



15th Biennial SGA Meeting
Glasgow, Scotland
August 27 -30 2019

Life with Ore Deposits on Earth

PROCEEDINGS VOLUME 4




University of Glasgow Publicity Services

ISBN 978-0-85261-965-0



9 780852 619650

© Society for Geology Applied to Mineral Deposits, 2019



The theme for this 15th edition is “Life with Ore Deposits on Earth”.

Suggested citation for the entire volume:

Proceedings of the 15th SGA Biennial Meeting, 27-30 August 2019, Glasgow, Scotland, 1897 pages.

Suggested citation for an individual paper:

Smith DJ, Jenkin GRT, Holwell DA, Keith M (2019) Challenges and Opportunities in Tellurium Supply. Proceedings of the 15th SGA Biennial Meeting, 27-30 August 2019, Glasgow, Scotland, pages 1654-1656.

Volume 1

Advances in understanding hydrothermal processes

Volume 2

Magmatic sulfide and oxide systems
Gold - from orogenesis to alluvial
Supergenes, gems and non-metallic ores

Volume 3

Magmatic-hydrothermal systems: from Porphyry to Epithermal
New discoveries – new views - Advances in the science of mineral exploration
New Techniques for ore discovery

Volume 4

Co-evolution of Life and Ore Deposits
Economics of ore deposits
The changing face of metal extraction - geology, biology and geometallurgy
Sustainable development of ore deposits
Mineral resources for green growth
Open Session

This publica cannot be reproduced in whole or in part without the permission of The Society for Geology Applied to Mineral Deposits (SGA).

A digital version of theses volumes is available from the SGA website at www.e-sga.org

SPONSORS

BHP



PEOPLE
MAKE
GLASGOW



AGNICO EAGLE

BOLIDEN



RioTinto



TABLE OF CONTENTS

Volume 4

Co-Evolution of Life and Ore Deposits

PLENARY 3: Hydrothermal Origins of Brucite, Banded Iron Formations, Transition Metal Sulfides and Life.....1398
Mike Russell

Microbial ecosystems and secondary ore formation, Las Cruces deposits (SW Spain).....1401
Fernando Tornos, Monike Oggerin, César Menor-Salván, Francisco Velasco

The Importance of Carbon in Ni-Cu-PGE Deposits.....1405
John Parnell, Joseph Armstrong

KEYNOTE: Geobiology of northern Australian mid-Proterozoic sedex Zn-Pb-Ag deposits...1409
Peter McGoldrick

Neoproterozoic microbial processes in chemical sediment diagenesis: evidence from the Aberfeldy barite deposits.....1413
Moles, Norman R., Boyce, Adrian J.

The importance of biological productivity for the formation of the George Fisher Zn-Pb-Ag deposit, Queensland, Australia.....1417
Philip Rieger, Joseph M. Magnall, Sarah A. Gleeson, Alexander Rocholl, Richard Lilly

INVITED: Biomineralization in modern seafloor hydrothermal chimneys: implications for microbe-metal interactions in ancient VMS deposits.....1421
Si-Yu Hu, Stephen J. Barnes, Anais Pagès, Joanna Parr, Ray Binns

How long does it take to form a sediment hosted Zn+Pb deposit?.....1425
Gary Mullen, Craig Barrie, Adrian Boyce, Drew Drummond

Toxic contribution of Kupferschiefer metals, hydrocarbon, and related Zechstein salines to the Permian extinction event.....1429
Stanley B. Keith, Jan C. Rasmussen, Volker Spieth

Hydrothermal activity as a probe of hydrosphere-lithosphere interaction and evolution of life on early Earth1433
Svetlana Tessalina, Vitor Barrote, Bryant Ware

Timing and composition of stratiform pyrite mineralization in black shales at Liblín (Teplá Barrandian Unit, Bohemian Massif).....1437
Jan Pašava, František Veselovský, Ondřej Pour, Lukáš Ackerman, Martin Svojtka, Robert A. Creaser

Economics of Ore Deposits

- KEYNOTE:** Economic challenges for mineral deposits.....1441
[John F.H. Thompson](#)
- A dynamic model for polymetallic Zechstein mineralisation based on the Milicz area of SW Poland.....1443
[Krzysztof Zieliński, Tomasz Bieńko, Jan Wierchowicz](#)
- Global Copper Resources and Reserves; Discovery is Not the Only Control on Supply.....1447
[Simon M. Jowitt, Gavin M. Mudd](#)
- Assessment of undiscovered Li resources in LCT pegmatites in Finland.....1451
[Timo Ahtola, Kalevi Rasilainen, Pasi Eilu, Niilo Kärkkäinen, Janne Kuusela, Panu Lintinen, Tuomo Törmänen, Tapio Halkoaho](#)
- Reassessment of the Sn-Co mineralization from the mica schists of the Krobica-Gierczyn area (SW Poland).....1454
[Alicja Pietrzela](#)
- The metallogenic potential of an old European mining region: the case of Sardinia (Italy).....1458
[Stefano Naitza, Sandro Fadda, Maddalena Fiori, Roberto Peretti, Francesco Secchi](#)
- Secondary gold structures: evidence of "new" gold's growth inside wastes of sulfide deposits.....1462
[Alfiia Khusainova](#)

The changing face of metal extraction – geology, biology and geom metallurgy

- KEYNOTE:** Geometallurgy - what's new and what's next1466
[Julie Hunt](#)
- INVITED:** Operational mineralogy: an overview of key practices in sample analysis, sample preparation and statistics.....1470
[Christopher Brough, James Strongman, John Fletcher, Mariola Zając, Rachel Garside, Corinne Garner, Libby Rose](#)
- From Exploration towards Predictive Geometallurgy - The Role of SEM-based Automated Mineralogy and Statistical Assessment.....1474
[Sandra Birtel, Kai Bachmann, Philipp Büttner, Raimon Tolosana Delgado, Karl Gerald van den Boogaart, Jens Gutzmer](#)

Metal deportment and ore variability of the Bolcana Porphyry Au-Cu system (Apuseni Mts, Romania) - Implications for ore processing.....	1478
Rosie Blannin, Laura Tusa, Sandra Birtel, Jens Gutzmer, Sabine Gilbricht, Paul Ivășcanu	
Mineralogical and textural key attributes for the geometallurgical evaluation of alkaline rare metal granites.....	1482
Lars H. Gronen, Sven Sindern, G. Regina F. Holtmann, André Hellmann, F. Michael Meyer, Janet L. Katzmarzyk, Hermann Wotruba, F. Michael Meyer	
Sulfide chemistry and trace element deportment at the metamorphosed Lappberget Zn-Pb-Ag-(Cu-Au) ore body, Sweden: Implications for Mineral Processing.....	1486
Glaciale Tiu, Nils Jansson, Christina Wanhainen, Yousef Ghorbani	
The use of geometallurgy in the processing of a complex copper-gold ore deposit.....	1490
R. Aliyev, F. Hedjazi, S.J. Westhead and A.J. Monhemius	
Evaluating processing attributes using hyperspectral mineralogy.....	1494
Nathan Fox	
Luminescence sorting to reduce energy use during ore processing.....	1498
Nicola. J. Horsburgh, Adrian. A. Finch	
Mapping and sampling for real-time development of mine plans in high-grade, narrow-vein, underground Mining.....	1501
Luke Palmer, Kathryn Moore, Gareth Thomas, Steve Broom, Richard Roethe, Dominic Roberts	
Platinum Behaviour in Sulfide and Oxide Melts during The Metallurgical Processing of Copper-Nickel Ores.....	1505
Sergei Fedorov, Alex Amdur, Ivan Blinov	
Beneficiation of parisite-rich rare earth ore from the Nam Xe South deposit, Vietnam.....	1508
Robert Möckel, Thomas Heinig, Alan Fernando Cardenas Vera, Jens Gutzmer, Gerhard Merker, Van Phan Quang	
Gold and critical element recovery with environmentally-benign Deep Eutectic Solvents.....	1512
Gawen R. T. Jenkin, Hugh Graham, Daniel J. Smith, Rumana Khan, Andrew P. Abbott, Robert C. Harris, David A. Holwell, Shaun D. Graham, Christopher J. Stanley	
KEYNOTE: The development and future impact of biotechnologies for mineral processing and metal recovery.....	1516
David Barrie Johnson	
Definition of geochemical domains in a chromite mine, Bushveld Complex, South Africa.....	1520
Kai Bachmann, Peter Menzel, Raimon Tolosana-Delgado, Jens Gutzmer	
Key ore textures influencing separation behaviour of ores.....	1524
Kate Tungpalan, Elaine Wightman, Cathy Evans	

A reliable method for the automated distinction of quartz gangue and epoxy resin with reflected light microscopy for geometallurgical characterization.....	1528
Ursula Grunwald-Romera, Juan Carlos Catalina, David Alarcón, Alfredo López-Benito, Ricardo Castroviejo	
Gold and silver mineralogy of the Liikavaara Cu-(W-Au) deposit, northern Sweden.....	1532
Mathis Warlo, Christina Wanhainen, Glenn Bark	
Geochemistry and quantitative mineralogy of REE-bearing phosphate stockpile ore from the Catalão Region, Brazil.....	1536
Tim Rödel, Gregor Borg	
The Cinovec Sn-Li deposit: Challenges for ore processing.....	1540
Alla Dolgoplova, Reimar Seltmann, Robin Armstrong, Chris Stanley, Jens Andersen, Gavyn Rollinson, Beth Simons, Chris Broadbent, Vitaly Shatov	
Mineral processing and mineralogical characterization of pre-concentrates from the Rondônia Tin Province, Brazil.....	1544
Simon Goldmann, Herwig Marbler, Frank Haubrich, Tiago Buch	
Processing waste of feldspar raw material as source of valuable metals: pre-full-scale laboratory study and search for optimum separation flowchart.....	1548
Tomáš Vrbický, Richard Příklad	
Graphite raw material in the Bohemian Massif - processing for future mining.....	1551
Michal Poňavič, Anna Vymazalová, Bohdan Kříbek, František Ptíčen, Jan Jelínek	
Remediation of cyanide within gold mine waste: an in-depth review of Prussian blue in aqueous solution.....	1555
Megan D. Welman-Purchase, Robert N. Hansen	
Fungal extraction of Se and Te from the Kisgruva Proterozoic volcanogenic massive sulfide deposit.....	1558
Xinjin Liang, Magali A.M. Perez, Joseph G. Armstrong, Liam A. Bullock, Jorg Feldmann, Laszlo Csetenyi, Geoffrey M. Gadd	

Sustainable development of Ore Deposits

PLENARY 1: Geoscience vision for future exploration and resource extraction.....	1562
T. Campbell McCuaig, Jillian Terry	
PLENARY 2: Responsibility in Mining: How to make difficult decisions.....	1566
Sarah Gordon	
KEYNOTE: Sustainability in the Mine Life Cycle.....	1570
R.J. Howell, C.R. Williams, R. Griffiths, H.E. Jamieson, J.V. Parshley	

Tools for foresight on land-use planning in mineral rich areas: A case from Northern Finland.....	1574
Mari Kivinen, Mira Markovaara-Koivisto, Pasi Eilu	
Life cycle assessment of European copper mining: A case study from Sweden.....	1577
Tobias C. Kampmann, Rodrigo A.F. Alvarenga, David Sanjuan-Delmás, Mats Lindblom	
Linking mineral processing simulation with Life cycle assessment (LCA) to forecast potential environmental impacts of small-scale mining technologies development.....	1581
Jérôme Bodin, Stéphanie Muller, Pablo Brito-Parada, Juliana Segura-Salazar	
Acid and Metalliferous Drainage (AMD): cause and effect, prediction and prevention – A journey through decades of experiences.....	1585
Alan M. Robertson, Greg A. Maddocks, Matthew G. Landers and Laura M. Jackson	
An economic and risk based appraisal of standardised waste management strategies: using fragmentation analysis to optimise the approach.....	1589
Steven Pearce, Diana Brookshaw, Andrew Barnes, Christopher Brough	
Utilising automated mineralogy and accelerated static tests to enhance kinetic testing evaluations.....	1593
Anita Parbhakar-Fox, Nathan Fox	
Geochemical considerations for improved management of sulfide mine tailings.....	1597
Matthew B.J. Lindsay, Michael C. Moncur	
KEYNOTE: Engagement and Emotional Response of the Narrative of Social License as reflected in the Dominance of the Minerals Sector in Traditional and Social Media.....	1601
Prof. Michael Hitch	
Secondary mineral assemblages associated with weathered mine and mill wastes, Cobalt Mining Camp, Ontario.....	1603
H.E. Jamieson, A. Dobosz, J. Clarke, K. Martin, R.J. Bowell, C. Kennedy	
INVITED: Increasing Value and Decreasing Environmental Risk by Reprocessing and Stabilizing Tungsten Tailings at Cantung Mine, NT, Canada.....	1607
Heather E. Jamieson, Brent Kazamel, Matt Leybourne, Agatha Dobosz, H. Falck	
Geoenvironmental characterisation of the King River Delta: A combined geophysical, geochemical and mineralogical approach.....	1610
Sibele C. Nascimento, Anita Parbhakar-Fox, Matthew J. Cracknell, Wei Xuen Heng	
Carbon Sequestration in Ultramafic Mine Waste: Potential for Carbon Neutral Mining	1615
Sterling S.S. Vanderzee, Gregory M. Dipple, Ian M. Power	
Environmental & social maturity as a new concept for self-assessment of best practice in a mining context.....	1619
Keiran Doyle, Olga Sidorenko	
Re-thinking the concept of small-scale mining for a European social context.....	1623
Olga Sidorenko, Rauno Sairinen, Kathryn Moore	

Gold mine tailings as future resources: long-term storage and behaviour of As and Sb phases.....1626
Kerr G, Weightman E, Craw D.

Characterization of serpentinites in Tolima and Antioquia (Colombia): analyzing their CO₂ sequestering potential through carbonation processes.....1630
Mónica Ágreda López, Carlos Augusto Zuluaga Castrillón, Iván Mateo Espinel Pachón

Mineral Resources for Green Growth

INVITED: Tracking the magmatic-hydrothermal transition in the phosphorus-rich Gatumba pegmatite dyke system (Rwanda) and its role on Sn mineralization1634
Niels Hulsbosch, Philippe Muchez

Assessment of scandium deportment and recovery potential in Li-Sn-W greisen deposit Cínovec/Zinnwald using EPMA, LA-ICP-MS and TIMA automated mineralogy.....1638
Jakub Výravský, Sebastian Hreus, Jan Cempírek, Michaela Vašinová Galiová

Lithium, REE and trace-element contents of stanniferous-greisen mica (Rondonia Tin Province, Brazil) and their relation to REE–Sn–Rare-metal occurrence.....1642
Frederico S. Guimarães, Anna Luíza R. de Oliveira, Lucas Eustáquio D. Amorim, Francisco J. Rios, José Vinícius Martins, Renato de Moraes

Discovery, delineation and development of Australia's first caesium deposit: Exploration implications from applied technology.....1646
Nigel W. Brand, David J. Crook, Stuart T. Kerr, Russel N. Panting, Sophie O. Perring. Christabel J. Brand

KEYNOTE sponsored by SoS TeaSe: Challenges of byproduct recovery of critical elements.....1650
Sarah M. Hayes, Nadine M. Piatak, Sarah Jane White, Robert R. Seal II

Challenges and Opportunities in Tellurium Supply.....1654
Daniel J Smith, Gawen RT Jenkin, David A Holwell, Manuel Keith

Tellurium and selenium systematics in mafic VMS from Cyprus: mineral, mound and regional scale controls.....1657
Andrew J. Martin, Iain McDonald, Katie A. McFall, Christopher J. MacLeod, Manuel Keith, Gawen R.T. Jenkin, Adrian J. Boyce

Te-rich protolith for PGE mineralisation in NE Scotland.....1661
Joseph Armstrong, John Parnell, Magali Perez, Jorg Feldmann

Minor and trace element concentrations in sphalerite and galena from the HYC Pb-Zn deposit and nearby prospects (McArthur Basin, Australia).....	1665
Joséphine Gigon, Julien Mercadier, Antonin Richard, Irvine R. Annesley, Ingrid Gautier, Chantal Peiffert, Andrew S. Wygralak, Roger G. Skirrow	
Germanium concentration associated to sphalerite recrystallization: an example from the Pyrenean Axial Zone.....	1669
Alexandre Cugerone, Bénédicte Cenki-Tok, Emilien Oliot, Manuel Munoz, Alain Chauvet, Fabrice Barou, Kalin Kouzmanov, Stefano Salvi, Vincent Motto-Ros, Elisabeth Le Goff	
Germanium, Gallium and Indium distribution in base metal sulfides from hydrothermal veins of the Ruhr and Bergisches Land districts, Germany.....	1673
Sören Henning, Torsten Graupner, Hans-Eike Gäbler, Simon Goldmann, Jolanta Kus, Thomas Krassmann	
Distribution of Indium in the Ánimas - Chocaya - Siete Suyos District.....	1677
Malena Cazorla Martínez, Marta Tarrés, Laura Gemmrich, Belén Torres, David Artiaga, Álvaro Martínez, Diva Mollinedo, Joan Carles Melgarejo, Lisard Torró, Osvaldo Arce, Pura Alfonso	
Ore mineralogy of the In-bearing Ayawilca Zn-Ag-Sn-Cu project, Pasco, Peru.....	1681
Diego Benites, Lisard Torró, Jean Vallance, Patrick Quispe, Jorge Sáez, Silvia Rosas, Álvaro Fernández-Baca, Jorge Gamarra, Antoni Camprubí, Lluís Fontboté	
Global cobalt resources, production and future sources of supply.....	1685
Carolyn Kresse, Gus Gunn, Eva Petavratzi	
Germanium and cobalt in sedimentary rock-hosted deposits of northwestern Alaska.....	1689
Garth E. Graham, Karen D. Kelley	
The genesis of Carlow Castle: A unique Australian orogenic Cu-Co-Au deposit in the Archean Pilbara Craton.....	1693
David Fox, Samuel Spinks, Mark Pearce, Margaux Le Vaillant, Robert Thorne, Milo Barham, Mehrooz Aspandiar	
Potential for low cost bioprocessing of Co and Ni from Nkamouna lateritic ore.....	1697
D. Sulaiman J. Mulroy, Victoria S. Coker, Jonathan R. Lloyd, Paul F. Schofield, J. Fred W. Mosselmans	
Sulphide trace element, sulphur isotope and hydrothermal alteration studies in the Juomasuo and Hangaslampi Au-Co deposits, Kuusamo belt, northeastern Finland.....	1700
Mikael Vasilopoulos, Jukka-Pekka Ranta, Ferenc Molnár, Hugh O'Brien, Yann Lahaye	
Trace elements in Cu-(Fe)-S sulphides from inactive hydrothermal vent sites at TAG, Mid-Atlantic Ridge.....	1704
Berit Lehrmann, Bramley J. Murton, Matthew J. Cooper, J. Andy Milton	
KEYNOTE: Recipes for Rare Earth Deposits.....	1708
Frances Wall	
The architecture and geochemistry of magmatic roof zones: implications for mineralization and exploration.....	1712
Adrian A. Finch, Will Hutchison, Anouk M. Borst, Nicola J. Horsburgh, Eva E. Stüecken	

The importance of post-collisional magmatism for global rare earth element resources.....	1716
Kathryn M Goodenough, Éimear Deady, Charles Beard	
Overview of the European phosphate deposits and occurrences: A project dedicated to phosphate mineralizations and associated critical raw materials.....	1720
Sophie Decrée, Christian Burlet, Thomas Goovaerts, Maria João Batista, Daniel P.S. de Oliveira, Khaldoun Al-Bassam, Boris Malyuk, Nolwenn Coint, Eoin McGrath, Heikki Bauert	
Mineral resources for green growth in the U.S.....	1724
Jeffrey L. Mauk, Nicholas A. Karl, Morgan Mullins, Carma A. San Juan, Germán Schmeda, Patrick Scott, Bradley S. Van Gosen	
Punctuated release of Lithium from Past Ignimbrite Eruptions: Key to Present Lithium-Brine Resources in the Western U.S. & Central Andes.....	1728
Albert Hofstra, Celestine Mercer, Erin Marsh, Alexandra Wallenberg, Mark Mihalasky, Scott Hynek	
The Geology and Mineralogy of High-Grade Rare Earth Element (REE-Th-U) Mineralization at Alces Lake, Saskatchewan (Canada).....	1732
Irvine R. Annesley, Kateryna Poliakovska, James Sykes, Krisztina Pandur	
Contrasting types of REE mineralisation in the Palaeoproterozoic Bergslagen ore province, Sweden: from syn-volcanic to late-orogenic.....	1736
Erik Jonsson, Per Nysten, Torbjörn Bergman, Martiya Sadeghi, Karin Högdahl, Fredrik Sahlström, Jaroslaw Majka	
Magmatic vs. hydrothermal – origin of parisite-hosted REE mineralization at Nam Xe, Vietnam.....	1740
Thomas Heinig, Robert Möckel, Joachim Krause, Jens Gutzmer, Van Phan Quang, Mathias Burisch	
Late- to post-magmatic controls on rare earth element mineralogy and the potential influence on subsequent ion adsorption ores.....	1744
Eva Marquis, Guillaume Estrade, Kathryn Goodenough, Martin Smith, Cristina Villanova-de-Benavent	
Resolving the structural state of heavy rare earth elements in lateritic ion adsorption clays.....	1748
Anouk M. Borst, Adrian A. Finch, Nicola J. Horsburgh, Martin Smith, Eva Marquis, Peter Nason, Guillaume Estrade, Kalotina Geraki, Kathryn Goodenough, Jindrich Kynicky, Xu Cheng	
KEYNOTE sponsored by SoS RARE: Isotopic constraints on ore-grade enrichment of rare earth elements in carbonatites: The Elk Creek carbonatite example.....	1752
Philip L. Verplanck, G. Lang Farmer, Craig A. Johnson, Heather A. Lowers	
Utilizing alteration (fenite) surrounding carbonatite intrusions as a REE and Nb exploration indicator.....	1756
Holly A.L. Elliott, Sam Broom-Fendley, Frances Wall	

Ore geometry and emplacement style of the carbonatite-hosted Morro do Padre Nb deposit.....	1760
Matheus Palmieri, José A. Brod, Pedro F. O. Cordeiro, José C. Gaspar, Paulo A. R. Barbosa, Tereza C. Junqueira-Brod, Sergio A. Machado, Bruno P. Milanezi, Luis C. Assis	
The giant Bayan Obo REE-Nb-Fe deposit, China: How did it come into being?.....	1764
Hong-Rui Fan, Kui-Fang Yang, Fang-Fang Hu, Shang-Liu	
Mechanisms for the generation of HREE mineralization in carbonatites: Evidence from Huanglongpu, China.....	1768
Martin Smith, Delia Cangelosi, Bruce Yardley, Jindrich Kynicky, Chen Xu, Wenlei Song, John Spratt	
Diversity of ores in carbonatite-related rare earth deposits.....	1772
Liu Yan	
Deposit or prospect? example from the Miaoya, Hubei province, China.....	1776
Dexian Zhang, Yan Liu	
Graphite occurrences in Northern Norway (Vesterålen-Lofoten, Senja).....	1780
Janja Knežević, Iain H.C. Henderson, Håvard Gautneb, Jan Steinar Rønning, Frode Ofstad, Bjørn Eskil Larsen	
Occurrences of energy critical elements; Lithium – Cobalt and Graphite in Europe, a preliminary overview.....	1784
Håvard Gautneb, Janja Knežević, Eric Gloaguen, Jérémie Melleton, Blandine Gourcerol, Tuomo Törmänen	
Typology of hard-rock Li-hosted deposits in Europe.....	1788
Blandine Gourcerol, Eric Gloaguen, Johann Tuduri, Jérémie Melleton	
Largest Spodumene lithium deposit of Western Europe.....	1792
Catia G. Dias, Filipa L. Dias, Alexandre M. C. Lima	
Tectono-magmatic constraints on tellurium-gold fertility, Fiji.....	1796
Rose H. Clarke, Daniel J. Smith, David A. Holwell, Jon Naden, Stephen Mann	
Pb-Sb/As sulfosalts from Săcărâmb Au-Ag-Te ore deposit (Romania).....	1800
George Dinca, Gheorghe C. Popescu, Daniel Birgaoanu, Oana-Claudia Ciobotea-Barbu	
Pt- and Pd-bismuthotellurides: phase relations in the Pt-Bi-Te and Pd-Bi-Te systems.....	1804
Polina V. Evstigneeva, Maximilian S. Nickolsky, Natalia V. Geringer, Anna Vymazalová, Aleksey N. Nekrasov, Dmitriy A. Chareev	
Separation of Selenium and Tellurium during Low-Temperature Diagenesis.....	1808
Magali Perez, John Parnell, Joseph Armstrong, Liam Bullock, Joerg Feldmann	
Iron-Oxide-Copper-Gold deposits as sources of tellurium, selenium, and other critical metals.....	1812
David Holwell, Sally Worbey, Daryl Blanks, Kate Canham, Richard Lilly	

The critical elements (V, Co, Ga, Sc, REE) enrichment of Fe-Ti-V oxide deposits related to Mesoproterozoic AMCG complex in Poland.....	1814
Mikulski Stanisław Z., Sadłowska Katarzyna	
Indium and other critical elements enrichment in cassiterite-sulphide mineralization from the stratiform tin deposits in the West Sudetes (SW Poland).....	1818
Mikulski Stanisław Z., Małek Rafał	
A review of the resource potential of cobalt in Europe.....	1822
Stefan Horn, Evi Petavratzi, Gus Gunn, Richard Shaw, Frances Wall	
Undiscovered Kuusamo-type cobalt-gold resources in Finland.....	1826
Kalevi Rasilainen, Pasi Eilu, Irmeli Huovinen, Jukka Konnunaho, Tero Niiranen, Juhani Ojala, Tuomo Törmänen	
Modelling ferromanganese crust distribution on seamounts for resource potential estimates.....	1830
Sarah A. Howarth, Isobel A. Yeo, Bramley J. Murton	
Geochemistry of REE-rich karst bauxite ore deposits from the Sierra de Bahoruco, Dominican Republic.....	1834
Thomas Aiglsperger, Bernhard Dold, Joaquín A. Proenza, Cristina Villanova-de-Benavent, Lisard Torró, Australia Ramírez, Jesús Rodríguez	
Sc redistribution during post-magmatic processes.....	1837
Sebastian Hreus, Jakub Výravský, Jan Cempírek, Michaela Vašinová Galiová	
Fenitisation associated with alkaline-silicate complexes. Implications for HFSE mobility in late-stage fluids, Gardar Rift, SW Greenland.....	1840
Krzysztof Sokół, Adrian A. Finch, Jonathan Cloutier, Madeleine C.S. Humphreys	
The Gakara Rare Earth Deposit, Burundi: geology, mineralogy, U-Th-Pb dating.....	1842
Ntiharizwa S, Boulvais P, Poujol M, Branquet Y, Midende G, Morelli C, Ntungwanayo J	

Open Session

Magnetite formation in the serpentinization of ultramafic rocks from Bangong-Nujiang suture zone, Tibetan Plateau.....	1846
Jing-Chao Li, Guo-Li Yuan, Hua-Sheng Shao	
Can low-titanium lamproite magmas produce ore deposits? Evidence from Mesozoic Aldan Shield lamproites.....	1850
Ivan F. Chayka, Andrey E. Izokh, Elena A. Vasyukova	

Peraluminous pegmatoids with several thousands of ppm of LREE in the Central Grenville Province.....	1854
François Turlin*, Aurélien Eglinger, Anne-Sylvie André-Mayer, Clara Deruy, Michel Cuney, Olivier Vanderhaeghe, Marieke Van Lichtervelde, Jean-Marc Montel, Abdelali Moukhsil, Fabien Solgadi	
Geochemical variations in pegmatites of the Cape Cross-Uis tin belt and Sandamap-Kranzberg tin belt, Namibia.....	1858
Philadelphia Mbingeneeko, Ansgar Wanke	
New geochronological constraints on the Lagoa Real uranium province.....	1860
Lucas Eustáquio Dias Amorim, Francisco Javier Rios, Lucilia Aparecida Ramos de Oliveira, Frederico Sousa Guimarães, Monica Elizetti Freitas, Ariela Costa Diniz, Mauro Cesar Geraldes, Evando Carele de Matos	
Iberian Pyrite Belt massive sulphide deposit stockworks: styles and comparison.....	1864
Emma Losantos, Guillem Gisbert, Fernando Tornos	
Topaz-rich breccias at the 1.9 Ga Kankberg Au-Te deposit, Skellefte District, Sweden.....	1868
Paulina Nordfeldt, Rodney L. Allen, Iain K. Pitcairn, Harold L. Gibson	
Indium and Gallium in Cu-Pb (Ag) sulphide deposits of the Otavi Mountain Land, Namibia; a LA-ICP-MS study.....	1872
Ester Shalimba, Ansgar Wanke, Sven Sindern	
Chemical characteristic of gersdorffite solid solutions in Stan Terg area, Kosovo.....	1875
Marcin Wojsław, Jaroslav Pršek, Sławomir Mederski, Burim Asllani, Jakub Kanigowski	
Thalcosite - a new mineral from the Kupferschiefer, Sieroszowice deposit, Poland.....	1879
Jadwiga Pieczonka, Adam Piestrzyński, Roman Jedlecki	
Nickel in shungite deposits.....	1883
Connor Brolly, John Parnell	
Coastal garnet and magnetite sands in the Erongo and Kunene regions of Namibia.....	1887
Stephanie Lohmeier, Bernd Lottermoser, Alexander Hennig, Daniela Gallhofer	
Detection of subsidence related to mining activity by using interferometric radar data: the Seruci-Nuraxi Figus coal mine case study (Sardinia, Italy).....	1890
Ammirati Lorenzo, Calcaterra Domenico, Di Martire Diego, Mondillo Nicola	
Developing adaptive expertise in exploration decision-making.....	1894
Marianne J. Davies, Rhys S. Davies	

Hydrothermal Origins of Brucite, Banded Iron Formations, Transition Metal Sulfides and Life

Michael J Russell

NASA Astrobiological Institute, Italy

Abstract. Most ores are precipitated at the interface between metal-bearing hydrothermal, and ambient surface fluids of highly contrasting chemistries and/or temperatures – e.g., Fe-Zn-Pb-rich fluids with surface microbial sulfidic waters. So, it was with the very first microbes: driven into being on our planet to resolve the disequilibrium between the fuels [$H_2 > CH_4$] emanating from submarine alkaline hydrothermal springs, with the oxidants [$CO_2 \gg NO_3^-$] dissolved in the acidulous Hadean Ocean. The two fluids were kept largely at bay by the precipitation of the iron minerals, green rust and mackinawite, at the spring/ocean interface. Thus, we can say that life – as an entropy generator – first hydrogenated, and hydrogenates still, carbon dioxide to produce a small, but ever-renewed stock of organic molecules, many of them chelating the transition metals and phosphates at the active sites of enzymes. Most of these enzymes act as engines, coupling exergonic reactions or steep gradients to the endergonic ones necessary to both start and sustain life. Entropy production in both ore deposition and life is in the form of heat, organic and inorganic waste as disseminations and detritus, guides to prospectors and predators alike.

1 Prospecting for disequilibria

The very delight in Earthly disequilibria – mountains, cliffs, caves and chasms – often leads the young to a love of geology. More cryptic forms of disequilibria – lineaments, cross-faulting, sites of maximum throw, geochemical and geophysical anomalies, types of magmatic intrusions – demark the staple hunting grounds of the exploration geologist. Strongly influenced by Dick Stanton (e.g. Stanton, 1960), my particular exploration interest was in ore deposits with affinities with hot springs, particularly in the so-called SEDEX type. Though the SEDEX theory of ore genesis was vigorously disputed in the mid 20th century, the discovery of the hot metal-rich brine pools in the Red Sea (Bischoff 1969), the sulfidic black smokers along oceanic ridges predicted by Corliss et al. (1977; and see Spiess et al. 1980), and the discovery of their ilk in ancient ores along with fossil vent-like fauna and trace element aureoles, brought it back into mainstream thinking (e.g., Russell 1974; Boyce et al. 1983,2003; Oudin and Constantinou 1984; Banks 1985).

However, although submarine alkaline hydrothermal systems developing in mafic to ultramafic terrains seem less enticing to the economic geologist than these, recent research papers could be taken to suggest that the deposition of the Archean Banded Iron Formations (BIFs) owed their origin to the mixing of Iron-rich ocean water with alkaline waters of possible hydrothermal origin

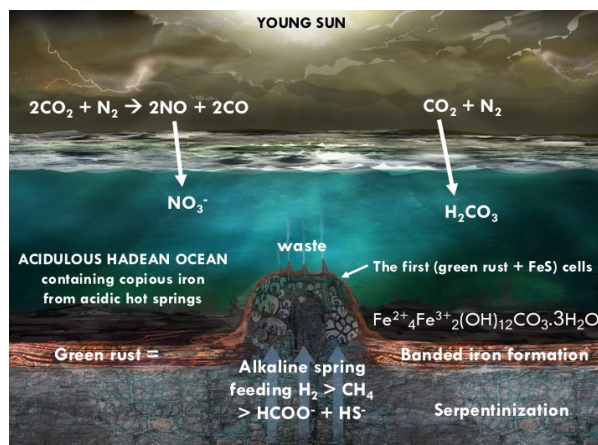


Figure 1. Diagram showing how green rust – the precursor to the Isua Banded Iron Formation and presumed Hadean BIFs – was precipitated from ocean water on meeting alkaline hydrothermal fluids (Isley, Abbott,1999; Halevy et al. 2017). Green rust and minor sulfides precipitated at the alkaline vent itself are the minerals that are argued here to have been instrumental in the emergence of life, mediating the disequilibria between the hydrothermal reductants and nitrate, a high potential electron acceptor that allowed the first cells to breathe (Nealson et al. 2002; Nitschke, Russell 2009; Wong et al. 2018) (after Branscomb and Russell 2018).

(Branscomb and Russell, 2018). The precursor to the magnetite in the BIFs appears to have been ferrous/ferric oxyhydroxide, viz., green rust ($[\sim Fe^{2+}_4Fe^{3+}_2(OH)_{12}][CO_3] \cdot 3H_2O$) accompanied by greenalite ($Fe^{2+}_{2.3}Fe^{3+}_{0.5}Si_{2.2}O_5(OH)_{3.3}$) and the occasional hisingerite ($Fe^{3+}_2Si_2O_5(OH)_4 \cdot 2H_2O$) (Génin et al. 2005; Tosca et al. 2016; Halevy et al. 2017; Russell 2017). These minerals are the ancient analogs to the ephemeral redox-resistant brucite ($Mg(OH)_2$) and the less soluble calcium carbonates precipitated at modern submarine alkaline springs (Figure 2). The Mg^{2+} today is supplied from ocean water (pH ~8) and precipitates on meeting the fluids with a higher pH (9-11) (Launay and Fontes 1985; Kelley et al. 2001; Okumura et al. 2016; Price et al. 2017; Russell, 2017). The general absence of sedimentary siderite at Isua – i.e., from the earliest Archean carbonic ocean – can be put down to its marked super-saturation in such fluids (Gäb et al. 2017).

1.1 From Astrophysics, through Geophysics to Geochemistry: It's Engines all the Way Up

The mineral exploration geologist must take account of the context of a promising mineral province, from the overall geological environment, through even to archeological clues. One way to think of orebodies is as an output of natural engines driven by thermal, chemical

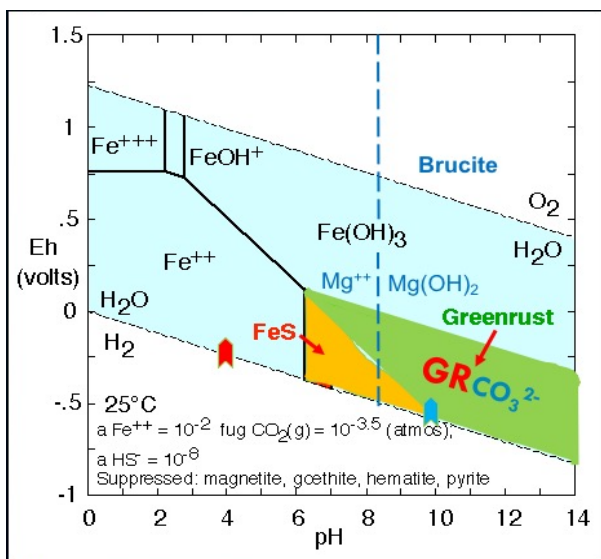


Figure 2. Eh/pH diagram (GWB: Bethke, 2007) contrasting the present conditions in the ocean at an alkaline hydrothermal vent with the acidulous Archean/Hadean ocean. Ephemeral brucite (magnesium hydroxide) and calcium carbonates (not shown) are precipitated around modern springs, whereas variable valence ferrous/ferric oxyhydroxide (carbonate green rust, GR_{CO_3}) and minor silicates, would have been precipitated around alkaline vents on the early Earth as shown in Figure 1 – the variable valence Fe replacing the redox-resistant Mg-hydroxide (Russell et al. 2001; Russell and Hall 2006; Russell 2017).

disequilibria that produce feedback systems often signaled by oscillatory phenomena (Cottrell 1979). Engines do work through harnessing disequilibria through involvement of autocatalysis whereby endothermic and/or endergonic activities are promoted through couplings to greater exothermic and/or exergonic disequilibria. Indeed, the entire evolution of the Universe can be considered in this way, from black holes feeding off stars and interstellar dust, through the nuclear processing within the stars themselves, the formation of planets, the convection currents that discharge their thermal gradients, some of them producing ore deposits and, given the appropriate disequilibria, gestating an informed and guided metabolism (Russell et al. 2013).

2 Resolving disequilibria between $\text{H}_2/\text{HCOO}^-/\text{CH}_4/\text{OH}^-/\text{HS}^-$ and $\text{CO}_2/\text{NO}_3^-/\text{NO}_2^-/\text{HPO}_4^{2-}/\text{H}_3\text{O}^+$

In the absence of life on the early Earth, far-from-equilibrium conditions at a submarine alkaline vent on the inorganic involved not only the disequilibria between the transition metals dissolved in the then ocean and the hydroxide and bisulfide in the alkaline hydrothermal fluid that resulted in the precipitation of green rust and mackinawite, but also those between $\text{H}_2/\text{HCOO}^-/\text{CH}_4/\text{OH}^-/\text{HPO}_4^{2-}/\text{HS}^-$ and $\text{CO}_2/\text{NO}_3^-/\text{NO}_2^-/\text{H}_3\text{O}^+$. In the latter case resolution was much more complex and, unlike ore deposition, never ending! This is because at its start the mineral precipitates could keep the alkaline and acidulous fluids apart excepting within the aqueous interlayers that characterize the green rust and

mackinawite minerals comprising the barriers, and admitting some leakage around their margins (Muñoz-Santiburcio, Marx 2017; Russell, 2018). In these circumstances, the variable valence green rust in particular could be coopted as a nano-engine or pump. For example, nitrate in the ocean could oxidize the proximal Fe^{2+} to Fe^{3+} ions which would then repel each other, having the effect of allowing access to nitrate to the aqueous interlayers, driven by the ambient proton gradient. The nitrate would then be promptly reduced to nitrite, and further reduced all the way to ammonia.

In these conditions oceanic CO_2 could also be hydrogenated to CO while CH_4 is oxidized to a methyl group, the two products combining in a complex series of reactions, to make acetate, the target molecule of life (Say Fuchs 2010; Berg et al. 2010). Further hydrogenations and carboxylations would lead to the longer chain carboxylic acids. At the same time the ammonia, reduced from the nitrate, is well placed to aminate the carboxylic acids to amino acids (Figure 3) (Barge et al. 2019).

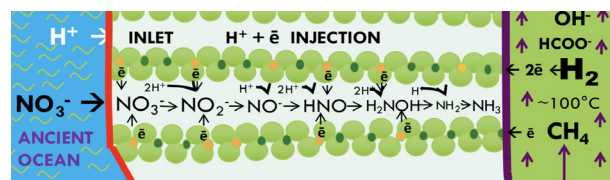


Figure 3. Cartoon demonstrating how green rust - separating the reduced and alkaline hydrothermal fluid from the relatively oxidized acidulous ocean – could have acted as a nitrate/nitrite reductase (cf. Fig. 1) (Hansen et al., 2001; Trolard, Bourrié 2012; Russell 2018).

Other “prebiotic” reactions, some of them endergonic, can be driven in the system as outlined in Russell (2018). For example, amino acids could be condensed to short peptides which in turn could capture the anions and cations of the transition elements (Milner-White and Russell 2005,2012; Harris, Szilagy 2016; Kim et al. 2018). The peptides, within, and extruded from interlayers of the green rust, would also spontaneously wrap themselves around phosphate available in the early ocean. In that state the orthophosphate could be condensed to pyrophosphate, the free energy currency of cells, driven by the ambient proton gradient (Milner-White, Russell, 2012; Russell et al. 2013; but see also Russell et al. 2013). And the green rusts would also be covered with peptide so forming the very first organic cells, fed with hydrothermal H_2 and CH_4 and “breathing” the ocean’s nitrate (Russell 2018).

3 Postscript

We could characterize the emergence of life from minerals at a submarine alkaline vent described above as “minerobiolization”. Of course, we are more accustomed to the involvement of microbial life in mineral deposition as its inverse; biomineralization. The attribution is returned as microbes bring about the precipitation of many sulfidic ores that otherwise might otherwise be dispersed and dissipated. For example, it has been shown that over 90% of the sulfide in the giant Navan

zinc-lead orebody as a result of microbial reduction of Mississippian seawater sulfate (Fallick et al. 2001),

Acknowledgement

The research described in this abstract was carried out at the Jet Propulsion Laboratory, California Institute of Technology, under a contract with the National Aeronautics and Space Administration, with support by the NASA Astrobiology Institute (Icy Worlds).

References

- Banks DA (1985). A fossil hydrothermal worm assemblage from the Tynagh lead-zinc deposit in Ireland. *Nature* 313:128-131.
- Barge LM, Flores E, Baum MM, VanderVelde DG, Russell MJ (2019). Redox and pH gradients drive amino acid synthesis in iron oxyhydroxide mineral systems. *Proc Natl Acad Sci* 116:4828-4833.
- Berg IA, Kockelkorn D, Ramos-Vera WH, Say RF, Zarzycki J, Hügler M, Alber BE, Fuchs G (2010) Autotrophic carbon fixation in archaea. *Nature Rev Microbiol* 8:447.
- Bethke CM (2007) *Geochemical and biogeochemical reaction modeling*. Cambridge University Press.
- Bischoff JL (1969) Red Sea geothermal brine deposits: Their mineralogy, chemistry and genesis. In *Hot Brines and Recent Heavy Metal Deposits in the Red Sea*, pp. 368-401, Springer-Verlag.
- Boyce AJ, Coleman M, Russell MJ (1983) Formation of fossil hydrothermal chimneys and mounds from Silvermines, Ireland. *Nature* 306:545-550.
- Boyce AJ, Little CT, Russell MJ (2003) A new fossil vent biota in the Ballynoe barite deposit, Silvermines, Ireland: evidence for intracratonic sea-floor hydrothermal activity about 352 Ma. *Econ Geol* 98:649-656.
- Branscomb E, Russell MJ (2018) Frankenstein or a submarine alkaline vent: Who is responsible for abiogenesis? Part 2: As life is now, so it must have been in the beginning. *BioEssays* 40:8. Doi: [org/10.1002/bies.201700182](https://doi.org/10.1002/bies.201700182)
- Corliss JB, Dymond J, Gordon LI, Edmond JM, von Herzen RP, Ballard RD, Green K, Williams D, Bainbridge A, Crane K, van Andel TH (1979) Submarine thermal springs on the Galapagos Rift. *Science* 203:1073-1083.
- Cottrell, A. (1979) The natural philosophy of engines. *Contemp phys* 20:1-10.
- Fallick AE, Ashton JH, Boyce AJ, Ellam RM, Russell MJ (2001) Bacteria were responsible for the magnitude of the world-class hydrothermal base-metal orebody at Navan, Ireland. *Econ Geol* 96:885-890.
- Gäb F, Ballhaus C, Siemens J, Heuser A, Lissner M, Geisler T, Garbe-Schönberg D (2017) Siderite cannot be used as CO₂ sensor for Archean atmospheres. *Geochim Cosmochim Acta* 214:209–225.
- Génin J-MR, Aïssa R, Géhin A, Abdelmoula M, Benali O, Ernstsen V, Ona-Nguema G, Upadhyay C, Ruby C (2005) Fougerite and FeII–III hydroxycarbonate green rust; ordering, deprotonation and/or cation substitution; structure of hydrotalcite-like compounds and mythic ferrosic hydroxide Fe(OH)_(2+x). *Solid State Sci* 7:545–572.
- Halevy I, Alesker M, Schuster EM, Popovitz-Biro R, Feldman Y (2017) A key role for green rust in the Precambrian oceans and the genesis of iron formations. *Nat Geosci* 10:135–139.
- Hansen HCB, Gulberg S, Erbs M, Koch CB (2001) Kinetics of nitrate reduction by green rusts: Effects of interlayer anion and Fe(II):Fe(III) ratio. *Appl Clay Sci* 18:81–91
- Harris TV, Szilagyi RK (2016) Protein environmental effects on iron-sulfur clusters: A set of rules for constructing computational models for inner and outer coordination spheres. *J Comp Chem* 37:1681-1696.
- Isley AE, Abbott DH (1999) Plume-related mafic volcanism and the deposition of banded iron formation. *J Geophys Res Solid Earth* 104:15461–15477.
- Kelley DS, Karson JA, Blackman DK, Früh-Green GL, Butterfield DA, Lilley MD, Olson EJ, Schrenk MO, Roe KK, Lebon GT, et al. (2001) An off-axis hydrothermal vent field near the Mid-Atlantic Ridge at 30°N. *Nature* 412:145-149.
- Kim DJ, Pike DH, Tyryshkin AM, Swapna GVT, Raanan H, Montelione GT, Nanda V, Falkowski PG (2018) Minimal heterochiral de novo designed 4Fe–4S binding peptide capable of robust electron transfer. *J Am Chem Soc* 140:11210-11213
- Launay J, Fontes J-C (1985) Les sources thermales de Prony (Nouvelle-Calédonie) et leurs précipités chimiques: Exemple de formation de brucite primaire. *Géologie de la France* 1:83–100.
- Milner-White J, Russell MJ (2005) Sites for phosphates and iron-sulfur thiolates in the first membranes: 3 to 6 residue anion-binding motifs (nests). *Origins Life Evol Bios* 35:19-27.
- Milner-White J, Russell MJ (2012) A peptide era heralding the emergence of life. *Genes* 2:671-688.
- Muñoz-Santiburcio D, Marx D (2017) Chemistry in nanoconfined water. *Chem Sci* 8:3444–3452.
- Nealson KH, Belz A, McKee B. (2002) Breathing metals as a way of life: Geobiology in action. *Antonie Leeuwenhoek Int J Gen Mol Microbiol* 81:215–222.
- Nitschke W, Russell MJ (2009) Hydrothermal focusing of chemical and chemiosmotic energy, supported by delivery of catalytic Fe, Ni, Mo/W, Co, S and Se, forced life to emerge. *J Mol Evol* 69:481–496.
- Okumura T, Ohara, Y, Stern RJ, Yamanaka T, Onishi Y, Watanabe H, Chen C, Bloomer SH, Pujana I, Sakai S, et al. (2016) Brucite chimney formation and carbonate alteration at the Shinkai Seep Field, a serpentinite-hosted vent system in the southern Mariana forearc. *Geochim Geophys Geosyst* 17:3775–3796.
- Oudin E, Constantinou G (1984) Black smoker chimney fragments in Cyprus sulphide deposits. *Nature* 308:349.
- Price R, Boyd ES, Hoehler TM, Wehrmann LM, Bogason E, Valtsson HP, Örlýgsson J, Gautason B, Amend JP (2017) Alkaline vents and steep Na⁺ gradients from ridge-flank basalts—Implications for the origin and evolution of life. *Geology* 45:1135-1138.
- Russell MJ (2018) Green rust: The simple organizing 'seed' of all life? *Life* 8:35; doi:10.3390/life8030035
- Russell MJ (2017) Life is a verb, not a noun. *Geology* 45:1143-1144.
- Russell MJ, Nitschke W Branscomb E (2013) The inevitable journey to being. *Phil Trans R Soc Lond B Biol Sci* 368:20120254. <http://dx.doi.org/10.1098/rstb.2012.0254>.
- Russell MJ, Hall AJ, Rahman L, Turner D (2001) Abiotic organic syntheses in deep submarine, alkaline hydrothermal systems catalysed by Fe⁰, mackinawite, violarite and green rust. In *Eleventh Annual VM Goldschmidt Conference Abstracts*.
- Russell MJ, Hall AJ (2006) The onset and early evolution of life. *Geol Soc Am Memoir* 198:1-32, doi:10.1130/2006.1198(01).
- Say RF, Fuchs G (2010) Fructose 1, 6-bisphosphate aldolase/phosphatase may be an ancestral gluconeogenic enzyme. *Nature* 464:1077-1081.
- Spieß FN, Macdonald, KC, Atwater T, Ballard R, Carranza A, Cordoba D, Cox C, DiazGarcia VM, Francheteau J, Guerrero J, Hawkins J, Hayimon R, Hessler R, Juteau T, Kastner M, Larson R, Luyendyk B, Macdougall JD, Miller S, Normark W, Orcutt J (1980) East Pacific Rise: hot springs and geophysical experiments. *Science* 207:1421-1433.
- Stanton RL (1960) General features of the conformable" pyritic" orebodies. *Can Inst Min Metall Trans* 63:22-27.
- Tosca NJ, Guggenheim S, Pufahl PK (2016) An authigenic origin for Precambrian greenalite: Implications for iron formation and the chemistry of ancient seawater. *Geol Soc Am Bull* 128:511-530.
- Trolard F, Bourrié G (2012) Fougerite a natural layered double hydroxide. In: *Gley soil: Habitus, structure, and some properties*. In: *Clay Minerals in Nature: Their Characterization, Modification and Application*, Chapter 3; doi:org/10.5772/50211
- Wong ML, Charnay BD, Gao P, Yung YL, Russell MJ (2017) Nitrogen oxides in early Earth's atmosphere as electron acceptors for life's emergence. *Astrobiology* 17:975-983.

Microbial ecosystems and secondary ore formation, Las Cruces deposits (SW Spain)

Fernando Tornos

Instituto de Geociencias (IGEO, CSIC-UCM), Madrid, Spain. f.tornos@csic.es

Monike Oggerin

Max-Planck-Institut fuer Marine Mikrobiologie, Bremen, Germany

César Menor-Salván

Universidad de Alcalá de Henares, Spain

Francisco Velasco

Universidad del País Vasco, Bilbao, Spain

Abstract. The zone of supergene alteration at the Las Cruces VMS deposit (Iberian Pyrite Belt) shows a complex arrangement of secondary assemblages which include a Cu-rich cementation zone, a zone enriched in Fe-Pb-Ag sulphides, another one with Fe-Pb-Ag carbonates and sulphates and remnants of a previous gossan. Geology, isotope geochemistry and microbiology show that these contrasting assemblages are controlled by different, very active and complex ecosystems, involving extremophilic microbes belonging to the iron, carbon and sulphur cycles. This unusual interaction between ores and microbes is due to the location of a previous mineralization in a zone of fluid mixing capped by a thick sedimentary sequence that isolated the system from the atmosphere.

1 Introduction

There is a direct relationship between ore deposits formed and modified in the critical zone and life, with the metabolism of microbes being able to dissolve and precipitate minerals. The influence of biologically-controlled redox reactions in the precipitation of ore assemblages has been described in a wide range of environments including volcanic- and sediment-hosted ore deposits, banded iron formations and zones of secondary enrichment. Here, microbial metabolism is able to accelerate usually kinetically-inhibited redox reactions which allow the quick supersaturation of minerals, especially carbonates and sulphides. While at temperatures at above ca. 200°C abiotic redox reactions are quick enough to form ore deposits, at the low temperatures where life is present (<120°C), they are too slow even for geological times (Ohmoto and Lasaga 1982; Machel 2001). Here, life takes advantage of these low reaction rates and obtains the energy needed for survival by accelerating redox equilibria. Biogenically-induced redox reactions are especially important in the deep and dark biosphere where there is no available oxygen and energy has to be obtained by the equilibrium of redox couples involving other electron acceptors. Furthermore, ore deposits are a preferred locus for the development of these ecosystems due to the presence of

liquid water and minerals having different redox states and the relatively high temperatures.

2 The Las Cruces deposit

The Las Cruces volcanogenic massive sulphide deposit, of late Devonian age, is located in the easternmost Iberian Pyrite Belt and below the shallow marine to continental sediments of the Guadalquivir basin, a Miocene to Holocene forearc basin to the Betic Alpine Range. The Las Cruces deposit is placed in the westernmost part of the basin and within a zone of major block compartmentalization controlled by large ENE-WSW Alpine faults. At the mine, the Tertiary sediments include a basal layer of sedimentary breccia and sandstone up to 20 m thick and overlain by more than 150 m of Messinian marl. The sandstone hosts nowadays an active aquifer recharged some 5 km north and hosting alkaline Ca-Mg rich water with large amounts of sulfate and carbonate but low chlorides. However, at the mine there is a second aquifer controlled by the faults – it permits the upflowing of hot (at depth with temperatures >100°C), also alkaline NaCl-rich waters also carrying sulphate.

The ore deposit is located in the contact between the basement and the Tertiary sediments, with the high-grade zones being controlled by one of the ENE-WSW faults. It consists of a large (>35 Mt) lens of massive sulphides situated between dark shale and underlying rhyodacite. The massive sulphides are dominated by pyrite with smaller amounts of sphalerite, galena, chalcopyrite and tetrahedrite-tennantite, between others and shows evidences of being deposited on an anoxic seafloor (Conde et al. 2007). It is underlain by a large stockwork dominantly hosted by rhyodacite and showing pervasive silicification and chloritization.

The primary mineralization was affected by the Variscan deformation and related very low-grade metamorphism and was again exposed to the surface at ca. 85 Ma. Subaerial oxidation during the late Cretaceous to Neogene formed a well-developed gossan and, perhaps, a small underlying cementation zone forming a secondary cap which would be similar to those of the

currently cropping out massive sulphide deposits of the Pyrite Belt such as Rio Tinto or Tharsis. The gossan is always enriched in goethite/hematite, barite, and Pb-Ag-Au-Hg dominantly in the form of different minerals of the jarosite group, mimetite and anglesite-cerussite but lacks of Cu- and Zn-bearing minerals (Velasco et al. 2013). At Las Cruces, beneath this zone, acid waters generated during the oxidation of pyrite reacted with shale and rhyodacite producing a zone of secondary advanced argillic alteration dominated by kaolinite and alunite that has been dated in 10-11 Ma (Tornos et al. 2017), which is interpreted as the epoch of major supergene alteration.

However, what makes Las Cruces different and unique is that the ore deposit was covered by the Tertiary sediments and isolated from the surface, something that changed dramatically the conditions of the system. Here, interaction between water circulating through the aquifers and the secondary mineralization lead to the formation of a set of unusual and previously undescribed rocks (Tornos et al. 2017) which include: (a) a red rock dominated by siderite with traces of anglesite-cerussite and jarosite. (b) A black rock composed of iron sulphides (greigite-smythite), galena and calcite with abundant accessory phases including silver, mercury and lead sulphides and sulphosalts, cinnabar and native gold (Blake 2008; Yesares et al. 2014; Tornos et al. 2017). (c) Epithermal-like veins dominated by pyrite, chalcopyrite, chalcocite, calcite and barite; (d) A large cementation zone controlled by the faults. This cementation zone shows a neat zonation with a core including a network of up to 50 cm thick veins of massive chalcocite and covellite and an external fringe were copper sulphides irregularly replace and coat fractures in the host pyrite, which is leached of Zn and Cu. The copper sulphides are accompanied by bornite and other sulphides uncommon in the supergene environment such as pyrite, chalcopyrite and enargite. (e) Late colloform coatings in open spaces having the same assemblages than the cementation zone.

Detailed studies on Las Cruces are those of (Doyle 1996; Knight 2000; Conde et al. 2007; Blake 2008; Scheiber et al. 2014; Tornos et al. 2017; Yesares et al. 2017).

3 Mineral assemblages and ecosystems

Combined geological studies, SEM, isotope geochemistry and microbiology have shown that the secondary rocks at Las Cruces host unequivocal evidences of a widespread microbial activity that seems to be the ultimate control on the formation of the unusual secondary assemblages and the extreme copper enrichment (Tornos et al. 2014; Tornos et al. 2019). (Blake 2008), on the basis of the mineral assemblage of the Black Rock and some $\delta^{13}\text{C}$ values was the first to quote that these unusual assemblages could be related to microbial activity.

The Red Rock is here interpreted as being the product of the partial reduction of a former gossan formed in pre-Tortonian times but when it was covered by the sediments and isolated from the atmosphere. The

dominant mineral here is siderite, which formation implies the reduction of the Fe^{3+} of goethite/hematite and an increase of the $f\text{O}_2$, something that stabilizes siderite vs iron oxides. $\delta^{13}\text{C}$ values of siderite (≈ -45 to -25‰) are interpreted as reflecting mixing of dissolved inorganic carbon (DIC) in the groundwater ($\approx 0\text{‰}$) with that of CO_2 unequivocally derived from the biogenic reduction of methane/light hydrocarbons. In this environment, sulphates and carbonates are stable suggesting that the assemblage formed in anoxic but not euxinic zones.

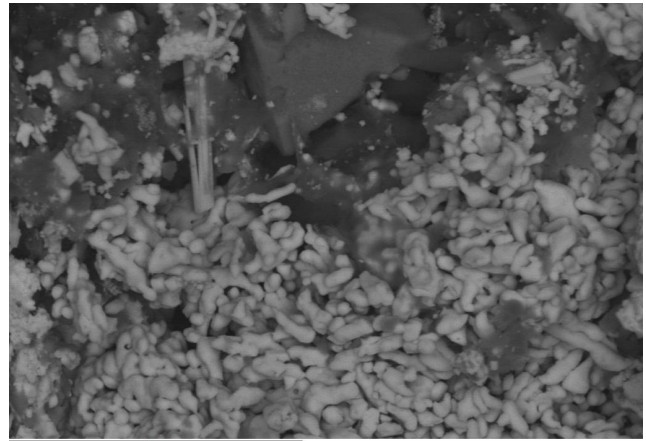


Figure 1. Bacteria coated and replaced by galena intergrown with euhedral proustite. Black Rock. SEM.

The Red Rock is replaced by the Black Rock due to the gradual growth of the galena at the expenses of the Pb-bearing carbonates and sulphates and the replacement of the siderite by the iron sulphides and calcite. While the calcite occurs as anhedral large crystals with no diagnostic evidences of microbial activity, the iron sulphides show colloform textures indicative of quick supersaturation and with superposition of different generations of chemically heterogeneous phases. Galena is dominated by textures resembling microbes and up to 10μ in length (Fig. 1). TEM shows that these structures are well preserved microbes including remnants of the original organelles and coated by galena. These highly metastable grains quickly evolve to skeletal crystals. Interestingly, intergrown with these galena bacteriomorphs there are euhedral crystals of proustite, jamesonite, and other sulphosalts suggesting that these minerals, despite being biogenically induced, don't fossilize microbes. $\delta^{34}\text{S}$ values of the unequivocally biogenic galena and iron sulphides are $+19$ to $+24\text{‰}$. These values are similar to the uppermost $\delta^{34}\text{S}_{\text{sulphate}}$ signatures (-17 to $+22\text{‰}$) of the nowadays circulating groundwater and strongly suggest that biogenic reduction of aqueous sulphate does not involve major isotope fractionation. Our interpretation is that in systems with excess of nutrients if compared with the electron acceptors, Rayleigh distillation produces only minor isotope fractionation (Tornos et al. 2014). The $\delta^{13}\text{C}_{\text{calcite}}$ values (≈ -40 to -20‰) are similar to those of the siderite of the Red Rock.

The underlying cementation zone shows no remnants of putative fossils replaced by copper sulphides or

Sulphur or carbon isotopes that could be used as tracers of biological activity. However, detailed SEM and CARD-FISH studies show that the cavities and cracks within the pyrite are infilled with sulphate-reducing bacteria and that covellite precipitates as minute euhedral crystals in the extrapolymeric substances that agglutinate the prokaryotes and that later coalesce as large crystals in the selvage of the veins. It is very likely that sulphate-reducing was accompanied by copper and iron reduction, something that promoted the saturation of the copper-iron sulphides.

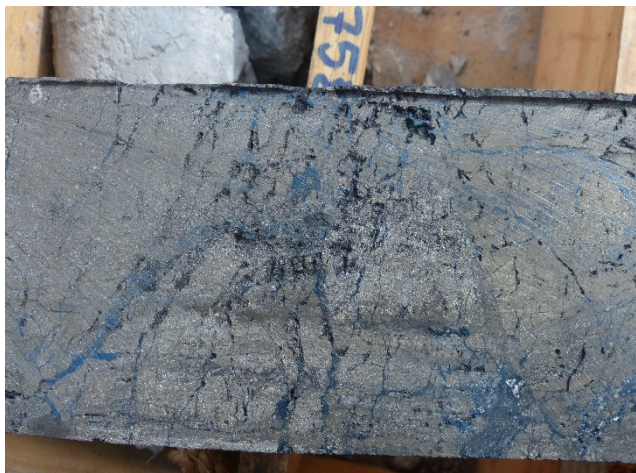


Figure 2. Veins of massive covellite crosscutting the massive sulphides. Bacteria infill the cavities and promote the precipitation of covellite. Width of the core: 6.4 cm.

4 Discussion and conclusions

The secondary mineralization of the Las Cruces deposit tracks the complex interplay between secondary mineralization and microbial activity. Microbiological studies (Tornos et al. 2019) show that these rocks include complex ecosystems that control the mineral assemblages. In the case of Las Cruces, the most striking effect of metabolism is the gradual reduction of Fe^{3+} , sulphate and Cu^{2+} to reduced iron, H_2S and Cu^+ . In the cementation zone this is accompanied by the production of CH_4 by methanogens while the methane seems to be oxidized in the overlying Red and Black rocks to CO_2 , producing siderite and calcite. Locally, these reduced assemblages are themselves oxidized, something probably related with the fluctuating geochemistry of the aquifers which are able to transport more oxidized water during the humid periods and reduced one in the dry ones. (Scheiber et al. 2018) have shown that the redox state of the inflowing waters is mainly due to the $\text{SO}_4/\text{H}_2\text{S}$ equilibria and microbial reduction that took place upstream of the Las Cruces deposit.

Cultures of mineralized samples show that there are prokaryotes belonging to other cycles than those of iron, carbon and sulphur and that the cementation zone hosts also abundant microbes with unknown roles and metabolism (Tornos et al. 2019). However, their metabolism is not able to neither induce the saturation of any minerals nor leave any geochemical imprint. Thus, their existence can only be traced by microbiological

techniques and when the microbes die is difficult to find evidences of their prior existence. The same holds true for the delicate crystals growing in the EPS or even the fossils in galena, which quickly recrystallize to skeletal shapes. These findings show that, probably, in most of the cases the evidences for microbial activity in ore deposits are just removed and leaving only some biomarkers and S-C isotopes as suitable tracers for a biogenic derivation. However, while carbon seems to be a rather definitive argument for the biogenic oxidation of hydrocarbons or methane, the interpretation of the sulphur isotopes is not so unequivocal. Although highly negative values reflect biogenic reduction of aqueous sulphate, the absence of such a ^{34}S depletion is not diagnostic of an abiogenic origin for the reduced sulphur. There are prokaryotes which produce no sulphur fractionation and even in systems with $\text{TOC} \gg \text{SO}_4$ can precipitate sulphides with $\delta^{34}\text{S}$ values similar to those of the coexisting sulphate.

Acknowledgements

Studies at Las Cruces have been supported by the Spanish SEIDI project RTI2018-094867-B-100 and EU projects ProMine and IPBSL. We thank Cobre Las Cruces SL and colleagues collaborating in different studies their support and help.

References

- Blake C (2008) The mineralogical characterisation and interpretation of a precious metal-bearing fossil gossan, las Cruces, Spain. Cardiff University, pp 207.
- Conde C, Tornos F, Doyle M (2007) Geology and litho-geochemistry of the unique Las Cruces VMS deposit, Iberian Pyrite Belt In: Andrew C Jea (ed) Digging Deeper Proceedings of the 9th Biennial SGA Meeting IAEG, Dublin, pp 1101-1104.
- Doyle M (1996) Las Cruces copper project, Pyrite Belt, Spain. Boletín Geológico Minero 107:681-683.
- Knight FC (2000) The mineralogy, geochemistry and genesis of the secondary sulphide mineralisation of the Las Cruces, Spain. University of Cardiff, Cardiff, pp 434.
- Machel HG (2001) Bacterial and thermochemical sulfate reduction in diagenetic settings — old and new insights. Sedimentary Geology 140:143-175. doi: [http://dx.doi.org/10.1016/S0037-0738\(00\)00176-7](http://dx.doi.org/10.1016/S0037-0738(00)00176-7).
- Ohmoto H, Lasaga A (1982) Kinetics of reactions between aqueous sulfates and sulfides in hydrothermal systems. Geochimica Cosmochimica Acta 46:1727-1745.
- Scheiber L, Ayora C, Vázquez-Suñé E, Soler A (2018) Groundwater-Gossan interaction and the genesis of the secondary siderite rock at Las Cruces ore deposit (SW Spain). Ore Geology Reviews 102:967-980. doi: <https://doi.org/10.1016/j.oregeorev.2017.07.001>.
- Scheiber L, Ayora C, Vázquez-Suñé E, Soler A, Yesares L, Nieto JM (2014) Groundwater-Gossan Interaction at the Las Cruces Ore Deposit (SW Spain) Macla 19.
- Tornos F, Oggerin M, Ríos Adl, Rodríguez N, Amils R, Sanz JL, Rojas P, Velasco F, Escobar JM, Gómez C, Slack JF (2019) Do microbes control the formation of giant copper deposits? Geology 47:143-146. doi: 10.1130/G45573.1.
- Tornos F, Velasco F, Menor-Salvan C, Delgado A, Slack JF, Escobar JM (2014) Formation of recent Pb-Ag-Au mineralization by potential sub-surface microbial activity. Nature Communications 5:4600. doi: 10.1038/ncomms5600.
- Tornos F, Velasco F, Slack J, Delgado A, Miguelez NG, Escobar JM, Gomez C (2017) The high-grade Las Cruces copper

- deposit, Spain: a product of secondary enrichment in an evolving basin. *Miner Deposita* 52:1-34. doi: 10.1007/s00126-016-0650-3.
- Velasco F, Herrero JM, Suarez S, Yusta I, Alvaro A, Tornos F (2013) Supergene Features and Evolution of the Gossans Capping the Massive Sulphide Deposits of the Iberian Pyrite Belt. *Ore Geology Reviews* 53:181-203.
- Yesares L, Saez R, Miguel Nieto J, Ruiz de Almodovar G, Cooper S (2014) Supergene enrichment of precious metals by natural amalgamation in the Las Cruces weathering profile (Iberian Pyrite Belt, SW Spain). *Ore Geology Reviews* 58:14-26. doi: 10.1016/j.oregeorev.2013.10.004.
- Yesares L, Sáez R, Ruiz De Almodóvar G, Nieto JM, Gómez C, Ovejero G (2017) Mineralogical evolution of the Las Cruces gossan cap (Iberian Pyrite Belt): From subaerial to underground conditions. *Ore Geology Reviews* 80:377-405. doi: <https://doi.org/10.1016/j.oregeorev.2016.05.018>.

The importance of carbon in Ni-Cu-PGE deposits

John Parnell, Joseph Armstrong
University of Aberdeen, Scotland, UK

Abstract. Nickel-copper-platinum group element (PGE) mineralization in ultramafic intrusions is commonly associated with organic matter, as graphite within the intrusion or as graphitic/carbonaceous country rocks. In most cases, the graphite has an isotopic composition that indicates a sedimentary rather than a magmatic origin. The graphite represents country rock assimilated into a magma, then re-precipitated from the melt, often associated with sulphide minerals. The graphitic country rocks are typically pyritic, and contributed sulphur and metalloids such as tellurium and selenium to the melt, which allowed precipitation of sulphide and telluride ores. Most of the richest post-Archean mineralized intrusions interacted with country rocks of Palaeoproterozoic age. All large nickel tonnage deposits of Palaeoproterozoic age, including Bushveld, are associated with carbonaceous matter. Even intrusions of Mesoproterozoic age (Duluth, Pants Lake, Voisey's Bay) were influenced by carbonaceous country rock deposited at least 500 million years earlier. Thus, the abundant organic matter deposited about 2 billion years ago has had a profound effect on global metallogeny.

1 Introduction

Organic materials (kerogen, bitumen, graphite) occur widely in ore deposits, and are particularly implicated in the genesis of certain types, including MVT lead-zinc deposits (Wu et al. 2013), roll front uranium-copper-vanadium deposits (Cumberland et al. 2016) and gold-uranium bearing quartz pebble conglomerates (Leventhal et al. 1987). Each of these is in sedimentary rocks, where most organic materials originate. Nickel-copper-PGE deposits, which occur in a diversity of ultramafic intrusions, also show a marked association with organic matter (Fig. 1), which has hitherto been little explored.

We review here the spatial relationship between carbon (as graphite) and Ni-Cu-PGE deposits, and emphasize that it occurs in the deposits so consistently, in varied time and space, that it must play a genetic role, most probably as a reductant. The presence of a reductant to induce low oxygen fugacity is an essential requirement of the genesis of Ni-Cu-PGE deposits, regardless of setting (Naldrett 1999; Ripley 2014).

Many instances of Ni-Cu-PGE mineralization are in mafic-ultramafic rocks emplaced at depth. Table 1 illustrates the diversity of occurrences, in time and space, of graphite-bearing ore deposits, most emplaced at a depth of about 10 km or greater. In most cases, despite the depth a source of abundant carbon was available in sedimentary/metasedimentary rocks, into which the intrusions were emplaced. In these examples, the intrusions clearly assimilated some of the host rock, which had been incorporated into the melt before the

carbon recrystallized as graphite. Graphite precipitates readily from carbon-sulphur melts due to a low solubility of carbon (Palyanov et al. 2006). There are yet other cases where graphite has not been reported in the deposits but where the wall rocks of the mineralized intrusion are carbon-rich, again so consistently that a genetic relationship is implied. Prominent examples where the host was carbonaceous are in Kabanga (Tanzania) and Noril'sk (Russia).

Table 1. Emplacement depths and carbon isotope compositions (Fig. 3) of graphite in cumulate rocks.

Deposit	Age	Emplacement	$\delta^{13}\text{C}$ (‰)
Stillwater, USA	2.7 Ga	10-15 km	-26 to -24
Bushveld	2.0 Ga	<8 km	-36 to -22
Voisey's Bay, Canada	1.33 Ga	9-11 km	-25 to -8
Duluth, USA	1.1 Ga	36 km	-37 to -19
Achankovil, India	470 Ma	>15 km	-10 to -7
Aberdeenshire, UK	470 Ma	16 km	-25 to -18
Bruvann, Norway	437 Ma	10 km	-21 to -14
Duke Island, USA	226 Ma	3-9 km	-28 to -26
N. Apennines, Italy	186 Ma	12-25 km	-5 to -4
Ronda, Spain	20 Ma	>30 km	-21 to -15
Hidaka Belt, Japan	10 Ma	23 km	-23 to -19
Hoggar, Algeria	~1 Ma	20-30 km	-25 to -14

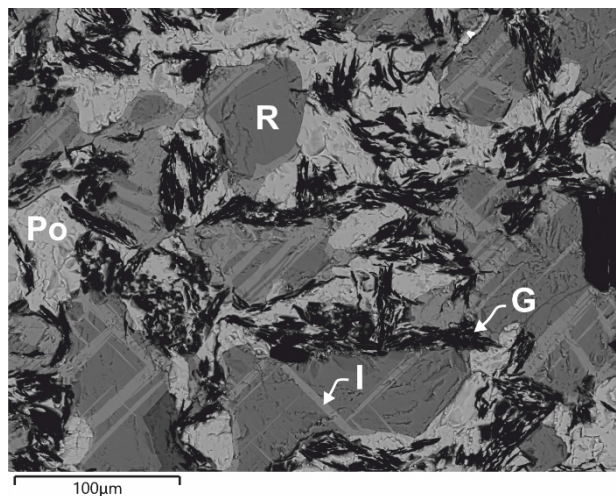


Figure 1. Graphite (black, G)-pyrrhotite (Po) intermixture through ilmenite (I) and rutile (R) from mineralized pegmatite in Ordovician ultramafic cumulates, Huntly, West Aberdeenshire. Cumulate is

mineralized by Ni-Cu-PGE (McKervey et al. 2007).

2 Role of carbon

Carbon has direct potential as a reductant. However carbonaceous sediments are very often also sulphidic, as the anoxic sedimentary environments that preserve carbon are also conducive to the precipitation of syndiagenetic sulphides, especially pyrite, by microbial sulphate reduction. Assimilation of the sulphidic sediment into melt liberates hydrogen sulphide that can also contribute to reduction, and may cause sulphide

saturation so that sulphide minerals precipitate out. This is fundamental to the mineralization process, by pulling metals including nickel out of the melt. Metalloids such as Se and Te enriched in the carbonaceous sediments are assimilated in the melt, in which Te can precipitate elements incorporating PGEs into tellurides (Fig. 2).

The sedimentary origin of the cumulate-hosted graphite is evident from carbon isotope data (Fig. 3). Most documented occurrences have isotopic compositions that are lighter than the typical range for mantle-derived carbon of -4 to -7 per mil, and more similar to the range for sedimentary organic carbon of -20 per mil and lighter.

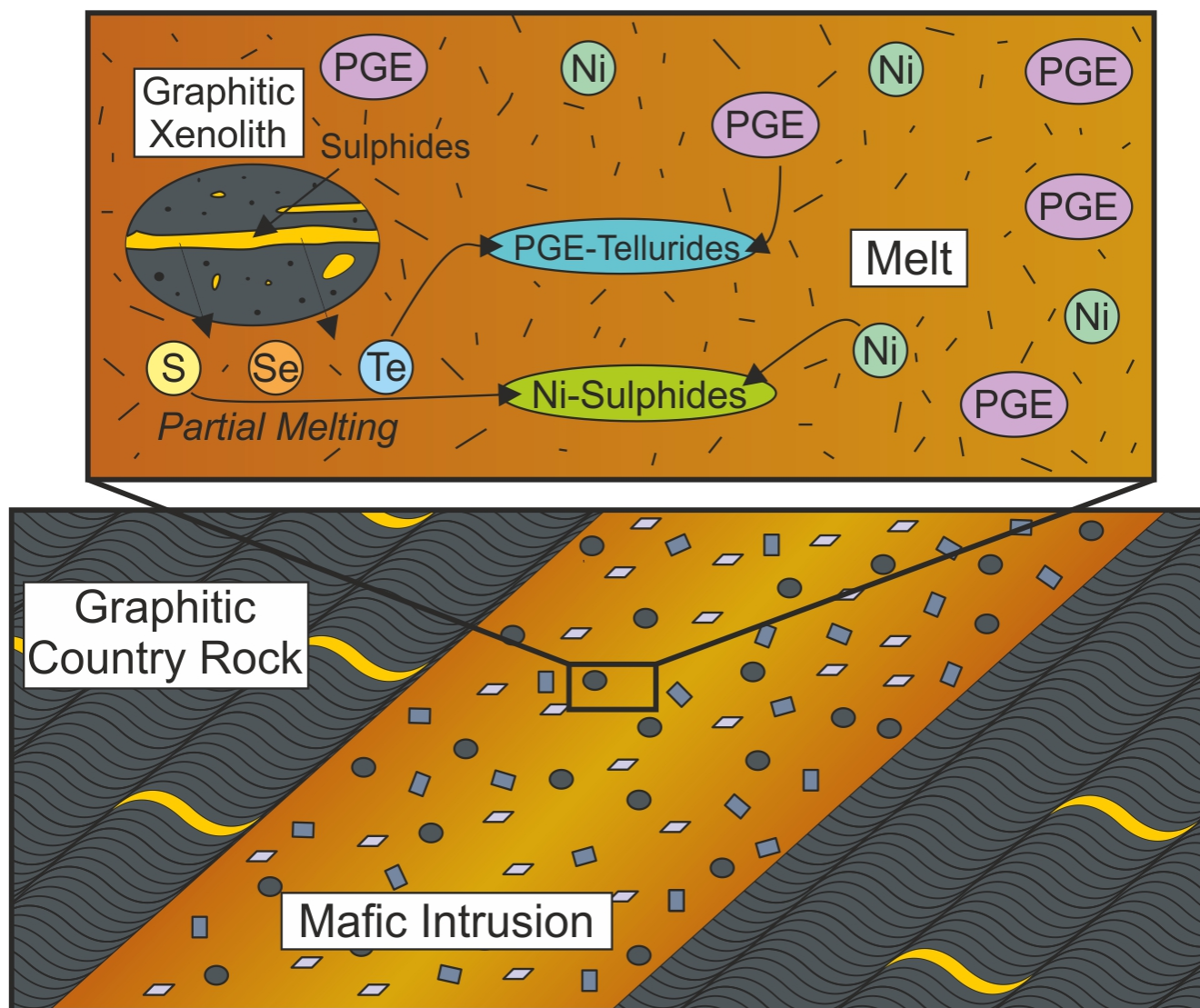


Figure 2. Schematic of graphitic, sulphidic xenolith in ultramafic intrusion, assimilated into melt to trigger precipitation of ore minerals (based on Samalens et al. 2017).

3 The Palaeoproterozoic

The distribution of the deposits through time calls for comment. Hoatson et al. (2006) have drawn attention to the abundance of Ni deposits in the mid-Palaeoproterozoic, about 1.9 Ga, based on evidence especially in Canada, South Africa, Australia and Finland.

In each of these deposits the host includes graphitic sediments, also of Palaeoproterozoic age. We are not aware of sizable Ni deposits of this age that are *not* hosted by graphitic sediments. They represent many of the largest Ni deposits in the world (Fig. 4). This implies that the abundance of Ni of this age is a consequence of the abundance of sedimentary carbon of this age, in turn

a probable consequence of a major escalation in photosynthetic activity.

The abundance of Palaeoproterozoic graphitic sediment is becoming increasingly evident. Carbon-rich deposition followed the Palaeoproterozoic Lomagundi Event, marked by a positive excursion in the carbon isotopic composition of marine carbonates (Kump et al. 2011; Martin et al. 2015). Geologists focus on non- or weakly metamorphosed sediments from which

geochemical and sedimentological signals can still be determined. This excludes sections that have been graphitized. However, the extent of carbonaceous deposition is recorded by graphitic exploration projects in Palaeoproterozoic successions in many parts of the world, including Canada, Brazil, Ghana, Tanzania, Zimbabwe, Australia, India, Korea, China, Greenland, Norway, Sweden and Finland.

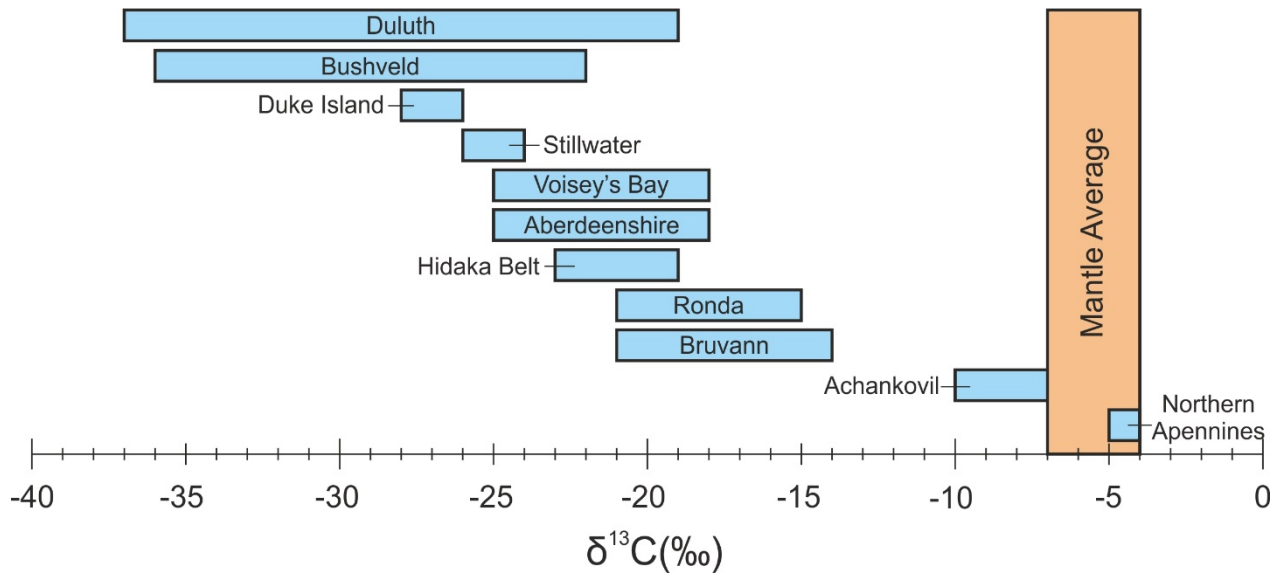


Figure 3. Carbon isotopic compositions of graphite in Ni-Cu-PGE mineralized ultramafic intrusions. Data from Buchanan and Rouse (1984), Crespo et al. (2006), Fuex and Baker (1973), Lerouge et al. (2001), Montanini et al. (2010), Rajesh et al. (2004), Ripley and Taib (1989), Ripley et al. (2002), Thakurta et al. (2008), Tomkins et al. (2012) and unpublished.

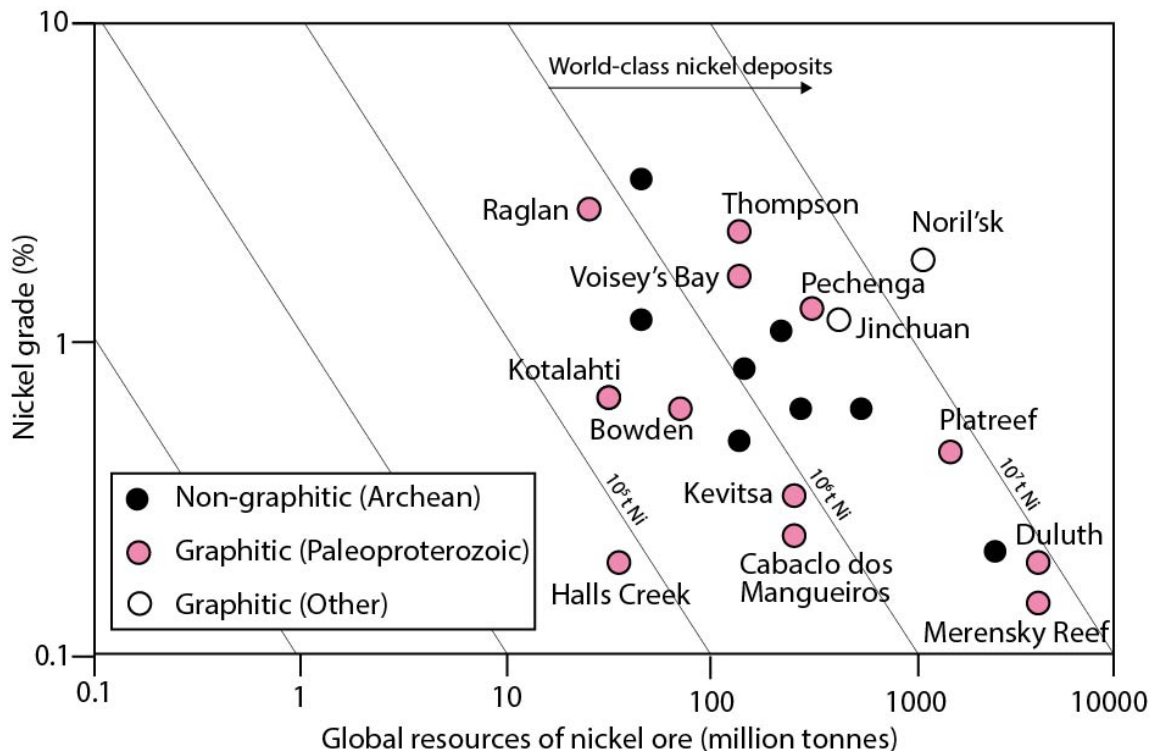


Figure 4. Nickel tonnages for largest deposits, modified from Hoatson et al. (2006), excluding impact-related Sudbury deposit. All non-Archean deposits were intruded into carbonaceous rocks, and almost all into Palaeoproterozoic carbonaceous hosts. Bushveld deposits are in Platreef and Merensky Reef.

4 Exploration

The evidence reported here suggests that ultramafic intrusions which cross-cut Palaeoproterozoic successions are potential exploration targets for Ni-Cu-PGE mineralization. Additionally, ultramafics are implicated in nickel enrichments into the original graphitic metasediments (Loukola-Ruskeeniemi & Lahtinen 2013). The carbonaceous sediments must have generated large volumes of hydrocarbons (Mancuso et al. 1989; Melezhik et al. 2009), which could also have interacted with any nickel that had been released from intrusions.

The association of nickel deposits and carbonaceous schists is so marked that graphite deposits are being discovered during exploration for metals in the Palaeoproterozoic, for example at the Neuron property in the Thompson Nickel Belt, Canada. In the Halls Creek Orogen, Australia, Cazaly Resources Ltd. have immediately adjacent licenses for nickel and graphite, i.e. they are likely to be discovered in close proximity. Similarly, if graphitic, pyritic sediments are a source of Te, they are a potential guide to exploring for PGEs.

Because rocks of Palaeoproterozoic age are usually metamorphosed, and contain graphite, they can be explored by measurement of electrical conductivity (Boerner et al. 1996; Zhamaletdinov 1996; Lindsay et al. 2018), which gives graphite deposits a preferential chance of detection. The link between graphite and nickel therefore means that this approach may help to detect metalliferous mineralization.

Acknowledgements

We are grateful to J. Johnston, J. Bowie and A. Boyce for skilled technical support. This work was partly supported by NERC grant NE/M010953/1.

References

- Boerner DE, Kurtz RD, Craven JA (1996) Electrical conductivity and Paleo-Proterozoic foredeeps. *Jour Geophys Res* 101:13775-13791
- Buchanan DL, Rouse JE (1984) Role of contamination in the precipitation of sulphides in the Platreef of the Bushveld Complex. In Buchanan DL, Jones MJ (eds) *Sulfide Deposits in Mafic and Ultramafic Rocks*. Spec Pub Inst Min Met: 141-146
- Crespo E, Luque FJ, Rodas M, Wada H, Gervilla F (2006) Graphite-sulfide deposits in Ronda and Beni Bousera peridotites (Spain and Morocco) and the origin of carbon in mantle-derived rocks. *Gondwana Res* 9:279-290
- Cumberland SA, Douglas G, Grice K, Moreau JW (2016) Uranium mobility in organic matter-rich sediments: A review of geological and geochemical processes. *Earth-Sci Revs* 159:160-185
- Fuex AN, Baker DR (1973) Stable carbon isotopes in selected granitic, mafic, and ultramafic igneous rocks. *Geochim Cosmochim Acta* 37:2509-2521
- Hoatson DM, Jaireth S, Jaques AL (2006) Nickel sulfide deposits in Australia: Characteristics, resources, and potential. *Ore Geol Rev* 29:177-241
- Kump LR, Junium C, Arthur MA, Brasier A, Fallick A, Melezhik V, Lepland A, Crne AE, Luo G (2011) Isotopic evidence for massive oxidation of organic matter following the Great Oxidation Event. *Science* 334:1694-1696
- Lerouge C, Auge, T, Lamberg P, Pineau F (2001) A stable isotope study of the Bruvann Ni deposit, Norway. In: Piestrzynski A (ed) *Mineral Deposits at the Beginning of the 21st Century*, Swets & Zeitlinger Publishers Lisse, 599-602
- Leventhal JS, Grauch RI, Threlkeld FE, Lichte CT (1987) Unusual organic matter associated with uranium from the Claude deposit, Cluff Lake, Canada. *Econ Geol* 82: 1169-1176
- Lindsay MD, Spratt J, Occhipinti SA, Aitken ARA, Dentith MC, Hollis JA, Tyler IM (2018) Identifying mineral prospectivity using 3D magnetotelluric, potential field and geological data in the east Kimberley, Australia. *Geol Soc Lond Spec Pubs* 453,247-268
- Loukola-Ruskeeniemi K, Lahtinen H (2013) Multiphase evolution in the black-shale-hosted Ni-Cu-Zn-Co deposit at Talvivaara, Finland. *Ore Geol Revs* 52: 85-99
- Mancuso JJ, Kneller WA, Quicke JC (1989) Precambrian vein pyrobitumen: evidence for petroleum generation and migration 2 billion years ago. *Precambrian Res* 44:137-146
- Martin AP, Prave, AR, Condon DJ, Lepland A, Fallick AE, Romashkin AE, Medvedev PV, Rychanchik DV (2015) Multiple Palaeoproterozoic carbon burial episodes and excursions. *Earth Planet Sci Letts* 424:226-236
- McKervey JA, Gunn AG, Styles M (2007) Platinum-group elements in Ordovician magmatic Ni-Cu sulfide prospects in northeast Scotland. *Canad Mineral* 45: 335-353
- Melezhik, VA, Fallick, AE, Filippov MM, Lepland A, Rychanchik DV, Deines, YE, Medvedev PV, Romashkin AE, Strauss H (2009) Petroleum surface oil seeps from a Palaeoproterozoic petrified giant oilfield. *Terra Nova* 21:119-126
- Montanini A, Tribuzio R, Bersani D (2010) Insights into the origin of mantle graphite and sulphides in garnet pyroxenite from the External Liguride peridotites (Northern Apennine, Italy). *Geol Soc Lond Spec Pubs* 337:87-105
- Naldrett AJ (1999) World-class Ni-Cu-PGE deposits: key factors in their genesis. *Mineral Deposita* 34:227-240
- Palyanov YuN, Borzdov YuM, Khokhryakov AF, Kupriyanov IN, Sobolev NV (2006) Sulfide melts-graphite interaction at HPHT conditions: Implications for diamond genesis. *Earth Planet Sci Letts* 250:269-280
- Rajesh VJ, Arima M, Santosh M (2004) Dunite, glimmerite and spinellite in Achankovil Shear Zone, South India: implications for highly potassic CO₂-rich melt influx along an intra-continental shear zone. *Gondwana Res* 7:961-974
- Ripley EM (2014) Ni-Cu-PGE mineralization in the Partridge River, South Kawishiwi, and Eagle intrusions: A review of contrasting styles of sulfide-rich occurrences in the Midcontinent Rift System. *Econ Geol* 109:309-324
- Ripley EM, Li C, Shin D (2002) Paragneiss assimilation in the genesis of magmatic Ni-Cu-Co sulfide mineralization at Voisey's Bay, Labrador: $\delta^{34}\text{S}$, $\delta^{13}\text{C}$, and Se/S evidence. *Econ Geol* 97:1307-1318
- Ripley EM, Taib NI (1989) Carbon isotopic studies of metasedimentary and igneous rocks at the Babbitt Cu-Ni deposit, Duluth Complex, Minnesota, U.S.A. *Chem Geol* 73:319-342
- Samalens N, Barnes SJ, Sawyer EW (2017) The role of black shales as a source of sulfur and semimetals in magmatic nickel-copper deposits: example from the Partridge River Intrusion, Duluth Complex, Minnesota, USA. *Ore Geol Rev* 81:173-187
- Tomkins AG, Rebryna KC, Weinberg RF, Schaefer BF (2012) Magmatic sulfide formation by reduction of oxidized arc basalt. *Jour Petrol* 53:1537-1567
- Wu Y, Zhang C., Mao J, Ouyang H, Sun J (2013) The genetic relationship between hydrocarbon systems and Mississippi Valley-type Zn-Pb deposits along the SW margin of Sichuan Basin, China. *Int Geol Rev* 55:941-957
- Zhamaletdinov AA (1996) Graphite in the Earth's Crust and electrical conductivity anomalies. *Izvest Physics Solid Earth* 32:272-288

Geobiology of northern Australian mid-Proterozoic sedex Zn-Pb-Ag deposits

Peter McGoldrick

Earth Sciences/CODES/IMAS – University of Tasmania, Australia

Abstract. The northern Australian mid-Proterozoic McArthur and Mount Isa Basins host four supergiant sediment-hosted Zn±Pb±Ag deposits, several smaller deposits and a number of sub-economic prospects. These formed at, or very close to, the sea floor when cool-warm, saline, oxidized brines ‘exhaled’ into anoxic (ferruginous) bottom water.

Host sediments are variably dolomitic, sideritic, pyritic and carbonaceous shales and siltstones, mostly deposited sub-storm wave base. Ores are present at several stratigraphic levels and ages range from ~1.65 Ga (Mount Isa) to ~1.59 Ga (Century).

The hosts and ores contain a variety of textures interpreted to have formed directly, or indirectly, by microbial activity. Chemical, isotopic and mass balance arguments suggest the (former) presence of vast quantities of microbial biomass. This prokaryote-dominated vent biota likely played a key role in the formation of the deposits by facilitating the production of reduced sulfur needed to fix base metals as metal sulfides.

Early eukaryotes living in these microbial communities may have experienced unique selection pressures in response to the deep, dark anoxic conditions in which they lived.

1 Introduction

Communities of diverse chemosynthetic microorganisms and macroscopic invertebrates associated with, and dependent on, deep sea hydrothermal vents and cold (hydrocarbon) seeps are among the most remarkable and unexpected biological discoveries of the last half century (Corliss and Ballard 1977, Paull et al. 1984). Fossil ‘vent biotas’ have been recognised in several locations. The oldest macroscopic examples are from Ordovician-Silurian massive sulfides in the Urals (Little et al. 1999; Georgeiva et al. 2018) and fossil microbial communities have been found in 1.43 Ga black smoker chimneys from north China (Li and Kusky 2007). Purported microorganisms have been reported from the oldest known (3.24 Ga) massive sulfides from the Pilbara of Western Australia (Rasmussen 2000).

Despite some historic arguments to the contrary, Australian mid-Proterozoic ‘sedex’ deposits formed at, or very close to, the sediment-water interface when warm(ish), dense, brines vented at the sea floor. In this review I will present textural and geochemical features from several Zn deposits and exploration prospects that indicate the former presence of microbial vent communities and argue some microbes played an integral role in ore formation.

2 Characteristics of the ‘sedex’ Zn systems

The northern Australian Proterozoic Zn Belt contains (or contained) more than a quarter of the world’s known Zn resource (Large et al., 2005). In the low metamorphic grade areas of the northern Mount Isa Basin, and in the McArthur Basin (Fig.1) the ores comprise stratiform, stacked, tabular lenses of laminated fine-grained base-metal sulfides. Metamorphism and deformation results in ores with coarser (‘recrystallised’) base metal sulfides and a more complex paragenesis. Host sequences are siltstones and carbonaceous shales with a ‘clastic’ dolomitic carbonate component. Mineralized intervals are often thicker than their lateral equivalents, indicating structurally controlled depocenters (‘sub-basins’) were favorable sites for ore formation (McGoldrick et al. 2010).

All deposits and prospects show Fe enrichment (‘halos’) in their host rocks. This is manifested as abundant fine-grained bedded and laminated pyrite, and/or Fe-carbonates (Large and McGoldrick, 1998; McGoldrick & Large, 1998).

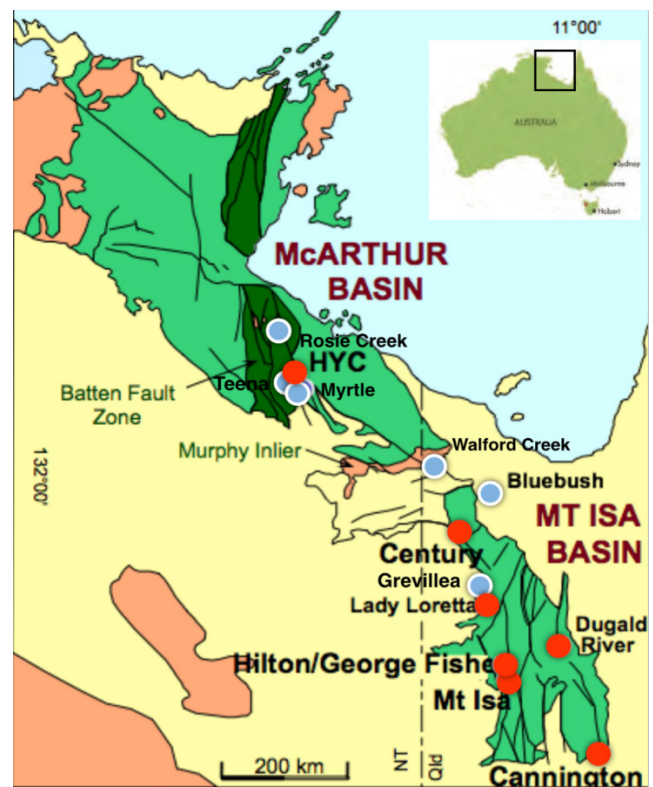


Figure 1. Location map showing the mid-Proterozoic McArthur and Mount Isa Basins and contained Zn±Pb±Ag mines and former mines (red dots) and sedex Zn prospects (blue dots).

3 Microbially mediated textures

3.1 Pyrite

Macroscopically, the bedded pyrite in all the northern Australian systems is very similar (Fig. 2a&b). Schieber (1990) compared Mount Isa bedded pyrite to pyritised microbial mat from the 1.4 Ga Newland Formation of Montana and suggested pyrite in northern Australian systems had a similar origin.

Microscopically much of the earliest generation bedded pyrite at Mount Isa comprises layers rich in small (5-10 micron) pyritohedra associated with carbonaceous matter (Painter et al. 1999) and 'classic' framboids have not been reported. By contrast, at HYC, Croxford and Jephcott (1972) described a variety of framboidal types (Fig. 2c&d). Carbonaceous spheres (interpreted as microbial fossil remains) have been extracted from Mount Isa pyrite (Love and Zimmerman 1961) and HYC ores (Hamilton and Muir 1974), and later work at HYC (Oehler and Logan 1977) revealed a diverse array of pyritised microbial forms preserved in black cherts.

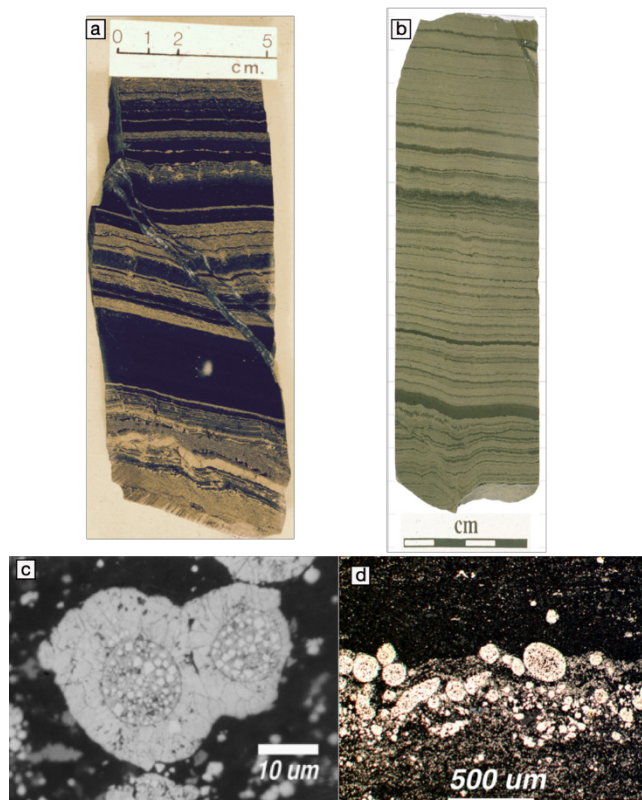


Figure 2. a. Bedded, crinkly-laminated pyrite from Mount Isa. b. Crinkly-laminated pyrite from Lady Loretta. c. 'Classic' framboids from HYC. d. Irregular ('amoeboid')-shaped macroframboids from HYC.

3.2 Other microbialites

There are several distinctive upwards-facing, curvy-planar, wavy and wrinkly structures present in a number of deposits reasonably interpreted as microbialites. Some of these would have stood proud of the sea floor (Fig. 3

a-d). These textures are preserved by a number of minerals, and mineral intergrowths (pyrite, carbonates, base metal sulfides). Small domal stromatolites with micro-unconformities are present in the sideritic inter-ore beds at Century (Fig. 3e)

Nodular or 'crusty' carbonate (\pm sphalerite) is a texture well developed peripheral to the HYC deposit (Ireland et al. 2004). In low grade Zn prospects (e.g., Myrtle, Grevillea) mineralisation is mainly this texture. Unmineralised examples from Bluebush prospect comprise sparry calcite aggregates separated by curve-planar pyrite and organic matter (Fig. 3f).

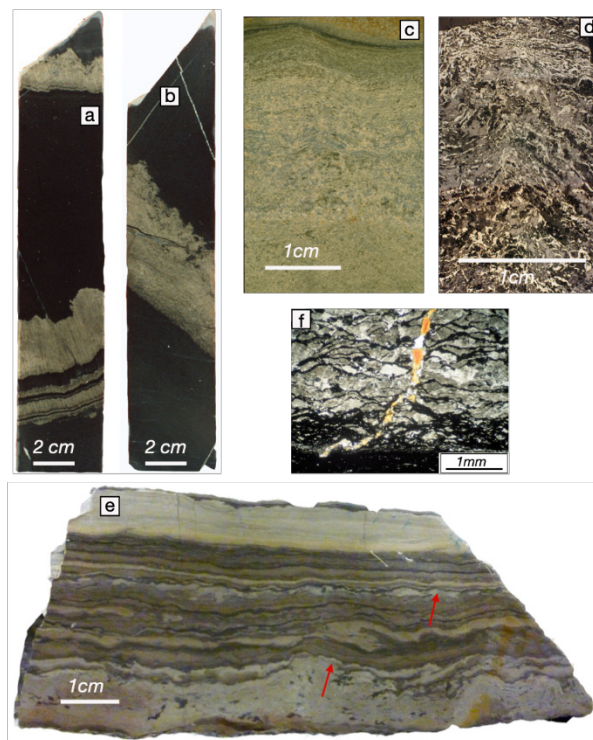


Figure 3. All photos oriented with stratigraphic younging direction to the top. All samples are of cut and polished hand specimens, except d & e, which are photomicrographs of thin sections. a&b. Crinkly-laminated pyrite beds with 'spiky' tops from Lady Loretta. c. Zinc mineralised crinkly-laminated pyrite-carbonate from Grevillea prospect. d. Reflected light photomontage of Grevillea mineralisation showing 'mini-stromatolite'. e. Microbially-laminated sideritic siltstone from inter-ore beds at Century (arrow indicates micro-unconformity associated with small stromatolites or thrombolites). f. Transmitted light photomicrograph of 'crusty' pyrite-calcite bed from Bluebush prospect.

4 Microbially mediated ore formation

High temperature 'smoker-type' sulfide deposits precipitate base metal sulfides (inorganically) in response to cooling and mixing on encountering cold seawater. In contrast, cool, oxidised sedex fluids require mixing with an exogenous source of reduced sulfur, or a mechanism to reduce sulfate already in the fluid, to form base metal sulfides. Thermochemical sulfate reduction has been proposed for deep subsurface mineralisation models (Broadbent et al. 1998), but is kinetically ineffective at temperatures below $\sim 140^\circ$ (Machel 2001). Biogenic

(microbial) sulfate reduction is an appealing alternative process for producing the required sulfide and the rate of BSR may be the fundamental control on the formation of high-grade mineralisation in these systems (Druschel et al. 2002, Maier and McGoldrick 2009). Recently, Johnson et al. (2018) argued that BSR facilitated by anaerobic oxidation of methane (AOM) generated the sulfide needed to form Palaeozoic sedex deposits in Canada. The crusty carbonate textures and concretions (Fig. 2j&k) associated with the northern Australian systems may indicate AOM operated in the Australian systems as well.

Under optimal ('goldilocks') conditions Australian Proterozoic seafloor vents would be self-sustaining producers of base metal sulfides ('bioreactors' - Fig.4). However, in the Fe-rich world of the Proterozoic deep oceans, many sedex systems produced low-grade or barren systems dominated by base metal anomalous pyrite (too much BSR) or ferroan-carbonates (too little BSR).



Figure 4. "Cloaca Professional" – art installation by Wim Delvoye on display at the Museum of Old and New Art (MONA), Hobart. Cloaca is locally referred to as 'the poo machine'. It comprises a series of small connected bioreactors that replicate the human digestive system – the device operates continuously, with food introduced daily at one end and solid waste excreted at the other.

5 Sedex systems and early eukaryotes

Undisputed eukaryote microfossils are present in 1.4 Ga rocks from northern Australia (Roper Group - Javaux et al. 2001) and Montana (Greyson Formation - Adam et al. 2017) and best estimates indicate the last eukaryotic common ancestor (LECA) pre-dates 1.5 Ga (Dacks et al. 2016). Various cryptic fossils suggest stem eukaryotes may have existed for more than half a billion years prior to LECA. However, biomarker chemistry for most of the Proterozoic is overwhelmingly dominated by prokaryotic compounds, suggesting eukaryotes were insignificant in terms of marine biomass (Brocks 2018). This may be real, or reflect sampling bias toward photic zone organic material. Recent microbial fossil discoveries from Century (McGoldrick and Satterthwait *in prep*) support the latter explanation and indicate biologically productive sedimentary vent sites in the deep dark anoxic Proterozoic oceans may have been important sites for eukaryogenesis (see also Porter et al., 2018).

Acknowledgements

My journey into the world of the mid-Proterozoic started at Mount Isa in 1978. Over the years numerous people contributed to the story presented here, and I would like to particularly thank Reid Keays, Bill Croxford, John Lovering, Peter Stoker, Rennie Blair, Steve De Cruif, Colin Robinson, Martin Neudert, Ross Logan, Brian Gulson, Neil Williams, Bill Perkins, Cees Swager, Greg Anderson, Wayne Nesbitt, Ross Large, Stuart Bull, David Cooke, Richard Keele, John Dunster, Mark Aheimer, Jamie Rogers, Tim Ireland, Alan Goode, Graham Carr, Andrew Allen, Peter Winefield, Rob Scott, David Selley, Josh Guilliamse, Ron Berry, Veryan Hann, Graeme Broadbent, Dugi Wilson, Poul Emsbo, Tim Lyons, Noah Planavsky, Clint Scott, John Slack, Cam Allan, Donna Satterthwait, Rod Maier, and Sean Johnson.

Funding supporting much of this research came from the University of Melbourne, the University of Tasmania, the Australian Research Council and AMIRA.

References

- Adam ZR, Skidmore ML, Mogk DW, Butterfield NJ (2017) A Laurentian record of the earliest fossil eukaryotes. *Geology* 45:387–390. doi.org/10.1130/G38749.1
- Broadbent GC, Myers RE, Wright JV (1998) Geology and origin of shale-hosted Zn-Pb-Ag mineralization at the Century deposit, Northwest Queensland, Australia. *Econ Geol* 93:1264–1294.
- Brocks JJ (2018) The transition from a cyanobacterial to algal world and the emergence of animals. *Emerging Topics in Life Sciences*, 2:181–190. doi.org/10.1042/ETLS20180039
- Corliss JB, Ballard RD (1977) Oases of life in the cold abyss. *Nat. Geogr.* 152:441–453.
- Croxford NJW, Jephcott S (1972) The McArthur lead-zinc-silver deposit, N.T. *Proc Australas Inst. Min Metall* 243:1-26.
- Dacks JB, Field MC, Buick R, Eme L, Gribaldo S, Roger AJ et al. (2016) The changing view of eukaryogenesis – fossils, cells, lineages and how they all come together. *J Cell Sci* 129:3695–3703. doi.org/10.1242/jcs.178566
- Druschel G, Labrenz M, Thomsen-Ebert T, Fowle D, Banfield J. (2002) Geochemical Modeling of ZnS in biofilms: An example of ore depositional processes. *Econ Geol* 97:1319–1329.
- Georgieva MN, Little CTS, Bailey RJ, Ball AD, Glover AG. (2018) Microbial-tubeworm associations in a 440-million-year-old hydrothermal vent community. *Proc Roy Soc B* 285:20182004. doi.org/10.1098/rspb.2018.2004
- Hamilton LH, Muir MD. (1974) Precambrian microfossils from the McArthur River lead-zinc-silver deposit northern territory, Australia. *Miner Deposita* 9:83–86.
- Ireland T, Large R, McGoldrick P, Blake M. (2004) Spatial distribution patterns of sulfur isotopes, nodular carbonate, and ore textures in the McArthur River (HYC) Zn-Pb-Ag deposit, northern territory, Australia. *Econ Geol* 99:1687–1709.
- Javaux EJ, Knoll AH, Walter MR. (2001) Morphological and ecological complexity in early eukaryotic ecosystems. *Nature* 412:66–69. doi.org/10.1038/35083562
- Johnson CA, Slack JF, Dumoulin JA, Kelley KD, Falck H. (2018) Sulfur isotopes of host strata for Howards Pass (Yukon-Northwest Territories) Zn-Pb deposits implicate anaerobic oxidation of methane, not basin stagnation. *Geology* 46:619–622. doi.org/10.1130/G40274.1
- Large R, McGoldrick P. (1998) Lithochemical halos and geochemical vectors to stratiform sediment hosted Zn-Pb-Ag deposits, 1. Lady Loretta Deposit, Queensland. *J Geochem Ex* 63:37–56.
- Large R, Bull S, McGoldrick P, Walters S, Derrick G, Carr, G. (2005) Stratiform and strata-bound Zn-Pb-Ag deposits in Proterozoic sedimentary basins, northern Australia. *Econ Geol* 100th Anniv

Vol:931–963.

- Li J, Kusky TM. (2007) World's largest known Precambrian fossil black smoker chimneys and associated microbial vent communities, North China: Implications for early life. *Gondwana Research* 12:84–100. doi.org/10.1016/j.gr.2006.10.024
- Little CTS, Herrington RJ, Maslennikov VV, Morris NJ, Zaykov VV. (1997) Silurian hydrothermal-vent community from the southern Urals, Russia. *Nature* 385:146–148. doi.org/10.1038/385146a0
- Machel H. (2001) Bacterial and thermochemical sulfate reduction in diagenetic settings - old and new insights. *Sed Geo*140:143–175.
- Maier RC, McGoldrick PJ. (2009) The Bluebush Zinc Prospect, NW Queensland: Multiple base metal mineralising events and a record of fluctuating redox conditions in late Palaeoproterozoic seas. *Geochim Cosmochim Acta*, Goldschmidt Conference Abstracts: A818.
- McGoldrick P, Large R. (1998) Proterozoic stratiform sediment-hosted Zn-Pb-Ag deposits. *AGSO J Aus Geo Geophys* 17:189–196.
- McGoldrick P, Winefield P, Bull S, Selley D, Scott R. (2010) Sequences, Syndimentary Structures, and Sub-Basins: the Where and When of SEDEX Zinc Systems in the southern McArthur Basin, Australia. *Soc Econ Geologists Spec Pub* 15:367–389.
- Oehler JH, Logan RG. (1977) Microfossils, cherts, and associated mineralization in the Proterozoic McArthur (HYC) lead-zinc-silver deposit. *Econ Geol* 72:1393–1409.
- Painter M, Golding S, Hannan K, Neudert M. (1999) Sedimentologic, petrographic, and sulfur isotope constraints on fine-grained pyrite formation at Mount Isa mine and environs, northwest Queensland, Australia. *Econ Geol* 94:883–912.
- Paull CK, Hecker B, Commeau R, Freeman-Lynde RP, Neumann C, Corso WP, et al. (1984) Biological Communities at the Florida Escarpment Resemble Hydrothermal Vent Taxa. *Science*, 226:965–967. doi.org/10.1126/science.226.4677.965
- Porter SM, Agić H, Riedman LA. (2018) Anoxic ecosystems and early eukaryotes. *Emerging Topics in Life Sci* 2:299–309. doi.org/10.1042/ETLS20170162
- Rasmussen B. (2000) Filamentous microfossils in a 3,235-million-year-old volcanogenic massive sulphide deposit. *Nature* 405:676–679./doi.org/10.1038/35015063
- Schieber J. (1990) Pyritic shales and microbial mats: significant factors in the genesis of stratiform Pb-Zn deposits of the Proterozoic? *Miner Deposita*, 25:7–14. doi.org/10.1007/BF03326378

Neoproterozoic microbial processes in chemical sediment diagenesis: evidence from the Aberfeldy barite deposits

Moles, Norman R.

School of Environment and Technology, UK.

Boyce, Adrian J.

Scottish Universities Environmental Research Centre (SUERC), University of Glasgow, UK

Abstract. Microbial- and diffusion-controlled diagenetic processes were significant in the formation of sulfide-, sulfate- and carbonate-rich stratiform mineralization hosted by Neoproterozoic graphitic metasediments near Aberfeldy in Perthshire, Scotland. In 1-10m thick beds of barite rock, barite $\delta^{34}\text{S}$ of $+36 \pm 1.5 \text{‰}$ represents the isotopic composition of contemporaneous seawater sulfate. Pronounced vertical variations in $\delta^{34}\text{S}$ (+30 to +41 ‰) and $\delta^{18}\text{O}$ (+8 to +21 ‰) occur on a decimetre-scale at bed margins. These excursions are attributed to early diagenetic alteration, while the barite sediment was fine-grained and porous, due to pulsed infiltration of isotopically diverse porefluids into the marginal barite. Fluid-mediated transfer of barium and sulfate into adjacent sediments contributed to barium enrichment and growth of millimetric sulfate crystals cross-cutting sedimentary lamination. Witherite, barytocalcite and norsethite occur only as small inclusions within crystals of pyrite. Barium carbonate formation is ascribed to early diagenetic processes that generated very low sulfate activity in pore waters. Subsequently, sulfidation reactions produced secondary barite + non-barium carbonates in the rock matrix. Comparatively low $\delta^{34}\text{S}$ (+16 to +22 ‰) in secondary barite indicate sulfur derived from reduced sulfide. Similar sulfide $\delta^{34}\text{S}$ ratios in the host sediments are consistent with microbial reduction of seawater/porewater sulfate.

1 Introduction

In modern and Phanerozoic shallow marine sediments, diagenetic processes are typically affected by bioturbation occurring within 0.1–0.4 m of the sediment-water interface and sometimes to depths of >1 m. This mixing speeds up reactions which would otherwise be limited by diffusion rates and homogenises light isotope compositions in the upper sediment layer (Goldhaber, 2003). In Precambrian marine sediments, the absence of burrowing organisms precluded mixing, consequently diffusion through pore water and pore water advection were the main processes affecting ionic concentration gradients and diagenetic mineralization.

Here we report evidence for microbial- and diffusion-controlled diagenetic processes in mid-Neoproterozoic sulfide-, sulfate- and carbonate-rich chemical sediments interbedded with organic-rich marine sediments.

2 Background

2.1 Barite deposition and diagenetic alteration

In modern ocean sediments, barite is not prone to diagenetic alteration after burial where oxic conditions prevail, but is soluble under reducing conditions especially in the presence of sulfate-reducing microbes and organic matter (e.g. Clark et al., 2004). Porewater sulfate reduction is ubiquitous in organic-rich sediments containing barite (e.g. Torres et al., 1996).

Some studies of sedimentary exhalative (sedex) barite deposits have proposed that barite precipitation occurred in the water column with finely crystalline barite deposited on the seabed (e.g. Lyons et al., 2006). However, in a study of non-hydrothermal sediment-hosted stratiform barite deposits worldwide, Johnson et al. (2009) found that many shows marked isotopic variation with values far removed from that of contemporaneous seawater. They conclude that the $\delta^{18}\text{O}$ and $\delta^{34}\text{S}$ values in barite had been modified by exchange with porewater sulfate from adjoining sediments in which sulfate was consumed by oxidation of organic matter or anaerobic oxidation of methane. The isotopic profiles resemble those of pore water sulfate observed in modern ocean sediments.

Modern seafloor barite deposits, and ancient sedex deposits that have not been strongly metamorphosed, contain barium carbonates that are invariably diagenetic in origin, often replacing pre-existing mineral phases such as barite or celtsian (e.g. Ansdell et al., 1989).

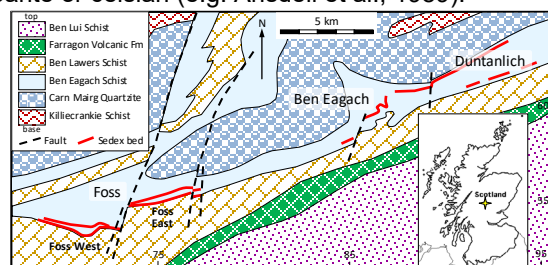


Figure 1. Bedrock geology in the vicinity of the barite deposits (map adapted from Coats et al., 1980 and Treagus, 2000). Inset map of Scotland with star indicating location of the area.

Magnall et al. (2016) report textural, mineralogical and isotopic evidence indicating that diagenetic replacement processes were dominant during barite and sulfide mineralization in the Tom and Jason shale-hosted massive sulfide (SHMS) deposits in the Selwyn Basin. They conclude that the interplay between biological activity, methanogenesis, seawater sulfate concentrations, and open system diagenesis are important to consider when interpreting $\delta^{34}\text{S}$ values in

SHMS and barite deposits from the geologic record.

It should be noted that sulfides are a major component of mineralization at Tom and Jason, and barite rarely forms thick beds (Gardner and Hutcheon, 1985) whereas in the Aberfeldy deposits described here, barite commonly forms metre-scale beds (Fig. 2) of nearly monomineralic rock often with low sulfide content.

2.2 The Aberfeldy barite deposits

Located in the mountainous region of central Perthshire in the Grampian Highlands of Scotland (Fig. 1), the Aberfeldy ore deposits represent the UK's largest resource of industrial barite (Treagus, 2000). The orebodies were discovered in the 1970s by the British Geological Survey (then 'IGS'). Barite production by Dresser Minerals from the Foss Mine commenced in the 1980s and since then about 40,000 tonnes annually has been extracted by M-I SWACO, a Schlumberger company. Barite rock is also worked intermittently from a small quarry on Ben Eagach. In the nearby Duntanlich deposit, an unworked resource of at least 7.5 million tonnes of barite is reported (M-I SWACO, 2014) in a structurally simple, tabular orebody. In 2016, planning permission was granted for an under-ground mine at Duntanlich and development is currently ongoing.

The Duntanlich orebody is stratigraphically lower than the barite beds in the Foss deposit although both are hosted in the Neoproterozoic Ben Eagach Schist Formation. This comprises mainly graphitic quartz muscovite schists, the protoliths of which were organic-rich mudstone and siltstone, enriched in barium and base metals in the vicinity of the deposits (Hall, 1993). Locally the schists are calcareous with thin beds of graphitic dolostone. The stratigraphically overlying Ben Lawers Schist Formation is calcareous and non-sulfidic, and contains barite and chert mineralization only in the lowermost strata. The presence of mafic volcanic components together with the sedex mineralization has been interpreted as evidence of high heat flow and convective circulation of hydrothermal fluids in a passive continental margin rifting environment (Coats et al., 1980; Russell, 1985; Hall, 1993; Treagus, 2000).

Subsequently in mid-Ordovician Grampian Orogeny, the sedimentary beds were tilted and distorted by several phases of folding and faulting, and subjected to amphibolite facies regional metamorphism (Moles, 1985; Treagus, 2000; Treagus et al., 2013).

The hydrothermal exhalative activity that precipitated barite sediment occurred in relatively shallow water as evidenced by localised reworking to form barite conglomerate (Moles et al., 2015) and lateral facies and thickness variations. Cherty rocks rich in quartz and barium aluminosilicates (celsian, cymrite, barium-rich micas) envelope the barite beds and extend laterally further than the barite as they precipitated on the seafloor in deeper parts of the sedimentary basin where anoxic conditions prevailed near the sediment-water interface. In some parts of the deposits, carbonate and sulfide rocks (mainly pyrite with lesser sphalerite and galena) occur within the mineralized beds. Occasionally all of these components occur together forming laminated beds.

Magnetite locally occurs in trace amounts instead of pyrite within thicker beds of barite. Pyrrhotite is a rare component of chert and carbonate rocks close to presumed hydrothermal vent sites (Hall, 1993).

The mineralized beds have sharp boundaries with the enclosing metasediments, and clastic sediments are seldom incorporated within the barite rock (Moles et al., 2015). These features suggest rapid deposition of the barite during hydrothermal exhalative episodes that were vigorous but short-lived and episodic. Seven such episodes are represented in the Foss deposit (labelled 1 to 7 in Fig. 2) although Foss Mine exploits just one barite bed, no. 5. Silicified, barium-enriched laminated sediment occurs locally in two contexts: stratigraphically below the mineralized beds, and as lateral equivalents located distal from the main locus of exhalative activity.

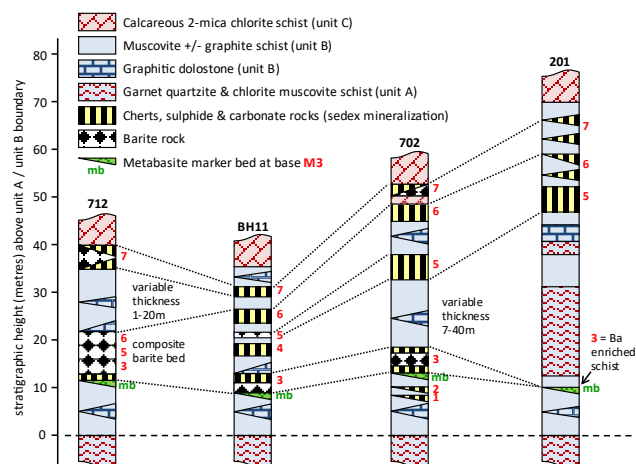


Figure 2. Representative vertical sections of mineralized beds illustrating the lateral variations across Foss East (Fig. 1). 3-digit numbers: Dresser Minerals boreholes. BH11: IGS borehole.

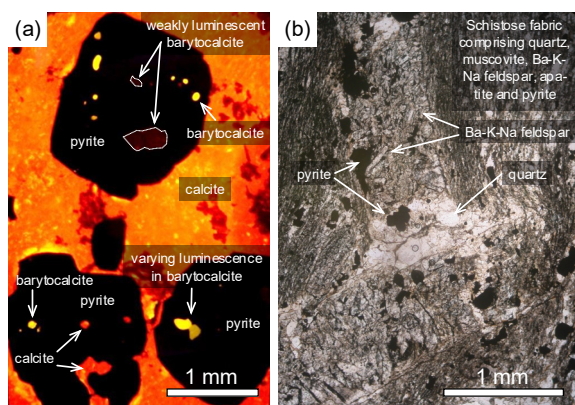
3 Mineralogical and isotopic evidence of diagenetic processes

3.1 Barium carbonates

Encapsulated within pyrite crystals in the bedded mineralization are small inclusions of sphalerite, barite and carbonates that have heterogeneous compositions in contrast with relatively homogeneous compositions of minerals in the rock matrix. The diverse composition of inclusions (Fig. 3a) suggests that due to encapsulation they were shielded from subsequent modification. We infer that these grains crystallized during the exhalative events and diagenesis of the chemical sediment.

The barium carbonates barytocalcite, norsethite and witherite occur only as tiny, pyrite-encapsulated grains within carbonate-bearing barite-sulfide rocks (Moles, 2015). They were initially identified by cold-source optical cathodoluminescence microscopy which revealed their distinctive luminescence colors (Fig. 3a). We infer that barium carbonates were formerly widespread within the chemical sediments and that later in the diagenetic / lithification sequence, matrix barium carbonate was replaced by barite + calcite or dolomite.

Figure 3 (a) Cathodoluminescence photomicrograph of pyrite-



barite-calcite rock showing inclusions of yellow-luminescent baryocalcite within pyrite and orange-luminescent matrix calcite. Sample from DH105, western Foss East. (b) Photomicrograph of pseudomorphs after ~1 x 5 mm barite porphyrotopes in mineralized sediment underlying the lower (#3) barite bed in the Foss deposit. Sample N81-43c from near IGS BH3, eastern Foss East (Fig. 1).

3.2 Pseudomorphs of diagenetic barite crystals

Fortey and Beddoe-Stephens (1982) illustrate a silicified metasediment from IGS BH9 (Foss West) that contains bladed 'porphyroblasts' ~1 mm wide and 4–7 mm long of Ba-K-Na feldspars with complex internal structures and inclusions of pyrite and trace barite. They suggested that the tabular structures are pseudomorphs of barite crystals that formed in the sediments during diagenesis, comparable to diagenetic barite laths cross-cutting sedimentary lamination observed in bedded sulfide ores (e.g. Lyons et al., 2006, Figure 7D).

We have found further examples of these features, illustrated in Fig. 3b. The complex internal structure indicates replacement processes during which the original barite was dissolved and replaced by pyrite, quartz and Ba-K-Na feldspar, the crystals of which often show growth perpendicular to the long edges of the tabular shape. The host rocks range from graphitic quartz-mica-feldspar schists to cherts and quartz-carbonate rocks within the stratiform mineralization. The pseudomorphs appear to have survived metamorphism because they are hosted by quartz- and/or feldspar-rich rocks which resisted the deformation that caused mica-rich rocks to develop a penetrative cleavage.

We infer that, prior to metamorphism, diagenetic sulfate crystals were common within the sediments and within silica- and carbonate-rich sedex mineralization.

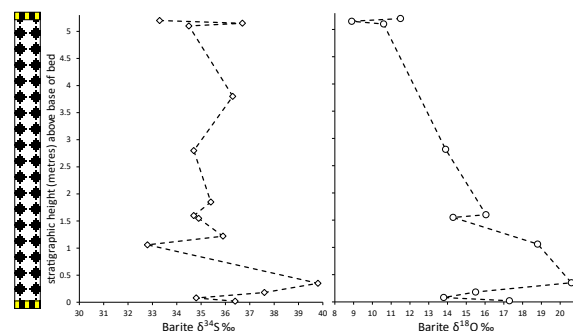
3.3 Isotopic composition of barite and sulfides

The sulfur isotopic composition of Aberfeldy barite and sulfides has been studied extensively with analyses published by Willan and Coleman (1983), Hall et al. (1991) and Moles et al. (2015). Based on analyses of 88 pure barite separates from the Aberfeldy deposits, Moles et al. (2015) showed that $\delta^{34}\text{S}$ values of $+36.5 \pm 1\%$ are typical across the entire geographical area and stratigraphic range. This is interpreted as the isotopic ratio of contemporaneous seawater sulfate which precipitated the Ba^{2+} exhaled in hydrothermal fluids.

However, upper and lower margins of barite beds

show atypically low ($+30$ to $+35\%$) and high ($+37$ to $+41\%$) $\delta^{34}\text{S}$ values varying over distances of centimetres to tens of centimetres (Fig. 4). Barite $\delta^{18}\text{O}$ values scatter about a mean of $+13.5 \pm 5\%$ and display variations similar to those of $\delta^{34}\text{S}$ near bed margins. These features are attributed to post-depositional isotopic modification while the barite sediment was fine-grained and porous, i.e. diagenetic alteration.

Figure 4. Stratigraphic profile through the barite bed intersected in



Foss East DH424 showing pronounced marginal excursions in isotopic composition (from Moles et al. 2015).

In Fig. 5, sulfide samples derived from the metasediments and mineralized sediments (clastic sediment impregnated with Ba and Si derived from hydrothermal solutions) are distinguished from sulfide and barite in the stratiform mineralization. It is apparent that sulfide $\delta^{34}\text{S}$ values vary widely in both the metasediments and mineralization, contrary to the two-fold division proposed by Hall et al. (1991) of lower $\delta^{34}\text{S}$ values in the metasediments and higher values in the mineralization. Sulfide $\delta^{34}\text{S}$ values of $+12$ to $+16\%$ in some metasediments are consistent with microbial reduction of seawater sulfate involving fractionation of around $+20 \pm 4\%$. However, values range up to $+23.5\%$ suggesting that other sulfur sources or fractionation processes contributed to produce the wide range in compositions.

We obtained further $\delta^{34}\text{S}$ data by both conventional and laser ablation analyses of samples selected on the basis of preserved diagenetic features. Barite and pyrite were separated from a sample of carbonate-sulfide-barite rock (702-4B) in which pyrite crystals contain relatively abundant inclusions of barium carbonates. The barite has a $\delta^{34}\text{S}$ value of $+14$ to $+16\%$ which is comparable to the isotopic composition of sulfides in sediments and is exceptionally low compared to normal barite rock at Aberfeldy (Fig. 5). Conversely, pyrite in the same sample reports $\delta^{34}\text{S}$ values of $+29$ to $+32\%$ which is outside the range of previously reported sulfides from Aberfeldy but is within the range of primary barite ratios.

In a laminated pyritic chert rich in barium carbonate inclusions (sample 505-15), individual dispersed crystals of pyrite have $\delta^{34}\text{S}$ values ($n=6$) ranging from 21.1 to 26.8 ‰ within an area of $<2\text{ cm}^2$. This remarkably wide range confirms that sulfur isotope heterogeneity existed at this scale in the precursor sedimentary rock and survived regional metamorphism.

Pyrite in three samples of mineralized sediment gave $\delta^{34}\text{S}$ values of $+27$ to $+29\%$, at the upper end of the 'normal' range for Aberfeldy sulphides (Fig. 5).

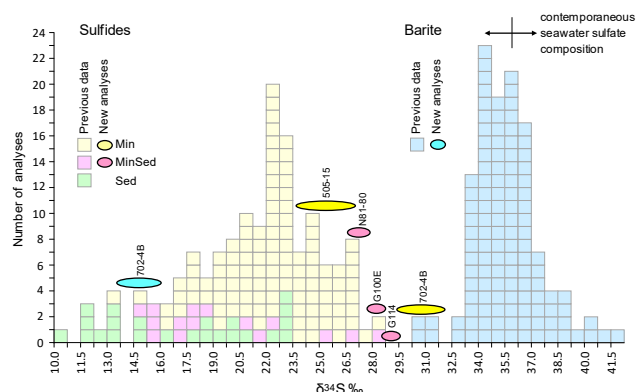


Figure 5. Histogram comparing $\delta^{34}\text{S}$ results for samples described here with previously published values from the Aberfeldy deposits. Min = sedex mineralization; MinSed = clastic sediment mineralized by hydrothermal material; Sed = metasedimentary host rock. Postulated seawater sulfate composition from Moles et al. (2015).

4 Summary of diagenetic processes

The barium carbonates and sulfate crystal porphyrotopes formed during diagenetic modification of the sediments prior to recrystallization during lithification and metamorphism. The barium carbonates precipitated within the sediments from porewaters that had very low sulfate ion activities due to microbial sulfate reduction. Under the highly reducing conditions, barium mobilised in the porewater infiltrated adjoining sediments where it was fixed by the precursors to barium muscovite and Ba-K-Na feldspars. Subsequent sulfidation reactions replaced the barium carbonates that were not encapsulated within inert crystals, and produced the matrix assemblage of calcite and/or dolomite plus secondary barite with an isotopic composition very different to primary barite that precipitated in the Neoproterozoic seawater. ^{34}S -rich secondary pyrite-sulfur was derived from reduction of pre-existing sulfate.

Fluxes of sulfate-bearing porewater derived from the organic-rich sediments diffused into the margins of the barite beds and modified the primary (seawater sulfate) isotope composition of the marginal barite. These fluxes had alternating enrichments in the light and heavy isotopes of sulfur and oxygen, creating layers of isotopically distinct barite rock parallel to bed margins. The isotopic perturbations preserve a record of the microbially-mediated porewater sulfate reduction and sulfate replacement processes that took place in the adjoining sediments. These are also evidenced by the growth in unconsolidated sediment of diagenetic sulfate porphyrotopes and their subsequent replacement by ^{34}S -rich sulfide-bearing pseudomorphs.

The barite bed-marginal isotopic excursions, and occurrences of sediment-hosted sulfate porphyrotopes, are not restricted to the base of barite beds but also occur at their tops. We infer that organic-rich clastic sediment was deposited soon after each exhalative event, before pore-sealing of the underlying chemical sediment, such that microbial activity in the overlying sediment generated isotopically diverse porewaters that infiltrated downwards into the barite sediment.

References

- Ansdell KM, Nesbitt BE, Longstaffe FJ (1989) A fluid inclusion and stable isotope study of the Tom Ba-Pb-Zn deposit, Yukon Territory, Canada. *Econ Geol* 84: 841-856.
- Clark SHB, Poole FG, Wang Z (2004) Comparison of some sediment-hosted, stratiform barite deposits in China, the United States, and India. *Ore Geol Rev* 24: 85-101.
- Coats JS, Smith CG, Fortey NJ, Gallagher MJ, May F, McCourt WJ (1980) Stratabound barium-zinc mineralization in Dalradian schist near Aberfeldy, Scotland. *Trans Inst Mining Metallurgy* 89: B110-122.
- Fortey NJ, Beddoe-Stephens B (1982) Barium silicates in stratabound Ba-Zn mineralization in the Scottish Dalradian. *Min Mag* 46: 63-72.
- Gardner HD, Hutcheon I (1985) Geochemistry, mineralogy and geology of the Jason Pb-Zn deposits, Macmillan Pass, Yukon, Canada. *Econ Geol* 80: 1257-1276.
- Goldhaber MB (2003) Sulfur-rich sediments. In: Holland HD and Turekian KK (editors-in-chief) *Treatise on Geochemistry Vol. 7 Sediments, diagenesis and sedimentary rocks*: 257-288.
- Hall AJ, Boyce AJ, Fallick, AE (1991) Isotopic evidence of the depositional environment of Late Proterozoic stratiform mineralisation, Aberfeldy, Scotland. *Chem Geol* 87: 99-114.
- Hall AJ (1993) Stratiform mineralization in the Dalradian of Scotland. In: Patrick RAD, Polya DA (editors) *Mineralization in the British Isles*, Chapman & Hall, London: 38-101.
- Johnson CA, Emsbo P, Poole FG, Rye RO (2009) Sulfur- and oxygen-isotopes in sediment-hosted stratiform barite deposits. *Geochim et Cosmochim Acta* 73: 133-147.
- Lyons TW, Gellatly AM, McGoldrick PJ, Kah LC (2006) Proterozoic sedimentary exhalative (SEDEX) deposits and links to evolving global ocean chemistry. In: Kesler SE, Ohmoto H (editors) *Evolution of Early Earth's Atmosphere, Hydrosphere, and Biosphere—Constraints from Ore Deposits*: Geol Soc America Memoir 198: 169-184.
- Magnall JM, Gleeson SA, Stern R A, Newton RJ, Poulton SW, Paradis S (2016) Open system sulphate reduction in a diagenetic environment – isotopic analysis of barite ($\delta^{18}\text{O}$ and $\delta^{34}\text{S}$) and pyrite ($\delta^{34}\text{S}$) from the Tom and Jason Late Devonian Zn-Pb-Ba deposits, Selwyn Basin, Canada. *Geochim et Cosmochim Acta* 180: 146-163.
- M-I SWACO (2014) Duntanlich Mine Plan. Presentation prepared by Dalgleish Associates Limited, Dunblane, Scotland.
- Moles NR (1985) Metamorphic conditions and uplift history in central Perthshire: evidence from mineral equilibria in the Foss celsian-barite-sulphide deposit Aberfeldy. *J Geol Soc London* 142: 39-52.
- Moles NR (2015) Barium carbonates as relicts of chemical sediment diagenesis in the Aberfeldy stratiform barite deposits, Grampian Highlands, Scotland (extended abstract). SGA 13th Biennial Meeting, Nancy, France.
- Moles NR, Boyce AJ, Fallick AE (2015) Abundant sulphate in the Neoproterozoic ocean: implications of constant $\delta^{34}\text{S}$ of barite in the Aberfeldy SEDEX deposits, Scottish Dalradian. In: Jenkin GRT, Lusty PAJ, McDonald I, Smith MP, Boyce AJ, Wilkinson JJ (editors), *Ore deposits in an evolving Earth*. *Geol Soc London Spec Publ* 393: 189-212.
- Russell MJ (1985) The evolution of the Scottish mineral sub-province. *Scott J Geol* 21: 513-545.
- Torres ME, Brumsack HJ, Bohrmann G, Emeis KC (1996) Barite fronts in continental margin sediments: A new look at barium remobilization in the zone of sulphate reduction and formation of heavy barites in diagenetic fronts. *Chem Geol* 127: 125-139.
- Treagus JE (2000) *The Solid Geology of the Schiehallion District*. British Geological Survey, Edinburgh. Memoir for Sheet 55W.
- Treagus JE, Tanner PWG, Thomas PR, Scott RA, Stephenson D (2013) The Dalradian rocks of the central Grampian Highlands of Scotland. *Proc Geologists Assoc* 124: 148-214.
- Willan RCR, Coleman ML (1983) Sulfur isotope study of the Aberfeldy barite, zinc, lead deposit and minor sulphide mineralization in the Dalradian metamorphic terrain, Scotland. *Econ Geol* 78: 1619-1656.

The importance of biological productivity for the formation of the George Fisher Zn-Pb-Ag deposit, Queensland, Australia

Philip Rieger^{1,2}, Joseph M. Magnall¹, Sarah A. Gleeson^{1,2}, Alexander Rocholl¹, Richard Lilly³

¹GFZ German Research Centre for Geosciences, Potsdam, Germany

²Free University of Berlin, Germany

³University of Adelaide, Australia

Abstract. The Carpentaria Province in Northern Australia is one of the most important districts for clastic-dominated (CD-type) massive sulphide deposits and comprises two of the world's oldest, well preserved hydrocarbon-bearing sedimentary basins. Paragenetically constrained pre-, syn- and post-ore pyrite from drill-core samples from the late Paleoproterozoic George Fisher deposit and its host rock were analysed by Secondary Ion Mass Spectrometry in order to obtain temporally and spatially resolved $\delta^{34}\text{S}_{\text{pyrite}}$ values. Together with petrographic observations, the $\delta^{34}\text{S}_{\text{pyrite}}$ values are interpreted to be the result of different sulphate reduction processes, which either directly or indirectly involve biological activity: (1) microbial sulphate reduction (MSR); (2) sulphate driven – anaerobic oxidation of methane (SD-AOM); (3) thermochemical sulphate reduction (TSR); and (4) recycling of sulphides. Altogether this highlights the importance of biological productivity for the formation of the George Fisher deposit and potentially for all CD-type deposits in the Carpentaria Province.

1 Introduction

The Proterozoic Mount Isa Inlier in the Carpentaria Province of northern Australia (Fig. 1) is one of the world's oldest sedimentary basins, in which substantial amounts of organic matter are well preserved (e.g. Chapman, 1999; Glikson et al. 2000). Moreover, the Carpentaria Province hosts some of the world's largest CD-type massive sulphide deposits (Large et al. 2005; Fig. 1). Linking both aspects, some authors have proposed that hydrocarbons may have played an important role in ore formation (e.g. Broadbent et al. 1998). Indeed, organic matter is an essential reactant during the reduction of sulphate to sulphide (Machel et al. 1995), of which there are biogenic (MSR and SD-AOM) and abiogenic (TSR) pathways.

Pyrite is a highly abundant sulphide phase in all CD-type deposits, which occurs as a primary gangue mineral phase throughout the paragenesis (pre-, syn-, post-ore). In the Carpentaria Province, fine-grained, spheroidal pyrite (fg-py) is a ubiquitous mineral phase associated with both the massive sulphide deposits and non-mineralised stratigraphy. It has been shown to be the paragenetically earliest sulphide phase (e.g. Grondijs and Schouten 1937; Eldridge et al., 1993; Chapman 2004), but its formation process is debated.

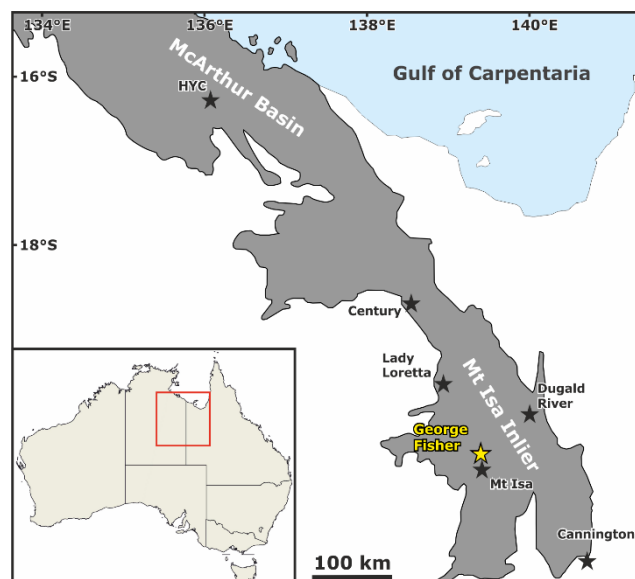


Figure 1. Simplified map of the Carpentaria Province (after Gibson et al., 2017); shown are the Mt Isa Inlier, the McArthur Basin and 7 major Zn-Pb-Ag deposits (asterisks); highlighted in yellow is the George Fisher Zn-Pb-Ag deposit, which is the subject of this study.

At the HYC deposit, fg-py has been interpreted to form by MSR in the water column (e.g. Ireland et al. 2004) or during early diagenesis (e.g. Eldridge et al. 1993). For the Mount Isa, George Fisher and Century deposits, fg-py precipitation by TSR has been proposed during late-stage diagenesis (Painter et al. 1999; Chapman 1999) or syn-deformation (e.g. Broadbent et al. 1998). The ore stages in the CD-type deposits of the Carpentaria Province consist of different generations of sulphide phases (mainly sphalerite, galena, pyrite and pyrrhotite), which show complex paragenetic relationships and were interpreted to have formed by MSR (e.g. Ireland et al. 2004), TSR (e.g. Broadbent et al. 1998) or by the recycling of sulphur from pre-existing sulphide phases (e.g. Grondijs and Schouten 1937).

The interpretation of sulphate reduction processes is typically based on sulphur isotope ($\delta^{34}\text{S}$) values, which is challenging for the northern Australian CD-type deposits due to the complex paragenesis and the very fine grain size of the sulphide phases. In this study, therefore, we use scanning electron microscopy (SEM) together with high resolution (spot size < 5 μm) *in situ* secondary ion mass spectrometry (SIMS) to spatially resolve the different generations of sulphide phases.

2 Geological setting

During the late Paleoproterozoic and early Mesoproterozoic, break-up and reassembly of the Nuna supercontinent led to the formation of the Mt Isa Inlier and the McArthur Basin (Gibson et al. 2017). The George Fisher deposit is hosted by carbonaceous siltstones and mudstones of the Urquhart Shale (ca. 1655 Ma), which is part of the Mt Isa Group within the Mt Isa Inlier (Chapman 2004). The deposit has been affected by several deformation events, resulting in complex macro- and microscopic structures (Chapman 2004).

3 Methods

Five drill-cores (4 from the George Fisher deposit and one from un-mineralised Urquhart Shale) were logged for lithology and paragenesis and sampled in this study. Representative samples were investigated petrographically and, target areas of paragenetically constrained sulphide phases were separated using a diamond core micro-drill (diameter of 4 mm). The micro-drill-cores (49) were set in epoxy mounts (3) together with pyrite reference material and coated with Au. Areas for isotopic analysis were then selected using the Scanning Electron Microscope (SEM).

The isotopic analyses of pyrite were carried out at GFZ Potsdam using a Cameca IMS 1280-HR instrument. Isotope ratios were acquired both for single-spot and multi-spot-transect analyses using a ~ 0.5 nA, mass filtered $^{133}\text{Cs}^+$ beam with a Gaussian density distribution focused to a < 5 μm diameter on the polished sample surface. The analyses points were then imaged by backscatter electron microscopy and mixed-analyses or data points of other phases than pyrite were rejected.

4 Results

4.1 Sulphide Paragenesis

Five generations of sulphides have been identified in this study. (1) pre-ore, fine grained pyrite; (2) three stages of hydrothermal sulphides (exclusive to George Fisher); and (3) a generation of coarse grained euhedral pyrite, which is limited to un-mineralised rocks. In the following, individual stages are described in terms of their relative timing of formation (paragenesis).

The first generation of pyrite (Py-0) occurs in laminated, carbonaceous siltstones of the background Urquhart Shale (Fig. 2a) and of the Urquhart Shale at the George Fisher deposit (Fig. 2b, c). Pyrite occurs as single grains or in grain aggregates and is typically spheroidal to subhedral and very fine-grained (< 10 μm ; Fig. 2c). It can be split into two sub-types: Py-0a forms spheroidal to sub-spheroidal cores, and is overgrown by Py-0b, which forms a porous, subhedral to euhedral overgrowth (Fig. 2c).

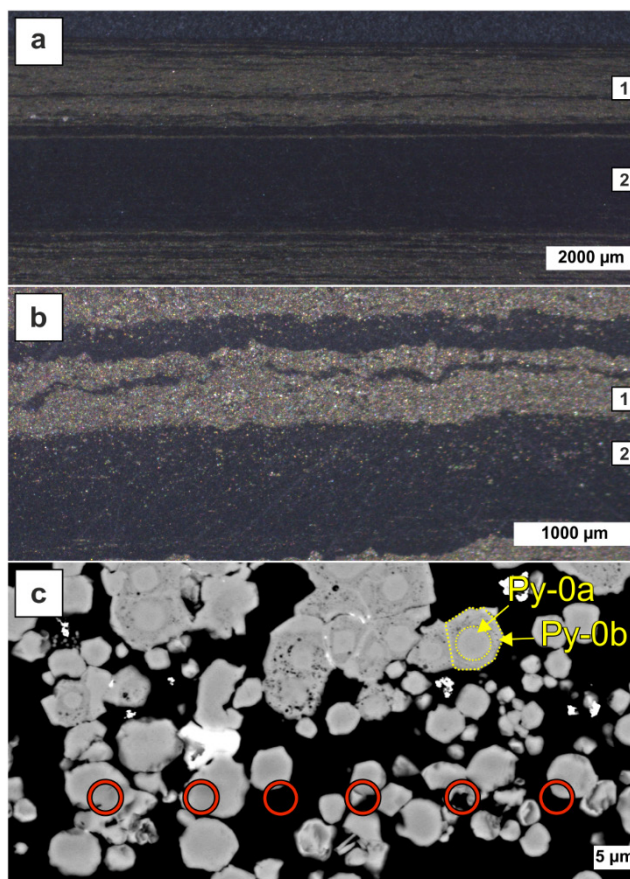


Figure 2. Binocular photomicrograph images of pyritic, carbonaceous siltstone (1) and carbonaceous mudstone (2) from un-mineralised Urquhart Shale (a) and from George Fisher (b); c) backscatter electron image of pyritic, carbonaceous siltstone; Py-0 consists of a spheroidal core (Py-0a) and a subhedral overgrowth (Py-0b); red circles indicate SIMS analysis spots.

The ore-stage sulphides clearly overgrow and replace pre-ore pyrite, and are differentiated in terms of texture, grain-size and abundance of different phases (pyrite, sphalerite, galena, pyrrhotite and chalcopyrite). Ore-stage 1 is strata-bound, consists of sphalerite, pyrite and galena (Sp-1, Py-1 and Gn-1) and is associated with coarse-grained ankerite. Ore-stage 2 occurs in veins and breccias and consists of galena, sphalerite, pyrite and pyrrhotite (Gn-2, Sp-2, Py-2 and Po-1). Within ore-stage 2, replacement textures of Py-0 by later sulphide phases are ubiquitous (Fig. 3). The last stage of sulphides (ore-stage 3) occurs strata-bound or as veins and breccias, and typically consists of pyrrhotite, pyrite, sphalerite, galena and chalcopyrite (Po-2, Py-3, Sp-3, Gn-3 and Ccp).

Coarse-grained, euhedral pyrite (Py-euh) occurs in carbonate beds and nodules overgrowing Py-0, but shows no temporal association to the ore-stage sulphides.

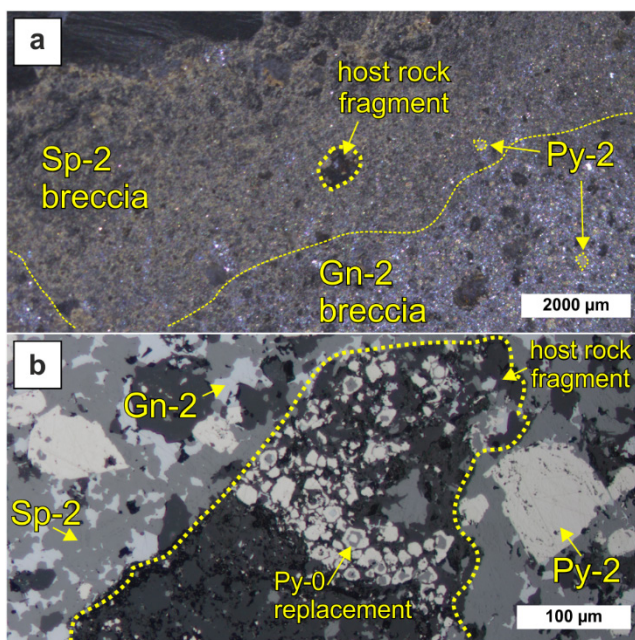


Figure 3. a) Binocular photomicrograph image of ore stage 2, comprising a typical high-grade George Fisher Sp-2- and Gn-2-ore breccia with Py-2 and host rock fragments; b) reflected light photomicrograph image of Gn-2, Sp-2, Py-2 and Py-0 in a host rock fragment; note that Py-0 was selectively replaced by Sp-2 and Gn-2.

4.2 Sulphur isotope composition of pyrite ($\delta^{34}\text{S}$)

The $\delta^{34}\text{S}$ values of 643 analyses of pyrite from George Fisher and the background Urquhart Shale are shown in Figure 4.

The $\delta^{34}\text{S}$ values of pyrite at George Fisher are distributed between -8.1 and +33.9 ‰ (n = 446; Fig. 4a). Py-0a and Py-0b preserve $\delta^{34}\text{S}$ values of -8.1 to +2.7 ‰ (n = 116) and -4.1 to +5.4 ‰ (n = 44) respectively. Ore stage pyrite has $\delta^{34}\text{S}$ values from +7.8 to +33.3 ‰ (Py-1; n = 76), +1.9 to +12.5 ‰ (Py-2; n = 154) and +23.4 to +28.2 ‰ (Py-3; n = 38). The $\delta^{34}\text{S}$ values of Py-euh are distributed between +7.2 and +33.9 ‰ (n = 18).

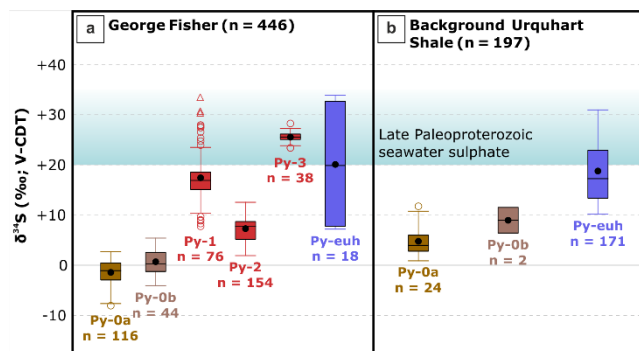


Figure 4. $\delta^{34}\text{S}$ (‰; V-CDT) values of pyrite (Py-0a, Py-0b, Py-1, Py-2, Py-3 and Py-euh) from George Fisher (a) and from background Urquhart Shale (b); note approximate $\delta^{34}\text{S}_{\text{seawater}}$ values of ≥ 20 ‰ derived from Strauss (1993), Gellatly and Lyons (2005) and Li et al. (2015).

The $\delta^{34}\text{S}$ values of pyrite in the background lithologies are distributed between +1.0 and +31.0 ‰ (n = 197; Fig. 4b). Pyrite-0a and Py-0b preserve $\delta^{34}\text{S}$ values of +1.0 to

+11.8 ‰ (n = 24) and +6.5 to +11.6 ‰ (n = 2) respectively. Py-euh preserves $\delta^{34}\text{S}$ values of +10.3 to +31.0 ‰ (n = 171).

5 Discussion

5.1 Pre-ore pyrite

At George Fisher, Py-0 is clearly overgrown or replaced (Fig. 3) by ore stage sulphides. Similarities in the morphology of Py-0, in mineralised and un-mineralised samples, provide good evidence that Py-0 formed in a pre-ore environment. Indeed, similar fine-grained pyrite is a feature of a number of other carbonaceous mudstones of Proterozoic age (e.g. Schieber 1989).

During anoxic diagenesis in marine sediments, there are 2 main pathways by which seawater sulphate is biologically reduced to sulphide (Jørgensen and Kasten 2006): (1) MSR and (2) SD-AOM. The resulting hydrogen sulphide reacts with reactive Fe to precipitate diagenetic pyrite (Sweeney and Kaplan 1973). Hydrogen sulphide produced by MSR is typically associated with a large kinetic fractionation from coeval seawater (e.g. Kaplan and Rittenberg 1964), meaning pyrite preserves $\delta^{34}\text{S}$ values that are considerably offset from seawater sulphate ($\Delta^{34}\text{S} = \delta^{34}\text{S}_{\text{seawater}} - \delta^{34}\text{S}_{\text{pyrite}}$). In Figure 4, $\delta^{34}\text{S}_{\text{Py-0a}}$ values preserve a large offset from Paleoproterozoic seawater, which is indicative of open system conditions where sulphate is not completely consumed.

More positive $\delta^{34}\text{S}$ values are indicative of more sulphate-limited conditions. Such conditions can occur due to consumption of sulphate by MSR followed by SD-AOM in diagenetic pore fluids (e.g. Magnall et al. 2016). This may be the case for slightly more positive $\delta^{34}\text{S}$ values in Py-0b, which is morphologically similar to euhedral overgrowths of fine-grained pyrite formed in modern marine sediments (Lin et al. 2016). Importantly, the lack of highly positive $\delta^{34}\text{S}_{\text{Py-0}}$ values shows that pyrite did not form under highly sulphate-limited conditions in the Urquhart Shale, either in the un-mineralised or mineralised samples.

The pre-ore timing of Py-0 and the overlapping $\delta^{34}\text{S}_{\text{Py-0}}$ values between un-mineralised and mineralised samples (Fig. 4) provide evidence that MSR in relatively open system conditions resulted in extensive pyrite formation before the onset of hydrothermal activity.

5.2 Ore-stage pyrite

The $\delta^{34}\text{S}$ values of ore-stage pyrite are distinctly higher than $\delta^{34}\text{S}$ values of pre-ore pyrite (Fig. 4), providing evidence that ore stage sulphides were most likely formed from sulphur derived from a different process.

Given the availability of hydrocarbons and sulphate (either as SO_4^{2-} seawater or in sulphate mineral phases), TSR can produce hydrogen sulphide under hydrothermal conditions (Machel 2001). This process may result in a temperature-dependent fractionation of $\epsilon^{34}\text{S} \leq 20$ ‰ from the initial sulphate, combined with the alteration of organic matter (Machel et al. 1995). Such fractionation

effects may explain the $\delta^{34}\text{S}$ values preserved by the ore-stage pyrites (Py-1, Py-2, Py-3) and, indeed, maturation of hydrocarbons has been observed at George Fisher (Chapman 1999). Additionally, the broad distribution of $\delta^{34}\text{S}_{\text{Py-1}}$ values is similar to $\delta^{34}\text{S}$ values of H_2S produced by TSR in sour gas reservoirs (e.g. Cai et al. 2003), providing evidence that TSR may have resulted in the formation of reduced sulphur and in the alteration of hydrocarbons at George Fisher during the ore-forming event.

Moreover, recycling of reduced sulphur within high-grade ore zones has been interpreted to be an important process for sulphide formation for the CD-type deposits in the Mount Isa Inlier (e.g. Grondijs and Schouten 1937; Chapman 1999). Indeed, replacement textures of pre-ore Py-0 (Fig. 3) and intermediate $\delta^{34}\text{S}_{\text{Py-2}}$ values between those of Py-0 and Py-1 in ore-stage 2 (Py-2; Fig. 4) provide evidence for recycling of sulphur within ore breccias at the George Fisher deposit.

6 Conclusions

Reduced sulphur in pre-ore and ore-stage pyrite at George Fisher and in the Urquhart Shale was most likely produced by several sulphate reduction processes (MSR, SD-AOM, TSR), all of which, either directly or indirectly, can be linked to biological processes: MSR and SD-AOM are directly dependent on biological activity, whereas TSR requires the availability and maturation of organic matter. Altogether, therefore, high biological productivity was likely an important requirement for the generation of reduced sulphur, and ultimately for ore formation, at the George Fisher deposit and throughout the Carpentaria Province.

Acknowledgements

We would like to thank the geology teams at Mount Isa Mines George Fisher operation and Mount Isa Mines Resource Development for the careful support during fieldwork and for access to the drill cores. Funding for this project was provided by a Helmholtz Rekrutierungsinitiative grant given to S. Gleeson. Furthermore, we acknowledge U. Dittmann and E. Lewerenz for sample preparation, O. Appelt, S. Mayanna, I. Schöppan and F. Wilke for assistance with backscatter electron imaging and F. Couffignal and M. Wiedenbeck for the analyses in the SIMS laboratory at GFZ Potsdam.

References

Broadbent GC, Myers RE, Wright JV (1998) Geology and Origin of Shale-Hosted Zn-Pb-Ag Mineralization at the Century Deposit, Northwest Queensland, Australia. *Econ Geol* 93:1264–1294.

Cai C, Worden RH, Bottrell SH, Wang L, Yang C (2003) Thermochemical sulphate reduction and the generation of hydrogen sulphide and thiols (mercaptans) in Triassic carbonate reservoirs from the Sichuan Basin, China. *Chem Geol* 202:39–57.

Chapman LH (1999) Geology and genesis of the George Fisher Zn-Pb-Ag deposit, Mount Isa, Australia. Ph.D. thesis, James Cook University.

Chapman LH (2004) Geology and Mineralization Styles of the George Fisher Zn-Pb-Ag Deposit, Mount Isa, Australia. *Econ Geol* 99:233–255.

Eldridge CS, Williams N, Walshe JL (1993) Sulfur Isotope Variability in Sediment-Hosted Massive Sulfide Deposits as Determined Using the Ion Microprobe SHRIMP: II. A Study of the H.Y.C. Deposit at McArthur River, Northern Territory, Australia. *Econ Geol* 88:1–26.

Gellatly AM, Lyons TW (2005) Trace sulfate in mid-Proterozoic carbonates and the sulfur isotope record of biospheric evolution. *Geochim Cosmochim Acta* 69:3813–3829.

Gibson GM, Hutton LJ, Holzschuh J (2017) Basin inversion and supercontinent assembly as drivers of sediment-hosted Pb–Zn mineralization in the Mount Isa region, northern Australia. *J Geol Soc* 174:773–786.

Glikson M, Mastalerz M, Golding SD, McConachie BA (2000) Metallogenesis and hydrocarbon generation in northern Mount Isa basin, Australia. In: *Organic Matter and Mineralization*:149–184.

Grondijs HF, Schouten C (1937) A study of the Mount Isa Ores. *Econ Geol* 32: 402–450.

Ireland T, Large RR, McGoldrick PJ, Blake M (2004) Spatial Distribution Patterns of Sulfur Isotopes, Nodular Carbonate, and Ore Textures in the McArthur River (HYC) Zn-Pb-Ag Deposit, Northern Territory, Australia. *Econ Geol* 99:1687–1709.

Jørgensen BB, Kasten S (2006) Sulfur Cycling and Methane Oxidation. In: *Marine Geochemistry*:271–309.

Kaplan IR, Rittenberg SC (1964) Microbiological Fractionation of Sulphur Isotopes. *J gen Microbiol* 34:195–212.

Large RR, Bull SW, McGoldrick PJ, Walters S (2005) Stratiform and Strata-Bound Zn-Pb-Ag Deposits in Proterozoic Sedimentary Basins, Northern Australia. *Econ Geol* 100th Anniversary Volume:931–963.

Li C, Planavsky NJ, Love GD, Reinhard CT, Hardisty D, Feng L, Bates SM, Huang J, Zhang Q, Chu X, Lyons TW (2015) Marine redox conditions in the middle Proterozoic ocean and isotopic constraints on authigenic carbonate formation: Insights from the Chuanlinggou Formation, Yanshan Basin, North China. *Geochim Cosmochim Acta* 150:90–105.

Lin Z, Sun X, Peckmann J, Lu Y, Xu L, Strauss H, Zhou H, Gong J, Lu H, Teichert BMA (2016) How sulfate-driven anaerobic oxidation of methane affects the sulfur isotopic composition of pyrite: A SIMS study from the South China Sea. *Chem Geol* 440:26–41.

Machel HG (2001) Bacterial and thermochemical sulfate reduction in diagenetic settings - old and new insights. *Sed Geol* 140:143–175.

Machel HG, Krouse HR, Sassen R (1995) Products and distinguishing criteria of bacterial and thermochemical sulfate reduction. *Appl Geochem* 10:373–389.

Magnall JM, Gleeson SA, Stern RA, Newton RJ, Poulton SW, Paradis S (2016) Open system sulphate reduction in a diagenetic environment – Isotopic analysis of barite ($\delta^{34}\text{S}$ and $\delta^{18}\text{O}$) and pyrite ($\delta^{34}\text{S}$) from the Tom and Jason Late Devonian Zn–Pb–Ba deposits, Selwyn Basin, Canada. *Geochim Cosmochim Acta* 180:146–163.

Painter MGM, Golding SD, Hannan KW, Neudert MK (1999) Sedimentologic, Petrographic, and Sulfur Isotope Constraints on Fine-Grained Pyrite Formation at Mount Isa Mine and Environs, Northwest Queensland, Australia. *Econ Geol* 94:883–912.

Schieber J (1989) Pyrite mineralization in microbial mats from the mid-Proterozoic Newland Formation, Belt Supergroup, Montana, U.S.A.. *Sed Geol* 64:79–90.

Strauss H (1993) The sulfur isotope record of Precambrian sulfates: new data and a critical evaluation of the existing record. *Precam Res* 63:225–246.

Sweeney RE, Kaplan IR (1973) Pyrite Framboid Formation: Laboratory Synthesis and Marine Sediments. *Econ Geol* 68:618–634.

Biom mineralization in modern seafloor hydrothermal chimneys: implications for microbe-metal interactions in ancient VMS deposits

Si-Yu Hu, Stephen J. Barnes, Anais Pagès, Joanna Parr, Ray Binns
CSIRO Mineral Recourses

Kliti Grice
WA-OIGC, Curtin University

Abstract. Seafloor massive sulfide deposits are modern analogues of ancient VMS deposits, and are important hosts for macro- and microorganisms, which have been suggested to play a significant role in mineral deposition and metal cycling. In this study, we report a detailed study of biom mineralization in a seafloor hydrothermal chimney collected from the PACMANUS basin, Papua New Guinea. We have identified four types of sulfides deriving from various microbial activities, occurring in distinct zones of the chimney structure. The sphalerite-dominated transition zone contains filaments, which have been mineralized to dufrenoyite. These mineralized filaments are often found in close associations with realgar and are interpreted to be by-products of As-oxidizing microbial activity. The barite-dominated outer zone of the hydrothermal chimney is characterized by the occurrence of Pb- or As-mineralized fungi. The fungi are believed to produce Pb- and As-sulfides at the cell surface during detoxification processes when in contact with a Pb- or As-bearing hydrothermal fluid. Framboidal pyrite and sphalerite are present in Fe-Mn oxide zone, and may result from sulfate-reducing microbial activity. Those biologically-derived minerals can be as proxies for tracing microbe-metal interactions in ancient VMS deposits for recognition of ancient analogous VMS deposits.

1 Introduction

Hydrothermal venting systems have been discovered on the seafloor since 1979 (Corliss et al. 1979), and then gradually been found in various geological settings, i.e. mid-oceanic ridge of various spreading rates and back-arc basins (German and Seyfried 2014). Those hydrothermal vents are of high importance in the deep ocean as they continually discharge warm and metal-rich hydrothermal fluids into the seawater, providing key nutrients to living organisms (Holden et al. 2012). Previous studies of microbe-metal interactions in seafloor hydrothermal systems have generally focused on the characterization of the microorganisms thriving under such extreme conditions using genomics techniques, however, the minerals deriving from the activity of these micro-organisms have been rarely characterized. These modern hydrothermal systems are considered analogues to ancient VMS deposits, which are known to host evidences of early life (Rasmussen 2000). Therefore, the

detailed characterization of biom minerals in modern hydrothermal chimneys can provide significant insights into ancient metabolic processes and microbe-metal interactions in ancient ore deposits.

2 Geological setting

The Manus Basin is back-arc extension basin, located in the Bismarck Sea, Papua New Guinea (Fig. 1). A series of spreading centers and transform faults are developed in the basin due to the subduction of the Solomon plate into the Bismarck plate along the New Britain Trench. The Eastern Manus basin is the back-arc extension developed in the remnant island-arc crust which has formed during the previous subduction along the Manus Trench (Binns and Scott 1993). The eastern Manus volcanic zone is located between the Djuai and Weitin transform faults, and develops east-west *en echelon* neovolcanic ridges and domes (Binns et al. 2007). The volcanic edifices are in northeast direction, normal to the extension direction, and the composition varies from basalt to dacite-rhyodacite. The active volcanic activity has resulted in the occurrence of numerous hydrothermal fields, i.e. PACMANUS (Papua New Guinea -Australia-Canada-Manus Basin) (Binns, 2014), Desmos (Seewald et al. 2015) and SuSu Knolls (Yeats et al. 2014), and has produced a large number of Cu-Zn-Pb-Ag-Au rich seafloor deposits (Binns and Scott 1993; Yeats et al. 2014).

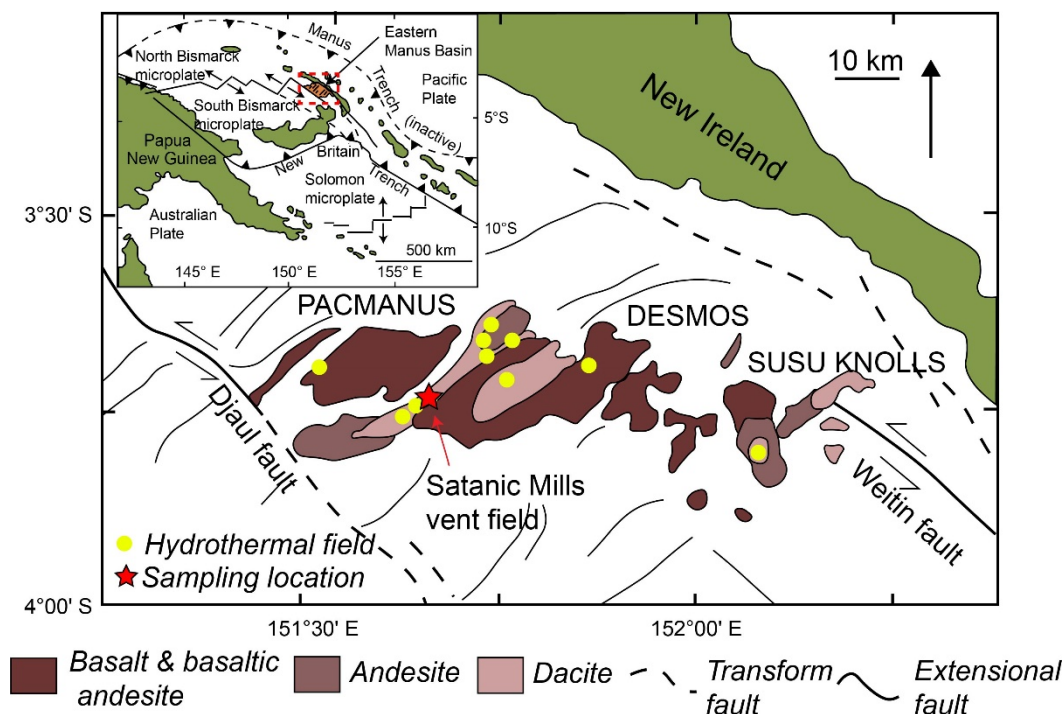


Figure 1. Geological setting of PACMANUS basin and sampling location. Modified from Binns et al. (2007).

3 Biomineralization within the chimney

3.1 Chimney description

This chimney sample (CSIRO ID: 118584) is a polymetallic sulfide chimney with multiple conduits (Fig. 2). It was collected by dredging from the Satanic Mills hydrothermal field (Fig. 1) (1,650 m below sea level). This sample includes distinct zones with a chalcopyrite-dominated zone in the center, a sphalerite-dominated transition zone, a sphalerite and barite-dominated outer zone, and a Fe-Mn oxide crust. The growth history of hydrothermal chimneys has been extensively studied and a variety of growth models have been proposed. Briefly, an initial porous wall with sulfate and fine-grained sulfides is formed during the initial mixing of hot hydrothermal fluids and cold seawater. During the continuous influx of hydrothermal fluids, sulfides and sulfates will fill in the porous wall and isolate hydrothermal fluids from seawater. Relatively high temperature sulfides (e.g. chalcopyrite) will be continually precipitated along the conduits when hot hydrothermal fluids pass through. When the hydrothermal activity weakens, low temperature minerals, such as realgar, galena and dufrenoyite (Pb-As sulfosalt), are precipitated within most of the zones and overgrow pre-existing sulfides. The unstable chimneys will collapse eventually and form the sulfide mounds which are important analogues of some ancient VMS deposits on land (Jamieson et al. 2013; Koski et al. 1994).

The aliquots were collected from various zones of the chimney sample, and prepared as polished thin sections. Optical microscopic observations, scanning electron microscopy (SEM), synchrotron x-ray fluorescence

microscopy (SXFEM) and transmission electron microscopy (TEM) were conducted to characterize the biominerals.

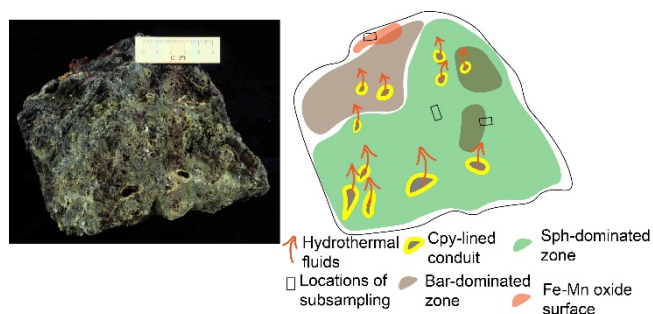


Figure 2. Photograph (left) and sketch diagram (right) of the chimney sample showing the distribution of chalcopyrite (Cpy), sphalerite (Sph), barite (Bar) and Fe-Mn oxide surface. The locations of sub-samples are indicated in the sketch diagram with rectangle boxes. Modified from Hu et al. 2019.

3.2 Biomineralization

Dufrenoyite mineralized filaments

Submicron-scale filaments, which have been mineralized into Pb-As sulfosalt (dufrenoyite), were observed mainly in the sphalerite-dominated zone (Fig. 3). They are observed in close associations with realgar (As_4S_4), reflecting mixing of hydrothermal fluids and seawater. Individual filaments present a dufrenoyite-dominated core and an organic-rich shell with high concentrations of carbon, nitrogen and phosphorus. We interpret the Pb-As rich filaments to be by-products of microbial metabolism, resulting from a detoxification strategy of As-oxidizing microorganisms exposed to warm Pb- and As-rich hydrothermal fluids during chimney growth.

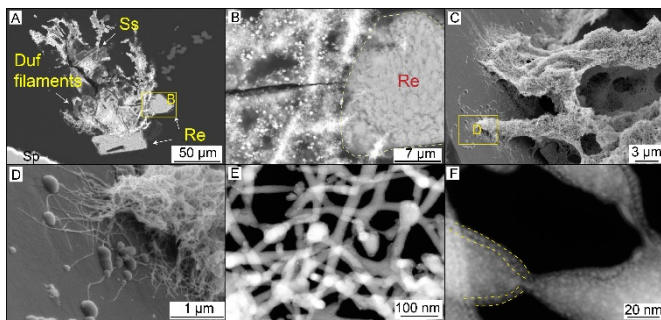


Figure 3. The features of dufrenoyite (Duf)-mineralized filaments. (A, B) SEM-BSE images showing the filaments intergrown with realgar (Re) in the vicinity of sphalerite (Sp). (C, D) SEM-SEM images of the filaments attached to barite surface and deposited by silica spheres (Ss). (E, F) STEM dark field images of a detailed observation of filaments. In (F), the filaments have a dense core with Pb, As and S (shown as relative bright) and lighter shell with C, N and P signatures (outlined with yellow dotted lines).

As- and Pb-mineralized fungi

A cluster of larger filaments (>10s microns) was observed in sphalerite and barite-dominated outer zone (Fig. 4). Individual filaments are larger than the sulfosalt-mineralized filaments mentioned above. These filaments are found in the cavities of sphalerite and barite. The filaments show morphological similarity to fungi in optical microscopic observation. In addition, SXFM elemental maps show that these filaments are enriched either in Pb or As, but not both. It is interpreted that when Pb- and As-rich hydrothermal fluids came in contact with fungi, Pb and As-rich sulfides accumulated at the surface of cells as the result of a fungal detoxification process. It is assumed that the cells would have died after being fully covered by sulfides.

Framboidal pyrite and sphalerite

A large quantity of framboidal pyrite and sphalerite were observed in the Fe-Mn oxide crust (Fig. 5). The cluster of pyrite is compact and occurs on the surface of the crust, whereas sphalerite is fine-grained and disseminated within what we interpret as biofilms in the outer part and within the crust. Sulfate-reducing microbes, which can produce fine-grained pyrite and sphalerite with such textures (Hu et al. 2018), have been extensively found in the outer zone of chimney structures (Nakagawa et al. 2004). Therefore, these pyrite and sphalerite framboids are likely reflecting the activity of sulfate-reducing microbes in this system.

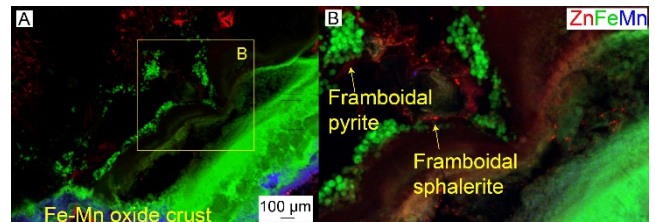


Figure 5. SXFM elemental maps. (A) Zn-Fe-Mn map showing the distribution of pyrite and sphalerite within the crust; (B) High magnification image of framboidal pyrite (green) and sphalerite (red).

4 Implications for ancient VMS deposits

Ancient VMS deposits are of high interest for early life studies (Rasmussen 2000). In the present study, various biominerals were observed in distinct areas of the hydrothermal chimney, from the sphalerite-dominated zones to the Fe-Mn oxide crust. From these results, it is inferred that microbial activity is strongly involved in the cycling of at least four key elements (As, Pb, Fe and Zn).

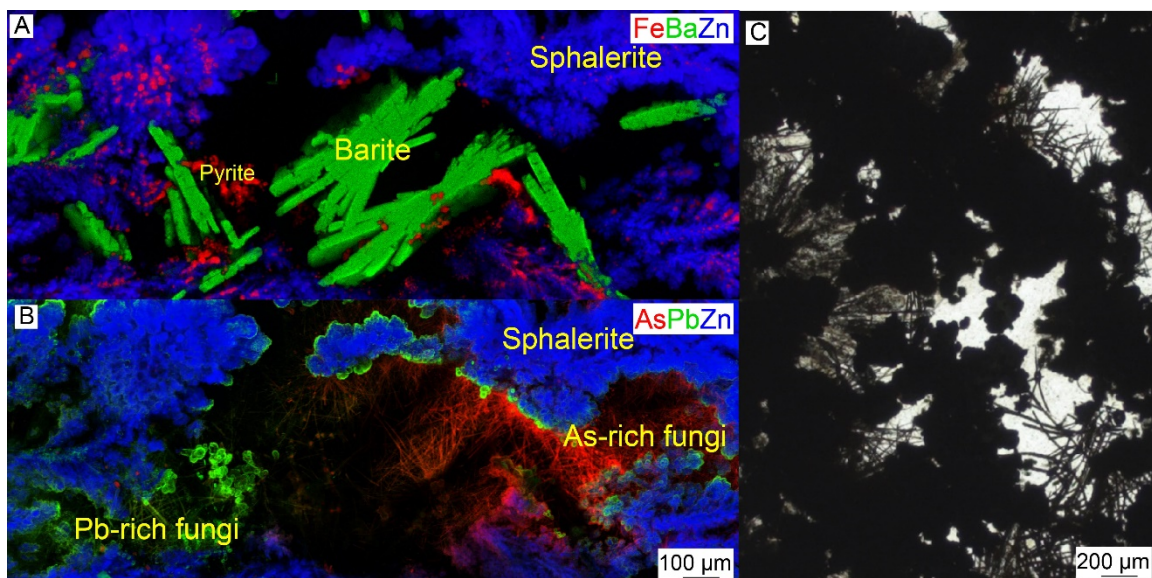


Figure 4. (A, B) SXFM elemental maps. (A) Fe-Ba-Zn map showing the distribution of pyrite, sphalerite and barite; (B) As-Pb-Zn map showing the distribution of As- and Pb-rich fungi in red and green respectively within the cavities of sphalerite and barite. (C) Optic microscopical image of the fungi in the cavities of sphalerite.

It is notable that As and Pb-based microbial activities have rarely been reported in hydrothermal chimneys. Arsenic has been suggested to be a driving factor in the origin of life (Kulp 2014). Therefore, the detection of As-related microbial metabolism in the modern hydrothermal chimneys of PACMANUS could shed light on As-based metabolism on primordial Earth.

Additionally, previous reports generally focused on studying the genomes of the microbial ecosystems present in hydrothermal chimneys, but did not make the link between the precipitation of minerals and microbial activities. In the present study, the observed biominerals have the potential to be used as proxies to trace early life signatures in VMS deposits. Their biologically-mediated origin can provide insights into the microbe-metal interactions occurring during the formation of ancient deposits. Meanwhile, the unique microbe-metal, mineral and structural associations in the hydrothermal chimneys of modern seafloor massive sulfide deposits may be of use to mineral exploration to recognise analogous ancient VMS deposits.

Acknowledgements

The authors would like to acknowledge the support for SXFM work, which was undertaken on the X-ray fluorescence microscopy beamline at the Australian Synchrotron (Proposal 12589), part of Australia's Nuclear Science and Technology Organisation (ANSTO). Dr Chris Ryan and Dr David Paterson are acknowledged for the assistance during data collection. S.H. and S.B. acknowledges the Research-plus postdoctoral fellowship funded by the Commonwealth Science and Industry Research Organization (CSIRO).

References

- Binns RA (2014) Bikpela: A large siliceous chimney from the PACMANUS hydrothermal field, Manus basin, Papua New Guinea. *Econ Geol* 109:2243–2259.
- Binns RA, Barriga FJ, Miller DJ (2007) Leg 193 Synthesis: Anatomy of an active felsic-hosted hydrothermal system, Eastern Manus Basin, Papua New Guinea. *Proc Ocean Drill Program, Sci Results* 193:1–71.
- Binns RA, Scott SD (1993) Actively forming polymetallic sulfide deposits associated with felsic volcanic rocks in the Eastern Manus Back-Arc Basin, Papua New Guinea. *Econ Geol* 88:2226–2236.
- Corliss JB, Dymond J, Gordon LI, Edmond JM, von Herzen RP, Ballard RD, Green K, Williams D, Bainbridge A, Crane K, van Andel TH (1979) Submarine Thermal Springs on the Galápagos Rift. *Science* 203:1073–1083.
- German CR, Seyfried WE (2014) *Hydrothermal Processes*. 2nd ed., Elsevier Ltd.
- Holden J, Breier J, Rogers K, Schulte M, Toner B (2012) Biogeochemical Processes at Hydrothermal Vents: Microbes and Minerals, Bioenergetics, and Carbon Fluxes. *Oceanography* 25:196–208.
- Hu SY, Barnes SJ, Glenn AM, Pagès A, Parr J, MacRae C, Binns R (2019) Growth History of Sphalerite in a Modern Sea Floor Hydrothermal Chimney Revealed by Electron Backscattered Diffraction. *Econ Geol* 114: 165–176.
- Hu SY, Evans K, Rempel K, Guagliardo P, Kilburn M, Craw D, Grice K, Dick J (2018) Sequestration of Zn into mixed pyrite-zinc sulfide framboids: A key to Zn cycling in the ocean? *Geochim Cosmochim Acta* 241:95–107.
- Jamieson JW, Wing BA, Farquhar J, Hannington MD (2013) Neoproterozoic seawater sulphate concentrations from sulphur isotopes in massive sulphide ore. *Nat Geosci* 6:61–64.
- Koski RA, Jonasson IR, Kadko DC, Smith VK, Wong FL (1994) Compositions, growth mechanisms, and temporal relations of hydrothermal sulfide-sulfate-silica chimneys at the northern Cleft segment, Juan de Fuca Ridge. *J Geophys Res* 99:4813–4832.
- Kulp T R (2014) Early earth: Arsenic and primordial life. *Nat Geosci* 7: 785–786.
- Martin W, Baross J, Kelley D, Russell MJ (2008) Hydrothermal vents and the origin of life. *Nat Rev Microbiol* 6:805–814.
- Nakagawa T, Nakagawa S, Inagaki F, Takai K, Horikoshi K (2004) Phylogenetic diversity of sulfate-reducing prokaryotes in active deep-sea hydrothermal vent chimney structures. *FEMS Microbiol Lett* 232:145–152.
- Rasmussen B (2000) Filamentous microfossils in a 3,235-million-year-old volcanogenic massive sulphide deposit. *Nature* 405:676–679.
- Seewald JS, Reeves EP, Bach W, Saccocia PJ, Craddock PR, Shanks WC, Sylva SP, Pichler T, Rosner M, Walsh E (2015) Submarine venting of magmatic volatiles in the Eastern Manus Basin, Papua New Guinea. *Geochim Cosmochim Acta* 163:178–199.
- Yeats CJ, Parr JM, Binns RA, Gemmill JB, Scott SD (2014) The SuSu Knolls hydrothermal field, Eastern Manus Basin, Papua New Guinea: An actively forming submarine high sulfidation copper-gold system. *Econ Geol* 109:2207–2226.

How long does it take to form a sediment hosted Zn+Pb deposit?

Gary Mullen

University of Glasgow

Craig Barrie

GeoMark Research

Adrian Boyce, Drew Drummond

Scottish Universities Environmental Research Centre

Abstract. Sediment hosted Zn+Pb sulphide deposits are the primary source of global lead and zinc. Their secular distribution is well defined, however the duration of individual mineralisation events is less so. By coupling modern H₂S production data from sedimentary/hydrothermal environments and metalliferous fluid flux calculations with data on the size concentration and distribution of the world class Navan Zn-Pb deposit in Ireland, it is postulated that the deposit could have formed within a relatively rapid, integrated timeframe of ~26,000 years. Ore fluid influx, driven by convection and seismicity, is assumed to be the most limiting factor. In this study, bacteriogenic sulphide availability is not considered to be a limiting factor.

1 Introduction

Massive Zn+Pb sulfide ore deposits, formed via the migration of metal-rich fluids into sedimentary basins, are a major resource. Literature discussing the genesis of these deposits is extensive (e.g. Anderson et al 1998; Garven et al 2002; Sangster 2002; Wilkinson et al 2005 etc.), but few consider the time required to deposit these ores (Converse et al 1984; Schardt and Large, 2009). Many estimates of timescales are ambiguous implying 'prolonged' or 'geologic' time-spans; and this reasonably reflects the general view. This lack of detail is unsurprising, as regardless of ore deposits origins, there are rarely markers preserved indicative of mineralization durations, and when examined in detail, the complexity of ores ensures that it is difficult to determine how many events contributed to total ore accumulation (Barrie et al 2009).

In simple terms four principal components are needed to generate massive sulfides: a source of sulfur, a source of metals, a fluid to transport the metals and a flow path to bring these elements together. Both efficiency and preservation potential must also be considered. A number of studies allow reasonable estimates of these essential variables (e.g. Rickard 1973; Wortmann et al 2001, 2007; Oliver 2001; Weber and Jorgensen 2002; Wilkinson et al 2009). In our calculations of ore event history timescales, we use the giant Navan Zn-Pb deposit in Ireland (Ashton et al 2010), as it is well researched and understood geologically, and allows us to blend published data on fluid metal concentrations, bacterial sulfide

production from modern and ancient analogs with models of integrated fluid flow to provide geologically realistic estimates. What emerges is that it may take a surprisingly short integrated period of influx, perhaps as quick as a few hundred or thousand years, to deliver and preserve more than 9.6 Mt of Zn and 2.4 Mt of Pb at Navan.

2 Geological Setting

The giant, world-class Navan Zn+Pb deposit is the largest Zn mine in Europe with in excess of 120 M tonnes grading ~8.1% Zn and ~2% Pb (Ashton et al 2010). The deposit forms an elongate, NE-trending ellipsoid which dips ~15° to the SW at the surface and flattens out at depth, and comprises stratabound sulfide lenses, hosted within Lower Carboniferous shallow water carbonates of the Dublin Basin (Fig. 1; Anderson et al 1998). The total area of the ore deposit covers approximately 5km x 1.2km with an average thickness of ~10m.

Mineralisation is dominated by sphalerite (ZnS) and galena (PbS) with lesser pyrite (FeS₂) and other sulfides and gangue mineral phases. Faulting exerts the major control on the disposition of ore, but distribution does not appear to be governed by a single structure (Blakeman et al., 2002). The deposit is instead spatially associated with several major ENE-trending extensional faults (Fig. 1), and areas of high Zn-Pb distribution in the main orebody clearly parallel NE-SW structural trends and are coincident with major faults or localized zones of minor extensional fracturing (Ashton et al 2010). Metal-rich fluid from depth utilized this complex fault network, and the inherent fracture-related permeability, to migrate into the host carbonates where it mixes with surface brines, enriched in H₂S derived from bacteriogenic reduction of seawater sulfate to generate mineralization (e.g. Anderson et al 1998; Fallick et al 2001; Blakeman et al 2002; Everett et al 2003). The exhalation of a metal-bearing brine towards the earth surface through complex fracture pathways is typical in all sediment-hosted sulfide deposits, as is the concept of mixing to cause ore deposition (McGowan et al 2003; Robb, 2005). In the case of the Irish deposits, there is clear evidence that this mixing took place close to, or certainly within a few 10's of meters (Wilkinson et al 2003) of the Lower Carboniferous seafloor: the involvement of fluids containing bacteriogenic sulfide produced in a system

open to seawater sulfate necessitates this (Anderson et al 1998; Fallick et al 2001; Wilkinson et al 2005b).

3 Developing the model

What are the rates and behaviour of comparable modern-day sedimentary shelves and hydrothermal mineralizing systems that can apply to developing a model for the timing of ore deposition at Navan?

3.1 H₂S Production in Modern Marine Settings

Navan formed in shallow water carbonate sequences, influenced by hydrothermal activity, where ~90% of the sulphide produced was bacteriogenic in origin (Fallick et al 2001). Modern sedimentary/hydrothermal environments can contain highly elevated concentrations of H₂S, such as the Australian bight with ~9000 nmol/l (Wortman et al 2001) and H₂S production rates of 3350 nmol cm⁻³ d⁻¹. The dominant control on production rates appears to be temperature (Weber and Jorgensen 2002).

3.2 Metal enrichment

The source of metals at Navan is the lower Palaeozoic basement lithologies (Everett 2003) Dissolved metal concentrations at Navan are not well defined; gangue minerals such as quartz record 3.6 - 26 ppm while sulphide minerals suggest 22 - 890 ppm Pb and 5000 ppm Zn (Wilkinson 2009).

3.3 Integrated flow dynamics

The main orebody at Navan is within a fractured/faulted relay ramp system, bounded to the NW and SE by major extensional faults. This fractured, permeable system would have facilitated the vertical migration of metal rich fluids and mixing with a cooler, more saline, sulphide rich brine (Blakeman 2002; Freeman and Everett 2000). Velocity: Modern flow rates at hydrothermal vents are recorded as being between 70 - 240 cm/s (Converse 1984), similar to the 100 - 200 cm/s for seafloor hydrothermal discharge (Schardt and Large 2009). Fluid velocities are dependent on several factors including exit temperature e.g. black smokers >180°C = > 150 cm/s (Converse et al 1984) and high salinity, which has been found to increase flow velocities by an order of magnitude (Koziy et al 2009, Yang 2006). Temperatures at Navan were in the region of 140-210°C and salinity at upto 26 wt% (Ashton et al 2015), suggesting relatively high velocity. However, in order to model mineralisation, you not only need to know fluid flow rates, but also the 'integrated area of influx' through which the metal-rich fluid enters the H₂S saturated host rocks. The larger the area of influx, assuming H₂S and metal concentrations are not limiting, the faster the rate of economic mineralization.

4 Modelling mineralisation at Navan

To understand potential timescales of mineralization in

ore deposits unavoidable assumptions about the conditions prevalent during mineralization need to be made. This includes estimating average rates of H₂S production, metal influx and concentration as well as behaviour and distribution of the ore and host rocks (e.g. Blakeman et al., 2002; Fallick et al., 2001; Wilkinson et al., 2009; Wortmann et al., 2001; Wilkinson, 2001; Weber and Jorgensen, 2002; Converse et al., 1984; Schardt and Large, 2009). The timescale defined by our model will be a minimum value that assumes continuous mineralization at conservative conditions. However, mineralizing systems switch on and off with 'pulses' of activity followed by hiatuses (e.g. Barrie et al., 2009) therefore, the 'lifetime' of ore genesis may in actuality be much longer than the actual timescale of mineralization. Due to the complexity of mineralization processes and the disrupted, chaotic and often superimposed nature of ore at Navan (Anderson et al., 1998) our results should be considered as a guide to understanding potential timescales of mineralization and not the definitive answer.

4.1 H₂S production potential at Navan

Current estimates of ore at the main orebody/SWEX are in the region of 120 Mt, with grades ~8% Zn and ~2% Pb (Ashton et al 2015). So, it can therefore be estimated that a minimum of ~3.5 Mt (3,476,888) of S must exist at Navan, in both sphalerite and galena (without accounting for the S in pyrite). The deposit has been shown to contain ~ 90% bacteriogenic sulphur (Fallick et al 2001), which equates to a minimum of 3,131,899 tonnes or 9.67 x 10¹⁰ moles of S. If these values are coupled with the volume of the ore at Navan (5 km x 1.2 km x 10 m) and H₂S production rates in sedimentary hydrothermal settings (e.g. Weber and Jorgensen 2001) then estimates can be made as to the length of the time required to form the orebody; assuming unlimited and constant metal input (Table 1)

Table 1. Table summarising the total time taken to generate sufficient H₂S for mineralization of the total volume of bacteriogenic ore at the Navan Zn-Pb Mine, Ireland. Variations in timescale reflect differing potential H₂S production rates.

Volume of Ore (cm ³)	H ₂ S Production Rate (nmol cm ⁻³ d ⁻¹)	Moles of S (cm ³ y ⁻¹)	Total time (years)
1E+14	3350	1.22E-03	0.79
1E+14	1500	5.48E-04	1.77
1E+14	200	7.30E-05	13
1E+14	12	4.38E-06	221
1E+14	1	3.65E-07	2,649
1E+14	0.1	3.65E-08	26,491

Geologically, these timescales are exceptionally short and while the calculations are essential in understanding timescales of H₂S production at Navan they assume an unrealistic situation. For this scenario to be representative of ore mineralization at Navan then supply of metals would have to be unlimited, while the integrated area of influx would need to be equal to the volume of ore.

4.2 Metal enrichment and fluid dynamics at Navan

Based upon the average grade of Zn (~8%) and Pb (~2%) at Navan and the total tonnage it can be estimated that there are 9.6 Mt of Zn and 2.4 Mt of Pb in the Navan

deposit (e.g. Blakeman et al 2002; Fallick et al 2001). To calculate how long it would take to generate this quantity of metals three variables need to be estimated:

(1) The concentration of dissolved metals in the hydrothermal ore fluid; set at 100 ppm Zn and 25 ppm Pb, based on the 4:1 ratio found at Navan and a conservative approximation of the data recorded by Wilkinson et al (2009)

(2) The rate at which the ore fluid is transported through fault conduits; set at 100 cm/s for an ore fluid of 180-200°C (Converse et al 1984)

(3) The 'integrated area of influx' by which the metal-rich fluid enters the H₂S rich host sediments.

The 'integrated area of influx' across which the ore fluid enters the host rocks is a major control on the timing of mineralization. Our model assumes an area of 1km x 10cm is available for this influx and considering the abundance of faulting at Navan this is again considered a conservative estimate Utilising these variables and an average ore fluid density of 0.95 (Wilkinson 2001) then it is possible to calculate the mass flow of the ore fluid into the carbonate host rocks using the formula:

$$(1) \dot{m} = rva$$

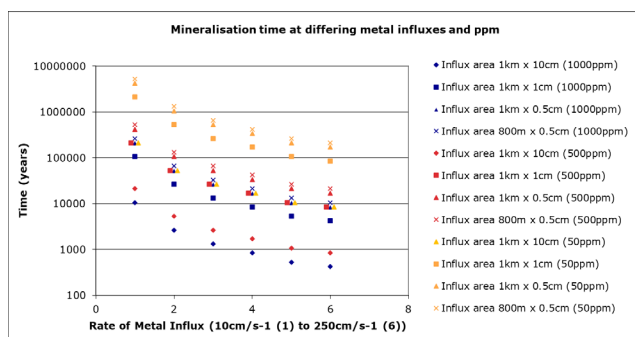
whereby \dot{m} = mass flow, r = ore fluid density, v = ore fluid velocity and a = integrated area of influx. Assuming a concentration of 100ppm Zn/25ppm Pb, a flow rate of 100cm/s and an influx area of 1,000,000 cm² then it would take 11,700 years to transport sufficient metals into the host rocks to form the Navan Zn-Pb Ore deposit. However, this timescale makes two big assumptions:

(1) The efficiency of sub-seafloor mineralization processes was 100% with no ore fluid and thus, dissolved metal escaping onto the seafloor and,

(2) The preservation of the ore deposit since formation has been 100%.

While it could be argued that the latter preservation potential, based upon the largely sub-seafloor nature of ore mineralization, may be a close representation of the situation at Navan, the former is unlikely. However, if mineralization efficiency is assumed to be, on average, 50% and preservation potential 90%, then even with an exceptionally low H₂S production rate of 0.1 nmol cm⁻³, it would take 26,000 years to generate the giant Navan Zn-Pb ore deposit (Table 1, 2). The authors consider all of the values used to calculate this timescale, to be a conservative representation of the conditions prevalent during genesis at Navan. If, however, you increase dissolved Zn concentration up to 1000ppm at flow rates of 100-200cm/s then ore mineralization will be completed in a few thousand years or only a few hundred if the maximum concentrations (5000ppm Zn) are considered viable during fluid pulses (Table 2).

Table 2. Table summarising the total time taken to generate and transport sufficient metals for mineralisation of the total volume of ore at the Navan Zn-Pb Mine, Ireland. Area of Influx, mineralisation efficiency and ore preservation potential all remain the same. Variations in timescale reflect differing metal-rich fluid flow rates and the concentration of dissolved metals.



5 Inhibition

While not addressed here, various recent studies have found the activity and growth of sulphate reducing bacteria, which are necessary for sulphide production, to be inhibited by high concentrations of sulphate, sulphide and metals (Azabou et al 2006, Cassidy et al 2015, Al Zuhair 2008, Kiran et al 2017). For example, toxic concentrations of Zn have been found at 150ppm (Azabou et al 2006) 13-40ppm (Kiran et al 2017) and 25 ppm (Morton et al 1991). The degree of inhibition appears to be genera specific. Therefore, any future calculations must account for the limiting nature of high metal and sulphide concentrations.

6 Summary

Based upon estimates of analogous conditions in the literature we propose that the integrated timescale for total economic ore mineralisation at Navan could have been completed in ~26,000 years. While this timescale may seem geologically short, it is similar to that proposed for other giant Zn deposits by Schardt and Large (2009) and also represents the timescale for total mineralization not for the lifetime of the deposit as a whole, which may in fact be much longer.

This study has two important conclusions: firstly, that H₂S production is unlikely to be a limiting factor in sulfide mineral genesis and secondly that the idea of 'prolonged' mineralization timescales for ore deposits is not based upon fact.

References

- Al-Zuhair, S., El-Nass, M., H., & Al-Hassani, H. (2008). Sulfate inhibition effect on sulfate reducing bacteria. *J Biochem Tech*, 1(2):39-44.
- Anderson, I.K., Ashton, J.H., Boyce, A.J., Fallick, A.E., and Russell, M.J., 1998, Ore depositional processes in the Navan Zn-Pb deposit, Ireland: *Economic Geology*, 93:535-563.
- Ashton, J.H., Blakeman, R., Geraghty, J., Beach, A., Collier, D., Philcox, M.E., Boyce, A.J. and Wilkinson, J.J., 2010, The Giant Navan Carbonate-Hosted Zn-Pb Deposit – A Review. *ZINC 2010 Extended Abstracts Volume*, Irish Association for Economic Geology, p. 97-102.
- Ashton, J. H., Blakeman, R. J., Geraghty, J. F., Beach, A., Collier, D., Philcox, M. E., Boyce, A. J., Wilkinson, J. J. (2015). The giant Navan Carbonate-hosted Zn-Pb deposit: a review. *Irish Association of Economic Geology*.
- Azabou, S., Mechichi, T., & Sayadi, S. (2007). Zinc precipitation by heavy-metal tolerant sulfate-reducing bacteria enriched on

- phosphogypsum as a sulfate source. *Minerals Engineering*, 20(2), 173-178. doi:10.1016/j.mineng.2006.08.008
- Barrie, C. D., Boyce, A. J., Boyle, A. P., Williams, P. J., Blake, K., Wilkinson, J. J., . . . Prior, D. J. (2009). On the growth of colloform textures: a case study of sphalerite from the Galmoy ore body, Ireland. *Journal of the Geological Society*, 166(3):563-582. doi:10.1144/0016-76492008-080
- Blakeman, R., Ashton, J.H., Boyce, A.J., Fallick, A.E., and Russell, M.J., 2002, Timing of interplay between hydrothermal and surface fluids in the Navan Zn+Pb orebody, Ireland: Evidence from metal distribution trends, mineral textures and $\delta^{34}\text{S}$ analyses: *Economic Geology*, 97:73-91.
- Cassidy, J., Lubberding, H. J., Esposito, G., Keesman, K. J., & Lens, P. N. (2015). Automated biological sulphate reduction: a review on mathematical models, monitoring and bioprocess control. *FEMS Microbiol Rev*, 39(6):823-853.
- Converse, D.R., Holland, H.D., and Edmond, J.M., 1984, Flow rates in the axial hot springs of the East Pacific Rise (21° N): implications for the heat budget and the formation of massive sulfide deposits: *Earth and Planetary Science Letters*, 69:159-175.
- Everett, C.E., Rye, D.M., and Ellam, R.M., 2003, Source or sink? An assessment of the role of the Old Red Sandstone in the genesis of the Irish Zn-Pb deposits: *Economic Geology*, 98:31-50.
- Fallick, A.E., Ashton, J.H., Boyce, A.J., Ellam, R.M., and Russell, M.J., 2001, Bacteria were responsible for the magnitude of the world-class hydrothermal base metal sulfide orebody at Navan, Ireland: *Economic Geology*, 96:885-890.
- Freeman, S.R., and Everett, C.E., 2000, Basement fault controls on carbonate hosted Zn-Pb mineralisation at Navan, Ireland, *GSA Annual Meeting: Reno, Nevada*.
- Garven, G., Bull, S.W., and Large, R.R., 2002, Hydrothermal fluid flow models of stratiform ore genesis in the McArthur Basin, Northern Territory, Australia: *Geofluids*, 1:289-311.
- Kiran, M. G., Pakshirajan, K., & Das, G. (2017). Heavy metal removal from multicomponent system by sulfate reducing bacteria: Mechanism and cell surface characterization. *Journal of hazardous materials*, 324:62-70.
- Koziy, L., Large, R., Bull, S., Selley, D., & Yang, J. (2006). Numerical modelling of the ore forming fluid migration in the sediment-hosted stratiform copper deposit, Zambian Copperbelt. *ASEG Extended Abstracts*, 2006(1):1-6.
- McGowan, R., Roberts, S., Foster, R.P., Boyce, A.J., and Collier, D., 2003, Origin of the copper-cobalt deposits of the Zambia Copperbelt: an epigenetic view from Nchanga: *Geology*, 31:497-500.
- Morton, R. L., Yanko, W. A., Graham, D. W., & Arnold, R. G. (1991). Relationships between metal concentrations and crown corrosion in Los Angeles County sewers. *Research journal of the water pollution control federation*, 789-798.
- Rickard, D., 1973, Limiting Conditions for Syndimentary Sulfide Ore Formation: *Economic Geology*, v. 68, p. 605-617.
- Robb, L.J., 2005, Introduction to ore-forming processes, Wiley-Blackwell, 373 p.
- Sangster, D.F., 2002, The role of dense brines in the formation of vent-distal sedimentary-exhalative (SEDEX) lead-zinc deposits: field and laboratory evidence: *Mineralium Deposita*, 37:149-157.
- Schard, C., and Large, R.R., 2009, New insights into the genesis of volcanic-hosted massive sulfide deposits on the seafloor from numerical modeling studies: *Ore Geology Reviews*, 35:333-351.
- Southgate, P.N., Kyser, T.K., Scott, D.L., Large, R.R., Golding, S.D., and Polito, P.A., 2006, A Basin System and Fluid-Flow Analysis of the Zn-Pb-Ag Mount Isa-Type Deposits of Northern Australia: Identifying Metal Source, Basinal Brine Reservoirs, Times of Fluid Expulsion, and Organic Matter Reactions: *Economic Geology*, 101:1103-1115.
- Weber, A., and Jorgensen, B.B., 2002, Bacterial sulfate reduction in hydrothermal sediments of the Guaymas Basin, Gulf of California, Mexico: *Deep-Sea Research I*, v. 49, p. 827-841.
- Wilkinson, J.J., 2001, Fluid inclusions in hydrothermal ore deposits: *LITHOS*, 55:229 - 272.
- Wilkinson, J.J., Boyce, A.J., Everett, C.E., and Lee, M.J., 2003, Timing and depth of mineralization in the Irish Zn-Pb orefield, in Kelly, J.G., Andrew, C.J., Ashton, J.H., Boland, M.B., Earls, G., Fusciardi, L., and Stanley, G., eds., *Europes major base-metal deposits: Dublin, Irish Association for Economic Geology*, p. 483-497.
- Wilkinson, J.J., Eyre, S.L., and Boyce, A.J., 2005a, Ore-forming processes in Irish-type carbonate-hosted Zn-Pb deposits: Evidence from mineralogy, chemistry, and isotopic composition of sulfides at the Lisheen Mine: *Economic Geology*, 100:63-86.
- Wilkinson, J.J., Everett, C.E., Boyce, A.J., Gleeson, S.A., and Rye, D.M., 2005, Intracratonic crustal seawater circulation and the genesis of subseafloor zinc-lead mineralization in the Irish orefield: *Geology*, 33: 805-808.
- Wilkinson, J.J., Stofell, B., Wilkinson, C.C., Jeffroes, T.E., and Appold, M.S., 2009, Anomalous Metal-Rich Fluids Form Hydrothermal Ore Deposits: *Science*, 323:764-767.
- Wortmann, U.G., Bernasconi, S.M., and Bottcher, M.E., 2001, Hypersulfidic deep biosphere indicates extreme sulfur isotope fractionation during single-step microbial sulfate reduction: *Geology*, v. 29, p. 647-650.
- Wortmann, U.G., Chernyavsky, B., Bernasconi, S.M., Brunner, B., Bottcher, M.E., and Swart, P.K., 2007, Oxygen isotope biogeochemistry of pore water sulfate in the deep biosphere: Dominance of isotope exchange reactions with ambient water during microbial sulfate reduction (ODP Site 1130): *Geochimica et Cosmochimica Acta*, 71:4221-4232.
- Yang, J. (2006). Finite element modeling of transient saline hydrothermal fluids in multifaulted sedimentary basins: implications for ore-forming processes. *Canadian Journal of Earth Sciences*, 43(9), 1331-1340. doi:10.1139/e06-021

Toxic contribution of Kupferschiefer metals, hydrocarbon, and related Zechstein salines to the Permian extinction event

Stanley B. Keith

MagmaChem Exploration, Sonoita, Arizona, USA

Jan C. Rasmussen

Jan Rasmussen Consulting & University of Arizona, USA

Volker Spieth

VS. GLOBALMETAL LLC, Tucson, Arizona, USA & University Stuttgart, Germany

Abstract. The Kupferschiefer metal-hydrocarbon system and related Zechstein salines constituted one of the most massive toxic chemical events in geologic history. Toxicity related to emplacement of the Kupferschiefer was focused at the Permo-Triassic boundary throughout northern Europe. Like many other Permo-Triassic extinction timelines, the event is marked by lightening of the carbon isotope signatures. The Kupferschiefer toxic brine plumes contributed a massive, ultra-deep hydrothermal (UDH), toxic component to the great Permian extinction event that attended breakup of the Pangaea supercontinent. Other giant toxic plumes present at that time included the Permian Basin, Tunguska system in SE Siberia, and Meishan Basin in China. The combined global-scale chemical toxicity of these giant hydrothermal plumes instantaneously extinguished most of the global marine biosystem.

1 Stratigraphic position of the Permian extinction in the Kupferschiefer

Significantly, the age of the Kupferschiefer spans the Permo-Triassic boundary, based on the combined Re-Os and illite ages. The boundary between the Permian and the Triassic can be placed at the top of the black shale of the Kupferschiefer and below the Zechstein carbonates (Figure 1). The current Permo-Triassic boundary is radiometrically calibrated at 251.9 Ma, which is approximately the same as the age of the high-quality illite data for the Kupferschiefer (Keith et al. 2018). This boundary also falls near the midpoint of the apparent age gap between 245.5 and 259 Ma in the Re-Os mineral dates (Figure 2).

One of the emergent characteristics of the Permian extinction event is the distinct and occasional lightening of carbon isotopes at the extinction time line, which is well-documented in the Kupferschiefer (Figure 3). Similarly, the lightening of the carbon isotopes is especially pronounced in the Meishan section in China, which is considered a reference section for the timing of the Permian extinction as per the documentation in Burgess and Bowring (2015) (Figure 4). Of additional interest is the presence of oil-window mature hydrocarbons near the top of the Kupferschiefer. The oil



maturation is inferred to have formed from hydrogen
Figure 1. Zechstein carbonates, Kupferschiefer black shale, with underlying Weissliegend (white sandstone) and Sandsteinschiefer of the Upper Rotliegend (red sandstone) showing thinness of the Kupferschiefer with Permian-Triassic boundary at top of the Kupferschiefer black shale. Age information discussed below allows an assignment of about 252 Ma to the upper boundary of the Kupferschiefer black shale. The extinction timeline is placed at the top of the black Kupferschiefer, and the base of the grey Zechsteinkalk sequence. Photo by Juergen Kopp showing Wettelrode Mine manager Erich Hartung observing the Kupferschiefer unit.

released from hydrogen sulfide to make sulfides from reaction with metalliferous chloride brines at the same time as the hydrogenation of the incoming deep-sourced kerogen muds. The regionally widespread hydrocarbons (both gas and oil) in the underlying Rotliegend hydrocarbon reservoirs may be a product of latest Permian kerogen hydrogenation (see Figure 6 in Keith et al. 2018). At the least, this reduced hydrogen would have been very toxic to the local biosphere in northern Europe.

Carbon isotope data for the Kupferschiefer show a similar lightening pattern (Figure 3). Carbon for kerogen samples in the Konrad section consistently lighten

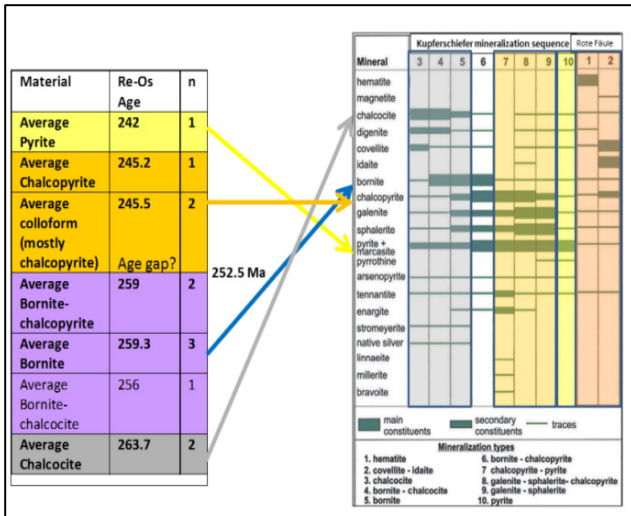


Figure 2. Re-Os ages on sulfides compared with modified paragenetic sequence for the Kupferschiefer (Alderton et al. 2016; Mikulski and Stein 2017; modified paragenesis is from Kopp et al. 2012; Rentsch and Knitzschke 1968; and Stedingk and Rentsch 2003). For a more detailed age discussion, see Keith et al. 2018.

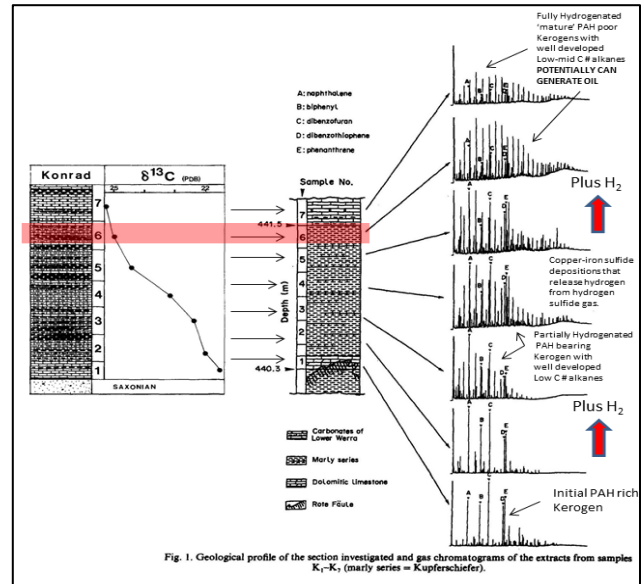


Figure 3. Carbon isotopes for kerogen hydrocarbon taken from the Konrad section. Pink bar indicates a potential oil generation window and extinction horizon associated with sample 6. Modified from Speczik et al. 1995.

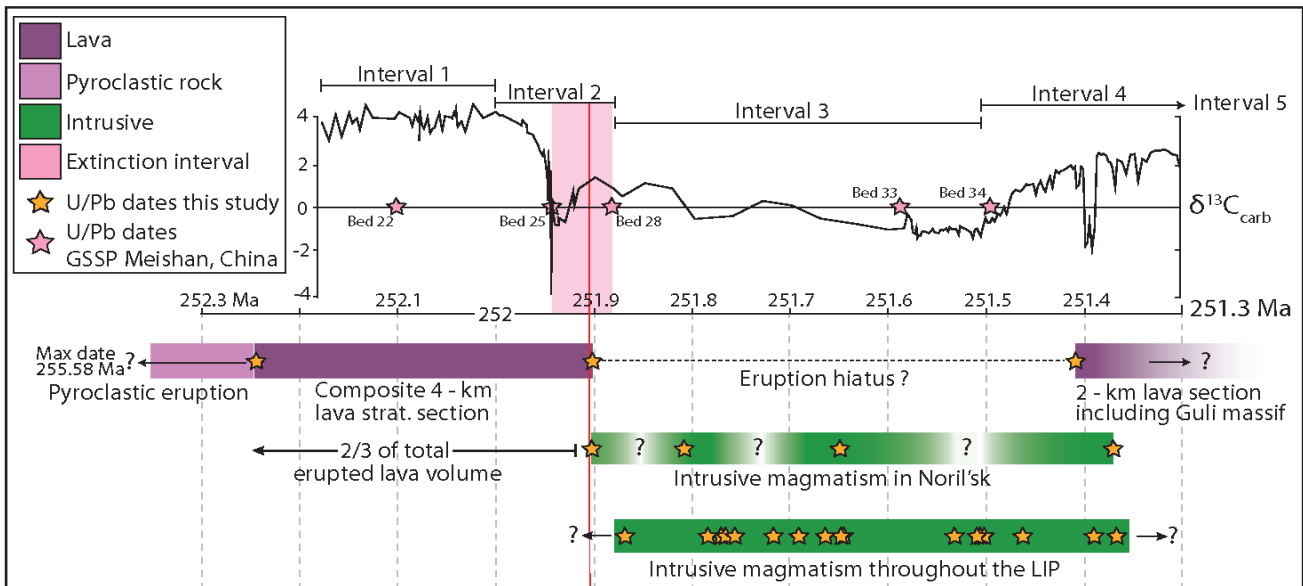


Figure 4. Timeline through the late Permian and early Triassic showing the record of Siberian Traps Large Igneous Province magmatism, the end-Permian mass extinction interval, and the carbonate carbon isotopic record (Fig. 4 from Burgess and Bowring 2015.)

upward in the section. The prospective oil generative sample exhibits a $\delta^{13}C$ ratio of -25.0. The oil generation also occurs at the dolomitic-illitic marl/calclitic Zechstein limestone transition that corresponds with the occurrence of zinc compounds. This carbon isotope lightening pattern is additionally consistent with up-section hydrogenation/reduction associated with hydrogen generation from sulfide and other hydrothermal mineral depositions (for example, illite and dolomite earlier in the sequence down section).

On a broader scale, the lightening of the carbon isotope (in this case kerogen carbon) reflects the input of reduced methane into the atmosphere-hydrosphere

columns. Obviously, the greenhouse gas nature of methane on a global scale can massively affect global warming and overall toxicity. When compared with the age date discussion above, the carbon isotope lightening can be correlated on a global basis with other carbon isotope profiles like the one shown for Meishan, China in Figure 4.

2 Correlation with other Permo-Triassic Deep Hydrothermal (UDH) mineral systems

In this regard, it is interesting that the well-calibrated Permo-Triassic boundary in the greater Tunguska region

of central Siberia and the Meishan region of northern China is also associated with a hiatus that is similar to the one we have inferred above in the Zechstein-Kupferschiefer sequence. The hiatus appears to be associated with the introduction of massive amounts of metalliferous brines into the Earth's atmosphere and hydrosphere systems. We concur, like Svensen et al. 2009; Polozov et al. 2016; and Fristad et al. 2015, that the end Permian hiatus, in addition to being an unconformity, is also a time of massive toxic brine influx, of which the Kupferschiefer is an example. Similar massive brine toxic plumes focused at the Permo-Triassic boundary were also introduced in North America in the Permian basin of Texas-New Mexico, and in the Phosphoria basin of the central Rockies, and in the Barents Sea of northern Norway. We infer these massive, toxic metal hydrothermal events are the cause of the well-known and highly debated, end Permian, extinction event.

The massive amounts of brines and acids would have been toxic to any life immediately above the eruption site and would have entombed any swimming animals above it, such as the pickled, metallized herring fossil in Figure 5. The super-sized, crustal-scale, mud-brine plumes created a massive chemical imbalance in the Earth's ecosystem that induced the well-known end Permian extinction event (Figures 6 and 7). The toxicity would have been maximized near the tops of the reductive black shale sequences, which mark the extinction event below the Zechstein at the top of the Kupferschiefer shale and elsewhere. Certainly, the toxicity would have continued into the saline intervals that mark the upper part of the Zechstein sequence. However, the global ecosystem rapidly recovered in the Triassic immediately after the metal-rich reduction event and salinity crisis ended.

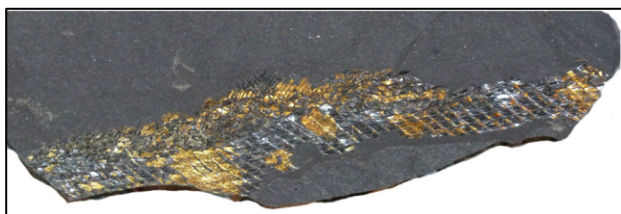


Figure 5. A witness to the Permian extinction. Fish fossil (*Palaeniscum Freiesiebeneri*) in the Kupferschiefer replaced by chalcocopyrite and chalcocite, Lubin, Poland (Lubin Kupferschiefer T-1, sample size 27 cm, collection of and photo by V. Spieth)

On a global scale, the UDH process operated in at least 7 basins at the end of Permian during the breakup of Pangaea and the great extinction event (Figure 6). Globally, UDH systems appear to be associated with instantaneous breakup of the northern half of the Pangea

supercontinent circa 252 Ma. The breakup may have been triggered by the gravitational instability that is inherent to supercontinent assemblies. These supercontinents can only survive for short intervals before they must gravitationally unload or rift. The rifting induces decompression and allows upwelling of mantle heat. The heating leads to dehydration of serpentosphere substrate into talc, which releases massive amounts of Mg-halogen-bearing, metalliferous hydrothermal brines. These brines ascend as large kerogen-charged, heavy hydrothermal, highly toxic brine plumes.

Hence, the Kupferschiefer and its larger Zechstein-Rotliegend system provide an insight, not only into metallogenic processes, but also into an entire earth scale, mantle-driven, ultra-deep, hydrothermal (UDH) geologic process. The individual system-scale involved the entire thickness of the crust in rift settings (Figure 7). The global extent and cumulative mass of the UDH process overwhelmed the biospheric system resulting in a world-wide extinction event.

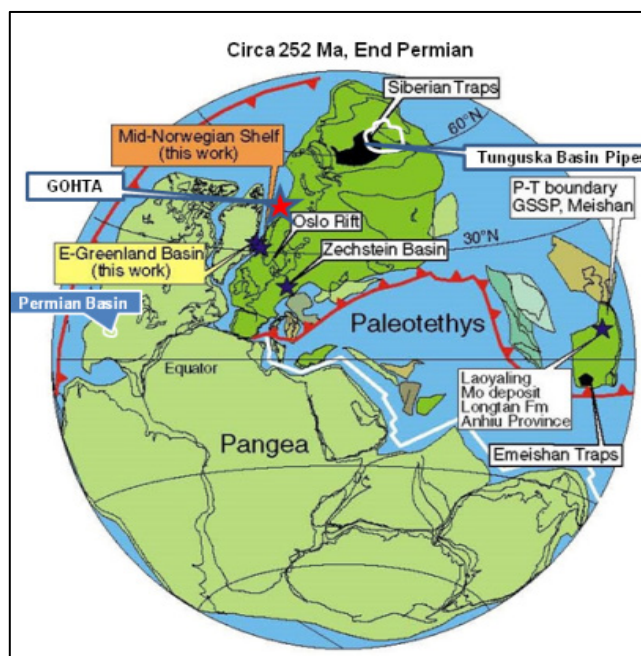


Figure 6. Geotectonic setting of the Permo-Triassic UDH extinction event. Modified from Georgiev et al. 2011.

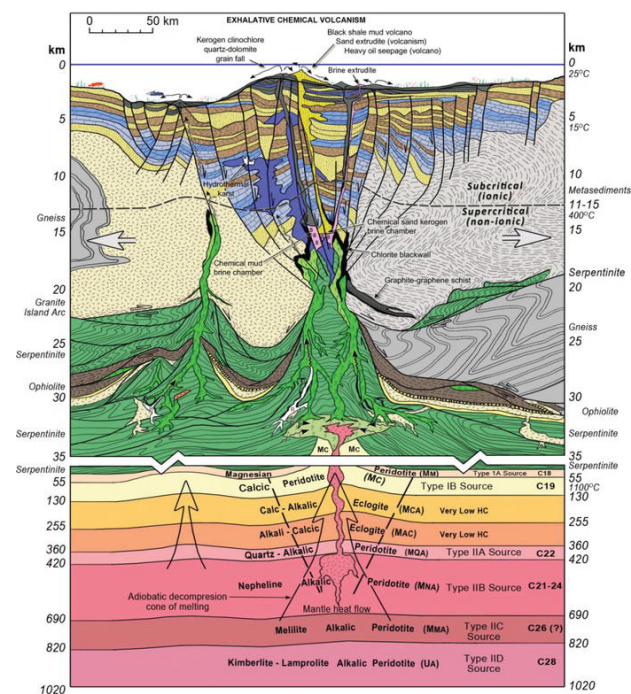


Figure 7a and 7b. Generic UDH model for failed rift/aulochoegen settings with text identifying major parts of the hydrothermal hydrocarbon component in the UDH process. Original figure contributed by Monte M. Swan, modified from Keith et al. 2018

References

- Alderton, Alderton DHM, Selby D, Kucha H, Blundell DJ. (2016) A multistage origin for Kupferschiefer mineralization. *Ore Geology Reviews* 79:535-543
- Burgess SD, Bowring SA (2015) High-precision geochronology confirms voluminous magmatism before, during, and after Earth's most severe extinction. *Science Advances (AAAS)* 28 August: 1–14.
- Fristad KE, Pedentchouk N, Roscher M, Polozov A, Svensen H (2015) An integrated carbon isotope record of an end-Permian crater lake above a phreatomagmatic pipe of the Siberian Traps. *Palaeogeography, Palaeoclimatology, Palaeoecology* 428:39–49.
- Georgiev S, Stein HJ, Hannah JL, Bingen B, Weiss HM, Piasecki, S (2011) Hot acidic Late Permian seas stifle life in record time. *Earth Planetary Sci Letters* 310:389–400.
- Keith SB, Spieth V, Rasmussen JC (2018) Zechstein-Kupferschiefer mineralization reconsidered as a product of Ultra-Deep Hydrothermal, mud-brine volcanism. *Al-Juboury AI (ed) Contrib to Mineralization Chapter 2:23–66.*
- Kopp JC, Spieth V, Bernhardt HJ (2012) Precious metals and selenides mineralisation in the copper-silver deposit Spremberg-Graustein, Niederlausitz, SE Germany. *Zeitschrift Der Deutschen Gesellschaft Fuer Geowissenschaften* 163/4:361–384.
- Polozov AG, Svensen HH, Planke S, Grishina SN, Fristad KE, Jerram DA (2016) The basalt pipes of the Tunguska Basin (Siberia, Russia). High temperature processes and volatile degassing into the end-Permian atmosphere: *Palaeogeography, Palaeoclimatology, Palaeoecology* 441:51–64.
- Rentsch J, Knitzschke G (1968) Die Erzmineralparagenesen des Kupferschiefers und ihre regionale Verbreitung – Freiburger Forsch.-H., C 231:189–211, Leipzig (Verl. Grundstoffind).
- Speczik S, Bechtel A, Sun YZ, Puttman W (1995) A stable isotope and organic geochemical study of the relationship between the Anthracosia shale and the Kupferschiefer mineralization (SE Poland). *Chemical Geology* 123:133–151.
- Steding K, Rentsch J (2003) Übersichtskarte Tiefliegende Rohstoffe und Energierohstoffe in Sachsen-Anhalt, Blatt II—

- Potenziale der Erze und Spate [General map of the low-lying energy resources and raw materials in Saxony-Anhalt, Sheet II—Potential of the ore and spar(?)], in *Digitale geowissenschaftliche Landesübersichtskarten von Sachsen-Anhalt im Maßstab 1:400,000* [Digital geoscience maps state of Saxony-Anhalt at a scale 1:400,000]. Landesamt für Geologie und Bergwesen Sachsen-Anhalt [State Agency for Geology and Mining Sachsen-Anhalt], scale 1:400,000 [In German].
- Svensen H, Planke S, Polozov AG, Schmidbauer N, Corfu F, Podladchikov Y, Jamtveit B (2009) Siberian gas venting and the end-Permian environmental crisis. *Earth Planetary Sci Letters* 277:490–500.

Hydrothermal activity as a probe of hydrosphere-lithosphere interaction and evolution of life on early Earth

Svetlana Tessalina, Vitor Barrote, Bryant Ware

John de Laeter Centre, The Institute for Geoscience Research (TIGeR), Curtin University, Australia

Abstract. Hydrothermal activity was present since the early days of our planet, and played a critical role in hydrosphere-lithosphere interaction and creating the suitable habitat for the appearance of life. Here we present a comprehensive study of a hydrothermal system at the North Pole Dome area, Dresser Formation, Pilbara Craton, as an example of co-evolution of hydrothermal activity and emerging life. This site stands out from later Archean counterparts by the presence of barium sulphate, and evoked several controversial models of the Early Archean paleo-environment as a potential habitat of early life. In this contribution, we present Re-Os elemental and isotopic composition of hydrothermal precipitates and the host sequence of volcano-sedimentary rocks. The Re-Os system was open, possibly due to on-going hydrothermal circulation with possible addition of Re. The Re contents in metalliferous and carbonaceous sediments are quite low, suggesting anoxic conditions during their formation. The gradual rise of oxygen by 2.7 Ga is evident from Re enrichment in black shales from the Nimbus deposit, Yilgarn Craton. The initial Os isotopic composition of Late Archean seawater, inferred from Re-Os regression, is close to the chondritic value, implying a predominantly hydrothermal/magmatic source of Os in the ocean.

1 Introduction

Hydrothermal venting associated with submarine volcanic activity occurs in the form of shallow subsea convection cells capable of releasing hydrothermal fluids into the ocean via either diffusive upflow over broad areas or focussed venting along structural corridors (e.g. ridge crests and flanks) (e.g. Brauhart et al. 1998). These hydrothermal fluids are comprised of a variable mixture of magmatic-hydrothermal fluids and evolved seawater that has reacted with the underlying rocks, causing most systems to be dominated by this evolved seawater signature (e.g. Franklin et al. 1981). Focused venting of hydrothermal fluids at the seafloor leads to rapid temperature decrease which in turn leads to the precipitation of massive amounts of sulphide / sulphate minerals, occasionally leading to the formation of economically important Volcanogenic Hydrothermal Massive Sulphide deposits (VHMS, Huston et al. 2010). As a consequence, the trace element and isotope geochemistry of precipitates from early Archean hydrothermal systems provide insights into both the early Archean lithosphere and the primitive ocean chemistry.

Hydrothermal activity was much more vigorous during the Archean than at present, due to higher global heat flow and/or the presence of a long-lived crustal / mantle

heat source. Some of the most conspicuous features of Archean hydrothermal activity are widespread silicification of volcanic host rocks and localised precipitation of barite (barium sulphate), a feature that indicates unique chemical conditions of the Early Archean oceans relative to the later Meso- and Neoproterozoic record (Huston and Logan 2004). Studies of these hydrothermal precipitates in early Archean volcanic rocks may provide important information linking the co-evolution of the lithosphere, the hydrosphere, and life on the early Earth (e.g. Van Kranendonk 2006; Van Kranendonk et al. 2008).

In submarine volcanic environments, hydrothermal fluids leach soluble elements from oceanic crust and lithosphere during water-rock interaction and transport of these elements into the hydrosphere (Huston et al. 2010). Many of these soluble elements precipitate at, or near, the seafloor during the mixing of high-temperature fluids and seawater; and supply the necessary nutrients for development of life.

The first record of early life in Australia was reported in ~3.49 Ga old rocks of the Pilbara craton, Western Australia. In the North Pole Dome area, the microbial activity was manifested by ³⁴S-depletion of sulphides, and occurrence of microbial methane with ¹³C as low as -56 ‰ in cherts-barite deposits. But paleo-environment and the tectonic setting of this possible habitat of life are still disputed. Two controversial models exist for the paleo-environment of this possible habitat of life. According to the first model, the stromatolite growth occurred in shallow evaporating brine ponds, separated from the sea, with primary gypsum precipitation, transformed into barite by later hydrothermal fluid circulation (Shen et al. 2001). Associated cherts were interpreted as evaporitic and clastic sediments which were silicified by later fluid circulation during either shallow seafloor alteration, structural doming at 3.3-2.9 Ga, or faulting during flood volcanism at 2.7 Ga. An alternative model of primary hydrothermal origin for barite and cherts was proposed more recently based on detail field mapping (Van Kranendonk 2006).

In this contribution, we evaluate the evolution of paleo-environmental conditions related to hydrothermalism and life evolution throughout the Archean era, starting from the oldest Early Archean North Pole Dome hydrothermal system with recorded traces of early life, as compared with the more developed Late Archean hydrothermal system within the Nimbus deposit area, where the evidence of microbial life are also described (Barrote et al. this volume).

2 Geological Context

2.1 Early Archaean North Pole Dome deposit, Pilbara Craton

The studied samples come from the low-grade metamorphosed Dresser Formation, which is a part of the Warrawoona Group at the North Pole Dome area in the Pilbara craton, Western Australia. This locality hosts bedded cherts and sulphide-barite horizons interlaid with well-preserved pillow basalts containing dense hydrothermal silica/chert ± barite feeder veins within the Dresser Formation (3.49 Ga, Van Kranendonk 2006). The metalliferous sediments (with mainly iron sulphides) and bedded carbonate with associated stromatolite-like structures are used in this study as a proxy for the Archaean seawater composition, as demonstrated by Van Kranendonk (2003) based on REE patterns.

2.2 Late Archaean Nimbus deposit, Yilgarn Craton

The Nimbus Ag-Zn-(Au) deposit is located near the margin between the Kalgoorlie and Kurnalpi Terranes in the Eastern Goldfields Superterrane (EGS) in the Yilgarn craton, Western Australia (see Barrote et al. this volume, for more details). This deposit was formed through the replacement of the host stratigraphy associated with c. 2705 Ma plume magmatism of the Kambalda Sequence (Hollis et al. 2017).

3 Results and Discussion

3.1 Timing of ore deposition / remobilisation

Certain isotopes of the metallic elements concentrated in hydrothermal precipitates are the daughter products of radioactive decay. For example, ^{187}Os is a product of the β -decay of ^{187}Re , making the Re-Os isotopic system an important geochronometer of hydrothermal processes, providing that the Re-Os system remains closed since the ore deposition event (e.g. Yang et al., 2009).

At the North Pole area, the Re-Os system was not closed, possibly due to repeated episodes of seafloor hydrothermal circulation giving rise to advanced argillic, phyllic, and prophyllitic hydrothermal alteration of footwall basalts (Van Kranendonk and Pirajno 2004). The Re/Os ratios of these altered basalts is about 3 times higher than that of komatiitic and overlying basalts from the area with Re/Os ~10 (Fig. 1).

The resetting of the Re-Os isotope system most likely occurred due to Re addition via hydrothermal fluids. The minimum age of this resetting event was estimated to be ca. 1.7 Ga, which may correspond to the reactivation of the system due to Proterozoic deformations related to nearby Capricorn orogeny (e.g., Spaggiari et al. 2008). However, this regression age is imprecise and will require application of additional geochronometers. These hydrothermal processes, however, didn't affect the Sm-Nd isotope systematic in the same rocks (Tessalina et al. 2010).

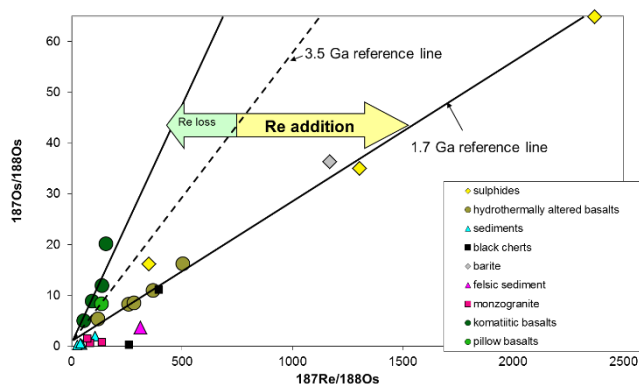


Figure 1. Re-Os isochron diagram for the hydrothermal precipitates, cherts, hydrothermally altered footwall basalts, and komatiitic basalts for North Pole Dome area. Note that the Re-Os system was open possibly due to addition of Re via hydrothermal circulation. The minimum age of the latest disturbance may be estimated at 1.7 Ga

At the Nimbus deposit, massive pyrite with colloform textures, situated at the top of the hydrothermal system, yield the Re-Os isochron age of 2719 ± 45 Ma (Barrote et al. this volume). The polymetallic epithermal-style mineralisation underneath this massive pyrite lens demonstrates open system behaviour, possibly due to pervasive hydrothermal circulation.

3.2 The Osmium isotope composition of Archean seawater

Because seawater – hydrothermal fluid mixing in submarine volcanic environments is the most important process driving sulphate/sulphide precipitation, the composition of seawater will have an influence on the chemistry of the hydrothermal products. Seawater chemical properties such as redox state and salinity will have a major influence on the behavior of hydrothermal fluids as they vent and a smaller influence on the ability of fluids to transport metal.

Metalliferous marine and organic-rich sediments carry exclusively seawater-derived Osmium (e.g., Peucker-Ehrenbrink et al. 1995), and can be used as recorders of variations in the Os isotopic composition of seawater in the past. In turn, the Os isotopic composition of seawater reflects a balance of input between eroded, radiogenic continental material and a non-radiogenic component derived either from the alteration of oceanic crust, erosion of ultramafic rocks, or dissolution of micrometeorite material. Consequently, this isotope system potentially provides a record of the relative changes in these sources over time, and variations in the Os isotope composition of seawater can be used to constrain climatic or tectonic driven changes in continental erosion or ocean circulation. In this case the Os isotopic system potentially offers a highly sensitive and distinct record of chemical weathering of the continents, but thus far robust records of seawater Os have proved difficult to retrieve.

The value of the initial Os isotopic composition from a Re-Os isochron records the $^{187}\text{Os}/^{188}\text{Os}$ isotope composition of the contemporaneous seawater at the time of sediment deposition, if the hydrogenous Os

fraction of organic-rich sediments dominates the detrital/extraterrestrial Os fraction (e.g. Ravizza et al. 1991). Determinations of the Os isotope composition of Precambrian seawater are limited (Kendall et al. 2016 and references therein). The seawater residence time of Os was possibly low under conditions of a predominantly anoxic Archaean atmosphere and ocean prior to the ca. 2.3 Ga Great Oxidation Event. However, for a predominantly anoxic Archean atmosphere and oceans, riverine transport of soluble Re and radiogenic Os from weathering and erosion of crustal rocks (major source of radiogenic Os to the oceans nowadays) would be negligible, resulting in deposition of Archean shales with low Re abundances and $^{187}\text{Re}/^{188}\text{Os}$ and $^{187}\text{Os}/^{188}\text{Os}$ ratios (e.g. Wille et al. 2007).

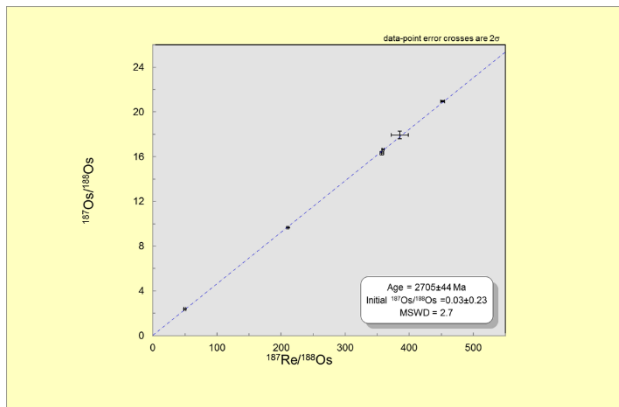


Figure 2. Preliminary Re-Os isochron diagram for black shales and syngenetic nodular pyrite from the Nimbus deposit area. The obtained age corresponds to the U-Pb age of volcanics in the area (Hollis et al. 2017).

Black shales and syn-sedimentary nodular pyrite from the Nimbus deposit area yield an isochron age of 2705 ± 44 Ma, with an imprecise initial $^{187}\text{Os}/^{188}\text{Os}$ isotopic composition of 0.03 ± 0.23 (Fig. 2). This $^{187}\text{Os}/^{188}\text{Os}$ is close to the chondritic value, and consistent with the dominance of the late Archaean marine Os budget by magmatic/hydrothermal and extraterrestrial inputs, which is typical of Precambrian marine shales deposited under an anoxic weathering regime.

Due to open behaviour of the Re-Os system at North Pole Dome area, we can't exactly estimate an initial Os isotopic composition of Early Archean seawater. However, a seawater component of the North Pole sedimentary carbonates is confirmed by seawater-like REE patterns with HREE enrichment and high Y/Ho ratios of ~ 45 . Thus, the $^{187}\text{Os}/^{188}\text{Os}$ ratios of 0.22 to 0.32 obtained for metalliferous and organic-rich sediments intercalating with sulphides, can be considered as a maximum estimate.

3.3 Redox state and early ocean chemistry

The widely recognised conclusion about the reduced state of the early Archaean atmosphere and hydrosphere is mainly based on sulphur mass-independent fractionation. This approach is more relevant to the atmosphere, because this fractionation effect is ascribed

to the photolytic breakdown of atmospheric SO_2 . The abundance of primary hydrothermal barite at early Archaean environments in the Pilbara has important implications for the composition of early Archaean ocean waters. It implies that the ambient seawater at the time of mineralization was sufficiently oxygenated to either stabilize SO_4^{2-} as the dominant sulphur species in seawater or to oxidize the H_2S present in the initial ore fluids to SO_4^{2-} . In either case, the precipitation of sulphate minerals during formation of early Archaean VHMS deposits may be consistent with their formation under oxic conditions. To evaluate this hypothesis, one can use the redox-sensitive group of elements including some of PGEs, Re and Mo. Their concentrations in recent marine sediments are highly variable as a result of redox-dependent solubility (which is the opposite of that of Fe), and the subsequent scavenging of the dissolved species under marine reducing conditions. Hence, PGE and Re-Os isotope studies on carbonate-rich and metalliferous sediments promise to provide a valid indicator for variations of atmospheric and marine redox conditions in the early Archaean. These chemical proxies appear to respond to subtle variations below the Fe-oxide buffer, and below the redox potential required for the development of negative Ce anomalies, and make it possible to study the early history of the atmosphere and hydrosphere. An advantage of this group of elements as redox proxies is that, unlike Fe, they are trace elements that cannot themselves buffer environmental redox conditions and that they appear to respond to low oxygen concentrations.

Our preliminary studies of metalliferous sedimentary rocks from the North Pole Dome area have shown low Re contents ranging from 0.07 ppb in metalliferous sediments up to 0.5 ppb in carbonate-rich sediment, and 2.1 ppb in black cherts, similar to 3.23 Ga old shales from Fig Tree Group from Barbeton (Wille et al. 2007), and consistent with anoxic conditions (Fig. 3). A general increase in Re and Mo concentrations, compared to the continental crust and North Pole Dome area, can be seen within the black shales associated with Nimbus deposit, where we observe enhanced Re and Os concentrations in a range from 2 to 150 ppb, indicating a weak $f\text{O}_2$ increase to levels where mass independent sulphur isotope fractionation still occurs in Late Archean time at 2.7 Ga (Caruso et al., 2018), or gradual rise of oxygen, consistent with observations from Transvaal supergroup shales (Wille et al. 2007). It should be noted that even if the upper part of the ocean was in equilibrium with a reduced atmosphere, the lower part of seawater column could be in disequilibrium, although still in a relatively reduced state (Huston and Logan 2004).

The late-Archaean sulphate-free VHMS deposits reflect an oceanic environment significantly more reduced than at present. Furthermore, the late Archaean globally, is widely recognized as a period of high global heat flow, growth and stabilization of continental crust and extensive degassing of the upper mantle. Some authors suggest that, during a time of rifting, hydrothermal discharge of reduced fluids can become extremely vigorous and potentially drive bottom waters to anoxia. This mechanism, together with transgressive

conditions, concomitant with the main period of VHMS generation during the late Archean could account for the absence globally of sulphates in these deposits.

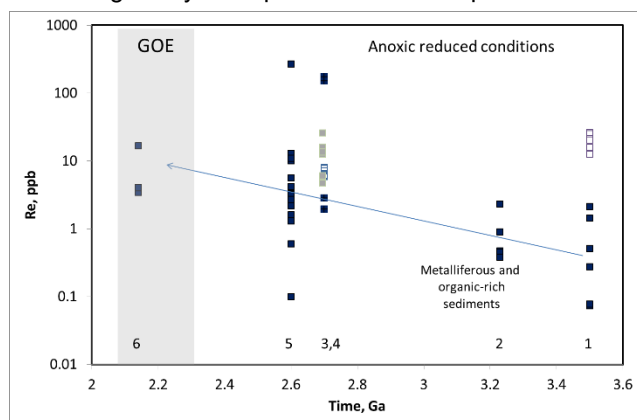


Figure 3. Re contents in sulphide ores (open squares), as well as metalliferous and organic-rich sediments (filled squares), versus time. From right to left: 1 – North Pole Dome area, this study; 2 – Fig Tree Group (Wile et al. 2007); 3 – Nimbus deposit black shale and sulphides (this study and Barrote et al. this volume); 4 – Joy Lake carbonaceous slates (grey squares; Yang et al. 2009); 5 – Ghaap Group black shales (Wille et al. 2007); 6 – Turee Creek Formation (Philippot et al. 2018). Note: GOE stands for Great Oxidation Event.

4 Conclusions

The hydrothermal activity at Archean time has promoted the lithosphere – hydrosphere interaction, provided nutrients and created an environment suitable for the early life. Comparison of Early Archean (North Pole Dome) and Late Archean (Nimbus) sites indicate the rise of oxygen towards the end of Archean. The Os budget in seawater was predominantly dominated by magmatic/hydrothermal input with negligible continental crust component via riverine erosion. Ongoing hydrothermal circulation did reset Re-Os system at North Pole Dome area, and late epithermal-style portion of the Nimbus deposit.

Acknowledgements

The authors acknowledge Prof Philippot for access to the samples and discussion of results; Prof McNaughton for ongoing support and scientific discussions; the Institut de Physique du Globe in Paris and John de Laeter Centre, Curtin University for the facilities, scientific and technical assistance.

References

Barrote V, Tessalina S, McNaughton N et al. (this volume) 4D history of the Nimbus VHMS ore deposit in the Yilgarn Craton, Western Australia: a multi-disciplinary approach.

Brauhart C, Groves DI, and Morant P (1998) Regional alteration systems associated with volcanogenic massive sulphide mineralisation at Panorama, Pilbara, Western Australia. *Econ Geol* 93:292-302.

Caruso S, Fiorentini ML, Hollis SP, et al. (2018) The fluid evolution of the Nimbus Ag-Zn-(Au) deposit: An interplay between mantle plume and microbial activity. *Precambrian Research* 317:211-229.

Franklin J.M., Lydon J.W., and Sangster D.M. (1981) Volcanic-

associated massive sulphide deposits. *Econ Geol* 75th anniversary volume: 485-627.

Hollis SP, Mole DR, Gillespie P, et al (2017) 2.7 Ga plume associated VHMS mineralization in the Eastern Goldfields Superterrane, Yilgarn Craton: Insights from the low temperature and shallow water, Ag-Zn-(Au) Nimbus deposit. *Precambrian Research* 291:119-142.

Huston DL and Logan GA (2004) Barite, BIFs and bugs: Evidence for the evolution of the Earth's early hydrosphere. *Earth Planet Sci Letters* 220:41-55.

Huston DL, Pehrsson S, Eglinton BM, Zaw K (2010) The Geology and Metallogeny of Volcanic-Hosted Massive Sulphide Deposits: Variations through Geologic Time and with Tectonic Setting. *Econ Geol* 105:571-591.

Kendall B, Creaser RA, Selby D (2016) ^{187}Re - ^{187}Os geochronology of Precambrian organic-rich sedimentary rocks. In: *Global Neoproterozoic Petroleum Systems: The Emerging Potential in North Africa* (Eds Craig et al). *Geol Society of London Special Publications* 326:85-107.

Peucker-Ehrenbrink B, Ravizza G, Hofmann AW (1995) The marine $^{187}\text{Os}/^{186}\text{Os}$ record of the past 80 million years. *Earth Planet Sci Letters* 130:155-167.

Philippot P, Avila JN, Killingsworth BA et al. (2018) Globally asynchronous sulphur isotope signals require re-definition of the Great Oxidation Event. *Nature Communications* 9:2245.

Ravizza G, Martin CE, German CR, Thompson G (1996) Os isotopes as tracers in seafloor hydrothermal systems: metalliferous deposits from the TAG hydrothermal area, 26°N Mid-Atlantic Ridge. *Earth Planet Sci Letters* 138:195-119.

Shen Y, Buick R, Canfield DE (2001) Isotopic evidence for microbial sulphate reduction in the Early Archean era. *Nature* 410:77-80.

Spaggiari CV, Wartho J-A, Wilde S (2008) Proterozoic deformation in the northwest of the Archean Yilgarn Craton, Western Australia. *Precambrian Research* 162:354-384.

Tessalina SG, Bourdon B, Van Kranendonk M, et al (2010) Influence of Hadaean crust evident in basalts and cherts from the Pilbara Craton. *Nature Geosci* 3: 214-217

Van Kranendonk MJ (2006) Volcanic degassing, hydrothermal circulation and the flourishing of early life on Earth: A review of the evidence from c.3490-3240 Ma rocks of the Pilbara Supergroup, Pilbara Craton, Western Australia. *Earth Sci Rev* 74:197-240.

Van Kranendonk MJ, Pirajno F (2004) Geochemistry of metabasalts and hydrothermal alteration zones associated with c. 3.45 Ga chert and barite deposits: implications for the geological setting of the Warrawoona Group, Pilbara Craton, Australia. *Geochemistry: Exploration, Environment, Analysis*, 4:253-278.

Van Kranendonk MJ, Philippot P, Lepot K et al. (2008) Geological setting of Earth's oldest fossils in the c. 3.5 Ga Dresser Formation, Pilbara craton, Western Australia. *Precambrian Research* 167:93-124.

Van Kranendonk MJ, Webb GE, and Kamber BS (2003) Geological and trace element evidence for a marine sedimentary environment of deposition and biogenicity of 3.45 Ga stromatolitic carbonates in the Pilbara Craton, and support for a reducing Archean ocean. *Geobiology* 1:91-108.

Wille M., Kramers J.D., Nagler T.F. et al. (2007) Evidence for a gradual rise of oxygen between 2.6 and 2.5 Ga from Mo isotopes and Re-PGE signatures in shales. *Geochim Cosmochim Acta* 71:2417-2435.

Yang G, Hannah JL, Zimmerman A et al (2009) Re-Os depositional age for Archean carbonaceous slates from the southwestern Superior Province: Challenges and insights. *Earth Planet Sci Letters* 280:83-92.

Timing and composition of stratiform pyrite mineralization in black shales at Liblín (Teplá Barrandian Unit, Bohemian Massif)

Jan Pašava, František Veselovský, Ondřej Pour
Czech Geological Survey, Czech Republic

Lukáš Ackerman, Martin Svojtka
Institute of Geology of the Czech Academy of Sciences, Czech Republic

Robert A. Creaser
Department of Earth and Atmospheric Sciences, Faculty of Science, University of Alberta, Edmonton, Canada

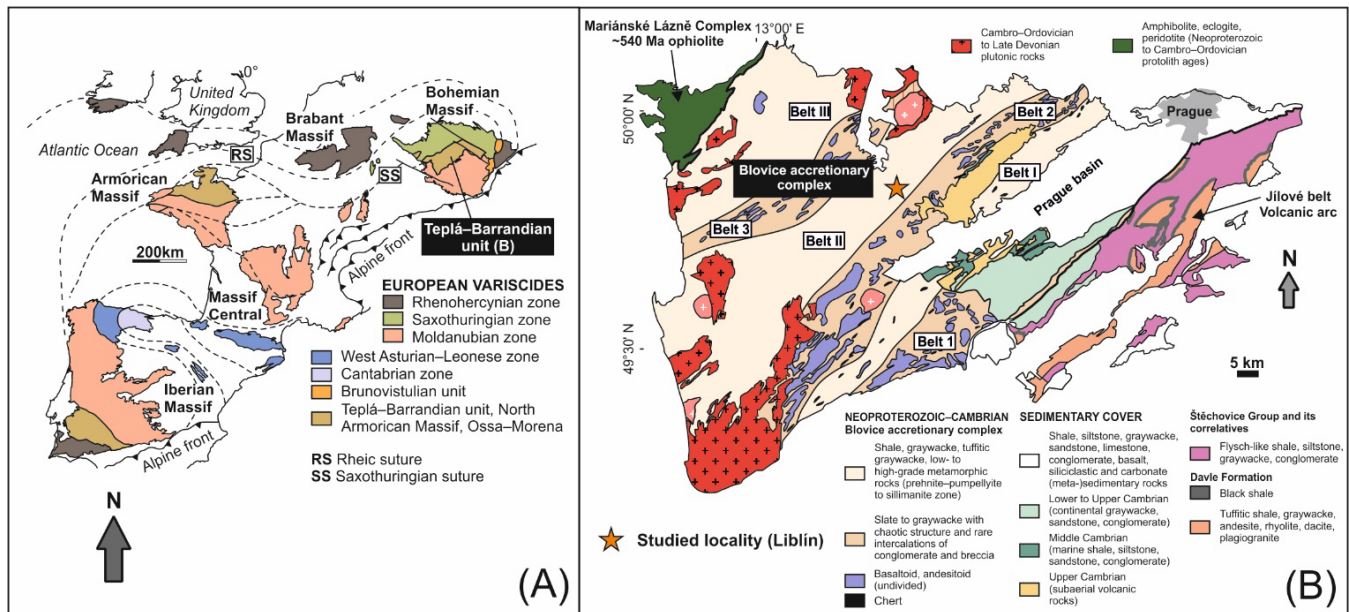


Figure 1. (A) Inferred paleogeographic position of the Teplá-Barrandian unit in the Avalonian-Cadomian belt on the northern active margin of Gondwana during the late Neoproterozoic. (B) Overview geologic map showing basement outcrop areas and principal lithotectonic zones of the Variscan belt in Europe. The Blovice accretionary wedge constitutes a major portion of the supracrustal Teplá-Barrandian unit in the center of the Bohemian Massif. (C) Simplified geologic map of the Blovice accretionary complex, emphasizing coherent belts (Belts I-III) alternating with ophiolitic mélanges (Belts 1-3). Modified from Hajná et al. (2013). Location of black shales hosting Fe stratiform mineralization at Liblín is shown by asterisk.

Abstract. Pyritic black shales represent one of the most widespread types of mineralization in the Bohemian Massif which were mined in the past for the production of the Bohemian sulfuric acid. They were considered to be of Neoproterozoic age. Here, we present new geochemical, geochronological and laser ablation ICP-MS data from pyritic black shales at Liblín - a part of the Teplá-Barrandian Unit (TBU). We suggest that these normal (non-highly metalliferous) black shales were deposited in suboxic/anoxic depositional environment during early Cambrian (Re-Os dating on pyrite - 505 ± 21 Ma), coinciding with the Cambrian explosion. Syn-sedimentary pyrite has significantly higher As, Ag, Cr, Mn, Pb, Sb and V concentrations when compared to recrystallized type, which is, however characterized by much higher Co, Cu and Se contents.

1 Introduction

The Bohemian Massif, a remnant of Middle-Late Paleozoic Variscan belt, is composed of four major units (Teplá-Barrandian, Moldanubian, Saxothuringian and Moravo-Silesian) characterized by different compositional and temporal tectonostratigraphic evolution (Kroner and Romer 2013 and references therein).

The Teplá-Barrandian Unit (TBU) includes predominant Neoproterozoic to Cambrian basement (~550-500 Ma) metamorphosed at low grade, intruded by volumetrically minor Cambro-Ordovician plutons and covered by Late Cambrian to Devonian sedimentary and volcanic rocks (e.g., Hajná et al. 2017 and references therein). The Cadomian basement of the TBU is represented by the Blovice accretionary complex (BAC) and Jilové belt (JB). The BAC developed during

subduction of an oceanic plate beneath the northern margin of Gondwana (Linnemann et al., 2014 and references therein) and exposes a complete section across an ancient subduction–volcanic arc system active from about 650–620 to ca. 480 Ma (Hajná et al. 2017 and references therein). The most notable feature of the BAC is that it consists of six fault-bounded linear belts, where three coherent domains of arc-derived and multiply recycled deep-marine siliciclastic rocks (Belts I–III; Fig. 1) represented by siltstones, slates, greywackes and (black)shales accompanied by cherts alternate with belts of ocean-floor-bearing (ophiolitic) mélanges (Belts 1–3; Hajná et al. 2013; Fig. 1) with basaltic rocks of highly variable composition. The Liblín locality belongs to the Kralovice–Rakovník belt (Belt II) characterized by very low-grade monotonous succession of graywackes rhythmically alternating with minor slates and siltstones interpreted as deep-water turbidites (Cháb and Pelc 1968). This belt is devoid of volcanic rocks except for only a few NE–SW-trending km-scale elongated bodies of alkali basalt and trachybasalt to trachyandesite. Well-preserved shallow-dipping bedding, syn-sedimentary textures, and general lack of pervasive deformation suggest that the Kralovice–Rakovník belt is the least deformed unit of the accretionary wedge (Hajná et al. 2013).

The region of the TBU has a long mining history of pyritic black shales, considered to be of Neoproterozoic/Ediacaran age, representing one of the most widespread types of mineralization in the Bohemian Massif (Kurzweil et al. 2015). Many locations including Liblín were exploited intensively from the 16th to 19th century for the production of the sulfuric acid (Slavík 1905; Pašava et al. 1996). Between 1833 and 1872, about 766,000 t of ore were mined at Hromnice, where an open pit remains.

Here, we present new geochemical characteristics of black shales and pyrite paralleled by Re–Os pyrite geochronology, developed in suboxic/anoxic environment and well preserved at the accretionary wedge. Our data provide new constraints on palaeoenvironment and metallogeny and timing of evolution of subduction process at the northern margin of Gondwana.

2 Results and discussion

2.1 Samples and methods

Eleven representative samples of black shales were collected in accessible gallery at the former pyrite deposit at Liblín. Major oxides were determined using a wet-chemistry method and selected trace elements were measured on an ICP-MS at the laboratories of the Czech Geological Survey in Prague. The polished sections with different types of pyrite grains were studied using an optical microscope and a FE–SEM Tescan Mira3 GMU, both housed at the Czech Geological Survey. Re–Os geochronology of the pyrite was carried out at the University of Alberta using protocols described in detail elsewhere (e.g., Morelli et al. 2010). The method includes

decomposition in a concentrated HCl–HNO₃ mixture in Carius Tubes with the presence of ¹⁸⁵Re–¹⁹⁰Os spike and Re and Os separation by ion exchange chromatography and solvent extraction, respectively. Both Re and Os fractions were analyzed for their isotopic compositions using negative thermal ionization mass spectrometry (N-TIMS). Fine pyrite microcrystals and framboids (272 analyses), and coarse-grained pyrite (analyses), have been analyzed *in-situ* for selected trace elements using an Element 2 high-resolution mass spectrometer coupled with a 193 nm ArF Analyte Excite excimer laser ablation system (Teledyne/Cetac), located at the Institute of Geology of the Czech Academy of Sciences (Prague).

2.2 Geochemistry of black shale

Concentrations of selected major oxides and trace elements (TE) are listed in Table 1. Based on average metal values, these facies can be considered normal black shales (e.g., Pašava 1996).

Table 1. Selected major (wt.%) and trace (ppm) elements in early Cambrian pyritic black shales from Liblín.

	min	max	mean
SiO₂	67.0	73.9	70.3
TiO₂	0.3	0.7	0.5
Al₂O₃	6.7	16.4	12.5
Fe₂O₃	0.2	4.4	1.6
FeO	0.1	0.6	0.3
MgO	0.6	1.8	1.2
MnO	0.008	0.023	0.015
CaO	0.01	0.09	0.04
Na₂O	0.1	3.1	1.6
K₂O	1.7	3.8	2.9
P₂O₅	0.026	0.046	0.035
TOC (wt.%)	0.8	7.0	3.2
S(pyrite)	0.01	3.1	0.6
As	12	52	23
Co	0	9	2
Cr	35	114	74
Cu	10	44	23
Mo	7	90	28
Ni	6	60	24
Pb	9	93	27
Sb	6	24	16
Se	0.2	10	2
U	8	25	14
V	231	983	575
Zn	5	154	62
Zr	93	204	159
V/Cr	5	11	7

It was documented by Pašava et al. (2018) that the positive correlation between TOC and V/Cr in both Ediacaran highly metalliferous black shales and normal black shales from the TBU justifies the use of this ratio as an indicator of paleoredox changes. Median value of V/Cr

~7 in our sample set indicates suboxic to anoxic conditions (Jones and Manning 1994) which were reported from different Cambrian locations worldwide (e.g. Sperling et al. 2015). Calculated Spearman correlation coefficients (*r*) indicate a significant relationship between TOC and Cr (*r*=0.81), V (*r*=0.79), Mo (*r*=0.78), S (*r*=0.72) and U (*r*=0.71). Sulfur shows the highest positive correlation with Fe and with Se (*r*=0.78), Co (*r*=0.743), Mo (0.72), U (*r*=0.66), and V (*r*=0.63).

2.3 Re-Os geochronology

Eight pyrite separates yield a Re–Os age of 505 ± 21 Ma (MSWD = 39) with initial $^{187}\text{Os}/^{188}\text{Os}$ value of 0.87 ± 0.12 (Fig. 2).

This age is younger than previously thought Neoproterozoic age (Pb–Pb age of 635 ± 45 Ma for black shales, Pašava and Amov 1993; U–Pb zircon age of 559.8 ± 3.8 Ma from tuffitic intercalations in black shale, Kurzweil et al. 2015). Our new age is, however, consistent with outcomes of the recent study of Hajná et al. (2017) who suggested that Ediacaran-aged orogeny was not abruptly terminated at the Neoproterozoic–Cambrian boundary, but represents succession of multiple, episodic accretion, deformation, and magmatic events and basin development from Ediacaran to early Ordovician.

It is also important to note that this new age coincides with the Cambrian explosion which was triggered by oxygenation (e.g., Canfield et al. 2008 and references therein) and/or other environmental, developmental and ecological causes (Zhang et al. 2014).

2.4 Geochemistry of pyrite

Basically, two types of pyrite were identified. Fine pyrite microcrystals and framboids concentrated in sedimentary bed (Fig 3A) and coarse-grained pyrite aggregates dispersed in matrix (Fig. 3B). Both types significantly differ in chemical composition (Fig. 3A, B).

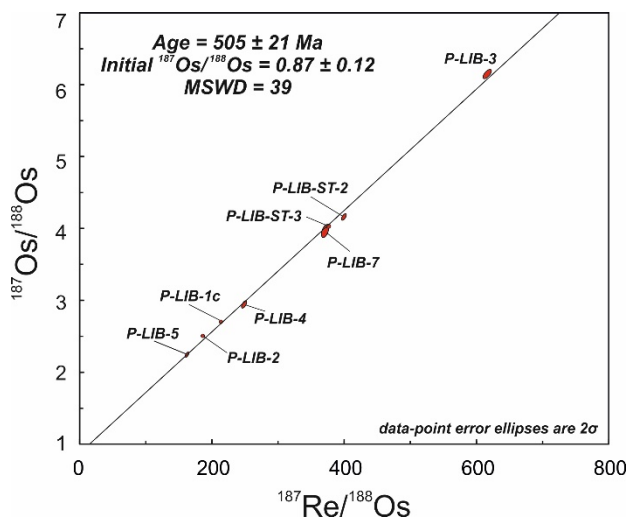


Figure 2. Re–Os regression age for eight pyrites from pyritic black shales at Liblín.

Levels of As, Ni, Pb, and Cu concentrations in our syn-sedimentary pyrite (Fig. 3A) are well comparable with those of average sedimentary pyrite reported by Gregory et al. (2015), however, pyrite from Liblín shows slightly higher Ag and Cd and much higher Sb and Zn values. Similarly, aged syn-sedimentary pyrite from the Que River Shale (505 Ma; Gregory et al. 2015) has almost identical mean As and Se values, much higher mean Co and Ni values and significantly lower mean Sb and V values. In syn-depositional pyrite from Liblín, Mo, Se and U are mostly homogeneously distributed while other TE show some zoning.

Large et al. (2019) used redox sensitive elements in synsedimentary pyrite for estimation of oxygen level through Proterozoic and Phanerozoic. Following this methodology and calculations after Yeung et al. (2017), we suggest that the mean concentration at the time of deposition of our black shales was about 16 wt% which is consistent with results reported by Large et al. (2019) and Berner et al. (2007).

3 Conclusions

The following outcomes resulted from the study of pyritic black shales at Liblín (TBU, Bohemian Massif):

1. Based on the chemistry of major and trace elements, they represent normal black shale (non-highly metalliferous facies), deposited in suboxic/anoxic environment.
2. Re–Os pyrite age of 505 ± 21 Ma indicates lower Cambrian deposition, which has an important geotectonic, palaeoenvironmental and metallogenetic implications.
3. Syn-sedimentary pyrite has higher mean As, Ag, Cr, Mn, Pb, Sb and V concentrations when compared to recrystallized one, which is, however characterized by higher mean Co, Cu and Se contents. Calculations based on redox-sensitive elements in synsedimentary pyrite indicate mean atmosphere O_2 value of ~16 wt. %.

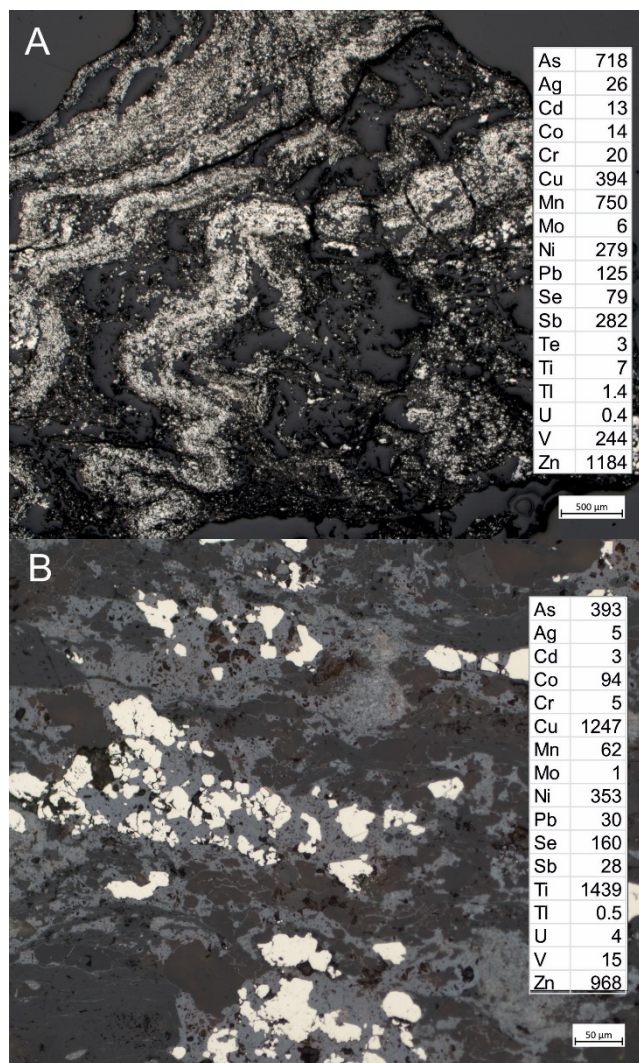


Figure 3. Photomicrographs of two types of pyrite in lower Cambrian black shales at Liblín with mean TE contents (in ppm). (A) Syn-sedimentary pyrite beds, (B) coarse grained pyrite aggregates (recrystallized). Axio Imager A2m, Carl Zeiss, Reflected light image, A. Vymazalová.

Acknowledgements

This study is a contribution to the Czech Science Foundation project 17-15700S and to the Institutional support RVO67985831 of the Inst Geol Czech Acad Sci and the Strategic Research Plan (DKRVO) of the Czech Geological Survey (2018-2022).

References

- Berner RA, Vandenbrooks JM, Ward PD (2007) Oxygen and evolution. *Science* 316:557-558
- Canfield DE, Poulton SW, Knoll AH, Narbonne GM, Ross G, Goldberg T, Strauss H (2008) Ferruginous conditions dominated later Neoproterozoic deep-water chemistry. *Science* 321: 949–952
- Cháb J, Pelc Z (1968) Lithology of Upper Proterozoic in the NW limb of the Barrandian area. *Krystalinikum* 6:141–167
- Gregory DD, Large RR, Halpin JA, Baturina EL, Lyons TW, Wu S, Bull SW (2015) Trace element content of sedimentary pyrite in

black shales. *Econ Geol* 110:1389-1410

- Hajná J, Žák J, Kachlík V, Dörr W, Gerdes A (2013) Neoproterozoic to early Cambrian Franciscan-type mélanges in the Teplá–Barrandian unit, Bohemian Massif: Evidence of modern-style accretionary processes along the Cadomian active margin of Gondwana? *Precambrian Res* 224:653–670
- Hajná J, Žák J, Dörr W (2017) Time scales and mechanisms of growth of active margins of Gondwana: A model based on detrital zircon ages from the Neoproterozoic to Cambrian Blovice accretionary complex, Bohemian Massif. *Gondwana Res* 42:63–83
- Jones B, Manning DAC (1994) Comparison of geochemical indices used for the interpretation of palaeoredox conditions in ancient mudstones. *Chem Geol* 111:111–129
- Kroner U, Romer RL (2013) Two plates - Many subduction zones: The Variscan orogeny reconsidered. *Gondwana Res* 24:298–329
- Kurzweil F, Drost K, Pašava J, Wille M, Taubald H, Schoeckle D, Schoenberg R (2015) Coupled sulfur, iron and molybdenum isotope data from black shales of the Teplá-Barrandian unit argue against deep ocean oxygenation during the Ediacaran. *Geochim Cosmochim Acta* 171:121–142
- Large RR, Mukherjee I, Gregory D, Steadman J, Corkrey R, Danyushevsky LV (2019) Atmosphere oxygen cycling through the Proterozoic and Phanerozoic. *Miner Depos* 54:485-506
- Linnemann U, Gerdes A, Hofmann M, Marko L (2014) The Cadomian Orogen: Neoproterozoic to Early Cambrian crustal growth and orogenic zoning along the periphery of the West African Craton-Constraints from U-Pb zircon ages and Hf isotopes (Schwarzburg Antiform, Germany). *Precambrian Res* 244:236–27
- Morelli RM, Bell CC, Creaser RA, Simonetti A (2010) Constraints on the genesis of gold mineralization at the Homestake Gold Deposit, Black Hills, South Dakota from rhenium–osmium sulfide geochronology. *Miner Depos* 45:461–480
- Pašava J, Amov B (1993) Isotopic composition of lead in Proterozoic anoxic metasedimentary and volcanogenic rocks from the Bohemian Massif (Czech Republic) with metallogenetic implications. *Chem Geol* 109:293–304
- Pašava J, Hladíková J, Dobeš P (1996) Origin of Proterozoic Black Shales from the Bohemian Massif, Czech Republic. *Econ Geol* 91: 63–79
- Pašava J, Chrastný V, Loukola-Ruskeeniemi K, Šebek O (2018) Nickel isotopic variation in black shales from Bohemia, China, Canada, and Finland: a reconnaissance study. *Miner Depos*, DOI 10.1007/s00126-018-0839-8
- Slavík F (1905) O kamenečných a kyzových břidlicích západočeských. *Rozpr Čes Akad*, č. 26, Praha.
- Sperling EA, Wolock CJ, Morgan AS, Gill BC, Kunzmann M, Halverson GP, Macdonald FA, Knoll AH, Johnston DT (2015) Statistical analysis of iron geochemical data suggests limited late Proterozoic oxygenation. *Nature* 523: 451–454
- Zhang X, Shu, DG, Han J, Zhang ZF, Liu JN, Fu DJ (2014) Triggers for the Cambrian explosion: Hypotheses and problems. *Gondwana Research* 25: 896–909

Economic challenges for mineral deposits

John F.H. Thompson

PetraScience Consultants Inc., Vancouver, Canada

Abstract. The definition of reserves for mineral deposits is based on codified metrics indicating that mineralization can be economically mined and that the commodity of interest can be recovered. In reality, this is only one step towards economic viability. Many other technical issues must be evaluated to define production costs, environmental management, and social performance. The resulting path to development is a multi-year exercise with numerous economic implications. Technical, social and business innovation will become increasingly important to success. Similarly, a strong foundation in earth science at both deposit and regional scales is vital to maximizing economic performance and minimizing impact.

1 Technical Challenges

Following the initial discovery of a mineral deposit, attention focuses on establishing the potential size of the discovery and the concentration (grade) of the key commodity or commodities. As exploration moves towards evaluation and potential development, technical work shifts to delineation drilling, definition of ore controls, conversion of resources to reserves, and preliminary work on mining and processing methods. These are all strongly influenced by geology – the geometry and depth of ore zones, lithologies and mineralogy, dilution and stripping ratios, and the resultant definition of economic cut-offs. Increasing drilling and evaluation adds confidence to resource and reserve estimation and provides sufficient data for preliminary economic assessment.

Decisions on appropriate mine and plant design are supported by a variety of traditional metallurgical test programs. While sophisticated, the cost of these programs tends to limit the number of tests, and hence extrapolation across large ore bodies involves major assumptions on continuity. Poor understanding of geological variability in ore bodies and associated waste, may result in poorly designed mines, start-up problems, and increases in capital and operating costs. Economic consequences include delays or even failure in extreme cases. Over the last ten to twenty years, efforts have been made to capture geological variability using exploration data augmented by quantitative mineralogy and physical rock property measurements. The resulting geometallurgy programs provide proxies for mining and metallurgical properties that can then be populated across the ore body to define variability. In the ideal case, energy consumption and recovery data can be estimated for each ore and waste block. These data can be converted into cost, net present value, and cut-off allowing for the creation of a fully optimized life of mine plan.

Full economic characterization of the ore body includes critical environmental parameters related to tailings and waste rock, as well as impacts related to the provision of energy, water, infrastructure, and access corridors. Energy requirements must be assessed in terms of source, cost, environmental impact, and greenhouse gas (GHG) emissions. The character of tailings and waste rock has implications for the design and cost of facilities, management of effluent (e.g., acid rock drainage), and closure costs. In some jurisdictions, a bond may have to be posted to cover closure costs, and is effectively included in the capital expenditure for the project. As with mining and processing, geological parameters are critical for defining waste characteristics, costs and associated risks.

This brief summary of technical challenges illustrates the complexity involved in assessing the economic viability of a new mineral discovery. Each stage of assessment involves significant costs and time commitments, which ultimately have economic implications if drawn out over many years. Clearly, larger, higher grade ore bodies will always have better base line economics and are more likely to weather technical challenges and delays, as well as the economic cycles that affect commodity prices. Thus, the focus for the future has to be both on discovering high quality ore bodies, as well as the proper technical assessment to optimize performance and economics.

2 Social Performance

Formal permitting processes are well established in many if not all mining jurisdictions. It has been recognized for many years, however, that potential mining projects must also achieve a social license to operate. This is acquired through a process of community engagement and consultation, formal or informal definition of benefits, and transparent definition of impacts. Community engagement requires the expertise of social scientists and other specialists who are familiar with local indigenous and non-indigenous groups.

The early days of exploration in an area can establish important first impressions with local people and, therefore, geoscientists need to be trained in the principles of community engagement. Early mistakes may be costly and some projects never recover from missteps at the exploration stage.

Most importantly, timelines for community engagement cannot be defined ahead of the process, and in many cases the result can be a drawn out over several years. Resulting delays, or outright opposition have major economic implications, again emphasizing the importance of critical programs from day one.

Regardless of the initial process, it is clear that a social

license is no longer sufficient for the long term relationship between mines and communities. Mining operations must strive for ongoing social performance, with associated investment and costs. It is difficult to build this into the conventional economic evaluation of a new discovery, but failure to do so ignores both the necessity and economic importance of social performance. The technical and financial assessment of a new discovery, for example in a due diligence process by a potential acquirer or third party provider of finance, is likely to spend a significant amount of time and effort evaluating community relations and related programs. In effect, a reserve defined by technical data may not truly qualify as a reserve if local communities are likely to oppose and prohibit development.

3 Innovation

Discovery, evaluation, and mine development are complex processes. Financial decisions are hampered by uncertainties related to commodity prices, natural variability of ore and waste, energy and water requirements, and social and environmental performance. All must be factored into economic assessment. Increasing costs and complexity of mine development, as well as societal expectations, are driving innovation efforts across the mining industry. This is influencing business, community involvement, and technical performance.

New ways to align major, mid-tier and junior exploration companies are being considered with the ultimate goal of increasing exploration efficiency and the probability of discovering high quality ore bodies. The focus on quality is critical for economic success. Companies are also considering novel business partnerships, for example creating joint operating facilities to exploit several different ore bodies, thus reducing the overall footprint. Mineral tenure in many jurisdictions encourages competition for what may ultimately be small pieces of the same resource. This rewards companies for their investments in exploration, but the result is numerous separate mining operations sometimes built within hundreds of meters of each other. Although consolidation has occurred in the past, broad public and local community pressure will increasingly demand the more efficient low impact facilities offered by consolidation. Progressive companies will seek partnerships that solve ownership and value challenges hence allowing the development of single efficient operations with long term benefits for all.

Mining operations have traditionally offered employment to members of local communities in the course of normal business, and in some cases as part of negotiated agreements. As mines become more automated, however, employment opportunities will be reduced removing a major opportunity for communities. Alternative benefits will need to be considered including joint infrastructure, the creation of businesses that both service the mine and community, and potentially equity involvement of communities in mines. Creative plans and innovative solutions will be required to bring these to

fruition, particularly if the goal is to create sustainable prosperity that goes beyond the life of the mine.

On the technical front, innovation is being driven significantly by digital transformation with sensor based data being acquired in exploration and across mining operations. Major efforts are being made to quantify rock variability with real-time data being used for sorting and grade engineering. Sorting removes waste from ore, effectively increasing grade and decreasing the energy and GHG emissions per unit of product produced.

Tragic tailings accidents have led to a new focus on decreasing the amount of tailings, and engineering safer storage facilities. Lack of progress on tailings will have a profound economic impact on mining, and the investment climate for new operations – a critical economic impact that is not easy to factor into the viability of individual projects.

To address investor and community concerns, sensor-based data across mining operations could be made available through open access platforms. The available data would facilitate third party certification that in turn would help companies demonstrate to their customers that their products contain responsibly sourced components and materials.

Innovation will provide solutions to the mining industry. In some cases, these will enhance economics by improving performance, but in other cases innovation may help with social acceptance while inevitably increasing costs. Conventional economic metrics will have to be adjusted to meet this reality.

4 The Role of Earth Science

Mineral deposits are the result of complex processes that have operated variably throughout Earth history. Understanding these processes is a critical part of mineral exploration, and will become increasingly important as conceptual approaches are used more effectively for deep targets.

Once discovered, characterizing rocks, ore and waste, and mapping variability will determine the economic viability of the mineralized zone, as well as technical, environmental, and to some extent, social performance.

Finally, mapping the Earth at a regional (e.g., water shed) scale and including bedrock and surficial geology, water resources, climate, biodiversity, population and human activity will provide the basis to truly assess choices, impacts and benefits related to the extraction of mineral resources individually and collectively.

Acknowledgements

Many people in, and associated with the mining industry are working hard to improve the industry so that it can provide vital products for society more effectively and cleanly. These people are responsible for many of the ideas and active programs that are summarized here.

A dynamic model for polymetallic Zechstein mineralisation based on the Milicz area of SW Poland

Krzysztof Zieliński, Tomasz Bieńko
Miedzi Copper Corp.

Jan Wierchowicz
University of Warsaw, Poland

Abstract. The present study describes an innovative approach to the calculation of polymetallic ore resources, which is an improvement over regulations concerning such deposits in Poland. These national provisions use the so-called copper equivalent grade, presenting the copper and silver content of ore as one figure based on monetary value and recovery rate. This leads to the underestimation of the resources of ore which also contains other metals, including zinc and lead, being particularly disadvantageous for deep deposits which require focusing on their richest parts and on all useful components of ore. This old approach omits the fluctuations of metal prices over time, whose impact on the equivalent grade is considerable. The presented improved method allows calculations of polymetallic grade for any number of metals, while tracing changes in this grade using arbitrarily selected time intervals. It also presents the monetary value of mineralisation, resulting in a dynamic model undergoing constant fluctuations. Average annual prices of Cu, Ag, Zn and Pb from the last 25 years were used for this study which focuses on deep Zechstein mineralisation of the Milicz area, Fore-Sudetic Monocline, SW Poland, as a representative example.

1 Introduction

The area described in this study constitutes a part of the Fore-Sudetic Monocline, a geological unit of south-western Poland known for its numerous occurrences of Zechstein ore mineralisation. The ore is of the stratabound type and consists primarily of copper sulphides with other metals also present, including significant amounts of silver, lead and zinc. Certain parts of the monocline are already an object of mining activity; however, the surroundings of the town of Milicz are one of many prospective areas of possible future ore extraction listed by the Polish Geological Institute (Wołkowicz et al. 2011).

According to Polish regulations, the resources of stratabound Cu deposits are to be calculated based on the so-called copper equivalent grade, a value taking into account both the copper and silver content of ore and presenting them as one percentage (Oszczepalski et al. 2016). This value is calculated using a predetermined formula based on the market values of those two metals and their metallurgical recovery rates (Bartlett et al. 2013). However, it does not account for constant changes in metal prices and it omits the presence of other valuable components of ore. It is an object of this study to modify

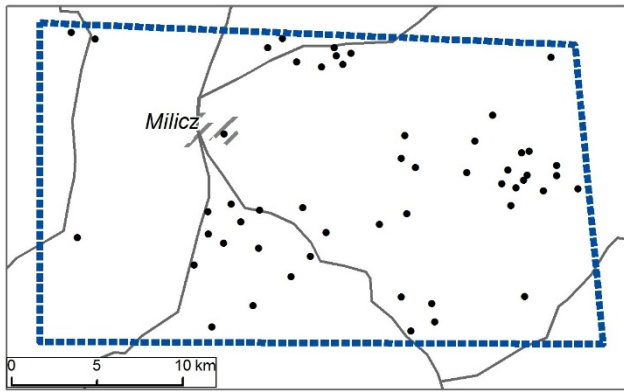
this methodology in order to show dynamic changes in estimated resources depending on the fluctuations of metal prices, and to incorporate other valuable metals into the formula.

2 Geological setting and source data

The studied area covering 578 km² is located in the Fore-Sudetic Monocline, which is characterised by the dipping of its strata in a general north-eastern direction. Its polymetallic mineralisation is associated with the so-called copper-bearing series, spanning up to several meters in the bottommost part of the Zechstein facies, above the lower barren Rotliegend facies. Going towards the top, the series consists of the Weissliegend sandstone, the locally occurring Basal Limestone, the Kupferschiefer shale and the Zechstein Limestone. On rare occasions, the orebody also reaches the bottom part of the overlying Lower Anhydrite.

The Zechstein base depth within the boundaries of the Milicz area ranges between 1500 m below ground level in the south and 1800 m in the north. This makes it an area of deep mineralisation with prospects of future extraction, which requires the recovery of the highest possible number of valuable elements from ore. In the studied area there are 52 historical boreholes, whose cores were sampled as part of an exploration project financed by Miedzi Copper Corp. (Oszczepalski et al. 2012b), as well as another task executed with the participation of a co-author of this paper (Oszczepalski et al. 2012a). Depending on the core, several to several dozen samples were collected in a continuous manner from the copper-bearing series. Some were analysed by Polish Geological Institute, others by Acme Analytical Laboratories Ltd., Vancouver, Canada. The results consisted of complete assays which listed the Cu, Ag, Zn and Pb contents of each sample, along with numerous other analysed elements.

A map presenting the boundaries of the research area and the studied boreholes is shown in Figure 1.



Key

- Research area
- Analysed boreholes
- Major cities
- Major roads



Figure 1. Location of the research area.

3 The old methodology

According to Polish regulations, calculations of stratiform Cu-Ag resources should use the following formula for copper equivalent grade (Oszczepalski et al. 2016):

$$Cu_e = Cu + 0.01 \cdot Ag$$

The symbol Cu_e stands for the copper equivalent grade [%], while Cu is the copper content [%] and Ag is the silver content of ore [ppm]. This means that 100 ppm of silver has the same economic value as 1% of copper, which is only true under specific conditions, and yet is applied to all calculations of such resources in Poland. The formula is valid for copper and silver prices amounting to US \$3.50/lb and US \$25/troy oz respectively, with the respective metallurgical recoveries of Cu and Ag being 89% and 85.5%. This is because 100 g of Ag in 1 tonne of ore would yield 85.5 g, or 2.75 oz, of recovered silver, which at a price of US \$25/troy oz would result in a value of US \$68.70. Also, 1% of copper would yield 19.6 lb Cu per 1 tonne of ore, which at this price is also equivalent to US \$68.70 (Bartlett et al. 2013). Therefore, e.g. a sample with 2% Cu and 50 ppm Ag has a copper equivalent grade of 2.5% Cu_e .

However, this formula does not take into account continuous changes in metal prices, also ignoring other valuable components of ore. This is particularly significant for great depths, like in the Milicz area, where future profitable extraction would require focusing on the richest parts of ore and the recovery of the highest possible number of useful elements.

4 The suggested new approach

This study uses the term polymetallic copper equivalent grade, as opposed to the aforementioned regular copper equivalent grade, to describe a percentage taking into

account not just those two, but also several other useful components of ore. In this case, lead and zinc were used as additional elements due to their significant percentages in certain core samples from the area in question, and also due to the sufficient amount of available data on those two metals. However, any number of other elements could be used as well, by applying analogical methodology.

The formula for the polymetallic copper equivalent grade developed by the authors in a previous paper (Zieliński and Wierchowicz 2018) is as follows:

$$Cu_{epol} = Cu + C_{Ag}^{-1} \cdot Ag + C_{Zn}^{-1} \cdot Zn + C_{Pb}^{-1} \cdot Pb$$

The symbol Cu_{epol} stands for the polymetallic copper equivalent grade, the symbols Cu and Ag have the same meaning as in the previous formula, while Zn and Pb are the zinc and lead content of ore [%], respectively. On the other hand, the symbols C_{Ag} , C_{Zn} and C_{Pb} are variables which the authors of this study have called equivalent gain coefficients, for silver, zinc and lead, respectively. They correspond to the grade of silver (in ppm), zinc (in %) and lead (in %) which would provide the same gain as 1% of copper. These coefficients are calculated using the following formulas:

$$C_{Ag} = \frac{R_{Cu} \cdot \$Cu}{0.0001 \cdot R_{Ag} \cdot \$Ag}$$

$$C_{Zn} = \frac{R_{Cu} \cdot \$Cu}{R_{Zn} \cdot \$Zn}$$

$$C_{Pb} = \frac{R_{Cu} \cdot \$Cu}{R_{Pb} \cdot \$Pb}$$

The symbols R_{Cu} , R_{Ag} , R_{Zn} and R_{Pb} represent the metallurgical recoveries of copper, silver, zinc and lead, respectively. The symbols $\$Cu$, $\$Ag$, $\$Zn$ and $\$Pb$ stand for the respective prices of copper, silver, zinc and lead expressed in US dollars per tonne (same price units were used for all metals to facilitate calculations). The value 0.0001 in the silver formula is necessitated by the difference between 1 ppm and 1%.

Recovery rates are variables which can be determined based on the technical capabilities of a given plant. As mentioned above, according to Bartlett et al. (2013) they amount to 89% for copper and 85.5% for silver. Other publications referring to polymetallic ores suggest 76.44% for zinc (Kursun and Ulusoy 2015); 90% for lead (Retman et al. 2014); 85.5%, 92.91% and 87.93% for copper, lead and silver, respectively (Chunlong et al. 2017); 96.4% for lead (Lorenzo-Tallafigo et al. 2019). The present study uses the lowest values from the abovementioned list, i.e. 85.5% for copper, 85.5% for silver, 76.44% for zinc and 90% for lead. Average annual prices of the four metals from the past 25 years and the resulting equivalent gain coefficients are presented in Table 1.

Table 1. The average annual prices of copper, silver, zinc and lead (source: www.indexmundi.com) and the resulting equivalent gain coefficients calculated for the years 1994-2018.

Price (US \$/tonne):	$\$Cu$	$\$Ag$	$\$Zn$	$\$Pb$
Equivalent gain coefficient:	C_{Ag}	C_{Zn}	C_{Pb}	
1994	2310.15	169774.92	997.84	548.13
		136.07	2.59	4.00
1995	2935.95	167202.57	1031.21	631.36
		175.59	3.18	4.42
1996	2294.18	167202.57	1025.08	774.28
		137.21	2.50	2.81
1997	2275.92	157877.81	1316.85	623.99
		144.16	1.93	3.46
1998	1653.79	178135.05	1024.37	528.74
		92.84	1.81	2.97
1999	1573.99	167524.12	1076.68	502.55
		93.96	1.64	2.98
2000	1813.72	159163.99	1128.27	454.00
		113.95	1.80	3.80
2001	1577.26	140514.47	884.95	476.03
		112.25	1.99	3.15
2002	1559.29	147909.97	778.86	452.55
		105.42	2.24	3.27
2003	1779.92	156913.18	828.14	515.38
		113.43	2.40	3.28
2004	2865.95	214147.91	1047.72	886.59
		133.83	3.06	3.07
2005	3681.47	235048.23	1381.60	976.31
		156.63	2.98	3.58
2006	6732.80	372025.72	3281.25	1289.98
		180.98	2.30	4.96
2007	7126.29	430225.08	3242.86	2584.75
		165.64	2.46	2.62
2008	6951.25	481993.57	1872.87	2086.67
		144.22	4.15	3.16
2009	5160.18	471061.09	1658.50	1722.45
		109.54	3.48	2.85
2010	7539.65	648874.60	2161.02	2148.83
		116.20	3.90	3.33
2011	8822.03	1133118.97	2192.13	2399.55
		77.86	4.50	3.49
2012	7960.65	1000643.09	1949.88	2064.26
		79.56	4.57	3.66
2013	7328.48	765594.86	1909.10	2138.64
		95.72	4.29	3.26
2014	6862.07	613183.28	2161.85	2095.47
		111.91	3.55	3.11
2015	5509.07	505466.24	1930.66	1787.79
		108.99	3.19	2.93
2016	4868.78	551768.49	2091.01	1866.91
		88.24	2.60	2.48
2017	6171.47	548553.05	2891.32	2314.88
		112.50	2.39	2.53
2018	6526.03	505144.69	2918.41	2238.22
		129.19	2.50	2.77

For instance, for a theoretical sample with 1.5% Cu, 30 ppm Ag, 0.3% Zn and 0.3% Pb, the polymetallic copper equivalent grade for average prices from the year 2018 would amount to 1.96%. However, using average prices from a decade earlier (2008) would result in a drop down to 1.88%. Going back another decade (1998), the produced result would be as high as 2.09%.

Once the polymetallic copper equivalent grade is known, it is possible to calculate the so-called productivity of each borehole, which is also a value used in Polish regulations to calculate metal resources. Its unit is kg/m²,

and therefore it provides information about how many kilograms of polymetallic copper equivalent can be extracted from 1 m² of area demarcated around a borehole. The suggested threshold value indicating a mineral deposit is 35 kg/m² (Oszczepalski et al. 2016). This calculation uses the following formula:

$$QCu_{epol} = \frac{\rho_r - Cu_{epol}(\rho_r - \rho_{Cu})}{100 \cdot \rho_r} \cdot \frac{Cu_{epol}}{100} \cdot th$$

The symbol QCu_{epol} stands for the polymetallic productivity, in this case taking into account Cu, Ag, Zn and Pb. The symbols ρ_r and ρ_{Cu} are the density of rock and copper, respectively [kg/m³], and th is the thickness of the mineralised interval. The value of ρ_r depends on the rock in which the ore is found (sandstone, shale, limestone, anhydrite). The final step is the calculation of the net value of mineralisation $\$Cu_{epol}$, expressed in American dollars per square metre:

$$\$Cu_{epol} = QCu_{epol} \cdot \$Cu \cdot 0.001$$

This figure represents simply the net value of polymetallic ore (in this case, Cu, Ag, Zn and Pb) *in situ*, not taking into account the costs of prospecting, mining, smelting, etc.

Once the polymetallic productivity and net value have been calculated for each borehole, the results can be presented on maps drawn separately for every investigated time period. Those maps present prognostic areas whose sizes are also variable over time. The resources of those areas can be calculated and their dynamic changes can be traced, along with fluctuations in the net value of ore present within their boundaries.

5 Results and discussion

Maps presenting the contour lines of polymetallic productivity and net value of mineralisation were prepared separately for each of the years 1994-2018 using the ordinary kriging method. Prognostic areas were delimited by lines corresponding to productivity value of 35 kg/m², in accordance with Polish guidelines (Oszczepalski et al. 2016). Inside those areas, resources of the polymetallic copper equivalent were calculated along with their net monetary value. A comparison between the minimum and maximum range of prognostic areas is presented in Figure 2, along with the contour lines of value in US \$/m² presented for the years 2002 (lowest copper price) and 2011 (highest copper price). A list of the total extents of prognostic areas and their polymetallic copper equivalent resources with their net values expressed in billions of dollars is presented in Table 2.

The smallest total size of all combined prognostic areas in the vicinity of Milicz corresponds to the year 1995, amounting to 21.589 km². This is also the year of their lowest total resources, amounting to 0.981 Mt. The largest total area and the highest resources correspond to the year 2011, amounting to 31.670 km² and 1.495 Mt, respectively. This means an increase in both the area and

resources by about a half compared to 1995.

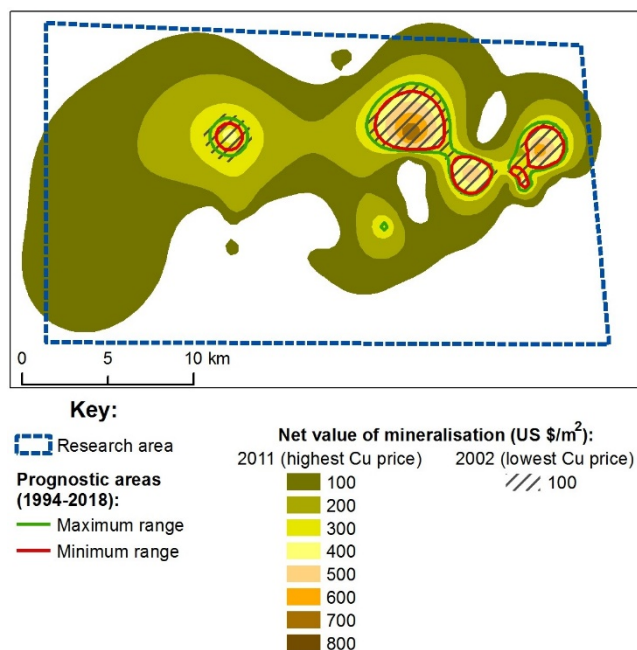


Figure 2. The minimum and maximum range of prognostic areas and the highest and lowest net value of mineralisation for average annual metal prices in the years 1994-2018.

Table 2. Changes in the total size, resources and net mineralisation value of prognostic areas based on average annual metal prices in the years 1994-2018.

Year	Prognostic areas		
	Total size (km ²)	Total resources (Mt)	Total net ore value (US \$ bln)
1994	24.090	1.104	2.494
1995	21.589	0.981	2.610
1996	24.584	1.124	2.536
1997	24.087	1.100	2.472
1998	30.337	1.414	3.034
1999	30.317	1.412	3.032
2000	27.044	1.248	2.704
2001	26.735	1.236	2.673
2002	27.374	1.270	2.737
2003	26.381	1.219	2.638
2004	24.191	1.109	2.902
2005	22.578	1.029	3.565
2006	21.890	0.992	6.498
2007	22.944	1.042	7.540
2008	23.186	1.061	7.358
2009	26.756	1.238	6.256
2010	25.591	1.182	8.863
2011	31.670	1.495	12.772
2012	31.264	1.474	11.496
2013	28.132	1.313	9.671
2014	26.119	1.208	8.215
2015	26.860	1.243	6.597
2016	30.441	1.424	6.933
2017	26.920	1.243	7.308
2018	25.215	1.156	7.269

On the other hand, the lowest net value of mineralisation has been calculated for the year 1997 and it amounts to US \$2.472 billion. The maximum value corresponds to the year 2011 and equals US \$12.772

billion, which is more than five times as high as the minimum value.

The presented methodology proves that a polymetallic mineral deposit which is not a subject of mining extraction, or even one with only inferred resources, still undergoes continuous dynamic changes. Not only do the fluctuations of metal prices affect the estimated net value of mineralisation; they also influence the range of an orebody, and therefore its resources. The applied formulas also enable the incorporation of numerous valuable components of ore into the calculations of resources. This is particularly important for deep deposits whose profitable extraction requires focusing on their richest parts.

References

- Bartlett S.C., Burgess H., Damjanović B., Gowans R.M., Lattanzi C.R. (2013) Technical Report on the copper-silver production operations of KGHM Polska Miedź S.A. in the Legnica-Głogów Copper Belt area of southwestern Poland. Micon International Limited. 170 p.
- Chunlong L., Yanwei G., Yongjun X., Hanping Z., Meng W., Xiangyu F., Shaojun B. (2017) Separation and Recovery Process of Copper-Lead-Silver-Barium Polymetallic Ore from Abroad [J]. Chin. J. Process Eng., 17(4):751-756.
- Kursun H., Ulusoy U. (2015) Zinc Recovery from a Lead-Zinc-Copper Ore by Ultrasonically Assisted Column Flotation. Particulate Science and Technology, 33, 4:349-356.
- Lorenzo-Tallafigo J., Iglesias-González N., Mazuelos A., Romero R., Carranza F. (2019) An alternative approach to recover lead, silver and gold from black gossan (polymetallic ore). Study of biological oxidation and lead recovery stages. Journal of Cleaner Production, 207:510-521.
- Oszczepalski S., Chmielewski A., Sowula W., Boratyn J., Piłkuła K., Zieliński K. (2012a) Ocena możliwości występowania cechsztyńskiej mineralizacji Cu-Ag na obszarze województw lubuskiego i wielkopolskiego na podstawie archiwalnych materiałów wiertniczych, w tym wierzeń naftowych (in Polish). Polish Geological Institute – National Research Institute. 196 p.
- Oszczepalski S., Speczik S., Małecka K., Chmielewski A. (2016) Prospective copper resources in Poland. Gosp. Sur. Miner. – Miner. Res. Manag., 32, 2:5–30.
- Oszczepalski S., Speczik S., Marks L. (2012b) Litologia, petrografia i cechsztyńska mineralizacja kruszcowa w wybranych profilach wiertniczych z rejonu Żmigród, Milicz, Sulmierzyce i Kalisz (in Polish). Polish Geological Institute – National Research Institute. 244 p.
- Retman W., Młynarczyk M., Grelewicz M., Kosowska M., Kosowski M., Krzysztynski K. (2014) Dokumentacja geologiczna złoża rud cynku i ołowiu „Zawiercie 3” w kategorii C1 + C2 + D w miejscowości: Zawiercie, Łazy, Rokitno Szlacheckie, Markowizna, Józefów, Poręba, gm. Zawiercie, Łazy, Ogrodzieniec, Poręba, pow. zawierciański, woj. śląskie (in Polish). Rathdowney Polska Sp. z o.o., Kraków. 93 p.
- Wołkowicz S., Smakowski T., Speczik S. (eds) (2011) Bilans perspektywicznych zasobów kopalni Polski wg stanu na 31 XII 2009 r. (in Polish). Polish Geological Institute – National Research Institute. 262 p.
- Zieliński K., Wierchowicz J. (2018) The equivalent copper producibility of polymetallic Cu, Ag, Zn, Pb mineralisation in the Fore-Sudetic Monocline as illustrated by the "Sulmierzyce-Odolanów" prospective area (in Polish with an English abstract). Zeszyty Naukowe IGSMiE PAN, 106:257-274.

Global copper resources and reserves; discovery is not the only control on supply

Simon M. Jowitt

University of Nevada Las Vegas, USA

Gavin M. Mudd

Environmental Engineering, School of Engineering, RMIT University, Australia

Abstract. Copper (Cu) is vital to modern life and has an often irreplaceable role in everyday infrastructure and technology. However, although clearly the world's endowment of extractable Cu is finite, global Cu production has increased over the past century, an increase that has been (more than) matched by significant growth in estimated Cu mineral reserves and mineral resources. Globally, some 2,301 deposits have reported Cu resources, split into 1,271 code-based and 1,030 non-code-based resources. A further 393 deposits have both resources and code-based reserves and a further 14 deposits have non-code-based reserves. These deposits contain 3,034.7 Mt of Cu, up from the 1,861.3 Mt reported in our 2010 study, including 640.9 Mt of contained Cu in reserves. The vast majority of mineral deposit types have recorded an average increase in Cu resources between 2010 (Mudd et al., 2013) and 2015, although grades are often similar, slightly lower (by ~5%), or are significantly lower depending on the mineral deposit type being considered. Porphyry deposits still dominate global Cu resources and reserves, containing ~75% of the contained Cu in our database. Equally unsurprisingly, Chile dominates global Cu resources and reserves, followed by the USA and Peru.

1 Introduction and overview

Copper (Cu) remains one of society's most widely used metals and plays a vital role in electronics, vehicles, telecommunications, electrical power generation and distribution systems, domestic and industrial piping, chemicals, currency and general infrastructure (e.g. (Gordon et al., 2006; Schlesinger et al., 2011; von Gleich et al., 2006)). The malleability, conductivity, and other unique characteristics of Cu means that these uses of this metal will continue for many decades to come. Recent concerns have also been raised about a variety of metals and minerals that are considered at potential supply risk but remain critical for numerous technologies and uses – the so-called “critical metals” (e.g., BGS, 2015; EC, 2017; Graedel et al., 2015; NRC, 2008). Although the metals considered critical varies on the viewpoint of the organization, country, or group of countries in question, these lists typically include the rare earth elements (REE), Ga, In, W, the platinum group elements (PGE), Co, Nb, Mo, Re, Sn, Li, V, Ni, Ta, Te, Cr, and Mn. Although this list does not include Cu, copper has a vital role in the supply of these critical metals as a number of these metals are predominantly sourced as a byproduct

of copper production (e.g. Se, Te, Mo, Re, Co; Jowitt et al., 2018). This means that understanding global copper resources is vital for not only determining where and how demand for this metal can and will be met in the future, and what may prevent this demand being met, but also what impact this Cu production may have on the supply of associated critical metals. Overall, to meet reasonable societal needs for Cu and possible critical metals derived from its mining, it is therefore fundamental to understand the dynamics of primary supply from the mining of mineral deposits containing Cu.

Mineral deposits are often viewed as ‘finite’ and ‘non-renewable’ resources as they are of a given size, have an average metal concentration, and once extracted cannot be replaced by the normal geological processes of mineral deposit formation, which often occur deep in the Earth's crust and can take millions of years. From a mining perspective, this means it is important to keep exploring for new deposits as known deposits are mined and then depleted. The amount of Cu known in mineral deposits is therefore a dynamic quantity, changing over time in response to exploration and mine production. There are two conceptual approaches to this situation – namely fixed stock or economic models, as reviewed briefly by IIED and WBCSD (2002), in detail by Tilton (1996) and more recently by Northey et al. (2018). The fixed stock approach assumes that there is a ‘finite’ quantity of mineable Cu (also referred to as ‘geological stocks’) and that we are possibly beginning to approach this value (e.g., Gordon et al., 2006). The economic approach assumes that as lower cost (or higher grade) deposits are depleted, ongoing demand will lead to higher prices which in turn make marginal or higher cost (and often lower grade) resources economic. There is also good evidence that although we are far from approaching geological stocks for potentially mineable Cu resources, the economic approach fails to account for the full complexity of issues affecting (and potentially controlling aspects of) Cu mining, especially social and environmental issues.

There is still misplaced concern, however, that the fixed stock approach is accurate and that we are therefore heading towards the point of ‘running out’. This perspective fails to appreciate the practices of the mining industry in assessing and reporting potentially mineable deposits, especially the wide variety of factors that are taken into account in such estimates. In particular, the terms reserves and resources have strict definitions in the mining industry and mean different things. For example,

reserves are considered economically mineable and relate to a specific mine plan (say for a 5-10 year horizon), while resources are geologically known but are less certain economically, may not have all necessary approvals for mining yet, and may relate to a 10-30 year planning horizon, or have no time expectation at all. This means that any assessment of reserves alone will necessarily appear to be modest in comparison to resources, as reserves relate to short-term mine plans. There are also numerous deposits that are known to be similar to existing deposits (or mines) but have not yet had reserves and/or resources formally estimated and/or publicly reported for them (e.g. Sakatti nickel (Ni)-Cu-PGE deposit, Finland) or are government or privately owned and are not bound by common stock exchange reporting requirements (e.g. Muruntau Au mine, Uzbekistan; Eloise Cu-Au mine, Australia). Combining these factors with ongoing exploration and active mining reinforces the fact that reserve and/or resource estimates are very dynamic over time and are invariably an underestimate of what could be mined in the near future (e.g. over the remaining decades of this century).

There are exceedingly few studies that examine the evolution of mineral reserves and resources over time and their conversion to mined production, including the various factors that can be crucial in hindering or facilitating such conversion. We recently published two studies of global Cu resources for the year 2010 (Mudd et al., 2013) and the year 2015 (Mudd and Jowitt, 2018; forming the basis of this abstract), showing that considerable Cu resources are available that could meet future demand a significant way into the future. In reality, the lack of detailed studies on reserves and resources trends over time combined with detailed assessments of key aspects that affect the conversion of resources to reserves and mined production remains a significant gap in the literature. This paper provides a new assessment of global Cu resources and reserves, discriminating between mineral resources and mineral reserves and examining the evolution of mineral resources over time coincident with production.

2 Global Cu resources and reserves

The 2,301 deposits compiled during this study contain Cu resources split between 1,284 code based and 1,017 noncode based resources. A further 393 deposits have both resources and code-based reserves and a further 14 deposits have non-code-based reserves. The most important values are arguably the significantly increased contained Cu in mineral resources (compared to the 2010 data of Mudd et al., 2013) at a total of 3,034.7 Mt Cu (Fig. 1), of which 2,489.4 Mt Cu is from code-based deposits and also includes the subset of mineral reserves containing 640.9 Mt Cu (637.6 Mt Cu of which is code based). The 2010 study recorded some 1,861.3 Mt Cu contained in mineral resources, meaning the 2015 estimate is a major advance in global Cu endowment, even if noncode data are excluded (i.e., 2,489.4 vs. 1,861.3 Mt Cu). All deposit types have greater 2015 resources than 2010 resources, often substantially so for

the major deposit types. The ore grades are generally similar, with some ~5% lower (e.g., porphyry, sediment-hosted stratiform/stratabound Cu, skarn, magmatic sulfides), others significantly lower (e.g., sediment-hosted Pb-Zn, VMS, manto Cu), and others with an increase in average grade (e.g., epithermal, intrusion-related Au; Fig. 1). These variations are typically related to the extent of deposits included, which is often greater in this study compared to the 2010 data presented in Mudd et al. (2013), but also to the changing mine plans for important deposits in each class. For example, the Telfer intrusion-related Au project has seen a marked reduction in reported resources and reserves in recent years (from a peak of 1,144.6 Mt at 0.09% Cu in 2011 to 360.4 Mt at 0.16% Cu in 2015; Newcrest Mining Ltd. data), indicating an effective conversion to a higher-grade mine plan to optimize costs and economic returns for the project.

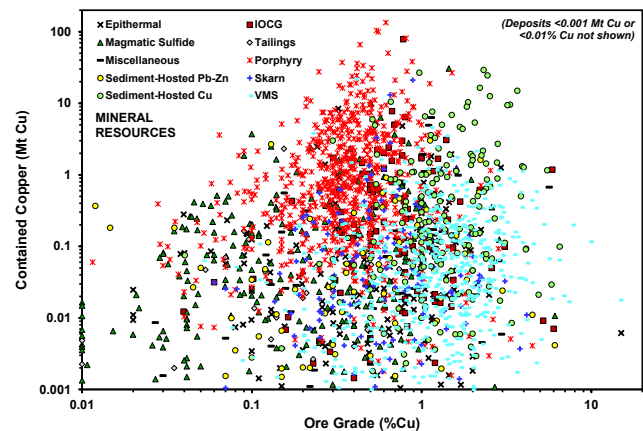


Figure 1. Relationship between Cu grades and contained Cu for 2015 mineral resources (Mudd and Jowitt, 2018).

2.1 Mineral deposit types

Porphyry deposits dominate global Cu resources (as expected), with ~75% of the total contained Cu in our database in both mineral resources and mineral reserves hosted by porphyry deposits. The next in size, almost an order of magnitude lower, is sediment-hosted stratiform/stratabound Cu deposits, whereas all other deposit types contain modest to insignificant Cu resources compared to porphyry deposits. Other unusual Cu-bearing deposit types include sea floor polymetallic nodules, unconformity U, and Ni laterites as well as a magmatic Fe-Ti-V oxide-related deposit. Our database also includes 26 and seven code- and noncode-based tailings resources, respectively, including five with code-based reserves, yielding some ~4.02 Mt Cu in tailings resources and reserves.

Some 21.1% of the total resources data is present in the form of reserves. This percentage of reserves within resources is similar across the majority of deposit types, although some have much higher (e.g., skarn) or lower (e.g., epithermal, sediment-hosted Pb-Zn, tailings) values. Several mineral deposit types have no Cu reserves at all (e.g., shale-hosted, unconformity U, native Cu, Ni laterite), perhaps reflecting their unconventional

nature and higher development risk (e.g. the Talvivaara mine in Finland; Mudd et al., 2017). For grades, the average ratio of reserves to resources is 1.09, with most falling between ~0.8 and ~1.4, although some deposits have much higher (e.g., sediment-hosted Pb-Zn) or lower (e.g., tailings) reserve grades. It also must be noted that there are several countries that clearly contain reserves present at operating mines, but where data is not reported publicly (e.g., Iran, Armenia, Uzbekistan, Serbia), indicating our data should be regarded as a minimum estimate.

2.2 Resources and reserves by country

In terms of country endowment, Chile has just over double the Cu endowment of its nearest competitor, the USA, which in turn hosts just under double the Cu endowment of Peru, with all countries closely spaced after this. It is important to note that only Bolivia and Botswana have fewer Cu resources remaining in 2015 than cumulative production by this time (both are minor Cu producers). All other countries have more Cu resources remaining in 2015 than cumulative production, many exceptionally so (e.g., United States, Australia, Argentina, Pakistan, Panama, Chile, etc.). This is again clear evidence of growing Cu endowments over time.

2.3 Largest and highest grade copper resources and reserves

The largest or highest grade deposits or projects in our database are Andina, which has the largest resource (133.9 Mt Cu), Escondida, which has the largest reserve (50.6 Mt Cu), Phu Tuxan (Phuda), which has the highest resource grade (15% Cu), and Sudbury (KGHM), which has the highest reserve grade (7.92% Cu).

3 Individual resource growth over time

We also undertook a comparison of Cu resources between 2010 and 2015 after deducting cumulative production between 2011 and 2015 (Fig. 2), allowing a quantitative assessment of the changes in global Cu resources during this time. Although there is some scatter in this graph, the overall pattern can be modelled using a best fit linear regression yielding an equation of $2015 = 1.1308 \times (2010 - \text{cumulative production})$ and a correlation coefficient of correlation of 0.947. This demonstrates that global Cu resources grew by an average of 13% between 2010 and 2015 on an individual project basis after allowing for cumulative production. This 13% growth is for projects that reported resources in 2010 and 2015, and does not consider new discoveries made during this time. This growth in Cu resources therefore demonstrates that global copper resources can increase not just by discovery, but as a result of the expansion of known resources. Growth of this type demonstrates the way the mining industry operates in terms of delineation of resources and, subsequently, the reserves needed for economical mine planning. That is, rather than the expensive drilling out of an entire mineralized system at

the spacing needed for resource estimation, only sufficient studies are completed to justify investment, a reality that is frequently overlooked or poorly understood (e.g., Sverdrup et al., 2014; Ragnarsdóttir and Sverdrup, 2015).

Mineral exploration is different from hydrocarbon exploration in that, unlike the three-dimensional seismic and other approaches used by the latter, mineral exploration advances in stages, with resources and reserves being delineated up to a point where X years of production can be defined rather than mining companies spending exorbitant amounts of money delineating the entirety of what may still be an incompletely understood system. This enables mining companies to generate revenue from initial production, with some of this revenue, and ideally profit, used to identify and delineate further resources. This is exemplified by the continued growth of the resources and reserves at Grasberg coincident with the production of millions of tonnes of Cu and millions of ounces of Au (e.g., Jowitt et al., 2013). One example of this is shown by the Marcapunta deposit in Peru (M in Fig. 2), where resources increased from 0.172 Mt Cu in 2010 to 1.95 Mt Cu in 2015, coincident with the production of 0.024 Mt Cu. This increase in resources was the result of a significant amount of near-mine exploration expenditure by the operator, Buenaventura. This also indicates that if the 2010 figure was taken as total resources rather than considering potential expansion, then the available Cu at this mine (and many other mines) would be significantly underestimated. The same applies to the Los Azules porphyry Cu project in Argentina (L in Fig. 2; increase in resources from 1.01 to 16.3 Mt Cu) and the Escondida-Main deposit in Chile (E in Fig. 2; increase in resources from 59.6 to 104.3 Mt Cu coincident with production of 5.39 Mt Cu).

There are some examples within our database that further highlight differences between 2010 and 2015 resource and reserve estimates. For example, Andina has grown from 113.6 to 133.9 Mt contained Cu, the main Escondida deposit has grown from 52.1 to 104.3 Mt Cu and is now joined by nearby resources that total 36.1 Mt Cu (Chimborazo, Pampa Escondida, and Pinta Verde), and Tenke Fungurume has grown from 16.7 to 29.2 Mt Cu. In terms of reserves, Andina has declined from 19.8 to 7.40 Mt Cu (in contrast to resource growth) and the main Escondida deposit has grown from 31.4 to 50.6 Mt Cu despite cumulative production during this time of 5.39 Mt Cu (i.e., 26.0 to 50.6 Mt Cu). Finally, the reserves at Tenke Fungurume have declined from 4.04 to 3.71 Mt Cu despite cumulative production during this time of 0.90 Mt Cu (i.e., 3.14 to 3.71 Mt Cu). These several examples show that mining projects can certainly expand (and should be expected to if successful) beyond initial or even fairly mature resources and coincident with significant production. This also begs the question of at what point a given mining project would become mature and start to decline in terms of resources and reserves and how this might differ between different deposit types.

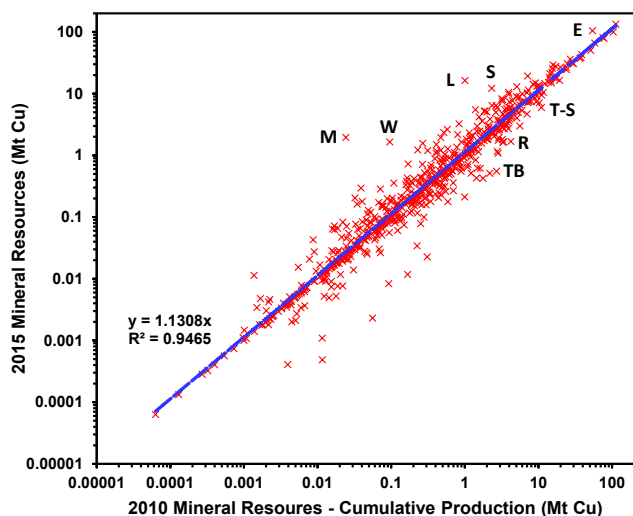


Figure 2. Comparison between 2015 (Mudd and Jowitt 2018) and 2010 (Mudd et al., 2013) mineral resources minus cumulative production (2011-2015). Notes: M – Marcapunta; W – Wellgreen; L – Los Azules; S – Spence; E – Escondida (Main); T-S – Trident-Sentinel; R – Robinson (Ely-Ruth); TB – Twin Buttes.

4 Conclusions

Global Cu resources as of 2015 included 2,301 deposits split into 1,284 code-based resources and 1,017 noncode-based resources. Some 403 of these projects have code-based reserves with a further four having noncode-based reserves. Global copper reserves are some 640.9 Mt of contained Cu, with global copper resources (including these reserves) being some 3,034.7 Mt of contained Cu (up from 1,861.3 Mt identified using 2010 data). These figures should be considered a minimum given the lack of reporting of Cu resources from some countries and projects. Porphyry deposits dominate global Cu resources and reserves, containing some ~75% of the contained Cu in our database, with Cu resources predominantly located in Chile, followed by the United States and Peru. The increase in global Cu resources is down to three main factors, namely deposit discovery, the incorporation of more resources within the database (i.e., better data coverage), and the growth of individual Cu resources (often coincident with production) by an average of ~13% between 2010 and 2015. This indicates the need for researchers to consider the methods used during the delineation of resources and reserves when examining global mineral resources, as using snapshots of resource data without consideration of their continued growth may lead to erroneous conclusions. This study indicates that Cu resources continue to grow over time coincident with production, indicating that although discovery—and, more importantly, brownfields expansion—is clearly important in terms of meeting increasing demands for Cu, we need to move beyond merely considering tonnes and grades. The fact that we have significant known Cu resources and reserves clashes with the increasing importance of environmental, political, logistical, and economical factors (among many others), meaning that these factors will become increasingly influential controls on the conversion of resources to reserves and the future supply

of Cu. In other words, just because it is a reported resource or reserve does not guarantee it will become production, and understanding the reasons why this does or does not occur is a topic that requires future investigation.

Acknowledgements

Financial support was provided by a small grant to both authors by the Resourcing Future Generations (RFG) initiative of the IUGS.

References

- British Geological Survey (2015) Risk list 2015—current supply risk for chemical elements or element groups which are of economic value. British Geological Survey, Keyworth, UK.
- European Commission (2017) The 2017 list of critical raw materials for the EU. DG Enterprise and Industry, Brussels, Belgium.
- Gordon RB, Bertram M, Graedel TE (2006) Metal Stocks and Sustainability: Proc Nat Acad Sci 103: 1209–1214.
- Graedel TE, Harper EM, Nassar NT, Reck BK (2015) On the materials basis of modern society. Proc Nat Acad Sci 112:6295–6300.
- International Institute for Environment and Development and World Business Council for Sustainable Development (2002) Breaking new ground: Mining, minerals and sustainable development. Earthscan, London.
- Jowitt SM, Mudd GM, Weng Z (2013) Hidden mineral deposits in Cu-dominated porphyry-skarn systems: How resource reporting can occlude important mineralization types within mining camps. Econ Geol: 108;1185–1193.
- Jowitt SM, Mudd GM, Werner TT, Weng Z, Barkoff D, McCaffrey D (2018) The Critical Metals: An Overview and Opportunities and Concerns for the Future. Soc Econ Geol Spec Pub 21: 25–38.
- Mudd GM, Jowitt SM (2018) Growing global copper resources, reserves and production: Discovery is not the only control on supply. Econ Geol 113:1235–1267.
- Mudd GM, Jowitt SM, Werner TT (2017) The world's lead-zinc mineral resources: Scarcity, data, issues and opportunities. Ore Geol Rev 80: 1160–1190.
- Mudd GM, Weng Z, Jowitt SM (2013) A Detailed Assessment of Global Cu Resource Trends and Endowments. Econ Geol 108:1163–1183.
- National Research Council (2008) Minerals, critical minerals and the U.S. economy. Committee on Critical Mineral Impacts on the U.S. Economy and Committee on Earth Resources, National Research Council (NRC) of the National Academies, Washington D.C., U.S.A.
- Northey SA, Mudd GM, Werner TT (2018) Unresolved complexity in assessments of mineral resource depletion and availability. Nat Resour Res 27:241–255.
- Ragnarsdóttir KV, Sverdrup HU (2015) Limits to growth revisited. Geoscientist 25:10–15.
- Schlesinger ME, King MJ, Sole KC, Davenport WG (2011) Extractive metallurgy of copper, 5th ed. Elsevier, Oxford.
- Sverdrup HU, Ragnarsdóttir KV, Koca D (2014) On modelling the global copper mining rates, market supply, copper price, and the end of copper reserves. Resour Conserv Recycl 87:158–174.
- Tilton JE (1996) Exhaustible resources and sustainable development: Two different paradigms. Res Pol 22: 91–97.
- von Gleich A, Ayres RU, Gößling-Reisemann S (2006) Sustainable metals management: Securing our future—steps towards a closed loop economy. Springer, Dordrecht, The Netherlands.

Assessment of undiscovered Li resources in LCT pegmatites in Finland

Timo Ahtola, Kalevi Rasilainen, Pasi Eilu, Niilo Kärkkäinen, Janne Kuusela, Panu Lintinen, Tuomo Törmänen, Tapio Halkoaho

Geological Survey of Finland, Finland

Abstract. Lithium resources in undiscovered LCT pegmatite deposits were estimated down to the depth of one kilometre in the bedrock of Finland using a three-part quantitative assessment method. Based on global data from 29 LCT pegmatite-hosted Li deposits we considered the best explored, we constructed a grade-tonnage model for our assessment. Nineteen permissive tracts were delineated for these deposits. Altogether, these tracts cover 22,404 km², which is 7% of the land area of Finland. The expected number of undiscovered Li deposits within the permissive tracts in Finland is 7, and these are estimated to contain, with a 50% probability, at least 510,000 t of lithium. Two thirds of the estimated undiscovered lithium resources in Finland are located within two permissive tracts in Western Finland. The assessment results indicate that at least 90% of the remaining lithium endowment within the uppermost 1 km of the Finnish bedrock is in poorly explored or entirely unknown deposits. Compared to global identified Li resource, these numbers are minor, but may be of importance for the near-future European Li battery industry. There has been no global assessments of undiscovered lithium resources to compare with the results from Finland.

1 Introduction

Presently, the world's sources of lithium under extraction are continental brines and pegmatites, whereas other sources, such as hectorite clay and jadarite deposits, have not been developed (Bradley et al. 2017; Jaskula 2018). In Finland, all the known lithium deposits and occurrences are hosted by pegmatites, and at least all the well-known lithium deposits are hosted by LCT pegmatites (Alviola 2012; Ahtola et al. 2015). Not even indirect indications of other types of lithium deposits are known from Finland.

We describe here the results of an assessment of undiscovered Li resources in LCT pegmatite-hosted deposits in Finland. Geological Survey of Finland (GTK) has carried out assessments of undiscovered mineral resources in Finland since 2008 (Rasilainen et al. 2010, 2016). Detailed results of the assessment of Li resources in Finland are reported in Rasilainen et al. (2018).

The GTK assessments are based on the three-part quantitative assessment method developed by the USGS (Singer 1993; Singer and Menzie 2010). The assessment process produces probabilistic estimates of the total amount of metals *in situ* in undiscovered deposits of selected types, down to the depth of one kilometre. The three-part method consists of (1) evaluation and selection or construction of descriptive models and grade-tonnage

models for the deposit types under consideration, (2) delineation of areas according to the types of deposits permitted by the geology (permissive tracts), and (3) estimation of the number of undiscovered deposits of each deposit type within the permissive tracts. The estimated number of deposits is combined with the grade and tonnage distributions from the deposit models to assess the total undiscovered metal endowment.

2 Lithium deposits in Finland

There are six well-known lithium deposits and over 30 partially explored occurrences in Finland (Fig. 1), all located in the southern half of the country and hosted by LCT pegmatites. The well-known deposits occur in a restricted area in central western Finland, in the Kaustinen area.

The Kaustinen lithium pegmatite province is hosted by Palaeoproterozoic supracrustal rocks. The dominant country rocks of the pegmatites are mica schists, metagreywackes, and metavolcanic rocks metamorphosed to amphibolite facies (Mäkitie et al. 2001). In the classification of granitic pegmatites (Černý & Ercit 2005), the lithium pegmatites of the Kaustinen province belong to the rare-element class of the LCT family, and more specifically to the albite-spodumene type of the lithium subclass (Ahtola et al. 2015). The pegmatites are dated to 1.79 Ga (Alviola et al. 2001) indicating intrusion during the late-orogenic stages of the Svecofennian orogeny (Lahtinen et al. 2009).

The Kaustinen LCT pegmatites occur as 1–30 m wide individual dykes up to 500 m long and dyke swarms up to 700 m in diameter (Kuusela et al. 2011; Ahtola et al. 2015; Keliber 2018).

Main minerals in the Kaustinen LCT pegmatites are spodumene, albite, quartz, K feldspar, and muscovite. Apatite, zinnwaldite, Nb–Ta oxides (Mn and Fe tantalites), beryl, tourmaline, fluorite, garnet (grossular), andalusite, calcite, chlorite, Fe–Mn phosphates, arsenopyrite, pyrite, pyrrhotite, and sphalerite have been detected in trace to minor amounts. Spodumene occurs as elongated, light green to light greyish, 0.5–50 cm long, lath-shaped crystals, which are oriented perpendicular to the wall-rock contacts. Spodumene is unevenly distributed in the dykes. In most cases, the spodumene content increases from the wall-rock contact towards the core of the dyke. At the wall-rock contacts, spodumene has usually been altered to muscovite (Sweco Industry 2016). For example in the Rapasaari deposit, the average spodumene content is 14.7 wt%, and, based on microprobe analyses, the average Li concentration of the spodumene is 7.21% Li₂O (Kuusela et al. 2011; Keliber

2018). The average contents of both Nb and Ta in the dykes vary between 20–80 ppm.

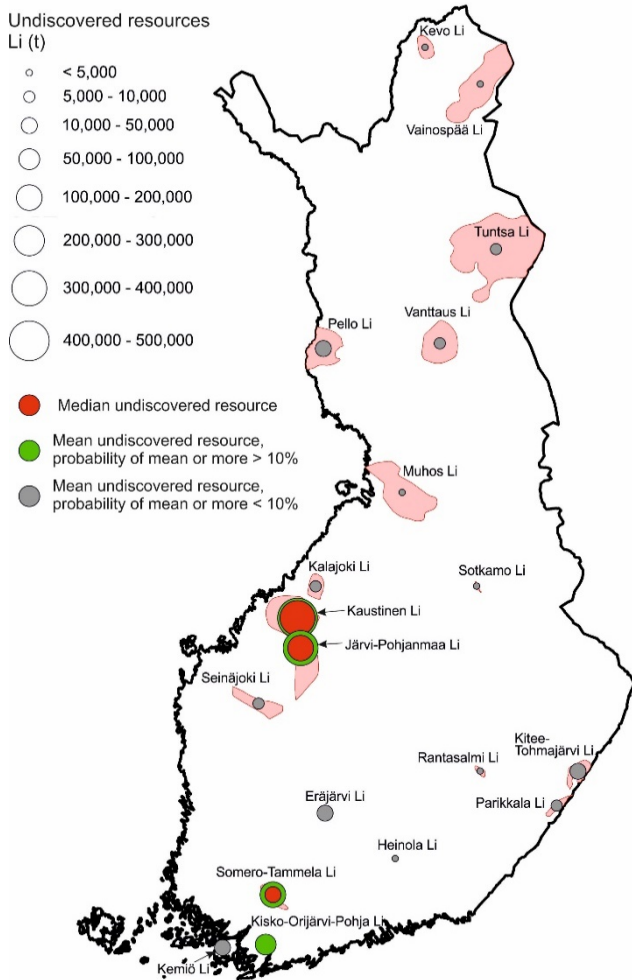


Figure 1. Permissive tracts for LCT pegmatite-hosted Li deposits in Finland. Note that the tracts are areas where geology allows these deposits to occur, not prospectivity.

3 Deposit model

The recently published mineral deposit model (Bradley et al. 2017) was used to identify the characteristic features of LCT pegmatites. This model was developed to support quantitative assessment of undiscovered lithium resources in LCT pegmatite-hosted deposits. The Finnish deposits were considered to comply with the model.

Grade and tonnage information was available for six LCT pegmatite lithium deposits in Finland and for 23 deposits from elsewhere ('global deposits'). The median tonnage of the global deposits (15.7 Mt) is almost 15 times larger than the median tonnage of the Finnish deposits (1.08 Mt), whereas there is no significant difference in the median Li grades between the global (1.19% Li₂O) and Finnish (1.20% Li₂O) deposits (Rasilainen et al. 2018). At least four of the six Finnish deposits with a published resource estimate are not totally delineated but remain open either at depth or along

strike, or both (Sweco Industry 2016). This, together with the similarity of average lithium grades in the Finnish and global deposits, suggests that there is no separate Finnish Li pegmatite population. Also, several of the global deposits are not entirely delineated. In any case, the number of Finnish deposits is too small for a stable deposit model, and hence, the global and Finnish data were jointly used to construct a grade-tonnage model for LCT Li pegmatite deposits. The distributions of Li grades and ore tonnages in the global model do not significantly deviate from lognormality, and there is no significant correlation between grade and tonnage.

4 Results and discussion

In total, 19 permissive tracts were delineated for LCT pegmatite-hosted Li deposits in Finland (Fig. 1). These tracts cover 22,404 km², which is about 7% of the total land area of Finland. The size of the tracts varies between 16 km² and 6624 km² with a median of 417 km² (Rasilainen et al. 2018). In most cases, the delineation of permissive tracts was based on reported existence of LCT pegmatite deposits or occurrences and late orogenic granites that could represent the source of the pegmatitic melts. In northern Finland, the tracts were delineated based on anomalous lithium concentrations in regional till geochemistry and reported observations of such tourmaline and/or beryl bearing pegmatites that were interpreted to belong to the LCT family.

The number of undiscovered deposits was estimated for each permissive tract. The expected (mean) number of undiscovered lithium deposits for a permissive tract, rounded to whole numbers, varies from zero to three deposits, and the sum of the mean estimates across all permissive tracts is seven deposits. Over 80% of the undiscovered deposits are estimated to be located within three permissive tracts: Kaustinen (38%), Järvi-Pohjanmaa (29%) and Somero-Tammela (15%).

The median estimate of the total *in situ* Li metal content in undiscovered LCT pegmatite-hosted deposits in Finland is at least 510,000 t of Li (Table 1), and 61% of this is estimated to be located in undiscovered deposits in the Kaustinen permissive tract (Fig. 1).

The identified Li resources in Finland are 51,000 t Li (Keliber 2018). The assessment results indicate that, at least, 90% of the remaining lithium endowment within the uppermost 1 km of the Finnish bedrock is in poorly explored or entirely unknown deposits.

The Kaustinen permissive tract and the surrounding larger Järvi-Pohjanmaa tract host the most important known and estimated undiscovered lithium resources in Finland. The Kaustinen deposits are under active development (Keliber 2018, 2019), and it can be expected that exploration within the area surrounding an operating lithium mine will in the future turn at least a part of the presently undiscovered resources into identified resources.

In a global or European-wide comparison, the Finnish identified and estimated undiscovered lithium resources are minor. The identified Finnish resources of 51,000 t of lithium (Keliber 2018) constitute 0.1% of the known world

resources, 2.1% of the European, and 3.7% of the EU lithium resources (Jaskula 2018). There have been no global assessments of undiscovered lithium resources to compare with the results from Finland.

In the EU and, especially, North-European context, the identified and assumed undiscovered resources may be of importance. The current mine production of Li within the EU is just 146 t Li, which is 0.4% of the global Li production (Reichl et al. 2018). According to the published updated definitive feasibility study for the Kaustinen deposits (Keliber 2019), based on an annual production of 12,000 t of lithium hydroxide, the annual output of the planned open pit mines could be 573,000 t of ore. This would facilitate an operating time of 13 years for the planned lithium hydroxide plant. According to our assessment (Rasilainen et al. 2018), there is a 90% probability that at least 2.1 Mt of undiscovered lithium pegmatite ore exist within the Kaustinen tract. If this resource was discovered, and assuming a similar reserve to resource ratio and concentrator throughput as in the published updated definitive feasibility study (Keliber 2019), the operating time of the lithium plant at Kaustinen could be increased by 40%. The discovery of new resources corresponding to the median estimate of undiscovered resources in the Kaustinen tract could increase the plant lifetime tenfold.

Considering the reliability of the assessment results, sensitivity analysis indicates that changes in grade and tonnage estimates have a much greater effect on the expected metal content in an assessment than changes in the expected number of deposits (Singer & Kouda 1999). This means that the greatest sources of possible error in the present assessments are associated with the grade-tonnage models used.

It is important that the grade and tonnage information included in the grade-tonnage model represents accurately total deposits of the correct deposit type. However, even deposits that are considered to be well known may contain undiscovered resources. Most of the deposits in our global grade-tonnage model might not be entirely delineated, and during the assessment process in 2017, new resource estimates were published at least once for several of the deposits. The updated estimates commonly had higher ore tonnages and somewhat lower lithium grades, resulting in an increased lithium metal content in the deposits. This indicates that the used grade-tonnage model underestimates the lithium contents of LCT pegmatite lithium deposits to some extent. Consequently, the amounts of lithium in the undiscovered resources estimated here are somewhat smaller than the true lithium contents in the undiscovered deposits.

Acknowledgements

We thank Laura Lauri for providing details and insights of Li deposits in northern Finland and Jussi Pokki for image preparation.

Table 1. Median (50% probability) and mean estimates of the undiscovered Li resources in LCT pegmatite-hosted deposits in Finland (Rasilainen et al. 2018).

Median estimate (t Li)	Mean estimate (t Li)	Probability of mean or greater	Probability of none
510,000	1,200,000	0.30	0.07

References

- Ahtola T, Kuusela J, Käpyaho A, Kontoniemi, O (2015) Overview of lithium pegmatite exploration in the Kaustinen area in 2003–2012. *Geol Surv Finland, Rep Invest 220*, 28 p
- Alviola R (2012) Distribution of rare element pegmatites in Finland. *Univ Helsinki, Inst Seismology, Rep S-56:1–4*
- Alviola R, Mänttari I, Mäkitie H, Vaasjoki M (2001) Svecofennian rare-element granitic pegmatites of the Ostrobothnia region, western Finland; their metamorphic environment and time of intrusion. *Geol Surv Finland, Spec Pap 30:9–29*
- Bradley DC, McCauley AD, Stillings LM (2017) Mineral-deposit model for lithium-cesium-tantalum pegmatites. *U.S. Geol Surv, Sci Invest Rep 2010–5070–O*, 48 p
- Černý P, Ercit TS (2005) The classification of granitic pegmatites revisited. *Can Miner 43*, 2005–2026
- Jaskula BW (2018) Lithium. *U.S. Geol Surv, Mineral Comm Summaries 2018:98–99*
- Keliber Oy (2019) Updated Definitive Feasibility Study, Lithium hydrpoxide production. Press conference Thursday February 28th, 2019, 22 p
- Keliber Oy (2018) Lithium Project, Definitive Feasibility Study – Executive Summary. Dated 14th June 2018, 60 p
- Kuusela J, Ahtola T, Koistinen E, Seppänen H, Hatakka T, Lohva J (2011) Report of investigations on the Rapasaaret lithium pegmatite deposit in Kaustinen–Kokkola, Western Finland. *Geol Surv Finland, Rep 42/2011*, 65 p
- Lahtinen R, Korja A, Nironen M, Heikkinen P (2009) Palaeoproterozoic accretionary processes in Fennoscandia. *Geol Soc Spec Publ 318:237–256*
- Mäkitie H, Kärkkäinen, N, Lahti SI, Alviola R (2001) Compositional variation of granitic pegmatites in relation to regional metamorphism in the Seinäjoki region, Western Finland. *Geol Surv Finland, Spec Pap 30:31–59*
- Rasilainen K, Eilu P, Halkoaho T, Iljina M, Karinen T (2010) Quantitative mineral resource assessment of undiscovered PGE resources in Finland. *Ore Geol Rev 38:270–287*
- Rasilainen K, et al. (2016) Assessment of undiscovered metal resources in Finland. *Ore Geol Rev 86:896–923*
- Rasilainen K, Eilu P, Ahtola T, Halkoaho T, Kärkkäinen N, Kuusela J, Lintinen P, Törmänen T (2018) Quantitative assessment of undiscovered resources in lithium–caesium–tantalum pegmatite-hosted deposits in Finland. *Geol Surv Finland, Bull 406*, 172 p
- Reichl C, Schatz M, Zsak G (2018) *World Mining Data. Vol 33.* Austrian Federal Ministry of Science, Research and Economy, Vienna, 250 p
- Singer DA (1993) Basic concepts in three-part quantitative assessments of undiscovered mineral resources. *Nonrenew Res 2:69–81*
- Singer DA, Menzie WD (2010) *Quantitative mineral resource assessments: An integrated approach.* Oxford University Press, New York
- Singer DA, Kouda R (1999) Examining risk in mineral exploration. *Natural Resources Res 8:111–122*
- Sweco Industry (2016) Pre-feasibility Study, Keliber Lithium Project. Report dated 14th March 2016, 215 p

Reassessment of Sn-Co mineralization in mica schists of the Krobica-Gierczyn area (SW Poland)

Alicja Pietrzela

Miedzi Copper Corp., Al., Poland

University of Warsaw, Faculty of Geology, Poland

Abstract. New investigation of the Krobica–Gierczyn mineralization, previously considered as the Sn-Co type, proved it to be polymetallic Sn-Co-Ni-Cu-Zn-Pb-Bi-As-Sb mineralization enriched with indium. The Krobica-Gierczyn area belongs to the Stara Kamienica mica schist belt, located in the western part of the Sudety Mountains. Tin and cobalt were mined here in the past; however, now this mineralization is considered to be below the cut-off grade. During microscopic examination main ore minerals were described, including pyrrhotite, chalcopyrite, sphalerite, pyrite, arsenopyrite, löllingite, galena, native bismuth and cassiterite. Chemical analyses using an SEM (EDS) and an EMPA revealed the occurrence of cobaltite, giessenite, willyamite and ikonolite. The last three minerals had not been described in this area before. Distribution of trace elements in the ore minerals, especially Co and In, was also studied, as they are critical metals of great economic value. Minerals containing Co include glaucodot, arsenopyrite and löllingite (up to 29.02wt%, 7.65wt% and 8.68wt% Co, respectively). Increased concentrations of In were noted in sphalerite and cassiterite (up to 0.11wt% and 0.15wt%). The documented concentrations of In could increase the economic value of the described mineralization.

1 Introduction

The Krobica-Gierczyn area is well known for its occurrences of tin mineralization (Jaskólski and Mochnacka 1958; Wiszniewska 1984; Michniewicz et al. 2006). Nowadays, tin is still an economically important metal, used in numerous modern technologies. Polish deposits of this metal were mined until the 19th century; however, now they are considered to have no economic value. Nonetheless, the shrinking world resources and prices that have remained high in the recent years could constitute a reason to pay more attention to these deposits. Documented occurrence of other valuable elements accompanying tin, like In, Co, Bi and Sb could be a reason for the reassessment of the economic value of mineralization in the Krobica-Gierczyn area.

Therefore, the aim of the study was to analyze ore mineralization, especially sulfides and sulfosalts accompanying tin, describe its mineralogical and textural features and analyze the chemical composition of each mineral. Particular emphasis was placed on trace elements, especially indium and cobalt, and their distribution in different minerals.

2 Geological setting

The Krobica-Gierczyn area is located in south-western Poland, in the western part of the Sudety Mountains. The Sudety Mountains constitute the north-eastern margin of the Bohemian Massif, which belongs to the internides of the Variscan Belt of Europe (Mazur et al. 2006). The main geological unit of the western part of the Sudety Mountains is the Karkonosze-Izera Massif, which is composed of the Variscan Karkonosze Granite and its metamorphic envelope. Its northern part includes the Izera Gneisses and several supracrustal complexes in the form of elongated belts (Mazur et al. 2006).

The Krobica-Gierczyn area belongs to the Stara Kamienica belt, which is the biggest and most diverse of all supracrustal complexes occurring among the Izera Gneisses (Michniewicz et al. 2006). The Stara Kamienica belt consists mostly of various types of metamorphic schists, probably of Precambrian age (Mazur et al. 2006). Main components of these schists include muscovite, biotite, chlorite, quartz, with garnets (mainly almandine) in their certain parts (Wiszniewska 1984; Michniewicz et al. 2006). Tin mineralization accompanied by sulfides and sulfosalts occurs in the central part of the Stara Kamienica belt (Fig. 1).



Figure 1. Geological sketch-map of the Karkonosze-Izera Massif (after Mazur et al. 2006).

3 Petrography and mineralogy of the ore

Cassiterite is the main tin mineral. It occurs in two forms: granular, often forming botryoidal aggregates, or "spongy". The size of cassiterite grains is usually smaller than 0.2 mm (Mochmacka 1985; Wiszniewska 1984). Polymetallic mineralization that accompanies cassiterite sometimes forms small lenses or impregnation veins, usually up to 1 cm thick, but most often it is disseminated in the host rock (Wiszniewska 1984). The most common ore minerals are pyrrhotite, pyrite, marcasite, sphalerite, chalcopyrite, galena, arsenopyrite, löllingite, bismuth, bismuthinite, cobaltite, nickeline, gersdorffite, tetrahedrite, stibnite, ilmenite and rutile (Jaskólski and Mochmacka 1958; Wiszniewska 1984; Cook and Dudek 1994; Michniewicz et al. 2006).

Local concentrations of sulfides and sulfosalts occur in the whole central part of the Stara Kamienica schist belt, while tin is limited to certain specific ore-bearing zones. They usually form lenses, concordant with the foliation of schists, with very variable length and thickness which reach several meters (Michniewicz et al. 2006).

4 Origin of the ore

The origin of mineralization is still a matter of discussion. The origin of cassiterite was considered as (1) sedimentary, syngenetic and later metamorphosed (Szalamacha and Szalamacha 1974); (2) hydrothermal, related to the granitic protolith of the Iżera Gneiss (pre-metamorphic) (Cook and Dudek, 1994; Michniewicz et al. 2006); (3) hydrothermal, related to the Variscan evolution of the Karkonosze Granite (post-metamorphic) (Jaskólski and Mochmacka 1958; Wiszniewska 1984; Mochmacka et al. 2015). Sulfides and sulfosalts are of hydrothermal origin; however, it is also a subject of debate whether the source of hydrothermal solutions was in the Iżera Granite or the Karkonosze Granite.

The main argument for the sedimentary genesis of cassiterite is that there seems to be a relationship between cassiterite and the lithology of schist protoliths, as tin occurs mostly in schists enriched with garnets (Szalamacha and Szalamacha 1974). However, it was proven that the shape of ore zones does not always correspond to the shape of zones containing garnets (Michniewicz et al. 2006). The hydrothermal origin of tin is supported by the fact that cassiterite occurs in paragenesis with sulfides and sulfosalts (Mochmacka 1985; Wiszniewska 1984), as well as by sulfur isotope analyses ($\delta^{34}\text{S}$) in sulfides accompanying tin mineralization (Berendsen et al. 1987). However, it is still unclear whether the mineralization was emplaced before or after the Variscan orogeny.

The genesis of mineralization was a long process which had a telescopic character, and each phase of this process had a different spatial extent (Wiszniewska 1984). There was probably a certain time gap between the emplacement of cassiterite and sulfides, as there are some major differences between their spatial distribution (Michniewicz et al. 2006).

5 Deposits

Up to 20 tin mines operated in the Krobica-Gierczyn area from the 16th to the first half of 19th century. East of Gierczyn, in Przecznica, there was also a cobalt mine (Madziarz 2008). Today, only old adits and dumps can be found in the area. In Krobica there is still an operating quarry where mica schists are being mined, but tin is not extracted anymore.

There are two tin deposits in the Stara Kamienica belt, documented in the 1970's by Polish geologists: "Krobica" and "Gierczyn". Indicated resources, calculated in categories C₁ and C₂ according to Polish criteria, are estimated at 5.5 million metric tons of ore containing on average 0.5% of tin. Inferred resources (category D) of the whole Stara Kamienica belt are estimated at 20 million metric tons of ore containing 100 thousand metric tons of metallic tin (Mikulski 2017). These resources are considered to be below the cut-off grade. Tin was the only subject of documentation in the Krobica-Gierczyn area. Knowledge on mineralogical and chemical composition of the sulfides/sulfosalts assemblage is not very detailed. For that reason, this mineralization is still a very interesting field of research.

6 Materials and methods

The following samples were analyzed in the study: samples from historical mines (containing the richest mineralization), samples collected from the Krobica quarry and samples collected from old dumps located close to historical mines. The samples comprise two main types: (1) composed mainly of chlorite, mica, quartz and minor garnets, in some cases with visible foliation; (2) composed of biotite, minor quartz and locally garnets. Garnets are usually hypautomorphic and exhibit brittle deformations. Samples were also collected from a massive sphalerite vein.

All of the samples were analyzed using the NIKON ECLIPSE E600 polarizing microscope in reflected light. Photomicrographs of the samples were taken and main ore minerals were identified. The ZEISS Sigma scanning electron microscope was used to confirm the identification of main ore minerals. BSE images of selected samples were examined and EDS analyses were then used to estimate their elemental composition. Samples containing the most interesting mineralization were chosen for further analyses using the CAMECA SX-100 electron microprobe analyzer. All of the analyses were conducted at the Faculty of Geology of the Warsaw University.

7 Results

7.1 Microscopic examination

In the first group, comprising samples from the old mines composed of chlorite and quartz, pyrrhotite is the most common mineral, usually accompanied by chalcopyrite and sphalerite (Fig. 2.A, B). Sphalerite very

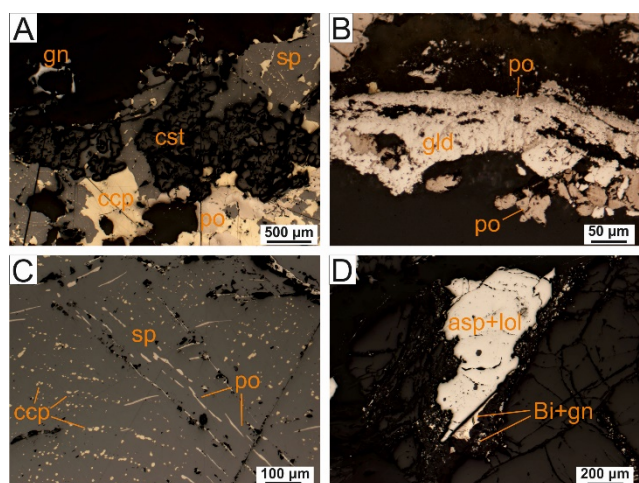


Figure 2. Reflected light images of the ores from the Krobica-Gierczyn area. **A.** Cassiterite (cst) forming intergrowths with sphalerite (sp), chalcopyrite (ccp), pyrrhotite (po) and galena (gn); **B.** Pyrrhotite (po) substituted by glaucodot (gld); **C.** Part of a sphalerite (sp) vein with exsolutions of pyrrhotite (po) (elongated) and chalcopyrite (ccp) (rounded); **D.** Arsenopyrite (asp) with intergrowths of löllingite (lol) accompanied by small aggregates of native bismuth (Bi) and galena (gn) inside of the garnet.

commonly contains rounded or elongated exsolutions of pyrrhotite and chalcopyrite (Fig 2.C). Other minerals observed in these samples include: galena, arsenopyrite (sometimes containing intergrowths of löllingite) and native bismuth. Covellite locally replaces chalcopyrite. Pyrrhotite is often replaced by secondary Fe-phases (pyrite/marcasite). Cassiterite was also observed in the discussed samples. It usually forms irregular aggregates or single isometric grains (Fig. 2.A).

In the second group, comprising samples from the old mines, composed of biotite and garnets, arsenopyrite is the main ore mineral. It commonly contains intergrowths of löllingite, often occurring in the central parts of arsenopyrite grains. Arsenopyrite locally contains intergrowths of native bismuth (Fig. 2.D). Native bismuth also forms small intergrowths with galena, disseminated within fractures in garnets. The discussed samples also contain minor pyrrhotite, chalcopyrite and sphalerite. Almost all of the samples from the old mines contain ilmenite and rutile. Their elongated grains are especially common in garnets.

In samples collected on site (in the quarry and from the dumps), mineralization is definitely less diverse. It consists mostly of pyrrhotite, native pyrite, ilmenite and rutile.

7.2 SEM + EDS

SEM analyses allowed the identification of more mineral phases. One of them is a lead sulfide containing bismuth, antimony and small admixtures of copper, silver and iron. Its chemical composition examined using the EDS suggests that this mineral could be giessenite $Pb_{27}(Cu,Ag)_2(Bi,Sb)_{19}S_{57}$ (Fig. 3.A). Another identified phase was a cobalt arsenic sulfide, accompanying pyrrhotite (Fig. 2.B). Its chemical composition indicates it could be a member of the cobaltite-gersdorffite series. In samples containing rich arsenopyrite and löllingite

mineralization, bismuth sulfide was also observed (Fig. 3.B). Chemical analyses using EDS suggest that this mineral could be ikonite $Bi_4(S,Se)_3$. The next identified phase is a cobalt-nickel antimonian sulfide accompanying chalcopyrite and native bismuth (Fig. 3.C). Its preliminary chemical composition is: 13.90-14.16wt% S, 58.94-59.36wt% Sb, 4.24-12.33wt% Co and 14.83-22.54wt% Ni. The total Co and Ni content is more or less constant and it amounts to approximately 27%. These results indicate it could be a member of the ullmannite ($NiSbS$) – costibite ($CoSbS$) series, like willyamite (Co,Ni)SbS.

Analyses of ore minerals that have already been identified in reflected light have shown that: (1) sphalerite almost always exhibits admixtures of indium; (2) arsenopyrite contains admixtures of Co and Sb; (3) löllingite contains admixtures of Co and Ni; (4) löllingite intergrowths in arsenopyrite are usually not observable in reflected light; they can only be examined in a BSE image (Fig. 3.D); (5) both minerals can contain intergrowths of galena, which are also not observable in reflected light; (6) tetrahedrite is present in one sample.

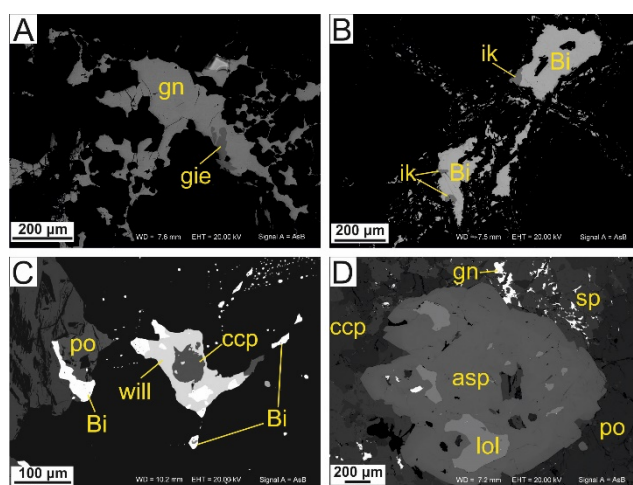


Figure 3. BSE images of ores from the Krobica-Gierczyn area. **A.** Galena (gn) with rounded intergrowths of giessenite (gie); **B.** Native bismuth (Bi) with intergrowths of ikonite (ik) inside the garnet; **C.** Willyamite (will) accompanied by chalcopyrite (ccp), native bismuth (Bi) and pyrrhotite (po); **D.** Arsenopyrite (asp) grain with intergrowths of löllingite (lol) and galena surrounded by pyrrhotite (po), sphalerite (sp), chalcopyrite (ccp) and galena (gn).

7.3 EMPA

5 samples were chosen for analyses using an electron microprobe. Selected results are shown in Table 1. The analyses revealed that In admixtures in sphalerite amount to between 0.05wt% and 0.11wt%. Concentrations of In were also noted in cassiterite (from 0.06wt% to 0.15wt%). Cassiterite also contains up to 0.4wt% Ta. Admixtures of Co in arsenopyrite can reach up to 7.65wt%, with up to 1.1wt% Sb. Concentrations of Ni were also noted (up to 0.71 wt%). Löllingite contains increased concentrations of Co, Ni and Sb reaching 8.68wt%, 2.86wt% and 0.58wt%, respectively. Galena in the analyzed samples contains up to 1.43wt% Bi and small concentrations of Ag (up to 0.36wt%).

The identification of giessenite and ikonite was

confirmed. The empirical formula of ikonolite is $\text{Bi}_{3,835-5,126}\text{Fe}_{0,019-0,193}\text{S}_3$ and the formula of giessenite is $\text{Pb}_{23,917-24,714}(\text{Cu}_{0,979-1,487}\text{Ag}_{0,687-0,954}\text{Fe}_{0,528-0,918})(\text{Bi}_{14,453-15,222}\text{Sb}_{5,169-5,506})(\text{S}_{56,865-57}\text{Se}_{0-0,135})$. The cobalt arsenic sulfide was also analyzed. It contains from 25.75wt% to 29.02wt% Co. Its formula indicates that this is cobaltite enriched with nickel and iron: $(\text{Co}_{0,689-0,758}\text{Ni}_{0,044-0,176}\text{Fe}_{0,092-0,174})\text{As}_{0,749-0,977}(\text{S}_{0,995-0,997}\text{Se}_{0,003-0,005})$.

Table 1. Mineral chemistry of some of the identified ores from the Krobica–Gierczyn area.

	sphalerite	arsenopyrite	löllingite	glaucodot	giessenite	ikonolite
S	33.34	16.23	1.21	20.17	16.75	10.38
Se	0	0.14	0.24	0.19	b.d.l.	b.d.l.
Ag	b.d.l.	b.d.l.	b.d.l.	b.d.l.	0.78	b.d.l.
As	b.d.l.	49.29	69.21	43.58	0	0
Bi	0	0	0	0	28.35	87.06
Cd	0.50	0	b.d.l.	0	0	0
Co	b.d.l.	5.80	6.68	26.51	0	0
Cu	0	0	0	b.d.l.	0.87	b.d.l.
Fe	6.36	28.45	20.06	5.23	0.46	0.21
In	0.09	0	0	b.d.l.	0	0
Ni	b.d.l.	0.21	2.03	5.20	b.d.l.	b.d.l.
Pb	0	0	b.d.l.	0	46.16	0
Sb	0	0.87	0.58	0	6.07	0
Zn	58.97	b.d.l.	0	0	0	0
Total	99.28	100.99	100.01	100.86	99.43	97.65

8 Conclusions

The performed studies documented the mineralogy of sulfides and sulfosalts occurring in the mica schists, as well as the chemical composition of the identified minerals, especially admixtures of trace elements like indium. This element has a great economic value as it is present on the list of critical elements which are crucial for modern technologies (Schwarz-Schampera and Herzig 2002). Nowadays, indium is obtained as a by-product of zinc ore processing. Its main sources are massive sulfides and deposits of tin-polymetallic mineralization. In-bearing sphalerite from tin-polymetallic deposits is extracted especially in Bolivia, China and Japan. In-bearing sphalerite usually displays textures called a “chalcopyrite disease” (Murakami and Ishihara 2013). The same textures are commonly observed in sphalerite from the analyzed samples. This indicates that it is reasonable to expect increased concentrations of indium in mineralization of the Stara Kamienica belt.

Although no In-bearing phases were found in the analyzed samples, indium is commonly present as structural admixtures in sphalerite and cassiterite. An indium mineral form the Krobica-Gierczyn area was recently described by other authors (Mikulski et al. 2018). That proves that studies on this matter should be continued. Elevated concentrations of indium, as well as other critical elements, may increase the economic value of this mineralization. Admixtures of cobalt in arsenic sulfides and sulfosalts were noted in the analyzed samples. Cobalt is also a critical metal and the reserves of this element in Przecznicza near Gierczyn may also have an economic value in the future. Chemical composition of the examined ores supports a genetic

relationship between ore mineralization and the Karkonosze Granite. The elevated concentrations of In and Ta in cassiterite may additionally confirm its hydrothermal origin. Petrographic data documenting the episodes of metamorphic recrystallization of cassiterite grains prove that metamorphic processes did not end after the main phase of mineralization.

Acknowledgements

This study was a part of a master’s project. The author would like to acknowledge Krzysztof Nejbert PhD (University of Warsaw, Faculty of Geology) for supervising the project and for assistance during the collection of samples and microanalyses.

References

- Berendsen P, Speczik S, Wiszniewska J (1987) Sulphide geochemical studies of the stratiform tin deposits in the Stara Kamienica chain (SW Poland). *Arch Mineral* 42:31-40
- Cook NJ, Dudek K (1994) Mineral chemistry and metamorphism of garnet chlorite-mica schists associated with cassiterite-sulphide-mineralization from the Kamienica Range, Iżera Mountains. S.W. Poland. *Chem Erde* 54:1-32
- Jaskólski S, Mochnacka K (1958) Tin deposits at Gierczyn in Iżera Mountains, Lower Silesia and attempt of elucidation their origin. *Arch Mineral* 22:17-106
- Madziarz M (2008) Relicts of former cobalt ore mines in Przecznicza in Lower Silesia. In: Zagożdżon PP, Madziarz M (ed) History of mining - an element of European cultural heritage, 1t. Wyd Polit Wr, Wrocław, pp 181-194
- Mazur S, Aleksandrowski P, Kryza R, Oberc-Dziedzic T (2006) The Variscan Orogen in Poland. *Geol Quart* 50:89-118
- Michniewicz M, Bobiński W, Siemiątkowski J (2006) Tin mineralization in the middle part of the Stara Kamienica Schist Belt (Western Sudetes). *Pr Państw Inst Geol* 185:1-130
- Mikulski SZ, Oszczepalski S, Sadłowska K, Chmielewski A, Małek R (2018) The occurrence of associated and critical elements in the selected documented Zn-Pb, Cu-Ag, Fe-Ti-V, Mo-Cu-W, Sn, Au-As and Ni deposits in Poland. *Biul Inst Geol* 427:21-52
- Mikulski SZ (2017) Tin ores. In: Szamalek K, Szufficki M, Malon A, Tyimiński M (ed) Mineral resources of Poland. Polish Geological Institute – National Research Institute, Warsaw, p 74
- Mochnacka K (1985) Structures and textures of ores from the Gierczyn tin ore deposit (Sudetes, Poland) and their genetic interpretation. *Mineral Pol* 16:85-93
- Mochnacka K, Oberc-Dziedzic T, Mayer W, Pieczka A (2015) Ore mineralization related to geological evolution of the Karkonosze-Iżera Massif (the Sudetes, Poland) - Towards a model. *Ore Geol Rev* 64:215-238
- Murakami H, Ishihara S (2013) Trace elements of Indium-bearing sphalerite from tin polymetallic deposits in Bolivia, China and Japan: A femto-second LA-ICPMS study. *Ore Geol Rev* 53:223-243
- Schwarz-Schampera U, Herzig PM (2002) - Indium. *Geology, Mineralogy and Economics*. Springer, Berlin
- Szalamacha M, Szalamacha J (1974) Geological and petrographic characteristic of schists mineralized with cassiterite on the basis of materials from the quarry at Krobica. *Biul Inst Geol* 279:58-89
- Wiszniewska J (1984) The genesis of ore mineralization of the Iżera schists in the Kamienieckie Range (Sudetes). *ArchMineral* 40:115-187

The metallogenic potential of an old European mining region: the case of Sardinia (Italy)

Stefano Naitza^{1,2}, Sandro Fadda², Maddalena Fiori², Roberto Peretti², Francesco Secchi^{2,3}

¹Dipartimento di Scienze Chimiche e Geologiche, Università degli Studi di Cagliari, Cagliari, Italy

²CNR – Istituto di Geologia Ambientale e Geoingegneria – Sede Secondaria di Cagliari, Cagliari, Italy

³Dipartimento di Chimica e Farmacia – Università degli Studi di Sassari, Sassari, Italy

Abstract. The current needs of supplying critical raw materials (CRM's) for the European Union lead to reconsidering the residual potential of many old districts in Western Europe. Sardinia was the most important Italian mining region, with some district (Iglesiente, Montevecchio) relevant at continental scale. Despite the intensive exploitation of last centuries, Sardinian districts still retains a metallogenic potential, involving: (1) large amounts of mine wastes; (2) marginal or poorly explored deposits; (3) new deposits, principally of precious metals and CRM's, emerging from new geological and metallogenic studies.

1 Introduction

Critical raw materials (CRMs) have been defined by EU Commission as a list of materials of high importance for EU economy and industry, for which there are concerns about supply risks, both for geological and geopolitical factors. The list is regularly updated and now comprises 27 CRMs, including large groups as HREEs, LREEs and PGMs (EU Commission, 2014, 2017). Moreover, from the first document of 2010, the Commission proposed a series of recommendations regarding EU policies on raw materials, indicating among the different lines of intervention the systematic re-evaluation of domestic mineral resources. Accordingly, in several ancient mining areas of Europe where old deposits have been mined for several centuries and are now considered as exhausted, new activities have begun to evaluate their residual potential in terms of CRMs resources.

The island of Sardinia represents one of these areas, as it has been the most important mining region in Italy. Sardinian districts hosted in the past several Pb-Zn-Ag deposits of continental relevance, as those of the Iglesiasiente and Montevecchio districts, which have been mined up to late 1990s. Even if the old resources can be considered technically exhausted by decades, the potential of the districts for new resources, also those falling within the CRMs list, remains to be assessed. Some resources are linked to marginal deposits of little economic interest at the time of the extensive exploitation of larger deposits; other resources are materials deriving from old mining activities (mine wastes, tailings), which constitute a major environmental problem in the region; moreover, further resources are mineral deposits up to now under-explored and never exploited for technical, economic as well as political/administrative reasons.

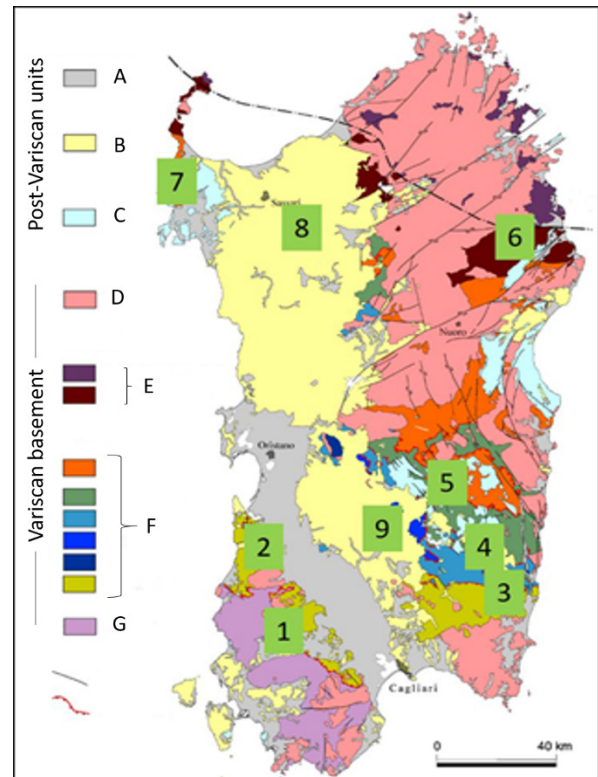


Figure 1. Schematic geological map of Sardinia (simplified and modified from Carmignani et al., 2001). A: Quaternary; B: Tertiary; C: Mesozoic; D: Variscan intrusive complexes; E: Variscan Axial Zone; F: Variscan Nappe Zone; G: Variscan Foreland. Numbers refer to the main mining districts cited in the text. 1: Iglesiasiente; 2: Montevecchio; 3: Sarrabus; 4: Gerrei; 5: Funtana Raminosa; 6: Lula; 7: Nurra-Argentiera; 8: Osilo and Logudoro; 9: Furtei.

2 The metallogenic framework of Sardinia

The Sardinian mineral deposits embrace a wide variety of types, resulting from the complex geological evolution of the island. Sardinian metallogenesis is multi-stage, encompassing several epochs from early Paleozoic to Quaternary. Schematically, seven different metallogenic periods may be recognized (Table 1): phases of relative metallogenic stasis alternated with metallogenic peaks marked by extensive mobilization, migration, concentration and re-concentration of elements to form different kinds of mineral deposits.

Table 1. Summary of the metallogenic periods in Sardinia (numbers refer to district reported in Figure 1)

DISTRICT	ORES	TYPE
<i>Pre-Sardic phase peak (early Cambrian-early Ordovician)</i>		
1	Ba, Pb	Evaporite
1	Fe-Zn-Pb	SEDEX
1	Pb-Zn	MVT
<i>Sardic phase period (middle-late Ordovician)</i>		
1	Ba, Zn-Pb	Karst, Supergene
3, 4, 5	base metals protoses	Sedimentary, volcanic exhalative
<i>Eo-Variscan period (late Ordovician-late Devonian)</i>		
3, 4, 5	Ti, Zr, LREE	Placers
7	Fe	Oolitic Fe
1, 3, 4, 5	base metals, U, V protoses	Sedimentary
<i>Variscan peak (Carboniferous – early Permian)</i>		
3, 4, 5	As-Sb-W-Au (Pb-Zn-Cu-Ag)	Orogenic Mesothermal
2, 6, 7	Pb-Zn (Ag, Ga-Ge-In), Ni-Co	Hydrothermal granite (OMP)-related “five elements-type” veins
5	Pb-Zn-Cu (Ag, Au)	Skarn, granite (OMP)-related
1, 2, 3, 4	Mo-W-Sn-F, F-Ba-Pb-Ag	Hydrothermal, greisen and skarn granite (YMP)-related
<i>Post-Variscan I period (Permian-Triassic)</i>		
1, 2, 3	F-Ba-Pb-Ag	Low-temperature veins
1	Ba, Zn-Pb	Karst, supergene
<i>Post-Variscan II period (Cretaceous)</i>		
7	bauxite	Paleosoil
<i>Cenozoic peak (Oligocene-Miocene)</i>		
8, 9	Au-Ag-Te-Cu	HS and LS epithermal, porphyry
1, 8	Mn	Volcano-Sedimentary/exhalative
8	Cu, Pb	Sedimentary

The **Pre-“Sardic phase” metallogenic peak** (early Cambrian- early Ordovician), resulted in the Pb-Zn ores of the Iglesias district (SW Sardinia). Accumulation of metals occurred in a sedimentary basin evolving from siliciclastic to carbonatic. Initial small evaporite deposits with barite were followed by SEDEX deposits with Fe-Zn sulfides and by very large MVT Pb-Zn sulfide deposits (Boni et al. 1996, and references therein). Ore deposition took place during transition from extensional tectonics and passive margin conditions (Cambrian), to compressive tectonics with folding in an active margin setting (Ordovician “Sardic phase”). SW Sardinia became an area of wide circulation of basinal brines that produced the MVT deposits. The **“Sardic phase” period** (middle-late Ordovician), followed crustal subduction and development of a magmatic arc whose evidences are widely exposed in E Sardinia. This phase resulted in a thick volcano-sedimentary succession with calc-alkaline magmatic products and arguably was a relevant phase of geochemical accumulation and formation of pre-concentrations of metallic elements into the geological pile of the upper crust (Garbarino et al., 1989). In SW Sardinia, mineralized deposits of karst and clastic type with barite and Pb-Zn sulfides originated in a continental environment. The **Eo-Variscan period** occurred in the Ordovician-late Devonian passive margin. In E Sardinia erosion of the volcanic arc produced marine placers of heavy minerals (zircon, rutile and LREE-bearing monazite: Loi et al. 1992). In NW Sardinia oolitic Fe

deposited in proximal siliciclastic sedimentary sequences. Silurian anoxic conditions led to widespread deposition of carbonaceous black shales, starting a new “pre-ore” phase of geochemical accumulation of a large set of elements (base metals, U, V). The onset of the Variscan collision (early Carboniferous) initiated a series of metamorphic, tectonic and magmatic events in which the **Variscan metallogenic peak** took place. The Variscan basement in Sardinia includes three tectonometamorphic zones (Fig.1): Axial Zone (North Sardinia), Nappe Zone (E Sardinia) and Foreland (SW Sardinia). During the post-collisional extension (late Carboniferous-early Permian), the basement was affected by extensional tectonics and intruded by various granitoid suites. Lithospheric delamination (Conte et al., 2017) triggered partial melting in the crust, with granitoid magma production and large-scale fluid circulation. Granitoids emplaced at high crustal levels during two main magmatic peaks (Old Magmatic Peak - OMP and Young Magmatic Peak – YMP, at 310-305 and 290-285 Ma, respectively: Conte et al., 2017). OMP granitoids are high-K, calc-alkaline, I-type (subordinately S-type) and B-bearing; YMP granitoids are in prevalence I-type ferroan, ilmenite-series and F-bearing. Naitza et al. (2015) schematized two main kinds of Variscan late-orogenic hydrothermal deposits: a) “orogenic” mesothermal As-Sb-W-Au deposits, not directly related to the granitoids, typical of SE Sardinia (Gerrei district), and b) granite-hosted/related deposits. The “orogenic” deposits of Gerrei are strictly structurally-controlled and related to regional folds and shear zones; they include some potentially economic target for gold (Garbarino et al., 2003). OMP-related deposits may include the large Pb-Zn hydrothermal veins of the Montevecchio (Cuccuru et al., 2016) and Lula districts and the Pb-Zn-Cu skarns of the Funtana Raminosa district (Central Sardinia). YMP-related and -hosted ores are more various and include numerous small Sn-W-Mo-Fe-As and Pb-Zn-Cu-Ag-F-Ba skarn, greisen, and hydrothermal vein deposits, mostly occurring in S Sardinia (Naitza et al., 2017). The **Post-Variscan I period** took place in a post-orogenic setting. The late Permian-early Triassic erosion and weathering of the basement led to extensive remobilization of the pre-existing ores. Boni et al. (1992) pointed out that several Pb-Zn-Cu-Ag-F-Ba vein deposits are associated to large-scale low-temperature fluid flows in the basement. In SW Sardinia, weathering of the Cambrian Pb-Zn MVT deposits produced large supergene Pb and Zn non-sulfide ores (Boni et al., 2003). In the same area numerous Ba deposits are related to karst processes (Garbarino et al., 1989). During Mesozoic, a long period of metallogenic stasis ended in middle Cretaceous (**Post-Variscan II period**) with the formation of bauxite deposits along a paleosurface within the carbonate sequences of NW Sardinia (Mameli et al., 2007). The Cenozoic drift and eastward migration of Sardinian-Corsican microplate from the European continent are crucial for the **Cenozoic metallogenic peak**. Migration was related with westward subduction and opening of the Liguro-Provençal back-arc basin. In Oligocene-Miocene large amounts of calc-alkaline volcanics were produced in W Sardinia. These tectonic

and magmatic events are associated with: 1) Cu-Au-Mo porphyry type deposits, related to andesitic intrusions; 2) high sulfidation Au-Cu-As-Te and low sulfidation Au-Ag-Sb-base metals epithermal deposits; (Fiori et al., 1994; Lattanzi, 1999) 3) stratiform to discordant volcano-exhalative and volcano-sedimentary Mn deposits in the Miocene volcano-sedimentary sequences; 4) Cu and Pb oxide deposits in clastic sediments at the top of the Miocene volcanics (Fadda et al., 1998).

3 The remaining metallogenic potential of Sardinian districts

Despite over one century of industrial mining, the Sardinian districts still preserve a significant metallogenic interest, and may be regarded as potential sources of raw materials, including several CRM's. Three kinds of sources must be considered: (1) mine wastes and tailing dam deposits from old mines; (2) known, but under-explored or under-exploited resources; (3) totally new themes and targets for mineral exploration.

3.1 Mine wastes as sources of raw materials.

The large Pb-Zn deposits of SW Sardinia districts (Iglesiente and Montevecchio) are now virtually exhausted. After the closure of the last mines (1999), a legacy of large volumes of mine wastes and tailings remains in the area. Only in SW Sardinia, the Regional Administration estimated about 66 million of cubic meters (Mm^3) of different mine wastes and tailings (Regione Autonoma Sardegna, 2003). The total tonnage of the ore deposits mined in the Iglesias MVT district amounted to 120-150 Mt of Pb and Zn sulfides; accordingly, 13 Mm^3 of wastes are now accumulated in the Iglesias valley, which hosts three of the largest mine sites. Among these wastes, the metallurgical red muds resulting from the electrolytic plant that in the Monteponi mine treated non-sulfide Zn ores have been identified as the most relevant potentially economic resource: about 3 Mm^3 of fine-grained deposits at an average of 8 wt% Zn, 1 wt% Pb and 400 ppm Cd (Buosi et al., 1999). In the Montevecchio district, wastes and tailings amount to 10.5 Mm^3 . The ore parageneses of hydrothermal veins exploited in the past display a wide list of metals, including Zn, Pb, Ag, Cu, Cd, Ge, Ga, In, Co, Sb (Moroni et al., 2019). Studies are currently underway by public agencies to assess the economic potential of these large wastes in terms of base metals and CRM's. In SE Sardinia, about 1 Mm^3 of mine and metallurgical wastes resulting from exploitation of Variscan "orogenic" or granite-related ores from Sarrabus and Gerrei district include potential sources of Sb, W and Au (e.g., Su Suergiu and Corti Rosas mines), Ag, F and Ba (e.g., Monte Narba mine). In Central Sardinia (Funtana Raminosa district), mining of Pb-Zn-Cu skarn ores left small wastes (0.35 Mm^3) of potential interest for base metals, Ag, Au, and several CRM's, including Ge, Ga, In and REE. The potential of mine wastes in the small districts of N Sardinia (i.e. Lula, Argentiera) is limited, although they likely include a set of CRM's as large as that of the Montevecchio district. Small volumes of mining

wastes are also present in Furtei (S Sardinia), the only mine that, between 1990's and 2000's exploited a high sulfidation epithermal deposit for gold: the wastes have been evaluated as interesting sources for Au and Te.

3.2 Under-explored or under-exploited resources

As documented in many European mining districts, also Sardinia include several minor deposits that in the past were considered sub-economic and are under-explored or under-exploited. Moreover, in major (and now exhausted) mineral deposits, there were marginal and under-exploited ores that may have some economic potential, in many cases for raw materials different from those mined in the past. A far from exhaustive list include, among others: 1) Mo ores (greisens, skarns, hydrothermal veins) related to YMP granites, occurring in different areas of the Sardinia batholith (Fadda et al., 2015; Naitza et al., 2017); 2) Ni-Co ores in "five elements"-type hydrothermal veins, associated to Montevecchio-type mineralization (Southern Arburès district: Cuccuru et al., 2016); 3) F-Ba ores, still unexploited, related to YMP granites (e.g. SE Sardinia districts: Monte Genis, Brunco Molentinu); LREE ores associated to fluorite deposits (e.g., Silius mine, SE Sardinia: Mondillo et al., 2017); "orogenic" Variscan Au deposits of Gerrei district in SE Sardinia (e.g.: Monte Ollasteddu, Dini et al., 2005); epithermal Au, Ag and Te ores associated to tertiary volcanics in Northern (Osilo district), Central (Montiferru area) and southern Sardinia (Cixerri area).

3.3 New themes and targets for mineral exploration

In last two decades, new geological studies have greatly improved the metallogenic framework of Sardinia, suggesting new themes, new targets for mineral exploration, as well as new metallogeneses. In many cases, this is associated with systematic re-evaluation of the old districts: for instance, a more precise knowledge of structural traps and the tectonic phases and correlated styles controlling the formation of "orogenic" gold ores in Gerrei district (Funedda et al., 2018) brings out new perspectives for an extension of Au explorations to the whole Paleozoic basement of Eastern Sardinia. In the same district, W (scheelite) occurrences frequently associated with "orogenic" Au ores are underexplored and probably deserve new consideration. In the old districts of SW Sardinia, Sn skarn deposits are related to YMP granites; highly mineralized cassiterite occurrences in proximal exoskarn environment suggest a possible new Sn metallogenic province (Naitza et al., 2017). In other cases, the integration between new geological data and sequential stratigraphy led to identify very rich zircon and monazite paleoplacers in late Ordovician rock sequences (Loi et al., 1992) as possible sources or metallogeneses of LREE. In the Funtana Raminosa district, recent studies suggest the possibility of further re-concentration of LREE in previously not exploited skarn deposits (Meloni et al., 2017).

4 Conclusions

Among the old mining regions of western Europe, Sardinia stands out for the variety of its mineralized deposits. In the light of the new studies on the geology and the metallogenesis of this region, many possible targets emerge for future explorations of different mineral resources, including several CRM's. These targets include primarily the mining dumps of the old districts and numerous marginal or under-explored deposits. New data from geological and metallogenic studies indicate possible new exploration themes and suggest that Sardinian districts still retain a metallogenic potential for the years to come.

Acknowledgements

This work was carried out under the CNR Project DTA.AD005.046. Authors are grateful to FdS-RAS for grant number F72F16003080002 (S. Naitza).

References

- Boni M, Gilg HA, Aversa G, Balassone G (2003) The "calamine" of southwest Sardinia: Geology, mineralogy, and stable isotope geochemistry of supergene Zn mineralization. *Econ Geol* 98:731-748
- Boni M, Iannace MA, Balassone G (1996) Base metal ores in the Lower Palaeozoic of South Western Sardinia. *Econ Geol* 75th Anniversary Volume, Special Publication 4:18-28
- Boni M, Iannace A, Köppel V, Hansmann W, Früh-Green G (1992) Late- to post-Hercynian hydrothermal activity and mineralization in SW Sardinia. *Econ Geol* 87:2113-2137
- Buosi M, Contini E, Enne R, Farci A, Garbarino C, Naitza S, Tocco S (2001) Contributo alla conoscenza dei materiali delle discariche della miniera di Monteponi: I "fanghi rossi" dell'éléttrolisi, caratterizzazione fisico-geotecnica, chimico-mineralogica, definizione del potenziale inquinante e proposte per possibili interventi. *Rend Ass Min Sarda* 104:49-93
- Carmignani L, Oggiano G, Barca S, Conti P, Salvadori I, Eltrudis A, Funedda A, Pasci S (2001) Geologia della Sardegna. Servizio Geologico d'Italia: Roma, 272 pp
- Conte AM, Cuccuru S, D'Antonio M, Naitza S, Oggiano G, Secchi F; Casini L, Cifelli F (2017) The post-collisional late Variscan ferroan granites of Southern Sardinia (Italy): Inferences for inhomogeneity of lower crust. *Lithos* 294-295:263-282
- Cuccuru S, Naitza S, Secchi F, Puccini A, Casini L, Pavanetto P, Linnemann U, Hofmann M, Oggiano G (2016) Structural and metallogenic map of late Variscan Arbus Pluton (SW Sardinia, Italy). *J. Maps* 12:860-865
- Dini A, Di Vincenzo G, Ruggieri G, Rayner J, Lattanzi P (2005) Monte Ollasteddu, a new late orogenic gold discovery in the Variscan basement of Sardinia (Italy)—Preliminary isotopic (^{40}Ar - ^{39}Ar , Pb) and fluid inclusion data. *Miner. Deposita* 40: 337-346
- EU Commission (2014) Report on Critical Raw Materials for the EU. Bruxelles, 41 pp
- EU Commission (2017) Communication on the 2017 list of Critical Raw Materials for the EU. Bruxelles, 8 pp
- Fadda S, Fiori M, Pretti S (1998) The sandstone-hosted Pb occurrence of Rio Pischinappiu (Sardinia, Italy): a Pb-carbonate end-member. *Ore Geol Rev* 12:355-377
- Fadda S, Fiori M, Matzuzzi C, Miscali M, Naitza S (2015) The metallogenic vocation of the second phase of the Hercynian magmatism: recent insights into the petrology of the Mo-bearing leucogranitic suite of SW Sardinia, Italy. *Proc. 13th Biennial SGA Meeting, Nancy, France* 2:721-724
- Fiori M, Grillo SM, Marcello A, Pretti S (1994) Mineral resources of the Oligocene-Miocene volcanic district of Monastir-Furtei (southern Sardinia). *Mem Soc Geol It* 48: 725-730
- Funedda A, Naitza S, Buttau C, Cocco F, Dini A (2018) Structural controls of ore mineralization in a polydeformed basement: Field examples from the Variscan Baccu Locci shear zone (SE Sardinia, Italy). *Minerals* 8:456
- Garbarino C, Grillo S, Padalino G, Tocco S, Violo M (1989) Lithospheric evolution and metallogenesis: The Pb-Zn-Fe-Ba mineralization of the Cambrian carbonatic platform, the sulphides of the Ordovician-Silurian volcanism and Hercynian magmatism of Sardinia. In: *The Lithosphere in Italy*, Acc Naz Lincei, Roma: 427-443
- Garbarino C., Naitza S, Tocco S, Farci A, Rayner J (2003) Orogenic Gold in the Paleozoic Basement of SE Sardinia. In: *Mineral Exploration and Sustainable Development*, Millpress, Rotterdam: 767-770
- Lattanzi P (1999) Epithermal precious metal deposits of Italy - an overview. *Min. Deposita* 34:630-638
- Loi A, Barca S, Chauvel JJ, Dabard MP, Leone F (1992) Analyse de la sédimentation post-phase sarde: les dépôts initiaux à placers du SE de la Sardaigne. *CR de l'Académie des Sciences, Paris*, 315 (II):1357-1364
- Mameli P, Mongelli G, Oggiano G (2007) Geological, geochemical and mineralogical features of some bauxite deposits from Nurra (Western Sardinia, Italy): insights on conditions of formation and parental affinity. *Int J Earth Science* 96:887-902
- Meloni MA, Oggiano G, Funedda A, Pistis M, Linnemann U (2017) Tectonics, ore bodies, and gamma-ray logging of the Variscan basement, southern Gennargentu massif (central Sardinia, Italy). *J Maps* 13:196-206
- Mondillo N, Balassone G, Boni M, Marino A (2017). Evaluation of the amount of rare earth elements -REE in the Silius fluorite vein system (SE Sardinia, Italy). *Periodico di Mineralogia* 86:121-132
- Moroni M, Naitza S, Ruggieri G, Aquino A, Costagliola P, De Giudici G, Caruso S, Ferrari E, Fiorentini M, Lattanzi P (2019). The Pb-Zn-Ag vein system at Montevecchio-Ingurtosu, southwestern Sardinia, Italy: a 21st century perspective from new mineralogical, fluid inclusion, and isotopic data. *Ore Geology Reviews* (submitted)
- Naitza S, Oggiano G, Cuccuru S, Casini L, Puccini A, Secchi F, Funedda A, Tocco S, (2015) Structural and magmatic controls on Late Variscan Metallogenesis: evidences from Southern Sardinia (Italy). *Proc. 13th Biennial SGA Meeting, Nancy, France* 1:161-164
- Naitza S, Conte AM, Cuccuru S, Oggiano G, Secchi F, Tecce F (2017). A Late Variscan tin province associated to the ilmenite-series granites of the Sardinian Batholith (Italy): the Sn and Mo mineralisation around the Monte Linas ferroan granite. *Ore Geol Rev* 80:1259-1278
- Regione Autonoma Sardegna (2003) Piano regionale gestione rifiuti - piano di bonifica aree inquinate. Cagliari: 255 pp

Secondary gold structures: evidence of "new" gold's growth inside wastes of sulfide deposits

Alfia Khusainova

*Sobolev Institute of Geology and Mineralogy, Siberian Branch of the Russian Academy of Sciences (IGM SB RAS),
Novosibirsk, Russia*

Novosibirsk State University (NSU), Novosibirsk, Russia

Abstract. The author has studied the morphology of native gold from three wastes of pyrite-barite-polymetallic deposits from the different regions of Siberia. The gold particles were studied using scanning electron microscopy. In this research the author has found that these gold growths were newly formed, bearing traces of growth and consolidation. The obtained results have shown that dissolved forms of gold have the high mobility. Moreover, these results illustrate the process of gold migration and precipitation on the different geochemistry barriers inside the gold-bearing wastes. Besides, the author has found that the secondary enrichment horizon was formed at the base of the wastes during more than 80 years.

1 Introduction

At the present time there are some obvious problems in research of gold morphology from gold-bearing wastes. First of all, there is a problem of gold diagnostic: discovered particles of gold could be authigenic or allothigenic. Secondary, there is a problem with a definition of the physical and chemical environmental conditions, which contribute to the processes of growth and dissolution of gold. Besides, microorganisms participate in the migration, dissolution, and precipitation of newly formed gold (Kuimova and Moiseenko 2006; Shuster and Reith 2018). Thirdly, there is a problem with a definition of period of time, for which the gold cycle occurs (dissolution – migration – precipitation) in the supergene zone (Shuster et al. 2017; Shuster and Reith 2018).

One of the evidence of supergene growth of gold is the presence of nano and micron-gold particles (Shuster et al. 2017; Shuster and Reith 2018; Wierchowicz et al. 2018). Most often, gold have the bacteriomorphic, leaf-shaped and "wire" forms, as well as idiomorphic, hexagonal, octahedral and triangular crystal forms.

The goal of this research is to study the morphology of gold particles from gold-bearing wastes of pyrite-barite-polymetallic deposits and to find out the nature of gold genesis in the supergene environment.

2 Sampling and methods

The objects of research are the wastes of the Ursk ore field (Salair Ridge) and the wastes of Zmeinogorsk factory (the Ore Altai).

The Ursk ore field is located in Kemerovo region, Russia. There are the wastes of the Novo-Ursk and Belokluch deposits on the territory of Ursk ore field. The

material was selected from vertical sections from different "lithological" interlayers. The Zmeinogorsk wastes are located in Altai Region, Russia. The material obtained as a result of research work on technological approbation.

Gold was enriched by the gravity method by using a pan. Research of the chemical composition of samples was conducted in the Analytical Center of multi-elemental and isotopes research SB RAS (Novosibirsk). The main results are obtained by a scanning electron microscopy (SEM) a LEO VP 1430 (Carl Zeiss, Germany) INCA Energy SEM 350 (Oxford Instruments), spectrometer in the JEOL 01430VP.

The main characteristic of these objects is that the deposits are of the same genetic type: gold in the primary ore is presented in the native form as well as in the associated form in sulfides (Bolgov 1937; Cherepnin 1957; Kovalev 1969). During 80 years, the wastes' material was undergone by the different physical, chemical and mechanical processes of transformation. As a result, the secondary enrichment horizon was formed at the base of the wastes of the Novo-Ursk and Belokluch deposits. The concentration of gold and silver was determined by the atomic absorption analysis (analyst Iliina V.N.). The concentration equals to Au 0.6 – 1.2 ppm and Ag 2.7 – 31.0 ppm. The gold particles were found in this horizon.

3 Results

As a result, during a research of gold morphology by SEM, the author has described the following morphology features. These features show that gold growths were newly formed and it forms in the supergene environment.

Nano- and micro-particles of gold were found in the gold surface, films of iron and manganese hydroxides, clay minerals and grains of barite. These particles have a size of about 200-300 nm. They have round and elongated shapes. Often they are located in both separate grains and clusters, mainly in the grooves or irregularities, but also they can be found on a flat smooth surface of gold. Besides, nano- and micro-particles of gold are related to films of iron and manganese hydroxides (fig. 1A), clay minerals, matrix gold particles (fig. 1B) and barite (fig. 1C).

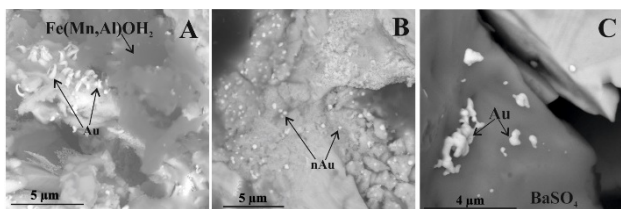


Figure 1. Nano- and micro-particles of gold are placed: A – in films of iron and manganese hydroxides; B – on the surface of matrix gold; C – on grains of barite.

The overgrowth of gold on the surface with the formation of larger aggregates. The overgrowths look like the aggregation of gold grains (fig. 2A, B), which begin their growth in the grooves or surface irregularities, then, gradually fill all available space. Often they have elongated and round shapes. The process of regular growth of one crystalline material on the surface of another one but at lower temperatures is called epitaxy.

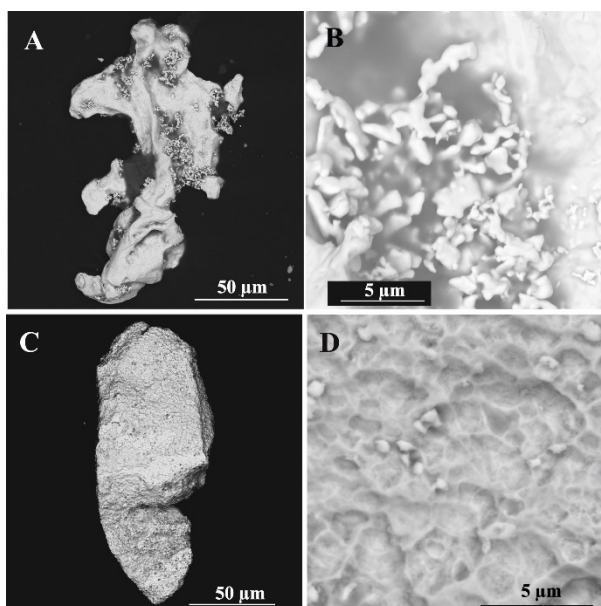


Figure 2. A – the overgrowths on the gold surface look like the aggregation of gold grains; B – scaled-up of fragment A; C – the overgrowths on the surface similar to neural network; D – scaled-up fragment C.

Another type of overgrowths is growth of separate grains on the surface of other grains of native gold (fig. 2C, D). These overgrowths have a round shape. Some gold particles have a surface similar to neural network, at the nodes of which rounded gold particles are deposited, forming a kind of “caps”. Then, this gold is evenly distributed and smoothed due to diffusion processes. Gold grows along special faces of the “neural grid”. The next example is the deposition of gold particles on uneven relief surfaces. With each subsequent injection of ore forming substance, the relief of gold becomes more and more uneven, forming a kind of “dunes”.

Sponge gold. It is known that spongy gold is formed in the supergene zones. Spongy formations were observed on the surfaces of the gold of the Novo-Ursky ore field, mainly on crystalline particles. These formations were found in grooves and surface irregularities, namely,

in various pits, holes, gaps. Probably, spongy gold is an intermediate state of gold’s growth between the stage of formation of massive homogeneous gold and newly formed one. Also, sponge gold is bound with the surface with films of iron and manganese hydroxides, barite inclusions, and clay minerals on which gold is also deposited. As a result, inclusions of minerals are captured and absorbed by the main mass of gold.

In addition, sponge gold was found on the gold’s surfaces of an aggregate structure. During a detailed study of particles of aggregate gold it was found that such gold is formed due to the formation of spongy forms. Then these forms are enlarged to globules or individual grains. Particles look like agglomerates and their shape is similar to dendrites. According to Osovetsky (2013), “aggregate gold” is gold, which consists of clearly distinguishable composite fragments, usually it has a globular structure (rounded shape), sometimes angular or columnar. Presumably, such gold particles were formed directly in the supergene environment, as evidenced by the presence of a variety of nano- and micro-particles of gold. This type of gold was found in the wastes of Zmeinogorsk wastes.

The formation of such gold occurs due to the formation of one or several crystalline centres, around which the growth of the main mass of gold takes place. Gold is deposited from solutions or colloids in the form of nano-sized particles of a rounded and/or elongated forms on various “seeds”. Such “seeds” are able to be compounds of iron hydroxides, clay minerals, barite and, gold. Then nano-particles are enlarged to micron size, gradually growing, layering on each other, creating a kind of spongy forms (fig. 3A). With their growth, natural porosity is formed (fig. 3D), which is unevenly distributed. As a result, these clusters can be very loose and brittle to mechanical stress. In parallel with the growth of nano- and microparticles, diffusion processes take place, namely, spongy accumulations of gold begin to penetrate each other, forming more massive aggregates (fig. 3B, C). Thus, unique particles (globules) of gold are formed (fig. 3E). At the same time, the external surface becomes relatively smooth and even, with preservation of porosity in some areas (fig. 3D). This mechanism is repeated for each individual globule. As a result, a larger gold agglomerate is formed (fig. 3F), in which the secondary (colloidal) unstructured gold is probably the binder. It is distributed unevenly in aggregates and it causes local cementation of fragments of the whole structure (Osovetsky 2013).

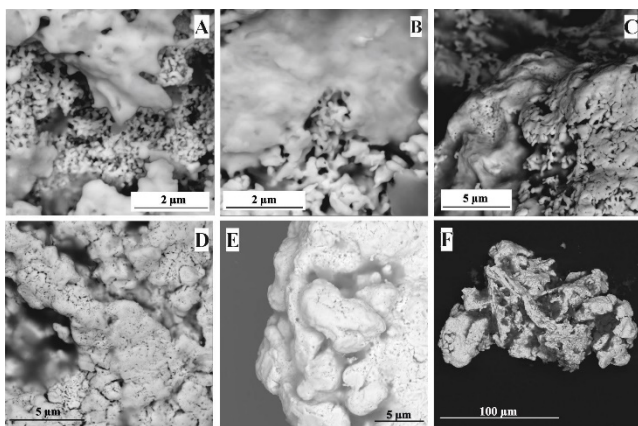


Figure 3. The formation of aggregate gold.

Another type of spongy forms is aggregations of spongy gold, which looks like “colonies of microorganisms”. One of their main features is a similar distribution over the entire surface of gold and a similar thickness. Perhaps this type of surface has formed during the life of microorganisms. It was also noted that the colony’s lithification process is in vivo and occurs synchronously with its growth (Amosov and Vasin 1993). This type of gold is characterized by the conservation of biogenic forms; therefore, we observe a similar distribution of newly formed gold. Particles with a size of 300-400 nm consist of thin elongated (like a needle) forms that build a spongy surface. Then, as in most other cases, there is a gradual merging (diffusion) of the two surfaces (the main massive gold and overgrowths).

Growth step. On the surface of gold, peculiar hollows of a funnel-shaped form were observed (fig. 3). One of their features is that the edges of the crystals are highly developed, but the inner space is not filled by mineral substance.

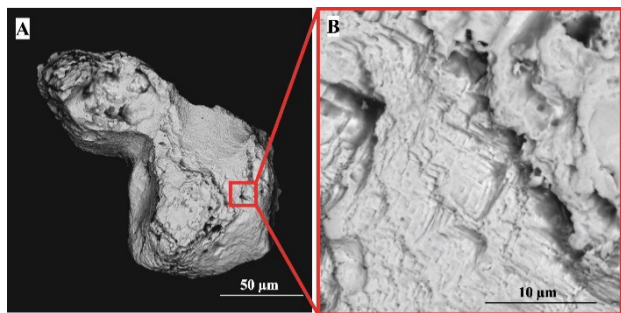


Figure 4. Growth step: A – common view of grain; B – scaled-up fragment.

The funnel-shaped form of depressions occurs when the diffusion limit exceeds during crystal growth (Krasnova and Petrov 1997). The growth of growth step occurs as a result of the rapid growth of crystals, when the stress is higher at the edges and corners than at the centers of crystals. The chemical composition of the medium can also affect the formation of skeletal crystals and these processes also take place with exceeding of the diffusion limit.

4 Discussion

During 80 years of wastes’ existence, due to physical, chemical and biological processes of differentiation and integration, a secondary enrichment horizon with visible supergene gold was formed at the base of the wastes. This gold could have been formed due to both abiotic and biotic processes during low-temperature mineral formation (<40 °C). Source of new gold can be sulfide minerals (Bolgov 1937; Cherepnin 1957; Kovalev 1969), which were released from minerals as a result of oxidation.

Earlier (Rikhvanov et al. 2017), a lot of research work was dedicated to studying microbiota in the wastes of the Novo-Ursky and Beloklyuch deposits. Representatives of the genus *Bacillus* dominate in samples of the Ursky soil and wastes, with the predominance of *B. Subtilis* in the cycle of sulfur-containing substances. In addition, (Reith et al. 2006) bacteria of the genus *Bacillus* is highly involved in the processes of dissolution, migration and growth of gold. Therefore, discovered structures of gold could be formed by microorganisms in the wastes.

Besides, the fact of low-temperature gold formation already has been established (Moiseenko and Marakushev 1987; Kuimova and Moiseenko 2006; Stewart et al. 2017). Research of gold formation’s temperature has shown the possibility of low-temperature mineral formation in the range from 30-40 to 90 °C (Moiseenko and Marakushev 1987). At the same time, microorganisms take an active part, which is confirmed by experimental works (Kuimova and Moiseenko 2006).

According to experimental data (Kuimova and Moiseenko 2006), the formation of biogenic gold is a multi-step process that includes three main stages: 1) a rapid process of biosorption of metals (Au, Ag, Pb) on the cell wall; 2) gold condensation on the crystallization centres, as a result of which reticular structures of gold are formed and bioforms are lithified; 3) transformation and further crystallization that leads to formation of loose aggregates of biogenic gold from biophilic elements (N, P, S).

Depending on the form of the presence of gold in solutions (ionic, colloidal) and specific characteristic of different groups of microorganisms (bacteria, mycelial fungi and yeast), different types of crystals and gold structures are formed. However, biocatalytic nucleation on microorganisms are followed by autoeptaxial growth of native gold on microfossils’ seeds through the interaction of system’s components and the surface of already existing gold. As a result of this interaction biomorphic structures can be destroyed (Kuimova and Moiseenko 2006).

5 Conclusion

Thus, the author has established the fact that discovered gold overgrowths is newly formed. The presence of nano- and micron size gold particles and the presence of newly formed phases on the surface of earlier particles, as well as growth steps, indicate that this gold has been grown in the wastes. The process of growth is continuous and it

occurs nowadays in the supergene environment as well. Besides residual gold can be dissolved, migrated and accumulated as native gold particles in the wastes of the supergene environment. A complex combination of gold aggregates of different ages indicate the duration of the process of its formation and continual changes in environmental conditions of mineral formation. Also, microorganisms have a key role in the formation of supergene gold.

Acknowledgements

Work is accomplished with support of IGM SB RAS and Ministry of Science and Higher Education of the Russian Federation.

References

- Amosov RA, Vasin (1993) SL Gold microfossils // *Ores and metals*. 3:101-107 [in Russian].
- Bolgov GP (1937) Salair sulfides, Ursk group of polymetallic deposits *Izv. Tomsk. Polytechnic Inst.*, №53 (11):45-96 [in Russian].
- Cherepnin VK (1953) The question of the composition and genesis of the ores of the Ursk deposits (Salair) *Izv. Tomsk. Polytechnic Inst.*, 90 [in Russian].
- Kovalev KR (1969) Features of the formation of ores of pyrite-polymetallic deposits of the North-Eastern Salair and East Tuva Candidate's dissertation of geol. mineral. sciences. Novosibirsk, 32 [in Russian].
- Krasnova NI, Petrov TG (1997) Genesis of mineral individuals and aggregates. St. Petersburg: Nevsky Courier, 228. [in Russian].
- Kuimova NG, Moiseenko VG (2006) Biogenic gold mineralization in nature and in experiment *Lithosphere*, 3: 83-95 [in Russian].
- Moiseenko VG, Marakushev SA (1987) Bacterial concentration, enlargement and "upgrading" of gold in the oxidation zone of gold deposits, weathering crusts and placers. Blagoveshchensk: AmurKNII, 45 [in Russian].
- Osovetsky BM (2013) Natural nanogold. Perm. state nat researches Univ. 176 [in Russian].
- Reith F, Rogers SL, McPhail DC, Webb D (2006) Biomineralization of Gold: Biofilms on Bacterioform Gold. *Science*, 313:233-236.
- Rikhvanov LP et al. (2017) Biogeochemical monitoring in the areas of tailing dumps of mining enterprises, taking into account microbiological factors of transformation of mineral components. Novosibirsk: Publishing House of the SB RAS, 437 [in Russian].
- Shuster J, Reith F, Cornelis G, Parsons JE, Parson JM, Southam G (2017) Secondary gold structures: relics of past biogeochemical transformations and implications for colloidal gold dispersion in subtropical environments. *Chem. Geol.* 450:154–164.
- Shuster J, Reith F (2018) Reflecting on Gold Geomicrobiology Research: Thoughts and Considerations for Future. *Endeavors Minerals*, 8:401.
- Stewart J, Kerr G, Prior D, Halfpenny A, Pearce M, Hough R, Craw D (2017) Low temperature recrystallisation of alluvial gold in paleoplacer deposits. *Ore Geology Reviews*, 88:43-56.
- Wierchowicz J, Mikulski SZ, Gąsiński A (2018) Nanoforms of gold from abandoned placer deposits of Wądroże Wielkie, Lower Silesia, Poland – The evidence of authigenic gold mineralization. *Ore Geology Reviews* 101:211–220.

Geometallurgy - what's new and what's next ...

Julie Hunt

Mineral Deposit Research Unit, University of British Columbia

Abstract. Geometallurgy is a team-based approach to characterising ore body variability and is used to assess the impact of geological parameters on the mining value chain. The increased use of the approach has led to upgrading of methods and equipment used to collect data, for example, small- and bench-scale systems for chemical, mineralogical, geotechnical and comminution data. New methods of analyzing and interpreting data are also being developed to provide statistically valid data needed for spatial modelling, for example modal mineralogy estimation, machine learning to incorporate data into spatial models, and innovative mathematical approaches. The use of geometallurgy has expanded to non-metallic deposits such as industrial minerals. In future, it could be used in emerging areas such as recovery of metals from electronic waste and characterization of carbon sequestration potential. Developments to reduce energy usage in mining, particularly in size reduction circuits, have led to the emergence of several innovative technologies (e.g. CAHM, eHPCC, CanMicro) along with improved ore sorting and upgrading methodologies to reduce the amount of material requiring size reduction. If these technologies become widely adopted, methods to assess the impacts of geological variability will need to be developed and incorporated into geometallurgical programs.

1 Introduction

Geometallurgy is a team-based approach to characterising variability within an ore body. The intent is to quantify the impact of geological parameters on the mining value chain from mining through comminution, metallurgical response, recovery and processing plus waste and tailings disposal as well as, for example, energy usage, CO₂ generation and social license to operate. The aim is to have 3D models that show the grade of valuable commodities plus other rock-related properties that may impact cost centers along the mining value chain (e.g. Hunt and Berry 2017). The models are intended to be used predictively to help mine planning and risk management – a ‘no surprises’ approach.

For geometallurgical modelling the data used need to be spatially constrained as well as quantitative. The link between results and the location of samples is important in outlining geometallurgical domains that can be exploited at a mineable scale. In order to create statistically valid sample distributions for modelling, data need to be abundant and thus relatively inexpensive to obtain. Below are some examples of ‘what’s new’ in terms of data collection and interpretation for geometallurgy plus some examples of emerging technologies that show significant promise in terms of reducing energy and water

use and are likely to be considered in future geometallurgy programs. Rock characteristics and properties related to the emerging technologies will need to be determined to incorporate them into geometallurgical modelling and domain definition. Small scale proxy-type tests may also be needed to define the geometallurgical domain model.

2 What’s new

Equipment and methods to collect data are continually being upgraded as well as ways to more rapidly and efficiently analyse and interpret large amounts of data. Some recent examples are described in the following sections.

It is also evident that geometallurgy is now being used in areas outside metallic deposits, such as the bulk commodities exploited in the mining of industrial minerals. Key differences between the industrial mineral and metallic ore sectors are discussed by Ellefmo et al. (2019) as they describe geometallurgical concepts used in industrial mineral production of marble and nepheline syenite.

2.1 Data collection

Development and improvement of hand held and bench scale equipment for collecting chemical assay or mineralogical data is continuing and routine use becoming more common. For example, McKinley et al. (2018) describe how near and shortwave infrared (NIR-SWIR) data collected using a handheld device are incorporated into 3D models for the Kisladag gold porphyry deposit in Turkey. Johnson et al. (2019) discuss how hyperspectral data collected from blast hole samples using an automated system are used in predicting recovery and throughput at the Phoenix Au-Cu porphyry-related skarn deposit, USA. Efforts are also being made to use data from the automated systems to provide information on geotechnical parameters of drill core. Harraden et al. (2019), for example, describe the use of surface models derived from laser profiling of oriented drill core to measure fracture orientations which can be used in determining rock quality designation (RQD) for incorporation in geotechnical models at the Cadia East porphyry deposit, Australia. Rafai et al. (2018) demonstrate the use of laser-induced breakdown spectroscopy (LIBS) for real-time geochemical applications on samples with complex mineralogy and varying surface topography.

Developments are continuing in scanning electron microscope-based automated mineralogy with ‘Mineralogic Mining’ (Graham et al. 2015) and ‘TESCAN TIMA’ (Hrstka et al. 2018) as fairly recent alternatives to

established MLA (SEM-mineral liberation analysis) and QEMSCAN (quantitative evaluation of materials by SEM) systems. Graham et al. (2015) describe a key point of difference of the Mineralogic Mining system as classification of the minerals using the weight percent contribution of elements and thus, the mineral stoichiometry. A capability to correlate light microscope, SEM and automated mineralogy mineral maps has also been developed. The TIMA system uses a unique X-ray spectrum clustering algorithm to lower the chemical detection limit and is optimized to deal with rapidly acquired low-count spectra (Hrstka et al. 2018).

New comminution tests are also being developed. As mentioned, geometallurgy requires abundant data to create statistically valid spatial models. One way of obtaining such data is via small-scale proxy type tests which, by design, use small sample size and are less expensive to perform. A recent example of a new development in this area is the 'rediscovery' of an old test as described by Heiskari et al. (2019). The testing follows from a review by Mwanga et al. (2015) and uses the results from a Mergan mill to predict Bond work index (BWI) values.

2.2 Data analysis

New methods of analyzing and interpreting data continue to be developed and improved. For example, methods to rapidly and inexpensively obtain bulk (modal) mineralogy continue to be tried. Escolme et al. (2019) describe using whole rock geochemical data to estimate bulk mineralogy using a combination of ternary diagrams and bivariate plots to classify alteration assemblages (i.e. alteration mapping) plus calculating mineralogy using linear programming for the Productora Cu-Au-Mo deposit, Chile. In an example from the industrial mineral sector, Silva et al. (2018) used X-ray fluorescence (XRF) and X-ray diffraction (XRD) data to compare two element-to-mineral conversion methods, one least squares-based and one regression-based. They demonstrate that the modal mineralogy of samples from the Nabbaren nepheline syenite deposit, Norway, was best estimated using a regression-based method. Also, in the bulk commodity sector, Parian et al. (2015) discuss a method to combine element-to-mineral conversion and quantitative XRD data to estimate bulk mineralogy for iron ore samples.

A comparison of machine learning methods was carried out by Lishchuk et al. (2019) to determine if process data (mass pull, liberation, particle size, recovery) could be effectively incorporated into spatial models of geometallurgical parameters at the Leveäniemi iron ore mine in Sweden. They were able to build acceptable spatial models for recovery and iron oxide liberation that could be used for geometallurgical mapping; they were less successful with comminution properties (grain size, BWI). The authors suggest tree methods tend to perform better than function methods in predicting non-additive variables such as recovery.

El Haddad et al. (2019) describe new methodologies for analysis of laser-induced breakdown spectroscopy (LIBS) data. They used a multivariate curve resolution –

alternating least squares (MCR-ALS) method for mineral identification and quantification and suggest the method could be scalable and used to gather automated mineralogy measurements in coarse rock streams. Recent developments in analysis of LIBS data in various fields, including mineralogy, are summarized in Jolivet et al. (2019).

The recently released Handbook of Mathematical Geosciences contains a chapter on Predictive Geometallurgy that discusses the state of the art and the need for new mathematical and computational developments to tackle problems arising from geometallurgical studies (Van den Boogaart and Tolosana-Delgado 2018).

3 What's next

There are continued efforts to reduce the quantity of energy used in size reduction circuits for mining; several examples of innovative technology are given in the following section. Ore sorting and upgrading is also being used to reduce energy consumption by decreasing the amount of material being processed. These new methods and devices have typically been tested at laboratory scale but if they become the disruptive technology that could revolutionise mining as suggested by their proponents then methods to assess the impact of geology, mineralogy and rock characteristics on these methods and technologies will need to be developed and incorporated into geometallurgical programs.

A geometallurgical approach could also be used to characterize process parameters in new areas of mineral production such as recovery of metals from electronic waste (e.g. printed circuit boards) as they continue to be tested (e.g. Arinanda et al. 2019). Carbon sequestration shows promise to offset carbon emissions and make marginal mines potentially viable and a geometallurgical approach could be used to help in characterizing the carbon sequestration potential of mine waste as the value of this previously untapped resource is increasingly explored (e.g. Dipple et al. 2018; McCutcheon et al. 2019).

3.1 Energy reduction and improved efficiency

Innovative approaches to reduce energy consumption and improved efficiency are being identified. These include the conjugate anvil hammer mill (CHAM), eccentric high pressure centrifugal comminution (eHPCC™), and combined microwave-assisted comminution and sorting (CanMicro; e.g. Canada Mining Innovation Council 2019; Impact Canada 2019).

The CHAM claims to have the potential to reduce energy consumption by up to 50%, and improve water and dust management (e.g. Nordell and Potapov 2015; Nordell et al. 2016).

eHPCC combines the breakage mechanisms of high pressure and high intensity attrition into one machine that reduces the particle size of run of mine feed (Roper 2015; Roper and Daniel 2016). The device is intended to be used without water, grinding balls and classification

circuits and the resulting efficiencies, including reduction in: energy and water use, wear and maintenance, capital and maintenance costs, are expected to be significant (Borissenko et al. 2015; eHPCC 2019).

CanMicro integrates microwave-assisted comminution and sorting to provide energy saving of up to 70% compared to conventional comminution circuits (CanMicro 2019). A short blast of high power microwaves is used to selectively break particles as differential heating of different minerals causes cracking along grain boundaries. The heating effect on ore minerals is used to sort particles and allow waste rock to be rejected.

4 Summary

The use of a geometallurgical approach to characterising variability within an ore body and its impacts on the mining value chain now has significant uptake and the increased use of the approach has led to advances in methodology and equipment used to collect and analyze data. At the macro scale (e.g. drill core samples), this includes increasing use of NIR-SWIR data in models used to predict recovery (e.g. McKinley et al. 2018; Johnson et al. 2019), the use of automated systems to obtain geotechnical information (e.g. Harraden et al. 2019), and the use of LIBS in samples with complex mineralogy (e.g. Rafai et al. 2018). At the micro scale, advances are continuing in SEM-based automated mineralogy with new developments presented by TESCAN TIMA and Mineralogic Mining (e.g. Hrstka et al. 2018; Graham et al. 2015).

New methods of data analysis and interpretation include, for example, developments in estimation of modal mineralogy in base and precious metal (e.g. Escolme et al. 2019), industrial mineral (e.g. Silva et al. 2018) and iron ore (Parian et al. 2015) deposits. The use of machine learning methods has been examined by Lishchuk et al. (2019) to assess the incorporation of process data into spatial models of geometallurgical parameters. El Haddad et al. (2019) discuss methodologies for the use of LIBS data. Significantly, the new Handbook of Mathematical Geosciences discusses the need for mathematical and computational developments to tackle problems arising from geometallurgical studies (Van den Boogaart and Tolosana-Delgado 2018).

There are continual efforts to streamline and increase efficiency throughout the mining value chain, particularly in terms of energy consumption in size reduction circuits. New proxy-type tests that use small sample size continue to be developed, such as the one described by Heiskari et al. (2019) that uses a Mergan mill to predict BWI. In addition, several innovative size reduction technologies (e.g. CAHM, eHPCC, CanMicro) are emerging along with improved ore sorting and upgrading methodologies (Nordell and Potapov 2015; Nordell et al. 2016; Roper 2015; Roper and Daniel 2016; Borissenko et al. 2015; eHPCC 2019; CanMicro 2019).

The use of geometallurgy is expanding and now includes non-metallic deposits such as industrial minerals and in future, it could be used in emerging areas such as

recovery of metals from electronic waste and characterization of carbon sequestration potential.

Acknowledgements

Thanks are offered to the many colleagues, collaborators and company personnel who have inspired geometallurgical developments, discussion and, most importantly, uptake in recent years and continue to push advances in this area.

References

- Arinanda M, van Haute Q, Lambert F, Gaydardzhiev S (2019) Effects of operation parameters on the bio-assisted leaching of metals from pyrolyzed printed circuit boards. *Minerals Engineering* 134:16-22
- Borissenko V, Roper LD (2015) A discounted average cost comparison of eHPCC against conventional Cu-S grinding circuit. e-hpcc.com/en/470-cost_benefits.html
- Canada Mining Innovation Council (2019) CMIC mineral processing teams selected as semi-finalists in the Crush It! Challenge. <https://mailchi.mp/cmhc/ccim/cmhc-board-update-2283077?e=647fd7e430>
- CanMicro (2019) <https://gcs-vimeo.akamaized.net/exp=1552258510~acl=%2A%2F1243349558.mp4%2A~hmac=e04d33828fe373a775eefcd6b0d2daa1ef0d3e601da0d63066f3d165407609ec/vimeo-prod-skyfire-std-us/01/4113/12/320569703/1243349558.mp4>
- Dipple GM, Carroll K, Power IM, Vanderzee S, De Baere B (2018) Mining to mitigate climate change. Abstracts AGU Fall meeting.
- eHPCC (2019) Reduce rocks to microns - Benefits. e-hpcc.com/en
- El Haddad J, de Lima Filho ES, Vanier F, Harhira A, Padiouleau C, Sabsabi M, Wilkie G, Blouin A (2019) Multiphase mineral identification and quantification by laser-induced breakdown spectroscopy. *Minerals Engineering* 134:281-290
- Ellefmo SL, Aasly K, Lang A, Vezhapparambu VS, Silva, CAM (2019) Geometallurgical concepts used in industrial mineral production. *Economic Geology* (in press).
- Escolme A, Berry RF, Hunt J, Halley S, Potma W (2019) Predictive models of mineralogy from whole rock assay data: Case study from Productura Cu-Au-Mo deposit, Chile. *Economic Geology* (in press).
- Graham SD, Brough C, Cropp A (2015) An introduction to ZEISS mineralogic mining and the correlation of light microscopy with automated mineralogy: a case study using BMS and PGM analysis of samples from a PGE-bearing chromite deposit. In *Proceedings Precious Metals 2015* 1-12
- Harraden CL, Cracknell MJ, Lett J, Berry RF, Carey R, Harris AC (2019) Automated core logging technology for geotechnical assessment: A study on core from the Cadia East porphyry deposit. *Economic Geology* (in press).
- Heiskari H, Kurki P, Luukkanen S, Sinche Gonzalez M, Lehto H, Liipo J (2019) Development of a comminution test method for small ore samples. *Minerals Engineering* 130:5-11
- Hrstka T, Gottlieb P, Skala R, Breiter K, Motl D (2018) Automated mineralogy and petrology – applications of TESCAN Integrated Mineral Analyzer (TIMA). *Journal of Geosciences* 63:47-63
- Hunt J, Berry R (2017) Geological contributions to geometallurgy. In *RFG2018 Abstracts, CIM-GAC-MAC*
- Impact Canada (2019) Crush it! Challenge. Government of Canada website <https://impact.canada.ca/en/challenges/crush-it>
- Johnson CL, Browning DA, Pendock NE (2019) Hyperspectral imaging applications to geometallurgy: Utilising blast hole mineralogy to predict Au-Cu recovery and throughput at the Phoenix mine, Nevada. *Economic Geology* (in press).
- Jolivet L, Leprince M, Moncayo S, Sorbier L, Lienemann C-P, Motto-Ros V (2019) Review of the recent advances and applications of LIBS-based imaging. *Spectrochimica Acta Part B* 151:41-53
- Lishchuk V, Lund C, Ghorbani Y (2019) Evaluation and comparison of different machine-learning methods to integrate sparse

- process data into a spatial model in geometallurgy. *Minerals Engineering* 134:156-165
- McCutcheon J, Power IM, Shuster J, Harrison AL, Dipple GM, Southam G. (2019) Carbon sequestration in biogenic magnesite and other magnesium carbonate minerals. *Environmental Science Technology*
<https://pubs.acs.org/doi/full/10.1021/acs.est.8b07055>
- McKinley S, Baker T, Öztaş Y (2017) Alteration at Kışladağ gold mine, Turkey: a progressive study in geology, geotechnics and geometallurgy. In *Proceedings Tenth International Mining Geology Conference 2017:51-62 AUSIMM*, Melbourne
- Mwanga A, Rosenkranz J, Lamberg P (2015a) Testing of ore comminution behavior in the geometallurgical context – a review. *Minerals* 5:276-297
- Mwanga A, Lamberg P, Rosenkranz J (2015b) Comminution test method using small drill core samples. *Minerals Engineering* 72:129-139
- Nordell L, Potapov A (2015) Novel comminution machine may vastly improve crushing-grinding efficiency. In: *Sixth international conference on semi-autogenous high pressure grinding technology*.
<https://www.scribd.com/document/363210553/Novel-Comminution-Machine-May-Vastly-Improve-Crushing-Grinding-Efficiency-081911-pdf>
- Nordell L, Potapov A, Porter B (2016) Comminution energy efficiency – understanding the next steps. *IMPC 2016, Quebec*.
http://conveyor-dynamics.com/wp-content/uploads/2016/05/COMMINUTION-ENERGY-EFFICIENCY-UNDERSTANDING-NEXT-STEPS_2016.pdf
- Parian M, Lamberg P, Möckel R, Rosenkranz J (2015) Analysis of mineral grades for geometallurgy: Combined element-to-mineral conversion and quantitative X-ray diffraction. *Minerals Engineering* 82:25-35
- Roper LD, (2015) A performance comparison of laboratory-scale eHPCC against conventional comminution. In M Evertson (Chair), *14th European Symposium on Comminution and Classification (ESCC2015)*, Chalmers University, Gothenburg, e-hpcc.com/en/402-downloads.html
- Roper LD and Daniel MJ (2016) Introducing eHPCC to International Mineral Processing Community. In *Proceedings of the XXVIII International Mineral Processing Congress (IMPC 2016)*, 10p. e-hpcc.com/en/402-downloads.html
- Silva CM, Sørensen BE, Aasly K, Ellefmo SL (2018) Geometallurgical approach to the element-to-mineral conversion for the Nabbaren nepheline syenite deposit. *Minerals* 8:325-345
- Van den Boogaart KG, Tolosana-Delgado R (2018) Predictive geometallurgy: An interdisciplinary key challenge for mathematical geosciences. In Daya Sagar B, Cheng q, Agterberg F (eds) *Handbook of Mathematical Geosciences*, Springer, Cham., pp.673-686

Operational mineralogy: an overview of key practices in sample analysis, sample preparation and statistics.

Christopher Brough, James Strongman, John Fletcher, Mariola Zając, Rachel Garside, Corinne Garner, Libby Rose

Petrolab Ltd

Abstract. Automated mineralogy has been variably utilized by mining companies for two decades, with numerous case studies demonstrating their value to the evaluation of an ore-body. Along with the original QEMSCAN® system there are now several automated mineralogy systems capable of providing comprehensive quantitative measurements of metrics relevant to process mineralogy. However, the current challenge is their application in operational contexts, with long turnarounds, the analysis of complex ore-bodies and single point data sets of dynamic systems. Operational mineralogy is an exciting new key branch of automated mineralogy that has been made possible by the development of ruggedised and versatile SEM systems, rapid sample preparation techniques and data visualisation tools. These advances enable mineralogy to be at the heart of short term operational decision making. This paper reviews some of these advances and current best practise, particularly in sample analysis options, sample preparation and particle statistics that are enabling rapid turnarounds. All work has been developed on the ZEISS Mineralogic platform, and the final presentation includes case studies of the implementation of operational mineralogy at different scales with examples from monthly auditing through to daily on-site support.

1 Introduction

Mineral processing operations are undergoing a shift in expectations of what can be achieved with process monitoring data, with much being drawn from the chemical, pharmaceutical and manufacturing industries. The key difference with mining and mineral processing and one reason for the lag in up take is that the ore feed material has significantly more variability than inputs in those industries. Therefore, alongside advances in automation and process control, there is a requirement to have a clear understanding of the impact of feed variability on the process.

The understanding of feed variability has typically been undertaken through process mineralogy assessments with a focus on representative sampling, understanding geometallurgical domains and characterizing likely process performance (e.g. Lotter et al 2011, Baum 2014), with consequential improvements on project cash flow (Lotter et al 2018a). As valuable as these assessments are, they usually represent single point datasets of dynamic systems and the current opportunity is to use mineralogy assessments in a continuous monitoring framework (Graham 2017, Kalichini et al. 2017). Understanding the routine impact of feed variability requires linking mineralogy, geochemical

assay data, and process performance together with a focus on trending datasets. This linkage is called “Operational Mineralogy” and ideally these trending datasets operate on a routine basis from monthly or weekly audits (on off-site or near-site automated systems) to preferably a daily or shift-by-shift resolution (through on-site automated systems). The implementation of these operational mineralogy systems is relatively new and very infrequent. To date examples have been observed from Cerro Verde (Fennel et al. 2005) and the Kansanshi mine (Kalichini et al 2017). This paper briefly reviews the advances that have made operational mineralogy possible together with key practices that are necessary for its implementation.

2 Operational Mineralogy

Operational mineralogy has developed as a branch of process mineralogy, which itself has been an integral part of mineral processing for the last half-century. Its development has been made possible by three specific advances, namely;

- i. Technological development of ruggedised fit-for-purpose and versatile site-based automated SEMs.
- ii. Developments in rapid sample preparation of mineralogy blocks.
- iii. Development of data visualisation tools to summarise large datasets into relevant metrics.

These changes allow routine mineralogy to be at the heart of operational decision making, and as such operational mineralogy marks a shift from traditional project focused mineralogy to dynamic mineralogy data deeply integrated with daily, weekly or monthly decision making. The first two of these advances are discussed below, along with the key consideration of particle statistics.

2.1 Ruggedised Versatile Automated SEMs

The first major step to automation in the process mineralogy field was the development of quantitative automated mineralogical systems, such as QEMSCAN® (Originally QEM*SEM) (Miller et al. 1982) and MLA (Gu and Napier-Munn 1997). These have driven improvements in ore characterisation, deportment studies and circuit surveys, becoming a critical part of project development and assessment. In recent years several new providers have continued the development of automated mineralogy systems including TIMA, INCA Mineral and ZEISS Mineralogic. Altogether these systems have made significant improvements in both throughput and repeatability. Critically, all these

automated systems provide quantitative measurements of grain and particle size distributions, liberation and also association data on a particle by particle basis. These advances have allowed automated mineralogy to become an integral component of process mineralogy.

At the core of all these automated mineralogy systems is a scanning electron microscope (SEM), a highly sensitive, analytical instrument and very much at home in a clean laboratory environment. Therefore, in the past simply transporting, installing and then servicing these instruments on a mine site was not practical other than on a few very large operations with dedicated or centralised labs. The development of mobile ruggedised systems for military applications, then the oil and gas industry, along with continued innovation of table top systems, means that the logistics of moving an instrument and installing on site have been greatly reduced.

MinSCAN, developed by Zeiss and using Mineralogic, is one such on-site ruggedised system and it benefits from recent advances in functionality and versatility (Graham et al 2015, Graham 2017). This system offers five analysis modes, all of which are user configurable (Figure 1 and see Graham et al. 2015). Deciding between the different analyses modes depends on the mineralogical complexity of the sample, what level of information needs to be obtained and how much time is available. For the mine site application, the routines must be consistent and robust.

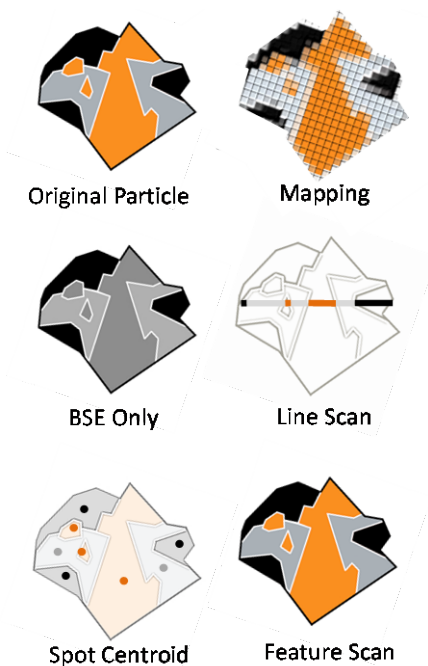


Figure 1. The five analysis modes on Zeiss Mineralogic.

Pixel mapping mode is the longest but most common analysis mode and produces the full suite of liberation and grainsize data. Textural information and throughput are determined by the pixel spacing, which is chiefly dictated by the mineralogical complexity of the sample (Figure 2). Line scan can provide rapid bulk mineralogy datasets and will incorporate much larger particle

populations than pixel mapping. However, grainsize data and liberation datasets are not available and on finer fractions the chance of acquiring poor edge spectra are greatly increased. BSE only is extremely fast and works very well for samples where the thresholds of target phases are distinct from one another and the gangue. For BSE only analysis all department information will be based on stoichiometric assumptions. Spot Centroid “MLA” mode and Feature Scan are also very fast and reduce edge and boundary effects, although as with BSE only they are heavily dependent on the distinct thresholding of the phases.

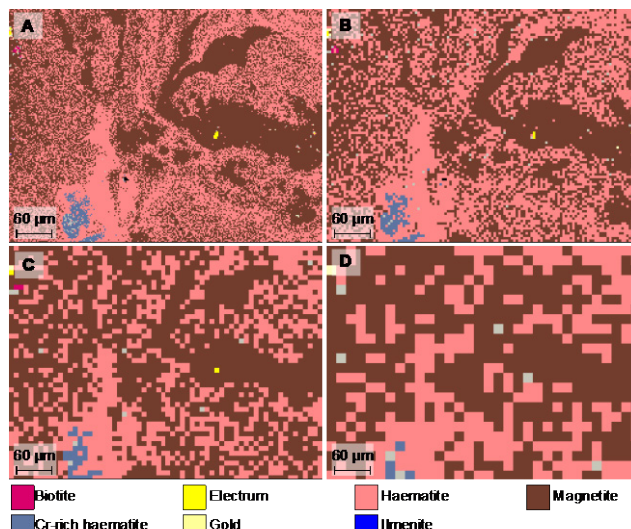


Figure 2. Trade off of speed against textural clarity at the same magnification but larger pixel spacing. (a) 2 µm (~28mins) and (b) 4 µm (~7mins) pixel spacing retaining the textures within the samples. (c) 8 µm (~3mins) pixel spacing retains the magnetite texture around the gold (right hand side) but loses the texture elsewhere. (d) 16 µm (46seconds) pixel spacing which is not suitable for analysis of this sample. No textures are preserved and the gold is not detected.

Along with analysis modes the image processing toolkits of modern automated systems, and particularly the Zeiss Mineralogic system are powerful, allowing for versatile operations in the segmentation and targeted analysis of particular phases. One such developed image processing routine is the bright phase search plus context (BPSC) that allows the analysis of bright phases (e.g. ore phases), along with a dilation zone into the surrounding particle (Figure 3 and see Brough et al. 2017). The image processing recipe works by defining two thresholds, one for the resin which is excluded and one for the target phase which is included. A dilation field is then applied to the target phase of a pre-determined width which spreads the analysis out in a border from the target phase into the surrounding host. If the host is a mineral phase then the border region is included in the analysis, but if the host is resin (i.e. the target phase is liberated), then there is no analysis of the border region. From this analysis the grain-size distribution and partial perimeter liberation of the target phase can be calculated, without the necessity to analyse the whole of the hosting particle. It is particularly useful in coarser size fractions where the target grain may be fine-grained even if the host particle

is coarse-grained, and allows the analysis to keep a fine step-size (i.e. fine resolution) to correctly resolve the ore textures. Furthermore, this BPSC analysis, coupled with a line scan analysis allows for the rapid assessment of bulk modal, deportment and basic liberation data increasing the throughput capacity of the automated analysis.

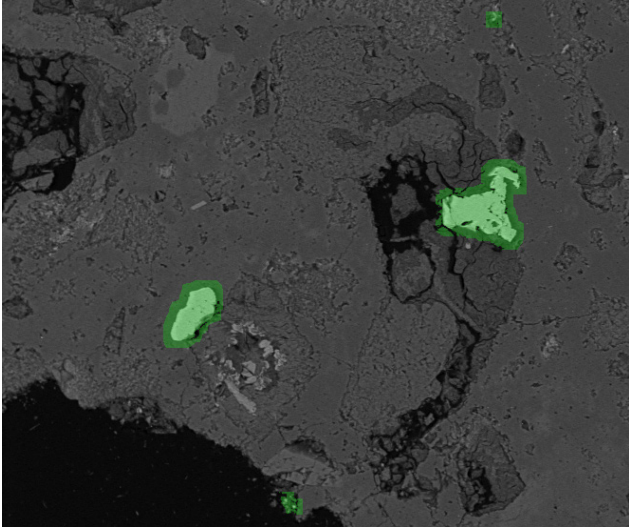


Figure 3. Image of a targeted BPSC routine (cf. Brough et al. 2017). Light green is the targeted phase. Dark green is the dilation zone of interest into the mineral host and the greys are remaining host phases unanalyzed. Black is the resin.

2.2 Sample preparation

Any operational mineralogy program requires quality samples on a rapid turnaround. Bad sampling (i.e. the collection of “specimens” rather than “samples”) equals bad data, and no amount of analysis can remove bias from a sample (Lotter et al. 2018b, Gy 1979). The sampling program should follow the assaying procedures for the targeted stream and ideally the mineralogy sample should be derived from assay reject. This allows a balance to be made between the elemental assays derived from mineralogical data to be compared against chemical assay. There needs to be a clear understanding of the potential error limits of the sampling method and analysis procedures. With operational mineralogy the focus is on trends, but equally it would be impossible to make an accurate mineralogical balance on a sample that is not suitable for metallurgical accounting.

Once collected the preparation of the samples into polished blocks requires a rapid turnaround. Whilst sample preparation techniques are usually subject to confidential in-house protocols there are several key principles that can be summarised. Particulate matter is generally denser than the resin it is being set in and subject to internal density differences as well (i.e. between ore and gangue phases). As such the differential density settling of particles, and therefore the incorrect estimation of modal mineralogy is a key potential problem (e.g. Sutherland and Gottlieb 1991, Kwitko-Ribeiro 2011). Sample preparation must therefore allow for the mixing of a suitably viscous resin and particulate matter in a thick

paste, with enough liquid to coat and fix the particles, but not so much that particles easily slide through the resin to the polishing surface. Included in the particulate matter will be a filler (e.g. graphite) to aid particle separation. Bubbles may form during preparation either from mixing, or from volatile release from the resin blend. These can be problematic due to the collection of fine dust within exposed bubbles on the polished surface and the potential for charging during analysis. As such preparation is undertaken under vacuum to remove excessive bubbles. Longitudinal sections (Figure 4) are an excellent tool for determining optimal preparation requirements and can be used in their own right if density settling is considered unavoidable (e.g. Coetzee et al. 2011).

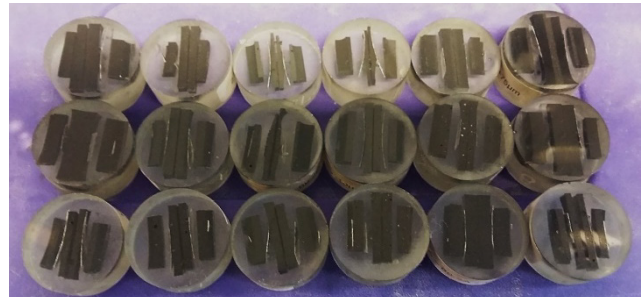


Figure 4. Longitudinal sections to study the effects of density settling under different conditions. From trials runs like this it's possible to determine optimal ratios of resin to particulate matter.

2.3 Particle statistics

All analysis techniques involve the collection of data from a subset of the total particle population. The number of particles to be analysed from each size fraction can be calculated using some of the general theory applied to the analysis of point-counting in petrographic studies but taking account of some more recent statistical studies. The published literature on the techniques of point-counting thin sections or polished blocks evolved from work in the early 19th and 20th century with some papers showing a particular focus on ore-minerals and ore concentrates (e.g. Chayes 1946, 1949). General rules for the estimation of error in point counting were provided in Barringer (1953) and were further elucidated in 1965 with the then seminal work of van der Plas and Tobi. Since 1965, their estimation became the benchmark for measuring point-count error and has been widely used by earth scientists. However, recent statistical studies (Howarth 1998 and references therein) have concluded that some of the assumptions built in to the 1965 paper were inaccurate, particularly as the required confidence interval around that estimation of error increases.

As such, using the Howarth (1998) paper as a blueprint and, in particular, equation (11) from that paper (itself derived from Blyth 1986), the measure of error can be used to calculate the number of particles that need to be analysed to reduce that error to an acceptable margin. It is noted that similar proposals have been put forward for a statistical approach based on the bootstrap method (Evans and Napier-Munn, 2013; Mariano and Evans, 2015). For operational mineralogy terms it is proposed

that the acceptable error for the relative error of a target phase present at an abundance of 10%, should itself be 10% (i.e. the measured value is $10\% \pm 1\%$). This is equivalent to an absolute error of $<0.5\%$ for a target phase present at an abundance of 1%.

The formula from Blyth (1986) estimated the error for the upper bound and lower bound corresponding to counts in the range;

$$p(n)_u = 100 \left(\frac{1}{N} \right) \text{ to } p(n)_l = 100 \left(\frac{N-2}{N} \right)$$

Within this range the upper and lower bounds on the estimate are given by;

$$p(n)_u = 100\text{BETA}(1 - \alpha, n + 1, N - n)$$

$$p(n)_l = 100[1 - \text{BETA}(1 - \alpha, n + 1, N - n)]$$

Where, N = number of grains analysed, n = number of target phases, α = confidence limit around that estimation and BETA is a statistical function.

Using their formulae, it is possible to calculate a solution for any given error margins. For example, if the acceptable error was deemed to be a 10% relative error around a target phase present at proportions of 10% ($10\% \pm 1\%$) with 95% confidence, then the solution comes as 2500 grains. This is equivalent to an absolute error of $<0.5\%$ for a target phase present at an abundance of 1%. 2500 grains would be sufficient for most operational contexts, and it should be noted that particle statistics can be improved for specific phases through targeted analysis (e.g. BPSC; Figure 3).

3 Conclusions

Operational mineralogy brings the tools for mineralogical characterisation into a continuous monitoring framework in order to build on-going trends in process response on a mine-site. Whilst optimal on a day-to-day or shift-to-shift basis these operational mineralogy techniques can be applied to weekly or monthly audits with the aim on integrating mineralogical information on feed variability with on-site decision making. Operational mineralogy has been made possible by key advances in ruggedised automated SEMs, the development of more powerful and versatile analytical software and best practice in rapid sample preparation and optimal particle statistics. These advances allow for rapid turnarounds and the presentation of key metrics to on-site and off-site stakeholders. Weekly and monthly audits represent a form of reactive control and are vital for understanding how the ore-body and processing conditions are changing. However, with day-to-day or shift-to-shift implementation there is the opportunity to move to predictive control of the processing operation, being able to adapt the processing operation to the incoming ore. This potential for day-to-day automated mineralogy is a key opportunity for mine-sites going forward.

References

Barringer AR (1953) The preparation of polished sections of ores and mill products using diamond abrasives, and their quantitative study by point counting methods. Bull. Instn Min.

Metall 63:21-41.

Blyth CR (1986) Approximate Binomial Confidence Limits. Journal of the American Statistical Association 81, 843 – 855.

Brough CP, Strongman J, Bowell R, Warrender R, Prestia A, Barnes A, Fletcher J (2017) Automated environmental mineralogy; the use of liberation analysis in humidity cell testwork. Minerals Engineering 107:112-122.

Coetzee LL, Theron SJ, Martin GJ, Merwe JD, and Stanek TA (2011) Modern gold deportments and its application to industry. Minerals Engineering 24:565–575

Chayes F (1946) Linear analysis of a medium-grained granite. American Mineralogist, 31:261-275.

Chayes F (1949) A simple point counter for thin-section analysis. American Mineralogist 34:1-11.

Evans CL Napier-Munn TJ (2013) Estimating error in measurements of mineral grain size distribution. Minerals Engineering 52:198-203.

Fennel M, Guevara J, Velarde G, Baum W, Gottlieb P (2005) QEMSCAN mineral analysis for ore characterization and plant support at Cerro Verde. 27th Mining Convention, Arequipa, Peru, Proceedings 1–11.

Graham S (2017) SEMs, mines and mineralogy – On-site automated mineralogy delivering an operational mineralogy approach for mine management. SGA conference, Quebec, 14th Biennial Meeting 1-4

Graham S, Brough C, Cropp A (2015) An Introduction to Zeiss Mineralogic and the correlation of light microscopy with automated mineralogy: a case study using BMS and PGM analysis of samples from PGE-bearing chromitite prospect. Precious Metals Conference 1-11

Gu Y, Napier-Munn T (1997) JK/Philips mineral liberation analyzer – an introduction. Minerals Processing '97 Conf. Cape Town, SA, 2

Gy PM (1979) Sampling of particulate materials – theory and practice. Elsevier, Amsterdam.

Howarth RJ (1998) Improved estimators of uncertainty in proportions, point-counting, and pass-fail test results. American Journal of Science 298:594-607.

Kalichini, MS Goodall, WR, Paul, EM, Prinsloo, A, Chongo, C (2017) Applied Mineralogy at Kansanshi mine -Proof of the Concept of On-Site Routine Process Mineralogy for Continuous Improvement of Plant Operations, Process Mineralogy.

Kwitko-Ribeiro R. (2011) New sample preparation developments to minimize mineral segregation in process mineralogy. 10th International Congress for Applied Mineralogy 411-417.

Lotter NO, Kormos LJ, Oliveira J, Fragomeni D, Whiteman E (2011) Modern Process Mineralogy: Two case studies. Minerals Engineering 24:638 – 650.

Lotter NO, Evans CL, Engstrom K. (2018a) Sampling – A key tool in modern process mineralogy. Minerals Engineering 116:196 – 202.

Lotter NO, Baum W, Reeves S, Arrue C, Bradshaw D (2018b) The business value of best practice process mineralogy 116:226 – 238.

Mariano RA, Evans CL (2015) Error analysis in ore particle composition distribution measurements. Minerals Engineering 82:36-44.

Miller PR, Reid AF, Zuiderwyk MA, (1982) QEM*SEM® image analysis in the determination of modal assays, mineral associations and mineral liberation. CIM-XIV International Processing Congress, Toronto Canada

Sutherland DN, and Gottlieb P (1991): Application of automated quantitative mineralogy in mineral processing. Minerals Engineering (4/7–11):753–762

Van der Plas L, Tobi AC (1965) A chart for judging the reliability of point counting results. American Journal of Science 263:87 – 90.

From exploration towards predictive geometallurgy - the role of SEM-based automated mineralogy and statistical assessment

Sandra Birtel, Kai Bachmann, Philipp Büttner, Raimon Tolosana Delgado, Karl Gerald van den Boogaart, Jens Gutzmer
Helmholtz Zentrum Dresden-Rossendorf, Helmholtz Institute, Germany

Abstract: Geometallurgical models are constructed to quantitatively predict how ores will behave during extraction and beneficiation. Depending on data availability, complexity of data and operational stage different classes of geometallurgical models can be distinguished: 1) resource potential, 2) recoverable resources, 3) first order predictive models, 4) predictive models, and 5) real-time mining models. Here, two case studies are presented where modal mineralogy and microstructural data obtained from SEM-based image analysis are combined with complementary analytical data and statistically assessed in order to predict raw material behaviour during mineral processing. For both case studies, the necessary steps to develop existing models into truly predictive geometallurgical models are outlined. The first case study concerns the recovery of Sn from a historic flotation tailings storage facility. The second case study centres on the recovery of PGE as by-products from a chromite ore deposit as a first order predictive geometallurgical model.

Introduction

Geometallurgy aims at increasing resource and energy efficiency during mineral exploitation and beneficiation by connecting disciplines along the raw material value chain (geosciences, mining engineering, minerals processing, extractive metallurgy, environmental engineering) with economics and appropriate mathematical modeling tools. By doing so, we expect to also reduce environmental impact and technical project risk. For this purpose all tangible data needed to understand the beneficiation characteristics of an orebody need to be obtained, aggregated and communicated.

The availability of quantitative data for the mineralogical and microstructural properties of ores from scanning electron microscope (SEM)-based image analysis (aka 'automated mineralogy') has provided an important key for the success of geometallurgy in the mining industry for the last 15 years (e.g., Hoal et al., 2009, Gregory et al., 2013). More recently, automated mineralogy has been also used to assess the presence and distribution of possible by-product or even penalty constituents (e.g. Minz et al., 2013, Frenzel et al., 2018).

Building upon this, predictive geometallurgy (van den Boogaart and Tolosana-Delgado, 2018) optimizes the mineral value chain based on a spatially resolved, precise and quantitative understanding of the geology and mineralogy of the ores, forecasting models of the

behavior of ores through beneficiation, and taking into account the mineral and operational economics. Thus, geometallurgical models can have different levels of complexity, which will depend on data availability and on the operational stage (Fig. 1):

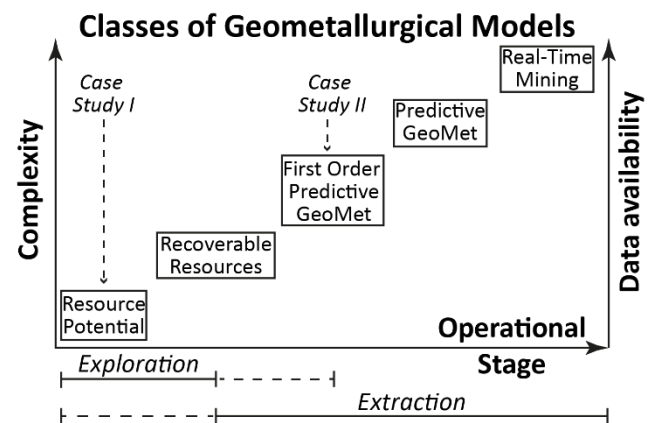


Figure 1: Classes of geometallurgical models. Complexity and resulting predictive power is strongly depending on the available amount of data, and hence on the current state of the operation. The two cases studies presented here are indicated. (GeoMet= geometallurgical).

- 1) **Exploration stage:** resource potential models and recoverable resource models provide information on geological, geochemical and mineralogical properties. Ideally, these properties may be interpolated at every locality, with their uncertainty; sometimes, these models include as well a first assessment on the behaviour during mineral processing.
- 2) **Extraction stage:** The extraction stage includes mining and beneficiation. Models in the extraction stage need to be predictive, as they provide information about: a) the strategy to sample the mining and beneficiation process at several scales; b) the prediction of behaviour of ores in the further process, and c) how to optimize of the operation. An economic assessment should always be part of such models.

Case studies

This contribution exemplifies the first steps of predictive geometallurgy with two different case studies (1) a resource potential model of Sn from a historic flotation tailings storage facility; and (2) a first order predictive

geometallurgical model for recovery of PGE as a by-product from a chromite ore deposit (Fig. 1).

2.1 Case study I: Resource potential model for tin recovery of a flotation tailings storage facility

A resource potential model of a tailings storage facility (TSF) at Tiefenbachhalde in the Erzgebirge (Germany) was created based the assessment and weighting of grade, modal mineralogy, liberation, grain size and flotation behaviour of tailings intersected by a series of drill cores (Büttner et al., 2018). The tailings originate from ores of the Altenberg Sn deposit, a world class greisen-type Sn deposit (Weinhold 2002). The TSF was in active use from 1952 to 1966 for flotation residues (Weinhold 2002). The dimensions of the TSF are ca. 350 m by 600 m with a maximum thickness of the TSF

deposits of ca. 30 m.

All available historic data was compiled, complemented by 10 drill cores produced from across the TSF area. The cores were logged; as the material appeared uniform on a macroscopic scale, 2 meters of drill core material was combined into one sample, generating 92 samples for analyses. After drying and deagglomeration polished grain mounts were prepared for mineral liberation analysis (MLA) and electron microprobe analysis, further material was wet sieved for laser granulometry and chemical assaying.

The current topography was obtained by a drone-borne survey (ground resolution 1.55 cm/px). For the 3 D reconstruction of the TSF the digital surface model of tailing body was combined with a digitalized topographic map from 1912 (1:25 000) as pre mining reference (Fig. 2)

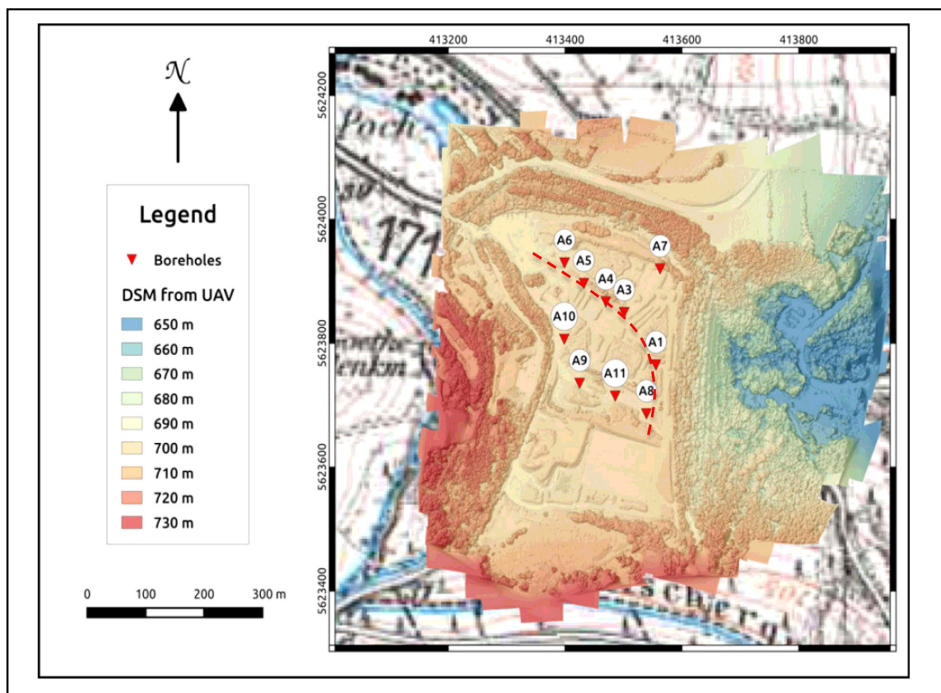


Figure 2: DSM acquired by airborne photogrammetric survey showing drill hole (here borehole) locations within topographic map of 1912 (1:25000, in Gauss-Krüger, Germany, Zone 4) as pre-filling reference. The red line shows the representative cross sections used in Fig. 2. Geographic coordinate system and Datum WGS84 UTM33N, Büttner et al. (2018)

Cassiterite turned out to be the only significant Sn bearing mineral, which contributes up to 0.2 wt% Sn in the tailings. Cassiterite is typically fine grained and well liberated (>80% by surface), implying that the liberation process during comminution was successful, whereas the concentration by flotation was insufficient. For developing a resource potential model illustrating the cassiterite content recoverable by flotation, relevant material parameters for beneficiation had to be defined. In absence of actual flotation testwork, a weighting strategy was proposed for the penalization of chemical Sn assays by the following parameters: particle size and liberation. This data was used to construct a 3D model; point data was interpolated by planar stratigraphic correlation. Fig. 3 shows a) the index concentration (IC) of SnO₂ (represented by elemental grade or cassiterite

grade), b) index of liberation (IL) the liberation of cassiterite grains (red > 89% by surface), c) index of particle size (IP) of cassiterite-bearing particles. D) Liberation- Concentration-Flotation value LCF: (red: LCF>0.07) illustrating the amount of cassiterite-bound tin that can realistically be recovered from the tailing by flotation. The output shows e.g. that considering only the grade would be misleading as the grade shows high values at the surface where liberation is low and particle sizes are large. Results of this study illustrate the importance of combining chemical grade data with quantitative mineralogical and microstructural information in any effort to objectively assess the residual value contained in industrial tailings or any other residue considering re-processing. Yet, this is

still not a truly predictive geometallurgical model. The latter will require knowledge of the actual behaviour of the tailings particles, i.e. lab based test work, ideally combined with particle tracking (Lamberg & Vianna 2007). A way of integrating such test work data with existing assay data into a coherent 3D geometallurgical model is discussed in the next case study.

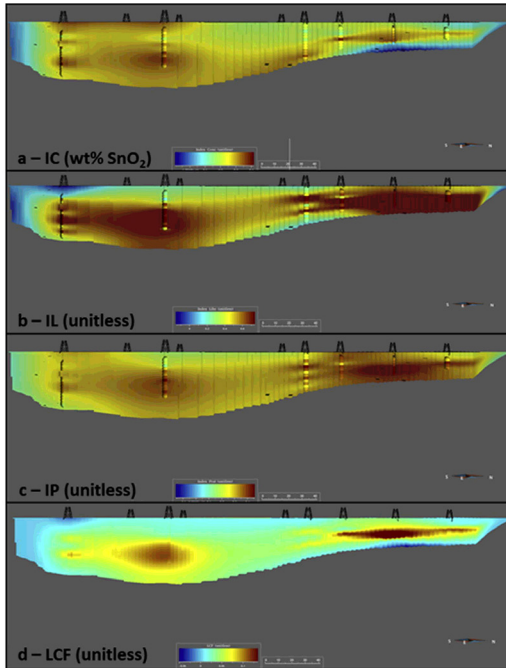


Figure 3: Spatial distribution of index figures along a representative N-S cross section through the Tiefenbachhalde: (a): IC (index concentration): cassiterite concentration (red 0.4 wt% Sn), (b): Index Liberation: Mineral liberation (red 80% liberation by free surface), (c): Index particle size: Mean particle size (red 30 µm equal circle diameter), (d): LCF: Liberation- Concentration- Flotation value (red: LCF>0.07), Büttner et al. (2018).

2.2 Case study II: First order predictive geometallurgical model for PGE recovery from a chromite ore deposit

A first order predictive geometallurgical model was created for an ore body comprising several chromitite seams at the Thaba mine, Western Bushveld Complex of South Africa. The focus of this study was the assessment of the potential for PGE recovery as a by-product. Here, a data-driven approach is presented using the whole available data set of primary (intrinsic) ore properties, such as bulk rock chemistry, mineral assemblage, mineral association and mineral grain sizes, to predict the PGE beneficiation potential in terms of probabilities (and therefore keeping track of uncertainty). A general geometallurgical framework for the development of the model is presented in Fig 4.

First, the geological architecture of the mine was evaluated and geochemical domains were defined (Bachmann et al. 2019 a, b). A rather pristine (least altered orthomagmatic) domain, a domain affected by hydrothermal alteration (e.g. along faults) and an oxidized zone affected by supergene alteration were distinguished.

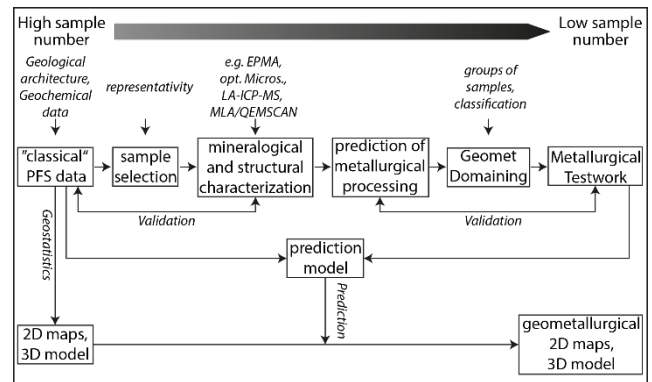


Figure 4: Flow sheet to develop a data-driven, first order predictive geometallurgical model. Bachmann et al. (2019 c)

Sample suites representing the different chromitite seams in drill cores and open pit exposures were characterized for modal mineralogy, including PGE mineralogy, mineral association and liberation as well as bulk rock chemistry. Pristine ore as well as hydrothermally altered ore samples were randomly collected from a series of drill core intersections of the LG-6, LG-6A, MG-1 and MG-2 chromitite seams. More than 100 individual drill core intersections were studied in detail using SEM-based automated image analysis. Samples were statistically clustered based on the mineral assemblage of platinum group minerals (PGM), base metal sulphides (BMS) and rock-forming minerals, such as chromite and silicates. Appropriate composite samples were created and used for beneficiation test work, including density separation and froth flotation. Results of output streams were evaluated by chemical assays and clusters were re-assessed and eventually merged according to the results achieved in terms of grade, recovery and yield of PGE. To define geometallurgical domains, these composited clusters were related back to well-known geological features by integration into a 3D model of the Thaba mine.

A spatially resolved geometallurgical model was subsequently developed for different chromitite seams by performing the following steps: i) Building a logistic regression model to relate the processability of the ore to chemical proxies, (ii) performing a geostatistical interpolation of a comprehensive geochemical dataset, and (iii) combining step (i) and (ii) to generate a space-resolved processability model. In this way, it was possible to define three final domains, one showing high and the other two with low potential for future PGE beneficiation (Fig.5). The result can be seen as a low budget, first order predictive geometallurgical model: a maximum of information was extracted from a minimum of data, by allowing lab work and data analysis to work iteratively. However, predictability is still limited, as we can only assess the probability that PGE recovery from a specific area would be more or less efficient. In the next step, costs should be taken into account, to be able to assess whether constructing a sub-circuit for PGE would be economically sound.

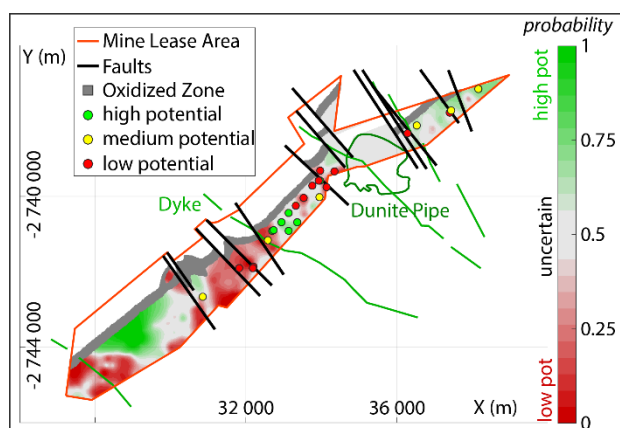


Figure 5: Geometallurgical model for beneficiation of PGMs as a by-product in Thaba mine, South Africa. Bachmann et al. (2019 c).

3 Conclusions

The approach outlined here is of general applicability to other metals and ore deposit types. It clearly illustrates the value of conducting predictive geometallurgical models already during the latter stages of exploration in a process that will benefit from regular follow-up and model updates during the phase of active exploitation. The two case studies serve to illustrate that predictive geometallurgical models can be constructed by a combination of geological insight and routine assay data with a limited amount of quantitative mineralogical and microfabric data through sound mathematical data treatment. To obtain fully fledged predictive geometallurgical models and real time mining, process optimization and hence economic assessment will be indispensable.

Acknowledgements

Both case studies were part of projects funded by German Federal Ministry of Education and Research (BMBF): Case study I was part of the 'SMSB' project, funded by within r3 program, (grant number BMBF 033R095). Case study II is a contribution to the German/South African R&D project 'AMREP' (grant number BMBF 033R119E).

References

- Bachmann K, Osbahr I, Tolosana-Delgado R, Chetty D, Gutzmer J (2018) Variation in platinum group mineral and base metal sulfide assemblages in the Lower Group chromitites of the western Bushveld Complex, South Africa. *Can Min* 56(5):723–743. <https://doi.org/10.3749/canmin.1700094>.
- Bachmann K, Menzel P, Tolosana-Delgado R, Schmidt C, Hill M, Gutzmer J (2019a) The use of assay data as a foundation for a geometallurgical model – the case of the Thaba Chromite Mine, South Africa. *J Geochem Explo.* <https://doi.org/10.1016/j.gexplo.2019.01.008>.
- Bachmann K, Menzel P, Tolosana-Delgado R, Schmidt C, Hill M, Gutzmer J (2019b) Multivariate geochemical classification of chromitite layers in the Bushveld Complex, South Africa. *Appl Geochemistry*. <https://doi.org/10.1016/j.apgeochem.2019.02.009>
- Bachmann K, Chetty C, Tolosana-Delgado R, Menzel P, Gilbricht S, Osbahr I, Van den Boogaart G, Gutzmer J (2019c) A first order geometallurgical model for PGE in a chromite ore. *Journal of Cleaner Production*, submitted.

- Büttner P, Osbahr I, Zimmermann R, Leifner, T, Satge L, Gutzmer J. (2018) Recovery potential of flotation tailings assessed by spatial modelling of automated mineralogy data *Minerals Engineering*, Volume 116:143-151,
- Frenzel M, Bachmann K, Carvalho JRS, Relvas JMRS, Pacheco N, Gutzmer J. (2018); The geometallurgical assessment of by-products - Geochemical proxies for the complex mineralogical department of indium at Neves-Corvo, Portugal *Miner Deposita* 1-24
- Gregory MJ, Lang JR, Gilbert S, Hoal, KO (2013) Geometallurgy of the Pebble Porphyry Copper-Gold-Molybdenum Deposit, Alaska: Implications for Gold Distribution and Paragenesis, *Economic Geology* 108:463-482
- Hoal KO, Stammer JG, Appleby SK, Botha, J, Ross JK, Botha, PW (2009) Research in quantitative mineralogy: Examples from diverse applications, *Minerals engineering* 22:402-408
- Lamberg P, Vianna S (2007) A technique for tracking multiphase mineral particles in flotation circuits, VII MSHMT- Ouro Preto, 195-202
- Minz F, Bolin H-J, Lamberg P, Wanhainen C (2013) Detailed characterisation of antimony mineralogy in a geo-metallurgical context at the Rockliden ore deposit, North-Central Sweden, *Minerals Engineering* 52, 95-103
- van den Boogaart, KG, Tolosana-Delgado R (2018) Predictive Geometallurgy: An Interdisciplinary Key Challenge for Mathematical Geosciences. *Handbook of Mathematical Geosciences*, Springer Verlag, 673-686
- Weinhold G. (2002) *Bergbau in Sachsen- Die Zinnlagerstätte Altenberg/Osterzgebirge*, ed: Sächsisches Oberbergamt Sächsisches Landesamt für Umwelt und Geologie, Freiberg Bd. 9

Metal department and ore variability of the Bolcana porphyry Au–Cu system (Apuseni Mts, Romania) – Implications for ore processing

Rosie Blannin, Laura Tusa, Sandra Birtel, Jens Gutzmer

Helmholtz-Zentrum Dresden-Rossendorf, Helmholtz Institute Freiberg for Resource Technology, Freiberg, Germany

Sabine Gilbricht

Institut für Mineralogie, Technische Universität Bergakademie Freiberg, Germany

Paul Ivășcanu

Eldorado Gold Corporation, Romania

Abstract. The maiden resource estimate for the Bolcana gold-copper porphyry defines 381 Mt at 0.53 g/t gold and 0.18% copper. The early stage of exploration provides the perfect opportunity for the application of geometallurgical studies, to enable optimisation of future mine and plant operations. Quantitative mineralogy and microfabric characterisation of crushed material and thin sections from seven 40 m drill core intervals were accomplished by Scanning Electron Microscopy based Mineral Liberation Analysis, complemented by X-ray Powder Diffraction. The mineralogy of the studied samples is highly variable, depending on lithology, mineralisation and alteration. The main Cu-bearing mineral is chalcopyrite, predominantly occurring in B and C veins. At shallow depths, secondary bornite and covellite form rims around chalcopyrite. Primary bornite occurs at greater depths in the system. Native gold grains are typically <10 µm and hosted by chalcopyrite or, to a lesser extent, pyrite. Electron Probe Microanalysis on four samples determined that gold concentrations in solid solution in selected sulphide minerals are <100 ppm. Copper and associated gold should be recoverable by flotation of chalcopyrite. The recovery of free gold and gold associated with pyrite may require additional processing steps.

1 Introduction

The Bolcana porphyry Au-Cu system, associated with Pb–Zn±Cu±Au±Ag intermediate-sulphidation epithermal veins, is located in the "Gold Quadrilateral" of the South Apuseni, Romania (Fig. 1; e.g. Cardon et al. 2008). Porphyry mineralisation comprises an early stage Cu-Au granodioritic porphyry overprinted by late-stage gold-rich microdiorite porphyry dykes, with variable quartz-magnetite-pyrite-chalcopyrite-bornite stockworks and disseminations of chalcopyrite and subordinate bornite hosted by dykes and coeval breccias (Dénes et al. 2015; Eldorado Gold 2018a; Ivășcanu et al. 2018; Milu et al. 2003). A maiden Inferred Resource of 381 million tonnes at 0.53 g/t gold and 0.18% copper, containing 6.5 million ounces of gold and 686,000 tonnes of copper, has been defined by Eldorado Gold (2018b).

A suite of samples from the Bolcana porphyry system was selected for metallurgical testing, with preliminary

rougher flotation tests achieving recoveries of up to 90% for Cu and 86% for Au (Eldorado Gold 2018b). This study aimed to quantitatively characterise the mineralogy and microstructures of samples selected for metallurgical testing, including both hand specimens and crushed samples, and assess the implications for mineral processing. Mineralogy and microfabric relationships play a significant role in the extraction of copper and gold from porphyry ores, and must therefore be considered during geometallurgical studies, for effective ore body management, optimisation and sustainable development of future mine and plant operations (e.g. Birtel et al. 2013; Cropp et al. 2013).

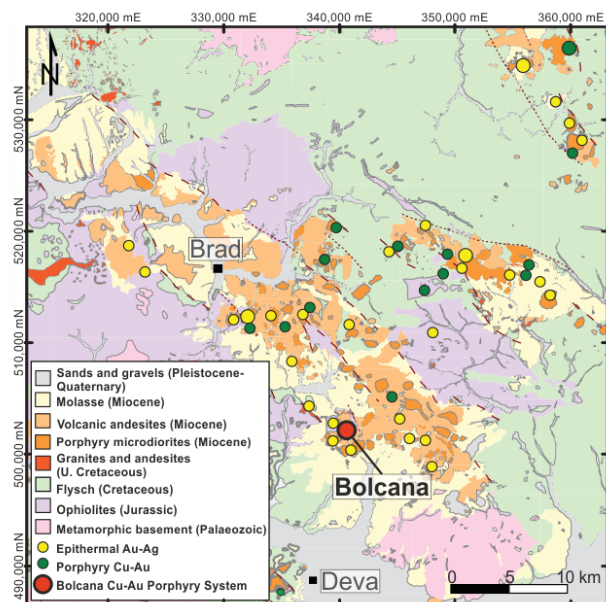


Figure 1. Simplified geological map of the "Gold Quadrilateral", South Apuseni Mountains. Epithermal Au-Ag and porphyry Cu-Au systems are highlighted. Modified after Ivășcanu et al. 2018.

2 Sampling and methods

Seven 40 m drill core intervals from two drill holes were selected for metallurgical testing: TRSD017 240–280 m, 346–386 m and 386–426 m; TRSD013 64–104 m, 152–192 m, 356–396 m and 758–798 m. The intervals were chosen

to represent alteration and mineralogical variability in the deposit (Eldorado Gold 2018b).

The drill holes were logged for lithology, alteration style, mesoscopic mineralisation and vein type. A suite of samples was selected to represent a range of sulphide mineralisation styles, vein types and alteration types, from which fourteen thin sections were prepared. A grain mount for each of the studied drill core intervals was prepared from crushed material (<600 µm).

Mineralogy, microstructure, mineral associations and deportment of the valuable elements were investigated in both sample types. Mineralogical studies were performed using Scanning Electron Microscopy (SEM) based Mineral Liberation Analyser (MLA) and X-ray Powder Diffraction (XRD). Bulk rock chemical assay data for 49 elements, provided by Eldorado Gold, was used to validate the mineralogical studies. Electron Probe Microanalysis (EPMA) was carried out on four samples with the purpose of studying gold deportment.

3 Results

3.1 Ore variability

Core logging identified eight lithologies and five alteration types within the studied intervals. These are characteristic of porphyry deposits, as well summarised by Sillitoe (2010). The lithologies include host porphyry, intermineral porphyries, late intermineral porphyry, late-mineral porphyry, magmatic breccia, phreatomagmatic breccia and magmatic hydrothermal breccia.

Argillic alteration is associated with fracture zones and late epithermal event(s). Phyllic alteration occurs in the shallow parts of the system, with a pyrite-white mica-clay assemblage. Potassic (biotite-feldspar-magnetite) alteration and sodic alteration occur at greater depths of the system. Sodic alteration is transitional between sodic-calcic and potassic alteration, with albite and labradorite contents exceeding the orthoclase content (Fig. 2). Magnetite-albite-chlorite-epidote (Mace) alteration, transitional between phyllic and sodic alteration assemblages, was also defined (Eldorado Gold 2018b).

Quantitative modal mineralogy was calculated from classified and processed MLA data, as seen in Figure 2.

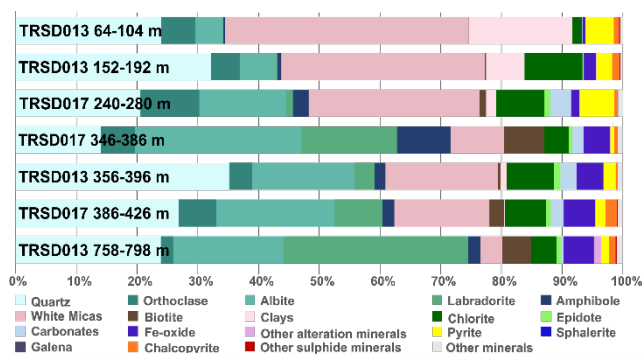


Figure 2. Modal mineralogy of crushed material samples, given by MLA results.

The rock-forming minerals include quartz, feldspars, and amphibole. Quartz content varies from ~15-35 wt%,

while feldspars tend to increase in content towards the centre of the system, from 10 wt% in the near-surface up to around 50 wt% at high depth. Amphiboles are typically a minor constituent throughout the intervals.

The main alteration minerals are micas, chlorite and clay minerals. Clay and white micas are dominant in the near-surface, related to phyllic alteration, and decrease with depth. Biotite content is linked to sodic and potassic alteration, occurring variably in the deeper intervals. Chlorite content is particularly associated with Mace alteration, remaining fairly constant at higher depths. Fe-oxide content, assumed to mainly comprise magnetite, according to XRD, increases with depth in relation to Mace and sodic alteration. Epidote, carbonates, gypsum, anhydrite, are typically minor and variable, but can reach up to ~3 wt% each, while some barite and fluorite may appear in relation with the distal polymetallic epithermal veins.

Pyrite content is most significant in phyllic alteration zones, at ~5 wt%, where it occurs as disseminations. Chalcocopyrite varies from ~0.3-2 wt%, while 'other sulphide minerals' bornite, covellite, chalcocite, sulphosalts (tetrahedrite and freibergite), sphalerite and galena are typically minor, at <0.1 wt%.

3.2 Vein types

The vein types most significant for controlling copper and gold distribution are seen in Figure 3.

In near-surface zones, phyllic-altered host porphyry is the dominant lithology, typically cut by quartz and quartz-magnetite veins, and with pyrite as the principal sulphide. Figure 3.A shows a high density of quartz stringers and pyrite-dominated sulphide stringers (D veins) cutting phyllic-altered host porphyry.

Early-forming A veins (e.g. Sillitoe 2010) are common throughout the porphyry system (Fig. 3.B). They are irregular, discontinuous and typically comprise quartz with low sulphide contents. In many cases, A veins were reopened and overprinted by later veins, resulting in chalcocopyrite and/or pyrite precipitation. An example of this can be seen in Figure 3.B, where an A vein is partially overprinted by a younger, cross-cutting B vein.

B veins, quartz veins with a sulphide centre-line (e.g. Sillitoe 2010), are the dominant vein type in many of the intervals, being particularly associated with intermineral porphyries. In Figure 3.B, the vein centre-line comprises intergrown pyrite and chalcocopyrite, with rims of bornite, chalcocite and covellite surrounding chalcocopyrite grains. In Figure 3.C, B vein (1) has a variable centre-line of pyrite, chalcocopyrite, magnetite and chlorite, whereas B vein (2) has a well-defined centre-line which transitions from pyrite- to chalcocopyrite-dominated. In Figures 3.B, 3.C and 3.D, the B veins have alteration haloes of muscovite and/or albite, which host disseminated pyrite and chalcocopyrite. The variability of the vein centre-lines and the presence of alteration haloes, which are characteristically absent for B veins, could imply that the veins have been overprinted at some stage.

C and D veins are sulphide-dominated veins typical of porphyry systems (e.g. Sillitoe 2010). D veins (Fig. 3.A) are typically pyrite-dominated, with an illite or sericite

selvage, whereas C veins (Figure 3.D) are chalcopyrite-dominated with no significant selvage.

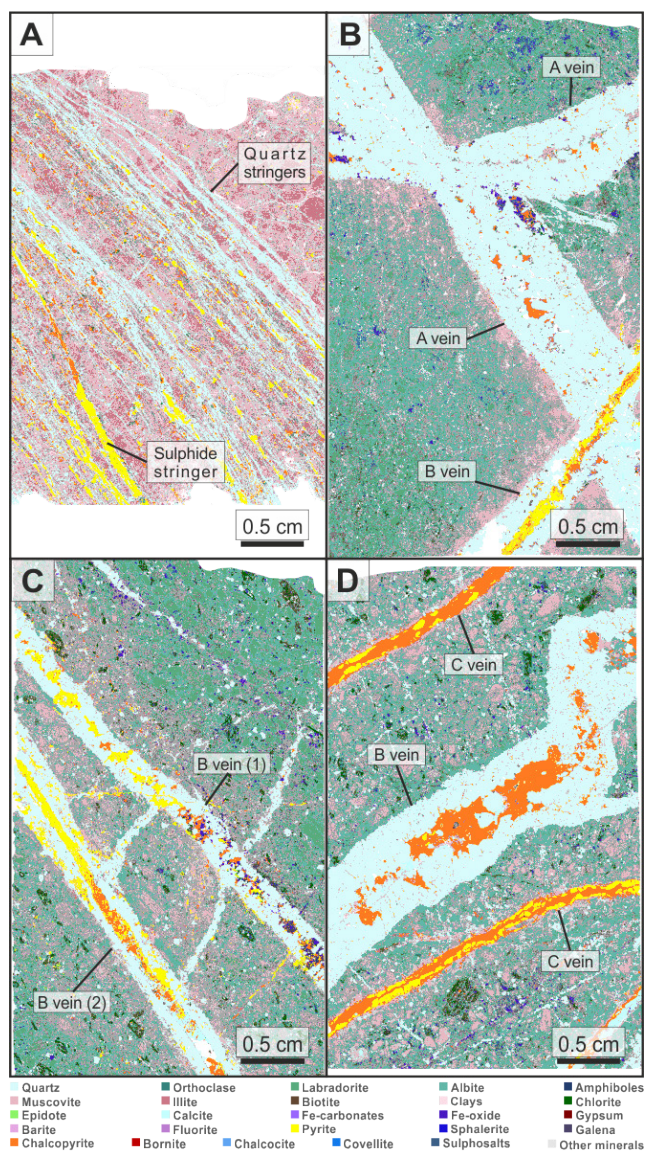


Figure 3. MLA false colour images of selected thin sections, with colour key. (A) TRSD013 83.7 m, phyllic-altered host porphyry with quartz and sulphide stringers; (B) TRSD017 360.8 m, magnetite-albite-chlorite-epidote-altered magmatic breccia with A and B veins; (C) TRSD017 410.9 m, sodic-altered fine intermineral porphyry with B veins; (D) TRSD017 398.2 m, phyllic- to magnetite-albite-chlorite-epidote-altered fine intermineral porphyry with B and C veins.

3.3 Copper deportment and variability

Copper is distributed between chalcopyrite, bornite, chalcocite, covellite and tetrahedrite. Chalcopyrite, which is typically hosted by A, B and C veins or found as disseminations, is the dominant Cu-bearing mineral, contributing 72-98% of Cu grade in the crushed material samples. The remaining Cu usually comes from bornite, which contributes ~10-15%. Chalcocite, covellite and sulphosalts are typically minor contributors to Cu grade.

Preferential associations of chalcopyrite with minerals other than the main rock-forming minerals are seen to

occur with pyrite and the other Cu-bearing minerals. Figures 4.A and 4.B represent the common occurrence of intergrown chalcopyrite and pyrite, which is seen to occur in B and C veins (Figs. 3.A, 3.B, 3.C and 3.D).

At shallow depths in the system, rims of secondary bornite and covellite form around chalcopyrite (e.g. Figs. 4.A-D), seen both in the crushed material samples and in B vein centre-lines in thin sections (Figs. 3.B and 3.E). Primary bornite (Figs. 4.E and 4.F) occurs at greater depths in the system. The replacement of chalcopyrite by secondary bornite tends to decrease with depth, as rims of chalcocite and covellite form around both chalcopyrite and primary bornite. Figure 4.G and 4.H show growths of minerals on bornite grain surfaces, identified as covellite and chalcocite by MLA.

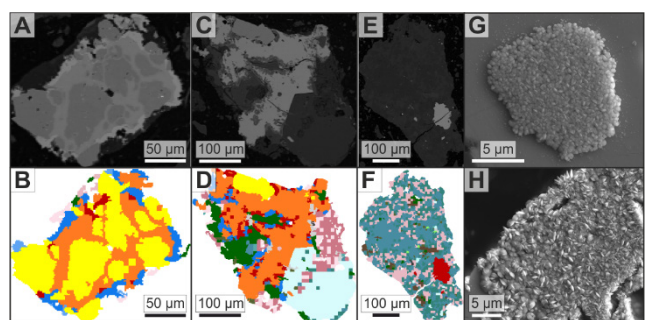


Figure 4. BSE images (A,C,E) and MLA false colour images (B,D,F) showing the association of chalcopyrite with other Cu-bearing minerals (A-D) and primary bornite (E,F), from crushed material samples TRSD013 164-168 m (A,B), TRSD013 152-192 m (C,D), TRSD017 386-426 m; SEM-EPMA images (G,H) of crystal growths on mineral surfaces, from crushed material sample TRSD013 758-798 m. See Figure 3 for key.

3.4 Gold deportment and variability

In the Bolcana porphyry system, gold has been found to occur as native gold grains. In total, 175 gold grains were identified. The grain size ranges up to 40 µm, but 80% of the gold grains are <10 µm (Fig. 5).

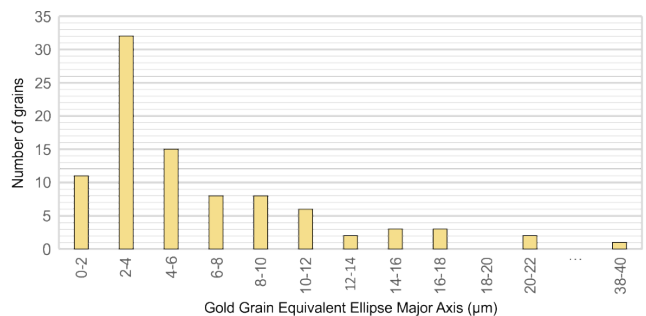


Figure 5. Gold grain size distribution for crushed material samples. The equivalent ellipse major axis of each grain as calculated in MLA Image Processing.

The Cu and Au grades are correlated, but there is no clear link between higher Au grades and higher bornite content, which is typical of porphyry deposits and therefore could be expected (e.g. Kesler et al. 2002). Instead, native gold grains are predominantly hosted by chalcopyrite (Figs. 6.A-B,E-H), variably in B vein centre-

lines, C veins and quartz veins. Over 60% of gold grains in the crushed material samples are associated with chalcopyrite. In the near-surface zones, where disseminated pyrite from phyllic alteration is significant, gold grains are commonly hosted by pyrite.

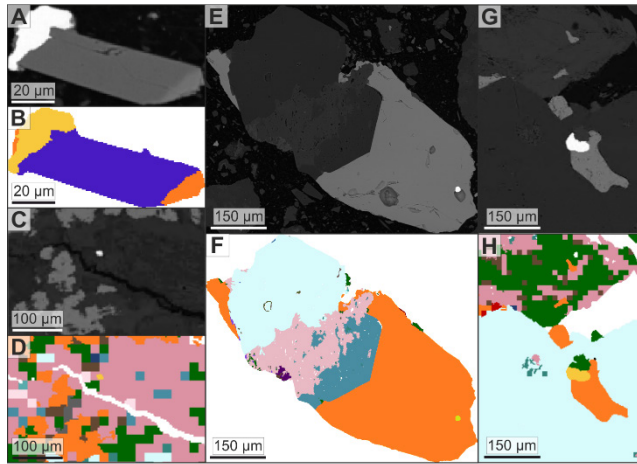


Figure 6. BSE images (A,C,E,G) and MLA false colour images (B,D,F,H) showing gold grains occurring in crushed material samples C-TRSD013 758-798 m (A,B), TRSD017 386-426 m (E,F) and thin sections TRSD013 160.0 m (C,D), TRSD013 764.8 m (G,H). See Figure 3 for key.

Around 30% of the gold grains in the crushed material samples are not associated with either chalcopyrite or pyrite. They occur as free gold at the boundaries of gangue and alteration minerals such as quartz, albite, muscovite, magnetite (Figs. 6.A-6.D). Typically, this occurs when gold is proximal to, but not hosted by, chalcopyrite grains, in veins or disseminated in the alteration haloes around veins (Figs. 6.C, 6.D).

The calculated gold assays from MLA are highly variable and do not fit the chemical assays, either exceeding or not reaching the assay values. This observation is attributed to a nugget effect, but may also imply that considerable amounts of gold are present in solid solution in sulphide minerals in some cases. EPMA on selected pyrite, chalcopyrite, bornite, covellite and chalcocite grains from the crushed material samples TRSD013 64-104 m, 184-188 m and 758-798 m, and TRSD017 386-426 m indicate that gold is absent in concentrations close to, or above, the detection limit of 100 ppm. However, gold could occur in solid solution in sulphide minerals at <100 ppm.

4 Summary and conclusions

The variability of copper and gold throughout the deposit are controlled by key factors including lithology, vein types, alteration, and how these factors vary with depth.

Copper is mainly distributed in chalcopyrite, with minor contributions from bornite, chalcocite, covellite and sulphosalts. Chalcopyrite predominantly occurs in B and C veins, hosted by sodic-potassic or Mace altered intermineral porphyries. At shallow depths, secondary bornite, chalcocite and covellite occur as rims around chalcopyrite grains, as a result of supergene and/or

epithermal processes. At greater depths, primary bornite occurs, with both chalcopyrite and primary bornite grains commonly having rims of chalcocite and covellite. Copper should be recovered by flotation of Cu-sulphides, assuming that their grain sizes would require a grinding size reasonable for milling and flotation.

Gold typically occurs as <10 µm grains, hosted by chalcopyrite or, to a lesser extent, pyrite. Therefore, gold is also typically found in B, C and D veins, or disseminated in the groundmass. Presumably, gold should be well recovered in a copper concentrate when associated with sulphides. Additionally, gold which may be in solid solution in sulphide minerals (<100 ppm) would also be recoverable by flotation. However, free gold associated with gangue in veins, or not attached to chalcopyrite grains in the groundmass, may be lost during processing, depending on grinding size and grinding behaviour.

Pyrite-hosted gold is common in the near-surface zones, related to phyllic alteration. Thus, depression of pyrite during flotation could cause gold to report to the tailings. More investigation is required to determine if a second stage of flotation will be required to recover pyrite, and how gold could be subsequently recovered.

Acknowledgements

Special thanks to our colleagues at the Helmholtz Institute Freiberg for discussions, for sample preparation and XRD, MLA and EPMA analyses. R.B. would like to thank Eldorado Gold for the invaluable fieldwork experience and support during the project.

References

- Birtel S, Wunderlich I, Gutzmer J (2013) Tracking ore mineral characteristics from mine to concentrate: the fate of electrum at the Cavanacaw gold deposit, Northern Ireland. 12th SGA Biennial Meeting 2013. Proceedings 1:306–309.
- Cardon O, Reisberg L, André-Mayer A, Leroy J, Milu V, Zimmermann C (2008) Re-Os systematics of pyrite from the Bolcana porphyry copper deposit, Apuseni Mountains, Romania. *Econ Geol* 103(8):1695–1702.
- Crope A, Goodall W, Bradshaw D (2013) The Influence of Textural Variation and Gangue Mineralogy on Recovery of Copper by Flotation from Porphyry Ore – A Review. The Second AusIMM International Geometallurgy Conference 30:279–291.
- Dénes R, Kiss G, Ivăşcanu P (2015) Petrographic and Geochemical Study of the Porphyry and Epithermal Mineralization in the Bolcana Magmatic- Hydrothermal System (Apuseni Mts, Romania). 13th SGA Biennial Meeting Proceedings 1:283–286.
- Eldorado Gold (2018a) Eldorado Gold Provides an Update on 2018 Exploration Programs.
- Eldorado Gold (2018b) Eldorado Gold Releases Updated Reserve and Resource Statement.
- Ivăşcanu P, Kulcsar Z, Dénes R, Baker T, Lewis P (2018) Bolcana Porphyry Au-Cu Deposit, Apuseni Mountains, Romania. AME Roundup 2018: Core Shack Abstract Guide.
- Kesler S, Chryssoulis S, Simon G (2002) Gold in porphyry copper deposits: Its abundance and fate. *Ore Geol Revs*, 21:103–124.
- Milu V, Leroy JL, Piantone P (2003) The Bolcana Cu-Au ore deposits (Metaliferi Mountains, Romania): first data on the alteration and related mineralisation. *CR Geosc* 335:671-680
- Sillitoe R (2010) Porphyry copper systems. *Econ Geol* 105:3–41.

Mineralogical and textural key attributes for the geometallurgical evaluation of alkaline rare metal granites

Lars H. Gronen, Sven Sindern, G. Regina F. Holtmann, André Hellmann, F. Michael Meyer
Institute of Applied Mineralogy and Economic Geology, RWTH-Aachen University, Germany

Janet L. Katzmarzyk, Hermann Wotruba
Unit of Mineral Processing, RWTH-Aachen University, Germany

F. Michael Meyer
German-Mongolian Institute of Resource Technology, Ulaanbaatar, Mongolia

Abstract. Alkaline granites can host notable reserves of rare metals (Zr, Y, Nb, REE). Mineralisation is commonly observed to be caused by post-magmatic alteration leading to fine and intricate intergrowth of ore minerals and associated gangue. Consequently, liberation of ore minerals requires intensive comminution, which is one aspect hampering the economic use of this deposit type. However, this study (part of r⁴-OptiWiM, Optimization of the value chain for polymineralic ores of economic strategic metals) shows that post-magmatic mineralisation also leads to textural heterogeneity, which is recognised to be the basis for improved mineral processing. Pseudomorph-like aggregates of ore minerals, often formed in a replacement reaction with precursor mafic magmatic minerals, permit efficient pre-concentration at coarser particle size fraction, requiring less energy consuming comminution. Process efficiency can be further enhanced due to presence of hematite associated with clustered ore minerals, which allows efficient magnetic separation. Thus, in addition to grade and a spectrum of ore minerals, other mineralogical and textural parameters are identified as significant for the economic exploitation. A geometallurgical approach links primary ore attributes to metallurgical processing and mine economics. It allows for definition of spatial deposit domains for improved mineral exploitation and prediction of mineral processing performance in the subsequent beneficiation chain.

1 Introduction

A geometallurgical evaluation of a mining operation considers all geological and mineralogical parameters of a deposit that are relevant for optimization of the entire process chain comprising mining, mineral processing, metallurgical procedures as well as final rehabilitation of mine sites (Dominy et al. 2018, Gutzmer 2014, Lund and Lamberg 2014). In addition to optimization of metal recovery other targets, such as waste reduction and minimisation of water-, chemicals- and energy consumption must be taken into account in order to achieve both, the most economic and the most environmental-friendly mining operation, respectively. Therefore, modern geometallurgy is based on integration of a multidisciplinary data set. In practice, integrating sound geological, mineralogical as well as processing or

metallurgical information is a crucial step and always a starting point to assess response of the ore to processing (e.g. Dominy et al. 2018).

Geometallurgy is particularly important for rare metal deposits and prospects in alkaline granites, many of which are not successfully exploited despite of numerous exploration attempts in the last years. Enrichment of rare metals (Zr, Y, Nb, Ta) and REE to enhanced grades in alkaline intrusions is the result of multi-stage and partially superimposing magmatic to hydrothermal processes leading to a remarkable spatial variability and heterogeneity in terms of mineral composition, grain size, mineral association, and texture (Gysi et al. 2016, Salvi and Williams-Jones 2005, Richardson and Birkett 1996). As a consequence of small grain sizes and intricate intergrowth, liberation sizes of ore minerals can be small. Mining operators have to apply intensive and energy-consuming grinding, as well as processing of fine fractions, to produce marketable concentrates with acceptable recoveries. In addition to causing high energy costs, the processing of fine fractions of polymineralic ores, comprising phases with different physical properties (e.g. density, magnetic susceptibility), is likely to be inefficient. Such impediments for efficient, economic and sustained mining are obstacles to the development of prospects associated with alkaline granites.

The importance of geometallurgy is demonstrated for alkaline Zr-REE-Y-Nb deposits (e.g. Khalzan Buregtei, Mongolia), in which liberation sizes for dominant ore minerals (zircon, Zr-silicates, REE-carbonates, pyrochlore) are mainly < 100 µm and can be as low as 10 µm (Katzmarzyk et al. 2018, Satur et al. 2014, Yang et al. 2015). Such properties primarily leave flotation as only suitable processing technique following energy and material consuming comminution. While flotation turns out to be effective for REE-carbonates, it cannot concentrate ore minerals with distinctly different physical properties, such as zircon and pyrochlore in the same step (Yang et al. 2015). Owing to the prices for Zr, Nb as well as for the HREE the latter ore minerals, which remain in the flotation tailings together with a large mass of gangue minerals, would represent a higher commodity value than the LREE predominantly recovered from carbonates. High process costs on one hand, and limited concentration efficiency on the other hand, would represent an obstacle to mining alkaline granite-hosted

ore bodies.

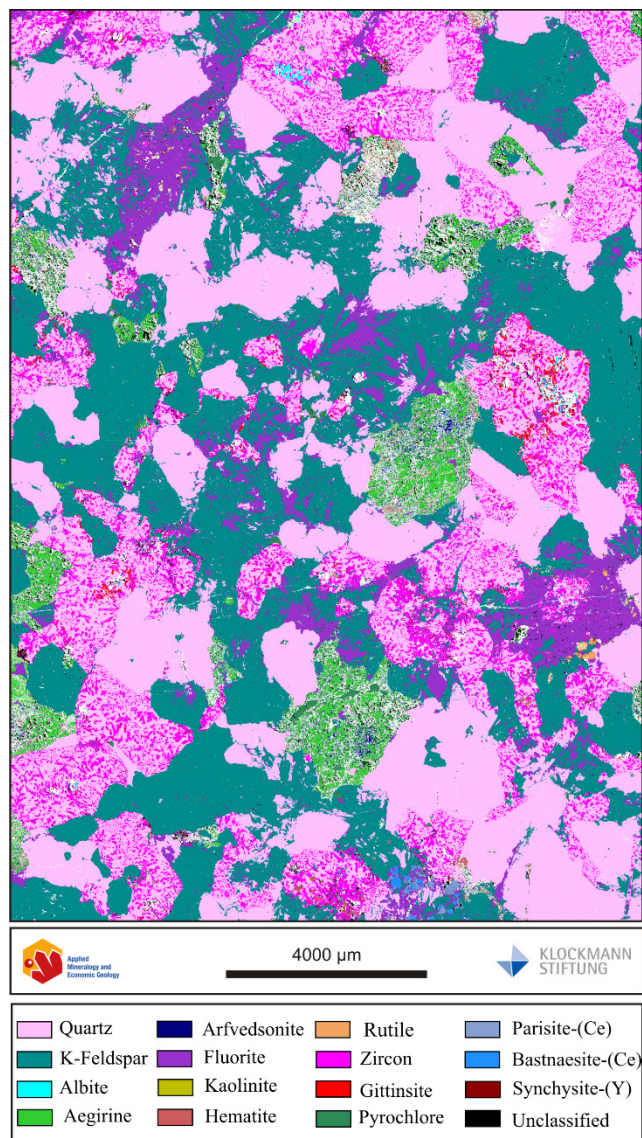


Figure 1. QEMSCAN® phase map showing zircon-quartz clusters associated with fluorite in alkaline granite.

2 The OptiWiM project

This contribution describes results from the OptiWiM project (Optimization of the value chain for polyminerale ores of economic strategic metals), funded within the r⁴ r&d programme “Raw materials of strategic economic importance for high-tech made in Germany” (Federal Ministry of Education and Research, Germany) which focusses on new approaches to improve the efficiency of rare metal mining in alkaline granites using the Khalzan Buregtei massif as a case study (www.fona.de).

The geology of this massif and the mineralogical and geochemical characteristics are described in detail by Kovalenko et al. (1995, 2009) and Kempe et al. (1999, 2015). According to Kempe et al. (2015), the major orebody contains 2.4×10^6 t ZrO₂, 3.5×10^5 t Nb₂O₅ and 4.9×10^5 t REE₂O₃ + 1.3×10^5 t Y₂O₃. In line with these previous studies, the ores analysed in this investigation

show average grades of 1.10 wt.% Zr, 0.14 wt.% Nb, 0.16 wt.% LREE (La-Eu), 0.06 wt.% HREE (Gd-Lu) and 0.09 wt.% Y (Katzmarzyk et al. 2018, Gronen et al. 2019). Mineralogical, geochemical and petrographic investigations were conducted on 100 samples taken from inspection lines cross cutting the outcropping part of the deposit.

Quartz, K-feldspar and albite are the dominant rock forming minerals and account in total for more than 70 vol.-% in all mineralized samples studied in this project. The mafic minerals arfvedsonite and aegirine are less abundant (< 5 vol. %) and can be observed only locally. All samples show variable proportions of HFSE ore minerals, such as Zr silicates, REE carbonates, pyrochlore, as well as of hematite, rutile, titanite, or fluorite.

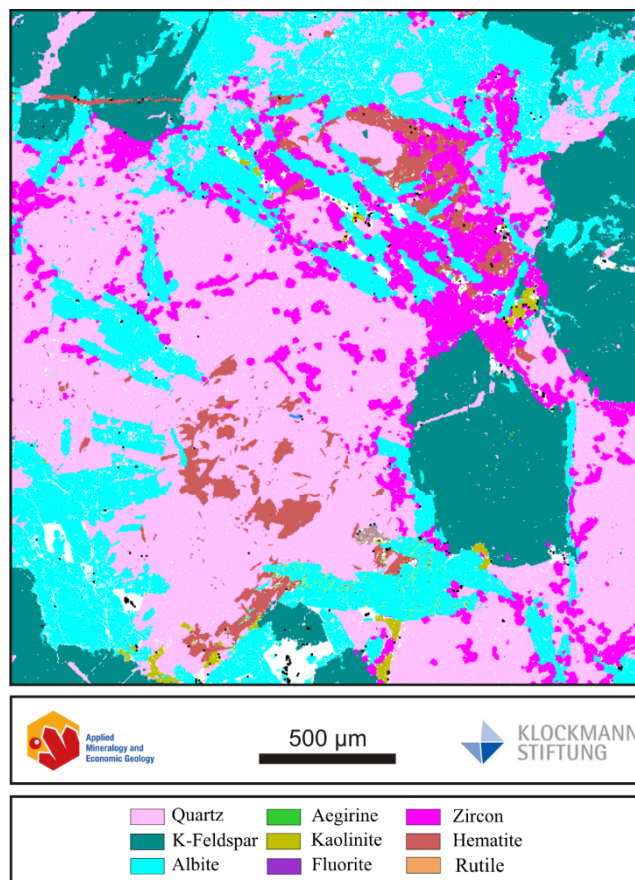


Figure 2. QEMSCAN® phase map, detailed view of zircon-quartz-hematite clusters.

Petrographic inspection revealed that, except for the major Nb carrier pyrochlore, all ore minerals of Zr and REE (zircon, Zr-silicates, REE-carbonates) can occur in pseudomorph-like association mainly replacing precursor magmatic arfvedsonite (Fig. 1). This leads to a concentration of ore minerals in clusters characterized by liberation sizes (approx. 250 µm) significantly exceeding those of individual ore minerals (45 – 100 µm). Furthermore, optical microscope and QEMSCAN® image analysis indicated that hematite is a characteristic constituent of clustered ore mineral aggregates (Fig. 2).

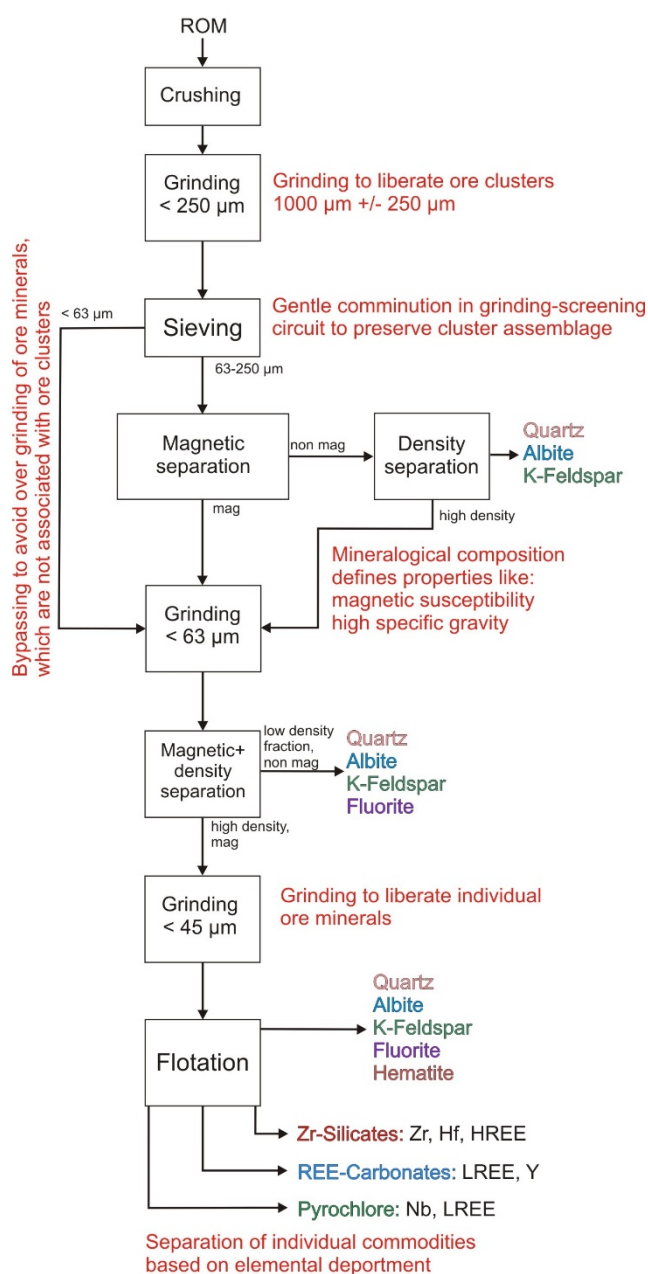


Figure 3. Beneficiation process for rare metal ores in alkaline granites characterized by clustered occurrence of ore minerals.

These textural properties allow pre-concentration of ore mineral clusters by magnetic separation which follows less energy consuming comminution to larger particle sizes of $< 250 \mu\text{m}$. Further comminution of the pre-concentrate and processing steps to concentrate zircon, Zr-silicates, as well as REE-carbonates, then only have to be applied to a significantly reduced fraction of the initial mass of the ore. This also implies a notable reduction of energy consumption, which was quantified by Katzmarzyk et al. (2018). Mineral processing test work conducted on a representative high volume ore sample of app. 1.5 t mass taken from the mineralized center of the deposit showed that 7 kWh/t can be saved due to comminution of a pre-concentrate. The reduced mass

flow further allows potential savings regarding decreased need and consumption of processing machinery, water supply and flotation chemicals for the further treatment of the pre-concentrate.

Sufficient size reduction by comminution is not only a prerequisite for mineral separation but it is also the step within mineral processing that has the highest energy demand. An improved beneficiation scheme for mineralised alkaline granites is depicted in Fig. 3.

Clustered occurrence of mafic minerals or Zr-silicates formed in a replacement reaction with magmatic or post-magmatic precursor minerals is also discovered in other alkaline granites (e.g. Strange Lake, Salvi and Williams-Jones 2005, Amis Complex, Brandberg, Schmitt et al. 2002). Taking into account that such mineral cluster formation, as well as the associations of ore minerals with hematite, is observed in other rare metal deposits formed in alkaline granitoids the approaches developed for Khalzan Buregtei are considered to be of general importance as steps towards more efficient and sustainable extraction of rare metal ores from alkaline granite deposits.

3 Implications for geometallurgical concepts

The mineralogical investigation in combination with processing test work performed in the OptiWiM project shows that evaluation of mineralogical and textural properties of mineralized alkaline granites are crucial for efficient beneficiation and optimized recovery.

Allowing efficient pre-concentration, the presence of ore mineral clusters and association of these minerals with hematite have a strong impact on energy and material consumption. This must be taken into account in an evaluation of design and costs of processing equipment. Furthermore, cluster size and ore mineral spectrum within clusters have an impact on initial grinding as well as on final beneficiation steps (Fig. 3).

In addition to grade and spectrum of ore minerals, other mineralogical and textural parameters are identified as significant for the evaluation of the rare metal ores as raw material for a process chain. This allows development of a new evaluation scheme applicable for the rating of ores observed in the Khalzan Buregtei alkaline granite deposit. Such evaluation and identification of the relevant mineralogical and textural attributes also represents the basis for definition of spatial deposit domains in a predictive geometallurgical model for improved mineral processing.

Acknowledgements

The OptiWiM project is funded by the German Ministry of Education and Research (BMBF, OptiWiM FKZ 033R162B). The support of R. Klinghardt (IML Klockmann Laboratory for Geometallurgy) to enable electron microprobe and QEMSCAN© analyses is gratefully acknowledged. Attendance of the SGA 2019 conference by LG was funded by the Klockmann Foundation (Aachen).

References

- Dominy SC, O'Connor L, Parbhakar-Fox A, Glass HJ, Purevgerel S (2018) Geometallurgy – A route to more resilient mine operations. *Minerals* 8, 560; doi:10.3390/min8120560
- Gronen LH, Sindern S, Katzmarzyk JL, Bormann U, Hellmann A, Wotruba H, Meyer FM (2019) Mineralogical and chemical characterization of Zr-REE-Nb ores from Khalzan Buregtei (Mongolia) - Approaches to more efficient extraction of rare metals from alkaline granitoids. *Minerals* 9 (4):217
- Gutzmer J (2014) Geometallurgy – Why metallurgists should communicate with geoscientists. *World of Metallurgy – Erzmetall* 67:54 – 58 (in German, English abstract)
- Gysi AP, Williams-Jones AE, Collins P (2016) Lithogeochemical vectors for hydrothermal processes in the Strange Lake peralkaline granitic REE-Zr-Nb deposit. *Economic Geology* 111:1241 – 1276. Katzmarzyk J, Gronen J, Wotruba H, Sindern S, Hellmann A, Meyer FM (2018) Geometallurgical investigation of the processing of REE-Y-Nb-Zr complex ore. IMPC International Mineral Processing Congress, September 15th – 21st 2018, Moscow, Russia, Abstract No. 2009-66
- Kempe U, Götze J, Dandar S, Habermann D (1999) Magmatic and metasomatic processes during formation of the Nb-Zr-REE deposits Khalzan Buregte and Tsakhir (Mongolian Altai): Indications from a combined CL-SEM study. *Mineralogical Magazine* 63:165 - 177
- Kempe U, Möckel R, Graupner T, Kynicky J, Dombon E (2015) The genesis of Zr-Nb-REE mineralization at Khalzan Buregte (Western Mongolia) reconsidered. *Ore Geology Reviews* 64:602 - 625
- Kovalenko VI, Kozlovsky AM, Yarmolyuk VV (2009) Trace element ratios as indicators of source mixing and magma differentiation of alkali granitoids and basites of the Haldzan-Buregtei massif and the Haldzan-Buregtei rare-metal deposit, Western Mongolia. *Petrology* 17:158 - 177
- Kovalenko VI, Tsaryeva GM, Goreglyad AV, Yarmolyuk VV, Troitsky VA, Hervig RL, Farmer GL (1995) The peralkaline granite-related Khalzan-Buregtei rare-metal (Zr, Nb, REE) deposit, Western Mongolia. *Economic Geology* 90, 530 -574
- Lund C, Lamberg P (2014) Geometallurgy – A tool for better resource efficiency. *European Geologist* 37:39 – 43.
- Richardson DG, Birkett TC (1996) Peralkaline rock-associated rare metals. In: Eckstrand OR, Sinclair WD, Thorpe RI (eds.) *Geology of Canadian Mineral Deposit Types*. Geological Survey of Canada, *Geology of Canada* 8:523 - 540
- Salvi S, Williams-Jones AE (2005) Alkaline granite-syenite deposits. In: Linnen RE, Samson IM (eds.) *Rare-element geochemistry and mineral deposits*. Short course notes 17, Geological Association of Canada, 315 - 341
- Satur J, Sanematsu K, Calabia B, Morita S, Kon Y, Takagi T, Yang XS, Naumanen A (2014) Recovery of REE-bearing minerals from a granite ore by dry magnetic separation and WHIMS-settling methods. IMPC 2014 XXVII International Mineral Processing Congress, Santiago, Chile, *Proceedings* 31 – 41
- Schmitt AK, Trumbull RB, Dulski P, Emmermann R (2002) Zr-Nb-REE mineralization in peralkaline granites from the Amis Complex, Brandberg (Namibia): Evidence for magmatic pre-enrichment from melt-inclusions. *Economic Geology* 97:399 - 413
- Yang X, Satur JV, Sanematsu K, Laukkanen J, Saastamoinen T (2015) Beneficiation studies of a complex REE ore. *Minerals Engineering* 71:55 – 64

Sulfide chemistry and trace element department at the metamorphosed Lappberget Zn-Pb-Ag-(Cu-Au) ore body, Sweden: Implications for Mineral Processing

Glaciale Tiu, Nils Jansson, Christina Wanhainen

Division of Geosciences and Environmental Engineering, Luleå University of Technology, Sweden

Yousef Ghorbani

Division of Minerals and Metals Engineering, Luleå University of Technology, Sweden

Abstract. The 58 Mt Lappberget Zn-Pb-Ag-(Cu-Au) ore body represents one of the largest and most significant polymetallic base metal sulfide deposits in Sweden. The complex mineralogical characteristics of the ore body pose particularly tough challenges for successful production forecast because of the mixed Zn-Pb-Cu base metals, the complex association of the beneficial Ag and Au, and the presence of influential elements such as Sb, Mn and Mg. Thus, a detailed mineralogical characterization study was conducted, focusing on the department of trace and minor elements (including credit and penalty elements). Mineral chemistry data derived from electron microprobe and laser ablation inductively coupled plasma mass spectrometry (LA-ICP-MS) analyses reveal the complexity in the composition and associations of the ore minerals, consisting of textural and chemical varieties of sphalerite, galena, chalcopyrite, iron sulfides, antimonides and sulfosalts. Recrystallization, re-mobilization and re-concentration of sulfide minerals, compositional banding, and ductile and brittle deformation textures (i.e. deformation twins on sphalerite, brecciation, bent cleavage planes, etc.) are observed throughout the deposit. The mineralogical and textural complexity and heterogeneity of the sulfide ore are reflected in the variability in grades and recovery from the processing plant.

1 Introduction

Located approximately 180 km northwest of Stockholm, the Lappberget ore body is part of Boliden Mineral AB's Garpenberg mine, Sweden's oldest still-operating mine. Recent research has shown that mining operation started as far back as 375 BCE (Bindler et al. 2017) and it has developed into one of the country's largest base metal mines. The mine targets several sulfide ore bodies distributed along the northwestern limb of the Garpenberg syncline (Figure 1). The ore bodies are commonly located in upright structural domes. Lappberget is the largest ore body in the mine with a combined mineral resource and ore reserve of 58 Mt at 3.42% Zn, 1.68% Pb, 0.06% Cu, 70 g/t Ag and 0.41 g/t Au (Högnäs 2018). It is hosted by intensely altered and metamorphosed felsic volcanic rocks and former limestone that are overlain by less altered metavolcanic rocks. Mineralization formed at c. 1.89 Ga, prior to ductile deformation and metamorphism during the

Svecokarelian orogeny (Jansson and Allen 2011). Allen et al. (1996) suggested that the mineralization was formed as a subsea-floor stratabound replacement-type deposit (SVALS-type), associated with a major caldera-forming volcanic event. The metamorphic grade is estimated at lower amphibolite facies with a peak metamorphic temperature of 550°C at pressures below 3.5 kbar (Vivallo 1985). The metamorphic overprint has made it uncertain whether calc-silicates in the ores formed during metamorphism (cf. metamorphosed VMS) or in conjunction with ore formation as in metasomatic skarn deposits (cf. Jansson and Allen 2011).

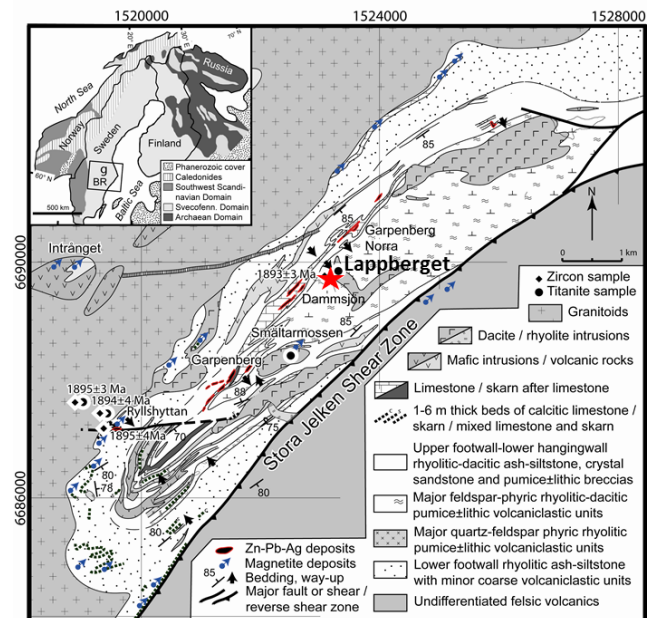


Figure 1. Regional geological map of the Garpenberg area with inset showing the location of the Bergslagen (BR) region where Garpenberg (g) is located (Jansson and Allen 2011b). Ages refer to dated metavolcanic rocks intrusions presented in Jansson and Allen (2011a). Grid is Swedish National Grid RT90.

The ore body is currently being mined and processed to produce four different concentrates: Zn, Pb, Cu and a gravimetric concentrate. The complex mineralogical characteristics of the ore body pose particularly tough challenges for successful production forecast because of the mixed Zn-Pb-Cu base metals, the complex association of the beneficial Ag and Au, and the presence of influential elements such as Sb, Mn and Mg. There are few studies addressing the sulfide ores from Garpenberg,

and the existing accounts mainly focus on other aspects of the deposits (e.g. Allen et al. 1996; Vivallo 1985). Currently, there is no published literature on the metallurgical assessment of the Lappberget ore body. Thus, this study aims to provide a detailed mineralogical characterization of the Lappberget sulfide ore body, focusing on the department of trace and minor elements (including credit and penalty elements). The result will provide constraints in identifying the metallurgical behavior of the ore during flotation, which can help a) improve the grade and recovery of the processing plant and b) determine its possible environmental impact.

2 Methodology

Drill core samples were collected from various sections of the ore body. Petrographic investigations were carried out on thin sections, using optical light microscopy and scanning electron microscopy (SEM). Sputter-coating with carbon was undertaken for all SEM and electron probe microanalyses (EPMA). Mineral chemistry data were derived for twenty-five thin sections on a CAMECA SX100 electron microprobe at the Geological Survey of Finland equipped with five wavelength-dispersion spectrometers (TAP, 2 LLIF, PET and LPET). All the sulfide analyses were determined using an accelerating voltage of 20 kV with a probe current and beam diameter of 40 nA and 1 micrometer, respectively. Natural minerals and metals were used as reference standards.

Quantitative trace element composition of sulfides was derived using a New Wave Research (NWR193) laser-ablation system coupled to an iCAP-Q quadrupole inductively coupled plasma mass spectrometer (LA-ICPMS, Thermo Scientific) at Luleå University of Technology. Spot sizes of 50 µm and 25 µm were used with a laser repetition rate of 5 Hz and a total acquisition time of 85 s (15 s background measurement, 30 s sample ablation and 40 s delay). The following isotope suites were analyzed: ³⁴S, ⁴⁹Ti, ⁵¹V, ⁵³Cr, ⁵⁵Mn, ⁵⁷Fe, ⁵⁹Co, ⁶⁰Ni, ⁶⁵Cu, ⁶⁶Zn, ⁶⁹Ga, ⁷³Ge, ⁷⁵As, ⁷⁷Se, ⁹⁵Mo, ¹⁰⁷Ag, ¹¹¹Cd, ¹¹⁵In, ¹¹⁸Sn, ¹²¹Sb, ¹²⁵Te, ¹⁸²W, ¹⁹³Ir, ¹⁹⁷Au, ²⁰²Hg, ²⁰⁵Tl, ²⁰⁸Pb and ²⁰⁹Bi, with a total sweep time of 0.840 s. ⁶⁶Zn was used as the sphalerite internal standard, ²⁰⁸Pb for galena and ⁵⁷Fe for the other sulfides. Data reduction was done using the IOLITE software package (Paton et al. 2011).

3 Ore mineralogy and texture

The Lappberget ore body contains sphalerite, galena, pyrite, pyrrhotite, chalcopyrite and magnetite as the main sulfide and oxide components. Trace amounts (generally <0.1 wt%) of tetrahedrite-tennantite ((Cu,Fe)₁₂(Sb,As)₄S₁₃), bournonite (PbCuSbS₃), freibergite ((Ag,Cu,Fe)₁₂(Sb,As)₄S₁₃), boulangerite (Pb₅Sb₄S₁₁), jamesonite (Pb₄FeSb₆S₁₄), dyscrasite (Ag₃Sb), gudmundite (FeSbS) and arsenopyrite (FeAsS) are also present. Rarer minerals present are cubanite (CuFe₂S₃), troilite (FeS), native antimony, native silver, allargentum (Ag_{1-x}Sb_x), nisbite (NiSb₂), ilmenite (FeTiO₃), gahnite (ZnAl₂O₄), and native arsenic. Sphalerite, pyrite and galena occur in all massive sulfide ores but in varying

proportions. Magnetite is only abundant in the uppermost and easternmost portion of the ore body (Jansson 2011).

The more plastic sulfide minerals (i.e. galena, chalcopyrite, sphalerite, pyrrhotite) display ductile deformation textures, interstitial overgrowth, annealing with triple junctions, and locally occur as inclusions in garnet and quartz. In contrast, the more rigid sulfide minerals (i.e. pyrite, arsenopyrite, tetrahedrite) exhibit cataclastic textures with gaps filled with plastic sulfide minerals, rounded grains, late euhedral open-space fill, and intergrowth and overgrowth textures (Figure 2). Tetrahedrite generally occurs as myrmekitic exsolutions in galena. Troilite only occurs as an exsolution in pyrrhotite, whereas cubanite is commonly present as exsolution lamellae in chalcopyrite but may also occur as individual grains. Silver minerals (i.e. dyscrasite, allargentum) are typically associated with the presence of tetrahedrite, Ag-rich chalcopyrite, cubanite, and alabandite.

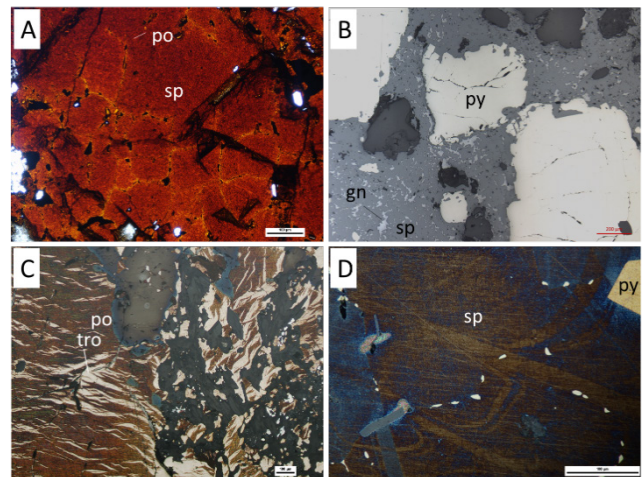


Figure 2. Photomicrographs of different sulfide textures. (A) annealed sphalerite grains showing triple junctions and pyrrhotite inclusions along boundaries (LPB1617-91.02, plain transmitted light), (B) tectonoclastic rotation and rounding of pyrite in sphalerite-galena matrix (LPB1101-246.03, reflected light), (C) coarse flame texture resulting from low temperature exsolution of troilite in pyrrhotite, which has undergone brecciation; sample etched with NaClO (LPB1103-198.32, reflected light), and (D) deformation twins in sphalerite; sample etched with NaClO (LPB3458-178.06, reflected light). Abbreviations: gn–galena, po–pyrrhotite, py–pyrite, sp–sphalerite, and tro – troilite.

3.1 Mineral chemistry of sulfide minerals

Sphalerite is the main Zn mineral in the Lappberget ore body and occurs in massive sulfide lenses, veins and disseminations. It commonly contains pyrrhotite or chalcopyrite inclusions. Results from this study show varying concentration of Zn, Fe and Mn (Figure 3), allowing four sphalerite populations to be identified: 1) Zn-rich (Fe- and Mn-poor), 2) Fe-rich, 3) Mn-rich and 4) Fe- and Mn-bearing. Zn-rich sphalerite contains elevated amounts of Cd, In, Co and Sb but lower Ga and Ge as compared to the other sphalerite populations.

Galena, the main Pb mineral in Lappberget, generally occurs with sphalerite. It exhibits a plastic behavior, typically occurring as an interstitial phase between

sphalerite and, less commonly, pyrrhotite and chalcopyrite. Mineral chemical analyses of galena reveal varying concentration of Ag, Sb and more rarely As in the crystal lattice. Galena may contain 0.01 – 0.24 wt% Sb, 0.01-1 wt% As and 0.10-0.20 wt% Ag. The high Sb and As content coincide with the presence of neighboring gudmundite and arsenopyrite, respectively.

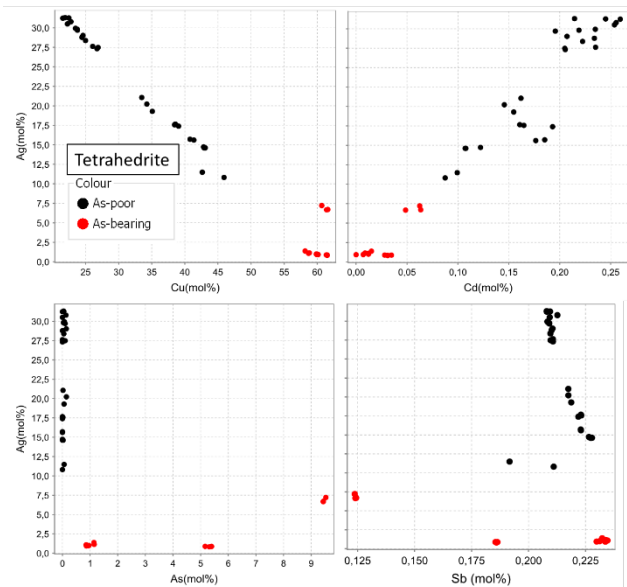
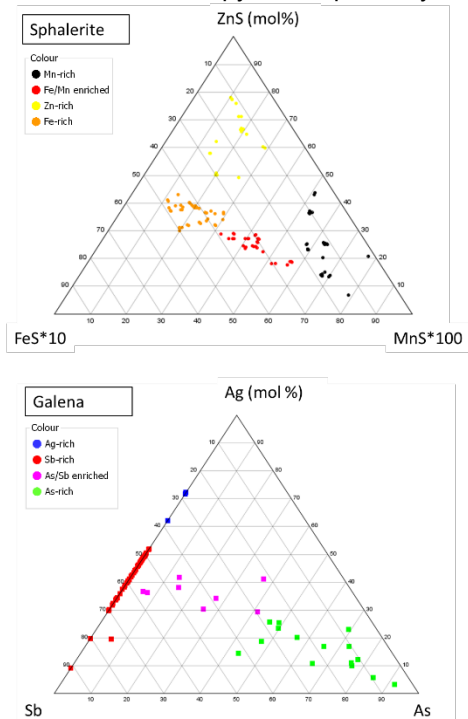


Figure 3. Plotted mineral composition of sphalerite, galena and tetrahedrite based on EPMA data, showing distinct element clusters.

Chalcopyrite is the most abundant Cu mineral in the deposit. It predominately occurs in the lower part of the deposit and is associated with Fe-rich silicates (e.g. biotite). Mineral chemistry of chalcopyrite from EPMA data shows an Ag-rich population of chalcopyrite. However, these results must be interpreted with caution

since petrographic analysis shows the presence of tarnished chalcopyrite grains, which according to LA-ICPMS analysis have a thin Ag_2S coating.

Tetrahedrite is the most abundant Ag-bearing mineral in Lappberget and serves as another Cu source. It typically occurs as exsolutions in galena, forming irregular grains 1-100 μm in size. Mineral composition varies considerably in Ag, Cu, Sb and As content (**Error! Reference source not found.3**). Silver shows a strong positive correlation with Cd and a negative correlation with Cu. The presence of As (>0.5 wt%) in tetrahedrite drastically lowers its silver content. Myrmekitic textures containing the assemblage tetrahedrite (secondary) + chalcopyrite + sphalerite + gudmundite + arsenopyrite + dyscrasite \pm native antimony \pm alabandite are possibly a result from the breakdown of earlier tetrahedrite grains.

Pyrite typically occurs as porphyroblasts in the massive sulfide ore and as disseminations in micaceous and quartzose hydrothermally altered rocks. Grain size varies widely from 100 to 2000 μm and the grains seldom display brittle deformation. LA-ICPMS analysis of pyrite samples shows varying trace element distribution as shown in Figure 4. Generally, inclusion-free pyrite has a low and homogeneous trace element distribution, whereas inclusion-rich pyrite contains elevated Ag, As and Co values.

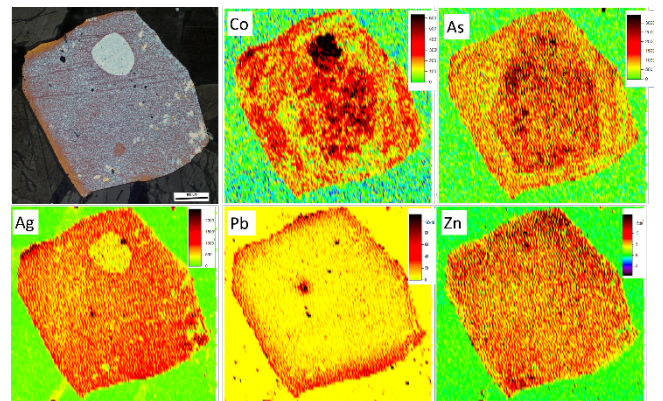


Figure 4 LA-ICPMS trace element mapping of subhedral inclusion-bearing pyrite, which reveals a Co-rich pyrite inclusion (distinguishable in the photomicrograph of the sample etched in NaClO) and an As-rich core (LPB1617-277).

In samples where sphalerite, galena, chalcopyrite, and pyrite co-exist, sphalerite is the primary host for Mn, Cd, Ga and Hg. Bismuth is preferentially concentrated in galena whereas Co, Ni and As is preferentially hosted by pyrite. Silver and Sb is highest in chalcopyrite followed by galena.

4 Implications for mineral processing

This detailed mineralogical characterization of the Lappberget ore body reveals the complexity in the composition and associations of the ore minerals, including various types of textural and chemical varieties of sphalerite, galena, chalcopyrite, iron sulfides, antimonides and sulphosalts. Recrystallization, re-mobilization and re-concentration of sulfide minerals, annealing of crystals, compositional banding, and ductile

and brittle deformation textures (i.e. sphalerite deformation twins on sphalerite, cataclasis, bent cleavage planes, etc.) are observed throughout the deposit.

The genetic classification of the Lappberget deposit is still unclear since primary textures are highly masked by subsequent metamorphism and deformation. This investigation shows that the formation and modification of the Lappberget sulfide ores occurred at varying physiochemical conditions, giving rise to the heterogeneity of the sulfide minerals. By inference, the resulting sulfide ore varieties are expected to behave differently during flotation. For instance, it is known that varying iron content in sphalerite can have different flotation kinetics (Boulton et al. 2005; Harmer et al. 2008). High Mn and Co content in sphalerite and high Bi and Sb content in galena are deleterious in the pyrometallurgical process (Sinclair 2009, 2005). During the smelting process, high levels of Zn in the copper concentrate and of Cu in the lead concentrate significantly reduce the recovery of copper and lead, respectively (Fountain 2013).

Antimony and As-bearing sulfosalts (e.g., tetrahedrite-tennantite, jamesonite, bournonite, boulangerite) are economically unattractive since Sb and As are highly volatile elements during thermal processes and require additional treatment to prevent hazardous emissions during smelting (Lane et al. 2016). Similarly, the presence of As-bearing minerals, such as arsenopyrite and native arsenic, which reports to the tailings, could pose environmental problems, if not properly managed. On the other hand, high Ag in tetrahedrite, galena and chalcopyrite are economically desirable as long as its effect on the beneficiation route is properly understood.

5 Conclusion

A detailed mineralogical and textural study of the Lappberget ore body highlights the complexity of the sulfide associations in the ore body reflecting a complex geological chain from the initial mineral formation to subsequent recrystallization, remobilization and deformation. The heterogeneity in composition and grain size of the ore minerals can significantly affect flotation performance. For complex ore bodies such as Lappberget, deleterious elements (e.g. As, Sb, Cd, Mn and Hg) should be included in the routine chemical analysis of drill cores to help identify local concentrations.

Acknowledgements

This study was financed by the European Union's Horizon 2020 research and innovation program under grant agreement No. 72267, as part of the MetallIntelligence network (www.metalintelligence.eu). The authors would like to acknowledge Boliden Mineral AB for allowing access to drill cores and assay data. Boliden Special thanks are given to Garpenberg geologists, especially to Lena Lilja, for providing valuable insights about the deposit geology and for their warm hospitality. Stefan Andersson, Magnus Olsson and Björn

Pederson (Boliden Garpenberg) are highly appreciated for their assistance during the logging and sampling campaign, as well as for their camaraderie and humor. Lassi Pakkanen (GTK Finland) and Riia Chmielowski (Luleå University of Technology) are thanked for the guidance in performing the EPMA and LA-ICPMS analysis, respectively.

References

- Allen R, Lundström I, Ripa M, Simeonov A, Christofferson H (1996) Facies analysis of a 1.9 Ga, continental margin, back-arc, felsic caldera province with diverse Zn-Pb-Ag-(Cu-Au) sulfide and Fe oxide deposits, Bergslagen Region, Sweden. *Economic Geology* 91: 979–1006. [doi:10.2113/gsecongeo.91.6.979](https://doi.org/10.2113/gsecongeo.91.6.979)
- Bindler R, Karlsson J, Rydberg J, Karlsson B, Berg Nilsson L, Biester H, Segerström U (2017) Copper-ore mining in Sweden since the pre-Roman Iron Age: lake-sediment evidence of human activities at the Garpenberg ore field since 375 BCE. *J. Archaeol. Sci. Reports* 12: 99–108. [doi:10.1016/j.jasrep.2017.01.019](https://doi.org/10.1016/j.jasrep.2017.01.019)
- Bolin NJ, Brodin P, Lampinen P (2003) Garpenberg-an old concentrator at peak performance. *Minerals Engineering*, 16: 1225–1229. [doi:10.1016/S0892-6875\(03\)00180-8](https://doi.org/10.1016/S0892-6875(03)00180-8)
- Boulton A, Fornasiero D, Ralston J (2005) Effect of iron content in sphalerite on flotation. *Minerals Engineering* 18: 1120–1122. [doi:10.1016/j.mineng.2005.03.008](https://doi.org/10.1016/j.mineng.2005.03.008)
- Du Rietz T (1968) Huvuddragen av Garpenbergstraktens bergbyggnad. *Sveriges Geologiska Underökning (C631)*: 22.
- Fountain C (2013) The whys and wherefores of penalty elements in copper concentrates. In *MetPlant 2013: Metallurgical Plant Design and Operating Strategies*, pp 502–518
- Jansson N (2011) The Origin of Iron Ores in Bergslagen, Sweden, and their Relationships with Polymetallic Sulphide Ores. Dissertation, Luleå University of Technology
- Jansson N, Allen R (2011) Timing of volcanism, hydrothermal alteration and ore formation at Garpenberg, Bergslagen, Sweden. *GFF* 133: 3–18. [doi:10.1080/11035897.2010.547597](https://doi.org/10.1080/11035897.2010.547597)
- Jansson N, Allen R (2011b) SIMS U-Pb Zircon Age Constraints on the Ages of Syn-volcanic Iron Oxide and Zn-Pb-Cu-(Ag-Au) Sulphide deposits, Garpenberg, Bergslagen, Sweden. In *SGA 2013: 12th SGA Biennial Meeting*
- Högnas J (2018) Boliden Summary Report, Resources and Reserves 2018, Garpenberg., Unpublished internal report for Boliden Mineral AB.
- Harmer SL, Mierczynska-Vasilev A, Beattie DA, Shapter JG (2008) The effect of bulk iron concentration and heterogeneities on the copper activation of sphalerite. *Minerals Engineering* 21: 1005–1012. [doi:10.1016/j.mineng.2008.02.014](https://doi.org/10.1016/j.mineng.2008.02.014)
- Lane DJ, Cook NJ, Grano, SR, Ehrig K (2016) Selective leaching of penalty elements from copper concentrates: A review. *Minerals Engineering* 98: 110–121. [doi:10.1016/j.mineng.2016.08.006](https://doi.org/10.1016/j.mineng.2016.08.006)
- Paton C, Hellstrom JC, Paul B (2011) Iolite: Freeware for the Visualisation and Processing of Mass Spectrometric Data. *Journal of Analytical Atomic Spectrometry* 26: 2508–2518. [doi:10.1039/C1JA10172B](https://doi.org/10.1039/C1JA10172B)
- Sinclair RJ (2005) *The Extractive Metallurgy of Zinc*. Carlton Victoria, Melbourne
- Sinclair RJ (2009) *The Extractive Metallurgy of Lead*. Carlton Victoria, Melbourne
- Vivallo W (1985) The geology and genesis of the Proterozoic massive sulfide deposit at Garpenberg, central Sweden. *Economic Geology* 80:17–32. [doi:10.2113/gsecongeo.80.1.1](https://doi.org/10.2113/gsecongeo.80.1.1)

The use of geometallurgy in the processing of a complex copper-gold ore deposit

R. Aliyev, F. Hedjazi, S.J. Westhead and A.J. Monhemius
Anglo Asian Mining plc, Baku, Azerbaijan

Abstract. The copper-gold ore deposit at Gedabek in western Azerbaijan is described, together with the various processes that are used to extract the gold, silver and copper from these ores. The processes include heap leaching, agitation leaching and flotation. Geometallurgy is used to classify the various types of ore found in this complex ore body and to determine the optimum processing route for each ore type. Examples of the ore classification system are given.

1 Introduction

The Gedabek Au-Cu-Ag deposit is located in the Gedabek Ore District in the Lesser Caucasus mountain range in north-western Azerbaijan. The Contract Area in which the Gedabek mine is situated is approximately 300 km² in size and is one of six Contract Areas held by the London-listed junior mining company, Anglo Asian Mining plc (“AAM”), under a Production Sharing Agreement with the Government of Azerbaijan (Figure 1). The AAM Contract Areas are located on the Tethyan Tectonic Belt, one of the world’s significant Cu/Au-bearing metallogenic belts.

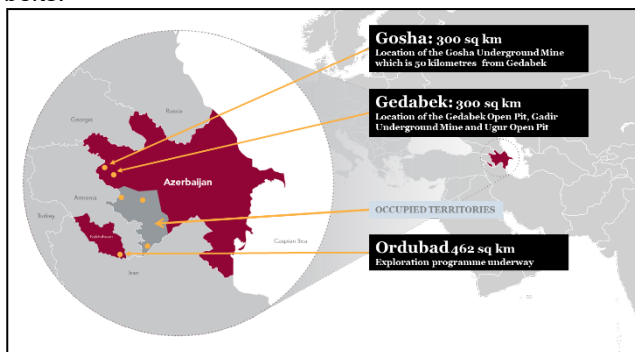


Figure 1. Map of Azerbaijan with locations of AAM Contract Areas

Exploitation of the ore at Gedabek has occurred intermittently since the Bronze Age. Old workings, adits and even pre-historic burial grounds can be identified in the region to this day. More recent mining activity began around 1849 when the Greek Mekhor Brothers, followed by the German Siemens Brothers Company in 1864, developed and operated the Gedabek Cu mine under an arrangement with Czarist Russian authorities. At least five large (>100,000t) and numerous smaller sulphide lenses were mined from 1849-1917, with exploitation ceasing at the onset of the Russian revolution.

During the 1990s, exploration work increased significantly at Gedabek, alongside attempts to reconcile then-current observations with historic production data. New adits were driven by Azergyzil (an Azeri government

mineral resources agency) in 1995 and trenching and dump sampling was conducted.

After signing the Production Sharing Agreements, AAM decided to twin four diamond holes (originally drilled during the Azergyzil campaign) in order to ascertain the validity of previous drilling and assays. This proved positive; so too were results from grab and core samples taken during due diligence, with the result that, in 2009, AAM developed the Gedabek deposit into an open pit mine, marking the company as the first Au/Cu producer in Azerbaijan in modern times. The satellite mines of Ugur (open pit) and Gadir (underground) have since also been developed by AAM within the Gedabek Contract Area and all three mines are operated by the Azerbaijan International Mining Company (“AIMC”), a wholly-owned subsidiary of AAM.

2 Geology of the deposit

The Gedabek ore deposit is located within the large Gedabek-Garadag volcanic-plutonic system. This system is characterised by a complex internal structure indicative of repeated tectonic movement and multi-cyclic magmatic activity, leading to various stages of mineralisation emplacement. The Gedabek ore deposit is located at the contact between Bajocian (Mid-Jurassic) volcanic rocks and a later-stage Kimmeridgian intrusion (Late Jurassic). The mineralisation is dominantly hosted in the local rhyolitic porphyry (known onsite as the ‘quartz porphyry’ unit), bounded by the volcanics (mainly andesites) in the west and a diorite intrusion to the east. The principal hydrothermal alteration styles found at Gedabek are propylitic alteration (encompassing the orebody) with quartz ± adularia ± pyrite alteration (forming the deposit) and argillic alteration (confined to the centre of the orebody).

Ore mineralisation is spatially associated with the quartz porphyry. Disseminated pyrite occurs pervasively through most of the deposit, with high concentrations of fine-grained pyrite found at its heart. Increased Au grades occur in the shallowest levels of Gedabek, predominantly in an oxidised zone in contact with the overlying waste andesites. A central brecciated zone continues at depth, as has been proven through exploratory drilling campaigns. Additionally, faulting running through the middle of the deposit has been shown to control the hydrothermal metasomatic alteration and associated Au mineralisation (causing the argillic alteration mentioned above).

The deposit geology was originally considered to be a “porphyry” style, whereas the current interpretation is that the deposit is HS-epithermal in nature. Mining of the

deposit since 2009 has provided a vast amount of data about the nature of the mineralisation and its structural control.

3 Ore processing at Gedabek

When the Gedabek mine started up in 2009, the ore, which initially was mainly oxidic in nature, was treated by cyanide heap leaching to produce pregnant leach liquor, from which gold was extracted by fixed-bed resin ion exchange. Resin ion exchange was used at Gedabek, instead of conventional activated carbon, because of the elevated copper concentrations in the leach liquors from the heaps, which typically contained about 1000 ppm Cu. In spite of the high Cu/Au ratios in the Gedabek leach liquors, which usually ranged from 500 to 1000, the excellent selectivity of the Minix resin used in the process was such that the Cu/Au ratio on the loaded resin was about one. In order to prevent copper from building up in the recirculating leach liquors, a SART plant (Sulphidisation-Acidification-Recycling-Thickening) was incorporated in the circuit to remove copper from solution as a copper-silver sulphide concentrate. A description of the operations at Gedabek in the early years of the mine, prior to the introduction of the agitation leach plant, was given in a paper by Hedjazi & Monhemius (2014).

As mining progressed, the ore became less oxidised and harder in texture, with the result that gold recoveries in the heaps started to decrease. In 2012, it was decided that agitation leaching should be introduced to operate in parallel with heap leaching, with high grade ore (>1.5 g/t Au) going to agitation leaching and low grade ore (<1.5 g/t Au) going to heap leaching. Accordingly, a 100 t/h stand-alone agitation leach plant, including resin-in-pulp solution processing, was designed, built, and commissioned by July 2013. The way in which the agitation leach plant was integrated into the original heap leach operation is illustrated by the flowsheet shown in Figure 2.

Following the introduction of the agitation leach plant, soluble copper became a much more important issue at Gedabek. Grinding the ore to minus 75 µm for agitation leaching, instead of crushing it to minus 25 mm for heap leaching, exposed much more of the copper minerals to direct contact with the cyanide leach solutions, which increased the rate and extent of dissolution of copper. Furthermore, as the mine went deeper, the copper grades of the ore tended to increase. The result of these factors was that the consumption of cyanide and hence the overall operating costs for producing gold became unacceptably high, so that steps had to be taken to modify the process to bring down the costs. To do this, a little-used technique that had been invented at the beginning of the 20th century, in the early years of cyanide leaching, was adopted. The technique involved the addition of ammonia into the cyanide leaching system to suppress the dissolution of copper, without adversely affecting the extraction of gold. A full description of the agitation leach plant at Gedabek, together with a discussion of the effects of adding ammonia into the cyanide leach, was published in 2018 (Hedjazi &

Monhemius, 2018).

After about one year of operation, ammonia additions at Gedabek were discontinued because the amount of soluble copper in the leach solutions had decreased naturally, due to changes in the ore mineralogy, which comprised more chalcopyrite and less cyanide-soluble secondary copper sulphide minerals.

The next development at Gedabek was the introduction in 2015 of a flotation plant to treat the tailings from the agitation leach plant to recover the copper sulphide minerals into a copper concentrate, together with some of the undissolved gold in the tailings. This additional process step increased the overall recoveries of both copper and gold. The plant was run in this configuration until the end of 2016 when, for operational reasons, it was decided to treat the stockpile of sulphide-rich ore that had been accumulated over several years. This change of feedstock necessitated a reconfiguration of the plant so that ore was first treated by flotation to produce a copper-gold flotation concentrate and then the flotation tailings were processed through the agitation leach plant to recover the gold remaining in the tailings by cyanide leaching. A paper comparing the performances of the plant in these two configurations was published in 2017 (Monhemius, Hedjazi & Saeedi, 2017).

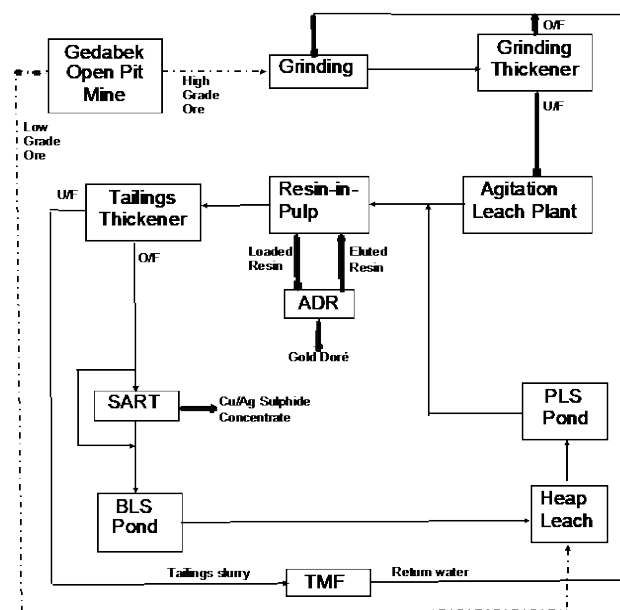


Figure 2. Flowsheet of the Heap Leaching and Agitation Leaching Circuits at Gedabek. (For key to acronyms, see Glossary)

In 2018, a second crushing and grinding circuit was installed, which enabled raw ore to be fed directly to the flotation plant, thus making flotation independent of the agitation leaching plant. The current set-up of the leaching operations at Gedabek closely resembles the pre-2015 configuration shown in Figure 2, but with the addition of an independent flotation plant operating in parallel. Furthermore, heap leaching has also undergone modification over the years. As well as using crushed ore (-25mm) as feed to the heaps, low-grade, run-of-mine (ROM) ore is also leached on separate heaps, without

any prior size reduction.

Thus in the current processing set-up at Gedabek, ore coming from the mine(s) has to be directed to one of five possible destinations, namely: (i) agitation leaching (AGL); (ii) flotation (FLT); (iii) crushed ore heap leaching (HLC); (iv) run-of-mine heap leaching (HLROM); or (v) stockpile (SPF). These various process routes result in three marketable products: (i) gold doré; (ii) copper flotation concentrate with significant gold credits; and (iii) precipitated copper sulphide with silver credits from the SART plant. The metal recoveries achieved in these processes are shown in the following table:

Processes	Recovery %		
	Au	Cu	Ag
AGL	75%	30%	66%
HLC	60%	30%	7%
HLROM	40%	20%	7%
FLT	60%	83%	68%
SPF	60%	83%	68%

The decision on which of these processing routes is optimal for any particular batch of ore is based on geometallurgical factors, such as gold grade, copper grade, cyanide leaching amenability and consumption, and ore mineralogy.

4 The use of geometallurgy

A geometallurgical system has been created to classify Gedabek ores, based on geology, oxidation state and laboratory assay results. The first stage in the classification process involves logging the lithology and oxidation state of the material at the drill site. The dominant ore-bearing lithologies are 'quartz porphyry', 'andesite', 'gossan', 'fault' and 'dyke' and oxidation state is classified as either 'oxide', or 'sulphide'. After assaying, samples are assigned their assay result in the database; the attributing lithology and oxidation state are also allocated. Critical grade ranges of gold and copper have been established, and the data are separated into these as in the table below:

Au range		
Au	↓	0.3 - 1 g/t
Au	○	1 - 3 g/t
Au	↑	3 - 999 g/t
Cu range		
Cu	↓	0 - 0.5 %
Cu	○	0.5 - 1 %
Cu	↑	1 - 10 %

The ore material is then assigned a 'criteria code', as shown in the example in the following table:

<i>lithology</i>	<i>mineral_zone</i>	<i>AU range</i>	<i>CU range</i>	<i>criteria_code</i>
Quartz Porphyry	Oxide	↑	↓	QO1
Quartz Porphyry	Oxide	↑	○	QO2
Quartz Porphyry	Oxide	↑	↑	QO3
Quartz Porphyry	Oxide	○	↓	QO4
Quartz Porphyry	Oxide	○	○	QO5
Quartz Porphyry	Oxide	○	↑	QO6
Quartz Porphyry	Oxide	↓	↓	QO7
Quartz Porphyry	Oxide	↓	○	QO8
Quartz Porphyry	Oxide	↓	↑	QO9

The code is set-up in the format of 'Lithology/Mineral Zone/Au&Cu Range' and this coding can be applied to the whole dataset; hence:-

Lithology	Oxidation	Au range	Cu range	
Quartz Porphyry	Q Oxide	○	↓ 0 - 0.5 %	1
AHQ-Contact rocks	A Transition	↑ 3 - 999 g/t	○ 0.5 - 1 %	2
Gossan	G Sulphide	○	↑ 1 - 10 %	3
Fault zone	F	○	↓ 0 - 0.5 %	4
Dyke	D	○	○ 0.5 - 1 %	5
		↓ 1 - 3 g/t	↑ 1 - 10 %	6
		○	↓ 0 - 0.5 %	7
		↓ 0.3 - 1 g/t	○ 0.5 - 1 %	8
		↓	↑ 1 - 10 %	9

For example, a sample comprising of transitional fault zone material assaying 2.5 g/t Au and 5% Cu would be assigned a criteria code of FT6. Metallurgical responses are obtained by subjecting each ore sample to a standardised cyanide leaching test to measure its gold and copper leaching recoveries and its cyanide consumption. These data are entered into the database and given a coding. By also adding empirical hardness ('soft', 'medium, or 'hard') to the coding, the classification can be used to guide drilling operations. This system alerts the driller to potential regions of increased hardness or abrasiveness that may impact drilling speed or the rate of drill bit replacement. It also has benefits in the crushing and grinding operations, where ore hardness can be used to estimate rate of steel grinding ball replacement (in the SAG and ball mills) or the frequency of part replacement or maintenance shutdown.

Since the introduction of flotation alongside leaching in the process plants, which was instigated in 2018, a simpler set of geometallurgical criteria was developed to determine the optimum process route, in which ore classification is based primarily on Au and Cu grades.

In general, all low gold grade ores are treated by heap leaching, either as crushed ore or run-of-mine (ROM) ore, except those with significant sulphidic copper grades, which are directed to flotation. For ores with higher gold grades, there are three processing alternatives, as described previously, i.e.

- i) Integrated mode A: with agitation leaching (AGL) ahead of flotation (FLT)
- ii) Integrated mode B: with FLT ahead of AGL
- iii) Parallel mode: with the AGL and FLT plants operating independently in parallel. This configuration almost doubles the total throughput of ore.

The choice of which mode is used and for what period of time is based on the availabilities of the different type of ore and their metal recoveries and production costs in

the various processes. The overriding objective is to maximize the NSR of the operations at any given time and this is the criterion that determines the selection of the processing route. Clearly, the market prices of gold, silver and copper and the selling terms of copper concentrates are important factors in this approach.

Currently, the processing plants are configured in parallel mode, with both agitation leaching and flotation being operated as independent units. The decision chart for parallel processing, which determines the optimum processing route for any particular ore type, as characterised by gold and copper assay values, is shown in Figure 3.

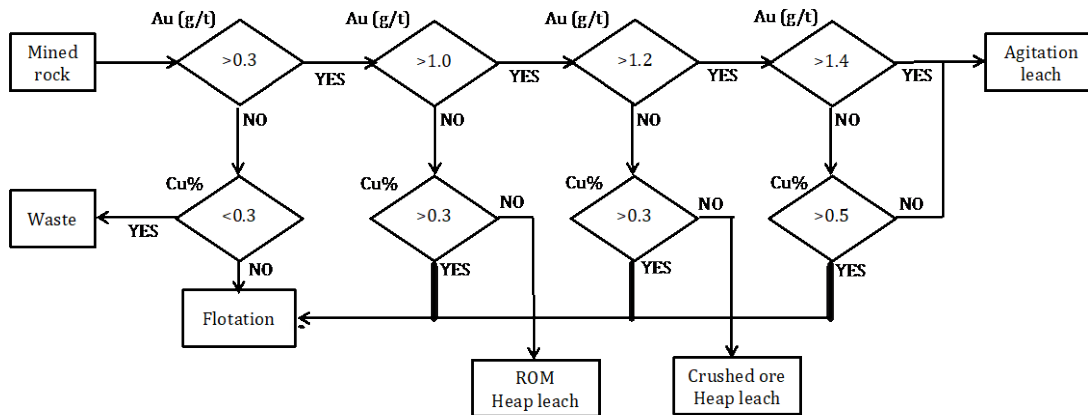


Figure 3. Decision chart to determine the optimum route for parallel processing based on gold and copper grade

Acknowledgements

The authors are grateful for the help of Katherine Matthews, project geologist at Anglo Asian Mining, in the preparation of this paper.

Glossary

AAM	Anglo Asian Mining plc.
ADR	Adsorption/Desorption/Recovery plant: where gold is eluted from the loaded resin and the stripped resin is returned to RIP, while the strip solution is electrowon to produce gold doré.
AGL	Agitation Leach plant.
BLS	Barren Leach Solution: recycled process solution used as feed to heap leaching.
FLT	Flotation.
HLC	Heap leaching of crushed ore.
HLROM	Heap leaching of run-of-mine ore
NSR	Net smelter return.
PLS	Pregnant Leach Solution: gold-bearing solution from heap leaching.
RIP	Resin-In-Pulp plant: where gold is extracted from the

5 Conclusions

A geometallurgical system has been created to classify Gedabek ores, based on geology, oxidation state, metal assay values and cyanide leaching response data. This classification is used primarily to determine the optimum processing routes for different classes of ore, through the processing options available at Gedabek, which are heap leaching, agitation leaching and flotation. Other benefits of the ore classification system are manifested in improved drilling and blasting performance and in reduced costs for comminution.

	agitation leach pulp and the PLS.
SART	Sulphidisation/Acidification/Recycling/Thickening plant: where Cu and Ag are precipitated from the cyanide leach liquor to produce a mixed Cu/Ag sulphide concentrate.
SPF	Ore stockpile
TMF	Tailings Management Facility.

References

Hedjazi F., Monhemius A.J. (2014) Copper-gold ore processing with ion exchange and SART technology. *Minerals Engineering*, 64:120-125. DOI: 10.1016/j.mineng.2014.05.025

Monhemius J., Hedjazi F., Saeedi H. (2017) Flotation and Leaching at Anglo Asian Mining's Gedabek Gold and Copper Mine in Azerbaijan. *Proceedings of COM2017 - The Conference of Metallurgists, hosting World Gold & Nickel Cobalt*, August 27-30, 2017, Vancouver, ISBN: 978-1-926872-36-0 Canadian Institute of Mining, Metallurgy and Petroleum. Paper No. 9707.

Hedjazi F., Monhemius A.J. (2018) Industrial application of ammonia-assisted cyanide leaching for copper-gold ores. *Minerals Engineering*, 126:123-129. DOI: 10.1016/j.mineng.2018.07

Evaluating processing attributes using hyperspectral mineralogy

Nathan Fox

CRC ORE/WH Bryan Mining & Geology Research Centre, Sustainable Minerals Institute, University of Queensland, Australia

Abstract. Geological variability occurs intrinsically in ore systems at a range of scales from 10-100s of meters to microns. Such variability includes rock type/lithology, alteration assemblage zonation and distribution of veins/faults. However, mineralogy represents a fundamental control on processing attributes (e.g., hardness) of different ore types. Such processing attributes are rarely confined to individual geological variables (such as rock type or alteration assemblage). Consequently, geometallurgical domain models built solely on lithology or alteration zone distribution are unlikely to capture the heterogeneity within an ore system. This study highlights the linkages between mineralogical variability and rock hardness, a processing attribute that influences throughput and energy consumption during comminution. Significantly, in the geometallurgical context, variables such as hardness may operate independently of geological variables. Integration of Equotip (impact hardness) and hyperspectral mineralogical data in this study highlights the co-dependence of these variables and emphasizes the benefit of high spatial resolution mineralogical data in evaluating processing attribute heterogeneity in mineralized systems.

1 Introduction

To meet the future demand for copper, gold and other metals, the minerals sector requires a combination of new exploration successes, optimisation of production/extraction efficiency and the ability to economically extract complex ore bodies in an environmentally conscientious way (e.g., Valenta et al., 2019). Economic value needs to be maximised across the entire mining chain from exploration to extraction, waste disposal and environmental management. An understanding of the spatial variability of physical processing parameters across an ore body is necessary for optimized extraction and scheduling, circuit design and waste management. Such approaches can mitigate against technical, economic and environmental risk and lead to long term cost benefits in an operation.

There is increasing appreciation that the metallurgical performance (e.g., throughput, grindability and flotability) of ores may be influenced not by grade alone, but by geological variables including lithology, alteration class and structure (e.g., Jackson and Young 2016). However, prediction of processing attributes based solely on geological domain models tend not to account for the true physical heterogeneity/variability of processing attributes

at the deposit-scale (Jackson and Young 2016). Emphasis is therefore required on mapping/measuring the short-range variability of the rock physical properties which influence metallurgical processing attributes. These properties include rock hardness (Keeney and Nguyen, 2014), mineralogy and 2D/3D texture (e.g., Evans et al., 2012; Perez-Barnuevo et al., 2018). To statistically measure/sample this variability, high spatial resolution analytical tools/techniques are required for integration into spatial geometallurgical models. Consequently, such tools need to be low cost, rapid and have cross-disciplinary applications.

Here we document the use of the CSIRO HyLogger, integrated with Equotip hardness measurements to highlight the relationships between material hardness and mineralogy at high spatial sampling resolution (<25 mm). These datasets are of mutual benefit across the mining value chain for heterogeneity mapping and have implications for predicting processing attributes, neutralizing domains and evaluating amenability to coarse waste rejection and sortability of complex ores.

2 Sample materials

2.1 Deposit Geology and Mineralisation-style

Two 30 m long drill core intervals were provided for this study from an Au-deposit located in the Eastern Goldfields of Western Australia. The study site is atypical of other shear zone hosted Au deposits in the region. It is characterized by a strong relationship between gold mineralization and monzonite intrusions which intrude volcanoclastic sandstone, conglomerate and sub-volcanic intrusions. The alteration is characterized by alternating sodic (albite-quartz-carbonate) and potassic (K-feldspar-quartz-biotite-magnetite) alteration zones ranging between 1 and 6 m in thickness. Chloritic alteration domains (chlorite-quartz-muscovite-carbonate) occur proximal to interpreted fault zones, but are typically barren. Although multiple quartz-carbonate vein sets occur in the deposit, there is no apparent relationship between veining and gold mineralization. Gold mineralisation is instead, broadly correlated with disseminated pyrite, and higher gold grades occur in the sodic alteration zones.

3 Analytical techniques

3.1 CSIRO HyLogger-3

The CSIRO HyLogger-3 is a semi-automated hyperspectral drill core scanning platform that measures spectral reflectance in the near-infrared (NIR), short-wave infrared (SWIR) and long wave infrared (LWIR; also known as thermal infrared, TIR) regions (Mason and Huntington 2012). Analysis of the NIR-SWIR spectra allows identification of a range of oxide (hematite, goethite), clay, phyllosilicate, sulfate, carbonate and other hydrous aluminosilicate minerals. The LWIR (or TIR) spectra are capable of identifying anhydrous silicates (e.g., quartz, feldspar, pyroxene), carbonates and other anhydrous aluminosilicates (Mason and Huntington 2012). During core analysis, the HyLogger acquires a high resolution linescan image, a laser profilometer surface profile and surface temperature in addition to spectral reflectance. The spectral reflectance measurements are continuously acquired during scanning and outputs are composited to 8 mm intervals for mineralogical identification and relative intensity estimation. By utilizing both NIR-SWIR and LWIR/TIR spectrometers, the HyLogger-3 is capable of identifying the majority of rock forming minerals that typically occur in zoned hydrothermal systems at high spatial sampling intervals.

3.2 PROCEQ Equotip hardness testing

The PROCEQ Equotip (Model-3) is a rebound hardness tester used to measure the impact hardness of drill core which represents a proxy for more expensive metallurgical tests (e.g., A*b) designed to predict the impact breakage energy required for different ore types (Keeney and Nguyen 2014). Equotip analyses are non-destructive, rapid (<10 sec. per measurement) and cost effective.

Compared to full-scale impact breakage metallurgical tests, the Equotip impact hardness proxy allows coverage of a larger proportion of the ore body and captures inherent hardness variability at higher spatial resolution. In this study, Equotip hardness measurements were taken every 24 mm along competent sections of half drill core greater than 100 mm in length, avoiding fractures and core edges. The sample spacing of 24 mm was equivalent to three Hylogger output intervals (IE. 3 x 8 mm). Raw data acquired by the Equotip are reported in Leeb's (Ls).

4 Results

Figure 1 shows a compilation log for a 30 m interval of drill core showing the down hole variability in i) logged lithology; ii) logged alteration; iii) gold grade; iv) Equotip hardness (Ls and Cusum); v) HyLogger mineralogy (TIR).

4.1 Downhole geological characteristics

The drill core interval shown in Figure 1, comprises variable lithologies including volcaniclastic sandstone and conglomerate, felsic intrusives and monzonite. The alteration shows some correlation to lithology with chloritic alteration constrained to the upper volcaniclastic

conglomerate and alternating intervals of sodic and potassic alteration broadly correlating with subtle lithological variations (Fig. 1).

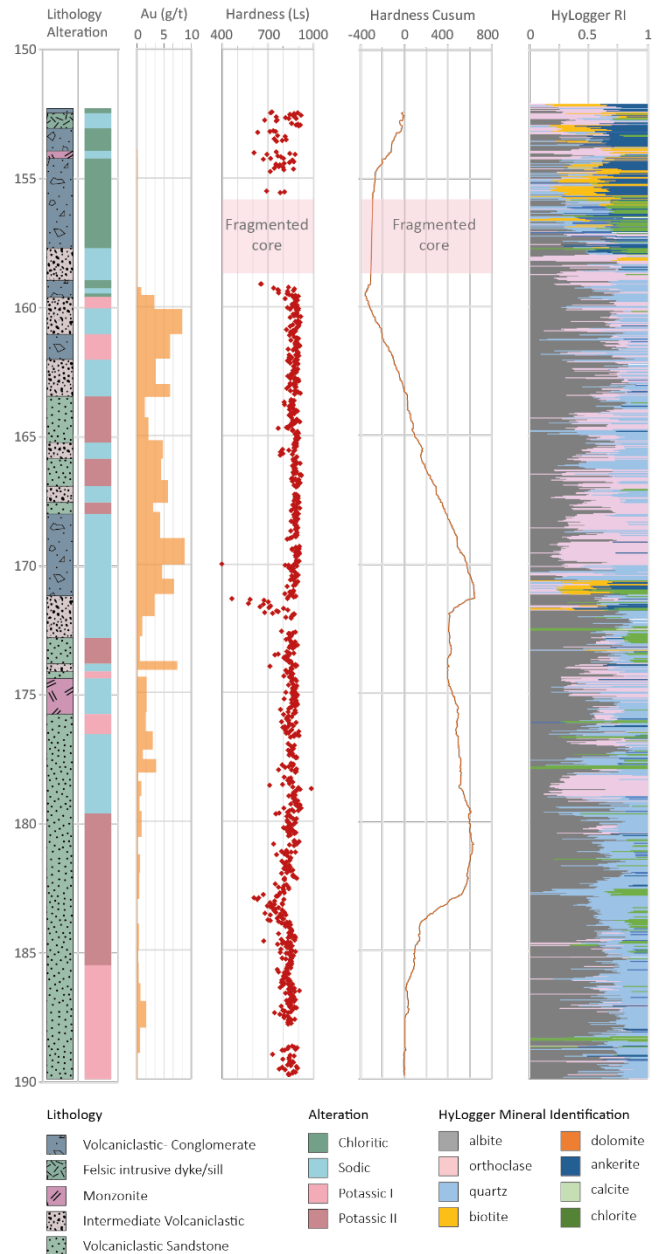


Figure 1. Graphic sketch log showing lithology, alteration class, Au grade, hardness (Ls) and hardness (Cusum) with corresponding HyLogger mineralogy.

Alteration intervals range between <1 and 8 m in apparent thickness throughout the hole, indicating highly heterogeneous lithological and alteration domains exist. The correlation of higher gold grades with sodic alteration zones is a characteristic observed both at the deposit-scale and in this drill core interval (Fig. 1). The upper chloritic alteration zone (~153 to 158 m) and the lower potassic alteration zone (180 to 190 m) are largely barren or very low grade (<1 g/t; Fig. 1).

4.2 Equotip hardness variability

Individual hardness point measurements (reported in Leeb's, Ls) spaced at 24 mm intervals along the drill core are shown in Figure 1. The upper 7 m of the intervals has less data points due to natural fragmentation of the core to individual fragments <50 mm in length, which are unsuitable for robust Equotip measurements.

From the point hardness data, a cumulative sum graph was calculated to determine the changes in the prevailing mean of the hardness values down hole. Cumulative sum (or cusum) charts are sensitive to deviations from the average values (in this case hardness, in Leeb's, Ls) for a given interval or domain (Napier-Munn, 2014). The cusum plots can therefore, be used to identify change points from the mean hardness value and identify areas of homogenous/heterogeneous mean hardness values.

The top 3 meters of the interval is characterized by variable hardness readings giving an initially erratic cusum deviation away from 0 (Fig. 1) indicating a zone of heterogeneous hardness. The hardness data gap (155.5 to 159.0 m) is represented by a line with no slope (vertical, parallel to y-axis). The first significant zone of constant hardness with low deviation from the mean hardness value occurs between 160 and 171 m, corresponding to an interval characterized by variable lithologies and alternating sodic and potassic alteration. This domain is expressed on the cusum plot as a slope with near constant gradient (Fig. 1) indicating low variability in hardness over this interval. Deviations from this slope correspond to changes in hardness as occurs at 171 m with a sharp decrease in the hardness value (Ls) and the cusum slope direction. The remainder of the interval shows variable hardness values and a corresponding steep profile on the cusum plot accounting for localized variability in the core hardness including a hardness decrease at ~184 m depth. Cusum charts are a useful tool to identify domains based on variability of the feature being measured (in this case, hardness). It can be noted that hardness domains do not directly correlate to either lithology breaks or changes alteration (Fig. 1).

4.3 Integration of HyLogger downhole mineralogy

A stacked bar chart of the HyLogger mineralogy is shown in the far right of Figure 1 as a relative intensity scale of mineral abundance normalized to 1, such that a relative intensity for albite of 0.5, would infer that albite constitutes approximately 50% of the rock mass. Consequently, changes in the relative intensity of the identified minerals can be used as a guide to down hole mineralogical variability.

The upper part of the drill hole is characterized by high dolomite, biotite and chlorite, moderate K-feldspar/quartz and low albite (Fig. 1). This corresponds to the low grade Au zone with variable hardness values between 600-900 Ls.

In contrast, the high-grade Au zone between 159 and 171 m is characterized by high, but variable albite, K-feldspar and quartz contents with sparsely distributed narrow intervals of carbonate (ankerite) and with no

significant biotite or chlorite detected (Fig. 1). The occurrence of abundant K-feldspar in the sodic alteration zones (e.g., 169 – 171 m) highlights the application of HyLogger to discriminate minerals that are difficult to identify visually or based on physical properties while logging. In terms of hardness variation in this zone, there is no significant difference in hardness ($\sim 900 \pm 25$ Ls) between potassic and sodic alteration zones despite variations in modal mineralogy. Localised softer intervals (750 – 800 Ls) are narrow and correlate directly with ankerite identified by the HyLogger (Fig.1).

The sharp decrease in hardness value at approximately 171 m identified in the change in slope of the hardness cusum plot coincides with increase in biotite, chlorite and ankerite and an absence of albite (Fig. 1). This is an unlogged zone marked by a change in lithology, but consistent alteration (sodic alteration) indicating that visually, this zone is discrete. Notably, this is still mineralized (1-4 g/t Au).

The lower 17 m of the interval shows highly variable mineral proportions. Both albite and quartz vary from <0.1 to 0.6 RI with generally very low relative intensities for K-feldspar, particularly in the potassic alteration zone between 180 and 190 m depth (Fig. 1). Unlike the upper sodic-potassic zone, this lower zone contains chlorite, dolomite and calcite, as determined by the HyLogger. Consequently, the measured hardness is more variable in this zone, including localized softer domains.

5 Discussion

5.1 Predicting Hardness from Mineralogy

Equotip impact hardness measurements provide hardness data analogous to unconfined compressive strength (UCS) of rocks (e.g., Aoki and Matsukura, 2008) and is a proxy measurement for standard metallurgical tests (e.g., A*b, BMWi; Keeney and Nguyen, 2014) to predict energy consumption related to feed material hardness.

The overall hardness of a rock depends on the physical properties of the minerals e.g., abrasion hardness (Mohs), tensile strength (Vickers hardness) and brittle behavior (Hunt and Berry, 2017). Significantly, the structural and textural arrangement of these mineral grains also affects hardness and comminution parameters (e.g., Hilden and Powell, 2017) together with the modal abundance of each mineral.

The hardness domains in the interval studied here are shown to be closely defined by mineralogical variations that occur at scales of <10 to 100 cm. Softer domains contain minerals such as biotite, ankerite/calcite/dolomite and chlorite with lower modal proportions of harder minerals such as albite, quartz and K-feldspar (Fig.1). The converse is true for the harder central potassic and sodic domains determined by Equotip measurements, these are dominated by hard phases (quartz, albite and K-feldspar) with low proportions of softer phases (Fig. 1).

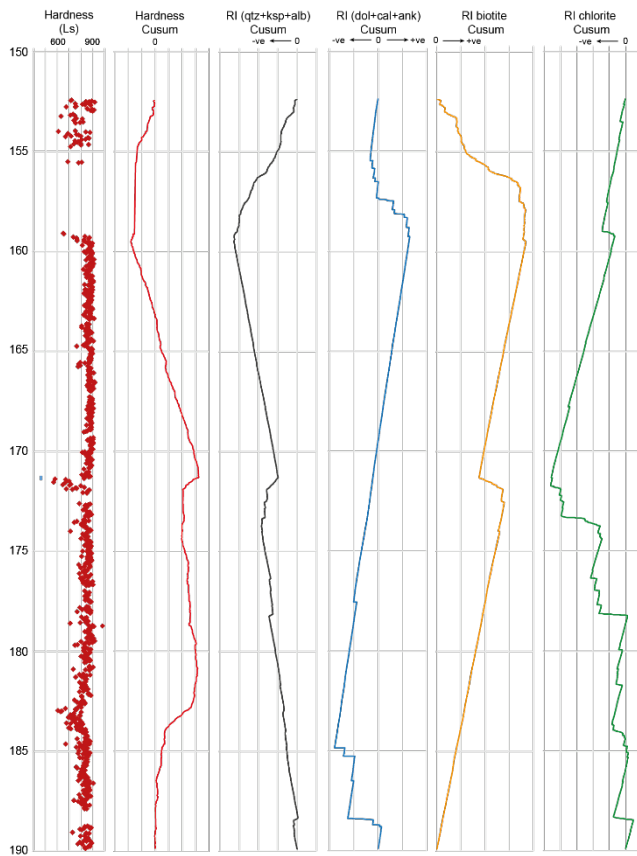


Figure 2. Raw Equotip data and cusum distribution plots for hardness compared to cusum plots for variation in Relative Intensity (RI) for hard and soft mineral phases. Abbrev. qtz, quartz; alb, albite; ksp, K-feldspar; dol, dolomite; cal, calcite; ank, ankerite.

Figure 2 compares hardness values (Ls) and cusum distributions against cusum distributions for the sum of relative intensities (RI) determined by the HyLogger for hard silicates (quartz+albite+K-feldspar) and softer phases including the sum of carbonate RI, biotite and chlorite. The trends in the cusum plots for each mineral or mineral class largely mimic the trend of the Equotip data cusum values which map harder and softer domains down hole. The ability of the HyLogger to determine relative intensity of silicate phases known to contribute to the overall strength (or hardness) of altered rock domains which typically produce lower A^*b values and higher BMWi values indicating higher energy consumption during comminution (e.g., Hunt and Berry, 2017) is considered critical for hardness domaining.

Cusum plots for the Relative Intensity of the softer mineral phases (carbonate, biotite and chlorite) similarly correspond to changes in domain hardness and in conjunction with the hard mineral groups are able to delimit harder and softer processing domains (Fig. 2).

Processing attributes related to hardness can therefore be defined based on semi-quantitative mineralogical abundance measured using the HyLogger at an analytical scale or resolution that captures intrinsic variability or heterogeneity across the rock mass. This information can be integrated with metallurgical test work which whilst carried out on fewer samples, can be used

to validate both Equotip and HyLogger measurements. These later two techniques are lower cost and can be readily applied at higher sampling densities across a deposit to complement geometallurgical and ore deposit knowledge characterization campaigns.

6 Conclusions

The detailed mineralogy determined by HyLogger provides high spatial resolution sampling that correlates measured hardness with observed variation in abundance and distribution of albite, quartz, K-feldspar, biotite, chlorite and carbonate. Hardness domains which will influence throughput and energy consumption are not constrained to specific lithology or alteration domains, indicating processing attributes must be mapped and modelled independently.

Acknowledgements

Jake Moltzen, Peter Harding and Steve Newett from the Department of State Growth at Mineral Resources Tasmania are acknowledged for HyLogging, data processing and access to core logging facilities.

References

- Aoki H, Matsukura, Y (2008) Estimating the unconfined compressive strength of intact rocks from Equotip hardness. *Bull. Eng. Geol. Env.* 67: 23-29
- Evans CL, Wightman EM, Yuan X (2012) Quantifying mineral grain size distributions for process modelling using X-ray microtomography. *Min Eng* 82: 78-83.
- Hilden M, Powell, M (2017) A geometrical texture model for multi-mineral liberation prediction. *Min Eng* 111: 25-35.
- Hunt J, Berry R (2017) Geological contributions to geometallurgy: A Review. *Geoscience Canada* 44: 103-118.
- Jackson J, Young M (2016) Ore type – Everything to someone but nothing to anyone. Third AusIMM International Geometallurgy Conference, Perth, WA, p. 267-274.
- Keeney L, Nguyen K, (2014) The use of Equotip as a hardness domaining tool. IMPC 2014 27th International Mineral Processing Congress.
- Mason P, Huntington JF (2012). HyLogger 3 components and pre-processing: An overview. Technical Note Northern Territory Geological Survey 2012-002
- Napier-Munn TJ (2014) Statistical Methods for Mineral Engineers. The University of Queensland/JKMRC.
- Pérez-Barnuevo L, Lévesque S, Bazin C (2018) Automated recognition of drill core textures: A geometallurgical tool for mineral process prediction. *Min Eng* 118: 87-96
- Valenta RK, Kemp D, Owen JR, Corder GD, Lebre E (2019) Re-thinking complex orebodies: Consequences for the future supply of copper. *Journ Clean Prod* 220: 816-826

Luminescence sorting to reduce energy use during ore processing

Nicola. J. Horsburgh, Adrian. A. Finch
University of St. Andrews, UK

Abstract. Rare Earth Elements (REE) are required for the production of all modern technological applications e.g. smartphones, televisions, computers, etc. The largest markets for REE are in the renewable energy and energy efficiency sectors. For example, REE are an essential component of magnets used in wind turbines and electric vehicles, also in energy efficient phosphors in LCD and LED displays. Although these materials are used in 'green' technologies the production of the raw materials is a major consumer of global energy production.

Comminution of ore in an average mining/processing operation accounts for nearly half of all energy used. Globally comminution is estimated to consume approximately 2% of electricity produced. With a move to responsible sourcing and increasing global demand for raw materials, new and innovative solutions are required to reduce environmental impacts and improve recovery.

Sorting of ore prior to grinding would significantly reduce energy requirements of processing. Automated sorting separates the ore material from gangue. In this study we investigate the potential of luminescence to fingerprint minerals so that these criteria can be used for smart sorting of REE minerals.

1 Introduction

Mineral processing requires ore minerals to be separated from gangue. The first stage is comminution, followed by beneficiation by gravity, magnetic, electrostatic separation or by froth flotation and/or leaching. Comminution accounts for 35-50% of total energy and mining costs (Curry et al. 2014, Herbst et al. 2003); an average mine uses approximately 6,700 kWh/kiloton of energy (Jeswiet and Szekeres 2016) and is the largest single component of mine energy usage, estimated to constitute 1.8% of electrical consumption globally (Naper-Munn 2015). However, if beneficiation were to separate ore from gangue at early stages of comminution, in particular prior to grinding (de Bakker 2014) there would be significant global energy savings. While grinding is done to improve liberation and increase the quality of the concentrate, grinding barren rock is energy intensive.

Sensor based sorting is one method of pre-concentrating ore. The potential for sensor based sorting is high within the mining industry, particularly since its use is commonplace within the recycling, food and manufacturing industries.

2 Sensor sorting

Sensor based sorting of run-of-mine (ROM) allows the removal of barren/gangue material and the separation of material into separate process streams, ideally concentrate and tailings, while at a coarse fraction reducing environmental impact by reducing water and energy consumption leading to increased productivity, yields and profits (Figure 1). Milling further down the processing stream accounts for 40% of mine electricity consumption (US Department of Energy Report 2007).

Automated sorting was first introduced to mining in the 1940s with the invention of radiometric sorting, followed by photometric sorting in the 1950'-70's (Salter and Wyatt 1991). Despite these early uses, showing potential applications and a widespread use in other industries, the uptake of sorting in mineral extraction has been slow with a few exceptions – notably precious metals and diamonds – due to the high value of the products. Technological advances increasing the resolution of detection have seen the adoption of sorting in some industrial mineral processing.

For mining companies to meet the increasing global demand for raw materials and technology metals, a shift towards more technical solutions that increase productivity and efficiency are required. Furthermore, the requirements to comply with ever-strengthening environmental legislation and the transition to sustainable low carbon-energy policies mean that the mining sector is under ever-increasing scrutiny. For all of these reasons, 'smart sorting' of ore offers substantial global benefits to mineral processing.

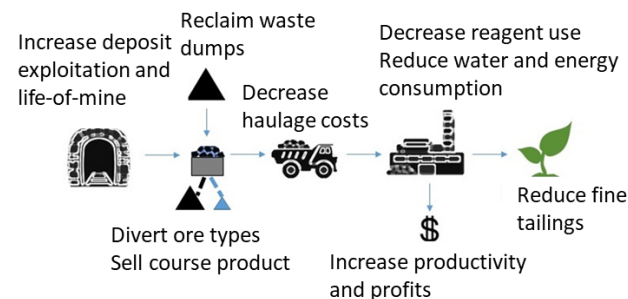


Figure 1. The main benefits of automated ore sorting.

3 Luminescence of REE

Emission spectra of REE are distinct and diagnostic due to the shielding of f-f energy cascades of lanthanide (Ln^{3+}) ions. Many natural REE bearing ore minerals are luminescent and, in this study, we demonstrate the viability of luminescence smart sorting of these minerals.

The luminescence spectrometry system at St Andrews

University (Finch et al. 2019) was used to investigate the luminescence emissions in response to radioluminescence (RL), also known as X-ray excited optical luminescence (XEOL), at room temperature and also as a function of temperature (-248 to 400°C) on a collection of REE minerals chosen to include all REE minerals that are being considered as potential REE ores. These include monazite, xenotime, eudialyte, fluorite, catapleite, wöhlerite and fluocarbonate minerals such as bastnaesite, parisite and ancylite. We present examples of the features observed in spectra to provide insights into the processes that are present in REE systems below.

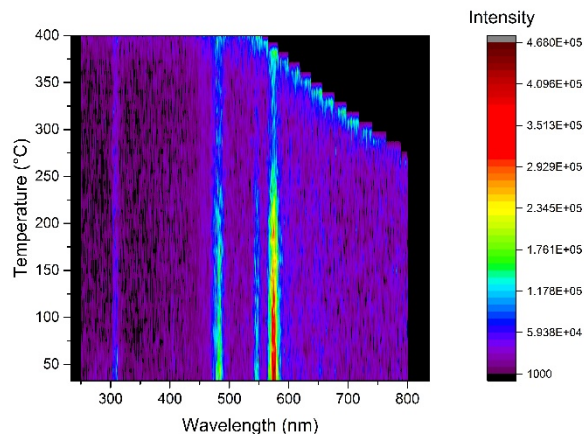


Figure 2. Spectra of monazite, (Herrebøkasa, Aspedammen, Østfold, Norway) from room temperature to 400 °C. Higher intensities show hot (red) colours, fading to cold (violet-blue). Note the characteristic narrow lines of REE emission which reduce in quantum efficiency as temperature increases. Intensity is in arbitrary units and blackbody radiation has been removed (top right corner).

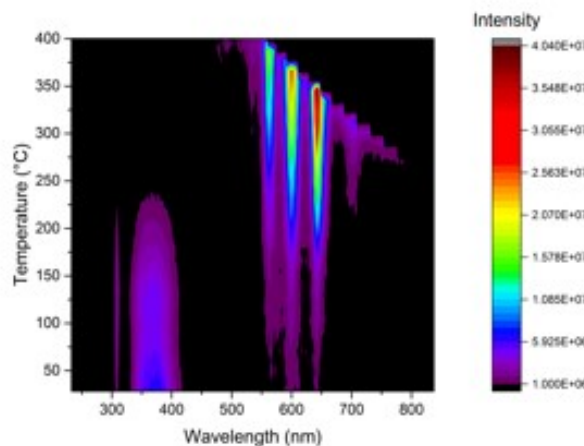


Fig. 3. Spectra of ancylite (QEQ195693, Qeqertaasaq, West Greenland) from room temperature to 400 °C. Higher intensities are hot (red) colours, fading to cold (violet-blue). Note the transfer of energy between REE on heating >200 °C. Intensity is in arbitrary units and blackbody radiation has been removed (top right corner).

Luminescence studies of REE mineral systems have focused on doped synthetic systems (e.g., containing one or two REE). This is not representative of natural mineral systems as minerals contain all REE (except Pm). Furthermore, elemental substitutions involving other

elements (potentially including quenching ions, e.g. Fe²⁺) and lattice damage from radiation all influence the energy transfer to REE and their quantum efficiency. Intra-ion Ln³⁺ transitions are spin forbidden and so energy transfer can only occur through interaction with the crystal lattice. The poor quantum efficiency of this process means that although there are multiple lanthanides present, only those ions that couple most efficiently with the crystal lattice are detected, producing sharp lines in the emission spectra. Dy³⁺ (480, 580 nm) dominates in monazite (Fig. 2) whereas Ce³⁺ (370 nm) is observed at room temperature in ancylite.

Changes in temperature affect the efficiency of energy transfer, particularly if it involves multiple REE. This results in temperature-induced, reversible Ln³⁺ shifts (e.g. Fig. 3). Luminescence hysteresis is observed, where irreversible changes occur on heating and some materials show strong thermoluminescence (light emissions associated with heating).

The luminescence responses are variable within mineral systems and by locality, reflecting the compositional and structural variations found in natural minerals. Characteristic shifts in the dominant lanthanide are observed as samples are heated (e.g. Fig. 3). The overall conclusion of our work from all of the minerals studied (including spectra not shown here) is that REE-bearing mineral systems give characteristic luminescence and that luminescence spectroscopy provides a means of fingerprinting the phase of a given mineral at a given locality.

4 Luminescence sorting

Current sorting technologies use X-rays and lasers as excitation methods, measuring X-ray transmission (XRT) and X-ray fluorescence (XRF) of industrial minerals, base/precious metals, and diamonds. Usually composition is explored by XRF or XRT but visible light is also emitted during X-irradiation and hence the upgrading of luminescence technology to existing sorting systems is viable.

The luminescence of minerals is sufficiently varied that it can be used as a sensitive identification tool. Even if an ore mineral does not luminesce strongly (e.g. eudialyte), we occasionally find that the associated gangue gives a signal. In this case one can remove the luminescent gangue material and comminute the ore phases without a signal. Hence luminescence-based sorting can be a discriminator to underpin smart sorting, if the basic characterisation of target minerals is determined for the locality of interest.

5 Conclusions

Luminescence is a route that potentially discriminates ore from gangue which can, in principal, be used to underpin smart sorting. This can be achieved by room temperature (RT) spectroscopy, comparing and contrasting RT and high temperature spectra and/or seeking TL responses. However, as we observe in our census of REE minerals, basic characterisation of target minerals is essential for

the locality of interest. It is rarely possible to determine accurately the luminescence properties of minerals from first principles, even in simple mineral systems.

Mining companies must meet the increasing global demand for raw materials and technology metals, coupled with an expectation towards more responsible mining. Therefore, there is an appetite for technical solutions such as this, which increases productivity and efficiency and reduces the carbon footprint of mining.

Acknowledgements

This work was carried out under the NERC-funded SOS RARE consortium [grant NE/M010856/1] and University of St. Andrews 7th Century Scholarship Fund. The Hunterian Museum, National Museum of Scotland, Natural History Museum, Oslo Henrik Friis, Josh Hughes and SoS RARE partners provided samples.

References

- BCS, Incorporated, 2007. Mining industry bandwidth study. In: U.S. Department of Energy, Industrial Technologies Program Report p47.
- de Bakker, J (2014) *Metallurgical and Materials Transactions E* 1: 8. doi:10.1007/s40553-013-0001-6
- Curry JA, Ismay MJL, Jameson GJ (2014) Mine operating costs and the potential impacts of energy and grinding. *Miner Eng.* 56:70-80
- Finch AA, Wang Y, Townsend PD, Ingle M (2019) A high sensitivity system for luminescence measurement of materials. *Luminescence* doi:10.1002/bio.3606
- Herbest JA, Lo YA, Flintoff B (2003) Size reduction and liberation. In Han KN, Fuerstenau MC (eds) *Principles of Minerals Processing*. Society for Mining, Metallurgy, and Exploration pp 61-115
- Jeswiet J, Szekeres A (2016) Energy Consumption in Mining Comminution. *Procedia CIRP* 48:140–145
- Napier-Munn T (2015) Is progress in energy-efficient comminution doomed? *Miner Eng* 73:1-6
- Salter JD, Wyatt NPG (1991) Sorting in the minerals industry: past, present and future. *Miner Eng* 4:7-11:779-796

Mapping and sampling for real-time development of mine plans in high-grade, narrow-vein, underground mining

Luke Palmer, Kathryn Moore

Camborne School of Mines, University of Exeter, UK

Gareth Thomas, Steve Broom

Metal Innovations Ltd.

Richard Roethe, Dominic Roberts

Mineco Ltd.

Abstract. Geological methods, such as sampling and mapping are key components in all mining operations. In underground, narrow-vein mines they are of particular importance as a small deviation from the ore-zone can result in a large loss of ore and be challenging to correct. This paper describes protocols for geological sampling that can be integrated with mine plans designed for new selective underground mining technology. A multistage sampling and surveying approach comprise different strategies that are tailored to different stages of the mining cycle. Collected data will be used to refine resource models and mine plans in real-time, providing greater geological control, improved grade control, enhanced mine planning and increased efficiency of selective mining. Continuous mining technology with increased geological certainty in high-grade deposits has the potential to greatly improve the economic viability of small mining operations with the potential to supply raw materials within Europe.

1 Introduction

Decreasing rates of discovery of large deposits, declining ore grades and increasing environmental costs in global mining operations, suggest that the diverse geological resource base in Europe can be re-investigated as a means to secure sustainable raw material supplies. To this end, the IMP@CT project aims to test the viability of small, modular, low-impact systems for small deposit mining in Europe. The project is developing the concept of Switch-On, Switch-Off (SOSO) mining for small, currently sub-economic, but well-understood ore deposits. These deposits can be extremely high grade, but do not provide the returns to justify high capital start-up costs of large-scale industrial mining. Thus, low-cost, high-mobility solutions are being investigated that can respond to rapid fluctuations in raw materials markets.

Selective mining approaches are enabled by the development of a reduced scale, prototype selective mining tool, with multiple functions, by Metal Innovations Ltd. The mining tool negates the need for drilling and blasting and can reduce the need for primary crushing. The operation of the mining tool facilitates geological sampling and mapping to reduce geological uncertainties associated with extraction in variable and complex ore bodies. In particular, the mine geologist can improve

resource estimation, short-term mine planning, and grade control.

Here, a sampling and mapping campaign methodology is presented, showing how detailed geological information can be used to increase recovery and decrease dilution through enhanced modelling. The methodology will be tested at the Olovo Lead Mine, located in the Federation of Bosnia and Herzegovina in central Europe, in conjunction with the selective mining tool. The results will be used to validate the viability of the method in an industrial setting and will demonstrate how enhanced mining strategies in real-time compare to traditional methods

2 Modern Underground Mining

Modern, industrial mining consists of a number of cycles that interlock over the mine life (see Rossi and Deutsch, 2013; Darling 2001). In underground mining for example, a cyclic sequence frequently includes drilling and blasting, mucking out (removing blasted material) and development for future extraction. Modern underground extraction for steeply dipping ore bodies commonly takes the form of either short or long-hole stoping methods (Fig. 1). Development in the ore zone is minimised to reduce the amount of dead ground and improve safety in what is commonly an unstable area. Lack of access requires that samples are obtained from ex-situ sampling points at access drives, blast holes or underground draw points. Geological sampling is required to ascertain the grade, and other properties, of the blocks being extracted. Key geological tasks that are linked to the mining cycle include resource estimation, short-term mine planning and grade control:

- Resource estimation involves using geological information, grade and density at a minimum, to calculate the possible mineral resources of a deposit. It is a computationally demanding stage, requiring modern software and trained users (Rossi and Deutsch 2013).
- Resources are transferred into reserves through the design of a mine plan, which details how the resources will be recovered and brought to the surface for processing (Darling 2011). Short-term mine planning is the practice of updating the original mine plan with increased certainty of

the structure and grade of the ore deposit.

- Grade control is the process by which ore and waste is designated at the point of mining so it can be dealt with correctly (Hoogvliet, Grieve and Sims 2014). This maximises the value of ore mined and fed to the mill (Shaw 1990). Grade control is ideally performed prior to fragmentation, so that ore and waste can be separated at an early stage. Ex-situ sampling at draw points compensates for lack of access in a closed ore stope.

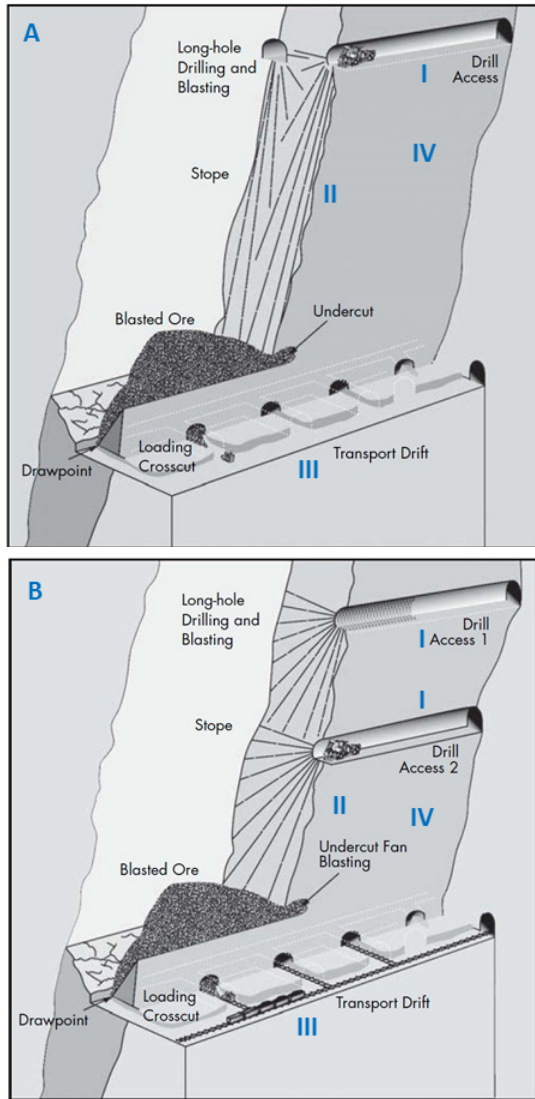


Figure 1. Common underground extraction open stoping methods, A) Long-hole or blasthole stoping and B) Sub-level open stoping. Common areas for sampling include drill access drives (I), blast holes (II) or ore draw points (III). The ore-zone (IV) is commonly weaker than the host rocks. Adapted from (Hamrin, 2001 and Pakalnis and Hughes, 2011).

3 Mining in a Switch-On, Switch Off context

SOSO mining builds upon traditional mining systems but considers that the whole systems approaches are required to reduce capital costs and speed up

deployment of technology to new deposits. A key tool that is being developed within the IMP@CT project is the Selective Mining Tool, developed by Metal Innovations Ltd. Rather than use drilling and blasting to fragment material for later processing, a boom-operated road-header is used within the ore-zone. Rotating picks on the road-header are applied to the active face, which liberates material from the face in a controlled, continuous manner.

The features of the technology that allow a high degree of control are its small-size, manual operation (in full view of the active mine-face), changing pick lacing and operating conditions. The narrow width of the technology further reduces the dilution of waste into the ore zone in narrow, high-grade deposits. Ore and waste zones can easily be extracted sequentially through operator management for increased geological control. The pick lacing, pressure and cutting speed can be used to control particle size and rate of advance..

4 Surveying and Sampling Methodology

4.1 Mine Plan

The new mining technology deployed in this project has necessitated the development of a specific, new mine plan to maximise the ore recovered, develop and respond to geological control and minimise potential risks. An under-hand, open stoping mining method first cuts in the ore-zone at the upper extent of the extraction area, and progresses by sequential extraction through horizontal slices (Fig. 2). This mine plan allows for a high degree of geological control by allowing access to the active faces during extraction for sampling and mapping whereas other stoping methods do not. Extensive geological mapping, sampling, and subsequent resource modelling that are performed during mining, reduces dilution and haulage costs.

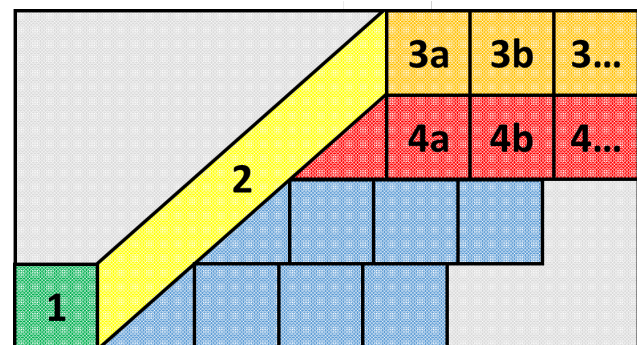


Figure 2. Schematic diagram of proposed sequential extraction of blocks within vein. 1) Horizontal development drive, in vein or perpendicular to the vein's strike. 2) Inclined production drive in vein. 3) Top cut with individual blocks labelled in order of extraction. 4) Second cut with individual blocks labelled in order of extraction. Mining would progress through the blue area if the entire stope were to be exploited. The grey area is dead ground.

4.2 Sampling and surveying

The multistage sampling and surveying approach is tailored to four different stages of the mining cycle.

(1). During development through barren waste rock (stage 1; Fig 2), there is little need to sample for grade. However, density is a key variable in resource estimation, for transferring volumetric grade data into mass, and rock hardness is key for safety considerations and predicting machine wear rates. Density is commonly under-sampled in exploration campaigns (Rossi and Deutsch 2013) and is included with in-situ analysis of rock hardness.

(2) Development of an incline within the ore zone (stage 2; Fig.2) necessitates a change in the sampling strategy. Geological mapping is now a key task as well as analysing for grade, via either, in-situ methods such as portable X-Ray Fluoresce analysis, or sampling in the field followed by analysis in a lab. Channel and grab sampling are amenable to narrow, high grade deposits (Dominy 2010). The suitability of sampling methods will be tested in relation to ore deposit variability in conjunction with geological mapping. Focus will be given to ore related structures and delineation of ore zones.

(3) True production will begin on the horizontal levels of the deposit (stage 3-; Fig. 2) where discrete blocks of material will be extracted. This stage marks the start of concentrated sampling activities.

(4) Sampling will continue on stage 4 (Fig. 2), but with greater access to geological faces due to the removal of blocks above (Fig. 3). Geological information will here be maximised to improve the efficiency of short-term mine planning and ore delineation.

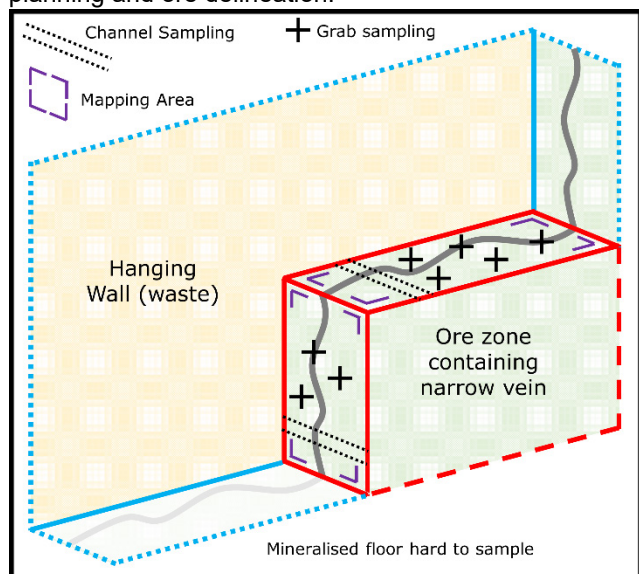


Figure 3. Sketch to show sampling and mapping activity within a vertical, high-grade vein, which has been exposed using selective mining technology. The red zone delineates the next block for extraction and the blue zone the limits of the open stope.

4.3 Real-time updating of geological and resource models

Direct access to the stope for generation of geological data can be used to update geological and resource models much faster and to a higher degree of detail than is possible with other narrow vein mining methods. The modelling workflow first involves definition of volumes and primary structures from initially available geological

data. Quantitative Kriging Neighbourhood Analysis (QKNA) is chosen as the most robust estimator that does not require significant computing power (Vann, Bertoli and Jackson 2003) for resource models.

Subsequently, the primary geological model is refined using new maps digitised in modelling software, by re-drawing the component strings of the wireframe and recalculating the resulting volumes (Fig. 4). Additionally, the primary resource model is enhanced by the incorporation of new grade, density and hardness data to improve the local estimate. The optimal parameters used to generate the QKNA estimate are maintained throughout the estimation process from the primary resource model, such that the addition of new data and refinement of the resource model is expedited. This results in increased definition of the ore zone in an enhanced geological model and it decreases significantly the time needed to produce a robust model.

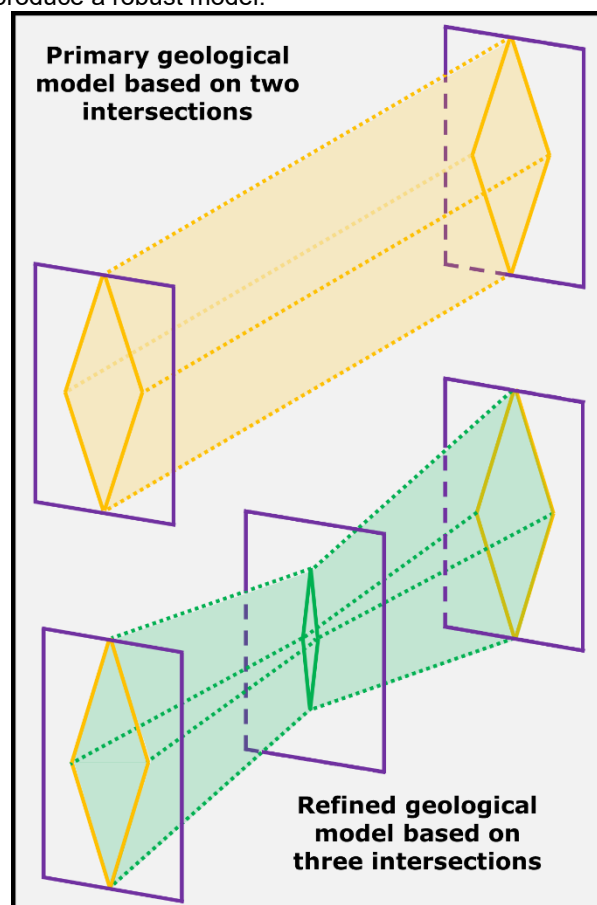


Figure 4. Schematic demonstrating the refinement of geological models with additional mapping data. The top image represents the primary wireframe model produced from two identical mapped areas and the bottom image the enhanced wireframe resulting when a third zone is included between the two previously mapped zones.

5 Case study: Olovo Lead deposit, Federation of Bosnia and Herzegovina

The methodology will be tested at the Olovo mine located 40km north of Sarajevo, the capital of the Federation of Bosnia and Herzegovina. The lead ore deposit lies within

Triassic limestones of the Internal Dinarides, marine sediments uplifted during the Himalayan-Alpine Orogeny (Hrvatović 2005). The predominant ore mineral is Cerussite (PbCO_3), with no primary textures and little primary mineralisation present. The structurally-controlled, vein mineralisation has varying thickness (up to 15m) and varies from weakly disseminated to high grade ore assaying up to 80% Pb. Gangue mineralogy is simple, with calcite, dolomite and quartz being the most common minerals, with minor kaolinite observed.

Lead mining in the Olovo region has a long history, indeed the name 'Olovo' derives from the Bosnian word for lead. Modern exploration started in the 1950s, but accelerated in the 1980s. This led to the development of numerous exploratory drifts and significant access into the ore-zone. Commercial extraction soon followed in the early 1990s, but was halted by the start of conflict in the region. Whilst the processing plant was completely destroyed, the underground workings remained relatively intact through very stable limestone. Mineco Ltd. acquired the concession in 2012 and has conducted intensive exploration works since then, whilst simultaneously re-developing infrastructure and preparing the project for production scheduled for later this year (Wardell-Armstrong 2013). It is an ideal case study for SOSO mining in Europe, due to both the stability of the underground infrastructure and the high-grade mineralisation.

The Olovo deposit is interpreted as supergene, due to the lack of mineral structure and the presence of hydrated minerals that are likely to have formed due to the ingress of meteoric waters. The monomineralic nature of the non-sulphide Pb ore has few global parallels. A comparable case study that has been well studied is the supergene Pb deposits of the Paroo Station Mine (formerly Magellan) in Western Australia (Sergeev, Burlow and Tessalina 2017). Whilst the classification of non-sulphide, vein-type mineralisation into supergene and hypogene end-members is relatively straightforward, differences remain as to how further classification is structured (Hitzman et al 2003 and McQueen 2005).

6 Conclusions and future work

We have determined the opportunities for changes to mapping and sampling protocols that are afforded by mine plans designed for selective small-scale mining tools. We have determined how new protocols can be incorporated into geological and resource models. We will test the application of this real-time data acquisition and modelling methodology in an industrial context (Olovo). We will discuss whether greater efficiency, recovery of the ore and reduction of unnecessary dilution of waste into the ore-stream are realised through better targeting as part of a mining strategy.

Acknowledgements

This project is funded by the EU Horizon 2020

Programme; Grant no 730411. Many thanks to the Mineco Project Development Team and Geomet d.o.o. for their help in facilitating site visits, sample collection, provision of data and many enlightening conversations.

References

- Darling P (2001) eds SME Mining Engineering Handbook (Englewood: Society for Mining, Metallurgy and Exploration)
- Dominy SC (2010) Grade Control Sampling Methods in Underground Gold Mines, Sampling Conference 2010, The Australasian Institute of Mining and Metallurgy: Melbourne
- Hamrin, H (2001) Underground mining methods and applications. In Hustrulid WA, Bullock RL (ed) Underground Mining Methods: Engineering Fundamentals and International Case Studies. Society for Mining, Metallurgy and Exploration, Littleton.pp-14
- Hitzman MW, Reynolds NA, Sangster DF, Allen CR, Carman CE (2003) Classification, Genesis, and Exploration Guides for Nonsulfides Zinc Deposits. *Econ Geol* 98:685-714
- Hoogvliet H, Grieve A, Sims D (2014) A Checklist for Grade Control. In Edwards AC (ed) Mineral resource and ore reserve estimation: the AusIMM guide to good practice, Second edition, Monography 30. Australasian Institute of Mining and Metallurgy, Carlton pp189-199
- Hrvatović H (2005) Geological Guidebook through Bosnia and Herzegovina Sarajevo, Geological Survey of Bosnia and Herzegovina
- McQueen KG (2005) Ore deposit types and their primary expressions. In: Butt CRM, Robertson IDM, Scott KM, Cornelius M (ed) Regolith Expressions of Australian Ore Systems. CRC LEME, Perth pp. 1–14
- Pakalnis RT, Hughes PB (2001) Sublevel Stopping. In. SME Mining Engineering Handbook, Darling P (ed) Society for Mining, Metallurgy and Exploration, Englewood
- Rossi ME, Deutsch CV (2013) Mineral Resource Estimation. Springer, New York
- Shaw WJ (1990) Management of grade control and mining geology – an overview, Strategies For Grade Control. AIG Bulletin 10, pp 1-7
- Sergeev N, Burlow R, Tessalina S (2017) The Paroo Station Mine supergene lead deposits, Western Australia: Geological and geochemical constraints, *Ore Geol Rev*, 80:564-593
- Wardell- Armstrong (2011) Olovo Lead Mine Bosnia, Internal Report.
- Vann J, Bertoli O, Jackson S (2003), Quantitative Kriging Neighbourhood Analysis for the Mining Geologist – A Description of the Method With Worked Case Examples In Proceedings of the Fifth International Conference on Mining Geology, Bendigo

Platinum behaviour in sulfide and oxide melts during the metallurgical processing of Copper-Nickel ores

Sergei Fedorov,

Institute of Metallurgy, Ural Branch of the Russian Academy of Sciences, Yekaterinburg city, Russian Federation

Alex Amdur

The Ural State Mining University, Yekaterinburg city, Russian Federation

Ivan Blinov,

Institute of Mineralogy, Ural Branch of the Russian Academy of Sciences, Miass city, Russian Federation

Abstract. Platinum extraction from sulfide copper-nickel ores is a multistage process. To make changes in the process technology to reduce metal loss the form in which platinum occurred in the matte and the slag is studied. The materials chosen for this study were compact Cu-Ni and impregnation sulphide ores. Polished sections of smelted products were studied using an optical and scanning electron microscope equipped with an energy dispersive console. The research work reveals that platinum in the matte occurs in the form of chemical compounds containing iron (tetraferroplatinum) and in that of intermetallic compounds containing Fe and Ni. Tetraferroplatinum represents needle-like formations with the length of 20 to 500 microns and with the thickness of up to 10 microns. It is located in the shell of intermetallic compounds. The discovered size effect establishes that the content of impurities in tetraferroplatinum (Cu and Ni) increases with the decrease in its thickness. The slag contains only Pt – Fe – Ni –based intermetallic compounds with a size of no more than 5–7 μm and floated from the matte by gas bubbles.

1 Introduction

The world's main platinum reserves are contained in the layered intrusions of ultrabasic rocks and in sulfide copper-nickel ores. Platinum extraction from sulfide copper-nickel ores is a multistage process. It includes smelting of a prepared concentrate in electric ore smelting furnaces, where the melt is separated into the sulfide matte and oxide slag. Although platinum is concentrated in the matte, a significant part of it remains entrapped in the slag, which results in loss of metal. To make changes in the process technology to reduce metal loss, it is necessary to study the form in which platinum occurs in these phases. This task appears to be important since platinum mineralogy has mainly been studied in mature slag dumps resulting from copper and nickel production (Makarov et al. 2016).

This research work aims at carrying out an experimental study of the forms in which platinum occurs in the matte and slag resulted from the ore smelting process in order to increase its extraction.

2 Materials and Methods

The materials chosen for this research work were compact Cu-Ni sulfide ore and impregnation copper sulfide ore. According to the data obtained from the research, the former consisted of 42.8 wt % pyrrhotite, 20.0 wt % chalcopyrite, 11.3 wt % pentlandite, 16 wt % magnetite, 9.9 wt % silicates as well as 1.5 g/t Pt. Impregnation ore contained 8 wt % sulfides in the form of chalcopyrite and pyrrhotite, with the Pt content amounting to 0.5 g/t.

Samples of ore were heated and melted in corundum crucibles placed in the resistance furnace with a graphite heater at a temperature of 1300 °C for 2 hours. The atmosphere in the furnace is carbon combustion products. Holding time is 1 hour, cooling with the furnace is 1 hour. Products discharged from the furnace were separated into the matte and slag. Polished sections (10 pieces) were prepared to study the mineral composition by means of an Axio Image optical microscope and a Tescan Vega 3 scanning electron microscope equipped with an Oxford Instruments X-act energy dispersive console. The electron beam with diameter of 2–3 μm made it possible to determine the chemical composition with micron accuracy. The elemental content was determined with the accuracy of 0.01-0.02 wt %. In some cases, in order to facilitate the microscopic analysis of particles containing platinum, Pt was added to the ores under examination in a specially prepared spongy form with a particle size not exceeding 100 μm in the amount of 2500-4800 g/t. The added platinum interacts with the ore components during heating, holding at high temperatures and cooling. The chemical composition of the sampling materials was determined by means of a S4 EXPLORER X-ray fluorescence spectrometer.

3 Results and Discussion

While being smelted, ore is separated into sulfide and oxide parts.

After copper-nickel sulfide ore with a natural platinum content (1.5 g/t) was smelted at the temperature of 1300 °C and held for 15 minutes, its sulfide part revealed skeletal tetraenaite crystals (FeNi) which contained single drop-shaped platinum-bearing intermetallic

particles with the size of less than 0.5 μm .

The addition of platinum to the ore made it possible to study the forms of its release in more details. The behaviour was similar to behaviour of natural platinum.

The research work reveals that Pt in the matte occurs in the form of intermetallic compounds and chemical compounds containing Fe and Ni and representing needle-like formations with the length from 20 to 500 μm and the thickness of up to 10 μm , Fig. 1. According to data obtained from chemical analysis (conducted with the help of an energy dispersive console) and X-ray phase analysis these formations are intergrowths of prismatic crystals which appear to be tetraferroplatinum. The crystals are in a double shell which is made up of Pt – Fe – Ni- based intermetallic compound with the thickness not exceeding 1 μm and with the Pt content ranging from 33.55 to 56.55 wt % and which in its turn is rimmed with Fe – Ni alloy. The latter is a chemical compound of tetrataenite. It can also occur separately from Pt compounds in the form of skeletal crystals.

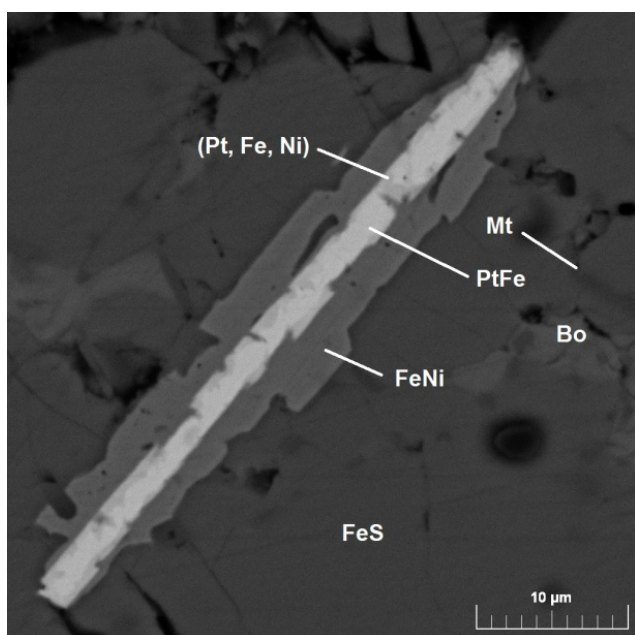


Figure 1. Needle -like tetraferroplatinum extractions (PtFe) in the shell made up of Pt, Fe, Ni and tetrataenite (FeNi) in the total sulfide melt (matte) consisting of troilite (FeS), bornite (Bo) and magnetite (Mt). Compact Cu-Ni ore melted at the temperature of 1300°C. BSE image.

Tetraferroplatinum contains Cu (0.79-2.64 wt %) and Ni (1.86-5.06 wt%) impurities, which is typical for this compound (Vatolin et al. 2016). As has been noted (Cabri et al. 1975), their content grows in a manner similar to that of dispersed Au particles with the decrease in tetraferroplatinum thickness (Fig. 2). The intermetallic compound (Pt, Fe, Ni) contains Cu (1.97-2.56 wt %) and Co (0.27-0.69 wt %) impurities.

According to the results of X-ray phase analysis, the slag consists of 72.4 wt % troilite 10.1 wt% bornite, 7.0 wt % tetrataenite, 4.9 wt % magnetite, 0.32 wt % tetraferroplatinum. Iron as a separate phase in metallic form is not detected.

The research makes it possible to trace the stages of

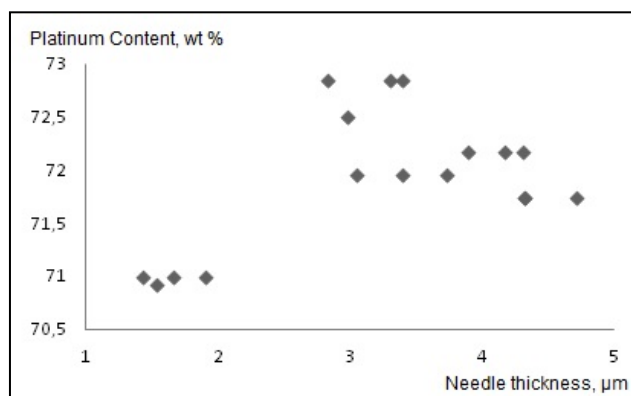


Figure 2. The relationship between the platinum content in the needle-like tetraferroplatinum formations and their thickness.

mineral crystallisation in the process of matte cooling. Tetraferroplatinum is the first to be extracted from the melt due to the high melting temperature. Its needle-like crystals penetrate all the mineral phases in the matte and are evenly distributed throughout the sulfide ingot. Then a thin metal shell of the alloy (Pt, Fe, Ni) crystallises on the tetraferroplatinum surface. Other platinum occurrences even in the form of impurities are not detected. Finally, tetrataenite also crystallises around platinum alloys. The last ones to be extracted from the melt are sulfides: troilite (with isometric, rounded grains) comes first and bornite comes last, thus occupying the remaining space and forming irregular grains. Magnetite occurs in small amounts in a thin shell of wustite, formed together with troilite, both of them having similar grain forms.

During the process of copper-nickel ore smelting, the oxide melt (slag) above the matte becomes porous due to the release of sulphurous gas bubbles. As can be seen from the micrograph (Fig. 3), these bubbles float matte drops up to 1.5 mm in diameter as well as irregular particles of Pt, Fe and Ni intermetallic compounds with a size of between 5 and 7 μm . Consequently, the drops appear in surface layers of the slag.

The oxide melt forms when the impregnation copper ore melts. The research reveals that a significant part of sulfide beads are present in the upper layers of the oxide melt, and all of them are attached to gas bubbles (Fig. 4). This fact also indicates that the flotation process is complete. The diameter of sulfide beads ranges from 8 to 170 μm while the diameter of gas bubbles reaches 300 μm . These beads as well as those in the matte are composed of troilite and bornite. Platinum metal added to the ore in the amount of 4.8 kg / t does not oxidise and occurs in the form of Pt-Fe intermetallic compounds of irregular shape. They are associated with sulfide beads. Since tetraferroplatinum is not formed, the Pt content is lower than that in the metallic phases in the matte, and it varies within the range of 55-63 wt %. The composition of even individual particles varies on the cross section. Impurities are represented by Cu (3.53-3.88) and Ni (0.95-2.52). The Fe-Ni shell is not detected due to the low nickel content in the ore under examination.

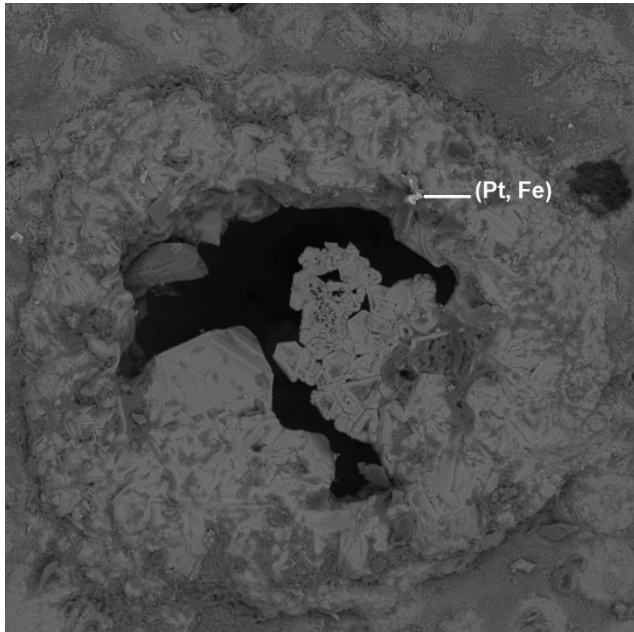


Figure 3. An intermetallic particle (Pt, Fe) on the surface of the oxide melt amid octahedral and skeletal crystals of Fe and Cu oxides. BSE image.

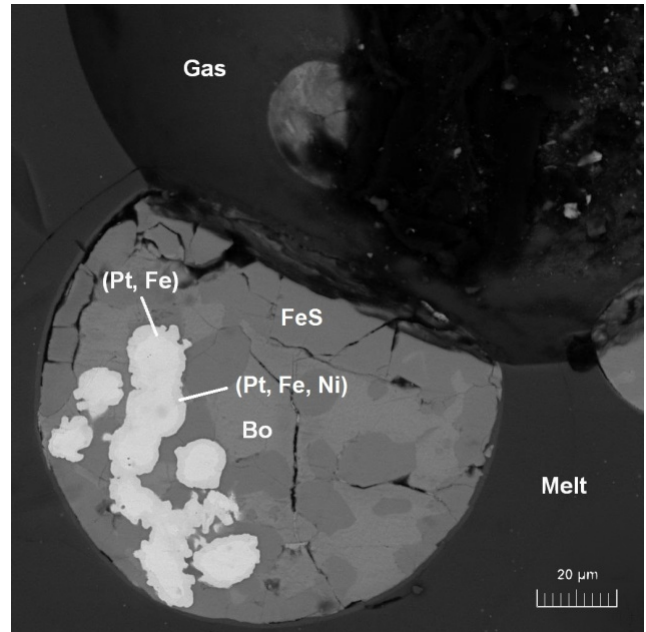


Figure 4. Sulfide droplet trapped by a gas bubble (Gas) in the oxide melt (Melt). The droplet consists of troilite (FeS), bornite (Bo), and Pt-Fe alloy (Pt, Fe). BSE image.

4 Conclusion

The research work reveals that platinum in the matte occurs in the form of chemical compounds containing iron (tetraferroplatinum) and in the form of intermetallic compounds containing Fe and Ni. Tetraferroplatinum represents needle-like formations with the length of 20 to 500 μm and with the thickness of up to 10 μm. It is located in the shell of intermetallic compounds. The discovered size effect establishes that the content of impurities in tetraferroplatinum (Cu and Ni) increases with the decrease in its thickness. The slag only contains Pt – Fe – Ni – based intermetallic compounds with a size of no more than 5–7 μm and floated from the matte by gas bubbles containing sulfur. The bubbles also float the matte drops with the diameter of up to 1.5 mm into the slag. Flotation leads to the loss of valuable metals including platinum.

Acknowledgements

This research work was carried out with support of RFBR grant No. 18-29-24081\18.

References

- Cabri LJ, Feather CE (1975) Platinum–iron alloys: a nomenclature based on a study of natural and synthetic alloys. *Can. Mineral* 13:117-126
- Makarov VA, Mikheev VG, Samorodsky PN (2016) Mineralogy of the slag heaps of the Norilsk Nickel Plant. *Gornyi Zhurnal* 3:50-55. doi: 10.17580/gzh.2016.03.11
- Vatolin NA, Amdur AM, Pavlov VV, Fedorov SA, Matushkina AN (2016) Content of impurities in dispersed ore gold particles depending on their size. *Doklady Physical Chemistry* 470/2:162-164. doi: 10.1134/S00125016161000 67

Beneficiation of parisite-rich rare earth ore from the Nam Xe South deposit, Vietnam

Robert Möckel, Thomas Heinig, Alan Fernando Cardenas Vera, Jens Gutzmer

Helmholtz-Zentrum Dresden-Rossendorf, Helmholtz Institute Freiberg for Resource Technology, Germany

Gerhard Merker

Merker Mineral Processing (MMP), Germany

Van Phan Quang

Faculty of Environment, Department of Environmental Engineering, Vietnam

Abstract. Parisite-rich rare earth element (REE) ores from the Nam Xe deposit in northern Vietnam were beneficiated on a lab scale. Beneficiation experiments included, amongst others, sensor-based sorting, magnetic separation and flotation. Particular analytical focus during all experiments was set on the grain size, association and intergrowth of the main REE carrier mineral parisite, which is finely intergrown with minerals of the barite-celestine solid solution series. All experiments were accompanied by mineral liberation analysis and chemical assays in order to be able to provide direction towards an optimal beneficiation strategy for this REE ore with its rather unique mineralogy. Special focus was set on the grain characteristics of the main REE carrier mineral parisite, which is finely intergrown above all with minerals from the barite-celestine solid solution series.

A multi-stage flotation technique was developed that uses an ambient rougher and a hot cleaner stage. Concentrates with 40% TREO grade with a total recovery of about 80% were achieved. It was shown that a combination with a sensor-based pre-sorting prior to the flotation can increase the input grade for flotation considerably by a nearly loss-free rejecting of virtually barren bed rock. The process combination developed holds good potential for further improvements.

1 Introduction

Nam Xe in northern Vietnam is a large REE deposit that can be subdivided in two geographic parts, located to the north and the south of the Nam Xe river and Ban Man-Phong Tho fault, respectively (Vlasov 1961; Nyugen et al. 2014; Heinig et al. 2019). This study is focused on ores from the southern part of the Nam Xe deposit. Here, mineralization comprises of up to 70 sub-parallel carbonatite dykes and lenses with an overall dimension of approx. 200 x 1000m and thicknesses of 0.3 to 2.5 m within basaltic rocks of Triassic age (Heinig et al. 2019).

Fong-Sam (2013) reported proven reserves at Nam Xe South to be 199,300t of REO and probable reserves to be 3.0 Mt of REO. REE concentrations reported for the Nam Xe South carbonatites are as follows: TREE from 3,400 to 6,100 ppm in calciocarbonatites, and from 43,200 to 163,900 ppm in ferrocyanatites, respectively (Nguyen 2013; Nguyen Thi et al. 2014).

Detailed mineralogical studies (Heinig et al. 2019) revealed that parisite $\text{Ca}(\text{REE})_2[\text{CO}_3]_3(\text{F},\text{OH})_2$ is the main REE-bearing mineral in the ores of Nam Xe South. Other rare earth fluoro-carbonates, such as bastnäsite $(\text{REE})[\text{CO}_3](\text{F},\text{OH})$ and synchysite $\text{Ca}(\text{REE})(\text{CO}_3)_2(\text{OH},\text{F})$ occur only in minor amounts. The ore also contains considerable amounts of baryto-celestine, i.e. minerals of the baryte-celestine solid solution series (Hanor 2000), calcite, biotite and magnetite. Especially the baryto-celestine is finely intergrown with parisite on a sub 100 μm -scale (Heinig et al. 2019).

The dominance of parisite as REE ore mineral and the close association between parisite and baryto-celestine render the mineralogy and mineral association of the REE ores of the Nam Xe South deposit as rather unique. Little is known about the mineral processing characteristics of parisite – as compared to the much more common bastnäsite (Pradip & Fuerstenau 2013) and monazite (Lucas et al. 2015). Extensive lab-scale beneficiation test work was thus carried out in order to assess possible processing routes for these ores.

2 Materials and methods

For processing experiments material from surface outcrops and two diamond drill cores (0512, 0709) of the Nam Xe South deposit was used.

Initial sensor-based sorting experiments were carried out to differentiate groups of host rocks and ores. “Red ore” represented carbonatite ore with the highest expected REE content; this was distinguished from REE-poor portions of the carbonatite dykes (including baryto-celestine and carbonates), “yellow ore” representing fenitized but barren host rocks, and “dark green” host rock. Sensor-based sorting (SBS) including different sensor set ups (optical, NIR, X-ray transmission, X-ray fluorescence) were used to separate these groups of materials. A second series of tests was made to separate host rock (“dark green” and “yellow ore”) from dyke material. For this final feasibility test we used a blend of ore material and host rocks (~50kg) with a ratio of 1:4, respectively. Experiments were done using the size fraction 16-31.5mm at the facilities of TOMRA, Hamburg, Germany.

For post-sorting comminution and beneficiation tests

host rocks and carbonatite dykes were mixed in an approximate 1:1 ratio to obtain a blend similar to an expected feed material from an eventual sensor sorted material from the mine. Material from more than ten individual carbonatite dykes and basaltic host rocks was mixed to form a total of 400 kg of sample blend that was available for beneficiation experiments including magnetic separation (MS), particularly wet high intensity magnetic separation (WHIMS), classification and desliming. Another comprehensive set of experiments was done with special focus on flotation.

To evaluate both the success and optimization potential of the above-described beneficiation test work a number of analytical methods were applied, including SEM-based image analysis on a Mineral Liberation Analyzer (MLA) and X-ray powder diffraction for mineralogical analysis, and X-ray fluorescence spectrometry and ICP-MS for chemical assays. MLA data was also used to determine the degree of liberation, grain size distributions, mineral associations, etc. These data were used in iterative steps to optimize parameters of subsequent flotation tests.

Up to now, no reference is known about beneficiation tests on REE-ores with parisite as main REE-mineral using SBS, MS and flotation.

3 Results and discussion

Custom beneficiation for unique, small scale deposits and mining operations typical aims for mass flow reduction and high recovery rate. This can be achieved by various methods, e.g., selective mining, sensor-based sorting before or in between comminution, magnetic separation, selective grinding and custom flotation. However, a deep

understanding of the deposit and the mineral properties is needed to select and design the suitable beneficiation methods.

Petrographic observations and MLA data of drill core surface rock samples reveal that the REE fluorocarbonate parisite is more abundant than bastnäsite. Parisite is fine-grained (10-300 µm) with typical euhedral and pyramidal crystals and is intimately associated with barytocelestine and calcite. Sample sections containing parisite display reddish colors and are optical distinguishable from the surrounding carbonatite minerals.

This sharp contrast between ore and gangue material, which not only applies to color but also to average electron density is used by XRT (X-ray transmission) sensor to presort the sample material. At a particle size of 16-31.5 µm, a sorting approach resulted in 88% product to product and 90% waste to waste rate for a 0.1% TREO cut-off and 100% product to product and 81% waste to waste rate for a 0.5% TREO cut-off. Almost all material from the host rock and barren gangue went into the waste fraction. With the final feasibility test on bigger scale, a very little REE-loss of less than 3 % in the virtually barren rejected host rock was confirmed.

Therefore, we conclude that a pre-enrichment via SBS is possible and favorable reducing the mass stream significantly and upgrading the beneficiation feed. Gangue mineral which have similar average electron densities are the remaining challenge of XRT sorting. In case of Nam Xe, barytocelestine and barite display no significant different signal compared to parisite and are part of the sorting concentrate.

Lab scale grinding tests were carried out to deal with the parisite-barytocelestine association of the XRT

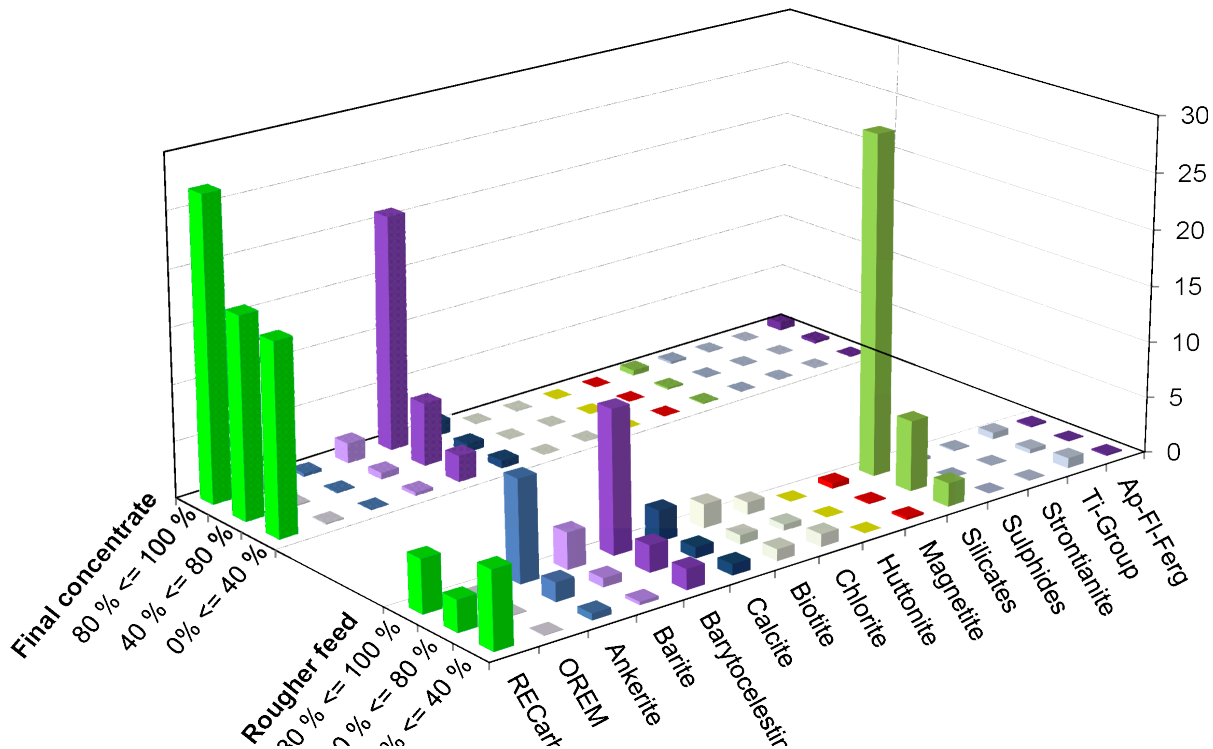


Figure 1: MLA mineral composition and liberation data of the final concentrate and rougher feed. All bars of the mineral group sum up to 100%.

product and to evaluate an optimal size-liberation fraction for batch flotation test series. Sieving and MLA data reveal an expected parasite liberation increase from the particle sizes fraction +180 μm where only 30 % of the parasite grains are >70 % liberated to – 10 μm where 98.8 % of the parasite grains are >70 % liberated. For the medium size fractions, the values of parasite showed elevated liberation for each of the fractions, starting with the 63-90 μm fraction where approximately 75% of the parasite display high liberation. For further beneficiation, this would mean an optimal composition after grinding and no further grinding down to <32 μm , since the fraction of 63-90 μm is already indicating elevated liberation values for the main target mineral with a particle size that is suitable for both flotation and magnetic separation.

A series of wet high intensity magnetic separation (WHIMS) experiments did not deliver conclusive results. On the one hand, a good separation was observed with magnetite deporting to the 1st product (low intensity magnetic product) and the majority of barytocelestine to the non-magnetic product. On the other hand, ankerite, the phyllosilicates, and Fe-silicates deported unspecifically. Even if the REE contents were almost doubled in the 3rd product (high intensity magnetic), no clear separation of parasite into one product could be achieved as they appear to deport in all products including the non-magnetic product. Although magnetic separation is described as feasible tool in bastnäs site beneficiation (e.g. Jordens et al. 2014, 2016) we could not find a suitable separation parameter.

In an experimental matrix on a 1:1 model blend of about 7 % REE-input grade, more than 50 flotation experiments were done. Thereby, the flotation reagents were chosen from a limited array of oleyl sarcosines, hydroxamtes, and lingo-sulphonates based on individual experience and literature for comparable bastnäs site flotation (Pradip & Fuerstenau 2013). Other parameters like pH, grain size (including de-sliming), and temperature were changed systematically.

The first flotation test series was setup as two-step rougher flotation with a scavenger followed by a 3 step cleaner flotation and a cleaner scavenger. MLA and bulk chemical analyses were carried out on the products of the flotation experiments, and evaluated with special regard to the rare earth carbonates and their grain characteristics. The data displayed an enrichment of REE fluorcarbonates by a factor of 2.2 in the rougher stage and 3.4 from feed to final cleaner concentrate. Furthermore, MLA data of the flotation stages reveal a problem with the parasite-barytocelestine association as barytocelestine reached similar enrichment factors like parasite and data of the cleaner tailing revealed a lack of parasite liberation (Fig. 2).

Due to these observations, flotation tests were redesigned with a two-step rougher flotation and a scavenger where the concentrate is re-fed into the wet milling followed by a wet re-grind of the rougher concentrate to minus 40 μm feeding into a 3 step cleaner flotation with a the scavenger of the first cleaner tailing. The cleaner scavenger concentrate is re-fed into the regrinding stage before the cleaners. MLA data revealed a REE fluorcarbonate enrichment by the factor of 2.5 in

the rougher stage and 4.4 (Table 1) from feed to final concentrate, respectively.

Table 1: MLA mineral composition data (wt%) of all REE fluorcarbonates and barytocelestine of the initial (first) and the final (last) flotation setup.

	REE-fluorcarbonate		Barytocelestine	
	[wt%]		[wt%]	
Test setup	first	last	first	last
Rougher feed	13.2	14.1	16.5	16.6
Rougher concentrate	29.3	36.0	34.8	36.5
Rougher scavenger conc.		26.5		24.9
Rougher tailing	1.1	1.6	2.7	5.3
Cleaner concentrate	44.9	61.9	40.9	29.1
Cleaner scavenger conc.		67.6	44.9	20.2
Cleaner tailing	11.7	18.3	27.9	41.5

Finally, TREO concentrate grades of more than 40 wt% were reached in the cleaner stage. The most effective way turned out to be a combination of cold (rougher) flotation on de-slimed ore at a coarser grain size (minus 100 μm), and a subsequent hot (cleaner) flotation after regrinding down to minus 40 μm . The REE loss of the de-sliming procedures was found to be below 8 %. In contrast to the initial liberation evaluation, the regrinding step was a need to get a better grade than 35 % REO.

Further tests including intensive screening of further collectors and additional depressants are supposed to reveal potential for further improvement of these results – particularly with respect to the parasite-barytocelestine separation.

4 Conclusion

We have shown for the first time that it is possible to beneficiate an uncommon parasite containing ore. In this case, a combination of sensor based sorting and subsequent two-step flotation setup led to concentrates with more than 40% TREO contents. Our experiments also revealed that parasite shows different beneficiation characteristics than common bastnäs site in terms of magnetic separation techniques and also flotation methods.

Physical Separation of the REE fluorcarbonates and barytocelestine will be the next challenge to further improve the concentrate, preliminary leaching tests of the achieved concentrates revealed promising results, nevertheless. Locked cycle tests or mini piloting is necessary to verify the lab scale results and unveil further optimization potential.

Acknowledgements

The team of the Faculty of Environment from Hanoi University of Mining and Geology is thanked for organizing the Vietnamese part of the project including sampling and data acquisition. The Vietnamese Ministry of Science and Technology (MOST, Code

NDT.02.GER/15) and the German Federal Ministry of Education and Research (BMBF, grant number: BMBF 033R120B) are acknowledged for funding this international research project (NAMXE). Furthermore, we thank the Hung Hai Group for providing access to exploration drill cores.

References

- Fong-Sam Y (2013) The Mineral Industry of Vietnam. 2011 Mineral Yearbook. USGS.
- Honor J S (2000) Barite-celestine geochemistry and environments of formation: Sulfate Minerals - Crystallography, Geochemistry and Environmental Significance, 40:193-275.
- Heinig, T, Burisch M, Möckel R, Phan Q V, Ebert D, Gutzmer (in prep.) Mineralogy, petrography and genesis of REE bearing carbonatite dykes, NamXE deposit, Vietnam
- Jordens A, Sheridan RS, Rowson A, Waters K (2014) Processing a rare earth mineral deposit using gravity and magnetic separation. *Minerals Engineering* 62:9-18
- Jordens A, Marion C, Langlois R, Grammatikopoulos T, Rowson NA, Waters KE (2016) Beneficiation of the Nechalacho rare earth deposit. Part 1: Gravity and magnetic separation. *Minerals Engineering* 99:11-122
- Lucas J, Lucas P, Le Mercier T, Rollat A, Davenport W (2015) Rare Earths: Science, technology, Production and Use. Elsevier B.V.
- Nguyen T (2013) Study on geochemistry of the South Nam Xe carbonatites, north-west Vietnam. Shizuoka University.
- Nguyen T, Wada H, Ishikawa T, Shimano, T (2014) Geochemistry and petrogenesis of carbonatites from South Nam Xe, Lai Chau area, northwest Vietnam. *Mineralogy and Petrology*, 108(3):371–390.
- Pradip P, Fuerstenau DW (2013) Design and development of novel flotation reagents for the beneficiation of Mountain Pass rare-earth ore. *Minerals and Metallurgical Processing*, 30(1):1-9
- Vlasov I (1961) Concluded report of exploring project on Nam Xe rare earth ore deposit (1958-1960 stage). Documented in Institute of Geological Informations Archives and Museum.

Gold and critical element recovery with environmentally-benign Deep Eutectic Solvents

Gawen R. T. Jenkin, Hugh Graham, Daniel J. Smith, Rumana Khan, Andrew P. Abbott, Robert C. Harris, David A. Holwell
University of Leicester

Shaun D. Graham, Rumana Khan
Carl Zeiss Microscopy Ltd., Cambridge

Christopher J. Stanley
The Natural History Museum, London

Abstract. Gold concentrates often contain significant enrichments of scarce or critical elements such as Te, Bi and Sb, but there are few financial incentives for recovery of these elements as by-products. Deep eutectic solvents (DES) may provide novel processing opportunities – these are a form of ionic liquid that are mixtures of salts such as choline chloride with hydrogen-bond donors such as urea. DESs are environmentally benign and the components are already produced in large quantities at low cost.

We have demonstrated that gold is rapidly dissolved in DES by iodine oxidation, whereas many base metal sulfides are unreactive or react only slowly. However, we show that trace minerals that host the majority of Te, Bi and Sb in a concentrate, such as native Te and Bi, tellurides, and Bi- or Sb-sulfosalts, are rapidly dissolved at similar rates to gold, suggesting routes to recovering gold *and* critical elements.

The etching rate shows systematic patterns in homologous mineral series, e.g. Ag_2Te leaches faster than Ag_2S which leaches faster than Ag_2Se . In all cases the selenide leaches the slowest. These observations, together with liberation analysis, enable us to predict and quantitatively model the bulk leaching behavior of ore concentrates and design bulk leach tests.

1 Introduction

Mineral deposits are geochemical anomalies where useful elements become highly concentrated by geological processes to the extent that they are economically exploitable. As well as concentrating target elements, such as gold, PGE or copper, these processes often enrich the ore deposit in a suite of geochemically related elements - a feature that is used in mineral exploration. For example, orogenic gold deposits can also be variably enriched in Te (Spence-Jones et al. 2018), Sb, W, Se, or Bi. Importantly, these associated elements are often categorized as critical or near-critical elements that are essential for modern technology, in particular environmental technologies, but may be subject to supply restrictions. However, recovery of critical elements as by-products alongside the main commodity (product) is either very inefficient or not carried out at all. This is because such by-products

contribute little value to the deposit due to low price combined with low volumes (e.g. Te, despite being nearly as rare in the Earth's crust as Au, has a monetary value ~400x less), and the prices of small commodities such as Te may fluctuate wildly, which deters a producer from investing in dedicated recovery circuits. One possible scenario is shown in Fig. 1a. Here much of the potential by-product is sent to tailings because it is not the focus of beneficiation. Even if some or all of the by-product is carried into the concentrate sent for refining generally the revenue returned from the refiner to the producer does not include any value for the by-product – even though the refiner may recover it and indeed make some profit on it. In some cases, a potential by-product may be classed as a penalty element by the refiner and actually reduce the revenue for the producer. Hence, in this example and many other scenarios, there is no financial incentive for the producer to optimize the recovery of the by-product, although for Se and Te sending them to the tailings may risk creating a future environmental liability.

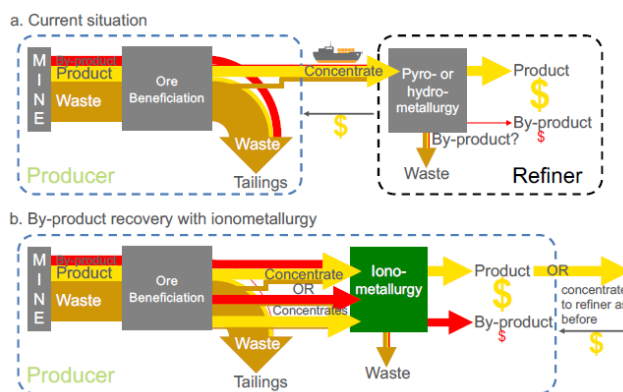


Figure 1. a. Scenario where critical element by-product containing minerals are not the focus of beneficiation and are dominantly sent to waste. Even if recovered by refiner no revenue is returned to producer. b. Possible change in processing if by-product elements can be recovered along with the primary product using DES. Product = Au, by-product = Bi, Te, Sb.

To find a mineral deposit, develop it, mine and crush ore, and extract the product metal, involves a substantial amount of energy (that translates to CO_2 footprint) and cost. Therefore, once ore is mined, the resource use is more efficient and has less impact on the environment if

the largest possible range of by-products can be extracted. This however requires a change to the current paradigm of resource use by making it economic to recover a greater range of by-products.

A notable feature of the elements Bi, Te, and Sb in many gold deposits, it that these elements tend to combine to form discrete minerals, rather than substitute into sulfides. Although these minerals are usually only present in trace concentrations this presents an opportunity for by-product recovery by targeted leaching of these minerals. It has previously been shown that DES have the potential to rapidly leach gold in a low-energy environmentally-benign process (Abbott et al. 2015; Jenkin et al. 2016). Here, we show that Bi, Te and Sb minerals are also rapidly leached in DES, opening the potential for their recovery along with the gold.

2 Methodology

Measurement of the etching rate of a range of minerals in a DES was carried out using the *in situ* method described in detail by Jenkin et al. (2016). In brief, target mineral grains were identified in polished blocks and thin sections and immersed in the DES for leaching. The depth of etching vs. time was determined by imaging the samples before and after etching with an optical profiling microscope and measuring the difference in surface relief across the mineral grain. Ideally, two or three leaching steps were measured, and etching was shown to be linear with time within error. Where only one measurement was possible the rate determined is a minimum. The DES used was Ethaline (1 mol choline chloride: 2 mol ethylene glycol) containing 0.1 molar iodine as the oxidizing agent. Experiments were run at 50°C unless otherwise stated and leach steps varied from 5-60 minutes.

3 Results

Measured etching rates vary over two orders of magnitude from 0.01-1 µm/minute (Fig. 2). The lower value is the practical limit of the method, and some slower etching may be occurring in other minerals, although usually visual observation shows no change suggesting they are unreactive. Previously it has been shown that silicate and carbonate gangue minerals are unreactive, as is pyrite under these conditions (Jenkin et al. 2016).

Our new data confirm that Au, as native gold and electrum, dissolves very rapidly, with electrum tending to dissolve faster. Jenkin et al. (2016) reported a *minimum* rate for electrum of 0.17 µm min⁻¹, whereas we show here rates ranging from that value (for an isolated grain in a placer sample) up to 0.56 µm min⁻¹. For comparison, the maximum rate of etching of gold by cyanide at 25°C is ~0.004 µm min⁻¹ (Wadsworth et al. 2000) – gold leaching rates with DES are 40-130 times faster. Our dissolution rate is at 50°C vs. 25°C used by Wadsworth et al. (2000) but room temperature dissolution with DES at realistic rates looks perfectly feasible. Our rates translate to complete leaching of even coarse gold grains in 1-2 hours in DES providing

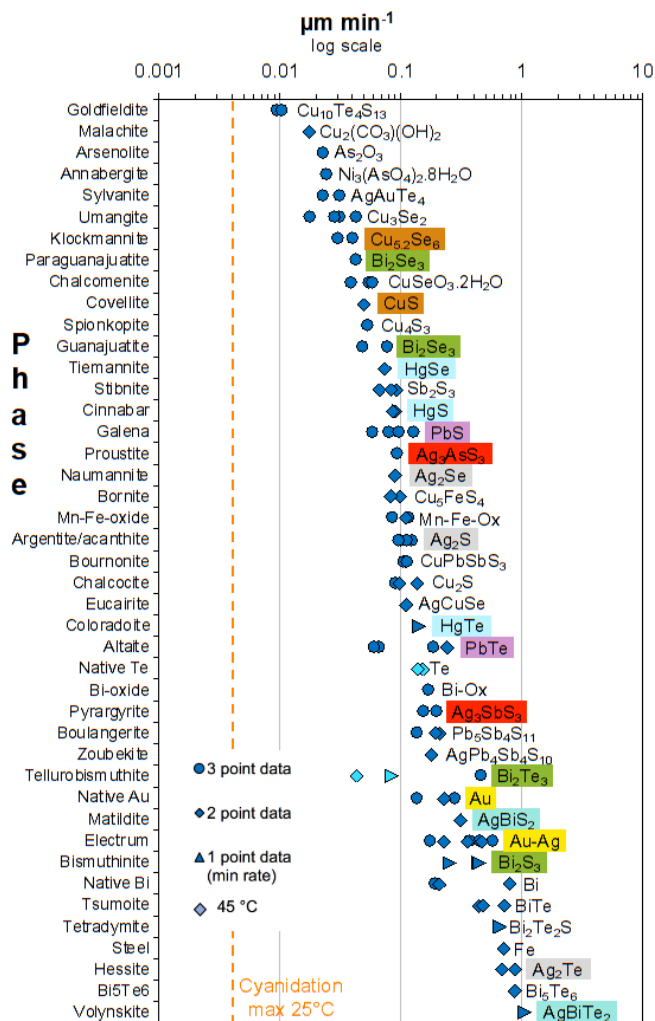


Figure 2. Etching rate data for a range of base metal and by-product bearing minerals in Ethaline with iodine oxidizing agent at 50°C (unless labelled otherwise). Homologous series of minerals are colour coded.

the potential as an alternative lixiviant to cyanide.

A range of Ag-, Bi- and/or Te-bearing minerals, including tellurides, sulfides, sulfoalts and native Bi and Te, are shown to etch as rapidly, and in some cases faster, than electrum. In contrast, Sb-bearing minerals tend to etch at slower rates, and selenides and copper minerals rather more slowly still – although still significantly faster than the cyanidation rate of gold and thus still a potentially viable leaching process.

Crystal chemical controls on etching rate can be identified by examining homologous series of minerals. In general either the sulfide or the telluride etches most rapidly, whereas the selenide is always the slowest. For example, Ag₂Te (hessite) etches much more rapidly than Ag₂S (argentite) which in turn is more rapid than Ag₂Se (naumannite). The same pattern is observed for mercury chalcogenides – with etching rates HgTe >> HgS > HgSe. For Bi chalcogenides etching rates are Bi₂S₃ > Bi₂Te₃ >> Bi₂Se₃. Interestingly there may be a distinction between the two polymorphs of Bi₂Se₃ with guanajuatite recording a 50% higher rate than paraguanajuatite. A possible alternative explanation for

the range of data for Bi_2Se_3 , and for some other minerals, is that different crystallographic faces may be etching at different rates in anisotropic structures – Jenkin et al. (2016) suggested a difference of 50% in the etching rate for tellurobismuthite (Bi_2Te_3) with etching parallel to the c-axis being faster than perpendicular to it. In general, it is difficult to precisely determine the crystallographic orientation of individual grains and so be definitive as to whether it is crystal structure or grain orientation that is causing the difference for Bi_2Se_3 .

Crystal chemical effects likely also explain the etching rate difference between the sulfosalts proustite Ag_3AsS_3 and pyrrargyrite Ag_3SbS_3 which etches twice as fast.

4 Case study – Bi leaching from gold ore

The *in situ* etching rate data can be used in combination with grain size and liberation data obtained from automated mineralogy to understand and ultimately predict bulk leach data with DES for specific ore concentrates. An example of bismuth leaching from a Colombian gold ore sample with DES is described here (Khan 2018).

4.1 Ore mineralogy and Bi and Se department

The ore is geochemically complex, containing significant concentrations of Bi and Se, along with Au and Ag. This is reflected in the mineralogy, with Se hosted completely within paraganajuatite Bi_2Se_3 , but Bi is distributed among a range of phases in addition to paraganajuatite including, bismuthinite Bi_2S_3 , native bismuth, matildite AgBiS_2 and cosalite $\text{Pb}_2\text{Bi}_2\text{S}_5$ (Fig. 3).

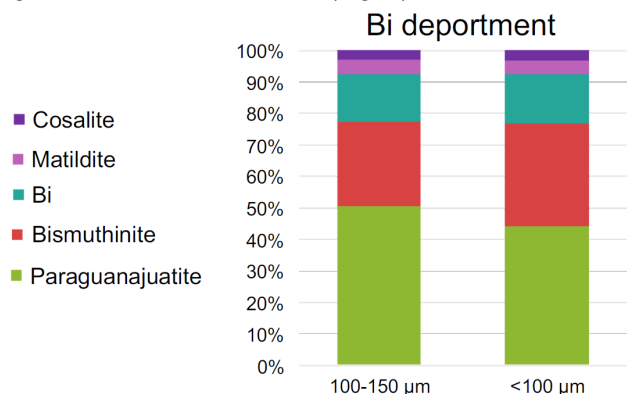


Figure 3. Bismuth elemental department in Colombian gold ore sample.

4.2 Bulk leaching methodology

Aliquots of 100 g of sample was added to 300 ml of Ethaline with 0.1M I_2 on a hotplate at 50°C. This amount of iodine represents a large over excess (~10x) of the amount required to oxidize the soluble metals in the sample. The solution was stirred for times ranging between 20 and 300 minutes and then the reaction was quenched by adding 300 ml of sodium thiosulfate at a concentration of 2M to convert the remaining iodine to non-reactive iodide (control tests have shown that thiosulfate does not react with gold under these neutral to

slightly acidic conditions). The residue was separated from the solution by centrifuge, washed 3 times with water to remove residual solvent, and then analyzed to determine the concentration of elements remaining.

Predicted leach-time curves for relevant minerals are calculated from the mineral etch rate data and maximum and minimum grain sizes using a shrinking sphere model and assuming that the minerals are perfectly liberated. No etch rate measurements have been possible on cosalite so it was assumed to etch at the same rate as matildite.

4.3 Bulk leaching results

Bismuth release is rapid in the first 20-30 minutes of leaching, with nearly 70% of Bi being released in these first steps (Fig. 4). Thereafter Bi release is negligible, and all data are within experimental error.

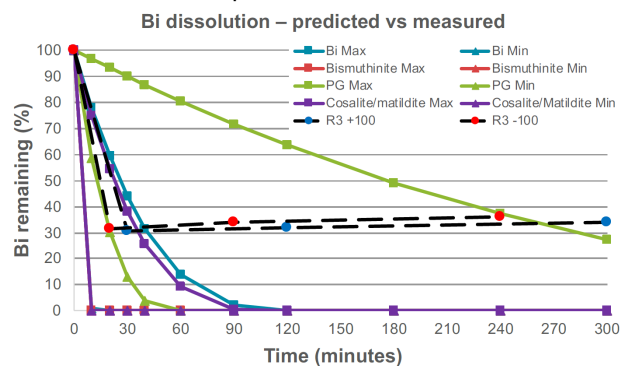


Figure 4. Bismuth leaching from two size fractions of Colombian gold ore in Ethaline with iodine oxidizing agent. Black dashed lines are measured leaching data, coloured curves are maximum and minimum predicted leach-time curves for different minerals from etch rate data and grain size estimates. Bismuthinite is fine grained and lies behind the lower cosalite curve. Initial Bi = 537 ppm <100 µm fraction, 689 ppm 100-150 µm fraction.

The remarkable dog-leg shaped release curve for Bi is actually well-explained from our knowledge of the etch rates of the component minerals and their liberation. Se is contained only in paraganajuatite which is relatively coarse-grained and relatively slow to etch (Fig. 2). As a result, Se-release (not shown) is slow and is still leaching at ~90 minutes – as well as very incomplete (only 10-20% released in 300 mins). The latter is an effect of the slow etching rate, but also the poor liberation with ~56% being classed as locked and therefore unavailable for leaching. Approximately half the Bi is also contained in paraganajuatite (Fig. 3) and so the slow/negligible release of Bi after 20-30 minutes can also be explained by the slow leaching and locked nature of the Bi_2Se_3 . In contrast, the other Bi minerals have leaching rates about 10x faster (Fig. 2), and bismuthinite, which contains about 25% of the Bi is the sample, is also much finer grained. In combination, this means that these phases leach rapidly and account for the early steep part of the Bi-release curve.

5 Implications

Our new data not only confirm that gold will be leached very rapidly with a DES solvent, but also demonstrate that a range of Bi, Te and Sb-bearing minerals will also be leached on similar timescales, subject to liberation. In contrast, major gangue phases including pyrite will be unaffected. This behavior presents the opportunity to leach not only the valuable gold product, but simultaneously extract the critical elements that have already been pre-concentrated into discrete trace minerals. This enables alternative processing scenarios such as that shown in Fig. 1b. Here, by-product elements can be extracted from concentrates along with gold using environmentally benign ionometallurgy with DES. This generates an additional revenue stream that can benefit the producer as it can be done in a smaller scale process in-house. Because the producer has a financial incentive to also focus on the by-products as well as the gold, the recovery of by-product bearing minerals in beneficiation circuits can be optimized. This in turn leads to greater resource use efficiency and diversifies supply of critical e-tech elements.

Acknowledgements

This work was funded by NERC Minerals Security of Supply (SoS) grant NE/M010848/1 Tellurium and Selenium Cycling and Supply (TeaSe) and the University of Leicester Research Impact Development Fund. R. Khan's MGeol project was supported by Carl Zeiss Microscopy Ltd and we are grateful to Dr Edward Hill for providing the Colombian samples.

References

- Abbott AP, Harris RC, Holyoak F, Frisch G, Hartley J, Jenkin GRT (2015) Electrocatalytic Recovery of Elements from Complex Mixtures using Deep Eutectic Solvents. *Green Chem* 17:2172-2179. DOI: 10.1039/C4GC02246G.
- Jenkin GRT, Al-Bassam AZM, Harris RC, Abbott AP, Smith DJ, Holwell DA, Chapman RJ, Stanley CJ (2016) The application of deep eutectic solvent ionic liquids for environmentally-friendly dissolution and recovery of precious metals. *Minerals Eng* 87:18-24, DOI: 10.1016/j.mineng.2015.09.026.
- Khan R (2018) The application of deep eutectic solvent ionic liquids as an alternative to mercury use in small scale gold mining in Colombia. Unpublished MGeol thesis, University of Leicester.
- Spence-Jones C, Jenkin GRT, Boyce AJ, Hill NJ, Sangster CJS (2018) Tellurium, magmatic fluids and orogenic gold: An early magmatic fluid pulse at Cononish gold deposit, Scotland. *Ore Geol Rev* 102:894-905. DOI:10.1016/j.oregeorev.2018.05.014
- Wadsworth ME, Zhu X, Thompson JS, Pereira CJ (2000) Gold dissolution and activation in cyanide solution: kinetics and mechanism. *Hydrometall* 57:1-11.

The development and future impact of biotechnologies for mineral processing and metal recovery

David Barrie Johnson

School of Natural Sciences, Bangor University, U.K.

Abstract. The continued upsurge in global demand for metals, both in scale and in the range used for industrial, domestic and “green” technologies, means that vast amounts of untapped primary resources will have to be exploited well into the foreseeable future. Traditional metal mining is a major consumer of energy and producer of carbon dioxide and has the reputation, often deserved, of having permanently degraded large areas of the terrestrial environment. The conflict of society’s hunger for metals but its increasing alarm of the environmental consequences of how they are obtained requires urgent resolution. Biotechnologies that can effectively extract metals from minerals and recover them, often selectively, from process liquors, have been used for over 50 years, but remain very much niche technologies. The potential for using the unique abilities of microorganisms for metal production is vast, but to realize this requires paradigm shifts in how mining industries operate.

1 History and *modus operandi* of biomining

Using microorganisms to extract and recover metals from ores has a long history. In the middle ages, miners at copper mines in Spain, China, Wales, and probably elsewhere, learned that, if they allowed shafts and adits to flood periodically, released the water into lagoons, and then added metallic iron to ponds, it was possible to recover metallic copper. The “transformation” of iron to copper was often perceived as a form of alchemy, but the same electrochemical reaction is still used widely to produce “cement copper” from pregnant leach solutions generated at dump biomining operations. The modern era of biomining began within a decade of the discovery of a bacterium that was shown to catalyse the oxidation of ferrous to ferric iron in low pH water bodies and the demonstration that this isolate and some related bacteria could accelerate the oxidative dissolution of pyrite (FeS₂), the most abundant sulfide mineral in the lithosphere. These bacteria have the ability to indirectly harness the energy “locked up” in sulfide minerals (as reduced sulfur and metals) and, in, degrading these they release metals that are integral to or associated with these minerals, most of which are retained in solution in low pH bioleach liquors, facilitating their downstream capture. Many commercially-important transition metals, such as copper, cobalt, nickel and zinc, occur either predominantly or in significant amounts in the lithosphere as sulfide minerals, whereas others, such as native gold and uranium (in uraninite) are associated with sulfidic minerals (pyrite, arsenopyrite, etc.) in some ore deposits. Depending on the nature of the target metal, these are either solubilised (bioleaching) or made accessible to

chemical extractants (bio-oxidation) in biomining operations.

Microorganisms involved in the bioleaching/bio-oxidation of sulfidic ores, and the mechanisms by which they accelerate their oxidative dissolution, are now well known (Schippers and Sand, 2013; Johnson, 2014; Harrison, 2016). Rather than this being the remit of a unique bacterium, >30 species are now known to play direct and indirect roles in biomining, and the key to their success is the fact that they operate as microbial consortia, rather than as individuals. A fundamental characteristic of all these species is that they are extremely acidophilic (i.e., they grow optimally at pH 3 or less) as biomining is carried out using low pH lixiviant solutions. Three groups of acidophilic microorganisms have been found in all biomining environments: (i) the “oxidant manufacturers”, acidophiles that oxidise ferrous to ferric iron, which acts as the primary chemical oxidant of pyrite and other sulfidic minerals; (ii) the “acid generators”, that oxidise the sulfur moieties in the minerals, generating sulfuric acid and thereby help to maintain acidity levels in the range that are suitable for biomining consortia (generally below pH 2) and the chemical attack of the minerals by soluble ferric iron; (iii) the “janitors”, which degrade organic carbon compounds exuded by active prokaryotes and lysed from dead cells, which would otherwise potentially accumulate and inhibit groups (i) and (ii).

2 Current status of mineral bioprocessing

The modern era of biomining began in the mid-1960s with the dump leaching of run-of-mine copper waste rocks in mines operated by the (then) Noranda corporation in the USA. Dump leaching is still commonly practised to recover copper, but the more precise engineering design of thin layer heaps has emerged as often more efficient (certainly in the time required to complete an operation) and has been used widely in Chile and elsewhere to bio-process mineral concentrates as well as crushed ore (Brierley and Brierley, 2013). *In situ* bioleaching, which essentially operates in the same way to the mediaeval practices, was used to extract residual uranium from worked out mines in Canada in the 1970s, and contrasts with tank leaching, used primarily as a preliminary stage to liberate gold from refractory ores, which is highly engineered but relatively rapid. However, despite its apparent “green credentials”, biomining has remained a niche rather than mainstream technology in the metal mining sector. Current estimates are that biomining accounts for ~15% of global copper production, 5% of gold, and smaller percentages of other metals (e.g., zinc,

nickel, and uranium). There are, however, a number of reasons for this, one being the relative slowness of the process compared with pyrometallurgical and alternative hydrometallurgical (e.g., pressure leaching) options. Bioprocessing in tanks generally takes several days to complete, heap leaching takes 1–3 years, while dump leaching can last up to or even well beyond five years. Other reasons include, as mentioned, the current limitation of bio-processing, at full-scale, to reduced ores only, the occasional mistrust of “bio”-based processes in some parts of the mining sector, and the need to maximise the use of existing large-scale investments, such as smelters, rather than to diversify into alternatives. There have also been a few situations where biomining has failed or has been linked with environmental problems. Protagonists of biomining have often also overplayed its green credentials. Many of the energy-demanding and CO₂-generating processes involved in conventional (smelting-based) mining are also, by necessity, used in biomining operations, in particular, tank leaching of mineral concentrates. Although the main microbial players in conventional biomining are autotrophic bacteria (i.e., they capture carbon dioxide) this minor advantage in net carbon budget is more than offset by the CO₂-producing pre-processing steps required. However, some of the emerging applications of mineral bioleaching, described below, can minimise or avoid some or all of the ore processing stages and thereby have potential major advantages in terms of carbon/energy budgets.

3 Niche applications for biomining

There are a number of existing situations where biomining has significant advantages over conventional mineral extraction and processing, such as bioleaching primary and secondary copper sulfide ores in sites where solvent extraction-electrowinning (SX-EW) plants have previously been installed for processing pregnant leach solutions (PLS) from acid-leaching of copper oxide ores. Bio-processing is also a feasible alternative in situations where producing a mineral concentrate is problematic, as with the polymetallic black schist ore at Talvivaara, Finland, where the high (~10%) graphite content of the deposit precluded the production of a suitable concentrate. Metal sulfide ores often contain significant concentrations of arsenic, which occurs in arsenopyrite (FeAsS), orpiment (As₂S₃), realgar (AsS/As₄S₄) and other minerals. Smelting mineral concentrates that contain high levels of arsenic incurs a penalty, which is often circumvented by blending these with other concentrates with lower arsenic contents, though the net amount of the metalloid released in gas plumes is ultimately unchanged. In hydrometallurgical mineral processing (which includes biomining), the arsenic released by oxidative dissolution of sulfide minerals is retained in solution (principally as arsenate, H₂AsO₄⁻) and can be effectively removed downstream by, for example, the adsorption onto positively charge ferric iron minerals or as the mineral scorodite (FeAsO₄·2H₂O) (though the

latter has to be crystallized to enhance its stability, which adds to costs).

One particular area where bioleaching can be highly effective, both in terms of metal recovery and environmental protection, is for processing solid mine wastes in general, and mine tailings in particular. Due to the fact that mineral separation techniques in the past were not as efficient as they are at present, historic tailings may still contain significant concentrations of valuable metals. These may be the original metal(s) that was mined or one or more other metals that were not considered at the time, on economic grounds, to warrant extraction. Since tailings deposits have already been through the cycle of extraction and haulage, grading, comminution, and froth flotation, bio-processing of these has particularly strong “green” credentials.

4 Recent innovations in mineral bioprocessing

Current biomining operations focus exclusively on reduced (sulfidic) ores and concentrates, where specialized microorganisms are used to accelerate the destruction of metal-containing minerals by the process of oxidative dissolution. Many commercially important metals also occur in significant abundance in oxidized ore bodies, such as laterites (e.g. an estimated 72% of terrestrial Ni reserves are thought to be found in laterites, though most of the metal currently comes from sulfidic ores). Nickel in limonite is associated mainly with ferric iron minerals, such as goethite (FeO(OH)). Consortia of acidophilic bacteria have been demonstrated to couple the oxidation of an electron donor to the reduction of ferric iron, promoting the dissolution of goethite and leading to the release of nickel from limonite ores (du Plessis et al., 2011; Johnson and du Plessis, 2015). This involves two processes: (i) abiotic acidic dissolution of goethite, and bacterially-catalysed reduction of the ferric iron liberated to ferrous. In order to do this, the bacteria require an energy source (electron donor) which, depending on the species used, can be organic (e.g. glucose) or inorganic (hydrogen or zero-valent sulfur). The latter (ZVS) is the most suitable, both in terms of cost and practical application. Cobalt in limonitic ores, together with some nickel, is chiefly deported in manganese (IV) minerals such as asbolane ((Ni,Co)_xMn(O,OH)₄·nH₂O). The ferrous iron generated by the bacteria can accelerate the reductive dissolution of asbolane, leading to the solubilisation of both manganese (as Mn²⁺) and cobalt, which have been shown to be closely synchronised.

The microbially-catalysed reductive dissolution of oxidized ores (sometimes referred to as “biomining in reverse gear”) is one application of what has been labelled “sulfur-enhanced bioleaching” (SEB). Sulfur is one of the most abundant elements in the lithosphere and ZVS is produced in vast quantities as a waste material, for example, in removing hydrogen sulfide from natural gas reserves. ZVS is used by many species of acidophilic microorganisms as an electron donor, and more rarely as an electron acceptor. In aerobic environments, ZVS oxidation is coupled to the reduction of molecular oxygen,

generating sulfuric acid while in the absence of oxygen, some acidophiles can couple the oxidation of ZVS to the reduction of ferric iron, as described above. The oxidative dissolution of many sulfide minerals, such as chalcopyrite and chalcocite, is net consumptive of proton acidity, which can be provided, at least in part, by the oxidation of minerals such as pyrite. Large concentrations of soluble iron tend to be generated as a consequence of this and, although ferric iron is required as the primary oxidant involved in the oxidative dissolution of sulfide minerals, excess amounts can be problematic, requiring removal and precipitation in bleed streams. SEB avoids this problem and can be used where acid-generating minerals are present in relatively small amounts in ores and tailings. SEB also provides the potential for ultra-low pH (<1.5) bioleaching, and the opportunity to change redox potential rapidly in bioleach liquors, which can be rapidly achieved by removing aeration of tanks or bioheaps, since sulfur-oxidising bacteria rapidly consume the remaining dissolved oxygen before switching to ferric iron as the alternative electron acceptor. Ferrous iron-rich leachates are less aggressive chemically and are more readily accessible for recovering soluble metals by solvent extraction or sulfide precipitation.

5 Using biotechnology to exploit currently untapped mineral and metal reserves

5.1 Deep *in situ* biomining

The term “deep *in situ* biomining” (DISB) has been used to describe an emerging approach for extracting and recovering base metals buried 1–2 km in the lithosphere (Johnson, 2015; 2018). DISB combines indirect bioleaching, where the abiotic dissolution of a sulfidic ore or concentrate by an acidic, ferric iron-rich lixiviant and the biological regeneration of oxidised iron following the stripping of the target solubilised metal(s), are spatially separated. *In situ* leaching (ISL) has been used for recovering uranium since 1959, and estimated to account for 51% of global U production in 2014, copper was also recovered using ISL in, e.g., Nevada and Arizona in the latter part of the 20th century. Major differences between DISB and conventional ISL are the depths of the target ore bodies and the techniques used to expose surfaces to flowing lixiviant solutions when this is necessary. Current ISL recovery of uranium involves extracting the metal from porous sediments and rock strata at relatively shallow depths, whereas hydrofracturing would be required to open up flow channels in a deep-buried massive sulfide deposit. While a paradigm shift would be required in both the mining industry and society, in general, to get to the point where DISB is both technically feasible and accepted, the potential advantages of this approach are enormous. Most high-grade base metal ores located close to the land surface have been worked out, but can still be found deep within the lithosphere. The green credentials of DISB are also strong: it avoids haulage and comminution, and therefore incurs greatly reduced energy costs and carbon-footprints, material of no value (~99% of a typical ore body) would remain

buried, leading to a vast reduction in waste material generated and dumped on the land surface, in contrast with current mining practices. The land surface area (“footprint”) required by a DISB operation would also be a fraction of that required by a conventional opencast metal mine.

5.2 Recovering metals from “natural biomines”

The term “solution mining” has been used to include both abiotic (e.g. acid leaching of Cu oxide ores and *in situ* leaching of U) and biologically-catalysed metal ore processing, as both involve the extraction of metals into acidic liquors and the downstream recovery of metals using SX-EW, ion-exchange or alternative methods. However, the microbially-catalysed dissolution of metal sulfides also occurs, advertently, both at operating mines and, more significantly, at abandoned mine sites. Natural biomines (as differentiated from engineered heap and dump biomines) are relic features (e.g., underground mines, mine wastes such as rock dumps and tailings) that generate run-off waters that contain concentrations of base metals that are high enough to make their recovery economically viable, and which require zero or minimal engineering to achieve this (Johnson, 2018). Sites of this kind are widespread throughout Europe and the USA, as well as other parts of the world that have historic mining operations. Although they can give the impression of being devoid of life, being often sparsely colonised, if at all, with vegetation, they are actually hot-spots of microbiological activity, particularly chemo-lithotrophic (“rock eating”) microorganisms that thrive by oxidising sulfide minerals made accessible by mining operations. Recovering metals from waters draining natural biomines has particularly strong green credentials, as not only are metal resources recovered without recourse to the usual energy-demanding steps, but environmental pollution is also simultaneously abated. Using biosulfidogenesis (the generation of hydrogen sulfide by some species of anaerobic bacteria) is particularly appropriate for recovering transition metals from streams draining natural biomines, as this can often be done selectively (e.g. by controlling solution pH) and this approach is also more suitable for efficient capture of metals when their concentrations are relatively small.

6 Perspectives on expanding biotechnologies in the mining sector

Although biomining is established as a proven biotechnology, it has not, as many had thought during its inception, revolutionised the mining industry but rather has remained as a more specialised, and often peripheral, application. Since its introduction, biomining has mostly focused on fine-tuning sulfide mineral bioleaching than more blue sky thinking and finding radically new directions and opportunities for using biological processing in the mining sector. Even so, areas of (mostly) laboratory-based research, such as reductive mineral bio-processing, have suggested how bio-processing could be used outside of conventional

bioleaching and bio-oxidation of sulfide ores and concentrates. By combining low carbon/energy solutions for metal extraction with environmental protection (e.g., considering the natural biomines as resources rather than wastes) in approaches that are economically sound, biotechnology has the potential to bring about major changes in the direction of how the 21st-century global community wins and recycles metals.

References

- Brierley CL, Brierley JA (2013) Progress in bioleaching: part B: Applications of microbial processes by the minerals industries. *Appl Microbiol Biotechnol* 97:7543–7552.
- du Plessis CA, Slabbert W, Hallberg KB, Johnson DB (2011) Ferredox: a biohydrometallurgical processing concept for limonitic nickel laterites. *Hydrometallurgy* 109:221–229.
- Harrison STL (2016) Biotechnologies that utilize acidophiles. In Quatrini R, Johnson DB (eds) *Acidophiles: Life in Extremely Acidic Environments*. Caister Academic Press: Haverhill, UK: 265–284.
- Johnson DB (2014) Biomining - biotechnologies for extracting and recovering metals from ores and waste materials. *Curr Opin Biotechnol* 30:24–31.
- Johnson DB (2015) Biomining goes underground. *Nat Geosci* 8:165–166.
- Johnson DB (2018) The evolution, current status and future prospects for using biotechnologies in the mineral extraction and metal recovery sectors. *Minerals* 8:343.
- Johnson DB, du Plessis CA (2015) Biomining in reverse gear: using bacteria to extract metals from oxidized ores. *Miner Eng* 75:2 – 5.
- Schippers A, Sand W (2013) Progress in bioleaching: fundamentals and mechanisms of bacterial metal sulfide oxidation - part A. *Appl Microbiol Biotechnol* 97:7529–7541.

Definition of geochemical domains in a chromite mine, Bushveld Complex, South Africa

Kai Bachmann, Peter Menzel, Raimon Tolosana-Delgado, Jens Gutzmer
Helmholtz Institute Freiberg for Resource Technology

Abstract. The Lower and Middle Group chromitites of the Bushveld Complex are the source of a very large portion of the global chrome supply. Yet, the effectiveness of chromite beneficiation circuits is highly sensitive to mineralogical and textural variations in feed composition. The use of geochemical proxies, based on data acquired routinely during the exploration and mining process may provide a cost- and time-efficient alternative to more time-consuming and expensive mineralogical analyses. Such an approach is presented in this study, which focuses on the LG-6, LG-6A, MG-1 and MG-2 chromitite seams at the Thaba mine located on the western limb of the Bushveld Complex. According to a sound statistical assessment, the chromitites of the Thaba mine area can be subdivided into three distinct domains, domains that constitute the suitable fundamental for a geometallurgical model. Accordingly, a least altered (orthomagmatic) domain is distinguished from a supergene altered domain and a domain affected by widespread hydrothermal alteration. The latter domain occurs below the depth of modern weathering, but in obvious proximity to faults and around a prominent dunite pipe. The orthomagmatic domain is represented by ores least affected by post-magmatic alteration processes. This domain occupies the centre of fault blocks below the extent of modern weathering.

1 Introduction

Besides vast resources of chromium, the Critical Zone of the Rustenburg Layered Suite (RLS) in the Bushveld Complex represents the largest global resource of platinum-group elements (PGE) as well as significant resources of Ni and Cu (e.g., Maier et al. 2013). A significant portion of the geological chromium and PGE resources is hosted together with chromite in a series of chromitite layers, subdivided according to their stratigraphic position in the Critical Zone into the Lower, Middle and Upper Groups (LG, MG, UG; Cousins and Feringa 1964). In general, LG and MG layers have a higher chromium content (>46% Cr₂O₃ in the LGs) and are mined for chromite, compared to the UGs (<42% Cr₂O₃). This trend is accompanied by a decrease of their Cr/Fe ratio from >1.8 to <1.3 (e.g. Viljoen 2016).

The bulk of the LG and MG chromitites extracted in the Bushveld Complex have an orthomagmatic mineral assemblage dominated by chromite (>50 wt% to 95 wt%) and associated gangue silicates, predominantly orthopyroxene and plagioclase (Kinnaird et al. 2002). This orthomagmatic assemblage has been noted to be affected by surficial weathering (down to 50 m; e.g. Junge et al. 2015) and hydrothermal alteration (e.g. Voordouw

et al. 2010). Becker et al. (2014) report an enrichment of alteration silicates (amphibole, chlorite, serpentine, talc) and Fe-oxides/hydroxides, as well as depletion in BMS (base metal and Fe sulfides) as a result of weathering.

This change in gangue mineralogy will have significant impact on the chromite beneficiation process, for both the grinding and the separation circuits. A shift in mineralogy towards alteration silicate-rich chromitite compositions will result in a higher amount of fines, which will reduce the performance of the subsequent unit operations (Murthy et al. 2011 and references therein). Equally important will be the effect of alteration on density separation techniques, such as spirals; an increase in fine particle sizes (<100 µm) will negatively impact the recovery during gravity separation – a significant amount of chromite will be lost to the tailings (Gence 1999). Murthy et al. (2011) reported that up to 25 % of the mineral value originally contained in the chromite ore is lost as slimes during beneficiation.

The scope of this study is to investigate the bulk geochemistry of a large number of drill cores of four chromitite seams of the Thaba mine (operated by Cronimet Chrome Mining SA (Pty) Ltd), to discuss the variability within and between the distinct seams and to separate the mine lease area into distinct geochemical clusters. These clusters are then related to the geological architecture in the mine lease area. The results are combined with knowledge concerning the quantitative mineralogical composition of selected samples achieved in Bachmann et al. (2018). This leads to the definition of domains that can be clearly distinguished based on their mineralogical, geochemical and geological characteristics. It is expected that these can also be used as a solid foundation of a geometallurgical model for the deposit.

2 Data and Methodology

To understand the geological architecture, a geological model of the Thaba mine focusing on four target chromitite layers and containing 771 chemical assays (LG-6: 339; LG-6A: 242; MG-1: 57; MG-2: 133) was developed. The geological model is based on 270 drill core logs containing collar location, depth and survey and geological information. The model is displayed in Figure 1 (see Bachmann et al, 2019, for reference). The data set provided by the mine owner, which comprises data for Cr₂O₃, FeO, Al₂O₃, MgO, SiO₂, CaO and P, was evaluated. Details on the quality of the data set, performed corrections for sample batches and analytical methods can be found in Bachmann et al. (2019).

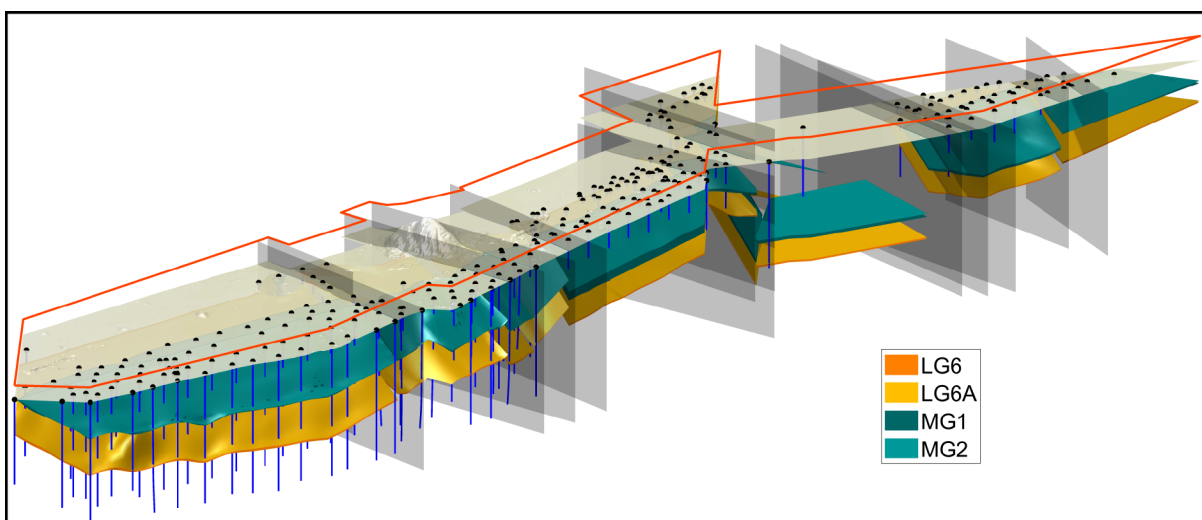


Figure 1 3D model geometry of the Thaba mine. 3D view of the surfaces representing the four target chromitite layers.

3 Results and Discussion

Cluster analysis was performed separately for LGs and MGs, respectively. Figure 2A displays a distinct separation into four clusters for geochemical data of the LG-6 and LG-6A. While cluster 1 represents samples high in Cr_2O_3 and low in CaO/SiO_2 , cluster 2 shows a slight but systematic shift to SiO_2 and CaO enriched compositions. Cluster 3 is dominated by outliers with high CaO and/or SiO_2 contents, while Cr_2O_3 shows, in general, lower concentrations. The “supergene” cluster represents all drill core intersections classified as cluster 2 and are within the first 50 m below surface. Whether the drill core intersections of this cluster were already altered prior to being exposed to weathering cannot be determined. Additionally, the results display systematic trends that are independent of the actual chromitite layer considered.

Figure 2B shows the results of the corresponding cluster analysis for MG-1 and MG-2. Note that PC3 is shown on the y-axis, displaying similar loadings as PC2 in Figure 2A. On the other hand, PC2 of the MGs corresponds to PC3 of Figure 2B (as well as PC3 of the LG's), showing strong loadings on phosphorous. Hence, due to limited data points, cluster discrimination for the MG chromitites is not as significant as for the LGs, but appears more “noisy”. Nevertheless, overall trends are similar to the LGs, representing a shift towards SiO_2/CaO richer compositions from cluster 1 through cluster 2 to the “Supergene” cluster. As shown in Figure 2A, cluster 3 predominantly represents outliers with either high phosphorous or CaO contents. Similar to the LG-6/LG-6A, trends do not distinguish MG-1 from MG-2.

3.1 Linking geochemistry with mineralogy

The mineralogy of chromitite seams of the LGs and MGs is well known and has been previously described in detail (e.g. Naldrett et al. 2012 and references therein), as well as for the Thaba Mine lease area (Bachmann et al. 2018).

Firstly, Cr_2O_3 occurs almost exclusively in chromite and mineral compositions of chromite show only slight variation, thus the assumption to link increasing Cr_2O_3 contents with increasing chromite concentrations is valid. Silicate minerals in primary orthomagmatic chromitites are orthopyroxene, minor clinopyroxene, olivine, feldspar (mainly plagioclase) and dark micas with biotitic compositions. This rock-forming mineralogy is well reflected by the available chemical assays, with minor exceptions, such as V, Ti, and Mn, usually accounting for not more than 1-2 wt% in total. Furthermore, iron was only measured as FeO, but in reality, iron is present as both FeO and Fe_2O_3 , which again will account for another few wt% in total. It can be concluded that the chemical assays contained in the database should account for >97 wt% of the total chemical composition of a typical orthomagmatic chromitite sample. Yet, there is a significant number of analyses with totals below 95 wt%. Analyses with low totals display a significant positive correlation with increasing SiO_2 and CaO concentrations, and are also marked by an abundance of alteration minerals, such as chlorite, talc, serpentine and amphibole (Bachmann et al., 2018). Furthermore, significant amounts of carbonate minerals such as calcite and dolomite are present in some samples. Hey (1999) documented that clay minerals (e.g. smectites) are common in chromitites affected by supergene alteration. These alteration minerals incorporate certain amounts of volatiles (water, carbonate) – constituents not included in the assay data set. Therefore, low totals are attributed to high abundances of alteration minerals. Alteration will, however, also change the relative abundance of certain elements within the data set. Due to the high resistance of chromite to alteration, the absolute amount of chromite will remain rather consistent, while the gangue mineral assemblage can change dramatically. An increase in volume of the seams, for example, will decrease the relative amount of chromite, hence, the Cr_2O_3 concentration decreases. All these parameters can be used as a proxy to detect alteration.

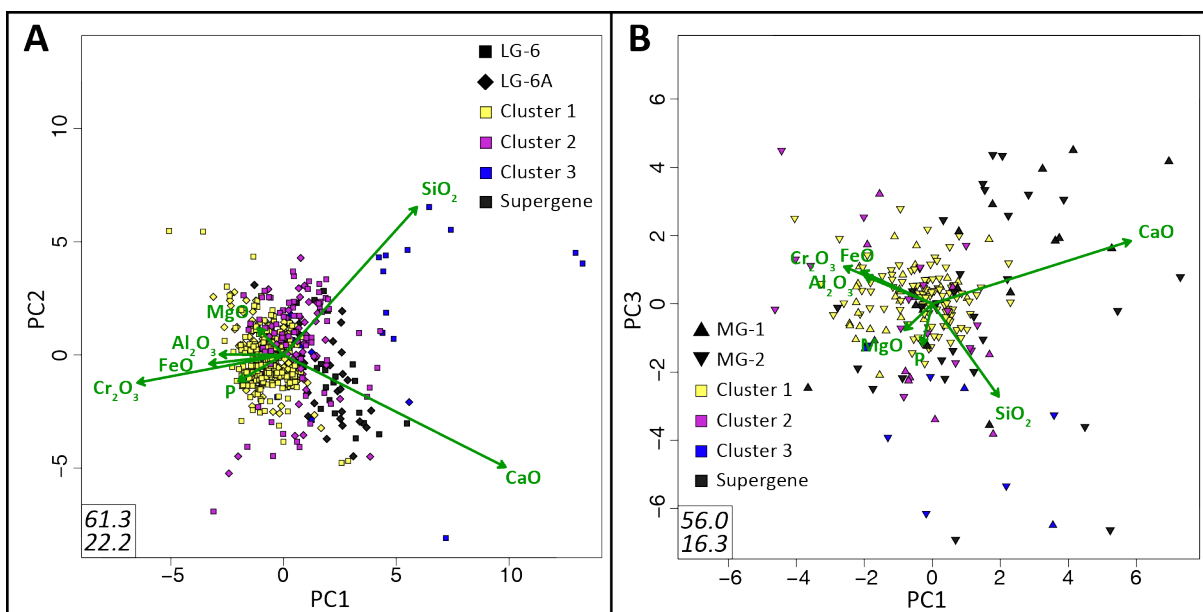


Figure 2 Compositional biplots of major element oxides and phosphorus showing (A) results of a cluster analysis of LG-6 and LG-6A chromitites (first (x-axis) vs. second (y-axis) principal components; PC) and (B) of MG-1 and MG-2 chromitites (first (x-axis) vs. third (y-axis) PC). The compositional contrast between LG-6/ LG-6A and MG-1/ MG-2, respectively, was minimized by matching the means of each seam.

3.2 From chemical clusters to geochemical domains

The integration of geochemical clusters into the geological 3D model allows recognition of the inherent relations between geochemistry and geological architecture. As shown in Figure 3, clusters form distinct geochemical domains. General trends are similar for both the LG-6 and LG-6A. While cluster 1 can be allocated to the southern part of the deposit, cluster 2 and the “supergene” cluster are, in general, located in the north of the mine lease area. Cluster 3 comprises outliers and can hardly be translated as a distinct geochemical domain, but points towards chemical anomalies within the deposit. For the LGs, cluster 1 shows homogeneous elemental distribution including high Cr_2O_3 , Al_2O_3 and FeO concentrations, while SiO_2 and CaO contents are low. The spatial distribution of this most pristine cluster seems to be connected to the distribution of troctolite. Troctolite is believed to cause metasomatization and/or replacement of orthomagmatic mineral assemblages (Voordouw et al. 2010) inducing increasing CaO and Al_2O_3 (plagioclase) and MgO (olivine) concentrations. However, we cannot observe such systematic changes in mineralogy in the majority of samples within cluster 1. Nevertheless, in the rare cases, when troctolites are emplaced in direct contact with the chromitite seams, they cause dramatic changes in the chemistry. Cluster 2 comprises chromitite samples affected by different types of alteration, with generally lower grades in Cr_2O_3 and increased SiO_2 and/or CaO . On the one hand, these alteration processes are associated with the Middellaagte IRUP (iron-rich ultramafic pegmatite; e.g. Scoon and Mitchell 1994) and form a halo of metasomatization/hydrothermal alteration. On the other hand, alteration is related to serpentinization within and

immediately around fault zones in the central portion of the mine lease area.

The “supergene” cluster forms a domain of supergene altered/oxidized ore and displays even lower Cr_2O_3 grades than the pristine and altered domains, while SiO_2 , CaO and FeO concentrations increase. As defined above and in accordance to literature (Junge et al. 2015), supergene alteration is restricted to intersections <50 m below surface. It appears reasonable to expect a rapid gradational contact between the supergene and pristine ore zones, although this remains to be tested. This notion is supported by results of the present study, because not all intersections <50 m are classified to the “supergene” cluster. Nevertheless, to define a transition zone between oxidized and pristine ores, the spatial resolution of the data set would have to be significantly higher. Similar to the LGs, integration into the geological geometry of the defined chemical clusters was performed for the MG chromitites. Due to the limited amount of data for the MG-1 (only ~50 intersections), defining precise domains using chemical clusters was challenging. Nevertheless, it can be stated that the data sets of MG-1 and MG-2 show a similar behavior; it appears thus reasonable to assume that both seams also have similar domains.

4 Conclusions

This case study illustrates how the combination of geochemical and geological data, complemented by tailored statistical evaluation, can provide a sound foundation for geometallurgical domaining and modelling. According to our assessment, three distinct geochemical domains are developed within the Thaba chromitite deposit. Firstly, the supergene altered domain is clearly differentiated from domains that are below the extent of modern day weathering. The chromitites below

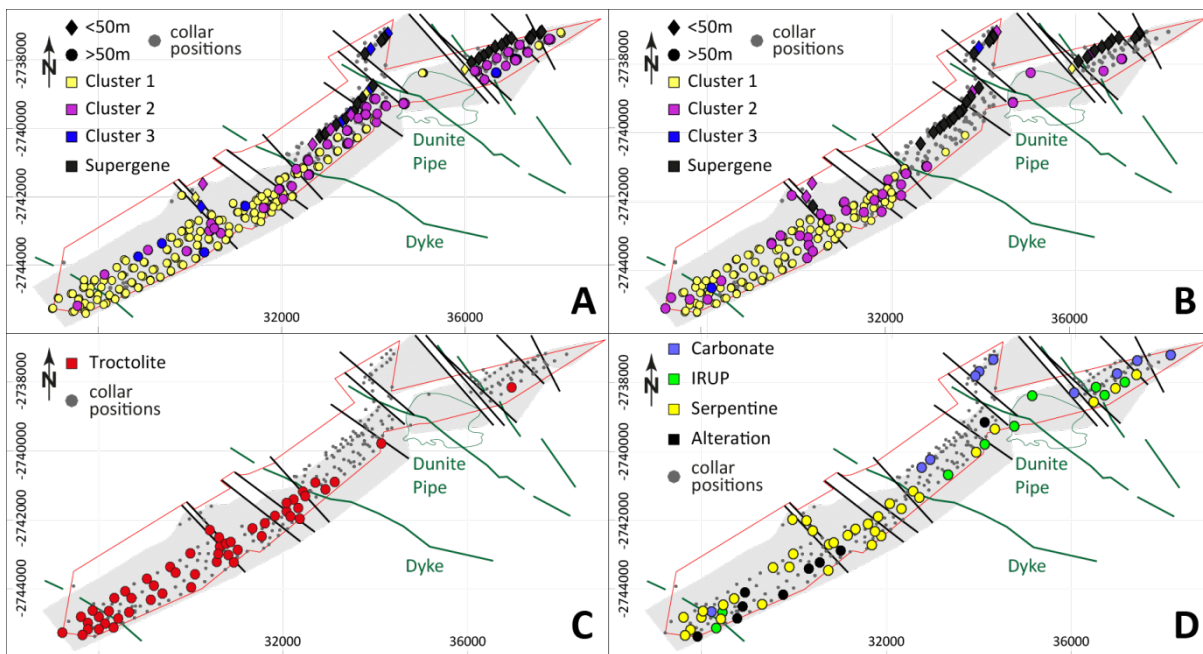


Figure 3 Maps of the mine lease area at the Thaba mine. Maps show all collar positions and the corresponding clustered geochemical data (according to Figure 10) of (A) the LG-6 and (B) the LG-6A. Maps displaying all alteration markers in close vicinity (150 m vertical and horizontal) to the seam intersections are shown in (C) for troctolite and (D) for all other alteration markers. Please note, all drill core intersections <50 m depth are displayed as diamonds; drill core intersections >50 m depth are shown as circles.

the depth of weathering can be further subdivided into a pristine domain with a predominantly orthomagmatic composition – and a domain affected by hydrothermal alteration processes. The latter domain is developed – sensibly – along fault structures and around the Middellaagte IRUP. These domains are crucial to design a sensible and tailored beneficiation process for chromitite ores, where the pristine domain will show superior processing characteristics for chromite beneficiation.

Acknowledgements

This is a contribution of the German/South African R&D project AMREP funded by the German Federal Ministry of Education and Research (BMBF; grant number BMBF 033R119E). We thank the Cronimet Mining Group for providing access to their core shed and drill core intersections from the Thaba mine and for the contribution of additional analytical data as well as information on the local geology and beneficiation.

References

Becker M, Wiese J, Ramonotsi M (2014) Investigation into the mineralogy and flotation performance of oxidised PGM ore. *Minerals Engineering* 65:24–32.

Bachmann K, Osbahr I, Tolosana-Delgado R, Chetty D, Gutzmer J (2018) Variation in platinum group mineral and base metal sulfide assemblages in the Lower Group chromitites of the western Bushveld Complex, South Africa. *Can Min*, <https://doi.org/10.3749/canmin.1700094>.

Bachmann K, Menzel P, Tolosana-Delgado R, Schmidt C, Hill M, Gutzmer J (2019a) The use of assay data as a foundation for a geometallurgical model – the case of the Thaba Chromite Mine, South Africa. *Journal of Geochemical Exploration*. doi.org/10.1016/j.gexplo.2019.01.008

Cousins CA, Feringa G (1964) The chromite deposits of the Western belt of the Bushveld Complex. In: Haughton SH (ed) *The geology of some ore deposits in Southern Africa*, Johannesburg.

Geological Society of South Africa 2:183–202.

Gence N (1999) Beneficiation of elazig-kefdag chromite by multi-gravity separator, *Tr. Journal of Engineering and Environmental Sciences* 23:473–475.

Hey PV (1999) The effects of weathering on the UG2 chromitite reef of the Bushveld Complex, with special reference to the platinum-group minerals. *South Afr J Geol* 102:251–260.

Junge M, Oberthür T, Kraemer D, Melcher F (2015) Distribution of platinum-group elements in pristine and near-surface ores from the Platreef, northern Bushveld Complex, South Africa. In: André-Mayer AS, Cathelineau M, Muches P, Pirad E, Sindern S (Editors). *13th Biennial SGA Meeting*, 955–958.

Kinnaid JA, Kruger FJ, Nex PAM, Cawthorn RG (2002) Chromitite formation—a key to understanding processes of platinum enrichment. *Applied Earth Science* 11(1):23–35.

Maier WD, Barnes S-J, Groves DI (2013) The Bushveld Complex, South Africa: formation of platinum–palladium, chrome- and vanadium-rich layers via hydrodynamic sorting of a mobilized cumulate slurry in a large, relatively slowly cooling, subsiding magma chamber. *Mineral Deposita* 48:1–56.

Murthy YR, Tripathy SK, Kumar CR (2011) Chrome ore beneficiation challenges & opportunities—a review. *Minerals Engineering* 24(5):375–380.

Naldrett AJ, Kinnaid J, Wilson A, Yudovskaya M, McQuade S, Chunnnett G, Stanley C (2009) Chromite composition and PGE content of Bushveld chromitites: part 1—the lower and middle groups. *Trans Inst Min Metall B* 118:131–161.

Naldrett AJ, Wilson A, Kinnaid J, Yudovskaya M, Chunnnett G (2012) The origin of chromites and related PGE mineralization in the Bushveld Complex: new mineralogical and petrological constraints. *Mineralium Deposita* 47:209–232.

Scoon RN, Mitchell AA (1994) Discordant iron-rich ultramafic pegmatites in the Bushveld Complex and their relationship to iron-rich intercumulus and residual liquids. *Journal of Petrology* 35(4):881–917.

Viljoen, M (2016) The Bushveld Complex. *Episodes* 39:239–268.

Voordouw RJ, Gutzmer J, Beukes, NJ (2010) Zoning of platinum group mineral assemblages in the UG2 chromitite determined through in situ SEM-EDS-based image analysis. *Mineralium Deposita* 45:147–159.

Key ore textures influencing separation behaviour of ores

Kate Tungpalan

W.H. Bryan Mining and Geology Research Centre, Sustainable Minerals Institute, The University of Queensland

Elaine Wightman

Julius Kruttschnitt Minerals Research Centre, Sustainable Minerals Institute, The University of Queensland

Cathy Evans

W.H. Bryan Mining and Geology Research Centre, Sustainable Minerals Institute, The University of Queensland

Abstract. Ore texture displays the fundamental ore properties that significantly influences processing behavior of ores. Of all texture characteristics, mineral grain size and mineral association are expected to have the greatest influence. These textural features can be used to predict the separation performance of ores. To obtain such micro-scale textural information is costly and time-consuming to be applicable to the entire deposit. Recent work has shown the contribution of vein-type mineralization in the separation behavior of ores. Since veins can be identified during core logging, it provides a cost-effective means of acquiring textural information relevant to mineral processing for the entire deposit. This can then improve geometallurgical characterization of separation performance, providing better understanding of separation variability within the deposit.

1 Introduction

The depletion of easily mined high-grade ore bodies has resulted in the industry being required to process lower grade, complex resources to meet the increasing demand for minerals (Albanese and McGagh 2011; Darling 2011; Randolph 2011). The trend is now towards mining and processing of low-grade and complex ores (Darling 2011; Yingling 1990). Such ores come with variable geological and mineralogical characteristics, and complex mineralogy and texture. Variable characteristics, and complex mineralogy and texture can result in large variations in metallurgical response and also causes challenges in processing (Carson 1995; Lorenzen and Barnard 2011; Yingling, 1990). Variability and the complex nature of ores are fundamental sources of risk that can often cause adverse economic impacts to mining operations (Dusci et al. 2007; Williams and Richardson 2004). Hence it is important to effectively characterize these types of ore bodies as early as possible in the project development process and assess their processing performance to enable the development of economic and optimized production.

2 Ore texture – key driver to mineral separation

A case study was performed on a copper porphyry deposit to assess its variability in separation performance. An integrated geometallurgical method was carried out to populate the exploration database with

copper recoveries. The method applied a principal component analysis on the database to divide the deposit according to similar geological and mineralogical characteristics. Each group had a distinct set of dominant geological and mineralogical characteristics, which were then used as input terms to predict copper recovery. The group-based modelling provided an indication of the key geological and mineralogical characteristics influencing copper recovery that were not evident in the original exploration database. Two drill core samples belonging to one group, and another two samples from another group were selected to undergo physical tests. The drill cores were crushed into particles; a sub-sample underwent flotation test and another sub-sample underwent texture measurement through the Mineral Liberation Analyser (MLA) (Fandrich et al. 2007). Each drill core sample was treated and analysed individually. The predicted and measured recoveries, and measured ore texture are shown in Table 1 and Fig. 1.

Table 1. Predicted and measured recoveries and grade

	Predicted Recovery, %Cu	Measured Recovery, %Cu	Measured Concentrate Grade, %Cu
Sample A.1	79	90±1	2.63±0.08
Sample A.2	89	80±4	4.36±0.94
Sample B.1	80	90±1	3.84±0.08
Sample B.2	90	85±3	3.92±0.08

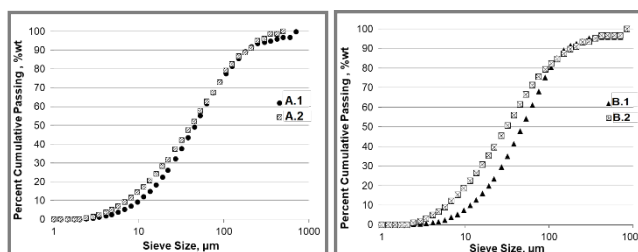


Figure 1. Comparison of the measured copper sulphides grain size distribution. (Left) Samples A.1 and A.2 have similar dominant geological and mineralogical characteristics, but A.1 exhibits slightly coarser copper sulphides grain size distribution and yielded higher measured copper recovery. (Right) Samples B.1 and B.2 also have similar dominant geological and mineralogical characteristics, but B.1 exhibits coarser copper sulphides grain size distribution and yielded higher measured copper recovery.

It was observed that there are discrepancies between experimental flotation recoveries and predicted recoveries. This indicated that the geological and

mineralogical data obtained from core logging which were used in the development of geometallurgical models for copper recovery were not capturing the underlying drivers for flotation response. However, the drill core samples yielded varying recoveries, which illustrates the usefulness of the integrated geometallurgical method in effective sampling of a variable deposit. Flotation is the most important and versatile separation technique that allowed the mining and processing of low-grade and complex ore bodies (Alexander et al. 2006). It is a complex process driven by several factors – from ore properties to operating parameters. It has been recognised that ore texture is representative of the fundamental ore properties that will determine the ease of mineral liberation and the subsequent mineral separation (Ferrara et al. 1989; Gaudin 1939; Jones 1987; King 1994; Petruk 2000). In metallurgy, the ore texture refers to the spatial arrangement, distribution, association, orientation, size and shape of the mineral grains that make up the ore (Barton 1991; Ferrara et al. 1989; Gaudin 1939; King, 1994; Preti et al. 1989). Of all texture characteristics, mineral grain size and mineral association are expected to have the greatest influence on processing behaviour (Evans 2010; Sutherland 2007; Tungpalan 2015). In the case study, it was found that the presence of coarser copper sulphide grains resulted in a higher degree of copper sulphides liberation as shown in Fig. 2, and higher copper recovery. The coarser mineral grains are easier to liberate compared to fine-grained minerals (Petruk 2000; Sutherland 1989). Consequently, the greater is the degree of liberation of the valuable minerals, it is highly likely that more valuable minerals will be recovered.

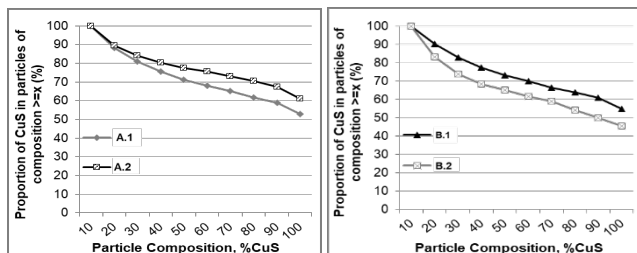


Figure 2. Comparison of the measured cumulative liberation of copper sulphide minerals. (Left) Sample A.1, having slightly coarser copper sulphides grain size distribution, yielded lower degree of liberation than A.2. This suggests that grain size is not the only key factor affecting the liberation of copper sulphides for these ores. (Right) Sample B.1, having coarser copper sulphides grain size distribution, yielded higher degree of liberation than B.2.

Mineral association also has an effect on the concentrate grade as well as the recovery. The case study showed that the ore where the copper sulphides are highly associated with sulphide gangue, particularly pyrite (Fig. 3), resulted in a higher copper recovery but lower concentrate grade. Since pyrite is a floatable mineral, particles (containing copper sulphides and pyrite) are more likely to float and hence have greater chances to be recovered. On the other hand, copper sulphides with higher degree of association with the non-floatable, non-sulphide gangue are less likely to be recovered, thus can lower the recovery.

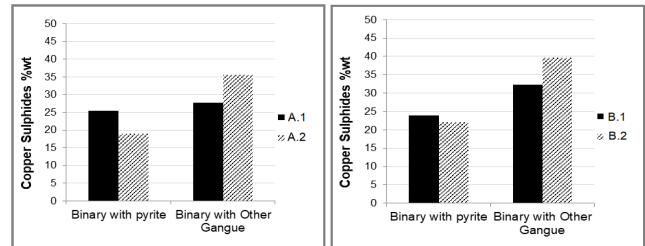


Figure 3. Comparison of the copper sulphides association with other minerals. (Left) The association between A.1 and pyrite is higher than between A.2 and pyrite; the association between A.1 and other gangue is lower than between A.2 and other gangue. The association of the copper sulphides with pyrite in sample A.1 could have caused its higher recovery despite having lower liberation of copper sulphides. This is also evident by the lower concentrate grade of sample A.1. (Right) The association between B.1 and pyrite is higher than between B.2 and pyrite; the association between B.1 and other gangue is lower than between B.2 and other gangue.

The results from analysis of the particles indicate that mineral grain size and mineral association are key textural drivers to separation behavior of ores. They provide valuable information for the grinding circuit and cleaner flotation. In particular, they could indicate the size to which the particles should be reduced to achieve optimum liberation. However, to obtain such detailed textural information is expensive and time-consuming to be practically applicable to the entire deposit. They are typically measured using high resolution measurement tools such as the MLA (Fandrich et al. 2007) and QEMSCAN (Sutherland and Gottlieb 1991). As a result, variability in separation performance within the deposit has not been fully understood. This points out the need to identify ore texture that are relevant to mineral separation at a larger scale i.e. drill core-scale. Recent works have shown the influence of mineralization styles in separation behaviour of ores, particularly of veins and disseminated grains (Tungpalan et al. 2017, 2018; Wightman et al. 2018). A drill core from the same copper porphyry deposit with evident veining structure was cut into semicircular slabs. Selected slabs were first analysed in the MLA to determine the extent of veining (Fig. 4). The slabs showed varied degree of sulphide veining from 11% to 22%. To investigate the influence of veining, the slabs were divided into two - those with $\leq 11\%$ of sulphide veining were nominated as low and those with $> 11\%$ were considered high. The slabs then underwent single impact breakage and analysed again in the MLA to measure the sulphides liberation. The measured sulphides liberation in the 600 micron particles (solid lines) and 300 micron particles (broken lines) are displayed in Fig. 5. It is evident that the presence of veins contribute to the ease of sulphides liberation. It was observed that the slabs with high extent of veining yielded higher degree of sulphides liberation. It was also observed that for the high veining, liberation of sulphides start to propagate even at 600 micron particles (indicated by the red line in Fig. 5). Whereas, in the low veining, sulphides start to liberate only at 300 microns.

Wightman et al. (2018) also examined the implications of disseminated grains on the liberation of gangue minerals. It was observed that the presence of disseminated grains, their grade and size distribution

have direct impact on the degree to which rejection of gangue minerals at coarse sizes is possible. The rejection of gangue at coarse particle size will also bring significant benefits in mineral processing.

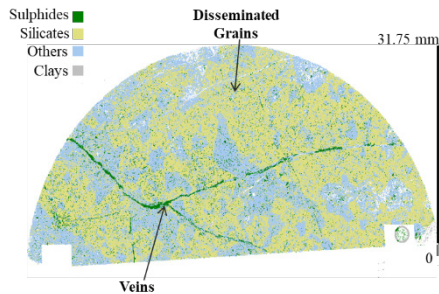


Figure 4. Slab image obtained from MLA showing veins and disseminated grains.

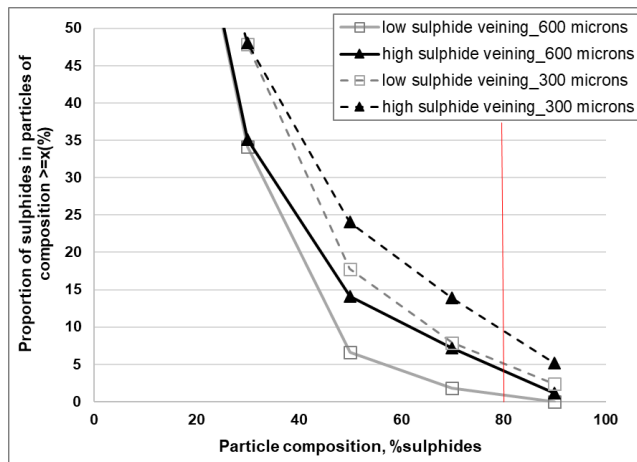


Figure 5. Cumulative liberation of sulphides measured from the slabs in the MLA. Greater veining contributed to an increased degree of sulphides liberation and contributed to propagation of liberated sulphides at coarser particle size.

More research work has to be done to gain better understanding of the role of veins and disseminated grains in separation behaviour of ores, particularly linking it with recovery. However, the work highlights the significance of vein-type mineralization in the ease of mineral liberation. The presence of veins contributes to an increased degree of liberation and also contributes to the propagation of liberated minerals at coarser particle sizes. Vein structures can be a proxy for separation performance, and is therefore a valuable tool for understanding potential mineral recoveries as early as the exploration phase. Since veins can be identified during drill hole logging without the use of expensive high resolution devices, it provides a cost-effective means of acquiring textural information relevant to processing for the entire deposit. The information from vein structures has potential benefits in improving geometallurgical characterization of separation performance, providing better understanding of the separation variability within the deposit. Logging of vein structures is therefore important and should include not only the type of vein but also the extent of veining.

3 Implications

It is apparent that the texture of the ore, particularly mineral grain size, mineral association and vein structures, have significant influence on copper sulphides liberation and copper recovery. This suggests the importance of describing texture to assess the separation performance of the deposit which then enables creation of strategies for optimized economic production. It is important to note that the scale at which detailed measurements of ore texture are undertaken is critical and needs to be carefully considered.

Acknowledgements

The authors would like to thank Professor Emmy Manlapig, Dr Luke Keeney, Professor Rick Valenta, Cong He, MLA staff and all their colleagues at the Sustainable Minerals Institute, The University of Queensland.

References

- Albanese T and McGagh J (2011) Future trends in mining. In Darling P (ed) SME Mining Engineering Handbook, 3rd edn. Society for Mining, Metallurgy and Exploration, Inc., USA, pp. 21-36.
- Alexander D, Bradshaw D, Manlapig E, Harbort G (2006) Froth Flotation. In Wills BA and Napier-Munn TJ (eds) Mineral processing technology: An introduction to the practical aspects of ore treatment and mineral, 7th edn. Butterworth-Heinemann, Oxford, pp. 267-352.
- Barton P (1991) Ore textures: problems and opportunities. *Mineralogical Magazine* 55:303-315.
- Carson DJ (1995) Geological-mineralogical controls on the metallurgical response of ores. Project Evaluation and Due Diligence short course, Prospectors and Developers Association of Canada, Ontario.
- Darling P (2011) Mining: Ancient, modern and beyond. In Darling P (ed) SME Mining Engineering Handbook, 3rd edn. Society for Mining, Metallurgy and Exploration, Inc., USA, pp. 3-9.
- Dusci M, Guibal D, Donaldson J, Voortman A (2007) Risk management through the use of 2D conditional Co-simulation at an underground gold Mine in Western Australia. In Dimitrakopoulos R (ed) Orebody modelling and strategic mine planning: Uncertainty and risk management models, 2nd edn. Spectrum Series, The Australasian Institute of Mining and Metallurgy, Victoria, pp. 103-110.
- Evans C (2010) Development of a methodology to estimate flotation separability from ore microtexture. Dissertation, The University of Queensland.
- Fandrich R, Gu Y, Burrows D, Moeller K (2007) Modern SEM-based mineral liberation analysis. *Int J Miner Process* 84:310-320.
- Ferrara G, Preti U, Meloy TP (1989) Inclusion, shape, mineral texture and liberation. *Int J Miner Process* 27:295-308.
- Gaudin AM (1939) Principles of mineral dressing. McGraw Hill, New York.
- Jones MP (1987) Applied mineralogy - A quantitative approach. Graham and Trotman, London.
- King RP (1994) Comminution and liberation of minerals. *Miner Eng* 7:12-140.
- Lorenzen L and Barnard MJ (2011) Why is mineralogical data essential for designing a metallurgical test work program for process selection and design?. In Dominy DS (ed) The First AUSIMM International Geometallurgy Conference, The Australasian Institute of Mining and Metallurgy, Melbourne, pp. 163-172.
- Petruk W (2000) Applied Mineralogy in the Mining Industry. Elsevier Science, The Netherlands.
- Preti U, Ferrara G, Meloy T (1989) Influence of particle shape on liberation. *Int J Miner Process* 25:17-28.

- Randolph M (2011) Current trends in mining. In Darling P (ed) SME Mining Engineering Handbook, 3rd edn. Society for Mining, Metallurgy and Exploration, Inc., USA, pp. 11-19.
- Sutherland DN (2007) Estimation of mineral grain size using automated mineralogy. *Miner Eng* 20:452-460.
- Sutherland DN, Gottlieb P (1991) Application of automated quantitative mineralogy in mineral processing. *Miner Eng* 4:753-762.
- Tungpalan K, Wightman E, Manlapig E (2015) Relating mineralogical and textural characteristics to flotation behaviour. *Miner Eng* 82:136-140.
- Tungpalan K, Wightman E, Manlapig E, Keeney L (2017) The influence of veins on mineral liberation as described by random masking simulation. *Miner Eng* 100:109-114.
- Tungpalan K, Wightman E, Manlapig E (2018) The role of vein-type mineralization in mineral liberation. *Miner Eng* 116:209-212.
- Williams SR and Richardson JM (2004) Geometallurgical mapping: A new approach that reduces technical risk. Proceedings of the 36th Annual Meeting of The Canadian Mineral Processors, Canadian Institute of Mining, Metallurgy and Petroleum, Ottawa, pp. 241-268.
- Yingling JC (1990) Circuit analysis: Optimizing mineral processing flowsheet layouts and steady-state control specifications. *Int J Miner Process* 29:149-174.

A reliable method for the automated distinction of quartz gangue and epoxy resin with reflected light microscopy for geometallurgical characterisation

Ursula Grunwald-Romera, Juan Carlos Catalina, David Alarcón, Alfredo López-Benito, Ricardo Castroviejo
Universidad Politécnica de Madrid, Spain

Abstract. The reliable distinction of gangue (typically quartz or silicates) and epoxy resin (commonly used to embed the sample, before polishing) is a pending problem for the widespread automated mineralogical characterization of ores and its application to geometallurgy. Traditional methods based on specular reflectance (**R**) measures are not able to distinguish between gangue and resin because of their similar R values. Different additives (colorants and fluorescein) have been investigated to alter the spectral signature of the resin in polished thin sections. Automated segmentation can commonly be achieved with colour dyes, only if R ratios are used, instead of R values. However, the results are most reliable with the addition of fluorescein. The acquisition of fluorescence images with the 20x objective, shows a high contrast between bright and dark areas (belonging to resin and mineral particles, respectively). This opens the way to the generalized application of automated methods of optical microscopy, such as the AMCO system, for geometallurgical characterization, with a notable increase in efficiency over traditional methods (point counter) and a significant cost reduction compared to electron microscopy.

1 Introduction

The reliable distinction of gangue (typically quartz or silicates) and epoxy resin in reflected light microscopy (through the measurement of specular reflectance in the visible and near infrared ranges, between 400 and 1000 nm), is a common problem for the automated geometallurgical characterization of ores with digital image analysis software. This is not a difficult problem in polished whole rock samples, because resin is present at the border only and can be easily isolated.

In milled ore concentrates, however, each ore grain or particle is surrounded by resin. This resin must be discriminated from gangue in order to carry out automated quantitative analysis of ore and gangue, or when the contours of the grains have to be recognized to define morphological properties. This distinction is therefore a requirement for a widespread application of automated optical microscopy, which warrants a notable increase in efficiency over traditional methods (point counter) and a significant cost reduction compared to electron microscopy.

Neumann and Stanley (2008) studied the possibility of discriminating quartz from commercial epoxy resins. They concluded: “*The close coincidence of specular reflectance for quartz and epoxy resins ensures that there*

is not relevant reflectance contrast between them, even when spiked with dyes. This data set is final, and precludes the application of reflectance in light optical image analysis for assessment of liberation, phase quantification, or any other signal that requires separation of resin from transparent minerals”. Delbem et al. (2015) propose for iron ore characterisation a semi-automated quartz/resin classification, defining first the particle contours, and then applying the measured R values inside each particle to identify its components, but the contour definition is not always straightforward.

The approach of this work is the direct definition of the particles based on the measured R values.

2 Background

This research benefitted from previous experiences in the GeMMe Lab (University of Liège) and in the Laboratory of Applied Microscopy (**LMA**, Universidad Politécnica de Madrid), kindly contributed by Pirard E., and Pérez-Barnuevo L., resp., which even if unsuccessful were instrumental to avoid repetition of useless attempts, including use of organic solvents to etch the polished epoxy surface, laser ablation, use of different additives to modify the surficial appearance or the refractive index (and R) of the resin, use of different types of dyes (yellow, blue and red), graphite powder, etc.

A common feature of these attempts was the use of polished blocks (**PB**), in which results are usually unsatisfactory, even with coloured resins, because the epi-illumination penetrating the surface of the block is transmitted and diffused within the resin and the gangue, and can be finally conveyed back to the surface through the transparent gangue grains, apparently tinting them with the resin's colour.

In 2017, a Grade's Thesis funded by a GIRMI-UPM grant (Grunwald-Romera 2017) brought forward Pérez-Barnuevo's work by studying the effect of different types of resin additives (the same yellow, red and blue dyes, plus fluorescein), in Polished Thin Sections (**PTS**). PTS have a typical thickness of 30 µm, thinner than the grain size of most samples, thus minimizing the presence of dyed resin under the grains. Should the grain size be smaller, thinner PTS might be prepared. This method proved to be quite effective, and therefore PTS were chosen as the standard sample preparation method for the tests that were performed later.

From 2016 to 2018, the LMA led the development of the AMCO System, an automated mineralogical characterisation system based on optical microscopy.

The work was carried out within a research project funded by EIT Raw Materials, with the participation of the University of Liège, the SME Thin Section Lab, and two mining companies (Cobre Las Cruces and KGHM). **AMCO** (which stands for Automated Microscopic Characterization of Ores), is the result of an upscaling of the CAMEVA system (Castroviejo et al. 2009, Catalina and Castroviejo 2017).

3 Materials and methods

A number of polished sections were prepared from two samples of quartz sand (IMOSAB and GUD), using two epoxy resins (FeroCa and Struers EpoFix Kit), and four dyes from Struers: the three AcryDye pigment-based liquid colorants (yellow, red and blue), and EpoDye (fluorescein in powder). Undyed polished sections were also prepared, for comparison.

Nine PTS, two with each dye plus one without, and two PB, one with EpoDye and one undyed, were prepared from IMOSAB sand in the labs of Complutense University of Madrid (UCM) by the first author for her Grade's Thesis (2017). A set of polished sections used FeroCa resin with 6 drops of AcryDye colorant for each one, while another set used EpoFix resin with 10 drops of AcryDye. For the sections with fluorescein, even if not exactly quantified, IMOSAB_F001 contained a larger amount of EpoDye than IMOSAB_F002.

Later on, five PTS and PB pairs from each sand sample (IMOSAB and GUD) were prepared at Thin Section Lab (Toul, France) using EpoFix resin and the same four dyes, plus one undyed.

Multispectral images of the polished sections were acquired at the LMA on a prototype of the AMCO system. The AMCO system prototype is based on a Leica DM6000 M reflected-light optical microscope integrating additional components, such as a fluorescence filter cube, a 12V/100W halogen light source with a custom hot mirror, a high-precision XY motorized stage, a filter wheel containing a large number of hard coated bandpass filters in the VNIR range, and a high-resolution monochrome video camera. The multispectral images are typically composed of 21 bands: 13 reflectance bands in the visible range from 400 to 700 nm with 25 nm bandpass (**BP**), 6 reflectance bands in the NIR from 750 to 1000 nm with 50 nm BP, a reflectance band in the NUV range centred at 370 nm with 36 nm BP, and an optional fluorescence band obtained through the L5 cube (excitation filter: BP 480/40 nm, dichromatic mirror: 505 nm, suppression filter: BP 527/30 nm), which is especially suited for fluorescein.

4 Multispectral measurements

Multispectral images of each of the polished sections were acquired with 5x, 10x and 20x objectives. For the images of the coloured resin sections, just the 20 reflectance bands were captured, as these resins do not exhibit significant fluorescence. However, for the images of the fluorescent resin sections, all the 21 bands (20 reflectance bands plus the fluorescence band) were

captured. The fluorescence band does not measure reflectance, but the intensity of the fluorescence of the sample. Because of this, it was necessary to adjust the integration time of the camera for the fluorescence band before the acquisition, to adapt it to the brightness level of the fluorescent resin, which depended on the amount of EpoDye added (higher amounts of fluorescein made the resin shine brighter, so it needed a shorter exposure time to prevent the image from becoming saturated).

Several images of each PB and each PTS were acquired with each objective, in order to determine the effect of the different dyes on the resin. These images were examined one by one with the AMCO image analysis software (Fig. 1). In each image, a number of rectangular boxes were manually drawn with the mouse on sufficiently uniform regions of the sand grains and the resin matrix, in order to select the gangue and resin regions used to conduct the study.

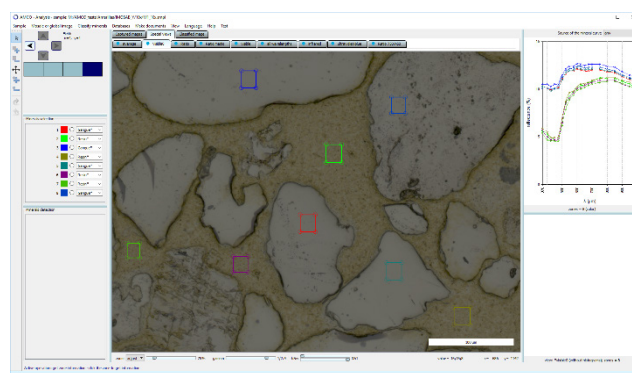


Figure 1. Window capture of AMCO image analysis software while examining an image of a polished thin section (IMOSAB-Y001)

The top-right graph of Figure 1 shows spectral curves measured on an image of a PTS prepared with yellow dye. Each curve is computed as the average (or the mode, at user's choice) of the multispectral R values of all the pixels contained within a region. The measured R values correspond in fact to apparent reflectance, which is higher than the nominal specular reflectance due to the well-known contribution of light diffused within the polished section (Criddle 1990). This effect is produced in transparent minerals by internal reflections, which are seen through the surface.

Measurements on PB show that the R values are very similar for gangue and resin, making automated distinction unreliable, while for PTS there are noteworthy differences. Therefore, for the rest of the discussion we will focus on PTS only.

5 Results and discussion

Figure 2 shows average spectral curves for gangue and resin from PTS prepared with resin dyed with the three colorants. Studying the curves, it can be realised that the R values of dyed resin regions are somewhat lower than the R values of gangue regions at some bands. These bands are typically the bands near the complementary colour of the dominant hue of the dye. For instance, with the yellow dye, resin appears significantly darker than

gangue in the bands closer to the blue range (between 400 and 500 nm).

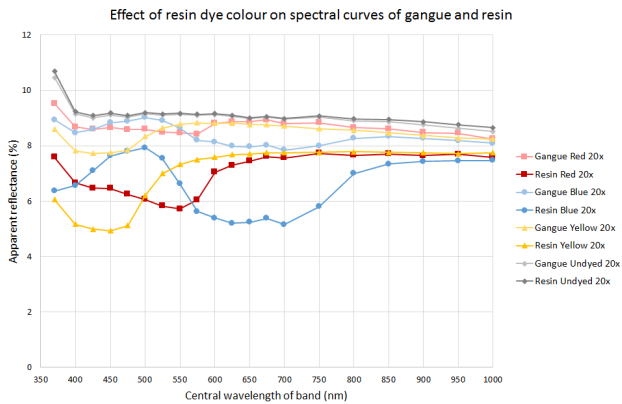


Figure 2. Effect of resin dye colour on measured spectral curves of gangue and resin

This spectrally uneven darkening of the resin can be exploited by computing ratio images of selected bands. Figure 3 shows a ratio image, in which each pixel is the quotient of the R value of the 425 nm band divided by the R value of the 700 nm band, for a PTS made with yellow-dyed resin. The difference in grey level between the gangue and the resin in this image is remarkable, as the bimodal histogram in Figure 4 clearly shows.

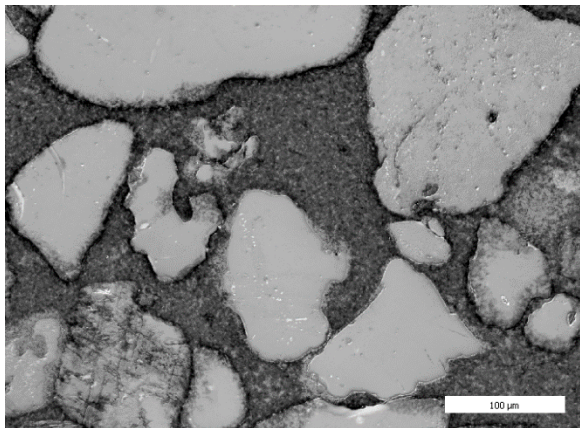


Figure 3. Ratio of 425 / 700 nm bands (yellow-dyed resin, 10x)

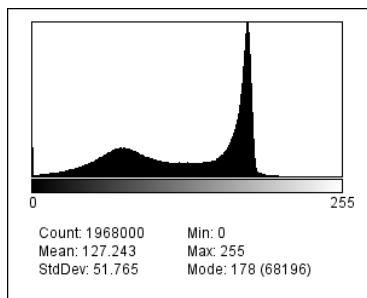


Figure 4. Histogram of the 425 / 700 nm ratio image of Figure 3

The behaviour of the three AcryDye colorants is similar, although the effect is less intense for the red and blue dyes than for the yellow. Depending on the amount

of colorant added, the aspect of the resin can change considerably. If the amount of dye is small, its pigments absorb part of the light that impinges on the resin, decreasing its apparent reflectance. As the amount of pigment increases, its particles make the resin behave like a higher-reflectance surface.

The magnification of the objective also has a clear effect in the separation between the spectral curves of gangue and resin: it is wider for the 5x and 10x objectives than for the 20x objective (Fig. 5). Nevertheless, 20x is the preferred magnification for ore characterisation, so the selected solution should be the one working best with 20x objectives.

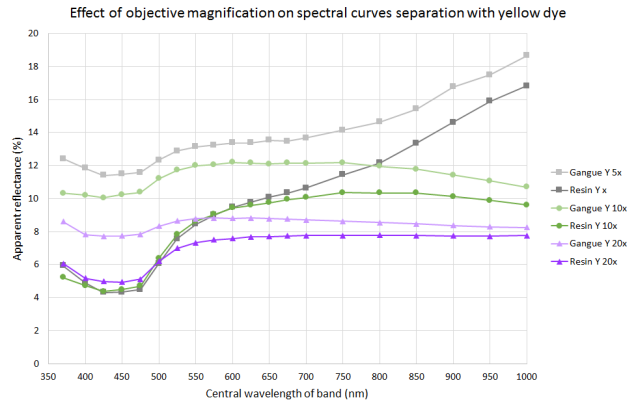


Figure 5. Effect of objective magnification on spectral curves separation

EpoDye behaves as a colorant very similarly to the yellow dye, and produces very good ratio images as well. However, its effect is even more outstanding when the image is acquired in fluorescence mode, as the resin appears bright while the gangue looks almost black, as Figure 6 shows. The histogram of fluorescence images is clearly bimodal (Fig. 7), implying a straightforward segmentation.

Therefore, the best solution is to use fluorescein as dye (EpoDye), and acquire a band in fluorescence mode, because of its higher effectivity with the 20x objective. While in bright-field mode differences between gangue and resin are small, in fluorescence mode resin becomes very bright and is clearly distinguished from mineral grains. Fluorescent minerals that might exist in the sample could be the only disadvantage of this method, but they are not common components of milled ore concentrates, and their fluorescence would also help to detect them.

6 Conclusion and applications

The results of this work for Polished Blocks (PB) agree with the conclusions reported by Neumann and Stanley (2008).

However, our work has shown that an effective method to distinguish between resin and gangue minerals is possible for Polished Thin Sections (PTS), without altering the properties of the ores or the gangue present in the sample.

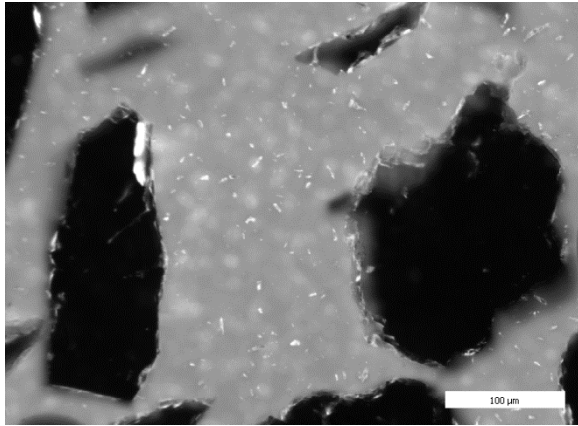


Figure 6. Image of fluorescence (fluorescein-dyed resin, 20x)

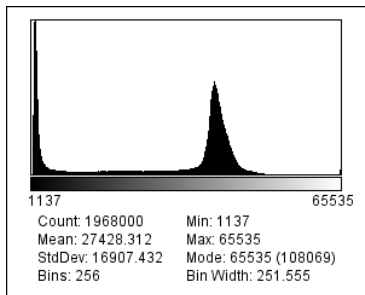


Figure 7. Histogram of the fluorescence image of Figure 6

Although all the studied colorant dyes can provide ratio images presenting a good discrimination between resin and gangue with 5x or 10x objectives, the best solution appears to be the use of the fluorescent dye, because of its high effectivity with the 20x objective, both for ratio and fluorescence images. This enables the application of Digital Image Analysis based on Reflected Light Microscopy to milled ore samples or concentrates.

With this solution, using PTS, the way to the generalized application of automated methods of optical microscopy for geometallurgical characterization is wide open. Nevertheless, for whole-rock studies automated identification of gangue minerals is possible even in PB, except for porosity measurement or for very porous samples, because the presence of resin is limited to the borders and can be easily isolated.



Figure 8. Mask for resin computed from image of Figure 6

The AMCO image analysis software incorporates a routine to implement the automated distinction between gangue and resin that creates a mask for the resin area, isolating the particles present in the microscopic field (Fig. 8). AMCO is thus able to offer an accurate modal analysis of milled ore concentrates, as well as whole-rock samples, automatically discounting the regions of resin from the sample.

Acknowledgements

This study has been undertaken as a UPM Grade Thesis and as a contribution to one of the scheduled tasks of AMCO (EIT Project no. 15039. 2016-2018), R+D+i Project funded by EIT Raw Materials, EU- H2020 Program. The colleagues of the AMCO Consortium (particularly TSL and E. Pirard and his ULiège team) and of the Sample Preparation Lab of the Department of Geochemistry and Petrology (Faculty of Geological Sciences, Madrid Complutense University) are thankfully acknowledged.



EIT RawMaterials is supported by the EIT, a body of the European Union

References

- Castroviejo R, Brea C, Pérez-Barnuevo L, Catalina JC, Segundo F, Bernhardt HJ, Pirard E (2009) Using computer vision for microscopic identification of ores with reflected light: preliminary results. Pp. 682-684, in: Williams et al., eds. Smart Science for exploration and Mining (Proc.10th biennial SGA Meet. Vol. 2. Townsville, Australia), ISSN: 9780980558685.
- Catalina JC and Castroviejo R (2017) Microscopía de Reflectancia Multiespectral: Aplicación al Reconocimiento Automatizado de Menas Metálicas. Rev. Metal. 53 (4):1-20. ISSN 0034-8570. doi: <http://dx.doi.org/10.3989/revmetalm.107>.
- Criddle A (1990) Microscope photometry, reflectance measurement, and quantitative colour. Chapter 6, pp. 135-169, in Jambor JL and Vaughan DJ, editors: Advanced Microscopic Studies of Ore Minerals. MAC Short Course 17, Ottawa.
- Delbem ID, Galéry R, Brandao PRG, Peres AED (2015) Semi-automated iron ore characterisation based on optical microscope analysis: quartz/resin classification. Miner. Eng. 82:2-13.
- Grunwald-Romera, U (2017) Detección de ganga en concentrados de planta por microscopía óptica de reflexión mediante métodos automatizados. Proyecto Fin de Carrera / Trabajo Fin de Grado, E.T.S.I. de Minas y Energía (UPM). <http://oa.upm.es/48414/>
- Neuman, R and Stanley, C J (2008) Specular reflectance data for quartz and some epoxy resins - Implications for digital analysis based on reflected light optical microscopy. Ninth International Congress for Applied Mineralogy, Brisbane 703-705.

Gold and silver mineralogy of the Liikavaara Cu-(W-Au) deposit, northern Sweden

Mathis Warlo, Christina Wanhainen, Glenn Bark

Division of Geosciences and Environmental Engineering, Luleå University of Technology, Sweden

Peter Karlsson

Exploration Department, Boliden AB,

Abstract. The Liikavaara Cu-(W-Au) deposit in northern Sweden is scheduled for production by the mining company Boliden AB in 2023. The ore will be processed in the plant of the nearby Aitik Cu-Au deposit. Copper will be the primary product and the trace metals Au and Ag will be byproducts. The trace mineralogy of Liikavaara, however, differs from that of Aitik and this might have implications on the mineral processing and recovery efficiency. Gold occurs mostly as free <10 µm-sized grains of native Au and electrum. Some Au is associated with native Bi, typically in <5 µm Bi-melt drops. Gold grains commonly form inclusions in quartz and sulfide minerals. Silver is found in electrum, hessite and acanthite. Hessite is the most abundant Ag mineral and it is commonly intergrown with pilsenite. Similar to Au, inclusions and crack-fillings of Ag in sulfides and quartz are most prominent. The small grain size, the diverse mineralogy, the association with Bi-phases, and the occurrence as inclusions in quartz may lower the recovery of Au and Ag in Liikavaara compared to Aitik, where Au and Ag phases are mostly bound in sulfides. Hence, adaptation of the processing parameters may be necessary in order to increase recovery of Au and Ag from the Liikavaara ore.

1 Introduction

The mineralogy, occurrence and distribution of trace metals in ore deposits often hold valuable information on ore genesis, but also their study is of interest from an economic perspective. Despite their low abundance, they can have a strong impact on the profitability of a mining venture. Trace metals like Au and Ag commonly add value as byproducts in mining operations. Other metals like Sb, As and U are deleterious. They either lower the quality of a primary commodity or require costly remediation to comply with environmental regulations. A good understanding of the trace metal mineralogy and its distribution in an ore deposit is therefore crucial to optimize profit and increase sustainability of a mining operation.

The Liikavaara Cu-(W-Au) deposit is an intrusion-related vein-style ore deposit in northern Norrbotten, Sweden (Fig. 1). It has a total resource estimate of 57.5 kton at 0.26% Cu, 0.06 g/t Au, and 2.2 g/t Ag (Boliden AB summary report 2018). Boliden AB holds the mining concession for the deposit and is currently in the mine development stage with estimated production to start in 2023. The deposit is enriched in a number of trace metals including Bi, Au, Ag, Sn, Te, and W. Gold and Ag are to

be produced as byproducts next to the primary production of Cu. Tungsten and other trace metals are currently not deemed profitable to extract. The Liikavaara ore will be processed in the plant of the nearby Aitik Cu-Au deposit. Despite their proximity, the two deposits show some differences in their mineralization (Warlo et al. submitted). This might affect the behavior of the ore during processing and ultimately the recovery efficiency. While the Aitik deposit has been described geologically in several studies (Monro 1988, Wanhainen 2005, Sammelin-Kontturi et al. 2011, Wanhainen et al. 2014), literature on the Liikavaara deposit are limited (e.g. Zweifel 1976, Warlo et al. submitted). Here, we present a detailed characterization of Au and Ag mineralogy in the Liikavaara deposit. The results should aid to optimize recovery efficiency of Au and Ag from the Liikavaara ore.

2 Geological background

The Liikavaara Cu-(W-Au) deposit is situated in the Gällivare area of the ore district of Northern Norrbotten, close to the world-class Aitik Cu-Au deposit (Fig. 1A). The deposit is situated in the eastern limb of a south-southeast dipping syncline and extends for about 1 km along strike, at a width of 100 m (Zweifel 1976). The ore body dips 80°W and is known to at least 400 meters depth (Zweifel 1976) (Fig. 1C, D). The ore is hosted by a metadiabase, which is partly altered and metamorphosed to biotite schist. The metadiabase intruded between metavolcaniclastic wall rocks ranging in composition from andesitic to basaltic (Estholm 2014, Warlo et al. submitted) (Fig. 1B–D). The rocks belong to the Muorjevaara Group and are of Svecofennian age (Zweifel 1976; Martinsson & Wanhainen 2004). A 1.87 Ga granodiorite intrusion in the footwall is suggested to be responsible for ore genesis and aplite dikes cutting the host rocks acted as pathways for the ore fluids (Fig. 1B–D) (Warlo et al. 2017, Warlo et al. submitted). Mineralization occurs predominantly in veins of quartz-tourmaline and calcite (Warlo et al. 2017, Warlo et al. submitted). Major ore minerals are chalcopyrite, pyrite, and pyrrhotite. Sphalerite, galena, scheelite, molybdenite, marcasite and magnetite are minor ore minerals. Whole-rock analyses show Bi, Au, Ag, Sn, and W to be prominent trace metals. Bismuth mineralogy is diverse and includes native Bi, Bi-tellurides and Bi-sulfides. Gold occurs as native Au and as grains of electrum. Silver is besides in electrum also found in hessite and acanthite. Tin occurs only in cassiterite and W in scheelite (Warlo et al. submitted). Warlo et al.

(submitted) present a paragenetic sequence where magnetite was formed first, followed by chalcopyrite, pyrite, and pyrrhotite. The minor sulfides formed later and the trace metal phases formed in an even later stage. Remobilization of the primary mineralization by hydrothermal fluids similar to the conditions in the Aitik deposit (Wanhainen & Martinsson 2003) is likely.

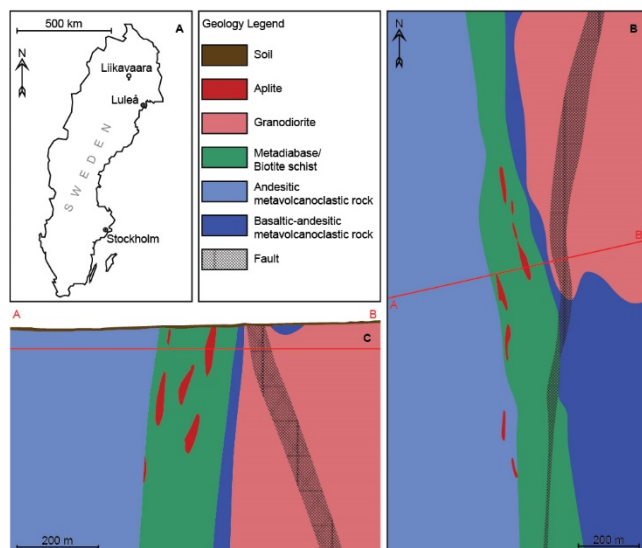


Figure 1. Geological map and profile of the Liikavaara Cu-(W-Au) deposit. **A.** Location of the deposit in northern Norrbotten, Sweden. **B.** Plan view of the Liikavaara Cu-(W-Au) deposit, at 100 m below surface. **C.** Cross section through the deposit (modified from Warlo et al. submitted).

3 Methods

In this study, sixteen thin section samples from the Liikavaara Cu-(W-Au) ore deposit were studied by light optical microscopy (LOM) and scanning electron microscopy (SEM).

Geochemical assays were used to select suitable drill core samples enriched in the targeted trace metals. Polished thin sections were prepared by Vancouver Petrographics LTD. The thin sections were studied with a Nikon ECLIPSE E600 POL optical microscope, in both transmitted and reflected light. Regions of interest were subsequently analyzed with a Zeiss Merlin FEG-SEM-EDS/WDS. Imaging was done in both secondary and backscattered electron mode.

4 Results

4.1 Gold

Gold in Liikavaara occurs in quartz-sulfide-tourmaline veins as native Au and electrum (Fig. 2A–D). Differentiation between the two phases is solely based on the Au/Ag ratio (anything >20% Ag is classified as electrum). Gold grains are typically <10 μm in size. They form rounded to angular grains and are partly elongated. The Au grains occur as inclusions and crack-fillings in especially quartz but also in the sulfides sphalerite, pyrite, and molybdenite (Fig. 2A–C). In places, they can also be

found spatially close to scheelite and tourmaline. Some of the Au grains are associated with Bi-minerals, especially native Bi and pilsenite (Bi₄Te₃) (Fig. 2A). For some Au grains, native Bi occurs in the form of melt-droplets with Au partitioning at the rim (Fig. 2D). These Bi-droplets are generally <5 μm and only observed in quartz.

4.2 Silver

The dominant Ag minerals in Liikavaara are hessite (Ag₂Te), electrum and acanthite (Ag₂S) (Fig. 2E, F). Similar to Au, the occurrence of Ag minerals is limited to veins of predominantly quartz and sulfides. Hessite occurs mainly tightly intergrown with pilsenite and occasionally with volynskite (AgBiTe₂). Hessite also forms inclusions at the rim of especially chalcopyrite but also other sulfides (Fig. 2E). At these sulfide rims hessite is commonly also in contact with calcite and tourmaline. Hessite grains vary in size from a few microns up to 100 μm. Acanthite is less common compared to hessite and the maximum observed grain size is ~30 μm. It occurs anhedral at the border of sulfide grains like pyrite and chalcopyrite and in contact with silicates (e.g. chlorite, tourmaline, quartz) and carbonates (e.g. calcite, ankerite) (Fig. 2F). The character and occurrence of electrum is described in 4.1.

5 Discussion

Introduction of Au- and Ag-minerals to the Liikavaara ore zone have previously been discussed to be the result of Bi-melt scavenging of Au and Ag from the footwall intrusion and subsequent deposition in veins in the ore zone (Warlo et al. submitted).

In the nearby Aitik deposit, Au occurs as native Au, electrum and amalgam, where electrum and amalgam are mostly found with sulfides, and native Au is typically associated with silicates. Gold grains are commonly <10 μm, but grains up to 35 μm have been observed (Wanhainen et al. 2003, Sammelin-Kontturi et al. 2011). Spatial variations in Au composition have been described, such as Ag-rich electrum and native Au common at depth and Au-rich electrum more distal to the core of the deposit (Sammelin-Kontturi et al. 2011). Sammelin-Kontturi et al. (2011) suggest this to possibly reflect differing conditions of Au/Ag deposition within the post-ore hydrothermal system but also highlight the possibility of multistage Au mineralization due to an IOCG (Iron Oxide Copper Gold) overprint at Aitik.

In Liikavaara no relationship between compositional and spatial variation of Au and Ag has been observed on deposit-scale. However, a contrast exists between round grains of native Bi with partitions of Au in quartz and partly elongated crack-infillings of electrum in sulfides. Furthermore, hessite and acanthite are mostly observed at the border of sulfides. This difference in character and occurrence of Au and Ag, in silicate and sulfide minerals in Liikavaara could indicate a multistage mineralization of Au and Ag similar to Aitik. Aside from Bi-melt scavenging, remobilization of Au and Ag from primary sulfides could

also have been a process involved in Au and Ag mineralization in Liikavaara.

Regarding mineral processing at the Aitik mine, the present method for Au and Ag recovery is Cu-flotation. This means the Au and Ag are floated with the copper minerals and later separated from the concentrate. Since

the ore from Liikavaara will be processed in the Aitik plant, a portion of Au from the Liikavaara ore will likely be lost to the tailings. This is due to the small Au grain size that limits floatability and the association with silicates that causes Au to go with the gangue.

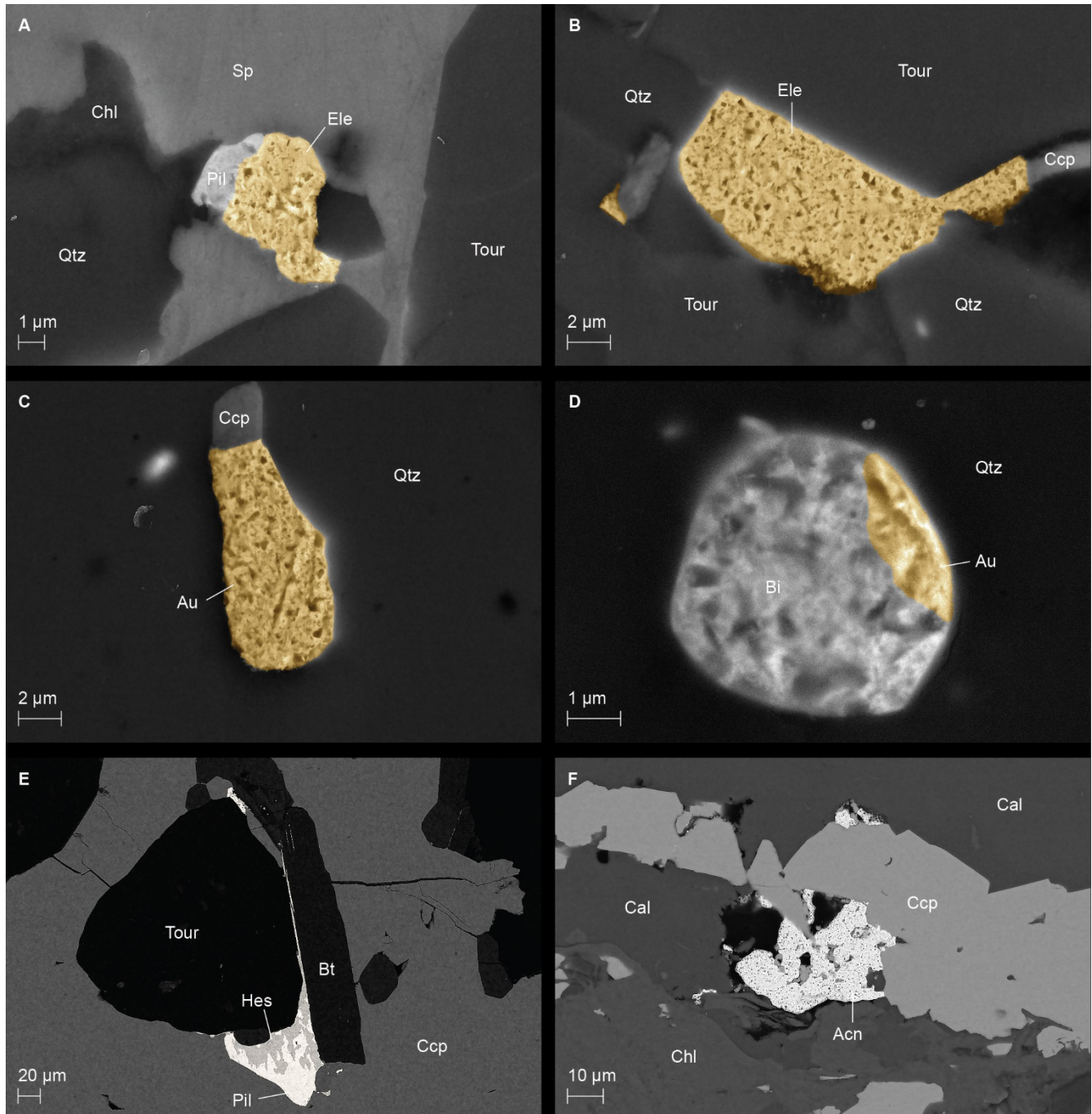


Figure 2. Secondary electron (A–D) and backscattered electron (E–F) images recorded by SEM. Gold is colored. The porous texture of Au is partly natural and partly an artefact of polishing. **A.** Electrum associated with sphalerite and pilsenite. **B.** Electrum and chalcopyrite associated with tourmaline and quartz. **C.** Native Au associated with chalcopyrite in quartz. **D.** Bismuth melt drop with Au, in a quartz matrix. **E.** Hessite intergrown with pilsenite at the boundary to chalcopyrite. **F.** Acanthite associated with chalcopyrite, calcite and chlorite. Abbreviations: Acn – acanthite, Au – gold, Bi – bismuth, Bt – biotite, Cal – calcite, Ccp – chalcopyrite, Chl – chlorite, Ele – electrum, Hes – hessite, Pil – pilsenite, Sp – sphalerite, Tour – tourmaline, Qtz – quartz

At present, it is likely that only the Au bound in sulfides will be recovered. Silver may have a higher chance for recovery. Acanthite and hessite are commonly associated with sulfides and grains are often >10 µm. However, hessite is mostly complexly intergrown with pilsenite, which may limit liberation and introduce unwanted Bi to the concentrate.

For a proper prediction of trace metal deportment during processing and a potential environmental impact more work is necessary. While samples were collected across the deposit, total sample volume was low and not all samples contained grains of Au and Ag. Therefore, to support representativeness of the findings of this study statistical analysis is required. For this, future work with automated quantitative mineralogy is planned. The characterization of Au and Ag mineralogy presented here provides an important basis to successfully plan and carry out quantitative analysis of the various minerals and textures.

Acknowledgements

Boliden AB is acknowledged for financing the analytical work in this study, which is part of a PhD project financed by CAMM² (Centre of Advanced Mining and Metallurgy), Luleå University of Technology. We gratefully thank Boliden AB for their continuous support and involvement in the project and for the permission to publish this abstract.

References

- Estholm M (2014) Identification of the host rocks and the environment of formation of the Liikavaara Cu-Au deposit, Norrbotten, Sweden. Bachelor thesis, Stockholm University
- Martinsson O, Wanhainen C (2004) Character of Cu-Au mineralizations and related hydrothermal alterations along the Nautanen deformation zone, Gällivare area, northern Sweden. *Econ Geol* 33:149-160
- Monro D (1988) The geology and genesis of the Aitik copper-gold deposit, Arctic Sweden. Dissertation, University of Wales, College of Cardiff
- Sammelin-Kontturi M, Wanhainen C, Martinsson O (2011) Gold mineralogy at the Aitik Cu-Au-Ag deposit, Gällivare area, northern Sweden. *GFF* 133:1-12
- Wanhainen C, Kontturi M, Martinsson O (2003) Copper and gold distribution at the Aitik deposit, Gällivare area, northern Sweden. *Appl Earth Sci*, 112(3):260-267
- Wanhainen C, Martinsson O (2003) Evidence of remobilisation within the Palaeoproterozoic Aitik Cu-Au-Ag deposit, northern Sweden: A sulphur isotope study. In: *Proceedings of the 7th biennial SGA meeting, Athens*, pp 1119-1122
- Wanhainen C (2005) On the origin and evolution of the Palaeoproterozoic Aitik Cu-Au-Ag deposit, northern Sweden: a porphyry copper-gold ore, modified by multistage metamorphic-deformational, magmatic-hydrothermal, and IOCG-mineralizing events. Dissertation, Luleå University of Technology
- Wanhainen C, Nigatu W, Selby D, McLeod C, Nordin R, Bolin N-J (2014) The distribution, character, and rhenium content of molybdenite in the Aitik Cu-Au-Ag-(Mo) deposit and its southern extension in the northern Norrbotten ore district, northern Sweden. *Minerals* 4:788-814
- Warlo M, Martinsson O, Wanhainen C, Karlsson P, Höglund S (2017) Mineralisation paragenesis of the Liikavaara Cu-(W-Au) deposit, northern Sweden. In: *14th SGA Biennial Meeting on Mineral Resources to Discover*, Quebec City, pp 971-974
- Warlo M, Wanhainen C, Martinsson O, Karlsson P (2019)

Mineralogy and origin of the intrusion-related Liikavaara Cu-(W-Au) deposit, northern Sweden. Submitted to *GFF*
Zweifel H (1976) Aitik - geological documentation of a disseminated copper deposit: a preliminary investigation. *SGU C720*, 80 pp

Geochemistry and quantitative mineralogy of REE-bearing phosphate stockpile ore from the Catalão Region, Brazil

Tim Rödel, Gregor Borg

Institute of Geosciences and Geography, Martin Luther University Halle-Wittenberg, Germany

Abstract. In this ongoing study, raw materials are being investigated for their potential as rare earth element (REE) sources. Amongst other sample groups, REE-mineral-bearing phosphate stockpile ore is analysed with respect to its quantitative mineralogical distribution and geochemical composition. Laser granulometry, ICP-MS geochemistry, SEM-EDX, and automated mineralogy tools are currently used. Total rare earth oxide (TREO) concentrations are as high as 0.7% to 0.9% but may reach up to 1.8%. Determining the fraction of extractable element content from a geometallurgical point of view is one major goal of the study. The phosphate ore consists predominantly of apatite, Fe-oxide minerals (hematite, magnetite, minor goethite) intergrown with ilmenite, quartz, and phyllosilicates like phlogopite or vermiculite. Minor, variable amounts of gorceixite, carbonates, rutile, and barite occur locally. Accessory heavy minerals are pyrochlore, Ba-pyrochlore, zirconolite, and baddeleyite. The main REE ore mineral is the REE-phosphate monazite with varying Ce-La-Nd proportions. Minor amounts of REE are also bound to pyrochlore, apatite, and zirconolite.

1 Preface

The REE have been classified as critical raw materials in 2014 due to supply risk, low end of life recycling rate and economic value (European Commission 2014). Important applications are diverse and uses in metallurgy as alloys, strong magnets (especially Nd-F-B magnets), ceramics or electronics (resistor materials) are common (Krishnamuthy and Gupta 2016). Diversifying the supply of critical elements for the European market is crucial in securing the future development of high-tech industries and limiting supply risks. The beneficiation of by-products from raw material production, tailings, and industrial residues (Binnemans 2015) enables society to pursue sustainable development by feeding previously unused resource potential into the economic value chain. Employing environmentally friendly processes without additional mining, reduces the ecological footprint, whilst improving economic profitability. As demonstrated by Pereira et al. (2019) assessing the geometallurgical properties of REE-bearing material might be useful in determining its economic potential as a by-product.

The recovery of REE as a by-product from phosphoric acid production for the fertilizer industry from the Catalão Region is the overall goal of the current study. Habashi (1984) estimated a possible global supply of 500,000 t of REE from 130 million t of annually treated phosphate rock based on a TREO content of up to 1%. Brazil hosts an estimated phosphate reserve of 170 million t with an

annual production of 5.4 million t (U.S. Geological Survey 2019). Consequently, a potential of an annual production of up to 25,000 t REE was estimated by Bardano and Gomes (2015) for sources from the Brazilian phosphate industry.

The run-of-mine stockpile phosphate ore from the Catalão Region presented here hosts the base inventory of available REE-mineral phases at the beginning of the process from ore to waste. Material streams during phosphate beneficiation including tailings are currently also investigated. Evaluating the source material's mineralogical composition is critical for selecting and optimizing further mineral beneficiation processes. One key objective of the current study is a comprehensive mineralogical description and assessment of the quantitative distribution of available mineral phases with regard to element recoverability and possible unwanted gangue. This includes particle size distribution, element composition of identified phases, and mineral intergrowth ("liberation").

2 Samples and methods

The analysed phosphate ore represents weathering products of alkaline igneous rocks from the Catalão Region, Brazil. Samples have been taken from pre-crushed blended stockpile material before phosphate beneficiation. Because of the unrefined nature, 60 % of the material is generally larger than 250 μm . Due to limited sample material available, no full sieving analysis was performed. Only the sample fraction passing 250 μm mesh was analysed using granulometry (Fig. 1).

The particle size distribution analyses were performed using a Cilas 920 laser diffraction granulometer with sample material in isopropanol suspension to prevent agglomeration of fine particles. Sieving lines of the analysed samples exhibit a similar shape and therefore similar characteristics. The grain size distribution is broad and 25 to 35 % of the analysed material is smaller than 25 μm . It was suspected that accessory heavy minerals are accumulated in the fine fraction below 80 μm . The particle size distribution analyses were performed using a Cilas 920 laser diffraction granulometer with sample material in isopropanol suspension to prevent agglomeration of fine particles.

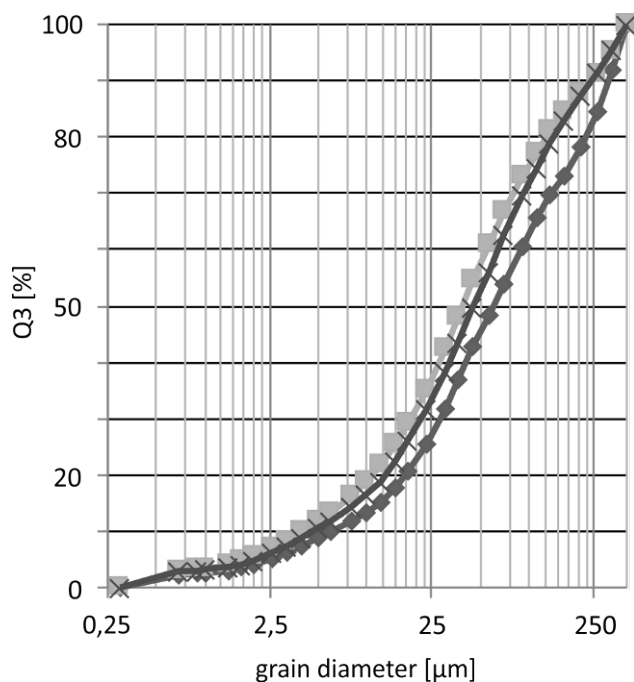


Figure 1. Particle size distribution of several run-of-mine phosphate ore samples passing 250 µm mesh. The cumulative sieving curve was created based on laser granulometry.

Sieving lines of the analysed samples exhibit a similar shape and therefore similar characteristics. The grain size distribution is broad and 25 to 35 % of the analysed material is smaller than 25 µm. It was suspected that accessory heavy minerals are accumulated in the fine fraction below 80 µm. For this reason, special emphasis was put on fine particle analysis. Grain mounts of representative sample splits from untreated samples, as well as milled and sieved (<125 µm mesh) material were prepared. Due to the heterogeneous particle size distribution, the subsequent additional sample preparation step proved necessary to achieve a homogeneous particle distribution in the granular polished sections. These will in turn improve the representability of the analysis using SEM-based automated mineralogy. Tests show that the results of the mineral distribution analysis for minerals occurring as large particles like Fe-oxides, quartz, or apatite have a much higher coefficient of variation (2- to 4-fold) in the untreated raw samples compared to milled and sieved material. Thus the absolute variations between individual measurements could be dramatically reduced by further crushing and sieving. For evaluating mineral and particle associations, the polished sections of raw untreated sample material remain of high importance nonetheless. Special precautions for avoiding nugget effects have to be taken, when working with this kind of heavy mineral target fraction.

Mineral distribution analyses were performed using the SEM coupled Bruker Quantax “feature analysis” tool and the “Advanced Mineral Identification and Characterization System” (AMICS). Both automated software tools are based on the collection of EDX spectra from segmented BSE greyscale images. Whereas the Bruker “feature analysis” tool is based on spectra

quantification, the AMICS system uses spectra shapes to match measured references. To this end a new database with relevant mineral phases was created for both systems to allow successful classification of detected spectra. Whereas Bruker “feature analysis” represents a more conservative particle counting approach, AMICS is a sophisticated software package based on MLA code. Compared to quantitative XRD with Rietveld method the techniques mentioned above allow a quantification of multiphase mineral systems (>10 phases), accessory minerals (content below 1%), or poorly crystalline phases. Additionally, information regarding mineral particle properties like size and liberation is generated. The mineral content can be expressed as area-, volume-, or weight-percent. Area percent is the actual measured particle property, based on segmented pixels, whereas volume is derived from a spherical model of the measured 2 D mineral area. Weight percent (wt %) is calculated from volume and mineral density. In this text mineral fractions are expressed as area %.

The geochemical analyses for major and trace elements were performed at the commercial laboratory “ALS Minerals”, Ireland using ICP-OES and ICP-MS. Digestion was achieved following lithium borate fusion. Non-destructive geochemical screening of sample material was achieved by portable XRF analysis with a ThermoScientific Niton XI3t.

3 Geochemical and mineralogical properties of stockpile phosphate ore

The investigated stockpile phosphate ore samples have a complex mineralogical composition and broad particle size distribution. Although homogenised after the mining operation, blending of the primary phosphate ore from different mining levels may result in variable geochemistry and mineralogy. Preliminary results of drill core material from different ore zones show a high variability in element composition and mineral inventory (Maak et al. 2019).

Major element concentrations of the selected and examined samples up to date are characterised by high Fe₂O₃ with 37 to 44% followed by CaO with 16 to 21%, SiO₂ with 15 to 18% and P₂O₅ with 12 to 16% (Fig. 2). Ba contents are generally elevated between 6000 to 9000 ppm, whereas Sr concentrations reach 3000 to 5,000 ppm. Nb contents of the analysed samples are as high as 2000 to 2,500 ppm but commonly above the detection limit (>2,500 ppm). TREO concentrations range between 0.7% to 0.9% but may reach up to 1.8%. These variations have to be considered when estimating the total rare earth element content available for further beneficiation. Generally, LREE exhibit a distinct enrichment compared to HREE. Ce, La, Nd and Pr are quantitatively the dominant REE.

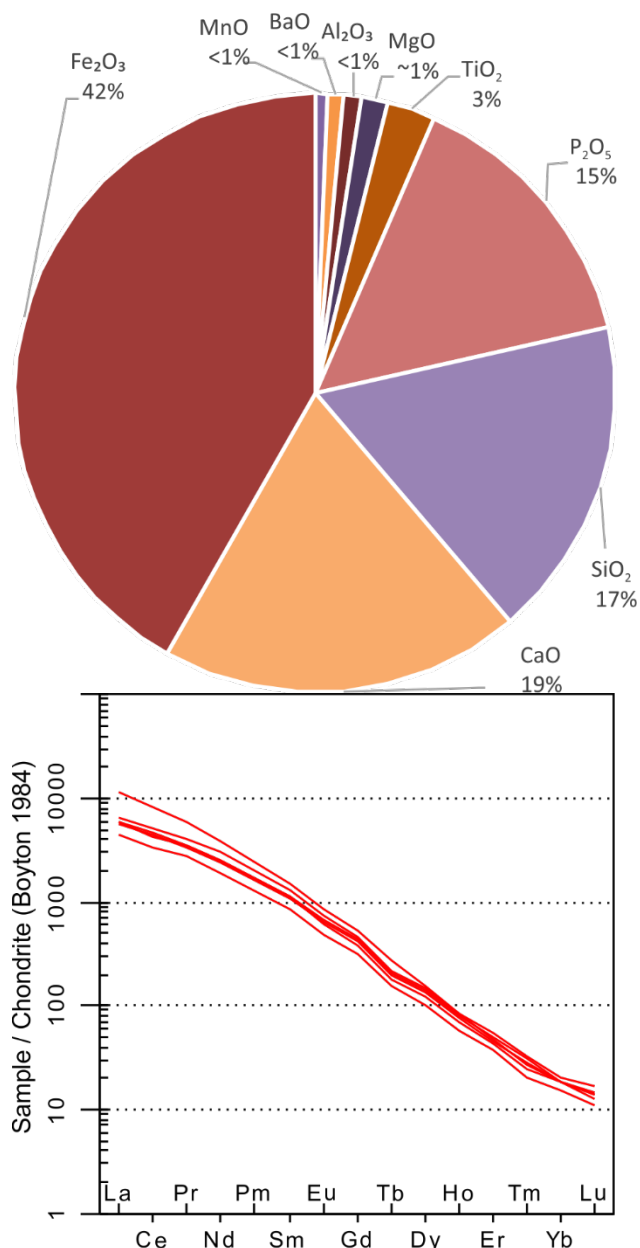


Figure 2. Mean concentration of major elements (see text for further explanation) and chondrite-normalized REE-patterns (Boyton 1984) for analysed stockpile ore samples.

Fe-oxide minerals (29-38% total area), apatite (32-39% total area), and quartz (19-23% total area) constitute the predominant rock forming mineral groups of the examined samples, which is in good accordance with the major element composition. Fe-oxides consist of varying amounts of martitised magnetite, hematite, goethite, and limonitic mixtures of goethite and clay minerals. Based on SEM-EDX analyses, Fe-carbonates like siderite are difficult to differentiate from Fe-oxide minerals but minor amounts of ankerite are easily distinguished by the presence of Ca in the spectra. Locally, Fe oxide minerals occur as large particles, intergrown with all occurring mineral phases, especially with quartz and apatite (Fig. 3). Ilmenite commonly occurs intergrown and overgrown by Fe-oxide minerals (most likely hematite) as fine exsolution lamellae. Species of Mg-bearing ilmenite have

also been detected. Total ilmenite content is relatively low between 1.5% to 3%. Other Ti-bearing minerals like titanite or rutile rarely make up more than 0.1% of the total mineral portion. Rutile primarily occurs as a Nb-bearing variety.

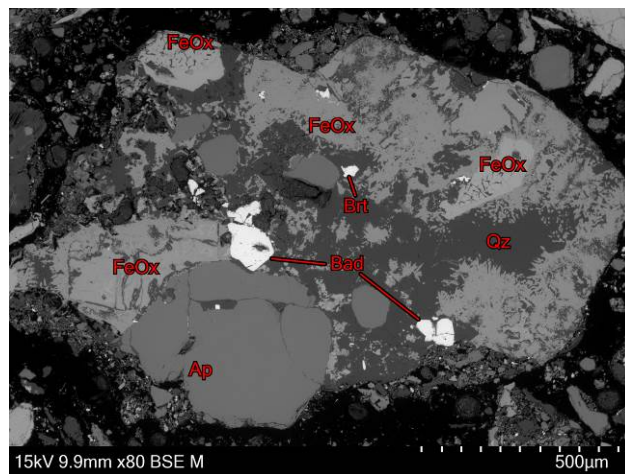


Figure 3. SEM-BSE image showing complex intergrowth of partly euhedral specular Fe-oxide minerals (FeOx) with quartz (Qz), subhedral apatite (Ap) and heavy minerals like baddeleyite (Bad) and barite (Brt).

The main phosphate carrier of the investigated samples is apatite with a P-80 between 205 and 950 µm. In the raw stockpile run-of-mine ore 55 to 70% of the total area of apatite particles are already liberated. Peculiar is its intergrowth and overgrowth of smaller Ba-alumophosphates (gorceixite). This mineral is occurring in low concentrations between 1 and 1.5% of the observed mineral particles. The presence of REE in apatite was detected but low concentrations prevent a semi-quantitative analysis using EDX.

Quartz occurs as particles with a P-80 between 325 and 770 µm. It appears as single particles but more commonly is intergrown with Fe-oxides or apatite. Quartz typically forms massive particles encapsulating euhedral apatite or specular hematite or as cementitious texture filling of fractures between larger apatite particles or Fe-oxides. Other silicates occur with varying combined quantities between 1.5 and 3%. Most common are Mg-bearing phyllosilicates like phlogopite, vermiculite, or chlorite. Carbonates are mainly represented by dolomite and only minor calcite.

Interesting from a raw material point of view are accessory heavy mineral fractions. Comparably large barite particles commonly occur in minor amounts around 0.25 to 0.35%. Pyrochlore and Ba-pyrochlore are common accessory Nb phases that occur in a fraction between 0.1 to 0.3 % but might reach up to 1.5%. Pyrochlore is commonly observed as euhedral to subhedral crystals, fully liberated or encapsulated by gorceixite, quartz, or apatite. Differing BSE grey-scale values originate from varying Ba-contents that occur in distinct zones or irregular schlieren. Zr-minerals like zirconolite (0.05 to 0.25%) and baddeleyite (0.05 to 1.5%) occur strictly as accessories. The Zr-oxide baddeleyite occurs liberated or intergrown with apatite. Rare

intergrowth occurs with Fe-oxides, quartz, or goethite. Zirconolite shows a less distinct affinity of intergrowth with specific mineral phases. Intergrowth was observed similarly with apatite, Fe-oxide minerals, goethite, and quartz. Zirconolite commonly contains low concentrations of REE.

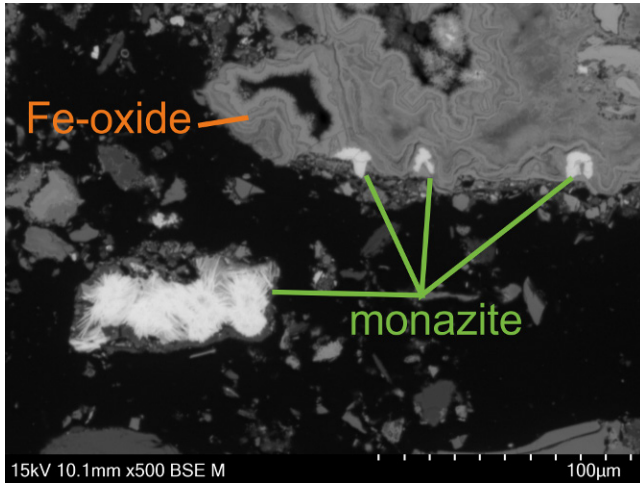


Figure 4. SEM-BSE image of a liberated fibrous monazite aggregate and intergrowth of fine botryoidal monazite with collomorphous Fe-oxide minerals.

Monazite hosts a large portion of the TREO content. Total amounts of this geochemically diverse mineral vary between 0.3 to 0.6 area %. This translates into 0.6 to 1 wt % of potentially accessible REE-mineral content. Rarely, even up to 2 wt % REE-phosphate have been documented. In conjunction with the TREO from geochemically analysed samples, monazite seems to account for 40 to 60 % of the REE content in the samples. Using that relationship could potentially help in predicting further processable quantities of REE. This estimation however is varying for different sample material groups. Monazite particles in the phosphate ore material generally show fine particle sizes with a P-80 between 37 to 43 μm (Fig. 5). The majority (80 wt %) of the particles have a diameter larger than 12 μm (applying a minimum measured particle size of 10 μm^2). A large portion of monazite is intergrown with apatite, quartz, and Fe-oxides. Monazite displays a variety of botryoidal, compact collomorphous, to radial fibrous mineral shapes (Fig. 4). Minute flaky radial monazite was observed as inclusions in apatite and goethite.

A high diversity of the mineral shapes might indicate several different monazite generations in the mined ore. Geochemically, monazite also shows a high variability besides the described morphological differences. Elements such as Sr, Ca, and F are commonly detected in monazite particles. So far, no systematic relationship between the trace element content and the specific mineral shape could be established.

Our results from the investigation of the phosphate ore will be put in further context with various process material from the phosphate beneficiation process. These results will hopefully assist to construct a robust and applicable system for the estimation of the recoverable total REE content in ores and process materials.

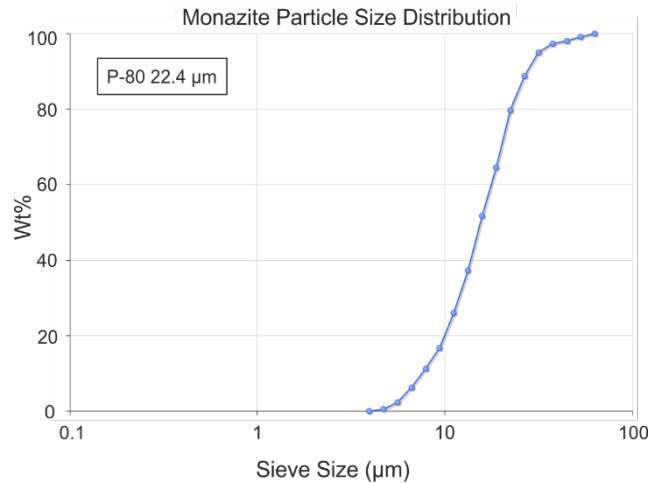


Figure 5. Mineral size distribution of exemplary fine-grained monazite in run of mine stockpile ore.

Acknowledgements

This project is funded by the German Federal Ministry for Education and Research (033R187C). Ceritech AG is greatly acknowledged for transferring know-how and arranging sample logistics.

References

- Bardano BMM, Gomes R (2015) Potencial de Aproveitamento de Fontes Secundárias para Terras Raras: Resíduos industriais, vol 86. CETEM Centro De Tecnologia Mineral
- Binnemans K, Jones PT, Blanpain B, van Gerven T, Pontikes Y (2015) Towards zero-waste valorisation of rare-earth-containing industrial process residues: A critical review. *J. o, Cleaner Production*
- Boynnton WV (1984) Cosmochemistry of the rare earth elements; meteorite studies. In: *Rare earth element geochemistry*. Henderson, P. (Editors), Elsevier Sci. Publ. Co., Amsterdam. 63-114.
- European Commission (2014) Communication from the commission to the European Parliament, the Council, the European Economic and Social Committee and the Committee of the regions, COM (2014) 297 final, Brussels
- Habashi F (1985) The recovery of the lanthanides from phosphate rock. *J Chem Tech Biotechnol* 35:5-14
- Krishnamurthy N, Gupta C (2016) *Extractive metallurgy of rare earths*, Second edition. CRC Press Taylor & Francis Group, Boca Raton, London, New York
- Maak, S, Kamrad, A, Borg, G (2019) Mineralogical and geochemical characteristics of alkaline phosphate ore from a supergene zone in the Catalão Region, Brazil. In this volume
- U.S. Geological Survey (2019) *Mineral commodity summaries*. U.S. Geological Survey, Reston, USA
- Pereira L, Birtel S, Möckel R, Michaux B, Silva AC, Gutzmer J (2019) Constraining the Economic Potential of By-Product Recovery by Using a Geometallurgical Approach: The Example of Rare Earth Element Recovery at Catalão I, Brazil. *Econ Geol*. doi: 10.5382/econgeo.4637

The Cinovec Sn-Li deposit: Challenges for ore processing

Alla Dolgoplova, Reimar Seltmann, Robin Armstrong, Chris Stanley
Natural History Museum, Department of Earth Sciences, London, UK

Jens Andersen, Gavyn Rollinson, Beth Simons
Camborne School of Mines, University of Exeter, UK

Chris Broadbent
Wardell Armstrong International, London, UK

Vitaly Shatov
VSEGEI St.Petersburg, Russia

Abstract. Mineralogical constraints for improving metal recovery at the Cinovec Sn-Li deposit in Czech Republic are discussed. We emphasize the importance of previously neglected mineralogical parameters that could significantly improve recovery of Li as the main commodity and of the most important by-products that include Sn, W, Ta and Nb. This research was performed in the frame of the h2020 FAME project aiming to catalyze the valorization of European tin, tungsten and lithium resources.

1 Introduction

The Cinovec-Zinnwald deposit is located in the eastern Erzgebirge/Krušné Hory area and extends across the Czech and German state border (Fig. 1). Both parts of the deposit are currently being explored by drilling for Sn-Li vein and greisen ores, accompanied by advanced ore processing tests.

Cinovec hosts the largest lithium resource in Europe, and one of the largest undeveloped tin resources in the World. A recently completed Preliminary Feasibility Study indicates that Cinovec has the potential to be the lowest cost hard rock lithium producer in the World (<https://www.europeanmet.com/cinovec-lithium-tin-project/>).

In our research, aiming to contribute to an increase in by-product recovery, we address some of the petrographic, mineralogical and geochemical criteria that affect ore processing.

2 Geological setting

The Zinnwald-Cinovec granite hosting world-class Sn-W-Li deposits forms an elliptical granite cupola outcropping 1.3 km in N-S direction. The W contact of the intrusion is steep, whereas the S, SE and E contacts plunge with 10 to 30°. The upper part of the intrusion is formed by lithium-albite granite, underlain by medium-grained protolithionite granite at a depth of 730 m beneath Cinovec (Štemprok and Šulcek 1969; Rub et al. 1983). In the cupola, the lithium-albite granite consists of two textural varieties: an older porphyritic granite and a younger medium-grained seriate granite that encloses the relicts of the porphyritic granite. Zinnwaldite is the predominant mica in the lithium-albite granite.

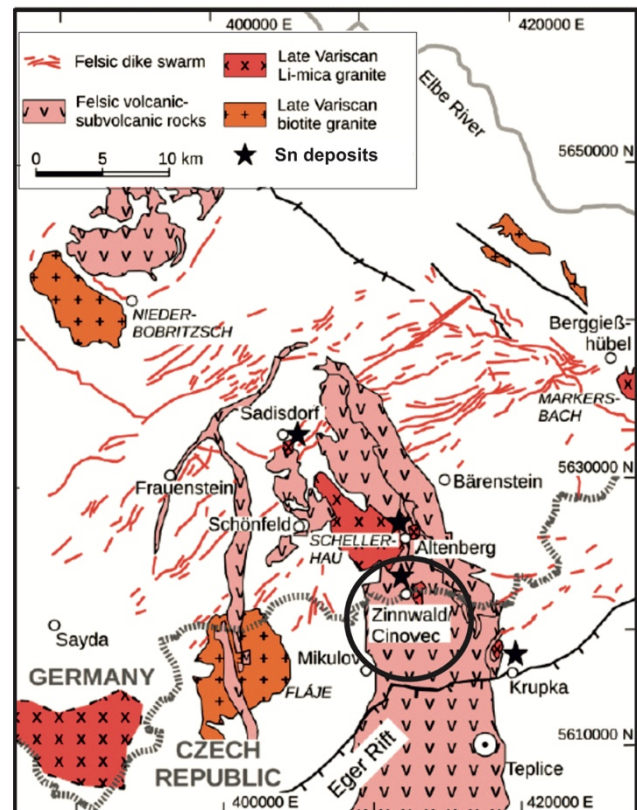


Figure 1. Late- to post-collisional highly evolved granite magmatism in the Erzgebirge, Germany-Czech border area. Asterisks show location of Sn deposits (from Zhang et al. 2017).

3 Mineralogical and petrographic study

The **lithium-albite granites** (synonyms: alkali feldspar granites or Li-F granites) contain on average 0.11 wt.% Li₂O and 4.62 wt.% K₂O. Plagioclase is absent, sodium feldspars are represented by albite with a low (<3 wt.%) anorthite content.

Main accessories are cassiterite, fluorite, topaz, columbite-tantalite in addition to rare bastnaesite, uranpyrochlor, uranmicrolite, strueverite, synchisite (Johan and Johan, 1993; Rub et al., 1998).

The **protolithionite granite** contains on average 0.05

wt.% Li₂O and 5.34 wt.% K₂O.

Main accessories are zircon, columbite, monazite, xenotime and rutile. Apatite is very rare.

The low-grade Li ore is confined to zinnwaldite with substantial Rb and Cs contents. In addition, the ore contains cassiterite, wolframite and scheelite as Sn and W carriers. Apart from this, the Sn and W concentrates contain considerable contents of Nb, Ta, and Sc.

The large petrographic and mineralogical variability of magmatic rocks and their alteration products is shown in figures 2 and 3; with quartz, potassic feldspar, albite, topaz, di- / trioctahedral micas, clays, and accessory minerals having main impact on metal recovery.



Figure 2. Mineralogical and petrographic variability of granites and greisens from Cínovec drill core (scale: half core sample NT-06 is 10 cm long).

Mica chemistry changes with compositional evolution of their granite hosts and it fingerprints the ore-generating potential of mineralized granitic systems as well as interaction of granite melts with their metamorphic wall-rocks. Furthermore, in highly evolved Li-F granite-ore systems such as Zinnwald-Cínovec, the magmatic-hydrothermal transition processes are characterized by intense “autometasomatic” fluid-rock interaction (Štemprok and Šulcek 1969).

Intrusive pulses and oscillating fluid release control continuous re-equilibration of mineral phases in time and space which explains the mica variability in the mineralized cupola with vertical petrographic zonation and mica zonation itself (Fig. 4).

The three observed genetic mica types include: magmatic-hydrothermal lithium mica (zinnwaldite, protolithionite, etc.), pseudomorph metasomatic replacements (high-Li: lepidolite) and tropomorph (low-Li: muscovite) metasomatic replacements.

The issue of accurate direct in-situ Li determination in micas, traditionally performed by recalculation of Li values from EPMA data using stoichiometry (Breiter et al. 2017, 2019), can be overcome by direct measurement of Li by LA-ICP-MS. The data obtained by the two methods correspond well to each other.

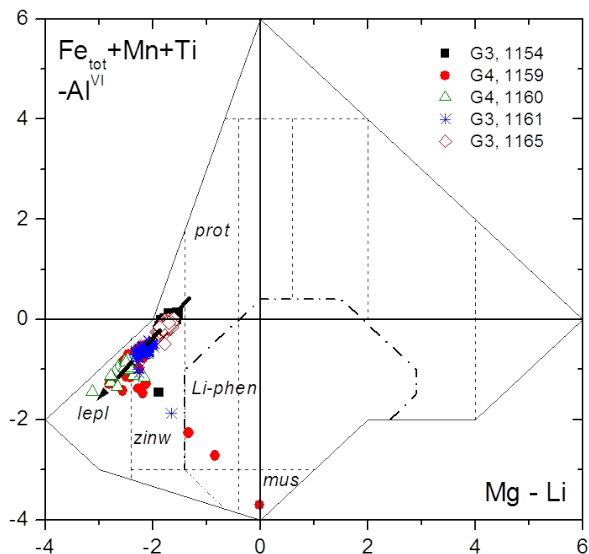


Figure 3. Mineralogical variability and evolution trends of lithium mica from Zinnwald-Cínovec (Fedkin et al. 2001): Li-Phengite - Zinnwaldite - Lepidolite (plot after Tischendorf et al., 1997).

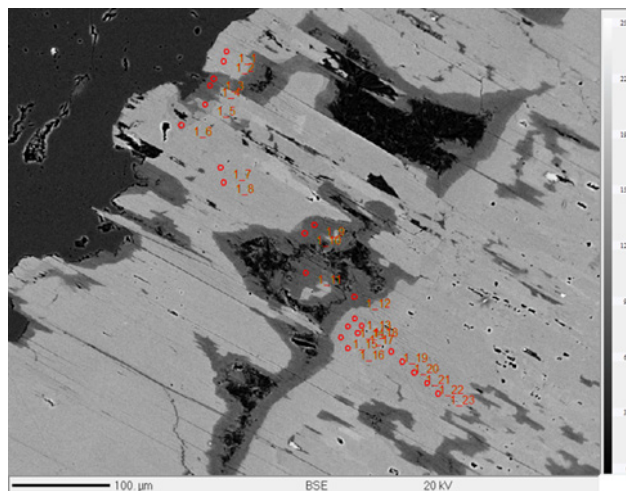


Figure 4. SEM BSE image of zinnwaldite with rims of retrograde muscovite.

4 QEMSCAN study

The QEMSCAN, an automated quantitative mineralogy technique, aids ore characterization for comminution. The

QEMSCAN analysis was carried out with the QEMSCAN® 4300 at Camborne School of Mines, University of Exeter (Fig. 5).

The studied ore is dominated by zinnwaldite (76 vol%) with minor clays (9 vol%), topaz (5 vol%) and quartz (4 vol%). Fluorite (1 vol%) partially replaces zinnwaldite, particularly along the cleavage planes of grains. The ore contains clusters of cassiterite (<50 µm, 0.01 vol%), locked primarily within zinnwaldite, less commonly fluorite.

Wolframite, columbite and scheelite are trace phases only (<0.01 vol%). Zircon, monazite, sulphides and uraninite are also trace phases only (<0.01 vol%) (Figs. 6, 7; Table 1).

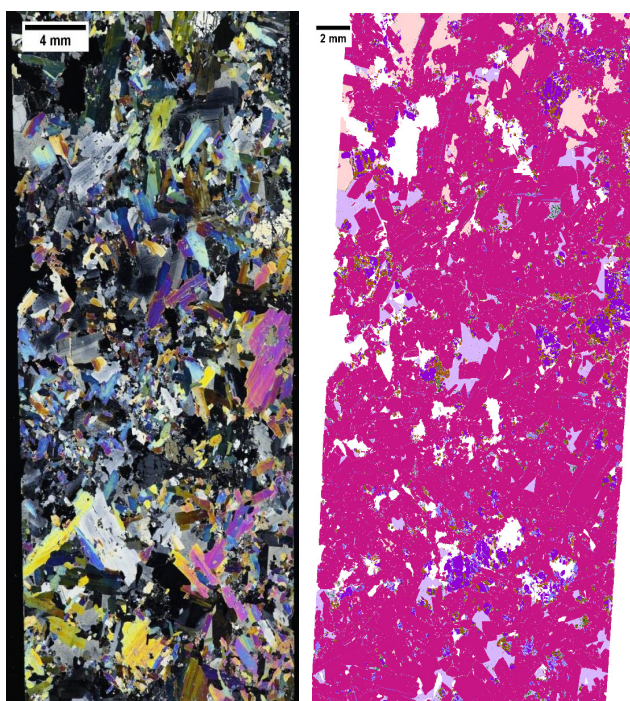


Figure 5. Visual appearance of thin section in transmitted light (left figure) and QEMSCAN® false colour map (right figure).

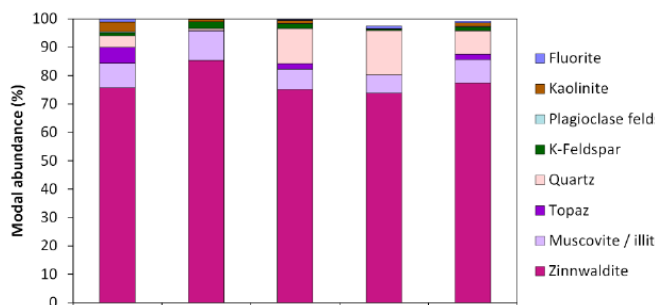


Figure 6. Modal abundances (vol%) for gangue and zinnwaldite.

Table 1. Mineralogical composition (Volume %) and size distribution identified by QEMSCAN (CSM University of Exeter).

Mineralogical composition (vol %)²

Zinnwaldite	75.67	Apatite	Tr.
Muscovite / illite*	8.78	Fe-Ox/CO3	Tr.
Topaz	5.51	Uraninite	Tr.
Quartz	4.15	Others	Tr.
Kaolinite	3.35	Galena	Tr.
Fluorite	1.11	Columbite	Tr.
K-Feldspar	0.98	Rutile	Tr.
Plagioclase feldspar	0.39	Scheelite	Tr.
Tourmaline	0.02	Wolframite	Tr.
Calcite	0.01	Bismuthinite	Tr.
Cassiterite	0.01	Sphalerite	Tr.
REE minerals	0.01	Chalcopyrite	n.d.
Chlorite	0.01	Cu arsenides	n.d.
Zircon	Tr.	Cobaltite	n.d.
Pyrite	Tr.		

Size distribution (max | min | mean)³

Zinnwaldite	6 mm	10 µm	521 µm
Cassiterite	145 µm	<10 µm	26 µm
Wolframite (Tr.)	-	-	≤15 µm
Scheelite (Tr.)	-	-	32 µm
Columbite (Tr.)	-	-	≤15 µm
REE minerals	120 µm	<10 µm	32 µm

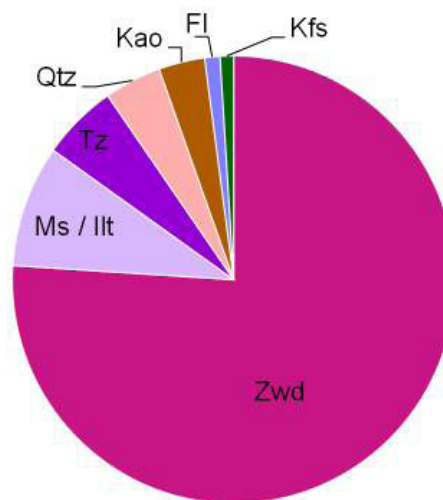


Figure 7. Visual representation of mineralogy (not <0.01 vol%): Gangue (+ zinnwaldite).

5 Optimising ore processing of Li-micas

Identifying key Li-bearing mineral phases has important implications for an optimized ore processing. Samples from the Cinovec deposit show a variety of main Li-bearing mineral phases such as zinnwaldite, muscovite and lepidolite (Fig. 8). Whereas the grain size distribution and density of the various mica phases are rather similar or in a close bandwidth, the magnetic behavior of Fe-Ti rich mica is the most contrasting petrophysical feature suggesting the application of magnet separation to achieve an optimized Li recovery. The magnetic susceptibility contrasts between zinnwaldite (paramagnetic) and lepidolite (diamagnetic) allow their successful separation. Muscovite is a common non-magnetic phase of late (retrograde) alteration, accompanying clayey phases in intergranular space, as zonal ongrowth, in cleavage of instable earlier Li mica or as replacement of tropomorphic alteration.

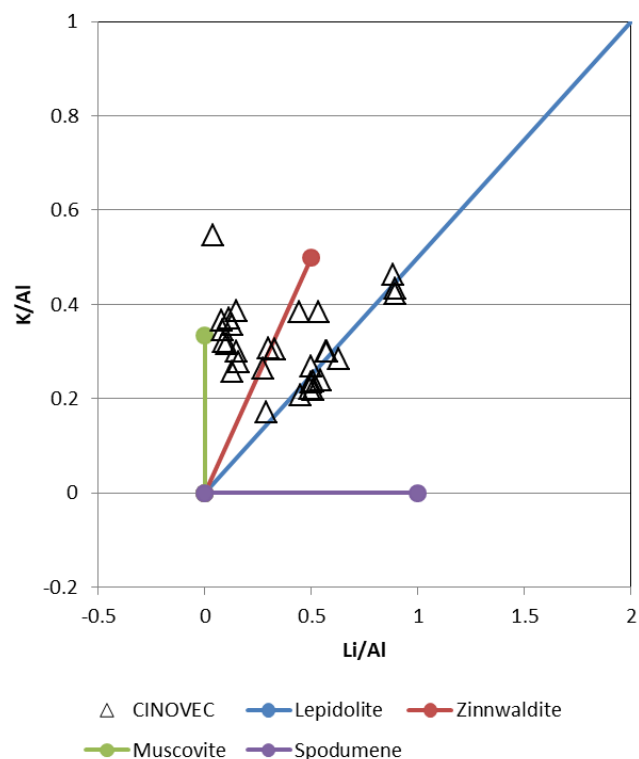


Figure 8. Li/Al vs. K/Al plot showing main Li-bearing phases at the Cinovec deposit.

6 Key challenges for ore processing

As key challenges for an optimized ore processing the following geological (petrographic, mineralogical, geochemical) constraints have been identified:

- Subhorizontal thin-layered anatomy of ore bodies (sheeted laccolite, alteration zones, flat ore bodies);
- Strong petrographic-mineralogical variability;
- Contrasting magnetic properties of mica phases;
- Variable grain size and strong Li zonation of mica;
- Low-temperature clayey alteration in intergranular

space could lead to Li loss in slimes;

- Problematic (or penalty) minerals: topaz – extremely hard and causes excessive wear on crushing and grinding equipment;
- Uraninite and pitchblende are trace radioactive minerals and could impact the final product if not removed.

A previously neglected mineralogical parameter but important for increased by-product recovery are the elevated contents of Nb and Ta in the alkali feldspar granites (outside the Li-Sn cut-off of the greisen ore bodies).

Acknowledgements

The research was co-funded by the EU Horizon 2020 Project “FAME”: *Flexible and Mobile Economic Processing Technologies* (grant #641650). The authors acknowledge the contributions of the whole FAME consortium for sample collection and preparation as well as scientific discussions that led to the development of this paper. We greatly appreciate the continuous support and cooperation of Neil Meadows, Pavel Reichl and Vojtek Sesulka of European Metals Holdings Ltd. / GEOMET, UK / Czech Republic.

References

- Breiter K, Ďurišová J, Hrstka T, Korbelová Z et al. 2017 Assessment of magmatic vs. metasomatic processes in rare-metal granites: A case study of the Cinovec/Zinnwald Sn-W-Li deposit, Central Europe. *Lithos* 292-293: 198-217.
- Breiter K, Hložková M, Korbelová Z, Vašinová Galiová M 2019 Diversity of lithium mica compositions in mineralized granite-greisen system: Cinovec Li-Sn-W deposit, Erzgebirge. *Ore Geology Reviews* 106: 12-27.
- Fedkin A, Seltmann R, Förster HJ 2001 Li-bearing micas as the fractionation indicator of tin granites: The Sadisdorf-Schellerhau granite suite, Eastern Erzgebirge. *Mineral Deposits at the Beginning of the 21st Century*, Piestrzynski et al. (eds). Swets & Zeitlinger Publishers Lisse: 409-412.
- Johan V, Johan Z 1993 Accessory minerals of the Cinovec (Zinnwald) granite cupola, Czech Republic, part 1. Nb-, Ta-, and Ti-bearing oxides. *Mineral. Petrol.* 49: 1-21.
- Rub MG, Pavlov VA, Rub AK, Štemprok M, Drábek M, Drábková E 1983 Elements of vertical zoning in the Cinovec massif of lithium fluorine granites (Czechoslovakia). In: *Correlation of magmatic rocks of Czechoslovakia and some districts of the USSR*. Izd. Nauka, 108-137, Moskva (in Russian).
- Rub AK, Štemprok M, Rub MG 1998 Tantalum mineralization in the apical part of the Cinovec (Zinnwald) granite stock. *Mineral. Petrol.* 63: 199-222.
- Štemprok M, Šulcek Z 1969 Geochemical profile through an ore-bearing lithium granite. *Econ. Geol.* 64: 392-404.
- Tischendorf G, Gottesmann B, Förster H-J and Trumbull RB 1997 On Li-bearing micas: estimating Li from electron microprobe analysis and an improved diagram for graphical representation. *Mineralogical Magazine*, 61, 809-834.
- Zhang R, Lehmann B, Seltmann R, Sun W, Li C 2017 Cassiterite U-Pb geochronology constrains magmatic-hydrothermal evolution in complex evolved granite systems: The classic Erzgebirge tin province (Saxony and Bohemia). *Geology* 45(12): 1095–1098.

Mineral processing and mineralogical characterization of pre-concentrates from the Rondônia Tin Province, Brazil

Simon Goldmann, Herwig Marbler

Federal Institute for Geosciences and Natural Resources (BGR)

Frank Haubrich

G.E.O.S. Ingenieurgesellschaft mbH

Tiago Buch

Companhia de Pesquisa de Recursos Minerais (CPRM) - Geological Survey of Brazil

Abstract. Processing tests are performed on pre-concentrates (about 60 kg each) from the Cachoeirinha and Bom Futuro mines to improve the recovery of cassiterite and columbite. The processing steps for the pre-concentrates include sample splitting, sieving, density and magnetic separation. The processing steps are accompanied by mineralogical characterization of the concentrates using scanning electron microscopy with Mineral Liberation Analysis software and geochemical analyses by handheld X-ray fluorescence. After sieving, both pre-concentrates can be successfully upgraded by density and magnetic separation to saleable concentrates at high grades and recovery.

1 Introduction

The present study is part of a cooperation project between the Federal Institute for Geosciences and Natural Resources (BGR), which is the Geological Survey of Germany, with Companhia de Pesquisa de Recursos Minerais (CPRM), the Geological Survey of Brazil. The aim of this study is the improvement of processing methods to optimize the recovery of cassiterite (major ore for Sn), columbite (major ore for Nb and Ta) and subordinate byproducts (e.g. zircon) to increase the economic output of marketable mineral concentrates from the Brazilian state of Rondônia. During a first reconnaissance study, geochemical analysis of pre-concentrates and tailings identified that quite a considerable amount of ore minerals is lost into the tailings during processing. This is the main reason for the processing tests in order to check if recovery could be improved. Here we show the results on pre-concentrate samples from the Cachoeirinha and Bom Futuro mines.

2 Geological setting

The Rondônia Tin Province is located in the southwestern part of the Amazonian Craton and is composed of Paleoproterozoic to Mesoproterozoic metamorphic rocks, which were intruded by several events of Rapakivi magmatism (A-type granites) between 1600 and 970 Ma (Fig. 1; Bettencourt et al. 1999).

The Sn-Ta-Nb deposits are closely associated with late-stage peraluminous, partly porphyritic alkali-feldspar

granites of the Younger Granites of Rondônia suite (998-974 Ma; Bettencourt et al. 1999). The primary mineralization styles are greisen bodies, quartz veins, and pegmatites. However, the exploited ores are mainly derived from the secondary alluvial and colluvial placer deposits, but also former tailings are re-processed. In Bom Futuro, 10 to 15 % of the production is also from primary ores.

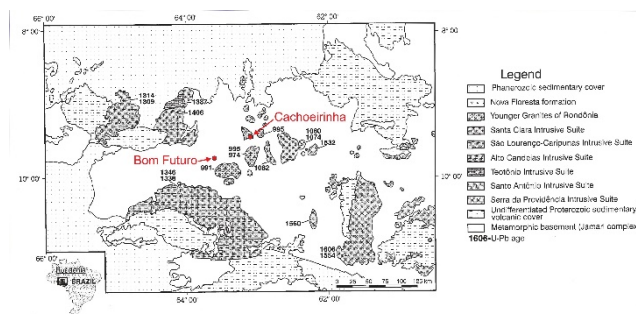


Figure 1. Geological map of the Rondônia Tin Province showing location of the respective sample sites. Insert shows the position of the map within Brazil (Bettencourt et al. 1999)

3 Materials and methods

3.1 Samples

Jigs are the initial processing step in the Cachoeirinha and Bom Futuro mines and bulk samples (about 60 kg each) are taken from the 2nd chamber of the jigs as starting material for further processing test work. The best quality is produced in the 1st chamber, but these concentrates are not treated for this study. Polished sections are prepared from these initial bulk samples (after sample splitting) and also from single processing steps during the test work.

3.2 Instrumental

Mineralogical parameters (like composition, grain size distributing and intergrowths) are identified using a FEI Quanta 650F scanning electron microscope with two Bruker energy-dispersive X-ray spectrometers (EDX) and Mineral Liberation Analysis (MLA) software. The MLA software uses the EDX system combined with

backscattered electron imaging to automatically identify mineral phases in ore concentrates by comparison of the X-ray spectra with those from standards stored in a database (Fandrich et al. 2007).

Geochemical analyses were performed using a Bruker S1 TITAN handheld X-ray fluorescence (XRF) on an aliquot of about 10 g of ground (<100 µm) sample for each processing step. The accuracy of the handheld XRF analyses are sufficient to monitor the enrichment or depletion of relevant elements along the processing path.

3.3 Mineral processing

The general processing procedure applied for the pre-concentrates includes sample splitting, sieving, density and magnetic separation. Subsamples of 1 kg from each pre-concentrate are sieved in 100 µm steps in order to determine which particle size fractions contain the largest amount of valuable material also in relation to mass of the respective fraction.

The enrichment of the heavy ore minerals takes place by density separation using a shaking table with a stroke length of 16 mm at 220 strokes per minute. For this purpose, the remaining bulk pre-concentrates are sieved into four particle size fractions with the following ranges: 63-250, 250-500, 500-710 and 710-2000 µm.

Subsequently, all heavy fractions (HF1 and HF2) from the shaking table are split into para- and diamagnetic fractions (the ferromagnetic fraction is very low) using a magnetic belt separator with a permanent magnet of fixed field strength of 1.1 Tesla.

4 Results and discussion

The pre-concentrate from Cachoeirinha (Fig. 2) is dominated by quartz and topaz, but also contains relatively high concentrations of cassiterite (~5 area%) as well as columbite (~2 area%). Cassiterite is present in high concentrations distributed over all particle sizes. Evaluated MLA data revealed that about 92 % of cassiterite is liberated. This is favorable for processing, because cassiterite is largely present as free grains and only a few grains are intergrown with other mineral phases. Especially in the small particle sizes, SnO₂ (representing cassiterite) is enriched up to 30 wt% and Nb₂O₅ + Ta₂O₅ (representing columbite) up to 15 wt% (Fig. 3). The highest concentrations of up to 5 wt% ZrO₂ (representing zircon) are in the <200 µm particle sizes. In terms of mass, the highest yield of SnO₂ (40 wt%) is in the coarse fraction >800 µm (Fig. 3), whereas Nb₂O₅ and Ta₂O₅ are distributed over the entire particle size range. The highest concentrations of ZrO₂ are only in the 100-200 µm fraction (Fig. 3).

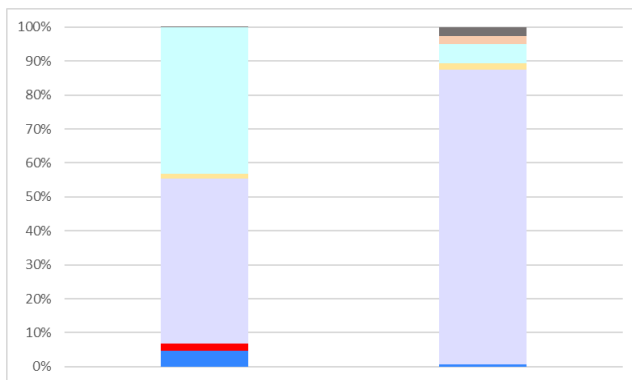
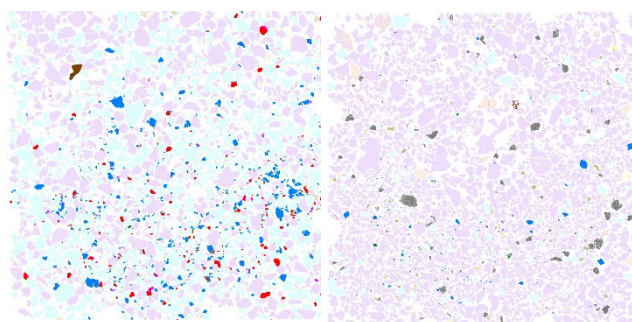


Figure 2. Classified MLA image of pre-concentrates (jig, 2nd chamber) from Cachoeirinha (left) and Bom Futuro (right) and their respective modal mineralogy (blue: cassiterite, red: columbite, violet: quartz, turquoise: topaz, grey: K feldspar, apricot: goethite, yellow: others)

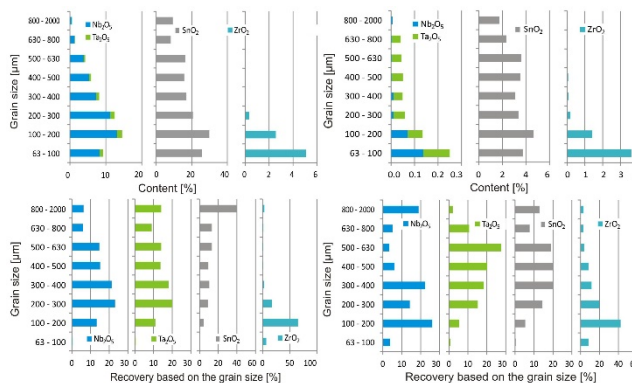


Figure 3. Element content (upper half) and recovery (lower half) dependent on grain size fraction of pre-concentrate from Cachoeirinha (left-hand side) and Bom Futuro (right-hand side)

Quartz is the major phase in the pre-concentrate from Bom Futuro, with minor topaz, goethite and potassium feldspar. Compared to Cachoeirinha, cassiterite is present in lower amounts (~0.6 area%) and columbite is lacking (Fig. 2). Cassiterite is highly liberated up to 97 %. The tin content ranges from 2 to 4 wt% SnO₂ and is rather uniformly distributed over the entire particle size range (Fig. 3). The highest concentrations of Nb₂O₅, Ta₂O₅ and ZrO₂ are in the small particle size ranges <200 µm, but are negligible in terms of mass. The largest proportions of SnO₂, Nb₂O₅ and Ta₂O₅ are >100 µm over the entire particle size range. However, high SnO₂ contents of 1 wt% are also in the >2 mm fraction, which represents about 18 % of total mass of the bulk sample.

4.1 Density separation

During density separation using a shaking table on the pre-concentrate from Cachoeirinha, cassiterite and columbite are almost completely recovered (recovery of >95 %) into the two heavy fractions (HF1 and HF2) and are nearly absent in the middlings (MD) and light fraction (LF). This applies to all four grain size fractions (Fig. 4). The highest mass of HF1 and HF2 is obtained from the 63-200 μm grain size fraction. Due to its small grain size of <200 μm , zircon is concentrated in the 63-250 μm grain size fraction (7.5 wt% ZrO_2) and has highest recovery in HF2 followed by HF1.

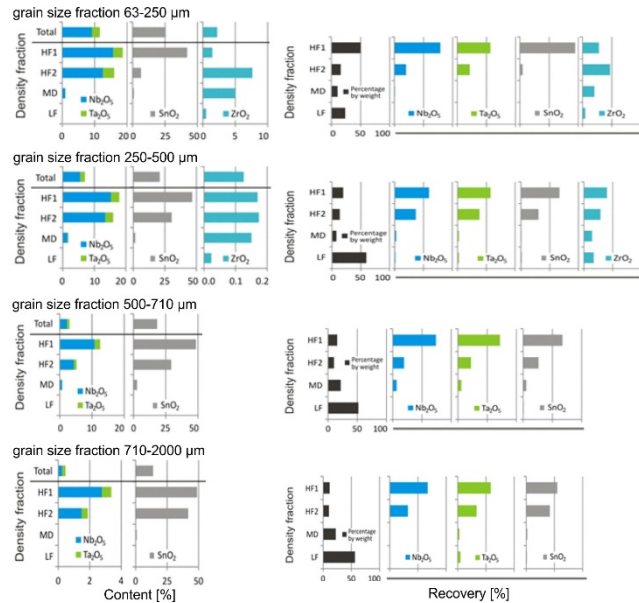


Figure 4. Element content (left) and element recovery (right) for heavy fractions (HF1 and HF2), middlings (MD) and light fraction (LF) from density separation for the different grain size fractions from Cachoeirinha. Top line shows the initial contents of the element oxides for each grain size fraction.

For Bom Futuro, cassiterite is also effectively concentrated especially into the heavy fractions (HF1 and HF2) for all four grain size fractions at >95 % recovery (Fig. 5). Both are almost absent in the middlings (MD) and light fraction (LF). The amount of $\text{Nb}_2\text{O}_5 + \text{Ta}_2\text{O}_5$ is significantly less compared to Cachoeirinha and is not present as single columbite grains. Zircon also plays a role in the 63-250 μm grain size fraction and has highest recovery in HF1.

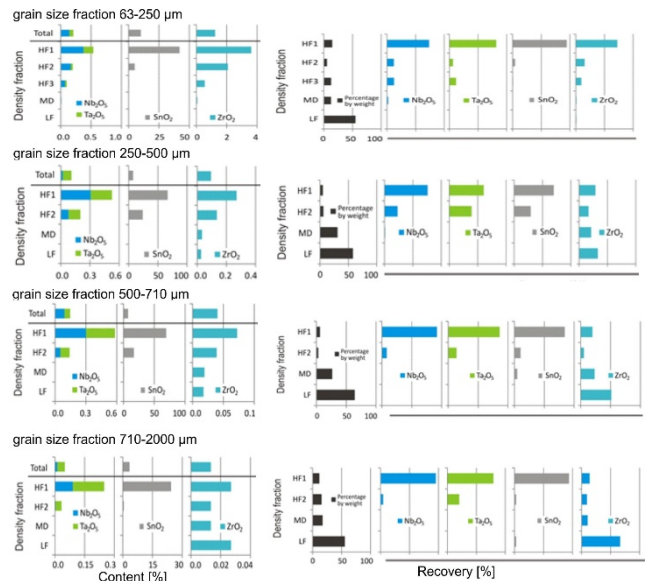


Figure 5. Element content (left) and element recovery (right) for heavy fractions (HF1 and HF2, HF3 just for 63-250 μm fraction), middlings (MD) and light fraction (LF) from density separation for grain size fractions from Bom Futuro. Top line shows the initial contents of the element oxides for each grain size fraction.

4.2 Magnetic separation

The heavy fractions from Cachoeirinha contain cassiterite, but also columbite. Both phases can be separated effectively by magnetic separation as cassiterite goes into the diamagnetic fraction, whereas columbite is concentrated in the paramagnetic fraction. In all diamagnetic fractions of HF1 and HF2, high SnO_2 concentrations are achieved with high recoveries of >80%. Overall, only a small amount of SnO_2 entered the paramagnetic fraction, which is possibly due to Fe-rich cassiterite, or cassiterite inclusions in columbite. Columbite was strongly enriched in the paramagnetic fraction. Part of the $\text{Nb}_2\text{O}_5 + \text{Ta}_2\text{O}_5$ were also transferred into the diamagnetic fraction because the cassiterite contains Nb and Ta, either as columbite inclusions, or incorporated as trace elements in the crystal lattice.

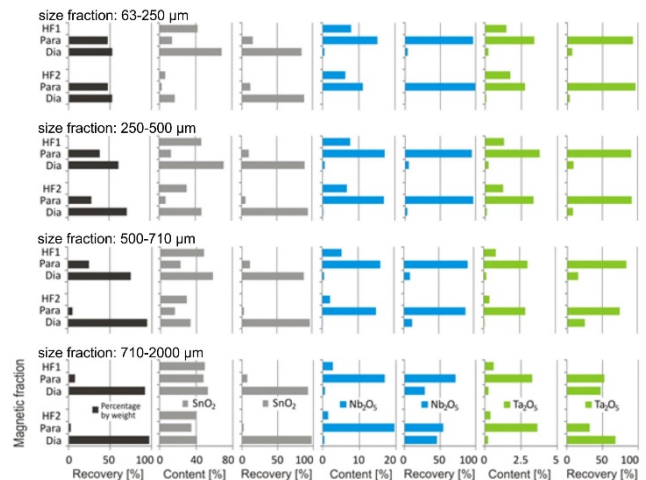


Figure 6. Concentrations and recovery rates in magnetic fractions for different grain size ranges from Cachoeirinha

For heavy fractions from Bom Futuro, cassiterite is recovered at high grades in all diamagnetic fractions, but some cassiterite is lost into the paramagnetic fraction. However, there is no significant enrichment in concentration compared to the heavy fractions from the shaking table. Individual columbite grains are not enriched.

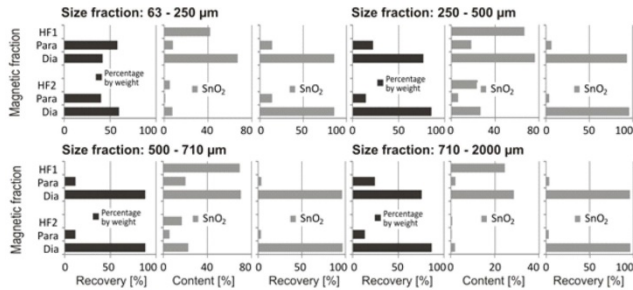


Figure 7. Concentrations and recovery rates in magnetic fractions for different grain size ranges from Bom Futuro

5 Conclusions

The valuable minerals in both pre-concentrates are almost completely liberated and can be successfully concentrated by a combination of density and magnetic separation.

The heavy minerals of interest in the bulk sample from Cachoeirinha are cassiterite, columbite, and zircon. Cassiterite and columbite can be enriched by density separation. Zircon is only enriched in the <200 µm grain size range. To achieve higher recovery for cassiterite and columbite, the HF1 and HF2 fractions should be further processed together. By magnetic separation, cassiterite and columbite can be separated effectively; columbite entering the paramagnetic fraction and cassiterite in the diamagnetic fraction. In the diamagnetic fraction, small amounts of Nb and Ta are present as trace elements or intergrowths in cassiterite. This Nb and Ta content in the cassiterite had to be rated as a loss and are transferred into the slag during tin smelting. However, the slags may be significantly enriched in Nb₂O₅ + Ta₂O₅ and can be considered as an additional raw material.

The valuable mineral at Bom Futuro is cassiterite. As the >2 mm portion contains up to 1 wt% SnO₂, the coarse fraction should be ground to <200 µm to recover this SnO₂ content. Subsequently, an enrichment of the cassiterite via the shaking table is possible. Magnetic separation (if at all) should take place at field strengths lower than 1.1 Tesla to avoid losses of cassiterite into the paramagnetic fraction. No Nb-Ta concentrate could be produced as the initial concentrations are too low and do not occur as individual minerals like columbite, but are present as trace elements within the lattice of other mineral phases.

Acknowledgements

We gratefully acknowledge the preparation of excellent polished sections by Don Henry and Andreas Heiner at BGR. We also would like to thank the companies

METALMIG and COOPERSANTA for access to their mine sites, permission to take samples and logistical support.

References

- Fandrich R, Gu Y, Burrows D, Moeller K (2007) Modern SEM-based mineral liberation analysis. *Int J Miner Process* 84:310-320.
- Bettencourt JS, Tosdal RM, Leite Jr. WB, Payolla BL (1999) Mesoproterozoic rapakivi granites of the Rondônia Tin Province, southwestern border of the Amazonian craton, Brazil: I. Reconnaissance U-Pb geochronology and regional implications. *Precambrian Res* 95:41-67

Processing waste of feldspar raw material as source of valuable metals: pre-full-scale laboratory study and search for optimum separation flowchart

Tomáš Vrbický, Richard Přikryl

Institute of Geochemistry, Mineralogy and Mineral Resources, Faculty of Science, Charles University in Prague, Czech Republic

Abstract. Leucogranites that are exploited at Krásno – Vysoký kámen deposit (Krásno ore district, Slavkov crystalline unit, western part of the Bohemian Massif, Czech Republic) are used as a feldspar raw material. These rocks are product of hydrothermal metasomatic alteration of Variscan granites. As the exploited material is utilized mainly by ceramic and/or glass industries, the content of harmful colourants presents a critical issue. Laboratory and small-scale processing trials by combination of magnetic and gravity separation aimed in reduction of the content of harmful phases. Mineralogical and chemical analyses of the obtained waste have shown that it is enriched in phases with high concentration of elements such as Li, Nb, and/or Ta which are considered as critical raw materials in EU.

1 Introduction

Feldspar-rich leucogranite formed by metasomatic / hydrothermal alteration of original granite makes one of the largest resources of feldspar raw material in the Czech Republic. Studied material consists mainly of albite and quartz accompanied with minor amounts of minor / accessory phases (Fe-, Mn-, Ti-rich phases partially with complex mineralogical binding with Nb-Ta, Li-micas, and apatite). The latest phases represent the major harmful components because their potential to cause colour changes in the final product.

As the exploited feldspar raw material is primarily used as one of the major components in the ceramic and glass industry, its quality is carefully controlled; this concerns specifically content of undesirable pigmentation components.

Due to overall mineralogy/geochemistry of the exploited deposit, part of excavated material is processed by newly installed dry magnetic separation. This processing results in generation of several tons of magnetic separate which is currently deposited nearby the quarry and can be generally viewed as a “waste” or currently non-usable by-product. However, extreme enrichment in phases such as Li-micas, and/or Nb-Ta-rich Ti-oxides lead authors to the idea on potential re-processing of the by-product and separation of individual phases which contain elements being currently classified as “critical raw materials” by EU and other countries.

The previous studies of the authors focused mainly on detailed mineralogy of the exploited raw material and on preliminary laboratory scale trials aiming to evaluate

individual processing methods for separation of individual phases. Considering the technical, economical, and ecological feasibility of available separation methods, combination of dry magnetic separation and air gravity concentrating table appeared to be very effective. Therefore, the recent study presents a step further: pre-industrial scale separation trials by using several tens of kg of by-product material. This step is a necessary for formulation of real, industrial-scale experiment which will use several tons of material and will be used as a basis for adoption of processing scheme in real feldspar raw material processing flowchart.

2 Geological setting

The main extracted raw material is alkaline - feldspar granite (albitic granite) which belonging to Krásno ore district situated in western part of Bohemian Massif (Czech Republic) (Pácal and Pavlu 1979). This feldspar deposit makes part of the granitic and locally greisenized stock Vysoký Kámen. (Sejkora et al. 2006). The deposit occupies an area of approximately 400 x 600 m in width and reaches a thickness to 190 m in depth (Hron and Kottnauer 2007). The exploited raw material is composed of prevalent feldspar minerals, specifically albite (Nosek 1997).

Granites are white to slightly pink, with an albite content of 30-50% and a K-feldspar content of 20-30%. In the case of feldspatite, feldspars form more than 75% of the mass.

Another important mineral is quartz (20 - 40%), which together with the feldspar is the main rock-forming minerals (Jarchovský 2006). Most rocks also contain mica, which are marked as Li - muscovite, cinvaldit or polyolithionite. The distribution of mica is very variable in the bearing area. Top quality parts contain mica only accessory, whereas in the edge parts of mine, it is possible to find large mica crystals up to several centimeters. Another mineral, whose representation is variable, is topaz. In some rocks topaz has not been found, while some samples have a content of about 10% (Hron and Kottnauer 2007). Another important mineral is apatite, whose representation is very variable, as in the previous case. The locality is mineralogically quite rich and contains many accessory minerals.

There are up to 15 cm large greenish berylliums. In quartz veins there are hemispherical aggregates of

radially arranged hematite crystals. Other minerals found include wolframite, bismuth, beryl, bertrandite, molybdenite or scheelite. (Beran 1999; Sejkora et al. 2006). In the area of the quarry was also discovered hollandite reaching several centimeters (Pauliš et al. 2014). In a cracks can be found significantly yellow-green (meta)autunite and autunite. (Pauliš 1990). In addition to these there are also younger alteration products such as russelite and clay minerals (Beran 1999). There are also muscovite, sericite and rutile (Jarchovský 2006). The site is mineralogically rich and there are supposed to be other minerals, especially phosphates.

3 Separation methods and results

According to the results of previous separation trials on laboratory scale done by the author, the small-scale separation experiments focused finding the optimum flow chart of separation techniques that would be further tested on full-scale. The general aims of these experiments were twofold: (1) increase of purity of feldspar raw material (i.e. removal of the phases bearing colourants – specifically Fe- and Ti-rich phases), and (2) effective separation of phases being present in the “waste” from previous step (i.e. trial to convert “waste” into the valuable byproduct(s)). Based on the results of previous laboratory study, the combination of dry magnetic separation and air gravity concentrating table proved to be very effective.

The combined gravity and magnetic separations were used to divide the material to individual components. Specifically, dry magnetic separation, wet shaking table and high density liquid was used. This process resulted in several fractions of relatively pure concentrates.

The main obtained concentrates are (Fig.1):

- 1 – Micas concentrate
- 2 – Apatite concentrate
- 3 – Nb-Ta rich concentrate
- 4 – Fe-Mn rich concentrate

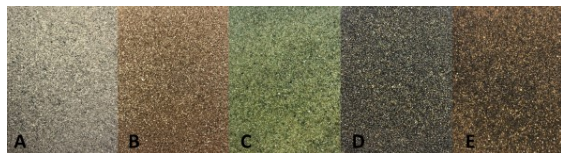


Figure 1. Photos obtained concentrates: A: primary material (magnetic concentrate), B: micas concentrate, C: Apatite concentrate, D: Nb-Ta-rich concentrate, E: Fe-Mn-rich concentrate.

Small-scale separation experiment focused on selection of optimal devices/processes that can be used for further processing (i.e. separation of individual components) of “waste” material generated during feldspar raw material processing. The specific interest was on separation of Li-rich micas and Nb-Ta minerals. About 50 kg of input material was employed for experiments.

The effectiveness of applied separation techniques was controlled through chemical analyses of the initial

input material and the end-products of the separation process by using XRF and SEM-EDS. For selected samples, content of specific light elements (e.g., of Li) was determined by wet silicate analysis. Control measurements of phase composition from powder XRD was done as well.

4 Discussion

4.1 Composition of magnetic concentrate

The studied material consists of several major minerals, which can be divided into almost pure fractions.

Micas are mostly represented by Li-micas with variable Fe content (Fig. 2). Some of mica are partially eroded and transformed to clay minerals.

Apatite occurs as microcrystalline aggregates, fill in cracks and also as zonal monocrytals.

Nb-Ta rich concentrate consist mainly of Nb-Ta rich rutile grains (Fig 3.) & less extant grains of Nb-Ta minerals (ferrocolumbite).

Fe-Mn oxides are represented mostly by hematite and hollandite. Which can make crystals even a few centimeters.

Last mineral that is in the material more abundant is topaz. Other minerals are only accessory.

4.2 Small-scale separation

Li mica separation

To obtain Li-rich micas concentrate, dry electro-magnetic separation appeared to be very effective. By using input material with 0.2 / 0.8 mm granulometry, it was possible to obtain relatively pure mica concentrate exhibiting 2.1 wt.% of LiO₂ in average.

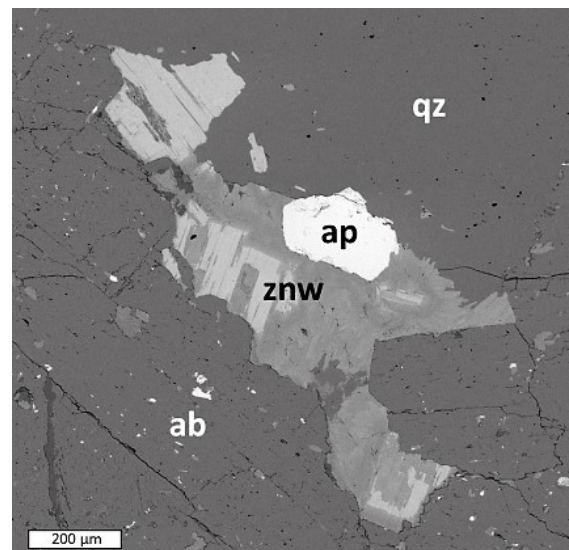


Figure 2. SEM (BSE) image: Li-rich mica (Zinnwaldite) grain with overgrown apatite.

Nb-Ta rich mineral separation

To obtain Nb-Ta rich phases, the wet gravity and dry gravity methods have been tested. Both of these methods were very effective and can be used to obtain

a concentrate containing first percents of Nb₂O₅. Air gravity concentration table appears to be proper and very effective method for heavy minerals concentrating.

Due to grain size of constituent minerals, the processing appeared to be most effective for input material having granulometry of 0.2/0.5 mm. Wet shaking table can also be employed for material with finer granulometry, but its use in operation would be much more complicated than in the optimum grain size distribution. Concerning the coarser input material (grain size above 0.5 mm), the separation of Li-, Nb-Ta-bearing phases is impossible as these phases are not liberated from the quartz-feldspar matrix. The effective separation is thus controlled by the optimum granulometry of the input material allowing for liberation of individual phases during crushing.

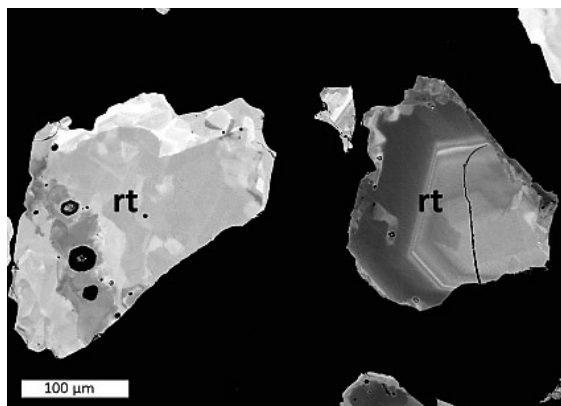


Figure 3. SEM (BSE) image: Heterogeneous Nb-Ta rich rutile grains.

5 Conclusions

The studied material consists of several major minerals, which can be divided into almost pure fractions, such as Li-micas, apatite and Nb-Ta minerals. Combination of dry magnetic separation and air gravity concentration table seems to be a very effective way on how to separate Nb-Ta-rich phases and Li-mica from material which is generated in feldspar raw material processing.

Acknowledgements

The financial support to this study from the Grant Agency of Charles University in Prague (Project No. GAUK 1352218) is highly acknowledged. We are also grateful for logistics, additional financial support and access to analytical techniques (XRF) and analytical support KMK GRANIT company.

References

- Beran, P. (1999) Nerosty cíno-wolframových ložisek Slavkovského lesa. Sokolov museum and library.
- Hron, M., Kottbauer, R. Punčochář, M. (2007) Krásno - ložiskový průzkum 2006, etapa průzkumu: podrobná, No. 2700981. Final report. Unpublished report.
- Jarchovský, T. (2006) The nature and genesis of greisen stocks at Krásno, Slavkovský les - western Bohemia, Czech Republic. Journal of the Czech Geological Society, 51: 201–216.

- Nosek, P. (1997) Přehodnocení ložiska Krásno - Vysoký Kámen. Surovina: živcové suroviny. Gekon, s.r.o., Praha 9. Unpublished report.
- Pácal, Z., Pavlů, D. (1979) Závěrečná zpráva dílčího úkolu 4/09-4 za léta 1976 - 1979 živcové suroviny - Krásno, Ústřední ústav geologický, Praha. Unpublished report.
- Pauliš, P. (1990): Autunit z Vysokého kamene (Krásno) u Horního Slavkova. Casopis pro mineralogii a geologii, 35, 1, 105–106.
- Pauliš, P., et al. (2014): Hollandit z Vysokého Kamene u Krásna. Minerál, 6, 22:530–532.
- Sejkora, J., et al. (2006): New data on mineralogy of the Vysoký Kámen deposits near Krásno, Slavkovský les area, Czech Republic. Journal of the Czech Geological Society, 51(1-2):43–55.

Graphite raw material in the Bohemian Massif - processing for future mining

Michal Poňavič, Anna Vymazalová, Bohdan Kříbek, František Ptíčen, Jan Jelínek
Czech Geological Survey, Prague, Czech Republic

Abstract. Critical raw materials in the Czech Republic have been studied under the frame of the project Competence Centre for Effective and Ecological Mining of Mineral Resources. The aim of this study was the improvement of graphite processing of the material samples from the Český Krumlov-Městský vrch deposit using the delamination of graphite-mica composite from the concentrate after the first flotation process. In order to delaminate the graphite-mica composite of the fraction grain size 100–150 µm, before the second flotation process, the destructive methods of ultrasound (US), frost cycles and repeated heating were applied. The process of destroying was tested at various US frequencies, at different intensities and times of processing (2 to 30 minutes). The delamination based on triple repeated frost cycles was performed at -18 °C and +24°C. Delamination based on repeated heating up to 150°C was conducted in two cycles. The most efficient improvement of ore processing has been shown by applying the method of delamination of graphite-mica composite after the second flotation.

1 Introduction

This study has been performed under the project Competence Centre for Effective and Ecological Mining of Raw Materials, funded by the Technology Agency of the Czech Republic (TA ČR) under the leadership of the Technical University of Ostrava (TUO). The aim of the project is to study critical raw materials (CRM) of the European Union (EU), assess the suitable resources of CRM in the Czech Republic and propose a possible efficient and environment-friendly way of their mining and processing.

One of the most important topics of the project is the detailed study of Czech graphite deposits. Graphite was declared to be a critical raw material due to its importance in crucial industries such as steel, lithium-ion batteries, and nuclear reactors. Lithium-ion batteries, widely used in cell phones, power tools and notebook computers, contain almost twenty times more graphite than lithium. Graphite being an essential ingredient in the production of the lithium-ion batteries that power the electrical and hybrid vehicles is forecasted to increase the demand in the future. Over 70 % of world production of natural graphite powders holds China, followed by Latin America, EU production of natural graphite powder is less than 1 %. The Czech Republic does not produce natural graphite domestically and is completely dependent on imports for graphite supply.

Since 2008 there is no mining of graphite in the Czech

Republic due to economic reasons but also due to difficulties in processing of the material. However, in the recent years there is an increased interest in reopening of graphite mining. All graphite deposits in the Czech Republic belong to the metamorphogenic type. They originated during the regional metamorphism of clayey sandy sediments rich in organic matter, which is also indicated by higher concentrations of S, P, V and Sr (Franěk et al. 2011). The deposits are located within the Bohemian Massif in two regions: South Bohemian Moldanubicum, and in the Moravian and Silesicum (Fig. 1). South Bohemian graphitic rocks have a character of graphitic gneisses and carbonates. Deposits in the Moravian-Silesian region occur in an area affected by lower grade metamorphism.

The most important deposits (Český Krumlov-Městský Vrch and others) occur in the Moldanubicum, particularly in the so-called Varied Group of Český Krumlov.

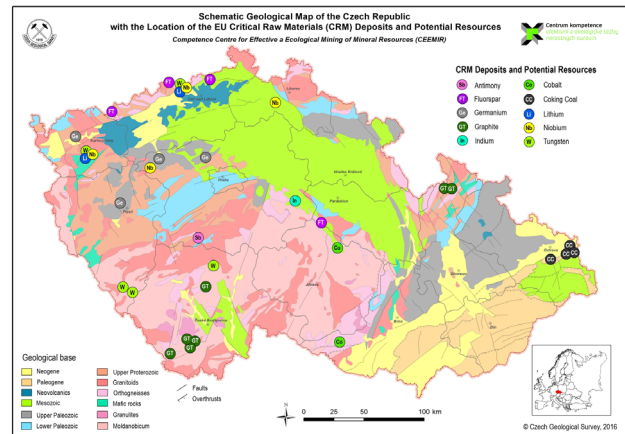


Figure 1. Schematic geological map of the Czech Republic, with the location of the EU CRM deposits and potential resources.

2 Samples and methods

The graphite deposit Český Krumlov-Městský vrch occurs in the central part of the Varied group of Český Krumlov, in the South Bohemian Moldanubicum region.

The deposit is hosted by graphitic paragneiss with a content of graphitic carbon from 8 to 30%. The material also contains blanched biotite, less common muscovite, sericitized and kaolinized feldspars, sillimanite, cordierite and apatite; pyrrhotite and pyrite are also very common, mostly in the form of sulphide impregnations (Tichý 2002). The raw material is formed by crystalline graphite of the size of flake from 0,001–0,5 mm. The deposit is comprised from five ore bodies; their geological structure is very complex (Fig. 2).

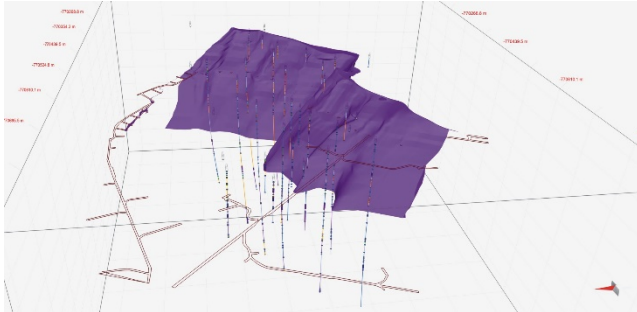


Figure 2. 3D model of the most important graphite ore body, Český Krumlov-Městský vrch deposit, after Jelínek et al. (in print).

We have collected a large volume of samples of graphitic raw material for the further technological tests (Fig. 3).



Figure 3. Macroscopic sample of graphite ore, underground mine, Český Krumlov - Městský vrch deposit.

The processing tests were performed at the TUO. The results of flotation tests have shown the low quality of primary flotation concentrate that proved a content of inner dust and low purity of graphitic flakes. The flakes of graphite are very often epitaxially grown on plates of biotite or white mica (Fig. 4). This, during the crushing and milling of the material, causes the formation of a graphitic composite. Therefore, the full process of flotation processing becomes impeded.

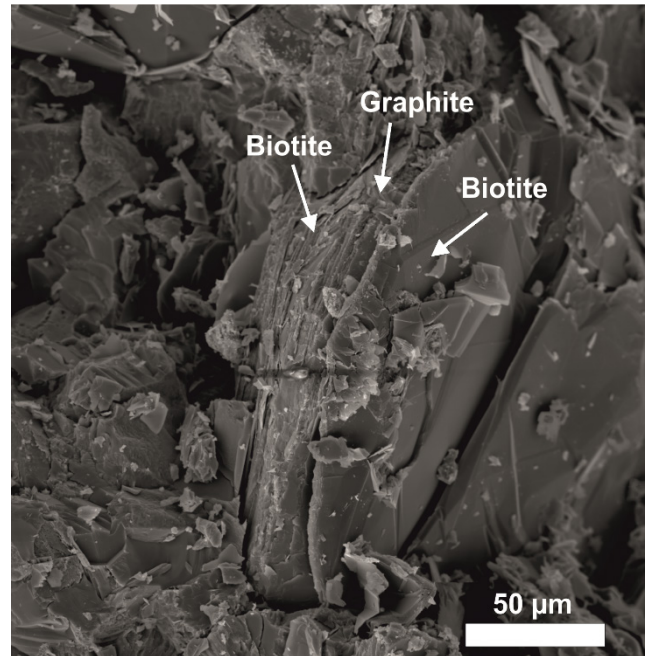


Figure 4. Natural flake of graphite showing fine layers of biotite and graphite, SEM image.

3 Results

The aim, at the Czech Geological Survey, was the improvement of graphite processing of the material samples from the Český Krumlov-Městský vrch deposit using the delamination of graphite-mica composite (Fig. 4) from the concentrate after first flotation process, performed at the TUO. The processing tests were performed at dry conditions after the crushing of graphite in jaw crusher and in oscillatory agate mill. Ultra-fine fraction below 100 µm was separated in air screener ASP HOSOKAWA-ALPINE up level of 40 µm and consequently chemical analyses were performed complemented by a magnetic separation of original milled rock of a fraction 40–100 µm. The Table 1. shows the analyses of selected elements for graphite contaminated by Fe sulphides with a low pH 4. Application of magnetic separation significantly improved to lower the content of sulphides (see Table 1).

In order to delaminate the graphite-mica composite of the fraction grain size 100–150 µm, before the second flotation process, the **destroying methods of ultrasound (US), frost cycles and repeated heating** were applied. The process of destroying was tested at various US frequencies from 20 to 40 kHz at different intensities and times of processing (2, 3, 5, 20 and 30 minutes).

Table 1 Chemical analyses of selected elements in raw graphite, non-magnetic fraction (non-mag), after magnetic separation (mag) and after the first floatation of non-magnetic part of graphite.

Graphite	Original	Non-mag	Mag	Flotation concentrate Non-mag	0-100 µm	40-100 µm	0-40 µm	40-100 µm	40-100 µm
								Non-mag	Mag
Fe	7.03	3.40	8.45	3.19	7.69	4.84	9.53	3.26	5.70
Ti	0.27	0.36	0.23	0.54	0.24	0.30	0.18	0.40	0.40
CaO	2.85	1.94	2.83	2.79	2.85	2.79	2.99	2.57	2.60
K ₂ O	2.52	2.30	2.25	2.06	2.69	2.13	2.84	2.09	2.13
S	5.92	4.24	6.22	1.93	6.37	4.21	7.32	4.14	4.87
Mn	0.35	0.15	0.36	0.27	0.23	0.25	0.23	0.15	0.23

Table 2 Annealing loss of graphite (non-mag fraction) after the first and second floatation, processing of graphite suspension before floatation US (20 kHz, 45°C) for 5, 15 and 30 minutes.

Graphite	Non-mag	Flotation concentrate non-mag	Flotation concentrace non- mag	Flotation concentrace non-mag	Flotation concentrace non- mag
	after 1 st floatation	after 2 nd floatation	after 5 min US after 2 nd floatation	after 15 min US after 2 nd floatation	after 30 min US after 2 nd floatation
Annealing loss (%)	38,5	64,9	69,0	81,8	89,5

4 Discussion

The Table 2. shows that the application of the delamination process using US increased the effect of the floatation. Therefore, the amount of combustible carbon (annealing loss) increased after floatation based on time of US application from 64.9 wt.% to 89.5 wt.%, in total of about 25 %. However, the increasement of content of combustible carbon is at the expense of the graphite flakes size. The higher intensity of US leads to flakes crushing (Fig. 5 c, d). The similar results obtained Łoś et al. (2013) and Guittonneau (2010).

The delamination based on triple repeated frost cycles was performed at -18°C and +24°C. Delamination based on repeated heating up to 150°C was conducted at two cycles. The most effective method of delamination of graphite-mica composite was the crushing using US, when the content of combustible particles increased from original 40% (in the concentrate after first floatation) to 95% after second floatation (Fig. 5).

The processing methods were applied for the first time on graphite from Czech Republic.

5 Conclusions

Reserves of graphite ores in the Czech Republic are substantial and reach up to about three millions of tons. The possibility of renewal of graphite mining in the territory of the Czech Republic is dependent on new technologies applied for graphite processing.

Graphite ores available in the Czech Republic contain

relatively high amounts of inorganic admixtures predominantly quartz, micas and pyrite and therefore these have to be separated during the ore processing. The sufficient improvement of ore processing has been shown by applying the method of delamination of graphite-mica composite after the second floatation.

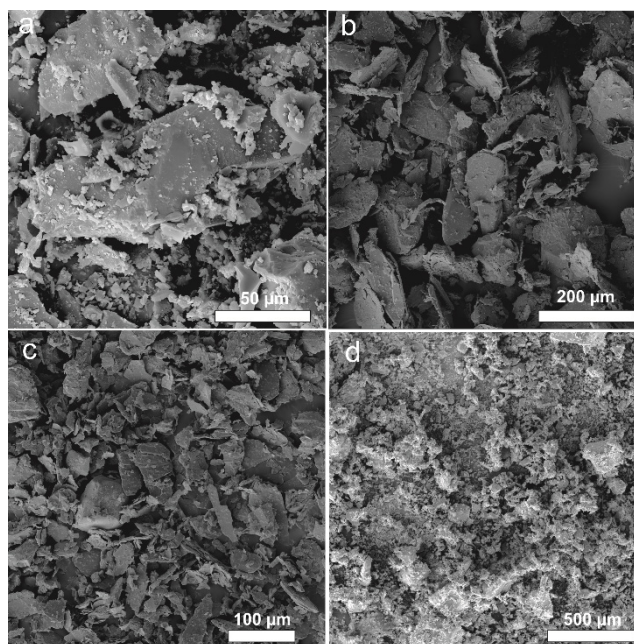


Figure 5. (a) Graphite before processing. (b) Graphite flakes from Lazec deposit. (c) Graphite after floatation before delamination. (d) Delaminated graphite. SEM images.

Acknowledgements

Financial support through the project „Competence Centre for Effective and Ecological Mining of Mineral Resources “(CEEMIR) from the Technology Agency of the Czech Republic (TA ČR), TE 02000029 is gratefully acknowledged.

References

- Franěk J, Schulmann K, Lexa O, Tomek Č, Edel J (2011) Model of syn-convergent extrusion of orogenic lower crust in the core of the Variscan belt: implications for exhumation of high-pressure rocks in large hot orogens. *J Metamorph Geol* 29:53–78.
- Guittonneau F, Abdelouas A, Grambow B, Huclier S (2010) The effect of high-power ultrasound on an aqueous suspension of graphite. *Ultrason Sonochem* 17:391–398.
- Jelínek H, Staněk F, Grygar R, Franěk H, Poňavič M (in print) Methodology to 3D modelling of a graphite deposits on the basis of archive data. *Geoscience Research Reports* 2018.
- Łoś S, Duclaux L, Alvarez L, Hawełek Ł, Duber S, Wojciech Kempniński W (2013) Cleavage and size reduction of graphite crystal using ultrasound radiation. *Carbon* 55:53–61.
- Tichý L (2002) Graphite ores between Cesky Krumlov and České Budejovice. (in Czech) *Uhlí-Rudy-Geologický průzkum* 9:29–33.

Remediation of cyanide within gold mine waste: an in-depth review of Prussian blue in aqueous solution

Megan D. Welman-Purchase, Robert N. Hansen
University of the Free State

Abstract. Cyanide (CN⁻) is used for gold extraction in mining, which creates a potential for dangerous environmental contamination. This research delves into the complexity of the ferro/ferri-cyanide complexes (such as Prussian and Turnbull's blue crystals) and their potential to be a resolution to this contamination. The Fe-CN bond of these complexes are believed to be stable and with the exact combination of bondings may create an inert substance. Although it has been mentioned that pH and redox conditions may affect this stability. This study involves the growth of Prussian and Turnbull's blue single crystals, the analysis of them using single crystal X-ray Diffraction, the affect that strong acids and UV-radiation will have on the stability of the crystals changing the following variables: light intensity, total dissolved salts, pH, temperature, solubility and cyanide complex concentrations. Resulting in the presentation of the best ferro/ferri-cyanide complex for the prevention of CN⁻ environmental contamination.

1 Introduction

Cyanide in the form of HCN is one of the most toxic chemicals known (Luque-Almagro et al. 2016). There are several industries; including metal plating, mining, synthetic rubber production, pharmaceutical, steel hardening, production of nitrile and nylon, photographic applications and gas production that either use or produce cyanide (Zagury et al. 2004; Akcil 2003). In the mining industry, cyanide is commonly used in the extraction of Ag and Au due to its' high affinity for these elements (Zagury et al., 2004) resulting in the mining industry using 20% of the world's cyanide production yearly (Luque-Almagro et al. 2011). Thus, the mining industry is responsible for the production and potential release of thousands of tons of waste which, along with cyanide, contains toxic metals such as, Hg, Pb and Cd (Luque-Almagro et al. 2016). The threat that cyanide has on human health and the environment is dependent on the chemical speciation (toxicity of the cyanide and physiochemical behaviour) (Meeussen et al. 1992). Cyanide in the gold mining industry can be classified into four categories: free cyanide (CN⁻ and HCN), readily soluble cyanide (KCN, NaCN), weak acid dissociable cyanide (CN^{WAD} – reasonably unstable containing Ni, Cu, Cd and Zn) and strong acid dissociable cyanide (CN^{SAD} – dissociate in acidic environments containing Au, Ag, Fe and Co) (Zagury et al., 2004). Free cyanide is the most toxic of these due to its high metabolic inhibition potential (Zagury et al., 2004). Free cyanide is produced during the dissociation and dissolution of cyanide complexes in aqueous solutions (Kuyucak and Akcil 2013). At a pH

below ~8.5, HCN is produced thus being the main volatilization conditions for free cyanide (Kuyucak and Akcil 2013). For optimum gold extraction, the pH needs to be 10.5 or greater causing the cyanide to form CN⁻ (Kuyucak and Akcil 2013). The high pH conditions minimise the volatilization of the cyanide (Kuyucak and Akcil 2013).

Soluble cyanide complexes include: NaCN, KCN and Ca(CN)₂, which dissipate completely in an aqueous solution (Kuyucak and Akcil 2013). The weakest cyanide complexes (referring to the chemical stability) are Zn and Cd complexes and the strongest complexes are Fe and Co (Kuyucak and Akcil, 2013). Strong acids and UV-radiation may dissociate these complexes releasing free cyanide (Kuyucak and Akcil 2013). Dissociation rate is affected by light intensity, pH, water temperature, complex concentration and TDS (total dissolved salts) (Kuyucak and Akcil, 2013).

According to Meeussen et al. (1992), cyanide is primarily treated and disposed of as iron-cyanide minerals or iron cyanide complexes such as Fe₄[Fe(CN)₆]₃. Fe₄[Fe(CN)₆]₃ is referred to as Prussian blue and Fe₃[Fe(CN)₆]₂ as Turnbull's blue (Weiser et al. 1942), although there is controversy surrounding these terms. The reason for the disposal is the alleged stability of such complexes (Kyle 1997) and the spontaneity of their production (Cosgrove et al. 1972). Other methods of treatment include sulphur dioxide and air process, hydrogen peroxide treatment, alkaline and breakpoint chlorination, biological treatments, among others (Akcil 2003).

Prussian blue can be found in two forms, soluble and insoluble (Adhikamsetty and Jonnalagadda 2009). Insoluble Prussian blue has the chemical formula of Fe₄[Fe(CN)₆]₃xH₂O and soluble Prussian blue has the chemical formula of KFe[Fe(CN)₆]_yH₂O (Adhikamsetty and Jonnalagadda 2009). Such minute alterations in the ions incorporated in the crystal structure can lead to the crystals being soluble or insoluble, thus the positioning of the ions in the crystal structure will reveal the solubility of the crystal.

According to the author's knowledge, single crystals of Prussian blue and Turnbull's blue have not yet been grown for the purpose of mining waste remediation. Crystal structures as published in Weiser et al. (1942) and Buser et al. (1977), see figure 1, have been calculated from powder diffraction. Crystals that have been produce are for other purposes such as for material sciences (Nai et al. 2018), for polymer research (Zheng et al. 2007), electrode research (Zadronecki et al. 1999), and so forth, which produce nano-sized crystals. Proving the significance of a crystal structure study, the study of

the positioning of ions in the crystal structure and the other factors that have been mentioned that affect the solubility of the crystals.

The aim of this study is to investigate the stability of the iron-cyanide minerals or iron cyanide complexes. Further studies will involve the implementation of the findings from this study.

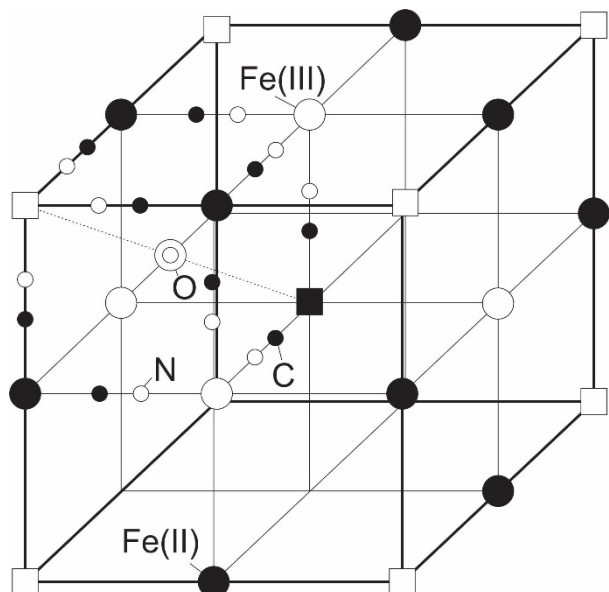


Figure 1. Calculated Prussian blue crystal structure from powder X-ray diffraction, modified after Bruser et al. (1977).

2 Methodology

The first method attempted to produce Prussian blue was by rapidly mixing an aqueous solution of ferric chloride and an aqueous solution of potassium ferrocyanide (Cosgrove et al. 1972). This produces a fine crystalline material, which can be seen in figure 2. The fine material is not sufficient for this study and thus a method of slow diffusion is needed.

The second method currently being attempted involves a single crystal grown using the method mentioned in Buser et al. (1977). A 7.5 mmol solution of $\text{FeCl}_2 \cdot 3/4\text{H}_2\text{O}$ along with 2.5 mmol $\text{K}_3[\text{Fe}(\text{CN})_6]$ were added to 500 ml 10 mol HCl/L (fig. 2). The solution is then placed in a desiccator containing water, as seen in figure 2. Turnbull's blue crystals are grown using a solution of FeCl_2 and $\text{K}_3\text{Fe}(\text{CN})_6$ (Weiser et al. 1942).

The third method that will be attempted is the crystal growth using the solvent diffusion/growth from gels method as described in Nishinaga (2015). Which involves the slow crystallization where two solutions interact.

3 Final thoughts

Humans are responsible for majority of cyanide environmental contamination. Methods to resolve this issue are of utmost importance. Although the key method of disposal is through ferro/ferricyanides, it can be concluded from the literature that there are many factors that influence the stability of these complexes. This

proves the significance of an empirical study of these systems.



Figure 2. a. Prussian blue fine-grained crystals produced from rapid mixing of two solutions (potassium ferrocyanide and ferric chloride). **b.** Two solutions used for the single crystal grow. 7.5 mmol solution of $\text{FeCl}_2 \cdot 3/4\text{H}_2\text{O}$ along with 2.5 mmol $\text{K}_3[\text{Fe}(\text{CN})_6]$. **c.** The 10 mol of HCl/L solution in a desiccator containing water.

Acknowledgements

Funding for this study is supplied by Iphakade - Earth Stewardship Science.

References

- Adhikamsetty RK, Jonnalagadda SB (2009) Kinetics and mechanism of Prussian blue formation. *Bull. Chem. Soc. Ethiop.* 23(1):47-54
- Akcil A (2003) Destruction of cyanide in gold mill effluents: biological versus chemical treatments. *Biotechnology Advances* 21: 501-511
- Buser HJ, Schwarzenbach D, Petter W, Ludi A (1977) The crystal structure of Prussian blue: $\text{Fe}_4[\text{Fe}(\text{CN})_6]_3 \cdot x\text{H}_2\text{O}$. *Inorganic Chemistry*, 16, 11, 2704-2710
- Cosgrove JG, Collins RL, Murty DS (1972) Preparation of ferrous ferricyanide. *Journal of the American Chemical Society*, 95, 4, 1083-1086
- Kuyucak N, Akcil A (2013) Cyanide and removal option from effluents in gold mining and metallurgical processes. *Mineral Engineering* 50:13-29
- Kyle JH (1997) Stability of metal-cyanide and hydroxide complexes. *World Gold '97 Conference*. 163-169
- Luque-Almagro VM, Blasco R, Martinez-Luque M, Moreno-Vivian C,

- Castillo F, Poldan MD (2011) Bacterial cyanide degradation is under review: *Pseudoalcaligenes* CECT5344, a case of an alkaliphilic cyano troph. *Biochem. Soc. Trans.* 39:269-274.
- Luque-Almagro VM, Moreno-Vivian C, Roldan MD (2016) Biodegradation of cyanide wastes from mining and jewelry industries. Elsevier. 38:9-13
- Meeussen JCL, Keizer MK, de Haan FAM (1992) Chemical stability and decomposition rate of iron cyanide in soil solutions. *Environ. Sci. Technol.* 26:511-516
- Nai J, Zhang J, Lou X (2018) Construction of single-crystalline Prussian blue analog hollow nanostructures with tailorable topologies. *Chem.* 4:1967-1982
- Nishinaga T (2015) Handbook of crystal growth, Volume 1 Part B. Elsevier. Amsterdam Netherlands
- Weiser HB, Milligan WO, Bates JB (1942) X-ray diffraction studies on heavy-metal iron-cyanides. *J. Phys. Chem.* 46(1):99-111
- Zagury GJ, Oudjehani K, Deschênes L (2004) Characterization and availability of cyanide in solid mine tailings from gold extraction plants. *Sci. Total. Environ.* 320:211-224
- Zadroncki M, Wrona PK, Galus Z (1999) Study of growth and the electrochemical behavior of Prussian blue films using electrochemical quartz crystal microbalance. *ElectroChem. Soc.* 146(2):620-627
- Zheng XJ, Kuang Q, Xu Tao, Jiang ZY, Zheng SH, Xie ZX, Huang RB, Zheng LS (2007) Growth of Prussian blue microcubes under a hydrothermal condition: possible nonclassical crystallization by a mesoscale self-assembly. *J.Phys. Chem.* 111:4499-4502

Fungal extraction of Se and Te from the Kisgruva Proterozoic volcanogenic massive sulfide deposit

Xinjin Liang¹, Magali A.M. Perez², Joseph G. Armstrong², Liam A. Bullock², Jorg Feldmann², Laszlo Csetenyi¹, Geoffrey M. Gadd¹

¹University of Dundee, Scotland, UK

²University of Aberdeen, Scotland, UK

Abstract. Microbial Se or Te reduction offers a potential route to biorecovery of these elements. Reduction is often efficient and large amounts of these metalloids can be removed from solution because of extensive precipitation of elemental forms. In this research, *Aureobasidium pullulans*, *Mortierella humilis*, *Trichoderma harzianum*, *Phanerochaete chrysosporium*, *Phoma sp.*, and *Phoma glomerata* were used to investigate their potential to extract Se and Te from selenium and tellurium resources in the Kisgruva Proterozoic volcanogenic massive sulfide deposit. All microorganisms were able to grow in selenium- and tellurium-containing sulfide ore liquid media and extract these elements from the ores. The findings are relevant to novel approaches for selenium and tellurium biorecovery from liquid and rock matrices as well as bioremediation.

1 Introduction

Many microorganisms are capable of transforming various selenium and tellurium species through methylation, oxidation, reduction and demethylation (Jacob et al. 2016; Eswayah et al. 2016). Filamentous fungi are capable of extracellular and intracellular synthesis of selenium particles making processing and biomass handling easier and hence perhaps more preferable than unicellular organisms (Mandal et al. 2006). The large amounts of extracellular produced enzymes and reductive proteins make fungi an unique investigation system (Gharieb et al. 1999; Gharieb and Gadd 2004; Espinosa-ortiz et al. 2017). Filamentous fungi like *Trichoderma harzianum* have been reportedly used for the extracellular biomass-free synthesis of silver nanoparticles. *T. harzianum* has been used as a biological control agent because of its multi-enzymatic system composed of chitinases, β -glucanases and proteases (Siddiquee et al. 2014). Several naphthoquinone and anthraquinone compounds from *T. harzianum* possess good reducing properties (Siddiquee et al. 2014). *Pseudomonas sp.* (Hunter and Manter 2009), *Alternaria alternata* (Sarkar et al. 2012), and *Phanerochaete chrysosporium* (Espinosa-Ortiz et al. 2015) were able to generate selenium nanoparticles from reduction of either selenate or selenite, while *Fusarium sp.*, *Penicillium citrinum* (Gharieb et al. 1999), *Saccharomyces cerevisiae* (Gharieb and Gadd 2004), and *Rhodotorula mucilaginosa* (Ollivier et al. 2011) can produce nanoscale elemental Te from tellurite. *P. chrysosporium* also produced mixed Se-Te nanoparticles when grown with selenite/tellurite (Espinosa-Ortiz et al. 2017). The application of microbial Se or Te reduction

offers a potential route for biorecovery of these elements

from solution and solid substrates.

This research explored the potential of selected fungal strains as selenium- and/or tellurite-reducing organisms and their potential to extract Se and Te elements from selenium and tellurium resources in the Kisgruva Proterozoic volcanogenic massive sulfide deposit. The objectives were to determine: (1) the effect of sulfide ores on fungal growth and morphology modification, (2) the different composition of sulfide ores before and after fungal growth, (3) Se and Te extraction rates after growth with selected fungi.

2 Sequential extraction and metalloid speciation in the Kisgruva sulfide ores

Sequential extraction and speciation were performed on Kisgruva sulfide ore samples 450, 456 and 459 to determine the total amounts of Se and Te associated with oxide minerals and organic matter (Bullock et al. 2018). Concentrations of selenium and tellurium species adsorbed to charged surfaces, such as oxide minerals, were determined using a phosphate buffer extraction method (Fig. 1 blue), while concentrations and speciation of selenium and tellurium bound to organic matter were examined by a sodium hydroxide extraction method (Fig. 1 orange). The Aqua regia residues method was used for total extractable concentrations of selenium and tellurium (Fig. 1 grey). Both selenite (SeO_3^{2-}) and tellurite (TeO_3^{2-}) were identified in sulfide ore crust samples by phosphate and sodium hydroxide extraction methods (Fig. 1), but elemental forms (Se^0 and Te^0) or selenate (SeO_4^{2-}) / tellurate (TeO_4^{2-}) were not detected. For sample 450, of the extractable Se (14.3% of total Se), only 39.5% was associated with oxide minerals, with 60.5% bound to organic matter (Se(-II)). For extracted Te (31.4%), 22% was associated with oxide minerals, and 78% with organic matter. Similar results were observed for sample 459, with total extractable Se, associated with oxide minerals and bound to organic matter of 27%, 20.9% and 79.1% respectively. For Te, the percentages were 24.2%, 20.9% and 79.1% respectively. More selenium was bound to organic matter in sample 456, compared to the other samples, with total extractable Se, associated with oxide minerals and bound to organic matter of 74.2%, 7% and 93% respectively. For Te, the respective percentages were 10.9%, 15.4% and 84.6%.

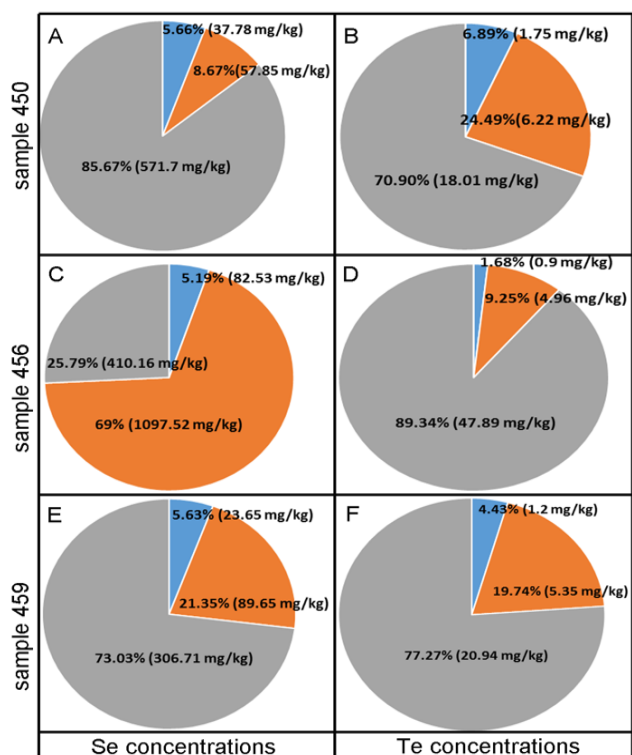


Figure 1. Se and Te speciation revealed by extraction with phosphate buffer (blue), sodium hydroxide (orange) and Aqua regia (grey) extraction methods for samples 450, 456 and 459. All values shown are means of at least three measurements with typical relative standard deviations of about 5%.

3 Tolerance indices of selected fungi grown with Kisgruva sulfide ores

Tolerance indices (TI) were used to compare fungal biomass yields grown in AP1 medium with or without sulfide ore samples (Fig. 2). A TI value lower than 100 indicates growth inhibition, whereas larger than 100 suggests growth stimulation. The tolerance indices for sulfide ore samples varied between different fungal strains. In the presence of samples 450, 456 and 459, all fungi showed growth reduction. For sample 450, growth of *P. chrysosporium*, *T. harzianum* and *Phoma. sp* was significantly ($P < 0.05$) inhibited by 43%, 19% and 51% respectively, while *A. pullulans*, *M. humilis* and *P. glomerata* showed relatively better tolerance (Fig. 2). In the presence of sample 456, *T. harzianum* showed the most inhibition (34%). There were no significant inhibitory effects on *P. chrysosporium*, and *Phoma. sp* in the presence of sample 459, while biomass yields were markedly reduced for *A. pullulans* and *M. humilis* (Fig. 2).

All fungi were able to grow in the presence of sulfide ore samples 450, 456 and 459 after 30 days incubation at 25°C. The original media pH values for samples 450, 456 and 459 were 3.9, 2.2 and 7.9 respectively. There were no significant differences in the media pH values on addition of samples 450 and 456. Compared to the controls grown in ore-free AP1 medium, growth of the fungal strains lowered the pH values from 3.9 to between 1.8 to 2.9 for sample 450, and from 2.2 to between 1.9 to 3 for sample 456. The pH values for sample 459 in the

presence of the fungi increased slightly after 30 days incubation except for *P. chrysosporium* and *Phoma. sp* (Fig. 2).

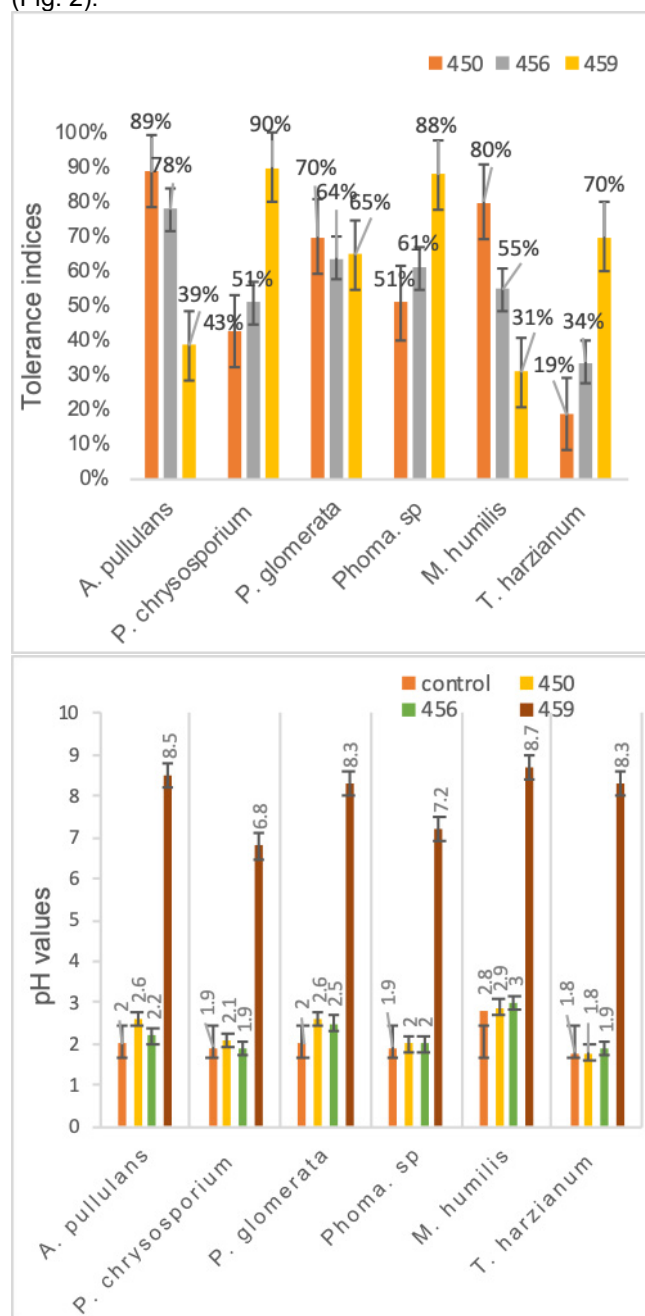


Figure 2. TI (tolerance indices) (top) and medium pH (bottom) for *A. pullulans*, *P. chrysosporium*, *M. humilis*, *T. harzianum*, *Phoma. sp* and *P. glomerata* grown in AP1 medium amended with samples 450, 456 and 459. All values shown are means of at least three measurements with typical relative standard deviations of about 5%.

4 Composition of the Kisgruva sulfide ores before and after fungal growth

The sulfide ore at the Kisgruva mine site was originally used for extraction of copper, sulfur and iron, but also contains high concentrations of selenium and tellurium. Elements present in the sulfide ore samples were determined by X-ray fluorescence (XRF) before and after

growth with fungi for 30 days. Both Se and Te were also present within the sulfide ores in pyrite and chalcopyrite (sample 450 and sample 459), which contained high concentrations of up to 688 ppm Se and 81 ppm Te (Bullock et al., 2018), together with the major and trace elements, including Fe, S, P, Al, Ca, K, Fe, Mg, Si, Ti, Co, Na, Ni, Cu, Zn, Cl, Pb, W and As. There were no significant differences observed with the composition of sulfide ore samples 450, 456 and 459 before and after fungal growth (Fig. 3, data for samples 456 and 459 not shown). The presence of fungi helped to leach most of the elements from the sulfide ore, however, only small proportional changes were observed for certain elements (Fig. 3). Since the XRF analysis assumes the sample matrix all in oxidic condition, the real compositions of the sulfide ore samples were too complicated to conclude by XRF on its own, it only gives oxidic composition percentages for elements detected, the further laser ablation analysis should give detailed element changes.

5 Fungal extraction of selenium and tellurium from Kisgruva sulfide ores

P. glomerata was chosen for further experiments, because of good tolerance of the sulfide ores. *P. glomerata* was grown on polished flat surfaces of samples 450 and 459 for 30 days on MEA plates to investigate its ability for selenium and tellurium extraction. Trace element analysis of polished sulfide ore blocks of generally inclusion-free pyrite was performed by using a new wave laser ablation system UP213 nm coupled to an ICP-MS Agilent 7900. Samples 450 and 459 were high in other chalcophile elements which showed a chemical affinity to Se and Te, such as Fe (380041 ppm, 633668 ppm), Cu (476 ppm, 2124 ppm), As (408 ppm, 376 ppm), Ag (26 ppm, 62 ppm), Au (0.2 ppm, 0.2 ppm), Hg (0.7 ppm, 1.4 ppm) Pb (1274 ppm, 189 ppm) and Bi (17 ppm, 30 ppm) respectively. Sulfide ore samples contained an average of 0.05% TOC (Fig. 4). All elements in the sulfide ore samples showed marked removal after growth with *P. glomerata*. Selenium and tellurium from sulfide ore samples 450 and 459 were extracted by *P. glomerata* with removals of 66-77% for selenium and 72% for tellurium confirmed by the laser ablation (LA) ICP-MS analysis (Fig. 4). Laser ablation analysis showed that Se, and Te to a lesser extent were present, even though Te was generally high throughout the pyrite phases (Bullock et al. 2018). For As, Se and Te, concentrations were higher towards the edges of the pyrite for samples 450 and 459. As well as a high content throughout pyrite, Se and Te also showed disseminated areas of high concentration, in some instances, up to 10,000 ppm and 1000 ppm respectively. Though the selected pyrite crystals were generally inclusion-free, these Se and Te hotspots may correspond to micron-sized Se^{2-} and Te^{2-} (Bullock et al. 2018). After growth with *P. glomerata*, Se and Te hotspot concentrations for sample 450 dropped down to 1000 ppm and 100 ppm respectively, while for sample 459, concentrations dropped down to 100 ppm on both selenium and tellurium (Fig. 4).

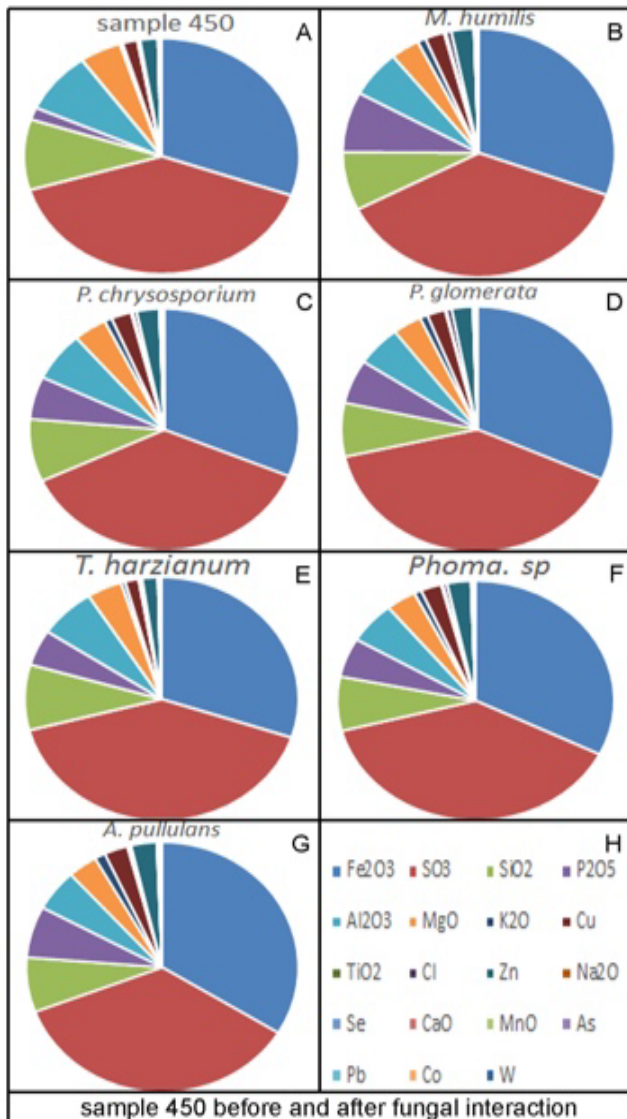


Figure 3. Elemental composition of sulfide ore sample 450 before and after fungal growth. Kisgruva sulfide ore sample was incubated with selected fungi in AP1 liquid media for 30 days at 25°C in the dark at 125 rpm. All values shown are means of at least three measurements with typical relative standard deviations of about 5%.

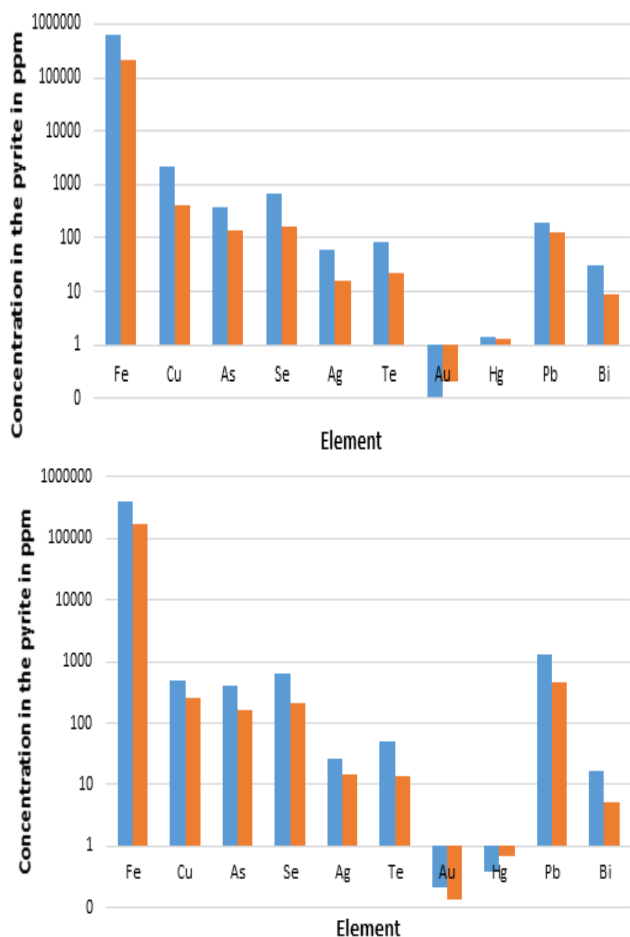


Figure 4. Concentrations of all elements in the sulfide ore samples 450 (top) and 459 (bottom) before (blue) and after (orange) growth with *P. glomerata* for 30 days at 25°C in the dark. Typical results are shown from one of at least three determinations.

6 Implications

Bioremediation and biorecovery of Se and Te from selenium- and tellurium-polluted environments suggest an environmentally-sustainable choice of treatment for contaminated soils, groundwater, wastewater and sediments (Liang and Gadd 2017). The potential application of bioextraction of Se and Te may be developed through established protocols and optimized processes. Previous research has demonstrated Se- or Te-species removal by fungi is accomplished through intracellular uptake or interaction with surface biomolecules such as proteins, amino acids and extracellular polymeric substances, while cellular biotransformation of selenium and tellurium oxyanions leads to reduction to elemental selenium and tellurium. Both elemental selenium and tellurium were found within the fungal biomass and in supernatants. A challenge in the biogenic production of selenium and tellurium nanoparticles is their purification from fungal biomass, because the formation of selenium and tellurium nanoparticles can be achieved both intracellularly and extracellularly: separation of particles from biomass without altering their properties, shape and size is challenging (Liang et al. 2019). These findings from the

fungal interaction with sulfide ore samples are relevant to novel approaches for biorecovery of these elements as elemental selenium and tellurium by the fungal surface biomolecules straight from the ore samples.

Acknowledgements

G. M. Gadd gratefully acknowledges research support from the Natural Environment Research Council [NE/M010910/1 (TeaSe); NE/M011275/1 (COG3)]. The authors also gratefully acknowledge the help of Dr Yongchang Fan (Materials and Photonics Systems Group, University of Dundee, Dundee, DD1 5EH, Scotland UK) for assistance with scanning electron microscopy.

References

- Bullock LA, Perez M, Armstrong JG, Parnell J, Still J, Feldmann J (2018) Selenium and tellurium resources in Kisgruva Proterozoic volcanogenic massive sulfide deposit (Norway). *Ore Geol Rev* 99:411-424.
- Espinosa-ortiz EJ, Gonzalez-Gil G, Saikaly PE, van Hullebusch ED, Lens PNL (2015) Effects of selenium oxyanions on the white-rot fungus *Phanerochaete chrysosporium*. *Appl Microb Biotechnol* 99:2405-2418.
- Espinosa-ortiz EJ, Rene ER, Guyot F, van Hullebusch ED, Lens PNL (2017) Biomineralization of tellurium and selenium-tellurium nanoparticles by the white-rot fungus *Phanerochaete chrysosporium*. *Int Biodeterior Biodegradation* 124:258-266.
- Eswayah AS, Smith TJ, Gardiner PH (2016) Microbial transformations of selenium species of relevance to bioremediation. *Appl Environ Microbiol* 82:4848-4859
- Gharieb MM, Gadd GM (2004) Role of glutathione in detoxification of metal(loid)s by *Saccharomyces cerevisiae*. *BioMetals* 17:183-188.
- Gharieb MM, Kierans M, Gadd GM (1999) Transformation and tolerance of tellurite by filamentous fungi: accumulation, reduction, and volatilization. *Mycol Res* 103: 299-305.
- Hunter WJ, Manter DK (2009) Reduction of selenite to elemental red selenium by *Pseudomonas* sp. strain CA5. *Curr Microbiol* 58:493-498.
- Jacob JM, Lens PNL, Balakrishnan RM (2016) Microbial synthesis of chalcogenide semiconductor nanoparticles: a review. *Microb Biotechnol* 9:11-21.
- Liang X, Gadd GM (2017) Metal and metalloid biorecovery using fungi. *Microb Biotechnol* 10:1199-1205.
- Liang X, Perez MAM, Feldmann J, Csetenyi L, Gadd GM (2019) Formation of selenium- and tellurium-containing nanoparticles during the growth of filamentous fungi. *Acce Microbiol* (doi: 10.1099/acmi.ac2019.po0286).
- Mandal D, Bolander ME, Mukhopadhyay D, Sarkar G, Mukherjee P (2006) The use of microorganisms for the formation of metal nanoparticles and their application. *Appl Microb Biotechnol* 69:485-492.
- Ollivier PRL, Bahrou A, Church TM, Hanson TE (2011) Aeration controls the reduction and methylation of tellurium by the aerobic, tellurite-resistant marine yeast *Rhodotorula mucilaginosa*. *Appl Environ Microbiol* 77: 4610-4617.
- Sarkar J, Saha S, Dey P, Acharya K (2012) Production of selenium nanorods by phytopathogen, *Alternaria alternata*. *Adv Sci Lett* 10:111-114.
- Siddiquee S, Rovina K, Yusof NA, Rodrigues KF, Suryani S (2014) Nanoparticle-enhanced electrochemical biosensor with DNA immobilization and hybridization of *Trichoderma harzianum* gene. *Sens Biosensing Res* 2:16-22.

Geoscience vision for future resource exploration and extraction

T. Campbell McCuaig, Jillian Terry

BHP Geoscience Centre of Excellence, Perth, Western Australia

Abstract. The resource landscape for the future is changing at an ever increasing pace. Discovery efforts have moved into the challenge of undercover exploration. Technological advances in terms of automation and AI are poised to transform extraction. Social pressures are demanding more environmentally and socially sustainable sourcing of material and energy resources for consumers. All of these changes will redefine the skill sets required in geoscience teams that discover, delineate and extract these resources, and what geoscience research, data collection and data management challenges and opportunities confront us to achieve this. Geoscientist's tasks will be elevated from manual and qualitative data gathering to high value, higher-order data validation, integration, quantitative AI-assisted interpretation and communication of knowledge to underpin decisions across all aspects of the mining value chain.

1 Resource Landscape

The resource industry is focused on sourcing and extracting material and energy resources for the needs society. The landscape in which this industry operates is facing an unprecedented rate of change to contextual factors that shape actors within it.

No one can predict the future. However, scenario planning can map out a range of plausible futures that could shape the type of geoscience, and capability of geoscientists that would be required to optimally manage resources in the future (e.g. Sykes and Trench 2016).

Emerging and continuing trends

There are a number of trends likely to continue to drive change into the future, highlighted in Figure 1. These trends include:

Increasing population and an increasingly technology-dependent population. In concert, these trends herald concomitant increasing material and energy resource demand.

Social pressures for environmental stewardship.

There are increasing calls from many sectors of society for action on environmental issues from global climate change to the local disruption of environment and communities around resource extraction operations. Industry is seeking to source resources in a sustainable manner that does not adversely affect the atmosphere, biosphere and hydrosphere.

Following from above, there is an increasing demand for renewable energy in an energy-constrained future. The pressures to limit the negative physical, socio-

economic and carbon footprint of resource extraction will redefine what is economic ore, affecting the entire mining chain - what type of resource accumulations we seek, what type of extraction and processing methods we employ, and how we manage resources from discovery through to closure (McCuaig et al. 2014).

A data-rich future. Our ability to collect data has outstripped our ability to effectively integrate and interpret it to optimise resource discovery and extraction efforts. This trend is leading to increasing adoption of data analytics, machine learning and artificial intelligence (AI) applied to exploration and extraction decisions. These efforts are aiming to maximise human intuition but minimise human bias through the power of the computer. Technology is also developing increasingly intimate data-human interfaces, allowing more efficient integration and interpretation of data.

Increasing automation. Just as the internet and mobile communications have transformed how we communicate, automation is transforming how we collect and manage data, and how we extract mineral resources. Automation also goes hand-in-hand with an increasing focus on safety, allowing humans to be taken out of the 'line-of-fire' throughout the exploration-extraction-closure value chain.

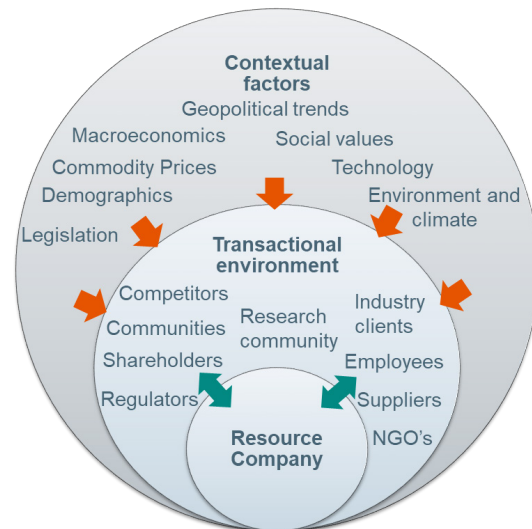


Figure 1. Contextual factors affecting the resources industry (after Ramirez and Wilkinson 2016; Sykes and Trench 2016).

Highly uncertain trends

While the trends previously discussed are widely accepted as continuing, there are others that are highly uncertain, in particular:

Advances in Technology that materially affect

commodity demand, including substitution, recycling, or new commodity demand. What will substitute hydrocarbons for energy density? What will substitute steel for construction? Either way, supplying any commodities in the future will still require geoscientists to source and extract them.

Geopolitical trends that affect access to resources. Will the current nationalistic wave sweeping the planet continue, or will globalism re-establish itself as the dominant trend? This will materially influence resource availability and therefore demand, as well as the capability and mobility of geoscientists.

2 The Future Geoscientist in the Resources Industry

How will these trends impact upon the skill sets required for geoscientists in the resources industry? Figure 2 illustrates the value chain in the resources industry, which can be broadly grouped into (1) exploration and discovery of resources, (2) resource appraisal (resource delineation, estimation, and analysis of potential economic extraction), (3) resource extraction and delivery to market, and (4) project closure. Also shown are the relative geoscience activities and skill sets in each step now, and in the possible futures shaped by the contextual factors discussed in the previous section.

2.1 Future exploration and discovery geoscience

The current technology package employed by mineral exploration companies has been optimized for discovery at or near surface. However, the near-surface search space is rapidly depleting for world class mineral deposits (Hronsky 2009). Future exploration is highly likely to focus in new search spaces under cover that were effectively 'blind' to historical exploration efforts and technology.

To predict and detect the presence of high quality mineralization in this new search space, a number of skill sets will need to be enhanced. Firstly, due to the increased cost of exploration under cover and difficulty in accessing ground to explore, targeting exploration in areas with the highest potential for success is of paramount importance. Adopting a multiscale systems approach will be required to enhance our ability to predict the spatial distribution of mineralisation through geologic time. Secondly, with the increased access to large and increasingly quantitative spatial datasets across a range of scales, data analytics and AI capabilities will likely be more heavily drawn upon in mineral exploration. Thirdly, the ability to accurately image and quantitatively model the subsurface will be required. Much geophysical data today is only qualitatively or semi-quantitatively integrated with geology. Future geoscientists must be able to critically assess, integrate and quantitatively interpret geological and geophysical datasets.

The exploration geoscience teams are often the point of 'first contact' with local community and government stakeholders and can make or break a company (and in fact the entire industry's) relationship with these groups. Environmental and social responsibility as well as cultural

awareness will continue to be key skill sets in the future explorer.

2.2 Future resource appraisal

Future resource appraisal will be heavily influenced by advances in computing power, uncertainty modelling, AI algorithms and automation. Many geological and resource models today are still based on a small number of deterministic scenarios, and model a limited range of parameters. Future resource modeling will allow the generation of multiple geological models and will comprise all geometallurgical parameters required for extraction, including geology, petrophysical properties, multielement geochemistry, structural, hydrological and geotechnical parameters, mineralogy and texture. Uncertainty in all of these parameters and the geological models themselves will be fully captured and quantified to inform accurate planning. The volumes of data at resource appraisal stage, and ability to generate multiple realisations of the subsurface, will require strong data analytical skills and be AI-enhanced.

Automation will strongly alter the workflow of the future geoscientist in this space. Gone will be the days of geologists undertaking time-consuming manual sampling and qualitative and subjective logging of drill core or mapping of surface or underground exposures. Instead, data will be collected automatically on drill core, and often down the drill hole, at surface or underground using drones in real-time. The task of the geologist will be elevated to data verification, synthesis, interpretation and communication of results to inform downstream decisions in the extraction process. Interpretation and communication will likely be aided by virtual reality where geoscientists can 'walk through' the data and models and modify them directly in 3D.

2.3 Future resource extraction

The highly-automated and high-volume real-time data availability and predictive analytics of the future resource extraction operation will dramatically change the role of the geoscientist. Predicting and monitoring the 4D performance of the rock mass in terms of metal content, contaminants and rock properties for mining engineering and probabilistic mine planning, processing stockpile management, water utilization, waste stream containment and storage and dynamic closure planning considerations will require a geoscientist to have a wide range of knowledge of the entire mining stream. Again, the days of labour intensive data collection will be gone. Geoscientists will only have restricted access to exposures due to the high degree of automation (less people in the 'line of fire') as well as potential advances in in-situ extraction technology. With the reduction of manual-intensive data collection, there is a high probability that future extractive activities will have fewer employees, including fewer geoscientists. However, geoscientists will be more focused on high value higher order tasks such as real-time data verification, integration and interpretation and delivery of knowledge to downstream users in the mining process.

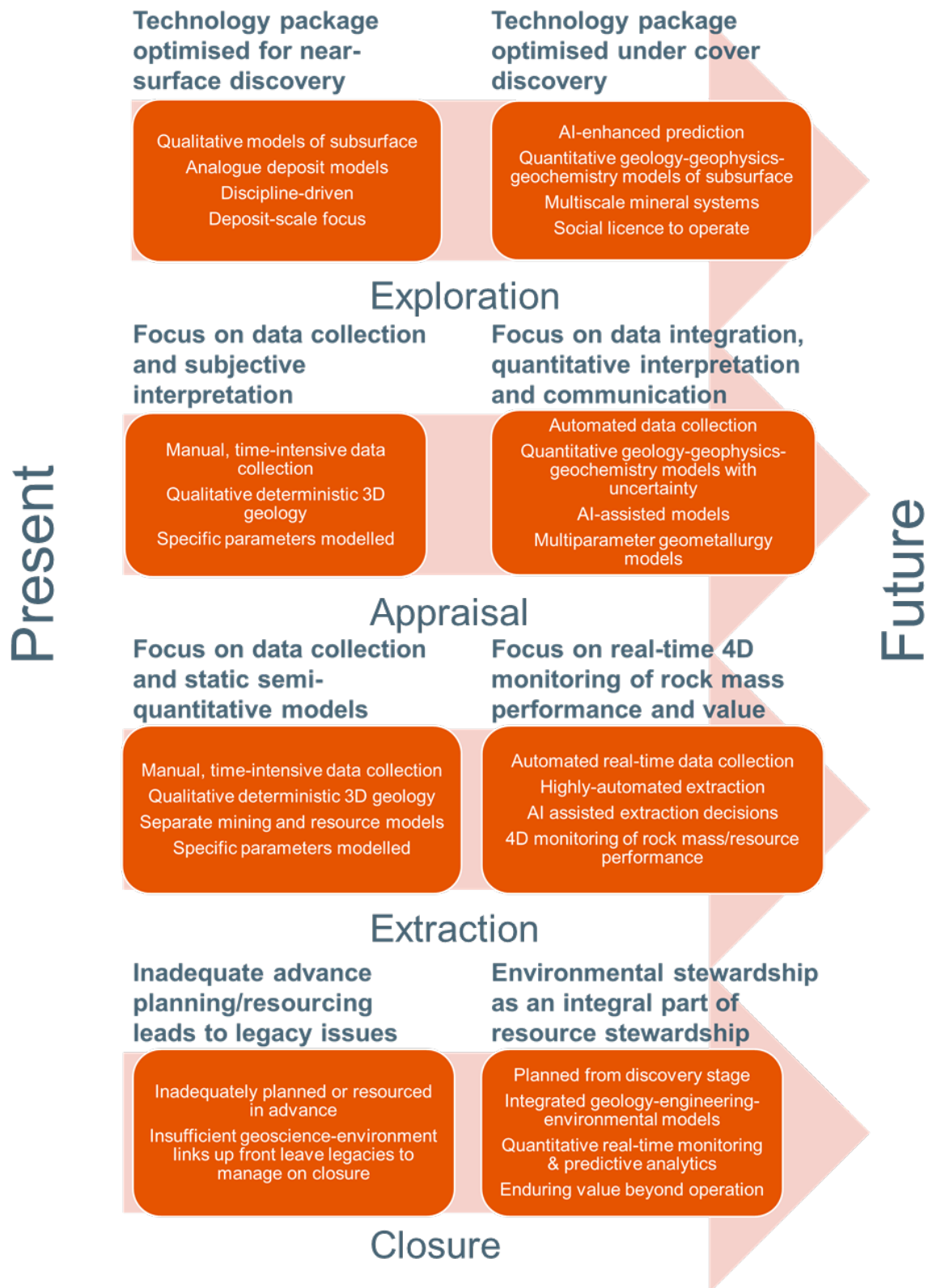


Figure 2. Resource value chain from exploration and discovery, through appraisal, extraction and eventual closure showing some major changes in geoscience focus and workflow from now into the future.

2.4 Future project closure

Project closure is often inadequately planned for and not resourced until late in the life of a mining operation. This practice is rapidly changing, and new resource projects coming online are required, prior to permitting, to increasingly consider the physical and environmental footprint of the operations. These considerations are not just during extraction, but past the life of the mine to ensure not only that any environmental impacts are minimized, but that enduring value is realized during and well beyond the life of the operation. This will require dynamic input to planning from environmental geoscientists from the discovery through to closure steps in the value chain.

3 Summary of impact on future geoscientists

Figure 3 shows select key skill sets required by the future geoscientist to be able to effectively contribute to the resource discovery and extraction industry. Clearly, it is a challenge to develop all of these skills in a single person, hence the need to be able to function in high-performing teams and communicate effectively. Nevertheless, the successful geoscientist will need to have an appreciation of all of these skills (and more).

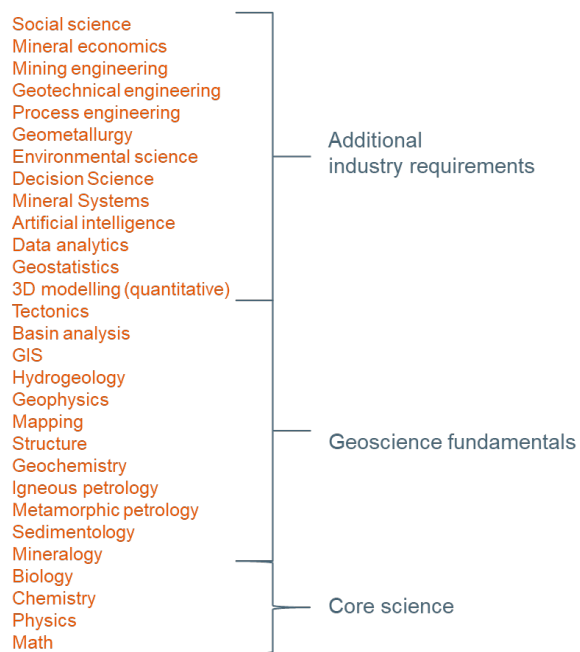


Figure 3. A partial list of disciplines in which the successful geoscientist of tomorrow's resources industry needs to be informed.

Not all of these can, will or should be taught in earth science departments in universities. Future geoscience teams in industry will involve people from a range of science disciplines, whose first degree may not be in geosciences, but instead physics, engineering, applied maths, etc. Furthermore, the future geoscientist will

require training post-first degree...whether as a second degree, or as short courses available through the host company or through a commercial or industry provider.

There is often debate about the relative value of becoming a generalist versus a specialist. To get breadth of knowledge, does one have to sacrifice depth of knowledge? It is envisaged that having a strong technical base in a core subject will always be a requirement from both the industry and the personal point of view. However, while specialist depth and no breadth is not desirable, similarly geoscientists need to be able to anchor to technical 'first principles' – especially in a future where automated and AI-assisted workflows can run the risk of becoming 'black box' approaches. Geoscientists are encouraged to seek to develop a broad base of technical knowledge and experience, but exercise curiosity and seek other areas in which they can develop sufficient depth.

No matter what mineral and energy resources are demanded by society in the future, the ability to effectively discover, appraise and extract these resources in a socially and environmentally sustainable way will all hinge on effective understanding of the subsurface, and how disruption of the subsurface will affect the surface biosphere-hydrosphere-atmosphere of the Earth system. This will require application of geoscience, and therefore skilled geoscientists.

The roles for geoscientists in the future extraction industry may be fewer, but they will clearly be more exciting – less focused on manual data collection, and more focused on data validation, integration, interpretation and communication of results throughout the value chain. However, the successful geoscientist in the extraction industry must take an active interest in the entire discovery-closure process and its impact on all stakeholders (including communities and the environment), focus innovative geoscience thinking onto identified material risks in this process, and effectively communicate to all downstream users of the geoscience information (McCuaig et al. 2000).

References

- Heyes J, Cooper T (2019) Strengthening BHPs closure Framework – a strategy to realise enduring value. In Proceedings of the 13th International Conference on Mine Closure, Perth, September (In Press)
- Hronsky JMA (2009) The exploration search space concept: key to a successful exploration strategy. CET Quarterly Newsletter 8.
- McCuaig TC, Vann J, Seymour C (2000) Dynamic links between geology and the mining process. In Proceedings Fourth International Mining Geology Conference.
- McCuaig TC, Vann JE, Sykes JP (2014) Mines versus mineralisation–deposit quality, mineral exploration strategy and the role of 'boundary spanners'. In Proceedings Ninth International Mining Geology Conference: 33-42.
- Ramírez R, Wilkinson A (2016) Strategic reframing: The Oxford scenario planning approach. Oxford University Press.
- Sykes JP, Trench A (2016) Using scenarios to investigate the long-term future of copper mining and guide exploration targeting strategies. In AusIMM International Mine Management Conference, Brisbane, Australia: 22-24.

Responsibility in Mining: How to make difficult decisions

Gordon, S. H.

Satarla Risk Management, London, UK

Department of Earth Sciences and Engineering, Imperial College London, UK

College of Business and Economics, Department of Accountancy, University of Johannesburg, South Africa.

Abstract. The often-conflicting requirements imposed by shareholders and society on mining companies can cause simple decisions to become far more complex than they initially appear. The desire to operate in a safe and sustainable manner whilst delivering significant returns on investment are not always possible.

The establishment of clear tolerance thresholds for risks faced throughout an organization are an increasingly common method through which to support teams when objectives conflict with one another. This technique empowers individuals to escalate risks that have the potential to jeopardize any aspect of a project, operation or team. Decision makers at the correct level of the organization, be they Project Manager, General Manager, CEO or Chairperson can then take accountability for balancing the management of key opportunities and threats.

Founded on a simple form of integrated, organization-wide risk management, this approach also addresses many regulatory requirements, increases the foresight required to improve the management of projects, and ensures that organisations truly live by their stated values.

1 Responsibility

The world is becoming increasingly “responsible”. Awareness of, and a desire to achieve the vision set out in documents such as the Sustainable Development Goals (SDGs) (United Nations 2015) is becoming the societal norm globally. While the specifics of each Goal continue to be debated, it is accepted by most that in order for the human population to survive, these challenges need to be addressed immediately.

1.1 Responsibility and mining

In order for many of the challenges set out in the SDGs to be addressed through the manufacturing of more sustainable technology and infrastructure, it is vital that access to a bountiful supply of resources ranging from copper to silver, REEs and lithium be maintained. Substitution and recyclability of these four example materials remains almost impossible (Dominish et al. 2019), placing the onus to meet global demand fully on the mining sector.

Mining as an industry therefore finds itself in a difficult position. While the provision of these materials is vital for global development, the extraction of non-renewable resources is inherently unsustainable as there is no intention to put those commodities back

where they were found. Sustainability principles can however be adopted when mining.

1.2 Conflicting objectives

Almost every mining and metals organization states objectives that include both the desire to mine and process materials safely and sustainably, whilst also delivering a healthy return on shareholder investment (e.g. Anglo American 2019, BHP 2019, Glencore 2019, Rio Tinto 2019). These are underpinned by values reinforcing the responsible nature in which they aim to operate.

These objectives are conflicting in that often the largest short term financial return can be gained by not truly adhering to the spirit of the stated company values. Decision makers therefore need to be prepared to relinquish a proportion of the potential financial return in order to adhere to the stated company values.

2 Trigger points for decision making

Ensuring the entirety of a team is aware of the point at which a decision needs to be made to manage an emerging conflict in objectives is critical. Assuming that every team member has the same tolerance for stretching the intent of an objective can lead to confusion and ultimate failure to achieve desired outcomes.

2.1 As low as reasonably practicable

Safety is often cited as the “number one priority” with slogans such as “zero harm” being common across the industry. However, if operators truly mean zero, humans either have to be removed from the mining environment which can be both costly and lead to forced social change regarding the level of employment available to communities bordering mining operations; or operations considered for closure. In many cases neither of these options are preferable.

As low as reasonably practicable (ALARP) (Health and Safety at work Act 1974) provides guidance as to the level of tolerance that can be introduced into the working environment with regards to safety. The definition set out by the Court of Appeal (in its judgement in *Edwards v. National Coal Board*, [1949] 1 All ER 743) is as follows:

“Reasonably practicable’ ... a computation must be made by the owner in which the quantum of risk is placed on one scale and the sacrifice involved in the

measures necessary for averting the risk (whether in money, time or trouble) is placed in the other, and that, if it be shown that there is a gross disproportion between them – the risk being insignificant in relation to the sacrifice – the defendants discharge the onus on them.”

Therefore, should controls be available that may reduce the risk posed by the often hazardous mining environment, they should either be implemented or mining be undertaken via an alternative method. Keeping the workforce safe should be the simplest decision, however due to competing expectations from shareholders versus society, can be made incredibly complex.

2.2 Establishing risk appetite and tolerance

Risk can be defined as the *effect of uncertainty on objectives, with the effects including both opportunities and threats* (International Standards Organisation 2018). All risks have an element of uncertainty, some of which can be quantitatively measured. Should an uncertain event not have the potential to impact on an organization’s objectives, by definition it is not a risk to that organization.

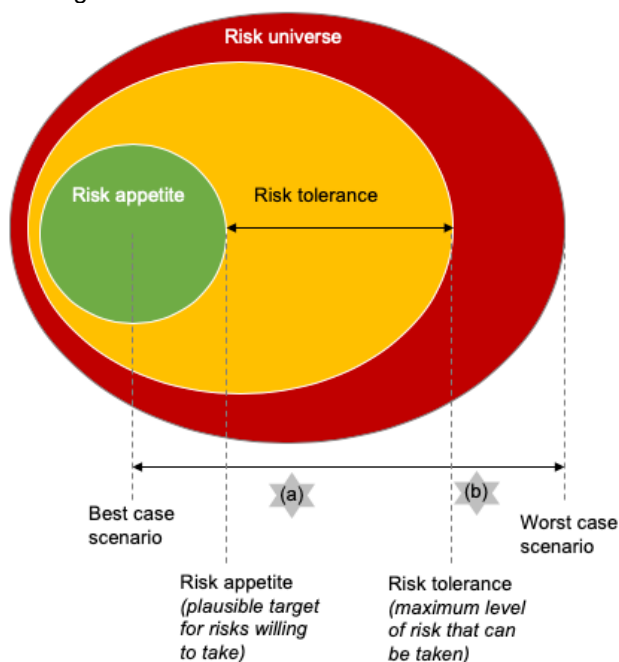


Figure 1. Risk appetite and tolerance. Risk appetite is the level of risk a team is willing to take; risk tolerance is the level of risk a team can take; the risk universe is all risks the organization faces, some of which are not tolerable (International Standards Organisation 2018). Example risk (a) is within the tolerable zone. The team can survive this risk in its current position. Example risk (b) is outside of the risk tolerance and action needs to be taken immediately to move it into the tolerable zone. If this does not happen prior to the risk occurring then the organization could cease to exist or a significant change to strategy is required.

The tipping point beyond which a risk becomes too large, either because the opportunity is so great that a change in strategy for the organization is warranted, or

because the threat posed goes beyond the stated values of the organization is sometimes called the risk tolerance level. Most organisations will define their risk appetite (the level of risk they are willing to accept), together with their risk tolerance level (the level of risk they can accept) (Fig. 1).

This set of criteria can be used to hold an organisation to account at the most senior level. The normality of including concepts such as risk tolerance in company reporting (Financial Reporting Council 2016) can be used deeper within organizations to ensure that responsible decisions are being made and actions taken to ensure risks are managed to within pre-defined tolerance limits.

3 Integrated risk-based decision making

Risk management is a formalized process for decision making. Entrenched in regulations and standards throughout the mining sector, the assessment and management of risk is part of daily life. The challenge is often to make it dynamic and valuable beyond the “tick the box” often required by a regulator.

3.1 The right tool for the job

A range of risk-based tools and techniques are common across different disciplines. For example, uncertainty modelling techniques for an ore body are common place for resource geologists; whilst an environmental expert will make use of scenario modelling; an engineer will often use Failure Mode Effects Analysis; and accountant will use techniques such as reverse stress-testing. The importance of using the correct tool for the job is critical. However, in order for risks to be compared with one another, they also need to be shared in a way that is understandable for those who are not an expert in each discipline.

Many organisations are therefore adopting a very simple central risk management process that can act as the anchor for risk-based decision making (Fig. 2).

3.2 Simple, proportionate risk management

The four-step risk management process (Fig 2) is aligned with all major risk management standards (including, ISO31000:2018, COSO Framework 2017). It is appropriate for mentally assessing simple risks such as those posed by crossing a road, to multi-billion dollar acquisitions.

3.3 Changing context

The internal and external context to an operation changes on a dynamic basis. For example, the collection and analysis of geoscientific data will change a team’s understanding of an ore body. Similarly, fluctuations in commodity markets may alter the economic viability of a project. Both internal and external changes in context should lead to a re-evaluation of the potential opportunity being explored.



Figure 2. Integrated risk management draws together all other types of risk management which may be undertaken across an organization. This simple form of risk management has four steps: (1) Define context and objectives. Describe the internal and external context in which you are operating, including any recent or anticipated changes. (2) Assess risks including the identification, understanding and evaluation of potential opportunities and threats. (3) Manage risks by putting in place appropriate controls. (4) Monitor and review the status of risks and effectiveness of controls through metrics, self verification and assurance.

3.4 “Black swans”

Black swans are those risks that an individual does not know about until they have been realized (Taleb 2007). These may be ore bodies that a geologist does not identify despite exploring in that area; or a fault in a piece of equipment that an individual is unaware of prior to it failing.

Often it is the knowledge that there are risks that “we don’t know we don’t know” (Rumsfeld and Myres 2002) that concerns an individual the most.

3.5 Identifying the “elephants” to manage the “black swans”

Many organisations are adopting the use of risk libraries. These help us to identify those risks that may be normal to the type of activity being undertaken. However, the risks that have more often significantly impact on a project or operation are those that we do not formally acknowledge or manage. These are increasingly termed the “elephant” risks.

Elephant risks can exist for a myriad of different reasons. An individual may assume that someone else is managing it, or suppress the risk for cultural reasons. Furthermore, an internal company process may insinuate that unless the risk triggers a gain or loss of a life or certain level of capital, it is not important.

By moving a team’s risks from “elephant” to “acknowledged” status, the potential for “black swan” events to occur are minimized.

For example, it has been suggested that the owners

of the Fundao waste dam at the Samarco iron ore mine were aware of the worsening integrity of the facility prior to its failure in November 2015. This unacknowledged risk has led to recent shareholder action in both the USA and UK.

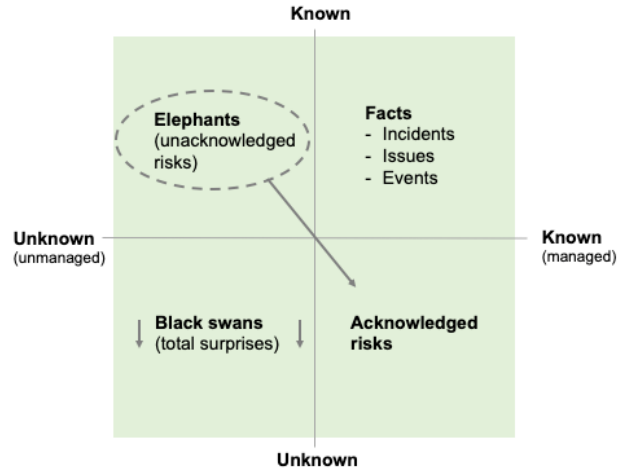


Figure 3. Adapted from the Johari window (Luft and Ingham 1955) and concept of “known knowns and known unknowns” (Rumsfeld and Myres 2002), this diagram demonstrates that by acknowledging “elephant risks”, the total number of black swans potentially faced by an organization will diminish.

3.6 Managing and monitoring risks

Ensuring that truly effective and meaningful controls are implemented is integral to the management of risks. A control is a task, object or process that actively changes the risk, either by changing the likelihood of it occurring or the consequence of the risk should it occur.

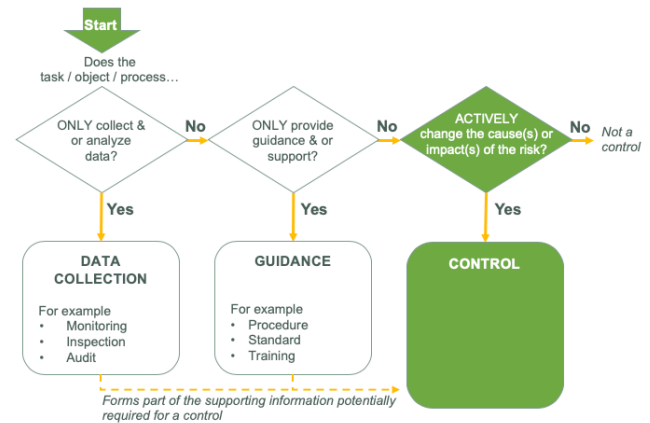


Figure 4. Control flowchart depicting that a control has to be a task, object or process that actively changes the risk.

Often monitoring or guidance activities are listed as controls, however these have no impact on the risk without being linked to a true control (Fig. 4).

3.7 Challenging our objectives

The four-step iterative process (Fig. 2) allows the following question to be posed: *Given the context in*

which we are operating coupled with the objectives we have set ourselves, the risks we face, and our ability to manage them, is it possible to achieve our objectives? If the answer is yes, carry on operating. If the answer is no, two options present themselves: 1) Allocate more time, capital, effort into managing the risks; or 2) Change the objectives.

This simple yet objective decision making process has allowed an increasing number of projects, operations and organisations to challenge their mode of operation and make changes where appropriate.

4 Responsible decision making for the long term

Many of the sustainability-based risks can be identified right at the beginning of a project. Unless managed, it is often these risks that then lead to the failure of the project at a future date. It can be increasingly difficult to explain the importance to investors of risks what may only come to fruition many years after a return on investment has been realized. Acknowledgement and management of these risks at the early stages is vital for the long term success of the project.

4.1 Ethical investment

Investors are increasingly seeking ethical opportunities in which to invest their capital. Currently these do not include mining due to the perception that the industry does not meet certain benchmarks centered on the SDGs. Only by formally and publicly moving towards transparent, long term, sustainable decision making will ethical investment begin to flow towards the vital activity that is mining.

4 Conclusions

Risk management can be that method through which difficult decisions are made in a responsible manner. No longer should it be the “tick box” risk assessment that is carried out on a daily basis to satisfy an auditor. The intent of risk management is to create a culture of transparency within the organizations that utilize it effectively, ensuring that decisions can be made at the right time to address risks. This dynamic and integrated form of organization-wide risk management not only provides a competitive advantage over peers, but also ensures a team can maintain its reputation by operating in a responsible manner.

Acknowledgements

We thank all of the clients and Associates of Satarla for contributing to this research.

References

- Anglo American (2019). Unlocking our full potential disciplined growth for a sustainable future. London: Anglo American plc
- BHP Billiton (2019). BHP Annual Report 2018. Melbourne: BHP Billiton
- Committee of Sponsoring Organizations of the Treadway Commission (2017). Enterprise Risk Management - Integrating with Strategy and Performance. United States: Committee of Sponsoring Organizations of the Treadway Commission
- Dominish, E., Teske, S. and Florin, N. (2019). Responsible minerals sourcing for renewable energy. Sydney: Institute for Sustainable Futures
- Financial Reporting Council (2016). The UK Corporate Governance Code. London: The Financial Reporting Council Limited
- Glencore (2019). Glencore Annual Report -Responsible sourcing the commodities for everyday life. Baar: Glencore
- International Standards Organization (2018). ISO 31000 - Risk management - Guidelines. Geneva: ISO.
- Luft, J. and Ingham, H. (1955). The Johari Window, a graphic model of interpersonal awareness. Proceedings of the western training laboratory in group development. Los Angeles: University of California, Los Angeles.
- Rio Tinto (2019). Rio Tinto Annual Report 2018. London: Rio Tinto.
- Rumsfeld, D. and Myers, R. (2002). DoD News Briefing - Secretary Rumsfeld and Gen. Myers.
- Taleb, N. (2007). The Black Swan: The Impact of the Highly Improbable. 1st ed. Penguin, London.
- United Kingdom government (1974) Health and Safety at Work etc. Act 1974.C37.
- United Nations General Assembly (2015). Transforming Our World: The 2030 Agenda For Sustainable Development. New York: United Nations.

Sustainability in the mine life cycle

R.J. Howell, C.R. Williams, R. Griffiths
SRK Consulting, Cardiff, UK

H.E. Jamieson
Queen's University, Canada

J.V. Parshley
SRK Consulting, Reno, USA

Abstract. As the earth's population grows, the pressure on natural resources becomes acute. Mining, once a foundation of human society is now often perceived negatively, despite the true but worn adage "if it cannot be grown, it has to be mined". 'Sustainable mining' now proliferates as a buzz-word, often incorrectly applied. Yet by its very nature, mining is rarely 'sustainable' but rather a finite process, the consumption of a resource. Despite this, aspects of mining can prove to be sustainable for example the exploitation of renewable minerals such as guano or evaporite salts. But sustainability is so much more than renewable materials. It incorporates a change in the philosophy and practices in mineral exploration and exploitation, it requires better education of generations to develop sustainable skills in society to continue mining and it seeks to minimize environmental and social disturbance whilst maximizing resource recovery. Another area where a sustainable philosophy is important is with closure of mines, aftercare of mining-dependent societies and potentially reuse of abandoned mines. Sustainability can cover a lot more in terms of development of alternative resources, appropriate development of infrastructure, improvement in land use, enrichment of society and in the preservation or restoration of the environment.

1 Introduction

"Humanity has the ability to make development sustainable- to ensure that it meets the needs of the present without compromising the ability of future generations to meet their own needs" (Brundtland, 1981).

Mining for metals has been a foundation of human society from pre-recorded history, with the winning of copper and gold from streams and oxidized ore deposits (Calas 2017). By its very nature, mineral deposits are rarely 'sustainable' as defined by Brundtland and the consumption is often seen as a limit to development (Meadows et al. 1972; Richards 2002; Kirsch 2010). Yet sustainability as a whole can be applied from exploration through to mine reclamation and after care.

The activity of mining consumes a resource as the development progresses (Kirsch, 2010). At some point a given mineral deposit will be physically or, more commonly, economically exhausted. Other than marine evaporates, guano phosphate and some soda ash deposits, mineral deposits are not renewed on a human time scale of sustainability (Howell 2017).

Sustainable mining as a philosophy can be applied to greenfields exploration (Grennan Clifford 2017), active operations (Erkayaoğlu and Demirel 2016; Gorman and Dzombak 2018), closure and reclamation (Espinoza and Morris 2017). Additional aspects include the re-assessment of old mining districts or sensitive development of a mining project to minimize or avert environment or community pressures (Espinoza and Rojo, 2017). Despite often long and active periods of mining, most mines do not close because of the exhaustion of all resource but rather because the resource that is left costs more to extract at prevailing metal prices than will be realized in revenue. As many resources reach this maturity or are abandoned, potential negative environmental impacts can and do occur. Historic writers from Pliny to Georgio Agricola and Hoover have commented on the waste associated with mines (Hoover and Hoover 1912), and the associated impacts to soil, vegetation and water. Therefore, another aspect of 'sustainable mining' is consideration of potential environmental impacts and the need to minimize or mitigate in operations and on closure (Aznar-Sánchez et al. 2019).

2 Renewable mineral resources

Although most mineral resources cannot be considered renewable on the scale of human life there are some that do get replenished on such a time scale. These deposits include those formed by; volcanic processes; evaporation; and biological processes.

Volcanic -related renewable minerals are many. Examples include geothermal associated deposits such as deep sea vents hosting base metal sulfides (e.g., the East Pacific Rise), sulfur or metal bearing fumarole deposits at surface, such as those in the Kuril Islands, geothermal precipitates and brines and groundwater enriched by brines (Singer 2014; Khomich et al. 2019). Other resources include soda ash and some potash deposits associated with circulating fluids in rift valleys, such as in the East African Ridge (Kun, 1965). Deep sea floor manganese-cobalt nodules are another possible renewable resource (Hein and Koschinsky 2014).

Marine evaporite salts are utilized globally for rock salt, iodide, bromide and occasionally in the production of potash. However, they also contain potential resources of boron and lithium. (Kun, 1965). Biological deposits that are renewable include the phosphate-rich guano deposits

(Van Kauwenbergh 1991).

One aspect not often listed as a renewable mineral resource is of course, water. In many mining areas, particularly arid areas, this precious resource can be a long-term sustainable source for urban water requirements and agriculture. It can be considered a renewable resource, such as in NW Spain, where flooded coal mines provide potential water resources for agriculture (Álvarez et al. 2018) and in Australia, where gold mine pit lakes provide drinking water (Kumar et al. 2009).

3 Improved efficiencies in mining

The discovery of high-grade mineral deposits is becoming rare and the development of deeper, lower grade and often metallurgically challenging ores, is becoming more common (Gorman and Dzombak 2018).

Figure 1 graphically depicts the mine life cycle and shows important cost items, both profit and loss, associated with a mining project over the life of a mine. As observed cost items are numerous and considerable cost and time outlay be required in order to provide engineering and operating plans that meet regulatory and public approval prior to any revenue generation. Decades of work may be required between exploration discovery and first production.

Mineral Exploration is the first step in the cycle. In an exhaustive study on the pillars of society development a report commissioned by the ‘club of Rome’ (Meadows et al. 1972) defined the “depletion of non-renewable resources” as a major concern that could limit societies advancement and lead to conflict.

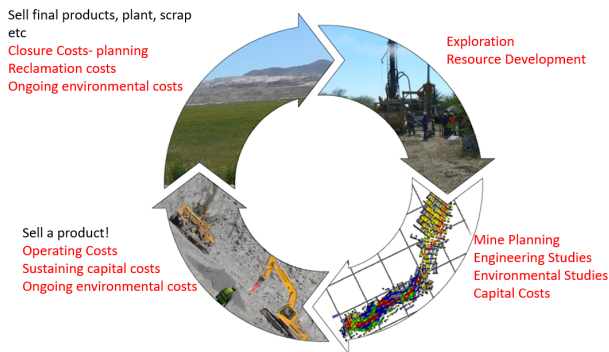
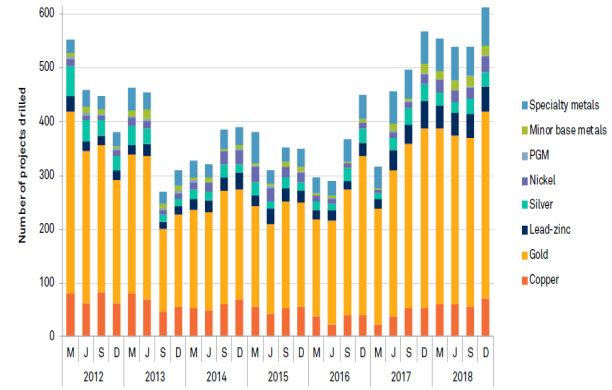


Figure 1. Revenue consumption and generation in the Mine Life Cycle (revenue in black; costs in red).

Fundamental to ensuring a slowdown in this depletion and shortage is the renewal of resources through mineral exploration and discovery (Grennan and Clifford, 2017). Despite this, exploration spending is limited generally to a few commodities (Figure 2).



Data as of Jan. 18, 2019.
PGM = platinum group metals
Source: S&P Global Market Intelligence

Figure 2. Summary of Exploration spending in 2018 (from S&P 2019).

More than half of exploration focus in 2018 was on gold. Yet zinc, along with speciality or critical metals, receive less than 20% of all exploration funding. This is even though these metals are all in depletion with less than a decade of known resource left (Laznicka 2010).

Sustainability plays a crucial role throughout the development of a mineral resource and need not be at the expense of shareholder return (Richards 2002). Rather, it is proposed to be a culture in which all stakeholders seek to minimize expenditure whilst maximising return in terms of financial reward, environmental compliance and positive community benefits (Gorman and Dzombak 2018).

The longer-term availability of mineral resources means ensuring that they are not sterilised from use. Mineral safeguarding is given little consideration in comparison to environmental issues and has resulted in the needless sterilisation of mineral deposits. Sustainable mining also means ensuring that mineral deposits are available for use by future generations. It is therefore necessary to consider not reclaiming them or providing alternative land use simply because they do not meet current economic criteria (Espinoza and Rojo 2017).

In terms of mining operations, a philosophy of sustainability to reduce unnecessary costs or impacts has been proposed to assess general mine operations (Laurence 2011), efficiency of open pit mining (Adibi and Atee-pour 2015), maximizing efficiency of explosives (Khademian and Bagherpour 2017), material handling (Erkayaoğlu and Demirel 2016) and water management and processing (de Villers 2017).

In addition, sustainability can also be applied in the Mine Life Cycle to education and training of current and future generations (Richards 2002). Sadly, this function tends to follow market forces with little investment during periods of low metal prices leading to poor succession planning and challenges in maintaining long term financial stability in many mining communities (Kirsch 2010).

As identified in several studies, the key to sustainable mining is often the sustainable development of skills base and intellectual resources appropriate for development now and in the future (Meadows et al. 1972; Brundtland 1981; Richards 2002; Grennan and Clifford 2017).

4 Advances in reclamation and restoration

Nearly all mines permanently change the surface of the earth and affect the physical and social environment. Therefore, planning for closure needs to begin early in the mine life cycle (IFC, 2007). Good international industry practice and some national regulations now stipulate that environmental and social closure be considered from the outset of project planning (Parshley and MacCallum 2016).

Most jurisdictions and good practice require that mine closure plans include measures to ensure long-term physical and chemical stability and address socio-economic considerations (ICMM 2019). In particular, closure of mine sites must address long-term public health and safety, and environmental protection as well as provide mitigation of social and economic impacts resulting from closure. During the last three decades the mining industry has developed technologies to address many of the technical issues associated with mine closure.

Future advances in technical closure are likely to be incremental rather than transformative. However, the industry has only recently begun to grapple with the social context of mine closure (Parshley and MacCullum 2016). Early and continued stakeholder engagement can minimize the impacts through education and management of expectations. However, in some contexts, post-closure economic opportunities are likely to be limited, and the impacts of closure on employees and local communities can be profound.

Even in developed nations stakeholder engagement regarding closure is essential to manage expectations and secure support for proposed closure actions. Some technical solutions such as perpetual care and water treatment are often seen as unattractive options that are rarely considered sustainable by any stakeholder (Kuyek 2011).

5 Mining legacy

The environmental legacies of metal mining are often dominated by large waste facilities, which can be sources of acid and metalliferous drainage, resulting in both local pollution and irreversible loss of some of the soluble minerals (Nordstrom et al. 2017). Re-mining these areas can lead to improvements in reclamation for example the Stibnite project in Idaho (Quinn, 2019).

In some cases, mines can be reused as aquaculture farms (Otchere et al. 2014) or even laboratories such as the SNOLAB in Sudbury, activity centres and zoos or botanical parks such as the Eden project (Pearman 2009). But in many cases the only use is to return to wilderness. This latter use does not betray a sustainable philosophy but rather demonstrates that pragmatic consideration is needed on a case by case basis.

6 Conclusions

Mining is only undertaken if a net positive long-term contribution can be made to the company. A sustainable approach ensures that net positive benefits to human and ecosystems are not contrary to this, but are sympathetic. Incorporating environmental, social and cultural issues can generate challenges in mine evaluation, but such an approach delivers lasting value to industry and society as a whole.

The longer-term availability of mineral resources is also essential, ensuring that they are not sterilised from use but instead are available for use by future generations, even if they are not economic today.

Sustainable mining is a philosophy that must be adopted by society as much as the mining industry. To conclude, for mining to be sustainable, the rate of consumption must not exceed the capacity to locate and develop replacement resources, recycle spent materials or develop suitable substitutes. It must also include sustainable environmental and community management in which exploitation or development does not compromise the needs of future generations or sustainable occupation of the plant. Sustainable mining implies that industry will use resources efficiently and economically, and that the land in which these resources occur will be managed with care and not endanger the planet's life support systems of air, water, soils and biota or the communities that rely on them.

References

- Adibi N, Atee-pour M (2015) consideration of sustainable development principles in ultimate pit limit design. *Enviro Ear Sci* 74: 4699-4718.
- Álvarez R, Ordóñez A, García R, Loredó J (2018) An estimation of water resources in flooded, connected underground mines. *Eng Geol* 232:114-122.
- Aznar-Sánchez JA, Velasco JF, Belmonte-Urena LJ, Manzano-Aguguliaro F (2019) Innovation and technology for sustainable mining activity: A worldwide research assessment. *J Clean Prod* 221: 38-54.
- Bowell RJ (2017) Perspective- what is sustainability in the context of mineral deposits? *Elements* 13: 297-298.
- Brundtland GH (1981) United Nations. Our Common world commission on Environment and Development, Oxford University Press. 400 p.
- Calas G (2017) Mineral resources and sustainable development. *Elements* 13: 301-306.
- Erkayaoğlu M and Demirel N (2016) A comparative life cycle assessment of material handling systems for sustainable mining. *JEM174*: 1-6.
- Espinoza RD, Morris JWF (2017) Towards sustainable mining (part II): Accounting for mine reclamation and post reclamation care liabilities. *Res Pol* 52: 29-38.
- Espinoza RD, Rojo J (2017) Towards sustainable mining (part I): Valuing investment opportunities in the mining sector. *Res Pol* 52: 7-18.
- Grennan EF, Clifford JA (2017) Resource sustainability- Geology is the solution. *Euro Geol* 44: 28-31.
- Gorman MR, Dzombak DA (2018) A review of sustainable mining and resource management: transitioning from the life cycle of the mine to the life cycle of the mineral. *Res, Conserv Rec* 137: 281-291.
- Hein JR, Koschinsky A. (2014) Deep-ocean ferromanganese crusts and nodules. *Enc Geochem* 13: 273-291.

- Hoover HC, Hoover LC (1912) *Georgius Agricola De Re Metallica*. Min Mag. 450 p.
- ICMM (2019) *Integrated Mine Closure Good Practice Guide*, 2nd Edition
- IFC (International Finance Corporation) (2007) *Environmental, Health and Safety Guidelines for Mining*. Washington DC. 228p.
- Khademian A, Bagherpour R (2017) Environmentally sustainable mining through proper selection of explosives in blasting operations. *Enviro Ear Sci* 76:166-171.
- Kirsch S (2010) Sustainable mining. *Dialect Anthro* 34:87-93
- Kun N de. (1965) *Mineral Resources of Africa*. Elsevier, London. 740 p.
- Kumar RN, McCullough CD, Lund MA (2009) Water resources in Australian mine pit lakes. *Min Tech*. 118: 205-212.
- Khomich VG, Boriskina NG, Kasatkina SG (2019) Geology, magmatism, metallogeny, and geodynamics of the South Kuril Islands. *Ore Geol Rev* 105: 151–162.
- Kuyek J. (2011) *The Theory and Practice of Perpetual Care of Contaminated Sites*. Report to Mackenzie Valley Environmental Impact Review Board. Alternative North. IAND, Ottawa, 145 p.
- Laurence D (2011) Establishing a sustainable mining operation: An overview. *J Clean Prod* 19: 278-284.
- Laznicka P (2010) *Giant Metallic Deposits*, 2nd edition: Heidelberg, Springer. 950 p.
- Meadows DH, Meadows DL, Randers J, Behrens III WW (1972) *The limits to Growth*. Report to the Club of Rome. New York: Universe Books. 270 p.
- Nordstrom DK, Howell RJ, Campbell K, Alpers CA (2017) *Challenges in Recovering Resources from Acid Mine Drainage*. Proceedings IMWA Conference, Finland, June 21-26 2017.
- Otchere F, Veiga MM, Hinton JJ, Farias RA, Hamaguchi R (2004) Transforming open mining pits into fish farms: Moving towards sustainability. *Natl Res For*. 28: 216-223
- Quinn S (2019) Midas gold. PDAC Gold commodities session. Proceedings PDAC, March 2019
- Parshley JV, MacCallum CS (2016) Attractive nuisances and wicked solutions; in *Mine Closure 2016 - A.B. Fourie, M. Tibbett (eds)*. March 2016.
- Pearman, G. (2009) *101 Things to Do with a Hole in the Ground*. Eden Project, 132 p.
- Richards J (2002) Sustainable Development and the Minerals Industry. *SEG Newsletter* 48, January 2002, 1, 8-10.
- Singer DA (2014) Base and precious metal resources in seafloor massive sulfide deposits. *Ore Geol Rev* 59: 66–72.
- S&P (2019) *World Mineral Exploration Trends 2018*. Market Intelligence Report 195. S&P, London. 12p.
- Van Kauwenbergh S.J. (1991) Overview of phosphate deposits in East and Southern Africa. *Fert. Res*. 30: 127–150.
- Villiers de JPR (2018) How to sustain mineral resources: Beneficiation and mineral engineering opportunities. *Elements* 13: 307-312.

Tools for foresight on land-use planning in mineral rich areas: a case from Northern Finland

Mari Kivinen, Mira Markovaara-Koivisto, Pasi Eilu
Geological Survey of Finland

Abstract. Foresight on land-use planning is gaining more importance in mineral rich areas. We present two tools which add detail on mineral potential planning: Mapping tool for regional considerations and a tool to scan conflicting interests on mineral deposit scale. A case study for the implementation of the mapping tool is provided for Northern Finland. Understanding the risks related to conflicting interests on land-use deepens the understanding of the future supply potential of mineral raw materials. It also increases the capabilities for early mitigation of disputes and conflicts and enhances the quality of planning for sustainable development on local societies.

1 Introduction

Land-use planning in areas where mining is an important industry benefits of foresight combining the information on mineral deposits and information of the demands from other livelihoods as well as the local people.

Foresight is essential as the raw material needs of the societies is diversifying and increasing, and major share of these resources need to be mined (Erdmann and Graedel 2011). At the same time the mineral deposits are getting more complex to mine and process, and occur in more difficult places in terms of environment and society. Valenta et al. (2019) argue, for example, that major proportion of deposits forming future copper supply involves environmental, governance and social risks. Understanding the risks related to conflicting demands on land-use in mineral rich areas deepens the understanding of the future supply potential of these raw materials. It also increases the capabilities for early mitigation of disputes and conflicts and enhances the quality of planning for sustainable development of local societies.

In our research we develop tools for foresight in land-use planning: A mapping tool to assess conflicting demands on land-use for mineral rich areas, and a scanning tool for conflicting interests related to individual mineral deposits. These tools could be used to support land-use planning as well as enhance social silencing on mineral exploration.

2 Assessing conflicting interests on land-use planning

2.1 A mapping tool: Mine and mineral deposit potentials

This planning tool reflects uncertainty and long time frames related to development of mineral deposits within context of other forms of land-use. It takes into account

the entire cycle from initial mineral exploration to complex final stage planning prior opening a mine. It recognizes reported but not developed mineral deposits, and adopts time scaling and narrative descriptions of uncertainty.

The methodology is initially described by Markovaara-Koivisto et al. (2017) in which the authors assess the nickel mining potential for Sodankylä region in Northern Finland. They found that there are large areas under restricting land-use forms in Sodankylä, of which the most important are nature conservation and housing. Restricting areas also overlap with high-prospectivity areas and indicate potential land-use conflict locations in the future. Markovaara-Koivisto et al. conclude that time scaling and narrative probability of mining activities helps in adding medium to long term perspectives in land-use planning in mineral rich areas.

In this paper the same methodology is adapted on a larger area in the Northern Finland which is described in the case study section.

2.2 Mineral deposits: Conflict palette

Technical, economic and environmental data available of an actual mine is usually scarce in the early stages of mineral exploration and mine planning. When the project proceeds, the amount and quality of information increases. However, the characteristics of the place in which the deposit is located and the general characteristics of the project itself can be assessed already in the early stages.

Eerola (2017) argues that people tend to see a mine already in the mineral exploration phase. Although there would not be a lot of information available or a project would be very small and with minimum socio-environmental impacts, the company benefits of preparing to handle with concerns stemming from other, even very different projects.

The information available for the early stage projects is mostly descriptive but can be contextualised by comparing to larger datasets. By contextualising it's possible to assess the presence of conflicts of interests related to a certain mineral deposit, and eventually a conflict potential. The aim is to define the most important elements that could propagate a conflict later on.

The palette brings together descriptive information about the project and the place where it's located, and considers the possible conflicts of interest stemming from these two. The focus is to provide first screening of issues potentially propagating disputes or conflicts later on during the mine planning process. The first aim is to support the planning of stakeholder dialogue and communications in companies working with early-stage

projects. The second aim is to bring socio-economic and environmental context in which mineral deposits are located more closely within the mineral deposit classification frameworks. This would benefit the comparisons of mineral deposits in terms of socio-environmental and eventually economic risk already in the early stages of the projects.

The examples of the conflict palette will be presented in the SGA 2019 conference on Glasgow, and published later by Kivinen and Giurco (*manuscript*).

3 Mapping case study in Central Lapland Finland

Jackson and Green (2015) ranked Finland as one of the top countries in the world for mining and exploration. While the Finnish Lapland can be largely regarded as under-explored it's having a good potential for gold, copper, and nickel deposits (Maier et al. 2015). Several foreign mining companies has started operations in the country since 1995, and the local population has awakened to the environmental risks that come along, and the local municipalities to the competition in land-use.

The case study described in this article is based on extensive mining-related datasets gathered at the Geological Survey of Finland (GTK) and research of the mineral prospectivity within Central Lapland. The datasets include the Mineral Deposit and Exploration Database (MdaE, <http://gtkdata.gtk.fi/MDaE/>), which contains spatial information of deposits, exploration and mining in Finland; the Fennoscandian Ore Deposit Database (Eilu et al. 2016), which contains numeric information of metallic mines, deposits and significant occurrences in Fennoscandia. The prospectivity assessment studies for the Central Lapland region include studies for magmatic nickel-copper (Nykänen et al. 2015), orogenic gold and iron oxide-copper-gold (IOCG) types of deposits (Nykänen and Ojala 2007, Nykänen et al. 2008a, 2008b). In addition to these data, we applied Mining Register Map Service maintained by TUKES (the Finnish mining permitting authority), which includes knowledge over all mining and exploration tenements in Finland (TUKES 2017).

Figures 1 and 2 show an example of value-adding mine and mineral potential -mapping tool. Figure 1 shows an information about mineral tenements and known mineral deposits. This is a general information commonly available for land-use planning. In figure 2, time scaling and narrative probability is added as well as mineral prospectivity within exploration claim areas. Mineral deposits are classified according to how close they are to the actual mining stage: What is the narrative probability to reach the mining stage and how long this would take. The figure 2 shows the situation in 2017 when many of the reported mineral deposits were actually undeveloped (marked with x). In addition, figure 2 includes nature conservation areas of which several overlap with high prospectivity areas. This information helps to add temporal and spatial detail to mineral information.

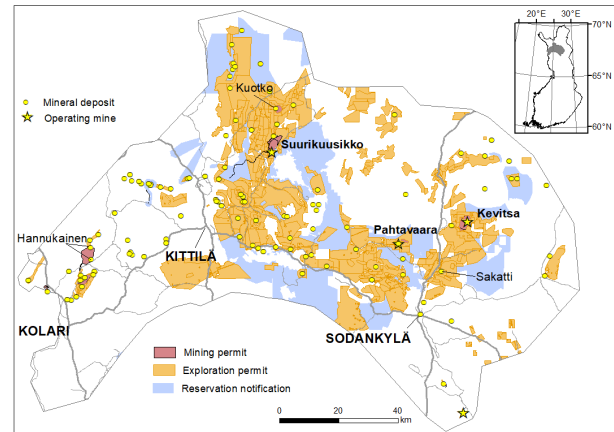


Figure 1. Case study area in Northern Finland with mining and exploration permits and known mineral deposits. Data sources: TUKES (2018) and GTK Mineral deposit and Exploration database (MdaE).

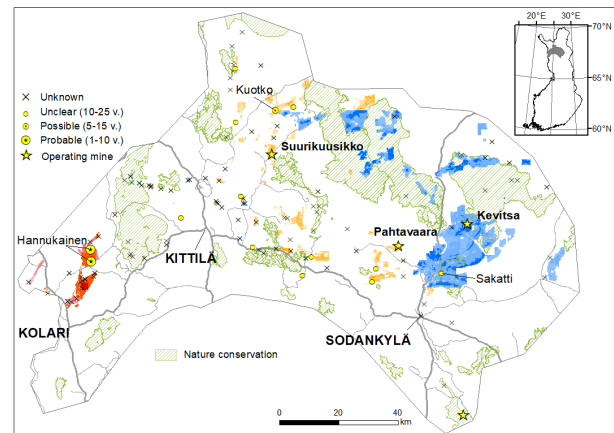


Figure 2. Sophisticated deposit and mineral exploration information provided by Mine and mineral deposit potential -mapping tool. Increasing mineral prospectivity is shown within exploration permit areas with darker color tones: Red color is for iron oxide-copper-gold, yellow is for orogenic gold and blue is for magmatic nickel-copper.

Acknowledgements

This study is a part of GovAda project in the ARKTIKO Program funded by the Academy of Finland (grant no. 283166).

References

Eerola T (2017) Corporate social responsibility in mineral exploration - The importance of communication and stakeholder engagement in earning and maintaining the social license to operate. Geological Survey of Finland, Report of Investigation 233. http://tupa.gtk.fi/julkaisu/tutkimusraportti/tr_233.pdf

Eilu P, Hallberg A, Bergman T, Bjerkgård T, Feoktistov V, Korsakova M, Krasotkin S, Lampio E, Lauri, LS, Litvinenko V, Philippov N, Sandstad JS, Shchiptsov V (2016) Fennoscandian Ore Deposit Database. Annual update. <http://en.gtk.fi/information/services/databases/fodd/index.html>. Accessed 25 February 2017

Erdman L, Graedel TE (2011) Criticality of Non-Fuel Minerals: A Review of Major Approaches and Analyses. *Environ Sci Technol* 45:7620-7630

Jackson T, Green KP (2016) Fraser Institute Annual Survey of Mining Companies 2015. Fraser Institute, Vancouver. <https://www.fraserinstitute.org/sites/default/files/survey-of->

- mining-companies-2015.pdf. Accessed 20 January 2017
- Kivinen M, Giurco D (Manuscript) How a place affects future mining: Defining a conflict palette for early stage mineral exploration and mine-planning projects. Unpublished manuscript
- Maier WD, Lahtinen R, O'Brien H (2015) *Mineral Deposits of Finland*. Elsevier, Oxford
- Markovaara-Koivisto M, Kivinen M, Eilu P (2017) Nickel mining potential for evaluating land-use pressure in the Sodankylä region, Finnish Lapland. SGA2017 proceedings, 20–23 August 2017, Quebec City, Canada
- Nykänen V, Groves DI, Ojala VJ, Gardoll SJ (2008a) Combined conceptual/empirical prospectivity mapping for orogenic gold in the northern Fennoscandian Shield, Finland. *Australian Journal of Earth Sciences*, 55, 39-59
- Nykänen V, Groves DI, Ojala VJ, Eilu P., Gardoll SJ (2008b) Reconnaissance-scale conceptual fuzzy-logic prospectivity modelling for iron oxide copper – gold deposits in the northern Fennoscandian Shield, Finland, *Australian Journal of Earth Sciences*, 55, 25-38
- Nykänen V, Lahti I, Niiranen T, Korhonen K (2015) Receiver Operating Characteristics (ROC) as validation tool for prospectivity models – a magmatic Ni-Cu case study from the Central Lapland greenstone belt, Northern Finland. *Ore Geol Rev* 71:853–860
- Nykänen V, Ojala J (2007) Spatial analysis techniques as successful mineral-potential mapping tools for orogenic gold deposits in the Northern Fennoscandian Shield, Finland. *Natural Resources Research* 16, 85-92
- TUKES (2017) Mining Register Map Service. <http://www.tukes.fi>. Accessed 20 February 2017
- Valenta RK, Kemp D, Owen JR, Corder GD, Lebre E (2019) Re-thinking complex orebodies: Consequences for the future world supply of copper. *Journal of Cleaner Production* 220:816-826

Life cycle assessment of European copper mining: A case study from Sweden

Tobias C. Kampmann

Luleå University of Technology, Sweden

Rodrigo A.F. Alvarenga

David Sanjuan-Delmás

Ghent University, Belgium

Mats Lindblom

Boliden Mineral AB, Sweden

Abstract. The application of the life cycle assessment (LCA) methodology in the mining sector has the potential to evaluate the environmental sustainability of the primary production of metals. As part of a wider project on developing LCA models and methods for mining, life cycle inventory (LCI) data have been collected at two European copper-producing mine sites, Aitik (Sweden) and Cobre las Cruces (Spain). Results from Aitik, including their impact analysis, identify the use of diesel and explosives, the emission of sulfur dioxide, as well as nitrogen and other emissions in the upstream supply chain of explosives and electricity, as significant contributors to the environmental impact. These outputs have influence on the impact categories Climate Change, Photochemical Ozone Formation, Acidification, as well as Terrestrial and Marine Eutrophication. Due to the increasing incorporation of LCA into legislative demands on the mining sector, mining companies need to establish the necessary infrastructure and framework to be able to provide the required data in a fast, transparent and cost-efficient manner. For this reason, some recommendations to improve communication and data management within the companies have been established from the experience gained within this project.

1 Introduction

Life cycle assessment (LCA) is a useful methodology to address environmental sustainability in the industry and is expected to be increasingly incorporated into the European legislation concerning industrial processes, including those in the mining and exploration sector. In addition, individual companies can highly benefit from the incorporation of life cycle research, through its potential to identify bottlenecks affecting the efficiency and environmental impact of industrial process chains.

The application of LCA in the metal/mining sector is still incipient, since there are only a limited number of studies published in the literature. Moreover, there is a general lack of availability of life cycle inventory data, including the case of copper. There is a demand from the copper sector to verify the robustness of existing datasets

(e.g. in commercial databases). In addition, the average global copper production datasets generated by the Copper Alliance (www.copperalliance.org) are not yet implemented into the available databases.

The focus of this life cycle impact assessment (LCIA) work is on the cradle-to-gate life cycle of copper, including the collection, analysis and interpretation of data from two active European mines: Aitik (Sweden) and Cobre las Cruces (Spain). The focus of this extended abstract is on the results of the Aitik case study.

Results will have important implications for the identification (and mitigation) of environmental hotspots of European copper production. This represents a crucial step towards the development of a sustainability profile of primary European metals production.

2 Background

2.1 The SUPRIM project

The project “Sustainable management of primary raw materials through a better approach in Life Cycle Sustainability Assessment” (SUPRIM)¹ aims to develop solutions and provide services to better address sustainability assessments in the raw materials sector. The main objectives of the SUPRIM project are:

- Development of a Life Cycle Impact Assessment (LCIA) method to address resource availability (‘depletion’) in sustainability assessment.
- Development of Life Cycle Inventory (LCI) datasets through case studies in collaboration with the industrial partners from the mining sector.
- Bringing the service to a broader audience, including the LCIA community, mining companies and their downstream users, policy makers and academia.

The aims of this project are to develop LCI datasets in collaboration with industrial partners from the mining sector and make environmental sustainability assessments of the cases using LCA, including the analysis of resource use – with the LCIA method developed within the project among the impact categories considered. In this framework, an analysis of the benefits of a product-oriented perspective in an environmental

¹ More information at <http://suprim.eitrawmaterials.eu/>

sustainability strategy of the mining sector has been published recently (Alvarenga et al. 2019).

2.2 Life cycle assessment (LCA)

The main purpose of LCA is to evaluate quantitatively the environmental impacts of a certain system or product. Its main strength is that it allows going from an inventory of the materials, emissions and other relevant flows within the boundaries of the system to the environmental impacts, revealing the environmental relevance of the different elements as well as the overall environmental performance. The LCA methodology is widely accepted and applied in science. Indeed, the methodology was standardised through the international standards ISO 14040 and ISO 14044 (ISO 2006a, b).

The LCA methodology is made up of four specific phases (goal and scope, inventory analysis, impact assessment and interpretation), as shown in Fig. 1. The workflow is commonly iterative, in order to ensure that all the phases in the study are consistent and coherent.

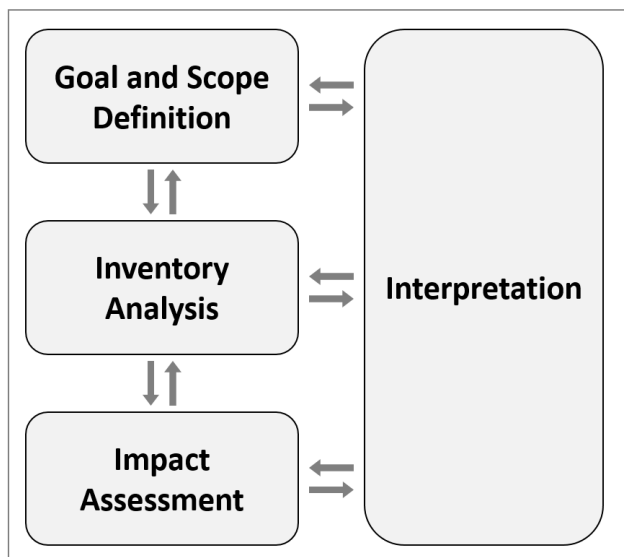


Figure 1. LCA framework. Adapted from ISO (2006a).

3 Methodology

3.1 Foreground data collection

The collection of the foreground LCI data (e.g. inputs and outputs of material, emissions to air, water and soil) was conducted using different sources in the company Boliden Mineral AB, operating the Aitik mine. Whenever possible, data already available from reports or specific databases were utilised. The following data sources were used during the process:

- *External reports*: Environmental reports delivered to environmental agencies
- *Internal reports*: energy audits
- *Internal information (software) system*: Aaro data bank
- *Estimations*: for instance, estimation of emissions

from work machineries, based on the parameter used in Aaro data bank

- *Direct correspondence* with staff from other sectors (e.g., Boliden Commercial)

The data were normalised to the production of 1 kg of copper cathode (functional unit). The data collection process took approximately 9 months. Boliden Mines acted as the central coordinator of data provision. This process required a substantial effort for the coordination and collaboration of the different internal contributors. More than 10 staff members were involved in the data collection, from four different departments/sub-companies (Boliden Mines, Boliden Commercial, Boliden Ronnskärsverken (Smelter), and Boliden Headquarters).

3.2 Software, background database, calculation method and impact category selection

To simulate the life cycle inventory regarding the environmental aspects, we used the database *ecoinvent* v3.3 and software *Simapro* v8.4.

The International Reference Life Cycle Data System (ILCD) Handbook, based on ISO 14040 and 14044 (ISO 2006a, b), was considered to conduct the LCA. This handbook is a guidance document, providing recommendations on models and characterisation factors to be used for impact assessment in applications such as LCA. This supports the analysis of emissions and resource consumption in a single integrated framework. The following impact categories have been selected to assess the environmental impacts of Aitik (and Cobre las Cruces):

- Climate Change
- Ozone Depletion
- Ionising Radiation
- Photochemical Ozone Formation
- Acidification
- Terrestrial Eutrophication
- Freshwater Eutrophication
- Marine Eutrophication

The characterisation factors were retrieved from the method "ILCD 2011 Midpoint+ v1.10" (European Commission 2012) for all impact categories except Climate Change. Regarding Climate Change, the characterisation factors were taken from "IPCC 2013 GWP 100a v1.03" (Joss et al. 2013; Myhre et al. 2013).

Some impact categories (e.g., human toxicity, ecotoxicity) were not included, since they lack a sufficiently robust LCIA model, as indicated in the Product Environmental Footprint guidelines by the European Commission (European Commission 2018).

4 Environmental assessment of copper production at Aitik

4.1 System boundaries

Processes for Aitik copper production have been divided into three sub-systems, for each of which LCI data (inputs and outputs) have been collected. These systems are the Aitik mine, the Aitik concentrator and the smelter. An

important characteristic of copper production at Aitik is that the smelter processes take place at geographically separate (ca. 410 km distant) facilities (Rönnskär, Skellefteå, Sweden). This smelter receives copper concentrate from several mines, as well as other metal concentrates (lead, zinc) and secondary material (scrap). As a result, the smelter produces, apart from copper cathode, various metals, metal sulfates or clinkers, as well as sulphuric acid, sulphur dioxide and iron sand. This made economic allocation procedures necessary in this study. A flowchart of the processes and the system boundaries for Aitik copper production is provided in Fig. 2.

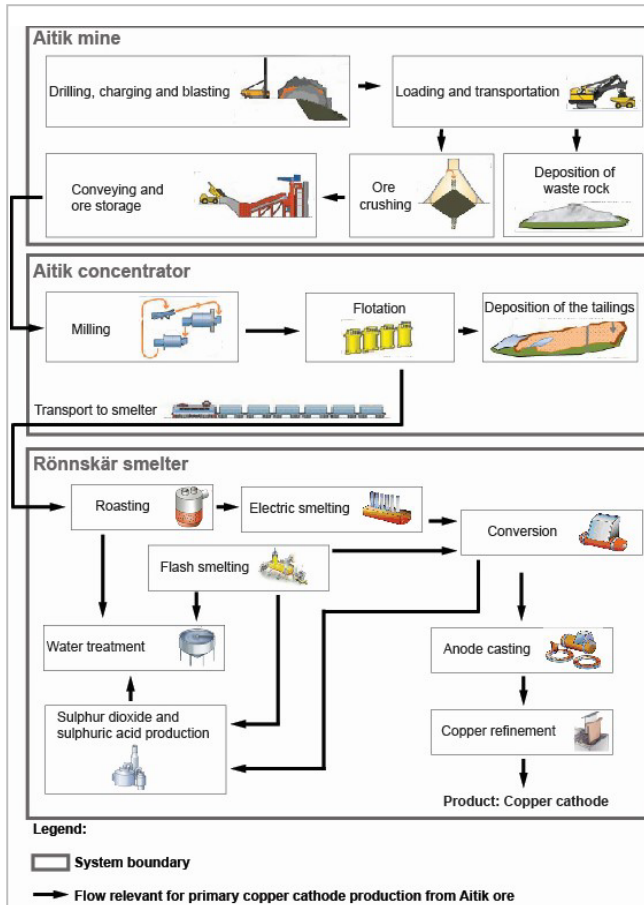


Figure 2. System boundaries for the Aitik LCIA case study, incl. the Rönnskär smelter (only primary-copper-relevant processes).

4.2 Environmental hotspots

Regarding the case study focused on Aitik Copper Concentrate, Fig. 3 shows the profile of the copper produced for the eight environmental impact categories considered. The relevant hotspots have been identified to support the industry on the management of environmental sustainability to reduce the footprint profile of copper production.

The main hotspots identified in the Aitik case are the following:

- Diesel and Explosives, at mine and concentrator, for climate change.

- Sulphur dioxide emissions at the smelter, affecting acidification and photochemical ozone formation.
- Nitrogen emissions to water, at mine and concentrator, for marine eutrophication.
- To a minor extent, NO_x , NH_3 , and SO_x emissions at the supply chain of electricity (at smelter, mine and concentrator) and explosives (at mine and concentrator), affecting a few impact categories (photochemical ozone formation, acidification, terrestrial and marine eutrophication).
- Electricity use in general, due to emissions in its supply chain affecting ozone layer depletion, ionizing radiation and freshwater eutrophication.

It is important to highlight that these results are referring solely to primary copper produced from Aitik copper concentrate.

As pointed out, diesel and explosives were the main hotspots identified in many impact categories. Compared with LCIA results obtained from the Cobre las Cruces copper production (part of the SUPRIM project, but not shown here), a correlation is apparent between deposit copper ore grade (<0.2 wt.% at Aitik, ca. 5 wt.% at Cobre las Cruces) and tonnage of explosives used in the mining process.

5 Suggestions for future LCA work in the mining sector

5.1 Structured communication and organization

One of the main issues regarding the data collection in this study was communication between LCA practitioners and industrial partners. Boliden Mineral AB, similar to many other mining companies, holds a complex structure that includes different, relatively independent departments and sub-companies (Boliden Mines, Boliden Smelter, Boliden Commercial, etc.), each conducting their own functions.

In order to improve these communication issues in future projects that involve LCI data collection processes, the definition of a key person of contact is advised. This contact person should be staff in a more central role and department in the organization, which may facilitate communication with the different departments.

Overall, the key message is that an optimal and efficient organization of the data collection is important to save efforts and resources along the development of an LCA study.

5.2 Comprehensive data management strategy

Another important point that might be crucial for the improvement of the efficiency of future LCI's is the adaptation of the data available at the mining company to the LCI requirements. This step requires substantial efforts due to the requirements to format certain data flows according to the requirements for LCI (e.g. allocations at the smelter).

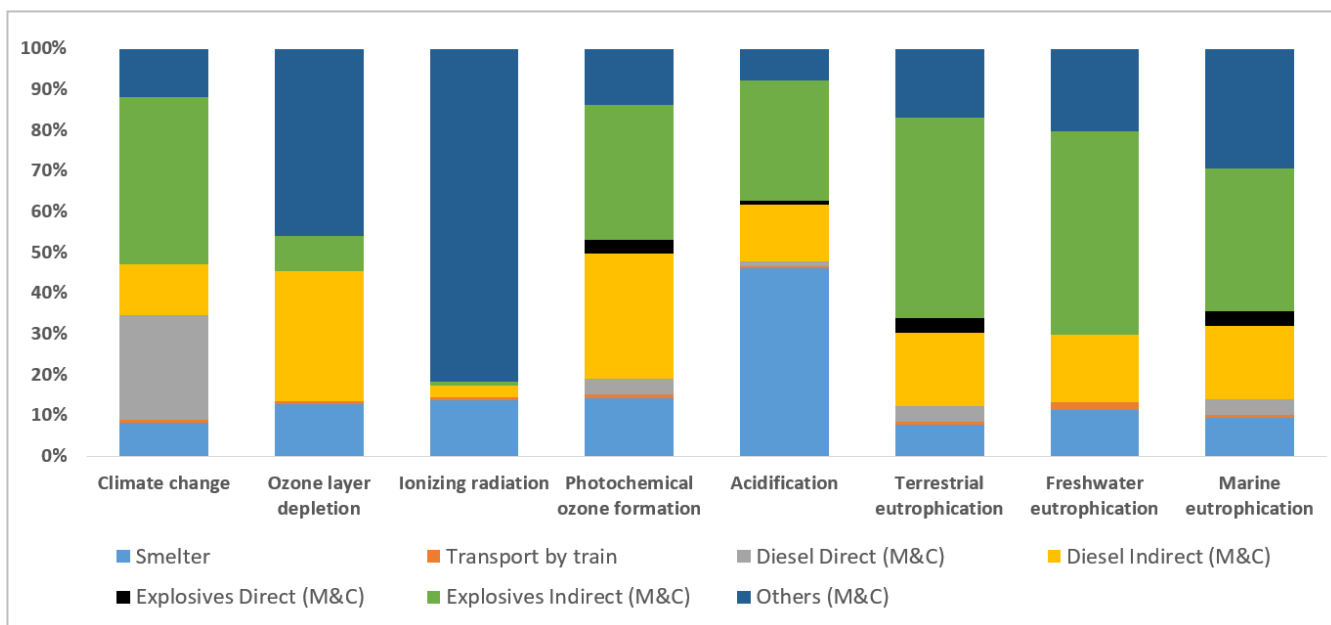


Figure 3. Contribution of the different elements of the system to the environmental impacts of copper production in the Aitik case study. Abbreviations: M&C = Mine and concentrator. An efficient LCI data collection will be possible only if the data needed in the LCI are linked with the data already available in the organization (e.g. data generated due to the legislation compliance). Thus, it is crucial to create awareness for this and employ existing tools that already collect data for LCA purposes. Such data may be already available in the allocated format, i.e., as emissions allocated to certain product systems of interest.

Therefore, we suggest that the data already collected for other purposes (such as environmental reports) could be structured and formatted for a life cycle study prior to the data collection work. This could be done through a more comprehensive data management strategy.

Acknowledgements

This study has been made possible through funding by EIT RawMaterials (SUPRIM Project number 16121). Workshop discussions with expert staff at the project partners Leiden University, Euromines, Boliden Mineral AB and Cobre las Cruces S.A. have aided to improve the approach to and the results of the work.

References

- Alvarenga RAF, Dewulf J, Guinée J, Schulze R, Weihed P, Bark G, Drielsma J (2019) Towards product-oriented sustainability in the (primary) metal supply sector. *Resour, Conserv and Recycl* 145:40–48.
- European Commission, Joint Research Centre, Institute for Environment and Sustainability (2012) Characterisation factors of the ILCD Recommended Life Cycle Impact Assessment methods. Database and Supporting Information. First edition. February 2012. EUR 25167. Luxembourg. Publications Office of the European Union; 2012.
- European Commission (2018) Product Environmental Footprint Category Rules Guidance. Version 6.3 - May 2018
- Joos F et al. (2013) Carbon dioxide and climate impulse response functions for the computation of greenhouse gas metrics: a multi-model analysis. *Atmos Chem Phys* 13:2793–2825.
- Myhre G et al. (2013) Anthropogenic and Natural Radiative Forcing. In: *Climate Change 2*. Cambridge University Press, Cambridge, United Kingdom and New York, NY, USA.
- ISO (2006a) ISO - International Organization for Standardization. 14040:2006 Environmental management - Life cycle assessment - Principles and framework.
- ISO (2006b) ISO - International Organization for Standardization. 14044:2006 - Environmental management -- Life cycle assessment -- Requirements and guidelines.

Linking mineral processing simulation with life cycle assessment (LCA) to forecast potential environmental impacts of small-scale mining technologies development

Jérôme Bodin, Stéphanie Muller

BRGM, Bureau de Recherches Géologiques et Minières, France

Pablo Brito-Parada, Juliana Segura-Salazar

Imperial College London, UK

Abstract. The IMPaCT European project proposes a solution that develops a new switch on-switch off (SOSO) mining paradigm to improve the viability of critical metals and other small complex deposits. It aims at developing small-scale mining along with mobile and modular beneficiation plants. Risks associated with such approach concern geological uncertainty, metallurgical variability and social acceptance. Sustainability of the developed technologies is of critical importance in the framework of IMPaCT. Potential environmental impacts are evaluated using life cycle assessment (LCA). LCA aims at quantifying exchanges between a system and the environment to translate them into impact indicators. Usually, LCA relies mainly on production data but in the case of new technologies development, often only experimental data are available. To deal with this gap, mineral processing simulation can provide consolidated and reliable data to forecast environmental impacts through LCA. The simulator-based USIM-PAC® software will assess the performance of a pilot plant commissioned for this project. The use of Monte Carlo algorithm regarding ore variability will allow evaluation of the effect upon metallurgical recovery and the generation of variable stream inputs/outputs for LCA. This work undertakes to link mineral processing simulation with LCA, resulting in comparisons between different mining strategies available for decision makers.

1 Introduction

In the context of the Raw Materials Initiative launched by the European Commission in 2008 (Directive 2008/98/EC 2008) that aims notably at ensuring access to raw materials and fostering a sustainable supply of raw materials from European sources, the goal of the European funded project IMPaCT is to unlock access to small complex mineral deposits, particularly of critical metals, in Europe.

The IMPaCT European project proposes a solution that develops a new switch on-switch off (SOSO) mining paradigm to improve the viability of many critical metals and other small complex deposits. The project's main objective is to develop a modularized mobile plant (MMP) concept that can economically operate different type of ores in different types of geological and geographical contexts. More specifically, the project aims at deploying and commissioning a pilot MMP that contains new

technological tools and methods related to mining, mineral beneficiation and waste and water management.

The project also focuses on developing good practices in terms of social acceptance and environmental sustainability. Particularly, the environmental sustainability of the developed new technologies is assessed through Life Cycle Assessment (LCA), notably its potential benefits compared with business as usual (BAU) solutions. Emerging technologies developed in the context of research projects usually have low technology readiness levels (European Commission 2015) since they are developed at lab or pilot scale. This means that operational data for foreground inventory modelling are only available at that scale. In this context, two challenges arise in the environmental assessment of IMPaCT technologies. The first one is the upscaling effect: how can we ensure that pilot technologies and BAU ones are comparable and that this comparison is underpinned by reliable data? The second one is the generic assessment of IMPaCT technologies: how can we provide conclusions depending on scenarios based on different geological and geographical contexts? This paper aims to treat these challenges by linking mineral processing simulation and life cycle inventory (LCI) in order to forecast the potential environmental impacts in the framework of small-scale mining technologies development.

Mineral processing simulation has already been used in several cases in the field of raw materials to simulate newly developed technologies (Villeneuve et al. 1995; Brochot et al. 2004; Menad et al. 2016). It has been used as well in environmental assessment of raw material recovery (van Schaik and Reuter 2010; Reuter and van Schaik 2015; Reuter et al. 2015; Rönnlund et al. 2016).

2 Mineral processing simulation

Developed by BRGM, and now commercialised by Caspeo, USIM-PAC® software is a steady-state simulator that allows mineral processing engineers to model and simulate unit and plant operations (Brochot et al. 2002). It includes as well hydrometallurgy and bio-hydrometallurgy models. The simulator is also able to take into account water and power consumption.

The simulator-based approach intends to describe as accurately as possible the behavior of the processed material along with performances of each unit operation included in the plant. Such an approach can be used for

early process design, feasibility studies, engineering, plant commissioning, plant operation and upgrading. Mineral processing simulation can deal with the challenge of upscaling, provided that a precise description of both the material and each unit operation is conducted, and that a large capitalization of knowledge has been acquired through laboratory and pilot tests, along with appropriate samples characterization.

Mineral processing simulation relies on a complete flowsheet design, along with a material model definition and several unit operations models adjusted on experimental mass balances. The flowsheet of the simulator describes the process as unit operations linked one to each other with material streams. The phase model describes the characteristics of the materials to be processed (water, solids, reagents), such as particle size distribution and mineralogical composition. The phase model description is of critical importance when it comes to use a steady-state simulator dedicated to mineral processing. Each unit operation is associated with a mathematical model whose level of complexity depends on the availability of experimental data and the purpose of the simulator. Calibration of predictive mathematical models for each mineral processing unit operation is mandatory to accommodate geological uncertainty and metallurgical variability, and to provide reliable results. Finally, the software includes a set of algorithms dedicated for data reconciliation, material balance, unit operation sizing and power consumption.

3 Life cycle assessment

LCA is a standardized technique (ISO 14040 2006) to quantify and assess the exchanges between a system and the environment regarding the consumption of resources (inputs), the emissions (outputs) and translates them as pressure on the environment (potential impacts) attributed to different products or processes over their entire life cycle. According to ISO 14040:2006, the application of LCA relies on four steps (Fig. 1):

- The goal and scope definition, where one defines the system boundaries and the functional unit, here the amount of metal production considered in a given context;
- The life cycle inventory aims at collecting and quantifying exchanges between the system defined previously and the environment;
- The life cycle impact assessment translates these exchanges in terms of potential environmental impacts and computes appropriate performance indicators.
- The interpretation phase discusses the results based on the defined context, performs scenario comparison, identifies the hotspots and if needed redesigns the process.

Environmental LCA is usually performed to compare products designs and processes routes (Norgate et al. 2007; Farjana et al. 2019), in order to find out which is the least harmful, or in other words, more eco-efficient. It gives decision-makers a set of environmental performance indicators and shows to what extent the

considered product or process is eco-efficient. In this way, one can also feedback to its own product or process design to make it more eco-efficient.

In this study, the Ecoinvent v3.4 database is used for the LCI background modelling and the LCA calculation is performed using Simapro v8.5 with the ILCD impact assessment method.

4 Concept

By definition, when one develops new technologies with specific processes, only laboratory or pilot scale data may be available. Are these data reliable and consistent in terms of mass and energy for example? Another issue arises as well: can we compare technologies with low TRLs (technology readiness level) with industrial technologies? This work undertakes to build a link between mineral processing simulation and LCA and to overcome limitations of LCA applied to new technologies by filling the data gaps and covering the upscaling step between experimental and operational.

Outputs of process simulation consist of each unit operation stream (solid and liquid flow-rate, composition, etc.), operating parameters, along with energy and reagents consumption. These data can act as direct inputs for the LCI foreground modelling (Fig. 1). In the case of the IMPaCT project, a mineral processing simulation is used to gather data specifically on the MMP operations at a semi-industrial pilot scale. Consumption of resources attributed to mining operations, modules and equipment transportation from one site to another is taken into account directly in the LCI foreground modelling. Given the particularity of modularity of IMPaCT technologies, the LCI foreground modeling must adapt to the type of treated mineral ores regardless of the geological and geographical contexts.

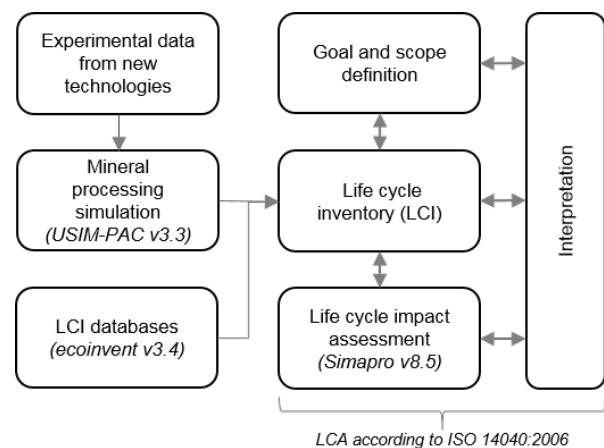


Figure 1. Block-flow diagram illustrating the concept of link between mineral processing simulation with LCA

The linking is performed through an Excel workbook that will consider outputs from simulation results, combined with additional models to complete the whole process chain (i.e. mining, transport, etc.). Outputs of the workbook, material and energy requirements and direct emissions, are imported into an LCA software (e.g. Simapro) to perform impacts calculation.

Case study application

In the framework of the IMPaCT project, the MMP is about to be deployed on two mining sites namely Olovo and Zajaca. The Olovo Pb-Zn deposit (MVT type) in Bosnia and Herzegovina is hosted by carbonate rocks predominantly limestones and where the ore minerals are mainly cerussite (PbCO_3) and minor smithsonite (ZnCO_3) (Palinkaš et al. 2008, 2016). The Zajaca Sb deposit in Serbia is mineralised with stibnite (Sb_2S_3) (Janković 1997; Radosavljević et al. 2013). The specificity of the raw material, the upstream supply needed regarding the conception, the configuration and the operation of the MMP will be different for each case study considered.

This work then undertakes to design a set of flowsheets, to elaborate mineralogical phase models, to choose and finally to calibrate each unit operation model according to each case study. The mineralogical phase model describes each considered ore with their specific:

- particle size distribution;
- density distribution of each size class;
- mineralogical composition of each particle type.

Additional parameters obtained from ore characterization tests, such as ore crushability and ore abrasiveness, are taken into account. The flowsheet is designed according to the equipment that are to be deployed on each site, including ore sorter, crusher, screen, mill, jigs, spirals, shaking tables, flotation cells, wastewater treatment and, eventually, hydrometallurgy. Calibration of predictive mathematical models for each unit operation are first performed with a testwork campaign realised after commissioning the MMP at the Olovo site.

Simulation results then provide mass balances and energy inputs of the MMP considering different scenarios of the LCI modelling. Additionally, the use of the Monte Carlo algorithm regarding ore variability permits evaluation of the effect upon metallurgical recovery, and also the generation of variable stream inputs/outputs for environmental assessment (LCA).

The functional unit will be one mass unit (kg or t) of ore concentrate and one mass unit of metal (lead or antimony) contained in the ore concentrate produced by a considered scenario. At the end, LCA calculations will result in an assessment of potential environmental impacts of the IMPaCT technologies for different considered mining scenario, when producing lead or antimony. Such an approach allows us to identify environmental hotspots within the process, which could help to drive a process eco-design feedback. Finally, another relevant analysis would be to benchmark the environmental impacts of the production of lead and antimony in Europe, or worldwide, against the production with IMPaCT technologies under development. Figure 2 presents a benchmark for 1 kg of lead production and its potential impact on climate change.

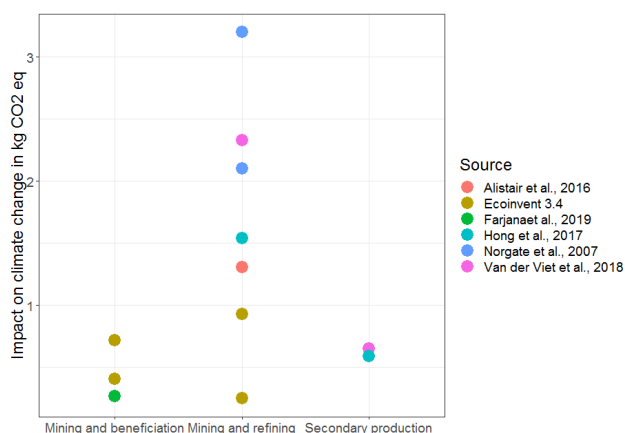


Figure 2. Benchmark of lead production potential impact on climate change (Norgate et al. 2007; Davidson et al. 2016; Hong et al. 2017; der Voet et al. 2019; Farjana et al. 2019).

6 Outlook

The outlook of this work within the IMPaCT project is to design an LCA tool that will allow a custom-made analysis to account for specificity, to conduct a comparative potential impacts assessment of different mining scenarios encompassing different types of resources, ore deposits and local contexts to illustrate the benefits of SOSO mining relative to traditional mining methods.

To link the different LCI foreground modelling specific to the functional unit using the MMP, while keeping the adaptability to assess different scenarios of MMP deployment, a link between mineral processing simulation outputs and LCI inputs is proposed in a specific Excel tool. This enables all the necessary information for LCI foreground modelling, as well as all information concerning the goal and scope of each scenario to assess (type of treated ore, amount treated, geographical context, etc.), to be taken into account in separate sheets. A complete LCI for the foreground process is then compiled, calculated and converted according to the Ecoinvent nomenclature, in a specific sheet of the tool that can directly be imported within Simapro to perform LCA calculations.

Inputs from mineral processing simulation towards LCA allow the environmental assessment of emerging technologies to be built on data that are consistent in terms of mass balance and more reliable especially when upscaling effects arise. This link is illustrated here in the context of the raw materials sector, but could be used in any other field where process design is used to develop emerging technologies. Finally, the developed tool provides the flexibility to assess different kinds of scenarios specific to the IMPaCT project. At the end, by answering the challenges of upscaling effects and adaptability, the results obtained can be used by decision makers for both eco-design approaches and benchmark assessments.

Acknowledgements

The IMPaCT project is funded by the EU Horizon 2020 Program, Grant no 730411.

References

- Brochot S, Durance M V., Villeneuve J, et al (2004) Modelling of the bioleaching of sulphide ores: Application for the simulation of the bioleaching/gravity section of the Kasese Cobalt Company Ltd process plant. *Miner Eng* 17:253–260. doi: 10.1016/j.mineng.2003.09.016
- Brochot S, Villeneuve J, Guillaneau J-C, et al (2002) USIM PAC 3: Design and Optimization of Mineral Processing Plants from Crushing to Refining. In: Symposium, Mineral processing plant Design, practice and control, Vancouver, Canada. Society for Mining, Metallurgy, and Exploration, pp 479–494
- Davidson AJ, Binks SP, Gediga J (2016) Lead industry life cycle studies: environmental impact and life cycle assessment of lead battery and architectural sheet production. *Int J Life Cycle Assess* 21:1624–1636. doi: 10.1007/s11367-015-1021-5
- der Voet E, Van Oers L, Verboon M, Kuipers K (2019) Environmental implications of future demand scenarios for metals: Methodology and application to the case of seven major metals. *J Ind Ecol* 23:141–155. doi: 10.1111/jiec.12722
- Directive 2008/98/EC (2008) Directive 2008/98/EC on waste (Waste Framework Directive) - Environment - European Commission
- European Commission (2015) Technology readiness levels (TRL)
- Farjana SH, Huda N, Mahmud MAP (2019) Life cycle analysis of copper-gold-lead-silver-zinc beneficiation process. *Sci Total Environ* 659:41–52. doi: 10.1016/J.SCITOTENV.2018.12.318
- Hong J, Yu Z, Shi W, et al (2017) Life cycle environmental and economic assessment of lead refining in China. *Int J Life Cycle Assess* 22:909–918. doi: 10.1007/s11367-016-1209-3
- ISO 14040 (2006) Environmental management — Life cycle assessment — Principles and framework. *Int Stand Organ*. doi: 10.1136/bmj.332.7550.1107
- Janković S (1997) The Carpatho-Balkanides and adjacent area: a sector of the Tethyan Eurasian metallogenic belt. *Miner Depos* 32:426–433. doi: 10.1007/s001260050110
- Menad N, Kanari N, Menard Y, Villeneuve J (2016) Process simulator and environmental assessment of the innovative WEEE treatment process. *Int J Miner Process* 148:92–99. doi: 10.1016/j.minpro.2016.01.018
- Norgate TE, Jahanshahi S, Rankin WJ (2007) Assessing the environmental impact of metal production processes. *J Clean Prod* 15:838–848. doi: 10.1016/J.JCLEPRO.2006.06.018
- Palinkaš L, Damyánov ZK, Borojević Šoštarić S, et al (2016) Divergent drift of Adriatic-Dinaridic and Moesian carbonate platforms during the rifting phase witnessed by triassic MVT Pb-Zn and SEDEX deposits; a metallogenic approach. *Geol Croat* 69:75–78. doi: 10.4154/GC.2016.06
- Palinkaš LA, Šoštarić SB, Palinkaš SS (2008) Metallogeny of the Northwestern and Central Dinarides and Southern Tisia. *Ore Geol Rev*. doi: 10.1016/j.oregeorev.2008.05.006
- Radosavljević SA, Stojanović JN, Radosavljević-Mihajlović AS, Kašić VD (2013) Polymetallic mineralization of the Boranja orefield, Podrinje Metallogenic District, Serbia: Zonality, mineral associations and genetic features. *Period di Mineral*. doi: 10.2451/2013PM0004
- Reuter MA, van Schaik A (2015) Product-centric simulation-based design for recycling: Case of LED lamp recycling. *J Sustain Metall* 1:4–28. doi: 10.1007/s40831-014-0006-0
- Reuter MA, van Schaik A, Gediga J (2015) Simulation-based design for resource efficiency of metal production and recycling systems: Cases - copper production and recycling, e-waste (LED lamps) and nickel pig iron. *Int J Life Cycle Assess* 20:671–693. doi: 10.1007/s11367-015-0860-4
- Rönnlund I, Reuter M, Horn S, et al (2016) Eco-efficiency indicator framework implemented in the metallurgical industry: part 1—a comprehensive view and benchmark. *Int J Life Cycle Assess*

- 21:1719–1748. doi: 10.1007/s11367-016-1123-8
- van Schaik A, Reuter MA (2010) Dynamic modelling of E-waste recycling system performance based on product design. *Miner Eng* 23:192–210. doi: 10.1016/j.mineng.2009.09.004
- Villeneuve J, Guillaneau JC, Durance M V. (1995) Flotation modelling: A wide range of solutions for solving industrial problems. *Miner Eng* 8:409–420. doi: 10.1016/0892-6875(95)00006-C

Acid and Metalliferous Drainage (AMD): cause and effect, prediction and prevention – a journey through decades of experiences

Alan M. Robertson, Greg A. Maddocks, Matthew G. Landers and Laura M. Jackson
RGS Environmental Pty Ltd

Abstract. Over the past three decades there have been significant advances in our understanding of the causes and potential effects of Acid and Metalliferous Drainage (AMD) from mining and mineral processing operations. Early recognition and management of AMD is necessary to produce a significantly better environmental outcome at mine closure. However, AMD remains a challenging subject that continues to be underestimated and long term management costs are often not correctly factored into company balance sheets. This paper presents an overview of the occurrence and potential impacts of AMD during the planning operational and closure phases of mining and mineral processing operations; and is based upon 25 years of experience at such operations both in Australia and around the world. Several case studies are integrated into the paper to provide relevant context and to 'bring the geochemical equations and concepts to life'. The presentation includes information on methods used to predict and prevent AMD, although it is recognised that in some cases AMD can only be mitigated and managed. Additional sources of useful information on AMD are also provided for further reading.

1 Introduction

One of the biggest challenges facing the mining and mineral processing industry is ensuring that proposed and operating mines are adequately designed, structured and maintained to prevent acid and metalliferous drainage (AMD). The mining industry has steadily improved its performance in this area with respect to the prevention and management of AMD.

Understanding the geochemical characteristics of potential mine waste materials at the exploration stage of a proposed mining operation is the key to developing and implementing an appropriate mine waste management plan and also contributes to successful mine closure. For larger mining companies such as Rio Tinto and BHP Billiton, prevention and management of AMD forms an integral part of internal standards which must be met before a project can proceed to the regulatory approvals stage. For some smaller mining companies, the risk of AMD can be an issue during downturns in the commodity price cycle, if the mine waste management plan is not implemented correctly, or there is a change in ownership of the mining operation.

Over the past three decades there has been a tremendous growth in the number of geochemical/AMD studies completed for mine waste storage facilities (e.g. waste rock dumps and tailings storage facilities) around

the world (Parker and Robertson 1998; MCA 2016). These studies are typically a pre-requisite to Regulatory approval and/or project finance, and form an integral part of mine planning, operation and eventual mine closure. If the principles of sustainable development are used as a framework for these studies, in line with accepted mining industry standards and principles (ICMM 2003), then this can significantly reduce the risk of AMD generation and potential environmental impacts.

It is typically during the mine planning stage that significant differences in key variables at each mining project become recognised (such as mine waste geochemistry, construction and final cover materials, climatic conditions, vegetation characteristics and stakeholder expectations), which leads to practical mine waste management design solutions varying considerably from site to site. Core decisions made during mine planning and operational stages can significantly limit the range of options available to site management for closure of mine waste storage facilities (INAP 2009). However, the timely acquisition and use of quality information on the nature of mine waste materials and their potential impact on the environment can be used to develop innovative design solutions and promote sustainable closure. This is shown in Figure 1 which illustrates management and closure options and costs over the life of a typical mine.

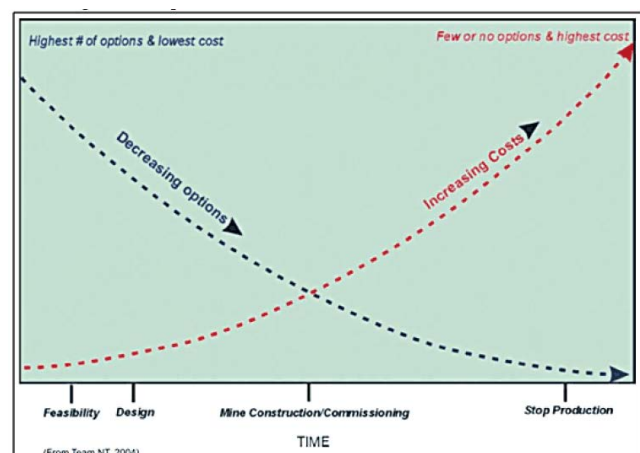


Figure 1. Closure options and costs across the life of mine after INAP, 2009.

The mining industry now recognizes that mining and associated mineral processing is a relatively short-term use of land that can present a number of environmental challenges and potential opportunities for beneficial post-

closure land use. Demonstration of successful mine planning and operation through to sustainable closure, retains a strong case for future access to resources, which not only benefits our industry, but society as a whole.

2 Planning

It is often during the pre-feasibility or feasibility stages of a mining project that key AMD studies are completed, and management decisions made regarding the fate of mine waste materials. Typically, samples of drill core from a range of drill holes in and around a target deposit are selected and subjected to a range of geochemical and mineralogical tests. In fact, there is often a wealth of mineralogical data on potential deposits that can be used to develop the scope of a geochemical assessment program and assist in determining AMD potential (Becker et al. 2018; Jackson et al 2018; and Opitz et al. 2018). The drill core samples may represent various waste rock lithologies and alterations as well as ore and low grade ore materials, each of which may need to be managed separately. Drill core samples representing ore may undergo mineral processing tests, producing tailings, which are also subjected to geochemical tests. The role of the geochemist at the planning stage is to select representative mine waste samples through interaction with other feasibility study team members, looking at the geology and mineralogy of the deposit, the mineral processing regime, potential surface water and groundwater interactions, and the design of conceptual mine waste storage facilities (e.g. waste rock dumps and tailings storage facilities).

There are generally no regulatory requirements regarding the minimum number of samples required to be obtained and tested for mine waste materials. However, technical guidelines for geochemical assessment of mine wastes has recently been published in Australia (COA 2016) and internationally (INAP 2009); and can be used as a framework for the development of a mine waste sampling and testing program. The sampling strategy should be based on the expected heterogeneity of the mine waste materials; potential for significant environmental and/or health impacts; size of operation; statistical sample representation requirements; waste volume; level of confidence in predictive ability; and cost.

Geochemical/AMD testing of mine waste materials is generally divided into two categories (static and kinetic tests). Static tests generally involve screening a relatively large number of samples to determine their geochemical characteristics (e.g. pH, salinity, potential for acid generation). Following screening, a subset of these samples is subjected to multi-element tests for total and soluble metals/metalloids contained in water extracts. Kinetic tests are generally reserved for a small number of samples to determine the geochemical characteristics of mine waste materials over time. In Australia, technical guidelines for static and kinetic geochemical testing of mine waste materials have been developed (AMIRA 2002). The information acquired from static and kinetic geochemical tests can be used as an input into a variety

of more advanced studies throughout the life of mine including block modelling of the waste rock materials, reactive transport models and prediction and development of closure completion criteria. These studies form part of the information required to develop optimal management strategies for mine waste storage facilities.

In the unfortunate event that AMD does occur at a mining operation, there are a number of water treatment processes that can be used to treat AMD, and these generally fall into the active and passive treatment categories. Active treatment typically involves the addition of alkaline materials to AMD at a treatment plant and although expensive, can be quite successful at treating AMD. The process does however generate a sludge material that can contain elevated concentrations of metals/metalloids and require management. Passive AMD treatment systems such as constructed wetlands are generally only used as a final polishing step following active treatment or where mining wastes have been well managed. However, AMD treatment could be viewed as an “admission of failure” because if mine wastes are characterised and well managed the need for AMD treatment processes could be avoided

3 Operations

In some cases, an expansion or new development at an existing mine mining operation can occur well after the mine has commenced operating and waste storage facilities are already in place. The McArthur River base metal (lead, silver and zinc) mine in the Northern Territory of Australia, for example, commenced as an underground operation in 1994/95 and plans for an open pit development were subsequently finalised in 2006. The open pit development required an Environmental Impact Assessment, a major component of which was a geochemical/ARD assessment of waste rock and tailings materials likely to be produced as a result of the planned expansion (Robertson 2005). For the waste rock characterisation test work, 656 drill core samples (representing 1 to 5m depth intervals) were selected from 35 drill exploration drill holes and subjected to static and kinetic geochemical AMD tests.

The static and kinetic test results were integrated into a geochemical block model for the final open pit design which involved significant interaction between the project geochemists and geological/mine planning personnel. The geochemical block model indicated that approximately 10 % of the waste rock material was Potentially Acid Forming (PAF) and that that this was restricted to the upper and lower pyritic shale rock types. The vast majority of the waste rock was found to be Non-Acid Forming (NAF) and the W-Fold Shale and Teena Dolomite domains were found to be a potential source of highly acid consuming material. As a result of this work, it was decided to selectively handle and encapsulate PAF shale waste rock materials in compacted clay cells within a NAF waste rock shell at a purpose-built waste rock emplacement facility. The geochemical kinetic tests were completed over a period of six years and results provided

insight into the likely quality on surface runoff and seepage quality from a range of PAF and NAF materials. The results of the geochemical tests and block modelling turned out to be a key issue with respect to project EIS approval and subsequent mine development.

Selective handling, placement and encapsulation of PAF mine waste materials can be an expensive and challenging exercise however for highly sulfidic materials, the benefits far outweigh the initial costs and challenges. At Ernest Henry lead zinc mine in Queensland, for example, visually identifiable PAF mine waste materials were selectively handled, placed and encapsulated within NAF waste rock materials in a manner that avoided the need for an expensive engineered cover system at mine closure (Figure 2).



Figure 2. Aerial view of waste rock dump construction

The final landform at the northeast end of the waste rock dump is shown in Figure 3. Encapsulation of PAF waste rock within the waste rock dump during construction was developed to essentially be an effective method of preventing AMD.



Figure 3. Waste rock dump final landform

4 Closure

There have been a number of publications in recent years focussing on the design for closure of mine waste storage facilities. If mine planning, completed during the feasibility stage, does not include the relevant studies to promote a comprehensive understanding of the geochemical nature of mine waste materials and potential ARD risk, mining companies can often be left with no alternative closure option other than to use an engineered cover system for mine waste storage facilities. Our understanding of the likely performance of cover systems has made significant advances over the past three decades. Whilst detailed numerical modelling and field trials of cover systems are favoured by some in the early stages and indeed throughout mine waste cover planning (MEND 2007), others appear to take a more pragmatic approach (Wilson 2008), with some questioning the validity of up-scaling the results from instrumented small-scale test plots to multi-hectare landforms (Campbell 2007). These publications contain a wealth of valuable information to guide closure planning design for mine waste storage facilities and highlight that, as an industry, we have come a long way towards our goal of sustainable closure. However, the significant variation in opinion also suggests that we still have some way to go to reach our goal of sustainable closure.

An example of a typical cover design solution for closure of an existing tailing storage facility (TSF) has been developed for an operating nickel mine located in a semi-arid to sub-tropical region of Australia. The design is based upon the existing knowledge base of the professional design team, the outcome of tailings geochemistry and mineralogy tests, the physical nature of the footprint materials, as well as knowledge of the physical nature of the construction and final cover materials. Infiltration modelling of the cover system design has been completed for the project along with hydrogeological and solute transport modelling. Other key factors for cover design included climatic conditions, site vegetation characteristics, and stakeholder input which led to regulatory approval in 2015 (Robertson et al. 2015).

Final closure of the TSF facility will be managed by constructing an enhanced store-and-release cover system over the tailings materials. The TSF will be divided into three cells for tailings deposition, which will result in the first cell (Cell A) being available for decommissioning and closure at an earlier stage than Cells B and C. This will provide an ideal opportunity to monitor and improve the performance of the TSF cover system before mine closure. Prior to closure of each cell, the central decant system will be converted into the main tailings discharge point and tailings will be deposited to create a “domed” surface (2-3% slope angle). The expected consolidation settlement of the tailings will be allowed for in the closure landform design. The TSF cover comprises a total depth of 3 m including a topsoil layer, growth layer and capillary break layer above the tailings surface. The TSF cover system will retain and store rainfall from most precipitation events and maintain a vegetated surface. Excess rainfall from extreme precipitation (cyclonic) events will be shed in a controlled manner from the TSF surface and released using a

spillway facility. The enhanced “store and release” cover system design for the TSF has been peer reviewed and found to align well with international best practice in the mining industry best practice.

Acknowledgements

The authors acknowledge the contributions from mining and mineral processing personnel and other key stakeholders at various mining operations over the past 25 years. The information and experiences presented in this paper would not have been possible without their valuable contributions.

References

- AMIRA (2002). ARD Test Handbook: Project 387A Prediction and Kinetic Control of Acid Mine Drainage. Australian Minerals Industry Research Association, Ian Wark Research Institute and Environmental Geochemistry International Pty Ltd, May 2002, Melbourne, VIC, Australia.
- Becker M Charikinya E Nthabane S Voigt M Broadhurst J Harrison STL Bradshaw D (2018). An integrated mineralogy-based modelling framework for the simultaneous assessment of plant operational parameters with acid rock drainage potential of tailings. In Proceeding of the 11th International Conference on Acid Rock Drainage, International Mine Water Association and WISA Mine Water Division Conference. Risk to Opportunity. 10-14 September 2018 Pretoria South Africa. pp 309-314.
- Campbell GD (2007). Isolation of reactive mine-wastes in the WA Goldfields. How arid-zone weathering and hydroecology simplify cover-design studies, Section 8.0 in Planning for Mine Closure. ACG Seminar. Perth, Western Australia. 14-15 June 2007. p41.
- COA (2016) Leading practice sustainable development program for the mining Industry. Preventing acid and metalliferous drainage. Commonwealth of Australia, Australian Capital Territory, Australia.
- ICMM (2003) International Council on Mining and Metals Sustainable Development Principles May 2003, ICMM,
- INAP (2009) *Global Acid Rock Drainage Guide (GARD Guide)*. Document prepared by Golder Associates on behalf of the International Network on Acid Prevention (INAP).
- Jackson LM Parbhakar-Fox A Fox N Cooke DR Harris A Savinova E (2018). Integrating hyperspectral analysis and mineral chemistry for geoenvironmental prediction. In Proceeding of the 11th International Conference on Acid Rock Drainage, International Mine Water Association and WISA Mine Water Division Conference. Risk to Opportunity. 10-14 September 2018 Pretoria South Africa. pp 1075-1080.
- MEND (2007) Macro-Scale Design and Performance Monitoring Manual. Mine Environment Neutral Drainage (MEND) Report No 2.21.5 prepared by O’Kane Consultants Inc., Ottawa, Ontario, Canada.
- Opitz A Broadhurst J Harrison S Bradshaw D Becker M (2018). Understanding mineralogy as a tool for Acid Rock Drainage characterisation. In Proceeding of the 11th International Conference on Acid Rock Drainage, International Mine Water Association and WISA Mine Water Division Conference. Risk to Opportunity. 10-14 September 2018 Pretoria South Africa. pp 424-429.
- Parker G Robertson AM (1999). Acid Drainage. Occasional paper published by the Australian Minerals and Energy Environment Foundation, November 1999, Melbourne, Victoria, Australia.
- Robertson AM (2005) Xstrata McArthur River Mine. Environmental management of overburden materials: Getting it right from the start. In Proceeding of International Conference on Mining and the Environment Metals and Energy Recovery, Swedish Association of Mines, Minerals and Metal Producers, June 22-July 1, 2005, Skelleftea, Sweden, pp 837-847.
- Robertson AM Swane IP (2008) Planning, operating and managing tailings storage facilities for sustainable closure – are we there yet? In proceedings of the 6th Australian Workshop on Acid and Metalliferous Drainage, Burnie, Tasmania, 15-18 April 2008, Australian Centre for Minerals Extension and Research (ACMER), Sustainable Minerals Institute, University of Queensland, QLD Australia, pp257-270.
- Robertson AM Kawashima N Smart R and Schumann R (2015). Management of pyrrhotite tailings: at Savannah Nickel Mine: A decade of experience and learning. Paper presented at the 10th International Conference on Acid Rock Drainage (ICARD) and Annual International Mining and Water Association (IMWA) Conference, April 21-24 2015, Santiago, Chile.
- Wilson G (2008) Why are we still battling ARD? In proceedings of the 6th Australian Workshop on Acid and Metalliferous Drainage, Burnie, Tasmania, 15-18 April 2008, Australian Centre for Minerals Extension and Research (ACMER), Sustainable Minerals Institute, Univ. of Queensland, QLD Australia, pp101-112.

An economic and risk based appraisal of standardised waste management strategies: using fragmentation analysis to optimise the approach

Steven Pearce¹, Diana Brookshaw², Andrew Barnes³, Christopher Brough⁴

¹Technical Director, Mine Environment Management (MEM) Ltd, Denbigh, UK

²Principal Environmental Scientist, Caulmert Limited, Bangor, UK

³Technical Director, Geochemic Ltd, Pontypool, UK,

⁴Senior Consultant Mineralogist, Petrolab Ltd, Redruth, UK,

Abstract. A technical research project has been instigated by Mine Environment Management Ltd (MEM) to determine how the application of fragmentation analysis to the characterisation, management and long-term planning of waste rock may provide opportunities to optimise project economics. Detailed laboratory-based heterogeneity testing including quantitative mineralogical analysis has been twinned with site-based fragmentation analysis to assess properties of as-mined waste at two operational sites. The technical assessment has involved analysis of geochemical and mineralogical properties across the range of particle size fractions represented by the mined waste product. The results indicate that fractionation of metal sulfides and carbonates as a result of fragmentation occurring during the mining process, is a key factor influencing the validity of a typical grade weighted cut-off grade and bulk property modelling approach to waste classification and modelling. It has been found that the geochemical properties of the waste as mined are not well represented by the bulk compositional values attributed in the waste block model. In addition, it has been found that if fragmentation analysis is used to inform economic assessment of long-term waste management costs, optimised waste management strategies can be identified that would otherwise have been missed.

1 Introduction

Typically, waste characterisation classification systems used as part of long term mine planning based on industry best practice geochemistry methods (Price 2009) are translated into mine planning and operations by the utilisation of block models (Pearce et al 2013). These block models are generally developed by the mine site geologist that have developed the ore reserve and geological model and define waste based on discrete grade weighted cut-off grades to differentiate between waste and ore zones, and wastes of different geochemical or physical properties (Pearce et al 2013). The use of a cut-off grade approach reflects an underlying assumption that waste rock properties can be defined and treated in block models as having static and bulk characteristics in the same manner as ore. That is to say that, once mined, the waste material block has the same intrinsic property as defined from the averaged value obtained from the block model. In most cases the

waste block model is integrated with the ore reserve block model, which in turn is generated from the geological block model. In general, the classification system used to define waste within these models is based on risk of acid and metalliferous drainage (AMD) and broad “catch all” definitions such as potentially acid forming (PAF) or non acid forming (NAF) are used (Price 2009). With respect to economic assessment, this approach typically assigns no economic “value” (negative or positive) to waste blocks irrespective of classification other than to consider load and haul costs for disposal. This lack of cost modelling is driven by the assumption that waste has no intrinsic value, and that additional costs of managing waste are adequately accounted for elsewhere such as in closure cost estimation. The adoption of these broad assumptions as part of typical waste management strategies is in many cases considered to reflect current best practice (MWEI BREF) given they are based on standardised and established mining approaches. The implication is that these approaches are considered to be adequate to capture risk and provide an optimised cost model for waste management. This study assess the validity of using waste characterisation methods that assume that the properties of the mined waste product can be accurately defined from grade averaged block modelling approaches. In particular the study focuses on the role of fragmentation that occurs during mining may have on project risk and economic assessment.

2 Fragmentation analysis

During the mining process blasting of ore and waste rock is designed and carried out to fracture the in-situ rock mass, to enable excavation and transport of the material. Run of mine (ROM) fragmentation is considered optimal when the material is fine enough and loose enough to ensure efficient excavation and loading operations. The blasting optimisation strategy is usually focussed on minimising total mining costs and maintaining the optimal ROM fragmentation characteristics (Kanchibotla et al 1999). Singh (2016) notes that “*the goal of efficient blasting is determined by investigating the relationship between blast design parameters and fragmentation. It is extremely important to make the connection between rock blasting results and their impact on the downstream operations. It is well accepted that fragmentation has a critical effect on the loading operations, but little*

quantitative information is available, upon which rational blasting strategies can be outlined". Although this reference is made with regard to downstream ore processing, it should be obvious that this statement would also apply to the consideration of the impact of the fragmentation profile on AMD risk and resultant management costs of the waste rock generated. Given the general lack of consideration of AMD risk in the cost model adopted for blasting strategies, it is clear that this aspect likely represents a significant source of missed opportunities for optimised waste management planning at mine sites. Fragmentation analysis is a common technique (e.g. Nov 2013, Mohamed 2019) used as part of economic optimisation of mining projects. The analysis involves assessment of the particle size distribution of mined material at various stages in the mining process, typically after blasting has occurred. The most utilised method to quantify fragmentation is the determination of the size distribution using digital imaging processing techniques. This method being low cost and practical and is the second reliable method after sieve analysis. In this method, images acquired from excavators, haul trucks, conveyor belts etc. are delineated automatically by using digital image processing techniques and size distribution of fragmented rocks is determined (Mohamed et al 2019). In recent years development and adoption of new automated imaging technology has significantly reduced the cost of carrying out the process, and as such more and better data can be gathered at lower cost. The technique is used to a great extent to assess blasting efficiency in ore zones as the as-mined particle size of ore material is a critical input to processing efficiency and cost. The technique is also used in waste zones but mainly to determine blast efficiency as part of assessing blasting costs. Because particle size has long been known to be a critical factor in the assessment of AMD risk of waste materials, an opportunity was identified to explore the potential to utilise the technology to supplement waste characterisation and management process.

The PSD profiles for three waste types from an operational open-pit base metal mine site, were collected between June 2016 and October 2017. The fragmentation analysis was carried out using automated Orica cameras fitted to two shovels operating onsite during this period. Recorded data was linked with the corresponding blast, material block and material type by following the progress of the shovels daily. Approximately ~32,000 images of blasted waste rock from 178 blasting events were processed and analysed (Figure 1). The PSD profiles of the three waste types are very similar to each other, indicating that blasting produces a consistent waste material product with respect to particle size, which is independent of waste type. The fine fraction accounts for a relatively small proportion of the overall waste mass with <20% mass being <10cm diameter.

Once the fragmentation profile for the blasted waste rock had been established, laboratory assessment of key particle size fractions was carried out to include compositional and mineralogical analysis.

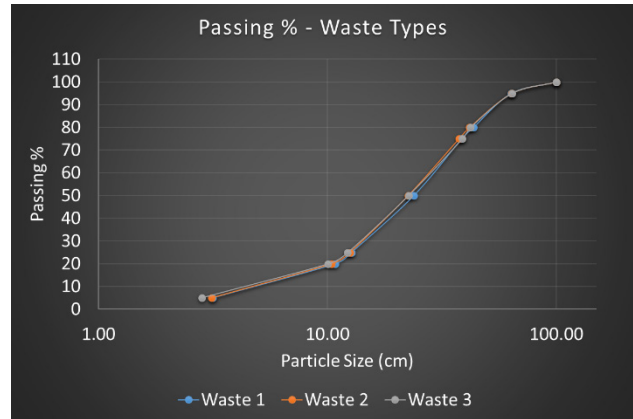


Figure 1. PSD profile for fragmentation analysis of 178 blasting events in open pit mining operations

2.1 Metal sulfide speciation

Nickel and copper concentrations for five, post-blast waste rock samples, was determined by four acid digest of the sample, followed by ICP analysis (Figure 2). The finest fraction of the samples (<2.36mm) has a notably higher concentration of Ni and Cu compared to the larger fractions indicating significant “upgrading” of metal content in the <2.36mm fraction. This effect was noted across all analysed samples. Mineralogical analysis was then carried out by Petrolab Ltd on one sample of <2.36mm size fraction and one >22mm size fraction samples using scanning electron microscopy (SEM). A polished block was prepared from each of the submitted sample fractions and carbon-coated to a thickness of 10 nm. Each block was analysed using a ZEISS EVO MA 25 scanning electron microscope (SEM) fitted with a Bruker xFlash 6|60 x-ray detector for energy-dispersive X-ray spectroscopy (EDX) analysis.

Table 1. SEM analysis results showing metal sulfides (pentlandite and chalcopyrite) and dolomite in <2.3mm fraction as weight %.

Mineral phase	<2.36mm	>22mm
Pentlandite	0.16%	0.03%
Chalcopyrite	0.2%	0.06%
Dolomite	0.44%	0.08%

Table 1 shows the results of the mineralogical analysis. Higher concentrations of Ni-bearing pentlandite, and Cu bearing chalcopyrite were reported for the <2.36mm fraction, where the highest concentrations of metals were recorded. The results indicate that blasting-related fragmentation significantly concentrates metal sulfides in the finer fraction, likely because of the presence of metal sulfides in veins/fracture fills. Cut-off grades for ore and waste at the site are defined based on metal sulfide content (processing is only effective at recovering metals from sulfide content). The significantly higher metal sulfide grades in the <2.36mm fraction therefore present an opportunity for metal recovery from this “waste” if this material were to be separated and processed as ore. The higher metal sulfide content and fine grain size both enhance the potential processing/recovery efficiency and lower cost.

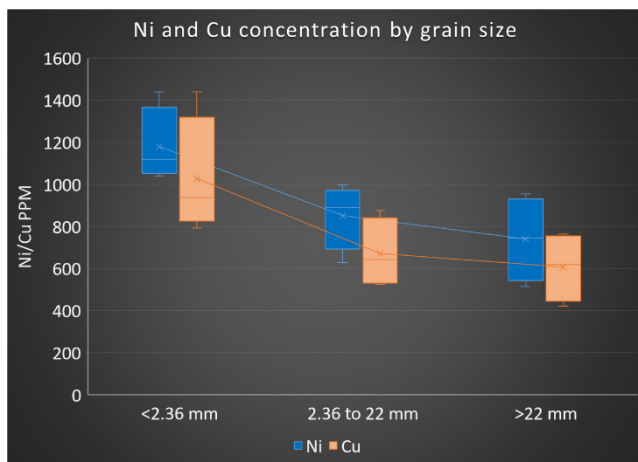


Figure 2. Box plot showing range, median and average concentrations of nickel and copper by particle size for 5 samples of waste rock post mining that have been split into 3 grain size fractions (15 samples total)

The higher surface areas and higher sulfide content of the fine fraction can cause an order of magnitude increase in sulfide oxidation rates and AMD loading making it the highest relative AMD risk. The results are important because the concentrating of metal sulfides in the finer fraction will increase the potential for AMD production relative to the assumed characteristics of the “bulk” material properties, estimated in the waste characterisation and block model. The block model assumes that all rock mass of the same grade-weighted-average value has the same geochemical properties. The further implication is that, conversely because metal sulfides are concentrated in the fines, the coarser materials will have a significantly lower AMD risk profile (lower grade, smaller surface area). As such, material that has been classified as higher risk with respect to AMD may be mined so as to have a significantly lower risk profile by optimising the waste blasting pattern in relation to fines generation. This highlights an opportunity to reduce waste management costs: the bulk of the high-risk classified material in the waste model and schedule can potentially be reclassified as lower-risk.

Figure 3 shows sulfur release from 2:1 leach tests carried out on different grain size fractions of the same sample. The >22mm fraction produces little if any sulfate. This lower reactivity reflects the lower metal sulfides present, and the low surface area, resulting in significantly lower AMD risk profile of this material. All of the fine fraction sample results exceeded the >22mm sulfur release amount significantly. In the block model the material is considered to have homogenous properties, however, the actual AMD risk profile of the grain size fractions represent order of magnitude differences. The relatively small volume of fine fraction material compared to the bulk highlights the overall benefit that separating this fine material would have on lowering waste management costs overall.

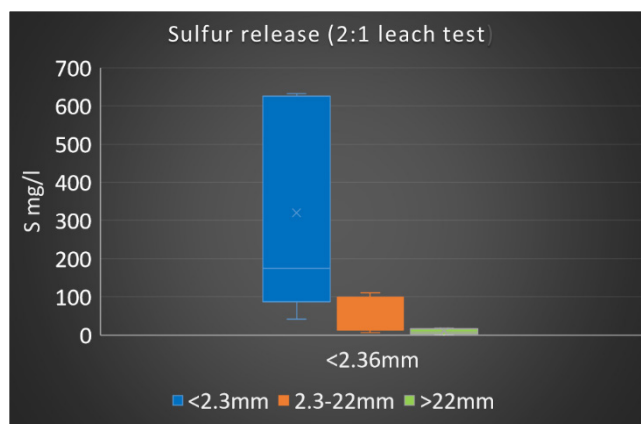


Figure 3. Box plot showing range, median and mean values for sulfur release in 2:1 leach tests for 5 samples split into 3 grain size fractions (15 samples total)

2.2 Carbonate speciation

Results from mineralogical analysis shown in Table 1 indicate that the carbonate dolomite is also concentrated in the <2.36mm fraction. This observation is important as the presence of carbonates in mine waste in the finer fraction is a key factor in AMD risk mitigation. Buffering of acidity generation by carbonate minerals is most significantly influenced by the finer particle size fractions where carbonate mineral reactivity rates are orders of magnitude higher.

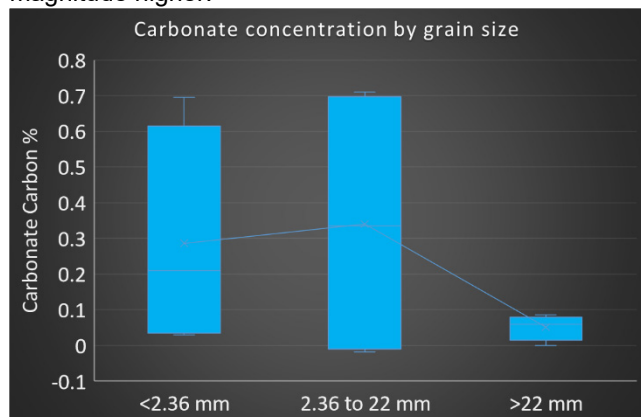


Figure 4. Box plot showing range, median and mean values for carbonate carbon for 5 samples split into 3 grain size fractions (15 samples total)

Analysis of carbonate content by grain size fraction for the 5 samples (Figure 4) shows carbonates are significantly concentrated in the finer fraction (2.36-22mm fraction as well as the <2.36mm fraction). The >22mm fraction has a much tighter range and values are very low indicating that the >22mm fraction is almost devoid of carbonates. The results suggest that concentrating of carbonates in the finer fraction will significantly increase potential buffering potential relative to the “bulk” properties. As such waste management costs could be reduced if material that was classified as higher risk in the waste model because of insufficient carbonate buffering, could be re-classified as lower risk because of higher relative carbonate to sulfide content. In addition further opportunity can be identified to utilise high carbonate, low

sulfide material which may have uses such as alkalinity producing cover, source material for “limestone” drains, source material for alkaline material to “blend” with higher risk material etc.

2.3 Implications for mine planning

Key findings of the assessment are that:

- (a) Fractionation may render larger particle sizes (>22mm) effectively inert when in the mine model they may be classified as having high AMD risk. As such a large potential cost saving can be identified by separating and re-classifying this material as lower risk material
- (b) Fractionation can cause carbonates to concentrate in the finer particle sizes which means that an alkalinity generating material could be created by screening this fraction out.
- (c) Fractionation causes significant upgrading in metal sulfide content in finer fractions meaning that metal grades move closer to that of ore than waste. There is an opportunity for this material to be separated and processed thus representing a source of recoverable metals.
- (d) Fractionation of metal sulfides into the finer grain size means that AMD risk may be underestimated by standard block modelling approach. This is because the model uses grade weighted cut off grades to determine waste class, which in turn is based on the relative reactivity of materials from laboratory testing at specific sulfide grades.
- (e) The separation and processing of the finer fraction with higher metal content presents an opportunity to significantly reduce project AMD risk. This is because the finer fraction with high metal sulfide fraction comprises the majority (>80%) of the potential total AMD risk from bulk mine waste mass. Processing of the material allows both removal of metals into product that will be sold offsite, and also the removal of the sulfide content to a different waste stream (tailings).
- (f) The use of fragmentation analysis to guide blasting patterns in waste zones may provide benefits as the physical properties of the waste product can be controlled at the source. Blasting can be tailored to produce a finer or coarser waste product that may allow some control over AMD risk, and may provide opportunities to recover both metals and carbonates that may provide positive cost benefits.

3 Conclusions

The use of waste “block models” to assess waste properties as part of mine planning, and the generation of waste schedules, has been increasingly used across industry over recent times. The research carried out by the authors demonstrates that this approach should be

viewed with caution, and further may be resulting in missed opportunities for optimising waste management economics. Classifying materials based on bulk grade weighted averages without assessing the actual properties of the as mined waste product may result in underestimation of potential AMD risks, and may result in recoverable metals being discarded in the waste stream. Fragmentation analysis has been identified as a potential means to assess the relative change to both the AMD risk profile, and metal recovery potential of the as mined waste. New technology allows for in-situ assessment of fragmentation during the mining process meaning that optimising the blasting process itself may realistically be used to “change” the AMD risk profile of the waste product and introduce another layer of AMD risk management. Further, this study demonstrates that opportunities to improve project economics can be identified such as identifying the recovery potential of potentially economic metals from material previously classified as “waste” along with recovery of carbonates that may have “value” on site for use as part of risk mitigation strategies.

References

- Mohamed F, Riadh B , Abderazzak S Radouane N , Ibsa T (2019). Distribution Analysis of Rock Fragments Size Based on the Digital Image Processing and the Kuz-Ram Model Cas of Jebel Medjounes Quarry. Aspects in Mining & Mineral Science.
- MWEI BREF: Best Available Techniques (BAT) Reference Document for the Management of Waste from Extractive Industries, in accordance with Directive 2006/21/EC; EUR 28963 EN; Publications Office of the European Union, Luxembourg, 2018; ISBN 978-92-79-77178-1; doi:10.2760/35297, JRC109657.
- K. Singh, M.P. Roy, R.K. Paswan, Md. Sarim, Suraj Kumar, Rakesh Ranjan Jha (2016). Rock fragmentation control in opencast blasting, *Journal of Rock Mechanics and Geotechnical Engineering* 8
- Noy. M.J. 2013. Automated rock fragmentation measurement with close range digital photogrammetry. In: the 10th International Symposium on rock fragmentation by blastic, new Delhi, India. Measurement and Analysis of Blast Fragmentation
- Pearce.S.R et al (2012), Managing closure risks by integrating acid and metalliferous drainage studies with mine scheduling – real world examples in: Proceedings of Mine Closure 2012, editors: Andy Fourie and M Tibbett, Australian Centre for Geomechanics, pp. 801-814
- Price (2009) Prediction Manual for Drainage Chemistry from Sulphidic Geologic Materials MEND Report 1.20.1
- Kanchibotla, S. S., Valery, W. and Morrell, S. (1999). Modelling fines in blast fragmentation and its impact on crushing and grinding. Explo'99: A Conference on Rock Breaking, Kalgoorlie, WA, 7-11 November 1999. Melbourne: AusIMM

Utilising automated mineralogy and accelerated static tests to enhance kinetic testing evaluations

Anita Parbhakar-Fox and Nathan Fox

Senior Research Fellow, W.H. Bryan Geology and Mining Research Centre, Sustainable Minerals Institute, University of Queensland, Australia.

Abstract. Three waste materials (A, B and D) were subjected to kinetic column leach tests to determine their acid forming characteristics. To improve predictions of their behaviour from the outset and to enhance the understanding of the water chemistry data collected over 156 weeks, column feed materials were characterised using automated mineralogy and a new accelerated static geochemical test. Initial measurements of the bulk mineralogy confirmed an abundance of magnesite and dolomite in Type A with trace pyrite (0.2 wt. %) identified however only 12% of this was liberated. Type B contained far less carbonate and was instead dominated by albite, magnesiohornblende and chlorite with minor pyrite (1.15%) again observed (with 12.5% liberated). Type D contained the highest pyrite (1.3 wt. %; 10% liberated) which was notably coarser (d_{80} of 550 μm) with the remainder comprising albite, actinolite, chlorite and tremolite and no carbonates. Accelerated static testing classified Types A, B and D as non-acid forming (NAF). Each waste type was predicted to be NAF in the kinetic trials which was observed. This study highlights that undertaking detailed column-feed characterisation allows behaviour of materials during kinetic trials to be predicted with a better understanding of mineral weathering and water chemistry afforded.

Introduction

The industry-wide trend towards mining larger, lower grade ores ultimately results in a net increase in the quantities of waste produced (Mudd and Jowett, 2018). For many ore deposit types (e.g., sedimentary exhalative, epithermal, porphyry) resulting mine waste materials may contain sulphides (e.g., pyrite; FeS_2 , pyrrhotite; $\text{Fe}_{(1-x)}\text{S}$) which under surficial conditions, will oxidise to produce sulphuric acid by processes collectively termed acid and metalliferous drainage (AMD) as described in Dold (2017). If this acidic drainage enters surface and ground waters, there is potential for metals/metalloids, at deleterious concentrations, to be introduced into surrounding ecosystems and ultimately become bioaccessible to humans (Dold, 2017). There is significant pressure on the mining industry to improve methodologies for predicting the behaviour of future mine wastes, in order to protect communities and reduce liabilities when the mine reaches the end of its life, as indicated by the social licence to operate having been identified as the top risk posed to the mining industry for 2019 (Ernest Young, 2019).

Traditionally, to predict the behaviour of mine waste material, two types of test work can be undertaken, static

(short term, low-cost) and kinetic (longer term, high-cost) tests. Static tests comprise a range of chemical tests which involve the determination of sulphur or sulphide-sulphur to calculate maximum potential acidity (MPA; using stoichiometric factors derived from pyrite oxidation reactions) and the titration of a sample to calculate its acid neutralising capacity (ANC). Subtraction of ANC from MPA gives the net acid producing potential (NAPP) which enables waste classification (based on the absolute acid forming potential), particularly when screened again net acid generation (NAG) pH values (Dold, 2017). Kinetic testing provides more reliable information for predicting the long term water chemistry with two main types of testing used, humidity cell (e.g., Brough et al., 2018) and column leach (e.g., Qian et al., 2017). However, this information is generated over a much longer time scale (i.e., the minimum a test can run is 20 weeks), and due to the costs involved, few are performed and can also be terminated too early, therefore the resulting data may be of questionable accuracy and not effectively included in mine planning decisions. Researchers (e.g., Bouguet et al., 2011; Opitz et al., 2016) have recognised there is a gap between static and kinetic testing which, in order to improve AMD predictions, needs to be bridged. Motivated by this, our study is part of a larger research project (with Petrolab Ltd and the University of Cape Town) aimed at introducing a new testing step, as a precursor to kinetic testing, which focuses exclusively on characterising column feed materials with detailed mineralogical assessments performed on size fractions to understand the texture of acid forming and neutralising minerals.

Sample materials from the Savage River iron-ore mine, Western Tasmania were used in this study. Waste at this site are classified as one of four types, Type A is carbonate bearing and is therefore considered alkaline, Type B is a neutral waste, Type C is a clayey gravel which is often used for capping and Type D contains pyrite so is regarded as potentially acid forming (PAF). Several waste rock piles, of different ages, are present at the site however the piles constructed by the current operator, Grange Resources, have been effectively built to minimise AMD. As newer parts of the deposit are being explored, early commencement of geoenvironmental characterisation work was initiated. At least 143 samples representative of Types A, B and D were subjected to detailed static testing, from which a preliminary waste model was developed. The aim of this study was to use new column feed tests and kinetic trials to confirm the geoenvironmental behaviour of these waste types in order to understand the risks posed and improve the understanding of how they might behave in a waste rock

pile.

Methodology

10 bulk samples (5 kg; - 4 mm) from each waste type were delivered to the University of Tasmania (UTAS) in July, 2015 and a composite sample prepared for each waste type. This material was riffle split and a representative portion of the column feed was used in a range of chemical and mineralogical tests. Static testing work included NAG testing (Dold, 2017), carbon-sulphur analysis using an Eltra 2000 instrument at UTAS and Sobek testing at ALS Global (Brisbane; method code: EA013). The Microwave Assisted Thermal Energy (MATE) pH test developed by Noble et al. (2015) as a proxy for kinetic trials was performed on all sample powders (2.5 g; $n=6$) at UTAS, with the derived leachates filtered ($<0.45 \mu\text{m}$), acidified (1% HNO_3) and analysed at the Central Science Laboratory (CSL), UTAS using an Element 2 HR-ICP-MS instrument with appropriate calibration standards, duplicates and blanks used.

To determine column feed mineralogy sample splits were micronised and analysed using a benchtop Bruker D2 Phaser XRD instrument with a Co X-ray source. Each sample was analysed for 1 hour (fixed divergence slit: 1 mm; range: $4\text{-}90^\circ 2\theta$; 0.02° step size, Fe-filter), with the resulting patterns processed in Eva 2.1 and Topas 2.0 softwares using the ICDD PDF 2012 database. Mineral liberation analysis was performed on splits of the same column feed material ($n=3$) using a FEI Quanta 600 mineral liberation analyser scanning electron microscope (MLA-SEM) at the CSL, UTAS. The X-ray modal analysis (XMOD) and sparse phase liberation (SPL) methods were selected to evaluate bulk mineralogy, pyrite grain size, grain shape, and mineral associations. A nickel standard was used. Data were processed in MLA Image Viewer to produce classified images for each sample based on a site-specific mineral library.

The kinetic columns were prepared in accordance with the AMIRA P387A ARD Testing Handbook free draining column leach procedure and is the most commonly used method in Asia-Pacific (e.g., Qian et al., 2017). A nominal grain size of -4 mm was used. In summary, each Buchner funnel was loaded with a piece of coarse 160 mm filter paper, sand (to improve drainage; 100 g) and riffle split representative portions of waste rock (2 kg). Four columns (Types A, B, D and a control cell) were established and followed a weekly cycle (days 1-5: heating under 275 W lamps; end-day 5: irrigation using fresh deionised water; days 6-7: free draining). On average, 500 ml was added to the columns. Leachates drained into conical flasks at the base and were collected weekly on day 7 for water chemistry assessments. Each week pH (Mettler Toledo S47 SevenMulti™ dual pH/conductivity meter) and EC (Euitech PC 450) measurements were taken following instrument calibration. Every 4 weeks, the column leachates were filtered ($0.45 \mu\text{m}$ PES Millipore filters) into pre-acidified (HNO_3) 70 ml vials and sent to ALS Global (Brisbane) for chemical analyses (method codes: EG020F, ED041G, EG035F) with the following elements measured: As, B, Ba, Be, Cd, Co, Cr, Cu, Hg, Mn, Ni, Pb, Se, V, Zn and

SO_4 . From weeks 55 onwards, additional leachates were collected for Ca and Mg analysis to assist with tracking the rate of neutralisation. The final six months' worth of leachates were analysed at the CSL, UTAS using the HR-ICP-MS instrument.

Results and discussion

Column feed characteristics

For Type A the bulk mineralogy was dominated by magnesite (32 wt. %), quartz (22 wt. %), dolomite (17 wt. %) and chlorite (10 wt. %) with only trace pyrite (0.2 wt. %) and magnetite (<1 wt. %). Detailed pyrite investigations reported a $p80$ of $260 \mu\text{m}$ with the largest particle size reported as $355 \mu\text{m}$. In total, only 12 % of pyrite grains were liberated. Pyrite was associated with quartz (29 %), chlorite (27 %), magnesiohornblende (11 %), epidote (6%) and magnetite (5.5 %; Figure 1). Notably, smaller grains (i.e., $<100 \mu\text{m}$) predominately associated with epidote. Only three pyrite grains were chalcopyrite associated, with no pyrite-carbonate associations.

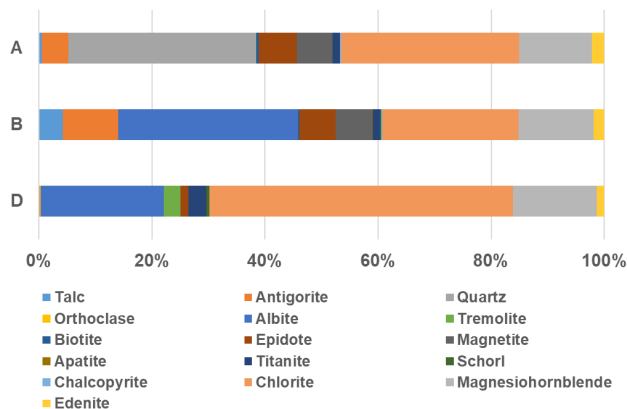


Figure 1. Mineral associations for locked pyrite grains observed in Type A, B and D waste materials as calculated by MLA-SEM.

The mineralogy of Type B was dominated by albite (35 wt. %), tremolite (18 wt. %), actinolite (15 wt. %) and chlorite (11 wt. %) with minor pyrite (1.15 wt. %) and trace magnetite (<1 wt. %) also identified. Carbonates were present but only in trace concentrations (<1 % dolomite (0.1 wt. %) and magnesite (0.14 wt. %)). Pyrite in this sample had similar properties to Type A with a $p80$ of $250 \mu\text{m}$ and a maximum particle diameter of $355 \mu\text{m}$. 12.5 % of pyrite was liberated and where locked, larger grains (i.e., $>100 \mu\text{m}$) were albite (27.5 %), chlorite (21 %), antigorite (8.5 %) and magnesiohornblende (11 %) associated with magnetite (5.6 %) and epidote (5 %) associating with smaller pyrite grains (Figure 1). Only a few grains (<10) were chalcopyrite associated, with again, no notable carbonate associations. The bulk mineralogy of Type D comprised of albite (25 wt. %), actinolite (19 wt. %), chlorite (18 wt. %) and tremolite (16 wt. %). Type D had the greatest quantity of pyrite (1.3 wt. %) but no measurable carbonates. Pyrite is present as large particles with a $p80$ of $550 \mu\text{m}$ and the largest

particle diameter of 600 μm measured. Approximately 10% of pyrite was liberated. Locked grains were associated with chlorite (48 %), albite (19 %), magnesiohornblende (13 %) and titanate (3 %; Figure 1).

Using the locked pyrite association data, each calculated percentage was multiplied by the mineral relative reactivity factor (at pH 5) given in Sverdrup (1990) and totalled to give a final score. As an example, if pyrite was 100 % associated with dolomite which is assigned a factor of 1 i.e., immediately dissolving, a score of 100 would be given. This could indicate that in a kinetic trial, the carbonates would rapidly dissolve in the initial weeks inducing pyrite liberation and a subsequent drop in pH may be observed. Conversely, if locked pyrite was 100 % associated with quartz classified as inert with a relative reactivity factor of 0.004, an overall score of 0.4 would be calculated and leachates evolved from a kinetic trial would be expected to be circumneutral for the duration of the test as pyrite liberation would be anticipated to occur at a very slow rate. By this calculation, these waste fall into the very slow weathering field, with Type D the most reactive due to its greater pyrite-chlorite associations (Figure 2). Considering all of these textural factors it is predicted that Types A and B will be NAF, whilst Type D leachates may be weakly acidic as 10% of pyrite is liberated with no measured carbonate.

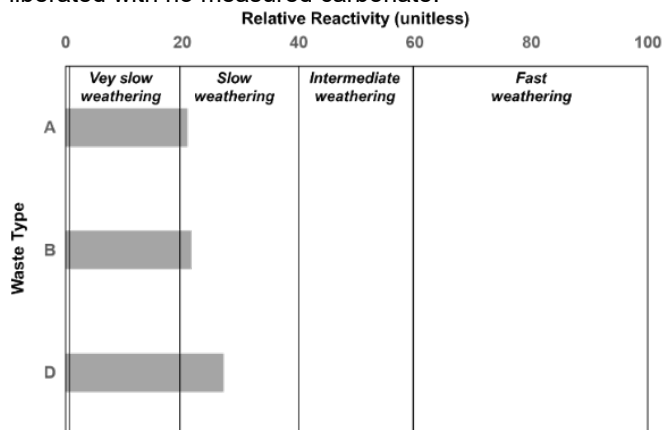


Figure 2. Relative reactivity of locked pyrite for Type A, B and D.

MATE pH values supported these predictions with average values of pH 7.7, 6.7 and 5.7 measured respectively for Types A, B and D classifying them as NAF if a cut-off criterion of pH 4.5 (for PAF or NAF) is used. NAG pH values differed with pH 8.1, 7.5 and 4.1 respectively measured classifying Type D instead as PAF. MATE pH leachates were classified as near neutral low-metal (Figure 3).

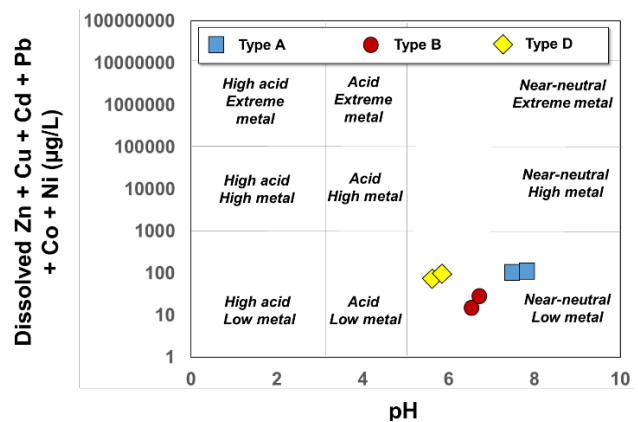


Figure 3. Modified Ficklin plot (after Plumlee et al., 1994) showing metal pollution characteristics based on the relationship between pH and sum of dissolved metals for Types A, B and D.

Kinetic trial results

A comparison of pH data from each cell (Figure 4) confirms that all cells, including the control, are consistently NAF for the duration of the 156 weeks if the same PAF/ NAF criterion of pH 4.5 is used. It is noted though, that high flushing rates as mandated by the procedure can increase carbonate dissolution and in a real field condition, these may actually be lower. If adjusted to pH 6 then Types A and B would still classify as NAF, but Type D would on two occasions have classified as PAF. i Type A, which contains the highest reservoir of carbonates, is the least acid forming, however in the final six months similar pH values were measured from the Type B cell (Figure 4), showing that when dealing with low-carbonate, low-sulphide waste, silicate buffering (via chlorite most likely) can maintain pH in the NAF realm. In these trials, passivating layers (i.e., iron (oxy)hydroxides doped with silicates and possibly sulphur/sulphate) on pyrite surfaces as described by Qian et al. (2017) are likely forming. However, to confirm this, surface chemistry analysis would need to be performed with Fe, O and Si specifically measured.

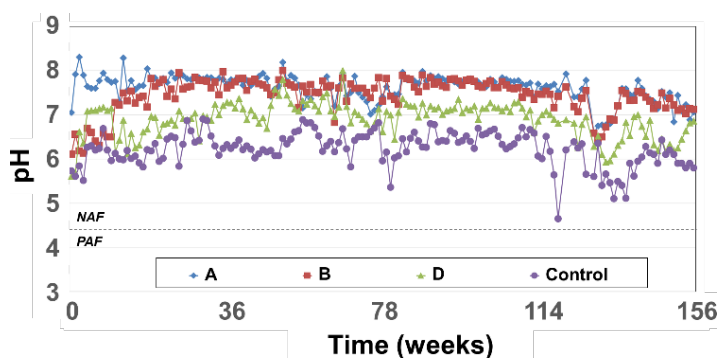


Figure 4. Leachate pH values for Types A, B, D and a control cell measured weekly for 156 weeks.

Measurements of dissolved sulphate (Figure 5) confirmed that Type A is the least acid generating, but surprisingly, Type B returns the highest quantities, which is consistent with it containing the highest liberated pyrite which also had the smallest $p80$ (250 μm) of the three

types suggesting this liberated finer-grained pyrite was more susceptible to oxidation. Measurements for Type D were comparatively low and relate to the lower quantity of liberated grains and the high association with chlorite potentially encouraging the rapid formation of passivating layers.

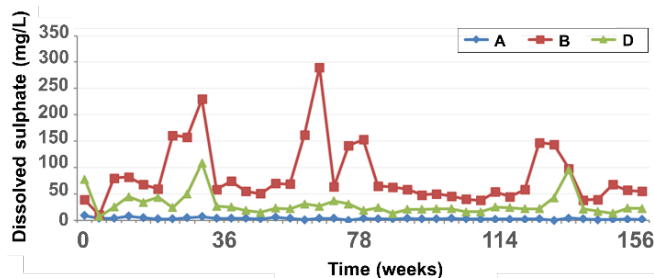


Figure 5. Dissolved sulphate (mg/L) for Types A, B, D measured weekly for 156 weeks.

Dissolved Ca + Mg (Figure 6) measurements showed the highest quantities for Type B despite there being a much lower content of dolomite and magnesite relative to Type A and relates to the higher rate of sulphide oxidation (Figure 5). The lowest quantity was measured for Type A despite having the largest carbonate reservoir and likely relates to the fact that the least sulphide oxidation occurred here to generate acid for carbonate dissolution.

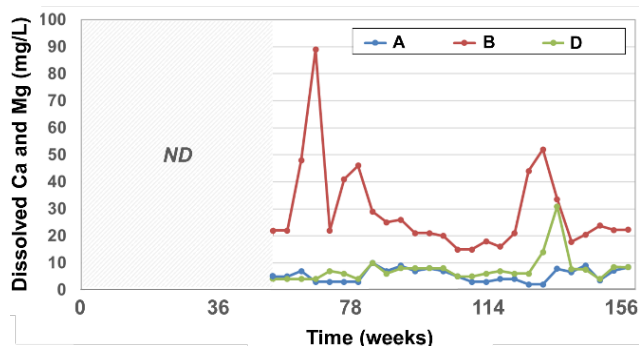


Figure 6. Dissolved calcium + magnesium (mg/L) for Types A, B, D measured from weeks 54 to 156 only (ND= no data).

Leachate chemistry data confirmed MATE pH classifications of low metals (Figure 3) with only Cu identified as a potential contaminant (avg. 0.006 mg/L Type A; 0.007 mg/L Type B and 0.006 mg/L Type D).

Conclusions

Three waste types from western Tasmania were subjected to column leach testing with the feed materials initially characterised using automated mineralogy and new chemical testing methods. Kinetic tests classified all three as NAF with Cu high in leachates. Type A is inert with a reservoir of dolomite and magnesite available for buffering acidity. Pyrite surface passivation reactions are occurring for Type B (enhanced by the presence of chlorite) and is likely to remain NAF. Pyrite in Type D is larger in diameter than other types but is encapsulated in silicates. Even if liberated, it will remain NAF as pyrite passivating layers appear to form rapidly. Further

investigations into the chemical nature of the passivating layers and experiments to test their longevity are recommended to confirm their durability, and inducing such layers may be a key control when managing similar low-sulphide mine waste materials. This research highlights that many procedural biases exist when using standard kinetic test approaches and they do not reflect real field conditions (i.e., order of magnitude higher flushing rates experienced in the lab, increased mineral surface areas relative to in the field). Thus, continual use of new technologies, in the lab and field, focussed on understanding the insitu mineralogy (sulphides, carbonates and reactive silicates) over a size fraction and mineral texture will facilitate better understanding of waste characteristics and drainage chemistry enabling better environmental outcomes.

Acknowledgements

Grange Resources and the ARC TMVC Hub (project number IH130200004) are thanked for funding and administering this project. Sibebe Nascimento (TMVC Hub, UTAS), Ashley Townsend (CSL, UTAS) and Laura Jackson (RGS) are thanked for analysing kinetic cell leachates, as is the reviewer for comments.

References

- Bouquet, N., Piccinin, R., Taylor, J. 2011. The benefits of kinetic testwork using oxygen consumption techniques and implications for the management of sulfidic materials. Proceedings of the 7th Australian Workshop on Acid and Metalliferous Drainage, Darwin, p. 117-129.
- Brough, C., Strongman, J., Bowell, R., Warrender, R., Prestia, A., Barnes, A., Fletcher, J., 2017. Automated environmental mineralogy; the use of liberation analysis in humidity cell testwork. Minerals Engineering, 107:112-122.
- Dold, B., 2017. Acid rock drainage prediction: A critical review. Journal of Geochemical Exploration, 172:120-132.
- Ernest Young: https://www.ey.com/en_gl/mining-metals/10-business-risks-facing-mining-and-metals (accessed 11th March, 2019).
- Mudd, G.M., Jowitt, S.M., 2018. Global resource assessments of primary metals: An optimistic reality check. Natural Resources Research, 27:.229-240.
- Noble T. L, Aalders, J.A., Lottermoser B. G, 2015. Development of the microwave assisted thermal energy (MATE) pH test. CRC ORE Technical Report 96, CRC for Optimising Resource Extraction, Brisbane, 50pp.
- Opitz, A., Becker, M., Broadhurst, J., Bradshaw, D., Harrison, S., 2016. The Biokinetic Test as a Geometallurgical Indicator for Acid Rock Drainage Potentials. AusIMM 3rd International Conference on Geometallurgy, Perth, 2016.
- Plumlee, G.S., Smith, K.S., Ficklin, W.H., 1994. Geoenvironmental models of mineral deposits and geology-based mineral environmental assessments of public land. USGS Open File Report 94-203. <https://pubs.usgs.gov/of/1994/ofr-94-0203/94-203.pdf>
- Qian, G., Schumann, R.C., Li, J., Short, M., Fan, R., Li, Y., Kawashima N., Zhou, Y., Smart, R., Gerson, A., 2017. Strategies for reducing acid and metalliferous drainage by pyrite surface passivation. Minerals, 7:42, doi:10.3390/min7030042
- Sverdrup, H., 1990. Kinetics of base cation release from chemical weathering of silicate minerals. Lund University Press – Chartwell-Bratt Ltd, London, 245pp.

Geochemical considerations for improved management of sulfide mine tailings

Matthew B.J. Lindsay

University of Saskatchewan, Canada

Michael C. Moncur

InnoTech Alberta, Canada

Abstract. Drainage emanating from sulfide tailings deposits can have widespread negative impacts on water quality. These impacts are generally associated with acidification or metal contamination resulting from sulfide-mineral oxidation. This weathering process contributes sulfate, metals, and trace elements to associated pore water and drainage. Consequently, tailings management and reclamation strategies are often focused on limiting oxygen availability and reducing water infiltration to minimize the formation and migration of sulfide-mineral oxidation products. Dry covers and, to a lesser extent, water covers have been used for tailings management and reclamation at mining operations worldwide. Reactive tailings amendments intended to limit migration of sulfide-mineral oxidation products have also been studied. Although both positive and negative geochemical responses are possible, specific outcomes are often non-intuitive and long-term studies examining the performance of these and other tailings management strategies are often lacking. In this paper, we briefly discuss geochemical considerations for implementation of tailings management approaches.

1 Introduction

Long-term chemical mass loading from sulfide mine tailings can have significant and widespread negative environmental impacts. These impacts are largely associated with the oxidative weathering of sulfide minerals, which can generate plumes of acid mine drainage (AMD) or neutral mine drainage (NMD). Therefore, tailings management approaches are commonly focused on (i) limiting the formation of sulfide-mineral oxidation products and (ii) minimizing the transport and discharge of these oxidation products. Johnson and Hallberg (2005) used the terms “source control” and “migration control” to describe options for AMD remediation, which includes both active and passive approaches. Similar approaches may be applied to manage the release and transport of dissolved metals and metalloids associated with NMD. Overall, tailings management approaches are intended to reduce contaminant source terms and associated mass loading to receiving environments. Here, we briefly review tailings geochemistry, discuss two passive tailings management approaches (i.e., tailings covers, reactive amendments), and consider potential geochemical implications associated with their implementation.

2 Tailings geochemistry

Tailings are commonly stored in near-surface deposits, where exposure to atmospheric oxygen and meteoric waters can promote sulfide-mineral oxidation. The oxidative weathering of pyrite [FeS_2], pyrrhotite [Fe_{1-x}S] and other sulfide minerals under these conditions contributes sulfate, metals, and associated trace elements to pore water and drainage (Lindsay et al. 2015). Protons generated during this process react with carbonate minerals to maintain near-neutral pH conditions sometimes referred to as NMD. Although acid neutralization reactions involving carbonates and, to a lesser extent, metal hydroxides can inhibit or delay acidification, ongoing sulfide-mineral oxidation combined with carbonate depletion may lead to AMD formation.



Figure 1. Pyrrhotite-bearing Au tailings in northwestern Ontario, Canada following deposition (top) and after one year of weathering (bottom).

The pH of tailings pore water and drainage has important implications for sulfide-mineral oxidation, precipitation of secondary phases, and element mobility. Sulfide-mineral oxidation rates are dependent upon several factors including oxygen availability, pH, temperature, and mineralogy. Assuming O_2 availability is not limited, oxidation rates are orders of magnitude higher at pH less than 5, where Fe(III) serves as the principal

oxidant. Under these conditions, O₂ reduction coupled with Fe(II) oxidation becomes the rate-limiting step in sulfide-mineral oxidation (Singer and Stumm 1970). Additionally, different sulfide minerals exhibit different susceptibility to oxidative weathering. Moncur et al (2009) developed a relative scale of weathering resistance for sulfide minerals, with pyrrhotite being the least resistant and pyrite among the most resistant of sulfide minerals commonly found in tailings deposits. Consequently, pyrrhotite-bearing tailings often weather more rapidly compared to tailings dominated pyrite or other sulfide minerals (Fig. 1).

Secondary phases are important controls on the transport of sulfide-mineral oxidation products within tailings deposits (Lindsay et al. 2015). Precipitation of Fe(III) (oxy)hydroxides and Fe(III) hydroxysulfates occurs within the oxidation zone, whereas hydrated Fe(II) sulfates may precipitate below the oxidation zone under anoxic conditions. The precipitation of these secondary phases is pH-controlled; ferrihydrite [Fe₁₀O₁₄(OH)₂·nH₂O] and goethite [αFeOOH] form at pH above 5, whereas schwertmannite [Fe₁₆O₁₆(OH)₁₂(SO₄)₂] and jarosite [KFe₃(OH)₆(SO₄)₂] forming under more acidic conditions. Extensive precipitation of secondary phases can lead to the formation of cemented layers commonly referred to as hardpans (Blowes et al., 1991; Fig. 2).



Figure 2. Thick accumulation of secondary Fe(III) (oxy)hydroxide and Fe(III) hydroxysulfate phases in highly-weathered pyrrhotite-rich Zn-Cu tailings in western Manitoba, Canada.

Ferrihydrite and schwertmannite are both metastable phases that transform to more crystalline phases over time. Ferrihydrite transforms to goethite under oxic conditions, whereas schwertmannite may transform to goethite or jarosite at pH below 3 (Acero et al. 2006). The formation and transformation of these secondary Fe(III) phases has important implications for the transport of potentially hazardous elements. Specifically, Cruz-Hernández et al. (2016, In Press) demonstrated that schwertmannite transformation to goethite and jarosite can lead to As, Cu, and Zn release.

Cationic metals (e.g., Cu, Ni, Zn) generally occur at higher concentrations and exhibit greater mobility in AMD

systems. Co-precipitation with Fe(III) (oxy)hydroxides (i.e., ferrihydrite, goethite) often limits Cu, Ni, and Zn concentrations at pH above 5. Consequently, hardpan layers comprised of Fe(III) phases are often contain high Cu, Ni, and Zn contents. In contrast, oxyanion-forming elements (e.g., As, Mo, V) often occur at elevated concentrations in neutral to alkaline pore water and drainage due to the limited sorption capacity of Fe(III) (oxy)hydroxides under these conditions. Incorporation of various elements (e.g., As, Cu, Ni, Pb, Zn) into Fe(III) hydroxysulfates (i.e., schwertmannite, jarosite) may also limit their mobility under acidic conditions. Similarly, the hydrated Fe(II) sulfate melanterite [FeSO₄·7H₂O] can contribute to Cu, Ni, and Zn attenuation within highly-weathered sulfide tailings (Moncur et al. 2005).

3 Tailings Management

Although other passive tailings management approaches exist, we have focused on cover systems and reactive amendments for the purposes of this paper.

3.1 Cover systems

Despite many design variations of varying complexity (INAP 2017), tailings covers generally fall into two categories: dry covers and water covers. Dry covers are designed limit oxygen and water fluxes to underlying mine wastes, and can also reduce erosion and support plant growth (Fig. 3). These covers may be constructed from soils, sediments, geosynthetics, or a combination of these materials. Non-reactive mine wastes may also be used for cover construction in locations where the availability of other materials is limited (e.g., Demers et al. 2008).



Figure 3. Revegetated dry soil cover over weathered pyrrhotite-bearing Ni-Cu tailings in central Ontario, Canada (top) and groundwater seepage at base of this tailings dam (bottom).

Similarly, water covers are used to limit oxygen

availability and, therefore, sulfide-mineral oxidation, acid generation, and metal leaching within. Water covers may be implemented through subaqueous disposal into freshwater or marine environments, or by flooding tailings in purpose-built impoundments (MEND 2018). Moncur et al (2015) reported that pyrrhotite-rich tailings stored for over 60 years under a 1-m water cover exhibited little evidence of oxidation compared to unsaturated areas of the same deposit (Fig. 4). Pore water within these subaqueous tailings was characterized by near-neutral pH and low dissolved metal concentrations, whereas the unsaturated tailings contained low pH pore water with extremely high dissolved Fe and SO₄ concentrations. However, ongoing oxidation and tailings resuspension are potential limitations for water cover use and have been reported at other mine sites (e.g., MEND 2018).



Figure 4. Revegetated dry soil cover over weathered pyrrhotite-rich Zn-Cu tailings in western Manitoba, Canada.

3.2 Reactive Amendments

Organic matter amendments including brewery waste, municipal biosolids, and pulp mill waste have been shown to promote sulfate reduction and metal attenuation within sulfide tailings (e.g., Hulshof et al. 2006; Lindsay et al. 2009). With this approach, sulfate reducing bacteria couple carbon oxidation with sulfate reduction to form H₂S and CO₂. Associated precipitation of Fe-S and Zn-S phases can limit migration of sulfide oxidation products including Fe, Zn, and associated trace elements. Lindsay et al. (2009) reported decreases in dissolved Fe and Zn concentrations of 25% and 60%, respectively, after four years in pyrite-rich Ag-Zn-Pb-Au tailings amended with brewery waste and municipal biosolids (Fig. 5). Other reactive amendments (e.g., fly ash, lime) have been used to promote metal attenuation through acid neutralization.



Figure 5. Dry-stacked pyrite-rich Ag-Zn-Pb-Au tailings used to test organic carbon amendments in southeast Alaska, USA.

4 Geochemical Considerations

Despite their intent to reduce chemical mass loading, tailings management approaches can have unintended geochemical implications. In particular, management approaches intended for (partially-)weathered sulfide tailings should be carefully considered.

Although dry covers can effectively reduce sulfide-mineral oxidation rates and the transport of associated reaction products, their use on (partially-)weathered tailings could promote transformation of metastable phases or metal mobilization. For example, the development of reducing conditions in tailings below soil covers may promote mobilization of Fe, As, and other elements. Paktunc (2013) found that organic carbon contributed by a biosolids cover promoted Fe and As mobilization in underlying tailings due to reductive goethite dissolution and reduction of As(V) to As(III). The transport and discharge of Fe, As, and other elements can lead to downgradient acidification and contamination (Fig. 3). In contrast, DeSisto et al (2017) reported that a low organic carbon soil cover did not promote As mobilization in underlying tailings; however, oxygen penetration limited development of reducing conditions and did not prevent sulfide-mineral oxidation.



Figure 6. Small boreal lake in western Manitoba, Canada following deposition of weathered pyrrhotite-rich Zn-Cu tailings.

Application of water covers to weathered tailings may also have unintended consequences. Dissolution of water-soluble secondary phases could lead to extensive acidification and metal contamination. For example, highly-weathered Zn-Cu tailings, which contained large amounts of melanterite, jarosite, and gypsum [CaSO₄·2H₂O] were deposited in a small boreal lake as part of an abandoned mine reclamation plan. This lake was subsequently dosed with quick lime to neutralize pH and limit dissolved metal concentrations. Metal attenuation was achieved via (co-)precipitation of Fe(III) phases (Fig. 5), which ultimately settled to the lake bottom. Although low dissolved metal concentrations were achieved, the long-term stability of the metal-rich sediments remains unknown, particularly in the presence of natural organic matter inputs from the surrounding watershed.

Reactive amendments may also have unintended geochemical implications for tailings management. Despite promoting extensive attenuation of Fe, Zn, and

SO₄, Lindsay et al. (2011a) observed temporary increases in pore water Fe and As concentrations during the development of reducing conditions associated with organic amendments. These initial increases were proportional to organic carbon availability, with higher amendment rates producing higher dissolved Fe and As concentrations (Lindsay et al. 2011b). Dissolved Fe and As concentrations declined with time due to sulfate reduction and metal-sulfide precipitation.

5 Summary

Tailings management strategies are generally intended to minimize the production and migration of sulfide-mineral oxidation products. Although this paper only touches on a few examples, changing geochemical conditions resulting from organic matter addition, subaqueous disposal or flooding, and associated pH changes can have both positive and negative implications. Therefore, it is critical that detailed geochemical investigations be undertaken when considering various options for tailings management.

Acknowledgements

We thank supervisors, colleagues, and students who we have had the pleasure to work with over the years. MBJL acknowledges support from the Natural Sciences and Engineering Council of Canada Industrial Research Chairs Program (Grant No. IRCPJ-450684-13).

References

- Acero P, Ayora C, Torrentó C, Nieto J-M (2006) The behavior of trace elements during schwertmannite precipitation and subsequent transformation into goethite and jarosite. *Geochim Cosmochim Acta* 70: 4130-4139.
- Cruz-Hernández P, Pérez-López R, Parviainen A, Lindsay MBJ, Nieto JM (2016) Trace element-mineral associations in modern and ancient iron terraces in acid drainage environments. *Catena* 47: 386–393.
- Cruz-Hernández P, Carrero S, Pérez-López R, Fernandez-Martinez A, Lindsay MBJ, Nieto JM (In Press) Impact of As(V) on precipitation and transformation of schwertmannite in acid mine drainage-impacted waters. *Eur J Mineral*.
- Demers I, Bussière B, Benzaazoua M, Mbonimpa M, Blier A (2008) Column test investigation on the performance of monolayer covers made of desulphurized tailings to prevent acid mine drainage. *Miner Eng* 21:317-329.
- DeSisto SL, Jamieson HE, Parsons MB (2017) Arsenic mobility in weathered gold mine tailings under a low-organic soil cover. *Environ Earth Sci* 76:773.
- INAP (2017) Global Cover System Design: Technical Guidance Document. International Network for Acid Prevention (INAP), Technical Report, 216 pp.
- Johnson DB, Hallberg KB (2005) Acid mine drainage remediation options: A review. *Sci Tot Environ* 338:3-14.
- Lindsay MBJ, Blowes DW, Condon PD, Ptacek CJ (2009) Managing pore-water quality in mine tailings by inducing microbial sulfate reduction. *Environ Sci Technol* 43:7086-7091.
- Lindsay MBJ, Blowes DW, Condon PD, Ptacek CJ (2011a) Organic carbon amendments for passive in situ treatment of mine drainage: Field experiments. *Appl Geochem* 26:1169-1183.
- Lindsay MBJ, Blowes DW, Ptacek CJ, Condon PD (2011b) Transport and attenuation of metal(loid)s in mine tailings amended with organic carbon: column experiments. *J Contam Hydrol* 125:26-38.
- Lindsay MBJ, Moncur MC, Bain JG, Jambor JL, Ptacek CJ, Blowes DW (2015) Geochemical and mineralogical aspects of sulfide mine tailings. *Appl Geochem* 57:157-177.
- MEND (2018) How to Assess Potential Biological Effects of Subaqueous Disposal of Mine Tailings – Literature Review and Recommended Tools and Methodologies. Mine Environment Neutral Drainage (MEND) Report 2.19.1, 158 pp.
- Moncur MC, Ptacek CJ, Blowes DW, Jambor JL (2005) Release, transport and attenuation of metals from an old tailings impoundment. *Appl Geochem* 20:639-659.
- Moncur MC, Jambor JL, Ptacek CJ, Blowes DW (2009) Mine drainage from the weathering of sulfide minerals and magnetite. *Appl Geochem* 24:2362-2373.
- Moncur MC, Ptacek CJ, Lindsay MBJ, Blowes DW, Jambor JL (2015) Long-term mineralogical and geochemical evolution of sulfide mine tailings under a shallow water cover. *Appl Geochem* 57:178-193.
- Moncur MC (2016) Surface Water Chemistry and Secondary Precipitate Mineralogy from Camp Lake: Post Remediation.
- Paktunc D (2013) Mobilization of arsenic from mine tailings through reductive dissolution of goethite influenced by organic cover. *Appl Geochem* 36:49-56.
- Singer PC, Stumm W (1970) Acid mine drainage: the rate-determining step. *Science* 167:1121-1123.

Engagement and emotional response of the narrative of social license as reflected in the social media

Michael Hitch

Department of Geology, Division of Mining, Tallinn University of Technology (TalTech), Tallinn, Estonia

Abstract. Social License is recognized as crucial in natural resource development. Much of the work to date that reflects on social license and social acceptance is built upon a social paradigm that conjoins the motives, hopes, and aspirations of multiple stakeholders that ultimately determine their respective behavior. Social License itself is the product of discourse, or the perception of events or conditions and may form the basis of the broader narrative or 'story'. Narratives today plays out in a highly dynamic and temporal way that evolve and change due to any number of psycho-social reasons including the use and nature of the language. This paper uses a proprietary and commercially available artificial intelligence algorithm to examine the positioning of a country's Social License narrative both in terms of long-term engagement and its emotional response in traditional and social media.

Social License evolves from discourse or the perception of the relative importance of the actors and relationships and events in a story, but on its own do not tell the whole story (i.e. the narrative). The narrative on the other hand, gives the broad strokes of a story.

Aristotle defined a 'story' as having four components, of which the most important is PLOT (i.e. the use of linguistic devices to convey causality, surprise, the unexpected, something that deviates from the canonical) and peripeteia or TROUBLE). There also must have a chronology (i.e. story unfolding over time), characters of greater or lesser virtue (i.e. heroes, villains etc.), and a setting (i.e. the 'stage'). A couple of millennia later, Kenneth Burke proposed the narrative pentad of Act + Actors + Scene + Agency + Purpose (Hershey and Branch 2011). All of these elements form the foundation of the phenomenon we refer to as 'Social License'.

Social License is best described as a metaphor (Thompson and Boutilier 2011). Social license itself really does not exist as a concrete 'thing', but rather a representation of a healthy relationship between parties that have different motives, values and perspectives. Over the past two decades, this concept has been widely applied within in the context of mining, oil and gas development and other resource development activities (Gehman et al. 2016; Raufflet et al. 2013; among others). The core around which social license can be developed is trust. This trust reflects the sincere and intense conviction to perform as promised, to communicate in a timely, complete and collaborative way, and to stand up and be accountable when issues arise. Without this level of mutual understanding, respect and meaningful dialogue natural resource development can be curtailed, delayed or postponed (Franks et al. 2014; Prno and Slocombe 2012, Thomson and Boutilier 2011). The chief

purveyors and promoters of Social License as a 'thing' tend to be the industrial proponents whose vested interest is to advance development as smoothly for corporate economic growth and return to shareholders. Communities and affected stakeholders see Social License as the means to exercise their right and privilege to self-determination.

Finally, Social License could be seen as this condition that exists in a particular place and time and shifting participants. It is fragile and occupies the space between a future that fosters some degree of dependence on natural resource production and all that entails, and a future that does not include this kind of economic activity. The occurrence of Social License is without judgement as any metaphor is, however has become the hallmark of corporate social engagement.

With the acceptance that social media is inextricably part of our lives, we have entered an era of *Digimodernism*, characterized by the interaction and relationship people have with communication technology (Kirby 2009). Narratives are in effect, broad strokes of a story without spelling out every emotive stop and intonation. They essentially convey an idea. This is amplified in the realm of *Digimodernisation*, where perceptions and narratives become 'true' by being the most compelling and most shared. It is the 'grand narratives' that are the ones that have the power to become larger than life and have the power to control people and their prevailing discourse (Foucault 1972).

As mentioned initially, the story or narrative needs a setting or stage. The current research examines how the narrative of Social License plays out in geographic locations where mining and mineral production are happening. Australia was used as a case due to the high dependence (+60%) of mineral production on their nation's economy. It would be reasonable to assume that if high levels of dependence of minerals for economic activity were the case, then the narrative surrounding Social License would also follow suit. Canada, although a significant mineral economy, relies far less on mining as a proportion of their nation's economic output. Finally, recognizing that Europe is not one huge geopolitical block, but rather a colourful tapestry of member nation states, has a collective economy that is dominated by the manufacturing sector and mineral production plays a very minor role in the big picture. In this case one might assume that the Social License narrative would be very localized and subdued.

Results from an AI-driven narrative analysis of social media has identified an inverse trend, where Australia had the least enduring Social License narrative and a highly negative tone, whereas Canada appears to

embrace the narrative and possess a strong emotional affinity to it. Selected European nations had a strong positive response to the narrative both in terms of its enduring of level of permanence and emotion.

The results of the study, suggest that due to the dominant nature of mineral production in Australia, there a sense of resolution may be in effect, whereas in Canada, the tenancy of mining is less dominant and the Social License narrative more significant. In the European case, those countries where mining play little or no importance in their economies, the Social License narrative is vibrant (i.e. in both a positive and negative sense). In countries like Greece, where mining is somewhat more important and topical in their social media outlets, the narrative is strong.



Figure 1. Significance of the SLO narrative

The study also examined the emotional response to social license. In this case, all three nations were rooted in a negative emotion. In the case of Australia, the narrative is associated with emotions fury, anger dislike. Canada on the other hand recorded emotional positive responses of favour, approval, closeness and joy. Greece sat squarely in the middle with no discernable emotional response.

The AI narrative analysis approach has its limitation in the very temporal nature of the 'story' and the tide of shifting opinions. To be most effective, this research approach needs to be assessed over time to map not only the permanence and emotional tone of a narrative, but also how it shifts with time.

References

Foucault M (1972). *The archaeology of knowledge* (A.M., Sheridan Smith, Trans.) Pantheon, New York

Franks DM, Davis R, Bebbington AJ, Ali SH, Kemp D, Scurrah M (2014) Conflict translates environmental and social risk into business costs. *Proceedings of the National Academy of Sciences of the United States of America*. 111/21:7576-7581

Gehman, J, Dara Y, Thompson D, Alessi D, Allen M, Goss G (2016) Comparative analysis of hydraulic fracturing wastewater practices in unconventional shale development: Newspaper coverage of stakeholder concerns and social license to operate. *Sustainability* 8:912

Hershey L, Branch J (2011) *Lexicon Rhetoricae: the narrative theory of Kenneth Burke and its application to marketing*, *Qualitative Market Research: An International Journal*, 14/2:174-18

Kirby A (2009). *Digimodernism: How new technologies dismantle the postmodern and reconfigure our culture*. Continuum, New York

Prno J, Slocombe DS (2012) Exploring the origins of 'social license to operate' in the mining sector: perspectives from governance and sustainability theories. *Resource Policy*, 37: 346-357

Raufflet E, Baba S, Perras C, Delannon N (2013) Social license. In: Idosu SO, Capaldo N, Zu L, Gupta AD (ed) *Encyclopedia of Corporate Social Responsibility*. Springer, New York

Thomson I, Boutillier RG (2011). Social license to operate. In: Darling P (ed), *SME Mining Engineering Handbook Society for Mining, Metallurgy and Exploration*, Littleton CO

Secondary mineral assemblages associated with weathered mine and mill wastes, Cobalt Mining Camp, Ontario

H.E. Jamieson, A. Dobosz

Department of Geological Science and Geological Engineering, Queen's University, Kingston, Ontario, Canada

J. Clarke

SRK Consulting, Vancouver, British Columbia, Canada

K. Martin

Wood, Mississauga, Ontario, Canada

R.J. Bowell

SRK Consulting, Churchill House, Wales, UK

C. Kennedy

Agnico Eagle Mines Limited, Toronto, Ontario, Canada

Abstract. The silver mining camp at Cobalt contains polymetallic wastes hosting metal of economic value (Ag, Co, Ni) and others other that are potentially hazardous (As, Sb). Mining in the early 20th century left many small deposits of mill wastes, waste rock, and tailings distributed throughout the area. The complex nature of the ores was a challenge for early metallurgists, which resulted in variable mill wastes from experiments in processing. The residues from the second half of the 20th century are less dispersed, and lower in metal content. Identification of the secondary minerals formed in situ in mine waste is critical to understand As solubility controls in the exposed tailings and waste rock. The situation is complicated in the Cobalt camp because of pervasive secondary (pre-mining) alteration. Here we report the identification of As- and Co-bearing tertiary minerals in mill wastes and tailings as part of an overall project designed to characterize the mobility of multiple metal and metalloids from primary ore to secondary pre-mining oxidation to tertiary (mine waste weathering) transformations.

1 Introduction

Silver was mined from the Cobalt area in northeastern Ontario, Canada from 1903 to 1989. A total of 17 M kg of Ag, 20 M kg of cobalt (Co), 7 million kg of nickel (Ni) and 2 million lbs of copper (Cu) was produced up to 1971 in the Cobalt-Gowganda Silver belt (Petruk et al., 1971). The area is currently a target for Co exploration (Bochove, 2017). Many small-scale mining operations were scattered through the camp and have left multiple residual legacy sites including mill sites, waste rock piles and tailings deposits. Arsenic is the primary element of environmental concern associated with the legacy mine sites and waste material (Dumaresq, 1993; MOE, 2011). The potential release of As from these materials is dependent on the stability of the As-bearing mineral

phases within the near surface environment. Unlike many ore deposits, where As is hosted in iron sulfides such as arsenopyrite and pyrite, and the mobility of As in weathering mine waste is controlled mainly by the stability of Fe oxyhydroxides and Fe-As oxidation products, the primary As-hosting minerals in the Cobalt ores were a complex mixture of sulfarsenides and arsenides (Table 1). The polymetallic nature of the mineralization (Ag-Co-Ni-Bi-As-Cu-Sb) was a challenge for the early mills, and has resulted in a complicated waste material that provides the opportunity to study the mobility in the near-surface environment of potentially hazardous elements and economically valuable elements, as well as some that fall into both categories. In the older legacy sites, there are processing wastes, that are highly variable as a result of multiple methods used in the early days to extract Ag. There are also to flotation tailings. Some of the processing wastes are exposed to the atmosphere, others are water-saturated and less oxidized. There has been partial remediation in some areas where soil covers waste that had been exposed for decades. There is sufficient carbonate in the host rocks to prevent extensive development of acid rock drainage (Kelly et al. 2007), but As is known to be mobile at near-neutral pH and has been released to surface water in the region (Dumaresq 1993). In addition to the complex primary mineralogy and variable post-depositional environments of the waste, Secondary oxidation of the ores is known to have resulted in arsenates such as erythrite-annabergite (the "cobalt bloom" used as an exploration guide) (Boyle and Dass 1971).

The overall objective of our research program is to understand how pre-mining and post-mining weathering processes affect the mobility of multiple elements (As, Sb, Co, Ni, Cu, Bi, Ag) in a polymetallic setting. This extended abstract is focused on As- and Co-hosting tertiary minerals in mill wastes and tailings. The results from this research will help understand the processes

controlling the release of potentially hazardous elements to the aquatic environment and provide guidance to explorationists pursuing new targets in a complex historic mining camp.

Table 1. Common ore and accessory minerals in the Cobalt camp (modified from Dumaresq 1993 and Petruk 1971)

	Mineral	Composition
Sulfarsenides	Cobaltite	CoAsS
	Gersdorffite	NiAsS
	Arsenopyrite	FeAsS
Arsenides	Nickeline	NiAs
	Safflorite	(Co,Fe,Ni)As ₂
	Loellingite	FeAs ₂
	Rammelsbergite	NiAs ₂
	Skutterudite	(Co,Ni,Fe)As _{3-x}
	Langisite	(Co,Ni)As
Sulfides	Chalcopyrite	CuFeS ₂
	Galena	PbS
	Sphalerite	ZnS
	Pyrite	FeS ₂
	Bornite	Cu ₅ FeS ₄
Stibnides and sulfstibnides	Breithauptite	NiSb
	Ullmanite	NiSbS
	Tetrahedrite	(Cu,Fe) ₁₂ Sb ₄ S ₁₃
Silver minerals	Native metals	Ag, Au, Bi, As
	Allargentum	Ag _(1-x) Sb _x
	Dyscrasite	Ag ₃ Sb
	Acanthite	Ag ₂ S
	Proustite	Ag ₂ AsS ₃
	Stephanite	Ag ₅ SbS ₄
	Pyrrargyrite	Ag ₃ SbS ₃

2 Geological Setting

The mineralized Ag-Co-Ni veins of the Cobalt-Coleman camp are spatially associated with both mafic sills of the Proterozoic Nipissing diabase and with the unconformity of Proterozoic clastic sediments of the Huronian supergroup which overlie Archean metavolcanic units (Andrews et al., 1986). The style of mineralization within the Cobalt-Coleman camp is classified as five-element (Ag-Bi-Co-Ni-As) style vein deposit (Kissin 1992). The Ag-Co-Ni mineralization is hosted within silica-carbonate veins which occur in all local lithologies including the Archean volcanics, Proterozoic sediments and the Nipissing diabase (Petruk, 1971).

3 Sampling and Analytical Methods

Samples were collected from the Nipissing High Grade

tailings, Nipissing High Grade mill, Nipissing Low Grade tailings, and Nipissing Low Grade mill (Figure 1). At the tailings sites, test pits were hand dug to approximately 40 cm, with samples collected from intervals of stratigraphic variation in colour and grain size. These waste materials are from the early stage of mining in the Cobalt camp (starting in 1903). More recent tailings from the Cart Lake area (1965-1983) were also sampled. More modern processing that produced the Cart Lake tailings was designed to recover not only Ag, but also Co and Ni hosted within arsenide and sulfarsenide minerals. Major and trace elements were determined using inductively coupled plasma atomic emission spectroscopy (ICP-AES) and inductively coupled plasma mass spectroscopy (ICP-MS) following a partial aqua regia digestion of equal parts HCl, HNO₃ and DI H₂O for 30 minutes. The characterization of the mineralogy of the samples was completed using SEM combined with automated mineralogy using mineral liberation analysis (MLA) and electron microprobe analysis.

4 Results

The Nipissing High Grade samples were higher in most metal(loid)s with mean concentrations in mill waste samples of 32600 mgkg⁻¹ As and 9727 mgkg⁻¹ Co (n=4) and in tailings samples of 12624 mgkg⁻¹ As and 5938 mgkg⁻¹ Co (n=7). The Nipissing Low Grade samples had mean concentrations in mill samples of 4930 mgkg⁻¹ As and 1236 mgkg⁻¹ Co (n=3) and in tailings samples of 2849 mgkg⁻¹ As and 711 mgkg⁻¹ Co (n=6). Silver concentrations were more than 1000 mgkg⁻¹ in the mill samples, reflecting the low recoveries in the early mills.

All tailings and mill samples analysed predominately consist of common silicate minerals including quartz, feldspar, chlorite, biotite, pyroxene, and hornblende. Together these silicate minerals comprise 90-95% of the

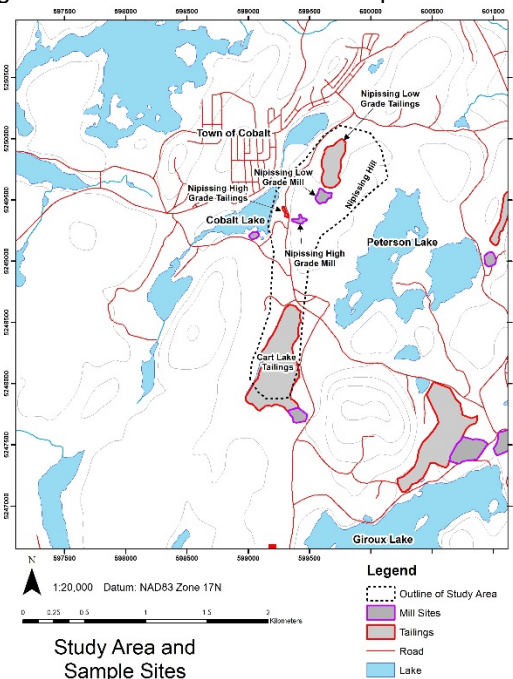


Figure 1. Outline of study area and location of sample sites

tailings samples, and 70% of the mill samples, with the remainder including sulfides, oxides and carbonates. Primary ore and accessory minerals observed in these samples include bravoite (Fe-NiS₂), cobaltite, gersdorffite, millerite (NiS), loellingnite, pyrite, realgar, plus solid solution series cobaltite-gersdorffite, safflorite-skutterudite), and (para)rammelsbergite-nickeline. Tertiary minerals formed in situ can be recognized by rimming, cementing and void-filling textures, and based on the known stability of these phases. A common tertiary phase is erythrite-annabergite-hörnesite solid solution (Figure 2).

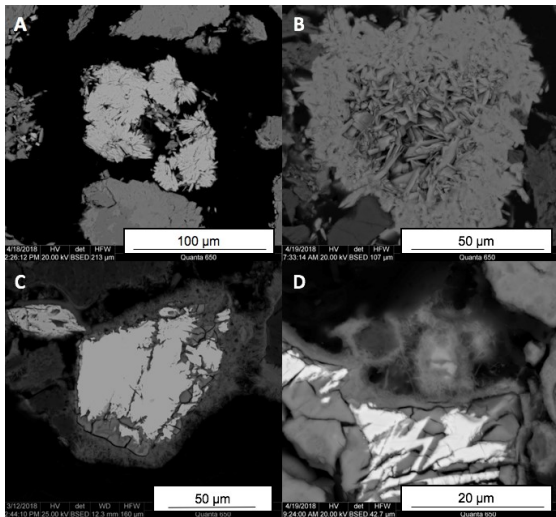


Figure 2. A) and B) NHGT002 (tailings) showing various texture of tertiary erythrite-annabergite-hörnesite. C) and D) NHGM014 (mill waste) Safflorite-skutterudite replaced by Co-Ni bearing Ca-Fe arsenate and rimmed by erythrite-annabergite-hörnesite.

Electron microprobe analysis shows that Ca and Fe are also present in this phase, which has an average composition of (Co,Ni,Mg)_{2.67}(Ca,Fe)_{0.3}(AsO₄)_{1.98}•7.67H₂O in the Nipissing High Grade tailings samples, and a similar composition in the High Grade Mill. Also present are a Ca-Fe arsenate tentatively identified as yukonite, and fine-grained mixtures that likely include both tertiary phases. Several grains of arsenic trioxide (arsenolite or its polymorph claudetite) were observed in mill and tailings, probably a remnant from roasting, although primary arsenolite has also been reported from this area (Kloprogge et al. 2006).

5 Discussion

Given that erythrite-annabergite has been previously recognized as a secondary mineral associated with Ag veins in this mining camp (Boyle and Dass 1971), the distinction between this phase as pre-mining, or forming in situ in the tailings might appear to ambiguous. However, the inclusion of significant amounts of Ca and Fe in the erythrite-annabergite-hörnesite solid solution in the tailings and mill samples appears to distinguish this as having formed in the mine waste deposits from recent oxidation. In fact, it is likely that the Ca and Fe became available for inclusion in the solid solution from

dissolution of carbonate minerals (calcite and ankerite) and sulfide oxidation in response to sulfide oxidation reactions tending to decrease pH. The tertiary solid solution formed in the tailings seems to have more Ca and Fe than previously reported (Jambor and Dutrizac 1995).

Arsenic trioxide, whether primary or secondary may be a source of high concentrations of dissolved As, given its high solubility. The experience from other mining camps where uncontrolled ore roasting emissions led to widespread arsenic trioxide in soil (Bromstad et al. 2017) and even lake sediments (Schuh et al. 2018) suggest that the dissolution of arsenic trioxide is kinetically-governed and it may persist in the environment for decades.

The mill samples and the near-surface tailings exhibit abundant tertiary mineral formation but a sample taken from water-saturated material 13 to 20 cm below the surface was dominated by primary As mineral species with minimal weathering textures, suggesting that sample is within a stable, water-saturated environment. Furthermore, there is an abundance of carbonate minerals in comparison to a sample taken closer to the surface, suggesting where the material is water saturated, carbonate is stable and not being consumed by any acid produced from dissolution of arsenides or sulfarsenides and may be precipitated in situ.

6 Conclusions

Based on the samples examined, the As- and Co-hosting secondary minerals in Cobalt area mine waste depend on depositional environment and mining history. Fine-grained, water-saturated tailings include more primary phases and carbonate. Erythrite-annabergite-hörnesite formed in situ includes more Ca and Fe than what has been reported from secondary (pre-mining) solid solutions. Further analysis of secondary and tertiary oxidation products is required to predict their influence on waste mineralogy and element mobility. Waste from the first era of mining in the early 20th century are particularly high in As, Ag and Co. Based on our samples, the more modern Cart Lake tailings are lower in these elements but have a larger volume than the Nipissing High Grade and Low Grade materials studied and thus may require consideration for their contribution to drainage.

References

- Andrews AJ, Owsiacki L, Kerrich R, Strong, DF (1986) The silver deposits of Cobalt and Gowganda, Ontario. I: Geology, petrology and whole-rock chemistry. *Can J Earth Sci* 23:1480-1506.
- Bromstad MJ, Wrye LA, Jamieson HE (2017) The characterization, mobility, and persistence of roaster-derived arsenic in soils at Giant Mine, NWT. *Applied Geochemistry* 82:102-118.
- Bochove D (2017) Cobalt rush in ... Cobalt brings nearly comatose Ontario town back to life <https://business.financialpost.com/commodities/ghost-town-of-cobalt-gets-first-jolt-from-teslas-electric-cars>
- Boyle RW, Dass AS (1971) The geochemistry of the supergene processes in the native silver veins of the Cobalt-South Lorrain area, Ontario. In Berry, L.G. (ed.), *The silver-arsenide deposits of the Cobalt-Gowganda Region, Ontario*. *The Can Min* 11, Part 1:358-390.

- Dumaresq CG (1993) The Occurrence of Arsenic and Heavy Metal Contamination from Natural and Anthropogenic Sources in the Cobalt Area of Ontario. M.Sc. thesis, Department of Earth Sciences, Carleton University, Ottawa.
- Jambor JL, Dutrizac JE (1995) Solid solutions in the annabergite-erythrite-hornesite synthetic system. *Can Min* 33:1063-1071
- Kelly J, Champagne F, Michel J (2007) Assessment of Metal Attenuation in a Natural Wetland System Impacted by Alkaline Mine Tailings, Cobalt, Ontario, Canada. *Mine Water Environ.* 26:181–190
- Kissin, SA (1992) Five-element (Ni-Co-As-Ag-Bi) veins, *Geoscience Canada*, v. 15(3).
- Kloprogge JT, Duong LV, Weier M, Martens WN (2006) Nondestructive Identification of Arsenic and Cobalt Minerals from Cobalt City, Ontario, Canada: Arsenolite, Erythrite, and Sphero-cobaltite on Pararammelsbergite, *Applied Spectroscopy*, 60(11):1293–1296.
- Ministry of Environment (MOE) (2011) Final Report: Cobalt-Coleman Mining Camp Soil Assessment. Terrestrial Assessment Unit Air Monitoring and Transboundary Air Sciences Section, Environmental Monitoring and Reporting Branch, Ontario Ministry of Environment.
- Petruk W (1971) Mineralogical Characteristics of the Deposits and Textures of the Ore Minerals; *in* The Silver-Arsenide Deposits of the Cobalt-Gowganda Region, Ontario, L.G. Berry (ed.), *Can. Min.* 11:108-139
- Petruk W, Jambor J, Boyle, RW (1971) History of the Cobalt and Gowganda area: *in* The Silver-Arsenide Deposits of the Cobalt-Gowganda Region, Ontario, L.G. Berry (ed.), *Can. Min.* 11: 1-
- Schuh CE, Jamieson HE, Palmer MJ, Martin AJ (2018) Solid-phase speciation and post-depositional mobility of arsenic in lake sediments impacted by ore roasting at legacy gold mines in the Yellowknife area, Northwest Territories, Canada. *App Geochem* 91:208-220.

Increasing value and decreasing environmental risk by reprocessing and stabilizing tungsten tailings at Cantung Mine, NT, Canada

Heather E. Jamieson, Brent Kazamel, Matt Leybourne, Agatha Dobosz
*Geological Sciences and Geological Engineering
Queen's University*

H. Falck
Northwest Territories Geological Survey

Abstract. Reprocessing mine waste to extract additional value is a potentially sustainable alternative to exploration and development of new mines. Combining the extraction of additional value and the reduction of deleterious elements, the environmental impact of stored mine tailings can be minimized, one of the goals of sustainable mining. At Cantung mine in northern Canada, tailings contain ore grade values of tungsten and minor additional value of copper and gold. The tailings are currently in steep-sided impoundments with little oxidation but some have spilled into the river and exhibit extensive oxidation and acidic drainage. Our long-term objective is to transform the Cantung mine from an inactive and environmentally problematic site in a vulnerable Northern setting to one where additional value can be extracted from tailings with a comprehensive remediation design that reduces environmental risk. Here we report on the first stages of the project: characterization of the tailings in terms of modal mineralogy, scheelite grain size and liberation, and acid-base accounting. The mobility of tungsten under the wide range of pH, Eh and variable mineralogy has also been studied.

1 Introduction

Tungsten is considered a critical metal, meaning that it has high economic importance and high risk of interruption of supply (Graedel et al. 2014). The Cantung mine is an unusually large and high-grade tungsten deposit located in the Northwest Territories in Canada and was the western world's largest producer during its operation from 1962 to 1985 (Figure 1). Despite the high grade (0.8 to 1% WO₃), the mine experienced numerous shutdowns during periods of low tungsten prices and profitability was hindered, in part, by problems with metallurgical recovery. Recently, the Canadian government has assumed responsibility for the site following insolvency of the previous operator. The site is in a remote, mountainous terrain near Nahanni National park and upstream of a First Nations community in an area subject to rapid climate change and elevated seismic risk. Currently, approximately 6.5 Mt of tailings are in steep-sided impoundments without adequate confinement, and 172,000 t in Flat River, actively eroding and producing acidic, metal-bearing drainage (Figure 2a and 2b). The tungsten content of the tailings is

comparable to ore grades from other operating or proposed mines.

Our long-term research objective is to create a comprehensive plan for reprocessing all tailings including those in the river, recovering previously-lost tungsten, producing a sulfide concentrate from which copper and gold might be extracted, and designing redispersion in a manner appropriate for the environmental sensitivities and geohazards relevant to the site. Ideally, the secondary recovery of tungsten would help defray cost of remediation.

This presentation is focused on two of our initial projects: (1) characterization of the Cantung tailings using automated mineralogy to better evaluate the potential of reprocessing based on scheelite concentration, grain size and liberation and the potential of the tailings to generate acid drainage, and (2) study of tungsten mobility in the tailings environment, and its dependence on pH, Eh and modal mineralogy.



Figure 1: Location of Cantung Mine



Figure 2. (top) view of Cantung site with tailings impoundment in foreground (photo E. Struzik). (bottom) oxidized tailings and iron-stained water near Flat River

2 Geological Background

Cantung is a skarn deposit situated in the Canadian Cordilleran, associated with Mid-Cretaceous felsic plutonic suites that were emplaced near the transition between shallower water carbonates of the Mackenzie Platform and siliciclastic rocks of the Selwyn Basin. The ore is hosted in the Ore Limestone, a relatively pure carbonate, and the Swiss Cheese Limestone, dolomitic siltstone and fine-grained impure limestone (Bowman et al., 1985).

3 Sampling and Analytical Methods

For the characterization project, fifty samples were collected from surface to 30 m depth in four tailings ponds, and one bulk sample from the Flat River tailings, which had been released during the early stages of mining. These samples varied in tungsten content from 0.11 to 0.65% W. Samples were prepared for detailed automated mineralogy by mounting a subsample in epoxy and hand polishing. They were analysed at Queen's University using the Mineral Liberation Analysis (MLA) system on an FEI Quanta 650 FEG Environmental SEM. Four types of analysis were done: (1) modal mineralogy, (2) liberation of scheelite, (3) particle size analysis of scheelite, and (4) acid-base accounting.

For the tungsten mobility project, porewater samples were collected using suction lysimeters and by centrifuging tailings samples. Surface waters were filtered through 0.45 μm filters. Samples were analysed

using high resolution inductively coupled mass spectrometry (HR-ICP-MS) and ion chromatography (IC). Tailings samples were collected from augered holes during lysimeter installation, and from the base of shallow ponds where surface waters were collected. Field pH, Eh, conductivity, and temperature were measured with a YSI 556 Multiprobe and an Accumet 115 Portable Meter.

4 Results

4.1 Modal Mineralogy

There is significant variation in the relative amounts of silicates, pyrrhotite, carbonates and oxides in the tailings, which may influence reprocessing design and environmental behavior. There is up to 30% pyrrhotite in the tailings, but little pyrite. The Flat River tailings exhibit extensive oxidation with less than 2% sulfide remaining, and 60% iron oxides.

4.2 Scheelite grain size and liberation

The scheelite grain size appears to be bimodal, based on the samples analysed to date (Figure 3). Loss of fine-grained scheelite is known to be problematic at other mines but the grain size analysis suggests that this is not the only reason for poor recoveries.

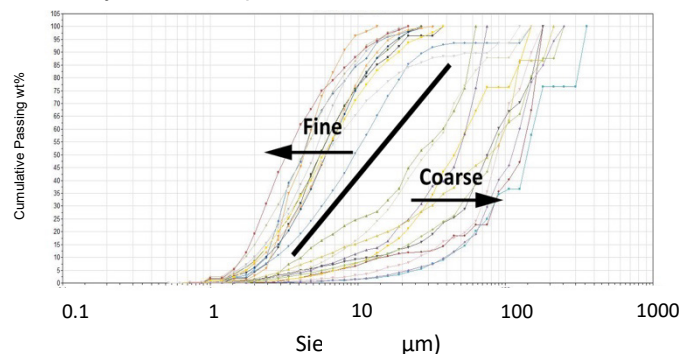


Figure 3. Grain size analysis of tailings. Vertical axis indicates cumulative passing in wt%.

Liberation of scheelite grains is variable (Figure 4) but the relatively small amount of unliberated grains suggests this is not the main reason for the loss of W to tailings. More than 50% of the scheelite is partially liberated.

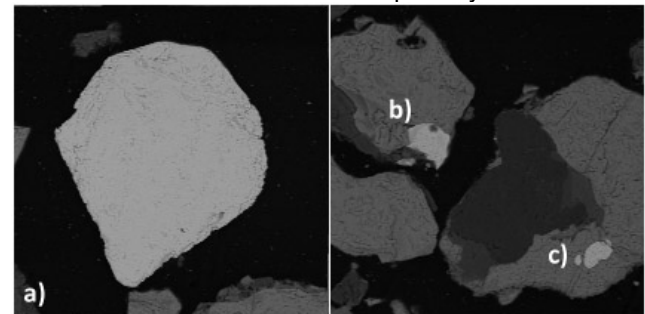


Figure 4. Degrees of liberation in scheelite a) Completely liberated. b) partially liberated. c) entirely unliberated.

4.3 Pyrrhotite Oxidation and Acid-base Accounting

The potential to produce acid was determined from modal mineralogy by calculating the sulfur content of acid-generating minerals. Neutralization potential was calculated based on the abundance of carbonate minerals, correcting for the presence of Fe and Mn carbonates. Results to date indicate that most of the tailings are potentially acid-generating, consistent with previous chemical tests. Field and SEM observations indicated variable degree of pyrrhotite oxidation (Figure 5).

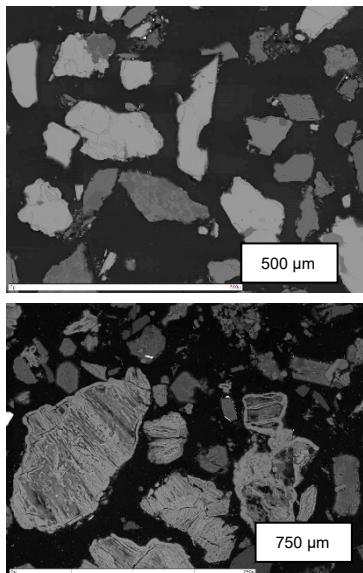


Figure 5. Unoxidized and oxidized pyrrhotite.

4.4 Identification of other ore minerals

Automated mineralogy provided the opportunity to locate rare grains of <10 µm sized electrum and native gold in several samples, mostly fully contained within either pyrrhotite or hornblende (Figure 6). Bismuth was found either as native bismuth or bismuthinite (Bi₂S₃). All samples except for the Flat River tails have at least a few particles of native Bi. Those samples highest in scheelite are also highest in native Bi. Generally, bismuthinite is rare in comparison to native Bi, but follows the same overall trends.

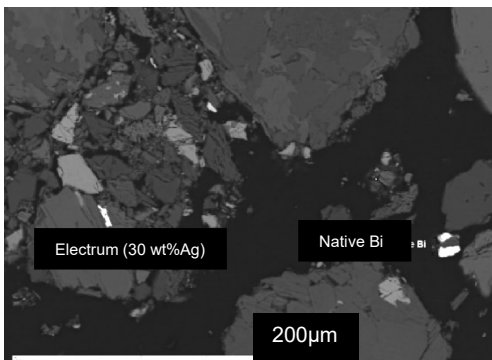


Figure 6. Electrum and native Bi in tailings

4.5 Mobility of Tungsten

Little is known about the transport and fate of tungsten in the mine waste environment and it has only recently been considered a potential human health hazards (Koutsospyros et al., 2006; Mohajerin et al., 2013). Dissolved tungsten is transported principally as tungstate oxyanions in most natural waters, and as thioanions in alkaline, highly sulfidic waters (Cui and Johannesson, 2017). At neutral to alkaline pH, the monomeric WO₄²⁻ species is dominant, but will protonate and polymerize with increasing acidity to form a number of ill-defined polytungstate species. Being negatively charged, tungstate anions will adsorb to positively charged mineral surfaces such as Iron oxides. The variable pH and Eh conditions (Figure 7), and striking differences in mineralogy mean that Cantung is an ideal place to study W mobility.

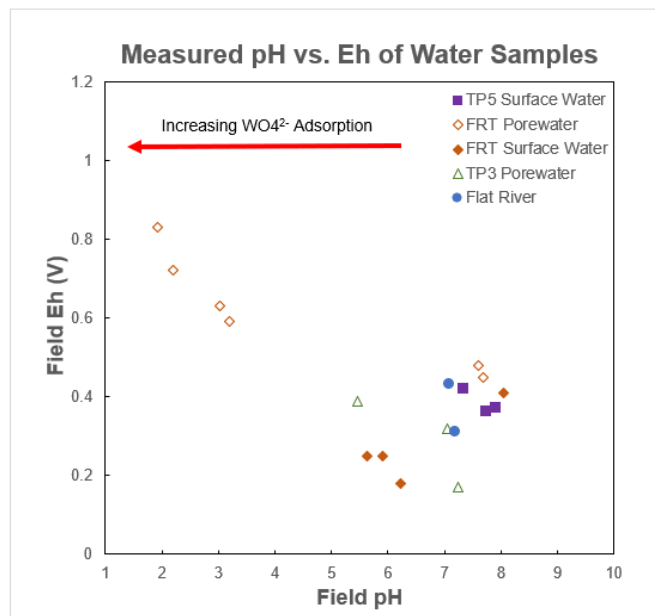


Figure 7. Eh v pH diagram for waters collected from Cantung tailings and Flat River.

5 Discussion

Reprocessing tailings is considered a more sustainable approach than opening new mines. When mining companies become insolvent, the mine may cease production and become a managed (or unmanaged) contaminated site. In the case of Cantung, the situation is complicated by the need to move the tailings from the impoundments that were constructed along the valley walls to a more geotechnically stable position. Other options have also been proposed, such as partially dewatered dry-stack storage. The generation of revenue from extracting the substantial amount of tungsten as well as the copper and gold from the tailings could be used to offset the costs associated with moving the tailings.

Characterization of the tailings is critical to design optimal reprocessing. Information of scheelite grain size and liberation is fundamental to improved gravity and

flotation design. The presence of significant amounts of pyrrhotite may also affect reprocessing and indicates that management of acidic drainage, especially if tailings are unsaturated, is required. Although tungsten is not regulated in mine effluent, understanding the mobility of a potentially hazardous element in the aquatic environment will provide useful information to regulators and communities.

6 Conclusions and future work

Results to date have shown that automated mineralogy is a useful technique when applied to tungsten tailings for quantifying modal mineralogy, measuring scheelite grain size and liberation, and mineralogically evaluating the potential for acidic drainage. The results indicated that although the relative proportions of minerals change from sample to sample, the ratio of sulfide (mostly pyrrhotite) relative to carbonate is always such that acid generation would be predicted. Field observations and previous characterization work (Mesh 2008) indicate that pH values in tailings pore waters and drainage are near neutral and there is a lag time for sulfide oxidation. However, the tailings released during the early years of mining directly into the river valley are highly oxidized with little pyrrhotite left and pore water pH values as low as 2. Clearly any design for future tailings disposal needs to prevent sulfide oxidation. The mobility of dissolved tungsten is known to be dependent on pH, which affects aqueous speciation and adsorption. Future work includes additional tailings characterization work, leach tests of current tailings, and those resulting from reprocessing experiments and a comprehensive study of co-existing water and tailings focused on understanding tungsten mobility.

References

- Bowman JR, Covert JJ, Clark AH, Mathieson GA (1985) The CanTung E Zone scheelite skarn orebody, Tungsten, Northwest Territories; oxygen, hydrogen, and carbon isotope studies. *Econ. Geol.* 80:1872-1895.
- Cui M, Johannesson KH (2017) Comparison of tungstate and tetrathiotungstate adsorption onto pyrite. *Chem Geol* 464:57-68
- Graedel TE, Gunn G, Espinoza LT (2014) Metal Resources, use and criticality. Chap. 1 in: Gunn G. *Critical Metals Handbook*, BGS-AGU-Wiley, 1-19.
- Kazamel BG, Leybourne MI, Jamieson HE, Falck H (2018) Factors Controlling Tungsten Mobility in Cantung Mine Tailings. *Yellowknife Geoscience Forum Abstract Volume* p. 108
- Koutsospyros A, Braida W, Christodoulatos C, Dermatas D, Strigul N (2006) A review of tungsten: from environmental obscurity to scrutiny. *J.Haz. Mat.* 136:1-19.
- Mohajerin TJ, Neal AW, Telfeyan K, Sasiharhan SM, Ford S, Yang N, Chevis DA, Grimm DA, Datta S, White CD, Johannesson KH (2013) Geochemistry of Tungsten and Arsenic in Aquifer Systems: A Comparative Study of Groundwaters from West Bengal, India, and Nevada, USA. *Water, Air, & Soil Pollution* 225.
- MESH Environmental (2008) Geochemical Characterization of the Cantung Mine Tailings, NWT. Report prepared for North American Tungsten

Geoenvironmental characterisation of the King River Delta: A combined geophysical, geochemical and mineralogical approach

Sibele C. Nascimento¹, Anita Parbhakar-Fox², Matthew J. Cracknell¹, Wei Xuen Heng³

¹Transforming the Mining Value Chain, ARC Industrial Transformation Research Hub, Centre for Ore Deposit and Earth Sciences (CODES), University of Tasmania.

²Senior Research Fellow, W. H. Bryan Research Centre, Sustainable Minerals Institute, University of Queensland

³School of Natural Sciences (Earth Sciences), University of Tasmania

Abstract. The Mount Lyell Mining and Railway company discharged nearly 95 Mt of tailings and 1.4 Mt of slag from its copper, gold and silver production into the Queen River from 1916 to 1994. Approximately 87.4 Mt of tailings has accumulated at the King River Delta. This research presents a geoenvironmental characterisation of the King River Delta that combines geophysical, geochemical and mineralogical data. Apparent resistivity and shear wave (V_s) profiles suggest the baseline of the tailings at 3–5 m depth. Low resistivity values (i.e., < 2 Ω -m) characterise the salt water intrusion, while resistivity values between roughly 5 to 12 Ω -m, below 15 m depth, suggests bedrock boundaries. Scanning electron microscope (SEM) analysis of sediments identifies pyrite, chalcopyrite, muscovite, quartz, chlorite, barite, and iron oxides in the tailings. Additionally, chemical analysis indicates high content of S and heavy metals (e.g., Fe, Cu, Co, Ni and Zn), which contribute to rapid acid formation and risk of metal leaching into the surrounded environment, confirmed by geochemical static tests.

1 Introduction

The Mount Lyell Mining and Railway Company, established in Queenstown in 1893, was the largest copper mining company on the west coast of Tasmania until 1994 (KoeHNken 1997). It produced over 1.3 Mt of

copper, 750 t of silver and 45 t of gold, which is equivalent to more than AU\$4 billion worth of metals in 1995 terms (McQuade et al. 1995).

A by-product of the extraction and concentration of these commodities were vast quantities of mine waste including approximately 53 Mt of waste rock, 97 Mt of sulfidic tailings and 1.4 Mt of slag. Tailings and slag were disposed into the Queen-King river system from 1916 to 1994 (Locher 1997) leading to acid and metalliferous drainage (AMD) generation at the river and environmental degradation, with Mt Lyell regarded as the most extreme example of AMD in Tasmania (Taylor et al. 1996). Currently these materials reside in overbank and river bottom sediments whereas 87.3Mt of tailings are stored within the delta (Figure 1) (Locher 1997). This research aims to establish the geoenvironmental characteristics of the King River Delta by combining geophysical, geochemical and mineralogical properties, which will further assist with reprocessing of tailings and rehabilitation planning of the Queen and King rivers and the King River Delta.

2 Methodology

Multi-channel analysis of surface waves (MASW) and DC resistivity were obtained in two parallel survey lines, displayed in Figure 2 (~ 400 m length). WinMASW was used to process the seismic data and resistivity was processed with RES2DINV.

Five trenches were dug for sediment and water sampling and further characterisation (Figure 2). The trenches were excavated with a shovel to ground water depth. Each trench was approximately 30–40 cm wide and 30–90 cm deep, depending on water table level. Between two and four sediment samples (depending on the trench depth), approximately 500 g each, were collected from each trench from different depths. A total of 18 sediment samples were collected.

Water quality measurements (i.e., pH) were taken in the field using calibrated portable devices. Samples were filtered (0.45 μ m PES filter) into 50 ml HDPE bottles, acidified with 1 ml of 1 % HNO_3 and transported in a cool box to for laboratory analysis using ICPMS to determine metal concentrations.

All analytical work was undertaken at the University of Tasmania laboratories. A Vanta handheld X-ray fluorescence (XRF) analyser was used for chemical

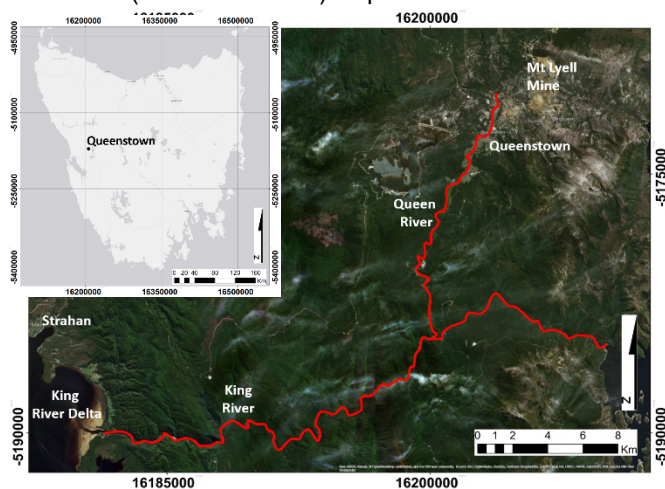


Figure 1. Location of study site in Western Tasmania and King River Delta

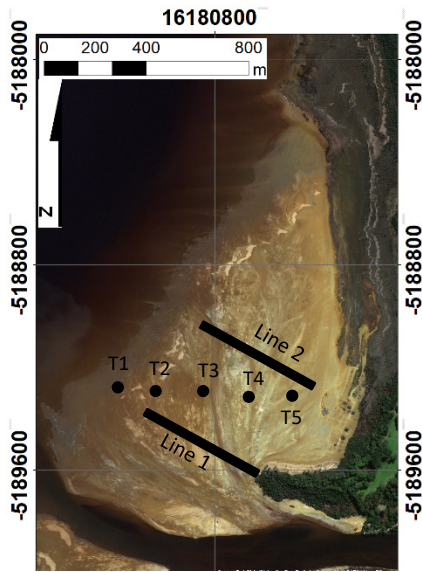


Figure 2. Trench locations and geophysics survey lines and ground traverse.

analyses of the sediments. Carbon, hydrogen, nitrogen and sulfur values were obtained using a Thermo Finnigan EA 1112 Series Flash Elemental Analyser. Static tests

(i.e., net acid generation (NAG) and paste pH tests) were undertaken to evaluate the acid producing potential of the sediments. For mineralogical characterisation, sediments were analysed using a Hitachi SU-70 field emission scanning electron microscope (FE-SEM).

Results and discussion

Geophysical survey

The Vs profiles indicate shear wave velocity of the tailings is less than 300 m/s for Line 1 (Figure 3) and less than 160 m/s for Line 2 classifying this material as dry sands according to Mavko (2005). All the profiles show a sudden

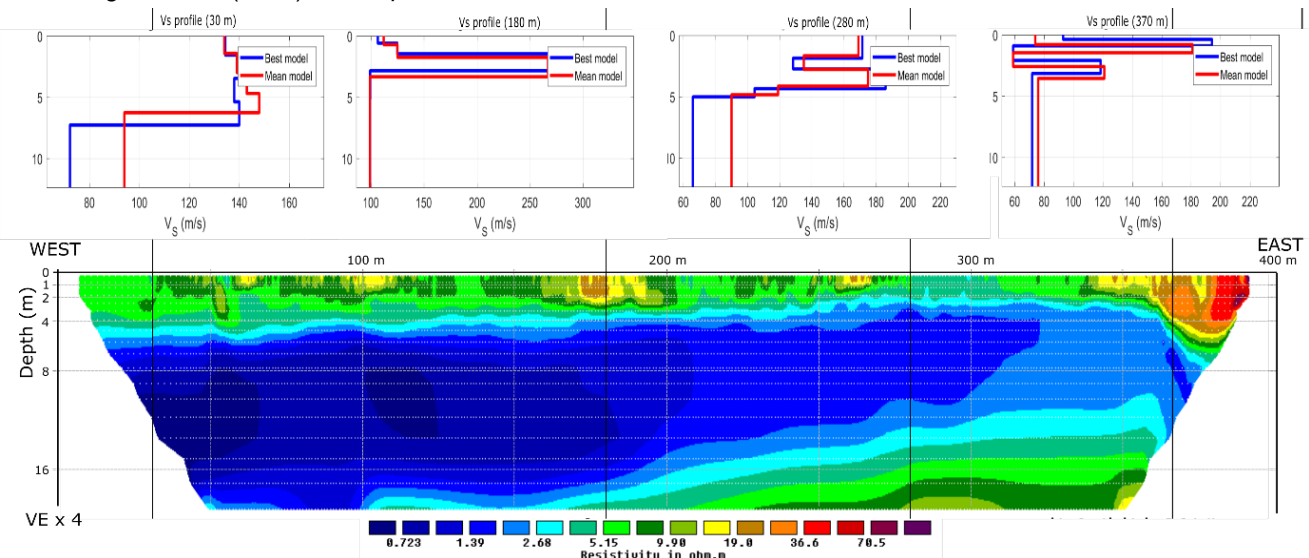


Figure 3. Modelled shear wave velocities and apparent resistivity carried out at Line 1.

decrease in seismic velocity between 3–8 m. This might indicate high pore water pressure at these depths (Telford et al. 1990) and likely saturation due to salt water intrusion. Below 10 m depth, the level of confidence is low and from this point onwards the seismic models are not reliable.

Apparent resistivity models (Figure 3) in the upper part of the profile (> 5 m) show a higher resistivity unit (> 20 $\Omega \cdot m$), indicating dry tailings. The underlying layer, from 5–15 m depth displays very low apparent resistivity values (i.e., < 2 $\Omega \cdot m$) suggesting this zone as saltwater intrusion (EM GeoSci 2018). Below 15 m, resistivity values increase to ~ 15 $\Omega \cdot m$, suggesting an interface with less porous materials, likely indicating bedrock.

A good correlation is observed between the Vs and apparent resistivity models and variations in the thickness of dry and saturated tailings is imaged. Preliminary interpretation classifies four layers. The topmost layer is dry loose tailings overlying wet loose tailings. Below this is the salt-water intrusion overlying bedrock.

3.2 Geochemical and mineralogical characterisation

The delta consists of layers of oxidized and un-oxidized tailings (Figure 4A), characterised by a typically bluish-grey coloured material and sandy texture, resulting from different flooding events at the King River. Damming of the King River in 1992 and cessation of dumping mine waste into the river in 1995 (Locher 1997) slowed the tailings supply in the delta leading to oxidation of the uppermost portion, creating a 20–30cm layer of reddish coloured tailings (Figure 4B).

Backscattered electron images indicate the presence of pyrite, chalcopyrite, iron oxides and sulphates, quartz, muscovite, chlorite, barite, rutile, florencite and carbonates in the tailings. Grains of liberated pyrite (Figure 5A) are detected on shallow sediments. In depth, liberated and euhedral pyrite crystals, encapsulated in quartz and chlorite were observed (Figure 5B). Element

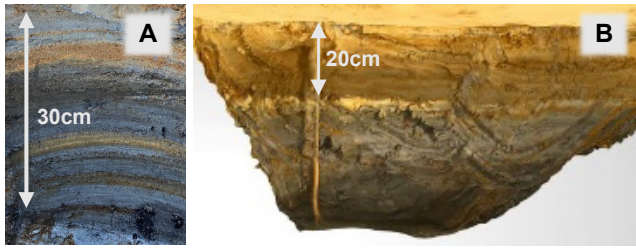


Figure 4. (A) Layers of oxidized and unoxidized tailings observed in the Delta and (B) 3D photogrammetric model (Agisoft Photoscan software) of a face of a trench with visible uppermost oxidized layer

mapping revealed these pyrite crystals as Co-bearing. Iron oxides rims and the presence of sulphate as rims and grains (Figure 5C), notably in the uppermost sediments, are indicators of tailings oxidation. Chalcopyrite grains were found associated mainly with muscovite, chlorite and quartz (Figure 5D).

Pore water collected from the trenches is acidic, ranging from pH 3.12–3.92. Chemical analysis reports high content of heavy metals, especially Fe (83.21–1109.63 mg/l), Cu (1.71–10.05 mg/l), Co (0.47–1.88 mg/l) and Zn (0.73–3.2 mg/l). These results suggest metals are being released within the delta instead of being absorbed into the sediment as consequence of the acid water (Osmond et al. 1998).

The delta tailings display high concentrations of Fe, Al, Cu and other transitional metals. Iron was found between 40,868–171,960 ppm while Al concentrations varied from 10,104–15,769 ppm and Cu content ranged from 373–3096 ppm. Other trace elements were also encountered in considerable concentrations such as Co (up to 505 ppm), Zn (up to 342 ppm) and Ni (up to 307 ppm). Copper concentration is observed to increase at depths below 20 cm, where fresh tailings are mostly present. Deleterious elements, such as As, were found in smaller concentrations (up to 50 ppm).

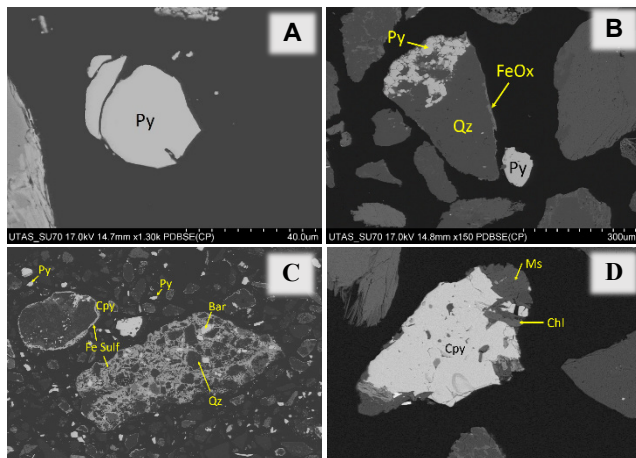


Figure 5. Backscattered electron images of (A) liberated pyrite, (B) encapsulated pyrite, (C) chalcopyrite and (D) iron sulphates. Abbreviations: Py, pyrite; Cpy, chalcopyrite; Ms, muscovite; Chl, chlorite; Qz, quartz; Bar, barite; FeOx, iron oxides; FeSulf, iron sulphate.

3.3 Geoenvironmental implications

Mineralogical and geochemical analyses show high metal content in the tailings and the presence of acid forming minerals (i.e., pyrite and chalcopyrite). Environmental concerns are clearly associated with the mine tailings, and the consequent release of their highly contaminating metal content (Martín-Crespo et al. 2018).

Geochemical static tests was performed in the samples as per Parbhakar-Fox et al. (2011) to predict acid formation of the tailings. Figure 6 indicates that all samples were potentially acid forming due to presence of S-bearing minerals (i.e., pyrite and chalcopyrite). The majority of samples will form acid rapidly on exposure, classifying them with a medium risk of ARD. A lag time and low risk of ARD is expected for sample 4 in trench 5 (T5S4). This sample has bluish-grey coloured unoxidized sediments. Encapsulated pyrite was found in this sample, which decreases the surface area for oxidation. Four samples reported high risk of ARD and immediate acid forming potential, two of these samples were collected from the uppermost oxidized layer (i.e., T1S1 and T2S1). Although these samples report lower S% (i.e., T1S1 = 1.58% and T2S1 = 0.93%), pyrite is typically liberated and finely grained, giving a large surface area available for oxidation. The deeper sample T4S4, returned the highest

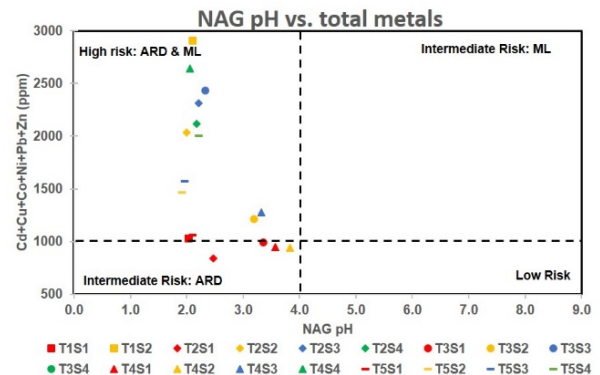


Figure 6. Classification of acid forming potential and lag-time to acid forming of trenches in the delta (PAF – potentially acid forming, ARD – acid rock drainage) (Parbhakar-Fox et al. 2011).

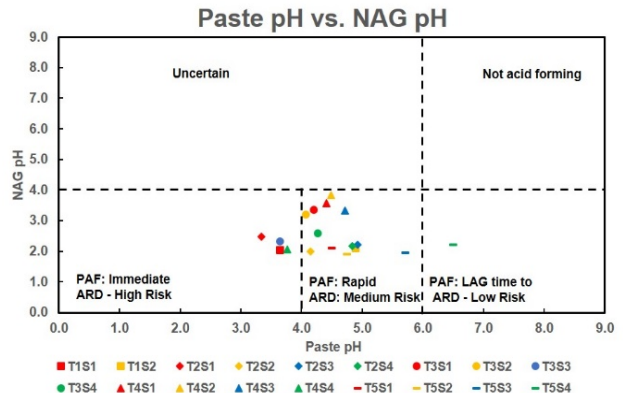


Figure 7. Modified Ficklin plot, adapted from Plumlee (1999), showing metals versus NAG pH for trenches in the delta (ARD – acid rock drainage, ML – metal leaching).

S content (i.e., S = 10.52%) and coarse particles of liberated pyrite thus supporting its classification in the high-risk field.

According to the modified Ficklin graphic (Figure 7), shallow samples (i.e., T2S1, T3S1, T4S1) were plotted as intermediate risk of ARD, indicating that top oxidized layer has lower metal leaching risk when compared to deeper sediments. The majority of samples returned high risk of ARD and metal leaching. Two samples with low pyrite content, T3S2 and T4S3 (S < 0.33%) are plotted in the high-risk field, indicating these samples are metal rich.

Further studies

This paper is part of the PhD project “Geo-environmental characterisation of historic mine tailings: Evaluating opportunities for reprocessing”. Further investigation is necessary to corroborate some of the assumptions made in this paper and for a better understanding of the tailings stored within the King River delta. For this, twenty trenches were excavated, and 100 samples collected within the delta. Similar analysis will be undertaken, and more characterisation techniques will be utilized (XRD, MLA, leach testing and LA-ICPMS) as well as the development of an automated sulphide alteration index.

The numerous tailings dumps and storage facilities around the world are likely to contain minable concentrations of valuable metals (Parbhakar-Fox 2016). For example, recent work has identified metal resources in regulated and monitored mine waste at Century Mine (Australia), Hellyer Gold Mine (Australia) and DRD Gold (South Africa). The current results of our research suggest that unregulated legacy dumps, such as those in the King River Delta and at other sites, e.g. Portman Bay (Gómez-García et al. 2015; Peña et al. 2013), can be evaluated for their metals reprocessing potential in the future.

Conclusions

Shear wave velocity and apparent resistivity geophysical models identified variations in tailings saturation towards the shoreline and constrain salt water and bedrock interfaces. The delta is formed by a top oxidized crust, composed mostly by liberated pyrite whilst deeper sediments have liberated and encapsulated pyrite. Iron oxide and sulphate rims are visible by backscattered images confirming the high oxidation at the uppermost layer. All the samples are acid forming at some extent and the high content of heavy metals at depth make this zone prone to metal leaching. Preliminary studies on pyrite texture, showed the direct influence of this parameter on acid formation as demonstrated by Parbhakar-Fox et al. (2011)

Acknowledgements

The ARC Research Hub for Transforming the Mining Value Chain (project number IH130200004) for supporting this project. Special thanks to David Cook,

Nathan Fox, Jay Thompson, Michael Roach, Samantha Lake and Laura Jackson (CODES, UTAS), Sandrin Feig, Ashley Townsend and Thomas Rodemann (CSL) for the guidance and assisting with the analysis.

References

- EM GeoSci, 2018, Typical Values for Rocks, DC Conductivity/Resistivity [online].
- Gómez-García, C., Martín-Hernandez, F., López García, J. Á., Martínez-Pagán, P., Manteca, J. I., and Carmona, C., 2015, Rock magnetic characterization of the mine tailings in Portman Bay (Murcia, Spain) and its contribution to the understanding of the bay infilling process: *Journal of Applied Geophysics*, 120:48-59.
- Koehnken, L., 1997, Mount Lyell remediation: final Report: Mount Lyell remediation research and demonstration program. Supervising scientist report, v. 126.
- Locher, H., 1997, Sediment transport in the King River, Tasmania. Mount Lyell Remediation Research and Demonstration Program. Supervising Scientist Report 120. .
- Martín-Crespo, T., Gómez-Ortiz, D., Martín-Velázquez, S., Martínez-Pagán, P., De Ignacio, C., Lillo, J., and Faz, Á., 2018, Geo-environmental characterization of unstable abandoned mine tailings combining geophysical and geochemical methods (Cartagena-La Union district, Spain): *Engineering Geology*, 232:135-146.
- Mavko, G., 2005, Conceptual overview of rock and fluid factors that impact seismic velocity and impedance: Retrieved, 11(11):2012.
- McQuade, C., Johnston, J., and Innes, S., 1995, Review of historical literature and data on the sources and quality of effluent from the Mount Lyell lease site: Supervising Scientist Report, v. 104.
- Osmond, D., Line, D., Gale, J., Gannon, R., Knott, C., Phillips, K., Turner, M., Coffey, S., Spooner, J., and Robillard, P., 1998, WATERSHEDSS: a decision support system for nonpoint source pollution control in predominantly agricultural watersheds.
- Parbhakar-Fox, A., 2016, Treasure from trash: how mining waste can be mined a second time: The conversation, <https://theconversation.com/treasure-from-trash-how-mining-waste-can-be-mined-a-second-time-59667>.
- Parbhakar-Fox, A. K., Edraki, M., Walters, S., and Bradshaw, D., 2011, Development of a textural index for the prediction of acid rock drainage: *Minerals Engineering*, v. 24, no. 12, p. 1277-1287.
- Peña, J. A., Manteca, J. I., Martínez-Pagán, P., and Teixidó, T., 2013, Magnetic gradient map of the mine tailings in Portman Bay (Murcia, Spain) and its contribution to the understanding of the bay infilling process: *Journal of Applied Geophysics*, 95:115-120.
- Plumlee, G. S., 1999, The environmental geology of mineral deposits: The environmental geochemistry of mineral deposits. *Society of Economic Geologists*. Part A, p. 71-116.
- Taylor, J. R., Weaver, T. R., McPhail, D. B., and Murphy, N. C., 1996, Characterization and impact assessment of mine tailings in the King River system and delta, Western Tasmania. Mount Lyell Remediation Research and Demonstration Program, Supervising Scientist Report 105
- Telford, W. M., Telford, W., Geldart, L., Sheriff, R. E., and Sheriff, R., 1990, *Applied geophysics*, Cambridge university press.

Carbon sequestration in ultramafic mine waste: potential for carbon neutral mining

Sterling S.S. Vanderzee, Gregory M. Dipple, Ian M. Power
The University of British Columbia, Vancouver, Canada

Abstract. The development and application of new technologies to reduce greenhouse gas (GHG) emissions and stabilize mine tailings will be beneficial for the mining industry and society. Ultramafic tailings can sequester carbon dioxide (CO₂) from the atmosphere and from industrial sources at ambient temperature and pressure if they contain highly reactive minerals such as brucite [Mg(OH)₂], certain hydrotalcites [Mg₆Fe₂(OH)₁₆Cl₂·4H₂O], and serpentine [Mg₃Si₂O₅(OH)₄]. The bulk dissolution of brucite and hydrotalcites, and mineral-surface dissolution of serpentine releases “labile magnesium” into tailings pore water which can then sequester CO₂ through the precipitation of cementitious magnesium carbonate minerals. In the process of sequestering CO₂ the cementitious minerals which are formed may stabilize the tailings and reduce the risk of a catastrophic tailings dam failure. We present mine planning tools to rapidly calculate labile magnesium abundance throughout a deposit by analyzing exploration whole rock data from drill core. Our analysis the Baptiste Nickel Deposit in Central B.C. suggests it has more than enough labile magnesium to potentially sequester all the CO₂ that would be produced by mining (11.4 tCO₂/kt rock mined, produced by haulage trucks). Furthermore, field observations and preliminary laboratory testing has indicated that carbonation can lead to cementation which may in turn stabilize stored tailings.

1 Introduction

Reducing greenhouse gas emissions and stabilizing mine tailings are important for the future of the mining industry and for society. The importance of stabilizing mine tailings is highlighted by recent events where the catastrophic failure of tailings dams resulted in loss of life and damage to the environment. Ultramafic tailings, commonly produced by nickel, diamond, platinum, and chromium mines, can potentially become stabilized when they react with carbon dioxide (CO₂) to form magnesium carbonate cement (Vanderzee et al., 2018). This can be accomplished through the exposure of the tailings to atmospheric and/or concentrated CO₂ from industrial flue gas. To make this process potentially economically viable, we must exploit the reactivity of “labile magnesium” and utilize whole rock analytical data from exploration to delineate its whereabouts within a mine.

We use the term labile magnesium to describe reactive “low-cost” magnesium cations that can be leached from tailings and into the pore water at ambient pressure and temperature. Sources of labile magnesium include the bulk dissolution of brucite {Mg(OH)₂} and hydrotalcite-group minerals such as iowaite {Mg₆Fe₂(OH)₁₆Cl₂·H₂O}

that are typically present in trace abundance in ultramafic tailings (Wilson et al., 2014). Another source of labile magnesium is mineral-surface leaching on the more abundant magnesium silicate minerals (e.g., serpentine {Mg₃Si₂O₅(OH)₄} (Thom et al., 2013). Here we consider 100% of the magnesium in brucite and hydrotalcites (pyroaurite), and 2.5% of the magnesium in serpentine to be labile (Vanderzee et al., 2019). Once released into the pore water of tailings, the labile magnesium ions can react with dissolved CO₂ species such as HCO₃⁻ to precipitate magnesium carbonate minerals such as nesquehonite {MgCO₃·3H₂O}, dypingite {Mg₅(CO₃)₄(OH)₂·5H₂O} and hydromagnesite {Mg₅(CO₃)₄(OH)₂·4H₂O}; (Wilson et al., 2014).

This process, termed “carbon mineralization”, occurs naturally at the Mount Keith nickel mine in Western Australia (Wilson et al., 2014). Without any intervention or costs, 11% of Mount Keith’s CO₂ emissions were offset due to the uptake of CO₂ from the atmosphere by labile magnesium-bearing tailings. Furthermore, reactive transport models infer that small changes in tailings management practices could allow the labile magnesium to fully react and offset up to 60% of the mine’s emissions (Wilson et al., 2014).

One of the challenges with applying this process at a mine site to stabilize tailings and significantly offset greenhouse-gas emissions is that the labile magnesium content within a single mineral deposit, and therefore within mine tailings, is highly variable due to the inherent geological variability. The abundance and spatial distribution of labile magnesium throughout a mineral deposit can be estimated from mineral abundance data. However, this technique is time and cost intensive and is not practical for mine planning reconnaissance studies that can require a mineral abundance analysis of several tens of thousands of samples. Alternatively, the problem can be solved by using estimations of mineral abundance that can be rapidly and inexpensively computed from whole-rock analytical data that are routinely collected on drill core as part of exploration.

In this paper, the authors apply the projection method of computing mineral abundance (Thompson, 1982; Raudsepp et al., 1999) to the whole-rock analytical data from exploration drill core from the Baptiste nickel deposit (MINFILE 093K 116; BC Geological Survey, 2018; Britten, 2017), which is part of the Decar nickel district in central British Columbia (BC) Canada.

A concept illustration showing how labile magnesium can be targeted at a mine site to help offset CO₂ emissions and stabilize tailings through carbon mineralization is shown in Figure 1. It should be noted that although the figure shows two options for promoting

the cement forming reactions by injecting air and/or flue gas into coarse and permeable tailings, other options exist. These include, but are not limited to, passive reaction with atmospheric CO₂ (naturally occurring at Mount Keith nickel mine), and the utilization of a CO₂-bearing gas in hydrometallurgical processes. It should also be noted that the kinetics of this process are

enhanced by promoting the supply rate of CO₂ to the tailings if labile magnesium is available. Therefore, it is intended for tailings that have sufficient buffering capacity relative to sulphide content such that acid rock drainage is not produced by increasing the exposure of tailings to atmospheric oxygen.

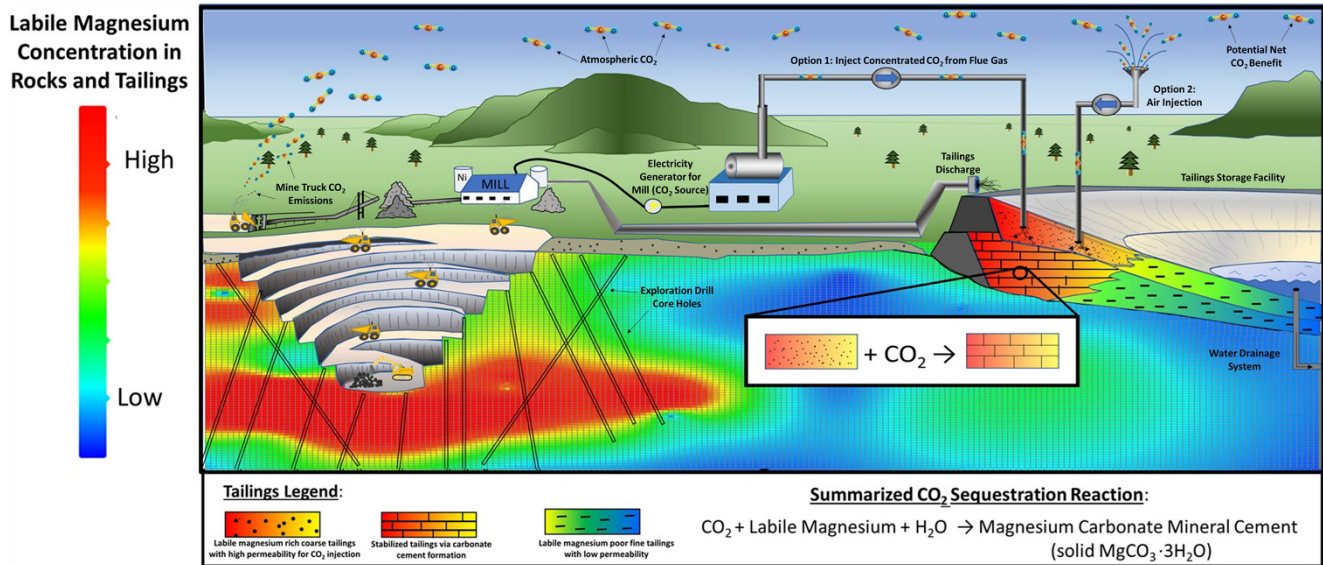


Figure 1. Concept illustration of promoting carbon mineralization at a mine site with labile magnesium-rich, and sulphide-poor tailings.

2 Results and implications

2.1 Calculating labile magnesium abundance and CO₂ sequestration potential.

Brucite and serpentine are the predominant sources of labile magnesium in the Baptiste nickel deposit. Accurate estimation of their abundance is therefore important for estimating labile magnesium abundance. A comparison between the measured and calculated abundance of brucite and serpentine is shown in Figure 2. The first 10 samples were used to calibrate the projection model and an additional 20 blind samples were analyzed after the projection model was built to test its accuracy.

This projection model calculates the abundance of model minerals that were selected by X-ray diffraction studies on 10 representative Baptiste samples. The projection model uses the whole-rock chemical data as input and then calculates the abundance of the model minerals that best explains the whole-rock chemical data (Raudsepp et al., 1999). Figure 2 shows that the projection model could provide useful mineralogical calculations. Where the projection model produced negative computed brucite abundances (1477 samples out of 7604), the values were set to zero. These negative numbers are an indication that there are minerals (trace or major) present in the sample that were not accounted for in the model.

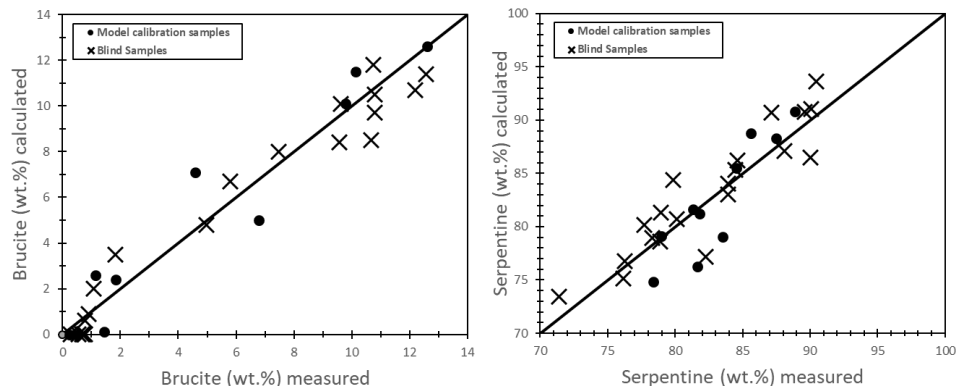


Figure 2. The measured abundance of brucite (left) and serpentine (right) versus the abundance calculated by the projection method (after Vanderzee et al., 2019).

The validated projection model was applied to 7,604 whole-rock assays from the Baptiste deposit to assess the heterogeneity in mineralogy and therefore heterogeneity in labile magnesium content. Histograms of calculated brucite and serpentine content within the Baptiste deposit are shown in Figure 3. Although more than 25% of the deposit is calculated to have no brucite, 75% contains brucite ranging from trace amounts to over 10 wt.%. Serpentine dominates the mineralogy of all samples.

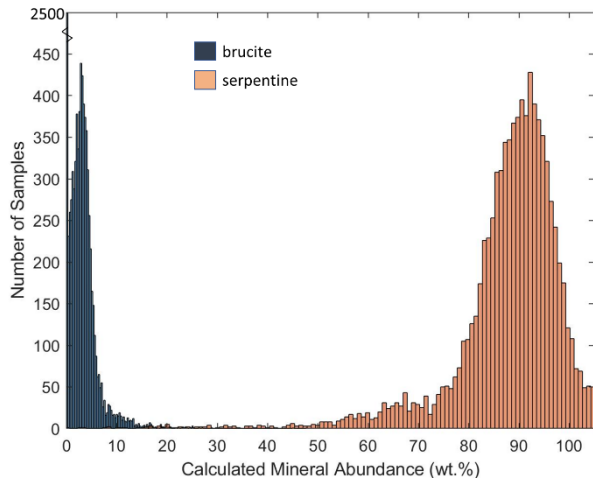


Figure 3. Histogram of the abundance of brucite and serpentine calculated by the projection model across the Baptiste nickel deposit. Samples described as waste rock or dikes in the geochemistry dataset were omitted. The mean brucite and serpentine content is 1.8 wt. % and 88.8 wt. % respectively (after Vanderzee et al., 2019).

The total labile magnesium content estimated from calculated brucite and serpentine content is plotted as weight percent MgO in Figure 4. This provides a preliminary assessment of the carbon sequestration capacity of mine tailings. To estimate greenhouse-gas emissions from mine operations, production data from the Mount Keith nickel mine in Western Australia, a serpentinite-hosted nickel deposit was used. At Mount Keith, natural gas is used to generate electricity for the ore processing facility. This accounted for ~66% of their CO₂ emissions and diesel-powered mining haul trucks account for the remaining ~34% (WMC Resources Ltd., 2002). In total, the mine produced 33.6 t CO₂/kt rock mined (Wilson et al., 2014); therefore, mines that use renewable or low-carbon energy sources still need to sequester 11.4 t CO₂/kt rock mined to be GHG neutral due to emissions from the haul truck fleet. From these data, it can be estimated that an average of 1.3 wt. % labile MgO is sufficient to make an open-pit nickel mine carbon neutral assuming hydroelectricity is used, and 3.9 wt. % labile MgO if natural gas is used for electricity generation. The Baptiste nickel mine is located near hydroelectric infrastructure; therefore, an estimated average of 1.3 wt. % labile MgO would provide sufficient capacity for carbon-neutral mining. Figure 4 shows that the projection model calculations give an average labile magnesium content of 2.3 wt. %. This suggests that the Baptiste deposit has more than enough carbon

sequestration capacity from labile magnesium to become a carbon neutral mine. Finally, if carbon mineralization efforts are focused on the most labile magnesium-rich tailings, only 30% of the tailings need to react with CO₂ to make the Baptiste mine carbon neutral over its lifetime (Figure 5).

These results may be typical of serpentinite-hosted nickel deposits. To help target the labile magnesium-rich areas of mineral deposits for carbon mineralization purposes, the authors propose using exploration geochemical data to make mineral abundance computations so that 3-D maps of labile magnesium (Figure 6) can be incorporated into the mine plan.

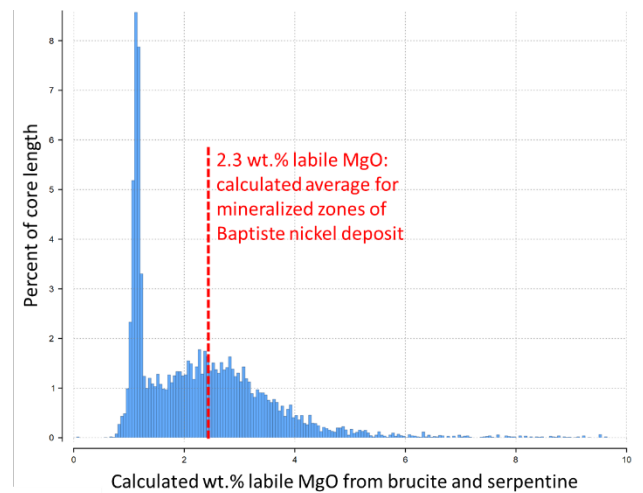


Figure 4. Histogram of the calculated labile magnesium content of drill core from the Baptiste nickel deposit (after Vanderzee et al., 2019).

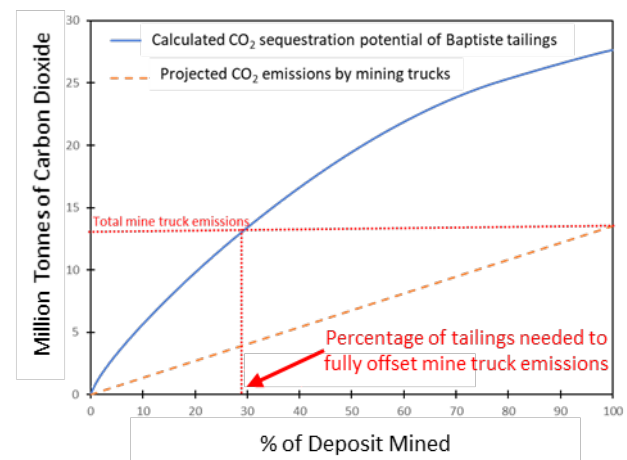


Figure 5. The projected CO₂ emission from nickel mining versus the percentage of the deposit that has been mined. The authors assume 1.8 Gt of rock will be mined as this represents the indicated reserve of the Baptiste deposit (FPX Nickel Corp., 2018). The solid line represents the potential rate of carbon sequestration if the most labile magnesium (MgO) rich zones are prioritized (after Vanderzee et al., 2019).

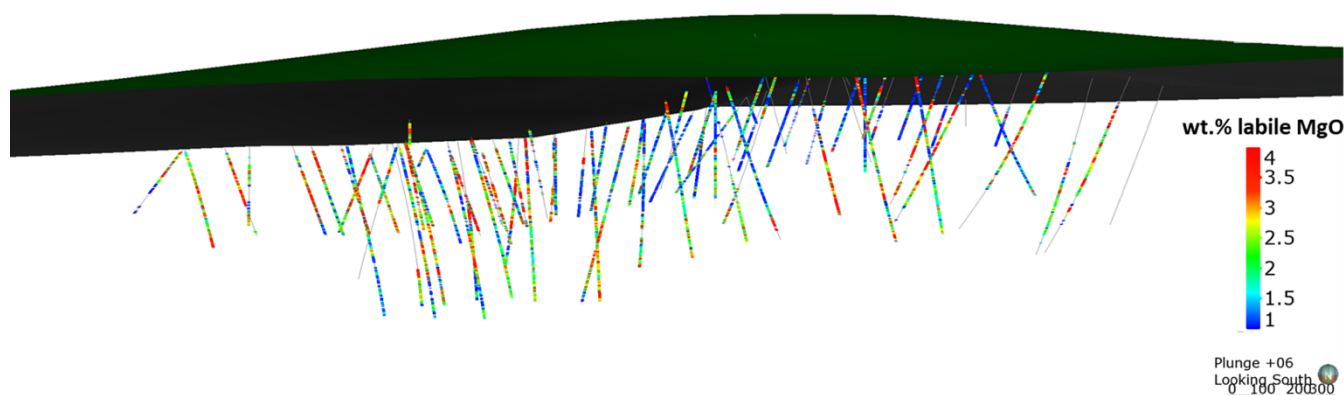


Figure 6. Computed labile magnesium abundance (in wt. % MgO) in mineralized drill core sections of the Baptiste nickel deposit, central British Columbia. Waste rock sections are shown in grey and were excluded from labile magnesium computations (after Vanderzee et al., 2019).

3 Conclusions and Future Work

Our calculations suggest that the Baptiste nickel deposit contains enough labile magnesium to potentially sequester all the CO₂ that would be produced by its mining trucks (11.4 t CO₂/kt rock mined) through carbon mineralization. This would make Baptiste GHG neutral if it used hydroelectric power, which is likely to be the case in BC, and carbon mineralization may stabilize the tailings at the same time. To improve, or at least complement, the accuracy of the labile magnesium estimations, other methods of computing mineral abundance can be applied to Baptiste. These methods include linear programming (Gordon and Dipple, 1999), phase equilibria (Connolly, 2005) and MINSQ (Herrmann and Berry, 2002). The next steps include thorough geotechnical testing on cemented tailings and investigating methods to further accelerate the reaction rates by promoting the transport of CO₂ into the tailings and conducting larger field-scale experiments. If the laboratory work can be verified at the field scale, carbon mineralization could prove to be of potential benefit to the mining industry and society.

Acknowledgements

In addition to FPX Nickel Corp., the authors acknowledge Geoscience BC and the Natural Sciences and Engineering Research Council of Canada for financial support of this project.

References

- BC Geological Survey (2018) MINFILE BC mineral deposits database. BC Ministry of Energy, Mines and Petroleum Resources, BC Geological Survey. <http://minefile.ca/> Accessed 8 November 2018
- Britten, R (2017) Regional metallogeny and genesis of a new deposit type-disseminated awaruite (Ni Fe) mineralization hosted in the Cache Creek terrane. *Economic Geology* 112 (3): 517-550.
- Connolly, JAD (2005) Computation of phase equilibria by linear programming: a tool for geodynamic modeling and its application to subduction zone decarbonation. *Earth and Planetary Science Letters* 236:524–541.
- FPX Nickel Corp. (2018) Developing Canada's next nickel district. FPX Nickel Corp. <https://fpxnickel.com/wp-content/uploads/2017/08/FPX-Nickel-Corporate-Presentation.pdf>

- Accessed 8 November 2018
- Gordon, TM. and Dipple, GM (1999) Measuring mineral abundance in skarn. II. A new linear programming formulation and comparison with projection and Rietveld methods. *The Canadian Mineralogist* 37:17–26.
- Harrison, AL, Dipple, GM, Power, IM and Mayer, KU (2015) Influence of surface passivation and water content on mineral reactions in unsaturated porous media: implications for brucite carbonation and CO₂ sequestration. *Geochimica et Cosmochimica Acta* 148:477–495.
- Herrmann, W and Berry, RF (2002) MINSQ – a least squares spreadsheet method for calculating mineral proportions from whole rock major element analyses. *Geochemistry: Exploration, Environment, Analysis*, 2:361–368.
- Raudsepp, M, Pani, E, Dipple, GM (1999) Measuring mineral abundance in skarn.1. The rietveld method using x-ray powder diffraction data. *The Canadian Mineralogist* 37:1-15.
- Thompson, JB, Jr. (1982) Reaction space: an algebraic and geometric approach. *Characterization of Metamorphism through Mineral Equilibria; Reviews in Mineralogy and Geochemistry* 10:33–52.
- Thom, JGM, Dipple, GM, Power, IM and Harrison, AL (2013) Chrysotile dissolution rates: implications for carbon sequestration. *Applied Geochemistry* 35 244–254.
- Vanderzee, SSS, Power, IM, Dipple, GM and Bradshaw, PMD (2018) Carbon mineralization in ultramafic tailings, central British Columbia: a prospect for stabilizing mine waste and reducing greenhouse gas emissions. *Geoscience BC Summary of Activities 2017: Minerals and Mining* 1 109–112.
- Vanderzee, SSS, Dipple, GM and Bradshaw, PMD (2019) Targeting highly reactive labile magnesium in ultramafic tailings for greenhouse-gas offsets and potential tailings stabilization at the Baptiste deposit, central British Columbia. *Geoscience BC Summary of Activities 2018: Minerals and Mining* 1 109–116.
- WMC Resources Ltd. (2002) WMC Resources Ltd Sustainability Report 2002; WMC Resources Ltd. https://www.bhp.com/-/media/bhp/documents/investors/reports/2002/wmc_sustainability_y2002.odf?la=en Accessed 8 November 2018
- Wilson, SA, Harrison, AL, Dipple, GM, Power, IM, Barker, SLL, Mayer, KU, Fallon, SJ, Raudsepp, M and Southam, G (2014) Offsetting of CO₂ emissions by air capture in mine tailings at the Mount Keith Nickel Mine, Western Australia: rates, controls and prospects for carbon neutral mining. *Journal of Greenhouse Gas Control*, 25:21–140.

Environmental & social maturity as a new concept for self-assessment of best practice in a mining context

Keiran Doyle

Camborne School of Mines, Penryn, UK

Olga Sidorenko

University of Eastern Finland, Finland

Abstract. Significant industrial and mining incidents have motivated widespread studies into the relationship between safety culture and the incidence of workplace accidents. Safety culture maturity has been used to develop a tool that enables organisations to self-assess their overall safety performance. In modern day mining operations, risks are also evaluated in terms of environmental and social (E&S) impacts, which is built into mine planning. In this work, we apply the principles of safety maturity to E&S factors to develop a novel approach to cultural maturity, allowing companies to self-scrutinize their operational practices from an E&S perspective. The culture models each comprise 5 levels that progressively increase in maturity, with the goal being to improve standards by implementing the criteria provided at each stage, based on factors such as community involvement, employment opportunities, energy use, etc. The case studies used to develop the model are located in Bosnia and Herzegovina where several mines recommenced operations recently following conflict in the region. This was chosen to consider the specific, complex challenges that are most influential in earning an SLO, and it is predicted that the outcome of a mining project is primarily influenced by the level of trust between the company and communities.

1 Introduction

Mining plays a major role in meeting the world's resource demands, with operations taking place across 6 continents, the largest of which being situated in countries such as China, Australia, South Africa, etc. Europe has a wealth of proven mineral potential (BRGM 2016), but very few of these prospects are feasible for large companies to exploit due to their small size & grade, close proximity to densely-populated settlements, and land use & tenement constraints. Obtaining social acceptance from the surrounding populations is difficult to achieve when they are led to believe that the risks associated with a mining operation outweigh the benefits, opting for the 'NIMBY' (Not in my back yard) attitude. Public perceptions of mining can also be adversely affected by past accidents that have resulted in loss of life and capital, which creates further difficulties in securing a social licence to operate from community stakeholders. So, establishing trust and rapport between companies and local populations, understanding their requirements and frequently communicating relevant updates are essential factors for maintaining strong relationships

during long term mining operations.

Safety culture has been the common denominator in a number of major industrial and mining incidents, including notably the BP Texas City refinery explosion, claiming 15 lives and injuring a further 180. The official investigation report concluded that the incident "was caused by organisational and safety deficiencies at all levels of the BP corporation... the extent of the serious safety culture deficiencies was further revealed when the refinery experienced two additional serious incidents just a few months after the disaster..." (CSB 2007). So, ensuring that an effective safety management system is implemented with a high level culture underlying those measures can considerably reduce the chance of major accidents occurring, as well as mitigating risks to a level that is as low as reasonably practicable.

2 The development of safety culture maturity

Early studies into safety culture established that employees develop their own perceptions of occupational safety based on the working environment that is significantly influenced by factors such as the level of management commitment to safety (Zohar 1980). The International Nuclear Safety Advisory Group (1991) first addressed safety culture as a concept and subsequently produced guidance documentation on how organisations may self-assess and continuously improve their safety best practice from a cultural perspective. The report defines safety culture as "...that assembly of characteristics and attitudes in organisations and individuals which establishes that, as an overriding priority, nuclear plant safety issues receive the attention warranted by their significance" (International Atomic Energy Agency 1991).

Hudson et al. (2000) reviewed the link between intrinsic motivation and safety culture, and found that the effects of a highly motivated workforce are; (a) less requirement for sites to dedicate time to occupational safety as every employee understands the importance of personal safety, and (b) more time being allowed for performance optimisation, in turn generating further profit while maintaining high safety standards.

The UK Coal Safety Way model was tested at a number of deep, surface and underground coal mines in 2011, which provided some insight into the culture of the mines in question, and allowed the authors to develop action plans for future improvement (Foster and Houlst 2011; 2013). This study showed that when attempting to

Resilient: High quality, integrated safety management is a way of life...

- Site-wide involvement in safety-related decisions and changes
- Risk assessment integral to all processes
- Comprehensive internal & external auditing
- Fully integrated communication

Enhanced: Company takes ownership of safety on their site...

- Employees and management work together on safety
- Training is high quality and comprehensive
- Safety meetings & discussions are thorough and decisive
- Risk assessments are regularly carried out

Preventative: Culture revolves around meeting compliance criteria...

- More safety-related discussions take place
- Emphasis on prevention of incidents
- Planned audits and regular monitoring
- Information from incidents is shared

Reactive: Incidents are investigated after they occur...

- Tends to be a blame culture
- Few meetings take place
- Limited communication
- Monitoring for compliance only

Simplistic: Mining is inherently unsafe, and always will be...

Figure 1. The safety culture maturity model applied to mining, comprising 5 stages of increasing maturity with associated criteria that should be met in order to make improvements in overall occupational safety culture. Edited from Anglo American Plc 2010; Foster and Hault 2011; 2013; The University of Queensland 2008.

improve the safety culture of an organisation, there is no 'one size fits all' model; each site or organisation should be investigated on a case-by-case basis. It is also important to consider that not all organisations will have the resources to make large steps towards high maturity, so areas for improvement should always be prioritised (Foster and Hault 2011; 2013).

In summary, occupational safety management is strongly influenced by the existing safety culture of the organisation, demonstrated by the prevailing attitudes and perceptions of the workforce, supervisory team and management towards safety issues (Glendon and Stanton 2000; Guldenmund 2000; International Atomic Energy Agency 1991). High levels of workplace culture can be defined by consistent enforcement and encouragement from managers towards employees regarding safety, freedom for employees to voice safety issues to management and supervisors, and regular meetings involving members from each hierarchical level ensuring fair representation and equal opportunity, (International Atomic Energy Agency 1991; Niskanen 1994; Simard and Marchand 1994; Zohar 1980). From the 1990's to present, the concept of safety culture maturity has been developed to suit various organisations and industries, moving from a model comprising 3 steps

from dependent to interdependent, to 5 levels from pathological to generative (Anglo American Plc 2010; Fleming 2001; Fleming and Lardner 1999; Hudson 2003; 2007; Hudson et al. 2000; The University of Queensland 2008; see Fig. 1). Later studies have utilised the 5 stage maturity model to assess safety culture in mining (Bascompta et al. 2018; Foster and Hault 2011; 2013; Stemn et al. 2019), coming to similar conclusions that management commitment to safety, effective site-wide communication, integrated safety management systems and safety focused meetings can all promote improvements in safety maturity. However, the principles of cultural maturity have not yet been applied to environmental and social aspects, so it is vital to first understand the main factors that define environmental and social sustainability, in order to establish appropriate requirements for each maturity level.

3 Environmental & social sustainability

The requirements of local communities affected by mining operations are a crucial consideration for companies assessing project feasibility. These "social stakeholders" have significant leverage in preventing projects from initiating, meaning a strong company-community relationship must be established before operations commence, thereby earning a social licence to operate (SLO). The expectations of the local community and stakeholders often exceeds the requirements set by law, meaning companies must go 'beyond compliance', because serious economic implications can be felt by those who do not meet the terms of the SLO (Gunningham et al. 2004). Horsely et al. (2015) stated 5 important sustainability cornerstones; financial, human, natural, social and physical. When mining operations commence in a populated region, these sources can be affected positively or negatively depending on the company's approach to sustainable practice. Kemp (2009) pointed out that mining companies are generally well resourced to meet community requirements, however progress in this respect is commonly hindered by corporate decision-making and governance that is positioned towards increasing production.

Hodge (2014) identified that the accelerating development of global communication channels are giving local communities a greater voice with regard to mining-related social issues. Walsh et al. (2017) found that public perceptions are negatively affected by a lack of consistent, two-way communication. The risk of difficulties arising during public consultation always exists, tends to vary with location, and can become a detriment to decision making if not carefully managed.

Therefore, establishing strong relationships early with communities, and demonstrating transparency in information disclosure throughout, can lead to greater trust between parties (Gunningham et al. 2004; Grubert 2018; Hodge 2014; O’Faircheallaigh 2010; Walsh et al. 2017).

The effective management and mitigation of E&S impacts in mining is primarily dictated by the existing attitudes towards the environment and communities by the operating company. So, those organisations that encourage sustainable working practices and open dialogue with local populations are demonstrating a high level of E&S maturity. By providing a novel tool that can assist other companies in understanding their own level of maturity, clear tasks and objectives can be set out that contribute to improving their E&S culture in existing and future mining operations.

4 E&S culture maturity model

Since safety culture has been shown to be an important leading indicator of H&S-related incidents, it would be reasonable to infer that the nature of environmental-related accidents and social-related conflicts can be

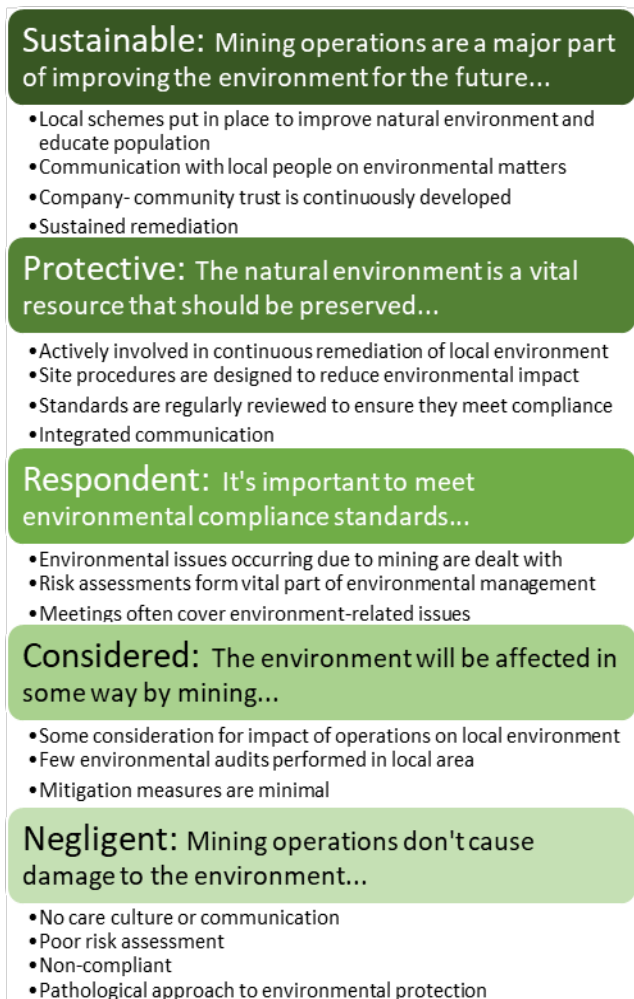


Figure 2. Environmental maturity model, with five stages which gradually improve in terms of environmental management, designed to inform best practice from a mining perspective.



Figure 3. Social maturity model, with five stages which represent systematic development in social management standards, advising companies on best practice.

influenced to an extent by a company’s socio-environmental culture, defined as the prevailing attitudes and perceptions of management and employees towards occupational risks and hazards that have direct and indirect implications for local & regional communities, authorities and ecosystems.

‘Negligent’ companies lack effective communication regarding environmental matters, little to no compliance with environmental standards, and minimal emphasis on environmental protection. Moderate to high maturity organisations (‘Considered’ to ‘Respondent’) demonstrate more consideration for the potential environmental impact of operations, carry out systematic environmental risk assessments and monitoring activities and meetings more regularly discuss environmental concerns. Companies at the highest tiers of environmental culture, ‘Protective’ and ‘Sustainable’ respectively, consider environmental protection to be a high priority by implementing the majority of community requests, showing commitment to remediation throughout the mine life, and supporting outreach and education programmes for local people (Fig. 2).

The social culture maturity model is similar in structure (Fig. 3), but instead it considers the typical features of a company’s social management system. ‘Inattentive’ and

'Inconsistent' companies demonstrate poor communication, a passive approach to dealing with local concerns and minimal compliance. 'Planned' organisations will consider potential social impacts in more depth during feasibility studies, carry out internal management meetings dedicated to social issues and regularly collaborate with community representatives. 'Integrated' and 'Entrusted' companies go beyond compliance, offer employment to local people, helping to develop personal skills whilst boosting economic growth. The strong relationships sustained throughout the mine life ensure conflict risk is reduced, and that disagreements are resolved swiftly. The model is designed to inform companies of best practice when working with local populations, and how a collaborative management style can accelerate the process of earning an SLO.

Table 1. Main factors informing environmental & social maturity criteria, tailored to a mining context.

Environmental	Social
1a: Policy & regulations	1a: Policy & standards
1b: Environmental impact assessment	2a: Corporate social responsibility
2a: Risk assessments	2b: Social impact assessment
2b: Hazard monitoring	3a: Community dialogue & decision-making
3a: Incident analysis & responsibility	3b: Outreach programmes
3b: Emergency measures	4a: Local employment opportunities
4a: Energy use	4b: Local education prospects
5a: Mine waste management	5a: Infrastructural investment
5b: Air quality management	6a: Conflict management
6a: Reclamation	

5 Conclusion

The principles of safety culture maturity have been useful for providing companies with guidance to improve their operating standards and practices. As mining often has positive and negative implications for environmental and social conditions, it is important to understand whether a company has the necessary level of maturity in order to make constructive changes. The optimal approach set out by the E&S culture maturity model is to operate in an environmentally sustainable way, where communities are entrusted with making decisions on issues that have effects on their quality of life. The journey towards high level maturity is guided by E&S management criteria (see Table 1), ensuring that each step up the maturity ladder is achievable regardless of company size or resources.

Acknowledgements

This paper was produced in partnership with the H2020 IMP@CT project, which has received funding from the EU Horizon 2020 research and innovation programme

under grant no 730411.

References

- Anglo American Plc (2010) Detailed Journey Workbook, in A3 Safety Risk Management Process Training Material. London.
- Bascompta M, Sanmiquel L, Vintro C, Rossell JM, Costa M (2018) Safety culture maturity assessment for mining activities in South America. *Work* 61:125–133.
- BRGM (2016) Minerals4EU. <http://minerals4eu.brgm-rec.fr/minerals4EU/>. Accessed: 15 February 2019
- CSB (2007) Investigation Report for BP Texas City Refinery Explosion.
- Fleming M (2001) Safety culture maturity model. Edinburgh. ISBN: 0717619192
- Fleming M, Lardner R (1999) Safety culture – the way forward. *The Chem Eng*, 16–18.
- Foster P, Hoult S (2011) Development and Use of a Safety Maturity Model as a Safety Assurance Tool in UK Coal Operations. In ICSMRI.
- Foster P, Hoult S (2013) The Safety Journey: Using a Safety Maturity Model for Safety Planning and Assurance in the UK Coal Mining Industry. *Mineral* 3:59–72.
- Glendon AI, Stanton NA (2000) Perspectives on safety culture. *Safety Sci* 34:193–214.
- Grubert E (2018) Relational values in environmental assessment: the social context of environmental impact. *Curr Opin Env Sust* 35:100–107.
- Guldenmund FW (2000) The nature of safety culture: a review of theory and research. *Safety Sci* 34:215–257.
- Gunningham N, Kagan RA, Thornton D (2004) Social License and Environmental Protection: Why Businesses Go Beyond Compliance. *Berk Law Schol Repos* 29(2):307–342.
- Hodge RA (2014) Mining company performance and community conflict: moving beyond a seeming paradox. *J Clean Prod* 84:27–33.
- Horsley J, Prout S, Tonts M, Ali SH (2015) Sustainable livelihoods and indicators for regional development in mining economies. *Extrac Indus Soc* 2(2):368–380.
- Hudson P, Parker D, Lawton R, Verschuur WLG, Van der Graaf GC, Kalf J (2000) The Hearts and Minds Project: Creating Intrinsic Motivation for HSE. In SPE International Conference on Health, Safety and the Environment.
- International Atomic Energy Agency (1991) Safety Culture: A report by the International Nuclear Safety Advisory Group.
- Kemp D (2009) Mining and community development: Problems and possibilities of local-level practice. *Community Dev J* 45(2):198–218.
- Niskanen T (1994) Safety climate in the road administration. *Safety Sci* 17(4):237–255.
- O'Faircheallaigh C (2010) Public participation and environmental impact assessment: Purposes, implications, and lessons for public policy making. *Environ Impact Asses* 30(1):19–27.
- Simard M, Marchand A (1994) The behaviour of first-line supervisors in accident prevention and effectiveness in occupational safety. *Safety Sci* 17:169–185.
- Stemn E, Bofinger C, Cliff D, Hassall ME (2019) Examining the relationship between safety culture maturity and safety performance of the mining industry. *Safety Sci* 113:345–355.
- The University of Queensland (2008) Minerals Industry Risk Management Maturity Chart. Brisbane.
- Walsh B, van der Plank S, Behrens P (2017) The effect of community consultation on perceptions of a proposed mine: A case study from southeast Australia. *Resour Policy* 51:163–171.
- Zohar D (1980) Safety Climate in Industrial Organizations: Theoretical and Applied Implications. *J Appl Psychol* 65(1):96–102.

Re-thinking the concept of small-scale mining for a European social context

Olga Sidorenko, Rauno Sairinen
University of Eastern Finland

Kathryn Moore
University of Exeter, UK

Abstract. In an attempt to secure access to minerals, European strategy includes the development of new models to mine metal and mineral deposits, in particular by means of small-scale operations. However, the application of traditional thinking and definitions of small-scale mining to a European concept of small-scale mining operations are problematic. The majority of existing research around small-scale operations refers to artisanal mining (Hilson and McQuilken 2014; Lahiri-Dutt 2018; Milanez and de Oliveira 2013), which occurs mostly in developing countries. Meanwhile, the discourse around social sustainability of mining operations is largely oriented to large-scale mining. An analysis of published literature has been undertaken in order to define the limiting characteristics of the term “small-scale mining” to modes of mining other than artisanal. Subsequently, we consider these limits in the context of strategy concerning the extractive industries, in order to re-conceptualize small-scale mining. This will enhance the precision of European small-scale mining discourse and avoid any ambiguity of definitions. We develop the concept of modern non-artisanal small-scale mining, which utilises modern industrial best practice standards and technological innovation with associated smaller workforces.

1 Introduction

Over the last decade, the European Union has articulated that its stability and the competitiveness of its economy are dependent on the import of raw materials, in some cases from vulnerable supply chains. In 2008, the European Commission (EC) launched The Raw Materials Initiative, which set a framework for more reliable and secure access to raw materials. The EC identified mining scenarios that have the potential to contribute to raw materials production in Europe: mining operations at greater depths, mining of non-conventional surface deposits and mining of small deposits (Strategic Implementation Plan 2013). Further, in 2011, the EC issued a list of 14 Critical Raw Materials, which was extended to 20 CRMs in 2014 and 27 CRMs in 2017. Rare earth elements serve as an example of a CRM: The domestic reserves of rare earth mineral in Europe account for less than 1% of mining production, though the potential for REE production in Europe is high (Goodenough et al. 2016; Rollat et al. 2016).

The imperative to unlock small deposits in Europe has triggered activities towards understanding the geological,

technological and economic step-changes that would be required. The IMP@CT project, funded by the EC Horizon 2020 programme, is developing a small-scale, compartmentalised whole systems mining approach for responsible extraction and processing of small deposits, including deposits of CRMs. The research is founded on the premise that a climate of increasing costs (including those relating to environment) from large deposits at decreasing grade may create a space in the market for small-deposit mining at high grades, with technological solutions that increase competitiveness.

This paper reviews the use of the concept “small-scale mining” in various contexts and discusses different connotations of the term.

2 “Small-scale mining” concept

For the last twenty years, discussions about “small-scale mining” have largely referred to artisanal mining activities. Terms have been used interchangeably, so that “small-scale mining” has effectively become a synonym for “artisanal small-scale mining” (ASM) (see e.g. Hilson 2006; Aryee et al. 2003).

Artisanal small-scale mining typically describes a poverty-driven activity, usually practiced in the poorest and most remote rural areas of a country by a largely itinerant and poorly educated populace with little other employment alternatives (World Bank 2013). ASM can include men and women working on an individual basis as well as those working in family groups, in partnerships, and enterprises involving hundreds or even thousands of miners (OECD 2016). 6 million people were directly engaged ASM in 1993, rising to 13 million in 1999, up to 30 million in 2014, and 40.5 million people were directly engaged in ASM in 2017 (IGF 2017). Since ASM is labour-intensive and the notion of “small-scale” relates to capital investment and the size of local enterprises, it may be expected that ASM production and revenue figures might be quite moderate and share an insignificant fraction of the global mining economy. The evidence is to the contrary and, in some cases, the cumulative amount of the mineral production by ASM can surpass that of large-scale operations. (Aubynn 2009; Zvarivadza and Tholana 2015). According to very rough estimates, the artisanal and small-scale mining produces around 15-20% of global minerals, including 80% of all sapphires, 20% of all gold, and 20% of diamonds (Buxton 2013, citing Estelle Levin 2012).

The relationship of ASM to large-scale mining (LSM)

by major mining companies has often been conflictual where both types of miners compete for the same resource, occupy the same concession or perceive one other as a threat (World Bank Group 2009; IGF, 2017). The LSM and ASM are frequently used in comparative studies representing two major (and opposite) paradigms of mining operations (e.g. Aubynn 2009; Luning 2014). Mineral governance frameworks tend to favour foreign direct investment by multinational companies over ASM, such that there are significant power imbalances, clashes over claims and the classification of ASM mining as illegal or extralegal (Siegel and Veiga 2009; IGF 2017).

The existing mining paradigm has led to the situation where mining activities that happen to be “formal” but “not so big” as LSM attract rare attention. Their operations remain largely invisible, particularly in comparison to multinational corporations. This establishes limits on the application of the term “small-scale” to other contexts and identifies a need for new research to address the issues of modern (not artisanal), potentially low-impact and sustainable small-scale mining operations.

3 Defining non-artisanal small-scale mining

In order to develop a clearer understanding of how the scales of formal mining projects can more effectively co-exist, the fundamental issue around meanings and definitions needs to be clarified. Early studies into the structure of the global mining industry established a hierarchical system dominated by “major” companies, who have an established practice of steering sectoral trends, and “intermediate” and “junior” companies that have corresponding practices (see e.g. Thomson and MacDonald 2001; Dougherty 2011). Artisanal small-scale mining does not sit neatly within the hierarchical and regulated global mining system.

A traditional description of “intermediate” is used for those companies that operate one or more small mines (see e.g. Thomson and MacDonald 2001) but the status of an “intermediate” company remains unclear since no comprehensive research on the performance of “intermediate” mining activities has been published. Additional terms that have been used in the published literature are “mid-tier resources companies” (Lyons et al 2016) and “smaller mining companies” (Shankleman 2009). In 2001, the ITDG (Intermediate Technology Development Group) defined small-scale mining in terms of a given production ceiling and the level of sophistication by which minerals are exploited. In this way, “small-scale mining is any single unit mining operation having an annual production of unprocessed material of 50,000 tonnes, or less as measured at the entrance of the mine” (Aryee et al. 2003 citing ITDG (2001)).

The new term “small-scale mining” which has started to appear recently in think tank and policy discussions, particularly in Europe, is different from conventional understanding. The implication of these characteristics is that the mining operations are likely to have a short duration, perhaps between 2 and 10 years, which will reinforce the small-scale of socio-economic impacts. It

also means that the local community will usually not suffer a big influence or disturbance from the mine culturally and socially, in terms of population structure etc. However, this potentially has both positive and negative implications. In small-scale mining that is legally and environmentally well-regulated, the scale of environmental impacts and risks should be smaller than in both large mines and ASM. This usually implies lower harm for neighbouring housing, other livelihoods and businesses in the area, although the risks are dependent on the mined metal and the use of chemicals. While small-scale mining would be appropriate for extraction from small mineral and ore deposits, there exists the potential that small-scale mining either by sophisticated and light technologies may be appropriate on large deposits for environmental and socio-economic reasons.

4 Questions of sustainability and social acceptance of non-artisanal small-scale mining

The concepts of social acceptance and social sustainability of mining operations have been increasingly used in the extractive sector to describe the complexity of mining-community relations and the commitment of mining companies to perform more sustainably. In this regard, it is essential to investigate how small-scale mining operations may be placed in wider sustainability discourses of the mining industry.

The discourses of large mining companies pre-empted considerable attention from economic/investment and academic sectors, which placed them under scrutiny. This is reflected not only in an increased number of case-studies about LSM, but also in the direction of the concepts about sustainable development of the mining industry. The idea of “sustainable mining” (Amezaga et al. 2010; Azapagic 2004), which has been widely adopted by academia over last decades, was initiated by major mining players in the late 1990s in response to global environmental movements against mining (Kapelus 2002; Franks 2014).

The geography of mining operations and shift of the production to developing countries have significantly influenced the agenda of sustainability performance of mining companies. Mining operations were widely seen as an engine for regional development and poverty reduction, which followed the global development discourse for the countries of the Global South. At the same time, strong sustainability research in the traditional mining countries of Australia and Canada have contributed other unique aspects to the global sustainability discussion. Since the preoccupations of large mining companies centred on large mines, with large workforces and large impacts, then the question arises as to whether concepts around sustainability and social acceptance can simply be scaled down for smaller forms of mining operations or whether concepts need to be re-evaluated.

5 Conclusion

The term “small-scale mining” has been widely used in the extractive industries; however, its meaning has become synonymous with practices that are globally recognized as “artisanal small-scale mining”. This paper attempts to shed light on how non-artisanal small-scale mining practices differ from conventional understanding. We will position the concept in relation to the current dual mining paradigm of large-scale and artisanal small-scale mining operation, describe its features and likely impacts, and delineate a reference frame for further discourses.

Acknowledgements

This paper was produced in partnership with the H2020 IMP@CT project, which has received funding from the EU Horizon 2020 research and innovation program.

References

- Amezaga, J. M., Rötting, T. S., Younger, P. L., Nairn, R. W., Noles, A. J., Oyarzún, R., & Quintanilla, J. (2010). A rich vein? Mining and the pursuit of sustainability. *Environmental Science & Technology*, 45(1):21-26.
- Arias, M., Atienza, M., & Cademartori, J. (2013). Large mining enterprises and regional development in Chile: between the enclave and cluster. *Journal of Economic Geography*, 14(1):73-95.
- Aryee, B. N., Ntibery, B. K., & Atorkui, E. (2003). Trends in the small-scale mining of precious minerals in Ghana: a perspective on its environmental impact. *Journal of Cleaner Production*, 11(2):131-140.
- Aubynn, A. (2009). Sustainable solution or a marriage of inconvenience? The coexistence of large-scale mining and artisanal and small-scale mining on the Abooso Goldfields concession in Western Ghana. *Resources Policy*, 34(1-2): 64-70.
- Azapagic, A. (2004). Developing a framework for sustainable development indicators for the mining and minerals industry. *Journal of Cleaner Production*, 12(6):639-662.
- Buxton, A. (2013). Responding to the challenge of artisanal and small-scale mining. *How can knowledge networks help*. IIED publication.
- Dougherty, M. L. (2011). The global gold mining industry, junior firms, and civil society resistance in Guatemala. *Bulletin of Latin American Research*, 30(4):403-418.
- Franks, D. M. (2015). *Mountain movers: Mining, sustainability and the agents of change*. Routledge.
- Goodenough, K.M., Schilling, J., Jonsson, E., Kalvig, P., Charles, N., Tuduri, J., Deady, E.A., Sadeghi, M., Schiellerup, H., Müller, A., Bertand, G., Arvanitidis, N., Eliopoulos, D.G., Shaw, R., Thrane, K., Keulen, N. (2016). Europe's rare earth element resource potential: An overview of REE metallogenic provinces and their geodynamic setting. *Ore Geology Reviews*, 72(1):838-856
- Hilson, G., & McQuilken, J. (2014). Four decades of support for artisanal and small-scale mining in sub-Saharan Africa: a critical review. *The Extractive Industries and Society*, 1(1):104-118.
- Hilson, G. M. (Ed.). (2006). *The socio-economic impacts of artisanal and small-scale mining in developing countries*. CRC Press.
- IGF (2017). Intergovernmental Forum on Mining, Minerals, Metals and Sustainable Development Global Trends in Artisanal and Small-Scale Mining (ASM): A review of key numbers and issues. Winnipeg: IISD.
- Jenkins, H. (2006). Small business champions for corporate social responsibility. *Journal of Business Ethics*, 67(3):241-256.
- Kapelus, P. (2002). Mining, corporate social responsibility and the “community”: The case of Rio Tinto, Richards Bay Minerals and the Mbonambi. *Journal of Business Ethics*, 39(3):275-296.
- Lahiri-Dutt, K. (Ed.). (2018). *Between the Plough and the Pick: Informal, Artisanal and Small-scale Mining in the Contemporary World*. ANU Press.
- Luning, S. (2014). The future of artisanal miners from a large-scale perspective: from valued pathfinders to disposable illegals?. *Futures*, 62 (2014):67-74.
- Lyons, M., Bartlett, J., & McDonald, P. (2016). Corporate social responsibility in junior and mid-tier resources companies operating in developing nations—beyond the public relations offensive. *Resources Policy*, 50: 204-213.
- Milanez, B., & de Oliveira, J. A. P. (2013). Innovation for sustainable development in artisanal mining: Advances in a cluster of opal mining in Brazil. *Resources Policy*, 38(4):427-434.
- OECD (Organization for Economic Co-operation and Development) (2011). *OECD Due Diligence Guidance for Responsible Supply Chains of Minerals from Conflict-Affected and High-Risk Areas*, OECD Publishing.
- Rollat, A., Guyonnet, D., Planchon, M., & Tuduri, J. (2016). Prospective analysis of the flows of certain rare earths in Europe at the 2020 horizon. *Waste Management*, 49: 427-436.
- Shankleman, J. (2009). *Going global: Chinese oil and mining companies and the governance of resource wealth*. Washington, DC: Woodrow Wilson International Center for Scholars.
- Siegel, S., Veiga, M.M. (2009). Artisanal and small-scale mining as an extralegal economy: De Soto and the redefinition of ‘formalization’. *Resources Policy* 34 (1-2):51-56
- Strategic Implementation Plan 2013. STRATEGIC IMPLEMENTATION PLAN FOR THE EUROPEAN INNOVATION PARTNERSHIP ON Raw Materials Part I.
- Thomson, I., and MacDonald, A. (2001). Corporate communication standards, practice and issues. Access to information: A key to building trust in the minerals sector. *MMSD, 2001*, 32. IIED publication.
- World Bank. (2013). *World Bank. Small-scale mining*. World Bank publications.
- World Bank Group, 2009. *Mining together: large scale mining meets artisanal mining – a guide for action*. Communities and Small-scale Mining (CASM), published by the World Bank/International Finance Corporation Oil, Gas and Mining Sustainable Community Development Fund (CommDev).
- Zvarivadza, T., Tholana, T. (2015). The tribute system as a funding model for artisanal small scale mining: a Zimbabwean case study. In: *Proceedings of the 23rd International Symposium on Mine Planning and Equipment Selection (MPES2015): Smart Innovation in Mining*. The Southern African Institute of Mining and Metallurgy. Sandton Convention Centre, Gauteng, South Africa, 851–860.

Gold mine tailings as future resources: long-term storage and behavior of As and Sb phases

Kerr G, Weightman E and Craw D.

Department of Geology, University of Otago, Dunedin, New Zealand

Abstract. Gold mine tailings contain sub-economic quantities of gold and therefore represent potential future resources if the gold price increases. Tailings should be managed to minimize the environmental impact and ensure they can be successfully reprocessed in the future. Elevated dissolved As, and in some cases Sb, can be a significant potential discharge issue at tailings storage facilities.

Mineralogical and geochemical characterization was undertaken on modern and historic mine wastes to evaluate their long-term behaviour. On a time-scale of years to decades, water-saturated sulfide-rich concentrate tailings were largely unoxidised and successfully reprocessed. Over longer timescales, unmanaged historic sulfide-rich concentrates show varying degrees of alteration, from minimally altered to fully oxidized. Tailings that have undergone roasting/pressure-oxidation processing now consist mainly of relatively stable iron oxides, iron arsenates, iron antimonates, and iron oxyhydroxides. Armoring of Au-bearing primary sulfides, and formation of stable secondary phases, can limit dissolved As and Sb concentrations in waters.

1 Introduction

Orogenic gold mining involves the excavation, crushing, concentration, and treatment of ore. This process generates significant quantities of mine wastes which typically have little economic value but must be contained to prevent environmental issues. Elevated dissolved arsenic, and in some cases antimony, is one of the most significant potential discharge issues at tailings storage facilities.

It is not possible to extract all gold from ore during the mining process due to recovery inefficiencies and dilution from wall rock, and some gold remains in mine wastes. Tailings therefore represent potential future resources from which the residual gold may be extracted as processing techniques improve. The re-mining of existing tailings is both economically advantageous and reduces waste burdens (e.g. Breytenbach 2016).

The long-term storage and re-mining of existing tailings presents different challenges to standard hard-rock (orogenic) mining. Tailings have undergone a range of ore processing techniques that have altered their physical, geochemical, and mineralogical properties and present their own environmental risks. For example, gold-bearing arsenopyrite (FeAsS) is commonly concentrated during processing, and tailings can be therefore be enriched in arsenopyrite and other sulfides. Sulfide concentrates may also be oxidized to liberate

encapsulated gold, producing oxide minerals such as arsenolite or claudetite (As_2O_3 ; Fig 1a), and oxidized Fe^{III} -bearing minerals including scorodite ($\text{FeAsO}_4 \cdot 2\text{H}_2\text{O}$; Fig 1a) and tripuhyite (FeSbO_4 ; Fig 1b).

Historic and modern mine wastes in New Zealand provide useful insights into the mineralogical and geochemical properties of mine processing wastes and the long-term stability of such materials.

2 Methods

Samples were collected at the active Macraes gold mine in Otago, southern New Zealand, and at the (now inactive) Globe Progress mine, and at a historic gold mine processing site, both on the West Coast, southern New Zealand. At Macraes mine, water quality monitoring is carried out for processing and environmental purposes and the data were made available for this study. Mineralogical studies were carried out on sulfide concentrate tailings and 'scales' collected from the pressure-oxidation autoclave. At the historic site, mineralogical and geochemical characterisation was undertaken and water samples were collected and analysed at Hill Laboratories, Hamilton, New Zealand.

Mineral identification was conducted on a PANalytical X'Pert PRO MPD PW3040/60 X-ray diffractometer (XRD) with a CuK_α source ($\lambda=1.5406\text{\AA}$). Scanning electron microscopy (SEM) imaging and analysis was undertaken on a Zeiss Sigma FEG scanning electron microscope with an Oxford Instruments XMax 20 Si drift energy dispersion X-ray detector (EDX).

3 Macraes gold mine

The Macraes orogenic gold mine has been in operation since 1990. The gold is typically disseminated, occurring in pyrite (FeS_2) and arsenopyrite. Between 1990 and 1993, a sulfide concentrate was produced via flotation of crushed ore, and this concentrate was fed directly to the cyanide system to extract the gold, after which the residues were stored in the concentrate tailings impoundment. From 1993, these sulfide-rich residues were combined with silicate tailings and discharged into a larger tailings dam: the Mixed Tailings Facility (MTF). In 1999, a pressure-oxidation autoclave was constructed to oxidize the sulfide-rich concentrate before the cyanidation step. The pre-1993 tailings, stored in the sulfide concentrates impoundment, were excavated and successfully reprocessed using the autoclave. From 2007, ore concentrate from OceanaGold's Globe Progress mine was transported and processed at Macraes treatment plant. In addition to pyrite and

arsenopyrite, the Globe Progress ore also contains stibnite (Sb_2S_3 ; 4 vol%; Milham and Craw 2009).

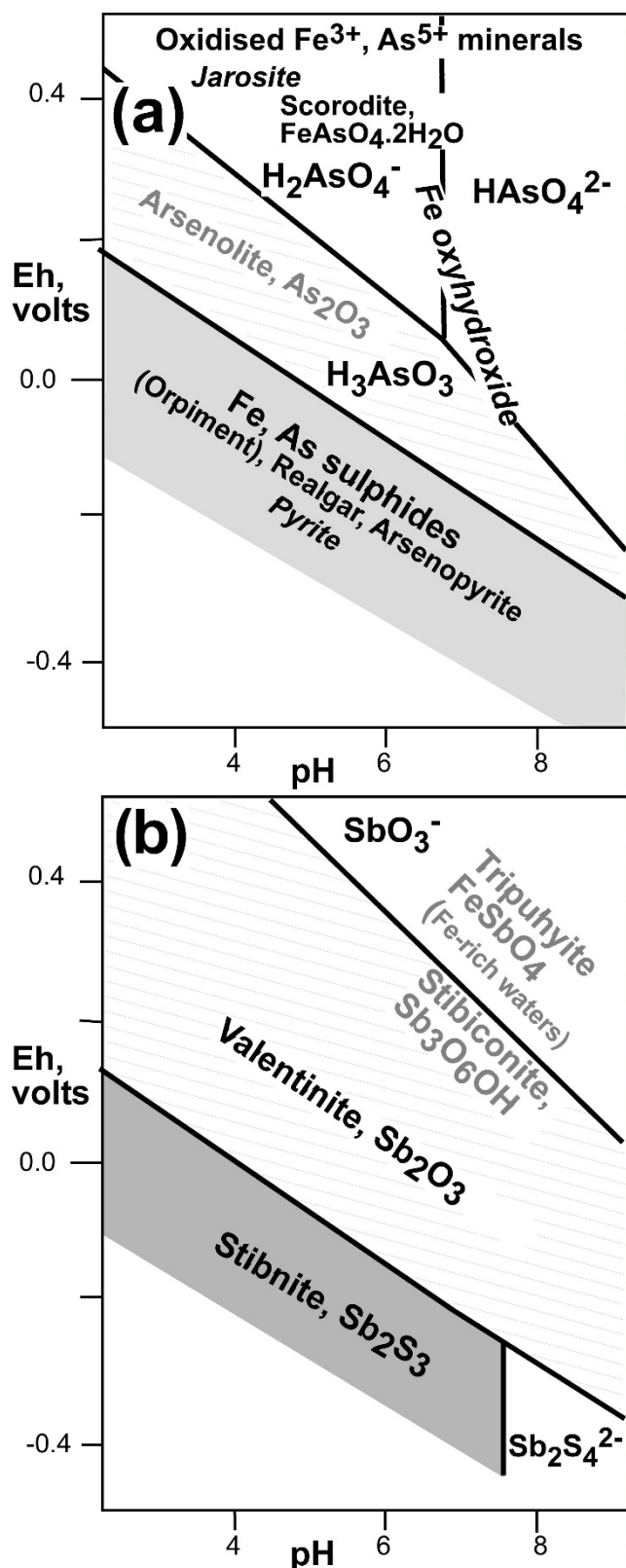


Figure 1. Mineral stability diagrams showing the geochemical relationships of As and Sb minerals in the surficial environment. Summary Eh-pH diagrams for oxidation of (a) pyrite and arsenopyrite, and (b) stibnite (compiled from Geochemists Workbench and Vink 1996).

3.1 Concentrate tailings impoundment (1990-1993)

Water monitoring data collected at the sulfide concentrate tailings impoundment from ca. 1990-2003, provides insights into the geochemical and mineralogical processes occurring during long-term storage (Craw et al. 2017).

Dissolved As levels in surface water were generally high (10's-100's of mg/L). Water pH was initially high (pH 10-11) as it was sourced from the alkaline cyanidation system (Craw et al. 2017). As the impoundment became inactive, downward percolating waters interacted with both tailings and the waste rock dam, and became mildly acidic (~ pH 6). During the monitoring period, the tailings remained saturated with only minor oxidation of sulfides in the top metre causing minor acidification and Fe-arsenate precipitation. Calcite, derived from the waste rock, reacted with the acid, producing high levels of dissolved sulfate (3000-6000 mg/L; Craw 2003). Dissolved sulfate concentrations subsequently dropped due to gypsum precipitation within the dam structure. Precipitation of iron oxyhydroxides adsorbed dissolved As. At the toe of the dam, As levels are generally below 1 mg/L and dissolved sulfate is ~2000 mg/L (Craw 2003).

Excavation and handling of the concentrates during re-processing resulted in minor oxidation of sulfides (Craw et al. 2017). As with the minor surface oxidation, calcite rapidly neutralized the acidified tailings waters and iron oxyhydroxides formed (Fig 1a).

3.2 Pressure-oxidation autoclave (1999)

In the pressure-oxidation autoclave, the sulfide-rich concentrate is oxidized at 225 °C and >3,000 kPa (residence time ca. 1 hr). Oxidation of pyrite results in a slurry pH of <2 (Craw 2006). Iron and arsenic are rapidly oxidized as they pass through the autoclave and Fe^{III} and As^V are the dominant species in the discharge waters. The oxidized slurry then undergoes cyanidation treatment to extract the gold.

During the autoclave process, mineral deposits ('scales') precipitate on the walls and agitators. These scales are composed of mm-cm thick layers with variable grain size and mineralogy that reflect chemical changes in the passing slurry. The scales provide insights into the geochemistry of the process waters. As the scales are ultimately deposited in the MTF, the mineralogy of this material is relevant to the long-term environmental management of the MTF.

In the first half of the autoclave, Ca sulfate, alunite ($\text{KAl}_3[\text{SO}_4]_2[\text{OH}]_6$), and ferrous sulfates dominate, and the principal As minerals are As^{III} oxides (arsenolite or claudetite; Fig. 1a, 2a). Antimony occurs in this section of the autoclave as a As-bearing iron antimonate (possibly tripuhyite; inferred from SEM-EDS analysis), closely associated with fine-grained hematite and ferrous sulfate (Fig. 1b, 2b). As oxidation progresses in the downstream half of the autoclave, ferric sulfates and jarosite precipitate (Fig. 1a; 2a). At the discharge point, jarosite, Ca sulfate, and ferric arsenate dominate (Craw 2006).

The jarosite is fine-grained (typically 1–10 μm) and contains little or no detectable As in solid solution (<0.2 wt% As; Kerr et al. 2015). Most arsenic is present as ferric arsenate (Fig 2a), which is intimately intergrown with the jarosite and Ca sulfate.

Water in the MTF has a pH of ~ 6 and high dissolved sulfate (Craw 2003). Under these conditions, jarosite dissolves relatively slowly and particles will survive for hundreds of years (Zahrai et al. 2013). Although the absence of solid solution As in the jarosite means no As will be directly mobilized, jarosite dissolution will further expose the intimately intergrown ferric arsenate to the tailings waters. At pH 6, the ferric arsenate dissolves at a faster rate than jarosite but also yields As-bearing ferric oxide/hydroxide precipitates (Roddick-Lanzilotta et al. 2002).

Dissolved Sb is not elevated in the Macraes waters despite the processing of Globe Progress ore (Weightman et al. 2018), indicating that the autoclave process assists in the removal of Sb through the formation of insoluble phases such as the As-bearing tripuhyite.

4 Historic tailings

As the tailings from the pressure-oxidation system are remixed and diluted approximately ten-fold with the silicate-rich flotation tailings, it is difficult to evaluate their long-term stability once in the MTF. As a proxy, we have examined historic tailings (ca. 90 years old) at an abandoned processing site. The historic processing of ore was similar to modern-day processing, albeit less technologically advanced, and involved sulfide mineral separation, oxidative roasting through the use of a furnace, and cyanidation.

Ferric iron oxides (e.g. hematite) and arsenolite were the principal waste products of the roaster furnace, and the hematite forms distinctly red tailings of which small quantities persist on site today. The hematite grains are porous and contain up to 4 wt% As and appear to have undergone only minor alteration. Similar results were observed at a nearby site with large volumes of hematite and low dissolved As levels (<0.01 mg/L; MacLachlan & Craw, 2017) indicating that hematite may be providing effective long-term As sequestration. Arsenolite is highly soluble and in most parts of the site has now been replaced by scorodite and ferric oxyhydroxide phases (Fig. 1a, Fig. 3a-d).

Unroasted sulfide concentrates remain on site and consist of quartz-bearing sand, rich in arsenian pyrite and arsenopyrite (Fig. 3). Arsenic content ranges from ~ 1400 mg/kg to 21 wt%. There are apparently steep redox gradients within the residues on the cm scale between largely original sulfides and fully oxidized residues that contain no sulfides and consist of almost pure Fe oxyhydroxide (Fig. 1a, Fig. 3b). Scorodite is an intermediate phase, which contributes to cementation and armoring of the sulfides. Arsenic in the Fe oxyhydroxides is 5-20 wt%, showing that at least some of the mobilized As has been adsorbed.

Fragments of timber framing are now intermixed with

the sulfide concentrates and have developed authigenic As sulfide (predominantly realgar, Fig. 1a, 3b,c). This organic debris has acted as a reductant within the predominantly oxidizing environment, causing dissolved sulfate to be reduced. This reducing microenvironment, which is sequestering As, is likely to persist until all wooden material has decomposed, after which the realgar will oxidize.

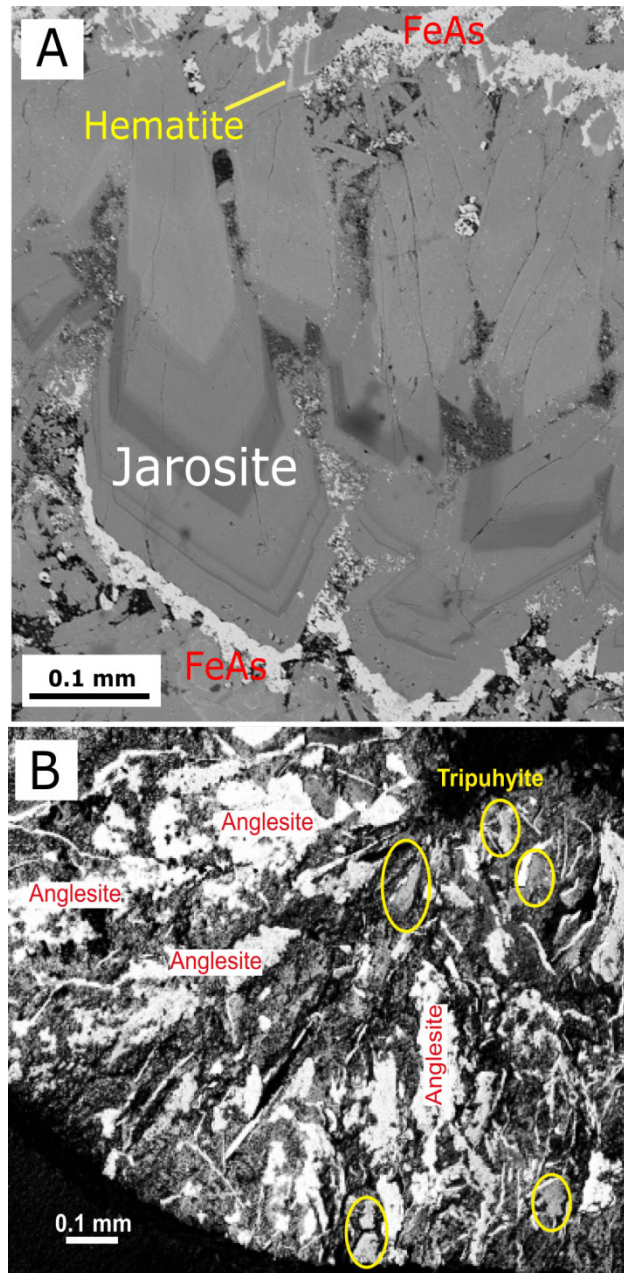


Figure 2. (a) Backscatter electron image of jarosite crystals in Macraes mine autoclave scale. Jarosite is shades of **grey** (darker higher Al content), **white** ferric arsenate (FeAs) or hematite, and **black** mounting medium (modified from Kerr et al. 2015). (b) Backscatter electron image of Sb-bearing minerals in autoclave scale. The coarse, very bright grains are predominantly anglesite (PbSO_4 ; lead derived from autoclave mortar), surrounded by a micron scale matrix of iron-antimony-arsenic-bearing oxide precipitate, with some larger grains of an As-bearing tripuhyite-like mineral. Black zone is ferrous sulfate.

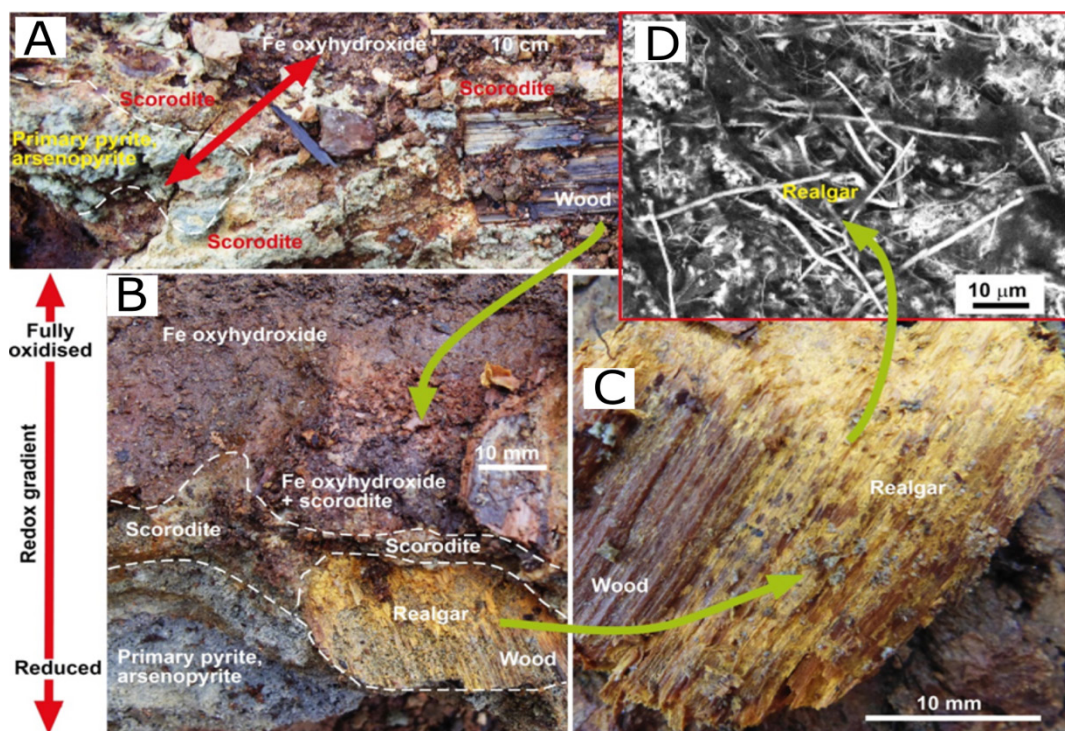


Figure 3. Weathered sulfide concentrate at an historic ore processing site. Primary arsenopyrite has weathered to Fe oxyhydroxide and scorodite (modified from Kerr and Craw 2018). Green arrows indicate progressively closer views of minerals; red arrows indicate redox gradients. (a) General view of tailings. (b) Close view of redox gradient showing primary arsenopyrite with oxidized scorodite and Fe oxyhydroxide. Low-temperature realgar has formed on fragments of wood. (c) Close-up photo of low temperature realgar. (d) SEM electron backscatter image of low temperature realgar.

5 Conclusions

- Mine tailings represent important future Au resources and to ensure their long-term stability, should be managed to minimize oxidation and secondary alteration.
- 13 year old tailings at a New Zealand mine, which had undergone only minimal surface oxidation, were successfully reprocessed.
- Dissolved As and Sb are low in the tailings dam, due to the formation of moderately stable phases in the autoclave (jarosite and tripuhyite) and formation of iron oxyhydroxides in the dam.
- Over longer timescales, unmanaged historic mine wastes show varying degrees of alteration, from minimally altered to fully oxidized.
- Armoring of primary sulfides, and formation of stable secondary phases, can limit dissolved As and Sb concentrations in waters at historic sites.

Acknowledgements

This research was funded by a New Zealand Ministry for Business, Innovation and Employment (MBIE) grant via CRL Energy Ltd. Additional funding was provided by Otago University. Logistical support was provided by OceanaGold Ltd and the Department of Conservation.

References

Breytenbach M (2016) Gold tailings retreatment an attractive

proposition in current environment. Engineering News.

Craw D (2003) Geochemical changes in mine tailings during a transition to pressure-oxidation process discharge, Macraes Mine, New Zealand. *J Geochem Explor* 80: 81–94.

Craw D (2006) Pressure-oxidation autoclave as an analogue for acid-sulphate alteration in epithermal systems. *Min. Dep.* 41:357-368.

Craw D, Kerr G, Malloch K, McLachlan C (2017) Storage of arsenic-rich gold mine tailings as future resources. *IMWA 2017*, Lappeenranta, Finland.

Kerr G, Druzbecka J, Lilly K, Craw D (2015) Jarosite solid solution associated with arsenic-rich mine waters, Macraes mine, New Zealand. *Mine Water and Environment* 34: 363-374.

Kerr G, Craw D (2018) Authigenic realgar and gold in dynamic redox gradients developed on historic mine wastes. *App. Geo.* 97:123-133.

Milham L, Craw D (2009) Antimony mobilization through two contrasting gold ore processing systems, New Zealand. *Mine Water Environ* 28:136–145.

McLachlan C, Craw D (2016) Characterisation of tailings at Prohibition Mine Site, Waiuta, Westland. *Proceedings of the 49th AusIMM NZ Branch Conference*, 259-268.

Roddick-Lanzilotta AJ, McQuillan AJ, Craw D (2002) Infrared spectroscopic characterisation of arsenate(V) ion adsorption from mine waters, Macraes Mine. *App. Geo.* 17: 445-454.

Vink BW (1996) Stability relations of antimony and arsenic compounds in the light of revised and extended Eh-pH diagrams. *Chem. Geo.* 130:21-30.

Weightman E, Craw D, Kerr G, Snow T (2018) Antimony mobilisation and attenuation during processing of gold ore. *Proceedings of the 51st AusIMM NZ Conference*, 421-429

Zahrai SK, Elwood Madden ME, Madden AS, Rimstidt JD (2013) Na-jarosite dissolution rates: the effect of mineral composition on jarosite lifetimes. *Icarus* 223:438–443.

Characterization of serpentinites in Tolima and Antioquia (Colombia): analyzing their CO₂ sequestering potential through carbonation processes.

Mónica Ágreda López, Carlos Augusto Zuluaga Castrillón, Iván Mateo Espinel Pachón
Universidad Nacional de Colombia

Abstract. The increasing trend of atmospheric carbon dioxide (CO₂) is a critical problem all around the world. In order to decrease CO₂ high concentrations, scientists are trying to generate mechanisms that can sequester this atmospheric gas. A viable alternative is to inject atmospheric CO₂ along with water in serpentinite-hosted aquifers where carbonation reactions will help sequestering the gas. With this in mind, is important to identify possible serpentinite reservoirs around the world that could potentially be used as CO₂ sequestration sites. In this work, we made a complete characterization of different serpentinites in two localities of Colombia, including their formation conditions and mineralogy. This allows us to identify critical areas in which CO₂ sequestering could be applied in the future.

We determined that the serpentines of Tolima have higher iron content (Baumite) and higher proportion of antigorite in relation to the polymorphs lizardite and chrysotile. In Antioquia, the serpentines are more magnesian with predominance of clinochrysotile over the other phases. In this way, it is proposed that Antioquia is a better locality for CO₂ sequestration.

1 Introduction

Serpentinites are rocks composed mainly by serpentine-group minerals formed by the alteration of ultramafic rocks, a process known as serpentinization. This process can occur in different geological settings including mid ocean ridges, subduction zones and mantle wedges (Deschamps et al. 2013). The process modifies the physical and chemical properties of the rocks, and this is commonly identified by reduction of seismic velocities and the increasing of peridotites' magnetic susceptibility. During the serpentinization process, density changes are dramatic due to the increasing content of water (13-15%) (Iyer 2007).

The most abundant serpentinite-group minerals are lizardite, chrysotile and antigorite with an idealized chemical formula $Mg_{2.813}Si_2O_5(OH)_{3.647}$ (Moody 1976). They are all trioctahedral phyllosilicates with different crystallographic structure and contrasting habit: lizardite appears like planar layers, chrysotile forms scrolled layers which tend to form cylindrical forms and antigorite possesses a modulated structure with periodical inversions of the tetrahedral-octahedral layers (O'Hanley 1996; Iyer 2007). These three minerals appear associated, in serpentinites. The maximum stable temperatures of serpentines are between 450-500°C and pressures from 3 to 3.5 kbar. Antigorite is the high-temperature stable polymorph (Prichard 1979).

Asbestiform types of serpentinites were commonly

used for their thermal and electrical properties. However, these minerals have been directly linked to diseases like mesothelioma and pneumoconiosis (Guillot and Hattori 2013).

Due to the climate change, the mineral carbonation through CO₂ sequestration has been one of the most important topics of investigation in the last decades. Many researchers integrated mineral carbonation processes in mining activities using ultramafic rocks and serpentinites in order to achieve the CO₂ sequestration obtaining at the same time financial benefits (Li et al. 2018). Power et al. (2013) *in-situ* industrial carbonation method in serpentinite-hosted aquifers is based on a chemical reaction that occurs naturally in subsurface conditions inducing a carbonation process by the injection of CO₂ directly to the rocks and precipitating magnesite. An experiment developed by Cipolli et al. (2003) showed that 33 g of CO₂ could be captured per kilogram of H₂O per year using serpentinites. In order to do this process more efficient, several conditions like reactive surface area, temperature, pH, solute transport, partial pressure of CO₂ and atmospheric conditions need to be considered (Bea et al. 2012).

The economic benefit is one of the most important factors in mining activities. Hitch and Dipple (2012) evaluated this through financial modeling and sensitivity analysis showing that the integration of industrial-scale mineral carbonation within mining operations is viable from a financial perspective.

2 Geological framework

The Colombian Andes are in a compressive tectonic regime with the collision of the South American, Nazca and Caribbean plates. Two main basement domains in the Colombian Andes can be differentiated: one with continental affinity (Eastern Cordillera and part of the Central Cordillera) and other with oceanic affinity (Western Cordillera and the west part of the Central Cordillera).

The serpentinites studied in this work were collected in the Central Cordillera (Antioquia and Tolima). This mountain range is mainly composed by metamorphic and igneous rocks from Cambrian to Cretaceous ages which are limited at west for the Otú-Pericos Fault and at east for the Romeral Fault System.

The serpentinites of Antioquia were collected from: 1) Diorita de Pueblito (Grosse, 1926), an amphibolite diorite composed by amphibole gabbros and peridotites formed by magmatic differentiation; Rodríguez and Vinasco

(2010) reported an U/Pb in zircon age for this unit of 233 ± 14 M.a. 2) Gabro de Heliconia or Gabros de Romeral (Mejía, 1894; Montoya and Pelaez, 1993), a gabbroic unit that surround the Diorita de Pueblito and located within the Romeral Fault System. This unit has a faulted contact with Diorita de Pueblito and Ultramafitas de Angelópolis (Tabares and Arredondo, 2006). A 126 Ma K/Ar in hornblende age was reported by Restrepo and Toussaint (1976). 3) Ultramafita de Angelópolis (González, 2001), a ultramafic unit with peridotites, serpentinitized dunites with ophiolitic affinity, gabbros and basaltic lavas.

Tolimas's serpentinites are part of the Cajamarca Complex (Maya and González, 1995; Cajamarca Group of Nelson, 1957), a Paleozoic low-grade metamorphic package with green schist, quartz-sericitic schists, phyllites, quartzites and marbles; this unit is bounded at the west by the Armenia Fan deposits and at the east by the Ibagué Batholith. The Cajamarca Complex is truncated at the west by the San Jerónimo Fault. The radiometric ages of the Cajamarca Complex can be classified in three groups: 345-240 Ma, 130-105 Ma and 75-55 Ma. The oldest ages correspond to Acadian Orogeny metamorphism; the others are related to subsequent metamorphic overprints (Rodríguez et al. 2005).

Methodology

We made a compilation of reported localities of serpentinites in Colombia (Fig.1). Rock samples were collected from two potential places and then characterized petrographically and metallographically, using polished thin sections, to identify the principal mineral assemblages, alterations and textures.

Samples chips were powdered in order to use X-Ray Diffraction with a Bruker D2 phaser diffractometer and the software DIFFRAC.EVA in order to identify the polymorphs of serpentine-group. The powder was also analyzed to obtain SEM-images using a Tescan Vega 3 to identify the morphology of polymorphs. Raman spectroscopy was used to established punctual mineral compositions with the Nicolet Omega dispersive XR equipment with a laser of 532 nm and 35 mW.

Additionally, the electron microprobe JEOL JXA-8230 was employed to semiquantitative and quantitative analysis and compositional maps with EDS and WDS spectrometers. Quantitative analysis were used to calculate stoichiometric formulas of spinel, magnetite, serpentine, olivine and pyroxene in order to identify the proportion of magnesium in the minerals that could potentially generate carbonation reactions to sequester atmospheric CO_2 , commonly represented by the reaction of olivine or serpentine with CO_2 to produce magnesite + quartz \pm H_2O (Power et al. 2013).

Finally, the samples were analyzed using the ICP-AES technique to obtain trace elemental compositions. The Bruker D2 phaser diffractometer, Tescan Vega 3, and the JEOL JXA-8230 instruments are hosted at the Universidad Nacional de Colombia.

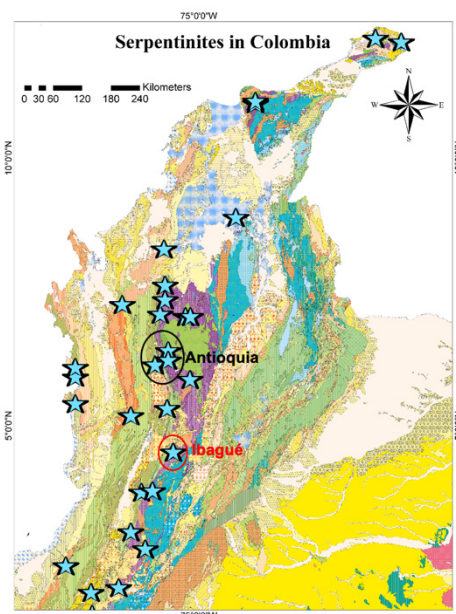


Figure 1. Localization of serpentinites outcrops in Colombia. The locations where the study was done, are marked in the map.

Results

4.1 Antioquia

Antioquia's rocks were collected in an abandoned magnesite mine. Magnesite was not found in the ultramafic serpentinitized rocks, because it was segregated in veins that were mined. The serpentinite tailings present intense fracturing (Fig. 2) which increases the reactive surface making those rocks a good prospect for applying the CO_2 sequestration through in-situ carbonation process (Power et al. 2013).



Figure 2. Outcrop of Antioquia's serpentinites in an abandoned magnesite mine. The rock is intensively fracture producing veins and veinlets that are filled with fibrous serpentine.

The studied samples present different grade of serpentinitization that is evident in the proportion of pyroxene, olivine and amphibole relicts. Mesh texture and bastites were identified. Additionally, these lithologies have veins and veinlets of the fibrous polymorph chrysotile. Magnetite appears disseminated and in veinlets along with chrysotile, due to the segregation of this mineral during the serpentinitization process (Fig. 3) (Huang et al. 2016).

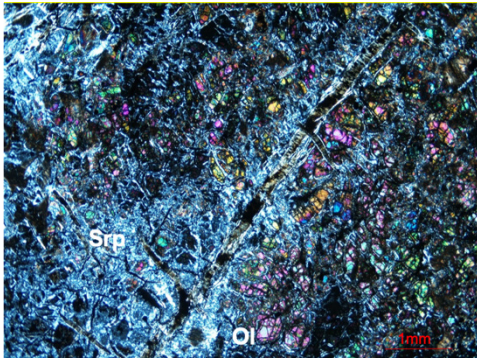


Figure 3. Cross polarized image of Antioquia's serpentinites. Olivine relicts can be observed placed in the center of mesh cells. A chrysotile veinlet crosses the section in NE-SW orientation.

The X-Ray Diffraction evidenced the presence of the following mineral phases: clinochrysotile $Mg_3Si_2O_5(OH)_4$, chamosite $(FeAlMg)_6(SiAl)_4O_{10}OH$, magnetite $FeOFe_2O_3$, marcasite FeS_2 , brucite $MgOH_2O$, antigorite $6Mg_3Si_2O_5(OH)_4$, lizardite-1T $Mg_3Si_2O_5(OH)_4$ and spinel $Ga_2Cd_{0.75}Cu_{0.25}O_4$.

Raman spectroscopy allow us to confirm the presence of chrysotile and lizardite, mainly within the veinlets, and the forsteritic component of olivines. SEM images also confirm the presence of the chrysotile polymorph as an important constituent of the rock (Fig. 4). If carbonation processes are planned to be implemented in this location, further considerations have to be taken in order to control the impact of chrysotile due to their associated health risks (Fubini and Fenoglio 2007).

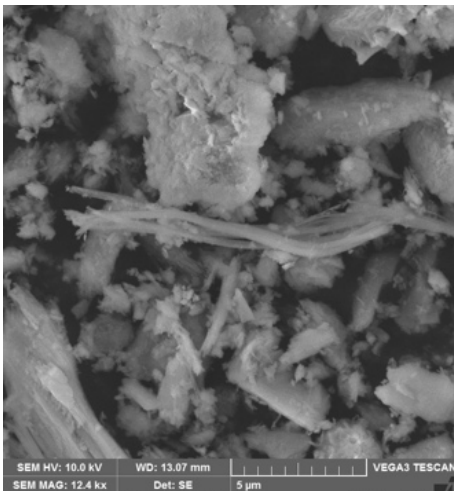


Figure 4. SEM image of the Antioquia's serpentinites showing the typical tubular morphologies of chrysotile.

Serpentine average calculated formula is: $(Mg_{2.77}Fe_{0.07}Al_{0.03})(Si_{2.05}O_5)(OH)_4$. Likewise, whole rock geochemistry shows an average of 35.45 wt% of magnesium in the serpentinized ultramafic rocks, which represent high magnesium concentrations that can be used to apply in-situ carbonation method (Table. 1).

Table 1. Percentages (wt%) of major elements obtained by whole rock geochemistry through ICP-AES in samples from Antioquia.

Sample	6	7	8	8A	12	13
SiO ₂	40.9	41.6	40	38.3	41.5	41
Al ₂ O ₃	1.63	1.9	0.77	3.62	1.22	2.82
Fe ₂ O ₃	7.86	8.02	6.58	7.96	8.19	8.1
CaO	1.41	2.35	0.17	1.08	0.49	3.01
MgO	36.3	36.8	36.9	34.1	35.5	33.1
Na ₂ O	0.06	0.14	<0.01	<0.01	0.02	0.05
K ₂ O	0.01	0.02	0.01	0.01	0.02	0.02
Cr ₂ O ₃	0.4	0.35	0.4	0.31	0.38	0.38
TiO ₂	0.03	0.07	<0.01	0.07	0.04	0.05
MnO	0.12	0.12	0.13	0.09	0.12	0.13
P ₂ O ₅	<0.01	0.01	<0.01	0.01	<0.01	0.01
SrO	<0.01	<0.01	<0.01	<0.01	<0.01	<0.01
BaO	<0.01	<0.01	<0.01	<0.01	<0.01	<0.01

4.2 Tolima

These rocks have a higher degree of serpentinization in comparison to the Antioquia's samples. No relicts of the ultramafic protolith were observed, and magnesite appears as anhedral crystals of approximately 550 microns in diameter. Serpentine is disposed in interpenetrating textures that indicates higher T-P condition than Antioquia's samples (Fig. 5). Magnesite appears as a product of the serpentinization process and may be explained by equations 1 and 2 of Johannes (1969):

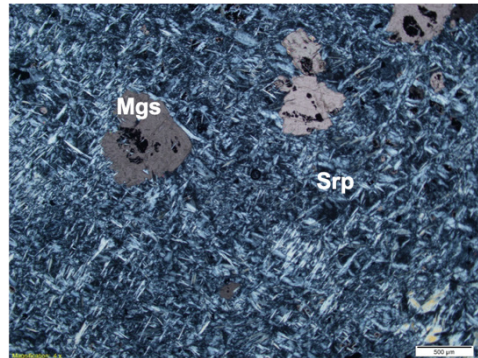
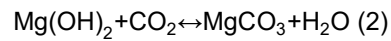
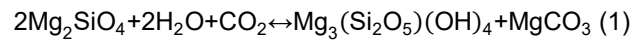


Figure 5. Cross polarized image of Tolima's serpentinites. Interpenetrating texture of serpentines is shown. Magnesite appears as anhedral crystals.

X-Ray Diffraction reveals the presence of antigorite $6Mg_3Si_2O_5(OH)_4$, eastonite $K-Mg-Fe-Al-Si-O-H_2O$, baumite-1T $(MgMnFeZn)_3(SiAl)_2O_5(OH)_4$, magnesite $Mg(CO)_3$, spinel $Mg(Al_{0.91}Fe_{0.09})O_4$ and chamosite $Fe_3Si_2O_5(OH)_4$.

Additionally, Raman spectroscopy and SEM images confirm the presence of antigorite as the main polymorph of serpentine-group (Fig. 6). This is a positive point compared to Antioquia's rocks because no health problems related to asbestos need to be considered.

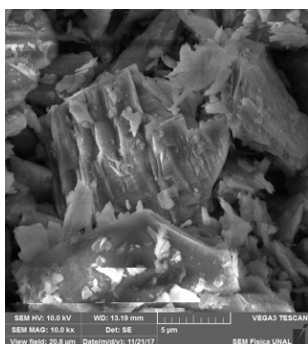


Figure 6. SEM image of the Tolima's serpentinites showing antigorite morphologies.

However, microprobe analyses show that the content of iron is higher in Tolima's serpentinites ($Mg_{2.63}Fe_{0.23}Al_{0.04}Cr_{0.01}(Si_{2.04}O_5)(OH)_4$) and the proportion of magnesium is lower than in Antioquia's serpentinites. This characteristic may reduce the utility of this lithologies in the sequestration process as magnesium is one of the principal reactants needed to complete the carbonation reaction.

Conclusions

The magnesium rich serpentine polymorph that predominate in Antioquia is clinochrysotile while in Tolima is antigorite. The presence of antigorite in Tolima's rocks, along with its interpenetrated texture and the absence of relicts of the ultramafic protholith, indicates that these rocks experienced higher T-P conditions during their serpentinization process than Antioquia's rocks.

Although samples from Antioquia were collected in an abandoned mine of magnesite, this mineral was not found in the studied rocks, because it was segregated in veins that were mined. In contrast, magnesite was found as anhedral crystals in Tolima's samples. This difference could be related to the T-P conditions, pH and presence of CO_2 rich fluids that allowed the formation of magnesite in the latest location.

Tolima's serpentinites presented three times higher iron content than Antioquia's rocks. The lower magnesium proportion of Tolima's serpentines in comparison to Antioquia's serpentines make the last a more suitable prospect to apply the CO_2 sequestration method through *in-situ* carbonation. However, the presence of chrysotile needs to be considered because of its potential health risks.

Localities sharing the characteristics reported in this investigation should be consider for applying potential CO_2 sequestration through *in-situ* carbonation process. The green characteristic of the technique could provide economic and environmental benefits in current and abandoned mines.

Acknowledgements

The authors thank the different laboratories of the Universidad Nacional de Colombia where most analysis were performed. We also thank Gloria Inés Rodríguez, Jimmy Fernández Lamus, Germán Bonilla Osorio, Ana Elena Concha Perdomo, Luis Demetrio López Carreño,

Jesús Alberto Ágreda Bastidas and the geologist Carolina Jimenez Triana for their help with the data acquisition process and with discussions about geology and mineralogy of serpentinites.

References

- Bea SA, Wilson SA, Mayer KU, et al (2012) Reactive Transport Modeling of Natural Carbon Sequestration in Ultramafic Mine Tailings. *Vadose Zo J* 11:0. doi: 10.2136/vzj2011.0053
- Cipolli F, Gambardella B, Marini L, et al (2003) Geochemistry of high-pH waters from serpentinites of the Gruppo di Voltri (Genova, Italy) and reaction path modeling of CO_2 sequestration in serpentinite aquifers. *Appl Geochemistry* 19:787–802. doi: 10.1016/j.apgeochem.2003.10.007
- Deschamps F, Godard M, Guillot S, Hattori K (2013) Geochemistry of subduction zone serpentinites: A review. *Lithos* 178:96–127. doi: 10.1016/j.lithos.2013.05.019
- Fubini B, Fenoglio I (2007) of Mineral Dusts. 407–414
- González H (2001) Memoria explicativa, Mapa Geológico del Departamento de Antioquia. Escala 1:400000. Medellín.
- Grosse E (1926) El Terciario Carbonífero de Antioquia
- Guillot S, Hattori K (2013) Serpentinites: Essential Roles in Geodynamics, Arc Volcanism, Sustainable Development, and the Origin of Life. *Elements* 9:95–98. doi: 10.2113/gselements.9.2.25
- Hitch M, Dipple GM (2012) Economic feasibility and sensitivity analysis of integrating industrial-scale mineral carbonation into mining operations. *Miner Eng* 39:268–275. doi: 10.1016/j.mineng.2012.07.007
- Huang R, Lin C-T, Sun W, et al (2016) The production of iron oxide during peridotite serpentinization: Influence of pyroxene. *Geosci Front* 8:1311–1321. doi: 10.1016/j.gsf.2017.01.001
- Iyer K (2007) Mechanisms of serpentinization and some geochemical effects. University of Oslo
- Johannes W (1969) An experimental investigation of the system $MgO-SiO_2-H_2O-CO_2$. *Am J Sci* 267:1083–1104. doi: 10.2475/ajs.267.9.1083
- Li J, Hitch M, Power I, Pan Y (2018) Integrated Mineral Carbonation of Ultramafic Mine Deposits—A Review. *Minerals* 8:147. doi: 10.3390/min8040147
- Maya M, González H (1995) Unidades litodémicas en la Cordillera Central de Colombia. *Boletín Geológico, Ingeominas* 11
- Mejía M (1894) *Geología y Geoquímica de las Planchas 130* (Santafe de Antioquia) 146 (Medellín Occidental)
- Montoya D, Pelaez I (1993) Ultramafitas y rocas relacionadas de Heliconia, Antioquia. Universidad Nacional de Colombia
- Moody JB (1976) Serpentinization: a review. 125–138
- Nelson H (1957) Contribution to the geology of the central and western cordillera of Colombia in the sector between Ibagué and Cali
- O'Hanley DS (1996) Serpentinites: Records of Tectonic and Petrological History
- Power IM, Wilson SA, Dipple GM (2013) Serpentinite carbonation for CO_2 sequestration. *Elements* 9:115–121. doi: 10.2113/gselements.9.2.115
- Prichard HM (1979) Contributions to Mineralogy and A Petrographic Study of the Process of Serpentinisation in Ophiolites and the Ocean Crust. *Contrib to Mineral Petrol* 68:231–241
- Restrepo J, Toussaint JF (1976) Edades radiométricas de algunas rocas de Antioquia, Colombia. *Boletín Ciencias la Tierra* 6:
- Rodríguez G, Gonzalez H, Zapata G (2005) *Geología de la Plancha 147 Medellín Oriental*
- Rodríguez JV, Vinasco C (2010) Fábrica y emplazamiento de la Diorita de Pueblito, NW Cordillera Central de Colombia: análisis de fábrica magnética y mineral. Universidad Nacional de Colombia, Sede Medellín
- Tabares G, Arredondo L (2006) Cartografía Geologica de 132 km2 entre los municipios de Angelópolis y Heliconia (Departamento de Antioquia, Colombia)

Tracking the magmatic-hydrothermal transition in the phosphorus-rich Gatumba pegmatite dyke system (Rwanda) and its role on Sn mineralization.

Niels Hulsbosch and Philippe Muchez

KU Leuven, Department of Earth and Environmental Sciences, Division of Geology, Belgium

Abstract. Fieldwork, petrography, Raman spectroscopy and fluid inclusion microthermometry were applied to the lithium-cesium-tantalum (LCT) Gatumba pegmatite dyke system (Rwanda) to track the magmatic-hydrothermal fluid transition and its role on cassiterite mineralization. The phosphorus-rich system illustrates a magmatic-hydrothermal fluid evolution from H₂O-NaCl-KCl-(CO₂,N₂) to H₂O-NaCl-LiCl-(CO₂,N₂) fluids during solidification from the border zone inwardly to the core zone. The Gatumba dyke system is a unique case-study because the montebrasite, carbonated Mn-fluorapatite, quartz core zone is mineralized in primary cassiterite. The high Li- and P-contents in the core zone, which lowers the crystallization temperature, explains the crystallization of magmatic-hydrothermal cassiterite in this pegmatite subsystem. A late-stage H₂O-NaCl-(CO₂,N₂) fluid caused subsolidus muscovitization of the magmatic fabric and precipitation of secondary cassiterite in greisen pockets.

1 Introduction

This study evaluates the role of magmatic-hydrothermal aqueous fluids in transporting, concentrating and precipitating cassiterite during crystallization and subsolidus replacement of lithium-cesium-tantalum (LCT) family pegmatite dykes. The extreme lithophile, rare-metal enrichment (Li, Rb, Cs, Be, Nb, Ta, Sn, etc.) in these highly peraluminous magmas has generally been interpreted as resulting from extended disequilibrium crystal fractionation of an undercooled melt. The presence, timing and petrogenetic importance of an aqueous fluid phase, coexisting with the melt, during internal textural and geochemical-mineralogical differentiation of pegmatites, is strongly debated (e.g. London 2014). However, studies indicate the potential importance of melt-fluid and melt-melt immiscibility in flux-rich pegmatite melts (Jahns and Burnham 1969; Webster et al. 1997). In addition, aqueous fluid exsolution is accepted to occur in shallow-level, miarolitic pegmatites that contain crystal-lined open cavities and show abundant fluid inclusions with the typical signature of aqueous fluids (Maneta and Anderson 2018; and references therein).

Consequently, this contribution aims to decipher the temporal and compositional evolution of magmatic-hydrothermal fluid exsolution in LCT pegmatites in order to understand the timing and role of water-saturation during pegmatite differentiation processes and late-stage crystallization at the magmatic-hydrothermal transition. The Early-Neoproterozoic LCT-family Gatumba dyke system (GDS) in Western Rwanda is selected because of

its internally zoned nature with Nb-Ta-oxides and cassiterite mineralization occurring in primary magmatic and secondary metasomatic replacement units. This work will consequently (1) describe the internal anatomy of the GDS, (2) identify mineral compositional variations by Raman spectroscopy, (3) describe the microthermometric properties of magmatic, magmatic-hydrothermal and metasomatic fluid system trapped in quartz, cassiterite, and montebrasite-amblygonite crystals and (4) characterize the evolution of these fluids.

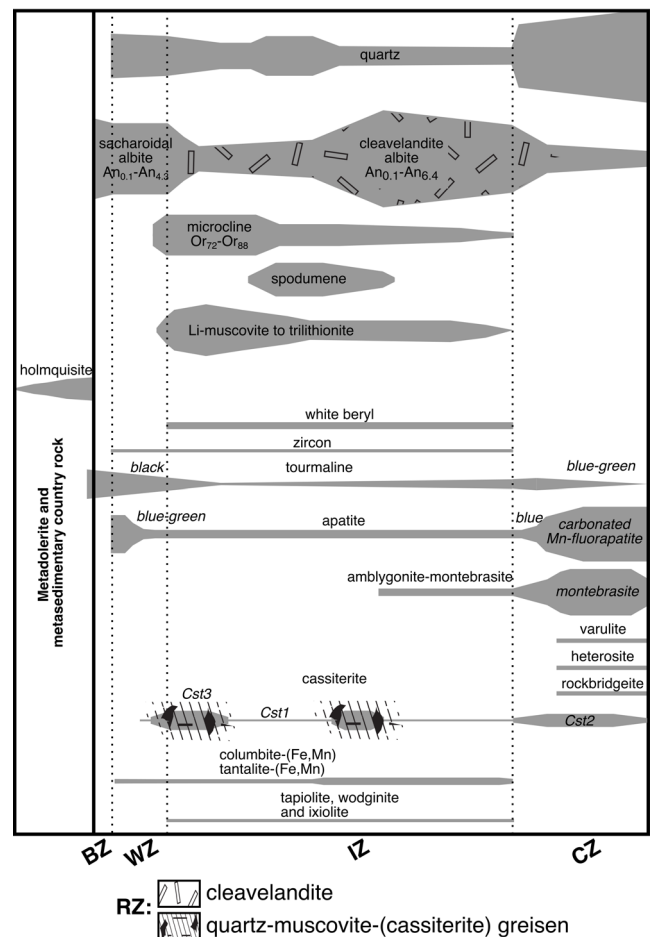


Figure 1. Internal anatomy of the Gatumba pegmatite Dyke System consisting of a border (BZ), wall (WZ), intermediate (IZ), core (CZ) and two replacement zones (RZs).

2 Results and interpretation

2.1 Internal anatomy of the GDS

Field observations in combination with a macro- and

microscopic study and Raman spectroscopic analyses of 64 hand-specimens enabled characterization of the internal anatomy of the GDS. It consists of border, wall, intermediate, quartz core and replacement zones (Fig. 1). The GDS is dominantly intruded along axial planar cleavage planes in greenschist-facies, Mesoproterozoic metasediments (S_0 and $S_1 \sim 260/50$) and bedding-parallel metadolerite sills ($S_1 \sim 270/30$). The pegmatite bodies locally crosscut the sills. The maximum length of the GDS is ~ 850 m and dyke thicknesses range between ~ 15 -40m in the metadolerites and ~ 3 -10m in the metasediments. Small pegmatitic stringers (m- to dm-wide) occur along the cleavage planes in the metasediments.

Contact metasomatism caused locally the development of holmquistite-bearing assemblages in the metadolerites. The border zone (BZ) of the GDS developed as a sharp 0.5-1 cm thin layer and consists of hypidiomorphic and fine-grained quartz, sacharoidal albite and inwardly flaring black tourmaline crystals. The wall zone (WZ) ranges in thickness between 5 cm and 4 dm. It developed an aplitic banding (~ 1 cm thick bands) which consists of medium-grained quartz, fine-grained albite and fine-grained, blue-green apatite. The aplite fabric (~ 15 cm thick) evolves dyke-inwards to a more coarse-grained (cm to dm) anisotropic fabric of inwardly elongate and flaring crystals of quartz, Li-rich micas, microcline, apatite and fine-grained albite. The latter fabric contains mm-scale tantalite-columbite crystals. The interior zone (IZ) demonstrates increased crystal sizes (m-scale) and has thicknesses varying from ~ 3 to ~ 10 m. This zone is dominated by asymmetrical and dominantly discontinuous bi- to tri-mineral assemblages consisting of perthitic microcline-quartz and Li-muscovite-spodumene-quartz. Both quartz and spodumene form as dm- to m-long elongated, euhedral crystals. Primary accessory phases consist of white beryl, zircon, tourmaline, apatite, amblygonite-montebbrasite, niobium-tantalum oxides and rare euhedral cassiterite. In addition, this zone is heavily affected by metasomatic replacement zones of cleavelandite after microcline ($>70\%$) and the subsequent development of quartz-muscovite-cassiterite greisen pockets (0.5-5 dm wide). The greisen pockets can extend towards the WZ. The major part of the cassiterite occurs as subhedral and solid-inclusion-rich phases in the greisens. The core zone (CZ) can occasionally develop as a coarse monomineralic quartz unit in thinner dyke parts. However, it often formed as a cogenetic assemblage of coarse quartz, amblygonite-montebbrasite and blue-apatite, together with minor fine-grained albite and euhedral cassiterite. Alteration of amblygonite-montebbrasite to varulite, heterosite and rockbridgeite is observed. Based on its primary mineralogy, the GDS can be classified as an LCT-family, rare-element class, complex spodumene-subtype pegmatite.

In summary, cassiterite occurs as a primary phase in magmatic-stage microcline, and in cleavelandite units, replacing microcline, from the IZ (i.e. Cst1), but also in assemblage with primary phosphates and quartz in the CZ (i.e. Cst2). Secondary cassiterite occurs abundantly in metasomatic-replacive greisen pockets (i.e. Cst3).

2.2 Raman spectroscopy of minerals

Raman analyses were performed with a Bruker Senterra in order to determine the mineralogical variation of amblygonite-montebbrasite ($n=14$), apatite ($n=17$), and cassiterite ($n=29$) in the GDS. The position and width of Raman bands of amblygonite-montebbrasite are related to its fluorine content and enable as such characterization (Rondeau et al. 2006). Montebbrasite-amblygonite in the CZ shows bands at 601.5 ± 0.5 cm^{-1} (PO_4^{3-} bending and AlO_6^{9-} stretching vibrations), at 1058.5 ± 0.5 cm^{-1} (PO_4^{3-} stretching vibration) and at 3369.9 ± 0.7 cm^{-1} (OH-stretching vibration) with a FWHM of 33.3 ± 1.4 cm^{-1} . These observations indicate a montebbrasite fluorine content of 1.8-4.5 wt.%, 0.5-4.1 wt.%, 1.4 wt.% and 2.3 wt.%, respectively, with an average of 1.8 wt.%. Based on the calibrated montebbrasite F-OH exchange reaction of London et al. (2001) this relates to a low, i.e. ~ 0.5 wt.%, fluorine content of the melt (maximum of 1.2 wt.%).

The Raman spectra of blue apatite in the CZ show PO_4^{3-} vibrations around 965 cm^{-1} (ν_1), 446 cm^{-1} (ν_2), 1060 cm^{-1} (ν_3) and 581 cm^{-1} (ν_4); indicating fluorapatite. The spectra are, moreover, strongly complicated with the presence of sets of (very) strong vibrations at 1222 cm^{-1} ($>\nu_{1,\text{PO}_4}$), 1322 cm^{-1} , 1422 cm^{-1} ($>\nu_{1,\text{PO}_4}$), and a set at 1510 cm^{-1} , 1582 cm^{-1} and 1710 cm^{-1} . The presence of ~ 1420 cm^{-1} vibrations in fluorapatite univocally points to carbonate substitution for phosphate (i.e. ν_{3a,CO_3} mode of ν_{3,CO_3} doublet) and requires a paired substitution or vacancies to maintain charge balance (Tacker 2008). The paired ~ 1500 cm^{-1} and ~ 1580 cm^{-1} peaks indicate carbonate substituting for fluorine, partially charge balanced with carbonate substituting phosphate (i.e. ν_{3b,CO_3} mode of ν_{3,CO_3} doublet). The other peaks may arise from Davydov splitting (Tacker 2008). The shift in position of the 284 cm^{-1} (Ca- PO_4 mode), 311 cm^{-1} (Ca-F mode) and 330 cm^{-1} (Ca-OH mode) peaks towards 266 cm^{-1} , 309 cm^{-1} and 350 cm^{-1} indicates, moreover, divalent cations substituting for Ca^{2+} (cf. Penel et al. 1997). The blue color of apatite in the CZ demonstrates manganese enrichment with dominantly Mn^{2+} substituting for Ca^{2+} . The color itself originates from Mn^{5+} substituting for P^{5+} (Hughes et al. 2004).

Raman spectra of the 3 cassiterite phases (Cst1, Cst2 and Cst3) all show the characteristic A_{1g} band at 633 to 634 cm^{-1} and a less-intense, broad B_{2g} band around 730 cm^{-1} which corresponds to the symmetric and asymmetric stretching of the Sn-O bonds, respectively (Wang et al. 1993). In addition, Cst1 and Cst2 phases contain a medium-weak band at ~ 774 cm^{-1} in combination with a medium-intense band at ~ 834 cm^{-1} . Cst3 contains strong bands at ~ 777 cm^{-1} , ~ 804 cm^{-1} (i.e. infrequent), ~ 833 cm^{-1} and ~ 876 cm^{-1} . The rarely observed ~ 804 cm^{-1} and abundantly-observed ~ 830 cm^{-1} bands are assigned to broad A_n peaks caused by heterovalent substitution of W^{5+} and $\text{Nb}^{5+} + \text{Ta}^{5+}$, respectively (Wang et al. 1993). The ~ 876 cm^{-1} bands are assigned to the A_g peak of columbite-(Mn). Moreover, Cst3 shows abundant 100 - 450 μm large columbite-(Mn) lamellae along its growth zones. Altogether, Cst1, 2 and 3 phases demonstrate paired substitution of

$2(\text{Nb,Ta})^{5+}+(\text{Fe,Mn})^{2+}$ for 3Sn^{4+} . In addition, the inclusion-rich Cst3 phase is characterized by profuse columbite-(Mn) exsolution.

2.3 Microthermometry

Detailed inclusion petrography and microthermometric measurements, with a synthetic fluid inclusion-calibrated Linkam THMS600 stage, were performed on 217 inclusions in quartz, montebasite and cassiterite from 24 wafer sections representing all zones. Only the thin BZ and the cleavelandite RZ could not be studied for inclusions due to the fine-grained and translucent nature of the host minerals. The phase transition temperatures (T_{fm} , $T_{\text{m,ice}}$, $T_{\text{m,hh}}$, $T_{\text{m,CO}_2}$, $T_{\text{m,clath}}$, $T_{\text{h,CO}_2}$ and $T_{\text{h,tot}}$) were determined by slow-rate cooling to -190°C and applying a cyclic heating-cooling method both to obtain precise measurements (especially for $T_{\text{m,ice}}$ and $T_{\text{m,hh}}$) and to avoid metastability and incomplete liquid solidification effects. Important to note is that when the inclusions were only cooled to approximately -130°C , no first melting around -70°C was observed but only a sudden change in the appearance of the aqueous phase around -35°C . The latter transition could then erroneously be identified as first melting.

On the basis of petrography, six (sub-)types of fluid inclusion could be identified (L1a - L1b, L2a - L2b, and L3a - L3b) for which the main characteristics are given in Table 1. The vapor phase of CO_2 -containing inclusions was analyzed with Raman spectroscopy, which detected N_2 up to 25 mol%.

Type L1 inclusions occur in quartz of WZ and IZ and are characterized by saline $\text{H}_2\text{O-NaCl-KCl-CO}_2$, N_2) fluids with ~ 20 wt.% NaCl and ~ 3 wt.% KCl. Both L1a and L1b subtypes are microthermometrically similar except for (1) the presence of $(\text{Ca}^{2+}, \text{Mn}^{2+}, \text{Fe}^{2+})$ -carbonates and paragonite as accidentally trapped solids in the L1a subtype, which is the predominant type in the WZ and (2) the $T_{\text{h,tot}}$ which averages 290°C for L1a and 355°C in L1b. The Na/K ratio lowers from (1) primary inclusions in growth zones in euhedral prismatic quartz to (2) (pseudo)secondary inclusions occurring as intragranular and interphase assemblages spatially related to partial microcline replacement in the cleavelandite RZ. (1). The prevalence of L1a towards the WZ, (2) lower $T_{\text{h,tot}}$ of L1a compared to L1b, (3) the presence of Mn^{2+} and Fe^{2+} carbonates as trapped solids in L1a, and (4) the presence of flaring-inwards black, $(\text{Fe-Mg})^{2+}$ tourmaline both in the BZ and country rocks, point towards (1) the importance of conductive cooling of the hot pegmatite-forming melt at its margins by the cooler, greenschist-facies country rocks (cf. London, 2014) and, (2) the influence of small-scale mobility of mafic-elements from the country rocks to the pegmatite marginal zones.

Type L2 inclusions occur in primary assemblages in the CZ minerals and show low first melting temperatures indicating LiCl enrichment. Occasionally, L2 inclusions show accidentally trapped Li-mica crystals.

L2a subtype inclusions occur in montebasite and Cst2 and demonstrate an $\text{H}_2\text{O-NaCl-LiCl}$ compositions with ~ 6 wt.% NaCl and ~ 10 wt.% LiCl, and a $T_{\text{h,tot}}$ of $\sim 300^\circ\text{C}$. L2b subtype inclusions occur in quartz and demonstrate $\text{H}_2\text{O-}$

$\text{NaCl-LiCl-CO}_2\text{-N}_2$ compositions with ~ 12 wt.% NaCl and ~ 1 wt.% LiCl, and a $T_{\text{h,tot}}$ of 290°C . L2b inclusions form a liquid CO_2 phase upon cooling. Although, L2a and L2b subtype inclusions occur in co-genetic montebasite-apatite-quartz-cassiterite assemblages, the fluid composition is dissimilar between montebasite-Cst2 (L2a subtype) and quartz (L2b subtype). Based on the (1) the lowering in LiCl content from L2a to L2b, (2) the increase in NaCl and CO_2 content from L2a to L2b, in combination with (3) a similar $T_{\text{h,tot}}$ for both subtypes, the evolution of L2a to L2b is interpreted to be caused by montebasite crystallization in a closed CZ. Montebasite formation consumes Li and H_2O which, in turn, forces the pristine $\text{H}_2\text{O-NaCl-LiCl}$ (L2a) fluid composition in the CZ towards the complementary $\text{H}_2\text{O-NaCl-LiCl-CO}_2\text{-N}_2$ composition (L2b). Although no measurable inclusions could be observed in the blue-colored carbonated Mn-fluoroapatite in the CZ, it is suggested that a L2b-subtype fluid was also involved in the formation of this mineral phase.

Type L3 inclusions are hosted as intergranular trails and massive 3D assemblages by mineral phases in the greisen RZ. L3 inclusions contain dominantly Na as cation. A major difference between the subtypes is the presence of a liquid CO_2 phase upon cooling in L3a inclusions. L3a subtype inclusions are hosted in quartz and show an $\text{H}_2\text{O-NaCl-(LiCl,KCl)-CO}_2\text{-(N}_2)$ composition with ~ 15 wt.% NaCl and a $T_{\text{h,tot}}$ of $\sim 280^\circ\text{C}$. L3b subtype inclusions are hosted in Cst3 and show $\text{H}_2\text{O-NaCl-(LiCl,KCl)-(CO}_2,\text{N}_2)$ compositions with ~ 14 wt.% NaCl and a $T_{\text{h,tot}}$ of $\sim 290^\circ\text{C}$. L3a and L3b inclusions are interpreted to represent the same fluid subsystem with slightly varying CO_2 partial pressures.

3 Discussion

Based on the paragenesis of the internal anatomy and the inclusions, the F-poor GDS illustrates a magmatic-hydrothermal fluid evolution from L1, L2 to L3 during solidification from the BZ inwardly to the CZ and subsolidus formation of (1) cleavelandite and (2) greisen RZs in the IZ. Inclusion petrography demonstrates the presence of magmatic saline $\text{H}_2\text{O-NaCl-KCl-(CO}_2, \text{N}_2)$ L1 fluids during early crystallization of the WZ and IZ of the GDS. The high Na/K ratio ($>> 1$) of the L1 fluid is typical for a magmatic fluid which equilibrated with an evolved peraluminous melt (e.g. Audéat et al. 2000) and appears to be controlled in the GDS by microcline fractionation in the WZ and IZ. The observed decrease of the Na/K ratio in the L1 fluid is dominantly caused by

Type	Phases	System	n	Zone	Host	Size (µm)*	Fill rate (%)*	Solids	T _m * (°C)	T _{m,th} * (°C)	T _{m,av} * (°C)	T _{m,co2} * (°C)	T _{m,avth} * (°C)	Th _{co2} * (°C)	T _{h,ut} * (°C)	N ₂ *(mol%)	NaCl wt.%**	LiCl wt.%**	KCl wt.%**	Salinities
L1a	S ₁₀ LV	H ₂ O-NaCl-KCl-(CO ₂ , N ₂)	54	WZ + IZ	Oz	10;60;23	5;32;16	paragonite, siderite, rhodochrosite, kutnohorite	-28.7;-23.4; -26.1	-22.9;-4.1; -20.3	-22.9;-15.2; -20.0	/	3.2;4.2;3.7 (n=4)	/	249;359;288	5;19;13	21.5±1.6	/	3.6±1.4	[3]
L1b	LV	H ₂ O-NaCl-KCl-(CO ₂ , N ₂)	47	WZ + IZ	Oz	6;48;25	6;48;18	/	-28.1;-23.3; -25.9	-22.8;-2.3; -17.1	-22.9;-13.8; -19.4	/	-4.7;2.6;-0.9 (n=16)	/	315;389;356	3;17;12	19.7±1.8	/	2.0±1.7	[3]
L2a	(S)LV	H ₂ O-NaCl-LiCl	40	CZ	Mon+ Cst2	6;130;25	4;5;16	Li-mica	-79.5;-64.4; -70.1	-36.6;-28.6; -31.9	-22.5;-13.3; -17.8	/	/	/	289;304;301	/	5.54±1.3	9.84±1.1	/	[1]
L2b	(S)LV	H ₂ O-NaCl-LiCl-CO ₂ -N ₂	27	CZ	Oz	12;54;22	17;27;22	Li-mica	-60.4;-56.0; -59.4	-22.9;-20.7; -22.2	-58.1;-56.6; -57.6	16.2;20.0; 2.2;3.7;2.7	18.8 (to V)	282;304;292	5;4;7	12.3±0.3	1.0±0.5	/	[1] [2]	
L3a	LV	H ₂ O-NaCl-LiCl-(KCl)CO ₂ -N ₂	28	greisen	Oz	9;31;15	12;15;13	/	-37.7;-29.8; -32.6	-20.1;-15.4; -17.7	-57.8;-56.6; -57.0	12.6;14.1; 13.5 (to V)	257;305;283	12;22;18	15.17±0.13	/	<0.02	<0.02	[2] [3]	
L3b	LV	H ₂ O-NaCl-(KCl)CO ₂ -N ₂	21	greisen	Cst3	11;50;24	8;15;10	/	-24.3;-19.5; -21.9	-11.1;-9.8; -10.3	-4.7;-2.1;-3.2 (n=6)	/	/	254;349;289	8;25;11	14.29±0.36	/	<0.02	[3]	

Values correspond to: *minimum; maximum; average. **average ± standard deviation
 [1] Dubois et al. (2010); [2] Bakker (1997); [3] Bodnar et al. (1989)
 Cst: cassiterite; Mon: montebraisite; Oz: quartz L: liquid; S: solid; V: vapor

Table 1. Microthermometric results of the GDS. excessive albitization. With further internal differentiation and solidification, the GDS melt-fluid system evolves to a Li-rich composition in the CZ as demonstrated by the L2 fluid. In the case of cassiterite mineralizations, literature melt-solubility data indicates that saturation of magmatic cassiterite is unlikely even for Sn-rich, highly-fractionated

peraluminous systems (Štemprok 1990) like the GDS. This explains the rare occurrence of magmatic cassiterite (Cst1) in the IZ. High contents of the fluxes P and Li in the CZ cause extended fractionation by lowering the crystallization temperature which, in turn, enables Sn-saturation and the precipitation of a more significant magmatic-hydrothermal cassiterite phase (Cst2). The L3 fluid is involved in greisen formation reactions and secondary cassiterite (Cst3) precipitation.

Acknowledgements

We thank Dr. K. Piessens and Dr. S. Decrée for the access to the Raman microscope at the Royal Belgian Institute of Natural Sciences. Research of NH is funded by a postdoctoral fellowship of the Research Foundation – Flanders (FWO). The financial support by research grant C14/17/056 of the KU Leuven Research Fund is acknowledged.

References

Audétat A, Günther D, Heinrich CA (2000) Magmatic-hydrothermal evolution in a fractionating granite: A microchemical study of the Sn-W-F-mineralized Mole Granite (Australia). *Geochim Cosmochim Acta* 64:3373-3393.
 Bakker RJ (1997) Clathrates: Computer programs to calculate fluid inclusion V-X properties using clathrate melting temperatures. *Comput & Geosci* 23:1-18.
 Bodnar RJ, Sterner SM, Hall DL (1989) SALTY: a FORTRAN program to calculate compositions of fluid inclusions in the system NaCl-KCl-H₂O. *Comput & Geosci* 15:19-41.
 Dubois M, et al. (2010) Investigation of the H₂O-NaCl-LiCl System: A Synthetic Fluid Inclusion Study and Thermodynamic Modeling from -50 degrees to +100 degrees C and up to 12 mol/kg. *Econ Geol* 105:329-338.
 Hughes JM, et al. (2004) Mn-rich fluorapatite from Austria: Crystal structure, chemical analysis, and spectroscopic investigations. *Am Mineral* 89:629-632.
 Jahns RH, Burnham CW (1969) Experimental studies of pegmatite genesis; I, A model for the derivation and crystallization of granitic pegmatites. *Econ Geol* 64:843-864.
 London D, Vi GBM, Wolf MB (2001) Amblygonite-montebraisite solid solutions as monitors of fluorine in evolved granitic and pegmatitic melts. *Am Mineral* 86:225-233.
 London D (2014) A petrologic assessment of internal zonation in granitic pegmatites. *Lithos* 184-187:74-104.
 Maneta V, Anderson AJ (2018) Monitoring the crystallization of water-saturated granitic melts in real time using the hydrothermal diamond anvil cell. *Contrib Mineral Petrol* 173:83.
 Penel G, et al. (1997) Infrared and Raman microspectrometry study of fluor-fluor-hydroxy and hydroxy-apatite powders. *J Mater Sci Mater Med* 8:271-276.
 Rondeau B, et al. (2006) A Raman investigation of the amblygonite-montebraisite series. *Can Mineral* 44:1109-1117.
 Štemprok M (1990) Solubility of tin, tungsten and molybdenum oxides in felsic magmas. *Miner Depos* 25:205-212.
 Tacker RC (2008) Carbonate in igneous and metamorphic fluorapatite: Two type A and two type B substitutions. *Am Mineral* 93:168-176.
 Wang R, Wu J, Dubessy J, Monchoux P (1993) Raman spectroscopy of Nb, Ta-Rich cassiterite in Beauvoir and Montebraisite granites, France. *Chin J Geochem* 12:353-390.
 Webster JD, Thomas R, Rhede D, Forster HJ, Seltmann R (1997) Melt inclusions in quartz from an evolved peraluminous pegmatite: Geochemical evidence for strong tin enrichment in fluorine-rich and phosphorus-rich residual liquids *Geochim Cosmochim Acta* 61:2589-2604.

Assessment of scandium deportment and recovery potential in Li-Sn-W greisen deposit Cínovec/Zinnwald using EPMA, LA-ICP-MS and TIMA automated mineralogy.

Jakub Výravský^{1,2} Sebastian Hreus², Jan Cempírek², Michaela Vašinová Galiová^{3,4}

¹TESCAN Brno, Czech Republic

²Department of Geological Sciences, Faculty of Science, Masaryk University, Czech Republic

³Institute of Chemistry and Technology of Environmental Protection, Faculty of Chemistry, Brno University of Technology, Czech Republic

⁴Central European Institute of Technology, Brno University of Technology, Czech Republic

Abstract. We investigated Sc content in minerals from Cínovec/Zinnwald greisen deposit. The highest content of Sc was found in ixiolite (avg. 2.09 wt.% Sc₂O₃), columbite (avg 1.34 wt% Sc₂O₃) and zircon (avg. 0.59 wt% Sc₂O₃). Three chemically distinct types of wolframite containing in avg. 0.06, 0.2 and 0.58 wt% Sc₂O₃, respectively were recognized. Cassiterite contains in average 0.068 wt% Sc. From the rock forming minerals, significant content of Sc was found only in zinnwaldite (avg. 63 ppm Sc) and muscovite (avg. 25 ppm Sc), whereas quartz, topaz, albite and K-feldspar contain very low Sc. TIMA was used to measure mineral mass proportions, grain size, deportment of elements and bulk composition of the samples. Because of low content of zircon and columbite in the studied rocks, they host significant fraction of whole rock Sc budget only in mica poor granites (~ 6 ppm Sc bulk). Higher bulk Sc concentrations in greisens are controlled predominantly by amount of micas (especially zinnwaldite) and the most Sc-rich samples (up to ~290 ppm Sc) are the ones most rich in wolframite. Grain size measurements showed, that median grain size of zircon, columbite, xenotime and ixiolite (10-40 µm) is several times lower compared to wolframite and cassiterite.

1 Introduction

Scandium is a light transitional metal with interesting applications for modern industry. The most important use of Scandium is alloying metal to Al-alloys. Al alloys with tenths of wt. % of added Sc have superior hardness and weldability (Ahmad 2003), and are used especially in the aerospace industry, resulting in lighter airplanes consuming less fuel. Other important applications are solid oxide fuel cells, where the electricity is produced directly by oxidation of the fuel (carbohydrates or hydrogen) in presence of solid electrolyte (typically Y₂O₃ doped ZrO₂). Replacement of Y₂O₃ doping with Sc₂O₃ increases ionic conductivity of the electrolyte and decreases necessary operating temperature, and therefore positively affects efficiency and lifespan of the cell (Fergus et al. 2016). Despite clear advantages of scandium, it is only seldom used, due to high prices and lack of reliable supply, so the whole market is limited to ca 10-15 t/year (USGS 2018).

Scandium abundance in the Earth's continental crust is 25 ppm in the upper and 7 ppm in the lower,

respectively (Wedepohl 1995). Due to similarity in ionic radii with Fe, Mg, Mn, Al, Zr, Sn and Ti (Shannon 1976), it is usually dispersed in mafic rock-forming silicates (amphiboles, pyroxenes, Fe-Mg micas) and/or resides in some accessory minerals (garnet, tourmaline, epidote, zircon, columbite, wolframite, cassiterite, rutile, etc.). For that reason, Sc-dominant minerals and economic-grade concentrations are generally rare.

2 The Cínovec/Zinnwald deposit

The Cínovec/Zinnwald deposit is located in the Krušné hory/Erzgebirge area on border between Czech Republic and Germany (majority of the reserves lies in the Czech Republic). Geologically, it belongs to the Saxothuringian zone of the Bohemian massif of Variscan age. The deposit is bound to ca. 1.4 x 0.3 km large, N-S elongated cupola of Cínovec granite, which intruded into rhyolite-filled Teplice caldera. The granite is post-collisional, A-type, slightly peraluminous, strongly fractionated, F, Li, Rb, Sn, W, Nb and Ta-enriched intrusion (Breiter and Škoda 2012; Breiter et al 2017a). The Li-Sn-W greisen mineralization is most extensively developed in the upper part of the cupola, typically not deeper than ca 200 m below the granite-rhyolite contact surface (Breiter et al. 2017a). Four textural types of the ore bodies were recognized in the deposit (Nessler and Seifert 2015; Breiter et al. 2017a): 1) Coarse-grained, flat, up to ca 1 m thick, quartz-zinnwaldite veins with wolframite and cassiterite, which formed in fractures parallel to the granite/rhyolite contact. 2) Mineralogically and texturally similar veins with steep dip and local enrichment by base metals sulphides. 3) Relatively finer-grained greisens in massive bodies up to several tens of meters large, which formed by direct metasomatic greisenization of the original granites. 4) Flat bodies of "mineralized granites" with dispersed fine-grained cassiterite occurring in the southern part of the deposit (deeper than greisens).

Interesting contents of Sc in some ore minerals, especially wolframite, from the Cínovec/Zinnwald deposit have been known for decades, and several tens of kg of Sc-oxide were recovered from the wolframite concentrate in the 1950 s (Brožek et al. 2011). More recently, Sc content of ore minerals from various greisen deposits (including Cínovec/Zinnwald) was investigated by Kempe and Wolf (2006). Johan and Johan (1994) and Breiter et

al. (2013; 2017b; 2019) also reported Sc content of various minerals from this deposit.

With current exploration by Geomet s.r.o. evaluating the possibility of reopening the deposit, new material from recent drill holes has become available. In this contribution, we studied thin sections from all rock types (granites, greisens, hydrothermal veins) by means of EPMA and LA-ICP-MS to measure Sc content in the ore and rock-forming minerals, and we used TIMA (Tescan Integrated Mineral Analyzer) to obtain mineral mass proportions, grain size distribution, deportment of Sc, bulk sample compositions, and to understand the complex polyphase textures on the micro to macro scale.

3 Materials and methods

Twenty-three samples from the 3 drill cores lying on N-S cross-section of the deposit were obtained and 100 µm thick thin section was made from each sample. The EPMA was used to measure chemistry of wolframite, cassiterite, columbite, ixiolite, rutile, scheelite, zircon, fluorite, monazite, xenotime and micas. Trace element content of micas, quartz and feldspars were investigated by LA-ICP-MS

Fifteen samples were scanned with TIMA (Tescan Integrated Mineral Analyzer). The machine is based on SEM with BSE detector and up to 4 SDD EDS detectors and uses combination of BSE intensity and EDS spectra to distinguish boundaries of individual phases (see more in Hrstka et al. 2018). The thin sections were analyzed using “dot mapping” mode (Hrstka et al 2018) with 1 µm BSE and 5 µm EDS grid. In the dot mapping mode, the BSE image is taken first, then initial segments are found, and they are covered by EDS points in selected coarser grid. After that, image segmentation is run again, this time taking into account also EDS data, to distinguish areas with similar BSE signal but different chemistry. If a segment smaller than EDS grid spacing is found during the BSE segmentation, one EDS point is placed in center of such segment, to recognize even the smallest BSE-distinct grains (typically the ore minerals). This mode provides reasonable compromise between robustness of the data and analytical time. Average composition of phases from EPMA, trace element data from LA-ICP-MS and densities from publicly available mineral databases were loaded into TIMA software to calculate deportment of elements, mass proportion of phases and bulk sample compositions (here only Sc is discussed).

4 Results

4.1 Scandium content in ore, accessory and rock-forming minerals

From the studied minerals, the highest Sc content was found in (apparently) secondary Nb-W-Fe-rich ixiolite spatially associated with Nb-Sc-rich wolframites (avg. 2.09 wt% Sc₂O₃ and maximum value of 4.86 wt% Sc₂O₃). After the ixiolites, highest concentrations of Sc reside in columbites (avg 1.34 wt% Sc₂O₃) and zircons (avg 0.59 wt% Sc₂O₃). Three distinct types of wolframite with

different minor element content were recognized: 1) Wolframite with Fe/Mn ratio close to the ferberite/hubnerite boundary with avg. ca 0.2 wt% Sc₂O₃ 2) Nb-enriched wolframite with Fe/Mn ratio close to the ferberite/hubnerite boundary with avg. ca 0.58 wt% Sc₂O₃ 3) near-endmember hubnerite poor in trace elements containing only 0.06 wt% Sc₂O₃ in average.

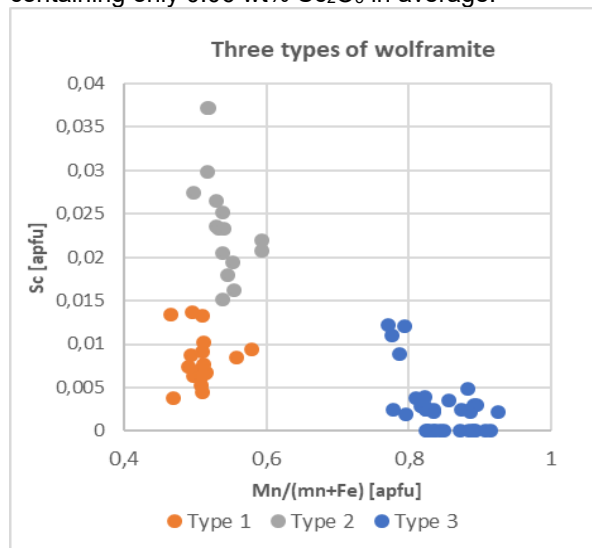


Figure 1. Plot showing 3 distinct types of wolframite, with different Sc, Nb and Mn content. See text for explanation.

The Sc contents in Nb-Ta rich rutile and cassiterite are relatively lower, but still significant (in average 0.16 wt% and 0.068 wt% Sc₂O₃, respectively, fig. 2). From the other minerals, Sc content was discovered in xenotime (avg 0.14 wt% Sc₂O₃), however the volume proportion of xenotime is very low in all studied samples. Concentrations of Sc in fluorite and monazite were systematically below the EPMA detection limit. In scheelite replacing wolframite, only a few points showed Sc content above the detection limit.

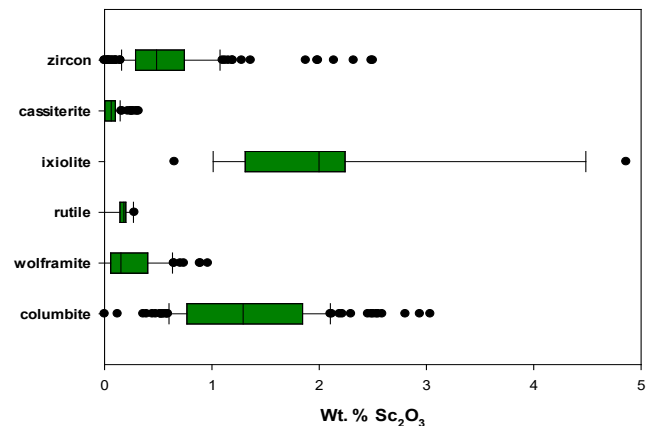


Figure 2. Box diagrams of Sc concentrations in selected minerals from Cínovec/zinnwald greisen deposit. Green boxes correspond to 2nd and 3rd quartile, vertical line in the green box represents median and the solid horizontal lines cover the range from 10 to 90% of the values.

From the rock-forming minerals investigated by LA-ICP-MS, the most important Sc-carrier by far is mica of zinnwaldite composition, containing between 43 and 88 ppm Sc, with average of 63 ppm. The zinnwaldite tends

to be more or less extensively replaced by muscovite, which could locally become the dominant mica. The Sc concentrations in secondary muscovite are about 2-3 times lower than in zinnwaldite (avg. 25.3 ppm). All other minerals are poor in scandium. Quartz contains 0.9 ppm, topaz 2.7 ppm (Breiter et al. 2013), albite < 0.5 ppm and K-feldspar 0.55 ppm.

4.2 Department of Sc and bulk Sc content of individual samples

Because the selected samples are very diverse with regard to rock type and content of ore minerals/micas, the differences in Sc distribution and bulk concentration will be showed on several typical examples.

1) Wolframite-rich hydrothermal vein: This sample is composed of (by mass): ~70% quartz, ~17% wolframite, ~6% micas, ~5% scheelite, ~0,12% ixiolite. Scandium is dominantly contained in wolframite (~ 87 %, 253 ppm) and ixiolite (~ 7%, 21 ppm). The total calculated Sc content of this sample is 287,7 ppm.

2) Cassiterite-rich greisen with extensive replacement of zinnwaldite to muscovite. This sample is composed of (by mass): ~60% quartz, ~21% muscovite, ~7% zinnwaldite, 1.78% cassiterite 0.02% columbite and 0.017% zircon. Scandium is dominantly contained in cassiterite (~ 41 %, 9 ppm) followed by muscovite (~ 25 %, 5.5 ppm) and zinnwaldite (~ 18 %, 4.6 ppm). Columbite and zircon host 6.8 and 4.1 % of bulk scandium, respectively. The total calculated Sc content of this sample is 22.2 ppm.

3) Mica-poor granite below the greisenized horizons. This sample is composed of (by mass): ~40% quartz, ~34% albite, ~22% orthoclase, 2.7% zinnwaldite 0.03% columbite and 0.023% zircon. Scandium is dominantly contained in columbite (~ 43 %, 2.8 ppm) followed by zinnwaldite (~ 25 %, 1.7 ppm) and zircon (~ 17 %, 1.1 ppm). The total calculated Sc content of this sample is 6.6 ppm.

4) Zinnwaldite-rich greisen with cassiterite. This sample is composed of (by mass): ~67% quartz, ~25% zinnwaldite, ~2.5% topaz, 0.54% cassiterite and 0.013% zircon. Scandium is dominantly contained in zinnwaldite (~ 75 %, 15.6 ppm) followed by cassiterite (~ 13 %, 2.7 ppm). The total calculated Sc content of this sample is 20.7 ppm.

From the obtained data it turned out, that zircon and columbite, although they are rich in Sc, are relatively significant Sc carriers only in the mica poor granites, which are generally poor in scandium (< 10 ppm bulk). The reason is their overall low abundance in the rocks (0 - 0.052 wt % for zircon and 0.002 - 0.074 wt % for columbite). The most important minerals responsible for high bulk contents of Sc in the rocks are wolframite and zinnwaldite.

4.3 Grain size distribution of relevant minerals

To understand the potential for individual Sc-bearing minerals to be recovered during ore processing, grain size distribution curves were constructed (fig.3). The

grain size is expressed as ECD (Equivalent Circle Diameter – a diameter of a circle, which would have the same area as the cross-section of the grain). Because the data are too detailed, it is not possible to stitch them, therefore, grains spanning across acquisition field boundaries are actually considered as 2 or more grains, resulting in systematic bias especially for large grains (the calculated values are smaller than real). However, the primary aim of this study was to show the dramatic difference in grain size of cassiterite and wolframite compared to zircon and columbite and to assess the mass fraction of valuable minerals residing in the smallest grains, which should not be affected by this issue.

Our results (fig.3) show, that cassiterite and wolframite form much larger grains compared to zircon, xenotime, Nb-Ta rutile and columbite and that these two minerals tend to be coarser in the veins, compared to massive greisens. Zircon, xenotime, columbite and Nb-Ta rutile form significantly smaller grains with median grain size ranging generally between 10-40 µm. Although ixiolite contains the highest concentrations of Sc out of all investigated minerals, it forms typically rather small, porous, spongy-like grains, which would be probably vulnerable to extensive disintegration during crushing/milling of the ore.

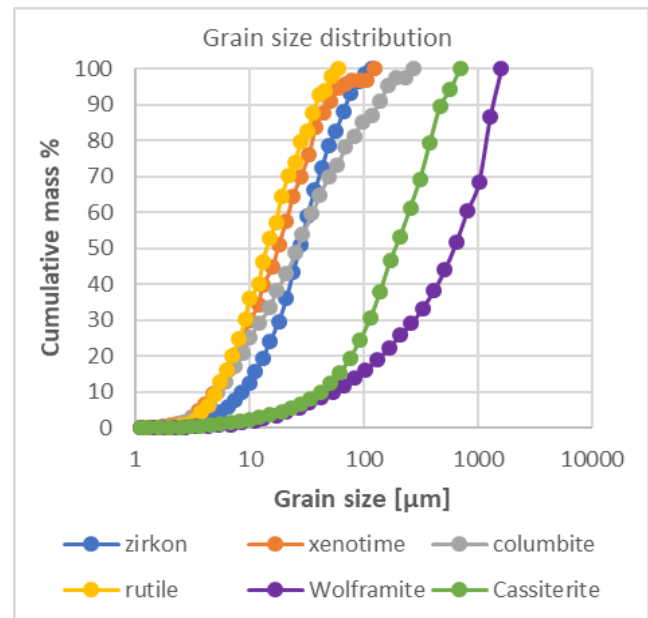


Figure 3: Cumulative grain size distribution curves for selected minerals from the Cínovec/Zinnwald deposit. The grain size is expressed as ECD (see text).

5 Conclusions

In Cínovec/Zinnwald deposit, the most important carriers of Sc in the greisens and ore veins are zinnwaldite and wolframite, whereas cassiterite becomes significant only locally in mica- and wolframite-poor samples. Granites poor in mica and ore minerals contain only about 6 ppm Sc bulk, which resides mostly in columbite and zircon. Zircon, columbite and other accessory minerals (xenotime, monazite, ixiolite...) could be potentially economically interesting due to their content of highly

prized metals (Sc, Nb, Ta, REE, Zr, Hf...), but their small grain size and low abundance complicates their recovery. On the other hand, significant concentrations of Sc (and Nb, Ta) in wolframite, zinnwaldite and cassiterite, which are the primary exploration targets could have a positive economic impact on mining operations.

The complex investigation of the samples by combination of EPMA, LA-ICP-MS and Automated mineralogy is beneficial, because on the one hand it provides (among others) quantitative data on deportment of elements in minerals, which can be used in further studies focused on understanding element behavior during magmatic, greisenization-related and post-greisenization processes, and on the other hand, we can obtain data relevant to the mining industry (grain size, associations...) at the same time from the same samples.

Acknowledgements

We thank Geomet s.r.o. for allowing us to collect the samples needed for this study.

References

- Ahmad Z, 2003. The properties and application of scandium-reinforced aluminum. *The Journal of The Minerals, Metals & Materials Society* 55:35-39. doi:10.1007/s11837-003-0224-6
- Breiter K., Škoda R (2012) Vertical zonality of fractionated granite plutons reflected in zircon chemistry: the Cínovec A-type versus the Beauvoir S-type suite. *Geologica Carpathica* 63(5):383-398. doi: 10.2478/v10096-012-0030-6
- Breiter K, Gardenová N, Vaculovič T, Kanický V 2013. Topaz as an important host for Ge in granites and greisens. *Mineralogical Magazine* 77:403-417.
- Breiter K, Ďurišová J, Hrstka T, Korbelová Z, Hložková Vaňková M, Vašinová Galiová M, Kanický V, Rambousek P, Knésl I, Dobeš P, Dosbaba M 2017a. Assessment of magmatic vs. metasomatic processes in rare-metal granites: a case study of the Cínovec/Zinnwald Sn–W–Li deposit, Central Europe. *Lithos* 292:198-217. doi: 10.1016/j.lithos.2017.08.015
- Breiter K, Vaňková M, Vašinová Galiová M, Korbelová Z, Kanický V 2017b. Lithium and trace-element concentrations in trioctahedral micas from granites of different geochemical types measured via laser ablation ICP-MS. *Mineralogical Magazine* 81:15-33
- Breiter K, Hložková M, Korbelová Z, Vašinová Galiová M 2019. Diversity of lithium mica compositions in mineralized granite-greisen system: Cínovec Li-Sn-W deposit, Erzgebirge. *Ore Geology Reviews* 106:12-27
- Brožek V, Dušek B, Novák M 2011. Chemické listy a české skandium po 55 letech. *Chemické listy* 105:285-314 (in Czech).
- Fergus J, Hui R, Li X, Wilkinson D.P, Zhang J, 2016. *Solid Oxide Fuel Cells: Materials Properties and Performance*. CRC Press, Boca Raton. 314p
- Hrstka T, Gottlieb P, Skála R, Breiter K, Motl D, 2018. Automated mineralogy and petrology - applications of TESCAN Integrated Mineral Analyzer (TIMA). *J. Geosci.* 63:47-63
- Johan, V., & Johan, Z. (1994). Accessory minerals of the Cínovec (Zinnwald) granite cupola, Czech Republic Part 1: Nb-, Ta- and Ti-bearing oxides. *Mineralogy and Petrology*, 51(2-4), 323-343.
- Kempe U, Wolf D (2006) Anomalously high Sc contents in ore minerals from Sn–W deposits: Possible economic significance and genetic implications. *Ore Geology Reviews* 28:103–122.
- Shannon RD (1976) Revised effective ionic radii and systematic studies of interatomic distances in halides and chalcogenides. *Acta Crystallographica A*32: 751–767
- U.S. Geological Survey, 2018, Mineral commodity summaries 2018:

U.S. Geological Survey, 200 p.,
<https://doi.org/10.3133/70194932>
Wedepohl KH (1995). The composition of the continental crust. *Geochimica et Cosmochimica Acta* 59:1217-1232.

Lithium, REE and trace-element contents of stanniferous-greisen mica (Rondonia Tin Province, Brazil) and their relation to REE–Sn–Rare-metal occurrence

Frederico S. Guimarães¹, Anna Luíza R. de Oliveira^{1,2}, Lucas Eustáquio D. Amorim¹, Francisco J. Rios¹, José Vinícius Martins³, Renato de Moraes³

¹*Centro de Desenvolvimento da Tecnologia Nuclear (CDTN-CNEN)*

²*Instituto de Geociências UFMG*

³*Instituto de Geociências USP*

Abstract. The Rondonia Tin Province hosts a polymetallic rare-metal association of Sn, Nb, Ta, Li, W. Mineral chemistry of Li-bearing mica from granite, greisenized granite and greisen of the province was analyzed by combined EPMA and LA-ICP-MS study. Post-magmatic micas are enriched in Li, Rb, F. Lithium incorporation in mica took place, at least partially, as coupled $Fe^{+2} + Al^{+3} \rightleftharpoons Li^{+} + Si^{+4}$ substitution. Post-magmatic micas also show strong depletion of Sn, W, Nb, Ta and Ti. Depleted metals precipitate as oxide inclusions in the newly formed mica, such as cassiterite, rutile, ilmenite and niobates-wolframates. Heavy REE are also depleted in relation to light REE during greisenization, and HREE minerals were also found as inclusions in post-magmatic mica. Weathered siderophyllite displays the highest total-REE contents of all samples, revealing REE mobility during weathering. The observations highlight the importance of greisen micas as records of the greisenization and also as rare metal and REE reservoirs.

1 Introduction

Global REE and rare-metal (Nb, Ta, Li, W) demand is growing and strongly motivated by technological advances: their availability is critical to several high-tech industries worldwide. Granitic Sn deposits are known to bear important Nb-Ta-W-Li occurrences (Ishihara 1980; Pollard 1983; Lehmann 1990; Pirajno 2009), and evolved granites have been suggested both in Brazilian deposits and worldwide as REE hosts (Santana 2013; Santana et al. 2015; He et al. 2017).

Greisen rocks are magmatic-hydrothermal systems formed over a series of complex multi-stage metasomatic processes over highly evolved granites. During evolved granite fractional crystallization, HFSE and volatile elements are progressively enriched in fluid phases. In late- to post-magmatic periods, such fluids interact with the very granitic rock that they originated from, or its country rock, subjecting them to K-feldspathization, albitization and greisenization as the relative activities of K^{+} , Na^{+} and H^{+} change (Pollard 1983; Pollard and Taylor 1986; Pollard et al. 1987; Pirajno 2009).

Micas are the main mineral formed during greisenization (Shcherba 1970; Pollard 1983). The micas themselves tend to be Li-bearing, somewhere on the siderophyllite-zinnwaldite-polyolithionite spectrum and

serve as particularly good rare-metal bearers, to the point of hosting them at ratios nearly the same as the ores, and releasing them to the fluid during greisenization (Shcherba 1970). Li and trace-elements are not readily quantifiable by EPMA analyses, and while Li estimates have been used in the past, several of them exist, with varying uses and results (Tindle and Webb 1990; Tischendorf 1997, 1999).

Recent studies have developed microchemical analyses in such micas via combined EPMA and LA-ICP-MS, with reasonable success (Li et al. 2015; Xie et al. 2015; Breiter et al. 2017, 2019).

Li-bearing mica of the greisens in Rondônia Tin Province (RTP), Rondônia state, Brazil, have been previously studied in PhD theses (Leite Júnior 2002; Sparrenberger 2003), but Li and trace-element content was only available through EPMA estimates and wet chemistry, which are inconclusive. Here we provide the first combined EPMA and LA-ICP-MS analyses for Li-bearing mica for the RTP, preliminary interpretations and its implications for the REE-Sn-Rare-metal occurrences.

2 Geological Setting

The RTP is the close-second largest Sn province in Brazil. The province is in the southwest Amazonian Craton, which is a succession of SW-verging, subparallel tectono-chronological provinces, with ages spanning from the Archean to the Neoproterozoic (Cordani et al. 1979; Tassinari and Macambira 1999; Santos et al. 2008; Scandolara et al. 2013).

The RTP is hosted by the 1800 to 1550 Ma Rio Negro – Juruena Province, and consists of a series of at least seven (Bettencourt et al. 1999), possibly eight (Payolla et al. 2001; Bettencourt 2006) intrusive suites with 1606-975 Ma ages. While the latest three are the most important in respect to Sn + W + Nb + Ta ± Be mineralization, cassiterite occurrences are widespread in all suites (Isotta et al. 1978; Amorim 1999; Santos Jr. 2015; Bettencourt et al. 2016).

The studied occurrence belongs to the Younger Granites of Rondonia Suite (YGR, 995-975Ma), Santa Bárbara and Duduca batholiths.

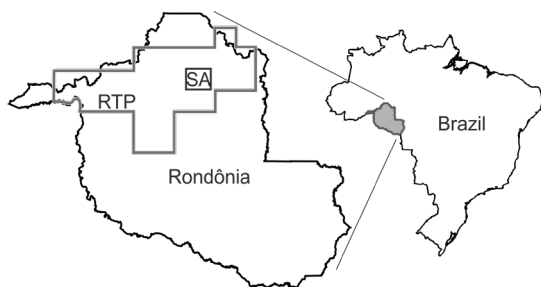


Figure 1: Localization map. RTP = Rondônia Tin Province. SA = Study area.

3 Petrography

The rocks consist of granites, greisenized granites and greisens. Granites are equi- to inequigranular and bear quartz, K-feldspar, albite and dark mica. Mica is intergranular or occurs as circular aggregates. Accessory minerals - zircon, ilmenite, rutile, fluorite, columbite, monazite, bastnäsite, britholite, topaz and cassiterite - are generally found as inclusions in mica aggregates. K-feldspathization and albitization textures are common.

Greisenized granites are equigranular rocks that preserve granitic igneous textures but had albite mostly replaced by mica. Mica hosts most accessory minerals.

Greisens are isotropic equigranular rocks that display reequilibrated textures and lack feldspar completely or almost completely. Cassiterite and columbite are abundant and occur as inclusions in dark mica.

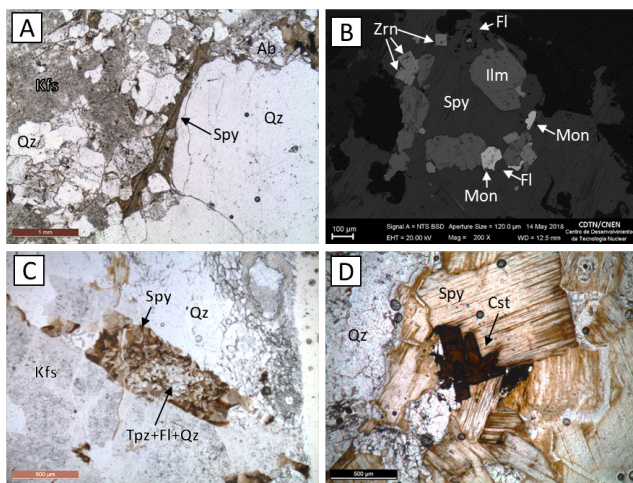


Figure 2: (A) Interstitial granite mica. (B) BSE image of accessory minerals as inclusions on mica aggregate. (C) Albite slab replaced by mica on greisenized granite. (D) Mica aggregate in greisen with cassiterite crystal. Cst = cassiterite; Fl = fluorite; Ilm = ilmenite; Kfs = K-feldspar; Mon = monazite; Qz = quartz; Spy = siderophyllite; TpZ = Topaz. Zrn = zircon.

4 Results

4.1 Major elements

There are two main compositional mica types in the rocks (Fig. 3A): a prevalent, trioctahedral type (siderophyllite grading to lithian siderophyllite), and a dioctahedral type (muscovite to lithian muscovite). Lithium estimates based

on EPMA SiO₂ content were more or less fitting for trioctahedral micas but lacking for dioctahedral (Fig. 3B). Lithium estimates based on F content were satisfactory for all mica types (Fig. 3C). Because of that, samples without LA-ICP-MS analyses had their Li content estimated via F content.

The trioctahedral and dioctahedral types are mainly separated by their Si, Al, Fe, Ti, Li and F content, as the Li-siderophyllite series is richer in the latter four. Additionally, the trioctahedral series displays negative Fe + Al (IV) x Si + Li correlation (Fig. 3D).

MgO and Na₂O contents are very low in all mica types (<1.8% and <0.3% respectively).

4.2 REE and trace elements

The rare metals (Nb, Ta, W) plus Ti and Sn show positive correlations, particularly amongst Li-siderophyllite (Fig. 4A). Highest rare metal and Sn contents are observed in mica from granites, and a few samples of mica from greisenized granite, a trend opposite to Li (Fig. 4B). Greisen mica follows with intermediate values, and the remaining mica samples from greisenized granites display the lowest values (samples circled in Fig. 4).

Total REE (REEt) content varies from <1 ppm to ~800 ppm, and lithology has no influence in it. However, the ratio between light REE and total REE is highly dependent on lithology (Fig. 4C). Mica from granites show the lowest values of this ratio while greisens display the highest. Some mica from greisenized granites has intermediate values, while others have ratios as high as the ones from greisen. Weathered siderophyllite displays higher REE totals amongst samples (samples marked with rectangles in Fig. 4).

5 Discussion

SiO₂-based Li estimates assume Li is incorporated via the coupled substitution Fe²⁺ + Al³⁺ <=> Li⁺ + Si⁴⁺ at the octahedral and tetrahedral site. This mechanism is present in trioctahedral mica as evidenced by the negative Fe + Al (IV) x Si + Li correlation (Fig. 3D) The correlation is present but not at a perfect 1:1 ratio, indicating another mechanism should also be in effect. Dioctahedral micas, on the other hand, show no correlation of these values (Fig. 3B) suggesting another Li-incorporation mechanism is predominant. This hypothesis also explains why SiO₂-based Li estimation was not accurate.

Lithium is a good proxy for greisenization since its contents rise consistently from granitic (magmatic) siderophyllite to greisenized-granite and greisen (postmagmatic) siderophyllite, towards the lower-left corner of the Mg_{li} x Fe_{al} diagram (Fig. 3A). Mg_{li} stands for Mg – Li and Fe_{al} for Fe(t) + Mn + Ti – Al (IV), in apfu (Tischendorf, 1997). Incipient weathering of siderophyllite moves samples towards the upper-right corner as Li is lost and Mg and Fe added.

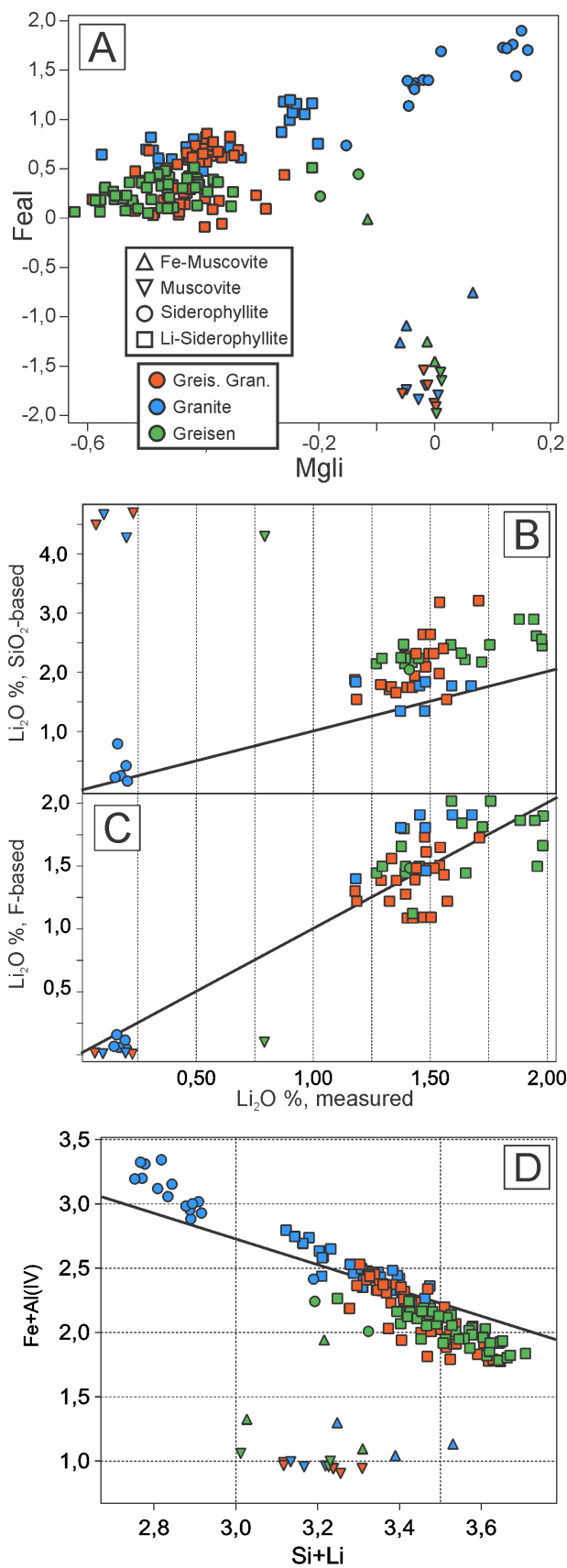


Figure 3. (A) MgLi versus Feal plot (Tischendorf, 1997). (B-C) Li₂O as measured via LA-ICP-MS versus Li₂O estimates based on EPMA SiO₂ and F content respectively. Solid lines have a slope of 1. (D) Fe+Al versus Si + Li plot, apfu. Solid line has a slope of -1.

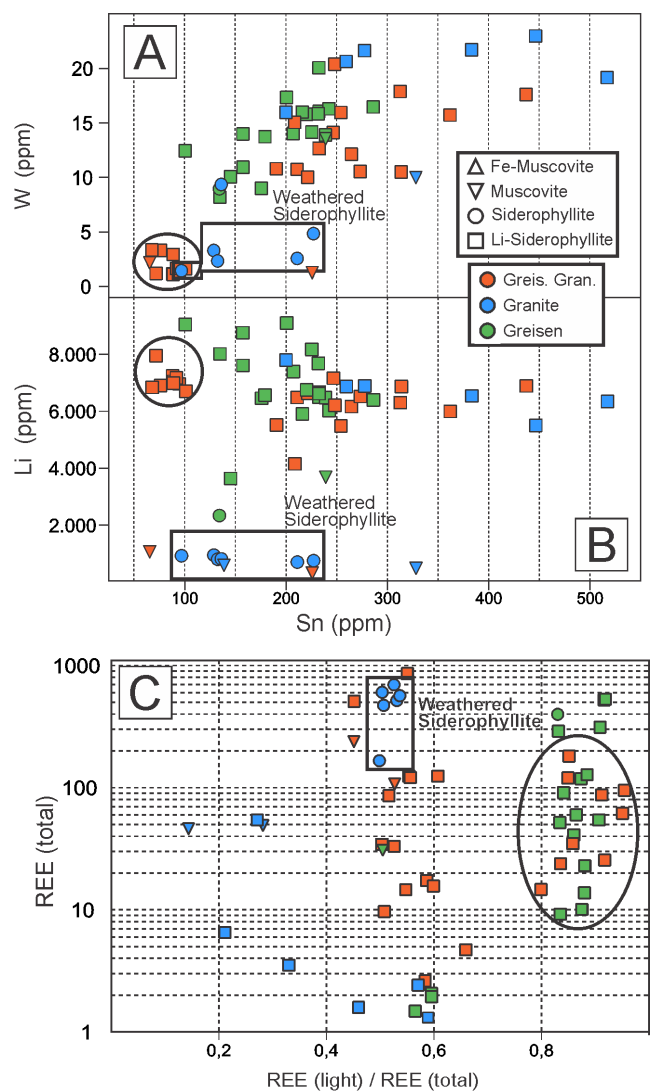


Figure 4. A-B: Sn in ppm versus W and Li respectively. C: Ratio of Light REE / REE(total) versus REE (total) in ppm.

Di octahedral micas bear little to no Li and have been interpreted as a late sericitization event. Magmatic mica hosts the highest contents of rare metal and Sn, and the lower contents observed occur in post magmatic mica from greisenized granite. Greisenized granites also retain some preserved igneous mica that bears high rare-metal content. Greisen texture has been fully reequilibrated, so mica trace-element composition cannot be distinguished between magmatic and post-magmatic stages. Greisenization seems to produce mica relatively depleted in HREE and enriched in LREE when compared to magmatic mica.

6 Implications

Micas are thought to be important reservoirs of Sn and rare metals in evolved granites (Shcherba 1970). During greisenization, said elements can be partitioned to the fluid and/or to precipitate as mineral inclusions as new mica is formed (Pirajno 2009). This process seems to be instrumental to ore formation at the RTP, particularly as

greisens and greisenized granites host cassiterite, niobates and wolframates mainly as inclusions on mica.

Moreover, while LREE minerals were observed as inclusions in mica in all rock types, HREE minerals were observed only as inclusions in mica from greisen and greisenized granite. Similarly, it is suggested that relative depletion in HREE from magmatic micas during greisenization could trigger HREE mineral formation.

High REE content on weathered siderophyllite suggests weathering has some bearing on REE mobilization on evolved granites.

Acknowledgements

We thank chief exploration geologist Henrile Meireles for access and support, CNPq (Projects 424909/2016-2 and 308781/2014-7), FAPEMIG (Project PPM 00357-17) and CDTN/CNEN (project 0614.26)

References

- Amorim JL (1999) Recursos Minerais. In: Scandola J (ed) *Geologia e Recursos Minerais do Estado de Rondônia*. CPRM, Brasília, pp 67–76
- Bettencourt JS (2006) SHRIMP-RG U-Pb ZIRCON GEOCHRONOLOGY OF GNEISS FROM THE RIO CRESPO INTRUSIVE SUITE, SW AMAZONIAN CRATON, RONDÔNIA, BRAZIL: New insights about Protolith crystallization and metamorphic ages. In: *South American Symposium on Isotope Geology*. pp 49–52
- Bettencourt JS, Juliani C, Xavier RP, et al (2016) Metallogenic systems associated with granitoid magmatism in the Amazonian Craton: An overview of the present level of understanding and exploration significance *Journal of South American Earth Sciences Metallogenic systems associated with granitoid m. J South Am Earth Sci* 68:22–49. doi: 10.1016/j.jsames.2015.11.014
- Bettencourt JS, Tosdal RM, Leite WB, Payolla BL (1999) Mesoproterozoic rapakivi granites of the Rondonia Tin Province, southwestern border of the Amazonian craton, Brazil-I. Reconnaissance U-Pb geochronology and regional implications. *Precambrian Res* 95:41–67. doi: 10.1016/S0301-9268(98)00126-0
- Breiter K, Hložková M, Korbelová Z, Galiová MV (2019) Diversity of lithium mica compositions in mineralized granite-greisen system: Cinovec Li-Sn-W deposit, Erzgebirge. *Ore Geol Rev* 106:12–27. doi: 10.1016/j.oregeorev.2019.01.013
- Breiter K, Vaňková M, Galiová MV, et al (2017) Lithium and trace-element concentrations in trioctahedral micas from granites of different geochemical types measured via laser ablation ICP-MS. *Mineral Mag* 81:15–33. doi: 10.1180/minmag.2016.080.137
- Cordani UG, Tassinari CCG, Teixeira W, et al (1979) *Evolução Tectônica da Amazônia com Base nos dados Geocronológicos*. In: *Segundo Congreso Geológico Chileno*. Arica, p 12
- He C, Xu C, Zhao Z, et al (2017) Petrogenesis and mineralization of REE-rich granites in Qingxi and Guanxi, Nanling region, South China. *Ore Geol Rev* 81:309–325. doi: 10.1016/j.oregeorev.2016.10.021
- Ishihara S (1980) The granitoid Series and Mineralization. doi: 10.1590/S1516-18462008000300012
- Isotta CAL, Carneiro JM, Kato HT, Barros RJL (1978) *Projeto Província Estanífera de Rondônia*. Porto Velho
- Lehmann B (1990) *Metallogeny of Tin*. Springer-Verlag
- Leite Júnior WB (2002) *A Suíte Intrusiva Santa Clara (RO) e a Mineralização primária polimetálica (Sn, W, Nb, Ta, Zn, Cu, Pb) Associada*. Universidade de São Paulo
- Li J, Huang XL, He PL, et al (2015) In situ analyses of micas in the Yashan granite, South China: Constraints on magmatic and hydrothermal evolutions of W and Ta-Nb bearing granites. *Ore Geol Rev* 65:793–810. doi: 10.1016/j.oregeorev.2014.09.028
- Payolla BL, Bettencourt JS, Leite Jr WB, Basei MAS (2001) The Rio Crespo intrusive suite: Geological U-Pb and Sm-Nd isotopic evidence for a major 143 Ga arc-related magmatism in the Rondonia state, SW Amazonian craton, Brazil. In: *3 South American symposium on isotope geology Extended abstracts*. Servicio Nacional de Geología y Minería, Chile, p 642
- Pirajno F (2009) *Hydrothermal processes and mineral systems*
- Pollard PJ (1983) *Magmatic and postmagmatic processes in the formation of rocks associated with rare-elements deposits.pdf*. *Trans Inst Min Metall (Section B Appl Earth Sci)* 92:
- Pollard PJ, Pichavant M, Charoy B (1987) Contrasting evolution of fluorine- and boron-rich tin systems. *Miner Depos* 22:315–321. doi: 10.1007/BF00204525
- Pollard PJ, Taylor RG (1986) Progressive Evolution of Alteration and Tin Mineralization: Controls by Interstitial Permeability and Fracture-Related Tapping of Magmatic Fluid Reservoirs in Tin Granites. *Econ Geol* 81:1795–1800. doi: 10.1055/s-2002-30668
- Santana IV (2013) *Caracterização Mineralógica e Geoquímica de Ocorrências de Terras Raras no Maciço Granítico Serra Dourada, Goiás/Tocantins, Brasil*
- Santana I V, Wall F, Botelho NF (2015) Occurrence and behavior of monazite-(Ce) and xenotime-(Y) in detrital and saprolitic environments related to the Serra Dourada granite, Goiás/Tocantins State, Brazil: Potential for REE deposits. *J Geochemical Explor* 155:1–13. doi: 10.1016/j.gexplo.2015.03.007
- Santos JOS, Rizzotto GJ, Potter PE, et al (2008) Age and autochthonous evolution of the Sunsás Orogen in West Amazon Craton based on mapping and U-Pb geochronology. *Precambrian Res* 165:120–152. doi: 10.1016/j.precamres.2008.06.009
- Santos Jr. PSM (2015) *Metalogênese do Depósito de Estanho Liberdade, Campo Novo de Rondônia - RO*. Universidade de Brasília
- Scandola JE, Fuck RA, Dantas EL, Souza VS (2013) Geochemistry of Jamari complex, central-eastern Rondônia: Andean-type magmatic arc and Paleoproterozoic crustal growth of the southwestern Amazonian craton, Brazil. *J South Am Earth Sci* 46:35–62. doi: 10.1016/j.jsames.2013.04.002
- Shcherba GN (1970) Greisens. *Int Geol Rev* 12:114–150. doi: 10.1080/00206817009475216
- Sparrenberger I (2003) *Evolução da Mineralização Primária Estanífera Associada ao Maciço Granítico Santa Bárbara, Rondônia*. Universidade de São Paulo
- Tassinari CCG, Macambira JB (1999) Geochronological provinces of the Amazonian Craton. *Episodes* 174–182. doi: 10.1080/00206819709465329
- Tindle AG, Webb PC (1990) Estimation of lithium contents in trioctahedral micas using microprobe data: application to micas from granitic rocks. *Eur J Mineral* 2:595–610. doi: 10.1127/ejrm/2/5/0595
- Tischendorf G (1999) The Correlation Between Lithium and Magnesium in Trioctahedral Micas: Improved Equations for Li₂O Estimation from MgO Data. *Mineral Mag* 63:57–74. doi: 10.1180/minmag.1999.063.1.07
- Tischendorf G (1997) On Li-Bearing Micas: Estimating Li from Electron Microprobe Analyses and an Improved Diagram for Graphical Representation. *Mineral Mag* 61:809–834. doi: 10.1180/minmag.1997.061.409.05
- Xie L, Wang RC, Groat LA, et al (2015) A combined EMPA and LA-ICP-MS study of Li-bearing mica and Sn-Ti oxide minerals from the Qiguling topaz rhyolite (Qitianling District, China): The role of fluorine in origin of tin mineralization. *Ore Geol Rev* 65:779–792. doi: 10.1016/j.oregeorev.2014.08.013

Discovery, delineation and development of Australia's first caesium deposit: Exploration implications from applied technology.

Nigel W. Brand

Geochemical Services Pty Ltd, The University of Western Australia

David J. Crook, Stuart T. Kerr, Russel N. Panting

Pioneer Resources Limited

Sophie O. Perring, Christabel J. Brand

Portable XRF Services Pty Ltd

Abstract. The Sinclair Caesium Deposit, discovered in 2016, delineated in 2017 and developed in 2018, is Australia's first mining operation to commercially extract the caesium-rich mineral pollucite. Economic caesium deposits are extremely rare, with only three known mining operations having produced commercial quantities of pollucite, including the Bernic Lake Mine (Manitoba, Canada), Bikita Mine (Zimbabwe) and the Sinclair Mine (Western Australia).

The formation of pollucite only occurs in extremely differentiated complex lithium-caesium-tantalum (LCT) pegmatites and given their size and rarity, caesium-rich deposits globally are either challenging to explore for or failed to form during the emplacement of the LCT pegmatite. The discovery and development of the Sinclair Caesium Mine has provided a rare opportunity to examine an extremely differentiated complex LCT pegmatite with applied technologies to provide an insight for future discoveries of economic caesium deposits.

1 Introduction

The announcement of a significant caesium (Cs) intersection (6m at 25.7% Cs₂O) associated with lithium-caesium-tantalum (LCT) pegmatites on the Pioneer Dome was reported by Pioneer Resources Ltd (PIO) on 4th October 2016 (PIO ASX 2016a). Follow-up drilling delineated a cluster of pollucite lenses, named the Sinclair Caesium Deposit (Sinclair), with an initial Mineral Resource Estimate of "10 500 t of the caesium ore pollucite with a grade of 17.1% Cs₂O" (PIO ASX 2017). The commencement of mining operations was reported on 13th September 2018 (PIO ASX 2018), less than 2 years from discovery.

Pollucite [(Cs,Na)₂(Al₂Si₄O₁₂) 2H₂O] is a rare mineral with a high value attributed to its high caesium content (~29.66% Cs₂O) which forms in extremely differentiated LCT pegmatite systems. Global supply is very constrained, and world resource estimations are unavailable (USGS, 2019). Caesium metal is sold in limited quantities under confidential contracts so a true market price is unavailable.

The uses of Cs include: the production of photoelectric cells, energy conversion devices such as fuel cells, magneto-hydrodynamic generators and polymer solar

cells, however its main use is in the manufacture of caesium formate brine, a heavy liquid (1.8 to 2.4 g/cm³) used in high-pressure, high-temperature well drilling for oil and gas.

2 Location and geological Setting

The Sinclair Caesium Deposit is located 35 km north-north west of Norseman in Western Australia or 125 km south-south east of Kalgoorlie.

The mine is located within the Archaean-aged Yilgarn Craton of Western Australia, within the Coolgardie Domain of the Norseman –Wiluna Greenstone Belt. The Coolgardie Domain is dominated by two large granitoid domes, the Pioneer and Widgiemooltha Domes; the long axes of which trend north to north-northwest respectively. The younger Binneringie Dyke, an east-west trending Proterozoic dyke, transects the sequence between the Widgiemooltha and Pioneer Domes.

The Pioneer Dome is defined by a granitoid core which has intruded older Archaean-aged gneiss (Fifty Mile Tank Gneiss) and a greenstone sequence. The greenstone sequence comprises a mafic suite (black shale, ultramafic and mafic volcanics, and gabbro intrusions) which in turn has been stratigraphically overlain by a thick sedimentary sequence. Pegmatite bodies have preferentially intruded into the greenstone sequence. The Pioneer Dome and surrounding lithoscape has been metamorphosed to greenschist and lower-amphibolite facies and has been multiply deformed resulting in isoclinal folding (Griffin 1989).

At least 13 clusters of pegmatites, including LCT pegmatites, have been identified along a 20 km strike length on the eastern flank of the Pioneer Dome (Fig 1). The East Pioneer pegmatite corridor comprises a narrow (<1 km wide) mafic suite of rocks trending roughly north-south, faulted up against the Fifty Mile Tank Gneiss. This corridor is dominated by strong north-south cleavages and pegmatite dykes occur in both the gneiss and greenstones (Griffin 1990). To date the only available dating is of the Fifty Mile Tank Gneiss dated at $\geq 2664 \pm 5$ Ma (Nelson 1997).

The pegmatite wall zones typically consist of quartz, K and Na feldspars, and muscovite, while core zone minerals include biotite, lepidolite, petalite, pollucite

(where present), tourmaline, and beryl.

Less deformed pegmatites consistently cut more deformed pegmatites which suggest that there were several episodes of pegmatite intrusion.

3 Discovery and applied technology

Conventional soil samples were collected over mapped pegmatites within the mafic-ultramafic stratigraphy of the East Pioneer pegmatite corridor. All soil samples were analysed using a lithium-Index Calibration developed for a field portable XRF in association with Pioneer as a proxy for lithium (PIO 2016a); used to prioritise areas of interest in the field.

Confirmation four-acid ICP-MS laboratory analyses were undertaken prior to detailed prospect mapping, rock chip sampling and a decision to drilling. Over 7,000 soil samples identified nine high priority and 15 mid-rank targets including PEG008a, host to the Sinclair.

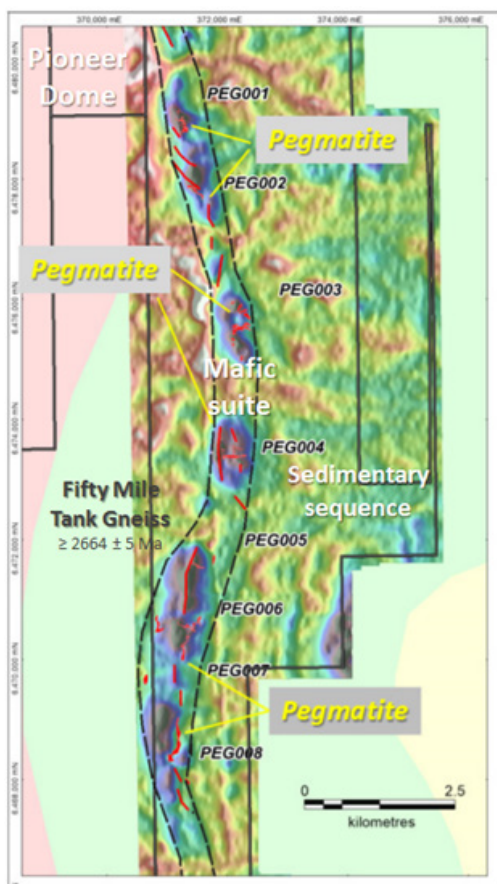


Figure 1. East Pioneer pegmatite corridor showing outcropping pegmatites (red) and main geological units in relation to total count (U, Th, K) radiometric image (PIO 2016b).

Commencement of an inaugural 5000m RC drilling programme in mid-2016 (PIO 2016b) identified both high grade lithium and caesium (PIO 2016a) being the discovery hole for the Sinclair Zone Caesium Deposit.

The discovery of pollucite and its subsequent extraction through mining provided Pioneer with a unique opportunity to investigate and understand the geology, mineralogy and geochemistry of such a rare deposit style

and provide insights for future exploration of caesium-rich deposits.

During the delineation and development of the Sinclair Mine, in addition to conventional laboratory four acid, fusion XRF assays and XRD mineral identification, a range of new, or more readily available, technologies were employed. These included RAMAN spectroscopy, short-wavelength infrared spectroscopy (SWIR), fourier-transform infrared spectroscopy (FT-IR), portable XRF (pXRF) and micro-XRF (μ XRF).

Throughout the extraction of the pollucite mineralisation pXRF was exclusively used for grade control, enabling rapid and accurate dataflow. RAMAN spectra for mineral identification were collected from grade control samples and are being used to augment geological mapping and mineral zonation definition ahead of the Company embarking on further exploratory drilling.

4 Sinclair LCT pegmatite

4.1 Pegmatite lithochemochemistry

Benchmarked against other known LCT pegmatites, the host pegmatite of Sinclair shows a very distinct and unique chemistry reflecting its extreme fractionation (Fig 2). The geochemistry of Sinclair will be discussed further in the talk.

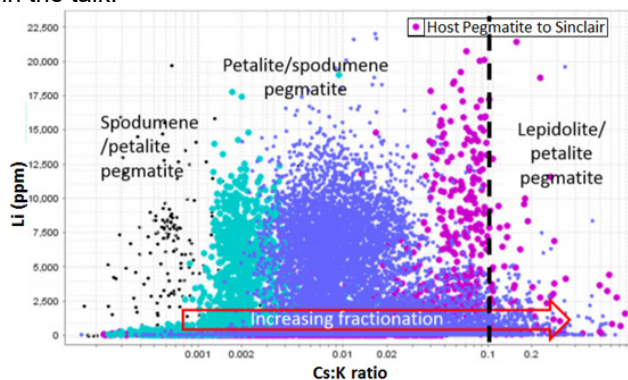


Figure 2. Cs:K ratio vs Li from three LCT pegmatites showing the extreme fractionation undertaken at Sinclair (purple).

4.2 Geology and mineralogy

Common with the Bernic Lake and Bikita Deposits, the Sinclair Deposit host LCT pegmatite consists of an outer pegmatite wall zone that is coarse grained, and dominated by plagioclase feldspar, muscovite and quartz with accessory garnet, tourmaline and beryl and an inner core zone composed of, in decreasing order, quartz, albite (cleavelandite), lepidolite, pollucite, petalite, zinnwaldite, eucryptite, beryl, amblygonite and topaz. The core zone is 'capped' by a thick (~35-40m) monomineralic potassium feldspar zone (Fig 3).

The pollucite mineralisation is monomineralic, similar to the Bernic Lake Deposit (London 2018), and forms small (~2-10m) discreet pods spatially associated with albite (cleavelandite), lepidolite, petalite and quartz.

To date, very minor instances of spodumene have

been detected, unlike pollucite zones described from Tanco (Stilling et al 2006) and Bikita (Dittrich et al 2018).

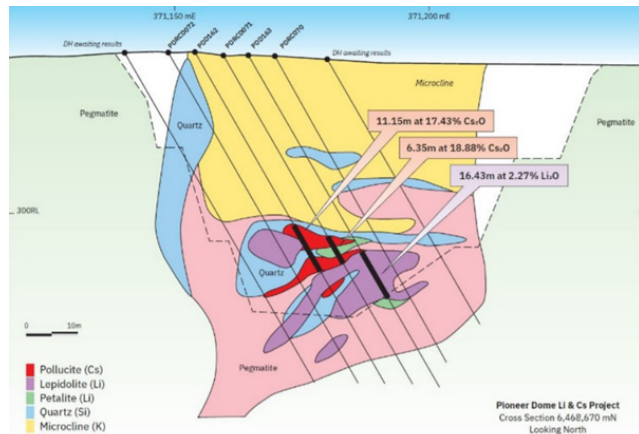


Figure 3. Geological cross section of Sinclair at 6468670mN with diagrammatic pit outline.

4.3 Mineral and chemical zonation in the core zone

During the development of the Sinclair Mine, grade control sampling was analysed using a matrix match Cs calibration on a countertop CTX XRF instrument, enabling rapid assay turnaround, which was of paramount importance due to the short time scale of operational cycles of the mining operation.

The use of the CTX pRFX instrument provided a comprehensive geochemical dataset, albeit without a Li analysis at the time.

To verify the presence of and distinguish between white lithium silicate minerals (eg petalite, eucryptite and spodumene) a RAMAN spectrometry application was developed.

Integrated results from the pXRF and RAMAN spectroscopy show a central core of discrete pollucite pods associated with quartz flanks and zoned by lepidolite and albite (cleavelandite). Zinnwaldite, petalite and eucryptite occur further outboard (Fig 4).

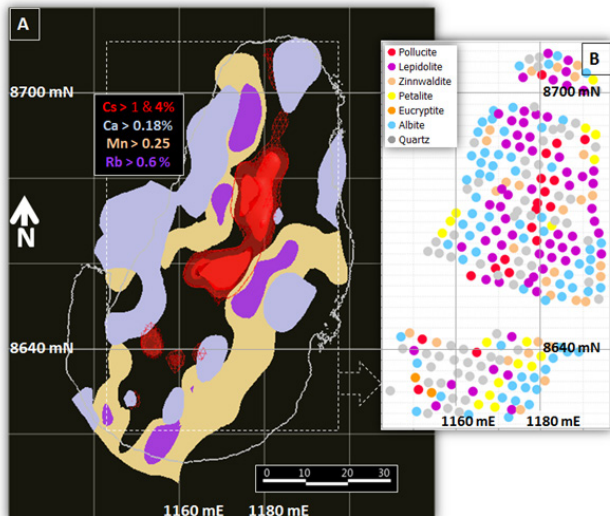


Figure 4. Plan section of Sinclair at 295 m RL showing a) selected

element concentration analyzed by pXRF and b) dominant mineral phase identified by RAMAN spectroscopy. Both data sets showing element and mineral zonation associated with the pollucite in the central core zone.

4.4 Pegmatite weathering

Published data on pegmatite weathering, associated regolith development and landscape evolution is rare to non-existent; and is a knowledge gap when exploring for LCT Pegmatites in deeply weathered terrains such as the Yilgarn Craton.

During the development of the Sinclair Deposit, zones of weathered pollucite were encountered typically associated with contacts and structures along which groundwater had penetrated. Weathered material collected during mining is being investigated using μ XRF following a successful trial which showed invading Ca and Sr veinlets from groundwater penetrating into amblygonite (Fig 5).

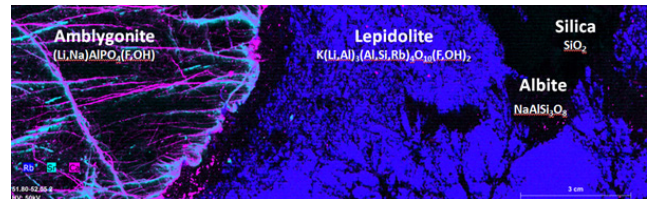


Figure 5. Micro XRF element map of amblygonite, lepidolite, quartz and albite (cleavelandite) from PDD167; 51.80 to 52.05 mdh showing invading Ca and Sr veinlets in amblygonite from penetrating ground waters.

5 Discussion and exploration implication

The discovery of a rare caesium deposit and its host LCT pegmatite has provided an opportunity to investigate and thus improve understanding of this style of mineralization utilizing Pioneer's extensive exploration and mining data sets to develop models for future discoveries.

The ongoing research into the geological setting of Sinclair has demonstrated its unique litho-geochemical signature and mineralogical characteristics of both fresh and weathered samples, using applied technologies that provide tools and applications that will be utilised in future exploration for Cs-rich LCT pegmatites.

Acknowledgement

The authors wish to acknowledge the effort of Pioneer Resources Limited staff, consultants and contractors associated with the discovery, delineation and development of Sinclair, Australia's first caesium mine and the continued and ongoing support from the Pioneer's Board of Directors.

References

Dittrich T, Seifert T, Schulz B, Hagemann S, Gerdes A, Pfänder J (2018) Lithium-Cesium-Tantalum pegmatites in Zimbabwe and Western Australia, and the formation of Neo-Archean massive (Cs)-pollucite mineralisations 10.13140/RG.2.2.14118.98888.
 Griffin TJ (1989) Widgiemooltha, Western Australia. Geological Survey of Western Australia 1:250,000 Geological Series

- Explanatory Notes.
- Griffin TJ (1990) Geology of the Granite-Greenstone Terrane of the Lake Lefroy and Cowan 1:100 000 sheets, Western Australia: Western Australia Geological Survey, Report 32, 53p.
- London D (2018) Ore-forming processes within granitic pegmatites. *Ore Geol Rev* 101:349-383.
- Nelson DR (1997) Evolution of the Archaean granite-greenstone terranes of the Eastern Goldfields, Western Australia: SHRIMP U-Pb zircon constraints. *Precam Res* 83: 57-81.
- Pioneer Resource Limited (2016a) Lithium-caesium discovery at Pioneer Dome. <http://www.pioneerresources.com.au/downloads/asx/pio2016100401.pdf>
- Pioneer Resource Limited (2016b) Pioneer announces a 5,000m RC drilling programme at its Pioneer Dome lithium project. <http://www.pioneerresources.com.au/downloads/asx/pio2016072701.pdf>
- Pioneer Resource Limited (2017) Mineral resource estimate for the Sinclair Caesium Project. <http://www.pioneerresources.com.au/downloads/asx/pio2017032201.pdf>
- Pioneer Resource Limited (2018) Pioneer commences mining operations at Sinclair caesium mine. <http://www.pioneerresources.com.au/downloads/asx/pio2018091301.pdf>
- Stilling A, Černý P Vanstone PJ (2006) The Tanco pegmatite at Bernic Lake, Manitoba.
- Xvi. Zonal And Bulk Compositions And Their Petrogenetic Significance. *Can Min* 44:599-623.
- U.S. Geological Survey (2018) Mineral commodity summaries 2018: USGS 200 p <https://doi.org/10.3133/70194932>.

Challenges of byproduct recovery of critical elements

Sarah M. Hayes, Nadine M. Piatak, Sarah Jane White, Robert R. Seal II
U. S. Geological Survey, Reston, VA, USA

Abstract. Ensuring adequate, affordable supplies of elements critical to green growth and other high technology devices is a growing challenge. Many critical elements are produced exclusively as byproducts of other commodities, meaning that their supply depends on recovery of the primary target commodity. Byproduct elements tend to be considered collectively, but some critical elements travel through ore-processing circuits with a primary commodity, making them more amenable to recovery, whereas others report to the waste streams. This behavior is dictated by the mineralogical hosts of critical elements and their deportment during processing. For example, germanium, critical in the manufacture of fiber optics, is commonly hosted within the lattice of the sphalerite that is targeted by zinc extraction; thus the potential for recovery is quite high. In contrast, most tellurium, which is used in CdTe-based solar panels, reports to the waste during the concentration of copper sulfide minerals from porphyry copper deposits. This contrast highlights the importance of understanding the identity and deportment of critical element-hosting phases when designing strategies for improving byproduct recovery.

1 Introduction

1.1 Elements critical to green growth

The elements identified as critical depend on the evaluators' frame of reference, but critical elements are often defined as having an important purpose and being subject to risk of supply disruption (e.g., NRC 2008; Graedel et al. 2012). Most recent literature on element criticality has originated from highly developed economies (U.S., E.U., and Japan) and focused on the availability of minor elements with specialized applications in high technology and green growth (Fig. 1; Hayes and McCullough 2018; Fortier et al. 2018). In many cases, these technology critical elements (TCE) are used in specialized applications without suitable substitutes, are geologically scarce or concentrated in a few geographic locations, or are not traded on commodity exchanges but are instead sold under, often private, fixed-price contracts between individual entities (Jaffe et al. 2011). Most of the elements that have frequently been identified as critical in Figure 1 (often evaluated and frequently identified as critical) are TCEs, which find application in green growth-related industries, including energy generation using solar (Ag, Cd, Te, In, Ga, Se and Ge) or wind (Nd, Pr, Dy, and Tb), energy transmission and storage (Li, Co, Ni, Sb, and graphite), and other technologies that underpin modern society (Nassar et al. 2016; Fortier et al. 2018).

Many critical elements are recovered as byproducts

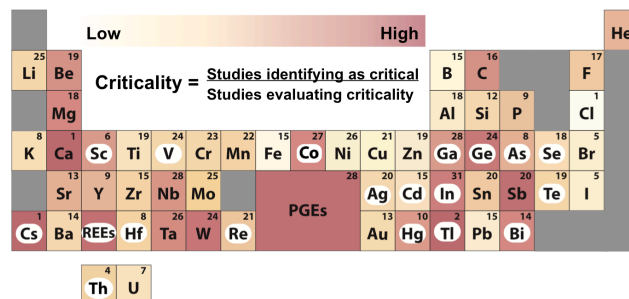


Figure 1. Summary of results of 32 comprehensive criticality studies published 2005-2018. Background color indicates criticality, calculated as the number of studies identifying each element as critical by the number of studies evaluating it. The values in the top right corner are the number of studies evaluating each element. Elements in white bubbles are primarily recovered as byproducts. Modified after Hayes & McCullough, 2018.

(Fig. 1), meaning that the economic viability of the mineral deposit is determined by production of a different mineral target(s) (Schulz et al. 2017). The classification of a particular element can change among deposits or as economic conditions fluctuate. Recovery of TCE as byproducts effectively decouples supply and demand because the availability of byproduct elements depends on both the production of a primary mineral commodity and the availability of a process to profitably recover the byproduct elements (Nassar et al. 2015). Sometimes, byproduct element-containing wastes are discarded without being processed due to the relatively insignificant value of the byproduct elements, inconsistent concentrations in the product stream, or a fundamental knowledge barrier of deportment or extractive technologies. Once diluted in a waste stream (e.g., tailings, slag, etc.) and decoupled from the value of the primary commodity, the potential for recovery from reprocessing becomes even more challenging, both from an economic and technological perspective.

1.2 All byproducts are not created equal

Although from a criticality perspective, byproducts often get treated collectively, the behavior of byproduct TCEs during extraction can be very different. The potential for increasing byproduct recovery depends on the behavior of byproduct TCEs throughout the extraction process of the target primary commodity. To date, relatively little work exists in the public domain on this topic. Further, our understanding of elemental cycling during ore beneficiation and processing is based primarily on limited studies that capture a snapshot of a mill feed flowing through concentration, smelting, roasting and refining processes (e.g., Ojebuoboh 2008; Licht et al. 2015). The utility of a single snapshot is limited given the heterogeneity within and among orebodies, deposit

types, and extractive processes.

Furthermore, byproduct elements may occur in a variety of mineral forms, which may or may not travel with the primary commodity through the physical and chemical separations applied during ore processing. Thus, mineralogy controls the department of byproducts throughout extraction processes.

1.3 This study: A tale of two byproduct elements

Tellurium and germanium are often identified as critical elements. Tellurium is used in CdTe-based photovoltaics and thermoelectric devices (USGS 2019). Germanium is used in fiber optics and other optical devices (USGS 2019). Both are recovered exclusively as byproducts. This study compares and contrasts the behavior of Te and Ge during the extraction processes of the primary commodities copper and zinc, respectively, to illustrate the importance of mineralogy for determining byproduct critical element recovery.

2 Methods

The department data presented here are from the literature (Kavлак and Graedel 2013; Ojebuoboh 2008; Licht et al. 2015). Each study reported the flow of a byproduct critical element throughout an extraction process in order to assess critical element department. In the Te case, this involved samples from a specific mine, mill, smelter, and refinery. Elemental analyses were then combined with mass through flux values in order to determine Te behavior throughout the process. The germanium flows are based on a global substance flow analysis using values mined from the literature.

Mineralogical characterization of Te- and Ge-bearing phases is also based largely on published sources. Te-bearing minerals have been examined in porphyry copper sulfide mill concentrates by electron microprobe using energy dispersive spectroscopy (Skidmore 2016). Other studies in hydrothermal ores have examined Te substitution into sulfides (George et al. 2015; George et al. 2016; George et al. 2017; Keith et al. 2018). Characterization of Ge in sphalerite has been ongoing since the early 1900s by a variety of techniques (Frenzel et al. 2014). Recent literature has focused on the mechanisms of Ge incorporation into sphalerite using x-

ray absorption spectroscopy (Cook et al. 2015; Belissont et al. 2016; Bonnet et al. 2016).

3 Results and Discussion

3.1 Byproduct element department and the role of mineralogy

Approximately 4.5 % of Te is recovered from the single operational stream examined and represents an overestimation of global flows because not all extraction operations recover Te. On a global basis, 0.5 % of Ge is recovered (Fig. 2). Regardless of the different study scopes, they highlight differences in the department of Te and Ge throughout their respective processes.

During the initial concentration step, 90 % of Te reports to the tailings. Additional Te losses of 50 % and 10 % occur during smelting and refining, respectively. In contrast, essentially all Ge remains with the primary Zn concentrate, which is either processed by hydrometallurgy (with <1 % loss Zn) or, less commonly, sent to a smelter. In contrast to Te, the majority of Ge is lost in Zn leach residues that are not processed to recover Ge.

3.2 Mineralogy matters!

The divergent behavior of these commodities during ore processing is explained by their mineral hosts. Tellurium occurs primarily within sulfides: pyrite, galena, and, to a lesser extent, chalcopyrite as (nano-)inclusions or in direct substitution (George et al. 2015; George et al. 2016; Keith et al. 2018). A small fraction of Te is present in a variety of telluride minerals, mostly of Ag and Bi, or sulfosalt minerals (Skidmore 2016). During Cu sulfide mineral concentration, most Te is lost because the flotation process is designed to send most pyrite and, incidentally, other Te-containing minerals to waste.

In contrast, Ge substitutes directly into the lattice of sphalerite, although the exact nature of the substitution is still actively debated in the literature (Bonnet et al. 2016; Cook et al. 2015; Belissont et al. 2016). Thus, the Ge accompanies the Zn through the extraction process until the sphalerite is decomposed, thereby decoupling the Zn and Ge. The identity and department of the mineralogical hosts of byproduct critical elements are essential for

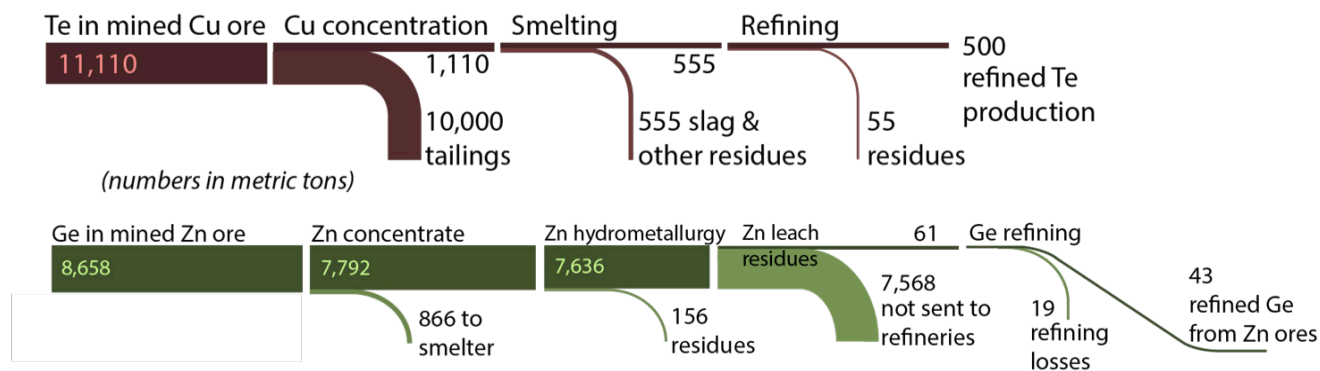


Figure 2. Department of tellurium and germanium during the extraction process of their respective primary commodity (values in metric tons). Modified after Kavлак and Graedel, 2013; Licht et al., 2015.

understanding their behavior and has important implications for improving byproduct recovery.

3.3 Implications for future supply of byproduct critical elements

The mineralogy and deportment of these elements in ore and during processing have important implications for the potential to increase recovery of these elements as byproducts in the short and long term. Perhaps in the near-term, the easiest strategy for recovering additional Te and Ge may simply be to increase the percentage of mining operations that implement recovery in their existing processes. This is identified in Figure 2 as the primary limitation to Ge recovery. However, if the concentration is below a currently economically viable cut-off grade or if adding an additional processing circuit is cost-prohibitive, this may not be feasible. Nassar et al. estimates that Te production could be increased by a factor of 3 by simply initiating more complete processing of ores (in prep.). Figure 2 indicates that Ge recovery could be increased to 62% percent, a potential huge short-term improvement, if all ores were amenable to processing by current methods.

On a longer time scale, improvements to byproduct recovery will depend on improvements to current recovery strategies, such as the smelting Cu ores that results in a 50% loss of Te, and Cu and Zn refining processes, in which 10% and 30% of Te and Ge are lost, respectively. Without a transformative change in extractive technologies, only incremental improvements are likely to be made in this way. However, even slight improvements to extraction efficiency could make a large difference in the industrially available Te or Ge, because extraction efficiencies are currently quite low.

For Te, the most impactful way to increase Te recovery would be to address the concentration of Cu minerals, where 90% Te is lost (Ojebuoboh 2008; Skidmore 2016). One strategy would be adding a secondary flotation circuit to target sulfide and Te-bearing minerals, which could be beneficial because Te is a penalty metal for smelters (Fountain 2013). This is not likely based solely on economic factors, but it is conceivable that environmentally-motivated regulations could support the recovery of byproduct critical elements. For example, if mines were required to recover pyrite to mitigate the acid generating potential of mine tailings, recovery of Te (and other critical elements) could potentially offset some of the added cost. Many mines already separate and stockpile pyrite to minimize acid mine drainage. Understanding the mineralogical hosts of byproduct critical elements is an essential first step in being able to identify and capitalize on opportunities to increase recovery in the future.

3.4 Future directions and challenges

Assessing the potential for byproduct recovery of critical elements is hampered by a lack of basic information on byproduct critical element behavior during ore processing and mineralogical hosts. Challenges include the

following:

1. The recovery of byproduct elements is, by definition, not critical to economic viability, and may not be of keen interest to industrial producers who focus on the primary commodity. The difference in scale between byproducts and primary commodities is highlighted by the 2018 estimated world production (excluding U.S.) of 120 and 440 metric tons of Ge and Te, respectively when compared with the primary commodity production of 21 and 13 *million* metric tons for Cu and Zn, respectively (USGS 2019).
2. Collection of representative samples is challenging, especially if the orebody is heterogeneous, ore processing conditions are unstable, or the element of interest is concentrated in low abundance phases that can contribute a “nugget effect” in chemical analysis. Determination of a representative distribution of trace phases in bulk ore samples is a challenge for both chemical and mineralogical analysis.
3. Challenges remain for the extractive technologies needed to profitably recover byproduct critical elements at low concentrations. Research is ongoing on topics such as the use of ionic liquids (e.g., Jenkin et al. 2016), but mainstream extractive technologies have not changed for base metals since flotation (1900s) and solvent extraction-electrowinning (SX-EW; 1960s). Tellurium is only recovered from the pyrometallurgical extraction of Cu and, as more Cu is recovered using SX-EW, the potential to recover Te may decrease. Recovery of byproducts may benefit from or be reduced by transformative shifts to new technologies.
4. The economics of increasing byproduct element recovery is tricky since a dramatic increase in supply is likely to result in a decreased market price. This complicates the implementation of byproduct recovery circuits where economics are initially marginal. Further, demand for these TCEs can be capricious as the demands evolve with technology.

Despite these challenges, widespread recent interest in critical elements may increase industrial engagement. Connection with green growth and high technology through recovery of byproduct critical elements could increase social license in mining. Recovering byproduct critical elements before they become diluted in mine wastes and enter the surficial environment could potentially limit liabilities from emerging new data on the potential toxicity of some critical elements.

Additional studies of byproduct TCE accumulation or loss in the extraction process will facilitate the design of extractive technologies to target these elements. This research could help bolster proactive measures, such as industry incentives or protective trade policies, that may be required to supply future industrial demands for byproduct critical elements.

Acknowledgements

The authors recognize and appreciate the discussions and constructive feedback of Jane Hammarstrom, Nedal Nassar, Jeff Mauk, and Dan Hayba during preparation. This work was supported by U.S. Geological Survey Mineral Resources External Research Program (USGS/G12AP20054) and the Eastern Mineral and Environmental Resources Science Center.

The authors declare no conflicts of interest. Any use of trade, firm, or product names is for descriptive purposes only and does not imply endorsement by the U.S. Government.

This licensed material constitutes "a work of the United States Government" as defined by the U.S. Copyright Act, 17 U.S.C. sec. 101; 17 U.S.C. sec. 105. A "work of the United States Government" is a work prepared by an officer or employee of the United States Government as part of that person's official duties and is not subject to copyright protection in the United States. However, copyright in a foreign country may apply.

References

- Belissont R, Muñoz M, Boiron M-C, Luais B, Mathon O (2016) Distribution and oxidation state of Ge, Cu and Fe in sphalerite by μ -XRF and K-edge μ -XANES: insights into Ge incorporation, partitioning and isotopic fractionation. *Geochimica et Cosmochimica Acta* 177:298-314. doi: <https://doi.org/10.1016/j.gca.2016.01.001>.
- Bonnet J, Cauzid J, Andre-Mayer A-S, Peiffert C, Caumon M-C, Rouer O, Mosser-Ruck R (2016) Trace element distribution (Cu, Ga, Ge, Cd, and Fe) in sphalerite from the Tennessee MVT deposits, USA, by combined EMPA, LA-ICP-MS, Raman spectroscopy, and crystallography. *The Canadian Mineralogist* 54:1261-1284. doi: 10.3749/canmin.1500104.
- Cook JN, Etschmann B, Ciobanu LC, Geraki K, Howard LD, Williams T, Rae N, Pring A, Chen G, Johannessen B, Brugger J (2015) Distribution and substitution mechanism of Ge in a Ge-(Fe)-bearing sphalerite. *Minerals* 5. doi: 10.3390/min5020117.
- Fortier SM, Nassar NT, Lederer GW, Brainard J, Gambogi J, McCullough EA (2018) Draft critical mineral list—Summary of methodology and background information—U.S. Geological Survey technical input document in response to Secretarial Order No. 3359 Open-File Report. Reston, VA, pp 26.
- Fountain C (2013) The whys and wherefores of penalty elements in copper concentrates Metallurgical Plant Design and Operating Strategies. Perth, WA, pp 502-518.
- Frenzel M, Ketris MP, Gutzmer J (2014) On the geological availability of germanium. *Mineral Deposita* 49. doi: 10.1007/s00126-013-0506-z.
- George L, Cook NJ, Ciobanu CL, Wade BP (2015) Trace and minor elements in galena: A reconnaissance LA-ICP-MS study. *American Mineralogist* 100:548-569. doi: 10.2138/am-2015-4862.
- George L, Cook NJ, Ciobanu CL (2016) Partitioning of trace elements in co-crystallized sphalerite-galena-chalcopyrite hydrothermal ores. *Ore Geology Reviews* 77:97-116. doi: 10.1016/j.oregeorev.2016.02.009.
- George L, Cook N, Ciobanu C (2017) Minor and trace elements in natural tetrahedrite-tennantite: Effects on element partitioning among base metal sulphides. *Minerals* 7:17. doi: 10.3390/min7020017.
- Graedel TE, Barr R, Chandler C, Chase T, Choi J, Christoffersen L, Friedlander E, Henly C, Jun C, Nassar NT, Schechner D, Warren S, Yang MY, Zhu C (2012) Methodology of metal criticality determination. *Environ Sci Technol* 46:1063-1070. doi: 10.1021/es203534z.
- Hayes SM, McCullough E (2018) Critical minerals: A review of elemental trends in comprehensive criticality studies. *Resources Policy in press*. doi: 10.1016/j.resourpol.2018.06.015.
- Jaffe R, Price J, Ceder G, Eggert R, Graedel T, Gschneidner KA, Jr., Hitzman M, Houle F, Hurd A, Kelley R, King A, Milliron D, Skinner BJ, Slakely F (2011) Energy critical elements: Securing materials for emerging technologies. American Physical Society, Washington, DC.
- Jenkin GRT, Al-Bassam AZM, Harris RC, Abbott AP, Smith DJ, Holwell DA, Chapman RJ, Stanley CJ (2016) The application of deep eutectic solvent ionic liquids for environmentally-friendly dissolution and recovery of precious metals. *Minerals Engineering* 87:18-24. doi: <https://doi.org/10.1016/j.mineng.2015.09.026>.
- Kavlak G, Graedel TE (2013) Global anthropogenic tellurium cycles for 1940-2010. *Resour Conserv Recycl* 76:21-26. doi: 10.1016/j.resconrec.2013.04.007.
- Keith M, Smith DJ, Jenkin GRT, Holwell DA, Dye MD (2018) A review of Te and Se systematics in hydrothermal pyrite from precious metal deposits: Insights into ore-forming processes. *Ore Geology Reviews* 96:269-282. doi: 10.1016/j.oregeorev.2017.07.023.
- Licht C, Peiro LT, Villalba G (2015) Global substance flow analysis of gallium, germanium, and indium: Quantification of extraction, uses, and dissipative losses within their anthropogenic cycles. *J Ind Ecol* 19:890-903. doi: 10.1111/jiec.12287.
- Nassar NT, Graedel T, Harper EM (2015) By-product metals are technologically essential but have problematic supply. *Sci Adv* 1:1-10.
- Nassar NT, Wilburn DR, Goonan TG (2016) Byproduct metal requirements for U.S. wind and solar photovoltaic electricity generation up to year 2040 under various Clean Power Plan scenarios. *Appl Energ*. doi: 10.1016/j.apenergy.2016.08.062.
- Nassar NT, Goonan, T (In preparation) Exploration of tellurium supply potential.
- NRC, National Research Council (2008) Minerals, critical minerals, and the U.S. economy. National Academies Press, Washington, DC.
- Ojebuoboh F (2008) Selenium and tellurium from copper refinery slimes and their changing applications. *World Metall* 61:33-39.
- Schulz KJ, DeYoung Jr JH, Seal II RR, Bradley DC (2017) Critical mineral resources of the United States—Economic and environmental geology and prospects for future supply. U. S. Geological Survey, Reston, VA.
- Skidmore A (2016) The behavior of tellurium during copper ore processing at the American Smelting and Refining Company (Tucson, AZ). Department of Chemistry and Biochemistry. University of Alaska Fairbanks, Alaska, Fairbanks.
- USGS, U. S. Geological Survey (2019) Minerals Yearbook: Volume 1. Metals and Minerals. U. S. Geological Survey, Washington,

Challenges and Opportunities in tellurium supply

Daniel J Smith, Gawen R T Jenkin, David A Holwell
University of Leicester, UK

Manuel Keith,
University of Leicester and Technische Universität Berlin, Germany

Abstract. Tellurium is vital to a number of emergent and growing technologies, including photovoltaic power and thermoelectric devices. It is however, one of the rarest elements in the Earth's crust, and future supply of Te is not without challenges. At present, Te is almost exclusively sourced from the reprocessing of waste materials from copper refining. There is potential for an increase in Te production from this source, but production statistics indicate that there has actually been a decrease in the efficiency of Te supply from this source. Alternatives are deposits in which Te is the dominant product (e.g. Dashuigou, China; Moctezuma, Mexico), mines where Te is a by-product (Kankberg), or mines in which Te may be recovered as a by-product. Tellurium enrichments are reported from epithermal Au, orogenic Au, VMS, IOCG and Carlin-type deposits. In many deposits, Te is likely hosted in pyrite – abundant but relatively low grade, and not always considered an ore phase. Tellurium in pyrite is unlikely to be recoverable with current technologies. Where Te occurs as stoichiometric component of gold, silver and other metal/metalloid minerals, recovery may be targeted. Co-recovery with precious metals is key to economic supply of Te.

1 Tellurium demand and supply

Tellurium is a chalcogen metalloid, with a small global demand for a variety of applications, including metallurgy, rubber vulcanization and as an additive in glass for telecommunication fibre optics. However, the last decade has seen a rapid growth in demand for tellurium in the electronics industry; Te is an increasingly important element in semi-conductors, photovoltaic cells, and thermo-electric devices. Photovoltaic power alone now consumes about 40% of world Te production (Anderson 2019).

The growth of Te consumption in modern technology has caused some researchers and analysts to suggest that in the future, Te demand could outstrip supply coupled with its low crustal abundance, has led to it being considered near-critical (Sykes et al. 2016)

Supply of Te is dominated by the reprocessing of anode slimes, waste products from copper refining. Crude tellurium is recovered alongside copper, gold, platinum group metals and selenium. Additional tellurium is sourced from the processing of waste stream from lead and nickel smelters. A significant boost in Te supply (Fig. 1) came from production at the Dashuigou deposit, Sichuan Province, China in 2017–8 (Anderson 2019). Alongside reprocessing anode slimes, China now accounts for over 60% of Te supply based on available

data. There remains a long term, strategic benefit in improving Te supply from a range of sources.

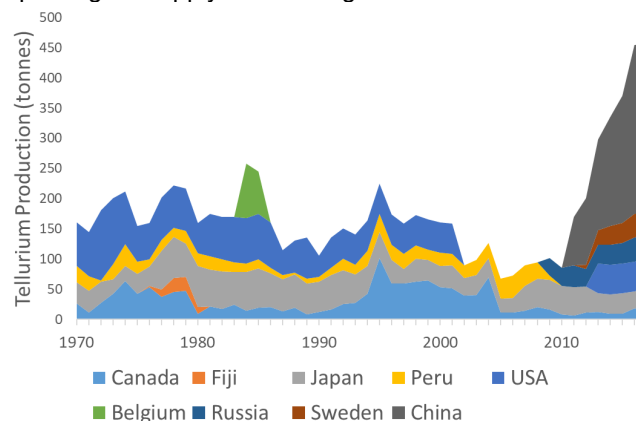


Figure 1. Tellurium production, 1970 – 2017. Data from BGS World Mineral Production statistics.

2 Reducing criticality

There are two principal routes to mitigate Te shortages – reducing the usage of Te in its applications, and increasing the production from existing or novel sources. In their review of Te supply risk-mitigation, Bustamante et al. (2018) outlined significant potential for “dematerialization” in photovoltaic CdTe thin film technologies in particular (e.g. Plotnikov et al. 2011). The implementation of end-use efficiencies, alongside fluctuations in the photovoltaic market, have contributed to Te prices remaining relatively low over recent years, after a spike in 2010 (Fig. 2).

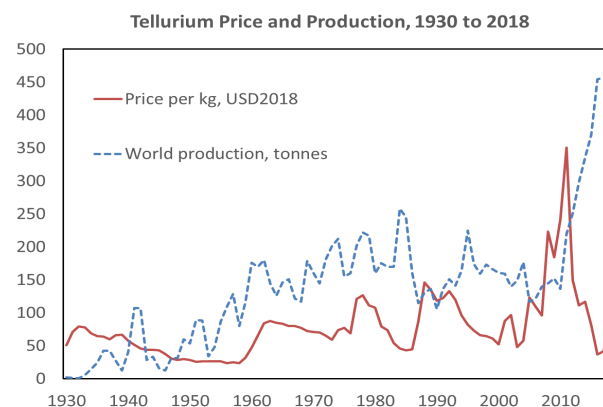


Figure 2. Tellurium price 1930–2018. Values indexed by US PPI (all commodities, NSA, from US Bureau of Labor Statistics). Data from USGS Historical Statistics and Mineral Commodity Summaries and BGS World Mineral Production Data.

Tellurium yield from anode slimes could realistically be doubled (Bustamante and Gaustad 2014a). However, the economic drivers for this are complex, as the profitability of anode slime reprocessing is dominated by the recovery of precious metals, not tellurium. Tellurium's status as a "by-product of a by-product" means that its production is weakly coupled to price changes.

A further challenge to Te production as a by-product from copper is that the intensity of recovery has declined over the last 30 years. This is a function of the changing nature of copper production, rather than a decline in the efficiency of anode slime reprocessing. A significant proportion of global copper demand is now met by heap-leaching and solvent extraction – electrowinning (SXEW) of low grade copper ores. This method offers no potential for the recovery of Te (Bustamante and Gaustad 2014b), so by-product intensity of production from copper has declined since the 1970s (Fig. 3).

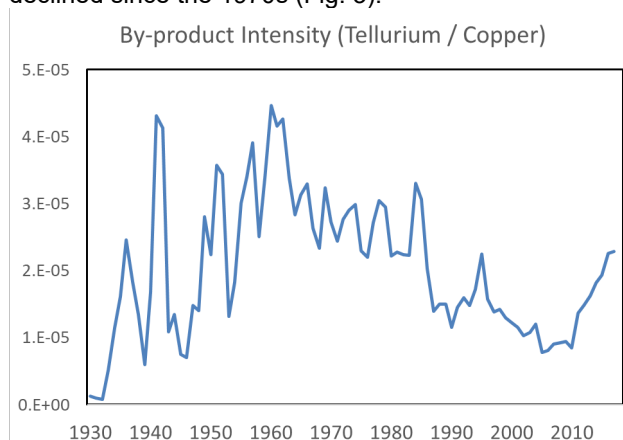


Figure 3. By-product intensity of tellurium (ratio of global Te production in tonnes to global Cu production in tonnes). Increase in intensity since 2010 reflects direct mining of Te from China, and discrepancies between USGS and UK production data (USGS withhold production data from 2004 onwards). After Bustamante et al. (2018).

Direct mining of Te resources is underway at the Te-Bi deposit at Dashuigou, and planned at Kankberg, Sweden, where it is a co-product with gold (Voigt 2018). These two deposits have or will have significant impact upon Te supply, and are likely to keep Te prices low for at least the next few years.

The economics of tellurium therefore make it a high risk commodity for producers; it has a growing but small market, and a number of potential mechanisms to reduce demand and/or increase supply – in some cases significantly and abruptly. The consequence of this is that increasing supply of tellurium is poorly incentivized from an economic perspective.

3 Mineralogy and Ore Deposits

As a chalcogen element, Te is typically associated with sulphide-rich ores of base and precious metals. Most recovery has been from copper deposits, but as the recovery is from refinery wastes, and run-of-mine ores are infrequently analysed for tellurium, it is not clear which specific styles of copper mineralisation Te is

particularly associated with (if any). Chalcopyrite cannot accommodate significant concentrations of Te; other minerals in polymetallic, Cu-rich deposits such as galena and arsenopyrite are more likely hosts for Te (Makuei and Senanayake 2018 and references therein).

Keith et al. (2018) reviewed Te concentrations in bulk rock and pyrite analyses. In many deposit classes, the concentrations of Te in pyrite overlapped with bulk rock Te – suggesting that in many cases, pyrite represents the main host for Te. In the majority of the deposits reviewed, pyrite was abundant but contained relatively low Te. As a consequence of this, much of the Te mined during the extraction of copper and other base metals is actually routed to the tailings (Kavliak and Graedel 2013).

Gold-silver deposits may also be enriched in tellurium. Pyrite is again an important host in terms of Te deportment, and is the main host (as with Au) in Carlin-type deposits (Keith et al. 2018). Tellurium can also occur as a stoichiometric component of gold and silver minerals, including calaverite ($AuTe_2$), hessite (Ag_2Te), and sylvanite ($[Ag,Au]Te_2$). Tellurium was recovered from the Vatukoula epithermal Au deposit (Fiji) in the late '70s, and more recently from Dashuigou and Kankberg (Fig. 1).

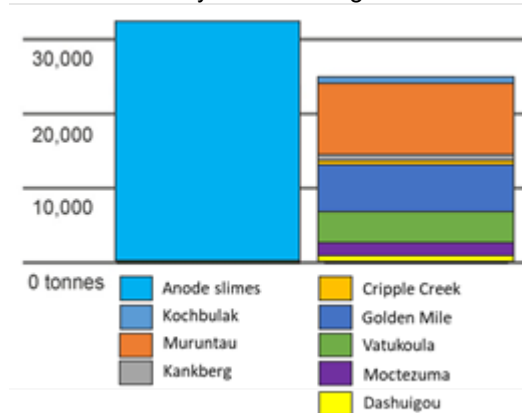


Figure 4 Tellurium resource potential from anode slimes and selected Au deposits. Data from Speirs et al. (2013), Green (2009) and Anderson (2019).

Epithermal gold telluride deposits represent a particularly attractive target for Te extraction. The precious metal tellurides are relatively common in the ores, and Te grades are relatively high (up to hundreds of ppm; Keith et al. 2018). The gold telluride deposits also include some of the largest epithermal deposits by contained gold (e.g. Ladolam & Porgera, PNG; Cripple Creek, USA). Epithermal gold telluride deposits are typically hosted in alkaline igneous rocks (Kelley and Spry 2016), and are interpreted to form in extensional, post-subduction tectonic environments (Richards 2009). The alkaline host rocks support high pH in well-equilibrated hydrothermal fluids (Smith et al. 2017), enhancing the solubility and transport of Te under epithermal conditions (Grundler et al. 2013). The resulting deposits often have distinctive alteration assemblages and gangue (Smith et al. 2017; Jensen and Barton 2000; Spry and Scherbarth 2006), with unusually vanadium-rich silicates, low amounts of silicification and limited quartz (relative to epithermal deposits hosted in silica-saturated calc-alkaline compositions) and a paucity

of acid-associated alteration (advanced argillic-type assemblages). They are therefore a deposit class that can be targeted for exploration, and have potential to yield both Au and Te.

4 Gold Telluride Metallurgy

Precious metal tellurides are generally refractory to hydrometallurgical processes including cyanidation (Dyer et al. 2017). As with Carlin-type auriferous pyrite, the concentrate is oxidized or roasted prior to leaching or cyanidation. Tellurium is typically lost during the pre-leach roast, and hence there is little to no recovery of Te from orogenic, epithermal or Carlin-type gold deposits, despite their Te enrichments (Keith et al. 2018).

Solvents that facilitate co-recovery of Te and Au will make gold deposits a major potential resource for Te, reducing dependency on anode slime processing and direct tellurium mining. Novel extraction techniques that show potential for gold-silver telluride processing include deep eutectic solvents (Jenkin et al. 2016). These are anhydrous salts, liquid at room temperature, that act as powerful solvents. As ionic liquids, they offer opportunities for electrochemistry, and hence selectivity in element dissolution and precipitation. They are environmentally benign and cheap to produce, and have low energy penalties during ore processing as they are effective solvents without pre-leach roasting, and do not require high temperatures during leaches to be effective.

5 Conclusions

Tellurium is in increasing demand for applications in electronics and clean energy technologies. Existing supplies have so far kept pace with demand, but there has been an increasing dependency on Chinese resources, and few signs that recovery of Te as a by-product from Cu refining will improve in efficiency. There are significant potential resources of tellurium within gold deposits (alkaline-associated epithermal, Carlin type and orogenic), that are now starting to be mined for gold and tellurium. New technologies and solvents in mineral processing, such as deep eutectic solvents, may facilitate the recovery of Au and Te from gold deposits, where they typically reside in refractory minerals such as calaverite and pyrite.

Acknowledgements

This research was funded by the Natural Environment Research Council (UK) grants NE/L002191/1 and NE/M010848/1 in the Security of Supply of Minerals programme.

References

- Anderson CS (2019) USGS Mineral Commodity Summary: Tellurium.
- Bustamante ML, Gaustad G (2014a) Challenges in assessment of clean energy supply-chains based on byproduct minerals: A case study of tellurium use in thin film photovoltaics. *Applied Energy* 123:397-414. doi: 10.1016/j.apenergy.2014.01.065.
- Bustamante ML, Gaustad G (2014b) The evolving copper-tellurium byproduct system: A review of changing production techniques & their implications. *Rare Metal Technology* 2014:11-16.
- Bustamante ML, Gaustad G, Alonso E (2018) Comparative Analysis of Supply Risk-Mitigation Strategies for Critical Byproduct Minerals: A Case Study of Tellurium. *Environ Sci Technol* 52:11-21. doi: 10.1021/acs.est.7b03963.
- Dyer LG, Sauber M, Dixon DG, Asselin E (2017) On the refractory nature of precious metal tellurides. *Hydrometallurgy* 169:488-495. doi: 10.1016/j.hydromet.2017.03.009.
- Green MA (2009) Estimates of Te and In prices from direct mining of known ores. *Progress in Photovoltaics: Research and Applications* 17:347-359. doi: 10.1002/pip.899.
- Grundler PV, Brugger J, Etschmann BE, Helm L, Liu W, Spry PG, Tian Y, Testemale D, Pring A (2013) Speciation of aqueous tellurium(IV) in hydrothermal solutions and vapors, and the role of oxidized tellurium species in Te transport and gold deposition. *Geochim Cosmochim Acta* 120:298-325. doi: 10.1016/j.gca.2013.06.009.
- Jenkin GRT, Al-Bassam AZM, Harris RC, Abbott AP, Smith DJ, Holwell DA, Chapman RJ, Stanley CJ (2016) The application of deep eutectic solvent ionic liquids for environmentally-friendly dissolution and recovery of precious metals. *Minerals Engineering* 87:18-24. doi: 10.1016/j.mineng.2015.09.026.
- Jensen EP, Barton MD (2000) Gold deposits related to alkaline magmatism In: Hagemann SG, Brown PE (eds) *Gold in 2000*. Society of Economic Geologists, Littleton, Colorado, pp 279-314.
- Kavlak G, Graedel TE (2013) Global anthropogenic tellurium cycles for 1940-2010. *Resour Conserv Recycl* 76:21-26. doi: 10.1016/j.resconrec.2013.04.007.
- Keith M, Smith DJ, Jenkin GRT, Holwell DA, Dye MD (2018) A review of Te and Se systematics in hydrothermal pyrite from precious metal deposits: Insights into ore-forming processes. *Ore Geol Rev* 96:269-282. doi: 10.1016/j.oregeorev.2017.07.023.
- Kelley KD, Spry PG (2016) Critical elements in alkaline igneous rock-related epithermal gold deposits In: Verplanck PL, Hitzman MW (eds) *Reviews in Economic Geology Society of Economic Geologists*, Littleton, CO.
- Makuei FM, Senanayake G (2018) Extraction of tellurium from lead and copper bearing feed materials and interim metallurgical products – A short review. *Minerals Engineering* 115:79-87. doi: 10.1016/j.mineng.2017.10.013.
- Plotnikov V, Liu X, Paudel N, Kwon D, Wieland KA, Compaan AD (2011) Thin-film CdTe cells: Reducing the CdTe. *Thin Solid Films* 519:7134-7137. doi: 10.1016/j.tsf.2010.12.179.
- Richards JP (2009) Postsubduction porphyry Cu-Au and epithermal Au deposits: Products of remelting of subduction-modified lithosphere. *Geology* 37:247-250.
- Smith DJ, Naden J, Jenkin GR, Keith M (2017) Hydrothermal alteration and fluid pH in alkaline-hosted epithermal systems. *Ore Geol Rev* 89:772-779.
- Speirs J, Gross B, Gross R, Houari Y (2013) UKERC Energy Materials Availability Handbook.
- Spry PG, Scherbarth NL (2006) The gold-vanadium-tellurium association at the Tuvatu gold-silver prospect, Fiji: conditions of ore deposition. *Mineral Pet* 87:171-186.
- Sykes JP, Wright JP, Trench A, Miller P (2016) An assessment of the potential for transformational market growth amongst the critical metals. *Appl Earth Sci* 125:21-56. doi: 10.1080/03717453.2015.1104055.
- Voigt B (2018) Boliden Summary Report: Kankberg –Åkulla Öst

Tellurium and selenium systematics in mafic VMS from Cyprus: mineral, mound and regional scale controls

Andrew J. Martin, Iain McDonald, Katie A. McFall and Christopher J. MacLeod
School of Earth and Ocean Sciences, Cardiff University, UK

Manuel Keith
Technische Universität Berlin & GeoZentrum Nordbayern, Universität Erlangen-Nürnberg, Germany
School of Geography, Geology and the Environment, University of Leicester, UK

Gawen R.T. Jenkin
School of Geography, Geology and the Environment, University of Leicester, UK

Adrian J. Boyce
Scottish Universities Environmental Research Centre, East Kilbride, UK

Abstract. Tellurium (Te) and selenium (Se) are critical elements used in the production of photovoltaic solar cells. Their criticality is paralleled by a poor understanding of their distribution and enrichment in a range of ore forming environments. This study aims at understanding Te and Se systematics on a range of scales in mafic VMS systems. To investigate this, >20 VMS of the Troodos ophiolite have been sampled. On a mineral scale, the distribution of Te and Se is not uniform between different sulfide phases; chalcopyrite is preferentially enriched in Se, averaging 1147 ppm (n=202), whilst pyrite averages 439 ppm (n=1570). In contrast, Te is preferentially incorporated in pyrite averaging 17 ppm compared to 6 ppm in chalcopyrite. Some VMS deposits exhibit evidence of Se remobilization leading to enrichment of Se in pyrite up to 4950 ppm. This demonstrates the significance of fluctuating fluid redox in VMS mineralisation and the enrichment of Se. Additionally, on an ophiolite scale, trace element distribution demonstrates a robust link between magmatic volatile influx and Te and Se enrichment in mafic VMS deposits.

1 Introduction

Tellurium and selenium are classified as critical in the European Union's Strategic Energy Plan (SET; Moss et al. 2013). They are critical components used in the production of photovoltaic solar cells. Currently, both Te and Se are produced as by-products through the electrolytic refining of Cu. The criticality of Te and Se is paralleled by a poor understanding of their enrichment in a wide range of ore forming systems.

This study investigates the distribution of Te and Se in mafic Volcanogenic Massive Sulfide (VMS) deposits. Mafic VMS are important sources of base metals, especially Cu (e.g. Galley et al. 2007). They form through the interaction of evolved hot (>350°C) seawater with oceanic crust in a range of extensional submarine environments (e.g. back-arc or MOR).

The principal source of metals in mafic VMS deposits is believed to be through the leaching of igneous rocks and

the formation of epidotes (e.g. Jowitt et al. 2012). However, it has been demonstrated in arc environments that a magmatic volatile phase may provide an additional source of metal in overlying VMS deposits (Yang and Scott 2002). This study presents in situ LA-ICP-MS analyses of sulfides from VMS of the Troodos ophiolite, Cyprus to constrain the distribution and enrichment of Te and Se in mafic VMS deposits.

2 The Troodos ophiolite, Cyprus

The 92 Ma Troodos ophiolite is the principal on-land analogue for Cyprus-type, mafic or Cu-Zn VMS mineralisation. Exceptional exposure, preservation of original seafloor spreading structures, and an apparent lack of metamorphic overprint make Troodos the ideal locality to investigate processes associated with mafic VMS hydrothermal systems (e.g. Hannington et al. 1998; Keith et al. 2016; Martin et al. 2019).

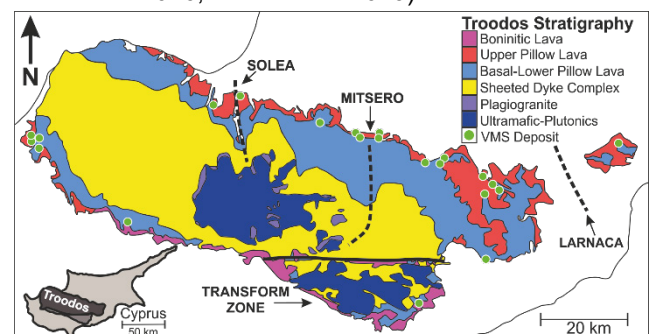


Figure 1: Simplified map of the Troodos ophiolite, Cyprus. Black dashed lines represent graben axes. Inset: location of Troodos massif within the island of Cyprus (after Martin et al. 2019)

Mafic VMS deposits are spatially associated with faults related to three rift structures; the Solea, Mitsero and Larnaca grabens (Fig. 1; Varga and Moores 1985). Grabens formed at the seafloor during periods of magmatic quiescence when spreading was accomplished via normal faulting and rotation of the upper crustal blocks in a bookshelf manner (Varga and Moores 1985).

Deposits range in size from <0.5 Mt to >16 Mt with a typical grade of ~2 wt.% Cu (Hannington et al. 1998). VMS deposits outcrop at the periphery of the ophiolite within the extrusive sequence; a series of basaltic to andesitic lavas. This study features VMS from across the entire ophiolite (Fig. 1), hence samples analysed represent a wide range of deposit- and regional-scale processes associated with the mafic VMS formation.

3 Mineral scale distribution of Te and Se

Trace elements are incorporated in sulfide minerals as either a lattice-bound substitution (stoichiometric or non-stoichiometric) or as nano- to micro-scale inclusions (Cook et al. 2009; Huston et al. 1995). The partitioning of Te and Se between different sulfide minerals is not uniform. Laser Ablation ICP-MS analyses of pyrite (n=1570), chalcopyrite (n=202), sphalerite (n=86) and covellite (n=8) have been used to constrain the incorporation behavior and mineral scale distribution of Te and Se in mafic VMS (after Martin et al. 2019, 2018).

This study demonstrates that chalcopyrite is enriched in Se averaging 1147 ppm (n=202) relative to pyrite at 439 ppm (n=1570). However, the concentration of Se is extremely variable in both minerals, ranging from below detection limit (<12 ppm) to 6158 ppm in chalcopyrite and 4950 ppm in pyrite. Covellite acts a sink for Se containing the highest average Se measured in this study at 1969 ppm, and the second highest Te at 9.6 ppm (n=8). Tellurium in pyrite averages 17 ppm (n=1570) compared to 6 ppm in chalcopyrite (n=200).

We demonstrate that the mineral scale partitioning of Te and Se is not uniform and will be affected by different co-precipitating sulfide phases (Martin et al. 2019; Fig. 2). In a pyrite-only system Te and Se will partition equally between individual pyrite grains. However, the precipitation of chalcopyrite leads to a depletion of Se in co-precipitated pyrite (Fig. 2). Sphalerite is a poor host for both Te and Se with the majority of analyses below detection limit (<12 ppm Se and 0.6 ppm Te).

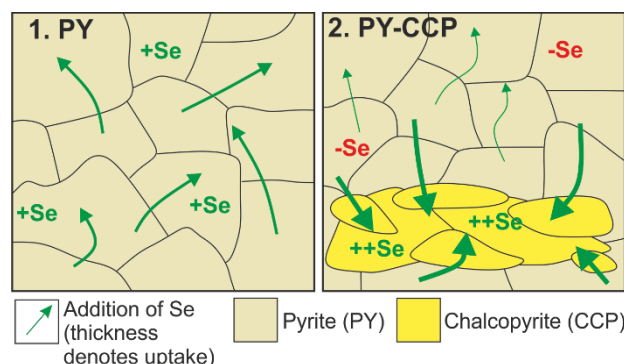


Figure 2. The effect of co-precipitation on Se during ore formation. Selenium is preferentially incorporated in chalcopyrite over pyrite.

Different Te and Se incorporation mechanisms can be defined by time resolved Laser Ablation ICP-MS analyses combined with the solubility limit of Te as a function of As in pyrite. Selenium appears to be uniformly hosted as a solid solution in both chalcopyrite and pyrite. A smooth time-resolved laser profile that exhibits co-variation with

S likely suggests its incorporation as a lattice bound substitution (Fig. 3; Huston et al. 1995). In contrast, Te exhibits different incorporation mechanisms, exhibiting both a smooth and jagged time resolved laser profile between different pyrite grains analysed. This suggests it is incorporated in either a lattice bound substitution or as micro inclusions, dependent on the sulfide grain analysed (Fig. 3). This is confirmed by the solubility limit of Te as a function of As in pyrite. Concentration above the Te solubility limit suggest an inclusion-related appearance, whereas concentrations below the solubility line indicate Te in a solid solution (Keith et al. 2018). Additionally, some VMS sulfides exhibit a moderate positive correlation between Bi and Te suggesting Te may be hosted as Bi-telluride inclusions (Martin et al. 2019).

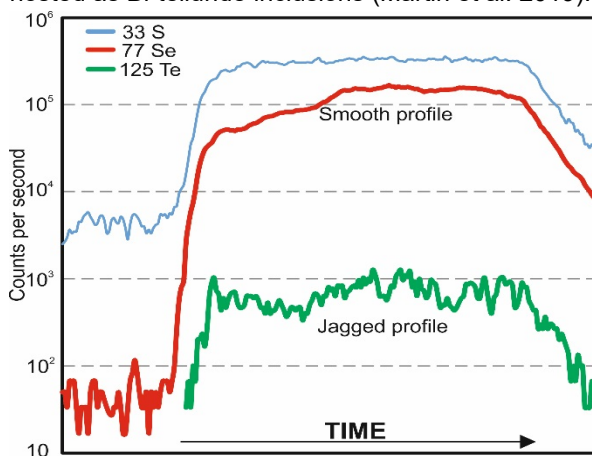


Figure 3. Time resolved analysis profile in pyrite for S, Se and Te. Selenium exhibits a smooth ablation profile whilst Te is more variable with a jagged profile.

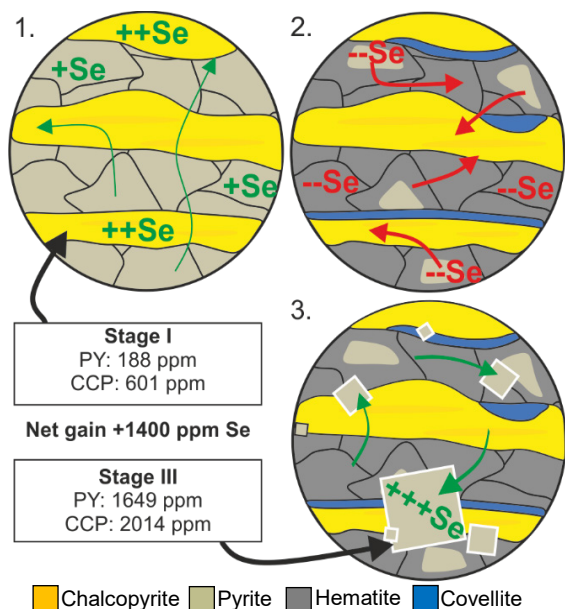
4 Extreme Se enrichment

The Apliki VMS in western Troodos exhibits an unusual enrichment in Se (Martin et al. 2018). The South Apliki Breccia Zone (SABZ) is located between two normal faults in the lower Apliki ore body. The zone is characterised by co-existing hematite, chalcopyrite and pyrite (Fig. 4). Laser ablation ICP-MS of sulfides from the SABZ identified late euhedral pyrite as being notably enriched in Se (Martin et al. 2018). Paragenesis of sulfides from the SABZ demonstrate the dissolution of stage I subhedral pyrite and formation of hematite followed by the later precipitation of euhedral stage III pyrite (Fig. 4). Hematite is not capable of incorporating Se in its mineral structure, therefore the dissolution of early stage I pyrite leads to release of Se to solution which is then readily incorporated in later stage III pyrite.

Laser ablation analysis of different paragenetic stages of pyrite reveals an addition of ~1400 ppm Se between stage I and III pyrite (Fig. 4). The enrichment of Se could relate to a late stage, Se-rich fluid pulse in the SABZ that may be responsible for Se enrichment in stage III euhedral pyrite. To elucidate the addition of a late stage Se-rich fluid pulse, isotope analysis of stage I and III pyrite was undertaken to assess if the enrichment of Se relates to an additional magmatic volatile (Se) rich fluid. Sulfur isotope ratios ($\delta^{34}\text{S}$) of pyrite (n=19) and

chalcopyrite (n=10) between stage I and III samples are indistinguishable at +4.2‰ ($\sigma = 1.2\text{‰}$) and +3.6‰ ($\sigma = 2.8\text{‰}$) respectively. Both values are consistent with the sourcing of metals from thermochemical or biogenic seawater sulfate reduction (Cretaceous seawater 17-19‰; Keith et al. 2016) and the leaching of Troodos igneous rocks (0-1‰; Alt 1994).

Figure 4. Paragenesis summary of Se enrichment at the SABZ. 1. Selenium is enriched in pyrite and chalcopyrite, 2. Hematite formation, Se is displaced, 3. Euhedral stage III pyrite acts as a sink for Se (after Martin et al. 2018).



5 Te and Se in mafic VMS

Using magmatophile trace element signatures (Te, Se, Bi, Au) and Se/S ratios of pyrite, we suggest that Te and Se enrichment in mafic VMS may be associated with increased magmatic volatile influx to the hydrothermal system. To assess this variation on a regional scale, we compare structural domains in the Troodos ophiolite; the Solea and Mitsero grabens (Fig. 1) and their associated VMS deposits.

Selenium/Sulfur ($\text{Se/S} \times 10^6$) ratios have been used as a proxy for magmatic influx in hydrothermal ore deposits (Huston et al. 1995; Layton-Matthews et al. 2013). A Se/S ratio >500 in pyrite indicates an increased magmatic influx in the VMS hydrothermal system, and all sediment starved ridges (e.g. Troodos) are expected to fall below 1500 (Layton-Matthews et al. 2013).

Selenium/Sulfur ratios for all Troodos pyrite (n=1570) range from 3 to 9238. The average Se ratio for the Solea graben is 481 (n=362) corresponding to an average Se concentration in pyrite of 251 ppm. In contrast Se/S ratios in the Mitsero domain are lower averaging 286 (n=183) with average Se concentrations of 183 ppm in pyrite. This suggests that the Solea and Mitsero structural domains could have experienced different amounts of magmatic volatile influx during VMS formation. We preliminarily link this to the spreading evolution of the Troodos ophiolite as

the Mitsero graben may have formed in an 'off axis' position or as a propagating ridge tip. In contrast, Solea is interpreted as representing a full magmatic-tectonic spreading ridge (Varga and Moores, 1985) and therefore experienced a relatively higher ingress of magmatic volatiles.

6 Comparison with modern SMS

Compared with modern mafic-hosted VMS deposits, Troodos sulfides are enriched in Te and Se. For example, maximum Se concentrations in pyrite from the TAG deposit, Mid Atlantic Ridge, are 10 ppm Te and 180 ppm Se (Grant et al. 2018; Fig. 5). In contrast, in Troodos maximum values in pyrite reach 332 ppm and 4950 ppm for Te and Se respectively (Martin et al. 2019). Perhaps more meaningful are median values; pyrite from TAG at 20 and 1.7 ppm for Se and Te respectively whilst Troodos VMS are 47 and 5.2 ppm (Grant et al. 2018; Martin et al. 2019).

This apparent enrichment in magmatophile elements, Te and Se in Troodos VMS relative to TAG suggests that TAG, on a trace element level, is not a comparable analogue to Troodos VMS as suggested by previous studies (e.g. Hannington et al. 1998). Data from Troodos VMS exhibit significant scatter, spanning almost the entire known range for back-arc, arc and MOR hydrothermal sulfides (Fig. 5). We suggest this reflects a variable magmatic influx into the Troodos VMS hydrothermal system on a regional scale, with the most enriched deposits experiencing an additional volatile source of Te and Se or in the case of Apliki, localized Se remobilisation. For example, elevated Te and Se at the Brothers caldera is attributed to an increased magmatic flux (e.g. de Ronde et al. 2011).

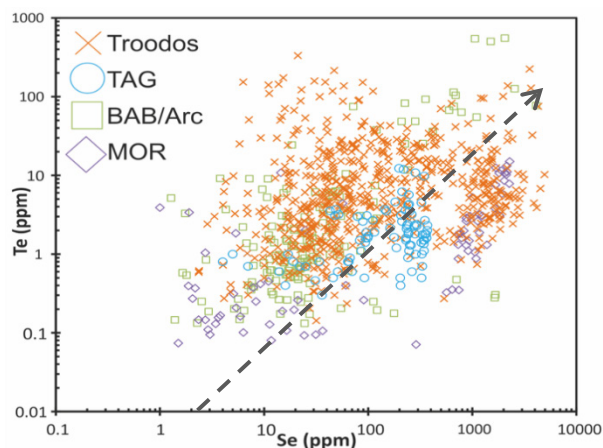


Figure 5. Tellurium vs. Se for Troodos and modern SMS in pyrite/marcasite. Grey dashed line is continental crust ratio for Te and Se (1/26; Keith et al. 2018). Data from: Grant et al. 2018; Keith et al. 2016b; Martin et al. 2019.

7 Summary and conclusions

This study demonstrates the complex distribution and enrichment of Te and Se at a range of scales in the mafic VMS hydrothermal system. On a mineral scale Se preferentially partitions into chalcopyrite and is probably incorporated in the sulfide crystal lattice in a solid

solution. In contrast Te is preferentially enriched in pyrite and may occur as both mineral inclusions and a lattice bound solid solution. This highlights the effect of co-precipitating sulfide phases on the Se budget of a mafic VMS mound (cf. Martin et al. 2019).

On a deposit scale we identify fluctuating redox and the dissolution of pyrite and formation of hematite as a key process in the localised enrichment of Se. The displacement of Se from early pyrite during oxidization to hematite and subsequent incorporation in later pyrite highlights the importance of seafloor oxidisation in the mobilisation and enrichment of Se.

Finally, we suggest that Troodos VMS preserve evidence of a variable magmatic volatile influx between different structural grabens (i.e. Solea and Mitsero). Furthermore, when compared with modern, mid-ocean ridge, mafic hosted analogues such as TAG, Troodos VMS are enriched in Te and Se, in some instances to levels comparable to volatile rich arc environments (e.g. Brothers). This demonstrates that whilst physicochemical ore-forming parameters and local remobilisation (e.g. SABZ) are important on a deposit scale, ultimately systematic regional enrichment of Te and Se is related to a magmatic volatile influx into the overlying hydrothermal system.

Acknowledgements

This research was funded under the NERC Security of Supply TeaSe consortium, grant NE/M010848/1. AJM acknowledges the support of the NERC Isotope Geosciences Facilities Steering Committee grant IP-1766-1117. We thank Alison McDonald, Dr. Andreas Zissimos and Dr. Costas Constantinou for their support during this research.

References

- Alt, J.C., 1994. A sulfur isotopic profile through the Troodos ophiolite, Cyprus: primary composition and the effects of seawater hydrothermal alteration. *Geochimica et Cosmochimica Acta*, 58(7);:825-1840.
- Cook, N.J., Ciobanu, C.L., Pring, A., Skinner, W., Shimizu, M., Danyushevsky, L., Saini-Eidukat, B., Melcher, F., 2009. Trace and minor elements in sphalerite: A LA-ICPMS study. *Geochim. Cosmochim. Acta* 73:4761–4791.
- de Ronde, C.E.J., Massoth, G.J., Butterfield, D.A., Christenson, B.W., Ishibashi, J., Ditchburn, R.G., Hannington, M.D., Brathwaite, R.L., Lupton, J.E., Kamenetsky, V.S., Graham, I.J., Zellmer, G.F., Dziak, R.P., Embley, R.W., Dekov, V.M., Munnik, F., Lahr, J., Evans, L.J., Takai, K., 2011. Submarine hydrothermal activity and gold-rich mineralization at Brothers Volcano, Kermadec Arc, New Zealand. *Miner. Deposita* 46:541–584. <https://doi.org/10.1007/s00126-011-0345-8>
- Galley, A., Hannington, M., Jonasson, I., 2007. Volcanogenic Massive Sulphide Deposits. *Miner. Depos. Can. Special publication No. 5*:141–161.
- Grant, H.L.J., Hannington, M.D., Petersen, S., Frische, M., Fuchs, S.H., 2018. Constraints on the behavior of trace elements in the actively-forming TAG deposit, Mid-Atlantic Ridge, based on LA-ICP-MS analyses of pyrite. *Chem. Geol.* 498:45–71. <https://doi.org/10.1016/j.chemgeo.2018.08.019>
- Hannington, M.D., Galley, A., Herzig, P., Petersen, S., 1998. Comparison of the TAG mound and stockwork complex with Cyprus-type massive sulfide deposits. *Proc. Ocean Drill. Program Sci. Results* 158:389–415. <https://doi.org/10.2973/odp.proc.sr.158.217.1998>
- Huston, D.L., Sie, S.H., Suter, G.F., 1995. Selenium and its importance to the study of ore genesis: the theoretical basis and its application to volcanic-hosted massive sulfide deposits using PIXE analysis. *Nucl. Instrum. Methods Phys. Res. Sect. B Beam Interact. Mater. At., Nuclear Microprobe Technology and Applications* 104:476–480.
- Huston, D.L., Sie, S.H., Suter, G.F., Cooke, D.R., Both, R.A., 1995. Trace elements in sulfide minerals from eastern Australian volcanic-hosted massive sulfide deposits; Part I, Proton microprobe analyses of pyrite, chalcopyrite, and sphalerite, and Part II, Selenium levels in pyrite; comparison with delta ³⁴S values and implications for the source of sulfur in volcanogenic hydrothermal systems. *Econ. Geol.* 90:1167–1196.
- Jowitt, S.M., Jenkin, G.R.T., Coogan, L.A., Naden, J., 2012. Quantifying the release of base metals from source rocks for volcanogenic massive sulfide deposits: Effects of protolith composition and alteration mineralogy. *J. Geochem. Explor.* 118:47–59. <https://doi.org/10.1016/j.gexplo.2012.04.005>
- Keith, M., Haase, K.M., Klemd, R., Krumm, S., Strauss, H., 2016a. Systematic variations of trace element and sulfur isotope compositions in pyrite with stratigraphic depth in the Skouriotissa volcanic-hosted massive sulfide deposit, Troodos ophiolite, Cyprus. *Chem. Geol.* <https://doi.org/10.1016/j.chemgeo.2015.12.012>
- Keith, M., Häckel, F., Haase, K.M., Schwarz-Schampera, U., Klemd, R., 2016b. Trace element systematics of pyrite from submarine hydrothermal vents. *Ore Geol. Rev.* 72, 728–745.
- Keith, M., Smith, D.J., Jenkin, G.R.T., Holwell, D.A., Dye, M.D., 2018. A review of Te and Se systematics in hydrothermal pyrite from precious metal deposits: Insights into ore-forming processes. *Ore Geol. Rev.* 96:269–282. <https://doi.org/10.1016/j.oregeorev.2017.07.023>
- Layton-Matthews, D., Leybourne, M.I., Peter, J.M., Scott, S.D., Cousens, B., Eglington, B.M., 2013. Multiple sources of selenium in ancient seafloor hydrothermal systems: Compositional and Se, S, and Pb isotopic evidence from volcanic-hosted and volcanic-sediment-hosted massive sulfide deposits of the Finlayson Lake District, Yukon, Canada. *Geochim. Cosmochim. Acta* 117:313–331. <https://doi.org/10.1016/j.gca.2013.05.002>
- Martin, A.J., Keith, M., McDonald, I., Haase, K.M., McFall, K.A., Klemd, R., MacLeod, C.J., 2019. Trace element systematics and ore-forming processes in mafic VMS deposits: Evidence from the Troodos ophiolite, Cyprus. *Ore Geol. Rev.* 106:205–225. <https://doi.org/10.1016/j.oregeorev.2019.01.024>
- Martin, A.J., McDonald, I., MacLeod, C.J., Prichard, H.M., McFall, K., 2018. Extreme enrichment of selenium in the Apliki Cyprus-type VMS deposit, Troodos, Cyprus. *Mineral. Mag.* 82:697–724. <https://doi.org/10.1180/mgm.2018.81>
- Moss, R.L., Tzimas, E., Kara, H., Willis, P., Kooroshy, J., 2013. The potential risks from metals bottlenecks to the deployment of Strategic Energy Technologies. *Energy Policy, Special section: Long Run Transitions to Sustainable Economic Structures in the European Union and Beyond* 55:556–564. <https://doi.org/10.1016/j.enpol.2012.12.053>
- Varga, R.J., Moores, E.M., 1985. Spreading structure of the Troodos ophiolite, Cyprus. *Geology* 13:846–850.
- Yang, K., Scott, S.D., 2002. Magmatic Degassing of Volatiles and Ore Metals into a Hydrothermal System on the Modern Sea Floor of the Eastern Manus Back-Arc Basin, Western Pacific. *Econ. Geol.* 97:1079–1100.

Te-rich protolith for PGE mineralisation in NE Scotland

Joseph Armstrong, John Parnell, Magali Perez, Jorg Feldmann
University of Aberdeen, UK

Abstract. The geological factors controlling the mineralisation of basic layered Ni-Cu-PGE intrusive deposits are often complex and debated at length. Many models of Ni-Cu deposit formation rely on assimilation of carbonaceous continental crust to reach sulphide saturation for ore formation, rather than through fractionation of the melt alone. The Ordovician 'Newer Basic Intrusions' in NE Scotland have historically been targeted for their Ni, Cu and minor precious metal enrichments (up to 700 ppb Au+Pt+Pd). The distribution of PGEs within these intrusions is variable, with the highest concentrations associated with sulphide-rich graphitic pyroxenites. The host rocks for these enriched intrusions are the sulphidic pelites and diamictites of the Dalradian Argyll Group. Sulphides within these strata are often enriched in tellurium, selenium and gold relative to average crustal values and there is considerable evidence for assimilation of this country rock within the ultrabasic intrusions. We propose here an ore formation model of Dalradian country rock assimilation, sulphide saturation and semi-metal enrichment of the intrusive melt. Tellurium enrichment within the melt resulted in localised PGE-telluride mineral formation, associated with graphitic xenoliths. It is possible that more extensive PGE mineralisation exists in similar settings in NE Scotland and globally.

1 Introduction

Ultramafic intrusive complexes are a major source of nickel (Ni), copper (Cu) and platinum group elements (PGE) globally (Bushveld Complex, Duluth, Vammala Nickel Belt, Aguablanca) (Thériault et al. 1997; Naldrett 1999; Pina et al. 2006; Ihlenfeld and Keays 2011; Makkonen et al. 2017; Samalens et al. 2017). As well as gold (Au), these deposits are often relatively enriched in other rare 'critical elements', including tellurium (Te) and selenium (Se), which are vital for the production of green technologies, such as photovoltaic cells. Understanding the mechanisms controlling accumulations of these elements is vital to identifying new deposits and securing their supply in the future. Current global production of Te and Se is primarily as a by-product of copper (Cu) refining, which limits future supply growth (Lu et al. 2015).

Here we investigate a model of PGE mineralisation in graphitic basic intrusions in NE Scotland, through crustal assimilation of sulphidic metasedimentary basement. Tellurium reserves within the metasediment-hosted Cononish Au deposit, Scotland, have recently been reexamined (Spence-Jones et al. 2018) and it is conceivable that other overlooked or unidentified enrichments in critical elements associated with metasediments may prove important as demand for these commodities increases. Accurate identification of the different mineralisation mechanisms in these complex

systems is key in targeted exploration.

2 Geological setting

The Grampian Highlands terrane of north-east Scotland (Fig. 1), bordered to the south by the Highland Boundary Fault and the north-west by the Great Glen Fault, can be split into three simplified units - Proterozoic basement, Devonian sedimentary rocks and Ordovician to Devonian intrusives. The Proterozoic metasedimentary Dalradian Supergroup (deposited c. 800–595 Ma; Halliday et al. 1989; Thomas et al. 2007), the stratigraphy of which has been well-characterized (Fig. 2), underlies and outcrops across the region. The intrusive units of the Grampian Terrane (granites and basic-ultrabasic layered sequences) formed during the Caledonian orogeny (475–400 Ma; Oliver et al. 2008), during subduction and closure of the Iapetus Ocean. This orogenic event also caused widespread regional metamorphism of the Dalradian Supergroup (Oliver et al. 2008). The Devonian 'Old Red Sandstone' in the north of the terrane comprises clastic sedimentary deposits, associated with the formation of the Orcadian basin to the north as a result of orogenic events in the Grampian Terrane (Kendall 2017).

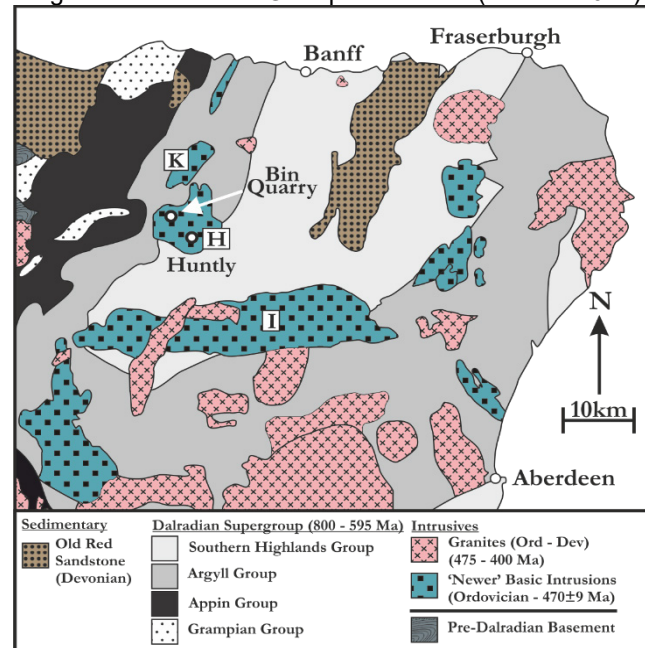


Figure 1. Simplified geological map of the Grampian Highlands terrane, NE Scotland: Illustrating the distribution of Proterozoic Dalradian metasediments, Caledonide intrusions and Old Red Sandstone. Intrusions: K = Knock; H = Huntly; I = Insch. Geological map after (Droop et al. 2003; Stephenson et al. 2013b). Dating ages (Halliday et al. 1989; Dempster et al. 2002; Thomas et al. 2007).

3 Caledonide PGE enrichment, NE Scotland

Platinum (Pt), palladium (Pd), Ni, Cu and minor Te, Au

and Co enrichments have previously been identified within the 'Newer' basic intrusive bodies in NE Scotland (Fletcher 1989; Gunn and Styles 2002; McKervey et al. 2007). These are basic-ultrabasic layered cumulate intrusions of Ordovician age, emplaced within the Dalradian Supergroup metasedimentary sequence. Timing of these ultrabasic intrusions was roughly coeval with the wider S-type granitoid emplacement in the region c. 470±9 Ma (Dempster et al. 2002; Oliver et al. 2008).

Two Ni-Cu (+minor PGE and Au) deposits of the Newer Basic Intrusions were identified as potentially prospective in the late 1960s and have been extensively studied since (Fletcher 1989; Fletcher et al. 1989; Gunn and Shaw 1992; Gunn and Styles 2002; McKervey et al. 2007). They comprise the Huntly and Knock intrusions (Fig 1) with values of 0.003–3.02% Ni, 0.002–6.46% Cu and maximum values of 584 ppb Pt and 381 ppb Pd across the two intrusions (Fletcher 1989; McKervey et al. 2007), though these are highly variable. Au concentrations vary between 1–179 ppb, with most values <20 ppb. The Ni, Cu, PGE and minor Au enrichments are primarily associated the sulphides

telluride, merenskyite, have been identified historically and are thought to be the main phase of PGE enrichment in these deposits (Fletcher 1989; Gunn and Styles 2002). The graphitic pyroxenites have Au+Pt+Pd concentrations up to 700 ppb (Gunn and Styles 2002).

The intrusions are layered basic and ultrabasic cumulates, gabbros and serpentinites with extensive disseminated sulphides, thought to be of magmatic origin. Localised deformation and sulphide mineralisation occurs along xenolithic shear zones, with common, but discordant pyroxene porphyritic mineralisation, abundant in graphite and sulphides (McKervey et al. 2007).

Existing models for the PGE-Ni-Cu mineralisation in the Younger Intrusions are complex and propose a magmatic sulphur source, with re-mobilisation and enrichment of sulphides associated with subsequent shear deformation and hydrothermal processes. While localised graphitic pyroxenites are known to have the highest precious metal concentrations in these deposits, previous works have discounted the influence of carbonaceous crustal assimilation on PGE mineralisation (Fletcher 1989; McKervey et al. 2007). The local host rock for these intrusions is the Dalradian Argyll Group (Fig. 1; Fig. 2), which is widely carbonaceous and sulphidic, with the potential to alter the bulk sulphur and trace element content of the melt during magmatic emplacement.

4 Dalradian crustal assimilation

Sulphides within carbonaceous schists, pelites and glacial diamictites in the Dalradian Argyll Group have been shown to contain anomalously high concentrations of Te, Au and Se (Parnell et al. 2017, 2018). Laser ablation inductively coupled plasma mass spectrometry (LA-ICP-MS) analysis of Argyll Group diamictites shows discrete Se and Te mineralisation within pyrite in these deposits (Fig. 3). SEM analysis has identified several discrete Te and Se mineral phases, including lead selenide, lead telluride, nickel telluride and bismuth telluride (Fig. 4). Given this mineralisation, these strata have the potential to act as protoliths for trace element enrichments during orogenic and magmatic processes. Partial melting of the country rock has long been recognized as a factor during the emplacement of the Ordovician intrusive suites in NE Scotland (Ashworth 1976; Droop et al. 2003; Johnson et al. 2015). Carbon (C) isotopic analysis of graphite from Bin Quarry, Huntly intrusion (Fig. 1) provide $\delta^{13}\text{C}$ values of -25.0 to -18.0‰, which are distinct from mantle derived values of $-5\text{‰} \pm 3$ (Horita and Polyakov 2015). Organic C is isotopically light, with an average $\delta^{13}\text{C}$ of -25‰ (Luque et al. 2012), indicating that the graphite in the Newer Basic Intrusions is derived from crustal contamination by organic C. The Argyll Group metasediments into which the Huntly and Knock intrusions were emplaced (Fig. 1), consist primarily of deep marine, carbonaceous schists and

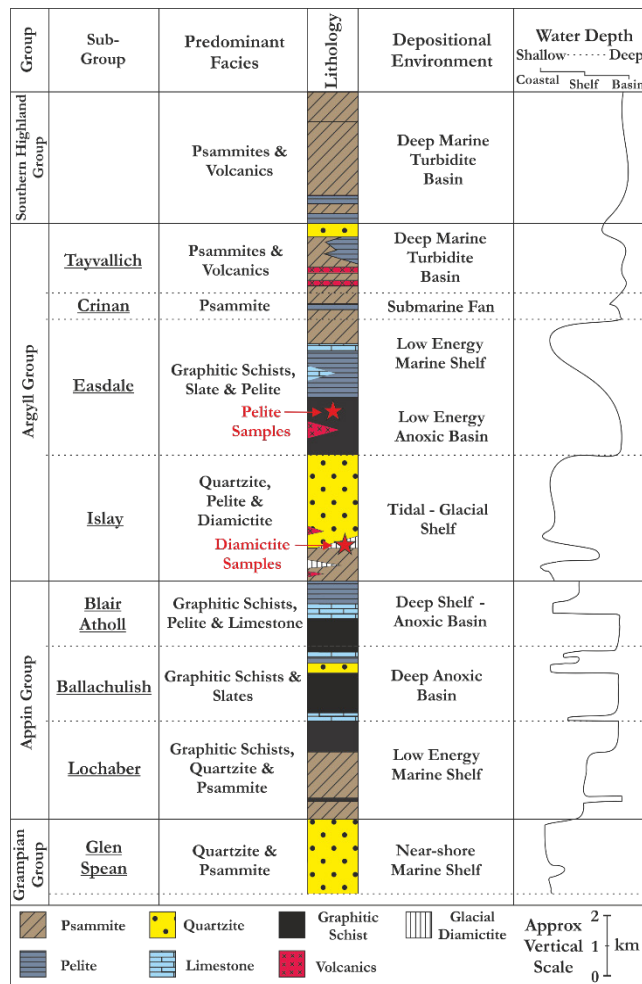


Figure 2. Simplified Dalradian stratigraphy in NE Scotland. After (Stephenson et al. 2013a, b).

pyrrhotite, chalcopyrite and pentlandite, within sulphidic gabbro-norite and graphitic pyroxene pegmatites (Fletcher 1989). Occurrences of the PGE-bismuth-

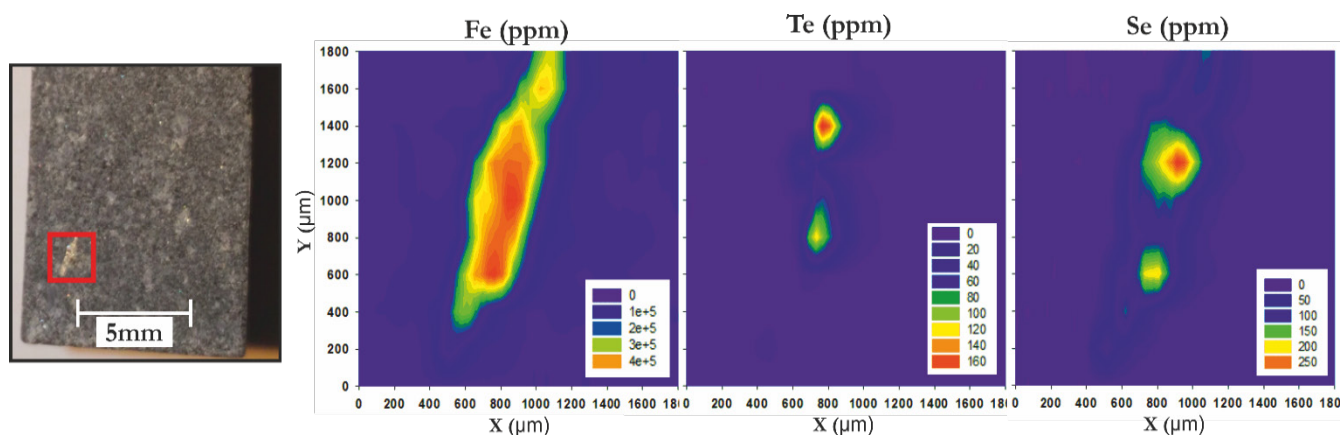


Figure 3. LA-ICP-MS maps of Fe, Te and Se concentration across sulphidic Argyll Gp diamicite sample. Te and Se enrichment within pyrite.

pelites, which are abundant in organic C (Fig. 2). Given the widespread graphitic mineralisation within the younger intrusions at Knock and Huntly, it is likely that localised crustal assimilation of the Argyll Group was significant during their emplacement.

Isotopic studies have previously concluded that the sulphur source within these intrusions is magmatic in origin, with $\delta^{34}\text{S}$ values between -1.7‰ and $+6.5\text{‰}$, which is comparable to typical magmatic values of $0\pm 3\text{‰}$ (Fletcher 1989). Given the variable nature of Argyll Group $\delta^{34}\text{S}$ compositions in Scotland, ranging from -15.5‰ to $+11.8\text{‰}$ (Parnell et al. 2017), distinguishing crustal sulphur input from primary magmatic sulphur can be difficult, as discussed in these previous studies.

The average S/Se ratio of sampled graphitic pyroxenites at Bin Quarry is 8440 (Table 1), which is significantly higher than the mantle maximum of 4350, indicating

contamination of the melt by crustal sulphur (Queffurus and Barnes 2015). These S/Se values are in agreement with previous studies from the ultrabasic intrusions in the region (McKervey et al. 2007). While the predominant sulphur source in these systems may be magmatically derived, a minor or localised Dalradian crustal component cannot be discounted. Tellurium and Se concentrations in the graphitic pyroxenites average 0.86 ppm and 7.1 ppm respectively, which is significantly higher than crustal averages of 0.03 and 0.09 ppm (Rudnick and Gao 2003; Hu and Gao 2008).

Table 1. Bulk rock ICP-MS data for graphitic pyroxenite samples, Bin Quarry, Huntly intrusion.

ID	Te (ppm)	Se (ppm)	S/Se	S (%)	Pt (ppb)	Pd (ppb)
A	0.34	3.8	7658	2.91	2	11
B	1.26	8.9	8236	7.33	3	26
C	0.99	8.6	9000	7.74	<2	43

5 Semi-metal input & PGE scavenging

Many models from comparable PGE-enriched Ni-Cu deposits (Duluth, Vammala, Aguablanca) propose that the assimilation of carbonaceous country rock increases the sulphide saturation in the melt, leading to precipitation of sulphides (Peltonen 1995; Pina et al. 2006; Samalens et al. 2017). Some of these models also propose that semi-metal enrichment from the country rock resulted in crystallization of accessory mineralised phases including graphite and PGE-tellurides.

Partial melting and assimilation of crustal sulphur from Dalradian sulphides is likely to have resulted in assimilation of the sulphide-hosted semi-metals (Te, Se and Au) within the Argyll Group, which would readily enter a sulphide under-saturated melt. Alternatively, partial melting of sulphidic, semi-metal enriched strata by a sulphide-saturated melt would result in semi-metal precipitation and potential scavenging of other chalcophile elements (Holwell and McDonald 2010).

It is conceivable that the partial melting of sulphidic Dalradian strata during emplacement of the Newer Basic Intrusions increased the trace element composition of the melt, particularly in the vicinity of the with an increase in sulphide saturation, is proposed here as a key mechanism for PGE scavenging and mineralisation in

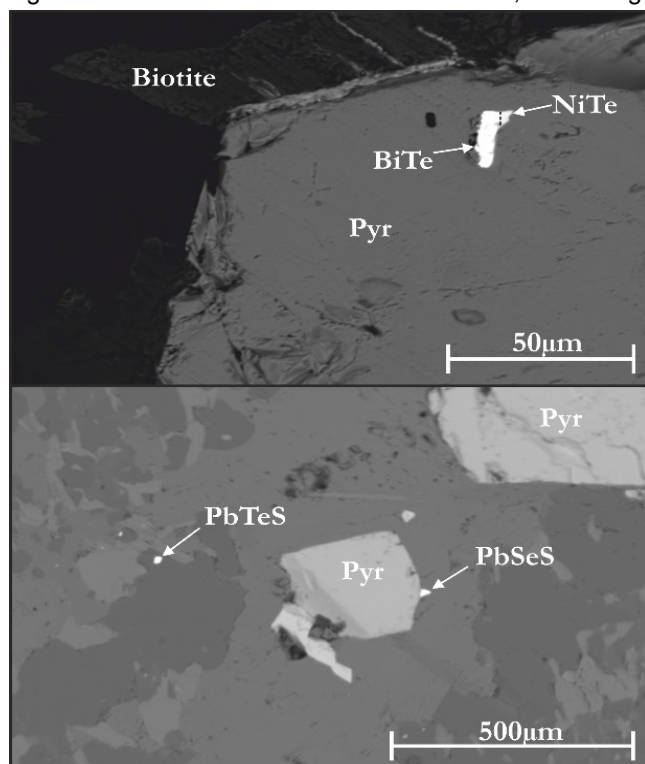


Figure 4. SEM imagery of discrete telluride mineralisation in glacial diamicite samples, Argyll Gp.

these intrusions. By comparison, precious metal concentrations at Knock and Huntly are significantly higher (max. 700 ppb Au+Pt+Pd) than those found at the Inch intrusion (Fig. 1), with a maximum of 13 ppb (Gunn and Shaw 1991). Cumulate sequences here are comparable with those at Knock and Huntly, with similar levels of shear deformation, though graphitic mineralisation is not a significant feature. The emplacement of the Inch intrusion, primarily within the Southern Highlands Group Dalradian strata (Fig.1–2), which is lacking in trace element enriched carbonaceous or sulphidic lithologies, suggests that differences in PGE content of these intrusions may relate to the varying trace element content of assimilated host rock. Therefore, crustal assimilation of Te-rich Argyll Group strata at the Huntly and Knock intrusions likely contributed to the formation of PGE minerals (specifically merenskyite) in these deposits. It is feasible that similar or more significant enrichments may be found in other intrusions emplaced within Te-enriched Dalradian country rock.

Acknowledgements

We are grateful to Adrian Boyce and John Still for skilled technical support. This work was supported by NERC grant NE/M010953/1.

References

- Ashworth JR (1976) Mineralogical magazine. *Mineral Mag* 40:661–682
- Dempster TJ, Rogers G, Tanner PWG, et al (2002) Timing of deposition, orogenesis and glaciation within the Dalradian rocks of Scotland: constraints from U–Pb zircon ages. *J Geol Soc London* 159:83–94
- Droop GTR, Clemens JD, Dalrymple DJ (2003) Processes and Conditions During Contact Anatexis, Melt Escape and Restite Formation: the Huntly Gabbro Complex, NE Scotland. *J Petrol* 44:995–1029
- Fletcher TA (1989) The geology, mineralisation (Ni-Cu-PGE) and isotope systematics of Caledonian mafic intrusions near Huntly NE Scotland. University of Aberdeen
- Fletcher TA, Boyce AJ, Fallick AE (1989) A sulphur isotope study of Ni-Cu mineralization in the Huntly-Knock Caledonian mafic and ultramafic intrusions of northeast Scotland. *J Geol Soc London* 146:675–684
- Gunn AG, Shaw MH (1992) Platinum-group elements in the Huntly intrusion, Aberdeenshire, north-east Scotland. Keyworth, Nottingham
- Gunn AG, Shaw MH (1991) Investigations for Cu-Ni and PGE in the Hill of Barra area, near Oldmeldrum, Aberdeenshire. Keyworth, Nottingham
- Gunn AG, Styles MT (2002) Platinum-group element occurrences in Britain: magmatic, hydrothermal and supergene. *Appl Earth Sci IMM Trans Sect B* 111:B2–B14
- Halliday AN, Graham CM, Aftalion M, Dymoke P (1989) Short Paper: The depositional age of the Dalradian Supergroup: U-Pb and Sm-Nd isotopic studies of the Tayvallich Volcanics, Scotland. *J Geol Soc London* 146:3–6
- Holwell DA, McDonald I (2010) A Review of the Behaviour of Platinum Group Elements within Natural Magmatic Sulfide Ore Systems. *Platin Met Rev* 54:26–36
- Horita J, Polyakov VB (2015) Carbon-bearing iron phases and the carbon isotope composition of the deep Earth. *Proc Natl Acad Sci* 112:31–36
- Hu Z, Gao S (2008) Upper crustal abundances of trace elements: A revision and update. *Chem Geol* 253:205–221
- Ihlenfeld C, Keays RR (2011) Crustal contamination and PGE mineralization in the Platreef, Bushveld Complex, South Africa: Evidence for multiple contamination events and transport of magmatic sulfides. *Miner Depos* 46:813–832
- Johnson TE, Kirkland CL, Reddy SM, Fischer S (2015) Grampian migmatites in the Buchan Block, NE Scotland. *J Metamorph Geol* 33:695–709
- Kendall RS (2017) The Old Red Sandstone of Britain and Ireland — a review. *Proc Geol Assoc* 128:409–421
- Lu DK, Chang YF, Yang HY, Xie F (2015) Sequential removal of selenium and tellurium from copper anode slime with high nickel content. *Trans Nonferrous Met Soc China* 25:1307–1314
- Luque FJ, Crespo-Feo E, Barrenechea JF, Ortega L (2012) Carbon isotopes of graphite: Implications on fluid history. *Geosci Front* 3:197–207
- Makkonen H V, Halkoaho T, Konnunaho J, et al (2017) Ni-(Cu)-PGE deposits in Finland – Geology and exploration potential. *Ore Geol Rev* 90:667–696
- McKervey JA, Gunn AG, Styles MT (2007) Platinum-group elements in Ordovician magmatic Ni-Cu sulfide prospects in northeast Scotland. *Can Mineral* 45:335–353
- Naldrett AJ (1999) World-class Ni-Cu-PGE deposits : key factors in their genesis. *Miner Depos* 227–240
- Oliver GJH, Wilde SA, Wan Y (2008) Geochronology and geodynamics of Scottish granitoids from the late Neoproterozoic break-up of Rodinia to Palaeozoic collision. *J Geol Soc London* 165:661–674
- Parnell J, Perez M, Armstrong J, et al (2017) A black shale protolith for gold-tellurium mineralisation in the Dalradian Supergroup (Neoproterozoic) of Britain and Ireland. *Appl Earth Sci (Trans Inst Min Met B)* 126:161–175
- Parnell J, Perez M, Armstrong J, et al (2018) Geochemistry and metallogeny of Neoproterozoic pyrite in oxic and anoxic sediments. *Geochemical Perspect Lett* 7:12–16
- Peltonen P (1995) Magma-country rock interaction and the genesis of Ni-Cu deposits in the Vammala Nickel Belt , SW Finland. *Mineral Petrol* 52:1–24
- Pina R, Lunar R, Ortega L, et al (2006) Petrology and Geochemistry of Mafic-Ultramafic Fragments from the Petrology and Geochemistry of Mafic-Ultramafic Fragments from the Aguablanca Ni-Cu Ore Breccia , Southwest Spain. *Econ Geol* 101:865–881
- Queffurus M, Barnes SJ (2015) A review of sulfur to selenium ratios in magmatic nickel-copper and platinum-group element deposits. *Ore Geol Rev* 69:301–324
- Rudnick RL, Gao S (2003) Composition of the continental crust. In: Holland HD, Turekian KK (eds) *Treatise on Geochemistry*, First. Elsevier B.V., pp 1–64
- Samalens N, Barnes S, Sawyer EW (2017) The role of black shales as a source of sulfur and semimetals in magmatic nickel-copper deposits: Example from the Partridge River Intrusion, Duluth Complex, Minnesota, USA. *Ore Geol Rev* 81:173–187
- Spence-Jones CP, Jenkin GRT, Boyce AJ, et al (2018) Tellurium, magmatic fluids and orogenic gold: An early magmatic fluid pulse at Cononish gold deposit, Scotland. *Ore Geol Rev* 102:894–905
- Stephenson D, Mendum JR, Fettes DJ, et al (2013a) The Dalradian rocks of the north-east Grampian Highlands of Scotland. *Proc Geol Assoc* 124:318–392
- Stephenson D, Mendum JR, Fettes DJ, Leslie AG (2013b) The Dalradian rocks of Scotland: An introduction. *Proc Geol Assoc* 124:3–82
- Thériault RD, Barnes S-J, Severson MJ (1997) The influence of country-rock assimilation and silicate to sulfide ratios (R factor) on the genesis of the Dunka Road Cu-Ni-platinum-group element deposit, Duluth Complex, Minnesota. *Can J Earth Sci* 34:375–389
- Thomas CW, Graham CM, Ellam RM, Fallick AE (2007) ⁸⁷Sr/⁸⁶Sr chemostratigraphy of Neoproterozoic Dalradian limestones of Scotland and Ireland: constraints on depositional ages and time scales. *J Geol Soc London* 161:229–242

Minor and trace element concentrations in sphalerite and galena from the HYC Pb-Zn deposit and nearby prospects (McArthur Basin, Australia)

Joséphine Gigon, Julien Mercadier, Antonin Richard, Irvine R. Annesley, Ingrid Gautier, Chantal Peiffert
Université de Lorraine, CNRS

Andrew S. Wygralak
Northern Territory Geological Survey

Roger G. Skirrow
Geoscience Australia

Abstract. Minor and trace elements can be extracted from sphalerite and galena as by-products of Zn and Pb respectively. Some of them (e.g. Ga, Ge, In in sphalerite) are essential for green technologies and have been classified as critical raw materials by many countries because of their high risks of supply shortage and impact on the economy (Hayes and McCullough 2018). In addition to their economic significance, trace elements in sphalerite and galena can be useful petrogenetic indicators for ore-forming processes (Frenzel et al. 2016). Here, sphalerite and galena from the giant HYC deposit and nearby prospects or deposits (Caranbirini and Myrtle) within the Batten Fault Zone in the Proterozoic McArthur Basin (Australia) have been analysed for the first time by LA-ICP-MS in order to determine their minor and trace element content. The comparison between data from the different ore lenses at HYC and the two nearby prospect and deposit and the calculation of temperatures derived from the composition of sphalerite (between 90 and 200°C) highlight both the potential critical element resource and the variable dynamics of the ore-forming systems in the study area.

1 Introduction

The Paleo- to Mesoproterozoic McArthur Basin (Northern Territory, Australia) is exposed over an area of about 180 000 km² and unconformably overlies Paleoproterozoic basement units. The basin hosts world-class and minor Pb-Zn resources that belong respectively to the stratiform Sediment Hosted Massive Sulphide (SHMS) and vein categories, especially within the Batten Fault Zone (Ahmad and Munson 2013, Figs. 1 and 2).

In an attempt to document the minor and trace element variability of Pb-Zn occurrences located at different places in a major fault system, the HYC and Myrtle deposits and the Caranbirini prospect located in the Batten Fault Zone have been sampled (Fig. 2) and analysed for major, minor and trace element content of sphalerite and galena by EPMA and LA-ICP-MS.

2 Sampling

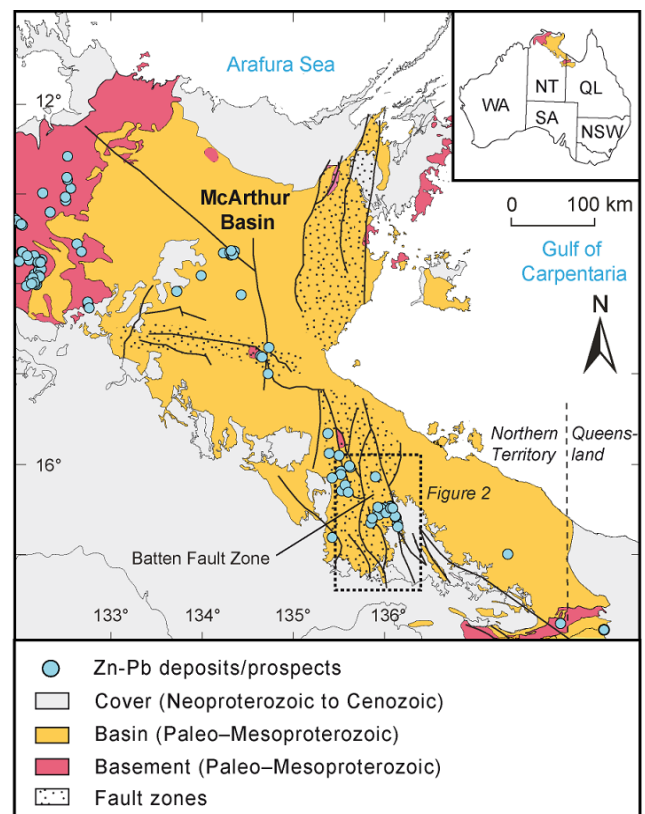


Figure 1. Simplified geological map of the McArthur Basin (Northern Territory, Australia). The crystalline basement, the McArthur Basin, the more recent sedimentary cover and the major faults and faults zones are indicated including the Batten Fault Zone (studied area). Modified after Ahmad and Munson (2013).

The sampled Pb-Zn deposits/prospects are all within 15 km from the Emu Fault, a major strike-slip basement-rooted crustal structure reaching 10 km in depth (Rawlings et al. 2004; McGoldrick et al. 2010). The HYC deposit is a world-class SHMS stratiform deposit with current JORC resource of 188 Mt @ 9.6% Zn, 4.5% Pb, 46g/t Ag (2018). It is located 2 km from the Emu Fault and is composed of eight different ore lenses (Fig. 3, Large et al. 1998). Here, five of the eight ore lenses were sampled together with one sample located below the main ore sequence, covering most of the ore sequence at HYC

(Fig. 3). HYC samples consist of laminated sulphide-rich shales, with sphalerite-galena-pyrite rich bands interlayered with mudstones and quartz-carbonate turbidites (Large et al. 1998, Fig. 4).

The Myrtle deposit is located 19 km south-southwest of HYC. Much of the resource mineralisation comprises stratiform laminated sulphides (sphalerite, galena and pyrite) layers, as well as disseminations in stratabound dolomite alteration lenses. The inferred resource are 43.6 Mt @ 4.09% Zn and 0.95% Pb (Rox Resources 2010).

The Caranbirini prospect is located within the Emu Fault, about 20 km north-northwest of the HYC deposit. Stratiform sulphides as well as sphalerite and galena in late carbonate veins have been sampled.

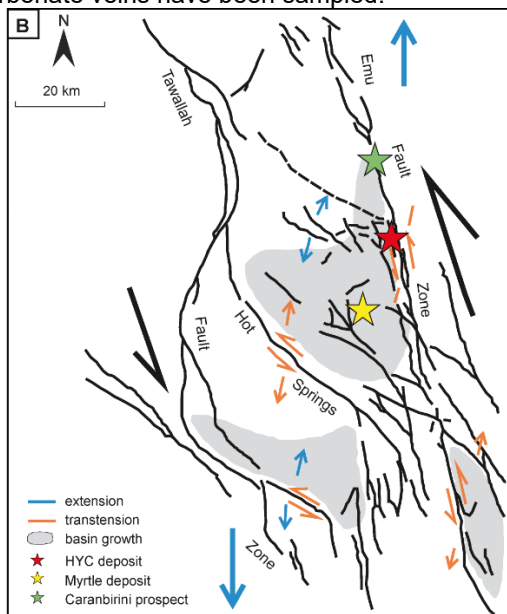


Figure 2. Structural map of the Batten Fault Zone and emplacement of the sub-basins and sampled locations (modified from McGoldrick et al. 2010 and Mukherjee and Large 2017).

2 Methods

All petrographic and geochemical analyses were carried out at GeoRessources Lab (Vandoeuvre-lès-Nancy, France). Petrographic investigation by was carried out using reflected light optical microscopy and SEM. Sulphides were analysed first by EPMA in order to establish major and minor element concentration (Fe, Zn, Pb and Cu) including internal standards (Pb and Zn) for further LA-ICP-MS analysis. LA-ICP-MS analysis was carried out to determine the major, minor and trace element concentration of sulphides. The analysed elements were V, Cr, Mn, Fe, Co, Ni, Cu, Zn, Ga, Ge, As, Se, Mo, Ag, Cd, In, Sn, Sb, Te, Au, Hg, Tl, Pb and Bi in sphalerite, and Mn, Fe, Co, Ni, Cu, Zn, Ga, Ge, As, Se, Ag, Cd, In, Sn, Sb, Te, Tl, Pb and Bi in galena. Detailed mineral mapping was carried out in order to select the most favourable zones within the grains (i.e. large enough to avoid contamination by surrounding minerals and devoid of mineral inclusions).

For LA-ICP-MS analyses, the spot size was from 24 to 44 μm for sphalerite and from 24 to 60 μm for galena, depending on the grain size and homogeneity of the

minerals. The limits of detection (LODs) were calculated according to the 3σ criterion of Longerich et al. (1996). All data points $< \text{LOD}$ were assigned the value of $\text{LOD}/2$.

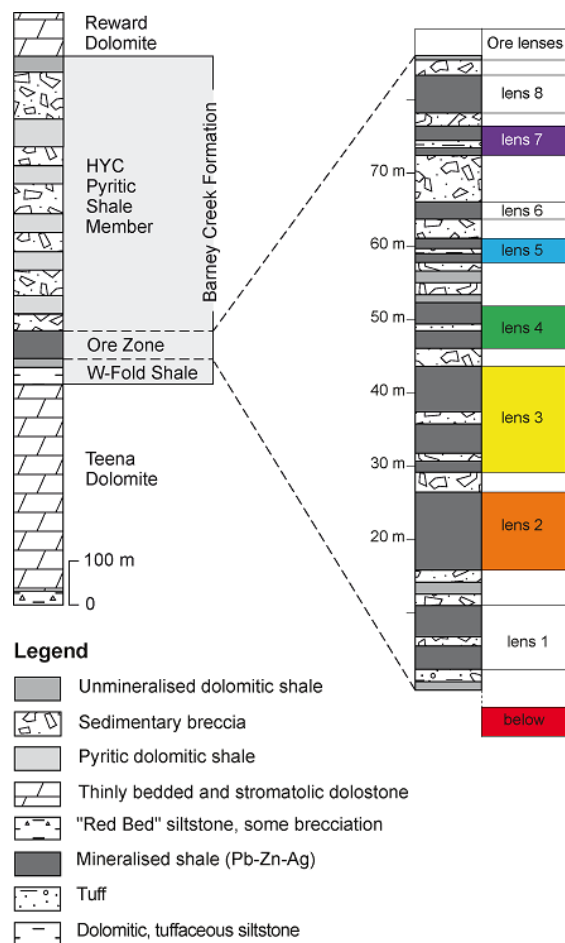


Figure 3. Simplified stratigraphic succession of the HYC deposit with location of the different ore lenses (Large et al. 1998). The sampled ore lenses (galena, lenses 2, 3, 4, 5 and 7) are identified by different colours reported accordingly in Fig. 5, 6 and 7.

3 Results

3.1 Sulphide petrography

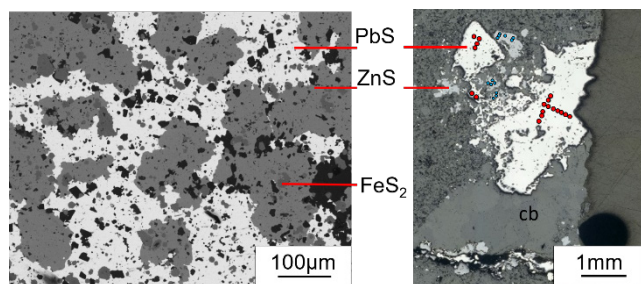


Figure 4. Examples of galena and sphalerite assemblages from the different studied areas. Left: sulphide-rich lamina from lens 2 at HYC showing the texture of galena (PbS), sphalerite (ZnS) and pyrite (FeS_2) (SEM). Right: sphalerite and galena cut by carbonate (cb) vein from sample Caranbirini 679.2m (reflected light). The blue dots are for sphalerite analyses and the red ones for galena.

No growth, recrystallization, zoning or alteration textures

in sphalerite and galena were observed. At HYC, the coarser galena grains show a poecilitic texture where galena crystals up to 1 mm show smaller (10 µm) inclusions of pyrite, sphalerite, carbonates and silicates (Fig. 4). At Myrtle and Caranbirini, sphalerite and galena are coarser (50 µm – 2mm).

3.2 Minor and trace element in sphalerite

Fe, Cu and Pb abundances have been cross-checked by EPMA to verify that the high contents were not due to the analysis of small inclusions. Figure 5 shows the composition results for Ga, Ge and In (used in green technologies and for temperature calculation), Mn and Fe (used for the temperature calculation) and TI (due to the presence of a TI anomaly at HYC).

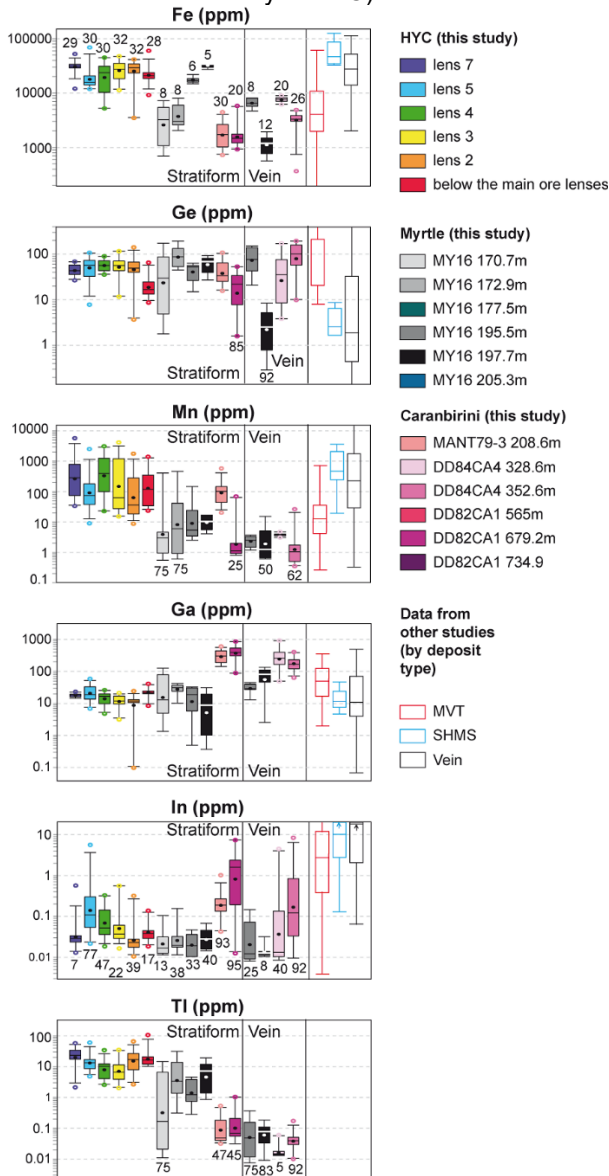


Figure 5. Box-and-whisker plots showing Fe, In, Ga, Ge, Mn and TI concentration in sphalerite at the HYC and Myrtle deposits and Caranbirini prospect (this study) and various deposit types (Frenzel et al. 2016). Lower whiskers, bottoms of boxes, central lines, tops of boxes and upper whiskers represent 5th, 25th, 50th, 75th and 95th percentiles respectively; circle represent outlier. The black dots are

for the mean. Numbers above the whiskers are the number of analysed spots (only written for Fe). The numbers below the whiskers are the percentage of analyses with values > LOD (=100% when not reported).

3.3 Minor and trace elements in galena

Galena at HYC shows high apparent concentrations of Fe (up to 4 %) and Zn (up to 10%) probably due to minor contamination by small inclusions of sphalerite and pyrite. Detailed investigation of element systematics indicate that the elements presented below are not affected by sphalerite contamination (Fig. 6).

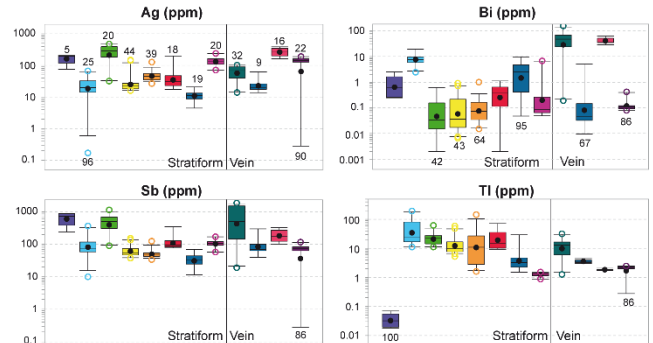


Figure 6. Ag, Bi, Sb and TI concentration in galena at the HYC and Myrtle deposits and Caranbirini prospect (see Fig. 5 for the legend).

3.4 Temperature estimate from sphalerite

Temperature of sphalerite precipitation was estimated using the Ga, Ge, Mn and In (in ppm) and Fe (in %) concentrations and the following equation (Frenzel et al. 2016):

$$T (^{\circ}\text{C}) = (-54.4 \pm 7.3) \times \ln \left(\frac{C_{\text{Ga}}^{0.22} * C_{\text{Ge}}^{0.22}}{C_{\text{Fe}}^{0.37} * C_{\text{Mn}}^{0.20} * C_{\text{In}}^{0.1}} \right) + (208 \pm 10)$$

The calculated temperature ranges from 133°C to 257°C with a median value of 182°C at HYC, from 38°C to 179°C with a median value of 105°C at Myrtle and from 21°C to 144°C with a median value of 84°C at Caranbirini (Fig. 7). The geothermometer is calibrated between 90 and 400°C and the temperatures under 90°C should not be taken into account.

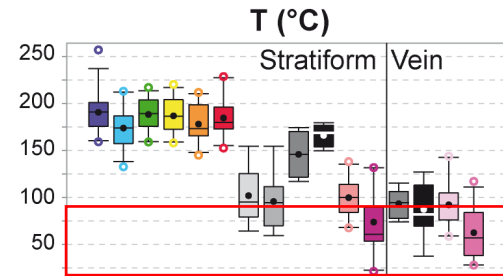


Figure 7. Estimated temperatures in sphalerites from HYC, Myrtle and Caranbirini calculated with the equation above (see Fig. 5 for the legend; Frenzel et al. 2016). Temperatures below the calibration range are highlighted in red.

4 Discussion and conclusions

The temperatures at HYC are consistent with what is expected (Large et al. 2005; Huston et al. 2006). At Myrtle

and Caranbirini, the low Fe, low In and high Ga content induce very low calculated temperatures. Even if some of the data are not in the calibration range, it is possible to infer a lower temperature at Myrtle and Caranbirini (stratiform and vein-type) than at HYC (stratiform only). This highlights significant variations in space and time (stratiform and later veins). Differences between the deposits may relate to fluid temperature and fluid flux, which in turn may relate to how well feeder fault conduits tap deep fluid reservoirs.

Sphalerite compositions are constant in the stratiform HYC deposit, meaning constant conditions of ore formation. Stratiform sphalerite present similar concentrations at Myrtle (except in Fe). At Caranbirini the stratiform sphalerite varies only in Mn concentration. Between all stratiform deposits/prospects, significant variations are observed, and only Ge content is similar in all of them. For vein-type sphalerite, compositions are constant at Myrtle and Caranbirini (with exception of Fe and Ge). When comparing stratiform and vein-type sphalerite, the variation magnitude and the orders of magnitude are similar. The trace element in sphalerite are compared to Mississippi Valley-type (MVT), SHMS and vein-type deposits (Fig. 5; Frenzel et al. 2016). For stratiform sphalerite, the grades obtained in this study are compatible with the one expected for Fe, Ga and Ge from SHMS deposits and slightly higher for Mn. In vein-type sphalerite Fe content is low and Ga content high. In all deposits, the In values are low and often < LOD (~0.04 ppm). It is interesting to note that in a sample with both stratiform and vein sphalerite the Fe content varies, which is expressed by different colours under the microscope.

The Ag, Bi and Sb content in galena is different depending on the lenses or deposits (Fig. 6). The highest Ag content are observed at Caranbirini and HYC, and high Bi values (>10 ppm) are present in two samples from Myrtle and one from Caranbirini. Trace elements in galena can be compared to the ones in the Mount Isa deposit (George et al. 2015) located in the adjacent sedimentary basin. The Bi values in the McArthur basin are lower than in Mount Isa (12–29 ppm) except from one sample at Myrtle and one at Caranbirini, very low for Ag and Sb compared to the 693–2355 ppm and 888–3032 ppm respectively in Mount Isa.

The Tl halo at HYC surrounding the deposit and extending at least 250 m into the hangingwall and 100 m into the footwall of the Emu Fault (Large et al. 2000) is visible through the composition of sphalerite and galena, where Tl content is 2–200 ppm compared to 4–230 ppm in pyrite (Mukherjee and Large 2017).

Even if the concentration trace elements in sphalerite and galena at HYC is in the average of these kind of deposits, the tonnage is so significant that the total amount of trace elements may reach a large tonnage. Yellishetty et al. (2017) estimated a potential stock of 10.9 kt Sb at HYC, consistent with the approximate values that can be calculated from the results present here and representing 3 times the 2018 production of Australia (U.S. Geological Survey 2019).

Acknowledgements

Glencore provided the samples for the HYC deposit, Teck for the Myrtle prospect and Northern Territory Geological Survey for Caranbirini.

References

- Ahmad M, Munson TJ (compilers) (2013) Geology and mineral resources of the Northern Territory. Northern Territory Geological Survey
- Cook NJ, Ciobanu CL, Pring A, et al (2009) Trace and minor elements in sphalerite: A LA-ICPMS study. *Geochimica et Cosmochimica Acta* 73:4761–4791
- Frenzel M, Hirsch T, Gutzmer J (2016) Gallium, germanium, indium, and other trace and minor elements in sphalerite as a function of deposit type — A meta-analysis. *Ore Geology Reviews* 76:52–78. doi: 10.1016/j.oregeorev.2015.12.017
- George L, Cook NJ, Ciobanu CL, Wade BP (2015) Trace and minor elements in galena: A reconnaissance LA-ICP-MS study. *American Mineralogist* 100:548–569
- Hayes SM, McCullough EA (2018) Critical minerals: A review of elemental trends in comprehensive criticality studies. *Resources Policy* 59:192–199
- Huston DL, Stevens B, Southgate PN, et al (2006) Australian Zn-Pb-Ag ore-forming systems: a review and analysis. *Economic Geology* 101:1117–1157
- Large RR, Bull SW, Cooke DR, McGoldrick PJ (1998) A genetic model for the HYC Deposit, Australia; based on regional sedimentology, geochemistry, and sulfide-sediment relationships. *Economic Geology* 93:1345–1368
- Large RR, Bull SW, McGoldrick PJ, et al (2005) Stratiform and Strata-Bound Zn-Pb-Ag Deposits in Proterozoic Sedimentary Basins, Northern Australia. *Economic Geology* 100th Anniversary Volume:931–963
- Large RR, Bull SW, McGoldrick PJ (2000) Lithochemical halos and geochemical vectors to stratiform sediment hosted Zn–Pb–Ag deposits. *Journal of Geochemical Exploration* 68:105–126. doi: 10.1016/S0375-6742(99)00084-9
- Longerich HP, Jackson SE, Günther D (1996) Inter-laboratory note. Laser ablation inductively coupled plasma mass spectrometric transient signal data acquisition and analyte concentration calculation. *Journal of analytical atomic spectrometry* 11:899–904
- McGoldrick P, Winefield P, Bull S, et al (2010) Sequences, synsedimentary structures, and sub-basins: the where and when of SEDEX zinc systems in the southern McArthur Basin, Australia. *Soc Econ Geol Spec Publ* 15:1–23
- Mukherjee I, Large R (2017) Application of pyrite trace element chemistry to exploration for SEDEX style Zn-Pb deposits: McArthur Basin, Northern Territory, Australia. *Ore Geology Reviews* 81:1249–1270
- Rawlings DJ, Korsch RJ, Goleby BR, et al (2004) The 2002 southern McArthur Basin seismic reflection survey. *Geoscience Australia, Record* 17:78
- Rox Resources (2010) ASX/Media release - Myrtle zinc resources continues to grow
- U.S. Geological Survey (2019) Mineral commodity summaries 2019: U.S. Geological Survey
- Yellishetty M, Huston D, Graedel TE, et al (2017) Quantifying the potential for recoverable resources of gallium, germanium and antimony as companion metals in Australia. *Ore Geology Reviews* 82:148–159. doi: 10.1016/j.oregeorev.2016.11.020
- (2018) Lead Zinc Silver factsheet and map. In: The Territory's Resources Commodities in the NT. https://core.nt.gov.au/__data/assets/pdf_file/0006/377619/LeadZincSilver-Factsheet.pdf

Germanium concentration associated to sphalerite recrystallization: an example from the Pyrenean Axial Zone

Alexandre Cugerone, Bénédicte Cenki-Tok, Emilien Oliot, Manuel Munoz, Alain Chauvet, Fabrice Barou
Géosciences Montpellier

Kalin Kouzmanov
University of Geneva

Stefano Salvi
Géosciences Environnement Toulouse

Vincent Motto-Ros
Institut Lumière et Matière

Elisabeth Le Goff
Bureau de Recherches Géologiques et Minières (BRGM)

Abstract. Germanium (Ge) is often found as trace element in undeformed sphalerite (ZnS). However, the presence of Ge-minerals (oxides, chloritoids and/or sulphides with up to 70 wt% Ge) is remarkable in Pb-Zn deposits from the Variscan Pyrenean Axial Zone. Their abundance is controlled by the chemical and/or the mechanical processes that affect rare element concentration from sulphides which have undergone deformation and metamorphism. In this study, we document the microstructures and chemical heterogeneities in sphalerite, based on EBSD (electron backscatter diffraction) coupled to LA-ICPMS *in situ* analyses. Deformation induces the dynamic recrystallization of sphalerite. Recrystallized domains have low Ge contents (1–50 ppm Ge) whereas porphyroclastic sphalerite grains commonly show higher Ge concentrations (up to 650 ppm Ge). Ge-minerals (up to 70 wt% Ge) are exclusively hosted by the Ge-poor recrystallized domains. We propose that Ge was removed from the sphalerite crystal lattice during sulphide recrystallization, and was subsequently concentrated in Ge-minerals, leaving behind a Ge-depleted fine-grained recrystallized sphalerite matrix. Numerous sulphide ore types enriched in rare elements like Pyrenean deposits may present recrystallization features and we suggest evaluating the potential of such deposits by integrating chemical and structural informations at the micrometer scale using state-of-the-art analytical techniques in exploration methods.

1 Introduction

Critical metals like Germanium (Ge), Gallium (Ga) or Indium (In) are often accommodated by the sphalerite lattice (Cook et al. 2009). These elements are presently exploited as by product in base metal deposits in low concentrations (up to several 1000s ppm ; Höll et al. 2007) as commonly observed in non-deformed sulphides (Cugerone et al. 2018a). However, the highest concentrations of zinc sulphide are hosted in

deformed/metamorphosed environments (Wilkinson 2013), but the presence of critical metals in these deposit-type has been poorly explored.

The impact of recrystallization on sulphide composition has been mostly studied in pyrite or arsenopyrite (Cook et al. 2013; Dubosq et al. 2018) and only few studies are available for sphalerite (e.g. Lockington et al. 2014; George et al. 2016). Lockington et al. (2014) compare diverse sphalerites that naturally endured different metamorphic imprints. A loss of trace elements like Pb, Bi, Ag is commonly observed associated to a re-incorporation of Fe, Cd, Mn, In. Homogenization of Cu in the sphalerite lattice is observed but data concerning Ge incorporation in sphalerite are lacking.

The studied sphalerites are located in the Pyrenean Axial Zone (PAZ) Pb-Zn district deposits. These Pb-Zn mineralizations were sampled from deposits mined in the past and represent an interesting natural material for studying the impact of orogenic deformation on sphalerite texture and chemistry. The occurrence of Ge-minerals such as brunogeierite $[\text{GeFe}_2\text{O}_4]$, briartite $[\text{GeCu}_2(\text{Fe,Zn})\text{S}_4]$ or carboirite $[\text{GeFeAl}_2\text{O}_5(\text{OH})_2]$ hosted in sphalerite has been reported in the PAZ (Johan et al. 1983; Cugerone et al. 2018a)

Combining textural (EBSD) and chemical (EPMA and LA-ICP-MS) analyses, our study aims at investigating the role of deformation/recrystallization on the behavior of trace elements in sphalerite, and, in particular the formation process of Ge-minerals.

2 Methods

Electron-BackScattered Diffraction (EBSD) maps were performed with a Camscan Crystal Probe X500FE SEM-EBSD at Geosciences Montpellier (CNRS-University of Montpellier, France). Operating conditions were 20 kV for the accelerating voltage and ~5 nA for the probe current with a working distance of 25 mm under 2 Pa low

vacuum. Samples were positioned horizontally and at the standard 70° angle of the EBSD detector. EDS maps were acquired simultaneously with electron backscatter pattern data. The measurement step was systematically below 5 µm. Oxford Instruments Aztec and Channel 5 softwares were used to generate EDS and EBSD maps.

Electron microprobe analyses (EMPA) were carried out using a Cameca SX100 (at the Service Inter-Regional Microsonde-Sud; Montpellier). Major, minor and trace elements were measured with a beam current of 100 nA and accelerating voltage of 20 kV. 14 elements were analyzed: standards, spectral lines, and spectrometers were as follows: Zn (Zn, L_α, TAP); S (FeS₂, K_α, PET); Fe (Fe₂O₃, K_α, LLif); Cd (CdS, L_α, LPET); Ge (Ge, K_α, LLif); Sb (GaSb, L_α, LPET); Cu (CuS, K_α, LLif); Ga (GaSb, K_α, LLif); Ag (Ag, L_α, LPET); Mn (Mn, K_α, LPET); Sn (Sn, L_α, PET); Pb (Pb, M_α, PET); As (GaAs, L_α, TAP); Si (CaSiO₃, K_α, TAP). Peak counting times ranged from 30 to 240 s (240 s for Ge). Germanium is analyzed on 2 LLif monochromators. The limit of detection for Ge and Cu, calculated by internal Cameca procedures, is reduced to 84 ppm and 110 ppm respectively. Ga, As, Ag, Pb, Sn, Sb, and Mn were below detection limit.

Laser ablation inductively coupled plasma-mass spectrometry (LA-ICP-MS) was used to determine trace elements concentrations in sphalerite. Analyses were carried out using an Excimer CompEx 102 coupled with a ThermoFinnigan Element XR available at the OSU-OREME AETE platform at the Montpellier University.

Laser ablation was performed at constant 5 Hz pulse rate with 140 mJ laser energy. Each measurement comprises 180 s of background measurement and 60 s of sample ablation (signal measurement), followed by a 60 s retention time to ensure a proper cell washout. Data were processed using the Glitter 4.0 software package.

The following isotopes were measured: ²⁹Si, ³⁴S, ⁵⁵Mn, ⁵⁷Fe, ⁵⁹Co, ⁶¹Ni, ⁶³Cu, ⁶⁵Cu, ⁶⁴Zn, ⁶⁹Ga, ⁷¹Ga, ⁷⁴Ge, ⁷⁵As, ⁷⁷Se, ⁹⁵Mo, ¹⁰⁵Pd, ¹⁰⁷Ag, ¹⁰⁹Ag, ¹¹⁰Cd, ¹¹¹Cd, ¹¹⁵In, ¹¹⁸Sn, ¹¹⁹Sn, ¹²⁰Sn, ¹²¹Sb, ¹²³Sb and ²⁰⁸Pb. Zn contents in sphalerite measured with EPMA were used as internal standard of the LA-ICP-MS analyses. MASS-1 reference was used as external standard (Dr. Stephen Wilson, personal communication) with a corrected 57 ± 1.75 ppm value for Ge. NIST SRM 610 was used as secondary external standard to identify possible instrumental drift. Ni, As, Mo, Se, Pd and Si concentrations were systematically below detection limits. Only Ge and Cu contents measured in sphalerite will be discussed in this paper.

3 Pb-Zn deposits in the Pyrenean Axial Zone

Pyrenean Pb-Zn deposits are hosted in the deformed Variscan (~325-290 Ma) Pyrenean Axial Zone exhumed during the collision between the Iberia and Eurasian plates since the Lower Cretaceous. Foliation trajectories exhibit a monotonous N080-N110°E trend with variable dip angles. Two main Variscan deformation events are recorded in the host-rock. A poorly expressed S₁ cleavage is often parallel to original stratification S₀ and is associated to regional M₁ Medium-Pressure Low-

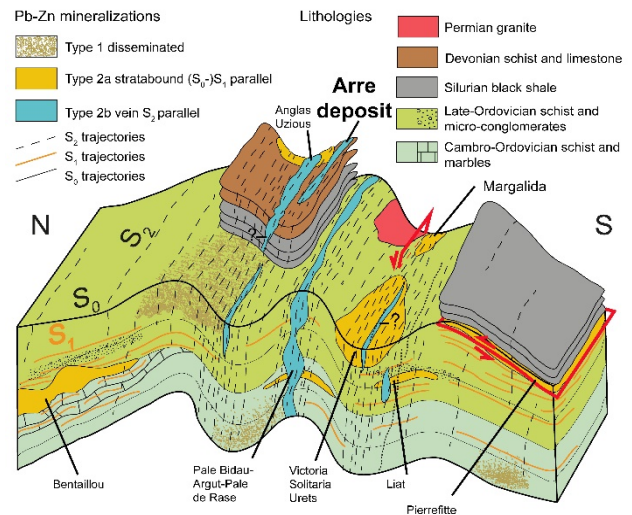


Figure 1: Schematic 3D sketch presenting the three main types of mineralization which are typically observed in the studied area and related to each studied deposit. Type 2b vein mineralizations appear in intensely S₂ deformed domains. Location of Arre deposit is noted (modified from Cugerone et al., 2018b)

Temperature (MP-LT) metamorphic conditions. A well-expressed S₂ cleavage is sub-vertical and superimposed to the previous structures. S₂ axial planar cleavage is associated to M₂ contact (HT-LP) metamorphic conditions, marked in the studied area with the appearance of cordierite.

Three Pb-Zn types of mineralization types are present in the PAZ and fully described in Cugerone et al. (2018b). In Figure 1, a schematic 3D sketch is shown and illustrates the major types of mineralization types. Type 1 corresponds to a minor disseminated mineralization, probably syngenetic and from an exhalative source. Type 2a is a stratabound mineralization, epigenetic and synchronous to the Variscan D₁ regional deformation event and (III) while Type 2b is a vein mineralization, epigenetic and supposed synchronous to the late Variscan D₂ regional deformation event.

Herein, we will only focus on the Type 2b Ge-rich mineralization and more precisely on Arre deposit (Cugerone et al. 2018b). Type 2b is an epigenetic sub-vertical vein-type mineralization (Fig. 2A) which has endured at least one deformation event, probably Variscan in age (D₂ in Cugerone et al. 2018b). These veins are composed of sphalerite and galena, with a small amount of pyrite, chalcopyrite, arsenopyrite and gangue of quartz-carbonate (Fig. 2B). Numerous Type 2b deposits are present in the Axial Zone (Cugerone et al. 2018b) and in this paper, we will focus on the Arre deposit. This Pb-Zn(-Ge) mineralization is hosted in Devonian calc-schist and marble rocks. Veins are oriented N070 E with sub-vertical dip (Fig. 2A).

4 Microstructural study

EBSD has been performed on Type 2b mineralizations

(Fig. 3A and 3B) to obtain textural and microstructural information. Sphalerite occurs with diverse grain size (from 10 μm to > 1 mm). Coarse grains are parent grains and are internally deformed. Smaller grains (< 100 μm)

mantled parent grains and also locally occur in twin boundaries. Three different textures are distinguished in sphalerite: dark domains and light domains that are

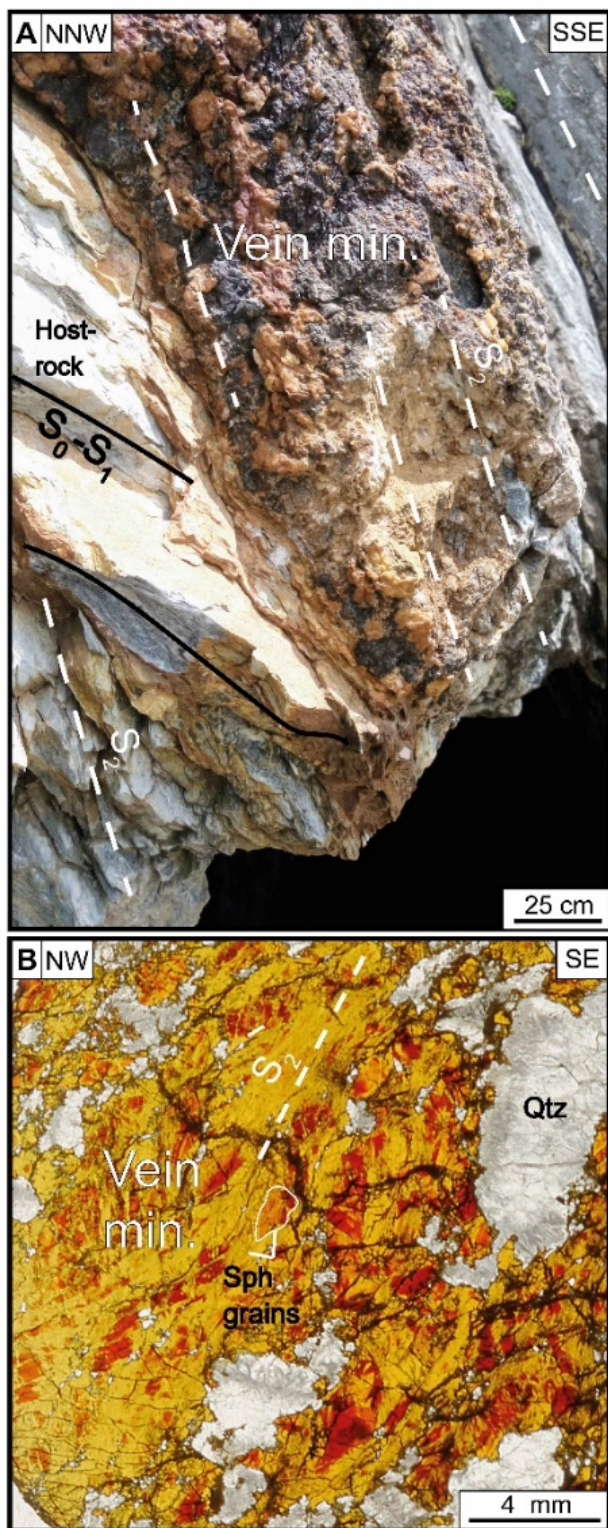


Figure 2: A: Pb-Zn Type 2b Vein in Arre deposit. B: Typical Pb-Zn Type 2b ore mineralization with color zonation in sphalerite and presence of superimposed S_2 cleavage (modified from Cugerone et al., 2018b; S_0-S_1 : S_0-S_1 foliation; S_2 : S_2 foliation; Qtz: quartz; Sph: sphalerite).

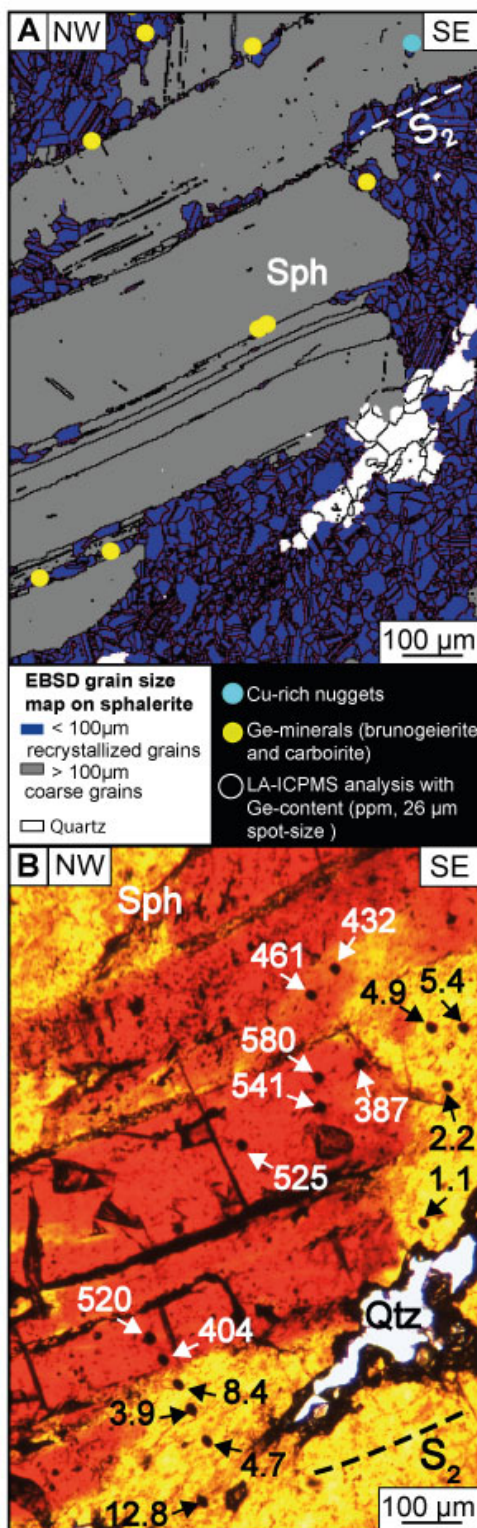


Figure 3: A: EBSD grain size map in sphalerite (Arre sample) with location of Ge and Cu rich phases. These minerals are preferentially located in recrystallized sphalerite domains. B: Corresponding area in transmitted light with LA-ICP-MS spot analyses associated to Ge-contents (in ppm). Note that the contrasts in color observed in Sph correspond to variations in Ge content. (S_2 : S_2 foliation; Qtz: quartz; Sph: sphalerite).

observed in coarse parent grains and recrystallized domains that are composed of newly formed smaller grains.

In the same area, an EDS chemical map is performed simultaneously to the EBSD acquisition, and so that the locations of Ge-minerals are reported (Figure 3A, yellow dots). Ge-minerals mainly consist of brunogeierite (GeFe_2O_4) and carboirite ($\text{GeFeAl}_2\text{O}_5(\text{OH})_2$); they are preferentially hosted in the small recrystallized sphalerite grain or located close to twin boundaries.

5 Ge and Cu in sphalerite

The location of LA-ICP-MS spot analyses was based on the EBSD grain size map so that chemical and textural information can be link each other. LA-ICP-MS spots are indicated in Figure 3B associated to their Ge-contents in zoned sphalerite as observed in transmitted light. Germanium distribution is highly zoned. In dark and light domains, the median content reaches 433 ± 21 ppm and 46 ± 2 ppm, respectively. In recrystallized domains, Ge content is typically low, with median Ge content is much lower with a median concentration of 4 ± 2 ppm. Heterogeneous Ge in sphalerite is positively correlated to Cu, especially in the dark and light domains with Cu median contents of 1012 ± 75 ppm and 102 ± 7 ppm respectively. Cu content is lower in recrystallized grains with a median value of 29 ± 9 ppm.

A mass balance calculation performed between the different Ge-bearing phases observed reveals an “equivalent” Ge concentration in primary non-deformed sphalerite of 700 ppm in average (Cugerone et al., in prep).

6 Discussion and conclusions

The studied sphalerites from the Arre deposit in the PAZ show remarkably heterogeneous sphalerite textures and related major and trace chemistry. The formation of Ge-rich minerals is mainly observed in close association with recrystallized sphalerite, so that deformation (supposed Variscan D₂) and recrystallization mechanisms are likely to play a major role in the Ge concentration process (Fig. 3a); leaving behind a Ge-depleted fine grained recrystallized sphalerite matrix.

Several textural and chemical analogues to these sphalerites may be present in Chinese deformed-MVT deposits (Ye et al. 2011), in Kipushi deposits (Belissont et al. 2016; Horn et al. 2018) but also in other sulphide minerals like chalcopyrite from VHMS deposit (Reiser et al. 2011; Belissont et al. 2019). Ores affected by recrystallization are likely to contain accessory minerals that can be potentially enriched in rare metals.

Acknowledgements

The authors thank the French Geological Survey (Bureau de Recherches Géologiques et Minières; BRGM) for funding through the national program “Référentiel Géologique de France” (RGF-Pyrénées). The authors gratefully acknowledge Christophe Nevado and Doriane

Delmas for the excellent thin sections preparation, Bernard Boyer and Olivier Bruguier for their involvement in EPMA and LA-ICP-MS analyses, respectively.

References

- Belissont R, Munoz M, Boiron M, Luais B, Mathon O (2019) Germanium Crystal Chemistry in Cu-Bearing Sulfides from Micro-XRF Mapping and Micro-XANES Spectroscopy. *Minerals* 9:1–12
- Belissont R, Munoz M, Boiron MC, Luais B, Mathon O (2016) Distribution and oxidation state of Ge, Cu and Fe in sphalerite by μ -XRF and K-edge μ -XANES: Insights into Ge incorporation, partitioning and isotopic fractionation. *Geochim Cosmochim Acta* 177:298–314.
- Cook NJ, Ciobanu CL, Meria D, Silcock D, Wade B (2013) Arsenopyrite-Pyrite Association in an Orogenic Gold Ore: Tracing Mineralization History from Textures and Trace Elements. *Econ Geol* 108:1273–1283
- Cook NJ, Ciobanu CL, Pring A, Skinner W, Shimizu M, Danyushevsky L, Saini-Eidukat B, Melcher F (2009) Trace and minor elements in sphalerite: A LA-ICPMS study. *Geochim Cosmochim Acta* 73:4761–4791.
- Cugerone A, Cenki-Tok B, Chauvet A, Le Goff E, Bailly L, Alard O, Allard M (2018a) Relationships between the occurrence of accessory Ge-minerals and sphalerite in Variscan Pb-Zn deposits of the Bossost anticlinorium, French Pyrenean Axial Zone: Chemistry, microstructures and ore-deposit setting. *Ore Geol Rev* 95:1–19.
- Cugerone A, Oliot E, Chauvet A, Gavalda J, Le Goff E (2018b) Structural Control on the Formation of Pb-Zn Deposits: An Example from the Pyrenean Axial Zone. *Minerals* 8:1–20.
- Dubosq R, Lawley CJM, Rogowitz A, Schneider DA, Jackson S (2018) Pyrite deformation and connections to gold mobility: Insight from micro-structural analysis and trace element mapping. *Lithos* 310–311:86–104.
- George LL, Cook NJ, Ciobanu CL (2016) Partitioning of trace elements in co-crystallized sphalerite-galena-chalcopyrite hydrothermal ores. *Ore Geol Rev* 77:97–116.
- Höll R, Kling M, Schroll E (2007) Metallogensis of germanium-A review. *Ore Geol Rev* 30:145–180.
- Horn S, Dziggel A, Kolb J, Sindern S (2018) Textural characteristics and trace element distribution in carbonate-hosted Zn-Pb-Ag ores at the Paleoproterozoic Black Angel deposit, central West Greenland. *Miner Depos* 1–18.
- Johan Z, Oudin E, Picot P (1983) Analogues germanifères et gallifères des silicates et oxydes dans les gisements de zinc des Pyrénées centrales, France; argutite et carboirite, deux nouvelles espèces minérales. *TMPM Tschermaks Mineral und Petrogr Mitteilungen* 31:97–119.
- Lockington JA, Cook NJ, Ciobanu CL (2014) Trace and minor elements in sphalerite from metamorphosed sulphide deposits. *Mineral Petrol* 108:873–890.
- Reiser FKM, Rosa DRN, Pinto ÁMM, Carvalho JRS, Matos JX, Guimaraes FMG, Alves LC, de Oliveira DPS (2011) Mineralogy and geochemistry of tin- and germanium-bearing copper ore, Barrigao re-mobilized vein deposit, Iberian Pyrite Belt, Portugal. *Int Geol Rev* 53:1212–1238.
- Wilkinson JJ (2013) Sediment-Hosted Zinc-Lead Mineralization: Processes and Perspectives: Processes and Perspectives, Treatise on Geochemistry, Second Edition. Elsevier, H Holland, K Turekian (ed), Amsterdam, Netherlands 219–249.
- Ye L, Cook NJ, Ciobanu CL, Yuping L, Qian Z, Tiegeng L, Wei G, Yulong Y, Danyushevskiy L (2011) Trace and minor elements in sphalerite from base metal deposits in South China: A LA-ICPMS study. *Ore Geol Rev* 39:188–217.

Germanium, Gallium and Indium distribution in base metal sulfides from hydrothermal veins of the Ruhr and Bergisches Land districts, Germany

Sören Henning
Leibniz University, Germany

Torsten Graupner, Hans-Eike Gäbler, Simon Goldmann, Jolanta Kus
Federal Institute for Geosciences and Natural Resources (BGR)

Thomas Krassmann
Mineral & Exploration Dr. Krassmann

Abstract. The increasing demand for high tech related trace elements and the high concentration of their supply supports the need for systematic investigations on Ge, Ga and In occurrences in ore deposits. The present work focuses on high tech trace element characteristics of historic hydrothermal base metal vein deposits of the Ruhr and the Bergisches Land districts (Germany). The mineralogy of 66 ore samples from 22 historic mine sites was determined by μ -EDXRF. High-resolution EMPA mapping and quantitative analysis of trace elements by LA-ICP-MS reveal incorporation mechanisms of high tech trace elements in the sphalerite structure. Despite the observed natural variability for minor and trace elements, low iron-bearing sphalerite of both studied vein districts contains moderate Ga concentrations incorporated in growth zoning structures. Indium occurs restricted to small grain domains outlining growth zoning structures in a few samples. Germanium is incorporated into the sphalerite structure in sector zoning patterns restricted to hydrothermal veins from the Ruhr district. Correlation trends and EMPA maps indicate coupled substitution processes in sector zoning involving Cu, Ag, (As, Pb) and Sb. Assessments on physicochemical fluid properties and possible metal sources suggest an influence of organic rich host rocks (Ruhr district) on the observed Ge enrichment.

1 Introduction

The rising resource demand, the high concentration of supply of strategic metals and the advancing development of modern technologies places new demands on the exploration and production of raw materials. So-called high tech trace elements such as germanium (Ge), gallium (Ga) and indium (In) gain rising importance for modern technologies (e.g. infrared optics, fibre optic cables, solar applications, LEDs) due to their characteristics as semiconductor elements and their infrared transmission properties.

Several studies indicate that these trace elements are occasionally incorporated in economically relevant concentrations in the base metal sulfides sphalerite and chalcopyrite (Cook et al. 2009). However, the transport, distribution and incorporation processes are poorly understood and systematic studies are missing.

During the recently completed research project "HTMET", a mineralogical-geochemical database on samples from historic German base metal mining districts was set up to evaluate the high tech trace element potential of these ores. It became apparent that differences in the trace element specialization of ores are dependent on the genetic deposit type. This is in agreement with economically oriented papers and case studies, where In-enriched sulfides in skarn and SHMS deposits, or Ge-specialized collomorphic sphalerite from MVT deposits, were investigated (Seifert and Sandmann 2006; Pfaff et al. 2011).

However, trace element concentrations in sulfides from hydrothermal vein deposits vary significantly depending on formation conditions, structural control of the deposits and metal sources. In order to reveal the reasons for differences in trace element concentrations, this study focuses on trace element distribution and incorporation mechanisms into sulfides of the two adjacent historic German base metal mining areas, the Ruhr and the Bergisches Land districts. The focus of this study are new insights into incorporation, distribution and transport mechanisms of Ge, Ga and In in hydrothermal systems. Besides textural and mineralogical investigations (μ -EDXRF, optical and scanning electron microscopy), quantitative trace element analysis (LA-ICP-MS) and high-resolution element mapping (EMPA) were carried out. Assessments of physicochemical fluid characteristics were used to constrain trace metal sources and will be complemented by fluid inclusion measurements and isotopic analysis.

2 Geological setting

The Ruhr Basin region is located in North Rhine-Westphalia in the Western part of Germany. The bedrock of the Ruhr area consists of alternate bedded and closely folded layers of Carboniferous mud- and sandstones. Fossil organic substances are embedded either as high-ash bituminous shale or as coal seams. Intensive post-Carboniferous tectonics led to a folding and faulting of the sedimentary rock sequences resulting in a complex block-faulting structure. In the course of this process, hydrothermal fluids were able to rise up and lead to the formation of hydrothermal base metal ore deposits

preferentially at the intersection of anticlinal axis of the Carboniferous mud- and sandstone and the normal faults (Richter 1997).

The adjacent Bergisches Land district is part of the Rhenish Massif that forms the southernmost part of North Rhine-Westphalia. The bedrock of the hydrothermal veins consists mainly of Devonian rocks. The strong-fissured Paleozoic rocks of the Rhenish Massif enabled the hydrothermal fluids to rise up and to form base metal ore veins with an intense accumulation in several ore districts. The base metal veins are mostly restricted to voids resulting of Northwest-Southeast to North-South trending cross faults (Ribbert 2012).

3 Mineralogical and textural properties

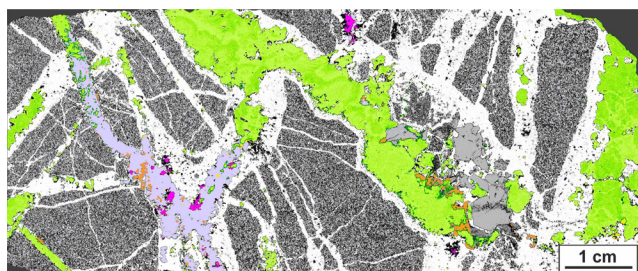


Figure 1. False color μ -EDXRF mineral distribution map showing textural properties of a typical ore sample (Lüderich, Bergisches Land district); i) sulfide minerals: sphalerite (green; color shades indicate varying Fe contents from dark (high) to light (low)), galena (magenta), chalcopyrite (yellow), iron sulfides (orange); ii) gangue minerals: quartz (white) and carbonates (purple); iii) silicified host rock (grey).

False color mineral distribution maps obtained for 66 ore samples out of 22 deposits by μ -EDXRF analysis (Flude et al. 2017) reveal a relatively simple mineral paragenesis for veins of both districts. Sphalerite (green) occurs either as bulky massive aggregates with a variable shape (Fig. 1) or on small fissures. Growth zoning structures are indicated by varying iron contents. The second most common sulfide in the analyzed samples is galena (magenta) that can occur as small inclusions up to large and nearly mono-mineralic lode fillings in both districts. Chalcopyrite (yellow) occurs as small phases in most samples, commonly embedded in, or associated with, sphalerite and galena, but not showing typical chalcopyrite disease. Massive chalcopyrite is more frequent in samples of the Bergisches Land district. Iron sulfides, either pyrite or marcasite (orange), occur in nearly all investigated hydrothermal veins as ubiquitous minerals in small amounts. However, the occurrence of massive marcasite minerals is typical of the Ruhr district. Quartz (white) is the main gangue mineral in most samples often occurring as rims around brecciated mud-, shale- and sandstone fragments or infiltrating and replacing the host rocks (grey). Carbonates (purple) such as siderite, ankerite or calcite were observed in many of the investigated samples of the multi stage mineralizations as well. Late stage barite does only appear in a few samples of the Ruhr district and is lacking in samples of the Bergisches Land district. Based on the mineral distribution maps, 3x3 cm sized polished sections

were prepared for further investigations on trace element concentrations.

4 Quantitative analysis of trace element concentrations in sphalerite

The major, minor and trace element concentrations in sphalerite and chalcopyrite grains were measured by LA-ICP-MS with up to 60 spots for each polished section. Measurements of sphalerite were quantified using a calibration method based on the matrix-matched sphalerite reference material MUL-ZnS-1, which has similar composition, ablation behavior and element fractionation behavior as typical natural sphalerite (Onuk et al. 2017). The concentrations of Ge and Ga in sphalerite from selected deposits of both districts are illustrated in figure 2 as box plot diagrams. Except for sphalerite 2 of the Auguste Victoria mine, sphalerite from the Ruhr district is characterized by elevated high tech trace element concentrations (median Ge: 24–81 ppm; Ga: 97–185 ppm) compared to the Bergisches Land district (median Ge: 1–6 ppm; Ga: 14–26 ppm). In both districts In occurs only in less than 5% of the measurements in detectable concentrations. The results of LA-ICP-MS analysis were validated by bulk ore geochemistry measured using ICP-OES/MS.

5 Distribution of trace elements in sphalerite

5.1 High resolution compositional mappings

Distribution and incorporation processes of high tech trace elements in sphalerite were investigated by high-resolution EMPA mapping of 2x2 mm large areas for selected samples. Semi-quantitative results for Ge and Ga are shown in figure 3. Germanium (Fig. 3a) is clustered in sector zoning patterns. These zones are enriched in Cu, Ag and Sb and depleted in Fe (not shown). In contrast to that, Ga (Fig. 3b), Cu and, to a minor extent, In are enriched in narrow bands (<50 μ m) outlining the sphalerite growth zone structures.

The heterogeneous distribution of trace elements in the sphalerite explains the high variability of the trace element concentration data obtained by 40 μ m laser spots shown above. These compositional zoning structures are explained by microscale crystallographic controls on the element fractionation along with alternating compositional variations in the fluid composition at the crystal fluid interface. According to Johan (1988), the growth zoning structures are related to 110 crystal faces whereas the sector zoning patterns exist at 111 planes of sphalerite crystals and may overlap the growth zoning structures.

5.2 Incorporation mechanisms

Correlation trends of LA-ICP-MS data illustrate the

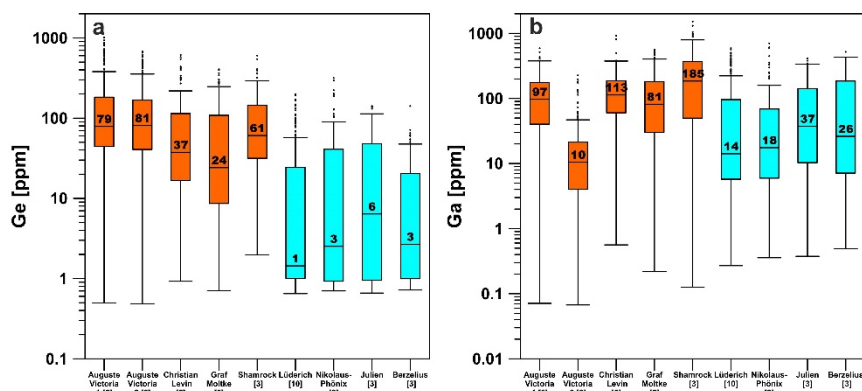


Figure 2. Box plot diagrams illustrating results of LA-ICP-MS trace element data for a) Ge and b) Ga for sphalerite from selected deposits of the Ruhr (orange) and the Bergisches Land (blue) districts; number of samples are shown in brackets and the median values are shown in the diagrams; results for Auguste Victoria mine were separated for two sphalerite generations.

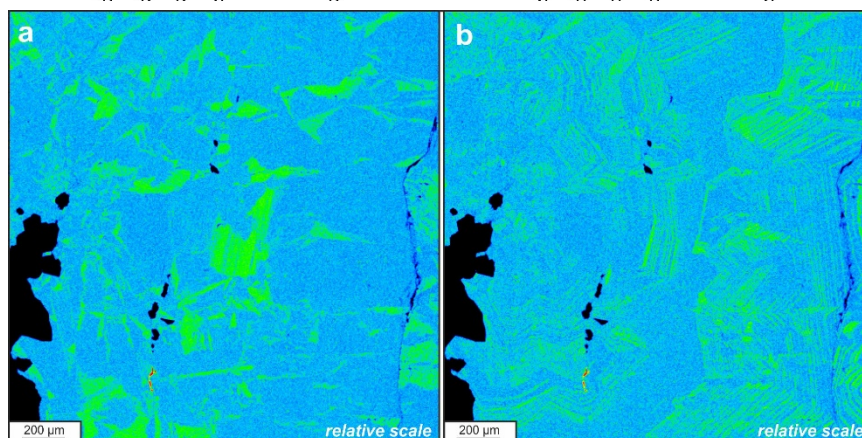


Figure 3. High-resolution EMPA mappings of sphalerite grains for a) Ge and b) Ga indicating incorporation in sector zoning patterns (Ge) and growth zoning structures (Ga) in the Ruhr district from blue (low) to green (high) concentrations (25 kV, 40 nA, 500 ms, 4 µm probe diameter).

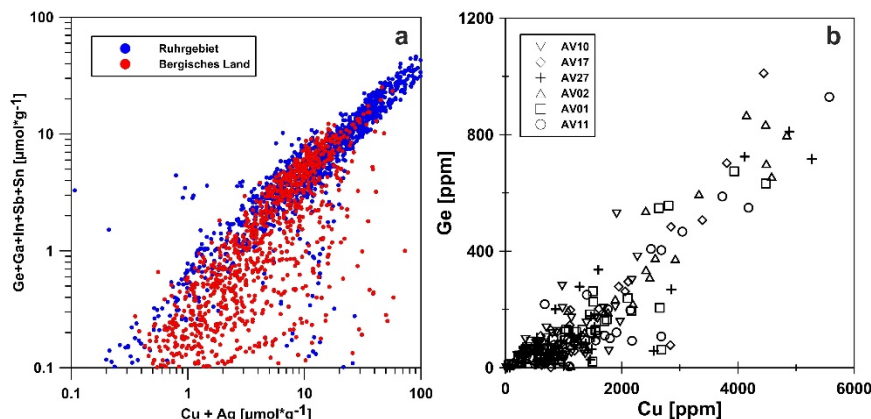


Figure 4. Correlation trends of LA-ICP-MS data indicating that a) tri- and tetravalent charged trace elements need monovalent cations to be incorporated into the sphalerite structure; b) strong positive correlation of Ge and Cu (Ag, Sb, (As, Pb)) was observed in samples from the Auguste Victoria (AV) mine in the Ruhr district indicating a coupled substitution process for sector zoning structures.

incorporation mechanisms of the high tech elements. Our data support the hypothesis of direct substitution of divalent cations (e.g. Fe^{2+} , Cd^{2+} , Mn^{2+}) against Zn^{2+} in the sphalerite structure (Cook et al. 2009). However, figure 4 shows that tri- and tetravalent cations (Ge^{4+} , Ga^{3+} , In^{3+} , Sb^{3+} and Sn^{3+}) need monovalent cations (Cu^+ , Ag^+) to be incorporated into the sphalerite structure in both districts (Fig. 4a). Figure 4b shows the strong positive correlation of Ge and Cu (LA-ICP-MS) for sphalerite 1 of the Auguste Victoria mine (Ruhr district), which was also observed in the EMPA data. The further strong positive correlation of Ge with Ag, Sb, (As, Pb) is in agreement with a coupled substitution process related to the sector zoning patterns (Johan 1988).

Due to the enrichment of In and Ga in narrow bands the correlation trends of LA-ICP-MS data of these areas are not as good as those for the sector zoning areas in the sphalerite. However, a distinct correlation of In^{3+} , Sn^{3+} and Cu^+ was observed.

6 Fluid characteristics and metal sources

The incorporation of major, minor and trace elements into the sphalerite structure is related to crystallographic control. But differences in trace element concentrations of the Ruhr and the Bergisches Land district cannot be explained by crystal growth alone as they show no significant differences in the incorporation mechanisms (Fig. 4a). Therefore, general variations in the sphalerite compositions may rather result from varying fluid properties and metal sources (Belissant et al. 2016).

Vitrinite reflectance analysis on associated hard coal samples and application of the “GGIMFis sphalerite geothermometer” (Frenzel et al. 2016) on trace element data indicate rather low temperatures for ore forming fluids in the Ruhr district (<200 °C). These results are in accordance with fluid inclusion literature data (Topp 1988). Calculated temperatures of hydrothermal fluids

from the Bergisches Land district (GGIMFIS) are only slightly higher (<255 °C) compared to those of the Ruhr district. The salinity of the fluids plays an important role in terms of metal transport. Fluid inclusion data indicate generally high, but variable salinities (up to 30 wt.% NaCl equiv.) and an increased amount of CaCl₂, for ore formation in both districts (Topp 1988).

Fluid properties as well as transport and incorporation processes are relatively similar in both districts. Further studies on fluid inclusions in ore and gangue minerals, the age of the mineralization (Rb/Sr), and the origin of sulfur ($\delta^{34}\text{S}$) are planned in order to reveal differences in the formation conditions of the two ore districts.

However, distinct differences in the host rocks of the ore deposits are obvious and may have resulted in significant differences of trace element enrichment for both districts. The moderate to high Ga concentrations in both districts may be explained by alteration of feldspar and mica in the host rocks as Ga³⁺ and Al³⁺ have the same charge and similar ionic radii.

As Ge compared to Ga is not enriched in all districts, a ubiquitous available source like release from silica mineral weathering (similar properties of Ge⁴⁺ and Si⁴⁺) does not seem to be very probable for the local Ge enrichment. The presence of coal seams in the Carboniferous layers and their immediate contact to the hydrothermal vein deposits is a distinct feature of the Ruhr district. As Ge is commonly enriched in peat, lignite or organic enriched environments, the coal seams may be a potential metal source. Horse tail plants that were widely distributed in the Ruhr district during Carboniferous are known to enrich Ge in their roots (Delvigne et al. 2009). Trace element studies on hard coal from the Ruhr district indicated concentrations of 1.20-1.98 ppm Ge, which are higher than those of the Saar area and other locations. As peat and lignite often have very high trace element concentrations and anthracite is known for very low trace element contents, it is expected that the trace elements were released during coalification. According to the massive silification, displacement, brecciation and the occurrence of coal debris in the hydrothermal veins from the Ruhr district, the presence of large volumes of matured coal seams may have a significant influence on the enrichment of Ge in sphalerite and chalcopyrite. The enrichment of Ge triggered by organic matter is discussed for MVT and Tsumeb-type deposits as well (Sahlström et al. 2017).

7 Conclusions

Mineralogical and geochemical investigations demonstrate that the distribution of high tech trace elements within sphalerite grains is highly inhomogeneous. High-resolution EMPA mapping indicate a preferential enrichment of Ge in sector zoning patterns. Correlation trends with other metals point to a Ge incorporation in the sphalerite lattice via coupled substitution of Zn. The enrichment of Ga, In, Sn and Cu appears in narrow growth zoning structure bands of the sphalerite grains. Sphalerite of hydrothermal vein deposits from the Ruhr district is characterized by clearly

elevated high tech trace element concentrations compared to sphalerite from the Bergisches Land district. We propose the silicified coal seams in the Carboniferous host rocks of the Ruhr district as the source for elevated Ge concentration in the cutting base metal veins.

Acknowledgements

The results of this study contribute to the BGR project RoStraMet and the r⁴-research project HTMET funded by the German government (BMBF). The authors would like to thank the affiliated and associated partners of the joint research project for providing sample material and for the exchange of ideas.

References

- Belissant R, Muñoz M, Boiron MC et al (2016) Distribution and oxidation state of Ge, Cu and Fe in sphalerite by μ -XRF and K-edge μ -XANES. *Geochim Cosmochim Acta* 177:298–314.
- Cook NJ, Ciobanu CL, Pring A et al (2009) Trace and minor elements in sphalerite. A LA-ICPMS study. *Geochim Cosmochim Acta* 73:4761–4791.
- Delvigne C, Opfergelt S, Cardinal D et al (2009) Distinct silicon and germanium pathways in the soil-plant system. Evidence from banana and horsetail. *J Geophys Res* 114.
- Flude S, Haschke M, Storey M (2017) Application of benchtop micro-XRF to geological materials. *Mineral Mag* 81:923–948.
- Frenzel M, Hirsch T, Gutzmer J (2016) Gallium, germanium, indium, and other trace and minor elements in sphalerite as a function of deposit type. *Ore Geol Rev* 76:52–78.
- Johan Z (1988) Indium and germanium in the structure of sphalerite. An example of coupled substitution with Copper. *Mineral Petrol* 39:211–229.
- Onuk P, Melcher F, Mertz-Kraus R et al (2017) Development of a Matrix-Matched Sphalerite Reference Material (MUL-ZnS-1) for Calibration of In Situ Trace Element Measurements by LA-ICP-MS. *Geostand Geoanal Res* 41:263–272.
- Pfaff K, Koenig A, Wenzel T et al (2011) Trace and minor element variations and sulfur isotopes in crystalline and colloform ZnS. *Chem Geol* 286:118-134.
- Ribbert KH (2012) *Geologie im Rheinischen Schiefergebirge. Bergisches Land.* Geologischer Dienst NRW, Krefeld.
- Richter D (1997) *Ruhrgebiet und Bergisches Land – Zwischen Ruhr und Wupper.* Bornträger, Stuttgart.
- Sahlström F, Arribas A, Dirks P et al (2017) Mineralogical Distribution of Germanium, Gallium and Indium at the Mt Carlton High-Sulfidation Epithermal Deposit, NE Australia, and Comparison with Similar Deposits Worldwide. *Minerals*, 7, 213.
- Seifert T, Sandmann D (2006) Mineralogy and geochemistry of indium-bearing polymetallic vein-type deposits. Implications for host minerals from the Freiberg district, Eastern Erzgebirge, Germany. *Ore Geol Rev* 28:1–31.
- Topp J (1988) *Mikrothermometrische Untersuchungen an Flüssigkeitseinschlüssen der Blei-Zink Lagerstätte Auguste Victoria (Ruhrkarbon) sowie Lüderich und Nikolaus-Phönix (Bergisches Land).* Diploma thesis. University of Göttingen.

Distribution of indium in the Ánimas – Chocaya – Siete Suyos District

Malena Cazorla Martínez, Marta Tarrés, Laura Gemmrich, Belén Torres, David Artiaga, Álvaro Martínez, Diva Mollinedo, Joan Carles Melgarejo
University of Barcelona, Spain

Lisard Torró
Pontifical Catholic University of Peru

Osvado Arce
Colegio de Geólogos de Bolivia

Pura Alfonso
Universitat Politècnica de Catalunya

Abstract. The Ánimas – Chocaya – Siete Suyos district in SW Bolivia hosts a Bolivian-type polymetallic vein mineralization composed mostly of cassiterite, sphalerite, pyrite, galena, stannite, lead sulfosalts, tin sulfosalts and silver sulfosalts. In addition to base (Zn, Sn, Pb) and precious (Ag) metals, important concentrations of In have been described. Systematic EPMA analyses have revealed that the highest concentrations are found in an early generation of sphalerite (up to 9.66 wt% In) and in stannite (up to 4.11 wt% In). Although In-bearing sphalerites are relatively Fe-rich (mostly between 6.0 and 18.1 mol % FeS), the atomic concentrations of these two elements do not yield any correlation. In contrast, In is positively correlated with Cu mostly along a $\text{Cu/In} = 1$ proportion pointing to a $(\text{In}^{3+} + \text{Cu}^+) \leftrightarrow 2\text{Zn}^{2+}$ coupled substitution. A relatively high activity of Cu during the crystallization of In-rich sphalerite is also supported by exsolutions of chalcopyrite and stannite.

1 Introduction

Indium (In) is currently considered a critical raw material because of its high market demand coupled to a high supply risk (European Commission 2017; Schulz et al. 2017). It is an essential component in modern technologies such as flat touch panels (as indium-tin oxide – ITO) and in the so-called green technologies such as photovoltaic cells. There are not mines that host indium as a primary commodity. This technological element, and others such as Ge, are mostly recovered as by-products from the production of other metals, chiefly zinc in sulfide minerals (i.e., sphalerite) even if important resources are described in tin ore as well (Schwarz-Schampera and Herzig 2002).

Important concentrations of In are described in the metalliferous belts in the Central Andean region (Fig. 1), particularly in the Andean tin belt (Schwarz-Schampera and Herzig 2002; Ishihara et al. 2011; Murakami and Ishihara 2013).

Mines in the Ánimas - Chocaya- Siete Suyos district are currently operated by several mining cooperatives. Ishihara et al. (2011) studied the concentration of trace

metals in 5 composite ore samples from Siete Suyos and Ánimas mines and reported whole rock In concentrations as high as 2510 ppm. Nevertheless, ore mineral chemistry has not been reported previously for this district and the mineralogical expression of In is hence unknown.

Here we present new data on the mineralogy and ore mineral geochemistry, with a particular focus on the critical metal In, to better understand its distribution at the district scale and along the paragenetic sequence.

2 Materials and methods

A total of 50 samples were examined for mineralogical and geochemical determinations. The distribution of the samples embraces the three deposits and for each, several veins and mining galleries at different depths in order to ensure a complete 3D representability at the district scale.

Forty polished thin and thick sections have been studied by optical and scanning electron microscopy (SEM) using an environmental Quanta 200 FEI, XTE 325/D8395 equipment with an INCA Energy 250 EDS microanalysis system at Centres Científics i Tecnològics of the University of Barcelona (CCiT-UB).

Mineral chemistry analyses of sulfide minerals and cassiterite were performed using a five-channel JEOL JXA-8230 electron microprobe (EPMA) at the CCiT-UB, operated at 20 kV acceleration voltage, 20 nA beam current, with a beam diameter of 5 μm .

3 Geological setting

The Ánimas – Chocaya – Siete Suyos district is located in the Potosí Department, 150 km south of the city of Potosí and near the town of Atocha. Physiographically, it sits in the western flank of the Eastern Cordillera, close to the Altiplano. The Eastern Cordillera is composed mostly of thrust, folded and variably metamorphosed Paleozoic marine sedimentary rocks, overlain by marine and non-marine Cretaceous sedimentary rocks (Suarez-Soruco 2000).

The district is included in the Quechisla mining group and belongs to the Andean (or Bolivian) tin belt, one of the metalliferous belts distinguished in the Central Andes

(Fig. 1; cf. Mlynarczyk and William-Jones 2005; Fontboté 2018). The Andean tin belt is confined to the Eastern Cordillera and extends along more than 1000 km from southern Peru to northern Argentina through Bolivia. In this belt, mineralization is triggered by reduced, peraluminous magmatism. In its southern portion, where the Ánimas – Chocaya – Siete Suyos district is located (Fig. 1), Sn, Sn-W and Sn-polymetallic mineralization is of late Oligocene and Miocene age (Arce-Burgoa 2009) and related to porphyritic intrusions and dome complexes including hydrothermal breccia pipes and collapse calderas (Heuschmidt et al. 2002; Arce-Burgoa 2009).

Mineralization in the Ánimas – Chocaya – Siete Suyos district is genetically associated to the Chocaya volcanic caldera complex of Miocene age (ca. 14–12 Ma; Heuschmidt et al. 2002). A lava and pyroclastic pile of dacitic composition is protruded by a central dome of the same composition. The volcanic complex is hosted by Ordovician sandstones and slates.

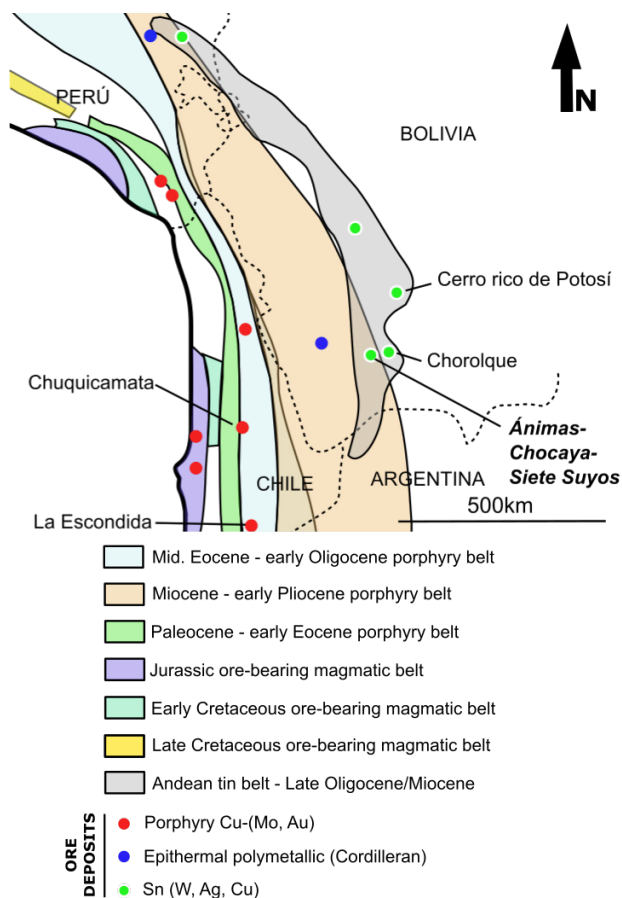


Figure 1. Schematic map of the Central Andes with the main mineralized belts and representative ore deposits. Modified from Fontboté (2018).

Volcanic and basement metamorphosed sedimentary rocks are crosscut by a NE-SW oriented network of veins that extends for more than 5 Km from the Siete Suyos mine (to the NE) to the Chocaya mine (to the SW); some veins have been exploited to depths of ~900 m (e.g., Burto and Colorada veins).

4 Mineralogy

The district has a zoned distribution of the ores, with a complex ore association in the central parts of the district, particularly at depth (Figs. 2–5), and chalcedony-barite veins, with lesser amounts of galena and sphalerite, in the marginal parts of the district.

The main ores in the central part of the district are sphalerite, pyrite and galena, accompanied by a gangue largely composed of quartz and siderite, with minor proportions of apatite, zircon and Al-rich phosphates. Other important phases usually found in the central and deep part of the mineralization include cassiterite, pyrrhotite, arsenopyrite, stannite, chalcocopyrite and tetrahedrite.

Minor phases scattered in the central part of the deposit, which may account for most of the silver content, include native silver, acanthite and silver-rich sulfosalts such as miargyrite, oscarkempffite, owyheeite, andorite, diaphorite, pyrargyrite, terrywallaceite, franckeite, staročeskéite and zoubekite; in addition, minor amounts of jamesonite, boulangerite, heteromorphite, semseyite, stibnite, wolframite, scheelite, and wurtzite also occurs.

Supergene products include minerals of the jarosite group, goethite, anglesite and smithsonite.

Hydrothermal alteration of the host rocks consists largely of silicification accompanied with argillitic and sericitic alterations in the central part of the district, and a propylitic halo with abundant chlorite at the margins.

5 Textures and paragenetic sequence

Vein infilling shows drusy or cockade growths of quartz and ore, often displaying banding or colloform arrangements, suggesting open space crystallization. In addition, late minerals may also occur as veinlets that crosscut earlier phases. Different generations of a same mineral species are revealed by changes in the textural patterns. Some minerals, in particular pyrite, arsenopyrite and sphalerite, show oscillatory zoning.

Early phases in the studied veins include quartz, cassiterite, arsenopyrite, a first generation of sphalerite, stannite and pyrite (Fig. 2). Cassiterite crystallized synchronously with quartz, even if the later formed during most of the mineralization lifespan in variable amounts. Arsenopyrite is largely replaced by pyrite suggesting a general earlier precipitation (Fig. 3). Sphalerite, the chief ore mineral in the district, probably crystallized during a protracted period. Early sphalerite is observed to form colloform bands overgrowing quartz and arsenopyrite, and by hosting myriads of chalcocopyrite and stannite exsolutions. The abundance of these exsolutions decreases toward inner, younger sphalerite bands giving way to interspersed bands with stannite (Fig. 2). Later generations of sphalerite are largely free of both chalcocopyrite and stannite exsolutions and intergrowths with stannite (Fig. 4). Galena is observed mostly as anhedral grains often replaced by late sphalerite (Fig. 5). Chalcocopyrite is rather scarce in the studied ore and, in addition to forming exsolutions in sphalerite, is observed veining this mineral (Fig. 4), suggesting later

crystallization.

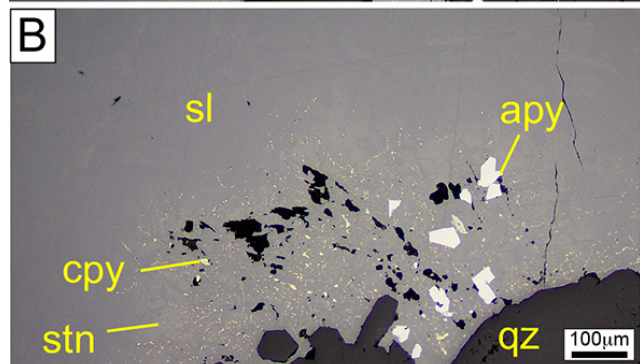
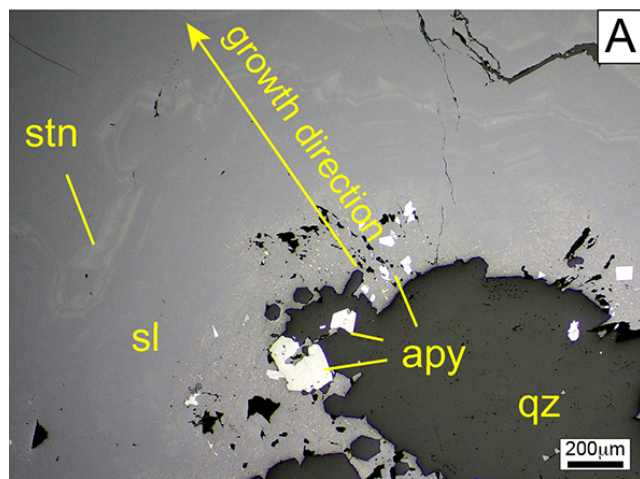


Figure 2. Microphotographs of ore mineralization from the Siete Suyos mine using reflected, plane polarized light. A) Colloform growths of sphalerite (sl) bands interspersed with stannite (stn) bands overgrew quartz (qz) and arsenopyrite (apy). B) The density of exsolutions of stannite and chalcopyrite (cpy) in sphalerite decreases toward younger growth bands.

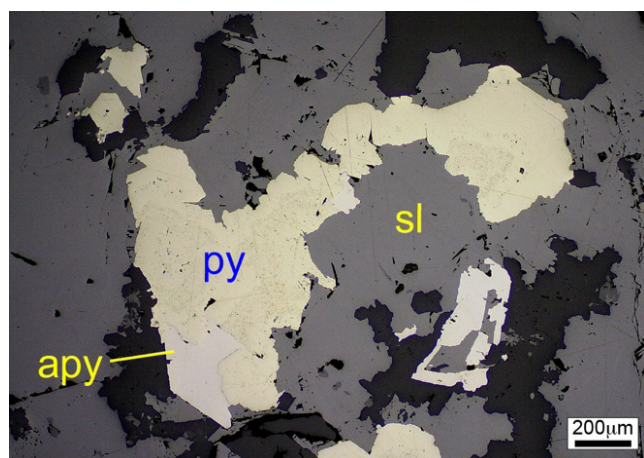


Figure 3. Arsenopyrite (apy) crystals were extensively replaced by pyrite (py), and both were replaced by a late generation of exsolution-free sphalerite (sl) in ore from the Siete Suyos mine (reflected, plane polarized light).

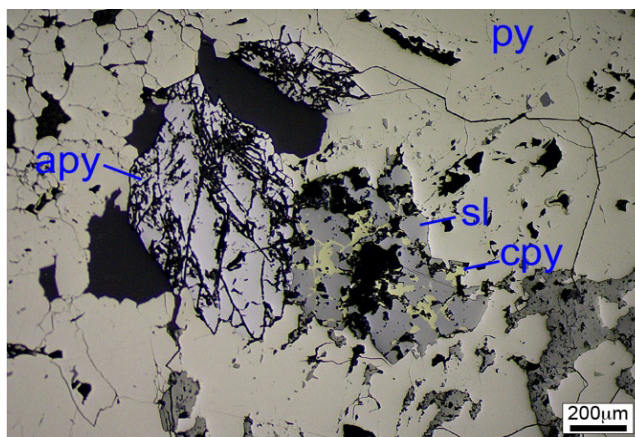


Figure 4. Arsenopyrite (apy) crystal replaced by pyrite (py), the second replaced in turn by sphalerite (sl). Chalcopyrite (cpy) veins sphalerite (sample from the Animas mine; reflected, plane polarized light image).

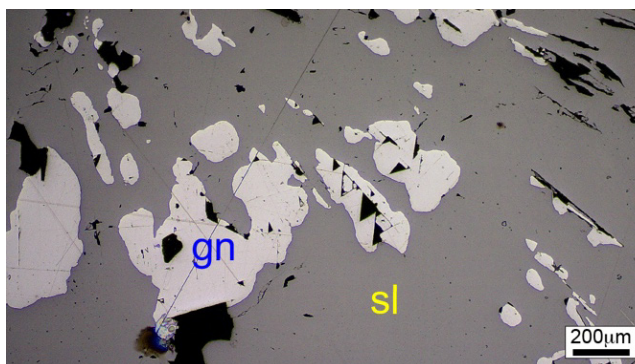


Figure 5. Galena (gn) grains are conspicuously replaced by a later generation of exsolution-free sphalerite (sl) in ore from the Animas mine (reflected, plane polarized light image).

Later phases include sulfosalts, mostly tetrahedrite (locally found in equilibrium with a second generation of stannite) and Pb sulfosalts that are almost synchronic with the crystallization of Ag sulfosalts. These phases crystallized in equilibrium with late sphalerite and a second generation of galena and Fe-carbonates (Fig. 6) In a few samples, late wurtzite has been identified.

Mineral	Early	→	Late
Quartz	—————		—————
Casiterite	—————		
Arsenopyrite	—————		
Pyrite		—————	
Sphalerite		—————	—————
Stannite		—————	—————
Galena		—————	—————
Chalcopyrite		—————	—————
Tetrahedrite			—————
Pb/Ag sulfosalts			—————
Fe-carbonate			—————

Figure 6. General, simplified paragenetic sequence of hypogene mineralization in the Animas and Siete Suyos mines.

6 Geochemistry of In-bearing ore minerals

Remarkable concentrations of In have been detected only in sphalerite and stannite. Contrasting compositions for sphalerite have been observed depending on the generation or in the vein system in which they crystallized. First-generation sphalerite is characterized by the highest In concentrations (up to 9.66 wt% in a sample from the Siete Suyos mine, up to 2.94 wt% in a sample from the Ánimas mine and up to 1.82 wt% in a sample from the Chocaya mine). In Siete Suyos and Ánimas ore, In-bearing sphalerite crystals are characterized by high Fe contents so that for sphalerite grains with In > 1.5 wt%, FeS is between 6 and 18 mol % in the Siete Suyos mine, and between 8 and 16 mol % in the Ánimas mine. In contrast, for sphalerite grains from the Chocaya mine with In > 1 wt%, the concentration of Fe is low, between 0.1 and 0.3 mol % FeS. A correlation between atomic proportions of In and Fe is not observed. In contrast, the atomic proportions of In yield a strong positive correlation with those of Cu, mostly at Cu/In=1. Some of the studied sphalerite grains yield a limited solid solution with stannite (up to 4 mol % Cu₂FeSnS₄).

Studied stannite yields a maximum content of In of 4.11 wt% in a sample from the Ánimas mine, whereas maximum concentration in stannite grains from the Siete Suyos mine is of 1.73 wt%. The concentration of In in stannite does not show clear correlation with other analyzed elements.

Analyzed cassiterite crystals yield only minor concentrations of In, up to 0.65 wt%.

7 Discussion

The strong correlation found between Cu and In in sphalerite grains from the Ánimas – Chocaya – Siete Suyos district at Cu/In=1 points to incorporation of In via a (Cu⁺ + In³⁺) ↔ 2Zn²⁺ coupled substitution, which has been amply identified in other districts worldwide for In-bearing sphalerite (Cook et al. 2011, and references therein). On the other hand, the occurrence of In in studied stannite favors a contextualization of the In mineralization in the (Zn,Fe)S – Cu₂FeSnS₄ – CuInS₂ pseudoternary system described by Oen et al. (1980), with a limited solid solution between the three endmembers (i.e., sphalerite, stannite and roquesite). The fact that In strongly correlates with Cu in the structure of sphalerite and is systematically found in first-generation sphalerite texturally characterized by hosting abundant chalcopyrite and stannite exsolutions suggests that Cu played a major role in the concentration of In. In contrast, the concentration of Fe in sphalerite is apparently disconnected of the initial concentration of In in this mineral. Nevertheless, high concentrations of FeS in sphalerite are described to favor diffusion of elements such as In in the structure of this sulfide and hence might have promoted local diffusion fronts enriched in roquesite solid solution (Schwarz-Schampera and Herzig 2002).

Acknowledgements

This study benefitted from the Peruvian CONCYTEC-FONDECYT-World Bank project 107-2018-BM, the budget granted by the Generalitat de Catalunya (Autonomous Government of Catalonia) to the Consolidated Research Group SGR 444 and the AECID project A3/042750/11. The help and hospitality extended by the miners from the Ánimas cooperative during sampling are gratefully acknowledged.

References

- Arce-Burgoa O (2009) *Metalliferous ore deposits of Bolivia*, 2 ed. SPC Impresores, La Paz
- Cook NJ, Sundblad K, Valkama M, Nygard R, Ciobanu CL, Danyushevsky L (2011) Indium mineralization in A-type granites in southeastern Finland: Insights into mineralogy and partitioning between coexisting minerals. *Chem Geol* 284:62–73
- European Commission (2017) Critical raw materials factsheets. https://ec.europa.eu/growth/sectors/raw-materials/specific-interest/critical_en. Accessed 05 March 2019
- Fontboté L (2018) Ore deposits in central Andes. *Elements* 14:257–261
- Heuschmidt B, Bellot de la Torre J, Miranda Angles V, Claire Zapata M (2002) Las Areas Prospectivas de Bolivia para yacimientos metalíferos. *Boletín del Servicio Nacional de Geología y Minería* 30, La Paz
- Ishihara S, Murakami H, Marquez-Xavalia MF (2011) Inferred indium resources of the Bolivian tin-polymetallic deposits. *Resour Geol* 2:174-191
- Jiménez N, López-Velásquez S (2008) Magmatism in the Huarina belt, Bolivia, and its geotectonic implications. *Tectonophysics* 459:85–106
- Lehmann B (1990) *Metallogeny of Tin*. Springer-Verlag Berlin, Heidelberg
- Mlynarczyk MSJ, William-Jones A (2005) The role of collisional tectonics in the metallogeny of the Central Andean tin belt. *Earth Planet Sc Lett* 240:656-667
- Murakami H, Ishihara S (2013) Trace elements of Indium-bearing sphalerite from tin-polymetallic deposits in Bolivia, China and Japan: A femto-second LA-ICPMS study. *Ore Geol Rev* 53:223-243
- Oen IS, Kager P, Kieft C (1980) Oscillatory zoning of a discontinuous solid-solution series: sphalerite-stannite. *Am Mineral* 65:1220-1232
- Schulz KJ, DeYoung JH, Seal RR, Bradley DC (2017) Critical mineral resources of the United States - Economic and environmental geology and prospects for future supply. U.S. Geological Survey Professional Paper. https://pubs.usgs.gov/pp/1802/pp1802_entirebook.pdf. Accessed on 03 December 2018
- Schwarz-Schampera U, Herzig PM (2002) *Indium: Geology, Mineralogy and Economics*. Springer-Verlag, Heidelberg
- Sinclair WD, Kooiman GJA, Martin DA, Kjarsgaard IM (2006) Geology, geochemistry and mineralogy of indium resources at Mount Pleasant, New Brunswick, Canada. *Ore Geol Rev* 28:123–145
- Suarez-Soruco R (2000) *Compendio de Geología de Bolivia*. Servicio Nacional de Geología y Minería, Yacimientos Petrolíferos Fiscales Bolivianos, Cochabamba

Ore mineralogy of the In-bearing Ayawilca Zn-Ag-Sn-Cu project, Pasco, Peru

Diego Benites, Lisard Torró, Jean Vallance, Patrick Quispe, Jorge Sáez, Silvia Rosas
Pontifical Catholic University of Peru

Álvaro Fernández-Baca, Jorge Gamarra
Tinka Resources Limited

Antoni Camprubí
Universidad Nacional Autónoma de México

Lluís Fontboté
University of Geneva

Abstract. The Ayawilca Zn-In-Ag-Sn-Cu project is located in the Central Andean polymetallic belt of Peru. It is a carbonate replacement deposit with strong similarities to porphyry-related epithermal polymetallic (“Cordilleran”) deposits in the Central Andes. Forty-two ore samples were studied for petrographic and ore mineral chemistry determinations. Within an early low sulfidation stage, the most important economically and volumetrically, three generations of Fe-rich sphalerite were identified, the second being characterized by fine disseminations of chalcopyrite and the highest indium contents (up to 1.58 wt% In). Although In-bearing sphalerite is characterized by high iron contents (between ~ 9 and 32 mol. % FeS), atomic concentrations of In and Fe do not show any visible correlation. In contrast, In and Cu correlate at $Cu/In = 1$ (at. proportions), which is compatible with a solid solution between sphalerite and roquesite.

1 Introduction

Indium (In) is a highly malleable post-transition metal, with a relatively low melting point and good electrical conductivity. This metal is considered a high-tech metal critical for the global economy (European Commission 2017). Its most valuable application is in the manufacture of LCD screens in the form of indium-tin oxide – ITO (Shanks et al. 2017). However, its uses also extend to the production of electroluminous panels, transistors, nuclear medicine, and alkaline batteries, among others. Indium is a trace element in the continental crust (~56 ppb; Rudnick and Gao 2014) and virtually absent in its elemental form. Although it forms some discrete minerals (e.g., roquesite $[CuInS_2]$), it mostly occurs in the structure of sulfides (chiefly in sphalerite, but also in stannite and chalcopyrite) or in tin oxides like cassiterite (Schwarz-Schampera and Herzig 2002; Cook et al. 2009). This fact explains its strong dependence on zinc production (Nassar et al. 2015).

Peru is currently the 7th largest producer of indium (European Commission, 2017) whose extraction is obtained mostly from sphalerite recovery, present in

most of Central Andes “Cordilleran” polymetallic deposits (e.g., Cerro de Pasco, Uchucchacua, and Colquijirca; Fontboté 2018). In 2012, Tinka Resources Ltd. discovered the Ayawilca zinc deposit (Fig.1) with a current estimated indicated resource of 11.7 Mt with 6.9% Zn, 0.16% Pb, 15 g/t Ag and 84 g/t In containing 983 t In and an additional estimated inferred resource of 45.0 Mt with 5.6% Zn, 0.23% Pb, 17 g/t Ag and 67 g/t In containing 3,003 t In as of November 26th, 2018 (CIM definition standards).

The goals of this work are 1) to define the ore mineralogy and assemblages to draw comprehensive paragenetic sequences and 2) to determine the chemistry of ore minerals, with special attention to the distribution of In.

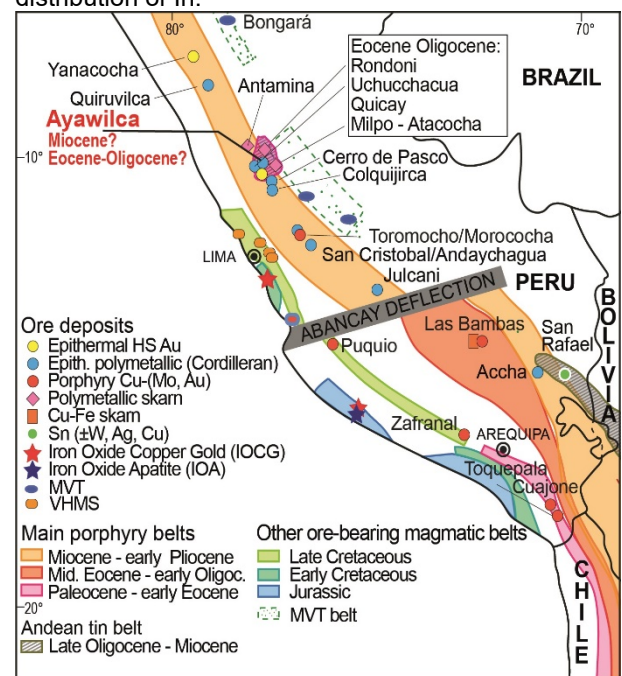


Figure 1. Map with the location of the Ayawilca project, the main Mesozoic and Cenozoic mineralized belts in the Central Andes and examples of representative ore deposits (modified from Fontboté 2018).

2 Geological setting

The Ayawilca deposit is located in the Department of Pasco, Peru, at 4,200 masl. It is interpreted to either belong to the Miocene polymetallic belt of Central Peru that includes the world-class porphyry-related deposits of Toromocho, Cerro de Pasco, Antamina and Yanacocha, or to the Eocene-Oligocene belt including Quicay, Atacocha, and Rondoní also related to calc-alkaline arc magmatism (Noble and Mckee 1999; Sillitoe 2004; Fontboté 2018). Main host rocks are Upper Paleozoic phyllites and Triassic to Cretaceous clastic, evaporitic and carbonate rocks that were deformed between the Upper Cretaceous and the Eocene, giving rise to the Marañón fold and thrust belt as the most important structural feature in the region (Cobbing and Sanchez 1996). Post deformation calc-alkaline arc-magmatism of Eocene-Oligocene and Miocene age occurs in the region although it has not been found in the Ayawilca project itself. The deposit consists of a blind zinc and tin mineralization mainly hosted by Upper Triassic to Lower Jurassic Pucará Group limestone. Mineralization occurs as 10 to 30-m-thick stacked lenses (“mantos”) associated with argillic alteration within the carbonate rocks (El-Rassi and Ross 2019). In addition, Zn-rich steep-dipping veins and minor high-grade mantos are found in the overlying Goyllarisquizga Group sandstones-siltstones of Cretaceous age.

3 Methodology

Forty-two polished sections were examined using an OLYMPUS BX51 optical microscope. A selection of these samples was examined on an environmental scanning electron microscope (SEM) Quanta 650 FEI, equipped with an EDAX-Octane Pro EDS microanalysis system at Centro de Caracterización de Materiales of the Pontifical Catholic University of Peru (CAM-PUCP). Operating conditions were 20 kV accelerating voltage and 5 nA in backscattered electron mode (BSE). Mineral chemistry analyses of sulfide minerals were performed using a five-channel JEOL JXA-8230 electron microprobe (EPMA) at the Centres Científics i Tecnològics of the University of Barcelona, operated at 20 kV acceleration voltage, 20 nA beam current, with a beam diameter of 5 µm.

4 Results

4.1 Ore mineralogy and textures

The main hypogene ore minerals in the Ayawilca project include pyrrhotite, sphalerite, chalcocopyrite, pyrite, magnetite, cassiterite and arsenopyrite and lesser amounts of stannite, tetrahedrite, freibergite, bismuthinite, native bismuth, galena, marcasite, mackinawite, herzenbergite [SnS], Pb/Ag sulfosalts (mainly stephanite and pyrargyrite) and intermediate product (a transition of pyrrhotite to mainly marcasite; Ramdohr 1969; Figs. 2 and 3 herein). At the deposit

scale, mineral assemblages define three stages of evolution similar to those recognized at the Cerro de Pasco Cordilleran deposit by Rottier et al. (2016, 2018) and other Cordilleran polymetallic deposits (Fontboté 2019). Stage A is the economically and volumetrically most important and consists of a low sulfidation assemblage of pyrrhotite, magnetite, Fe-rich sphalerite, chalcocopyrite, arsenopyrite and, occasionally, cassiterite and stannite. It is frequently overprinted by coarse euhedral/subhedral pyrite that forms the main part of Stage B. An intermediate sulfidation assemblage including siderite, galena, a Fe-poor sphalerite, Pb-Ag sulfosalts, kaolinite and dickite forms Stage C.

Figure 2 shows a paragenetic sequence for the ore mineralization in “mantos”, which are essentially composed of an early Fe-As sub-stage, with magnetite, pyrrhotite and arsenopyrite, a subsequent sub-stage of Sn-Cu-Zn sulfides, followed by Stage B with pyrite and a later mineral assemblage of Ag-Pb sulfosalts. Three generations of sphalerite, all rich in Fe, have been observed in the Stage A: 1) star-shaped inclusions in massive chalcocopyrite (high temperature; Fig 3a), 2) aggregates of anhedral to subhedral crystals, with fine-grained chalcocopyrite, mackinawite and pyrrhotite disseminations and 3) grains with only local Cu-Fe sulfide disseminations. Both the second and the third generations of sphalerite were replaced by stannite (Stage A) and, in places, by chalcocopyrite.

Samples from veins located in the northeastern area have a mineralogy that is largely equivalent to that described for “mantos” ore. In veins from the northwestern part of the deposit, Ag and Cu sulfosalts are conspicuous and associated with abundant galena and sphalerite. Iron-poor sphalerite postdating Fe-rich sphalerite occurs in phyllite-hosted veins, suggesting reopening of the fluid pathways.

MINERALOGY	STAGE A (LS)	STAGE B	STAGE C (IS)
Magnetite	---		
Pyrrhotite	---	--	
Quartz	-----		
Arsenopyrite	---		
Chalcocopyrite	---	--	
Fe-rich sphalerite	--	---	
Mackinawite		---	
Cassiterite		--	
Stannite		---	
Herzenbergite			
Cu sulfosalts			--
Fe-poor sphalerite			---
Bismuthinite			--
Native Bismuth			--
Galena			---
Pb/Ag sulfosalts			-----
Pyrite		---	
I.Product/Marcasite		---	---
Siderite			---

Figure 2. Paragenetic sequence for “mantos” hypogene ore mineralization. Intermediate P = intermediate product (see main text); LS = low sulfidation; IS = intermediate sulfidation.

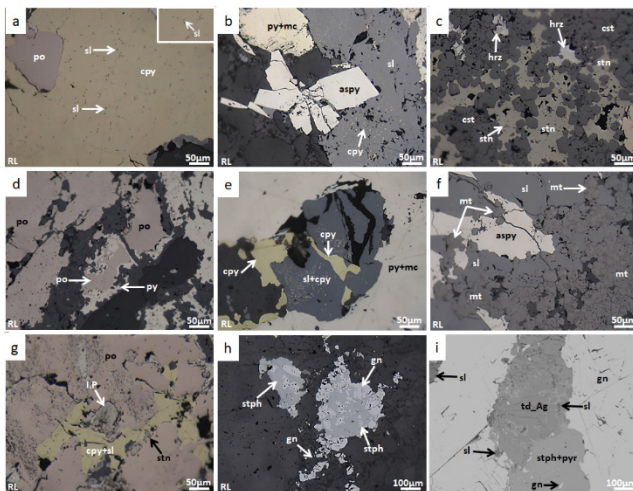


Figure 3. Photomicrographs of ore mineralogy in “mantos”: a) Pyrrhotite occluded in chalcopyrite; the latter with fine inclusions of sphalerite “stars” (1st generation). b) Arsenopyrite crystals with microfractures filled by a 2nd generation of sphalerite (with fine disseminations of chalcopyrite). Pyrite + marcasite (intermediate product) c) Cassiterite with interstices filled by stannite and herzenbergite. d) Pyrrhotite replaced by pyrite from their edges. e) Sphalerite included in pyrite and replaced by a third generation of chalcopyrite. f) Magnetite grains (slightly brownish gray) disseminated in arsenopyrite and clean sphalerite. Photomicrographs of distal veins: g) Chalcopyrite with inclusions of sphalerite “stars” and stannite in pyrrhotite which has been partially altered to intermediate product. h) Galena replaced by stephanite. i) Galena (gn) with remains of sphalerite and replaced by argentian tetrahedrite, stephanite and pyrrargyrite, taken with SEM, BSE mode. Abbreviations: aspy: arsenopyrite; cpy: chalcopyrite; cst: cassiterite; gn: galena; hrz: herzenbergite; I.P: intermediate product; mc: marcasite; mt: magnetite; po: pyrrhotite; py: pyrite; pyr: pyrrargyrite; sl: sphalerite; stn: stannite; stph: stephanite; td_Ag: argentian tetrahedrite; RL: reflected light.

4.2 Ore mineral geochemistry

Relatively high In concentrations have been obtained in Stage A sphalerite and stannite. The highest In concentrations are recorded in sphalerite grains of the second generation in “mantos” (up to 1.58 wt% In) with relatively high Fe (9 to 32 mol. % FeS at In > 0.20 wt%). In Stage C sphalerite in “mantos”, with FeS as low as 3 mol. %, In is below its detection limit. Analyzed Stage A sphalerite grains from NE veins have concentrations of In between 0.20 and 0.50 wt% and FeS between 17 and 18 mol. %. Sphalerite grains from NW veins are In-free at any FeS (between 1 and 33 mol. % FeS). Therefore, In-bearing sphalerite is systematically rich in Fe, but Fe-rich sphalerite is not always enriched in In. On the other hand, the atomic proportions of In and Fe do not show any visible correlation. In contrast, in the binary diagram in Fig. 4b, most sphalerite grains with In values above the detection limit fall along the Cu/In=1 line. In the ternary diagram in Fig. 4a, analyzed sphalerite shows a relatively low dispersion along the sphalerite-chalcopyrite, sphalerite-stannite and sphalerite-roquesite tie-lines. Stannite yields up to 0.49 wt% In in “mantos” and up to 0.32 wt% In in NE veins.

Tetrahedrite group minerals (Stage C) from Aywilca yield relatively high silver contents, between 11.38 and 20.04 wt% Ag, and Ag/(Ag+Cu) ratios in the range

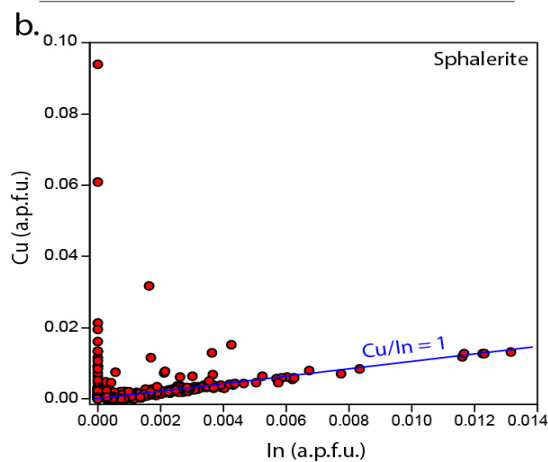
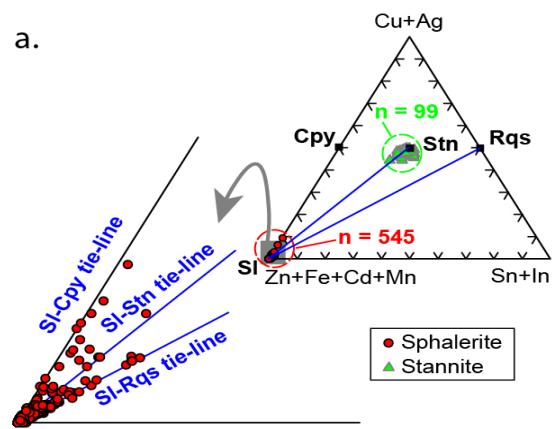


Figure 4. a) Cu+Ag - Zn+Fe+(Cd+Mn) - In+Sn ternary plot of sphalerite and stannite minerals from the Aywilca project. b) Cu - In binary plot of sphalerite from the Aywilca project. Abbreviations: cpy: chalcopyrite; rqs: roquesite; sl: sphalerite; stn: stannite.

between 0.33 and 0.56. The As/(As+Sb) ratios are between 0.004 and 0.030. Accordingly, tetrahedrite group minerals correspond to argentian tetrahedrite, with structural formula $(Cu_{5.96}Ag_{3.77})(Zn_{0.62}Fe_{1.48})(Sb_{4.00}As_{0.01})S_{12.78}$ and freibergite, with structural formula $(Cu_{4.57}Ag_{5.45})(Zn_{0.43}Fe_{1.60})(Sb_{4.00}As_{0.05})S_{12.2}$.

5 Conclusions and final remarks

Aywilca Zn-In-Ag-Sn-Cu Stage A low sulfidation mineralization is mostly composed of pyrrhotite, Fe-rich sphalerite, chalcopyrite, pyrite, magnetite, cassiterite and arsenopyrite and lesser amounts of stannite and herzenbergite. Idiomorphic coarse-grained pyrite and marcasite replacing pyrrhotite (Stage B) are postdated by siderite, Fe-poor sphalerite, tetrahedrite, freibergite, bismuthinite, native bismuth, galena, stephanite and pyrrargyrite.

The highest values of In are found in a second generation of Fe-rich sphalerite within Stage A, characterized by fine disseminations of chalcopyrite. In-rich sphalerite grains are systematically rich in Fe, but the reverse is not true; the atomic proportions of these two elements do not correlate. Indium is positively correlated

with Cu mostly at Cu/In=1 suggesting a $(\text{Cu}^+\text{In}^{3+}) \leftrightarrow 2\text{Zn}^{2+}$ coupled substitution, and an incorporation of In as a solid solution with roquesite (Schwarz-Schampera and Herzig 2002).

Sillitoe RH (2004) Musings on future exploration targets and strategies in the Andes. In: Sillitoe RH, Perelló J, Vidal CE Andean metallogeny: Mineralization styles, new discoveries, and deposit updates: Society of Economic Geologists Special Publication 11:1–14.

Acknowledgements

This study benefitted from the Peruvian CONCYTEC-FONDECYT-World Bank project 107-2018-BM. We would like to thank the staff of Tinka Resources Ltd. for the help and hospitality during sampling tasks.

References

- Cobbing J, Sánchez AW (1996) Mapa Geológico del Cuadrángulo de Yanahuanca, Departamento de Pasco (Hoja 21-j): Instituto Geológico, Minero y Metalúrgico CD
- Cook NJ, Ciobanu CL, Pring A, Skinner W, Danyushevsky L, Shimizu M, Saini-Eidukat B, Melcher F (2009) Trace and minor elements in sphalerite: a LA-ICPMS study. *Geochim Cosmochim Acta* 73:4761-4791
- EI-Rassi D, Ross D (2019) Technical report on the mineral resource estimate for the Ayawilca property, Department of Pasco, Peru, NI 43-101 Report. Available online <https://www.tinkaresources.com/assets/docs/reports/2019-01-09-43-101.pdf>. Accessed 6 March 2019
- European Commission (2017) Critical Raw Materials. Available online: <https://publications.europa.eu/en/publication-detail/-/publication/7345e3e8-98fc-11e7-b92d-01aa75ed71a1/language-en>. Accessed 28 February 2019
- Fontboté L (2019) Systematic trends in the evolution of porphyry-related epithermal polymetallic ("Cordilleran") deposits"- Biennial SGA Meeting, Glasgow (this volume)
- Fontboté L (2018) Ore deposits of the Central Andes. *Elements* 14:257-261
- Nassar NT, Graedel TE, Harper EM (2015) By-product metals are technologically essential but have problematic supply. *Sci. Adv.* 1-10
- Noble DC, McKee E (1999) The Miocene metallogenic belt of central and northern Peru. In: Skinner BJ (ed) *Geology and Mineral Deposits of the Central Andes*. Society of Economic Geologists, especial publication 7, pp 155-193
- Pfiffner OA, Gonzalez L (2013) Mesozoic–Cenozoic Evolution of the Western Margin of South America: Case Study of the Peruvian Andes. *Geosciences*, 3:262-310
- Ramdohr, P (1969) *The ore minerals and their intergrowths*. El Sevier, Amsterdam, 1192 pp
- Rottier B, Kouzmanov K, Casanova V, Wälle M, Fontboté L (2018) Cyclic dilution of magmatic metal-rich hypersaline fluids by magmatic low-salinity fluid: A major process generating the giant epithermal polymetallic deposit of Cerro de Pasco, Peru: *Economic Geology*: 113, 825-856
- Rottier B, Kouzmanov K, Wälle M, Bendejú R, and Fontboté L (2016) Sulfide replacement processes revealed by textural and LA-ICP-MS trace element analyses: Example from the early mineralization stages at Cerro de Pasco, Peru: *Economic Geology*: 111:1347-1367
- Rudnick RL, Gao S (2014) Composition of the continental crust. In: Turekian HD, Holland KK (eds) *Treatise on Geochemistry*, 2nd edn. Elsevier, Oxford, pp 1-51
- Schwarz-Schampera U, Herzig PM (2002) *Indium: Geology, Mineralogy and Economics*. Springer-Verlag, Heidelberg, 257 pp
- Shanks WCP, III Kimball BE, Tolcin AC, Guberman DE (2017) Germanium and indium, chap I. In: Schulz KJ, DeYoung JH, Jr Seal, RR II Bradley DC (eds) *Critical mineral resources of the United States Economic and environmental geology and prospects for future supply*: U.S. Geological Survey, Professional Paper 1802, pp I1–I26.

Global cobalt resources, production and future sources of supply

Carolyn Kresse, Gus Gunn, Eva Petavratzi
British Geological Survey, UK

Abstract. Cobalt is a critical metal with numerous applications in new and green technologies. Global demand, particularly for use in lithium-ion batteries, is forecast to increase rapidly. Consequently, to ensure security of cobalt supply, it is important to diversify the cobalt supply base, to expand our knowledge of its occurrence in known mineral deposits and to identify new resources. Cobalt may be enriched in a variety of geological settings. The most important deposit types with cobalt resource potential are sediment-hosted stratabound copper deposits, nickel-cobalt laterite deposits and magmatic nickel-copper deposits. About 60 per cent of mined cobalt is a by-product of copper mining, mainly in the Central African Copperbelt. The remainder is derived from several other deposit types, although less than two per cent is from primary cobalt producers such as Bou Azzer in Morocco. Potential new onshore sources of cobalt are widespread in the United States, Canada, Australia, the DRC, Zambia and Madagascar, and offshore in deep-sea manganese nodules and cobalt-rich ferromanganese crusts.

1 Introduction

The European Union (EC 2017) classifies cobalt as a critical metal. More than half of global mine production of cobalt is from the DRC, a country noted for its political and economic instability and the association of mining with armed conflict and the use of child labour. Cobalt is widely used in a range of hi-tech applications, most notably in decarbonising the transport sector. Cobalt is an important constituent of the cathodes in most lithium-ion batteries used in electric vehicles (EV). The recent growth in the global EV market and its forecast continued expansion will inevitably lead to increased demand for raw materials such as cobalt (IEA 2018). Consequently, in order to ensure future security of supply, it is becoming increasingly important to diversify the global supply base for cobalt. Improving our deposit models for cobalt enrichment in the crust will facilitate the identification of new resources.

2 Deposit types

Cobalt is found in economic concentrations in three main deposit types: sediment-hosted stratabound copper deposits (SHSC); nickel-cobalt laterite deposits; and magmatic nickel-copper (-cobalt±PGE) sulfide deposits (Naldrett 2004; Mudd et al. 2013). The largest cobalt-producing region is the Central African Copperbelt (CACB) in the DRC and Zambia, with some large deposits also known in Australia, Russia, Cuba, New

Caledonia and Canada (Fig. 1).

SHSC deposits (Taylor et al. 2013) are not only the world's second largest source of copper, but are also the most important source of cobalt accounting for approximately 60 per cent of global cobalt mine production (Brown et al. 2019).

Nickel laterites associated with ultramafic rocks may also contain appreciable concentrations of cobalt between 0.025 and 0.18% (Berger et al. 2011; Slack et al. 2017). The Murrin Murrin deposit in Western Australia (Gaudin et al. 2005) and the Goro deposit in New Caledonia (Wells et al. 2009) are examples of some of the world's many large nickel-cobalt laterite deposits. The manganese-rich Nkamouna cobalt-nickel deposit in Cameroon is one of the few in which cobalt would be the principal economic metal to be mined (Lambiv Dzemua and Gleeson 2012). Ore reserves in this and the nearby Mada deposit were 68.1 million tonnes grading at least 0.26% Co (SRK 2011), representing possibly one of the largest undeveloped cobalt reserves in the world.

Magmatic nickel-copper (-cobalt±PGE) deposits comprise: (1) magmatic sulfide deposits; and (2) magmatic PGE deposits in layered intrusions. Magmatic sulfide deposits account for about 60 per cent of global nickel production (Naldrett 2004) with cobalt contents of the iron-nickel-copper sulfide ores in some deposits reaching 500–1000 ppm (Mudd et al. 2013). Globally, two prominent nickel-copper districts exist each containing more than 20 million tonnes of nickel metal: Sudbury, Ontario, Canada and Noril'sk-Talnakh, Russia (Schulz et al. 2014). Naldrett (2004) reported an average Co grade of 0.038% in the Sudbury ores. Ore reserves in the Noril'sk-Talnakh deposits amount to 215 million tonnes grading 0.016% Co (Noril'sk Nickel 2014).

The most important magmatic PGE deposits in layered intrusions are located in the Bushveld Complex in South Africa, the Great Dyke in Zimbabwe and in the Stillwater Complex in the United States. Hitzmann et al. (2017) reported Co grades of 0.03% in Bushveld ores, and appreciable amounts of cobalt (7–18 wt%) in manganese-cobalt-nickel-copper-oxides and hydroxides at the Great Dyke (Oberthür et al. 2013).

Cobalt may also be concentrated in a variety of other geological settings and deposit types including: cobalt-copper-gold deposits in metasedimentary rocks; cobalt-rich vein deposits; iron-oxide-copper-gold deposits (IOCG); volcanogenic massive sulfide deposits; black shale hosted nickel-copper-zinc-cobalt deposits etc.

Significant concentrations of cobalt occur in iron-manganese-rich nodules and cobalt-rich crusts, although to date no cobalt has been extracted from these. Iron-manganese-rich nodules, typically 1–5 cm in size, found

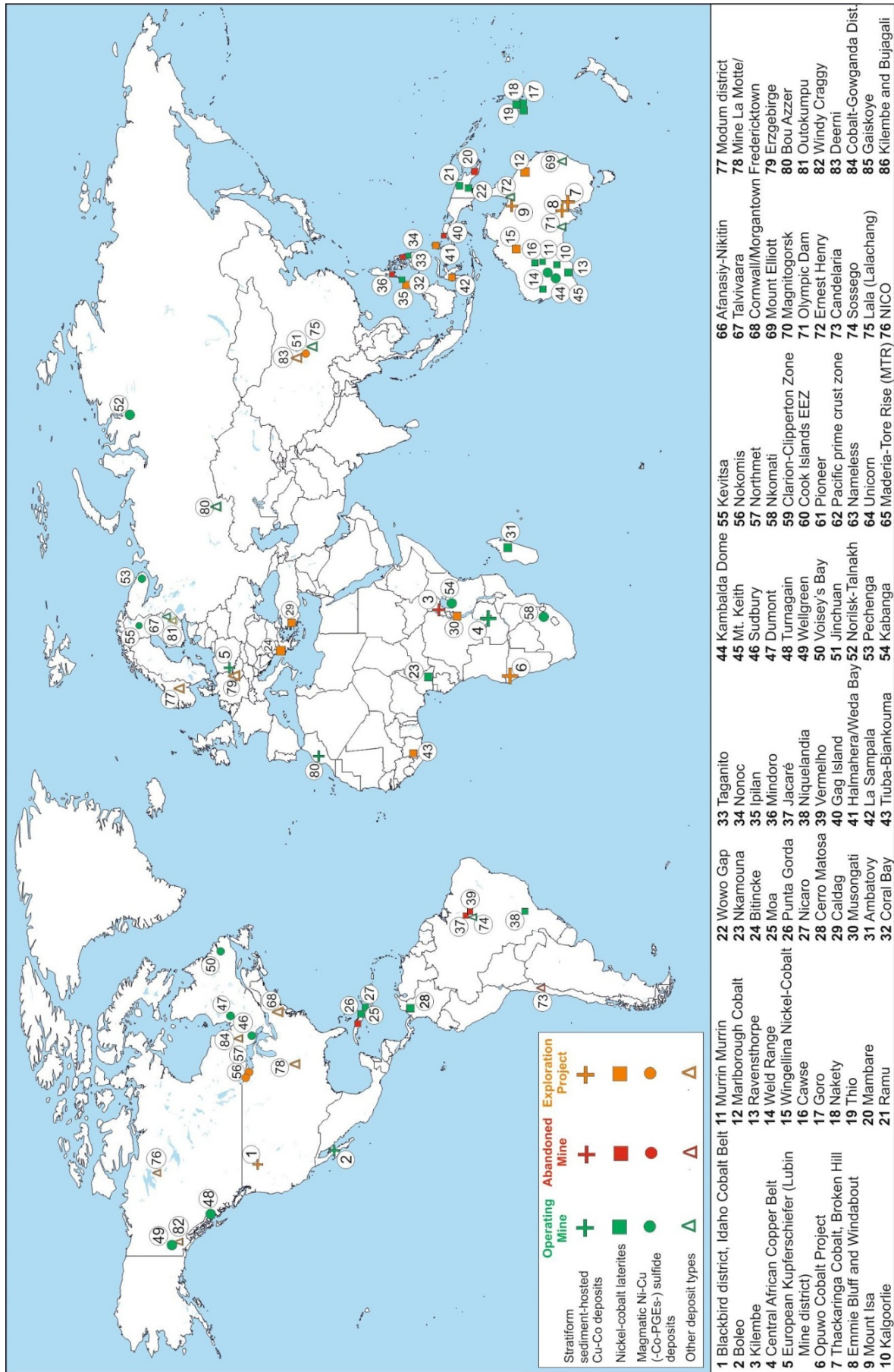


Figure 1: Selected cobalt deposits worldwide (Co content > 0.05 million tonnes*) (operating, abandoned, exploration project). *Estimated Co contents of exploration projects may be lower than 0.05 million tonnes. Other deposits include: Black shale-hosted Ni-Cu-Zn-Co, Fe-Cu-Co skarn and replacement deposits, Iron oxide Cu-Au (-Ag-U-REE-Co-Ni), Metasedimentary rock-hosted Co-Cu-Au, MVT sulfide deposits, Cobalt-rich vein deposits, VMS sulfide deposits, Cobalt-rich vein deposits, VMS sulfide deposits (Data from Mudd et al. 2013; Slack et al. 2017; company reports, websites and other publications)

at water depths of 4.5–6 km, may be strongly enriched relative to the Earth's crust in nickel, copper and cobalt (Hein et al. 2013).

The largest known occurrences are located in the eastern equatorial Pacific Ocean between the Clarion and Clipperton fracture zones (CCZ), in the Cook Islands Exclusive Economic Zone (EEZ), in the Penrhyn-Samoa Basin, in the Peru Basin, and in the Pioneer area of the central Indian Ocean (Hein et al. 2013). Cobalt grades in these nodules seldom exceed 2000 ppm, but, given the high nodule densities and the vast extent of these fields, the resource potential is very large.

Ferromanganese crusts are thickest and most metal-enriched on the flanks of seamounts at water depths of 800–2500 m. They are most abundant in the north-west Pacific Ocean. The Prime Crust Zone (PCZ) in the central and western equatorial Pacific is currently of greatest economic interest (Hein et al. 2013). The cobalt content of these crusts can be up to 2 wt%, but generally averages between 0.30 and 0.67 wt% (Hein et al. 2013).

3 World resources and reserves

The terrestrial cobalt resource is about 25 million tonnes (USGS 2019). The largest share of global resources, about 15 million tonnes, is located in the CACB in the DRC and Zambia (Hitzmann et al. 2017). In the CACB most economic cobalt resources occur in the Congo Copperbelt (CCB) and the Western portion of the Zambian Copperbelt (ZCB). The Tilwezembe structure (in the CCB) contains some of the most cobalt-rich deposits; several have grades sufficient for primary cobalt production, e.g. Kisanfu (1.1% Co) (Hitzmann et al. 2017).

Various estimates of cobalt resources in iron-manganese nodules and crusts on the seafloor should be considered as indicative geological endowments and are not mineral resources in the strict sense. USGS (2019) reports more than 120 million tonnes of cobalt resources in the Atlantic, Indian and Pacific oceans. Hein and Koschinsky (2014) reported that the CCZ alone contains 21 billion tonnes of nodules with a cobalt content of 40 million tonnes. Based on a mean cobalt content of 0.66%, the estimated total cobalt resource in the PCZ is about 50 million tonnes (Hein et al. 2013).

Global cobalt reserves amount to 6.9 million tonnes (USGS 2019). The DRC has the largest share of the reserves with about 49.5 per cent (3,400,000 tonnes), followed by Australia (17.5 per cent), Cuba (7.3 per cent) and the Philippines (4.1 per cent) (Fig.2).

4 World production

More than half of global mine production of cobalt comes from the DRC, which produces about 59 per cent of the total. Other significant producers include New Caledonia, China, Canada, Australia, Cuba, Zambia and Morocco (Brown et al. 2019). Almost all cobalt is produced as a by-product. In the DRC and Zambia, it is a by-product of the extraction of copper from SHSC deposits, while elsewhere most cobalt production is a by-product of nickel mining. For example, in Cuba, New Caledonia and

Madagascar the cobalt is derived from nickel-cobalt laterite deposits. Elsewhere, for example in Canada and Russia and China, most cobalt is extracted from magmatic nickel sulfide deposits. In Australia and Brazil, cobalt is derived as a by-product of mining both laterite and magmatic sulfide deposits. At only one operating mine, Bou Azzer in Morocco, is cobalt extracted as the main economic product (Bouabdellah et al, 2016). In contrast to mine production, refined cobalt production (both metal and chemicals) is dominated by China, which produces about 58 per cent of the world total, with other substantive cobalt refining capacity in Finland (10 per cent) and Zambia (2.1 per cent). China sources more than 90 per cent of its feed material for the production of refined cobalt from the DRC, with the DRC itself producing only 0.2 per cent of the world's refined cobalt (Brown et al. 2019).

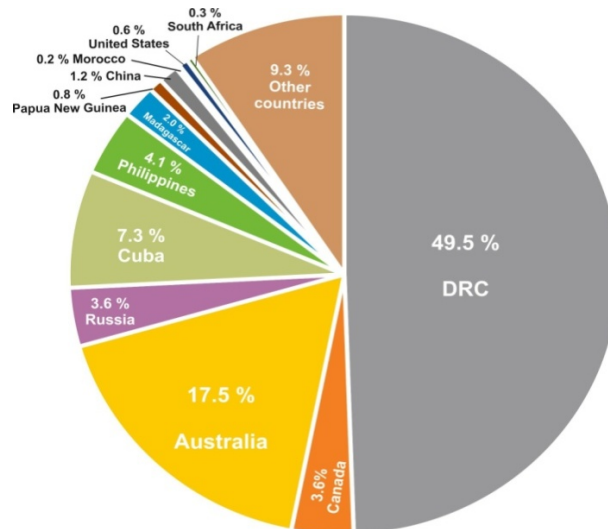


Figure 2. World cobalt reserves by country (USGS Mineral Commodity Summary 2019).

5 Expanding the resource base

Until recently, the small size of the global market for cobalt (about 100,000 tonnes contained metal per annum) and its price have meant that it has not been economic to mine cobalt alone. However, with rapidly growing demand and a concomitant rise in the price of cobalt, there has been significant growth in exploration for new cobalt resources. Numerous targets are being investigated worldwide. For example, Battery Mineral Resources is prospecting in the Ontario Cobalt Belt, where numerous projects demonstrate high-grade cobalt values ranging from 1.5% to 21%, and mineral resources of 72,000 tonnes grading 1.27% Co (Battery Mineral Resources 2018). Fortune Minerals Ltd plans to develop a mine at the NICO deposit in Canada, where mineral reserves total 33 million tonnes, containing c. 37200 tonnes of cobalt in open pit and 600 tonnes underground (Fortune Minerals Ltd 2014). The Thackaringa Cobalt Project in Australia has indicated resources of 72 million tonnes at 852 ppm Co for 61.5 kilo tonnes contained cobalt (Cobalt Blue Holdings 2018). At the Opuwo Cobalt Project in Namibia a mineral resource of 112.4 million

tonnes grading 0.11% Co has been identified (Celsius Resources Ltd 2018).

Increasing demand for cobalt is also driving exploration for new deposits in European countries, where only limited deposits are known. In 2017 the EU launched a European Battery Alliance aimed at creating a competitive EV manufacturing sector throughout Europe (<https://www.eba250.com/>). A key objective of the Alliance is to evaluate the potential for resources of battery raw materials in the EU. Ores in the Kupferschiefer deposits in Poland, mined by KGHM Polska Miedz S.A., have average contents of 50–80 ppm Co (Pazik et al. 2016). Boreal Metals Corp. owns several projects in Scandinavia, focusing on new targets in known mining districts, e.g. the Los Cobalt Mine, Sweden and the Modum project, Norway (Boreal Metals Corp. 2019). The Geological Survey of Finland has started a major programme to identify areas favourable for the occurrence of battery raw materials in Finland to ensure future supply in Europe (GTK 2018). Important Ni-Co laterites are found in the region stretching from Serbia through to Turkey, but many of them are still undeveloped. The current bulk Ni-Co production comes from Greece, accounting for about 1% of world production of Ni with other mines in Turkey, Albania, and Kosovo. The Mokra Gora deposit in Serbia is a potentially large but low-grade redeposited lateritic deposit, indicating a resource of more than 1 billion tonnes at 0.7% Ni and 0.05% Co. Newly advanced technologies regarding mineral processing could make the region more attractive for Ni and co-recovery of Co (Herrington et al., 2016).

Acknowledgements

The authors are grateful to BGS colleagues, Simon J. Kemp and Stefan Horn, for their reviews of this paper. The authors publish with the permission of the Executive Director, British Geological Survey (UKRI).

References

Battery Mineral Resources (2018) Investor Presentation, 20 pp https://www.batterymineralresources.com/site/assets/files/4814/investorpresentation_bmr_12_18.pdf.

Berger VI, et al. (2011) Ni-Co Laterite Deposits of the World—Database and Grade and Tonnage Models, USGS Open-File report, 26 pp.

Boreal Metals Corp. (2019) Corporate Presentation http://www.borealmetals.com/_resources/presentations/corporate-presentation.pdf.

Bouabdellah, M., Maacha, L., Levresse, G., Saddiqi, O., 2016, The BouAzzer Co–Ni–Fe–As (\pm Au \pm Ag) District of Central Anti-Atlas (Morocco): A Long-Lived Late Hercynian to Triassic Magmatic-Hydrothermal to Low-Sulphidation Epithermal System. In *Mineral Deposits of North Africa* (pp. 229–247). Springer, Cham.

Brown TJ, et al. (2019) World Mineral Production 2013–17. British Geological Survey, Keyworth, Nottingham.

Celsius Resources Ltd (2018) Building an Extensive Cobalt Resource in Namibia, Africa down under <http://clients3.weblink.com.au/pdf/CLA/02015894.pdf>.

Cobalt Blue Holdings (2018) Financial Report <https://www.cobaltblueholdings.com/thackaringa-resource/>.

EC, 2017. Critical Raw Materials Factsheets: Cobalt. <https://publications.europa.eu/en/publication-detail/-/publication/7345e3e8-98fc-11e7-b92d-01aa75ed71a1/language-en>.

Fortune Minerals Limited (2014) Technical Report on the Feasibility Study for the NICO Gold-Cobalt-Bismuth-Copper project

Northwest Territories, Canada, 385 pp.

Gaudin A, et al. (2005) Clay mineralogy of the nickel laterite ore developed from serpentinised peridotites at Murrin Murrin, Western Australia, *Aust J Earth Sci* 52: 231–241.

Geological Survey of Finland (2018) Geofoorumi Stakeholder magazine http://verkkoletti.geofoorumi.fi/wp-content/uploads/sites/1/2019/01/geofoorumi_2_122018_naytto.pdf.

Hein JR, et al. (2013) Deep-ocean mineral deposits as a source of critical metals for high- and green-technology applications—Comparison with land-based resources. *Ore Geol Rev* 51:1–14.

Hein JR, Koschinsky A (2014) Deep-Ocean ferromanganese crusts and nodules. In *Treatise on Geochemistry*, Elsevier, Amsterdam, 2: 273–291.

Herrington R, et al. (2016) Bauxite and Nickel-Cobalt Lateritic Deposits of the Tethyan Belt. *Econ Geol* 19:349–387.

Hitzman MW, Bookstrom AA, Slack JF, Zientek ML (2017) Cobalt—Styles of deposits and the search for primary deposits: USGS Open-File Report, 47 pp, <https://doi.org/10.3133/ofr20171155>.

IEA (2018) Global EV Outlook 2018. Towards cross-modal electrification. International Energy Agency.

Lambiv Dzemua G, Gleeson SA (2012) Petrography, mineralogy, and geochemistry of the Nkamouna serpentinite—Implications for the formation of the cobalt-manganese laterite deposit, southeast Cameroon. *Econ Geol* 107:25–41.

M2Cobalt (2017) Technical Report for the Bujagali and Kilembe Properties https://www.m2cobalt.com/images/pdf/Technical_Report_m2Cobalt.pdf.

Mudd GM, et al. (2013) Quantifying the recoverable resources of by-product metals—The case of cobalt, *Ore Geol Rev* 55:87–98.

Naldrett AJ (2004) *Magmatic Sulfide Deposits: Geology, Geochemistry and Exploration*, Berlin, Germany: Springer.

Norilsk Nickel (2014) Annual report <https://www.companyreporting.com/sites/default/files/annual-report-index/norilsk-nickel-annual-report-2014.pdf>.

Oberthür T, et al. (2013) The oxidized ores of the main sulphide zone, Great Dyke, Zimbabwe: Turning resources into minable reserves – mineralogy is the key, *J South Afr Inst Min Metall* 113:191–201.

Pazik PM, et al. (2016) World production and possible recovery of cobalt from the Kupferschiefer stratiform copper ore. In *E3S Web of Conferences*, EDP Sciences 8:01063.

Roberts S, Gunn G (2014) Cobalt. *Critical Metals Handbook*, pp 122–149.

Slack FJ, Kimball BE, Shedd KB (2017) Cobalt Chapter F of *Critical Mineral Resources of the United States - Economic and Environmental Geology and Prospects for Future Supply*. Professional paper 1802-F. USGS.

Schulz KJ, Woodruff LG, Nicholson SW, Seal II RR, Piatak NM, Chandler VW, Mars JL (2014) Occurrence model for magmatic sulfide-rich nickel-copper-(platinum-group element) deposits related to mafic and ultramafic dike-sill complexes: Chapter I in *Mineral deposit models for resource assessment*. USGS.

SRK Consulting (2011) Technical Report Nkamouna and Mada deposits <https://www.sec.gov/Archives/edgar/data/1398005/000119312511161283/dex991.htm>.

Taylor CD, et al. (2013) Descriptive models, grade-tonnage relations, and databases for the assessment of sediment-hosted copper deposits—With emphasis on deposits in the Central African Copperbelt, Democratic Republic of the Congo and Zambia. USGS Scientific Investigations Report, pp 154.

United States Geological Service, Mineral Commodity Summary, U.S. Geological Survey, Reston, Virginia: 2019.

Wells MA, et al. (2009) Mineralogy and crystal chemistry of “garnierites” in the Goro lateritic nickel deposit, New Caledonia, *Eur J Mineral* 21:467–483

Germanium and cobalt in sedimentary rock-hosted deposits of northwestern Alaska

Garth E. Graham, Karen D. Kelley
U.S. Geological Survey, USA

Abstract. Cobalt and germanium are critical elements that are essential for a number of technological applications. Northern Alaska hosts several deposits and occurrences that contain significant amounts of these elements. For example, whole rock geochemistry data show that the clastic-dominated Pb-Zn Anarraaq deposit contains up to 820 ppm Ge (median 110 ppm) and samples from the Bornite carbonate-hosted Cu (Pb-Zn) deposit contain tens of thousands of ppm Co. Mineral chemical data indicate that the Ge is hosted primarily in sphalerite in the Pb-Zn systems but the Ge concentrations vary greatly, due in part to a zoning in sphalerite and/or a complex paragenesis with multiple stages of sphalerite with variable Ge contents. Establishing the paragenesis and mineral chemistry in both Pb-Zn and Cu deposits is important for understanding the deportment of the critical elements like Ge (and Co). The deposits in northern Alaska are significant potential sources of Co and/or Ge, should they ultimately be developed.

1 Introduction

Globally, sedimentary rock-hosted lead-zinc and carbonate-hosted polymetallic deposits are potential sources for a number of critical elements including Co, Ga, Ge, and In (e.g., Marsh et al., 2016; Schulz et al., 2017), which are becoming increasingly important. Cobalt is mostly used in cathodes in rechargeable batteries and in superalloys for jet engines. Germanium is an important component in fiber optic cable and solar arrays, among other applications. In sedimentary rock-hosted deposits, cobalt typically resides as cobaltiferous pyrite and/or other cobalt-bearing minerals. Germanium can occur in Ge-bearing minerals (e.g., renierite, germanite) or as lattice substitutions or nano inclusions in sulfide minerals, particularly sphalerite.

The United States has limited domestic production of both Co and Ge, and thus is highly reliant on international sources (USGS, 2019). Identification of additional domestic sources for these metals is in the national interest. Northern Alaska contains two types of sedimentary rock-hosted deposits that are known to contain significant Co and/or Ge. The clastic-dominated Pb-Zn (CD Pb-Zn) systems include the world-class Red Dog deposit and satellite deposits (Anarraaq, Lik), and the Drenchwater deposit to the east. The carbonate-hosted polymetallic deposits include the Cu-rich Bornite (Ruby Creek) and Omar prospect, along with a number of additional Pb-Zn dominated occurrences in the Baird Mountains. In this contribution, we summarize reconnaissance USGS geochemical results that

demonstrate known and potential deposits/occurrences that contain enrichments of Co or Ge that could be resources under appropriate market conditions.

2 Geologic background

The CD Pb-Zn deposits (commonly termed SEDEX) of northern Alaska are hosted in Paleozoic passive margin black shales/mudstones with locally abundant carbonate turbidites and chert of the Mississippian Kuna Formation (Fig. 1).

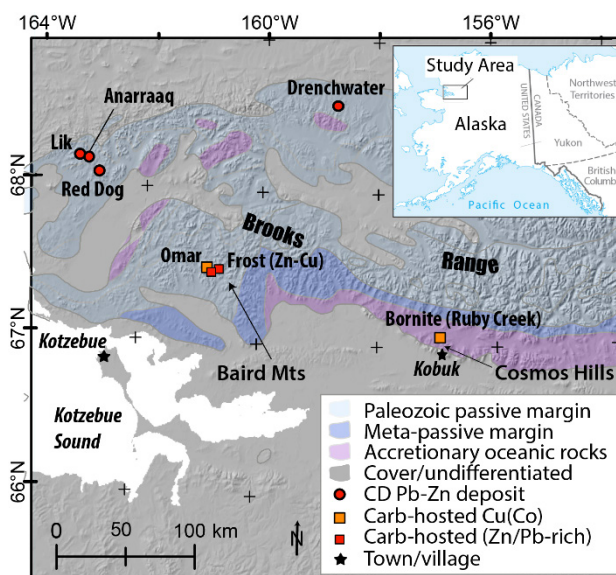


Figure 1. Generalized geology and select Zb-Pb and carbonate-hosted base metal deposits map of northwestern Alaska.

These deposits occur in one of several tectono-stratigraphic assemblages of dominantly sedimentary rocks that were juxtaposed during the Late Jurassic to Tertiary Brookian orogeny on the northern edge of the Brooks Range. (e.g., Moore et al., 1994). Voluminous volcanic and intrusive plugs are recognized only in the vicinity of the Drenchwater deposit, located ~200 km east of Red Dog (Werdon, 1996). Mineralised rocks in ore zones contain laminated to chaotic semi-massive to massive sulfides typically dominated by sphalerite, with lesser galena and pyrite. At some deposits (e.g., Red Dog), vein ores are economically significant. Multiple sphalerite stages are recognized at Red Dog and Anarraaq (Kelley et al., 2004a,b, Smith, 2017). Both deposits are interpreted to have formed in the shallow subsurface through precipitation of sulfides from basal brines by replacement of barite and/or carbonate in the clastic-dominated stratigraphy.

Table 1. Summary statistics for whole rock samples from select CD Pb-Zn and carbonate-hosted polymetallic deposits of northwestern Alaska. Data (except Ga) for Red Dog, Anarraaq, and Drenchwater (DW) are from Graham et al. (2009). These data are part of an Alaska statewide compilation (Granitto et al., 2013). Average crustal abundance values from Wedepohl (1995). All values are in parts per million (ppm).

Deposit(# samps)	Co			Cu			Ga			Ge			Pb			Zn		
	Min	Mediar	Max	Min	Median	Max	Min	Mediar	Max	Min	Mediar	Max	Min	Median	Max	Min	Median	Max
CD Pb-Zn																		
Red Dog (19)	<1	29	97	<10	140	480	0.5	3	25	1.3	16	60	640	25200	163000	29000	133000	371000
Anarraaq (11)	<1	7	145	<10	12	163	0.5	1	18	16	110	820	980	66900	124900	84400	199000	464500
DW (12)	7	15	44	69	130	740	1	13	49	8	23	88	236	5910	178000	1730	140000	249000
Carb.-hosted																		
Bornite (21)	9	176	16300	129	43500	571000	<1	1	24	<0.5	2.2	48	23.5	150	410	16	166	217000
Baird Cu (14)	<1	132	4320	3630	44600	343000	<0.02	0.3	9.7	<0.5	8.3	110	<5	180	2500	70	1500	16600
Baird-Zn (22)	<1	1	935	6	83	1090	<0.02	4.9	22.7	<0.5	11	98	22.6	1760	70100	12800	82700	484000
Baird Zn-Cu (4)	<1	1	3	1990	7780	40500	43	64	111	9.1	22	91	11	27	130	105000	253000	306000
Baird-Pb (4)	<1	1	2	21	33.55	288	1.6	2.2	9	1.9	2	2.3	12700	49650	59400	2640	2985	6370
Crustal avg.		24			25			15			1.4			14.8			65	

The Cu to Zn-rich carbonate-hosted polymetallic systems are located on the southern side of the Brooks Range (Fig. 1). The largest of these is the Bornite (Ruby Creek) deposit, located in the Cosmos Hills, and hosted in a 1-km-thick sequence of Silurian and Devonian metacarbonates (Hitzman et al., 1986). Mineralisation occurred in synsedimentary or later breccias and involved replacement of breccia matrix and early pyrite by copper minerals, minor sphalerite and galena and carrollite, and lesser reneirite and germanite (Bernstein and Cox, 1986, Hitzman et al. 1986). Mineralisation is interpreted to predate regional greenschist metamorphism. The Omar deposit, a copper-rich orebody located 180 km west of Bornite in the Baird Mountains, is a possible analog, with high cobalt concentrations (Fig. 1; Jansons, 1982; Folger and Schmidt, 1986). Several Zn(Pb) dominated prospects occur in the vicinity of Omar, sometimes with significant Cu (Frost occurrence labeled as Baird Zn-Cu in Fig. 1).

3 Reconnaissance whole rock geochemistry

Whole rock geochemical data for select deposits and occurrences are summarized in Table 1. These data indicate highly variable enrichments of Co and/or Ge. Cobalt concentrations are generally not enriched in CD Pb-Zn deposits (max 145 ppm, median concentrations <30 ppm; Table 1) compared to average continental crust. However, cobalt is highly enriched in some samples from both the Bornite deposit and the Omar Cu prospect, in the Baird Mountains (maximum 16,300 and 4,320 and median concentrations of 176 and 132 ppm, respectively).

Gallium concentrations approximate or are lower than crustal averages in CD Pb-Zn samples (median concentrations of 1 to 16.5 ppm), but a maximum concentration of 49 ppm was reported in mineralised tuff at Drenchwater (Table 1). Ranges are similar in most of the carbonate-hosted systems, although four Zn and Cu-rich surface samples at the Frost occurrence near Omar yielded 43 to 111 ppm Ga. Based on our limited dataset from the Bornite deposit, the highest Ga concentrations of 15 to 24 ppm occurred in poorly mineralised shale.

The Anarraaq deposit has distinctly elevated Ge concentrations, with maximum and median concentrations of 820 and 110 ppm, respectively from grab samples, consistent with previous reports (Jennings and King, 2002). Red Dog and Drenchwater CD Pb-Zn deposits have significantly lower median concentrations of ~16 and 23 ppm, respectively. Germanium concentrations are also elevated at Frost (Baird-Zn-Cu on Table 1).

4 Mineral chemistry

Mineral chemistry data are available for a few of the CD Pb-Zn deposits but not the carbonate-hosted deposits considered here. At the Red Dog deposit, four different paragenetic stages of sphalerite are recognized, including stage 2 yellow-brown sphalerite and stage 3 red-brown sphalerite that together comprise the majority of the ore (Kelley et al., 2004a). Median concentrations of 149, 103, 82, 247 ppm Ge in these stages, were established by laser ablation inductively coupled mass spectrometry (LA-ICP-MS). Stage 2 and 3 sphalerite also contains median concentrations of Co of 102 and 149 ppm, higher than pyrite associated with these generations (median 60 and 7 ppm, respectively).

Germanium concentrations in sphalerite samples from other deposits, including Anarraaq, Drenchwater and Lik are summarized in Graham et al. (2009). Limited sphalerite chemical data for Anarraaq indicate high Ge concentrations (median ~420 ppm) relative to 94 to 140 ppm median value for other deposits, including volumetrically dominant stages 2 and 3 at Red Dog (Fig. 2). More recently, Smith (2017) established qualitatively significant variations in Ge concentrations in different generations of sphalerite from Anarraaq.

Elemental associations of Ge differ among stages and deposits. For example, despite some data scatter, Ag displays a positive correlation with increasing Ge associated with different stages of sphalerite at Red Dog. In contrast, Anarraaq samples show no systematic relationship between Ge and Ag, but Ge displays positive correlation with Mn and Tl concentrations (the absolute concentrations of which are higher than those at Red

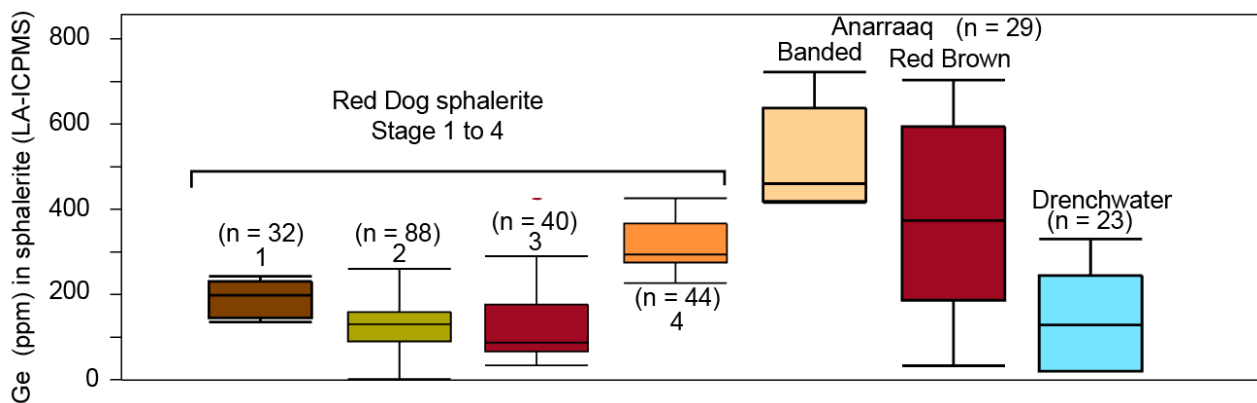


Figure 2. Boxplots showing the ranges of germanium concentrations in LA-ICPMS analyses of sphalerite from the Red Dog, Anarraaq, and Drenchwater CD Pb-Zn deposits. Note the difference in concentration ranges for the better characterized Red Dog sphalerite generations (relatively narrow) versus lesser characterized samples from Anarraaq and Drenchwater. Data included from Graham et al. (2009).

Dog) in two distinctly different sphalerites (banded and red-brown; Fig. 2) from different parts of the deposit.

5 Discussion

5.1 Comparison to domestic production and deposits

The critical mineral endowment of some of the northern Alaskan deposits is significant and could be important for future supply. In 2018, only 500 tonnes of Co were produced in the US (USGS, 2019, page 50). The recent inferred resource estimate of 77 million pounds of Co at Bornite in combined open-pit and underground zones with different Cu cut-off grades (Trilogy Metals, Inc. 2018) equates to approximately 34,900 tonnes of Co. This makes Bornite one of two recently delineated Co-bearing sedimentary-rock hosted deposits in the US (the other being the Black Butte deposit in Montana). The similarity of Omar to Bornite with respect to geology and geochemical signatures opens the potential for additional resources. However, additional extensive work is necessary to assess the potential of this very remote deposit.

Domestic production numbers for Ge are not currently available, although zinc concentrates from the US are sent to Canada for smelting for Ge recovery (USGS, 2019). Some of these ores are assumed to be from Red Dog, which had previously reported concentrations of 79 ppm Ge in zinc concentrate (Alaska Department of Environmental Conservation, Tennessee. Massive sphalerite/sphalerite concentrate chemistry show Ge concentrations appreciably higher than Red Dog, at ~200 to 390 ppm (Bonnett et al., 2016). However, these concentrations are approximately the same as the median values in Anarraaq sphalerite (a proxy for concentrate results).

5.2 Mineral residence

The LA-ICP-MS data for sphalerites demonstrate complex trace element associations both within the paragenetic evolution of a given deposit and among

deposits. Even within the well-studied Red Dog deposit significant ranges of Ge exist in each of the four stages. In the more poorly characterized samples used for the reconnaissance work at Anarraaq and Drenchwater, broad ranges in Ge concentrations undoubtedly reflect either zoning within single crystals or treatment of different paragenetic stages as a single population (Fig. 2). The work of Smith (2017) demonstrates major variation in Ge and other trace element concentrations in the different stages, with irregular and patchy character specifically for Ge at the micron to millimeter scale within a single crystal.

These data also suggest that there may be different chemical processes at the stage or deposit scale that control trace element compositions of sphalerite. For example, the positive correlations between Ge and Mn for most Anarraaq sphalerite analyses could be recording a redox control on sphalerite formation. Anarraaq ores contain abundant organic matter that could have served as a reductant (Kelley et al. 2004b).

The absence of any noted Ge-bearing phases at Anarraaq, despite the high concentrations of Ge contrasts with reports of Ge-bearing (and Co-bearing) phases at Bornite, which contains lower absolute Ge concentrations as suggested by our limited sample suite. Cugerone et al. (2018) suggested that the abundance of accessory Ge-minerals and Ge-poor sphalerite in Variscan Pb-Zn vein deposits was a consequence of recrystallization of sphalerite by a metamorphic overprint that expelled many of the trace element impurities, including Ge. Similar processes may have, at least in part, caused formation of Ge-(and Co-bearing) phases in Bornite. Such greenschist metamorphic conditions have not impacted the CD Pb-Zn deposits. Textural and mineral chemistry analyses from the carbonate-hosted deposits may help answer this question.

6 Conclusions

Geologic evidence demonstrates that there is significant resource potential for both Co and Ge in different sedimentary rock-hosted deposits of northwestern Alaska. Mineral chemistry studies highlight the

complexity of the controls on Ge concentrations on the micro- through macro scales. As society seeks additional critical element resources, it is essential to develop a strong understanding of paragenetic relationships within deposits to define the department of elements of interest. Combined with an evolving understanding of why they occur in certain stages we will enhance our capability of predicting where these resources might occur.

Acknowledgements

We thank Jane Hammarstrom and Erin Marsh for their comments on earlier iterations of this abstract.

References

- Alaska Department of Environmental Conservation (2002) Table 2-1: Composition of Red Dog lead and zinc concentrates (revised 6-7-05). https://dec.alaska.gov/spar/csp/docs/reddog/03dmts_ra_tables-april2005.pdf. Accessed 22 February 2019
- Bernstein LR, Cox DP (1986) Geology and sulfide mineralogy of the Number One Orebody, Ruby Creek copper deposit, Alaska. *Econ Geol* 81: 1675-1689
- Bonnett J, Mosser-Ruck R, Caumon MC, Andre-Mayers AS, Cauzid J, Peiffert C (2016) Trace element distribution (Cu, Ga, Ge, Cd and Fe) in sphalerite from the Tennessee MVT deposits, USA, by combined EMPA, LA-ICP-MS, Raman spectroscopy, and crystallography. *Can Mineral* 54:1261-1284
- Cugerone A, Cenki-Tok B, Chauvet A, Le Goff E, Bailly L, Alard O, Allard M, (2018) Relationships between occurrence of accessory Ge-minerals and sphalerite in Variscan Pb-Zn deposits of the Bossost anticlinorium, French Pyrenean Axial Zone: chemistry, microstructures and ore-deposit setting. *Ore Geol Rev* 95:1-19
- Folger PF, Schmidt JM (1986) Geology of the carbonate-hosted Omar copper prospect, Baird Mountains, Alaska: *Econ Geol* 81:1690-1695
- Graham GE**, Kelley KD, Slack JF, Koenig, AE (2009) Trace elements in Zn-Pb-Ag deposits and related stream sediments, Brooks Range Alaska, with implications for Tl as a pathfinder element. *Geochem: Explor Environ Anal* 9:19-37
- Granitto M, Schmidt JM, Shew NB, Gamble BM, Labay KA (2013) Alaska Geochemical Database, Version 2.0 (AGDB2)—including “best value” data compilations for rock, sediment, soil, mineral, and concentrate sample media. US Geol Surv Data Series 759:20 pamphlet and database, 1 DVD, <https://pubs.usgs.gov/ds/759/>
- Hitzman MW, Proffett JM, Schmidt, J, Smith TE (1986) Geology and mineralization of the Ambler District northwestern Alaska. *Econ Geol* 81:1592-1618
- Jansons U (1982) Cobalt content in samples from the Omar copper prospect, Baird Mountains, Alaska, US Geol Surv Open File Report MLA 109-82:16 http://dggs.alaska.gov/webpubs/usbm/mla/text/mla109_82.pdf. Accessed 25 February 2019
- Jennings S, King AR (2002) Geology, exploration history and future discoveries in the Red Dog district, western Brooks Range, Alaska. In Cooke D, Pongratz J (eds) *Giant Ore Deposits: Characteristics, genesis and exploration*, Center for Ore Deposit Research, Hobart Australia, pp. 151–158
- Kelley KD, Leach DL, Johnson CA, Clark JL, Fayek M, Slack JF, Anderson VM, Ayuso RA, Ridley WI (2004a). Textural, Compositional, and Sulfur Isotope Variations of Sulfide Minerals in the Red Dog Zn-Pb-Ag Deposits, Brooks Range, Alaska: Implications for Ore Formation. *Econ Geol* 99:1509–1532
- Kelley KD, Dumoulin JA, Jennings S (2004b). The Anarraaq Zn-Pb-Ag and barite deposit, northern Alaska: Evidence for replacement of carbonate by barite and sulfides. *Econ Geol* 99:1577–1591
- Marsh EE, Hitzman MW, Leach DL (2016) Critical elements in sediment-hosted (clastic-dominated Zn-Pb-Ag, Mississippi Valley Type Zn-Pb, sedimentary rock-hosted stratiform Cu, and carbonate-hosted polymetallic deposits): A review. *Rev Econ Geol* 18: 307-321
- Moore TE, Wallace WK, Bird KJ, Karl SM, Mull CG, Dillon JT (1994) Geology of northern Alaska. In Plafker , Berg HC (eds) *The Geology of Alaska*: Geol Society of America, pp. 49-138
- Schulz KJ, DeYoung JH Jr, Seal II RR, Bradley DC (eds.) (2017) *Critical mineral resources of the United States—Economic and environmental geology and prospects for future supply*. US Geol Surv Prof. Paper 1802:797. doi.org/10.3133/pp1802.
- Smith D (2017) *Lithophile and Chalcophile Elements in Sphalerite from the Anarraaq Sediment-Hosted Zn-Pb-Ag Deposit, Red Dog District, Alaska*, Masters thesis, University of Alberta, 117 p
- Trilogy Metals Inc., 2018. Trilogy Metals Inc. NI 43-101 Technical Report on the Bornite Project, Northwest Alaska, USA. July 20th 2018 https://trilogymetals.com/assets/docs/Technical_Report_for_the_Bornite_Co_Update_2018_07_20-F.pdf. Accessed 22 February 2019
- U.S. Geological Survey, 2019, Mineral commodity summaries 2019: US Geol Surv, 200 p., <https://doi.org/10.3133/70202434>. ISBN 978-1-4113-4283-5.
- Wedepohl KH (1995) The composition of the continental crust. *Geochim. Cosmochim. Acta* 59: 1217–1232
- Werdon MB (1996) Drenchwater, Alaska; Zn-Pb-Ag mineralization in a mixed black shale; volcanic environment, in Coyner, A.R., and Fahey, P.L., eds., *Geology and ore deposits of the American Cordillera: Reno, Nev., Geol Soc Nevada Symp Proceed*, pp 1341–1354

The genesis of Carlow Castle: a unique Australian orogenic Cu-Co-Au deposit in the Archean Pilbara Craton

David Fox, Samuel Spinks, Mark Pearce, Margaux Le Vaillant, Robert Thorne

CSIRO Mineral Resources, Australian Resources Research Centre, Australia

David Fox, Milo Barham, Mehrooz Aspandiar

The Institute for Geoscience Research (TIGeR), School of Earth and Planetary Sciences, Curtin University, Australia

Abstract. Carlow Castle is a Cu-Co-Au deposit situated within the western Pilbara Craton of Western Australia. Whilst Carlow Castle is the oldest discovered copper deposit in the Pilbara region, having been initially discovered in 1882 (Ruddock 1999), no detailed study of the ore mineralisation has ever been undertaken. After being long abandoned, a recent drilling campaign through 2018 uncovered an economically significant and geologically complex system of Cu-Co-Au mineralisation with a current resource estimate for Carlow Castle of 7.7Mt @ 1.06g/t Au, 0.51% Cu, and 0.08% Co (Artemis Resources Limited 2019), making it one of Australia's most significant Cu-Co-Au deposits. Recent analysis suggests that Carlow Castle is a hydrothermal Cu-Co-Au deposit, with mineralisation hosted in sulphide-rich quartz veins throughout a pervasively chloritised shear zone in an Archean mafic volcano-sedimentary sequence. Within these ore veins, the sulphide mineralogy is dominated by pyrite (FeS₂), chalcopyrite (CuFeS₂), chalcocite (Cu₂S), and cobaltite (CoAsS). Here we present the findings of the first detailed study on the nature of the Cu-Co-Au mineralisation at Carlow Castle and propose an orogenic model for the genesis of this unique deposit.

1 Introduction

The Carlow Castle Cu-Co-Au deposit occurs in the West Pilbara region of Western Australia, ~10 km SW of Roebourne, ~25 km SE of Karratha, and ~1500 km NE of Perth. The present JORC (2012) compliant resource for Carlow Castle is 7.7 Mt @ 1.06 g/t Au, 0.08% Co, and 0.51% Cu (Artemis Resources Limited 2019); making this one of Australia's most significant Cu-Co-Au deposits (Britt et al. 2017). This follows major exploration and drilling campaigns by Artemis Resources through 2017 and 2018 resulting in the discovery of this resource proximal to the previously abandoned Carlow Castle Cu mine. Here it is proposed that Carlow Castle's genesis most closely matches the conventional genetic model for an orogenic Au deposit, however its particularly cobaltiferous ore mineralisation makes it unique among orogenic Au deposits, which are not commonly observed to be strongly enriched in Co (Groves et al. 1998). This is topical given the present broad interest in Co as a critical battery metal and the increasing drive for Co exploration to ensure security of supply as the adoption of electric vehicles increases and renewable energy storage becomes of greater importance to the global energy industry (Olivetti et al. 2017). The necessity to better understand the genesis of

Co mineralisation is additionally compounded by existing risks in the supply security of Co pertaining to the fact that >50% of Co is presently sourced from the Democratic Republic of Congo (US Geological Survey 2018). Given the economic significance of this deposit, the current broad interest in Co deposits, the recency of this discovery, its unique Cu-Co enrichment, and the lack of any existing literature on this deposit this study introduces this unique class of Co-rich orogenic Au deposits with insights into the genesis of Carlow Castle specifically. It is anticipated that by providing insights into the unique combination of processes required to form Co-rich orogenic Au deposits, and determining how these differ from conventional orogenic Au genetic models, that exploration for these deposits can be enhanced.

2 Geological background

The Pilbara Craton is an Archean craton that covers ~400,000 km² in the northwest region of Western Australia and is divided broadly into the Archean North Pilbara granite-greenstone terrain (3.6-2.8 Ga) and the overlying Mount Bruce Supergroup of Archean to Paleoproterozoic age (2.77-2.3 Ga), which primarily occurs along the southern edge of the craton within the Hammersley and Fortescue Basins (Ruddock 1999; Smithies et al. 1999; Van Kranendonk et al. 2002). Carlow Castle is hosted in a volcano-sedimentary sequence within the West Pilbara Superterrane of the northwest Pilbara Craton (Hickman 2016). This volcano-sedimentary sequence is denoted as the Ruth Well Formation; forming part of the Roebourne Group, which is in turn a component of the Karratha Terrane (Hickman 2016; Ruddock 1999). Within the Ruth Well Formation, the mineralisation at Carlow Castle occurs proximal to the Regal Thrust; a regionally significant thrust fault that is interpreted to have formed immediately before or during the original formation of the West Pilbara Superterrane (3.16-3.07 Ga) (Hickman 2016; Van Kranendonk et al. 2007). This may have coincided with the Prinsep Orogeny, where obduction of the Regal Formation onto the Karratha Terrane formed the Regal Terrane and the continued convergence of the Regal Karratha, Regal, and Sholl terranes caused their amalgamation into the West Pilbara Superterrane (Hickman 2016). This was followed by the collision of the West Pilbara Superterrane and the East Pilbara Terrane from ~3.068-3.066 Ga (Hickman 2016).

3 Cu-Co-Au mineralisation

3.1 Style of mineralisation

The mineralisation at Carlow Castle deposit is hosted in a heavily altered dominantly mafic volcano-sedimentary sequence, within the Ruth Well Formation (Ruddock 1999). With this considered, it is often difficult to constrain the primary lithology within which Carlow Castle's mineralisation is hosted due to extensive hydrothermal alteration that has produced a pervasively chloritised and silicified host lithology. However, based on previous studies of the Ruth Well Formation, it is likely that this host lithology was dominated by a volcanic sequence of mafic to ultramafic rocks with minor chert and carbonaceous shale beds (Hickman 2016; Ruddock 1999; Van Kranendonk et al. 2006). Within the Ruth Well Formation, the Co-Cu-Au mineralisation typically occurs within 100 m of the surface and this mineralisation occurs broadly in two styles. The first, and most significant, style of mineralisation is structurally-hosted, where mineralisation occurs in quartz-carbonate and sulphide veins through brecciated and sheared basalt. The second style of mineralisation occurs near to the surface, overlying the structurally-hosted sulphide mineralisation, as an oxidised supergene layer. Within this oxidised layer, there is partial to complete replacement of the original sulphide mineralisation with secondary Cu-oxide and carbonate minerals.

3.2 Structure and extent

Carlow Castle occurs within a heavily tectonised zone through the Ruth Well Formation, proximal to the regionally significant Regal Thrust. Reflecting this, the Ruth Well Formation at Carlow Castle hosts evidence of several generations of deformation. Brittle deformation is intense through portions of Carlow Castle, where the Ruth Well Formation proximal to the ore zone is heavily brecciated and this brecciation forms a network of quartz infilled fractures. In addition to these brittle structures, there is also extensive evidence of ductile deformation at Carlow Castle, where quartz and sulphide veins throughout the Ruth Well Formation in portions of the ore zone are heavily sheared and folded. These brittle and ductile structures at Carlow Castle are both observed to host mineralisation, which occurs infilling these structures as networks of quartz-sulphide veins. The formation of these structures was clearly critical to the genesis of this mineralisation as they provided permeable structures to allow Carlow Castle to act as a regional focus for migrating mineralising fluids. This includes those that may have flowed along the proximal Regal Thrust, to which gold mineralisation is more broadly associated (Hickman 2016).

3.3 Mineralogy

The structurally-hosted mineralisation at Carlow Castle occurs broadly in two sulphide-dominated mineral assemblages. The first of these is a chalcocite-cobaltite-gold assemblage, whilst the second is composed predominantly of a pyrite-chalcocopyrite assemblage. In addition to these minerals, other minerals are observed to occur in these assemblages in minor or trace volumes. These mineral assemblages are summarised in Table 1.

Table 1. Summary of two distinct ore mineral assemblages that occur through Carlow Castle Cu-Co-Au deposit.

	Mineral Assemblage One	Mineral Assemblage Two
Cu	Chalcocite (Cu ₂ S), ±Chalcocopyrite (CuFeS ₂)	Chalcopyrite, ±Chalcocite
Co	Cobaltite (CoAsS)	± Cobaltite
Au	Gold (Au)	± Gold
Other	±Pyrite (FeS ₂), ±Uraninite (UO ₂)	Pyrite, ±Tellurobismuthite (Bi ₂ Te ₃), ±Hessite (Ag ₂ Te)

The two mineral assemblages appear to occur independently of one another; they do not appear to reflect a broad scale mineralogical or geochemical zonation within the ore body at Carlow Castle. With this considered, Assemblage Two forms the majority of the structurally-hosted sulphide mineralisation throughout Carlow Castle, whilst Assemblage One occurs primarily in vein networks that are limited to the particularly Cu, Co, Au-rich portions of Carlow Castle.

Petrographic analysis of the sulphide mineralisation within the Carlow Castle ore body provide insights into the genesis of this mineralisation. Within Assemblage One (Fig. 1) the dominant sulphide minerals are chalcocite and cobaltite, occurring in varying amounts from almost entirely cobaltite to almost entirely chalcocite. Generally, within these veins cobaltite occurs as aggregates of euhedral-subhedral crystals hosted in a mix of quartz and siderite. Networks of thin chalcocite veinlets commonly occur through these cobaltite-rich veins, typically surrounding cobaltite grains and filling in networks within these larger quartz-carbonate veins.

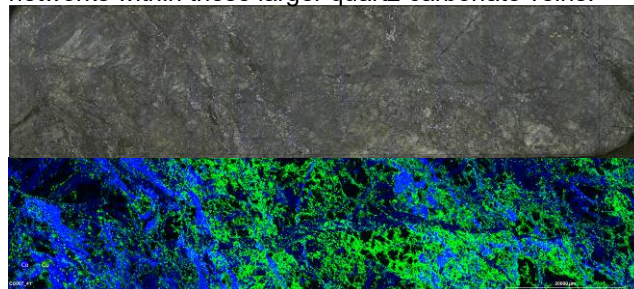


Figure 1. Mosaic and XRF map of veined chalcocite and cobaltite-rich Assemblage One. Note here that on the XRF map green corresponds to Cu and blue corresponds to Co. This sample is ~22 cm long.

Notably, there is a clear genetic relationship, within this assemblage, between cobaltite and gold mineralisation as the native gold is observed to occur virtually exclusively as inclusions within grains of cobaltite. Additionally, trace inclusions of chalcocopyrite and uraninite are also observed within these grains of cobaltite. Finally, it is interesting to note that pyrite, when it does occur within this assemblage, is commonly observed to be partially replaced by chalcocite; where chalcocite surrounds pyrite and occurs as penetrating lamellae throughout.

Assemblage Two (Fig 2.) is defined by an intergrown assemblage that is primarily composed of chalcocopyrite

and pyrite. Where this assemblage occurs in quartz-carbonate veins, pyrite and chalcopryrite tend to be anhedral and form stringy veinlet networks infilling space between quartz. These veinlet network of chalcopryrite and pyrite are occasionally associated with blocky grains of euhedral to subhedral cobaltite. Assemblage Two also occurs in particularly sulphide-rich veins where gangue quartz-carbonate is limited and instead the chalcopryrite and pyrite compose virtually all of these veins, here these sulphides are massive with intergrown anhedral pyrite and chalcopryrite but are commonly also intergrown with chlorite from the pervasively altered host rock. Interestingly, in massively textured samples of Assemblage Two, cobaltite is less common in comparison to the more quartz-rich veinlet textured samples. Further within assemblage Two, gold is notably less common in general in comparison to Assemblage One. However, gold does occur within Assemblage One in trace quantities and it is commonly associated with chalcopryrite. Finally, there is a clear association between the tellurides hessite and tellurobismuthite and pyrite as these tellurides occur exclusively as inclusions within pyrite.

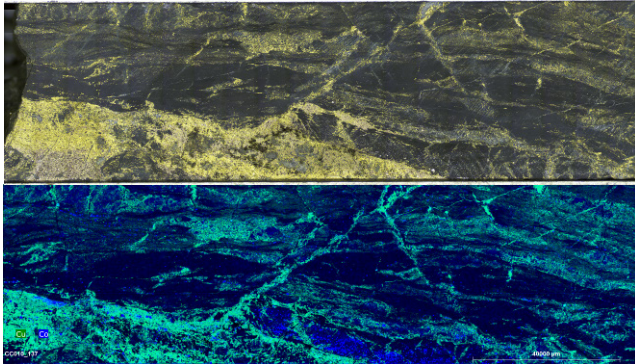


Figure 2. Mosaic and XRF map of veined chalcopryrite and pyrite-rich Assemblage Two with minor cobaltite. Note that on the XRF map green corresponds to Cu and blue corresponds to Co. This sample is ~20 cm long.

3.4 Geochemistry

Strong enrichments are observed in Cu, Co, Au at Carlow Castle. Several interesting relationship are observed between elements within the ore body; most notably correlation coefficients of 1.00 for Co:As, 0.95 for Ag:Cu, 0.83 for Au:Co, 0.69 for Au:Cu, 0.61 for Cu:Co. The perfect positive correlation between Co and As confirms mineralogical observations that all of the Co within the deposit is hosted in cobaltite. Additionally, the strong positive correlation between Au and Co provides additional geochemical evidence of the previously mentioned genetic relationship between Co and Au mineralisation observed in Assemblage One. Conversely, the comparably less strong positive correlation between Co and Cu suggests that these two metals do not always occur in association, as has been observed mineralogically above.

4 Genesis

As no detailed study of Carlow Castle has previously

been conducted, very little beyond superficial ideas regarding the metallogeny of this deposit exist (Hickman 2016; Ruddock 1999). With this considered, the interpretation proposed here is that Carlow Castle represents an orogenic hydrothermal Cu-Co-Au deposit, this is congruent with suggestions regarding Carlow Castle's genesis posited by Ruddock (1999) and Hickman (2016) based on broad-scale observations. This is proposed due to the fact that Carlow Castle exhibits several geological characteristics that are typical of orogenic gold deposits. On a broad scale, the first of these characteristics is Carlow Castle's regional situation in an Archean greenstone belt and, on a smaller scale, within a rift-related volcano-sedimentary succession (Groves et al. 1998; Hickman 2016; Van Kranendonk et al. 2010). Additionally, the occurrence of Carlow Castle within the West Pilbara Superterrane, a collisional accretionary superterrane that formed at ~3.068 Ga during the Prinsep Orogeny (Hickman 2016), provides a classic tectonic setting for an orogenic gold system (Goldfarb et al. 2001; Groves et al. 1998). On a deposit scale, the strong structural control on mineralisation, occurrence through a heavily tectonised zone proximal to the regionally significant Regal Thrust fault, pervasive quartz-carbonate veining, extensive chloritic hydrothermal alteration, and the otherwise clear hydrothermal origin of Carlow Castle are similarly typical of orogenic mineral systems (Saunders et al. 2014; Groves et al. 1998; Goldfarb et al. 2001).

As Carlow Castle has been classified here as an orogenic Cu-Co-Au deposit, its genesis is inextricably linked to the ~3.068 Ga Prinsep Orogeny during the amalgamation of the Karratha, Regal, and Sholl Terranes into the West Pilbara Superterrane and the subsequent convergence of the West Pilbara Superterrane and the East Pilbara Terrane (Van Kranendonk et al. 2007; Hickman 2016). Given its close proximity to the Regal Thrust, which is believed to have formed during the Prinsep Orogeny or the prior convergent 'Karratha Event' around ~3.16 Ga (Hickman 2004; Van Kranendonk et al. 2010), the formation of this thrust and the associated tectonization at Carlow Castle was key to the genesis of the Cu-Co-Au mineralisation. This is because although the timing of the mineralisation at Carlow Castle is not yet constrained relative to these tectonic events and the formation of the Regal Thrust, the Regal Thrust and the tectonised zone at Carlow Castle were at very least key to the genesis of this mineralisation in that they provided conduits and a regional fluid focus for migrating ore fluids. Whilst the source of these fluids and their metal enrichment is not yet constrained, Hickman (2016) suggested that the proximal sediments of the Nickol River Formation may have provided a source of gold due to the deposition of detrital gold into these sediments; shed from eroded gold deposits in the East Pilbara Terrane. However, there is no strong evidence to directly support this hypothesis and further study is required to constrain the metal source for Carlow Castle. With this considered, the uniquely strong enrichment of Co and Cu in this deposit implies a unique metal source relative to other orogenic Au systems. If the formation of this mineralisation was synchronous to the Prinsep Orogeny

then it is likely that this ore fluid would have been produced by metamorphic devolatilization (Cox 2005; Tomkins 2013). The Cu-Co-Au rich ore fluid would have been channeled through permeable structures along the Regal Thrust and focused into the brecciated and sheared zone at Carlow Castle. Once channeled into third-order structures, metal deposition would have most likely occurred due to wall rock interaction with the mafic volcanic rocks and carbonaceous shales of the Ruth Well Formation (Morey et al. 2007; Phillips and Powell 2010; Hickman 2016).

5 Implications

The primary significance of Carlow Castle stems from its unique Cu-Co-Au metal association and its unique ore mineralogy given its interpreted genesis as an orogenic Au deposit. Although Carlow Castle does bear some broad mineralogical, textural, or structural similarities to other rare examples of Co mineralisation in some orogenic terranes (e.g. Bou Azzer, Morocco and Idaho Cobalt Belt, USA), Carlow Castle is distinguished by its Archean age; significant Cu-Au enrichment; and lack of Ni enrichment. Given the recency of the discovery of major structurally-hosted Cu-Co-Au mineralisation at Carlow Castle (Artemis Resources Limited 2019), the purpose of this research is to provide the first overview of the geology of Carlow Castle and nature of its mineralisation, as there is no other existing literature focused on Carlow Castle. This work is particularly topical due to the strong Co enrichment within Carlow Castle and the current broad interest in Co deposits due to the dramatic increase in Co prices through 2017 and 2018 (London Metal Exchange 2019), driven by projections of increased demand from the battery sector due to Co's status as a key metal in Li-ion batteries (US Geological Survey 2018). Because of its unique enrichment in Cu and Co, understanding the unique combination of processes necessary to form this deposit and how they differ from the conventional model for orogenic Au deposits are of broad significance as they could assist with exploration efforts for other cobaltiferous orogenic Au deposits. This is particularly significant given the present lack of supply security for cobalt.

Acknowledgements

This research was supported by an Australian Government Research Training Program Scholarship and a CSIRO Mineral Resources postgraduate student scholarship. Artemis Resources Ltd. are acknowledged for their financial, logistical, and material support.

References

Artemis Resources Limited (2019) Carlow Castle Au-Cu-Co Resource Grows by 71% to 7.7Mt.
 Britt A, et al. (2017) Australia's Identified Mineral Resources 2017. Geoscience Australia, Canberra.
 Cox SF (2005) Coupling between Deformation, Fluid Pressures, and Fluid Flow in Ore-Producing Hydrothermal Systems at Depth in the Crust. *Economic Geology* 100th Anniversary Volume:39-75.
 Goldfarb RJ, et al. (2001) Orogenic gold and geologic time: a global

synthesis. *Ore Geology Reviews* 18:1-75.
 Groves DI, et al. (1998) Orogenic gold deposits: A proposed classification in the context of their crustal distribution and relationship to other gold deposit types. *Ore Geology Reviews* 13:7-27.
 Hickman AH (2004) Two contrasting granite-greenstone terranes in the Pilbara Craton, Australia: evidence for vertical and horizontal tectonic regimes prior to 2900 Ma. *Precambrian Research* 131:153-172.
 Hickman AH (2016) Northwest Pilbara Craton: a record of 450 million years in the growth of Archean continental crust. Geological Survey of Western Australia, Perth, pp 104.
 JORC (2012) Australasian Code for Reporting of Exploration Results, Mineral Resources and Ore Reserves. The Joint Ore Reserves Committee of The Australasian Institute of Mining and Metallurgy, Australian Institute of Geoscientists and Minerals Council of Australia.
 London Metal Exchange (2019) LME Cobalt. London Metal Exchange.
 Morey A, et al. (2007) The structural controls of gold mineralisation within the Bardoc Tectonic Zone, Eastern Goldfields Province, Western Australia: implications for gold endowment in shear systems. *Mineralium Deposita* 42:583-600.
 Olivetti EA, et al. (2017) Lithium-Ion Battery Supply Chain Considerations: Analysis of Potential Bottlenecks in Critical Metals. *Joule* 1:229-243.
 Phillips GN, Powell R (2010) Formation of gold deposits: a metamorphic devolatilization model. *Journal of Metamorphic Geology* 28:689-718.
 Ruddock I (1999) Mineral occurrences and exploration potential of the west Pilbara. Western Australia Geological Survey, Perth, Western Australia, pp 63.
 Saunders JA, et al. (2014) 13.15 - Geochemistry of Hydrothermal Gold Deposits In: Holland H, Turekian K (eds) *Treatise on Geochemistry*. 2 edn. Elsevier, Amsterdam, pp 383-424.
 Smithies RH, Hickman AH, Nelson DR (1999) New constraints on the evolution of the Mallina Basin, and their bearing on relationships between contrasting eastern and western granite-greenstone terranes of the Archean Pilbara Craton, Western Australia. *Precambrian Research* 94:11-28.
 Tomkins AG (2013) On the source of orogenic gold. *Geology* 41:1255-1256.
 US Geological Survey (2018) Mineral commodity summaries 2018. U.S. Geological Survey, pp 200p.
 Van Kranendonk MJ, Hickman AH, Smithies RH, Nelson DR, Pike G (2002) Geology and Tectonic Evolution of the Archean North Pilbara Terrain, Pilbara Craton, Western Australia. *Economic Geology* 97:695-732.
 Van Kranendonk MJ, Hickman AH, Smithies RH, Williams IR, Bagas L, Farrell TR (2006) Revised lithostratigraphy of Archean supracrustal and intrusive rocks in the northern Pilbara Craton, Western Australia. Western Australia Geological Survey, pp 57p.
 Van Kranendonk MJ, Smithies RH, Hickman AH, Champion D (2007) Review: secular tectonic evolution of Archean continental crust: interplay between horizontal and vertical processes in the formation of the Pilbara Craton, Australia. *Terra Nova* 19:1-38.
 Van Kranendonk MJ, Smithies RH, Hickman AH, Wingate MTD, Bodorkos S (2010) Evidence for Mesoarchean (~3.2Ga) rifting of the Pilbara Craton: The missing link in an early Precambrian Wilson cycle. *Precambrian Research* 177:145-161.

Potential for low cost bioprocessing of Co and Ni from Nkamouna lateritic ore.

D. Sulaiman J. Mulroy^{1,2}, Victoria S. Coker¹, Jonathan R. Lloyd¹, Paul F. Schofield², J. Fred W. Mosselmans³

¹The University of Manchester,

²The Natural History Museum

³Diamond Light Source

Abstract. The Nkamouna laterite, S.E. Cameroon, a uniquely Co-Ni enriched laterite hosts ~54Mt of proven and probable ore reserves. Co and Ni, plus local enrichments of Ba ($\leq 1\text{wt}\%$) and Ce ($\leq 0.35\text{wt}\%$), are associated with Mn(III/IV)-oxides e.g. lithiophorite, asbolane, and hollandite group phases. Biostimulation of indigenous microbial communities with a carbon source (glucose) under anaerobic conditions promoted generation of organic acids, e.g. acetate, through fermentation and provided dissimilatory metal reducing bacteria (DMRB) with potential electron donors to support reduction of $\text{Mn}^{3+}/\text{Mn}^{4+}$ ore minerals to Mn^{2+} causing release of target metals. In addition to standard geochemical analytical techniques a range of spectroscopic techniques have been used to confirm; 1) the mineralogy of the deposit with respect to Co, Ni and Ce and; 2) the divalent oxidation state of solid and soluble Co (and Mn) products generated through bioreduction of the ore. Complementary experiments on synthetic phases, e.g. Co-Ni-asbolane, with pure cultures of the DMRB *Geobacter sulfurreducens* showed total dissolution of the mineral phase. Preliminary results indicate a potential method for bioprocessing of the ore utilising organic carbon as the energy source and on scale-up could supplant glucose with low-cost organics e.g. cellulosic agricultural waste reducing reagent costs for metal extraction.

1 Introduction

Cobalt (Co) has been labelled “critical” by various national/supranational institutions (Slack et al. 2017; European Commission. 2017) and is ranked 10th out of 41 elements in terms of supply risk (BGS. 2015). 2018 supply was dominated the Democratic Republic of Congo (~60%) (Shedd. 2019) however historical political instability has previously caused supply shortages and elevated prices (Slack et al. 2017; Mudd et al. 2013). Concerns regarding the trade of conflict minerals at times mined using child labour (Diemel. 2018; de Haan and Geenen. 2016) have highlighted the importance of finding other sources of Co. Production has increased significantly from 1960 (~14.2kt) to 2018 (~140kt) (Kelly and Matos. 2017; Shedd. 2019) and demand is likely to increase further due to requirements for environmental- and hi-tech applications (Roberts and Gunn. 2013) such as superalloys for gas turbines and jet engines (Mouritz. 2012), rechargeable batteries for electric cars and electronics (Nitta et al. 2015; Perner and Vetter. 2015), catalysts for petrochemical processing (Javadli and de Klerk. 2012) and emerging uses e.g. magnetic

nanoparticles (Johannsen et al. 2005; Byrne et al. 2013) all serving an increasing world population with growing energy demands (United Nations. 2015; United Nations. 2018).

A potential alternative source is the Nkamouna laterite in S.E. Cameroon (Lambiv-Dzemua et al. 2013) which is the focus of this work. Bioprocessing methods for other lateritic ores have attracted recent attention as low-cost alternatives to conventional hydrometallurgical processes. Initial studies have focused on bioleaching with sulphuric acid generated from sulphur by acidophilic bacteria, e.g. *Acidithiobacillus* (Smith et al. 2016). Bioleaching via biostimulation of indigenous anaerobic neutrophiles remains a poorly characterized alternative. Here, organic carbon, including agricultural waste, e.g. corn stover (He et al. 2016) or palm-oil mill effluent (Rana et al. 2017), could be used to generate organic acids through cellulosic degradation (Ichikawa et al. 2018) aiding in breakdown of ore minerals (Lindsay et al. 1991) with further metal release promoted by DMRB e.g. *Geobacter* species (Lloyd. 2003).

2 Samples

There are two lateritic horizons of significant interest in terms of economic mineralization, the Lower Breccia (LB) and the Ferralite (FL). LB, (average thickness ~3m), is volumetrically subordinate to FL (average thickness ~12m), but hosts higher grades of Mn and Co (Fig. 1). Samples from both FL and LB horizons are used in this study in order to understand the differences in microbiomes vertically through the profile and their potential role in controlling trace metal solubility and mobility. Additional samples were selected from the upper limonite/ferruginous hardpan capping the laterite, a spoil heap and a highly Co- and Ni-enriched region of the southern trench.

3 Co-Ni Mineralogy

X-ray diffraction (XRD) was performed at the School of Earth and Environmental Sciences, University of Manchester, UK, in order to constrain mineralogy and mineralogical proportions and link to bulk-sample geochemical data obtained through X-ray Fluorescence. Lambiv-Dzemua et al. (2013) confirmed the presence of Co and Ni primarily in phylломanganates, e.g. lithiophorite, asbolane and intermediates thereof.

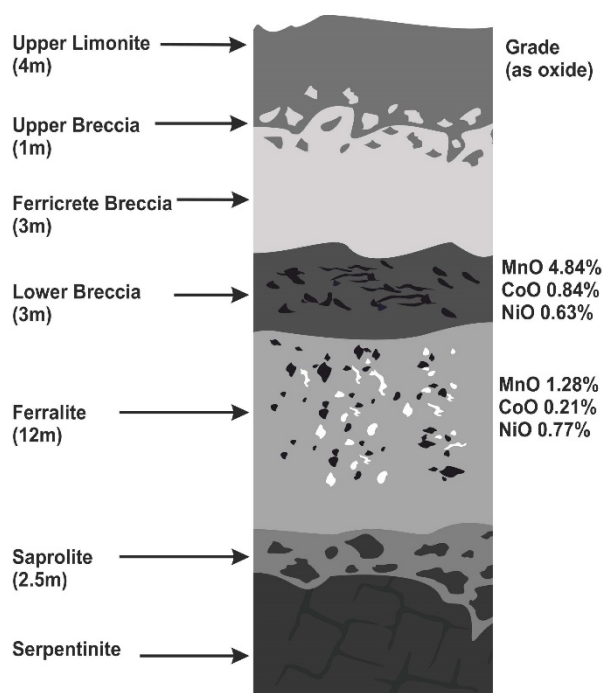


Figure 1. Profile through the Nkamouna laterite showing main horizons and thickness. Adapted from Lambiv-Dzemua et al. (2013).

Building on this work Co and Ni *K*-edge Extended X-ray Absorption Fine Structure (EXAFS) were performed at beamline I20, Diamond Light Source (DLS), UK, to fully constrain mineralogical sites. In lateritic environments Co is typically present as octahedrally coordinated ($_{oh}$) Co^{3+} (Manceau et al. 1986), with an ionic radius (IR) of $\sim 0.53\text{\AA}$, and has been previously demonstrated to be incorporated into the Mn-oxide sheet of phyllo-manganates due to similarities in IR with Mn^{3+}_{oh} ($\sim 0.58\text{\AA}$) and Mn^{4+}_{oh} ($\sim 0.54\text{\AA}$) (Manceau et al. 2000). Ni, exhibiting significant differences in both IR ($\sim 0.69\text{\AA}$, Ni^{2+}_{oh}) (Shannon, 1976) and valence, with respect to Mn^{3+}/Mn^{4+} occupies different sites dependent on a range of factors including height in profile and availability of mineral forming elements e.g. Mn and Al. These factors combined with redox conditions can either promote or inhibit incorporation of Ni into mineral phases.

Additional analyses performed on beamline 6.3.1 at the Advanced Light Source (ALS) synchrotron, Berkeley, CA, USA, allowed evaluation of valence and coordination of Mn in the ore through X-ray Absorption Spectroscopy (XAS) at the $L_{3,2}$ -edge. Speciation of Mn in the ore, as the main constituent of the Co- and Ni-bearing oxide phases, has implications regarding the stability of these poorly defined minerals and therefore consequences in terms of phase-deconstruction and metal release during applied bio-processing methods.

4 Ore Incubation and Bio-Extraction

Samples were incubated in a synthetic groundwater with glucose as a carbon source and monitored at selected time-points for changes in fluid chemistry. Changes in Fe^{2+} (labile and aqueous), aqueous Fe, Mn, Co, Ni and Ba, and volatile fatty acids (VFAs) were measured by

ferrozine assay, Inductively-Coupled Plasma Atomic-Emission Spectroscopy (ICP-AES) and Ion Chromatography, respectively. All samples showed Fe-reduction, release of Mn, Co, Ni and Ba, and generation of VFAs, e.g. formate, lactate and acetate, concomitant with reduction in pH. Differences in key geochemical parameters can be linked to a combination of factors including height in the laterite profile, mineralogy and geochemistry, which all affect the microbiome of each sampled region. Similarly, both rates of release and proportions of metals released can be linked to samples' vertical location as well as mineralogy and present considerations with respect to ore beneficiation especially where phases with high sorption capacity, e.g. Fe(III)-oxyhydroxides and clays, are abundant in the ore (Eylem et al. 1990; Ugwu et al. 2017).

5 Speciation of Bio-Extraction Products

Speciation of both Co and Mn in post-reduction aqueous phases was assessed through Co- and Mn *K*-edge X-ray Absorption Near Edge Structure (XANES), performed at beamline I20, DLS, UK. Results confirmed breakdown of Mn(III/IV)-oxides promoting release of Mn and Co to solution. Solid phase XANES analyses at the Mn and Ni *K*-edges were performed at beamline B18, DLS, UK and show both structural and speciation changes in the minerals with incubation. Supporting *L*-edge XAS results from 6.3.1, ALS, allowed characterisation of the solid phase, with respect to relative proportions of Mn^{4+} , Mn^{3+} and Mn^{2+} , with bulk reduction occurring relative to unstimulated ore. These techniques and their ability to define bioextraction products have underpinned this study.

6 Co-Ni-Asbolane Bioreduction

A poorly crystalline Co-Ni-asbolane, with high concentrations of Co and Ni, was synthesized by oxidative precipitation and characterized by XRD and Selected Area Electron Diffraction (SAED). Energy Dispersive X-ray Spectroscopy (EDS) and ICP-AES confirmed elemental proportions. XAS at the Mn-, Co- and Ni *L*-edges, performed at 6.3.1, ALS, allowed a tentative structure to be proposed based on speciation and coordination of Mn, Co and Ni.

The phase was suspended in bicarbonate buffer and reduced using a pure culture of *Geobacter sulfurreducens* using Na-acetate as electron donor. Dissolution and metal release was noted, consistent with the bioreduction mechanisms implied in the more complex sediment systems above.

7 Implications

Microbial consortia indigenous to Nkamouna ore offer an extraction method representing a way of integrating agro-industrial waste into the extraction of critical metals from lateritic ore and should offer cost-benefits by removing import and transport costs of elemental sulphur/sulphuric acid typically used in lateritic ore processing (Oxley et al.

2016). This will help offset the carbon footprint of reagent transport as well provide an extraction route with lower environmental risk. Gangue material from the ore, e.g. Fe-oxide rich waste, can be potentially repurposed for transformation into valuable by-products (Joshi et al. 2018).

Acknowledgements

This work has been done as part of the CoG3 project, funded as part of the NERC sponsored SoS Minerals project. Thanks are due to Richard Patrick, without whom I would not be doing this project, Gideon Lambiv-Dzemua for assistance during sample collection, Paul Lythgoe and Al Bewsher (SEES, UK) for performing ICP-AES and IC analyses, John Waters and Heath Bagshaw (SEES, UK) for aid in mineralogical analyses, Alpha N'Diaye (ALS, USA) for aid in XAS experimental setup, Shusaku Hayama (DLS, UK) for aid in XANES/EXAS experimental setup, Laura Newsome (CSM, UK) for help throughout the main experiment, and Agustin Solano-Arguedas and Dawn Buchanan (SEES, UK) for help on numerous beamtimes.

References

BGS (2015) Risk List 2015 British Geological Survey - Commodity Statistics <https://www.bgs.ac.uk/mineralsuk/statistics/risk-list.html>

Byrne JM, Coker VS, Wincott PL, Vaughan PL, Tuna F, Arenholz E, Van der Laan G, Patrick RAD, Lloyd JR, Telling ND (2013) Controlled cobalt doping in biogenic magnetite nanoparticles. *J R Soc Interface* 10

de Haan, J, Geenen, S (2016) Mining cooperatives in Eastern DRC: The interplay between historical power relations and formal institutions. *J Exis* 3:823-831

Diemel JA (2018) Authority and access to the cassiterite and coltan trade in Bukama Territory (DRC). *J Exis* 5:56-65

European Commission (2017) Communication from the Commission of the European Parliament, the Council, the European Economic and Social Committee and the Committee of the Regions on the 2017 list of Critical Raw Materials for the EU. <https://eur-lex.europa.eu/legal-content/EN/TXT/PDF/?uri=CELEX:52017DC0490&from=EN>

Eylem C, Erten HN, Götürk H (1990) Sorption-desorption behaviour of barium on clays. *J Environ Radioact* 11 (2):183-200

He T, Jiang Z, Wu P, Yi J, Li J, Hu C (2016) Fractionation for further conversion of raw corn stover to lactic acid. *Sci Rep* 6:38623 1-11

Ichikawa S, Ichihara M, Ito T, Isozaki K, Kosugi A, Karita S (2018) Glucose production from cellulose through biological simultaneous enzyme production and saccharification using recombinant bacteria expressing the β -glucosidase gene. *J Biosci Bioeng*. In Press

Javadli R, de Klerk A (2012) Desulfurization of heavy oil. *Appl Petrochem Res* 1:3-19

Johannsen M, Gneckeuvow U, Eckelt L, Feussner A, Waldofner N, Scholz R, Deger S, Wust P, Loening SA, Jordan A (2005) Clinical hyperthermia of prostate cancer using magnetic nanoparticles: Presentation of a new interstitial technique. *Int J Hyperth* 21:637-647

Joshi N, Filip J, Coker VS, Sadhukhan J, Safarik I, Bagshaw H, Lloyd JR (2018) Microbial reduction of natural Fe(III) minerals; toward the sustainable production of functional magnetic nanoparticles. *Front Environ Sci* 6:127.1-127.11

Kelly TD, Matos GR (2017) Historical statistics for mineral and material commodities in the United States (2017 version): USGS Data Series 140. <https://minerals.usgs.gov/minerals>

[/pubs/historical-statistics/](https://pubs/historical-statistics/)

Joshi N, Filip J, Coker VS, Sadhukhan J, Safarik I, Bagshaw H, Lloyd JR (2018) Microbial reduction of natural Fe(III) minerals; toward the sustainable production of functional magnetic nanoparticles. *Front Environ Sci* 6:127.1-127.11

Lambiv-Dzemua G, Gleeson S, Schofield PF (2013) Mineralogical characterization of the Nkamouna Co-Mn laterite ore, southeast Cameroon. *Min Dep* 48:155-171

Lindsay WL (1991) Iron oxide solubilisation by organic matter and its effect on iron availability. *Plant Soil* 130: 27-34

Lloyd JR (2003) Microbial reduction of metals and radionuclides. *FEMS Microbiol. Rev* 27:411-425

Manceau A, Llorca S, Calas G (1986) Structural Chemistry of Mn, Co and Ni in some natural manganese-oxides. *J Phys Colloques* 47; C8-703-C8-707

Manceau A, Schliegel ML, Musso ML, Sole VA, Gauhtier C, Petit PE, Tolard F (2000) Crystal chemistry of trace elements in natural and synthetic goethite. *Geochim Cosmochim Acta* 64:3643-3661

Mouritz AP (Ed.) (2012) Introduction to aerospace materials. In: *Introduction to aerospace materials: 1-14*. Online: Woodhead Publishing

Mudd GM, Weng Z, Jowitt SM, Turnbull ID, Graedel TE (2013) Quantifying the recoverable resources of by-product metals: The case of cobalt. *Ore Geol. Rev.* 55:87-98

Nitta N, Wu F, Lee JT, Yushin G (2014) Li-ion battery materials: present and future. *Mater Today* 18 (5):252-264

Oxley A, Smith ME, Caceres O (2016) Why heap-leach nickel laterites? *Min. Eng.* 88:53-60

Perner A, Vetter J (2015) 8 – Lithium-ion batteries for hybrid electric vehicles and battery electric vehicles. In: SCROSATI B, GARCHE J, TILLMETZ W (Eds.) *Advances in battery technologies for electric vehicles: 173-190*. Online: Woodhead Publishing

Rana S, Singh L, Wahid Z, Liu H (2017) A recent overview of palm oil mill effluent management via bioreactor configurations. *Curr Pollution Rep* 3:254-267

Shannon RD (1976) Revised effective ionic radii and systematic studies of interatomic distances in halides and chalcogenides. *Acta Cryst A* 32:751-767

Shedd KB (2018) USGS Mineral Commodity Surveys – Cobalt 2018. Available: <https://minerals.usgs.gov/minerals/pubs/commodity/cobalt/mcs-2018-cobal.pdf>

Shedd KB (2019) USGS Mineral Commodity Surveys – Cobalt 2019. Available: <https://minerals.usgs.gov/minerals/pubs/commodity/cobalt/mcs-2019-cobal.pdf>

Slack JF, Kimball BE, Shedd KB (2017) Cobalt. In: SCHULZ KJ, DEYOUNG JH, SEAL RR, BRADLEY DC (eds.). *Critical mineral resources of the United States - economic and environmental geology and prospects for future supply*. US Geological Survey Professional Paper 1802: F1-F40

Smith SL, Grail BM, Johnson BD (2016) Reductive bioprocessing of cobalt-bearing limonitic laterites. *Min Eng* 106: 86-90

Ugwu IM, Sherman DM (2017) Irreversibility of sorption of cobalt to goethite (α -FeOOH) and disparities in dissolution of aged synthetic Co-goethite. *Chem Geol* 467:168-176

United Nations (2015) World population prospects – Key findings and advance tables. https://esa.un.org/unpd/wpp/publications/files/key_findings_wpp_2015.pdf

United Nations (2018) World urbanization prospects 2018. <https://population.un.org/wup/Publications/>

Sulphide trace element, sulphur isotope and hydrothermal alteration studies in the Juomasuo and Hangaslampi Au-Co deposits, Kuusamo belt, northeastern Finland

Mikael Vasilopoulos, Jukka-Pekka Ranta
University of Oulu, Finland

Ferenc Molnár, Hugh O'Brien, Yann Lahaye
Geological Survey of Finland, Espoo, Finland

Abstract. The Juomasuo and Hangaslampi Au-Co deposits are hosted by the Paleoproterozoic Kuusamo belt in northeastern Finland. Sulphur isotope and trace element data from sulphides indicate that the geochemically distinct, Au-Co and Co-only enrichments were formed from fluids of different origin. Accordingly, sericite alteration is typical in the zones of the Au-Co enrichment, whereas the chlorite-biotite-amphibole alteration occurs in relation to the Co-only mineralization. Variation in the composition of host rocks does not seem to have a strong control on the type of mineralization.

1 Introduction

Finland currently produces 66% of the EU cobalt supply, extracted from sulphide ores from the Sotkamo, Kevitsa, Hitura and Kylahti mines (European Commission 2018). With the cobalt demand related to rechargeable batteries expected to rise in the following years, the importance of Finland's cobalt resources becomes even more pronounced. A better understanding of the formation processes of the already known Co-rich deposits is needed to enhance successes of exploration for new deposits.

This study concentrates on the Juomasuo and Hangaslampi Au-Co deposits, which are located in northeastern Finland, approximately 45 km north of the town of Kuusamo (Fig. 1). These deposits are situated in the Paleoproterozoic Kuusamo belt (KB) and are part of the Kuusamo-Kuolajärvi orogenic gold metallogenic area (Eilu et al. 2012), comprising several epigenetic Au-Co-Cu occurrences (Pankka 1992; Vanhanen 2001). Previous studies proposed different genetic classifications for the Au-Co-Cu mineralization including iron-oxide-copper-gold (IOCG), orogenic gold with atypical metal association, epithermal gold, Blackbird-type and syngenetic type (Pankka 1992; Vanhanen 2001; Eilu & Pankka 2009; Slack et al. 2012). The Juomasuo deposit is the most important known epigenetic-hydrothermal Au-Co deposit in the Kuusamo belt. Hangaslampi is situated approximately 1 km south from Juomasuo and is also mainly enriched in Au and Co. Cu, Mo and REE are the most typical associated trace metals in these deposits. For the purpose of better understanding the hydrothermal processes that led to

the mineralization in Juomasuo and Hangaslampi we applied *in situ* multi- and single collector LA-ICP-MS

analytical techniques to study sulphur isotope and trace element characteristics of sulphide minerals from these deposits. Additionally, we utilized whole-rock geochemical data in order to classify the heavily altered host rocks and to study the control of the alteration mineralogy on the mineralization types with different metal associations at Juomasuo.

2 Regional geological setting

The KB is a part of the larger Karasjok-Kuusamo-Lake Onega belt that extends from northern Norway to the Lake Onega in Russia (Pankka 1992). The rocks comprising this belt are part of the Karelian supracrustal formations. Their age ranges from 2.5 to 1.9 Ga (Silvenoinen 1972, 1992). The KB was at least partially formed in an intracratonic failed rift setting related to the Paleoproterozoic breakup of the Archean Karelian craton (Hanski & Huhma 2005). The KB consists of several formations of volcanic and sedimentary origin,

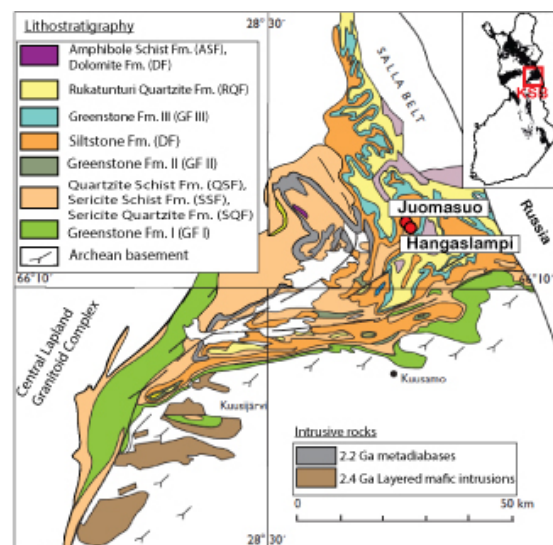


Figure 1. Simplified geological map of the Kuusamo belt. Modified after Laajoki (2015) and Vanhanen (2001).

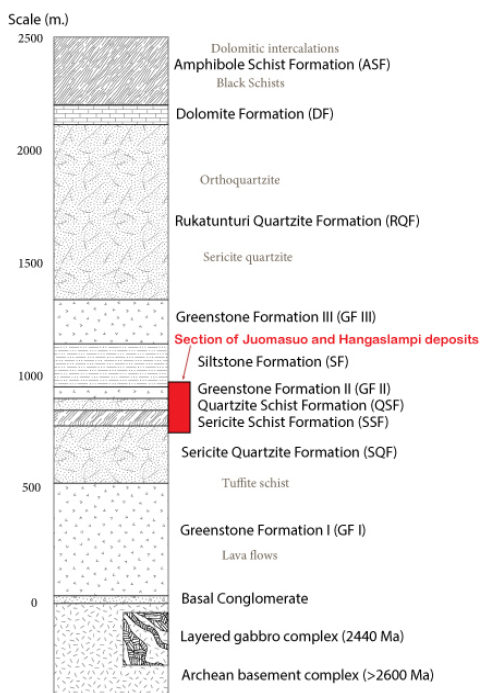


Figure 2. Stratigraphic column of the Kuusamo belt showing the location of Juomasuo and Hangaslampi in the stratigraphy. Modified after Silvennoinen (1972) and Vanhanen (2001).

including three or four stages of mafic volcanism with associated mafic sills and dykes (Pankka 1992). The stratigraphy of the Kuusamo belt was defined by Silvennoinen (1972) (Fig.2).

The stratigraphic sequence of the KB underwent deformation and regional metamorphism during the Svecofennian orogeny (1.9-1.8 Ga; Silvennoinen 1972, 1992). The metamorphic grades vary from lower greenschist facies in the central parts of the belt to upper amphibolite facies in the western parts, near the contact with the Central Lapland Granitoid Complex. Higher metamorphic grades are also present in the eastern part of the KB. Mineralization has been mostly encountered near the upper and lower boundaries of the Greenstone Formation II (GF II), but some mineralization is also hosted by the upper part of the Rukatunturi Quartzite Formation (RQF) (Vanhanen 1990, 2001) (Fig. 2).

3 Geology and mineralogy of the Juomasuo and Hangaslampi Au-Co deposits

The host rocks of the Juomasuo deposit are characterised by strong albitisation but the mineralised zones also contain quartz, chlorite, biotite, sericite, carbonate, amphibole and talc in addition to albite. The most abundant sulphide is pyrrhotite followed by pyrite and lesser chalcopyrite. Cobaltite can be found in the Co-rich parts of the ore as inclusions in pyrrhotite and sometimes in pyrite. Cobaltpentlandite is also present mainly as exsolutions in pyrrhotite. Molybdenite, rutile, magnetite, native Au and tellurides (altaite, tellurobismuthite and melonite) are noteworthy accessories in the deposit. The Juomasuo deposit consists of one major mineralized zone and several

smaller adjacent sulphidized zones (Vanhanen 2001). The total mineral resource estimate for the Juomasuo deposit is 2.37 million tonnes grading at 4.6 g/t Au and 0.13 wt% Co and an additional 5.04 million tonnes of Co resources without Au grading at 0.12 wt% Co (Dragon Mining 2014).

The orebodies at Hangaslampi occur in a local antiform structure just below the GF II (Vanhanen 2001). The resource estimates amount to 403 thousand tonnes grading at 5.1 g/t Au and 0.06 wt% Co and an additional 180 thousand tonnes of ore grading at 0.1 wt% Co without Au (Dragon Mining 2014). The gangue minerals at Hangaslampi comprise albite, quartz, chlorite, biotite, sericite, lesser carbonate, amphibole and accessory tourmaline, apatite and zircon. The most common sulphide is pyrite. Pyrrhotite has a weak presence and is mostly found as inclusions in pyrite and magnetite and sometimes as disseminated grains in the silicates where it is occasionally associated with chalcopyrite. Cobaltite is rare in Hangaslampi and cobaltpentlandite occurs sporadically as exsolutions in the disseminated pyrrhotite. Magnetite is more widespread compared to Juomasuo. Other common accessory ore minerals at Hangaslampi include molybdenite and some minor tellurides.

4 Lithogeochemistry at the Juomasuo deposit

Previous studies have described the heavily altered and metamorphosed rocks at Juomasuo and Hangaslampi mainly on the basis of the dominating alteration minerals (Pankka 1992; Vanhanen 2001). For the Juomasuo deposit, the Dragon Mining Ltd. provided a detailed lithogeochemical dataset for the purpose of our studies and we utilized this database for the geochemical classification of the protoliths of the altered rocks. We combined drill core observations with immobile element ratios and recognized the following six rock types: ultramafic rock, mafic rock, intermediate rock, felsic rock, metasediment and albitite (Fig.3). By plotting the samples belonging to the Au-Co and Co-only type of ores on the Nb/Y-Zr/TiO₂ discrimination diagram, it is evident that both types of mineralization are present in all of the rock types, apart from the albitites and the ultramafic rocks (Fig. 3).

A second application of the lithogeochemical database was to calculate Molar Element Ratios (MER) to determine the control of the alteration mineralogy on the different types of mineralization. The MER diagrams (Fig. 4) show that different types of alteration affected different rock types. By plotting the gold and cobalt grades together with the MER data for the metavolcanic rocks it seems that gold enrichment is mainly associated with sericite alteration and much less with chlorite-biotite alteration (Fig. 4). Co enrichment is strongly associated with chlorite-biotite and amphibole alteration and additionally with sericite alteration (Fig. 4). Similar trends can be demonstrated for the metasediments.

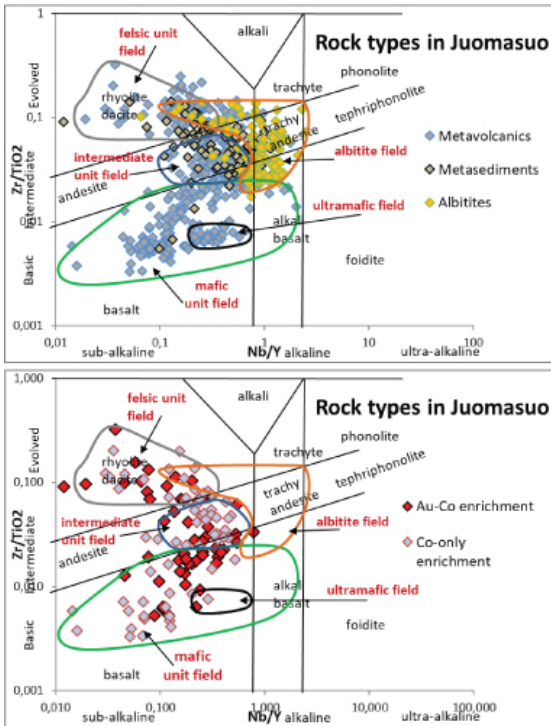


Figure 3. Fields for each rock unit recognized at Juomasuo on the Nb/Y-Zr/TiO₂ discrimination diagram (Pearce, 1996); Metasediments do not have a separate field as they are a mixture of both felsic and mafic components.

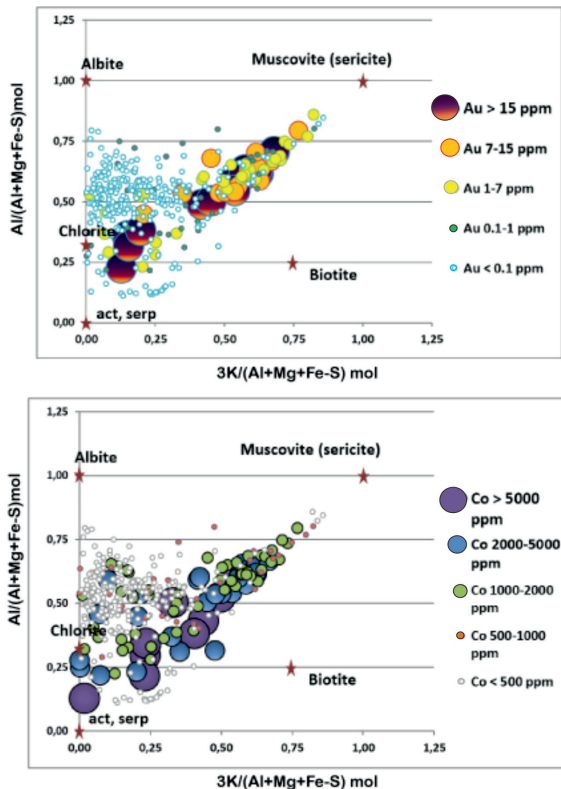


Figure 4. MER diagrams for metavolcanic Juomasuo samples. The selected molar elemental ratios of the axes represent well the alteration mineralogy of Juomasuo by allocating a specific position in the diagram to the most important alteration minerals.

5 Sulphur isotope and trace element data

Systematic sulphur isotope analyses were performed on pyrite, pyrrhotite and chalcopyrite from Juomasuo and Hangaslampi with the use of multi-collector LA-ICP-MS. Trace element contents of the same sulphide grains were determined by single-collector LA-ICP-MS analyses. Analytical spots for sulphur isotope and trace element determination were placed next to each other. Matrix-matched sulphide standards were used during these analyses.

Sulphides from the ore zones at Juomasuo have $\delta^{34}\text{S}$ values between -2.6 and +6.9 (median +3.45) and at Hangaslampi between -0.9 and +9 (median +5.3). Sulphides from barren samples range from -0.5 to +13.5. Whereas most of the values are positive, there is a shift to negative or near-zero values in some sulphides in both deposits (Fig. 5). By examining the Co/Ni ratio of pyrite grains from different mineralization types, distinct mineralization stages become evident: one represented by distinctly high Co/Ni ratios and one with low Co/Ni ratios. Pyrite grains with high Co/Ni ratios show a relatively narrow range of positive $\delta^{34}\text{S}$ values, whereas the grains with low Co/Ni ratios have a wider range of $\delta^{34}\text{S}$ values including all the negative ones (Fig. 5). A similar trend is present for the Se/S ratios of the two stages with the high Co/Ni pyrite having a narrow range of low Se/S ratio values and the low Co/Ni pyrite having

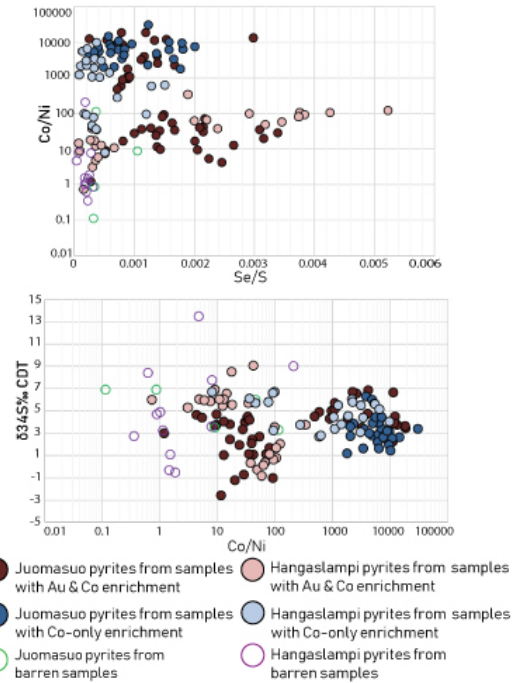


Figure 5. Results of sulphur isotope and trace element analyses on pyrite from Juomasuo and Hangaslampi.

a wider range. Other trace elements also vary systematically within the two Co/Ni ratio categories (Fig. 6). The Co/Ni ratio is mostly controlled by the Ni content of sulphides with differences up to two orders of magnitude (Fig. 6).

The wider range of $\delta^{34}\text{S}$, Se/S ratios and the relatively

high Ni, Se and Te contents in the low Co/Ni category could indicate a mixing of different fluid and sulphur sources. The low Co/Ni stage comprises mainly Au-Co mineralization in both deposits. The high Co/Ni category on the other hand has a narrow range of $\delta^{34}\text{S}$ and Se/S ratios and low Ni, Se and Te contents. The high Co/Ni stage could thus be attributed to a single hydrothermal event and a homogeneous sulphur source. The high Co/Ni stage mainly includes Co-only mineralization with some Au-Co mineralization included in Juomasuo.

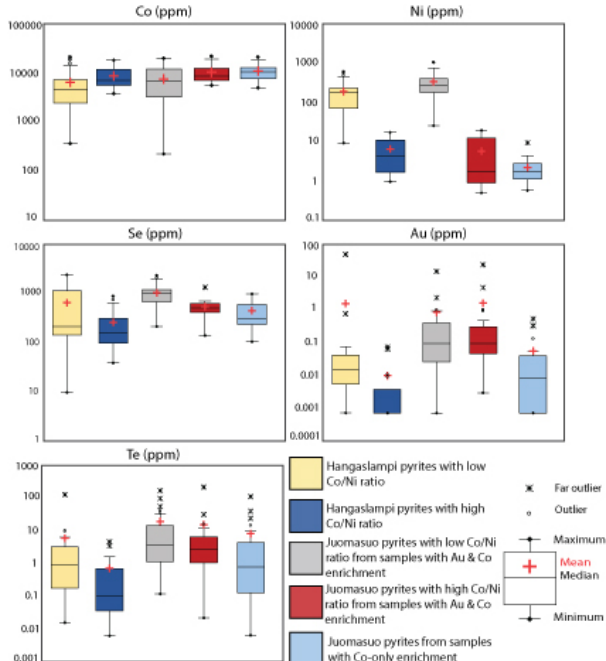


Figure 6. Box and whisker plots with logarithmic scales for analyzed pyrite from Juomasuo and Hangaslampi.

6 Summary and conclusions

The Juomasuo and Hangaslampi Au-Co deposits are characterized by multi-stage hydrothermal processes that are recorded in the sulphur isotope and trace element characteristics of sulphides. A hydrothermal stage responsible for the accumulation of the Co-only ores in both deposits, and some Au-Co mineralization in Juomasuo, deposited pyrite characterized by high Co/Ni ratios, low Se/S ratios and positive $\delta^{34}\text{S}$ values showing a relatively narrow range of values. Pyrite from a different stage of hydrothermal activity that created mostly Au-Co mineralization in both deposits is characterised by low Co/Ni ratios, a wide range of Se/S ratios, $\delta^{34}\text{S}$ values and high Ni, Se and Te contents. The distinct sources of parent fluids are also supported by contrasting alteration parageneses of the same lithologies depending on enrichment type. The Au-Co mineralization in Juomasuo mainly occurs within sericite alteration zones whereas the Co-only mineralization is hosted by chlorite-biotite-amphibole alteration. These results are in agreement with the U-Pb dating of hydrothermal monazite from Hangaslampi suggesting two major stages of mineralization, one at 1.85 and the other at 1.81 Ga (Pohjola et al., 2017).

Acknowledgements

This work was supported by grants from the Vilho, Yrjö and Kalle Väisälä foundation, the K.H. Renlund foundation and by the Academy of Finland # 281670 – MinSysPro project.

References

- Dragon Mining (2014) Asx announcement, 18 March 2014: Resource updates lift Kuusamo ounces. http://www.dragonmining.com/static/files/41/2014-03-18_resource_updates_lift_kuusamo_ounces.pdf Accessed 01 March 2019.
- Eilu P, Korsakova M, Äikäs O (2012) F040 Kuusamo-Kuolajärvi Co-Au. In: Eilu, P (Ed.) Mineral deposits and metallogeny of Fennoscandia. Geological Survey of Finland, Special Paper 53: 306-310.
- Eilu P & Pankka H (2009) FINGOLD – A public database on gold deposits in Finland. Version 1.0. Geological Survey of Finland. Digital data product 4.
- European Commission (2018) Report on Raw Materials for Battery Applications (SWD (2018) 245/2 final) <https://ec.europa.eu/transport/sites/transport/files/3rd-mobility-pack/swd20180245.pdf> Accessed 02 March 2019
- Hanski E & Huhma H (2005) Central Lapland greenstone belt. In: Lehtinen, M., Nurmi, P.A. & Ramo, O.T. (Eds.) Precambrian Geology of Finland – Key to the Evolution of the Fennoscandian Shield. Amsterdam, Elsevier: 139–194.
- Laajoki K (2005) Chapter 7 Karelian supracrustal rocks in Lehtinen M, Nurmi PA, Rämö OT (ed.) Developments in Precambrian Geology. Elsevier, volume 14: 279-341.
- Pankka H (1992) Geology and mineralogy of Au-Co-U deposits in the proterozoic Kuusamo volcanosedimentary belt, northeastern Finland. A dissertation. Michigan Technological University, Geology.
- Pearce JA (1996) A users guide to basalt discrimination diagrams. In: Wyman, D. A. (Eds.) Trace Element Geochemistry of Volcanic Rocks: Applications for Massive Sulphide Exploration. Geol. Assoc. Canada, Short Course Notes 12: 79-113.
- Pohjola E, Molnár F, O'Brien H, Huhma H, Tiljander, M, Sorjonen-Ward P, Lukkari S, Johanson B (2017) U-Pb geochronology of monazite from the Hangaslampi gold deposit in the Paleoproterozoic Kuusamo schist belt, northern Finland: implications for dating multi-stage mineralizing events. Proceedings of the 14th SGA Biennial Meeting, vol. 3: 1039-1042.
- Silvennoinen A (1972) On the stratigraphic and structural geology of the Rukatunturi area, northeastern Finland. Geological Survey of Finland, Bulletin 257.
- Silvennoinen A (1992) General geological setting and deep fracture structures in the Kuusamo-Kuolajärvi-Paanajärvi area. In: Silvennoinen, A (ed.) Deep fractures in the Paanajärvi-Kuusamo-Kuolajärvi area. Proceedings of a Finnish-Soviet Symposium in Finland on September 18-21, 1989. Geological Survey of Finland, Special Paper 13: 5-10.
- Slack JF (2012) Strata-bound Fe-Co-Cu-Au-Bi-Y-REE deposits of the Idaho Copper Belt: multistage hydrothermal mineralization in a magmatic-related iron oxide-copper-gold system. Economic Geology 107: 1089-1113.
- Vanhänen, E (1990) Sulfidimalmi- ja kultatutkimukset Kuusamon ja Sallan kuntien alueilla vuosina 1983-1988 kohteissa Vilkaslampi, Painanteenniitty, Maitokoski, Perttuma-aapa, Juhonlampi, Pulealampi, Manalanniemi (In Finnish). Geological Survey of Finland, Unpublished report M19/4524/-90/2/10.
- Vanhänen E (2001) Geology, mineralogy and geochemistry of the Fe-Co-Au-(U) deposits in the Paleoproterozoic Kuusamo Schists Belt, northeastern Finland. Geological Survey of Finland Bulletin 399.

Trace elements in Cu-(Fe)-S sulphides from inactive hydrothermal vent sites at TAG, Mid-Atlantic Ridge

Berit Lehrmann, Bramley J. Murton
National Oceanography Centre-Southampton, UK

Matthew J. Cooper, J. Andy Milton
School of Ocean and Earth Science, University of Southampton, UK

Abstract. Metals such as cobalt, tin, germanium, silver and selenium that are vital in high-technology applications and for transition to a low-carbon economy are frequently termed 'critical'. To determine whether seafloor massive sulphide (SMS) represent a potential future source of critical metals, copper minerals from hydrothermal mounds at different stage of development and age, located in the TAG area (Mid-Atlantic Ridge), were analysed by in-situ laser ablation inductively coupled plasma-mass spectrometry (LA-ICP-MS). The results show that critical metals reach concentrations up to several hundreds of ppm. However, the distribution of these elements is very heterogeneous even on the scale of a single sample suggesting. Future mining operation of SMS will target these deposit primary for base and precious metals with critical metals being extract as by-products.

1 Introduction

There is growing demand for a range of minerals required in green energy and high-tech applications. These are typically referred to a 'critical'. (Zepf et al 2014). Land-based mining activities are increasingly focusing on more remote and technically challenging environments (Carvalho 2017) that often result in a higher environmental impact. Seafloor massive sulphide deposits, which form through hydrothermal venting in today's oceans, may contribute to the resource of critical metals in the future (Hannington et al 2011). While recent estimates of the resource potential for base and precious metals of modern SMS are 600 Mt with a median grade of 3 wt.-% copper, 9 wt.-% zinc, 2 g/t gold and 100 g/t silver (Monecke et al 2016), the inventory of critical metals associated with SMS and their fate during alteration processes are poorly understood.

This paper presents insights into the trace element distribution in copper sulphide (chalcopyrite, idaite, chalcocite and covellite) minerals from different aged, inactive SMS sites from the TAG hydrothermal area at 26°09'N on the Mid-Atlantic Ridge (Fig. 1). Our in-situ LA-ICP-MS data show that the trace element budget of fresh chimney samples and weathered sulphide blocks differs by several orders of magnitude. In addition, a variation in trace elements between surface and sub-surface samples of the same mound can be observed. Such information is critical in the decision process for economically feasible exploitation strategies of SMS where critical metals will contribute to the overall resource as by-products..

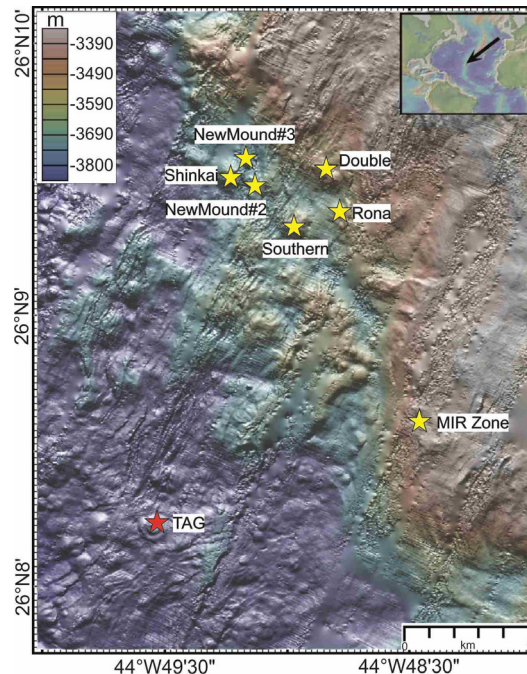


Figure 1. Bathymetric map (data source GeoMapApp: KN142-05 (TAG94), DSL120 2m grid White) of the TAG hydrothermal area and the location of the active and inactive hydrothermal sites studied in this project. The inset shows the locations on the Mid-Atlantic Ridge.

2 Geological Setting

The TAG hydrothermal area is one of the largest and best studied hydrothermal systems on earth (Rona et al 1986, 1993; Tivey et al 2003; Humphris et al 2015). Several active and relict hydrothermal sites, predominantly forming sulphide mounds are present in an area of 5x5 km. These mounds vary in size, stage of development and age. The active TAG mound, located in the southwest of the area, is currently in an active high-temperature stage, i.e. metal-rich black smoker fluids of ~365°C are discharged through multiple chimneys (Humphris et al 2015). North-northeast of the TAG mound several hydrothermal extinct mounds occur: Southern, Rona, Double, New Mound #2, New Mound #3 and Shinkai. Radiometric dating of sulphides from Double and Shinkai yield ages of 50 ka and 2-23 ka, respectively (Lalou et al 1995). Based on the proximity of New Mound #2 and #3 to Shinkai and Southern and Rona to Double it is assumed that these mounds are of similar development stages as the slope angles of the mounds, indicating the degree of anhydrite dissolution at depth, are very similar (Hannington et al 1998, Murton et al

2018).

3 Methodology

Thirteen copper-rich surface and subsurface samples, collected during expedition JC138 on *RRS James Cook* using a multipurpose robotic underwater vehicle and a robotic lander-type seafloor drill were investigated in this study. Samples were described macroscopically and studied under transmitted and reflected light to reveal their mineralogical composition.

Trace elements were analysed by LA-ICP-MS using a New Wave UP 193FX laser coupled to a Thermo Scientific XSeries 2 quadrupole ICP-MS at the University of Southampton. The ICP-MS operated with a plasma power of 1350 W, He (1 l/min) and N (0.01 l/min) were used as carrier gases while Ar acted as plasma (13 l/min) and auxiliary gas (0.8 l/min). Laser pulse frequency was set at 5 HZ and a laser energy density of 5-6 J/cm² was chosen. The total analysis time for each spot was 45 s, including 20 s for gas blank analysis. A beam diameter of typically 25 µm and on occasion of 18 µm was used according to crystal size of the different copper sulphides.

In total 34 isotopes were monitored for quantitative analysis as well as mass positions of ⁷⁷ArCl and ⁸³Kr in order to quantify any interferences on ⁸²Se. NIST-610, NIST-612 (Jochum et al 2005) and MASS-1 (Wilson et al 2002) were used as external calibration standard. Analytical precision was monitored by the repeated analysis of the standards yielding <5% RSD for reported elements in this study on NIST610 (except Se 7.1 %) and <10% RSD on MASS-1. To monitor the instrument drift the sulphide standards were analysed for several times during an analytical day. After measurement the trace element concentrations were calculated with the PlasmaLab 2.6.1.335 software (Thermo Scientific) using Fe as internal standard determined by electron microprobe analysis on a Cameca-SX100 at the University of Edinburgh. Minimum detection limits were calculated following the protocol of Longerich et al 1996.

4 Results

4.1 Petrography

Massive sulphides recovered from the surface of Shinkai, New Mound #2 and #3 comprise chimneys and fragments of chimney material (Fig. 2A) whereas samples from Southern and Rona Mound comprise sulphide breccia and massive sulphide blocks (Fig. 2B). These samples are quite similar from drill core samples obtained from Southern, Rona and MIR Zone.

The interior of the chimney sample comprises an orifice of predominately chalcopyrite with an intercalated layer of idaite (Fig. 3A). Extending outwards, coarse-grained tetrahedral chalcopyrite is present that is altered to covellite along grain boundaries.

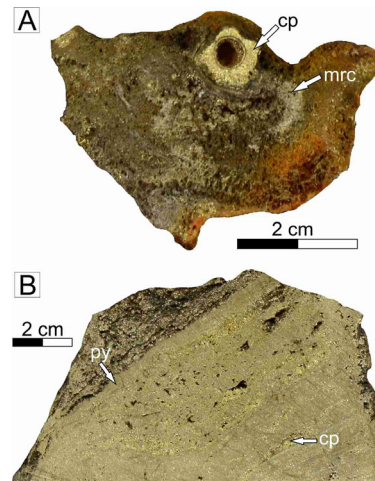


Figure 2. Representative sulphides obtained from inactive sulphide mounds from the TAG area. **(A)** Chimney with a chalcopyrite-rich orifice surrounded by marcasite; New Mound #2, 55-1A. **(B)** Massive sulphide talus comprising of pyrite with intercalated layers of chalcopyrite; Southern Mound, 21-3. Mineral abbreviations: cp: chalcopyrite, py: pyrite, mrc: marcasite.

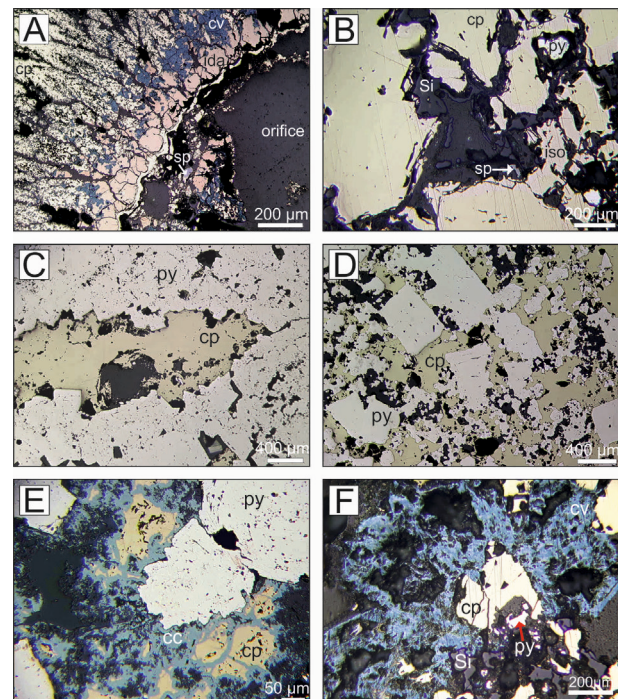


Figure 3. Reflected photomicrographs of representative mineral assemblages from sulphides samples from inactive mounds. **(A)** Cross-section of chimney comprising of tetrahedral shaped coarse-grained chalcopyrite, subhedral idaite altered to covellite along grain boundaries; New Mound #2, 55-1A. **(B)** Coarse-grained chalcopyrite with exsolution lamella of isocubanite and coated by a thin layer of amorphous silica; New Mound #3, 55-6A. **(C)** Massive recrystallized pyrite with intercalated layers of chalcopyrite; Southern Mound, 50-14. **(D)** Aggregates of pyrite surrounded by chalcopyrite; MIR Zone, 73-18. **(E)** Pyrite clasts surrounded by chalcopyrite that is altered to chalcocite along micro-fractures; Rona Mound, 45-7C. **(F)** Chalcopyrite surrounded by covellite with traces of amorphous silica and pyrite; New Mound #3, 55-6A. Mineral abbreviations: cp: chalcopyrite, iso: isocubanite/cubanite, ida: idaite, cc: chalcocite, cv: covellite, py: pyrite, sp: sphalerite, Si: amorphous silica.

Other chimney material from New Mound #3 comprises coarse-grained chalcopyrite that shows exsolution

lamella of isocubanite (Fig. 3B). Surface and subsurface samples from Southern, Rona and MIR Zone are formed of massive recrystallised pyrite that is intercalated with chalcopyrite layers (Fig. 3C) or coarse-grained cubic pyrite that is surrounded by massive chalcopyrite (Fig. 3D). Chalcopyrite is either altered to chalcocite along micro-fractures (Fig. 3E) or is surrounded by aggregates of fibrous covellite (Fig. 3F).

4.2 Trace element inventory of copper sulphides from different sites

Cobalt concentrations differ between chalcopyrite and other copper phases. While chimney material from New Mound #3 (55-6A) has on average cobalt content of 177 ± 30 ppm ($\pm 1\sigma$), chalcopyrite from the chimney of New Mound #2 (55-1A) yields concentrations of 0.12 ± 0.07 ppm cobalt (Fig. 4A). The chalcopyrite from the sub-surface samples at Southern and Rona yield an order of magnitude higher cobalt concentration, of 0.84 ± 0.33 ppm and 3.28 ± 3.62 ppm, respectively.

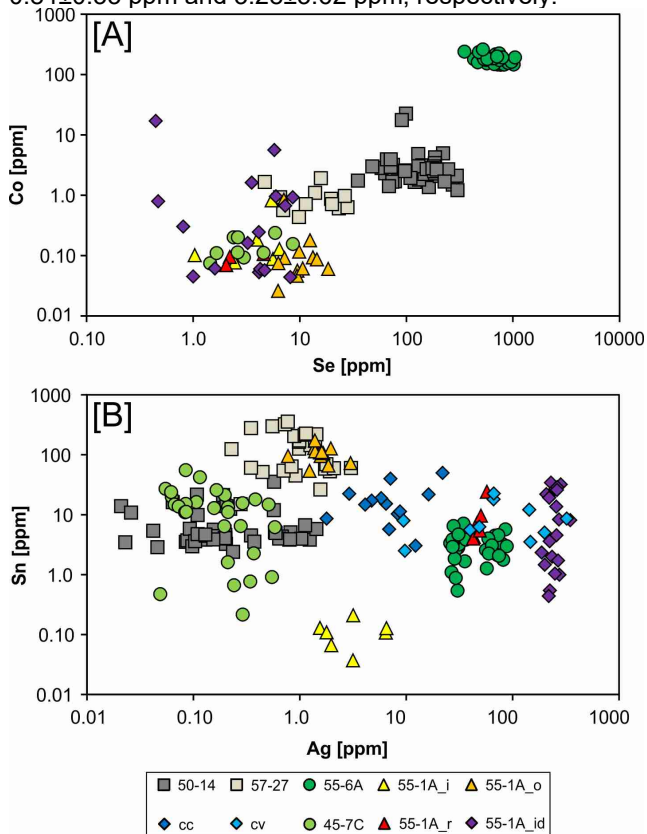


Figure 4. Log-log plots of trace elements concentrations in copper minerals from several inactive sulphide mounds at the TAG area. (A) Cobalt (Co) versus Selenium (Se) and (B) Tin (Sn) versus silver (Ag). Chimney 55-6A and 55-1A differ with regards to their trace element concentration, while sub-surface samples 50-14 and 57-27 show similar trace element pattern. Copper phases other than chalcopyrite can be quite enriched in silver.

A similar pattern can be observed for selenium concentrations. Again the chimney (55-6A) yields the highest concentration of 679 ± 152 ppm Se, the other chimney (55-1A) shows average concentrations between 4.17 ± 1.9 and 10.4 ± 3.6 ppm. Again the sub-surface

samples have intermediate selenium concentrations.

Tin concentrations are very similar in the majority of samples and copper phases (Fig. 4B). One sub-surface sample (57-27) and one generation of chalcopyrite from a chimney (55-1A) yield very high tin concentrations of 140 ± 97 ppm and 104 ± 30 ppm, respectively. In contrast chalcopyrite from the inner conduit of 55-1A shows the lowest tin concentrations (0.11 ± 0.05 ppm).

Silver is predominately enriched in idaite, chalcocite and covellite rather than in chalcopyrite with the highest concentration being detected in idaite (246 ± 35 ppm). The only exception is chalcopyrite from the other chimney (55-6A) where a concentration range between 26-89 ppm is observed.

Other elements such as gallium, germanium, indium and bismuth also show elevated concentrations of up to several hundreds of ppm in some samples and copper phases.

4.3 Trace element concentrations in one chimney sample

Trace element distribution is not only heterogeneous on a mound scale but also varies within a single sample. This can be observed in different chalcopyrite generations and idaite from chimney 55-1A (Fig. 5). While silver and cobalt yield the highest concentrations in the idaite, selenium and tin are enriched in the chalcopyrite of zone two. Chalcopyrite from the inner layer (zone 4) has elevated concentrations of germanium (287 ± 136 ppm).

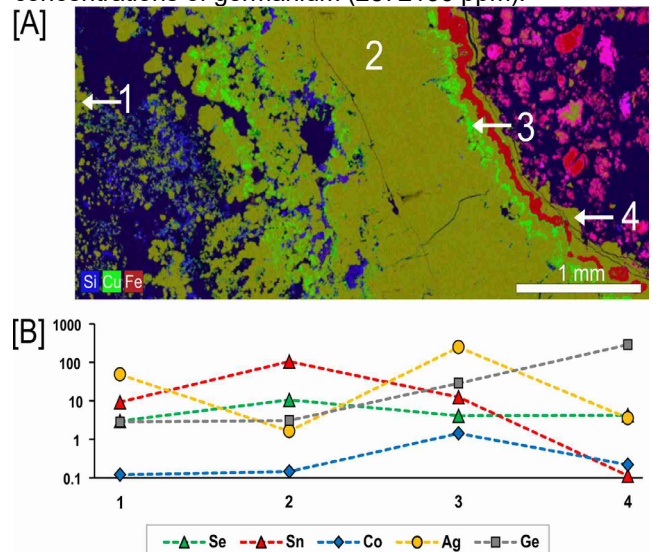


Figure 5. Variations of trace element concentrations within one chimney samples from New Mound #2. (A) Scanning electron microprobe map illustrating the major element distribution on the scale of several mm. Zone 1 is coarse grained chalcopyrite (referred to as 55-1A_r in figure 4), zone 2 is massive chalcopyrite forming the outer layer of the orifice (55-1A_o), zone 3 comprises idaite and zone 4 is chalcopyrite that forms the inner layer of the orifice (55-1A_i). (B) Log-line plot showing the change of concentrations across the four zones. Concentrations plotted are the mean values.

5 Conclusions

Bulk geochemical data for fresh chimney samples and sub-surface drill core from the literature suggest that

chimney samples from SMS deposits have the highest variety and concentrations of trace elements (Monecke et al 2016). However, in-situ LA-ICP-MS data provides further insight. Certain chimneys are enriched in high-temperature trace elements such as selenium and tin (Maslennikov et al 2009). Notably, some recrystallised chalcopyrite from subsurface samples can also exhibit this trace element signature whereas other sub-surface samples as well as surface material do not appear to host any significant quantities of trace elements. Secondary copper minerals can incorporate high concentrations of silver but do acquire many other trace elements.

In summary, our data show that copper phases can host critical metals at concentrations of up to several orders of magnitude, but their distribution is highly variable even at the scale of individual samples.

Acknowledgements

We thank the officers and crew of the *RRS James Cook*, and the shipboard technical and scientific party for their constant help and support throughout expedition JC138. Thanks to Duncan Muir from Cardiff University (SEM-time) and Chris Hayward from University of Edinburgh (EMPA-time). This work was funded by the European Union Seventh Framework Program (EU-FP7) “Blue Mining: breakthrough solutions for the sustainable deep-sea mining value chain” under grant No. 604500.

References

- Carvalho FP (2017) Mining industry and sustainable development: time for change. *Food and Energy Secur.* 6:61-77. doi: 10.1002/fes3.109
- Hannington MD, De Ronde CEJ, Petersen S (2005) Sea-Floor Tectonics and Submarine Hydrothermal Systems. In: Hedenquist JW, Thompson JFH, Goldfarb RJ, Richards JP (eds) *Economic Geology One Hundredth Anniversary Volume*, Soc. Econ. Geol., Littleton, pp 111–141
- Hannington M, Jamieson J, Monecke T, Petersen S, Beaulieu S (2011) The abundance of seafloor massive sulphide deposits. *Geol.* 39:1155–1158. doi:10.1130/G32468.1
- Humphris SE, Tivey MK, Tivey MA (2015) The Trans-Atlantic Geotraverse hydrothermal field: A hydrothermal system on an active detachment fault. *Deep Sea Res. Part II* 121:8–16. doi:10.1016/j.dsr2.2015.02.015
- Jochum KP, Herwig K, Lammel E, Stolland B, Hofmann AW (2005) GeoReM: A New Geochemical Database for Reference Materials and Isotopic Standards. *Geostand. Geoanalytical Res.* 29:333-338. doi.org/10.1111/j.1751-908X.2005.tb00904.x
- Lalou C, Reyss JL, Bricet E, Rona PA, Thompson G (1995) Hydrothermal activity on a 105-year scale at a slow-spreading ridge, TAG hydrothermal field, Mid-Atlantic Ridge 26°N. *J. Geophys. Res.:* 100 17855–17862. doi:10.1029/95JB01858
- Longerich HP, Jackson SE, Günther D (1996) Laser Ablation Inductively coupled plasma mass spectrometric transient signal data acquisition and analyte concentration calculation. *J. Anal. At. Spectrom.* 11: 899-904. 10.1039/JA9961100899
- Maslennikov VV, Maslennikova SP, Large RR, Danyushevsky LV (2009) Study of Trace Element Zonation in Vent Chimneys from the Silurian Yaman-Kasy Volcanic-Hosted Massive Sulfide Deposit (Southern Urals, Russia) Using Laser Ablation-Inductively Coupled Plasma Mass Spectrometry (LA-ICPMS). *Econ. Geol.* 104: 111-1141. 10.2113/gsecongeo.104.8.111
- Monecke T, Petersen S, Hannington MD, Grant H, Samson IM (2016) The minor element endowment of modern seafloor massive sulphides and comparison with deposits hosted in ancient volcanic successions. In: Verplanck PL, Hitzman MW (eds.) *Rare Earth and Critical Elements in Ore Deposits*, Soc. Econ. Geol. Knoxville, pp. 245–306.
- Murton BJ, Shipboard Scientific Party (2018) Cruise Report: Expedition JC 138: 29th June–8th August 2016, Mid Atlantic Ridge, 26° 8.38'N, 44° 49.92'W. National Oceanography Centre Southampton. https://www.bodc.ac.uk/resources/inventories/cruise_inventory/reports/jc138.pdf. Accessed 01 March 2019
- Rona PA, Klinkhammer G, Nelsen TA, Trefry JH, Elderfield H (1986) Black smokers, massive sulfides, and vent biota at the Mid-Atlantic Ridge. *Nat.* 321: 33–37. doi:10.1038/321033a0
- Rona PA, Bogdanov YA, Gurvich EG, Rimski-Korsakov A, Sagalevitch AM, Hannington MD, Thompson G (1993) Relict hydrothermal zones in the TAG hydrothermal field, Mid-Atlantic Ridge 26°N, 45°W. *J. Geophys. Res.* 98:9715–9730. doi:10.1029/93JB00552
- Tivey MA, Schouten K, Kleinrock MC (2003) A near-bottom magnetic survey of the Mid-Atlantic Ridge axis at 26°N: Implications for the tectonic evolution of the TAG segment. *J. Geophys. Res.* 108:2277–2789. doi:10.1029/2002JB001967
- Wilson SA, Ridley WI, Koenig AE (2002) Development of sulfide calibration standards for the laser ablation inductively-coupled plasma mass spectrometry technique. *J. Anal. At. Spectrom.* 17:406-409. doi: 10.1039/b108787h
- Zepf V, Reller A, Rennie C, Ashfield M, Simmons J, BP (2014). Materials critical to the energy industry: an introduction. https://www.bp.com/content/dam/bp/pdf/sustainability/group-reports/ESC_Materials_handbook_BP_Apr2014.pdf. Accessed 15 June 2016

Recipes for Rare Earth Deposits

Frances Wall

Camborne School of Mines, University of Exeter, UK

Abstract. Rare earth elements (REE) are essential for a range of clean and digital technologies and the use of some such as neodymium is forecast to increase markedly. A wide variety of rocks can host (REE) ore deposits and although the complete REE series (except Pm that has no naturally occurring stable isotope) are ingredients of all types of deposits, concentrations of the individual REE can range from parts per million to tens of weight percent giving much variation in grade and degree of light and heavy REE enrichment. There is no single recipe for a 'perfect' REE ore deposit. All have advantages and disadvantages but it is possible to review and distill some overall patterns regarding the processes that concentrate REE. Firstly, REE are strongly influenced by their cation size, including the effect of the lanthanoid contraction, which controls, their partitioning into magmas and minerals. Second, element complexing and transport in hydrothermal solution is a key step in changing from light to heavy REE ratios, and thirdly, REE in weathering environments are strongly controlled by mineral solubility. Most of the recipes for REE deposits involve multiple steps of enrichment.

1 Introduction

Rare earth elements (REE), defined by IUPAC as the 15 lanthanoids plus Sc and Y and divided here into 'light REE' (LREE, La – Sm) and 'heavy REE' (HREE, Eu-Lu), are needed for a wide range of clean and digital technologies. Demand for Nd in particular is expected to rise sharply owing to its use in permanent magnets for electric vehicles and wind turbines.

Most REE are mined in China: LREE are produced from several carbonatite-related deposits and HREE, as well as some LREE, are produced from, usually small, ion adsorption clay deposits distributed across southern China. This combination of economic importance and the supply risk that comes from one country's domination of production, leads to the designation of REE as critical raw materials. Heavy REE are subject to the greatest potential supply risk but essential for magnet additives, phosphors and medical applications.

Recent reviews of REE and REE ore deposits include Verplanck and Hitzman (2016), Voncken (2016), Wall (2014), Chakhmouradian and Wall (2012). Wall et al. (2017) put REE deposits into the context of responsible sourcing and discussed that each type has relative merits for REE content, efficient processing, low radioactivity, by-product recovery etc but that there is no such thing as the perfect REE deposit (so far). The aim of this review is to take a slightly different approach from usual to highlight the main controls on concentration of REE into ore deposits.

2 REE ore deposits

REE can be concentrated to potential economic levels in a wide variety of rocks and minerals (Table 1). The most ore minerals in REE deposits are bastnäsite-(Ce) and monazite-(Ce) (Table 1). Other fluorocarbonates such as parasite-(Ce) and synchysite-(Ce) are also common. Xenotime-(Y) is rare as the major mineral but can dominate in some deposits. The mineral assemblages in carbonatite deposits can be complex but the most diverse range of minerals occurs in alkaline rocks (Table 1). Ion adsorption clays are weathered rocks, usually granites, in which the REE are adsorbed onto the surface of clays. Exactly what constitutes an economic concentration of REE depends on which REE are present. For the LREE, concentrations will usually need to be weight percents. For HREE, concentrations of hundreds of ppm may be sufficient.

Table 1. Examples of REE deposits (operating mines in bold)

Locality	Rock type	Main minerals	Main control
Lovozero, Russia	Nepheline syenite	loparite	Partition
Kvanefjeld, Greenland	Nepheline syenite	steenstrupine	Partition
Norra Kärr	Nepheline syenite	eudialyte	Partition
Mountain Pass, USA	Carbonatite	bastnäsite	Partition
Songwe Hill, Malawi	Altered carbonatite	synchysite, apatite	Mobility
Gakara, Burundi	REE-rich veins	bastnäsite monazite	Mobility
Browns Range, Australia	Hydrothermal	xenotime	Mobility
Orissa, India	Mineral sand placer	monazite	Solubility
Mt Weld, Australia	Weathered carbonatite	monazite	Solubility
Southern China	Ion adsorption	n/a	Solubility

3 Cation size and the lanthanide contraction - Partition

The systematic decrease in REE cation radius with increasing atomic number, called the lanthanide contraction, is the foundation of much of the natural behaviour of REE (Fig. 1). Many geoscientists will have

used trace element geochemistry of REE as tracers and indicators of geological processes. Cation size variation is just as important in controlling ore deposit levels of REE. First, it explains the association of REE with each other, because they have very similar cation sizes and properties and will partition and substitute together. The gentle change in size from LREE to HREE is sufficient to fractionate the LREE from the HREE, and result in their being hosted in different minerals. A good example is monazite (La,Ce,Pr,Nd)PO₄ the phosphate host for LREE versus xenotime (YPO₄) that hosts the heavy REE. Deposits with predominantly LREE minerals, such as monazite, bastnäsite, synchysite, and parisite are often termed LREE deposits. They have been the main source of REE for industry. There are far fewer HREE deposits. Notable examples are Browns Range, Australia, Area 4 at Lofdal, Namibia and some of the Chinese ion adsorption deposits. Other deposits, including alkaline rocks and most ion adsorption clays, have overall LREE enrichments but higher proportions of HREE, and usually particularly Y than the carbonatitic strongly LREE-enriched deposits (Goodenough et al. 2018).

Cerium and Eu, the two REE with different oxidation states in natural systems (Fig. 1) can be separated from the +3 cations in ore deposits under some conditions.

The REE 'balance problem' is always uppermost in exploration company considerations. Demand for the individual REE does not correlate neatly with supply. The gentle lanthanoid contraction means that REE are never separated from each other (except occasionally for Ce and Eu). Production of Nd, for example, will require mining much larger amounts of the other LREE, La and Ce.

The close cation size of Th and U to the REE (Fig. 1) is important and problematic because the actinides substitute for the REE into many minerals, especially in monazite. Radioactivity is often the greatest public concern about REE mining. Generally, Th substitution into REE minerals is greater at higher temperatures and lower in low temperature hydrothermal environments and weathering. The much smaller cation size of Sc³⁺ compared with all of the other REE (Fig. 1) leads to its different geochemical behaviour and concentration

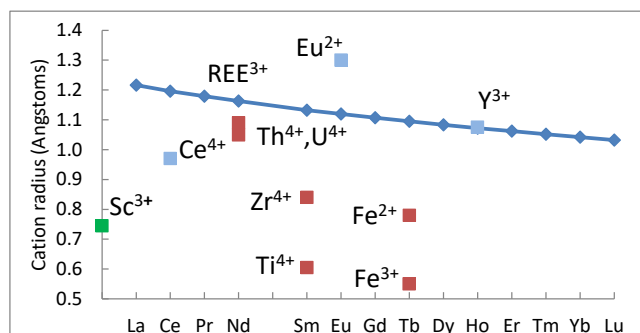


Figure 1. Atomic number vs cation radius for REE³⁺ cations, to show the lanthanoid contraction. Sc, Th, U, Zr, Ti, Fe are plotted in arbitrary positions on the x axis in order to compare cation radii. Modified after Siegfried et al. (2018). Cation radii from <http://abulafia.mt.ic.ac.uk/shannon/radius.php>

with elements such as in zirconium and iron minerals

rather than with the other REE. Bayan Obo, the world's largest LREE deposit is also a large Sc deposit but the Sc is hosted in aegirine rather than in the REE minerals (Williams-Jones and Vasyukova 2018).

4 Fluid complexation and transport - Mobility

Concentration of REE by fluid transport, in subsolidus post-magmatic systems, especially in alkaline rocks and carbonatites, and by hydrothermal systems in other rock types, is key to forming many deposits, and especially to forming HREE ore deposits. Magmatic fractionation will tend to concentrate LREE and it seems from recent published studies that hydrothermal activity is important in making the most HREE-enriched ore deposits. In nepheline syenites fluid activity can help or hinder formation of an ore deposit. REE concentrated into eudialyte, for example, can be altered to more complex, and difficult to process, assemblages of minerals (Borst et al, 2016). Remobilisation of REE can also help to raise concentrations to ore deposit levels, as at Thor Lake, Canada (Sheard et al. 2012). In most carbonatite systems, the REE minerals form in transition environments and by subsequent hydrothermal processes, including remobilization from the original igneous rock.

The role of various ligands is still not entirely clear. Fluoride used to be the most popular ligand proposed to promote REE mobility but the importance of chlorine instead, especially for LREE, was argued by Williams-Jones et al. (2012). Lower temperatures (<200°C) seem to be important in forming more HREE-enriched deposits such as the apatite/synchysite combination at Songwe Hill (Broom-Fendley et al. 2016). Smith et al (2018) and Richter et al. (2018) both cite the probable role of sulphate ligands as well as chloride to form rocks enriched in HREE at Huanglongpu, China and Browns Range, Australia.

5 Mineral Solubility

Mineral solubility, together with resistance to breakdown during erosion and transport is the key attribute in determining which minerals accumulate in mineral sand placer deposits. Monazite and subsidiary xenotime are the main REE hosts in mineral sands, which if it were not for their radioactivity would certainly still be used as a main source of REE (Mudd and Jowett 2016).

Weathering environments that have not been subject to erosion are also important. The main mine producing REE outside of China is at Mt Weld, Western Australia. Here, monazite has formed in lateritic weathered carbonatite, following release of REE from more soluble minerals such as apatite and carbonate, and removal of the more soluble elements such as Ca (Lottermoser 1990). The resulting laterite is much more REE-rich than the original igneous carbonatite.

Mineral solubility is also an important factor in the formation of ion adsorption clay deposits. These may consist of mildly weathered saprolite or strongly altered laterite. The REE are adsorbed to the surface of the clay

minerals and can be released by ion exchange with chemicals such as ammonium sulphate. If insoluble minerals such as monazite and xenotime are the main REE carriers in the original rock, then they will remain unaltered in the weathered profile, and there will be no release of REE, and thus no ion adsorption REE deposit. Conversely, if soluble REE minerals (e.g. synchysite-(Y)) are present in the original rock, they will break down and release REE in the profile. With the right groundwater conditions and presence of kaolinite or halloysite clays, they may form an ion adsorption deposit (Sanematsu and Watanabe 2016). The formation of HREE-enriched soluble precursor minerals can require a discrete stage of hydrothermal mineralization, (Xu et al. 2017).

6 Discussion and conclusion

This classification necessarily simplifies the geological processes involved but it shows the key controls in the various environments (Fig. 2). Partition, controlled by cation size in magmatic environments, the importance of hydrothermal systems and the role of low temperature hydrothermal fluids in concentrating HREE over LREE. It also demonstrates *the contrasting importance of the insoluble minerals needed to create mineral sand deposits and the soluble minerals required to produce ion adsorption clays*. Most recipes for REE deposits require more than one process of enrichment.

Acknowledgements

This work was funded by the SoS RARE NERC Grant NE/M011429/1, (www.sosrare.org) and HiTech AlkCarb European Union Horizon 2020 research and innovation programme, grant agreement 689909, (www.carbonatites.eu). All colleagues who have taken part in these projects and contributed results are gratefully acknowledged.

References

Borst AM, Friis H, Andersen T, Nielsen TFD, Waight TE., Smit MA (2016) Zirconosilicates in the kakortokites of the Ilmaussaq complex, South Greenland: implications for fluid evolution and high-field-strength and rare-earth element mineralization in apatitic systems. *Mineral Mag* 80:5-30.

Broom-Fendley S, Brady AE, Wall F, Gunn G, Dawes W (2017) REE minerals at the Songwe Hill carbonatite, Malawi: HREE-enrichment in late-stage apatite. *Ore Geol Rev* 81:23-41.

Chakhmouradian AR, Wall, F (2012) Rare earth elements: minerals, mines, magnets (and more). *Elements* 8: 333–340.

Cook NJ, Ciobanu CL, O’Rielly D, Wilson, R, Das K, Wade B, (2013) Mineral chemistry of Rare Earth Element (REE) mineralization, Browns Range, Western Australia. *Lithos* 172–173:192–213.

Goodenough KM, Wall F, Merriman D (2018) The Rare Earth Elements: Demand, Global Resources, and Challenges for Resourcing Future Generations, *Nat Resour Res* 27:201.-216.

Lottermoser, BG (1990) Rare-earth element mineralization within the Mt. Weld carbonatite laterite, Western Australia. *Lithos* 24:151-167.

Mudd GM, Jowitt SM (2016) Rare earth elements from heavy

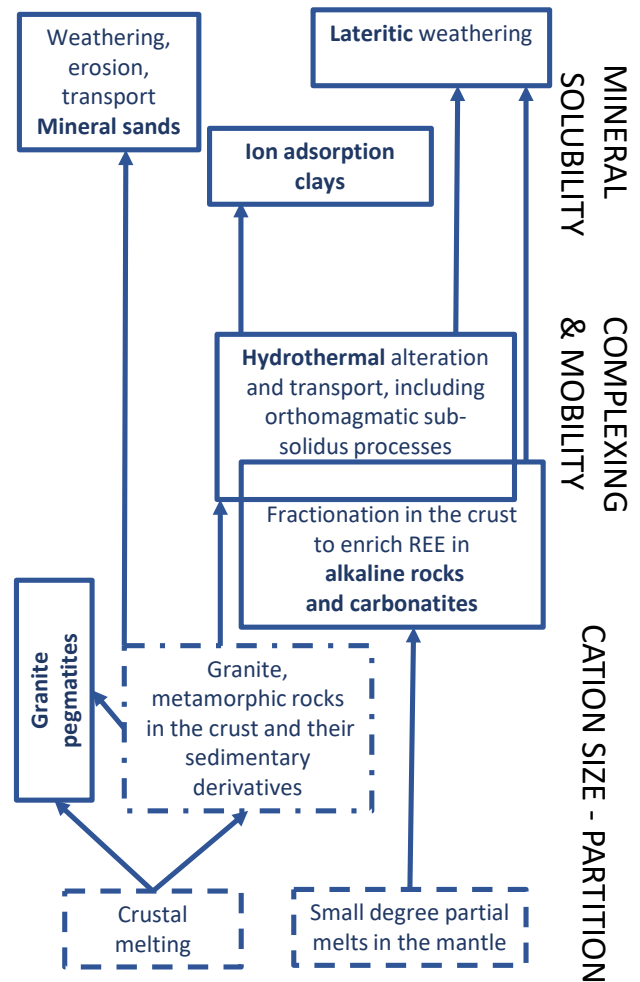


Figure 2. Summary of key controls, stages and routes to the formation of REE ore deposits. Dashed lines show key steps that do not form ore deposits. Granite pegmatites have previously been mined for REE but tend to be small and radioactive, and are not discussed in the text

mineral sands: Assessing the potential of a forgotten resource. *Applied Earth Science* 125: 107–113.

Richter L, Diamond LW, Atanasova P, Banks DA, Gutzmer J (2018) Hydrothermal formation of heavy rare earth element (HREE)– xenotime deposits at 100°C in a sedimentary basin. *Geology* 46:263-266.

Sheard ER, Williams-Jones AE, Heiligmann M, Pederson C, Trueman DL (2012) Controls on the concentration of zirconium, niobium, and the rare earth elements in the Thor Lake rare metal deposit, Northwest Territories, Canada. *Econ Geol* 107: 81–104.

Sanematsu K, Watanabe Y (2016) Characteristics and genesis of ion adsorption-type rare earth element deposits. In P. Verplanck & M. Hitzman (Eds.), *Rare earth and critical elements in ore deposits* (Vol. Reviews in Economic Geology 18:55–79). Littleton, Colorado: Society of Economic Geologists.

Siegfried P, Wall F, Moore K (2018) In search of the forgotten rare earth. *Geoscientist* 28 (10):10-15.

Smith M, Kynicky J, Chen Xuc, Song W, Spratt J, Jeffries T, Brtnicky M, Kopriva A, Cangelosi D (2018) The origin of secondary heavy rare earth element enrichment in carbonatites: Constraints from the evolution of the Huanglongpu district, China. *Lithos* 308–309:65–82.

- Smith MP, Moore K, Kavecsánszki D, Finch AA, Kynicky J, Wall F (2016). From mantle to critical zone: A review of large and giant sized deposits of the rare earth elements, *Geoscience Frontiers* 7:315-334.
- Verplanck PL, Hitzman M (2016) Rare earth and critical elements in ore deposits (Vol. Reviews in Economic Geology 18). Littleton, Colorado: Society of Economic Geologists.
- Voncken JHL (2016) The rare earths elements An introduction. SpringerBriefs in Earth Sciences.
- Wall F. (2014) Rare Earth Elements, Pp 312-339 in: *Critical Metals Handbook*, edited by Gus Gunn, Wiley-Blackwell.
- Wall F, Rollat A, Pell R (2017) Responsible sourcing of critical metals. *Elements* 13:313–318.
- Williams-Jones AE, Vasyukova, O (2018) The Economic Geology of Scandium, the Runt of the Rare Earth Element Litter. *Econ Geol* 113:973-988.
- Williams-Jones AE, Migdisov, A, Samson, IM (2012) Hydrothermal Mobilisation of the Rare Earth Elements - a Tale of "Ceria" and "Yttria". *Elements* 8:355-360.
- Xu C, Kynicky J, Smith MP, Kopriva A, Brtnický M, Urubek T, et al. (2017) Origin of heavy rare earth mineralization in South China. *Nature Communications* 8: 14598

The architecture and geochemistry of magmatic roof zones: implications for mineralization and exploration

Adrian A. Finch, Will Hutchison, Anouk M. Borst, Nicola J. Horsburgh, Eva E. Stüecken
University of St Andrews

Abstract. Magmatic roof zones are unique environments in which magma composition and physical properties can be radically different to those in the main reservoir. The most chemically-evolved melts and volatiles concentrate in the roof and late-stage roof zone processes are implicated in rare element mineralisation. Here we critically review processes in roof zones alongside field observations from the Gardar Rift Province in Greenland. We also present new sulfur isotope ($\delta^{34}\text{S}$) constraints on the origins and evolution of roof zone fluids. Most $\delta^{34}\text{S}$ variation takes place during late-magmatic and hydrothermal stages, and clear differences occur between three alkaline systems (Ilímaussaq, Motzfeldt and Ivigtût) that host REE/Zr/Nb deposits. At Ilímaussaq, the magmatic series is exceptionally reduced (below QFM buffer) and roof zone $\delta^{34}\text{S}$ remains narrow (0–3 ‰). At Motzfeldt, a more oxidizing roof zone, $\delta^{34}\text{S}$ ranges from –12 ‰ in late-stage fluorite veins to +12 ‰ where local crust has been assimilated. Ivigtût is intermediate varying between –5 to +5 ‰. $\delta^{34}\text{S}$ relates to temperature and redox variations and highlights the appearance of sulfate during fluid evolution. We demonstrate the potential of S isotopes as a redox and temperature proxy. We discuss the pointers that may indicate a mineralised roof zone at depth.

1 Introduction

The contact between a magma reservoir and the overlying country rock (or 'roof zone') is impossible to observe directly in active volcanic systems and very rarely exposed at ancient plutonic systems (Yoshinobu et al., 2003; Johnson et al., 2011). Melts and volatiles concentrate in the roof and inject dykes and veins into the host rock; these disintegrate the layers of surrounding country rock and cause them to be assimilated into the magma (Žák et al., 2012). Although such processes are commonly invoked to explain volcanic-magmatic

processes, rarely can they be examined in the field and as such they remain poorly understood.

Magmatic roof zones represent unique environments at the interface between the magma and country rocks (Paterson et al., 2012). The magma and its roof interact in many ways, combining physical interaction with the envelope (dyking, stoping and cooling) and chemical reactions (crustal assimilation and metasomatism). The roof will also accumulate low-density melts or bubbles from the chamber that rise through buoyancy. Field evidence confirms that roof zones have atypical compositions and textures, and are often the sites of ore deposits. This is because volatiles (e.g., H_2O , CO_2 , F and Cl) form complexes with metals and mobilise critical elements within alkaline systems. Thus roof zone processes may localise metal deposits and enhance the grade of mineral deposits associated with alkaline magmas (e.g. Kogarko, 1990; Kovalenko et al., 1995; Salvi & Williams-Jones, 2006).

The present contribution reviews the physical and chemical processes that take place in roof zones. We discuss each process in the context of field evidence and novel geochemical data from natural laboratories in Southern Greenland. Finally, we draw together the evidence for each process occurring in natural roof zones and draw insights into how roof zone architecture and composition influence mineralisation.

2 Regional Setting: Gardar Province

The Gardar Province in South Greenland (Fig. 1) comprises an ancient rift that was volcanically and tectonically active between 1300 and 1100 Ma (Upton, 2013 and references therein). The region is endowed with several major deposits in REE, Ta and V, and

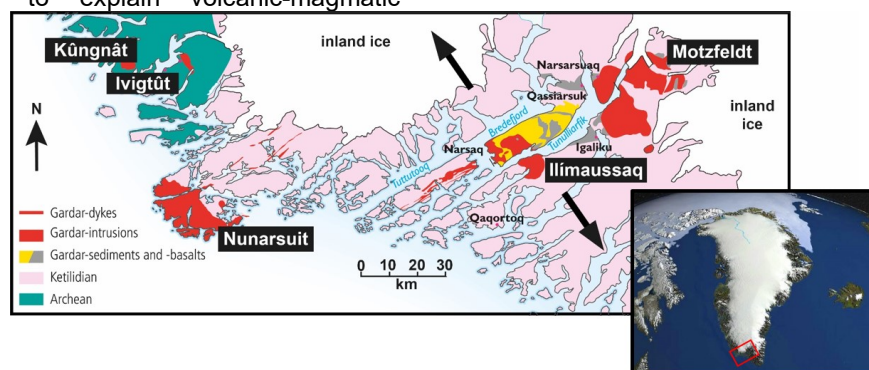


Figure 1. A simplified geological map of the Gardar Province in Greenland showing the location of the main magmatic intrusions (Ilímaussaq, Motzfeldt and Ivigtût) considered here. Extension vectors for the late Gardar rifting are shown by the black arrows.

recent glacial erosion has exposed exceptional three-dimensional sections through the roofs of several ancient alkaline complexes. These exposures present some of the finest examples of 'frozen-in' roof process zones and, because there have been multiple phases of Gardar rifting (summarized in Fig. 1) through varying lithologies (Archean vs. Ketilidian crust), a wide range of magmatic processes can be examined.

3 Sulfur isotopes – a new proxy for REE mineralization and exploration

One of the key goals of resource geology is to develop proxies that track magmatic and metasomatic processes, and indicate mineral prospectivity. Sulfur is an important volatile in alkaline magmas and, although the isotopic composition of sulfide and sulfate from magmatic-hydrothermal systems has been studied for several decades (Seal, 2006), only a few investigations have studied sulfur isotopes of alkaline bodies and associated REE deposits (Farrel et al., 2010; Gomide et al., 2013). Sulfur isotopes in igneous systems are sensitive to magmatic-hydrothermal processes.

3.1 Mineral $\delta^{34}\text{S}$

The partitioning of sulfur isotopes between mineral species is dependent on the oxidation state and temperature of the system (Seal, 2006). Temperature variations generally have a small effect on the sulfur isotope fractionation between H_2S and crystallizing sulfide minerals (Ohmoto & Goldhaber, 1997). This is shown in Fig. 2a where experimentally derived S isotope fractionation factors between sulfide, sulfate and H_2S are shown as a function of temperature. Different S-bearing minerals have different fractionation factors and an important point is that the temperature-dependence of isotope fractionation between two phases can be used for geothermometry (Seal, 2006). When $\delta^{34}\text{S}$ is measured in co-existing mineral phases, for example sphalerite and galena, then temperature can be estimated assuming the two minerals formed together and in equilibrium.

Redox state of the evolving magma and fluid is also a major control on mineral $\delta^{34}\text{S}$. This is because at higher oxidation states, sulfate will become stable which tends to be enriched in ^{34}S , and will have correspondingly higher $\delta^{34}\text{S}$ (Fig. 2a). In systems containing both sulfate and sulfide, the former will always display higher $\delta^{34}\text{S}$ values due to sulfur isotope fractionation between these species (e.g. Mitchell & Krouse, 1975; Seal, 2006). Conversely, in systems where no sulfate minerals are stable the $\delta^{34}\text{S}$ will largely remain close to typical magmatic values of $0 \pm 3 \text{‰}$. Thus changing proportions of oxidized and reduced sulfur species in the magma and late-stage fluids $\Sigma \text{SO}_4 / \Sigma \text{H}_2\text{S}$ is an important control on $\delta^{34}\text{S}$. This has been shown for thermodynamic calculations for fenitizing fluids from Swartbooisdrif, north-western Namibia (Drüppel et al., 2006), which show changes from positive to negative $\delta^{34}\text{S}$ in the early to late sulfide mineralization which marks an increase in oxygen

fugacity ($f\text{O}_2$) and a systematic increase in the $\Sigma \text{SO}_4 / \Sigma \text{H}_2\text{S}$ ratio of the fluid (Fig. 2b)

3.2 Whole-rock $\delta^{34}\text{S}$

Sulfur isotope analysis of whole-rock samples can also be used to understand magmatic processes. In this case $\delta^{34}\text{S}$ provides information on magma source and assimilation processes (i.e. changes to the bulk rock sulfur, rather than subtleties of temperature and redox). Recent studies of mid-ocean ridge basalts (MORB), show that asthenospheric upper mantle has a $\delta^{34}\text{S} < 0 \text{‰}$ and, more probably, $\leq -1.4 \text{‰}$ (Labidi et al., 2012). $\delta^{34}\text{S}$ of plume-derived magmas are broadly similar to MORB values. Primitive high-MgO Icelandic basalts show $\delta^{34}\text{S}$ from -2.0‰ to $+0.4 \text{‰}$, with a mean of -0.8‰ (Torssander, 1989), while $\delta^{34}\text{S}$ of plume lavas in the British Palaeogene Igneous Province have values of $-2.3 \pm 1.5 \text{‰}$ (Hughes et al., 2015). Metasomatized mantle at subduction zones generally has $\delta^{34}\text{S}$ values ranging from $+1.5 \text{‰}$ to $+10 \text{‰}$ since seawater sulfate ($\sim 20 \text{‰}$) is introduced and recycled by arc volcanism (de Hoog et al., 2001). In addition, magma-crust interactions alter the $\delta^{34}\text{S}$ of the magma if the S isotopic composition of the country rocks is significantly different from the magma. For example, sedimentary rocks with organic sulfide are $\sim 20 \text{‰}$ lighter than magmatic values, while evaporative sulfate may have $\delta^{34}\text{S}$ signals that are $\sim 20 \text{‰}$ higher than magmatic values. Careful isotopic fingerprinting of magma throughout the crystallization sequence is needed to distinguish between magma source and contamination (Ohmoto & Goldhaber 1997).

4 Architecture of magmatic roof zones and key processes

4.1 Magma emplacement and physical interactions

A substantial magma body will change the properties of the rocks above it. This may be mechanical, i.e. a buoyant magma at depth would reactivate regional faults, lifting the rocks above it. Alternatively, the loss of magma at depth (perhaps by lateral magma migration) may cause caldera collapse (Walter & Troll, 2001). The magmas may degas, allowing water, carbon dioxide and sulfur-bearing phases to rise along faults, lubricating them and thereby facilitating fault movement.

The magma in the roof zones also interacts physically with the envelope. The roof zone shows both plastic and brittle deformation processes. For example, at Motzfeldt, suites of inclined sheets sourced from the magma penetrated the country rocks above and around the chamber. Sheeting exploited fabrics in the country rocks (e.g. bedding in sediments and vertical faults). We infer that repeated emplacement progressively amplified the number and width of the minor intrusions, ultimately leading to xenoliths, physically detached from the roof.

As magma interacts with the colder roof, it chills and becomes more plastic. As cooling progresses, a growing

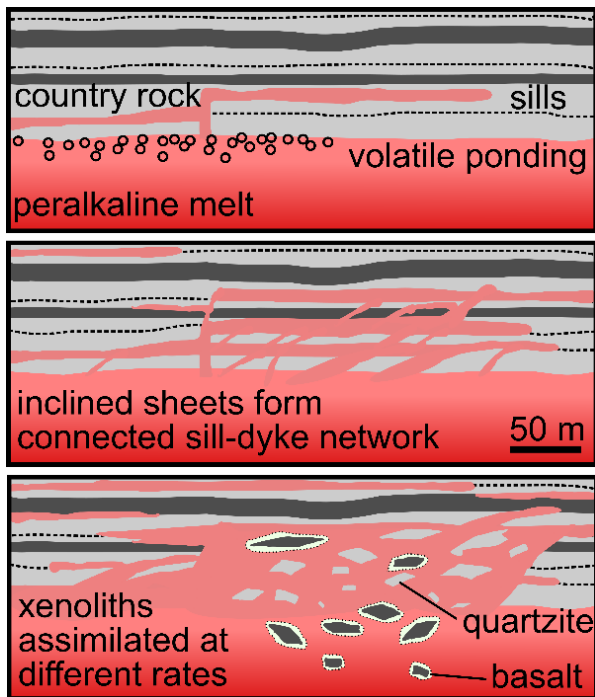


Figure 2: Summary of roof zone magma emplacement and assimilation processes in alkaline systems.

chill zone of crystal mush will form against the roof, physically insulating the roof rocks from the magma and thereby suppressing chemical interaction between them. Eventually a coherent semi-solid roof zone will form, maintained by the temperature gradients with the country rock. The roof zone may be gravitationally unstable; parts of it may periodically detach to fall back into the body of the chamber. Alternatively, the roof zone may be intruded by inclined sheets of magma from below (Paterson et al. 2012; Žák et al. 2012). The repeated inclined sheeting in the roof zone moves down, away from magma intruding country rocks, towards magma repeatedly intruding the chilled, plastic, partly crystallised magma carapace, which we call the 'Hot Sheeted Roof' (Finch et al. 2019). At Motzfeldt, the Hot Sheeted Roof is preserved as complex syenitic variants with compositional and textural variability but without internal chilled contacts.

4.2 Crustal Assimilation

Heating of the country rocks substantially modifies roof rheology. Such changes would be greatest very close to the contact and fade away laterally. The rocks may be heated sufficiently to become plastic and deform, or ultimately they may melt. Melting would create a discrete (probably granitoid) secondary melt, which may then mingle with the primary melt (creating a heterogeneous mingling zone) or may blend to provide a homogenous but contaminated hybrid melt unique to the roof region (Huppert & Sparks, 1988). In addition to physical melting, roof rocks and magma may chemically react, locally producing a rock with a new texture but one which retains the 3-dimensional structure of the xenolith.

4.3 Melt and Volatile Accumulation

A lens of low density magma may form at the top of the magma chamber. This may be a less dense, more evolved melt which will rise to the chamber roof creating magma stratification. Similarly, low-density volatile-rich magmas would rise. Any secondary boiling in the chamber would create bubbles which rise rapidly, conveying volatiles efficiently to the chamber roof. Analysis of biotite in the roof zone of Motzfeldt, for example, shows elevated fluorine levels, significantly greater than those lower in the chamber. We infer that the roof zone is atypically volatile-rich (Finch et al., 1995).

Irrespective of how it has formed, the lens of atypical magma can remain undisturbed at the roof because of contrasting composition and viscosity; a boundary layer may form and convection currents operate below the roof, effectively isolating it from the remainder of the chamber. At both the Kūngnāt and Nunarsuit complexes, there are subhorizontal xenolith horizons which extend km along strike. These appear to be where a convection cell has transported xenoliths which have been parked beneath a thickness of roof magma or roof rocks. The roof may constitute an isolated lens of magma crystallising largely independently, or consolidated but hot roof rocks. Such observations indicate that cooling and chemical modification (e.g. by assimilation) can progress in the roof without the modified magma convecting the products immediately away. Hence as the magma assimilates xenoliths of country rock, a small amount of assimilation results in substantive local changes in composition.

4.4 Metasomatic Alteration

When the magmatic system in the roof zone is solidified, continued alteration may occur through metasomatism by magmatic fluids (Cathelineau, 1986). These may exsolve from the magma lower in the chamber, and rise through the solidified roof. Because a magmatic fluid is derived from a magma similar, but not identical, to that of the roof, the resulting chemical changes are subtle. These include coarsening textures in exsolved feldspar (e.g. perthite) and the formation of turbidity. Mafic minerals may be altered to microcrystalline biotite and iron oxides. However when the fluid extends beyond the igneous rocks of the roof, the substantive temperature and compositional contrasts will trigger reaction. This reaction might occur by two mechanisms. First, it may be a reaction between the fluid and the country rocks. At the roof of Motzfeldt and in the envelope of the Igdlersigalik Centre, fluorine-rich hydrothermal fluids attacked the arenite country rocks, replacing quartz with feldspar and precipitating alkali mafic minerals such as aegirine and arfvedsonite (Sokół et al., this conference). White arenite in the roof was replaced by a pink saccharoidal feldspar-quartz rock. The second mechanism may be that hot magmatic fluids interact with colder meteoric fluids circulating above the intrusion. As the hot, metal-rich fluid meets a cold one, precipitation is favoured. Such a mechanism is envisaged for the formation of, for example, Volcanic Massive Sulfide deposits (Lydon, 1984).

4.5 Microenvironments beneath major rafts

Similar processes to those beneath the roof may also be seen underneath some substantial rafts. Analysis of the fluorine content of the mica beneath a substantive (100 m+) wide basalt xenolith lower down in the Motzfeldt centre showed elevated F contents similar to those in the roof (Fig. 5). One interpretation is that volatiles or volatile-rich magmas rise through the chamber, ponding when their upwards ascent is impeded. Alternatively the rafts may once have been the roof itself with roof-zone processes taking place beneath it. Latterly, the roof zone may have detached and sunk through the chamber. It also means that micro-roof environments can develop beneath substantive xenoliths and these may also be sites of smaller scale mineralisation.

5 Conclusions

Roof zones are a key aspect of igneous geology and are often implicated in the genesis of metal deposits. Physical and chemical interaction between magma and the rocks above the chamber create gradients in temperature, composition and physical properties. These interact to give mineralisation in and around the roof.

New sulfur isotope techniques have potential for REE prospecting since they are able to fingerprint the metasomatised mantle sources that generate and feed alkaline-carbonatite systems. Further, sulfur isotopes are a powerful tool for identifying early to late-stage magmatic fluids and the temperature and redox evolution that has taken place. More case studies and isotopic modelling are required to advance the technique further.

Acknowledgements

This work was funded by the NERC SoS RARE consortium [NE/M010856/1 to AMB, AAF & NJH] and has received funding from the European Union's Horizon research and innovation programme under grant No 689909 [AAF, WH].

References

Cathelineau, M., 1986. The hydrothermal alkali metasomatism effects on granitic rocks: Quartz dissolution and related subsolidus changes. *J. Petrol.* 27:945–965. doi:10.1093/ptology/27.4.945

de Hoog, J.C.M., Taylor, B.E., Van Bergen, M.J., 2001. Sulfur isotope systematics of basaltic lavas from Indonesia: Implications for the sulfur cycle in subduction zones. *Earth Planet. Sci. Lett.* 189:237–252. doi:10.1016/S0012-821X(01)00355-7

Drüppel, K., Wagner, T., Boyce, A.J., 2006. Evolution of sulfide mineralization in ferrocarnatite, Swartbooisdrif, northwestern Namibia: Constraints from mineral compositions and sulfur isotopes. *Can. Mineral.* 44:877–894. doi:10.2113/gscanmin.44.4.877

Farrell, S., Bell, K., Clark, I., 2010. Sulphur isotopes in carbonatites and associated silicate rocks from the Superior Province, Canada. *Mineral. Petrol.* 98:209–226. doi:10.1007/s00710-009-0101-2

Finch, A.A., Parsons, I., Mingard, S.C., 1995. Biotites as Indicators of Fluorine Fugacities in Late-Stage Magmatic Fluids: the Gardar Province of South Greenland. *J. Petrol.* 36:1701–1728.

Finch, A.A., McCreath, J.A., Reekie, C.D.J., Hutchison, W., Armour-Brown, A., Anderson, T. and Simonsen, S.L., 2019. From Mantle to Motzfeldt: A Genetic Model for Syenite-hosted Ta, Nb-mineralisation. *Ore Geology Reviews*, in press.

Gomide, C.S., Brod, J.A., Junqueira-Brod, T.C., Buhn, B.M., Santos, R.V., Barbosa, E.S.R., Cordeiro, P.F.O., Palmieri, M., Grasso, C.B., Torres, M.G., 2013. Sulfur isotopes from Brazilian alkaline carbonatite complexes. *Chem. Geol.* 341:38–49. doi:10.1016/j.chemgeo.2013.01.006

Hughes, H.S.R., et al., 2015. Contrasting mechanisms for crustal sulphur contamination of mafic magma: evidence from dyke and sill complexes from the British Palaeogene Igneous Province. *J. Geol. Soc. London.* 172:443–458. doi:10.1144/jgs2014-112

Huppert, H.E., Sparks, R.S.J., 1988. The generation of granitic magmas by intrusion of basalt into continental crust. *J. Petrol.* 29, 599–624. doi:10.1093/ptology/29.3.599

Johnson, S.E., Jin, Z.H., Naus-Thijssen, F.M.J., Koons, P.O., 2011. Coupled deformation and metamorphism in the roof of a tabular midcrustal igneous complex. *Bull. Geol. Soc. Am.* 123:1016–1032. doi:10.1130/B30269.1

Kogarko, L.N., 1990. Ore-forming potential of alkaline magmas. *Lithos* 26, 167–175. doi:10.1016/0024-4937(90)90046-4

Kovalenko, V.I., 1995. The peralkaline granite-related Khaldzan-Buregtey rare metal (Zr, Nb, REE) deposit, western Mongolia. *Econ. Geol.* 90:530–547. doi:10.2113/gsecongeo.90.3.530

Labidi, J., et al. 2012. Determination of multiple sulfur isotopes in glasses: A reappraisal of the MORB $\delta^{34}\text{S}$. *Chem. Geol.* 334:189–198. doi:10.1016/j.chemgeo.2012.10.028

Lydon, J.W., 1984. Ore deposit models-8. Volcanogenic massive sulphide deposits Part I: A descriptive model. *Geosci. Canada* 11.

Mitchell, R.H., Krouse, H.R., 1975. Sulphur isotope geochemistry of carbonatites. *Geochim. Cosmochim. Acta* 39:1505–1513. doi:10.1016/0016-7037(75)90152-0

Ohmoto H, Goldhaber MB (1997) Sulfur and carbon isotopes. In: *Geochemistry of Hydrothermal Ore Deposits*. Barnes HL (ed) J Wiley and Sons, 517–611

Paterson, S.R., et al., 2012. Formation and transfer of stoped blocks into magma chambers: The high-temperature interplay between focused porous flow, cracking, channel flow, host-rock anisotropy, and regional deformation. *Geosphere* 8, 443–469. doi:10.1130/GES00680.1

Salvi, S., Williams-Jones, A.E., 2006. Alteration, HFSE mineralisation and hydrocarbon formation in peralkaline igneous systems: Insights from the Strange Lake Pluton, Canada. *Lithos* 91, 19–34. doi:10.1016/j.lithos.2006.03.040

Seal, R.R., 2006. Sulfur Isotope Geochemistry of Sulfide Minerals. *Rev. Mineral. Geochemistry* 61:633–677. doi:10.2138/rmg.2006.61.12

Torssander, P., 1989. Mineralogy and Sulfur isotope ratios of Icelandic rocks. *Contrib. to Mineral. Petrol.* 102, 18–23.

Upton, B.G.J., 2013. Tectono-magmatic evolution of the younger Gardar southern rift, South Greenland, Geological Survey of Denmark and Greenland Bulletin.

Walter, T.R., Troll, V.R., 2001. Formation of caldera periphery faults: An experimental study. *Bull. Volcanol.* 63:191–203. doi:10.1007/s004450100135

Yoshinobu, A.S., et al., 2003. A view from the roof: Magmatic stoping in the shallow crust, Chita pluton, Argentina. *J. Struct. Geol.* 25:1037–1048. doi:10.1016/S0191-8141(02)00149-9

Žák, J., et al. 2012. Magma emplacement process zone preserved in the roof of a large Cordilleran batholith, Wallowa Mountains, northeastern Oregon. *J. Volcanol. Geotherm. Res.* 227–228:61–75. doi:10.1016/j.jvolgeores.2012.03.001

The importance of post-collisional magmatism for global rare earth element resources

Kathryn M Goodenough, Éimear Deady and Charles Beard
British Geological Survey, Edinburgh, UK

Abstract. The rare earth elements are critical metals for modern technology, and are most commonly found in deposits associated with alkaline igneous and carbonatite complexes. Although much research has focused on alkaline-carbonatite magmatism in intraplate settings, in reality many REE deposits occur in post-collisional settings. This review of post-collisional REE deposits demonstrates that they typically show evidence for liquid immiscibility between potassic alkaline magmas and F-, Ba- and REE-rich carbonatitic melts or carbo-hydrothermal fluids. The carbonate-rich melts/fluids rise through the magmatic system and are emplaced at shallow levels, forming the main REE deposits in such complexes. A detailed understanding of the processes operating in these systems can be used to generate geomodels that will be useful for exploration targeting in post-collisional complexes.

1 Introduction

The rare earth elements (REE) are critical metals for which demand is growing as they are used in a wide range of technologies. Neodymium (Nd), praseodymium (Pr) and dysprosium (Dy) are considered to be the most critical of the REE, due to their use in high strength magnets that are needed for the motors of electric cars and wind turbines (Goodenough et al. 2018).

Primary resources of the REE are found in a range of settings, but all known large and giant-sized deposits are associated with alkaline igneous rocks and carbonatites (Smith et al. 2016). Alkaline-carbonatite igneous complexes are most commonly associated with continental intraplate magmatism, but can also occur at plate boundaries, typically as part of post-collisional magmatic suites. Post-collisional magmatism is often voluminous, and occurs in a period of 'relaxation' generally post-dating continental collision by 25-75 Ma; emplacement of magmas is commonly linked to movement along major transcurrent shear zones (Sylvester 1989; Bonin 2004). Post-collisional alkaline magmatic rocks are typically potassic to ultrapotassic, with rarer sodic compositions (Bonin 2004).

Much research relating to alkaline igneous rocks and carbonatites, and their associated mineralization, has focused on continental intraplate settings (Dostal 2017). However, many significant REE deposits worldwide are associated with post-collisional alkaline-carbonatite magmatic complexes. This contribution reviews some of the key characteristics of post-collisional REE deposits, and builds up a preliminary model for these magmatic-mineralised systems.

2 REE deposits associated with post-collisional magmatism

The majority of well-known REE deposits formed in post-collisional settings are Mesozoic to Cenozoic in age, and relatively shallow levels of the alkaline-carbonatite magmatic suite are exposed at the surface. Common rock-types include shallow-level syenitic, phonolitic and trachytic intrusions and carbonatite dykes, with the REE mineralization hosted in breccias, carbonatite dykes and carbo-hydrothermal veins. Alkaline rocks are typically potassic to ultrapotassic in composition, whilst the REE deposits are carbonate-dominated and enriched in F, Ba, and the REE.

The most economically important REE deposits associated with post-collisional magmatism lie in the Mianning-Dechang REE belt of southwestern China, which includes the Maoniuping and Dalucao REE deposits. These deposits occur as veins, lenses and breccias of barite-fluorite-bastnäsite-calcite ore with a range of alkaline silicate minerals (Guo and Liu 2019). They are associated with post-collisional syenite-carbonatite complexes of Cenozoic age, which were emplaced into the Himalayan collision zone during shearing on regional strike-slip faults (Liu et al. 2015; Hou et al. 2009). REE deposits in post-collisional alkaline-carbonatite complexes are also known from elsewhere in China, for example at Miaoya (Xu et al. 2015).

In Turkey, Cenozoic post-collisional alkaline-carbonatite suites are associated with a number of fluorite deposits. One of these, the Kizilcaören deposit, comprises lenses and veins of fluorite-barite-bastnäsite ore which represent a REE deposit (Öztürk et al. 2019). Igneous rocks in the area are represented by shallow-level phonolitic to carbonatitic intrusions.

In Southern Mongolia, the Lugin Gol, Mushghai Khudag and Bayan Khushu alkaline complexes show a suite of syenitic to trachytic intrusions associated with carbonatite and phonolite dykes, magnetite-apatite rocks, and fluorite-barite-carbonate veins (Baatar et al. 2013; Nikolenko et al. 2018). At Mushghai Khudag, the magnetite-apatite rocks represent the most important REE mineralization, but the carbonatitic dykes and veins in all complexes are also significantly REE-enriched (Kynicky et al. 2019). These complexes are not well-dated, but are thought to be late Jurassic in age, part of an alkaline magmatic province that formed in association with a tectonic transition from contractional to extensional deformation during the late Jurassic (Meng 2003).

In the USA, Cenozoic post-collisional alkaline magmatic complexes were emplaced towards the end of

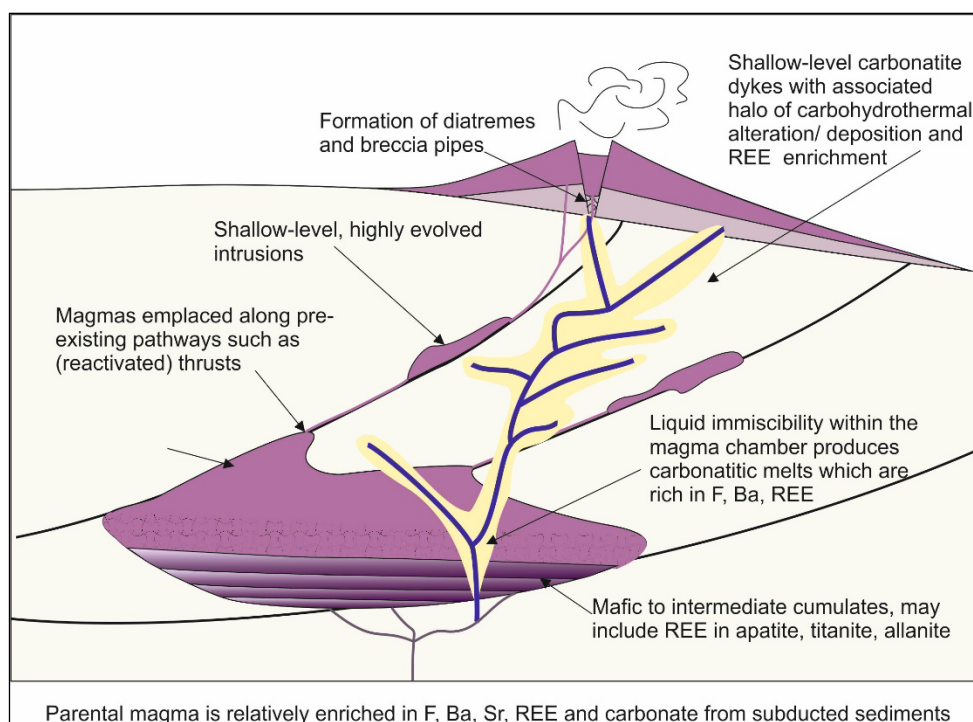


Figure 1. Schematic figure indicating the components of a post-collisional alkaline-carbonatite REE deposit.

the Laramide Orogeny, and include several REE deposits (McLemore 2018). These include the Gallinas Mountains of central New Mexico, which host Cenozoic, syn- to post-collisional alkaline intrusives with associated REE deposits in breccia pipes and fault-hosted breccias. The REE deposits comprise the fluorite-bastnäsite-barite-calcite-quartz breccia matrices (Olivo et al. 2000). The Bear Lodge REE deposit in Wyoming is also hosted in an alkaline-carbonatite complex within this belt. The most heavily-explored part of the deposit is in the Bull Hill diatreme, comprising a breccia pipe with a stockwork of carbonatite veins and dykes; REE mineralization is related to multiple phases of carbo-hydrothermal activity within this diatreme (Moore et al. 2015). Carbonatite dykes and veins extend throughout much of the alkaline complex, and some peripheral zones are HREE-enriched (Andersen et al. 2016).

It is evident that in most deposits in post-collisional settings, the REE mineralization occurs in carbonate- and fluorite-dominated ore bodies, which are associated with potassic alkaline igneous rocks. These REE deposits are likely to have formed by liquid immiscibility of a carbonatitic melt (or carbothermal fluid) from the alkaline silicate magma at deeper levels in the system (Kynicky et al. 2019). The REE, F, and Ba were all preferentially partitioned into the carbonatitic phase, as indicated by experimental data (Song et al. 2015). These volatile-rich carbonatitic melts/carbothermal fluids were subsequently emplaced at shallow levels as dykes, sheets, and in the matrix of breccia pipes. Such immiscible melts/ fluids may have also formed REE mineralization at deeper levels in the igneous complexes; to understand this it is necessary to investigate older and more deeply eroded examples.

3 Understanding the deeper levels of post-collisional REE deposits

Few REE deposits associated with deeper levels of alkaline-carbonatite complexes have been positively recognized as post-collisional. However, the Proterozoic Mountain Pass REE deposit is associated with ultrapotassic alkaline igneous rocks and was likely formed in a post-collisional setting. These ultrapotassic rocks are relatively enriched in Ba and the LREE, and have allanite, apatite, monazite, fluorite and magnetite as accessory minerals (Castor 2008). The REE deposit is in a tabular carbonatite body that is enriched in barite, bastnäsite and monazite.

Similar features are recognized in the post-collisional Silurian alkaline intrusions of the NW Highlands of Scotland, which were emplaced at the end of the Caledonian orogeny, and are characterized by ultrapotassic, high Ba-Sr compositions (Fowler et al. 2008; Goodenough et al. 2011). The complexes largely comprise under- to oversaturated syenites with minor carbonatites. The main REE enrichment has been recognized in the form of biotite-magnetite-allanite-apatite veins in syenites at the Cnoc nan Cuilean locality (Walters et al. 2013). These veins represent pathways exploited by late-stage, fluorine- and carbonate-rich fluids or melts rising through the magma chamber. Late allanite-monazite-fluorocarbonate veins also form the REE mineralization at the Ditrău Alkaline Complex in Romania, which was emplaced after the Variscan orogeny (Honour et al. 2018).

Such examples are consistent with immiscibility of a F-Ba-REE-rich carbonatitic melt within the alkaline magma chamber and subsequent migration upwards through the magmatic system.

4 Genesis and evolution of REE-enriched magmas in post-collisional settings

Parental magmas in post-collisional settings are commonly potassic to ultrapotassic, and enriched in Ba, Sr, and the LREE. These compositional features are considered to be derived from an enriched mantle source that has interacted with subducted continental material (or melts/fluids derived from the subducting material) and subsequently been melted (Couzinié et al. 2016). This enriched mantle source must typically also have been rich in carbonate; carbonate is stable in the shallower parts of modern subduction zones, but is eventually extracted through formation of carbonatitic melts, which metasomatise the overlying lithospheric mantle (Dasgupta and Hirschmann 2010). Compilations of Sr, Nd and Hf data for post-collisional alkaline complexes are consistent with addition of continentally-derived material into the mantle source.

An overarching model for the formation of REE deposits associated with post-collisional alkaline magmatism can be summarized as follows. Small-degree partial melting of the enriched mantle source, triggered by 'relaxation' and extension of the orogenic belt, produces a parental magma that is relatively rich in F, CO₂, K, Ba, Sr and the LREE. Such magmas are emplaced along major crustal structures, reactivated in an extensional manner, into magma chambers at medium levels in the crust. Evolution by fractional crystallization produces trachytic/syenitic magma compositions which are volatile-rich, and thus eventually a fluorine-rich carbonatitic melt is formed by liquid immiscibility. These carbonatitic melts rise through the magma chamber and into the overlying country rocks, to be emplaced as REE-enriched dykes and veins with associated metasomatic alteration.

The HiTech AlkCarb project is developing new geomodels for REE mineralization in alkaline igneous rocks and carbonatites, which will incorporate information about complexes in post-collisional settings. A schematic diagram illustrating some of the features of this type of mineralized system is shown in Figure 1.

5 Conclusions

REE deposits in post-collisional alkaline-carbonatite complexes represent a discrete sub-type, which should be distinguished in exploration geomodels. They can be identified by regional tectonic setting and by the K-, Ba- and LREE-rich nature of the associated alkaline igneous rocks. The REE deposits at the upper levels of these complexes will typically take the form of carbonatitic dykes and veins or carbo-hydrothermal ore bodies, which are enriched in fluorite, barite and fluorocarbonates. At deeper levels, carbonatites and alteration zones within the alkaline complexes may be enriched in monazite, allanite and apatite which have the potential to represent significant REE mineralization.

Acknowledgements

This research is part of the HiTech AlkCarb project which

has received funding from the European Union's Horizon 2020 research and innovation programme (grant agreement No 689909).

References

- Andersen AK, Clark JG, Larson PB, Neill OK (2016) Mineral chemistry and petrogenesis of a HFSE(+HREE) occurrence, peripheral to carbonatites of the Bear Lodge alkaline complex, Wyoming. *American Mineralogist* 101:1604-1623. doi: 10.2138/am-2016-5532.
- Baatar M, Ochir G, Kynicky J, Iizumi S, Comin-Chiaramonti P (2013) Some Notes on the Lugiin Gol, Mushgai Khudag and Bayan Khoshuu Alkaline Complexes, Southern Mongolia. *International Journal of Geosciences* 4:1200.
- Bonin B (2004) Do coeval mafic and felsic magmas in post-collisional to within-plate regimes necessarily imply two contrasting, mantle and crustal, sources? A review. *Lithos* 78:1-24. doi: <https://doi.org/10.1016/j.lithos.2004.04.042>.
- Castor SB (2008) THE MOUNTAIN PASS RARE-EARTH CARBONATITE AND ASSOCIATED ULTRAPOTASSIC ROCKS, CALIFORNIA. *The Canadian Mineralogist* 46:779-806. doi: 10.3749/canmin.46.4.779.
- Couzinié S, Laurent O, Moya J-F, Zeh A, Bouilhol P, Villaros A (2016) Post-collisional magmatism: Crustal growth not identified by zircon Hf–O isotopes. *Earth and Planetary Science Letters* 456:182-195. doi: <https://doi.org/10.1016/j.epsl.2016.09.033>.
- Dasgupta R, Hirschmann MM (2010) The deep carbon cycle and melting in Earth's interior. *Earth and Planetary Science Letters* 298:1-13. doi: <https://doi.org/10.1016/j.epsl.2010.06.039>.
- Dostal J (2017) Rare Earth Element Deposits of Alkaline Igneous Rocks. *Resources* 6. doi: <https://doi.org/10.3390/resources6030034>.
- Fowler MB, Kocks H, Darbyshire DPF, Greenwood PB (2008) Petrogenesis of high Ba–Sr plutons from the Northern Highlands Terrane of the British Caledonian Province. *Lithos* 105:129-148. doi: <https://doi.org/10.1016/j.lithos.2008.03.003>.
- Goodenough KM, Millar I, Strachan RA, Krabbendam M, Evans JA (2011) Timing of regional deformation and development of the Moine Thrust Zone in the Scottish Caledonides: constraints from the U–Pb geochronology of alkaline intrusions. *Journal of the Geological Society* 168:99-114. doi: 10.1144/0016-76492010-020.
- Goodenough KM, Wall F, Merriman D (2018) The Rare Earth Elements: Demand, Global Resources, and Challenges for Resourcing Future Generations. *Natural Resources Research* 27:201-216. doi: 10.1007/s11053-017-9336-5.
- Guo D, Liu Y (2019) Occurrence and geochemistry of bastnäsite in carbonatite-related REE deposits, Mianning–Dechang REE belt, Sichuan Province, SW China. *Ore Geology Reviews* 107:266-282. doi: <https://doi.org/10.1016/j.oregeorev.2019.02.028>.
- Honour VC, Goodenough KM, Shaw RA, Gabudianu I, Hirtopanu P (2018) REE mineralisation within the Ditrău Alkaline Complex, Romania: Interplay of magmatic and hydrothermal processes. *Lithos* 314-315:360-381. doi: <https://doi.org/10.1016/j.lithos.2018.05.029>.
- Hou Z, Tian S, Xie Y, Yang Z, Yuan Z, Yin S, Yi L, Fei H, Zou T, Bai G, Li X (2009) The Himalayan Mianning–Dechang REE belt associated with carbonatite–alkaline complexes, eastern Indo-Asian collision zone, SW China. *Ore Geology Reviews* 36:65-89. doi: <https://doi.org/10.1016/j.oregeorev.2009.03.001>.
- Kynicky J, Smith MP, Song W, Chakhmouradian AR, Xu C, Kopriva A, Galiova MV, Brtnicky M (2019) The role of carbonate-fluoride melt immiscibility in shallow REE deposit evolution. *Geoscience Frontiers* 10:527-537. doi: <https://doi.org/10.1016/j.gsf.2018.02.005>.
- Liu Y, Hou Z, Tian S, Zhang Q, Zhu Z, Liu J (2015) Zircon U–Pb ages of the Mianning–Dechang syenites, Sichuan Province, southwestern China: Constraints on the giant REE mineralization belt and its regional geological setting. *Ore Geology Reviews* 64:554-568. doi:

- <https://doi.org/10.1016/j.oregeorev.2014.03.017>.
- McLemore VT (2018) Rare Earth Elements (REE) Deposits Associated with Great Plain Margin Deposits (Alkaline-Related), Southwestern United States and Eastern Mexico. *Resources* 7. doi: <http://dx.doi.org/10.3390/resources7010008>.
- Meng Q-R (2003) What drove late Mesozoic extension of the northern China–Mongolia tract? *Tectonophysics* 369:155-174. doi: [https://doi.org/10.1016/S0040-1951\(03\)00195-1](https://doi.org/10.1016/S0040-1951(03)00195-1).
- Moore M, Chakhmouradian AR, Mariano AN, Sidhu R (2015) Evolution of rare-earth mineralization in the Bear Lodge carbonatite, Wyoming: Mineralogical and isotopic evidence. *Ore Geology Reviews* 64:499-521. doi: <https://doi.org/10.1016/j.oregeorev.2014.03.015>.
- Nikolenko AM, Redina AA, Doroshkevich AG, Prokopyev IR, Ragozin AL, Vladykin NV (2018) The origin of magnetite-apatite rocks of Mushgai-Khudag Complex, South Mongolia: mineral chemistry and studies of melt and fluid inclusions. *Lithos* 320-321:567-582. doi: <https://doi.org/10.1016/j.lithos.2018.08.030>.
- Olivo GR, Williams-Jones AE, Samson IM (2000) The Genesis of Hydrothermal Fluorite-REE Deposits in the Gallinas Mountains, New Mexico. *Economic Geology* 95:327-341. doi: 10.2113/gsecongeo.95.2.327.
- Öztürk H, Altuncu S, Haniççi N, Kasapçı C, Goodenough KM (2019) Rare earth element-bearing fluorite deposits of Turkey: An overview. *Ore Geology Reviews* 105:423-444. doi: <https://doi.org/10.1016/j.oregeorev.2018.12.021>.
- Smith MP, Moore K, Kavecsánszki D, Finch AA, Kynicky J, Wall F (2016) From mantle to critical zone: A review of large and giant sized deposits of the rare earth elements. *Geoscience Frontiers* 7:315-334. doi: <http://dx.doi.org/10.1016/j.gsf.2015.12.006>.
- Song W, Xu C, Veksler IV, Kynicky J (2015) Experimental study of REE, Ba, Sr, Mo and W partitioning between carbonatitic melt and aqueous fluid with implications for rare metal mineralization. *Contributions to Mineralogy and Petrology* 171:1. doi: 10.1007/s00410-015-1217-5.
- Sylvester PJ (1989) Post-Collisional Alkaline Granites. *The Journal of Geology* 97:261-280. doi: 10.1086/629302.
- Walters AS, Goodenough KM, Hughes HSR, Roberts NMW, Gunn AG, Rushton J, Lacinska A (2013) Enrichment of Rare Earth Elements during magmatic and post-magmatic processes: a case study from the Loch Loyal Syenite Complex, northern Scotland. *Contributions to Mineralogy and Petrology* 166:1177-1202. doi: 10.1007/s00410-013-0916-z.
- Xu C, Kynicky J, Chakhmouradian AR, Li X, Song W (2015) A case example of the importance of multi-analytical approach in deciphering carbonatite petrogenesis in South Qinling orogen: Miaoya rare-metal deposit, central China. *Lithos* 227:107-121. doi: <https://doi.org/10.1016/j.lithos.2015.03.024>.

Overview of the European phosphate deposits and occurrences: a project dedicated to phosphate mineralizations and associated critical raw materials

Sophie Decrée, Christian Bulet, Thomas Goovaerts

Royal Belgian Institute of Natural Sciences, Geological Survey of Belgium

Maria João Batista, Daniel P.S. de Oliveira

Geological Survey of Portugal (LNEG)

Khaldoun Al-Bassam

Czech Geological Survey

Boris Malyuk

Geoinform of Ukraine

Nolwenn Coint

Geological Survey of Norway (NGU)

Eoin McGrath

Geological Survey Ireland

Heikki Bauert

Geological Survey of Estonia

Abstract. Critical Raw Materials (CRM) listed by the European Commission are raw materials that are economically and strategically important for the European economy, with uncertainties/risks related to their supply and sourcing from countries outside the EU. Phosphate is listed among these CRM, as are other commodities associated with phosphate mineralization (REE and F, for instance). Phosphate deposits and occurrences are widely distributed in Europe. However, most of them have not been studied in detail for some time, especially with respect to their potential for CRM. The identification of the economic potential of phosphate deposits, whether they are of sedimentary or igneous origin, could significantly contribute to secure access to many commodities listed as critical by the EC. The aim of the project presented here (funded by the H2020- ERA-NET Cofund Action) is to provide an up-to-date overview of phosphate mineralizations (and economically interesting black shales) in Europe, with special emphasis on their CRM content, as well as to stimulate and encourage further work on the known or newly reported phosphate deposits and occurrences in Europe. This abstract presents (i) the goals and methodology of the project, and (ii) the first outcomes under the form of a database and maps.

1 Frame of the project

GeoERA (a H2020 ERA-NET Cofund Action) is a research program aiming to gather the European Geological Surveys around common research themes. The main objective of GeoERA is to contribute to the optimal use and management of the subsurface in

Europe. One of the four topics of interest concerns the raw materials.

Under the umbrella of this GeoERA “Raw Material” theme, the FRAME (Forecasting and Assessing Europe’s Strategic Raw Materials Needs) project – which started on the 1st of July 2018 – aims to expand the strategic and CRM knowledge through a compilation of mineral potential and metallogenic areas of critical raw materials resources in Europe. One of the work packages (WP4 - “Critical Raw Materials in phosphate deposits and associated black shales”) is specifically dedicated to the assessment of economic potential of igneous and sedimentary phosphate deposits (and their host black shales) in Europe, especially regarding CRM. This sub-project is detailed in section 3 of this abstract.

2 Interest in phosphate and associated Critical Raw Materials

Phosphorus is an element that is essential for living plants and animals. It is mostly found as apatite *sensu lato*, which occurs mainly in sedimentary marine phosphorite. An increase in the phosphorus demand of about 2% per year is expected in the global market (EC 2015), mostly to produce fertilizers.

Phosphate deposits and occurrences are widely distributed in Europe (Fig 1). Their ages vary from the Archean to the Pleistocene (Fig 2). However, the EU is a net importer of natural phosphates, with an average of 4,000,000 tonnes of natural phosphate-rich material imported per year (EC 2015). In 2014, phosphate rock was added to the list of critical raw materials (CRMs) for

the EU (EC 2014). With the CRM list, the EU policy aims, among others, (1) to ensure European industrial competitiveness through a fair and sustainable supply of raw materials from global markets (EC 2014), and (2) to encourage the domestic production of these raw materials and new mining activities in the EU (EC 2016).

In addition to phosphorus, other CRM can be recovered from phosphate deposits, such as rare earth elements (REE) and fluorapatite (the commercial name of fluorite). The EU is also a significant importer of these commodities (EC 2015).

Phosphate deposits represent a potential source of REEs (Christmann 2014; Ihlen et al. 2014; Emsbo et al. 2015; Goodenough et al. 2016). Apart from the endowment in REE in these deposits (whether they are sedimentary or igneous in origin; Fig 3), the key potential for production of REE from apatite deposits is the easy extraction, compared to most conventional REE prospects (Pereira and Bilal 2012; Emsbo et al. 2015). Beside the REE, phosphate rocks can contain up to 3-4% of F. The recovery of F compounds is possible with all of the existing technologies in phosphate processing. Accordingly, phosphate rocks represent another possible source of fluorine (McKelvey 1967; Gorecki 1994).

In addition, it must be emphasized that black shales, which can contain significant amounts of valuable trace elements, such as Be, Sb, V, Co, Ni, Mo, PGM, Cr and Zn (e.g., Huyck 1989), often host sedimentary phosphorite. They are also interesting with regard to (precious) metals, which they may host (McKelvey 1967).

3 Description of the project

This subproject “Critical Raw Materials in phosphate deposits and associated black shales” aims to provide an overview about phosphate mineralizations (and associated economically interesting black shales). It will comprise detailed mineralogical and geochemical characterization of key phosphate deposits of sedimentary and igneous origin. These metallogenic, mineralogical and geochemical studies will help to decipher the processes leading to CRM enrichment in these deposits. Since part of the phosphorites in Europe are hosted within metalliferous black shales, the latter will be considered as well, with the view of a combined and rational exploitation of these resources. Another aim is the development of a procedure to prepare and analyze samples from phosphate deposits. It would be helpful in providing internally consistent geochemical data at a European level for this type of mineralization. Finally, the data from the project will contribute to databases, such as those from Minerals4EU, the European Union Raw Materials Knowledge Base (EURMKB), SRT RM1, EGDI, and the GeoERA Information Platform.

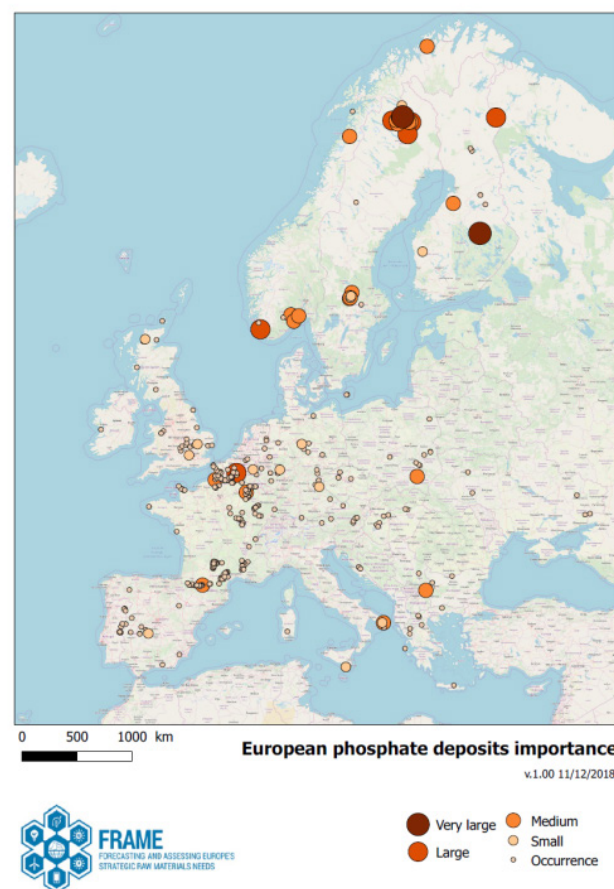


Figure 1. Phosphate deposits and occurrences in Europe. Deposit size: Small (>X) 2,000,000; Medium (>X): 20,000,000; Large (>X): 200,000,000; Very large (>X): 2,000,000,000 tonnes.

More precisely, the objectives are the following ones:

- (1) Acquisition of new mineralogical and geochemical data on selected phosphate deposits and occurrences.
- (1) Careful investigation of a selection of key phosphate deposits representative of the different types of phosphate mineralization encountered in Europe. The goal will be (i) to provide an up-to-date scientific overview about the genesis of phosphate deposits in Europe, (ii) to determine more clearly the potential for CRM (and their speciation) in phosphate deposits (and their metalliferous black shale hosts), and (iii) to investigate the processes leading to their enrichment.
- (2) Establishment of a procedure for sample preparation and analysis of phosphate samples with the objective of providing internally consistent geochemical data on a European level.
- (3) Development of an enhanced database compiling data collected during this project and information from the literature and older databases.

4 First outcome: Overview of the phosphate deposits and occurrences in Europe

4.1 Database

The new database will provide information about the

potential of phosphate mineralization to host CRM, and help to identify new areas of interest for CRM, based on such criteria as: (i) the different commodities/CRM associated with phosphate deposits (REE, F, V, U and Y); (ii) the size of the deposits according to their known tonnages; (iii) the type and origin of the phosphorus-phosphate mineralizations and deposits; (iv) the age of the deposits/occurrences and the host rock; (v) the commodities/CRM (Be, Sb, Co, PGM, V and Cr) in the associated black shales, when applicable and available.

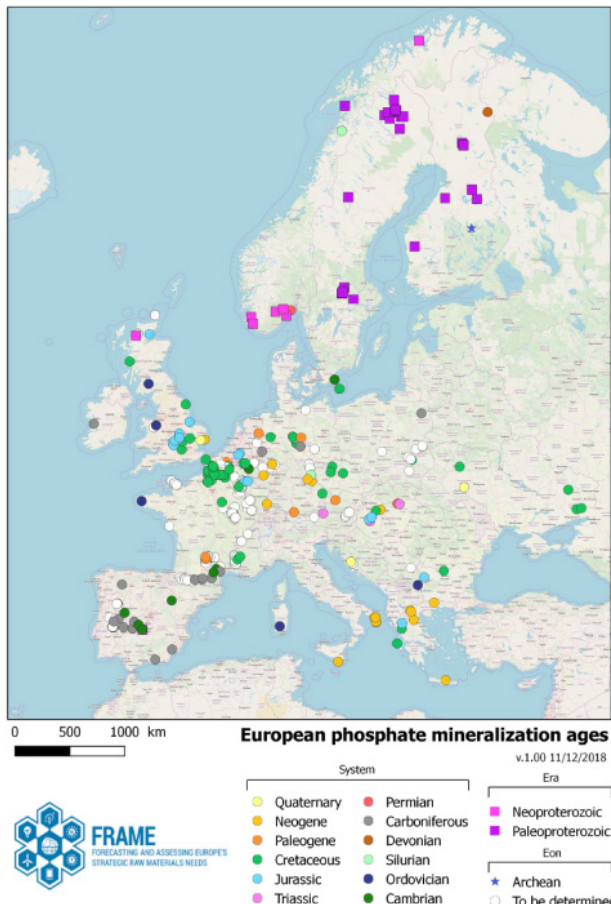


Figure 2. Map illustrating the phosphate deposits/occurrences according to their age (System/Period for Phanerozoic mineralization, Era for Proterozoic mineralization, and Eon for Archean mineralization).

The data sources used to fill in this new database are ProMine, FODD (Fennoscandian Mineral Deposit Database), SIORMINP (Sistema de Informação de Ocorrências e Recursos Minerais Portugueses), and Mine records database (Ireland). In addition, information extracted from approximately 60 references, including some very recent ones, is integrated.

The compiled database presents 429 phosphate deposits and occurrences throughout Europe. This is undoubtedly one of the most complete (if not the most complete) databases about phosphate mineralizations of the continent. Taken as a whole, it shows the diversity and potential regarding phosphate mineralization in Europe fairly well (Fig 3).

4.2 Maps

The maps drawn from the database constitute an added value to the database itself, since they allow visualization at a glance of the most striking features concerning phosphate mineralization in Europe. Here are examples:

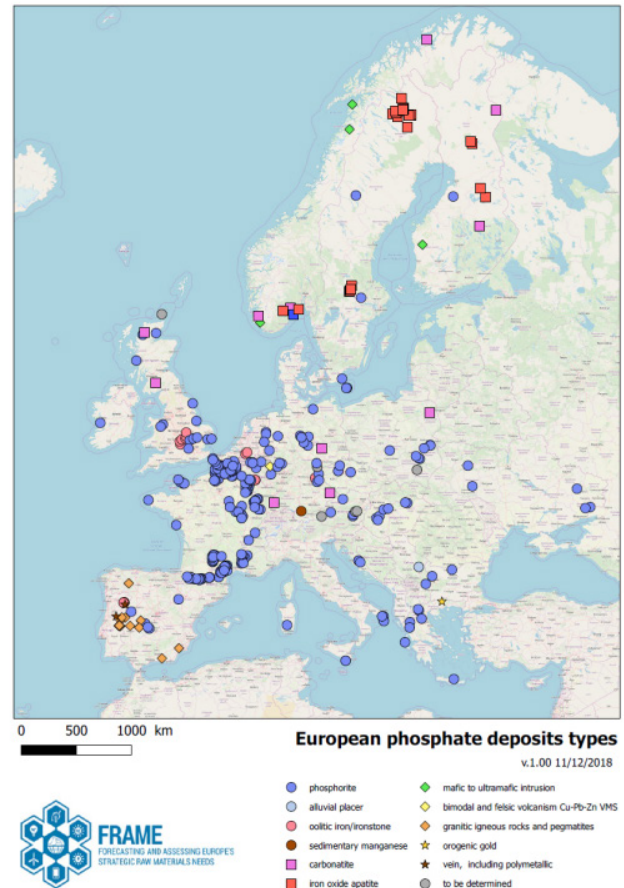


Figure 3. Mineral deposit type of phosphate mineralizations and deposits in Europe.

The first one (Fig 1) presents the known locations of phosphate deposits and occurrences in Europe. The size of the symbol used on the map directly relates to the size of the deposit (not yet UNFC compliant but aiming to be at the end of the project).

The second map (Fig 2) shows the deposits/occurrences according to their age. This map allows considering the regions where important phosphogenic events have occurred. This is also of interest because the potential in CRM of sedimentary phosphate deposits is highly dependent on their age and the environment/settings in which they formed.

The last map (Fig 3) allows discrimination of the different “Mineral Deposit Types” (according to Inspire; EC 2007). This map gives clues about the metallogenic provinces and the genetic type of the phosphate mineralization. Among the deposit types encountered are:

(1) Sedimentary phosphorites that are the most abundant and widely distributed phosphate deposits/occurrences in Europe. Three main episodes of phosphogenesis occurred during the Lower Paleozoic,

the Upper Cretaceous, and the Tertiary.

(2) Phosphate mineralizations related to alkaline complexes and carbonatites, as at Siilinjarvi (Archean in age), and Sokli (dated Devonian), both being located in Finland.

(3) Apatite deposits associated with Neoproterozoic anorthosite complexes (e.g., the noritic Bjerkreim-Sokndal layered intrusion, Norway) and monzonitic complexes (e.g., the Paleoproterozoic Lofoten-Vesteralen Mangerite Complex and the Permian Larvik Plutonic Complex of the Oslo Paleorift, Norway).

(4) Apatite iron ores (AIO), which are mostly found in the large districts of northern Norrbotten and Bergslagen, Sweden. A large part of the igneous deposits are located in the Fennoscandian Shield. The genetic type of the mineralization has an influence on the potential in CRMs of the deposit. For instance, REE content in magmatic apatite is usually higher than in apatite formed in a sedimentary environment.

Both maps in Figs. 2 and 3 aim at identifying new areas of interest for CRM and constraining the potential of the deposits. The new geochemical data to be acquired during this project will help to better constrain these zones.

5 Future work and prospects

In the future, an enhanced database will be developed, compiling the present database and new mineralogical and geochemical data collected during the project.

The combination of these new data sets will lead to (i) a better understanding of the CRM distribution and enrichment (grade) within these deposits, and constrain the processes, which have led to these enrichments, and (ii) identify and highlight the potential of these deposits regarding the CRMs. Research continues.

Acknowledgements

This project has received funding from the European Union's Horizon 2020 research and innovation program under grant agreement No 731166.

References

- Christmann P (2014) A forward look into rare earth supply and demand: a role for sedimentary phosphate deposits? *Procedia Engineering* 83:19-26
- EC (European Commission) (2007) Establishing an Infrastructure for Spatial Information in the European Community (INSPIRE). <https://eur-lex.europa.eu/legal-content/EN/TXT/HTML/?uri=CELEX:32007L0002&from=EN>. Accessed 11 March 2019
- EC (European Commission) (2014) On the review of the list of critical raw materials for the EU and the implementation of the Raw Materials Initiative. <http://eur-lex.europa.eu/legal-content/EN/TXT/PDF/?uri=CELEX:52014DC0297&from=EN>. Accessed 9 December 2016
- EC (European Commission) (2015) Report on Critical Raw Materials for the EU. Critical Raw Materials Profiles. <http://ec.europa.eu/DocsRoom/documents/11911/attachments/1/translations>. Accessed 9 December 2016
- EC (European Commission) (2016). Critical Raw Materials. <https://ec.europa.eu/growth/sectors/raw-materials/specific->

- interest/critical_fr. Accessed 9 December 2016
- Emsbo P, McLaughlin PI, Breit GN et al (2015) Rare earth elements in sedimentary phosphate deposits: Solution to the global REE crisis? *Gondwana Res* 2:776-785
- Goodenough KM, Schilling J, Jonsson E et al (2016) Europe's rare earth element resource potential: An overview of REE metallogenetic provinces and their geodynamic setting. *Ore Geol Rev* 72:838-856
- Gorecki HJ (1994) Utilization of fluorine from phosphate fertilizer plants. In: Hodge CA, Popovici NN (eds) *Pollution control in fertilizer production*, CRC press, pp 299-336.
- Huyck HLO (1989) Metalliferous Black Shales and Related Ore Deposits. In: Grauch RI, Huyck HLO (eds) *Proceedings, United States Working Group Meeting, International Geological Correlation Program Project 254*, USGS Circular 1058:42-56
- Ihlen PM, Schiellerup H, Gautneb H, Skår Ø (2014) Characterization of apatite resources in Norway and their REE potential—a review. *Ore Geol Rev* 58:126-147
- McKelvey VE (1967) *Phosphate deposits* (No. 1252-D), USA Govt Print Off
- Notholt AJG, Sheldon RP, Davidson D (1989) Europe-Introduction. In: Notholt AJG, Sheldon RP, Davidson D (eds) *Phosphate deposits of the world: volume 2, phosphate rock resources*, Cambridge University Press, Cambridge
- Pereira F, Bilal E (2012) Phosphoric acid extraction and rare earth recovery from apatites of the Brazilian phosphatic ores. *Rom J Miner Dep* 85:49-52

Mineral resources for green growth in the U.S.

Jeffrey L. Mauk, Nicholas A. Karl, Morgan Mullins, Carma A. San Juan, Germán Schmeda, Patrick Scott, and Bradley S. Van Gosen
U.S. Geological Survey, USA

Abstract. The objective of the U.S. Geological Survey's mineral deposit database project is to develop a comprehensive 21st century geospatial database that is the authoritative source of the most important mines, mineral deposits, and mineral districts of the United States. Since May 2017, the project has focused on critical minerals. Data for critical minerals that are produced as products are relatively robust, whereas data for byproducts are commonly of much poorer quality. For example, rare earth elements occur principally in deposits hosted by alkaline igneous rocks, but there is potential for production from waste from phosphate rock mining. Lithium has been recovered from pegmatites and brines, but other Li-bearing deposit types that may go into production have been delineated. Cobalt may be produced as a byproduct from a wide range of mineral deposit types, whereas Te is a byproduct of copper ore. Significant opportunities for research exist that could help identify new sources of critical minerals, and might also help increase production and recovery from existing sources.

1 Introduction

The rate of technological change is astonishing and accelerating. Smart phones, smart cars, advanced defense systems, green technology, and many other applications rely on an essential array of elements and compounds that were almost unused three decades ago. The uneven geological and geographic distribution of these elements and the orebodies that produce them, combined with estimates of political stability, have led to the development of critical minerals lists by different nations and organizations.

This paper summarizes significant mineral deposits, as measured by production and resources, that are available for green growth applications in the U.S. Related databases for the U.S. Geological Survey's mineral deposit database project are on the web at https://www.usgs.gov/energy-and-minerals/mineral-resources-program/science/usgs-mineral-deposit-database?qt-science_center_objects=4#qt-science_center_objects. Herein, we critically assess knowledge gaps that impede our ability to evaluate and estimate supply chain risk and possible new sources of materials. We conclude by delineating important avenues for future research to more fully assess the availability of mineral resources to meet the globally increasing growth in green technologies.

2 Mineral deposits and resources for green growth in the U.S.

This contribution focuses on rare earth elements (REEs), Li, Co, and Te, which are some of the most important critical minerals for green growth. We consider deposits with past production or resources that exceed specific cut-off values, so as to consider only deposits that may be significant in a global economy.

2.1 Rare earth elements

The REEs represent a prime example of a critical mineral resource. In the 21st century, the REEs have gained visibility due to: (1) the recognition of the essential, specialized properties that REEs contribute to modern technology, as well as (2) China's dominance in production and supply of the REEs, and (3) international dependence on China for the majority of the world's REE supply. Since the late 1990s, China has provided 85–95% of the world's REEs, while the U.S. is highly dependent on REEs for their use in high technology devices, clean energy components, and defense technologies (Jowitt et al. 2018; Van Gosen et al. 2018).

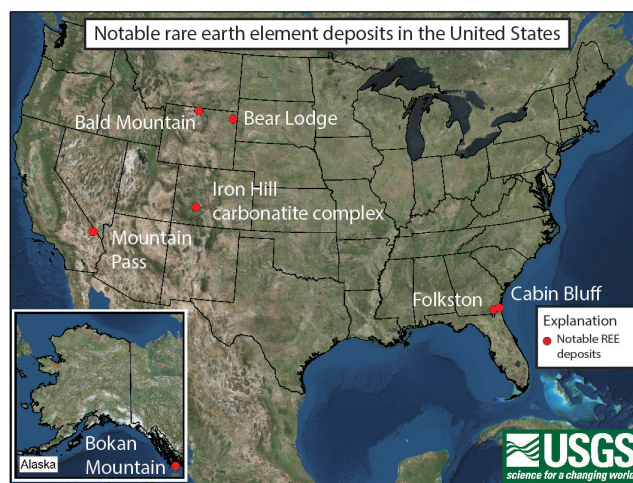


Figure 1. Distribution of notable REE deposits in the U.S.

The deposits with the largest REE endowments in the U.S. are carbonatites at Iron Hill, Colorado; Mountain Pass, California; and Bear Lodge, Wyoming. These are examples of REE deposits hosted by alkaline igneous rocks, which is the predominant source of REEs on a global basis (e.g., Chakhmouradian and Wall 2012; Van Gosen et al. 2018, and references therein). In addition to these conventional resources, every year approximately 56,000 t of REEs are mined, beneficiated, and put into

solution, but not recovered, by operations associated with the global phosphate fertilizer industry (Emsbo et al. 2015; Emsbo et al. 2016). Metallurgical trials are currently underway to attempt to recover REEs from the 2Gt of waste material from phosphate mining operations in Florida, which contains approximately 600 kt of REEs (Zhang et al. 2019).

2.2 Lithium

Lithium is necessary for strategic, consumer, and commercial applications. The primary uses for Li are in batteries, ceramics, glass, metallurgy, pharmaceuticals, and polymers. The commodity is traded in three primary forms: mineral concentrates, mineral compounds (from brines), and refined metal (electrolysis from lithium chloride). Lithium mineralogy is diverse; it occurs in a variety of pegmatite minerals, such as amblygonite, lepidolite, and spodumene, and in the clay mineral hectorite (Kesler et al. 2012; Bradley et al. 2017).

In the U.S., Li was first mined from pegmatites in South Dakota in the late 1800's. As of 2019, the only deposit in the U.S. that is producing Li is the Clayton Valley brine deposit in Nevada. Because the U.S. is not a significant producer of Li, it is primarily imported to the U.S. from Chile and Argentina to meet consumer needs for the commodity. In 2018, the U.S. imported more than 50% of its Li (U.S. Geological Survey 2019), and for this reason, Li has been included as a critical mineral as defined by the USGS in response to Executive Order 13817 and Secretarial Order No. 3359 (Fortier et al. 2018).

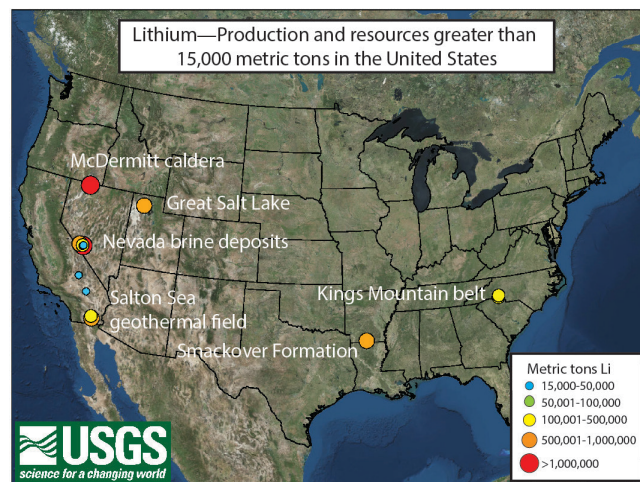


Figure 2. Distribution of Li deposits in the U.S.

Past production of more than 15,000 metric tons (t) Li in the U.S. has come from pegmatite deposits of the Kings Mountain belt in North Carolina, and from the Clayton Valley brine deposit in Nevada. This production mimics global production, where pegmatites and brines are the predominant sources of Li (Kesler et al. 2012). The U.S. has other resources that contain more than 15,000 t Li, including oilfield brines of the Smackover Formation in Arkansas, closed-basin brines in Nevada and California, Li-rich clay minerals such as those in the McDermitt caldera in Nevada, geothermal brines such as

those in the Salton Sea geothermal fields in California, and the Great Salt Lake in Utah (Bradley et al. 2017; Karl 2019).

2.3 Cobalt

Cobalt has diverse uses because of its properties, which include ferromagnetism, hardness, wear-resistance, low conductivity, and high melting point. The primary uses for Co are in rechargeable battery electrodes, and in superalloys used to make gas turbine engines. In 2017, the U.S. imported 72% of its Co (U.S. Geological Survey 2019).

Cobalt mineralogy is diverse; it occurs in a variety of sulfide, arsenide, sulfarsenide, and oxyhydroxide minerals. In the U.S., Co could be derived as a byproduct from mineral deposits that primarily produce other metals, including Ni, Cu, Zn, and Pb. The range of deposit types that may produce Co is diverse, and includes laterite deposits (Puerto Rico), volcanic hosted massive sulfide deposits (Ducktown, Tennessee), Mississippi Valley type deposits (Missouri), magmatic Ni-Cu-PGE deposits (Minnesota), sediment-hosted massive sulfide deposits (Black Butte, Montana; Idaho cobalt belt), and Kipushi deposits (Bornite, Alaska) (Burger et al. 2018; Fig. 2).

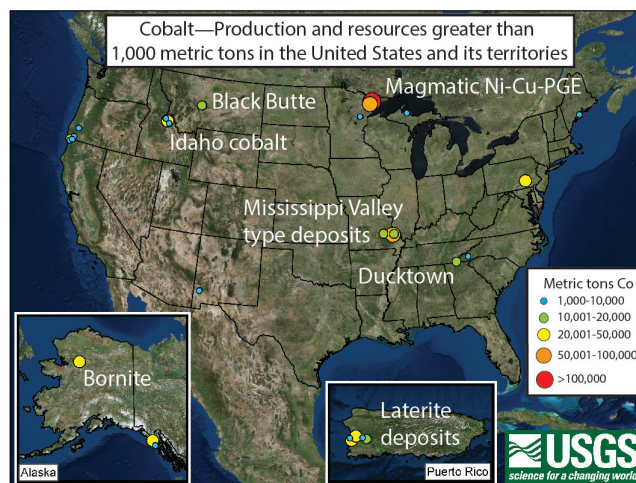


Figure 3. Distribution of Co deposits in the U.S.

2.4 Tellurium

The main use of Te is for Cd-Te film in solar cells; other common uses are in thermoelectric cooling instruments, and as an additive to Cu, Pb, and steel alloys to improve machine efficiency (Goldfarb et al. 2017). In 2018, the U.S. had an import reliance of more than 75% for Te (U.S. Geological Survey 2019). Tellurium principally occurs in Au, Ag, and PGE telluride minerals; less is known about its distribution as a minor and trace element in sulfide minerals (e.g., George et al. 2017; Keith et al. 2018, and references therein). Tellurium is principally recovered from anode slimes as a byproduct of electrolytic copper refining, and in the U.S., the main producers of Te are likely the porphyry Cu deposits of the western U.S. However, because it is a byproduct mineral, Te production is rarely reported; only Butte, Montana has

historic production records (Fig. 4).

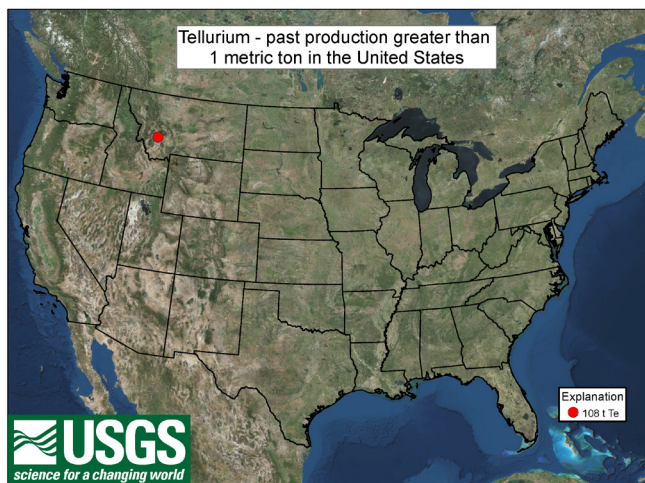


Figure 4. Distribution of Te deposits in the U.S.

2.5 Gallium, germanium, indium, antimony, and graphite

Other elements and minerals that are important for low-emission energy production, storage, and usage include Ag, Cd, Ga, Ge, In, Ni, Sb, Se, and graphite (Nassar et al. 2016; Hayes et al. 2019). Of these, Ga, Ge, In, Sb, and graphite have been listed as critical minerals in the U.S. (Fortier et al. 2018). The first four—Ga, Ge, In, and Sb—are byproduct elements whose resources and production are not widely reported. Graphite, Ga, and In were 100% imported to the U.S. in 2018, Sb was 85% imported, and Ge was >50% imported (U.S. Geological Survey 2019).

Graphite differs from most other critical minerals because it is a mineral, rather than an element or element group, and therefore it is classified and valued differently. Natural graphite occurs as vein, amorphous, and disseminated flake deposits, which form 1%, 44% and 55% of the graphite market, respectively (Industrial Minerals 2019). Vein and flake graphite command the highest prices due to the higher quality of that material; graphite quality is determined by flake size, carbon purity, and industry-specific technical attributes of the flakes. Although the U.S. currently has no graphite production, the Graphite One project in Alaska has an NI 43-101 compliant indicated resource of 10.3 Mt with 7.3% graphite, and an inferred resource of 71.2 Mt with 7.0% graphite (Eccles et al. 2015).

3 Discussion

The commodities described herein encapsulate many of the challenges and opportunities that are inherent with the growth of the critical minerals industry. This section discusses some of those challenges and opportunities.

The majority of the critical minerals are primarily recovered as byproducts, and in many cases, this leads to profound ignorance of their production and recovery. Because byproduct production does not impact a company's balance sheet, there is no obligation to report them to stakeholders or to the public domain. This is

nice illustrated by Te, where Butte, Montana is the only deposit in the U.S with recorded production values, even though Te has likely been recovered from anode slimes from many porphyry Cu deposits in the western U.S. There is an opportunity for industry to collaborate with researchers to more completely document supply and production of byproduct critical elements. This could provide essential guidance on the next generation of research topics that need to be addressed to ensure supply of critical minerals.

Knowledge of the department of critical minerals varies from excellent in the case of most critical mineral products, to poor for many byproducts. The array of analytical tools that are now available make this an exciting avenue for research that can provide first-order constraints on the recoverability of critical minerals from different deposits and deposit types.

Critical minerals have small, and in many cases volatile markets compared to ferrous, base, and precious metals (Jowitt et al. 2018). Where critical minerals are potential byproducts from deposits, the small market value of potential contributions from these byproducts may provide little incentive to tackle mineral processing challenges, which may hinder critical mineral production. In a world where social license plays an increasingly important role in determining whether prospects can become mines (e.g., Karakaya and Nuur 2018, and references therein), can operating mines derive additional, non-financial benefits by producing critical minerals?

Production of many critical minerals relies on a chain of prerequisites, as illustrated by the possible recovery of Co from the Bornite deposit in Alaska. Bornite lacks critical infrastructure, and cannot go into production before a road is built to the site. Bornite is a copper deposit, and therefore its economic viability rests on its ability to produce copper profitably. The Co resides in co-occurring arsenian pyrite, and current plans are to recover that Co from a separate metallurgical stream (Davis et al. 2016). Therefore, successful recovery of Co from Bornite relies on building a road to access the deposit; economic production of Cu; and successful and economic recovery of Co from a separate metallurgical stream. Any break in this chain would result in no production of Co. Many other byproduct commodities have similarly tenuous production chains.

The small market size and limited production of many critical minerals makes them potentially vulnerable to disruptors. For example, the estimated REE endowment of the waste slimes from Florida phosphate mines—600 kt—exceeds, by more than an order of magnitude, the 28 kt of REE oxides of indicated resources at Bokan Mountain, Alaska. Recovery of byproduct REE from the phosphate industry could transform REE production and availability (Emsbo et al., 2015; 2016). Similarly, the diverse types of Li occurrences that are currently undergoing evaluation shows the potential for disruption; the Li marketplace could be transformed if a specific deposit type can outproduce others at a lower cost.

Many critical minerals report extensively to waste, and some were never considered for recovery until relatively recently (e.g., Jowitt et al. 2018; Hayes et al. 2019, and

references therein). Consequently, one potential avenue for critical mineral recovery is from mine dumps and tailings of former operations (McLemore and Frey 2018). Although conceptually appealing, it must be recognized that weathering of ore materials may change the mineralogical site of critical minerals, which in turn may significantly impact mineral processing and recovery. As above, the array of analytical tools that are now available make this an exciting avenue for future research.

4 Conclusions

In conclusion, the U.S. is making progress with delineating possible domestic sources of critical minerals. However, as illustrated by the examples shown here, this effort is often complicated by a lack of publicly available data that report byproducts recovery. Thus, key priorities for future research include collaboration between industry and researchers to document current production of byproduct critical minerals from different deposits. Improved analytical techniques provide the ability to carefully evaluate where critical minerals reside in ore and waste materials; and collaboration with metallurgists will be necessary to optimize recovery using existing processes, and to develop new recovery processes. Small market size and limited production make critical minerals particularly vulnerable to disruptive changes—the next decade will undoubtedly bring about unexpected quantum shifts in supply and demand.

Acknowledgements

We thank Jesse Bellora, Meredith Burger, Tom Carroll, Keith Long, and Tyler Reyes for their assistance in compiling data releases for several critical elements. Any use of trade, product, or firm names is for descriptive purposes only and does not imply endorsement by the U.S. government.

References

Bellora JD, Burger MH, Van Gosen BS, Long KR, Carroll TR, Schmeda G, Giles SA (2019) Rare earth element occurrences in the United States (ver. 3.0, March 2019). U.S. Geological Survey data release, <https://doi.org/10.5066/F7FN15D1>.

Bradley DC, Stillings LL, Jaskula BW, Munk L, McCauley AD (2017) Chapter K. Lithium In: Schulz KJ, DeYoung JH, Jr., Seal RR, Bradley DC (eds) Critical mineral resources of the United States—Economic and environmental geology and prospects for future supply. U.S. Geological Survey Professional Paper 1802, pp K1–K21.

Burger MH, Schmeda G, Long KR, Reyes TA, Karl NA (2018) Cobalt deposits in the United States. U.S. Geological Survey data release, <https://doi.org/10.5066/P9V74HIU>.

Chakmouradian AR, Wall F (2012) Rare earth elements: Minerals, mines, magnets (and more). *Elements* 8:333-340.

Davis B, Sim R, Austin J (2016) NI 43-101 technical report on the Bornite project, northwest Alaska, USA. 169 p.

Eccles DR, Nicholls S, Hough R (2015) 2015 Indicated and inferred mineral resource estimate at the Graphite Creek property, Alaska, United States. Edmonton, Alberta, Canada, 138 p.

Emsbo P, McLaughlin PI, Breit GN, du Bray EA, Koenig AE (2015) Rare earth elements in sedimentary phosphate deposits: Solution to the global REE crisis? *Gondwana Research* 27:776-785.

Emsbo P, McLaughlin PI, du Bray EA, Anderson ED, Vandenbroucke T, Zielinski RA (2016) Rare earth elements in sedimentary phosphorite deposits: a global assessment Rare earth and critical elements in ore deposits. *Society of Economic Geologists: Reviews in Economic Geology*, v. 18:101-113.

Fortier SM, Nassar NT, Lederer GW, Brainard J, Gambogi J, McCullough EA (2018) Draft critical mineral list—Summary of methodology and background information—U.S. Geological Survey technical input document in response to Secretarial Order No. 3359. U.S. Geological Survey Open-File Report 2018–1021, 15 p.

George LL, Cook N, Ciobanu C (2017) Minor and trace elements in natural tetrahedrite-tennantite: Effects on element partitioning among base metal sulphides. *Minerals* 7, 25 p.

Goldfarb RJ, Berger BR, George MW, Seal RR, II (2017) Chapter R. Tellurium In: Schulz KJ, DeYoung JH, Jr., Seal RR, Bradley DC (eds) Critical mineral resources of the United States—Economic and environmental geology and prospects for future supply. U.S. Geological Survey Professional Paper 1802: R1-R27.

Hayes SM, Piatak NM, Seal RR, II (2019) Challenges of byproduct recovery of critical elements. SGA 2019 abstracts, IN PRESS.

Industrial Minerals (2019) <https://www.indmin.com/Graphite.html>. Accessed 06 March 2019.

Jowitt SM, Mudd GM, Werner TT, Weng Z, Barkoff DW, McCaffrey D (2018) The critical metals: An overview and opportunities and concerns for the future In: Arribas R AM, Mauk JL (eds) *Metals, Minerals, and Society: Society of Economic Geologists Special Publication* 21: 25–38.

Karakaya E, Nuur C (2018) Social sciences and the mining sector: Some insights into recent research trends. *Resources Policy* 58:257-267.

Karl NA (2019) Lithium deposits in the United States. U.S. Geological Survey data release, IN REVIEW.

Keith M, Smith DJ, Jenkin GRT, Holwell DA, Dye MD (2018) A review of Te and Se systematics in hydrothermal pyrite from precious metal deposits: Insights into ore-forming processes. *Ore Geology Reviews* 96:269-282.

Kesler SE, Gruber PW, Medina PA, Keoleian GA, Everson MP, Wallington TJ (2012) Global lithium resources: Relative importance of pegmatite, brine and other deposits. *Ore Geology Reviews* 48:55-69.

McLemore VT, Frey B (2018) Making abandoned mine lands (AML) profitable—workshop proceedings and abstracts. New Mexico Bureau of Geology and Mineral Resources Open-File Report 597.

Nassar NT, Wilburn DR, Goonan TG (2016) Byproduct metal requirements for U.S. wind and solar photovoltaic electricity generation up to the year 2040 under various Clean Power Plan scenarios. *Applied Energy* 183:1209-1226.

U.S. Geological Survey (2019) Mineral commodity summaries 2019. U.S. Geological Survey, 200 p.

Van Gosen BS, Verplanck PL, Seal RR, II, Long KR, Gambogi J (2018) Rare-earth elements, Chapter O In: Schulz KJ, John H. DeYoung J, Seal RR, II, Bradley DC (eds) Critical mineral resources of the United States—Economic and environmental geology and prospects for future supply. U.S. Geological Survey Professional Paper 1802: O1-O31.

Zhang J, Alledini G, Jin Z, DePaoli D, Anderson C (2019) Characterization study of an abundant secondary resource for yttrium and heavy rare earths Smart Mining: Resources for a connected world—2019 SME annual conference and expo. Denver, Colorado, p. 209.

Punctuated release of Lithium from past ignimbrite eruptions: key to present Lithium-brine resources in the Western U.S. & Central Andes

Albert Hofstra, Celestine Mercer, Erin Marsh, Alexandra Wallenberg

U.S. Geological Survey, Denver Inclusion Analysis Laboratory, USA

Mark Mihalasky

U.S. Geological Survey, Spokane Field Office, USA

Scott Hynek

U.S. Geological Survey, Utah Water Science Center, USA

Abstract. Lacustrine evaporite basins with significant Li resources in the western U.S and central Andes were filled over millions of years concurrent with volcanism. Since felsic ignimbrites are voluminous and contain more Li than andesites, their pre- and post-eruptive concentrations of Li were determined to evaluate Li mobility. Comparisons of the Li content of melt inclusions to those of pumice or whole rock show that Li-enriched ignimbrites release up to 98% of their Li into soluble salts that are removed by meteoric water whereas Li-poor ignimbrites release as little as 36%. Calderas trap about 1/3 of the Li released from such eruptions, with the remainder deposited in adjacent basins. Small volume eruptions of Li-enriched tuff can release tens of megatonnes into one basin whereas large volume eruptions of ordinary tuff spread a similar amount over many basins. Large volume eruptions of Li-enriched tuff can spread gigatonnes of Li over many basins.

The punctuated release of large amounts (tens to thousands Mt) of Li from successive ignimbrite eruptions into closed drainage basins increases resource potential, is more than enough to form world-class Li-brine and -clay resources (tenths to several Mt) and should be included in mass-balance, exploration, and assessment models.

1 Introduction and Background

The growing demand for Li, driven by the burgeoning Li battery industry, has fueled a global exploration boom for pegmatites and lacustrine brine and clay deposits. About half of the world's present and future Li resources occur in brine and clay layers in lacustrine evaporite basins (Bradley et al. 2018). A common factor that can explain the heterogeneous distribution of Li-brine and -clay resources over space and time in the western U.S. and central Andes is the eruption of ashflow tuff and tephra into closed basins from which Li can be leached by surface water, groundwater and geothermal fluids (Coolbaugh et al. 2018).

As summarized by Bradley et al. (2018), Li-brines form under arid climatic conditions by the evaporation of meteoric water, which results in the formation of salt flats or salars. Gypsum, halite, and sometimes potash and

borate, precipitate at the surface while conserved elements such as Li and Mg are concentrated in residual brine. Residual brines are dense and sink into basin aquifers where they accumulate over time. The Li-clay deposits in these basins likely formed by hydrolysis of volcanic ash by Li-brines over a range of T°C (Stillings & Godfrey, 2018).

Recent studies of Li-brine deposits in closed drainage basins (e.g. Salar de Atacama; Munk et al. 2018) have used present rates of Li input in surface water and groundwater coupled with the evaporation rate to estimate the time required to concentrate the amount of Li present in the basin. Leachate analyses of volcanic rocks in these basins show that only about 2% (~0.5 ppm) of the Li is released into surface water or groundwater, which is similar to concentrations in present day surface and groundwater. Hence, the approach used in these studies did not consider the punctuated release of large amounts of Li from past ignimbrite eruptions. This is a significant flaw because many lacustrine evaporite basins are long lived and occur in or near coeval volcanic fields. For example, the Salar de Atacama basin has been in its present configuration for ~10 Ma over which time it was blanketed by several ignimbrite eruptions (Evenstar et al. 2016).

Because Li is an incompatible element, the Li content of felsic melts depends on the amount of continental crust assimilated by mantle-derived magmas and the degree of fractional crystallization (Benson et al. 2017). The mass of Li released from ignimbrite eruptions (Eq. 1) can be estimated from the volume and density of tuff, the pre-eruptive concentration of Li in silicate melt inclusions in phenocrysts (Fig. 1), and the post-eruptive concentration of Li in pumice or whole rock (Hofstra et al. 2013). For crystal-rich ignimbrites, the mass fraction of glass must be estimated. The areal distribution and thickness of tuff can be used to apportion the amount of Li released from each eruption into closed basins.

Equation 1. Li Released (t) = Volume of tuff (m³) x density of tuff (t/m³) x mass fraction of glass x [mass fraction of Li in melt inclusions – mass fraction of Li in pumice or whole rock]

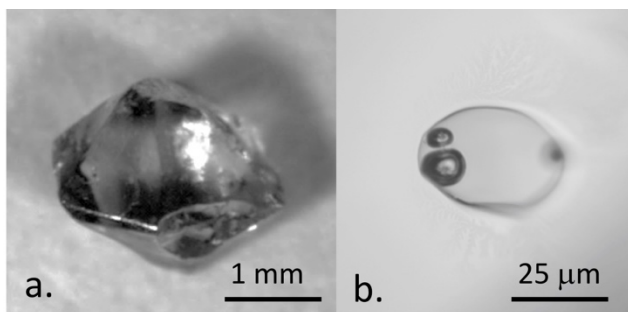


Figure 1. Quartz phenocryst **a.** with melt inclusion **b.** containing 4000 ppm Li from the Spor Mountain Tuff (Hofstra et al., 2013).

The aim of this report is to demonstrate that the vast majority of the Li transferred from ashflow tuffs and tephra into closed drainage basins occurs in a punctuated fashion during or soon after each eruption. Hence, the volcanic history and life span of closed lacustrine evaporite basins is the key to their present Li-endowments.

2 Western United States

In the western U.S., previous studies of melt inclusions and pumice glass or whole rock show that upon or soon after eruption, 36-98% of the Li present in magma is released into surficial environments (Hofstra et al. 2013; Benson et al. 2017). Moreover, Li-enriched melts release a greater percentage of their contained Li. The results also show that small volume eruptions of enriched tuff (e.g. Spor Mtn, 21.7 Ma, 10 km³, 3750 ppm Li) release significant amounts of Li (55 Mt) into small areas whereas large volume eruptions of ordinary tuff (e.g. Bishop, 0.8 Ma, 600 km³, 74 ppm Li; Fig. 2a) spread similar amounts (41 Mt) over large areas. Large volume eruptions of enriched tuff (e.g. tuff of Long Ridge, 16.3 Ma, 1080 km³, 1600 ppm Li; Fig. 2b) release enormous amounts of Li (3685 Mt) over large areas. Consequently, successive eruptions into closed basins increase resource potential.

Clayton Valley in southwest Nevada has a 0.3 Mt Li-brine resource that has been in production since the 1960s (Bradley et al. 2018) and a newly defined 0.02 Mt Li-clay resource (Barrie et al. 2018). It is located about 100 km east of the source caldera for the Bishop Tuff and Bishop tephra is 3-7 m thick in Clayton Valley, consistent with the westerly trade winds. The small volume of Bishop tephra deposited in the ~1400 km² Clayton Valley drainage basin (4.2 km³) released about 0.29 Mt of Li. In the Pliocene, small volume, rhyolite tuffs and flows exposed on the east side of Clayton Valley released about 83% and 53% of their contained Li (200 ppm) into the drainage basin (Hofstra et al. 2013). The amount of Li released (Fig. 2a) from 1 km³ of CV tuff (0.32 Mt) is similar to the amount of Li in brine. Together or individually, the Bishop Tuff and CV tuff can explain the known Li resource.

The Miocene McDermitt caldera in northwest Nevada contains a 1.7 Mt Li-clay resource (Lithium Americas, 2018). It was the only significant closed drainage basin in the volcanic field. Since the calderas in this field contain

about 1/3 of their eruption volumes, about 1/3 of the 3685 Mt of Li released from the tuff of Long Ridge (Fig 2b) was likely trapped in the McDermitt caldera. Only 1.5% of this amount is present in the known Li-clay resource. It is therefore possible that the caldera contained a much larger Li-brine resource in the past that either drained into underlying aquifers or discharged into the Pacific.

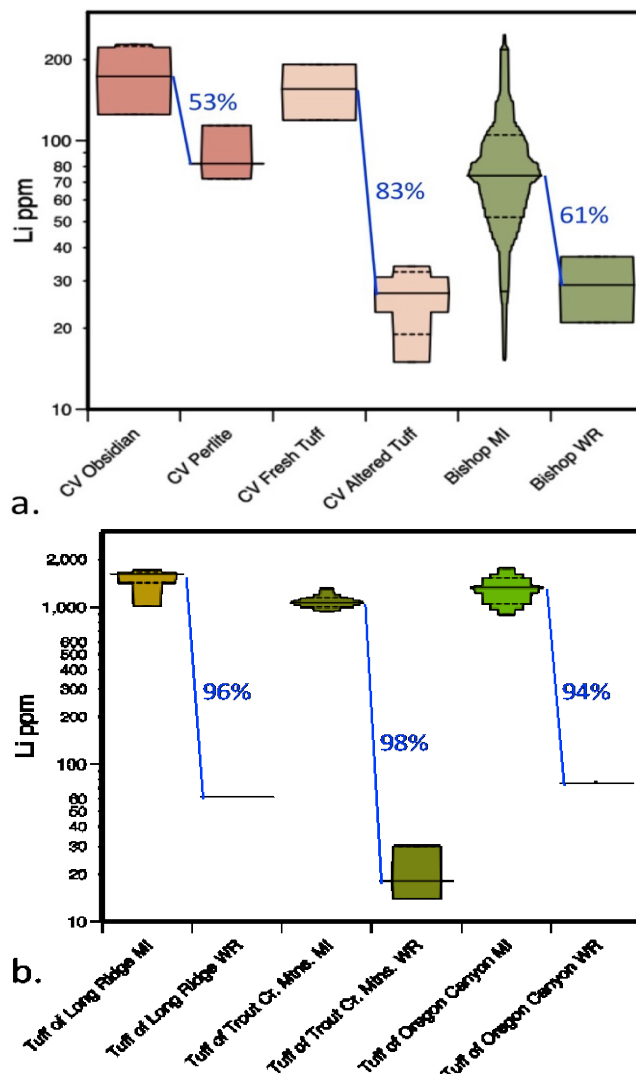
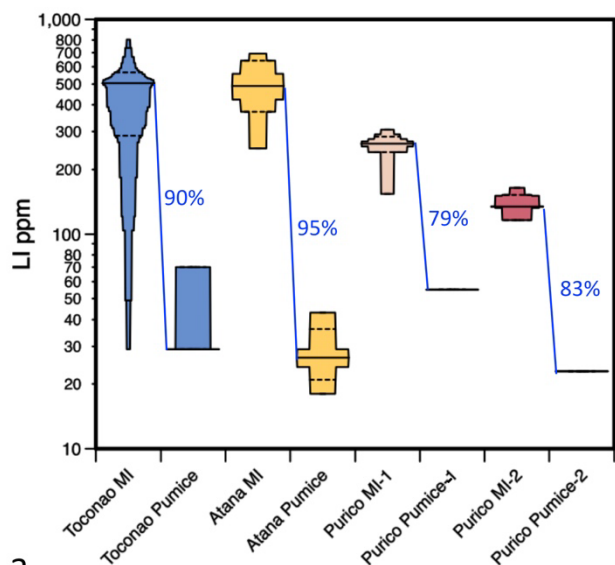


Figure 2. a. Percent Li released from Clayton Valley (CV) rhyolites, Bishop Tuff and **b.** peralkaline rhyolites in the McDermitt volcanic field. Data from Anderson et al. (2000), Price et al. (2000), Hildreth et al. (2007), Benson et al. (2017). Median values were used to calculate the Li depletions shown. Abbreviations: melt inclusion (MI) and whole rock (WR).

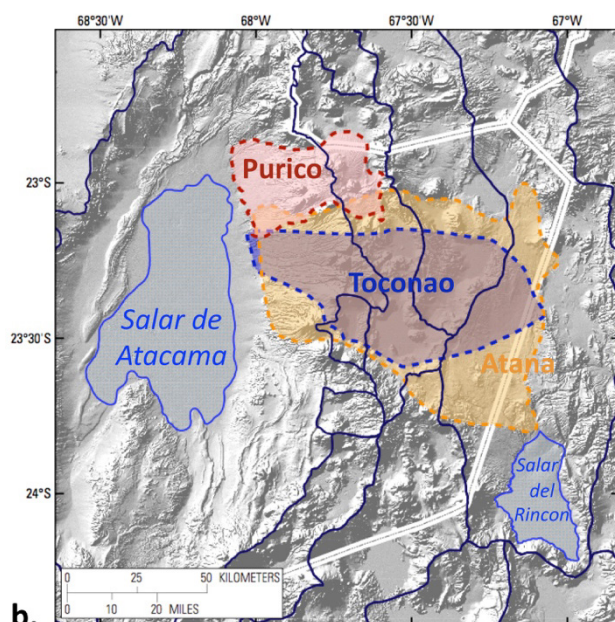
3 Central Andes

In the central Andes of Bolivia, Chile and Argentina, numerous ignimbrite eruptions blanketed closed drainage basins over the past 10 m.y. (Kern et al. 2016) and several basins contain Li-brine resources (Munk et al. 2016). Many are west of eruptive centers, consistent with easterly trade winds. The Li-content of melt inclusions and pumice have only been determined for three ignimbrites that erupted into the Salar de Atacama

and Salar del Rincon basins at 4 Ma (Toconao and Atana) and 1 Ma (Purico) (Fig. 3a,b).



a.



b.

Figure 3. a. Percent Li released from the 4.00 Ma Toconao, 3.96 Ma Atana, and 0.98 Ma Purico-1 & -2 ignimbrites. Data from Lindsay et al. (2001), Schmitt et al. (2001), Burns et al. (2015), Kern et al. (2016), and this study. b. Distribution of ignimbrites relative to closed drainage basins and salars.

The calculated amount of Li released from these eruptions (Eq. 1) is as follows: Toconao 90 Mt, Atana 1000 Mt, and Purico 15 Mt. The Salar de Atacama basin captured about 275 Mt of the 1105 Mt of Li released from these ignimbrites and the Salar del Rincon basin about 315 Mt of Li; the remainder went into intervening basins (Fig. 3b). The Salar de Atacama brine resource contains about 7.5 Mt of Li at an average grade of 1400 ppm and the Salar del Rincon 0.2 Mt at an average grade of 400 ppm. The known Li brine resources account for only 2.7%

and 0.6% of the Li released, which suggests either that most of the Li was not concentrated in brine or that additional Li-brine or -clay resources are present at depth. The latter alternative is supported by the mismatch in accumulation times for NaCl (~50 Ma) and Li (~2 Ma) in the Salar de Atacama (Munk et al. 2018). Since halite is buoyant and brine is dense, the mismatch may be due to the loss of Li-brine from the bottom of the basin along permeable structures or depletion of Li from brine into clay minerals, as observed in other basins.

4 Model & Conclusions

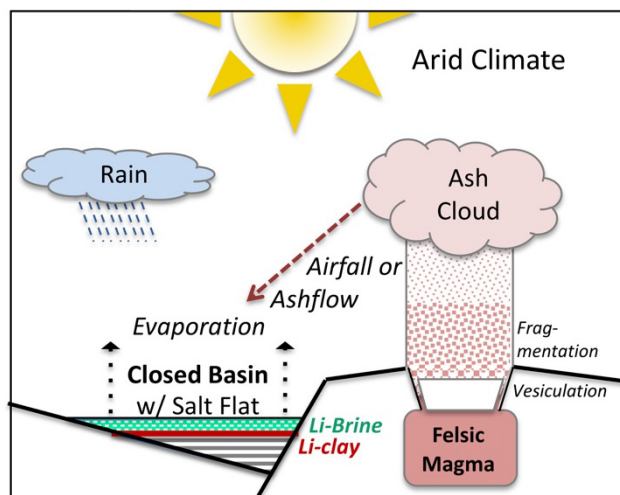


Figure 4. Model (after Hofstra et al., 2013), see text for further description.

In this model, felsic crustally contaminated magmas erupt and deposit ash into closed drainage basins in arid climatic zones. Calderas trap a significant fraction of each eruption. The pressure drop during magma ascent and eruption results in fluid saturation, vesiculation of melt, and fragmentation of glass. Because the diffusion rate of Li rivals that of helium at magmatic temperatures (Richter et al. 2003), Li in melt or glass diffuses into vesicles and out to shard surfaces. Li partitioned into magmatic fluid condenses onto shard surfaces or dust particles in the form of soluble Li-salts. The initial flush of meteoric water, from rain or snowfall, through tuff or tephra dissolves Li-salts and drains into closed drainage basins (e.g. calderas or grabens) where it is concentrated by evaporation. Li-enriched melts release up to 98% of their contained Li in this manner. Residual Li in tuff is less abundant and resides in relatively insoluble phenocrysts such that only about 2% is leached by subsequent flushes of surface water or groundwater. The resulting Li-brine may react with basin sediments (e.g. ash layers) to form Li-clay deposits and/or descend along structures into permeable aquifers, where it may reside for thousands to millions of years. Successive ignimbrite eruptions into a closed drainage basin increase the amount of Li that can be concentrated into Li-brine and -clay deposits; thus, well situated basins blanketed by several Li-enriched ignimbrites, such as the Salar de Atacama are the most prospective.

All of the closed drainage basins in the western U.S. and central Andes with significant Li resources were filled during periods of volcanism. The punctuated release of large amounts of Li from successive ignimbrite eruptions into these drainage basins increases resource potential, is more than enough to form world-class Li-brine and -clay resources and should be included in mass-balance, exploration, and assessment models.

Isotopic fractionation by chemical diffusion between molten basalt and rhyolite: *Geochimica et Cosmochimica Acta*, v. 67, p. 3905-3923.

Schmitt AK (2001) Gas-saturated crystallization and degassing in large-volume, crystal-rich dacitic magmas from the Altiplano-Puna, northern Chile. *J Geophys Res* 106:30561-30578.

Stillings LL, Godfrey L (2018) Isotopic Composition of Lithium in Lithium-bearing Clays from the Southwestern US. AGU Fall Mtg. Abstract V14B-34.

References

- Anderson AT Jr, Davis AM, Lu F (2000) Evolution of Bishop Tuff rhyolitic magma based on melt and magnetite inclusions, and zoned phenocrysts. *Jour Petrol* 41:449-473.
- Barrie CT, Peek B, Whittaker P (2018) Lithium clay deposits of the Zeus Property, Eastern Clayton Valley, Nevada. AGU Fall Mtg. Abstract V14B-32.
- Benson TR, Coble MA, Rytuba JJ, Mahood GA (2017) Lithium enrichment in intracontinental rhyolite magmas leads to Li deposits in caldera basins. *Nature Commun* 270 DOI: 10.1038/s41467-017-00234-y
- Bradley DC, Stillings LL, Jaskula BW, Munk LA, Bradley AD (2018) Chapter K. Lithium. In: *Critical mineral resources of the United States—Economic and environmental geology and prospects for future supply*, U.S. Geological Survey Professional Paper 1802:K1-K21.
- Burns DH, De Silva SL, Tepley-III F, Schmitt AK, Loewen MW, (2015) Recording the transition from flare-up to steady-state arc magmatism at the Purico-Chascon volcanic complex, northern Chile. *Earth Plan Sci Let* 422:75-86.
- Coolbaugh MF, Stillings LL, Hickson CJ (2018) Relationship of Cenozoic volcanic activity to lithium concentrations in playas and sediments around the world and implications for genesis of lithium-enriched brines. AGU Fall Mtg. Abstract V14B-25.
- Evenstar LA, Hartley AJ, Archer SG, Neilson JE (2016) Climatic and halokinetic controls on alluvial-lacustrine sedimentation during compressional deformation, Andean forearc, northern Chile. *Basin Res* 28:634-657.
- Hildreth W, Wilson CJN (2007) Compositional zoning of the Bishop Tuff. *Jour Petrol* 48:951-999.
- Hofstra AH, Todorov TI, Mercer CN, Adams DT, Marsh EE (2013) Silicate melt inclusion evidence for extreme pre-eruptive enrichment and post-eruptive depletion of lithium in silicic volcanic rocks of the western United States—Implications for the origin of lithium-rich brines. *Econ Geol* 108:1691-1701.
- Kern JK, DeSilva SL, Schmitt AK, Kaiser JF, Iriarte AR, Economos R (2016) Geochronological imaging of an episodically constructed subvolcanic batholith: U-Pb in zircon chronochemistry of the Altiplano-Puna volcanic complex of the central Andes. *Geosphere* 12:1054-1077.
- Lindsay JM, Schmitt AK, Trumbull RB., DeSilva SL, Siebe W, Emmermann R (2001) Magmatic evolution of the La Pacana caldera system, central Andes, Chile: Compositional variation of two cogenetic, large-volume felsic ignimbrites, *J Petrol*, 42:459-486.
- Lithium Americas (2018) Thacker Pass, the largest known lithium resource in the United States and the next large-scale lithium mine. <http://www.lithiumamericas.com/thacker-pass/>
- Munk LA, Hynek SA, Bradley DC, Bout D, Labay K, Jochens H (2016) Lithium brines: A global perspective. *Rev Econ Geol* 18:339-365.
- Munk LA, Boutt DF, Hynek SA, Moran BJ (2018) Hydrogeochemical fluxes and processes contributing to the formation of lithium-enriched brines in a hyper-arid continental basin. *Chem Geol* 493:37-57.
- Price, JG, Lechler PJ, Lear MB, Giles TF (2000) Possible volcanic source of lithium in brines in Clayton Valley, Nevada. In: Cluer JK, Price JG, Struhsacker EM, Hardyman RF, Morris CL, eds., *Geology and Ore Deposits 2000: The Great Basin and Beyond*, Geol Soc Nev Symp Proc, Reno, Nevada, May 15-18, 41-248.
- Richter, FM, Davis, AM, DePaolo, DJ, and Watson, EB, 2003,

The geology and mineralogy of high-grade Rare Earth Element (REE-Th-U) mineralization at Alces lake, Saskatchewan (Canada)

Irvine R. Annesley and Kateryna Poliakovska
Université de Lorraine - École Nationale Supérieure de Géologie, France

James Sykes
Appia Energy Corp., Canada

Krisztina Pandur
First Geolas Consulting, Canada

Abstract. The Alces Lake property (Canada) is an emerging high-grade rare earth element (“REE”) deposit of critical REEs for the “green technology” industry. Surface channel samples and diamond drillhole results have identified total rare earth oxide (“TREO”) concentrations exceeding $\gg 20$ wt% TREO within multiple zones at/near surface. In 2018, Appia Energy Corp. carried out a summer exploration program, comprising: 1) overburden stripping of seven REE surface-outcropping zones, 2) collection of 844 channel samples, 3) collection of 6 heavy mineral beach sand samples, and 4) completion of the first-ever property diamond drill program. The latter included 15 diamond drill holes within the Charles, Ivan, and Wilson zones. The Alces Lake REE mineralization is hosted within polyphase anatexites containing massive braided biotite schist and quartzofeldspathic pegmatite augen. The REEs are completely hosted within monazite (REE-Th-rich phosphate), as red, coarse grains (i.e., as individual grains, banded, or clustered masses exceeding 75% monazite within the Ivan and Dylan zones). Alces Lake monazites yielded a crystallization age of 1927.1 \pm 1.2 Ma, which places mineralization within the Taltson-Thelon Orogeny. Petrographic studies reveal that the monazite crystals are euhedral to rounded, suggesting undisturbed crystalline growth for the former and physically active “magmatic entrainment from source” for the latter.

1 Introduction

The rare earth elements (REE) have gained a lot of attention over the past 10-15 years; mainly because they are interpreted to be critical metals for green/military technologies, and are in short supply due to the tight supply chain control (i.e., monopoly) by China. This has taken place despite the fact that: 1) REE mineralization is not rare, 2) REEs occur in a wide range of geodynamic settings, and 3) REEs have been the “flavour of the day” for much recent exploration activities. As a result of recent worldwide increases in exploration for REE deposits, many new resources/reserves have been defined globally (Wall 2014; Goodenough and Wall 2016; Goodenough et al., 2016). A large number of these new discoveries are located in Canada (Mariano and Mariano 2012). The Alces Lake property (SK, Canada)

has become a significant, emerging high-grade rare earth element (REE) deposit of critical rare earth metals that are required for the “green technology/battery metal” industry. Here we present 2017-2018 surface channel samples and diamond drill hole results from Alces Lake; including identified total rare earth oxide (“TREO”) concentrations $\gg 20$ wt% TREO within multiple zones at/near surface.

2 Regional Geological Setting and Historical Exploration

The Alces Lake property is located immediately north of Lake Athabasca and the Athabasca Basin. The Alces Lake project area is 14,334 hectares (35,420 acres) in size, and is 100% owned by Appia Energy Corp. The site is approximately 34 km east of Uranium City and 135 km west of Stony Rapids.

Alces Lake is located within the Beaverlodge Domain; one of the major lithotectonic domains of northern Saskatchewan (Fig. 1). The Beaverlodge Domain was host to >17 individual uranium mines; having produced a total of 70 M lbs. U₃O₈ at an average grade over 0.20 wt% U₃O₈ between 1950 and 1980 (Normand 2014).



Figure 1. Lithotectonic domains and location of Alces Lake; immediately north of the world-renown U-rich Athabasca Basin in northern Saskatchewan. Figure is courtesy of Appia Energy; Geology and lithotectonic domains after Lewry and Sibbald 1978; Annesley et al. 2005; Card et al. 2007; Norman 2014.

Historic exploration for uranium and rare earth elements on the Alces Lake property and surrounding area occurred over four separate timeframes: 1950-1955, 1966-1968, 1975, and 2010-2013 (Normand 2014).

Three zones of surface mineralization on the Alces Lake property were first discovered by radiometric prospecting in the 1950's; including the Alces Lake rare earth showing(s). In 2013, a new high-grade rare earth surface discovery, the Ivan zone, was discovered 90 m NE of the Alces Lake zone.

3 Alces Lake Geology

The Alces Lake area is underlain by Archean and Paleoproterozoic rocks of the Beaverlodge Domain (Fig. 2; Normand 2014). Lithological units on the Alces Lake property include: 1) Archean granitic gneiss, 2) Paleoproterozoic metasedimentary gneiss (pelitic-psammopelitic [+/- graphite], quartzite, amphibolite, pyroxenite, diatexite), and feldspathic gneiss, 3) Paleoproterozoic syn- to late-anatectic pegmatites, 4) Paleoproterozoic late-orogenic to metasomatic biotite schist, pegmatite augen and monazite accumulations (the REE mineralized system). The basement rock package of metasedimentary gneiss is similar to that observed within the Beaverlodge uranium deposits. The property boundary is approximately 28 km N of the current day Athabasca Basin margin. The St. Louis Fault, a regional scale fault, runs ENE-WSW within the northern portion of the property below the Alces Lake waterbody. This fault is a major tectonic boundary between the Beaverlodge and Train Domains (Figs. 1 and 2, Normand 2014).

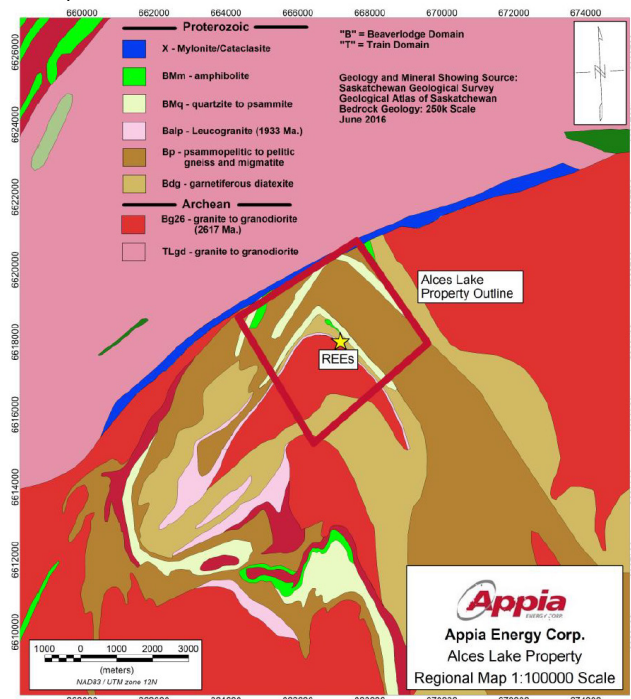


Figure 2. Geological setting of Alces Lake in the Beaverlodge Domain (modified after Normand 2014). Figure is courtesy of Appia Energy.

The fault zone hosts >3 uranium deposits, all of which produced over 45 M lbs U3O8 between 1950 and 1980.

4 Alces Lake mineralization

To date, all of the REE elements are hosted primarily (~100%) within monazite (Fig. 4); with a minor amount component of Y within xenotime.

The Alces Lake REE mineralization is hosted within a lithological mixture of late-orogenic to metasomatic polyphase anatectites that contain massive braided biotite schist and quartzofeldspathic pegmatite augen, with equal distribution of monazite accumulations within both schist and pegmatite. Biotite schist, which is also typically sulphide-rich, shows signs of remobilization along/within massive biotite schlieren. This mineralized anatectic system appears to be in sharp contact and clearly cross-cut previously solidified gneissic material; suggesting late orogenic development. The Alces Lake geological suite lies within a regional synformal anticline, with the eastern limb hosting the REE zones; suggesting folding controls on the mineralization deposition (Fig. 3).

Mineralized System – Schematic

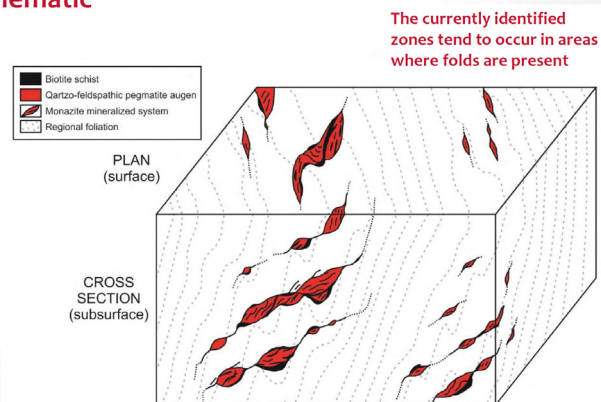


Figure 3. Schematic 3D block diagram of the Alces Lake mineralized system within a regional scale folding configuration; fully scalar from outcrop to district to regional scale.

The REE mineralization system occurs in both Archean orthogneisses and Paleoproterozoic metasediments. The REE mineralization appears to be consistent within all zones and rock types; occurring as isolated grains to 1 to 3 cm thin lenses to isolated massive clusters to massive clusters (up to m's thick) of 1 to 3 mm-sized grains (average) of monazite (Fig. 4).

At Alces Lake, the REEs are completely hosted within monazite (REE-Th-rich phosphate). The monazite is red in color, coarse-grained (0.5 to 3.0 mm in width); forming as isolated grains, banded, or as clustered masses exceeding >75% monazite within the Ivan and Dylan zones. Previous studies of Alces Lake monazite have suggested a crystallization date of 1927.1 +/- 1.2 Ma, which places mineralization within the Taltson-Thelon Orogeny. Petrographic studies reveal that the monazite crystals are euhedral to rounded; suggesting undisturbed crystalline growth for the former and a physically active "magmatic entrainment from source" for the latter.

The REE ratios are consistent from one zone to another; regardless of variable grades or of rock type hosting the mineralized system. In particular, Nd and Pr account for approximately 20% and 5% of the REEs, respectively.

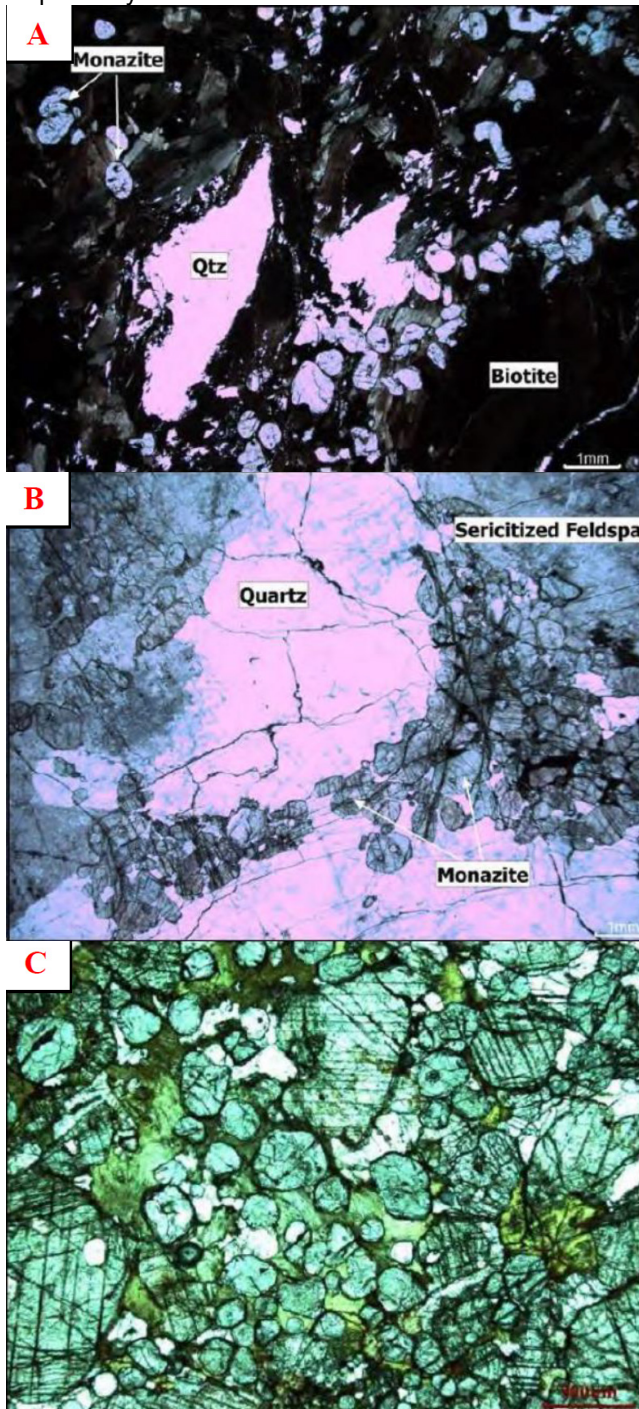


Figure 4. Summary figure for “monazite”; the REE host mineral of the Alces Lake REE-TH-U deposit: a) monazite hosted within biotite, b) monazite hosted within quartz and altered feldspar, and c) large concentrated aggregate of monazite (>50%). Figure is courtesy of Appia Energy Corp. Petrographic observations in plane polarized light using transmitted and reflected light microscopes on a JEOL JXA-8900 Superprobe electron microprobe situated at the University of Saskatchewan.

5 Alces Lake prospecting and drilling

Three zones of surface mineralization on the Alces Lake property were first discovered by airborne and ground radiometric prospecting in the 1950’s; including the Alces Lake rare earth showing(s). A new high-grade rare earth surface discovery, the Ivan zone, was discovered 90 m NE of the Alces Lake zone in 2013.

Radioactivity measurements of the Alces Lake outcrops and boulders have consistently exceeded 56,000 total counts per second (off-scale radioactivity) as measured with a RS-125 Super-Spec hand-held spectrometer, and sourced mainly from Th-rich minerals (i.e., monazite).

A total of seven high-grade REE zones have been discovered as of 2018; six of which are at surface, and one is within 15 m of the surface. These include: Bell (surface) at 10.239 wt% TREO (2.223 wt% CREO), Charles (surface) at 9.656 wt% TREO (2.163 wt% CREO), Charles Lower (sub-surface) at 8.868 wt% TREO (2.049 wt% CREO), Dante (surface) at 13.763 wt% TREO (3.057 wt% CREO), Dylan (surface) at 31.827 wt% TREO (7.259 wt% CREO), Ivan (surface) at 22.711 wt% TREO (5.242 wt% CREO), Wilson (surface) at 9.398 wt% TREO (2.062 wt% CREO). CREO was calculated as the sum of Pr₆O₁₁, Nd₂O₃, Eu₂O₃, Tb₄O₇ and Dy₂O₃.

In addition, a total of three REE zones with grades compatible with halos surrounding high-grade zones have been discovered to date; one of which is at surface, and two which are within 15 m of the surface: Ivan Middle (sub-surface) at 0.379 wt% TREO (0.083 wt% CREO), Ivan Lower (sub-surface) at 0.315 wt% TREO (0.072 wt% CREO), and Wilson South Central (surface) at 0.622 wt% TREO (0.144 wt% CREO).

Also, there are at least four REE showings and prospects, which require detailed follow-up; having grades similar to those zones above: Danny (surface) at 9.961 wt% TREO (2.525 wt% CREO), Hinge (surface) at 4.718 wt% TREO (1.171 wt% CREO), Wilson NW (surface) at 2.481 wt% TREO (0.630 wt% CREO), and Wilson SE (surface) at 1.066 wt% TREO (0.257 wt% CREO).

5.1 2018 prospecting and drilling program

During the summer of 2018, Appia Energy Corp. carried out a field exploration program for REEs, which consisted of: 1) overburden stripping of 7 REE surface-outcropping zones (Bell, Charles, Dante, Dylan, Ivan, Wilson, Wilson South-Central), 2) collection of 844 systematic channel samples, 3) collection of 6 heavy mineral black beach sand samples (see Mudd and Jowitt 2016), and 4) completion of the first-ever diamond drill program on the Alces Lake property.

A total of fifteen short diamond drill holes (“DDH”) were collared in three different REE zones (Charles, Ivan, and Wilson) that were previously exposed at surface as part of the overburden stripping program. Twelve of these holes intersected REE mineralization, of which ten intersected high-grade Total and Critical REEs (CREE). Two drill holes, CH-18-000 and CH-18-004, were

abandoned and re-collared as CH-18-001 and CH-18-004A, respectively.

Also significantly, three new sub-surface occurrences without surface expressions were intersected within 12m true depth below the surface of the Charles and Ivan zones; the Charles Lower, Ivan Middle, and Ivan Lower zones. The best drill hole analytical results of the Program were from drill hole CH-18-008 within the Charles Lower Zone, which returned 10.02 wt% TREO over 3.55m. It is noteworthy that the sub-surface zones discovered by the drilling remain open in all directions.

The depth extensions of the surface REE zones (Charles, Ivan and Wilson) were traced down to a range of 0.43 to 7.27 metres true depth from surface and remain open with the exception of the Charles N-S subzone, which was closed off at 1.95 m depth from surface. In particular, the drill hole analytical results from the Charles N-S subzone were higher grades than those witnessed at surface; for example 10.12 wt% TREO over 0.9 m returned from DDH CH-18-007.

6 Discussion

The Alces Lake Property encompasses some of the highest-grade total and critical REE mineralization in the world, hosted within seven surface showings that remain open at depth. Critical rare earth elements (CREE) are defined here as those that are in short-supply and high-demand for use in permanent magnets and modern electronic applications (i.e., Neodymium (Nd), Praseodymium (Pr) and Dysprosium (Dy)). The Alces Lake REO geochemical assay results are ranked presently as the highest-grade REE occurrences in Canada. Results to date showcase world-class REO grades that are comparable to (locally possibly better than) those encountered in the historical REE-producing Steenkampskraal (South Africa) and Mountain Pass (USA) deposits; as well as the currently producing high-grade Gakara Rare Earth Project (Burundi, East Africa) and the Mt. Weld CLD mine (Australia). The latter produced over 12% of the global REE supply in 2017.

As of September 2018, four of the seven REE zones exposed at surface have been drill-tested. Diamond drilling was focused within an area measuring 1.5 hectares (3.7 acres), which represents a very small portion of the Alces Lake property, further attesting to the exploration potential of the Property. The Alces Lake REE grades have been compared with global REE deposit grades.

These comparable high grades are world-class, thus Appia plans to continue their diamond drilling and reconnaissance exploration on the Alces Lake property in 2019 with a >3,000 meter program designed to continue defining and evaluating the currently known surface and sub-surface zones, as well as testing other high-priority target areas. This planned drilling program will be carried out concurrently with a detailed ground gravity survey exploring for subsurface REE zones, and additional overburden stripping / channel sampling of at least nine other REE showings identified during the previous exploration programs.

7 Conclusions

The Alces Lake Property encompasses some of the highest-grade total and critical REE mineralization in the world, hosted within seven at/near surface showings that remain open laterally and at depth.

The 2018 diamond drilling program verified the concepts of a working geological model, as well as indicating that REE mineralization continues well below the surface. Most importantly, the sub-surface discoveries provide evidence that the Alces Lake property remains highly prospective for additional REE zones to be discovered; both laterally and at depth. As a result of a significant number of years of erosion of these REE zones, we are only seeing the tail ends of saucer-shaped REE zones at surface. The sub-surface provides the untapped potential for discovering fully-intact high-grade REE bodies at depth.

Acknowledgements

The two senior authors acknowledge the permission to publish by Appia Energy Corp. SGA2019 reviewers are thanked for their review and editorial comments.

References

- Annesley IR, Madore C, Portella P (2005). Geology and thermotectonic evolution of the western margin of the Trans-Hudson Orogen: evidence from the eastern sub-Athabasca basement, Saskatchewan. *Canadian Journal of Earth Sciences*, 42:573-597.
- Card CD, Pana D, Portella P, Thomas, DJ, Annesley IR (2007). Basement rocks to the Athabasca basin, Saskatchewan and Alberta. In Jefferson, C. and Delaney, G., editors, EXTECH IV: Geology and Uranium EXploration TEChnology of the Proterozoic Athabasca Basin, Saskatchewan and Alberta, pages 69-87. Geological Survey of Canada Bulletin 588.
- Goodenough KM, Schilling J, Jonsson E, Kalvig P, Charles N, Tuduri J, et al. (2016). Europe's rare earth element resource potential: An overview of REE metallogenetic provinces and their geodynamic setting. *Ore Geology Reviews*, 72(Part 1):838-856.
- Goodenough KM and Wall F (2016). Critical Metal Mineralogy: Preface to the special issue of Mineralogical Magazine. *Mineralogical Magazine*, 80(1):1-4.
- Lewry JF and Sibbald TII (1980). Thermotectonic evolution of the Churchill Province in Northern Saskatchewan. *Tectonophysics*, 68:45-82.
- Mariano AN and Mariano A (2012). Rare earth mining and exploration in North America. *Elements*, 8(5):369-376.
- Mudd GM and Jowitt SM (2016). Rare earth elements from heavy mineral sands: Assessing the potential of a forgotten resource. *Applied Earth Science*, 125(3):107-113.
- Normand C (2014). Rare Earths in Saskatchewan: Mineralization Types, Settings, and Distributions; Saskatchewan Ministry of the Economy, Saskatchewan Geological Survey, Report 264.
- Wall F (2014). Rare earth elements. In A. G. Gunn (Ed.), *Critical metals handbook* (pp. 312-339). London: Wiley.

Contrasting types of REE mineralisation in the Palaeoproterozoic Bergslagen ore province, Sweden: from syn-volcanic to late-orogenic

Erik Jonsson, Per Nysten, Torbjörn Bergman, Martiya Sadeghi

Department of Mineral Resources, Geological Survey of Sweden (SGU), Uppsala, Sweden

Karin Högdahl, Fredrik Sahlström, Jaroslaw Majka

Department of Earth sciences, Uppsala University, Uppsala, Sweden

Abstract. The Bergslagen ore province in south central Sweden is one of the most metallogenetically diverse of the classic mining regions in the Fennoscandian shield. Although most prolific with regards to iron and base metal production, Bergslagen was also the first place where hard-rock mining for extraction of rare earth elements (REE) took place, and exploration for them is ongoing. Major deposit types hosting REE mineralisation are apatite-iron oxide (Kiruna-type) ores, Bastnäs type magnetite-skarn mineralisations and rare metal-enriched granitic pegmatites. These deposits represent a variety of geological processes that led to the formation of a diverse suite of REE minerals over a total time span of some 100 M.y., from early orogenic and syn-volcanic intrusive-related as well as hydrothermal processes, to late-orogenic intrusive-related ones.

1 Introduction and background

In today's industry and society the rare earth elements (REE, often separated into less sought-after light ones, LREE, and higher-value heavies, HREE) are key to a vast range of products, from basic yet high-tech utilities, via research and military technologies, to extensive applications within present and emerging "green" and "fossil free" energy systems. The recent increase in demand for REE for the latter technologies, combined with a global supply situation entirely dominated by China has led to worldwide interest in REE mineralisations both old and new (e.g. Wall 2014).

The Palaeoproterozoic Bergslagen ore province is the most classic and ancient mining region in the Fennoscandian shield, featuring diverse deposit types that have been worked at least since medieval times (e.g. Tegengren 1924; Geijer and Magnusson 1944). Although most metal mining has been focused on iron oxide and base metal sulphide deposits, noble and rare metals have also been exploited. The main ore-bearing sequence consist of c. 1.91-1.88 Ga dacitic to rhyolitic metavolcanic rocks with marble interlayers that were deposited in a continental back-arc basin setting (Allen et al. 1996; Fig. 1). During the Sveco Karelian orogeny, these rocks were subjected to polyphase deformation and regional metamorphism (e.g. Stephens et al. 2009). Syn-volcanic activity generated an absolute majority of the base metal and iron oxide deposits, as well as REE mineralisations, ranging from apatite-iron oxide ores, to

REE-skarn deposits. In contrast, rare metal pegmatites mainly formed at c. 1.82-1.78 Ga (Romer and Smeds 1994, 1997), during a late-orogenic stage.

2 REE mineralisations in Bergslagen

2.1 Granitic pegmatites

Within the greater part of the Bergslagen ore province (Fig. 1), the most important notable granitic pegmatites are either of NYF-affinity, carrying Y-HREE-rich minerals (oxides and silicates) and mainly concentrated in the northwestern-northern and north/eastern parts, whereas LCT-type pegmatite fields are particularly found in the southeastern part of the area, typically associated with extensive areas of pelitic meta-sedimentary rocks such as in the Utö area (Fig. 1; e.g. Smeds 1990).

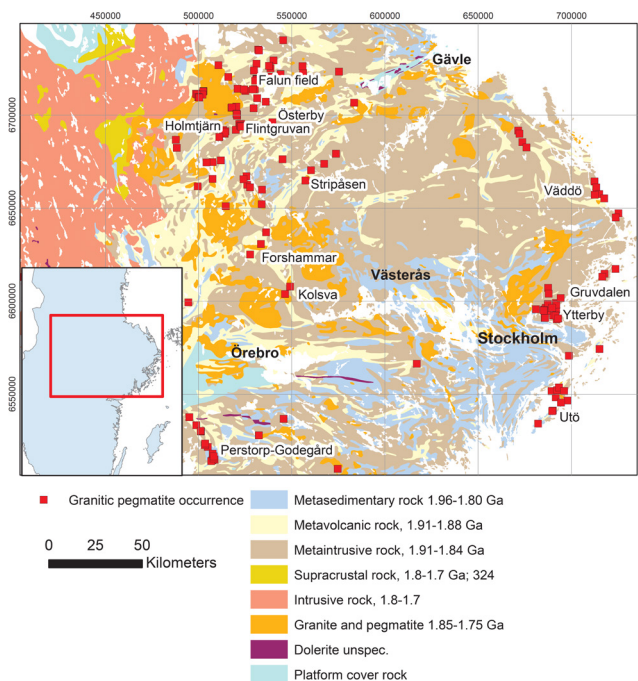


Figure 1. Overview bedrock geology map of the Bergslagen ore province (inset map showing the location in south central Sweden), with marked locations of major granitic pegmatites and pegmatite groups mentioned in the text. From SGU databases.

The well-known, historical pegmatite quarry at Ytterby,

north of Stockholm [with abundant Y+HREE-rich minerals such as gadolinite-(Y), fergusonite-(Y) and yttrantalite-formanite-ichikawaite-(Y)] is, together with other occurrences such as Gruvdalen, part of the easternmost broad grouping of HREE-enriched NYF-dominated pegmatites. Y-HREE-silicates, e.g. yttrialite-(Y) and thalénite-(Y) are important in some pegmatites, such as Holmtjärn, Österby and in the Falun field, while oxidic Y-HREE-bearing phases predominate in others, such as at Flintgruvan and Kolsva (Fig. 1).

The formation of a majority of pegmatites with available age datings is clearly related to the final, late-orogenic phase of the Svekokarelian orogeny, peaking around 1.8 Ga.

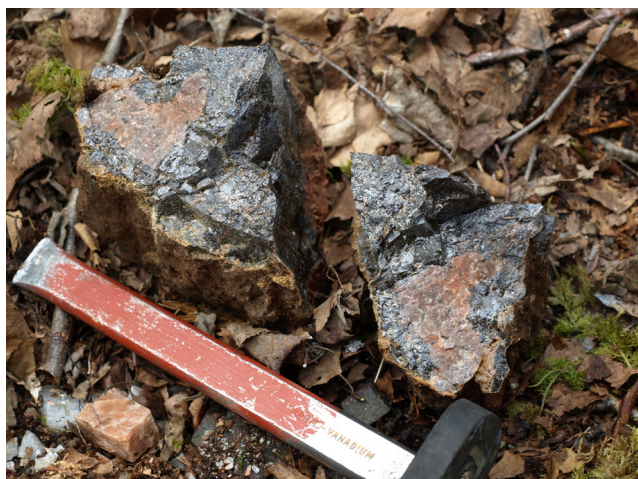


Figure 2. Coarse aggregates of Y+HREE-rich silicates at the Holmtjärn granitic pegmatite, northwestern Bergslagen, featuring inter alia yttrialite-(Y). Length of chisel is c. 20 cm.

As most of the known rare metal-enriched granitic pegmatites in Bergslagen are of small to moderate size with highly variable contents of REE-bearing minerals, they are therefore mostly not amenable to mining in any modern industrial sense; yet, some dykes (or fields) are more extensive, and the potential for new discoveries clearly remains.

2.2 Apatite-iron oxide ores

The apatite-iron oxide ores of Bergslagen are represented by a few deposits in the northwestern part of the province (Fig. 3), in contrast to the great number of iron oxide skarn deposits (thousands). The largest of these now closed mines, Grängesberg and Blötberget (Fig. 3), have been worked extensively and constitute the largest iron ore concentration in southern and central Sweden, with abundant ore left underground. Based on their mineralogy, geochemistry, geometry and host-rock relations, these deposits clearly represent Kiruna-type deposits (e.g. Jonsson et al. 2013, and references therein). They formed at an early stage of the volcanic activity in Bergslagen, with indicated ages near 1.9 Ga (e.g. Högdahl et al. 2013). Besides the main commodity, iron in the form of magnetite and hematite, fluorapatite and associated REE-bearing phosphates and silicates in these multi-million tonne ores represent potential

reserves of REEs as well as of phosphorus, particularly as possible by-products of iron mining.

Fluorapatite is a key mineral in the apatite-iron oxide deposits, mostly occurring as fine-grained aggregates in the magnetite ore, and often exhibits a banded or schlieren-like structure in it. Already in the 1970s significant REE contents were found to be present in the fluorapatite, and although programs including chemical analytical work as well as concentration tests were performed during the time of active mining at Grängesberg (cf. Back 1991), the largest and most well-studied of these deposits, it never led to any full-scale beneficiation. Characteristic of these deposits is that Si and (Y+REE) in the fluorapatite exhibit a distinct positive correlation, as opposed to Na and (Y+REE) (Harlov et al. 2002; Jonsson et al. 2016). This is the result of REE incorporation by the coupled substitution $\text{Si}^{4+} + (\text{Y}+\text{REE})^{3+} = \text{P}^{5+} + \text{Ca}^{2+}$. In the Grängesberg ores, the fluorapatite is typically high in Ce, La, Nd, and Y. REEs are also carried by monazite-(Ce), xenotime-(Y), allanite-(Ce) and variably REE-enriched epidotes, as well as in Ce-LREE-dominant REE-fluorocarbonates of synchysite-bastnäsite-type; additionally, a gadolinite-(Ce)-like mineral has also been observed (Jonsson et al. 2016). Within the variably phyllosilicate-altered immediate host rocks that exhibit enrichment in the REEs, these are hosted by minor allanite-(Ce), fluorapatite, monazite-(Ce), REE-fluorocarbonates and gadolinite-like minerals.

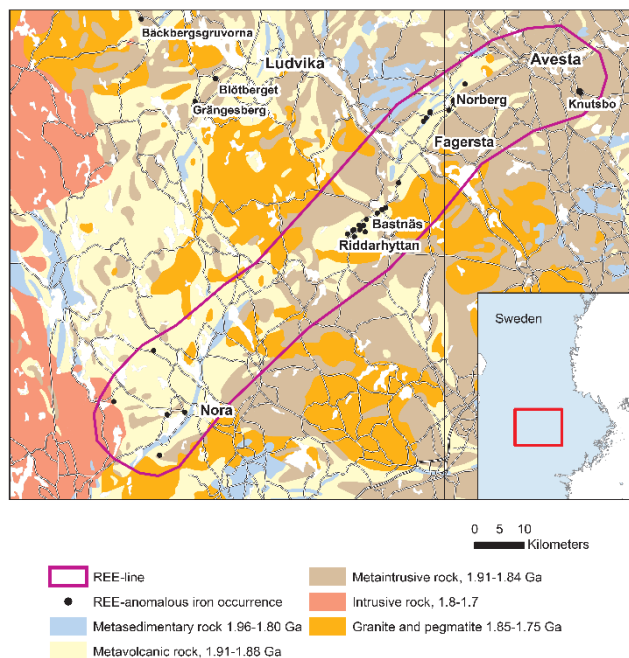


Figure 3. Bedrock geology map over west-central Bergslagen with marked locations for the major apatite-iron oxide deposits in the Ludvika area, and the Bastnäs-type REE-mineralisations of the REE-line (outlined in purple). From SGU databases.

Based on mineralogical and mineral-chemical studies, including high resolution microprobe data, fluorapatites in the Grängesberg ore are chemically and texturally variable, and overall contain between c. 0.5 up to close to 2.5 w% $(\text{Y}+\text{REE})_2\text{O}_3$ (Jonsson et al. 2016). The most

likely interpretation of the variable REE contents and textures is that primary REE contents of a majority of fluorapatites have been depleted through post-crystallisation fluid overprinting. The associated REE-bearing phosphates (monazite, xenotime) and silicates (allanite) formed through fluid-mediated remobilisation of REEs from primary fluorapatite, and subsequent formation of these secondary, REE-enriched phases, mainly as dissolution and reprecipitation as monazite, but also by more distal remobilisation and formation of allanite through reactions with groundmass silicates (Fig. 4; Jonsson et al. 2016). The REE-fluorocarbonates, in turn, formed at even later, low-temperature conditions. Overall, the Grängesberg fluorapatites exhibit the following ranges in contents of discrete REEs (average of 481 electron microprobe point analyses, all in wt% oxide): Ce 0.01-0.6; La 0.01-0.2; Nd 0.03-0.39; Pr 0.02-0.13; Y 0.02-0.24; all others were below the analytical detection levels (Jonsson et al. 2016). Average total REE contents for apatites from discrete assemblage types range from 0.19 wt% (Y+REE)₂O₃ in an altered metavolcanic rock (phyllosilicate-rich alteration assemblage) to between 1.7 and 2.5 wt% (Y+REE)₂O₃ in apatite-rich units in magnetite ore (Jonsson et al. 2016).

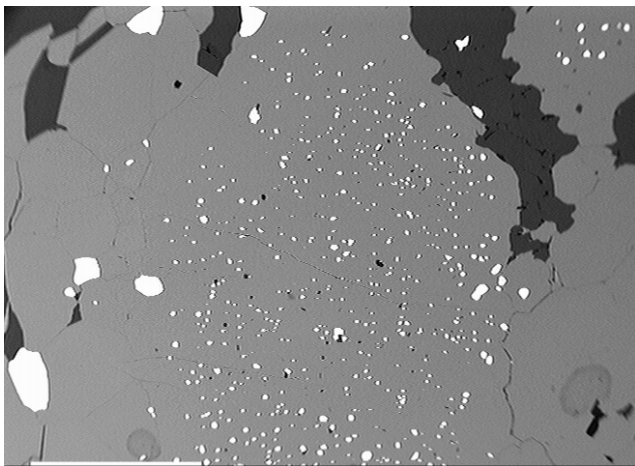


Figure 4. Back-scattered electron (BSE) image showing peripheral coarser-grained and central finer-grained inclusions of monazite-(Ce) in a medium-grey fluorapatite. Magnetite-apatite ore from the Grängesberg mine, north-eastern Bergslagen. Scale bar equals 200 μm.

Allanites occurring associated with the ores are primarily rich in Ce and La. As expected, monazite carries large amounts of REE, mainly Ce, and is an important accessory REE mineral; yet, the abundance of monazite associated with fluorapatite varies significantly. Xenotime-(Y) hosts major Y+HREE, but is much less abundant than monazite and allanite. Bulk analyses of dump samples at Grängesberg yielded up to 0.7 wt% total REE, comparable to contents in the other apatite-iron oxide deposits in Bergslagen (Högdahl et al. 2015).

2.3 Bastnäs type REE-magnetite skarn deposits

The Bastnäs-type REE deposits are skarn-hosted iron oxide, locally polymetallic (± Cu, Au, Co, Bi, Mo...) mineralisations that carry in part very REE-rich

assemblages. They occur along a discontinuous, c. 100 km long, narrow belt of felsic metavolcanic rocks with skarn-bearing marble interlayers, for which the name “the REE-line” has been introduced (Fig. 3; Jonsson and Högdahl 2013). Major deposit clusters are located in the Nora, Riddarhyttan and Norberg areas (Fig. 3). These deposits are characterised by the occurrence of locally very abundant REE-rich silicate minerals such as cerite-(Ce) and allanites (*sensu lato*), but also including REE-fluorocarbonates such as bastnäsite-(Ce). Overall, these mineralisations exhibit a quite complex and diversified REE mineralogy. The deposit type was named after the Nya Bastnäs mine field (Geijer 1961), the site of the original discovery of Ce, as well as the type locality of numerous REE minerals, such as bastnäsite-(Ce), cerite-(Ce), törnebohmit-(Ce) and several others (cf. Holtstam & Andersson 2007; Holtstam et al. 2014, and references therein). Additionally, the mine Ceritgruvan in the Nya Bastnäs field was most likely the first hard-rock deposit specifically mined for rare earth elements.

The REE-rich iron oxide skarn deposits (Fig. 3) occur together with associated BIF occurrences, as well as similar skarn mineralisations without known elevated REE contents. The major iron ore horizons, magnetite-dominated skarns and hematite-dominated banded iron formations, are stratiform and overall likely to be of volcano-sedimentary origin (e.g. Holtstam et al. 2014). The skarn-hosted mineralisations follow narrow marble horizons within the metavolcanic rocks. The main phase of hydrothermal alteration of the volcanic units probably took place during an essentially syn-volcanic stage around 1.90-1.88 Ga, as is also suggested by the near, spatial association of extensively altered, originally volcanic rocks with those that are essentially unaltered except for a later (regional) metamorphic overprint. Near the actual deposits, these rocks were strongly hydrothermally altered, and subsequently transformed during regional (Svecokarelian) metamorphism into cordierite and/or andalusite-bearing mica schists or “mica quartzites”. Ductile folding of host rocks as well as REE-mineralised assemblages has been recorded, and the mineral assemblages in the studied deposits mostly exhibit recrystallised textures, indicating that they formed at an early stage of the orogenic evolution (Fig. 5). The origin of the Bastnäs-type deposits has been debated over time, and they are now generally interpreted as being the result of skarn-forming reactions between pre-existing carbonate rocks and medium to high-temperature, metal-rich (including the REEs) hydrothermal fluids (e.g. Sahlström et al. 2015; Holtstam et al. 2014, and references therein). The formation of local REE silicate mineralisation in other host rocks, and specifically banded iron formations (BIFs) is suggested to be related to the same (epigenetic) process forming the skarns, rather than synchronous with the formation of the BIFs (Jonsson & Högdahl 2013).

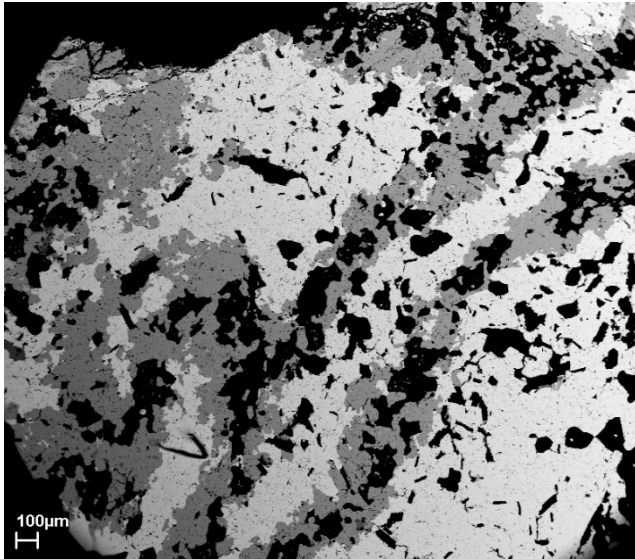


Figure 5. BSE image of folded, recrystallised REE-silicates from the Högfors mines, northeast of Bastnäs, central part of the REE-line, showing the pre-tectonic nature of this mineralisation type. Light grey is cerite-(Ce), medium grey is a västmanlandite-(Ce)-like mineral. Gangue silicates are black.

3 Summary and conclusions

The formation of REE-enriched mineralisation in the Bergslagen province was extensive and diverse during some 100 M.y. of the Svecokarelian orogeny and represents an important geodynamic stage for such deposits in the contexts of both the Fennoscandian shield and Europe (Goodenough et al. 2016). Besides the three major groups of mineralisations described here, several recently discovered and so far poorly studied ones also exist; some with potential genetic links to these three major groups, as well as some that seem rather unique. All mentioned deposit types will be described in a forthcoming report from the Geological Survey of Sweden (SGU), in part based on work performed during the EURARE project, summarising the known REE mineralisation in Sweden.

Additionally, just outside the southern edge of Bergslagen proper are the presently studied c. 1.8 Ga hydrothermal Olserum-Djupedal deposits (Andersson et al. 2018), which suggest further exploration potential along the border of the province. It is clear that the Palaeoproterozoic rock units of the Svecokarelian Bergslagen ore province and its surroundings represent one of the major REE provinces in Europe.

Acknowledgements

We acknowledge financial support from the EU to the now finished EURARE project (European Community's Seventh Framework Programme, FP7/2007-2013, under grant agreement no. 309373), as well as from the Swedish Research Council (VR) to Uppsala University, and from the Geological Survey of Sweden (SGU).

References

- Andersson SS, Wagner T, Jonsson E, Fusswinkel T, Leijd M, Berg JT (2018) Origin of the high-temperature Olserum-Djupedal REE-phosphate mineralisation, SE Sweden: a unique contact metamorphic hydrothermal system. *Ore Geol. Rev.* 101, 740-764.
- Back F (1991) Grängesbergs malmfält. Slutrapport Grängesbergs Gruvor AB (unpublished report). 10 pp.
- Geijer P (1961) The geological significance of the cerium mineral occurrences of the Bastnäs type in central Sweden. *Ark. Mineral. Geol.* 3:99-105
- Geijer P, Magnusson NH (1944) De mellansvenska järnmalmernas geologi. *SGU Ca* 35, 654 pp.
- Goodenough KM, Schilling J, Jonsson E, Kalvig P, Charles N, Tuduri J, Deady EA, Sadeghi M, Schiellerup H, Müller A, Bertrand G, Arvanitidis N, Eliopolous DG, Shaw RA, Thrane K, Keulen N (2016) Europe's rare earth element resource potential: an overview of metallogenetic provinces and their geodynamic setting. *Ore Geol. Rev.* 72:838-856.
- Harlov DE, Andersson UB, Förster HJ, Nyström JO, Dulski P, Broman C (2002) Apatite-monzite relations in the Kiirunavaara magnetite-apatite ore, northern Sweden. *Chem. Geol.* 191:47-72.
- Högdahl K, Troll VR, Nilsson KP, Jonsson E 2013: Structural evolution of the apatite-iron oxide deposit at Grängesberg, Bergslagen, Sweden. In: E Jonsson et al. (eds.), *Mineral Deposit Research for a High-Tech World, 1650–1653*.
- Högdahl K, Jonsson E, Kritikos A, Sahlström F (2015) Turning yesterday's waste into tomorrow's treasure: searching for base and critical metals in central Sweden's ancient mine dumps. In: AS André-Meyer et al. (eds.), *Mineral Resources in a Sustainable World, 757-760*.
- Holtstam D, Andersson UB (2007) The REE minerals of the Bastnäs-type deposits, south-central Sweden. *Can. Mineral.* 45:1073-1114.
- Holtstam D, Andersson UB, Broman C, Mansfeld J (2014) Origin of REE mineralisation in the Bastnäs-type Fe-REE-(Cu-Mo-Bi-Au) deposits, Bergslagen, Sweden. *Mineral. Dep.* 49:933-966.
- Jonsson E, Högdahl K (2013) New evidence for the timing of formation of Bastnäs-type REE mineralisation in Bergslagen, Sweden. In: E Jonsson et al. (eds.), *Mineral deposit research for a high-tech world, 1724-1727*.
- Jonsson E, Troll VR, Högdahl K, Harris C, Weis F, Nilsson KP, Skelton A (2013) Magmatic origin of giant central Swedish "Kiruna-type" apatite-iron oxide ores. *Sci. Rep.* 3:1644, 1-8.
- Jonsson E, Harlov D, Majka J, Högdahl K, Persson-Nilsson K (2016) Fluorapatite-monzite-allanite relations in the Grängesberg apatite-iron oxide ore district, Bergslagen, Sweden. *Amer. Mineral.* 101:1769-1782.
- Romer R, Smeds SA (1994) Implications of U-Pb ages of columbite-tantalites from granitic pegmatites for the Palaeoproterozoic accretion of 1.90-1.85 Ga magmatic arcs to the Baltic Shield. *Prec. Res.* 67:141-158.
- Romer R, Smeds SA (1997) U-Pb columbite chronology of post-kinematic Palaeoproterozoic pegmatites in Sweden. *Prec. Res.* 82:85-99.
- Sahlström F, Jonsson E, Högdahl K, Harris C, Troll VR, Jolis EM (2015) O and C isotope study of Bastnäs-type rare earth element mineralisation, Bergslagen, Sweden. *PacRim* 2015: 439-443.
- Smeds SA (1990) Regional trends in mineral assemblages of Swedish Proterozoic granitic pegmatites and their geological significance. *Geol. Fören. Stockholm Föhr.* 112:227-242.
- Stephens MB, Ripa M, Lundström I, Persson L, Bergman T, Ahl M, Wahlgren CH, Persson PO, Wickström L (2009) Synthesis of the bedrock geology in the Bergslagen region, Fennoscandian Shield, south-central Sweden. *SGU Ba* 58:259.
- Tegengren FR (1924) Sveriges ädlare malmer och bergverk. *SGU Ca* 17:406.
- Wall F (2014) Rare earth elements. In: AG Gunn (ed.), *Critical Metals Handbook*, J. Wiley & Sons, 312-339.

Magmatic vs. hydrothermal – origin of parisite-hosted REE mineralization at Nam Xe, Vietnam

Thomas Heinig, Robert Möckel, Joachim Krause and Jens Gutzmer

Helmholtz-Zentrum Dresden-Rossendorf, Helmholtz Institute Freiberg for Resource Technology, Germany

Van Phan Quang

Faculty of Environment, Department of Environmental Engineering, Hanoi University of Mining and Geology, Vietnam

Mathias Burisch

Institute of Mineralogy, Technische Universität Bergakademie Freiberg, Germany

Abstract. The REE mineralization of Nam Xe, Vietnam, provides important new insights into paragenetically complex carbonatite-related REE mineral formation associated with the transition from magmatic to hydrothermal conditions. Carbonatite dykes at Nam Xe comprise of calcite, ankerite and barite; these are crosscut by younger veins consisting of rare earth fluorocarbonates, fine-grained barytocelestine and calcite. The dominant rare earth fluorocarbonate is parisite $[(\text{REE})_2\text{Ca}(\text{CO}_3)_3\text{F}_2]$ with only minor bastnäsite and synchysite. Petrographic observations reveal that REE-mineralization is polystadial. Early bastnäsite associated with the magmatic stage is subsequently replaced by parisite in the presence of a Ca-CO₃-rich carbothermal fluid. Parisite is then again overprinted by a Sr-rich hydrothermal fluid resulting in the formation of REE-enriched parisite and calcite.

1 Introduction

Within the last decade, the supply of rare earth elements (REE) received considerable public attention (Goodenough et al. 2018). As a consequence, numerous REE exploration projects were initiated (Massari and Ruberti 2013) on a large number of different ore deposit types (Goodenough et al. 2018). Carbonatites have been of particular relevance to recent exploration efforts, as some of them are known to contain high concentrations of REEs (Verplanck 2015). Carbonatites are defined as igneous rocks composed of more than 50 wt% carbonate and less than 20 vol % quartz (Le Maitre 2002). Many carbonatites are formed as central plugs in alkali intrusive complexes or as dykes, sills, or breccia bodies (Singer 1986). Based on origin and shape, they are subdivided into primary carbonatites formed by asthenospheric mantle-derived magmas, carbonatites formed by pneumatolytic melting of crustal rock and carbonate-rich rocks associated with potassic and sodic peralkaline magmas from metasomatized lithospheric mantle (Mitchell 2005). REE enrichment in carbonatites is still rather tentatively attributed to different processes, e.g., orthomagmatic processes or hydrothermal fluid-rock interaction, subsolidus metasomatic redistribution of REEs, and sequestration of REE into secondary minerals (Verplanck 2015). Significant enrichment of REE grades can also be related to chemical weathering of the

carbonatite host rock.

Carbonatite-related mineralization is typically enriched in light REE (LREE) with the REE fluorocarbonates (bastnäsite, parisite, synchysite, ancylite) and phosphates (monazite and apatite) as the most common ore minerals (Kanazawa and Kamitani 2006; Verplanck 2015; Wall and Zaitsev 2004). Bastnäsite is particularly common and of major economic relevance (Goodenough et al. 2018).

The present contribution provides a first description of the geological setting, mineralogy and mineral paragenesis of REE mineralization associated with a series of carbonatite dykes at Nam Xe, in the northwestern region of Vietnam (Fig 1). Preliminary results show that REE deposition is polystadial and related to both magmatic and hydrothermal processes.

2 Geological Setting

Carbonatite dykes form a series of ca. 70 sub-parallel intrusions into a thick succession of basanite-trachybasalts of Triassic age (Chung and Jahn 1995; He et al. 2007; Searle 2006). The dykes strike in NW-SE direction and dip between 20 and 30° to the southwest. An extensive drilling campaign in 2012 confirmed that these dykes continue with depth throughout the entire exploration area (~340 m lateral, 400 m vertical).

The dominant regional tectonic feature in the area is the Song Da zone, which is described as an intracontinental rift structure of Mesozoic age (Metcalf 1988; Polyakov et al. 1998; Nguyen et al. 2014; Tran et al. 2016). This rift zone extends from the Vietnamese coastline striking southeast-northwest to the Vietnam-China border with the Nam Xe carbonatite dykes being located near at the northwestern limit. The dykes are situated at the intersection of Ban Man-Phong Tho fault (Fig. 1) and synclinal faults (Vlasov 1961) which offsets the Triassic basalt and the surrounding Permian limestone and other Paleozoic sediments (Metcalf 1988; Chung and Jahn 1995; Polyakov et al. 1999; Searle 2006; Nguyen et al. 2014; Tran et al. 2016).

Carbonatites are exposed as lenses and dykes on the surface which extend for hundreds of meters with thicknesses up to several meters (Fig. 1). The carbonatites have previously been subdivided into two compositional types, namely ferro- and calcio-carbonatite

(Chi et al. 2010; Nguyen et al. 2014; Vlasov 1961). At their contact to the host rock, all carbonatite types are surrounded by zones of fenitization where the fenites show a transition starting from an inner carbonate-rich, to a biotite and finally an aegirine-rich composition (Nguyen et al. 2014).

K-Ar age data of 28.0 Ma (Chi et al. 2010) and 44.0 Ma (Nguyen et al. 2014) suggest a close relationship of carbonatite magmatism with Paleogene volcanism of the Fansipan range to the north. Isotopic and trace-element data has, however, been used to invoke distinct and unrelated sources for these two magmatic events (Nguyen et al. 2014).

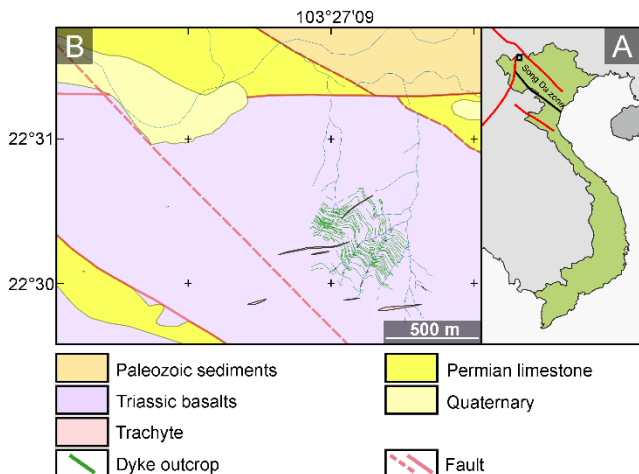


Figure 1. (A) A Map of Vietnam with the location of the investigated area in northwest Vietnam (square). (B) Geological map of the Nam Xe area. South Nam Xe dykes (green lines) are situated on a north facing mountain slope south of the east-west striking Ban Man-Phong Tho fault. This fault greatly offsets Triassic basalts and Permian limestones.

3 Samples and Methods

The geological context of REE mineralization at Nam Xe was studied during a field visit in 2016. A series of diamond drill cores obtained in 2012 was available for investigation and sampling on site. The present contribution includes samples from two drill cores (0512, 0709), which were complemented by field samples. Representative samples of half core from 21 dykes were prepared as polished thin sections.

Polished thin sections were characterized using transmitted and reflected-light microscopy. Furthermore, a scanning electron microscope (SEM; FEI Quanta 650F) was used to acquire backscatter electron (BSE) images and energy dispersive X-ray (EDX) single grain analyses for detailed petrographic sample characterization as well as semi-automated thin section mapping (MLA; GXMAP) for modal composition and mineral association (Bachmann, 2017).

Parasite compositions were determined using a JEOL JXA-8530F HyperProbe equipped with a field emission gun and five wavelength-dispersive X-Ray spectrometers. The measurements were run at an acceleration voltage of 15 kV and a beam current of 30 nA using a defocused beam of 10 to 20 μm diameter.

Online quantification was done with the ZAF matrix correction and further offline corrections were performed according to the measurement protocol of Osbahr et al. (2015). Furthermore, drift corrections were calculated for C, Mg, Sr, Ba, Ca, S and applied assuming a linear machine drift between two reference material blocks. Elemental concentrations were removed from the data set if their value was below 3.4 times the JEOL software displayed limit of detection and subsequent if their relative 3-sigma standard deviation exceeded 50% (Burisch et al. 2018).

4 Results

Most of the carbonatite dykes at South Nam Xe can be classified as coarse-grained calico-carbonatites dominated by calcite, closely associated with aegirine, arfvedsonite, biotite, apatite and magnetite (Chi et al. 2010; Nguyen et al. 2014; Vlasov 1961). Two minor but distinct compositional types are observed, including foliated calico-carbonatite with phlogopite rather than aegirine, and ferro-carbonatite consisting of ankerite, calcite, rare earth fluorcarbonates, fluorapatite, K-feldspar and Ba-, Sr-sulfates (Nguyen et al. 2014).

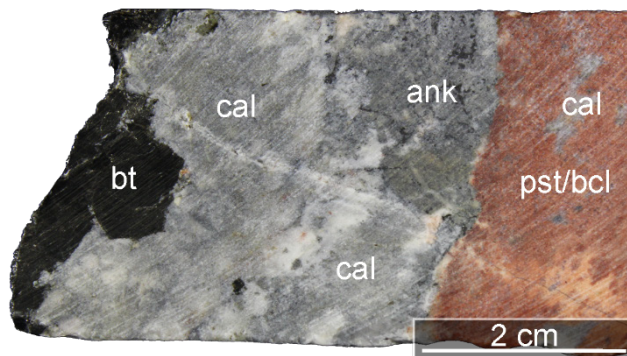


Figure 2. Scanned image of dyke from rim (left) to center (right). The rim is characterized by coarse crystalline biotite (bt) followed by coarse crystalline calcite (cal). The crystal size of ankerite (ank) and calcite decreases towards the REE-fluorcarbonate contact. On the right side of the sharp carbonate - REE-fluorcarbonate contact 60 - 150 μm parasite crystals occur in a fine crystalline barytocelestine-calcite matrix.

This study observed for all dykes an often symmetrical structure having calcite, ankerite and minor barite at the center of the dykes and biotite and magnetite more abundant towards the contact of the dykes with the host rock. Aggregates and veins of REE-fluorcarbonates in a fine-grained barytocelestine and calcite matrix are distinctively younger than the coarse crystalline carbonatite mineral assemblage (Fig. 2).

MLA and EMPA analyses of the REE fluorcarbonates show that parasite $[(\text{REE})_2\text{Ca}(\text{CO}_3)_3\text{F}_2]$ is more abundant than bastnäsite. Parasite is intimately associated with barytocelestine and calcite. Different REE-fluorcarbonates can be discriminated according to their stoichiometric ratio of REE fluorcarbonate $[\text{REEFCO}_3]$ and calcium carbonate $[\text{CaCO}_3]$. Parasite has a ratio of 2:1 and is compositionally in between bastnäsite (1:0) and synchysite (1:1) (Fig. 3; Alles et al. 2018).

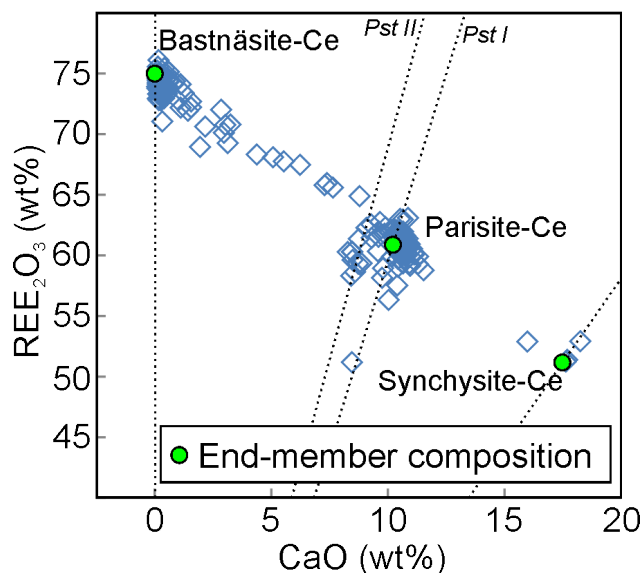


Figure 3. EMPA data for REE fluorcarbonates from Nam Xe plotted as REE_2O_3 vs. CaO (blue rhombus). Dotted lines indicate the different $\text{REE}_2\text{O}_3/\text{CaO}$ ratio of bastnässite-Ce, parisite type 1 (pst I), and parisite type 2 (pst II).

Bastnäsite $[(\text{REE})(\text{CO}_3)\text{F}]$ exhibits 5-120 μm sized crystals associated with parisite and barytocelestine. In one of all investigated ore veins, bastnäsite was the only REE fluorcarbonate present having 300 μm to 1 mm sized idiomorphic, pyramidal crystals associated with mainly strontianite and minor calcite. Parisite occurs in two distinct generations, which are often closely associated (Fig. 4). The first generation (pst I) is fine-grained (10-300 μm) with typical euhedral and pyramidal crystals (Fig. 4). Pst I is characterized by a uniform $\text{REE}_2\text{O}_3/\text{CaO}$ ratio of 5.8 ± 0.2 (Fig. 3) and has a relative high calcium and a low REE content. The second generation of parisite (pst II) replaces pst I together with calcite. It occurs mostly in direct contact to pst I and is intimately intergrown with calcite (Fig. 3). The clear petrographic discrimination between pst I and pst II is supported by the $\text{REE}_2\text{O}_3/\text{CaO}$ ratio of pst II at 6.8 ± 0.35 . However, the compositional differences between both parisite generations are relative small with pst II tending towards higher $\text{REE}_2\text{O}_3/\text{CaO}$ ratios.

5 Discussion and Conclusion

Magmatic and hydrothermal processes – or a combination of both have been invoked by previous authors to explain REE-rich mineralization associated with carbonatites (e.g., Mariano 1989; Wall and Mariano 1996; Zaitsev et al. 2002; Williams-Jones et al. 2012; Song et al. 2016). In some cases a combination of magmatic and hydrothermal processes involving water-bearing fluids has been invoked (e.g., Wall and Mariano 1996; Zaitsev et al. 2002; Moore et al. 2015).

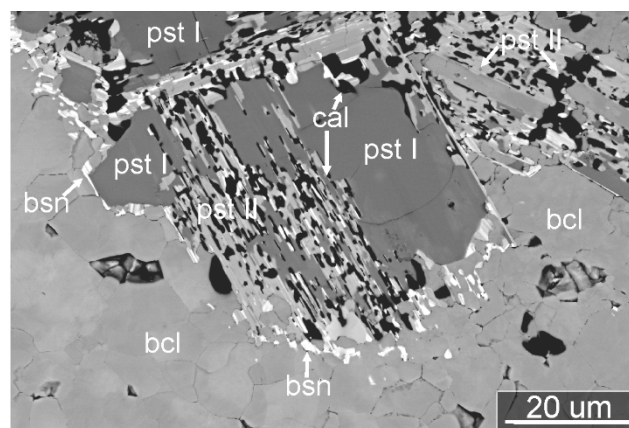


Figure 4. Contrast-enhanced BSE image of a crystal of parisite within a matrix of barytocelestine. The original crystal outline of parisite (pst I) is still visible and outlined by the presence of bastnäsite (bsn). Noteworthy is the alteration of pst1 to parisite type 2 (pst II) and calcite (cal).

REE enrichment at the in Nam Xe deposit is a consequence of multiple mineralization stages. The association of fine-grained calcite, strontianite and barytocelestine suggest a magmatic origin of bastnäsite (Castor 2008) at temperatures above 600 $^{\circ}\text{C}$ (Wyllie et al. 1996). The alteration of bastnäsite to pst I is attributed to the presence of post-magmatic Ca-, and CO_3 -rich carbothermal fluids (Giebel et al. 2017). Pst II replaces pst I, which is related to the influx of a Sr- and CO_3 -rich hydrothermal fluid. Concomitantly, barite is altered to barytocelestine and carbonates hosting the REE-fluorcarbonate veins are recrystallized resulting in smaller grains and increased strontium content towards the contact. Polystadial mineral-fluid reactions, which happened across the magmatic-hydrothermal transition of the Nam Xe carbonatite system, resulted in redistribution and substantial enrichment of REE in the dykes. Bastnäsite, common in the major REE carbonatite deposits (Voncken 2016), is replaced by two generations of parisite forming a unique REE fluorcarbonate deposit.

Acknowledgements

The team of the Faculty of Environment from Hanoi University of Mining and Geology is thanked for organizing the Vietnamese part of the project including sampling and data acquisition. The Vietnamese Ministry of Science and Technology (MOST, Code NDT.02.GER/15) and the German Federal Ministry of Education and Research (BMBF, grant number: BMBF 033R120B) are acknowledged for funding this international research project (NAMXE). Furthermore, we thank the Hung Hai Group for providing access to the samples of their drilling campaign.

References

- Alles J, Ploch A-M, Schirmer T, Nolte N, Liessmann W, & Lehmann B (2019) Rare-earth-element enrichment in post-Variscan polymetallic vein systems of the Harz Mountains, Germany. *Mineralium Deposita*, 54(2):307-328
- Bachmann K, Frenze, M, Krause J, & Gutzmer J (2017) *Advanced*

- Identification and Quantification of In-Bearing Minerals by Scanning Electron Microscope-Based Image Analysis. *Microscopy and Microanalysis*, 23(3):527-537.
- Burisch M, Hartman, A, Bach, W, Krolop P, Krause J, and Gutzmer J (2018) Genesis of hydrothermal silver-antimony-sulfide veins of the Bräunsdorf sector of the classic Freiberg silver mining district, Germany.: *Mineralium Deposita*, v. (2018).
- Castor S B (2008) The Mountain Pass rare-earth carbonatite and associated ultrapotassic rocks, California. *Canadian Mineralogist*, 46:779–806.
- Chi, N. T Flower, M and Hung, D T (2010) Carbonatites in Phong Tho, Lai Chau Province (NW Vietnam): Their Petrogenesis and Relationship with Cenozoic Potassic Alkaline Magmatism, 1-46
- Chung S L and Jahn B M, (1995) Plume-Lithosphere Interaction in Generation of the Emeishan Flood Basalts at the Permian-Triassic Boundary: *Geology*, 23(10):889-892.
- Giebel R J, Gauert C D K , Marks M A W , Costin G and Markl G (2017) Multi-stage formation of REE minerals in the Palabora Carbonatite Complex, South Africa. *American Mineralogist* 102:1218–1233.
- Goodenough K M, Wall F, & Merriman D (2017) The Rare Earth Elements: Demand, Global Resources, and Challenges for Resourcing Future Generations. *Natural Resources Research*, 27(2):201-216.
- He B, Xu Y G, Huang X L, Luo Z Y, Shi Y R, Yang Q J, and Yu S Y (2007) Age and duration of the Emeishan flood volcanism, SW China: Geochemistry and SHRIMP zircon U-Pb dating of silicic ignimbrites, post-volcanic Xuanwei Formation and clay tuff at the Chaotian section: *Earth and Planetary Science Letters*, v. 255(3-4):306-323.
- Kanazawa Y, and Kamitan, M, (2006) Rare earth minerals and resources in the world: *Journal of Alloys and Compounds*, v. 408-412:1339-1343.
- Le Maitre R W, (2002) *Igneous rocks : a classification and glossary of terms : recommendations of the International Union of Geological Sciences, Subcommittee on the Systematics of Igneous Rocks*, in Le Maitre, R. W., ed.: Cambridge, U.K. ;, Cambridge University Press.
- Mariano A N (1989) Nature of economic mineralization in carbonatites and related rocks. In K. Bell, Eds., *Carbonatites: Genesis and evolution*, p. 149–176. Unwin Hyman, London.
- Metcalfe I, (1988) Origin and assembly of south-east Asian continental terranes: Geological Society, London, Special Publications, 37(1):101-118.
- Moore M, Chakhmouradian A R, Mariano A N, and Sidhu R (2015) Evolution of rare-earth mineralization in the Bear Lodge carbonatite, Wyoming: Mineralogical and isotopic evidence. *Ore Geology Reviews*, 64:499–521.
- Mitchell R H (2005) Carbonatites and carbonatites and carbonatites: *Canadian Mineralogist*, 43:2049-2068.
- Nguyen T N, Wada H, Ishikawa T, and Shimano T (2014) Geochemistry and petrogenesis of carbonatites from South Nam Xe, Lai Chau area, northwest Vietnam: *Mineralogy and Petrology*, 108(3):371-390.
- Polyakov G, Balykin P, Hoa T T, Phuong N T, Thanh H H, Hung C, Ponomarchuk V, Lebedev Y N, and Kireev A (1998) Evolution of the Mesozoic-Cenozoic magmatism of the Song Da rift and its contouring structures: *Geologiya i Geofizika*, 39(6):695-706.
- Polyakov G V, Hoa T T, Akimtsev V A, Balykin P A, Phuong N T, Thanh H H, Hung C Q, Nien B A, Tolstykh N D, Glotov A I, Petrova T E, and Van V V (1999) Ore and geochemical specialization of Permo-Triassic ultramafic-mafic complexes in North Vietnam: *Geologiya i Geofizika*, 40(10):1474-1487.
- Searle M P, (2006) Role of the Red River Shear zone, Yunnan and Vietnam, in the continental extrusion of SE Asia: *Journal of the Geological Society*, 163:1025-1036.
- Singer D A (1986) Descriptive model of carbonatite deposits: Mineral deposit models: U.S. Geological Survey Bulletin 1683:52-53.
- Tran T-H, Polyakov G V, Tran T-A, Borisenko A S, Izokh A E, Balykin P A, Ngo T-P, and Pham T-D (2016) Intraplate magmatism and metallogeny of North Vietnam, Springer.
- Verplanck P L (2015) A Review of Rare Earth Element Ore-Grade Enrichment in Carbonatites: *Mineral Resources in a Sustainable World*, 1-5:1041-1044.
- Voncken J H L (2016) *The Rare Earth Elements - An Introduction*. 10.1007/978-3-319-26809-5.
- Vlasov I (1961) Concluded report of exploring project on Nam Xe rare earth ore deposit (1958-1960 stage). : Documented in Institute of Geological Informations Archives and Museum. Hanoi (in Vietnamese). p. 169.
- Wall F, and Mariano A N (1996) Rare earth minerals in carbonatites: a discussion centred on the Kangankunde Carbonatite, Malawi. In A.P. Jones, F. Wall, and C.T. Williams, Eds., *Rare Earth Minerals: Chemistry, Origin and Ore Deposits*. Mineralogical Society Series, p. 193–226. Chapman and Hall, London.
- Wall F, and Zaitsev A N (2004) Phoscorites and Carbonatites from Mantle to Mine: the Key Example of the Kola Alkaline Province.: *London (Mineralogical Society Series, Volume 10): Mineralogical Magazine*, 70(2):237-237.
- Zaitsev A N, Demény A, Sindern S, and Wall F (2002) Burbankite group minerals and their alteration in rare earth carbonatites—source of elements and fluids (evidence from C–O and Sr–Nd isotopic data). *Lithos*, 62:15–33.
- Williams-Jones A E, Migdisov A A, and Samson I M (2012) Hydrothermal mobilisation of the rare earth elements—a tale of “ceria” and “yttria”. *Elements*, 8:355–360.
- Wyllie P J, Jones A P, and Deng J (1996) Rare earth elements in carbonate-rich melts from mantle to crust. In A.P. Jones, F. Wall, and C.T. Williams, Eds., *Rare Earth Minerals: Chemistry, Origin and Ore Deposits*. Mineralogical Society Series, p. 77–103. Chapman and Hall, London.

Late- to post-magmatic controls on rare earth element mineralogy and the potential influence on subsequent ion adsorption ores

Eva Marquis

University of Brighton

Guillaume Estrade

Géosciences Environnement Toulouse

Kathryn Goodenough

British Geological Survey

Martin Smith, Cristina Villanova-de-Benavent

University of Brighton

Abstract. The rare earth elements (REE) Nd, Dy and Pr are critical metals for low carbon technologies that require high field strength permanent magnets and rechargeable batteries. The majority of the global heavy REE (HREE: Gd-Lu) supply, which includes Dy, is sourced from ion adsorption deposits. At the Ambohimirahavavy Alkaline Complex, northwest Madagascar, thick laterite profiles with variable ion exchangeable REE content develop from a range of protoliths, which vary in both REE concentration and REE-host mineralogy. Proportions of REE within these ores are controlled by their relative concentrations and host-minerals in the protolith lithologies. 'First-order' magmatic processes generally control the REE concentration of the protolith, such as fractional crystallisation and melt differentiation, whereas the REE-host mineralogy is influenced by the melt conditions and late- to post-magmatic evolution of the residual melt and fluids. This late- to post-magmatic evolution may result in mineral assemblages that are susceptible or resistant to dissolution during supergene processes.

1 Introduction

Neodymium, Dy and Pr are critical metals for low carbon technologies that require high field strength permanent magnets and rechargeable batteries (Goodenough et al 2018). In REE deposits these three critical elements are found together with the other lanthanides, and most REE deposits are strongly enriched in light REE (LREE: La-Eu) but have low heavy REE (HREE: Gd-Lu) content.

The majority of the global HREE supply, which includes Dy, is sourced from ion adsorption deposits (European Commission 2017). These supergene deposits contain over 50% of their REE in an ion exchangeable form (Sanematsu and Watanabe 2016), typically adsorbed to the surface of clay minerals, which are liberated using weak electrolyte solutions (Moldoveanu and Papangelakis 2012). This ease of extraction, coupled with the low radioactivity and relatively elevated HREE content compared to other major REE sources (e.g. carbonatite-associated

deposits, typically strongly LREE-enriched), makes these deposits ideal HREE sources. Other REE deposits with relatively elevated HREE-content include hydrothermally altered carbonatite-associated (e.g. Huanglongpu District, China – Smith et al 2018) and alkaline to peralkaline igneous rock-associated (e.g. Ilímaussaq Alkaline Complex, Greenland; Strange Lake, Canada – Marks and Markl 2017) occurrences.

Most known ion adsorption deposits are developed upon muscovite and/or biotite granites, which have experienced variable hydrothermal alteration, such as those of the Nanling Range, southern China (Li et al 2017). Principal controls on the development of ion adsorption ores include: 1) tropical to temperate climate to enable intense chemical weathering, 2) low to moderate denudation rates to allow preservation of regolith profiles and 3) parental rocks containing REE-bearing minerals susceptible to dissolution during chemical weathering (Sanematsu and Watanabe 2016; Li et al 2017). The Ambohimirahavavy Alkaline Complex (AAC) is a unique example of ion adsorption ores derived from alkaline to peralkaline igneous rocks, and thus encompassing two REE deposit types – ion adsorption and alkaline to peralkaline rock-associated deposits.

By integrating the paragenesis of REE-host minerals and whole rock geochemistry, the effect of late magmatic to post-magmatic alteration on the REE-bearing mineralogy is evaluated for peralkaline granitic dykes (PGD), nepheline syenites (NS) and alkali feldspar syenites (AFS) of the AAC. From this, we discuss the importance of late- to post-magmatic processes on the development of easily degradable REE-mineral assemblages for the subsequent development of ion adsorption ores.

2 Climate, topography and geological setting

Northwest Madagascar has a tropical climate, with average annual temperatures > 25°C and precipitation of >200 mm/annum in the AAC area (Desharnais et al 2014). Regolith profiles have an average thickness of 13.5 m and maximum of 40 m (Desharnais et al 2014).

An annular ridge forms a topographic high, surrounding a central caldera, in the southeast of the AAC and the northwest is comprised of a series of hills and valleys with elevations ranging from sea level to 713 m.

The AAC is a sub-volcanic alkaline to peralkaline complex of the Cenozoic Ampasindava Alkaline Province. It comprises a suite of coeval silica-undersaturated to silica-oversaturated intrusive syenitic to granitic and extrusive volcanoclastic units (Estrade et al 2014a). There are two main intrusions, the Tsarabariabe Intrusion in the northwest and the annular Ampasibitika Intrusion in the southeast. The Ampasibitika Intrusion hosts unusual eudialyte-bearing peralkaline granitic dykes, which are mineralised with respect to REE (up to 2.24 wt. % REE₂O₃; Gilbertson 2013), and thus this intrusion has been the main interest for studies into REE mineralisation associated with the AAC (Estrade et al 2014b; 2018). There are three major intrusive units of this intrusion: the silica-undersaturated Ankobabe Hybrids (NS and associated mafites), the silica-neutral AFS that are the main intrusive lithology of the intrusion, and the silica-oversaturated marginal dyke swarm, which consists of variably altered microsyenite dykes and PGD (see geological map in Estrade et al 2014a). Peralkaline units may contain agpaite (complex Na-Ca-K-Zr-silicates) and/or miaskitic (simple HFSE-phases, e.g. zircon, titanite etc.; Marks and Markl 2017) lithologies.

3 Whole rock geochemistry

Whole rock geochemical data are available for rocks of the Ampasibitika Intrusion from this study and Estrade et al (2014a 2014b). The AFS, NS and PGD of the Ampasibitika exhibit a range of K/Rb ratios of <115 for PGD and >150 for AFS and NS (Fig. 1A). The total Rb content increases exponentially with decreasing K/Rb, with an order of magnitude difference between the lowest values of the AFS and highest of the PGD. There is a similar trend recorded for the total REE (Σ REE) concentrations, with Σ REE generally increasing with decreasing K/Rb (Fig. 1B).

4 REE host mineralogy

Host mineralogy of the REE is highly heterogeneous. There has been extensive research on pseudomorph assemblages after eudialyte for the Ampasibitika PGD (Estrade et al 2014b 2018), which is summarised in the following section. New information on the REE-host mineralogy is described for NS and AFS of the Ampasibitika Intrusion.

Peralkaline Granitic Dykes

Eudialyte group minerals (EGM) occur as late magmatic accessory phases and early magmatic rock forming mineral phases alongside other agpaite minerals in transitional miaskitic-agpaite and agpaite granites of the PGD (Estrade et al 2018). Secondary pseudomorph assemblages of unidentified Ca-Na-zirconosilicates or zircon and quartz resulting from the destabilisation of EGM during interaction with Ca-bearing fluids are a common feature (Estrade et al 2018).

Cathodoluminescence imagery highlights the multiple generations of quartz present in these dykes and the occurrence of late dendritic zircon with the final generation (Fig. 2A). Other REE-bearing minerals associated with PGDs include monazite and pyrochlore; these occur as intermediate to late-stage phases and are interstitial to the earliest quartz generation (Fig. 2B).

Nepheline Syenites

Fluorapatite is the most common REE-bearing mineral phase in amphibole-dominated NS. These apatites exhibit oscillatory zonation patterns and REE-rich overgrowths (Fig. 2C) that correspond to the crystallisation of late arfvedsonite amphibole, aegirine and analcime. Rare, unidentified Na-Ca-zirconosilicate, interleaved with pyrochlore, and monazite occur as late interstitial phases associated with analcime (Fig. 2D).

EGM occur as intercumulus phases in aegirine-dominated NS (Fig. 2E). These EGM are variably destabilised to pseudomorph assemblages of Na-Ca-zirconosilicate, fluorite-(Y) and monazite (Fig. 2F).

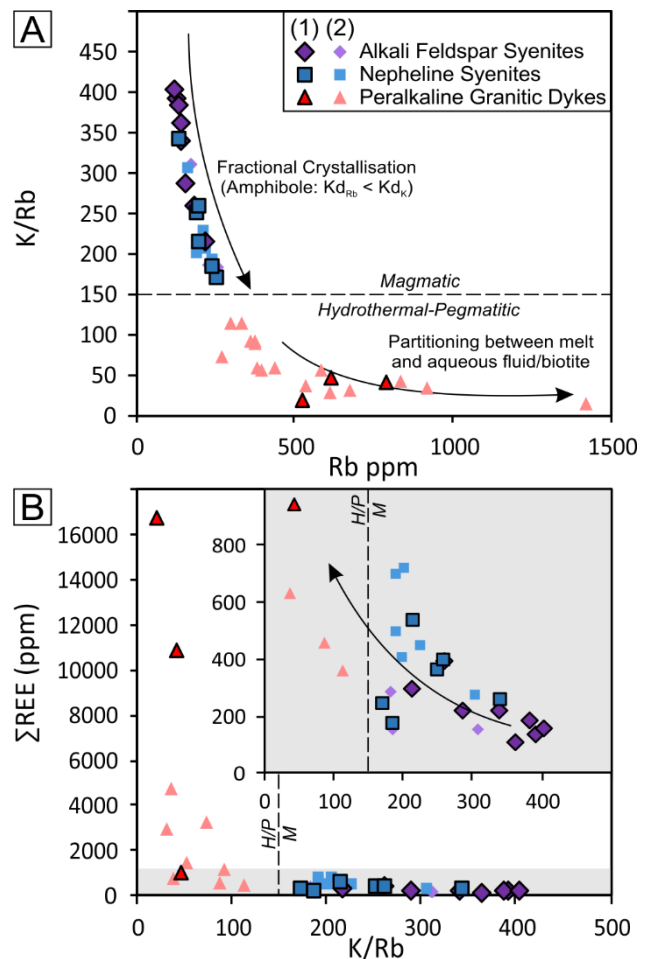


Figure 1. Bivariate plots of **a.** K/Rb vs. Rb and **b.** Σ REE vs. K/Rb (Bottom) showing magmatic (M) to hydrothermal/pegmatitic (H/P) subdivision at K/Rb \approx 150 defined by Shaw (1968). Data sources: (1) This Study and (2) Estrade et al 2014a 2014b.

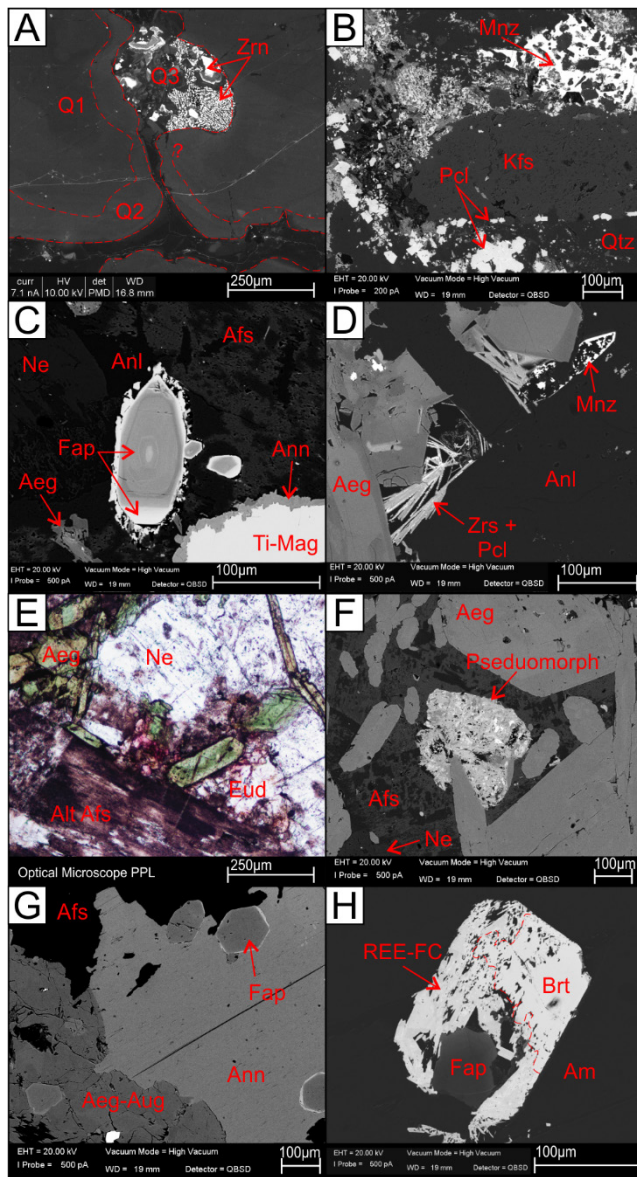


Figure 2. SEM (cathodoluminescence, CL; backscatter electron, BSE) imagery and photomicrograph (plain polarised light, PPL) of characteristic REE-host mineralogy of units the Ampasibitika Intrusion. **a.** PGD: SEM CL image showing three generations of quartz (Q1 – Q3) and dendritic zircon (Zrn) + Q3 pseudomorph assemblage; **b.** PGD: SEM BSE image of ‘poikilitic’ monazite (Mnz) with potassic feldspar (Kfs) inclusions and pyramidal pyrochlore (Pcl). **c.** NS (amphibole- dominated): SEM BSE image with oscillatory-zoned fluorapatite (Fap) with bright REE-rich fluorapatite rim associated with analcime (Anl); **d.** NS (amphibole- dominated): SEM BSE image of amphibole-NS with late unidentified Na-Ca-zirconosilicate (Zrs) interleaved with pyrochlore and monazite in interstitial space between analcime and aegirine (Aeg). **e.** NS (aegirine- dominated): PPL image of intercumulus eudialyte (Eud) located between earlier nepheline (Ne) and alkali feldspar (Afs) and associated with acicular aegirine; **f.** NS (aegirine-dominated): SEM BSE image of pseudomorph assemblage of Na-Ca-zirconosilicate, fluorite (F), monazite and analcime. **g.** AFS: SEM BSE image of fluorapatite inclusions in intercumulus aegirine-augite (Aeg-Aug) and annite (Ann), bright rims indicate REE-enriched apatite; **h.** AFS: SEM BSE image of apatite with britholite (Brt) mantle partially replaced by REE-fluorocarbonate (REE-FC) hosted in intercumulus amphibole (Am). *Other abbreviations:* Qtz, quartz; Ti-Mag, titanomagnetite; Alt Afs, altered/sericitised alkali feldspar.

Alkali Feldspar Syenites

Fluorapatite is a common early to intermediate-magmatic mineral phase of the AFS. Where associated with intercumulus amphibole and annite, apatite is variably mantled by late-magmatic monazite (Fig. 2G). Proximal to carbonate-rich alteration assemblages and miarolitic cavities, monazite is partially to completely replaced by REE-fluorocarbonate phases (Fig. 2H).

5 Discussion

5.1 ‘First-order’ magmatic controls on protolith REE content

Trends in K/Rb and Rb can be used as a proxy for the degree of fractional crystallisation and differentiation experienced by parental magmas (Fig. 1A), with lower K/Rb indicating that the parental melts are more evolved. Very low K/Rb ratios of <150 are proposed to mark the transition from magmatic to pegmatitic or hydrothermal processes (Shaw 1968). This proposal is consistent with the trends observed for granites and syenites of the Ampasibitika Intrusion; the PGD, which are pegmatitic, have K/Rb <150 in contrast to the AFS and NS that have higher K/Rb ratios and are magmatic cumulates that have undergone variable degrees of fractional crystallisation.

The abundance of REE generally increases with decreasing K/Rb ratios (Fig. 1B), and thus, the greater the degree of fractional crystallisation and differentiation experienced by the parental magma prior to emplacement, the greater the overall REE content of the final rock. This is coherent with the expected incompatible behavior of REE in most rock-forming minerals and their affinity for the melt phase during fractional crystallisation and melt differentiation.

5.2 Late- to post-magmatic controls on REE-host mineralogy

Conditions promoting EGM saturation in magmas include strongly peralkaline compositions, and high Zr and Cl melt compositions (Sørensen 1997; Ghiesse et al 2014; Estrade et al 2018). Subsequent destabilisation of EGM to Na-Ca-zirconosilicates is promoted by decreases in Cl melt content and increases in H₂O activity (Marks and Markl 2017; Estrade et al 2018), potentially triggered by the exsolution of a fluid phase during the latter stages of crystallisation. Estrade et al (2018) proposed that late exsolution of a fluid phase and interaction with external Ca-rich fluids destabilised the EMG to form the zircon + Q3 pseudomorph assemblage of the peralkaline granite PGD. The complete destabilisation of EGM to Na-Ca-zirconosilicate, fluorite (F), monazite and analcime in the aegirine-rich NS suggests the presence of a Ca, F, and P enriched fluid that interacted with the EGM. Due to the incompatibility of Ca and P in Na-rich silicate mineral phases, these elements may become enriched in the final volatile-rich melt. As such, an external fluid source may not be required to promote the destabilisation of EGM to Na-Ca-zirconosilicate pseudomorph assemblages.

In the amphibole-dominated NS, REE-enrichment in the residual melt/fluid phase is evident by the

development of REE-rich fluorapatite rims around earlier REE-poorer fluorapatite as well as the presence of monazite, Na-Ca-zirconosilicate and pyrochlore as a final phase after analcime. Na-Ca-zirconosilicates are interstitial to analcime and therefore crystallised from the final aqueous melt/fluid phase. For agpaitic Na-Ca-zirconosilicate phases to stabilise in place of eudialyte or zircon the late melt or exsolved fluid would have had a high $\alpha\text{H}_2\text{O}$ (Marks and Markl 2017).

Fluorapatite in the AFS records the enrichment of REE in the residual melt phase, with the development of REE-enriched fluorapatite rims and britholite mantles associated with intercumulus annite and amphibole respectively. Replacement of britholite by REE-fluorcarbonate minerals indicates an F^- and CO_3^{2-} rich fluid phase, which was either exsolved from the residual melt or externally derived.

5.3 Implications for subsequent ion adsorption ores

During chemical weathering, protolith mineral phases break down at different rates and form a variety of alteration products. The final mineral assemblage produced from the weathering of rocks is comprised of the least soluble minerals (e.g. kaolinite, Fe-oxide/hydroxide) and resistant primary minerals (zircon, quartz, etc.; Anand and Paine 2002). REE-fluorcarbonates are susceptible to dissolution when exposed to acidic solutions, eudialyte will decompose to Fe- and Al-oxide/hydroxide assemblages (Zakharov et al 2011) and apatite to secondary REE-phosphate phases, whereas monazite and zircon are resistant to dissolution (Sanematsu and Watanabe 2016).

As such, the development of zircon pseudomorphs after eudialyte will decrease the availability of REE for ion adsorption ores, as would the presence of monazite as the main REE-host phase. Development of REE-fluorcarbonates would promote the release of REE during subsequent weathering, thus is beneficial to the development of ion adsorption REE ores. However, the presence of phosphate-rich phases (e.g. apatite) may result in the sequestration of REE into secondary phosphates, which would trap REE in non-ion exchangeable phases.

6 Conclusions

Magmatic fractional crystallisation and differentiation promote the enrichment of REE in the most evolved melts of the Ampasibitika Intrusion. However, the exsolution or introduction of late volatile-rich and/or aqueous fluids strongly influences development of REE minerals susceptible or resistant to dissolution during supergene processes. Thus, although the protolith may be highly enriched in REE, late- to post-magmatic alteration may result in the development of mineral phases unsuitable of the subsequent development of ion adsorption ores (e.g. PGD), whereas lower grade protoliths (e.g. AFS) may contain REE-host minerals that will release their REE-budget during weathering enabling the formation of ion

exchangeable REE.

Acknowledgements

This work was supported by the National Environment Research Council (NERC) SOS:RARE project (NE/M011267/1). Scanning electron microscopy and rock preparation for geochemical analyses were carried out at the British Geological Survey. Whole rock geochemical analysis was done at the University of Brighton (ICP-MS) and by ALS Global (XRF).

References

- Anand RR, Paine M (2002) Regolith geology of the Yilgarn Craton, Western Australia: implications for exploration. *Aust J Earth Sci* 49:3-162.
- Desharnais G, Camus Y, Bisailon C (2014) NI 43-101 Technical Report on Resources for the Tantalus Rare Earth Ionic Clay Project, Northern Madagascar, Prepared for Tantalus Rare Earths AG. SGS Canada Inc.
- Estrade G, Salvi S, Béziat D et al (2014a) Unusual evolution of silica-under-and-oversaturated alkaline rocks in the Cenozoic Ambohimirahavavy Complex (Madagascar): Mineralogical and geochemical evidence. *Lithos* 206:361-383.
- Estrade G, Salvi S, Béziat D et al (2014b) REE and HFSE mineralization in peralkaline granites of the Ambohimirahavavy alkaline complex, Ampasindava peninsula, Madagascar. *J Afr Earth Sci* 94:141-155.
- Estrade G, Salvi S, Béziat D (2018) Crystallization and destabilization of eudialyte-group minerals in peralkaline granite and pegmatite: a case study from the Ambohimirahavavy complex, Madagascar. *Mineral Mag* 82:375-399.
- European Commission (2017) Study on the review of the list of critical raw materials. European Commission, Brussels.
- Giehl C, Marks MAW, Nowak M (2014) An experimental study on the influence of fluorine and chlorine on phase relations in peralkaline phonolitic melts. *Contrib Mineral Petrol* 167:1-21.
- Goodenough KM, Wall F, Merriman D. (2018) The Rare Earth Elements: Demand, Global Resources, and Challenges for Resourcing Future Generations. *Nat Resour Res* 27:201-216.
- Li YHM, Zhao WW, Zhou M (2017) Nature of parent rocks, mineralization styles and ore genesis of regolith-hosted REE deposits in South China: An integrated genetic model. *J Asian Earth Sci* 148:65-95.
- Marks MAW, Markl G (2017) A global review on agpaitic rocks. *Earth Sci Rev* 173:229-258.
- Moldoveanu GA, Papangelakis VG (2012) Recovery of rare earth elements adsorbed on clay minerals: I. Desorption mechanism. *Hydrometallurgy* 117:71-78.
- Sanematsu K, Watanabe Y (2016) Characteristics and genesis of ion adsorption-type rare earth element deposits. In: Verplank PL, Hitzman MW (ed) *Rare Earth and Critical Elements in Ore Deposits*, *Rev Econ Geol* 18:55-79.
- Shaw DM (1968) A review of K-Rb fractionation trends by covariance analysis. *Geochim Cosmochim Acta* 32:573-601.
- Smith M, Kynicky J, Xu C et al (2018) The origin of secondary heavy rare earth element enrichment in carbonatites: Constraints from the evolution of the Huanglongpu district, China. *Lithos* 308-309:65-82.
- Sørensen H. (1997) The agpaitic rocks – an overview. *Mineral Mag* 61:485-498.
- Zakharov VI, Maiorov DV, Alishkin AR, Matveev VA (2011) Causes of insufficient recovery of zirconium during acidic processing of Lovozero eudialyte concentrate. *Russ. J. Non-ferrous Metals* 52:423-428.

Resolving the structural state of heavy rare earth elements in lateritic ion adsorption clays

Anouk M. Borst, Adrian A. Finch, Nicola J. Horsburgh
University of St Andrews, UK

Martin Smith, Eva Marquis, Peter Nason
University of Brighton, UK

Guillaume Estrade
France Paul Sabatier University, France

Kalotina Geraki
Diamond Light Source

Kathryn Goodenough
British Geological Survey, UK

Jindrich Kynicky
Mendel University Brno, Czechia

Xu Cheng
Peking University, China

Abstract. Lateritic Ion Adsorption Deposits (IADs) are the world's dominant source for heavy rare earth elements (HREE: Gd-Lu), currently mostly mined from China. IADs in Brazil, Madagascar and South East Asia may provide alternative supply for HREE. However, the exact nature of REE in the IADs is unclear; for example whether deposits elsewhere are directly analogous to the easily-leachable Chinese laterites, and whether the REE are truly adsorbed, structurally bound in clays or hosted in other mineral phases.

This study compares economically mineralized IADs from the Zhaibei granite, China to prospective IADs developed on peralkaline igneous rocks from Madagascar. We use synchrotron X-Ray Fluorescence (SXRF) element mapping and X-ray Absorption Spectroscopy (XAS) to study the distribution and coordination state of light and heavy REE. We explore sites of adsorption to clays and the presence of HREE in other mineral phases. The Malagasy and Chinese laterites have kaolinite as the dominant REE-hosting clay phase, with minor halloysite. XAS data demonstrate that the REE occur as 8 to 9-coordinated outer-sphere basal surface complexes on kaolinite, rather than 5- or 6-coordinated edge complexes, or 6- or 8-coordinated interlayer complexes, thus confirming the truly adsorbed nature of REE in lateritic IAD's from both localities.

1 Introduction

Heavy rare earth elements (HREE, Gd-Lu) are classed as 'critical metals' because of their ubiquitous use in modern technologies and renewable energy solutions and because restricted access to these metals would hinder technological development for green energy

solutions (e.g. Goodenough et al. 2017). At present, lateritic IADs from Southern China account for c. 80% of global heavy REE supply (Weng et al 2015). They formed through weathering of granitic bedrock (Li et al. 2017; Sanematsu and Watanabe 2016). Despite being relatively low grade (0.05 - 0.2 wt.% total RE₂O₃, incl. Y₂O₃) and small compared to carbonatite or alkaline hosted REE deposit types (Smith et al 2016, Weng et al 2015), exploitation of IADs is economically viable through low-cost in situ or heap leaching (Bao and Zao, 2008; Wall et al. 2017). The assumption is that the majority of REE (>50%) are loosely adsorbed onto the surfaces of clay minerals, and hence, are 'ion exchangeable'.

While most Chinese laterites developed on granites with relatively low heavy REE contents, a primary control on heavy REE enrichment into the laterite profile is the REE-hosting mineralogy of the protolith and their susceptibility to weathering (Li et al. 2017, Xu et al 2017). Compared to granite, peralkaline igneous rocks typically contain orders of magnitude higher total REE contents and are also relatively enriched in heavy REE compared with carbonatites (Chakhmouradian and Wall 2012). Moreover, they may contain complex alkali-HFSE phases such as eudialyte, which are highly susceptible to late-magmatic hydrothermal alteration and subsequent supergene weathering (Estrade et al., 2018; Borst et al. 2016). Laterites developed over such protolith types may therefore be more favourable for the development of high grade IADs with high proportions of leachable heavy REE.

In this work we characterize economically mineralized laterites from Southern China, developed on the Zhaibei granite (Yiangxi Province; Xu et al. 2017, Wang et al. 2015), and compare them to soils developed on

peralkaline granite and syenite from the Cenozoic Ambohimirahavavy complex in Madagascar (Estrade et al. 2014). We characterize the REE-hosting mineralogy in both laterites and identify the local bonding environment of the clay adsorbed heavy REE fraction.

2 Samples and mineralogy

2.1 Zhaibei, China

Samples from the Zhaibei granite in China were obtained from surface exposed profiles into mineralized laterite. The sample selected for analysis was taken from the upper 2 m of a 12 m laterite profile and shows a total of 1000 mg/kg REE leachable with ammonium sulphate solution, with 37% HREE (Eu to Lu plus Y) developed on biotite granite (dominated by quartz, K-feldspar, plagioclase and biotite) with small quantities of muscovite and amphibole. Rare earth element mineralization in the bedrock occurs in accessory zircon, apatite, monazite, REE-fluorcarbonates, xenotime and fluorapatite (Wang et al. 2015). The pedolith sample was prepared by mounting rock fragments and disaggregated soil materials in epoxy resin, followed by polishing to provide a flat surface for analysis. Examination by SEM (at the University of Brighton) shows the lateritic mineralogy to be dominantly kaolinite, K-feldspar, quartz (Fig. 1a) and iron oxides with minor illite, and accessory relict zircon and rutile. X-ray diffraction indicates that kaolinite is the dominant clay mineral, with minimal halloysite present.

2.2 Ambohimirahavavy, Madagascar

The Ambohimirahavavy complex is a Cenozoic caldera complex in Northern Madagascar which is in the advanced stages of mineral exploration. It hosts IADs in a 1 to 30 m thick laterite profile formed by tropical weathering. The complex comprises peralkaline granite, pegmatitic dykes and a syenite ring dyke (Estrade et al. 2014). Samples for this study included pedoliths and saprolites from a hand-dug weathering profile on rhyolite and trachyte, and boreholes and drill cores of soil profiles on REE mineralized peralkaline granite and pegmatite dykes. Samples for XAS analyses were selected to reflect a range in REE grades, and to allow for mineralogical comparison of different bedrock and depths along the laterite profile.

A sample with the highest grades in leachable REE (1962 mg/kg REE, 29% HREE), derived from the base of a hand-dug pit, was prepared as an epoxy resin impregnated polished thin section from intact blocks of pedolith. SEM examination shows it to contain kaolinite, K-feldspar, Fe and Mn oxyhydroxides with accessory zircon and micron-sized cerianite (Fig 1b). K-feldspar and zircon are present as microscopic relict phases. X-ray diffraction shows the clay fraction to be kaolinite, halloysite and gibbsite. Analysis of orientated clay samples shows comparable levels of kaolinite and halloysite, but kaolinite is visibly dominant. Pedolith and saprolite samples developed over REE mineralized peralkaline granite pegmatite dykes (Estrade et al. 2018)

demonstrate variable degrees of weathering and primary bedrock mineralogy. Magmatic and late-stage hydrothermal minerals include albite, K-feldspar and quartz with minor amounts of zircon, Ca-REE fluorcarbonates, pyrochlore and aeschynite-(Ce). The latter may be spatially correlated, occurring together in pseudomorphs after primary eudialyte (Estrade et al. 2018). The Ca-REE-fluorcarbonates are associated with partially decomposed magmatic pyrochlore which has zones enriched in Pb (Fig 2c).

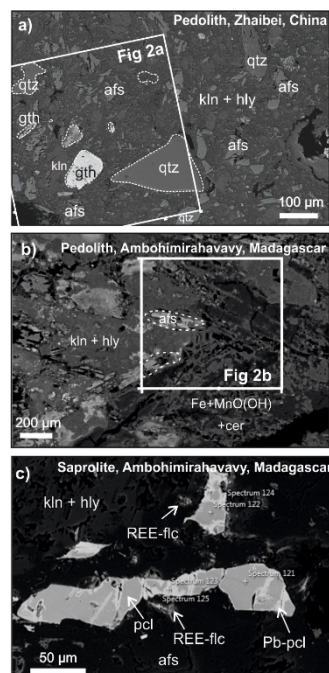


Figure 1. Back-scatter electron images. (a) Pedolith sample from Zhaibei, China, showing relict alkali feldspar and quartz and supergene gibbsite, Fe-Mn oxyhydroxides (gth), kaolinite and halloysite. (b) Pedolith sample from Madagascar showing a similar mineralogy with Fe-Mn oxyhydroxides and cerianite. (c) Pyrochlore with late-stage alteration forming Pb-rich pyrochlore and REE-fluorcarbonate as relict primary REE-phases in saprolite from Madagascar. White boxes indicate locations of element maps shown in Figure 2.

3 X-Ray Absorption Spectroscopy

3.1 Experimental set-up and data processing

We use X-ray Absorption Spectroscopy (XAS, including SXRF maps, XANES and EXAFS) of soil samples and leachates to study the distribution and local bonding environment of REE in these deposits.

XAS measurements were carried out at the I18 micro-focus beamline, Diamond Light Source, Didcot, UK. The I18 beamline is designed for high spatial resolution analyses of heterogeneous samples within the 2-20.7 keV energy range, and set up for SXRF mapping, μ -XRD and μ -XAFS (Mosselmans et al. 2009). Measurements were run at room temperature (~ 295 K), in fluorescence mode using a 3×3 μm focused beam. Standards were measured as powders or crystals (gem-quality diamond and zircon) on KAPTON[®] tape, and Y and Nd solutions

were held in a metallic liquid cell sealed between KAPTON® tape.

Yttrium K-edge (17038 eV) and Nd L₃-edge (6208 eV) X-ray absorption spectra were measured as proxies for light and heavy REE, respectively. We chose Y as it can be analyzed on the K-edge, which has no significant interference from absorption edges of other elements over the measured energy range, and Nd because natural materials contain no Pm, allowing a longer *k*-range in the EXAFS spectrum than other lanthanides.

All data were normalized and processed using the Athena and Artemis Demeter Perl packages for XAS analyses following the IFEFFIT program (Ravel and Newville, 2005). A total of 187 EXAFS measurements and 16 XRF maps were completed, including 134 analyses of pressed powder pellets, resin blocks and thin sections from China and Madagascar, and 53 analyses of standards and diamond blanks including synthetic and natural mineral samples and solutions of Y and Nd.

3.2 SXRF element mapping and XANES

Selected areas in thin section and the resin blocks were targeted for detailed SXRF elemental mapping to visualize areas of REE enrichment associated with clays and relict bedrock phases such as zircon, pyrochlore and REE-fluorocarbonates (i.e. parisite-(Ce), synchysite-(Ce)). The different REE-hosting phases were then targeted for in situ XAS measurements. Here we focus only on results of the clay-hosted REE fraction (medium REE concentrations, and compare these to mineral standards. Element maps of REE-enriched pedoliths from both localities (Fig 2) demonstrate local enrichment of Y (in red) within and along the boundaries of kaolinite and halloysite.

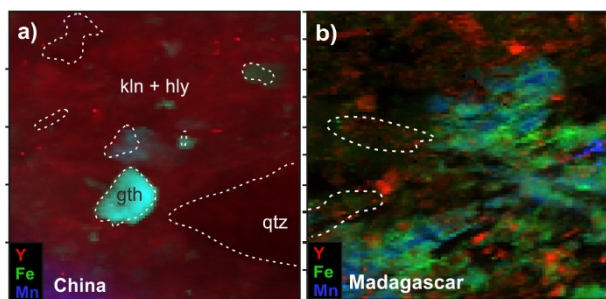


Figure 2. 118 SXRF elemental maps (500x500 μm) produced using Dawn software of (a) Chinese pedolith sample and (b) Malagasy REE-rich lower pedolith sample. Corresponding features visible in accompanying BSE images (Fig 1) are highlighted in white dashed lines. Tick marks are spaced at 100 μm.

The clay-adsorbed Y fractions as determined from BSE and SXRF element maps all show identical Y K-edge XANES and were merged to improve signal to noise ratios. Average spectra for the clay hosted Y fraction in the pedolith from China, and the Malagasy pedolith and saprolite samples are shown in Figure 3. They most closely resemble XANES obtained for REE-fluorocarbonates and Y in aqueous solution, in which the REE respectively occur in low point-symmetry 9-fold coordination (3x F, 6x O) and 8-fold coordination (8x OH)

(Ni et al 2000; Diaz-Moreno 2000).

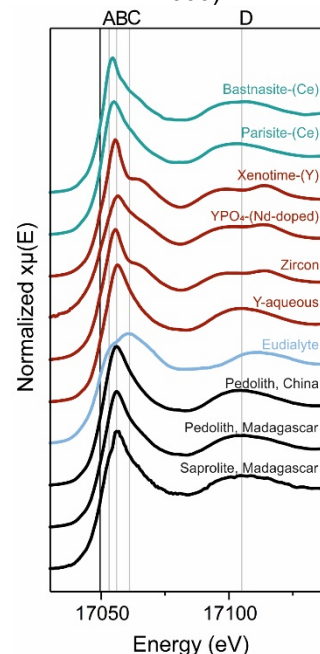


Figure 3 Normalized Y K-edge XANES spectra for REE-mineral standards with REE in different coordination states (from top to bottom, CN=9 in green, CN=8 in red, CN=6 in blue). Black lines represent merged spectra for clay hosted REE fractions in the Malagasy and Chinese pedolith and saprolite samples.

3.3 Yttrium coordination state from EXAFS

Quantitative refinement of the EXAFS for the Malagasy and Chinese clays are shown in Figure 4. The EXAFS spectra were fitted to theoretical scattering paths using Artemis Demeter Perl software to constrain the number of nearest neighbour oxygen atoms associated with water or hydroxyl groups, or fluorine, and their average bond distances. Best fits were obtained for a simple hydration sphere comprising 8.1 - 8.6 ± 0.9 oxygens at average distances of 2.35 - 2.38 ± 0.01 Å and significant structural disorder (large Debye-Waller factors).

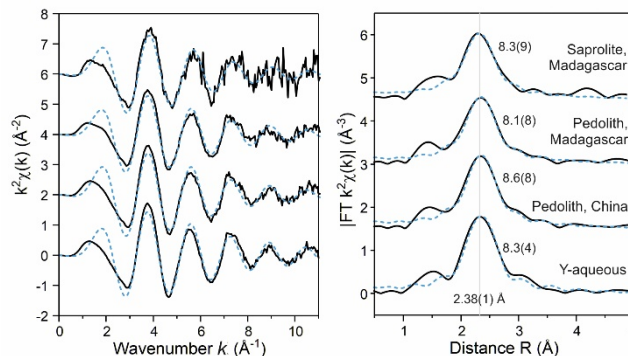


Figure 4 Left: EXAFS oscillations in *k*-space for the clay-hosted Y fractions, and Y in aqueous solution. Black lines indicate measured spectra. Blue stippled lines indicate fitted spectra. Right: Radial distribution functions showing best fit coordination numbers and average bond distances of nearest neighbor oxygens to yttrium.

4 Conclusions

Laterite samples from the Zhaibei granite was compared to laterite from the Ambohimirahavavy complex in

Madagascar. Ammonium sulphate leaching studies demonstrate high levels of exchangeable REE associated with kaolinite. Scanning electron microscopy shows that REE are released from primary phases during late-magmatic alteration and subsequent supergene weathering. Y K-edge XANES for the Chinese and Malagasy clay-hosted REE fractions are comparable to XANES of Y in aqueous solution and of REE-fluorocarbonates, where Y are respectively inferred to be 8 and 9 coordinated (Fig 3). This suggests a similar 8 to 9-fold hydration environment for Y associated with kaolinite in the laterites.

The structural state of Y associated with kaolinite from pedolith and saprolite samples was further constrained from quantitative EXAFS refinements. This yielded best fit coordination numbers of $8.1 - 8.6 \pm 0.9$ with average Y-O bond distances of $2.35 - 2.38 \pm 0.01 \text{ \AA}$ (Fig 4). Fits to a structural model of REE in parisite-(Ce), with 3 F and 6 O in the first coordination shell, were less successful. This suggests that the REE are truly adsorbed to the clays, and not hosted in micro- or nanoscopic particles of REE-fluorocarbonates. We therefore conclude that REE-adsorbed kaolinites from Madagascar and China are direct structural analogues, where REE are present as easily exchangeable 8 to 9 coordinated, hydrated, outer sphere, basal surface complexes on kaolinite, rather than structurally bound 5-6 coordinated edge complexes, or 6 coordinated interlayer complexes. Our data thus confirms a similar absorption mechanism at both deposits and explains the easily leachable nature of the REE.

Acknowledgements

This work was funded by the NERC SOSRARE consortium [grants NE/M010856/1 (to AMB, AAF and NJH), NE/M011267/1 (to MS, GE and EM) and NE/M01116X/1 (to KG)]. We thank Diamond Light Source for beam time awarded at the I18 beamline [grants SP14793 and SP15903]. SOSRARE partners and Lynn Boatner (ORNL, USA) provided samples and standards.

References

- Bao, Z. & Zhao, Z. (2008). Geochemistry of mineralization with exchangeable REY in the weathering crusts of granitic rocks in South China. *Ore Geol Rev* 33:519-535.
- Borst, A. M., Friis, H., Andersen, T., Nielsen, T. F. D., Waight, T. E. & Smit, M. A. (2016). Zirconosilicates in the kakortokites of the Ilímaussaq complex, South Greenland: Implications for fluid evolution and high-field-strength and rare-earth element mineralization in apatitic systems. *Min Mag* 80:5-30.
- Chakhmouradian, A. R. & Wall, F. (2012). Rare Earth Elements: Minerals, Mines, Magnets (and More). *Elements* 8:333-340.
- Díaz-Moreno, S., Muñoz-Páez, A. & Chaboy, J. (2000). X-ray Absorption Spectroscopy (XAS) study of the hydration structure of yttrium(III) cations in liquid and glassy states: Eight or nine-fold coordination? *J of Phys Chem A* 104:1278-1286.
- Estrade, G., Béziat, D., Salvi, S., Tiepolo, M., Paquette, J.-L. & Rakotovo, S. (2014). Unusual evolution of silica-under-and-oversaturated alkaline rocks in the Cenozoic Ambohimirahavy Complex (Madagascar): Mineralogical and geochemical evidence. *Lithos* 206:361-383.
- Estrade, G., Salvi, S. & Béziat, D. (2018). Crystallization and destabilization of eudialyte-group minerals in peralkaline granite and pegmatite: a case study from the Ambohimirahavy

- complex, Madagascar. *Min Mag* 82:375-399.
- Goodenough, K. M., Wall, F. & Merriman, D. (2017). The Rare Earth Elements: Demand, Global Resources, and Challenges for Resourcing Future Generations. *Nat Resources Res*, 1-16.
- Li, Y. H. M., Zhao, W. W. & Zhou, M.-F. (2017). Nature of parent rocks, mineralization styles and ore genesis of regolith-hosted REE deposits in South China: An integrated genetic model. *J of Asian Earth Sci* 148:65-95.
- Mosselmans, J. F. W., Quinn, P. D., Dent, A. J., Cavill, S. A., Moreno, S. D., Peach, A., Leicester, P. J., Keylock, S. J., Gregory, S. R., Atkinson, K. D. & Rosell, J. R. (2009). I18 - the microfocus spectroscopy beamline at the Diamond Light Source. *J of Synch Rad* 16, 818-824.
- Ni, Y., Post, J. E. & Hughes, J. M. (2000). The crystal structure of parisite-(Ce), $\text{Ce}_2\text{CaF}_2(\text{CO}_3)_3$. *Am Min* 85:251-258.
- Ravel, B. & Newville, M. (2005). ATHENA, ARTEMIS, HEPHAESTUS: data analysis for X-ray absorption spectroscopy using IFEFFIT. *J of Synch Rad* 12, 537-541.
- Smith, M. P., Campbell, L. S. & Kynicky, J. (2015). A review of the genesis of the world class Bayan Obo Fe-REE-Nb deposits, Inner Mongolia, China: Multistage processes and outstanding questions. *Ore Geol Rev* 64:459-476.
- Wang, L., Xu, C., Zhao, Z., Song, W. & Kynicky, J. (2015). Petrological and geochemical characteristics of Zhaibei granites in Nanling region, Southeast China: Implications for REE mineralization. *Ore Geol Rev* 64:569-582.
- Weng, Z., Jowitt, S. M., Mudd, G. M. & Haque, N. (2015). A detailed assessment of global rare earth element resources: opportunities and challenges. *Econ Geol* 110:1925-1952.
- Xu, C., Kynický, J., Smith, M. P., Kopriva, A., Brtnický, M., Urubek, T., Yang, Y., Zhao, Z., He, C. & Song, W. (2017). Origin of heavy rare earth mineralization in South China. *Nat Comms* 8, 14598.

Isotopic constraints on ore-grade enrichment of rare earth elements in carbonatites: the Elk Creek carbonatite example

Philip L. Verplanck¹, G. Lang Farmer², Craig A. Johnson¹, Heather A. Lowers¹

¹U.S. Geological Survey, Denver Colorado, USA

²University of Colorado, Boulder, Colorado USA

Abstract. Magmatic, hydrothermal, and weathering processes play important roles in enrichment of rare earth elements (REEs) in carbonatites. We utilized multiple isotopic systems to evaluate the origin of the REE mineralization of the Elk Creek carbonatite, Nebraska, United States. Nd and Sr isotopes were used to evaluate the source of the REEs, the age of the carbonatite, and open-system behavior. The ϵ_{Nd} (1.9 to 3.0, median of 2.4) is consistent with a lithospheric mantle source for the REEs. Sr_i ranges from 0.70289 to 0.70748. The lower Sr_i values are consistent with a mantle reservoir, but the higher values suggest input from other sources (open-system behavior). Multiple generations of dolomite were observed. Generation 1 (Dol I) is well crystallized, contains inclusions, and is intergrown with coarse apatite. Fine dolomite (Dol II) surrounds Dol I in some units, is poorly crystalline, and contains more Fe, Mn, and Sr than Dol I. Calcium and oxygen isotope analyses of Dol I plot in or near the primary igneous carbonate field, whereas Dol II extends to greater values ($\delta^{13}C$ to -1, $\delta^{18}O$ to 23). Ore-grade REE mineralization occurs in veins that cut units containing Dol II, suggesting that REEs were remobilized and enriched by late-stage fluids.

1 Introduction

Carbonatites are the primary source of niobium and light rare earth elements (REEs) and are potential sources of other critical elements. Compared to many mineral deposit systems, relatively little work has been done to constrain important questions concerning the distribution of mineralized carbonatites, the processes responsible for ore-grade enrichment, and the timing of ore forming processes. Isotope geochemistry can play an important role in addressing these unknowns regarding carbonatite ore genesis because the composition of these intrusive-related deposits lends itself to a multi-isotope approach. Radiogenic isotopes (including Nd, Sr, and Pb) can constrain the age and origin of the ores as well as open versus closed system behavior. Stable isotopes (including C, O, and S) can constrain the origin of the ores and open and closed system behavior. It is an ideal situation to have an isotopic system that matches one of the ore commodities, such is the case with neodymium in carbonatites. Strontium is generally quite enriched in carbonatites because of its similar charge and ionic radius to calcium. Similarly, carbonatites lend themselves to calcium and oxygen isotopic analysis because these elements are found in multiple minerals. Sulfide and

sulfate minerals are also present in many carbonatites, and thus sulfur isotopes are another tool that can be employed. By utilizing a multi-isotope approach, data can be gathered from a variety of minerals that formed throughout the paragenesis.

This abstract will highlight the utilization of a multi-isotope approach to constrain REE enrichment in the Elk Creek carbonatite, located in southeastern Nebraska, USA. The multi-lithologic Elk Creek carbonatite is associated with other alkaline intrusives. The carbonatite, reported to be the largest niobium resource in the United States, contains zones enriched in REEs. This intrusive complex is buried by more than 200 m of Pennsylvanian marine sedimentary rocks and Quaternary glacial till. Alkaline intrusive units associated with the carbonatite include syenites and subordinate mafic dikes. The carbonatite and alkaline intrusives intrude into Precambrian granite and gneiss on the eastern margin of a major rift zone in the basement rocks (the Mid-Continent rift) where the rift has been offset by one of a series of southeasterly trending structures. Age determinations of the carbonatite range from ~ 500 to 570 Ma.

In 1970, a geophysical survey identified a positive gravity anomaly, and the following year the carbonatite was discovered when drilled by the state of Nebraska (Carlson and Treves 2005). Between 1973 and 1986, MolyCorp Inc. undertook an extensive exploration program at the site, including over 100 drill holes that amassed ~46,800 m of core. Our study utilizes a subset of the archived MolyCorp drill cores to evaluate REE enrichment in carbonatites. MolyCorp geologists divided the carbonatite into three primary lithologies: apatite beforite, barite beforite, and magnetite beforite; beforite is a dolomite-rich carbonatite. Brecciated carbonatite is also present in some of the cores, and much of the carbonatite was overprinted by various fluids. Zones of ferruginous alteration resemble "rodbergite" as described at the Fen complex, Norway.

2 Geology and geochemistry

The apatite beforite is the most voluminous carbonatite unit in the Elk Creek complex; it consists of dolomite and apatite with variable amounts of quartz, fluorite, phlogopite, pyroxene, chlorite, feldspar, magnetite, sulfides, barite, and REE-rich phases that include parisite, synchysite, bastnäsite, and monazite. Zones enriched in pyrochlore (the primary Nb host mineral) or

REE-phases occur quite sporadically in this unit. Apatite is either disseminated or occurs in narrow bands.

The magnetite befsrite consists of dolomite, magnetite, ilmenite, hematite, barite, and quartz, with variable amounts of rutile, apatite, fluorite, phlogopite, pyroxene, sulfides and pyrochlore. Much of the magnetite befsrite is brecciated, with magnetite befsrite occurring as clasts and/or as the matrix.

The barite befsrite is the least voluminous lithology. It consists of dolomite, barite, and quartz with minor or variable apatite, fluorite, phlogopite, pyroxene, feldspar, chlorite, sulfides, and contains the highest abundance of REE phases, which include parisite, synchysite, bastnäsite, and monazite. The barite befsrite primarily occurs as veins and dikes, a few millimeters to meters in width, but thicker zones (tens of meters thick) have been identified in a few cores.

Our work has documented a range in REE concentrations and patterns within the carbonatite. The chondrite-normalized REE patterns of apatite befsrite samples display a typical carbonatite pattern (Fig. 1) with moderate enrichment in the light REE (La 118-1780 ppm), no Eu anomaly, and a negative slope. Samples of apatite befsrite with the highest LREE content (>500 ppm La) contain late-stage fluorocarbonates (parisite, synchysite, and bastnäsite) and phosphates (monazite). The fluorocarbonates occur as clusters of fine needles, sometimes in a radiating morphology, which were first

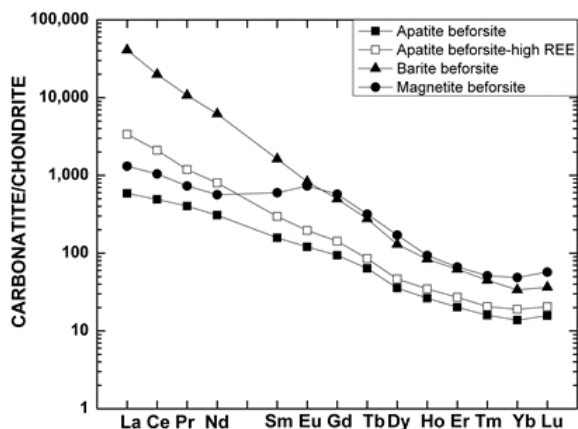


Figure 1. Chondrite-normalized REE diagram displaying various carbonatite lithologic units of the Elk Creek carbonatite. Median values used for apatite befsrite, apatite befsrite-high REE, barite befsrite, and magnetite befsrite.

identified during the Molycorp exploration studies. Similarly, the monazite occurs as fine needles, in radiating or random orientations. The barite befsrite contains the most REE-rich zones within the Elk Creek carbonatite with La as much as 53,100 ppm, Ce as much as 66,900 ppm, and Nd as much as 13,100 ppm; their chondrite-normalized REE patterns display typical carbonatite REE patterns (Fig. 1). Similar to the apatite befsrite, samples of barite befsrite with the highest LREE content contain late-stage fluorocarbonates and

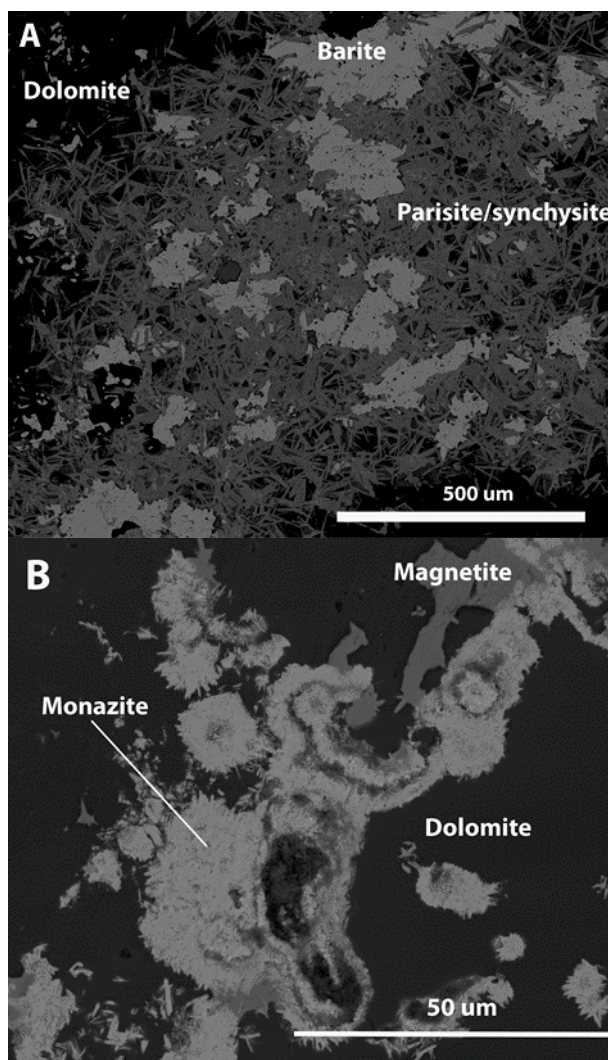


Figure 2. SEM backscattered electron images of REE phases in barite befsrite unit of Elk Creek carbonatite. A. REE fluorocarbonates. B. Monazite infilling in barite befsrite.

phosphates (Fig. 2). The magnetite befsrite, the carbonatite unit that contains much of the Nb mineralization, has an anomalous REE pattern displaying enrichment of the more valued middle and heavy REEs (Eu, Gd, Tb, and Dy) relative to lower mass La, Ce, and Nd, and higher mass Tm, Yb, and Lu (Fig. 1). Studies are underway to determine the hosts of these elements in the magnetite befsrite.

Detailed petrographic and scanning electron microscope (SEM) work have identified multiple generations of dolomite. The first generation (Dolomite I) is well crystallized and contains inclusions. It can be found intergrown with coarse apatite in apatite befsrite (Fig 3A). The apatite befsrite samples that contain only Dolomite I have lower REE concentrations than apatite befsrite samples that contain multiple generations of dolomite. Dolomite I also occurs in the magnetite befsrite where it is surrounded by a finer dolomite (Dolomite II; Fig 3B). Dolomite II is poorly crystalline and contains higher concentrations of Fe, Mn, and Sr than Dolomite I. A fine-grained dolomite, similar to Dolomite II, is the primary dolomite found in the barite befsrite.

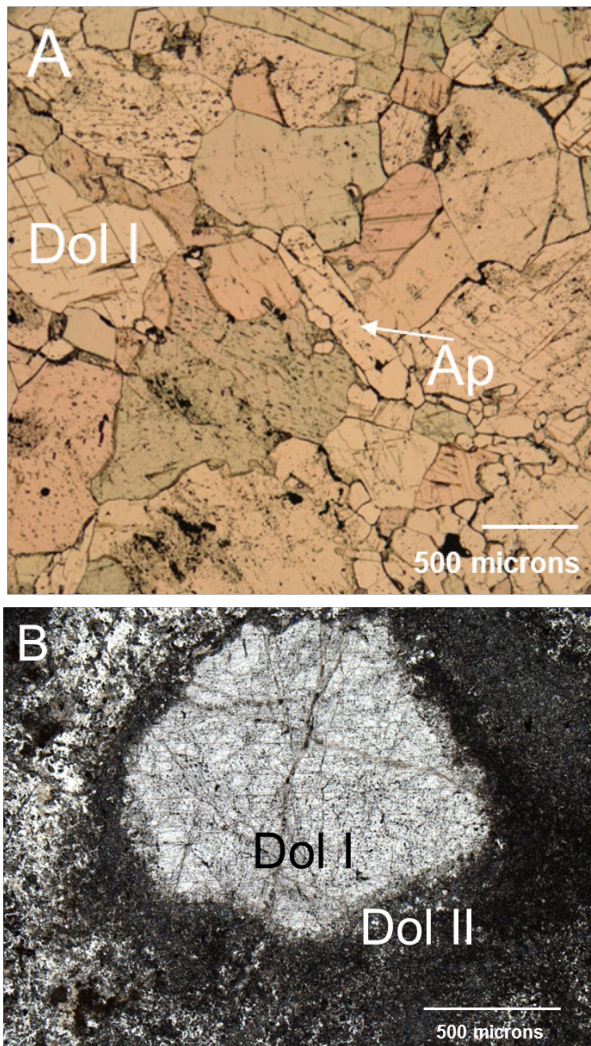


Figure 3. Photomicrographs displaying two generations of dolomite. A) coarse-grained apatite beforite with Dolomite I. B) Magnetite beforite with Dolomite I surrounded by Dolomite II.

3 Isotope geochemistry

Neodymium and strontium isotopes were used to evaluate the source of the REEs, the age of the carbonatite, and open-system behavior. Whole rock samples of each lithology were analyzed. The initial ϵ_{Nd} (1.9 to 3.0, median of 2.4) is consistent with a lithospheric mantle source for the REEs. Sr_i values range from 0.70289 to 0.70748. The lower Sr_i values occur in the apatite beforite and are consistent with a mantle reservoir, but the higher values suggest input from other sources including post-formation alteration (open-system behavior).

Because of the range in elemental concentrations of Sm and Nd, the Nd isotopic data can be used to calculate an age for the carbonatite (570 ± 37 Ma). This age is similar to the few previously reported ages (~500-550 Ma (Carlson and Treves 2005). Furthermore, because the Nd isotopic data lie along a linear array, the REE ore had a single source.

Utilizing a micro drill on characterized billets, samples

of various dolomites were obtained for calcium, oxygen, and strontium isotopic determinations. Carbon and oxygen isotope analyses of Dolomite I plot in or near the Primary Igneous Carbonate field, whereas Dolomite II extends to greater values ($\delta^{13}C$ to -1, $\delta^{18}O$ to 23) (Fig. 4). Dolomite II samples with the highest $\delta^{18}O$ and $\delta^{13}C$ values occur in zones of ferruginous alteration that resemble “rodbergite” as described at the Fen complex, Norway. These samples also have significantly higher Sr isotopic compositions, suggesting open system behavior; the timing of this event could be substantially later than the ore forming event.

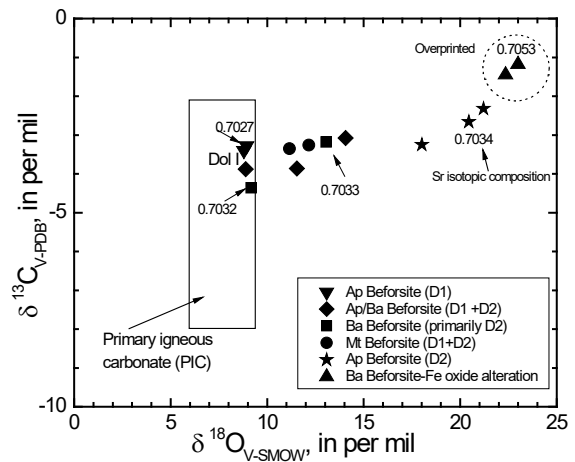


Figure 4. Variations in carbon and oxygen isotopic compositions of dolomite from various lithologies in the Elk Creek carbonatite with strontium isotopic values from the same aliquots. Ap=apatite, Ba=barite, Mt=magnetite, D1=Dolomite I, D2=Dolomite II. Field for primary igneous carbonate from Deines (1989).

Most of the Dolomite II samples lie along a trend away from the Primary Igneous Carbonate field and display a substantial increase in $\delta^{18}O$ (11 to 21) and only a slight increase in $\delta^{13}C$ (-3.5 to -2.5). This systematic variation could result from a decrease in temperature during crystallization or the input of fluids with higher $\delta^{18}O$ and $\delta^{13}C$ values. Because there is little change in the Sr isotopic compositions of the dolomites, open system behavior is less likely. This suggests that no external fluids are required to form the second generation dolomites.

4 Conclusions

Radiogenic and stable isotopic data on well-characterized samples can provide important constraints on ore-grade enrichment of REEs in carbonatites. Since Nd is an ore element, the Nd isotopic data provide direct information for the source of the ore. If there is sufficient Nd and Sm elemental concentration variation, then a carbonatite age can be calculated. If multiple ore forming events occur, Nd isotopic data can help determine if the Nd was derived from different sources, from the same source, or remobilized from within the carbonatite. The Sr isotopic data complements the Nd but is more sensitive to later events. Many carbonatites display a range in Sr

isotopic compositions suggesting that open system processes are common. This open system behavior may occur long after crystallization.

Stable isotopic data can provide additional insight into ore forming processes. C, O, and S can reside in ore and gangue minerals that form throughout the life of the deposit, and thus with well constrained samples, these data can provide important constraints on ore-grade enrichment processes.

Acknowledgements

This work was supported by the US Geological Survey's Mineral Resources Program (MRP), in part through the MRP External Research Program.

References

- Carlson MP, Treves SB (2005) The Elk Creek Carbonatite, Southeast Nebraska-An overview. *Natural Resources Research* 14: 39-45
- Deines P (1989) Stable isotope variations in carbonatites. In Bell K (ed) *Carbonatites: Genesis and Evolution*. Unwin Hyman, London, 301-359

Utilizing alteration (fenite) surrounding carbonatite intrusions as a REE and Nb exploration indicator

Holly A.L. Elliott, Sam Broom-Fendley, Frances Wall
Camborne School of Mines, University of Exeter, UK

Abstract. Carbonatites are the world's primary source of rare earth elements (REE) and niobium (Nb). China currently monopolizes the market, producing >95% of the world's supply. In order to meet UK government greenhouse gas emission targets, a reliable and sustainable supply of REE and Nb must be established in order to produce green technologies such as electric cars and wind turbines. The location of many carbonatite complexes are currently known, however the economic potential of few have been explored. Detailed petrological and geochemical analysis of fenite (metasomatic alteration surrounding carbonatite systems) has provided criteria to determine whether the source intrusion is enriched in these critical metals. Fenite micro-mineral assemblages enriched in REE and Nb indicate that the source of the fenitizing fluids is similarly enriched in these metals. Fenite apatite morphology and luminescence can also be used to indicate REE-enrichment in the source intrusion, showing systematic increases in Na, Sr and total REE (TREE) concentration from core to rim or homogenous late-stage crystals. These fenite alteration patterns are vertically and horizontally extensive, and can therefore be seen at a variety of erosion levels, providing a means of determining the economic potential of a system before undertaking expensive drilling campaigns.

1 Introduction

Carbonatites are often associated with high concentrations of a multitude of economically important minerals such as iron, copper, titanium, fluorite and uranium (Heinrich 1966; Mariano 1989; Pell 1996). In addition, carbonatites are the most important source of rare earth elements (REE) and niobium (Nb) (Wall 2014; Goodenough et al. 2016), both high profile critical metals considered imperative to technological advancement and the production of green technologies.

Despite the global distribution of both carbonatites and REE deposits, China currently produces >95% of the world's supply of REE (EC, 2017), causing vulnerability to future supply. REE are used in the production of neodymium-iron-boron magnets, which are important constituents of green technologies, such as electric cars and wind turbines. The UK government has recently committed to reducing greenhouse gas emission by at least 80% and ensuring every car and van is zero emission by 2050 (DTOLEV 2015; DBEIS 2018). Therefore, the future demand for REE is expected to increase dramatically (Yang et al. 2017).

Models relating to carbonatite and alkaline systems has not progressed considerably since that initially proposed by Le Bas (1977). However, this model has its limitations including lack of temporal relationships, ore

formation processes and alteration. In order to ensure a sustainable and reliable source of REE for the future, new geomodels must be developed to enable exploration companies to better understand carbonatite systems and any critical metal-enrichments they contain.

2 Fenites and fenitization

Cooling and crystallizing carbonatite melts release multiple pulses of alkali-rich fluids (Morogan 1994; Le Bas 2008) which metasomatise the surrounding country rock during a process called fenitization. Traditionally, fenitization is considered to involve the addition of alkalis and the removal of silica (Brögger 1921; Bardina and Popv 1994). The resulting alteration is zoned both horizontally and vertically. A potassic fenite aureole which is typically brecciated and consists predominantly of alkali feldspar and metal oxides (Le Bas 2008; Doroshkevich et al. 2009) forms proximal to the intrusion, and a sodic fenite aureole characterized by veins of sodic pyroxenes and amphiboles forms distal to the intrusion.

3 Fenite as an exploration indicator

Until recently, the vast majority of research focused on carbonatite intrusions due to their economic importance, with fenite being relatively neglected in the literature. However, alteration patterns have been used with great success in the past to find other magmatic-related ore deposits such as porphyry copper (e.g. Sillitoe 2010). Fenite has the potential to be used in a similar way to explore for REE and Nb deposits.

3.1 Field relationships

Fenite aureoles form a distinct pattern of alteration that allows vectoring toward the source intrusion. The rocks themselves are easily recognizable in the field, without the need for expensive lab techniques. In addition, alteration can extend >1 km away from the source intrusion and can be exposed at a variety of erosion levels.

Evolution of carbonatitic magmas by fractional crystallization causes incompatible REE to be concentrated in later or last carbonatite differentiates (Heinrich 1966; Le Bas 1981; Wall 2014). Each phase of carbonatitic magmatism is associated with the release of fenitizing fluids, leading to multiple stages of fenitization which are represented as different assemblages or vein generations in the country rock. As such, the complexity of the fenite reflects magma evolution, and therefore the likelihood of REE-enrichment in the source intrusions.

Although brecciation is not recorded at every REE-rich carbonatite complex, there is a strong correlation between the presence of breccia and mineralization. Seventy percent of REE-enriched carbonatites are associated with brecciated fenite (Elliott et al. 2018), however the lack of observations at other sites may have been due to the literature focus or level of erosion. Widespread brecciation associated with carbonatite emplacement indicates the explosive release of fluids and volatiles from the evolving magma (Verplanck et al. 2014). The presence of these fluids and volatiles attest to the evolution and crystallization of the carbonatite magma, the same processes that concentrate incompatible REE in the residual melt, therefore it is logical that an association between brecciation and mineralization would exist.

3.2 Micro-mineral assemblages

Fenitizing fluids contain ligands such as chloride-, fluoride-, sulphate-, phosphate-, and/or carbonate anions, which can form complexes with REE and Nb, greatly enhancing their solubility in aqueous fluids (Andersen 1986; Haas et al. 1995; Williams-Jones et al. 2012; Tsay et al. 2014). Fenitizing fluids transport these critical metals into the surrounding fenite, where they precipitate as REE and Nb-enriched micro-mineral assemblages (Hogarth 2016; Bodeving et al. 2017; Dowman et al. 2017).

We have found micro-mineral assemblages enriched in REE and Nb globally (e.g. Songwe Hill, Malawi; Mountain Pass, USA; Sokli, Finland) and their presence in fenite could be used to determine the level of critical metal enrichment in the source intrusion.

3.3 Apatite characteristics

Apatite is a brilliant mineral for recording metasomatic activity, and the properties and composition of fluids (e.g. Harlov 2015). Apatite within fenite aureoles is typically zoned, fingerprinting the changing chemistry of multiple pulses of fenitizing fluids as the source intrusion evolves. Changes in chemical composition between these zones can be seen by contrasting luminescence colors under cold-cathodoluminescence (CL). Fenite apatite morphology and luminescence has been studied to investigate whether it can be used to determine if a carbonatite complex is REE-enriched.

4 Fenite apatite geochemical data

Fourteen carbonatite localities were selected, including REE-enriched and poor systems from US, Europe, Africa, and Asia. Fenite apatite was imaged used CL and then zones were analyzed for major element (using EPMA) and trace element (using LA-ICPMS) geochemistry.

Three main groups have been identified based on morphology and geochemical composition. Group 1 are concentrically zoned apatite. These can be found at both REE-enriched and poor complexes but with distinct differences. REE-poor systems display fenite apatite with

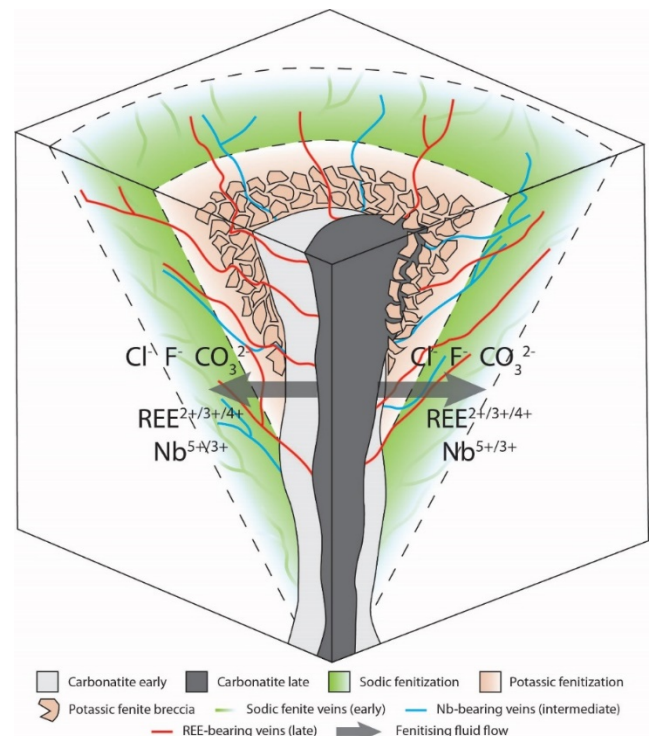


Figure 1. 3D model showing idealized fenite alteration patterns surrounding multiple generations of carbonatite intrusions. Fenitizing fluids contain ligands that mobilize Nb and REE into the surrounding fenite aureole. Adapted from Elliott et al. 2018.

unregimented zoning both between and within complexes. This is reflected in their chaotic composition, with no discernible trends. REE-enriched complexes displaying concentrically zoned apatite always have a core which luminesces green, rich in Mn and most likely inherited from the protolith, surrounded by one or multiple purple luminescing rims. These crystals display increasing Na, Sr and total REE (TREE) concentration from core to rim.

Group 2 apatite are only found in fenite surrounding REE-enriched systems. These are late-stage and homogenous, displaying little to no variation in their blue-purple luminescence and are also enriched in Na, Sr, Th and TREE.

Group 3 apatite display evidence of hydrothermal alteration, such as being strung out by later veins, partial replacement by porous material or stringer textures with patchy luminescence. The composition of these crystals is variable, reflecting the hydrothermal alteration. However, this alteration can have the effect of preferentially mobilizing light REE (LREE).

5 Discussion

5.1 Utilizing fenite during exploration

Fenite alteration aureoles are easily identified by hand specimen in the field, allowing vectoring toward the source intrusion. However, if the source intrusion has not yet been exposed by erosion, it requires expensive drilling campaigns to determine any critical metal-enrichment present.

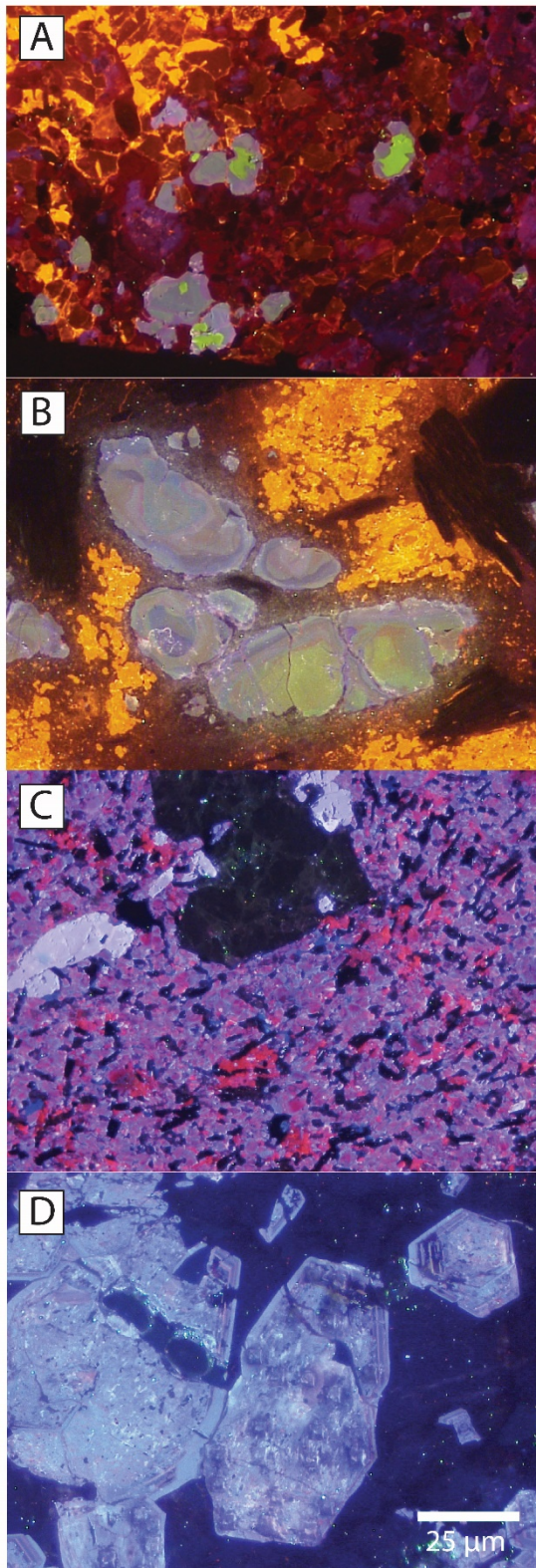


Figure 2. Cold cathodoluminescence images **A:** Group 1 apatite morphology from a REE-enriched complex showing green luminescing Mn-rich core surrounded by multiple purple luminescing REE-rich rims. Lofdal, Namibia. **B:** Group 1 apatite morphology from REE-poor complex showing unregimented layering. Tororo, Uganda. **C:** Group 2 apatite morphology showing homogenous blue-purple luminescing crystals. Mountain Pass, USA. **D:** Group 3 apatite morphology showing porous sponge-like alteration. Sokli, Finland.

Using the criteria outlined in this paper, provides the ability to use the fenite mineralogy as a means to determine whether further exploration of a site is warranted. The large vertical and horizontal extent of fenitization means that it can be exposed at a variety of erosion levels where an intrusion might not be. The presence of enriched micro-mineral assemblages and Group 1 and/or 2 apatite crystals can be used to indicate the enrichment of the source intrusion in REE and/or Nb.

5.2 Implications of hydrothermal alteration

Group 3 apatite display evidence of hydrothermal alteration, which can have the effect of preferentially mobilizing LREE, and concentrating HREE in the residual crystal. HREE-enrichment is rarer within carbonatite complexes and these elements are more valuable.

Spongy, porous crystals and stringer textures indicating the occurrence of hydrothermal alteration, have also been observed in intrusions at Songwe Hill, Kangankunde and Tundulu, Malawi (Broom-Fendley et al. 2016a; 2016b; 2017); Chipman Lake, Canada; and Sokli Finland (Chakmouradian et al. 2017). This indicates that although it is not currently considered economical to exploit metals from fenite aureoles, the alteration provides evidence for processes that are occurring inside the more economical carbonatite intrusion.

Acknowledgements

This research is part of the HiTech AlkCarb project which has received funding from the European Union's Horizon 2020 research and innovation programme under grant No 689909.

References

- Andersen T (1986) Compositional variation of some rare earth minerals from the Fen complex (Telemark, SE Norway): implications for the mobility of rare earths in a carbonatite system. *Min Mag* 50: 503-509.
- Bardina NY, Popov VS (1994) Fenites: systematics, formation conditions and significance for crustal magma genesis. *Min Obsh* 113:485-497.
- Bodeving S, Williams-Jones AE, Swinden S (2017) Carbonate-silicate melt immiscibility, REE mineralizing fluids, and the evolution of the Lofdal intrusive suite, Namibia. *Lithos* 268: 268-271:383-398.
- Brögger WG (1921) Die eruptivegestein des kristianiagebietes, IV. Das fengebietet in telemark. *Norwegen. Naturv. Klasse* 9:150-167.
- Broom-Fendley S, Styles MT, Appleton D, Gunn G, Wall F (2016a) Evidence for dissolution-reprecipitation of apatite and preferential LREE mobility in carbonatite-derived late-stage hydrothermal processes. *Amer Min* 101:596-611.
- Broom-Fendley S, Heaton T, Wall F, Gunn G (2016b) Tracing the fluid source of heavy REE mineralisation in carbonatites using a novel method of oxygen-isotope analysis in apatite: the examples of Songwe Hill, Malawi. *Chem Geol* 440: 275-287.
- Broom-Fendley S, Brady AE, Wall F, Gunn G, Dawes W (2017) REE minerals at the Songwe Hill carbonatite, Malawi: HREE-enrichment in late-stage apatite. *Ore Geol Reviews* 81:23-41.
- Chakmouradian AR, Reguir EP, Zaitsev AN, Couëslan C et al (2017) Apatite in carbonatitic rocks: compositional variation, zoning, element partitioning and petrogenetic significance. *Lithos* 274-275:188-213.

- Department for business, energy and industrial strategy (2018) Clean growth strategy executive summary. <https://www.gov.uk/government/publications/clean-growth-strategy/clean-growth-strategy-executive-summary> Accessed 15 September 2018.
- Department for Transport, Office for Low Emission Vehicles (2015) <http://webarchive.nationalarchives.gov.uk/20160805060601/https://www.gov.uk/government/news/uk-government-pledges-bold-ambition-for-electric-cars> Accessed 15 September 2018.
- Doroshkevich AG, Viladkar SG, Ripp GS, Burtseva MV (2009) Hydrothermal REE mineralization in the Amba Dongar carbonatite complex, Gujarat, India. *Can Min* 47:1105-1116.
- Dowman E, Wall F, Treloar PJ, Rankin AH (2017) Rare earth mobility as a result of multiple phases of fluid activity in fenite around the Chilwa Island Carbonatite, Malawi. *Min Mag* 81:1367-1395.
- Elliott HAL, Wall F, Chakmouradian AR et al (2018) Fenites associated with carbonatite complexes: a review. *Ore Geol Reviews* 93:38-59.
- European Commission (2017) Study on the review of the list of critical raw materials. *Criticality Assessments*.
- Goodenough KM, Schilling J, Jonsson E et al (2016) Europe's rare earth element resource potential: AN overview of REE metallogenic provinces and their geodynamic setting. *Ore Geol Rev* 72:838-856.
- Haas JR, Shock, EL, Sassani DC (1995) Rare earth elements in hydrothermal systems: estimates of standard partial molal thermodynamic properties of aqueous complexes of the rare earth elements at high pressures and temperatures. *Geochim Cosmochim Acta* 59:4329-4350.
- Harlov DE (2015) Apatite: a fingerprint for metasomatic processes. *Elements* 11:171-176.
- Heinrich EW (1966) *The geology of carbonatites*. Rand McNally & Company, Chicago.
- Hogarth DD (2016) Chemical trends in the Meech Lake, Québec, carbonatites and fenites. *Can Min* 54:1105-1128.
- Le Bas MJ (1977) Magmatic and metasomatic processes. In: Le Bas MJ (ed) *Carbonatite-nephelinite volcanism: an African case history*. John Wiley & Sons, pp 263-278.
- Le Bas MJ (1981) Carbonatite magmas. *Min Mag* 44:133-140.
- Le Bas MJ (2008) Fenites associated with carbonatites. *Can Min* 46:915-932.
- Mariano AN (1989) Nature of economic mineralization in carbonatite and related rocks. In: Bell K (ed) *Carbonatites: genesis and evolution*. Unwin Hyman, pp 149-176.
- Morogan V (1994) Ijolite versus carbonatite as sources of fenitization. *Terra Nova* 6:166-176.
- Pell J (1996) Mineral deposits associated with carbonatites and related alkaline igneous rocks. In: Mitchell RH (ed) *Undersaturated alkaline rocks: mineralogy, petrogenesis, and economic potential*. No. 24 in *Mineralogical Association of Canada Short Course Series*. *Min Assoc Can*, pp 271-310.
- Sillitoe RH (2010) Porphyry copper systems. *Econ Geol* 105:3-41.
- Tsay A, Zajacz Z, Sanchez-Valle C (2014) Efficient mobilization and fractionation of rare-earth elements by aqueous fluids upon slab dehydration. *Earth Planet Sci Lett* 398: 101-112.
- Verplanck PJ, Van Gosen BS, Seal RR, McCafferty AE (2014) A deposit model for carbonatite and peralkaline intrusion-related rare earth element deposits. In: *Mineral Deposit Models for Resource Assessment*. No. 2010-5070-J in *Scientific Investigations*. US Geological Survey, pp 1-58.
- Wall F (2014) Rare earth elements. In: Gunn G (ed) *Critical Metals Handbook*. John Wiley & Sons, pp 312-339.
- Williams-Jones A, Migdisov AA, Samson I (2012) Hydrothermal mobilization of the rare earth elements: a tale of "Ceria" and "Yttria". *Elements* 8: 355-360.
- Yang Y, Walton A, Sheridan R et al (2017) REE recovery from end-of-life NdFeB permanent magnet scrap: a critical review. *J Sustain Metall* 3:122-149.

Ore geometry and emplacement style of the carbonatite-hosted Morro do Padre Nb deposit

Matheus Palmieri¹, José A. Brod², Pedro F. O. Cordeiro³, José C. Gaspar⁴, Paulo A. R. Barbosa, Tereza C. Junqueira-Brod², Sergio A. Machado⁵, Bruno P. Milanezi⁵, Luis C. Assis

¹*Centro de Desenvolvimento de Tecnologia Nuclear*

²*Universidade Federal de Goiás*

³*Pontificia Universidad Católica de Chile*

⁴*Universidade de Brasília*

⁵*CMOC International Brasil*

Abstract. The Morro do Padre niobium deposit contains important unexploited niobium resources within carbonatite-associated rocks and laterites of the Catalão II complex, Brazil. The deposit can be divided into three zones: a) The Lower Hypogene Zone; b) The Upper Hypogene Zone; c) The Laterite Zone. The Hypogene Zone is defined by dike swarms of nelsonites (magnetite-apatite-carbonate-phlogopite-pyrochlore rocks) and carbonatites cutting country rocks. Two main nelsonite phases occur: i) the N1 apatite-rich nelsonites and ii) the N2 magnetite-rich nelsonites. Additionally, two carbonatite phases are recognized: C1 calcite carbonatite and C2 dolomite carbonatite. The hypogene mineralization is defined by the abundance of nelsonite dikes, particularly N2, which are modally rich in pyrochlore. 3D modelling based on the drill hole database suggests a general EW elongated, pipe-like shape for these intrusions which, unlike other examples in the province, are not intruded directly into a coeval alkaline silicate plutonic series. This can be readily explained by the Morro do Padre deposit representing the emplacement of nelsonite and carbonatite dikes in the roof of a larger carbonatite complex.

1 Introduction

Carbonatite complexes containing phoscorite rocks (magnetite-apatite-olivine) are rare in the geological record, with only around 20 occurrences known worldwide (Krasnova et al. 2004; Wall and Zaitsev 2004). They are, however, extremely relevant as mineralizing systems, since igneous complexes containing associations of phoscorite, carbonatite, and alkaline silicate rocks have a strong potential for ore deposits. These include a wide variety of mineralization styles such as P, Nb, Cu, REE, Ba, Ti, vermiculite and lime, among others. The majority of the world's production of Nb comes from carbonatite complexes, particularly those in the Alto Paranaíba Igneous Province (APIP), in Brazil. The two biggest sources of production are mines in giant reserves in the Araxá complex (Gierth and Baecker 1986; Issa Filho et al. 1984) and smaller deposits in the Catalão I complex (Cordeiro et al. 2011) and Catalão II complex (Palmieri et al. in submission). Together, these deposits represent ca. 85% of the global niobium production (Mitchell et al. 2015).

In spite of having been mined for more than 40 years,

ore formation processes associated with these carbonatite-hosted niobium deposits have not been satisfactorily explained in comparison to processes observed in other well-known Nb-barren carbonatite complexes.

This work is part of a larger research to be submitted for publication covering a systematic study of ore geometry, paragenetic sequences, mineral chemistry and lateritization in Morro do Padre. The aim is to understand what makes these APIP carbonatites highly fertile for niobium mineralization and provide information to help build both advanced exploration models and refined ore processing technologies. To address this, we present a discussion on the structure and mineralization styles of the hypogene deposit of Morro do Padre on the basis of geophysical and ore modelling data. Our goal is to provide a complete emplacement model that takes into account the time-space evolution of this mineralizing system.

2 The Alto Paranaíba Igneous Province (APIP)

The Late-Cretaceous alkaline rocks of southern Goiás and western Minas Gerais states, in central Brazil, spread over an area of 25,000 km² and have been grouped under the designation of Alto Paranaíba Igneous Province, APIP, by Gibson et al. (1995). The province consists mainly of kamafugitic lavas and plugs, with subordinate kimberlite and lamproite diatremes and alkaline-carbonatite plutonic complexes. This extensive magmatic activity is interpreted as the result of the impact of the Trindade mantle plume head under central Brazil, at ca. 90 Ma, which melted the overlying metasomatized sub-continental lithospheric mantle to produce voluminous ultrapotassic magmas (Thompson et al. 1998). In spite of the wide range of rock types, the carbonatite complexes in the APIP have a strong ultrapotassic character and kamafugitic affinity. They are also co-genetic with numerous small kamafugite pipes occurring throughout the province and with kamafugite lavas and pyroclastics of the Mata da Corda Group (Araujo et al. 2001). The chronological, spatial and petrological affinity of kamafugites and carbonatites led Brod et al. (2000) to propose that they derived from the same parental melt.

3 The Morro do Padre deposit

The Morro do Padre Niobium deposit is hosted in the southern part of Catalão II, an APIP carbonatite complex in the state of Goiás. Along with the Boa Vista Nb deposit, 100 m to the west, Morro do Padre is represented by dike swarms of carbonatites and magnetite-apatite rocks (Figure 2), named here as nelsonite (Yegorov 1993) emplaced within fenitized Precambrian phyllites and amphibolites. The northern part of the Catalão II complex, on the other hand, resembles the other APIP complexes which can be roughly depicted as an outer silicate plutonic series and an inner carbonatite-phoscorite core.

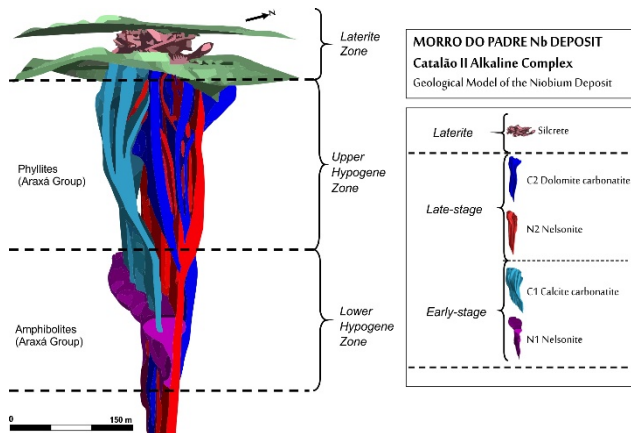


Figure 1. Geological model of the Morro do Padre Nb deposit and associated lithologies (Palmieri 2011).

On the basis of currently available drill core information and for modelling purposes, we subdivided the deposit into three distinct vertical sections from bottom to top into the Lower Hypogene Zone, the Upper Hypogene Zone and the Laterite Zone.

The hypogene ore is characterized by a complex system of crosscutting dikes of pyrochlore-bearing carbonatites and nelsonites hosted within country-rock phyllites and amphibolites. The general envelope of the hypogene ore reveals an E-W trend due to a dominant regional country rock fracture system, which albeit not the most pervasive, is also observable in regional magnetometry and satellite images (Palmieri 2011). The laterite ore developed over these fresh rocks through pedogenetic processes and compounded their mineralogical and textural complexity. The relationships between nelsonite-, carbonatite- and country rock-dominated units in the Upper Hypogene Zone of the Morro do Padre deposit are shown in Figure 1. Note that the geological units depicted in the model represent zones of high abundance of nelsonite and carbonatite, rather than continuous igneous bodies. Separation of hypogene and laterite ore zones is important for mining and ore processing because these ores have different geometallurgical behavior (e.g. Ribeiro 2008).

The Lower Hypogene Zone is 400 m wide and it was intercepted from 460 to 600 m of depth, where drilling ended. This zone is dominated by horizontally layered calcite-carbonatites (C1) and nelsonites (N1) hosted by fenitized amphibolites of the Neoproterozoic basement. N1 nelsonites occur in this zone as rhythmic layers of

apatite-nelsonite and pegmatoidal nelsonite. The Lower Hypogene Zone is cut by late-stage nelsonite (N2) and dolomite carbonatite dikes that proceed upwards to define the Upper Hypogene Zone.

The Upper Hypogene Zone is roughly 400 m thick and 140 m wide, but unlike its lower counterpart, it is dominated by stockworks of crosscutting pyrochlore-bearing nelsonite (N2), dolomite carbonatite and calcite-carbonatite dikes (usually a few centimeters thick, more rarely up to 1-2 m), with minor syenite and pyroxenite. These dikes cut fenitized Precambrian phyllites and subordinately amphibolites and quartzites, of the Brasília Belt.

The Laterite Zone is 470 m long, 160 m wide and represents the relatively thin (75 m) upper part of the Morro do Padre deposit. This zone poses additional challenges to the understanding and modeling of the mineralization because ores may have inherited the heterogeneity from primary mineralization but were overprinted by variable degrees of complex soil formation processes, up to near obliteration of primary hypogene features. Thus, unlike the hypogene ore, this zone is horizontally divided based on mineralogical and chemical characterization, from base to top into the Micaceous Ore, the Silcrete Ore and the Kaolinite-Oxide Ore.

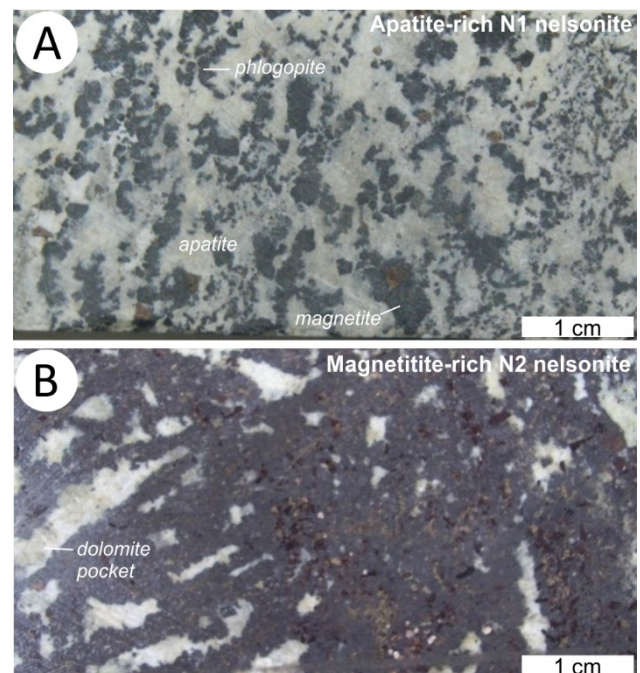


Figure 2. Pyrochlore-bearing nelsonite samples from the Morro do Padre Deposit **a.** Apatite-rich N1 nelsonite; **b.** Magnetite-rich N2 nelsonite with dolomite pockets (Palmieri 2011).

4 Discussion

The Morro do Padre deposit is hosted in the southern part of the Catalão II complex, a carbonatite complex that was poorly known until Palmieri (2011) reported on exploration efforts performed in the last 20 years. Field and core logging observations and geophysical data (Fig. 3), collected during multiple exploration campaigns, indicate that Catalão II is, in fact, comprised of two main

intrusions: a southern one, which hosts the Morro do Padre deposit, and a northern one. Both of them show carbonatite-related rocks but with wide variation of emplacement styles that can be explained by emplacement at different depths or levels of the intrusive system.

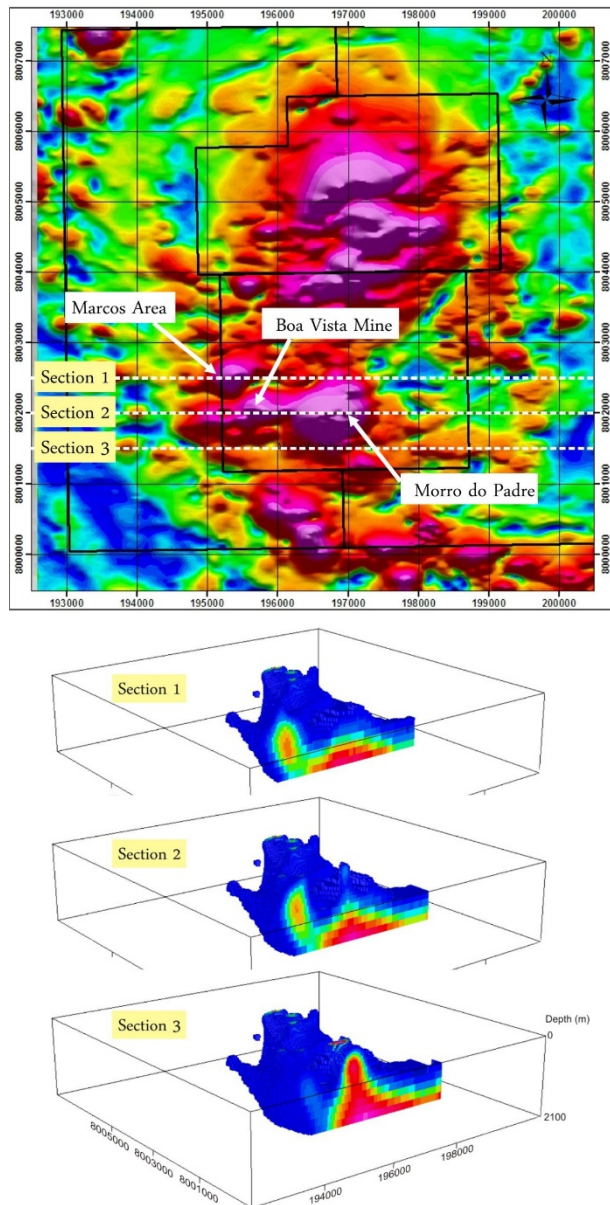


Figure 3. Analytical signal image of the Catalão I complex and magnetic modelling of the southern part of Catalão II, where the Morro do Padre Nb deposit is hosted (Palmieri 2011).

The northern part of Catalão II is a concentric, layered intrusion with an outer ultramafic rim and a phoscorite-carbonatite core as multiple intrusions, akin to other APIP complexes such as Tapira and Salitre (Brod et al. 2013; Barbosa et al. 2012), and constitutes the core of the carbonatite complex system. The southern part of Catalão II, on the other hand, is represented by nelsonite and carbonatite dikes cutting metasedimentary basement rocks and could be interpreted as the roof of a deeper

former pluton.

Geophysical modelling contributes to the suggestion of a deeper and larger magma chamber below 1000 m, at depths not yet reached by drilling (Fig. 3). In this model, the magnetic anomalies represented at surface by the nelsonite dikes that define the Morro do Padre and Boa Vista Nb deposits are rooted in a deeper magnetic anomaly.

Some fundamental differences between these two deposits, however, must be highlighted. The Morro do Padre hypogene zone has abundant carbonatites (C1 and C2) along with N1 and N2 nelsonites, rendering country rocks subordinate, although still present, in the mineralized section. In the Boa Vista Mine, on the other hand, carbonatite and nelsonite dikes are more scattered, implying not only a volumetrically more important contribution of barren metavolcanics and metasedimentary country rocks, but also a variation of emplacement level/depth between them, with the Boa Vista Mine representing a higher intrusive level, compared with the Morro do Padre deposit.

4.1 Emplacement styles

Within Morro do Padre, vertical lithological zoning of the hypogene zone can be indicative of the mode of emplacement of these magmas at different depths. The Lower Hypogene Zone, for example, can be interpreted as the result of the infilling of a small chamber or sill at the contact between amphibolite and quartzite country rocks. Such a contact zone would be prone to allow for magmas to pond and undergo several stages of differentiation and recharge, producing horizontal cyclic units which characterize the deeper part of Morro do Padre.

The Upper Hypogene Zone, on the other hand, would start to form with the ascension of C1 carbonatite magma upwards through quartzite country rocks. As suggested by crosscutting relationships, the entire system would be later cut by magmas that crystallized into the N2 nelsonites and C2 carbonatite, therefore implying that N2 and C2 represent a later stage in the evolution of the complex. It is noteworthy that both the carbonatite and nelsonite units tend to splay upward, suggesting that lower lithostatic pressure at the higher parts of the structure allowed a larger number of open fractures to be permeated by magmas.

These textural and lithological zoning features imply that magmas responsible for Morro do Padre percolated unusually during their ascension. Similarly, to pure carbonatite magmas whose fundamental structural units lack the ability to polymerize (Treiman 1989), the magmas responsible for originating the Morro do Padre niobium deposit emplaced as thin dikes, which is consistent with very low viscosity. Such extremely low-SiO₂, low-viscosity liquids are incapable of forcing their intrusion and forming large massive igneous bodies showing instead, a rather “runny” behavior, seeping through existing fractures with ease. This behavior implies that a given magma (e.g. a carbonatite or a nelsonite) will intrude as a zone of parallel and braided thin dikes rather than as a single body. An important

consequence of this feature is to render the mapping of individual dikes ineffective in any useful scale. These features, in association with small magma volumes and the configuration and structures of the wall rocks, lead to their emplacement as multiple phases of vertical or sub-vertical swarms of thin dikes and veins, rather than as massive bodies.

5 Implications

The majority of the hypogene mineralization in Morro do Padre is given by the abundance of N2 dikes, which are modally rich in pyrochlore and that, together with C2 dolomite carbonatites, comprise the latest stage of the evolution of Morro do Padre. The genesis of such magnetite-apatite rich rocks, however, remains a matter of debate given the importance of liquid immiscibility in carbonatite systems. In the case of N2 and C2, which appear to be coeval, it is not clear whether they are a pair of magmas related by liquid immiscibility or two stages of a single crystal fractionation process. Recent experimental and melt inclusions work support the existence of iron melts able to explain 'iron lavas' from El Laco and other cordilleran equivalents (Tornos et al 2016). An oxide-phosphate melt would be able to explain the occurrence of nelsonite and phoscorite dikes in the APIP, however, evidence for such melts is still largely textural (dike emplacement and nelsonite pockets/droplets within carbonatites and vice-versa). On the other hand, the textural features depicted in figure 2 suggest that the N1 sample has an equigranular texture (Fig. 2a) that could easily be produced by *in-situ* crystallization from either a phosphate-oxide or carbonatite magma, but N2 (Fig. 2b) could be explained as accumulations on a carbonatite dike wall. The suggested alternatives are not mutually exclusive, so the interplay between carbonatite and nelsonite magmas in Catalão II, in general and as a niobium ore formation process merits further petrological research is needed to test the relative role of the various differentiation processes involved.

Acknowledgements

This work was supported by CNPq - Brazilian Council for Research and Development (Grants 480259/2009-7 - Universal; 550376/2010-0 - CT-Mineral and 306650/2007-0) and Anglo-American Brazil (Mineração Catalão and Copebrás), for which the authors are most grateful.

References

- Araujo ALN, Carlson RW, Gaspar JC, Bizzi LA (2001) Petrology of kamafugites and kimberlites from the Alto Paranaíba Alkaline Province, Minas Gerais, Brazil. *Contrib to Mineral Petrol* 142:163–177.
- Barbosa ESR, Brod JA, Junqueira-Brod TC, Dantas EL, Cordeiro PFO, Gomide CS (2012) Bebedourite from its type area (Salitre I complex): A key petrogenetic series in the Late-Cretaceous Alto Paranaíba kamafugite-carbonatite-phoscorite association, Central Brazil. *Lithos* 144–145:56–72.
- Brod JA, Gibson SA, Thompson RN, Junqueira-Brod TC, Seer HJ, Moraes LC, Boaventura GR (2000) The Kamafugite-Carbonatite association in the Alto Paranaíba Igneous Province (APIP) Southeastern Brazil. *Brazilian J Geol* 30:408–412.
- Brod JA, Junqueira-Brod TC, Gaspar JC, Petrinovic IA, Valente SC, Corval A (2013) Decoupling of paired elements, crossover REE patterns, and mirrored spider diagrams: Fingerprinting liquid immiscibility in the Tapira alkaline-carbonatite complex, SE Brazil. *J South Am Earth Sci* 41:41–56.
- Cordeiro PFO, Brod JA, Palmieri M, Oliveira CG, Barbosa ESR, Santos RV, Gaspar JC, Assis LC (2011) The Catalão I niobium deposit, central Brazil: Resources, geology and pyrochlore chemistry. *Ore Geol Rev* 41:112–121.
- Gibson SA, Thompson RN, Leonardos OH, Dickin AP, Mitchell JG (1995) The late cretaceous impact of the trindade mantle plume: Evidence from large-volume, mafic, potassic magmatism in SE Brazil. *J Petrol* 36:189–229.
- Gierth E, Baecker ML (1986) A mineralização de nióbio e as rochas alcalinas associadas no complexo Catalão I, in: Schobbenhaus, C. (Ed.), *Principais Depósitos Mineraiis Do Brasil*. MME/DNPM, Brasília, 456–462.
- Issa Filho A, Lima PRAS, Souza OM (1984) Aspectos da geologia do complexo carbonatítico do Barreiro, Araxá, MG, Brasil, in: CBMM (Ed.), *Complexos Carbonatíticos Do Brasil: Geologia*. CBMM, São Paulo, 20–44.
- Krasnova NI, Petrov TG, Balaganskaya EG, Garcia D, Moutte D, Zaitsev AN, Wall F (2004) Introduction to phoscorites: occurrence, composition, nomenclature and petrogenesis. In: Wall, F., Zaitsev, A.N. (Eds.), *Phoscorites and Carbonatites from Mantle to Mine: the Key Example of the Kola Alkaline Province*. Mineralogical Society Series, London, 45–79.
- Mitchell, R. H., 2015. Primary and secondary niobium mineral deposits associated with carbonatites. *Ore Geology Reviews*, 64:626-641.
- Palmieri, M., 2011. Modelo Geológico e Avaliação de Recursos Mineraiis do Depósito de Nióbio Morro do Padre, Complexo Alcalino-carbonatítico Catalão II, GO. Universidade de Brasília.
- Ribeiro CC (2008) Geologia, Geometalurgia, Controles e Gênese dos depósitos de fósforo, terras raras e titânio do Complexo Carbonatítico Catalão I, GO. Universidade de Brasília.
- Tornos F, Velasco F, Hanchar JM (2016) Iron-rich melts, magmatic magnetite, and superheated hydrothermal systems: The El Laco deposit, Chile. *Geology* 44:427–430.
- Thompson RN, Gibson SA, Mitchell JG, Dickin AP, Leonardos OH, Brod JA, Greenwood JG (1998) Migrating Cretaceous-Eocene magmatism in the Serra do Mar Alkaline Province, SE Brazil: melts from the deflected Trindade mantle plume? *J Petrol* 39:1493–1526.
- Treiman AH (1989) Carbonatite magma: properties and processes, in: Bell, K. (Ed.), *Carbonatites: Genesis and Evolution*. Unwin Hyman, London, 89–104.
- Wall F, Zaitsev AN (2004) Phoscorites and Carbonatites from Mantle to Mine: the Key Example of the Kola Alkaline Province. Mineralogical Society Series 10, London.
- Yegorov LS (1993) Phoscorites of the Maymecha-Kotuy ijolite-carbonatite association. *Int Geol Rev* 35:346–358.

The giant Bayan Obo REE-Nb-Fe deposit, China: How did it come into being?

Hong-Rui Fan^{1,2}, Kui-Fang Yang^{1,2}, Fang-Fang Hu^{1,2}, Shang-Liu^{1,2}

1. Key Laboratory of Mineral Resources, Institute of Geology and Geophysics, Chinese Academy of Sciences, China

2. College of Earth Science, University of Chinese Academy of Sciences, China

Abstract. The world's largest Bayan Obo REE deposit is hosted in the massive dolomite, and nearly one hundred carbonatite dykes occur in the vicinity of the deposit. The carbonatite dykes, corresponding to different evolutionary stages of carbonatite magmatism, can be divided into three types: dolomite, co-existing dolomite-calcite and calcite. The latter always has the highest REE content. The ore-hosting coarse-grained dolomite represents a Mesoproterozoic carbonatite pluton and the fine-grained dolomite resulted from the extensive REE mineralization and modification of the coarse-grained variety. The first episode mineralization is characterized by disseminated mineralization in the dolomite. The second or main-episode is banded and/or massive mineralization, cut by the third episode consisting of aegirine-rich veins. The mineralization is rather variable with two peaks at ~1400 Ma and 440 Ma. The early peak corresponds in time to the intrusion of carbonatite dykes. The later significant thermal event resulted in the formation of late-stage veins. Bayan Obo deposit is a product of mantle-derived carbonatitic magmatism, which was likely related to the breakup of Columbia. Some remobilization of REE occurred due to subduction of the Palaeo-Asian oceanic plate during the Silurian.

1 Introduction

Bayan Obo is the largest rare earth element (REE) ore deposit and the second largest niobium deposit in the world, and also a large iron ore deposit in China. More than 80% of the REE resources in China are situated in the Bayan Obo region. Since the discoveries of Fe ores in the Main Orebody in 1927 by Mr. Daoheng Ding and REE minerals in 1935 by Mr. Zuolin He at Bayan Obo, many studies have been carried out, particularly in the last two decades, on the geological background, mineral constituents, geochronology and geochemistry. However, owing to the complicated element/mineral compositions and the occurrence of several geological events at Bayan Obo, the genesis of this giant REE ore deposit, including its potential ore-forming sources, particularly with regard to the mechanism of REE enrichment, still remains subject to intense debate.

2 Regional and ore geology

The Bayan Obo deposit is located approximately 90 km south of the China and Mongolia border, at the northern margin of the North China Craton (NCC), bordering the Central Asian Orogenic Belt to the north. Gentle fold structures, composed mostly of the low grade

metasedimentary units of the Mesoproterozoic Bayan Obo Group, are distributed from south to north in the region. The deposit, hosted in massive dolomite, occurs in one of the syncline cores. To the north of the ore body, a complete sequence of the Bayan Obo Group is exposed in the Kuangou anticline, which is developed on Paleoproterozoic basement rocks with a distinct angular unconformity. The low grade clastic sequences of the Bayan Obo Group represent the sedimentary units deposited within the Bayan Obo marginal rift, which correlates with the Mesoproterozoic continental breakup event of the NCC. The ore-hosting dolomites, covered by K-rich slate, extending 18 km from east to west and approximately 2 km wide, were once considered as a component of Bayan Obo Group. The origin of the dolomites is still disputed, with proposals for both sedimentary or carbonatite-related origins.

Basement rocks at Bayan Obo are composed of Neoproterozoic mylonitic granite-gneiss (2588±15Ma), Paleoproterozoic syenite and granodiorite (2018±15Ma), and biotite granite-gneiss and garnet-bearing granite-gneiss (~1890 Ma). Dioritic-granitic plutons, composed of gabbro, gabbroic diorite, granitic diorite, adamellite, and biotite granite, are distributed within a large area in the south and east Bayan Obo mine. These plutons were once regarded as intruding from Devonian to Jurassic. New geochronology data reveal that these plutons were formed in a post-collisional tectonic regime at convergent margins in the late Paleozoic in a narrow time interval from 263 to 281 Ma, with a peak age of 269 Ma, consistent with plate subduction during the closure of the Palaeo-Asian Ocean. It has been proved that REE mineralization at Bayan Obo has no direct relationship with these late Paleozoic granitoids.

REE reserves at Bayan Obo are 57.4 million metric tons (Mt) with an average grade of 6% RE₂O₃. Niobium reserves are estimated at 2.2 Mt with an average grade of 0.13% Nb₂O₅, and total Fe reserves are at least 1500 Mt with an average grade of 35%. REEs in the ores are rich in LREE, mostly are Ce, La and Nd, which occupy >90% LREE. There are nearly one hundred carbonatite dykes at Bayan Obo, intruded into the basement rocks and/or the Bayan Obo Group. The dykes are usually 0.5 to 2.0 m wide, 10 to 200 m long, and strike generally to the northeast or northwest. It is significant that some dykes have metasomatized the country rocks on both sides of the contact zones, producing fenites characterized by the presence of sodic amphiboles and albite. The major constituent minerals in the dykes are dolomite and calcite, which are associated with subordinate apatite, monazite, barite, bastnäsite, and

magnetite. The REE contents in the different carbonatite dykes vary from ca. 0.02 to ca. 20 wt%.

The mine is composed of three major ore bodies: the East, Main and West Orebodies. Relative to the West Orebody, the East and Main Orebodies occur as larger lenses, underwent more intense fluoritization, fenitization and hosted more abundant REE and Nb mineralization. Fluorite appears in the fenitized dolomite, and riebeckite and phlogopite are observed in the K-rich slate. The REE ores are defined to be four types, namely the riebeckite, aegirine, massive, and banded types. The principal REE minerals are bastnäsite-(Ce) and monazite-(Ce), and are accompanied by various REE and Nb minerals, such as huanghoite, aeschynite-(Ce), fergusonite, and columbite. The iron minerals are magnetite and hematite. The main gangue minerals include fluorite, barite, alkali amphibole, apatite, quartz and aegirine.

Based on ore occurrences and crosscutting relations, three important REE mineralizing episodes can be identified at the simplest level. The first episode is characterized by disseminated mineralization, which contains monazite associated with ferroan dolomite, ankerite and magnetite, concentrated along fractures and grain boundaries in the relatively unaltered/massive dolomite. The second or main-episode is banded and/or massive mineralization, which shows a generalized paragenetic sequence of strongly banded REE and Fe ores showing alteration to aegirine, fluorite and minor alkali amphibole. The banded and massive ores are cut by the third episode consisting of aegirine-rich veins containing coarser crystal fluorite, huanghoite, albite, calcite, biotite, and/or pyrite.

3 Genesis of carbonatite dyke and ore-hosting dolomite

Abundant carbonatite dykes occur adjacent to the eastern and southern of the Bayan Obo mine and particularly within the Kuangou anticline. The dykes can be divided into three types: dolomite, co-existing dolomite-calcite and calcite type, corresponding with different evolutionary stages of carbonatitic magmatism. The latter always has higher REE content. Field evidence of incision contact shows that a dolomite carbonatite dyke was cut by a calcite one, showing that the emplacement of the calcite dyke is later than the dolomite one. Geochemical data show that Sr and LREE contents in the dykes gradually increase from dolomite type, through calcite-dolomite type, to calcite type. This trend might be resulted from the crystal fractionation of a carbonatitic magma.

The origin of the ore-hosting dolomite at Bayan Obo has been addressed in various models, ranging from a normal sedimentary carbonate rocks to volcano-sedimentary sequence, and a large carbonatitic intrusion. All arguments have been supported with reference to the trace element and isotopic composition of the dolomite. Based on elemental geochemistry, and C, O, and Mg isotopic geochemistry, the ore-hosting dolomites are strongly enriched in LREEs, Ba, Th, Nb, Pb, and Sr, and have very different (PAAS)-normalized REE patterns.

The evidence obtained shows that the ore-hosting dolomite at Bayan Obo was mainly derived from the mantle (Yang et al., 2011).

A relatively small volume of coarse-grained dolomite occurs at Bayan Obo mainly in the West Orebody, as well as in the northern part of the Main Orebody. The rocks are composed predominantly of coarse-grained euhedral-subhedral dolomite, associated with evenly distributed fine-grained apatite, magnetite, and monazite. The fine-grained dolomites are distributed widely and constitute the main part of the deposit. They commonly also appear massive in outcrop and consist predominantly of dolomite or ankerite, which is mostly fine-grained, ranging from 0.05mm to 0.1 mm in diameter. The coarse-grained and fine-grained facies of the dolomite occurring at Bayan Obo introduced additional complexities into the interpretation of their genesis.

Field observations in the northern part of the Main Orebody revealed that the coarse-grained dolomite intruded into the Bayan Obo group quartz sandstone as apophyses. However, the geochemical characteristics of the coarse-grained dolomite are not consistent with those of the fine-grained dolomite. The major and trace element contents of the coarse-grained dolomite are very similar to the calcite-dolomite carbonatite dykes at Bayan Obo. Data from those samples overlap within the magnesio-carbonatite region on the CaO-MgO-(FeO+Fe₂O₃+MnO) classification diagram, and show similar REE contents and distribution patterns on a chondrite-normalized abundance diagram. The similar geochemical characteristics of coarse-grained dolomite and calcite-dolomite carbonatite dykes, and the intrusive contact between the coarse-grained dolomite and wallrocks, indicate that the coarse-grained dolomite is likely an earlier phase of calcite-dolomite carbonatite stock, which did not witness the subsequent mineralization event from the residual carbonatitic melts, probably because it is located far from the main mineralized zone. The fine-grained dolomite from the Main, East and West Orebody differs from the coarse-grained dolomite in their major, trace element and REE characteristics. The fine-grained dolomite shows major element compositions comparable to that of the dolomite carbonatite dykes. All the samples fall in the field of dolomite carbonatite dykes on the CaO-MgO-(FeO+Fe₂O₃+MnO) classification diagram. The REE content and distribution patterns of the fine-grained dolomite samples, however, are similar to those of the calcite carbonatite dykes.

The REE content in the dolomite carbonatite dykes is relatively low, as compared to the extreme accumulation in the calcite carbonatite dykes at Bayan Obo. It is noted that the REE minerals in the fine-grained dolomite occur as ribbons or aggregates. It has been found that the REE minerals are distributed around dolomite phenocrysts in the fine-grained dolomite and, therefore, formed. These observations lead us to believe that the fine-grained dolomite represents an early stage large-scale dolomite carbonatite pluton, and the superposed REE mineralization was derived from the later calcite carbonatite magma.

4 REE mineralizing time

According to the occurrences of rocks/veins related to the mineralization in the Bayan Obo deposit, four types of REE mineralization are identified, including carbonatite dyke, ore-hosting dolomite marble, banded REE–Nb–Fe ore, and late-stage REE vein. Geochronology on these four types of mineralization, using U–Th–Pb, Sm–Nd, Rb–Sr, K–Ar, Ar–Ar, Re–Os, and La–Ba methods, has been reported in the last two decades. However, various dating methods gave different mineralization ages, resulting in long and heated debates. A compilation of age data for the Bayan Obo REE mineralization has a wide range, from >1800 Ma to ~390 Ma, with two peaks at ~1400 Ma and 440 Ma. The earliest ages, reported from zircons in the carbonatite dykes by SHRIMP or ID-TIMS with ages > 1800 Ma, are largely thought to be inherited zircons derived from the Palaeoproterozoic basement in the area. There are three main opinions on mineralization ages.

Mesoproterozoic mineralization: Nakai et al. (1989) first reported REE mineral La–Ba and Sm–Nd isochron date of 1350 ± 149 Ma and 1426 ± 40 Ma, respectively. In addition, Zhang et al. (2003) obtained mineral Sm–Nd isochron dates for ores at the Main and East Orebodies of 1286 ± 91 Ma and 1305 ± 78 Ma, respectively. We report here a whole-rock Sm–Nd isochron from nine carbonatite dykes yielding a slightly older age of 1354 ± 59 Ma. Zircons collected from a carbonatite dyke were analyzed by conventional isotope dilution thermal ionization mass spectrometry (ID-TIMS). The results are an upper intercept age of 1417 ± 19 Ma. This age is confirmed by SHRIMP U–Pb analysis of zircon from the same carbonatite dyke, which gave a $^{207}\text{Pb}/^{206}\text{Pb}$ weighted mean age of 1418 ± 29 Ma.

Early Paleozoic mineralization: Chao et al. (1997) made numerous Th–Pb dates for monazite and bastnäsite samples at Bayan Obo, and provided isochron ages for monazite mineralization ranging from 555 to 398 Ma. They proposed that intermittent REE mineralization of the Bayan Obo deposit started at about 555 Ma, and the principal mineralization occurred between 474 and 400 Ma. We used Sm–Nd dating of the REE mineral, huanghoite, and single-grain biotite Rb–Sr dating, showing concordant isochrons corresponding to 442 ± 42 Ma and 459 ± 41 Ma, respectively.

Two-stage mineralization: Campbell et al. (2014) reported SHRIMP dating of extremely U-depleted (<1 ppm) zircons from banded ores in the East Orebody. Their ^{232}Th – ^{208}Pb geochronological data reveal the age of zircon cores with Mesoproterozoic ages as 1325 ± 60 Ma and a rim alteration event with Caledonian ages as 455.6 ± 28.27 Ma. Zhu et al. (2015) reviewed Sm–Nd isotopic measurements which were undertaken to constrain the chronology of REE mineralization events at Bayan Obo, and considered that a series of ages between ca. 1400 Ma and 400 Ma resulted from thermal disturbance and do not imply the existence of additional mineralization events. They proposed that the earliest REE mineralization event was at 1286 ± 27 Ma using a Sm–Nd isochron of coarse-grained dolomite and the carbonatite dikes in their vicinity, and a significant thermal

event at ca. 400 Ma resulted in the formation of late-stage veins with coarse crystals of REE minerals

5 Nature of ore-forming fluids and sources

The study of the nature of ore-forming fluids at Bayan Obo is limited by the post depositional history of the ores, particularly in the earliest stages of the paragenesis like banded ores. Several possible sources of ore-forming fluids have been proposed for the Bayan Obo deposit, including deep source fluids, anorogenic magma, magmatic and metamorphic fluids, mantle fluids, and carbonatite magma/fluids. Which source of ore-forming fluids best favor REE mineralization is still disputed.

The available data on the oxygen, carbon, strontium and niobium isotope composition of the carbonatites, dolomites and obviously sedimentary limestones at Bayan Obo are taken to indicate that the large and coarse-grained dolomite was an igneous carbonatite, and that the finer grained dolomite recrystallized under the influence of mineralizing solutions which entrained groundwater. Sun et al. (2013) systematically investigated the Fe isotope compositions of different types of rocks from the Bayan Obo deposit and related geological formations, such as carbonatites, mafic dykes, and Mesoproterozoic sedimentary iron formation and carbonates. The Fe isotope fractionation between magnetite and dolomite, and between hematite and magnetite at Bayan Obo is small, indicating that they formed in very high temperature conditions. It is proposed that the Fe isotope systematics for the Bayan Obo deposit is consistent with those of magmatic products, but different from those of sedimentary or hydrothermal products reported previously. They concluded that the Bayan Obo ore deposit is of magmatic origin.

The nature of ore-forming fluids has been studied in fluid inclusions trapped in banded and vein ores at Bayan Obo (Fan et al., 2006). Three types of fluid inclusions have been recognized: two or three phase CO₂-rich, three phase hypersaline liquid-vapor-solid, and two phase aqueous liquid-rich inclusions. Microthermometry measurements indicate that the carbonic phase in CO₂-rich inclusions is nearly pure CO₂. Fluids involving in the REE–Nb–Fe mineralization at Bayan Obo might be REE–F–CO₂–NaCl–H₂O system. The coexistences of hypersaline brine inclusions and CO₂-rich inclusion with similar homogenization temperatures give evidence that immiscibility took place during REE mineralization. The original H₂O–CO₂–NaCl fluid with higher REE contents probably derived from a carbonatite magma. The presence of REE-carbonates as an abundant solid in inclusions in the ores shows that the original ore-forming fluids were very rich in REE, and therefore, laid a foundation to produce economic REE ores at Bayan Obo.

6 Possible ore genesis

The Bayan Obo deposit was likely associated in space and time with large-scale carbonatitic magmatic activity (ca. 1400 to 1300 Ma) in response to the long-term rifting and magma evolution in the north margin of North China

Craton. The depleted mantle model age (T_{DM}) from the Nd isotope data on carbonatite dyke and ore-hosting dolomite samples ranges from 1610 to 1790 Ma, and coincides with the initiation of the Bayan Obo rift (ca. 1750 Ma). Along with the prolonged and slow extension of the Bayan Obo rift, the mantle lithosphere underwent low degree of partial melting leading to the production of carbonatite magma at the final stage of break up of the Columbia supercontinent (ca. 1400-1200 Ma). Through continuous evolution (crystal fractionation), abundant LREE accumulation occurred in the terminal calcite carbonatite magma, which was then superposed on the early dolomite carbonatite pluton, thus resulting in the formation of the giant Bayan Obo REE deposit.

As the Bayan Obo ore deposit is LREE and Th enriched, U depleted, and has very low Sm/Nd and U/Pb values and low $^{206}\text{Pb}/^{204}\text{Pb}$ ratios, it is difficult to obtain high resolution Sm-Nd, U-Pb ages for banded and massive REE mineralization in the East and Main Orebodies. The zircons in the carbonatite dyke at Bayan Obo provide a unique record of the early mineralization history of the region. The timing of the early episode of REE mineralization of the Bayan Obo deposit obtained from REE minerals and ore-hosting dolomite, ca. 1400-1300 Ma, is consistent with the reported ages of REE-rich carbonatite dykes, implying a genetic connection. Geochemical evidence from element content and Nd isotope compositions also imply that ore-hosting dolomite and the carbonatite dykes have a close relationship to a magmatic origin. A significant thermal event at ca. 440 Ma resulted in the formation of late-stage veins with coarse crystals of REE minerals. However, the REE mineralization developed during this event resulted from remobilization of REE within the orebodies, and any potential contribution from external sources was minimal. Thus, this late mineralization event might make no significant contribution to the existing ore reserves. The ages of ca. 440 Ma may be related to subduction of the Palaeo-Asian oceanic plate during the Silurian.

It can be concluded that the Bayan Obo giant deposit is a product of mantle-derived carbonatitic magmatism at ca. 1400 Ma, which was likely related to the breakup of Columbia. Some remobilization of REE occurred due to subduction of the Palaeo-Asian plate during the Silurian, forming weak vein-like mineralization (Fig. 1).

Acknowledgements

Prof. Frances Wall is thanked for her constructive and valuable comments. This study is financially supported by the National Key Research and Development Program (Grant No. 2017YFC0602302).

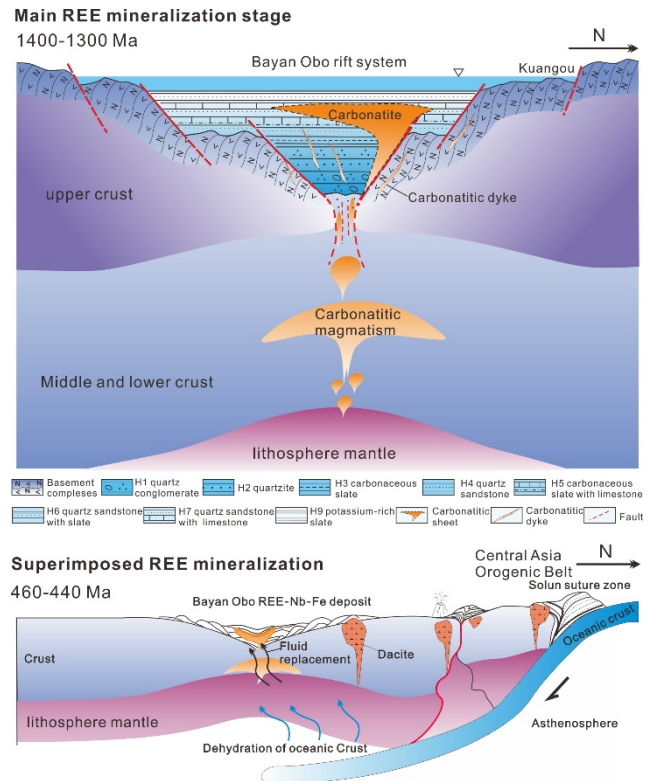


Figure 1. Two stage mineralization model for the formation of the giant Bayan Obo deposit

References

- Campbell LS, Compston W, Sircombe KN, Wilkinson CC (2014) Zircon from the East Orebody of the Bayan Obo Fe-Nb-REE deposit, China, and SHRIMP ages for carbonatite-related magmatism and REE mineralization events. *Contributions to Mineralogy and Petrology* 168:1041
- Chao ECT, Back JM, Minkin JA, Tatsumoto M, Wang J, Conrad JE, MaKee EH, Hou Z, Meng QS (1997). The sedimentary carbonate-hosted giant Bayan Obo REE-Fe-Nb ore deposit of Inner Mongolia, China: A cornerstone example for giant polymetallic ore deposits of hydrothermal origin. *US Geology Survey Bulletin* 2143:1-65
- Fan HR, Hu FF, Yang KF, Wang KY. (2006) Fluid unmixing/immiscibility as an ore-forming process in the giant REE-Nb-Fe deposit, Inner Mongolian, China: evidence from fluid inclusions. *Journal of Geochemical Exploration* 89:104-107
- Nakai S, Masuda A, Shimizu H (1989) La-Ba dating and Nd and Sr isotope studies on Bayan Obo rare earth element ore deposit, Inner Mongolia, China. *Economic Geology* 84:2296-2299
- Sun J, Zhu X, Chen Y, Fang N (2013) Iron isotopic constraints on the genesis of Bayan Obo ore deposit, Inner Mongolia, China. *Precambrian Research* 235:88-106
- Yang KF, Fan HR, Santosh M, Hu FF, Wang KY. (2011) Mesoproterozoic carbonatitic magmatism in the Bayan Obo deposit, Inner Mongolia, North China: Constraints for the mechanism of super accumulation of rare earth elements. *Ore Geology Reviews* 40:122-131
- Zhang ZQ, Yuan ZX, Tang SH, Bai G, Wang JH (2003) Age and Geochemistry of the Bayan Obo Ore Deposit. Geological Publishing House, Beijing, pp 1-222 (in Chinese with English Abstract)
- Zhu XK, Sun J, Pan C (2015) Sm-Nd isotopic constraints on rare-earth mineralization in the Bayan Obo ore deposit, Inner Mongolia, China. *Ore Geology Reviews* 64: 543-553

Mechanisms for the generation of HREE mineralization in carbonatites: Evidence from Huanglongpu, China.

Martin Smith¹, Delia Cangelosi, Bruce Yardley², Jindrich Kynicky³, Chen Xu⁴, Wenlei Song⁵, John Spratt⁶

¹School of Environment and Technology, University of Brighton, UK

²School of Earth and Environmental Sciences, University of Leeds, UK

³Mendel University in Brno, Brno, Czech Republic

⁴School of Earth & Space Sciences, Peking University, Beijing, China

⁵Department of Geology, Northwest University, Xi'an, China

⁶Natural History Museum, London, UK

Abstract. The Huanglongpu carbonatites, Qinling Mountains, China, are exceptional as they form both an economic Mo resource, and are enriched in the HREE compared to typical carbonatites, giving a metal profile that may closely match projected future demand. The carbonatites at the level currently exposed appear to be transitional between magmatic and hydrothermal processes. The multistage dykes and veins are cored by quartz which hosts a fluid inclusion assemblage with a high proportion of sulphate daughter or trapped minerals, and later stage, cross-cutting veins are rich in barite-celestine. The REE mineral paragenesis evolves from monazite, through apatite and bastnäsite to Ca-REE fluorocarbonates, with an increase in HREE enrichment at every stage. Radio-isotope ratios are typical of enriched mantle sources and sulphur stable isotopes are consistent with magmatic S sources. However, Mg stable isotopes are consistent with a component of recycled subducted marine carbonate in the source region. The HREE enrichment is a function of both unusual mantle source for the primary magmas and REE mobility and concentration during post-magmatic modification in a sulphate-rich hydrothermal system. Aqueous sulphate is a none specific ligand for the REE, and this coupled with crystal fractionation lead to HREE enrichment during subsolidus alteration.

Introduction

The rare earth elements have become a focus of intense economic interest because of the restriction in supply caused by a focus of production in China, coupled with increasing use in renewable energy and high technology applications. Rare earth element resources are dominated by concentrations associated with alkaline igneous rocks, notably carbonatites.

Element enrichments in carbonatite tend to be in the light REE (La to Nd). Middle to HREE enriched carbonatites do occur however, and may have REE distributions which are a closer match to project future REE demand than typical carbonatites (Goodenough et al., 2017). Here we present data on the geochemical and mineralogical evolution of the Huanglongpu carbonatites, China (Fig. 1), which show overall REE patterns that bridge a gap between typical and HREE mineralised carbonatites (Smith et al., 2018).

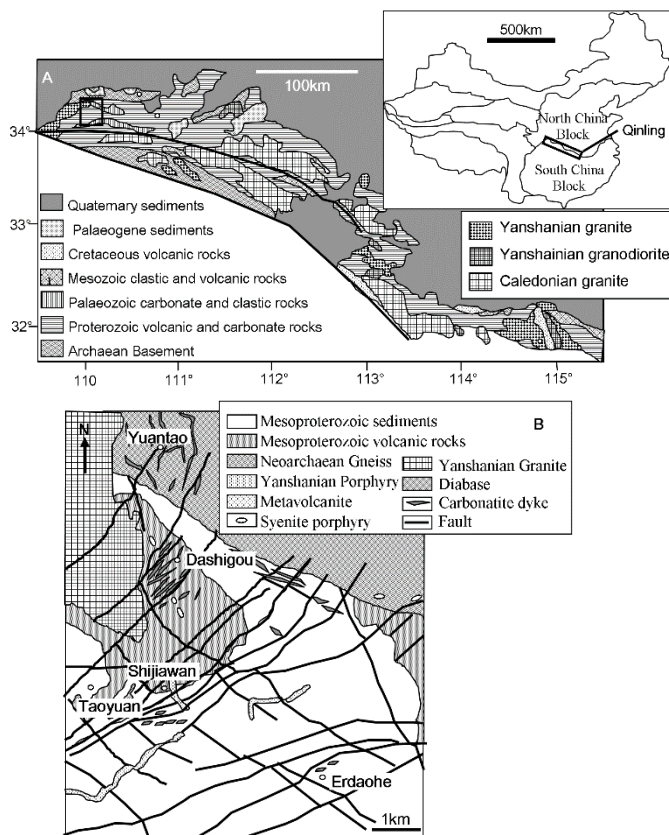


Figure 1: (A) Geological map of the eastern Qinling Mountains showing the location of the Huanglongpu area. Inset shows the overall location within China in relation to major crustal blocks. (B) Geological map of the Huanglongpu Mo-district (highlighted in bold in A). Maps adapted from Xu et al. (2010).

2 Geology

The Huanglongpu district is composed of four carbonatite-related orefields (Fig. 1) with a total ore reserve of N180 Kt of Mo. Re-Os dates indicate the dykes are 50-90Ma older than porphyry mineralisation in the district and hence not related to overprinting sulphide mineralisation (Song et al., 2016; Stein et al., 1997). The ore bodies occur discontinuously over a total distance of 6 km and an area of 23 km².

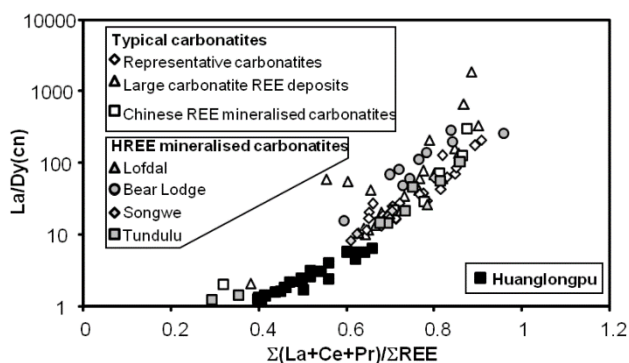


Figure 2: Comparison of ratios characterising the REE pattern for the Huanglongpu carbonatites with typical carbonatites (diagram and references from Smith et al., 2018).

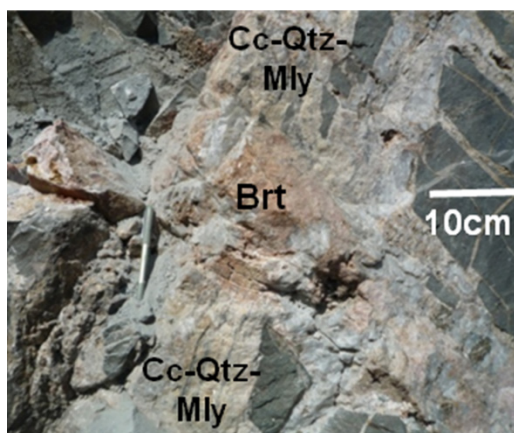


Figure 3: Example of field relationships in the Huanglongpu carbonatites, with a calcite-quartz-molybdenite dyke cross-cut by a conjugate barite-rich dyke (Smith et al., 2018)

The carbonatite dykes are highly parallel, predominantly dipping N to NNW, at steep angles (strike/dip ~260/50–88°N) and consist of calcite, kutnahorite, quartz, potassium feldspar, barite, pyrite, galena, sphalerite, molybdenite, monazite, Ca-REE-fluorcarbonates, apatite, britholite, pyrochlore, uraninite, REE fluorides, burbankite, celestine, strontianite and brannerite. Minor fluorite is found at Shijiawan and Yuantao. The dykes range in thickness from ~10m to ~0.1m (Fig. 3) with lateral extents ranging from 10m to N1 km. Rarer dykes occur in orientations conjugate to the main set (strike/dip ~350/50–80°E). Minor offsets suggest this set may be slightly later than the main set, although the conjugate orientation and presence of conjugate veins merging with the main set suggest they were very nearly contemporaneous. Barite-celestine bearing dykes and veins cut the earlier carbonate-quartz-sulphide bearing dykes (Fig. 3). Quartz is dominantly restricted to cores of dykes and may be mainly hydrothermal in origin. This suggests the primary dykes may have been calico-carbonatite in composition although the bulk dyke composition is silico-carbonatite. In the carbonatites, molybdenite occurs mainly as disseminated grains and intergranular and fracture-hosted films, sometimes associated with pyrite, galena and sphalerite suggesting a subsolidus, hydrothermal origin for at least some of the sulphide assemblage. Disseminated molybdenite is also

found along fractures in fenitized gneiss near its contact with the dykes. The overall HREE enrichment of the Huanglongpu carbonatites has been previously related to a recycled ocean crust component in the lithospheric mantle indicated by Nd-Sr radioisotope studies and Mg stable isotope analyses of calcite (Song et al., 2016). This primary source control has been proposed to be enhanced by fractional crystallisation of calcite, with the dykes at the current level of exposure representing relatively HREE-enriched carbonate residuum (Xu et al., 2007).

3 Results

3.1 REE mineral paragenesis

The earliest stage of REE mineralization is the formation of monazite-(Ce) as eu- to subhedral crystals within calico carbonatite. Monazite is a potentially magmatic phase as it is fractured, and the fractures subsequently filled by the sulphide mineral assemblage, specifically molybdenite. Additional potentially early REE-bearing phases include pyrochlore, apatite, zircon and parisite which occurs intergrown with galena and molybdenite. Monazite is overgrown and replaced by apatite, which is in turn overgrown and replaced by britholite-(Ce) ($\text{REE}_3\text{Ca}_2\text{SiO}_4\text{F}$) (Fig. 4). The formation of britholite is accompanied by the formation of allanite-(Ce) in the surrounding rock. Both are common in the quart-rich cores to the dykes. Within the fluorcarbonate assemblage early bastnäsite-(Ce) and parisite-(Ce) are replaced by parisite-synchysite-(Ce) syntaxial intergrowths, and by röntgenite-(Ce). At the same time as the development of the REE mineral paragenesis the early niobium phases undergo alteration. Early aeschynite-(Ce) is altered to urano-pyrochlore, which is then altered to pyrochlore with uraninite inclusions.

3.2 Mineral chemistry

Analyses of REE and niobate mineral chemistry were carried out by EMPA and LA-ICPMS at the Natural History Museum, London. Figure 5 shows typical chondrite normalized REE patterns for phosphates and fluorcarbonates. In all cases the mineral chemistry is dominated by the LREE, and all REE minerals are the Ce-dominant variety. However, there is a clear distinction in HREE contents between monazite and apatite and britholite, with the latter being significantly more HREE-rich. The same is also true of the fluorcarbonates, and aeschynite, urano-pyrochlore and pyrochlore, with the level of HREE enrichment increasing in later paragenetic stages (Fig. 5). When minerals are normalized to their precursor phase identified from textural studies, it becomes apparent that at every stage of alteration the REE minerals become more HREE-rich (Fig. 6).

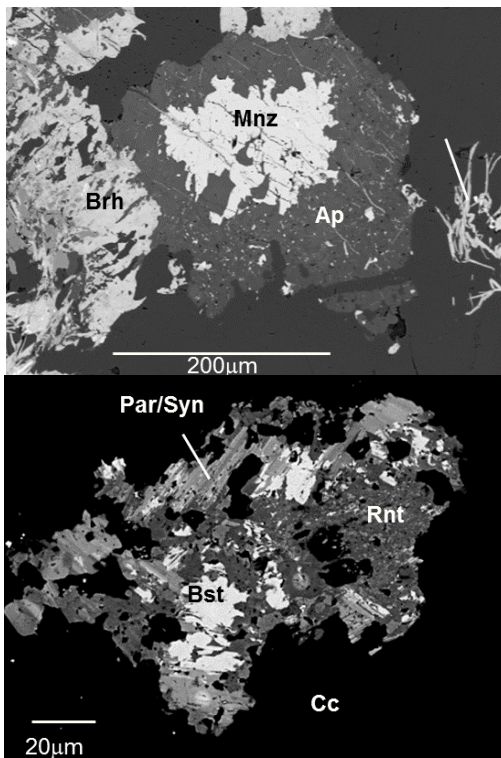


Figure 4: Examples of mineral textures at Huanglongpu as backscattered electron images. (A) Monazite replaced by apatite, which is in turn replaced and overgrown by britholite. (B) Bastnäsite overgrown by syntaxially intergrown pariste and synchysite, followed by röntgenite. (Smith et al., 2018).

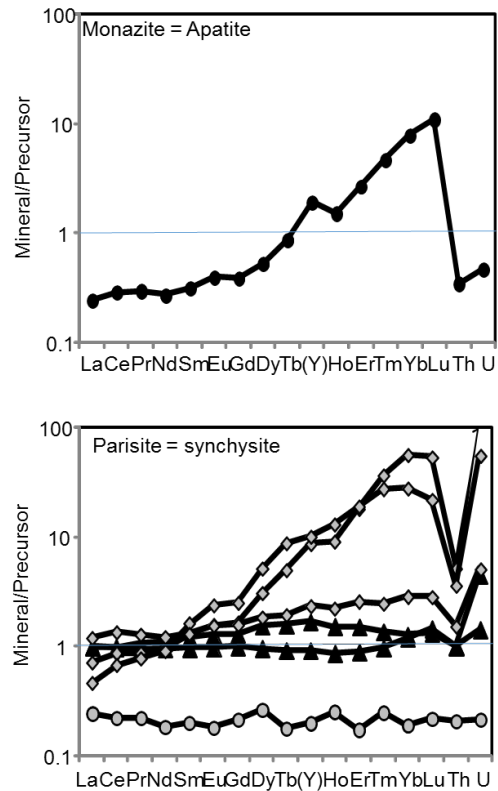


Figure 6: Composition of minerals in reaction textures normalised to the precursor phase for phosphates and fluorcarbonates (Smith et al., 2018).

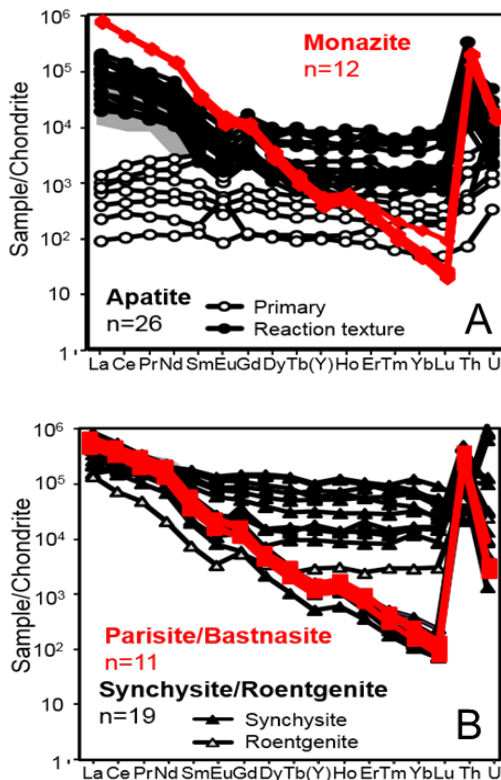


Figure 5: Chondrite normalized REE patterns for phosphates and fluorcarbonates from Huanglongpu. Determined by LA-ICPMS. Th and U are included to illustrate actinide behavior (Smith et al., 2018).

3.3 Fluid evolution

Fluid inclusions in quartz have been studied by Song et al, (2016) and as part of this study. Early aqueous-carbonic fluid inclusions containing sulphate minerals contain nearly pure CO₂, and have salinities in the aqueous phase determined from clathrate melting of 5–19 wt% NaCl equivalent, although high SO₄ contents may mean these estimates are significantly in error. These inclusion decrepitate on heating, and so homogenisation temperatures cannot be determined. They occur in assemblages with liquid CO₂ inclusions. Laser Raman spectroscopic data from inclusions in quartz cores to the carbonatite dykes indicate arcanite (K₂SO₄), anhydrite (CaSO₄), glauberite (Na₂Ca(SO₄)₂), apthitalite (K,Na)₃Na(SO₄)₂ and gorgeyite (K₂Ca₅(SO₄)₆·H₂O) within fluid inclusions (Fig. 7). The wide range in solids suggests heterogeneous trapping following sulphate saturation triggered by mixing with a CO₂-rich fluid, or with CO₂ generated by reactions of the acid sulphate fluid with carbonatite calcite. Fluid inclusions in fracture-fill quartz and calcite are typically 2 phase aqueous liquid plus vapour inclusions. These homogenise between 265 and 120 °C, and have salinities from 6 to 15wt% NaCl eq. Early quartz and calcite from Huanglongpu analysed by SIMS mostly give δ¹⁸O values close to 10 ‰. The very small fractionation between the two minerals is indicative of near-magmatic temperatures. Thin crack-fills of secondary quartz, identified by CL imaging, are of very similar composition to the primary quartz, but a

secondary crack-fill calcite is around 3 ‰ heavier, which may indicate a temperature below 200°C if both crack-fills equilibrated.

Overall these data suggest that initial REE mineralisation took place at late magmatic temperatures. Early fluid inclusions were heterogeneously trapped from sulphate saturated brines which either mixed with CO₂-rich fluids, or generated CO₂ via water-rock interaction between 300 and 200 °C and 100-50 MPa. Late hydrothermal quartz deposition and the alteration of REE minerals took place down to 120°C, at pressures below 100 MPa. These fluids were present throughout REE mineral deposition.

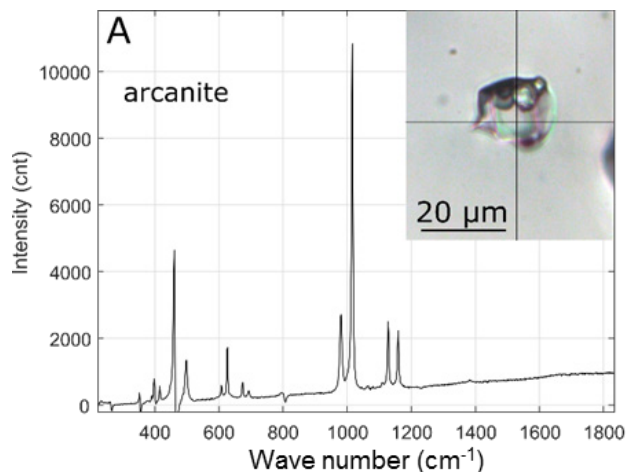


Figure 7: Example of a laser Raman spectrum of fluid inclusion hosted minerals in quartz hosted fluid inclusions from Huanglongpu. In this case the solid phase is identified as arcanite (K₂SO₄).

4 Discussion and conclusions.

Previous studies have demonstrated that the relative HREE enrichment of the Huanglongpu carbonatites relates to the primary magmatic source, with potential inputs from sedimentary carbonate recycled into the mantle via subduction (Song et al., 2016), followed by fractional crystallisation of LREE-rich phases resulting in further HREE enrichment of the residual carbonatite magma (Xu et al., 2007). This initial enrichment has been enhanced at the current level of exposure by hydrothermal processes involving sulphate-rich brines from sub-solidus temperatures down to ~120°C.

The REE mineral paragenesis evolved throughout this process. Monazite and possibly some LREE-rich fluorcarbonates formed as magmatic phases. Subsequent depletion of the residual magma in the REE, coupled with increasing Ca-activity resulted in the reaction of monazite to apatite. The onset of hydrothermal conditions, marked by the quartz cores to the dykes, caused the reaction of apatite with REE-bearing hydrothermal fluids to form britholite. Continuous cooling and dilution of this system resulted in calcite dissolution and the formation of progressively more Ca-rich REE fluorcarbonates.

The presence of sulphate as the dominant ligand in the hydrothermal fluid resulted in preferential transport

and deposition of the HREE during mineral alteration. Experimental studies have shown that most common ligands (in particular Cl⁻) promote preferential solubility of the LREE (Migdisov et al., 2009; Tropper et al., 2011). However, SO₄²⁻ shows no preferential complex ion formation with the REE, and may therefore have leached the REE from HREE enriched calcite without significant fractionation (Migdisov and Williams-Jones, 2008). Sulphate enrichment in carbonatites may therefore be important in the development of HREE-rich mineral assemblages, alongside specialised magmatic source regions.

Acknowledgements

This work was supported by the NERC SOS:RARE project (NE/M011267/1) and NERC Ion Microprobe facility grant IMF639/1017.

References

- Goodenough KM, Wall F, Merriman D. (2018) The Rare Earth Elements: Demand, Global Resources, and Challenges for Resourcing Future Generations. *Nat Resour Res* 27:201-216.
- Migdisov A.A., Williams-Jones A.E., Wagner T. 2009. An experimental study of the solubility and speciation of the Rare Earth Elements (III) in fluoride- and chloride-bearing aqueous solutions at temperatures up to 300°C. *Geochimica et Cosmochimica Acta* 73, 7087–7109.
- Migdisov A.A., Williams-Jones A.E. 2008. A spectrophotometric study of Nd(III), Sm(III) and Er(III) complexation in sulfate-bearing solutions at elevated temperatures. *Geochimica et Cosmochimica Acta* 72, 5291–5303.
- Song, W., Xu, C., Smith, M.P., Kynicky, J., Huang, K., Wei, C., Li Zhou, Shu, Q. 2016. Origin of unusual HREE-Mo-rich carbonatites in the Qinling orogen, China. *Scientific Reports* 6:37377 | DOI: 10.1038/srep37377.
- Smith M, Kynicky J, Xu C et al (2018) The origin of secondary heavy rare earth element enrichment in carbonatites: Constraints from the evolution of the Huanglongpu district, China. *Lithos* 308-309:65-82.
- Stein, H.J., Markey, R.J., Morgan, M.J., Du, A., Sun, Y., 1997. Highly precise and accurate Re–Os ages for molybdenite from the East Qinling–Dabie molybdenum belt, Shaanxi province, China. *Economic Geology* 92, 827–835.
- Tropper, P., Manning, C.E., Harlov, D.E. 2011. Solubility of CePO₄ monazite and YPO₄ xenotime in H₂O and H₂O–NaCl at 800 °C and 1 GPa: Implications for REE and Y transport during high-grade metamorphism. *Chemical Geology* 282, 58–66
- Xu, C., Campbell, I.H., Allen, C.M., Huang, Z.L., Qi, L., Zhang, H., Zhang, G.S. 2007. Flat rare earth element patterns as an indicator of cumulate processes in the Lesser Qinling carbonatites, China. *Lithos* 95, 267–278.

Diversity of ores in carbonatite-related rare earth deposits

Liu Yan

Institute of Geology, Chinese Academy of Geological Sciences, Beijing, PR China.

Abstract. Carbonatite-related REE deposits have various ore type characteristics, including the scales and ore-formation structures. The Cenozoic Mianning–Dechang (MD) rare earth element (REE) belt in eastern Tibet has several carbonatite-related REE deposits, with large and medium scales and a series of ore types such as brecciated, weathered and disseminated. According to petrographic studies, REE mineralization occurred with large scale overprinted gangue minerals such as barite, fluorite, calcite formed at the last hydrothermal stage and all these REE ores formed within an limited ranges of temperature and pressure. According to new detailed geological mapping, the variety of different ore types are a result of local tectonic structure rather than different depths. For instance, brecciated and weathered ores in the Dalucao deposit were controlled by frequent brecciation and fracture activities around the deposit. Ore veins controlled by tensional fissures arose by the same Haha fractures in Maoniuping deposit. As a result of fewer tectonic activities, disseminated ores only are found only in Lizhuang deposit. Thus, these various types of ores were controlled by different tectonic structures. Despite the various ores types, REE originate directly from the carbonatite-syenite complex. The ore variety is mainly caused by the different ore-controlling structures.

1 Introduction

The genesis of carbonatite-related REE deposits is not a simple one-stage process of ore deposition. Because of this complexity and the variety of ores, deciphering the evolution of these deposits is a challenging task that requires a meticulous study of petrography, geochemical characteristics of ores, tectonic activities, and variations in the distribution and composition of their constituent minerals. The Cenozoic Mianning-Dechang (MD) belt (Liu et al., 2015a) offers excellent opportunities for studying the genesis of variety of carbonatite-related REE ores.

The MD belt (Fig. 1) is situated in eastern Tibet and western Sichuan (southwestern China), and measures about 270 km in length and 15 km in width (Fig. 2). The MD belt contains REE deposits that all formed under the same geological conditions, but these deposits have various grades, reserves, and REE mineralization styles. As such, study of these deposits with regards to REE mineralization may further our understanding of the formation of large carbonatite-associated REE deposits (CARDs).

Schematic illustrations of models for CARD formation have been set up by Hou et al. (2015) including a variety of carbonatite-related deposits. This model includes a variety of orebodies formed by fluids exsolved from REE-rich carbonatitic magmas emplaced at shallow

crystal levels. Lateral migration, replacement, open-space filling, and focused discharges of ore-forming fluids produced semi-stratabound (Bayan obo-style), disseminated (Lizhuang or Mountain Pass-style), stringer-stockwork (Maoniuping -style) and breccia pipe (Dalucao-style) orebodies, with associated fenitization and K-silicate alterations, respectively (Hou et al. 2009). This model has been obtained from the depth of the ores, ore-controlling structures and appearance of carbonatite-related ores, but comparison of these deposits in terms of the formation of various types and scales of ores are still unclear.

Herein, based on literature studies and this work, the origin (carbonatite-syenite complex), formation stages, evolution and composition of ore-forming fluids and the local structural controls on the shape of orebodies have been systematically compared.

2 Geology of REE deposits in the Mianning-Dechang Belt

The MD Belt, which is in western Sichuan Province, southwest China, is ~270 km long and 15 km wide (Fig. 1). The NS-trending belt of carbonatite-nordmarkite complexes (Fig.2), bounded by the Yalongjiang and Anninghe strike-slip faults, intrudes the Proterozoic crystalline basement rocks and Paleozoic-Mesozoic sedimentary sequences. In individual complex, carbonatites occur as sills, dykes, stocks, and hypabyssal intrusions within the nordmarkite intrusions. The belt hosts the Maoniuping, Muluozhai, Lizhuang, and Dalucao REE deposits (Fig. 2) and contains a total estimated resource of over 3 Mt of light rare earth oxides (REO) (Hou et al., 2009).

The location of the Maoniuping nordmarkite-carbonatite pluton is controlled by the Haha strike-slip fault, which is a secondary structure with respect to the MD fault. Most carbonatite bodies (referred to as “sills” in previous publications) are in the northern part of the intrusion (Guangtoushan section). Although the currently mined part of the deposit (Dagudao section) contains some carbonatite bodies, their proportion is relatively small. This section consists predominantly of quartz nordmarkite, which hosts a stockwork grading into multiple branching veins of variable thickness. Fenitization, manifested by mica-, sodium clinopyroxene- and amphibole-rich zones, is very prominent at Dagudao, where it is spatially associated with REE mineralization.

In contrast to the other deposits in the MD belt, the REE ores at Maoniuping are hosted by a structurally complex system of mineralized veins, veinlets and stockwork zones, which has an “S”-like outline in plan view and extends roughly in a NNE-SSW direction (Fig. 2A). This configuration suggests that the mineralization was controlled by strike-slip faulting. Geological cross-sections along a series of exploration lines, constructed

on the basis of drill-core data, suggest that the Dagudao section is the core area of the Maoniuping deposit (Yuan et al. 1995).

Thick veins are particularly common in the southeastern part of the Dagudao section, i.e. down-slip from the core area. Breccias are composed of angular wall-rock nordmarkite clasts set in a matrix of ferromagnesian silicates (predominantly, sodium clinopyroxene and amphibole). Locally, pervasively fenitized older metamorphic rocks are also present as clasts.

The Muluozhai REE deposit is divided into the Diaoloushan and Zhengjialiangzi areas, which contain six main orebodies. The deposit is in the northern segment of the MD Belt and is controlled by the strike-slip Yalongjiang Fault, which connects with the Xianshuihe Fault to the north. The Permian units are part of a thick sequence of Permian–Triassic marble and basalt with minor sandstone and other clastic sediments. The REE-mineralization is hosted in veins and veinlets along the fractured contact between metadiabase and nordmarkite or marble.

The Lizhuang carbonatite–nordmarkite complex intrudes metamorphosed Silurian–Triassic clastic and carbonate rocks (Fig. 2C). The complex is 100–150 m wide, 400 m long, and consists of NNW–SSE-striking carbonatite sills and a nordmarkite pluton. The main REE orebody is elongate parallel to the contact zone between the carbonatite–nordmarkite complex and the surrounding wall rocks. The principal ore mineral is bastnäsite, which formed synchronous with the alteration of the carbonatite–nordmarkite complex (Fig. 3E). In contrast to the other deposits in the MD Belt, ore mineralization could be found in nordmarkite and carbonatite in the Lizhuang deposit respectively (Fig. 3F).

The Lizhuang deposit comprises massive fluorite–quartz–calcite–bastnäsite ores and minor brecciated ores. The individual orebodies are 30–100 m long and 2.2–11.6 m thick (Fig. 2C). There are four types of ore; yellow-banded, stockwork, black brecciated, and the principal brown-colored disseminated ore.

The Dalucao deposit is the only deposit in the southern part of the MD belt, and contains three orebodies (No. 1, No. 2, and No. 3; Fig. 2D). No. 1 and No. 3 orebodies are hosted in breccia pipes within carbonatite–nordmarkite host rocks, and have similar grades, at 1.0–4.5 % REO. Both pipes are elliptical in plan-view, with long-axes of 200–400 m and short-axes of 180–200 m. The pipes extend downwards for >450 m. The REE mineralization was controlled by the Dalucao Fault. Faulting and brecciation facilitated the circulation of ore-forming fluids and provided space for REE precipitation.

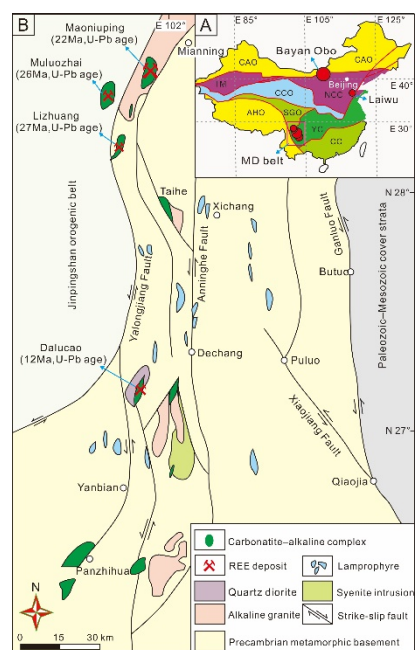


Figure 1. Location, geology, and tectonics of the Maoniuping, Muluozhai, Lizhuang, and Dalucao REE deposits. A) Overview map of the tectonic regions of China. NCC - North China Craton, TM - Tarim Block, YC - Yangtze Craton, CC - Cathaysia Craton, CAO - Central Asia Orogeny, CCO - Central China Orogeny, AHO - Alps-Himalaya Orogeny, SGO - Songpan-Ganze orogeny. B) Geological map showing the distribution of Cenozoic carbonatite–alkaline complexes in western Sichuan and the locations of reactivated faults and illustrating clearly that the faults cut the nordmarkite and carbonatite bodies. (modified from Yuan et al., 1995).

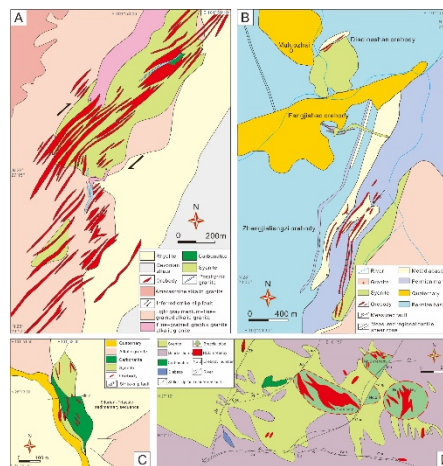


Figure 2. (A) Simplified geological map showing the distribution of carbonatite–alkaline complexes and associated REE orebodies within the Maoniuping deposit (modified from 109 Geological Brigade of Sichuan Bureau of Geology and Mineral Resource, 2010). (B) Geological map of the Muluozhai ore district (Institute of Multipurpose Utilization of Mineral Resources, Chinese Academy of Geological Sciences, 2008). (C) Schematic geological map showing the key features of the nordmarkite–carbonatite complex and associated REE orebodies within the Lizhuang deposit (modified from Hou et al., 2009). (D) Geological map showing the key features of the nordmarkite–carbonatite complex and associated REE orebodies within the Dalucao deposit (modified from Yang et al., 1998).

Despite multiple phases of brecciation (four events are

recorded in each of the pipes), mineralized veins and ores are contained wholly within altered nordmarkite at Dalucao (Liu et al., 2015b). The ores are weathered, brecciated, and dominated by fine-grained REE minerals (Fig. 3D) (Liu et al., 2015b, c). Brecciated ores are the main ore type, and it is notable that coarse-grained REE minerals are rare in the Dalucao deposit. Clasts within the breccia pipes are dominantly of magmatic origin, or are composed of carbonate minerals. Pyrite, fluorite, barite, celestine, muscovite, quartz, and REE minerals all occur throughout the matrix. In the No. 3 orebody, REE-mineral-bearing hydrothermal carbonate veins crosscut the other breccias, and represent another type of breccia ore.

3 Alteration and formation stages

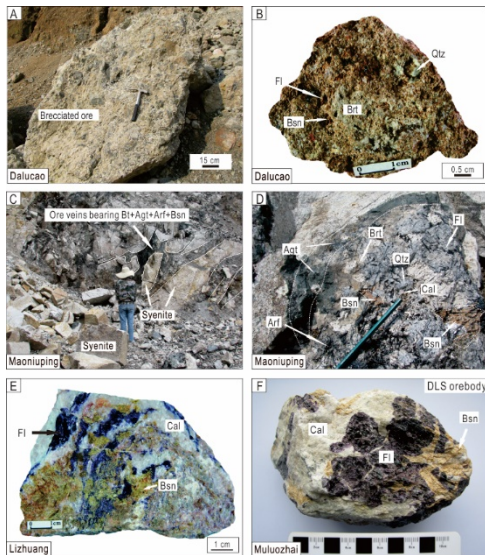


Figure 3. Macroscopic features of bastnäsite from the MD REE belt. (A) Brecciated ore in orebody No. 3 of the Dalucao deposit. (B) Weathered ore containing fluorite, quartz, barite, and bastnäsite in orebody No. 1 of the Dalucao deposit. (C) Ore veins containing a bastnäsite–aegirine–augite–arfvedsonite–biotite assemblage in syenite at Dagudao, Maoniuping deposit. (D) Mineral zoning from aegirine–augite, arfvedsonite, fluorite, calcite, barite, quartz, to bastnäsite within fractures in syenite. (E) Disseminated ore containing bastnäsite overprinting fluorite and calcite. (F) Typical massive ores containing fluorite, calcite, pyrite, and bastnäsite, Diaoloushan orebody, Muluozhai deposit. Mineral abbreviations are as follows: Brt (barite), Bsn (bastnäsite), Bt (biotite), Cal (calcite), Cls (celestine), Fl (fluorite), Gp (gypsum), Py (pyrite) and Qtz (quartz). From Guo and Liu (2019).

Alteration to biotite is the main alteration of syenite by hydrothermal fluids in these REE deposits. Gangue minerals such as fluorite, quartz, calcite and barite formed and overlapped with the biotite formation. In contrast, in the Maoniuping deposit, strong alteration of syenite by biotite–aegirine–augite–arfvedsonite was found. This is rare among these four deposits and may explain the formation of such a large REE deposit. In the Dagudao REE orebody at Maoniuping. The mineralized veins are invariably zoned; from the contact inwards, biotite- and K-feldspar-rich selvages are followed by zones dominated by aegirine–augite and arfvedsonite, and a core composed predominantly of barite, fluorite,

calcite, and bastnäsite.

Among the REE belt, various types of ores can be found such as weathered ore, brecciated ore, ore veinlet or veins. According to the mineral assemblages, bastnäsite is the predominant REE mineral with lesser amounts of monazite and others. Also, in these ores, the bastnäsite always formed at the later stages during the evolution of hydrothermal fluids.

Generally, magmatic, pegmatitic and hydrothermal stages are main stages for the whole process for the formation of carbonatite-related REE deposits. Among these deposits, it is the large deposits such as Dalucao and Maoniuping deposits rather than the small deposits that have pegmatitic stages.

4 Typical stable mineral assemblages in various types of ores in MD REE belt

According to the scale, stages, mineral assemblages and their characteristics in individual stages, a comparative summary of these four deposits could be obtained. Generally, the stable mineral assemblage containing fluorite, barite, calcite and bastnäsite occurs in a late hydrothermal stage in the various ore types. As fluid inclusions in bastnäsite crystals have low homogenization temperatures below 350°C and pressures of 2.0–2.4 kbar. (Zheng and Liu, 2019), large scale bastnäsite mineralization is only found during the late stage of hydrothermal fluid evolution. Actually, typical ores along Mianning–Dechang REE belt commonly include fluorite, barite, calcite and bastnäsite. Without fluorite, REE ores commonly have low grades below 2%. Among this mineral assemblage bearing bastnäsite, Ca, Ba, Sr, REE and F, SO_4^{2-} , CO_2 are closely related to each other, implying they are important for REE transport and precipitation. Also, in recent studies, Cl⁻ is also regarded as the important ion for the transport of REE (Liu et al., 2018).

5 Sources of REE metals

Although the Dalucao, Maoniuping, Lizhuang, and Muluozhai REE deposits have various ore types and styles of mineralization, they are all hosted by similar carbonatite–syenite complexes.

According to the four stages after the emplacement of carbonatite–syenite complex, bastnäsite formed at the latest stage after the magmatic stage, pegmatite stage and hydrothermal stage. Petrographic investigations suggest that the bastnäsite within these deposits formed after the precipitation of fluorite, celestine, and barite minerals (Liu and Hou, 2017).

Except bastnäsite has high content of REE, minerals such as barite, celestine, and fluorite from both pegmatite and hydrothermal stages along the MD belt have the similar REE patterns and trace elements compositions with those of carbonatite–syenite complex. Also, all these minerals from various stages and carbonatite, syenite have similar Sr–Nd–Pb isotopic compositions to the hosting carbonatites and syenites, suggesting that the carbonatites, syenites, and REE mineralization are

intimately related in origin.

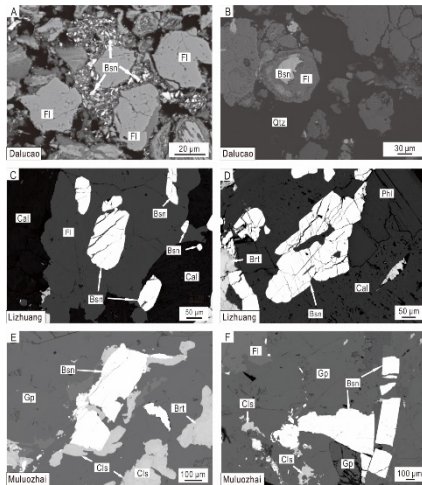


Figure 4. BSE images of REE ores in the MD belt. (A) bastnäsite in breccias overprinting fluorite in orebody No. 3, Dalucao deposit. (B) Weathered ore in orebody No. 1, Dalucao deposit. (C) and (D) Disseminated ore containing bastnäsite overprinting fluorite, calcite, and barite from the Lizhuang deposit. (E) and (F) Typical massive ores from the Diaoloushan and Zhengjialiangzi orebodies of the Muluozhai deposit, respectively, showing bastnäsite overprinting celestite, gypsum, and fluorite. Collectively, these images show that the REE mineralization overprinted earlier gangue minerals and therefore developed during the later stage of the hydrothermal evolution. From Guo and Liu (2019).

6 Local structure controlling orebody

Due to the scales and different types of faults and the distance between REE deposits, the effects on carbonatite-syenite complex and their wallrocks are quite different. For example, in the Maoniuping and Dalucao deposits, strong and frequent effects by faults led to the large amount of ore veins in Guangtoushan orebody in Maoniuping deposit and both brecciated and weathered ores in Dalucao deposit. But for Lizhuang REE deposit, with less effect from tectonic activities, only disseminated ores were found. In previous studies, it is assumed that REE could not be transported easily. But in the Maoniuping and Zhengjialiangzi deposits, wallrock such as alkali granite and marble, also hosts veinlet or veins. In fact, most of the ore occurs in the marble. In general, REE have been transported for relatively long distances into various types of wallrock.

Various types of ores point to one result that REE ores could be found in various types of fissures. Only in these fissures, pressures and temperatures could drop dramatically with infiltration of meteoric water. Then, REE mineralization mainly occurred under the similar conditions.

7 Conclusions

Despite various types of ores, REE mineralization occurs under a limited ranges of temperatures and pressures. Thus, the depth of the ores is not the main control on the various types of ores. Despite the different ore types, mineral assemblages of fluorite, calcite, barite and

bastnäsite are stable in the higher grade ores rather than barite and bastnäsite and other mineral assemblages (<2%). This mineral assemblage reflects the effective transport and precipitation of REE during the evolution of hydrothermal fluids as F, SO₄, Cl and CO₃ and REE could form complexes that are destroyed under lower temperature and pressure. According to the geological setting and observation, local tectonic setting controls the ore formation. Brecciation and fissures caused the brecciated ore, ore veins and veinlets. The disseminated ore formed under less active tectonic conditions.

Acknowledgements

The study was funded by the Natural Sciences Foundation of China (grant no. 41772044).

References

- Guo D X, Liu Y, 2019. Occurrence and geochemistry of bastnäsite in carbonatite-related REE deposits, Mianning-Dechang REE belt, Sichuan Province, SW China, *Ore Geol Rev* 107:266–28
- Hou ZQ, Tian SH, Xie YL, Yang ZS, Yuan ZX, Yin SP, Yi LS, Fei HC, Zou TR, Bai G, Li XY (2009) The Himalayan Mianning-Dechang REE belt associated with carbonatite-alkaline complexes, eastern Indo-Asian collision zone, SW China. *Ore Geol Rev* 36:65–89
- Hou ZQ, Liu Y, Tian SH, Yang ZM, Xie YL (2015) Formation of carbonatite-related giant rare-earth-element deposits by the recycling of marine sediments. *Sci Rep* 5:10231
- Liu Y, Hou ZQ (2017) A synthesis of mineralization styles with an integrated genetic model of carbonatite-syenite-hosted REE deposits in the Cenozoic Mianning-Dechang REE metallogenic belt, the eastern Tibetan Plateau, southwestern China. *J Asian Earth Sci* 137:35–79
- Liu Y, Chen ZY, Yang ZS, Sun X, Zhu ZM, Zhang QC (2015a) Mineralogical and geochemical studies of brecciated ores in the Dalucao REE deposit, Sichuan Province, southwestern China. *Ore Geol Rev* 70:613–636.
- Liu Y, Zhu ZM, Chen C, Zhang SP, Sun X, Yang ZS, Liang W (2015b) Geochemical and mineralogical characteristics of weathered ore in the Dalucao REE deposit, Mianning-Dechang REE Belt, western Sichuan Province, southwestern China. *Ore Geol Rev* 71:437–456
- Yuan ZX, Shi ZM, Bai G, Wu CY, Chi RA, Li XY (1995) The Maoniuping rare earth ore deposit, Mianning County, Sichuan Province. Seismological Publishing House, Beijing, p 150 (in Chinese)
- Zheng X, Liu Y, 2019. Mechanisms of element precipitation in carbonatite-related rare-earth element deposits: evidence from fluid inclusions in the Maoniuping deposit, Sichuan Province, southwestern China. *Ore Geol Rev* 107, 218-238

Deposit or prospect? example from the Miaoya, Hubei province, China

Dexian Zhang

Key Laboratory of Metallogenic Prediction of Nonferrous Metals and Geological Environment Monitor (Central South University), Ministry of Education, Changsha, China
School of Geosciences & Info-physics, Central South University, China

Yan Liu

Key Laboratory of Deep-Earth Dynamics, Institute of Geology, Chinese Academy of Geological Sciences, China

Abstract. The Miaoya carbonatite–syenite complex is prospective for REE and is ideal for studies of the formation of REE deposits. Mineralization at this prospect includes carbonatite-, syenite-, and mixed-type, all are low REE grade (below 1 %).

XRD and EMPA analyses reveal that REE minerals are low in all samples (<5%), consistent with the fact that few monazite, bastnäsite and other REE minerals are visible under the microscope. LA–ICP–MS analyses reveal that apatite and calcite in carbonatite have the highest REE concentrations. Isotope ratios of Sr and Nd for REE-mineralized and altered carbonatite and syenite rocks are similar to those of fresh carbonatites and syenites. These observations are interpreted as recording REE mineralization that originates directly from the unmineralized carbonatite–syenite complex rather than other host rocks. Carbon and oxygen isotope ratios of hydrothermal calcite are consistent with low-temperature alteration subsequent to ore formation.

The low REE of the Miaoya prospect compared with other carbonatite-syenite hosted deposits may reflect: 1) as supported by petrography, minimal tectonic deformation in the area resulting in 2) restricted cycling of hydrothermal solutions that led to 3) minimal fluid scavenging from REE-rich apatite and calcite for local REE re-deposition and concentration.

1 Introduction

China is known for its wide range of REE deposits, which have been producing since the 1980s. The genesis of China's giant carbonatite-hosted REE deposits involved a sequence of tectonic, magmatic, and hydrothermal events that produced a complex assemblage of rocks and mineralization styles. REE deposits in China have attracted the attention of geologists in recent decades due to their high-grade, large-scale, and low Th content. The existing models for REE deposit formation include two important processes: REE-rich hydrothermal fluids exsolved from carbonatite-syenite complex then formed a REE deposit through precipitation of a combination of fluid cooling, mixing and phase separation.

The Miaoya REE prospect is hosted by a carbonatite–syenite complex in the Qinling Belt, China. Concentrations of REE, Ba, Sr, and other elements in this prospect are relatively high, similar to those at other large REE deposits such as those at Maoniuping and

Dalucao. However, the REE minerals at the Miaoya prospect are rare than those deposits, which suggests that not all fertile carbonatites produce viable REE deposits. In the present study, XRD, LA-ICP-MS, EMPA, XRF, ICP-MS were employed to investigate trace element concentrations and the ratios of Sr, Nd, C, and O isotopes. Based on these results and the geological setting, the factors responsible for the low REE grades at the Miaoya prospect are subsequently discussed.

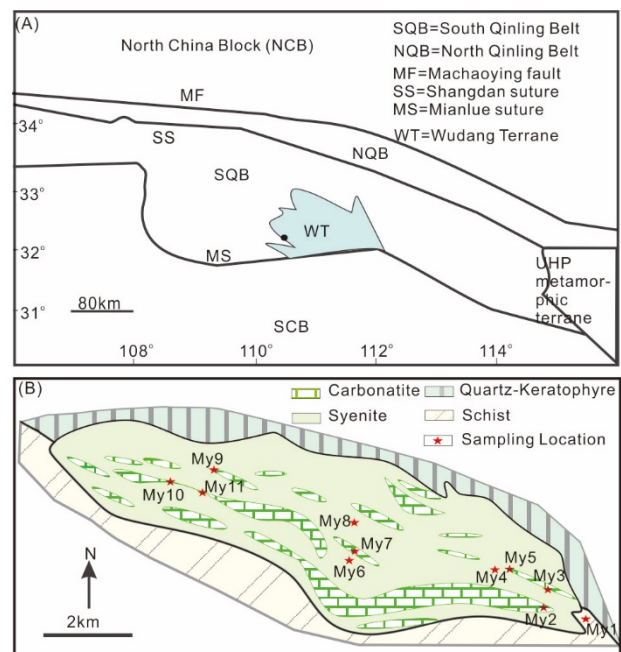


Figure 1 Sketch Geological Map showing the location of the Miaoya REE prospect (modified after Xu et al. 2010a).

2 Geological setting

The Miaoya REE prospect is located in the western area of the Wudan Terrane of the Qinling Belt. Forty-five shows have been discovered in a 12 square kilometer area with a total resource of 1.3 Mt TR₂O₃ (Total weight in Metric tons of Rare Earth Element Oxides) and 0.9 Mt Nb₂O₅ (Ma et al. 1981). The prospect is hosted in a carbonatite-syenite complex (Xu et al. 2010a; 2010b) which intruded along the fault belt between the schist of the Lower-Silurian Meiziya group and the Proterozoic meta-quartz keratophyre of the lower Sinian Yaolinghe group of the Nahua formation. Carbonatite intruded the syenite as stocks and minor dikes. Li (2018) reported that

a biotite K-Ar age yielded an age of 278 Ma for carbonatite. The U-Pb age of small oscillatory-zoned zircon from carbonatite was 147 ± 0.5 , while the U-Pb age of large euhedral oscillatory-zoned zircon from carbonatite was 766 ± 25 Ma (Xu et al. 2012; 2015). Syenite predominantly consists of K-feldspar with minor albite, biotite, quartz, sericite, plagioclase, and calcite. Carbonatite consists of fine to medium grained calcite and minor K-feldspar, albite, augite, biotite, fluorapatite, columbite, bastnäsité, ilmenite, pyrochlore, quartz, monazite, aeschynite, ilmenorutile, rutile, and minor sulphides. The REE minerals, dominated by monazite and bastnäsité, fill fractures in calcite and feldspar.

3 Results

3.1 Chemical composition of syenite and carbonatite

A total of 11 carbonatite and syenite samples were analyzed. The results show that the carbonatites are characterized by: (1) low SiO₂, generally less than 20%; (2) low Al₂O₃ due to lacking of Al-silicates; (3) high CO₂ content, generally 25%-40%; (4) CaO+ MgO+ Fe₂O₃+ FeO ranging from 35% to 50%; and (5) compared to other igneous rocks, carbonatite contains higher TiO₂, MnO, BaO, SrO, and P₂O₅. The syenite has relatively higher SiO₂ (36.0%-60.6%), Al₂O₃ (11.8%-20.2%), Fe₂O₃ (2.58%-4.35%), K₂O (4.09%-8.40%) than carbonatite (SiO₂: 3.15%-13.5%; Al₂O₃: 0.60%-5.77%; Fe₂O₃: 0.92%-1.28%; K₂O: 0.17%-2.18%) while lower CaO (0.71%-16.8%) than carbonatite (36.3%-48.8%).

Typical samples of syenite and carbonatite ores are enriched in large-ion-lithophile elements. The light REE (La, Ce, Pr, Nd, Sm, and Eu) content of the samples (5800–74,000 ppm) is ~46–164 times those of the heavy REE (Gd, Tb, Dy, Ho, Er, Tm, Yb, Y, and Lu)

3.2 REE minerals in the Miaoya prospect

Both syenite and carbonatite samples have different mineral assemblages. Macroscopic and microscopic examination reveals the carbonatite contains higher amounts of calcite (58.5- 92.0 vol.%), mica (3.00-25.8 vol. %), apatite (1.1-17.3 vol.%), ankerite (2.0-13.9 vol.%), and minor plagioclase (0-0.9%), K-feldspar (0.5-1.0 vol.%), chlorite (0-3.0% vol.%), and quartz (0-5.0% vol.%), while the syenite samples are composed mainly of feldspar (16.0-25.9vol.%), mica (21.2-56.7vol.%), quartz (9.5-20.8vol.%), calcite (0-27.0vol.%), ankerite (0-17.0vol.%), and apatite (0-4.4vol.%). The most obvious characteristics are that syenite contains relatively high amount of plagioclase, mica and quartz while carbonatite has more calcite and ankerite. Our XRD, SEM, BSE imaging, and EMPA data indicate that monazite, rather than bastnäsité, is the main primary REE mineral in the carbonatite at the Miaoya prospect, and monazite crystals are fine grained (10-100 µm), and rarely coarser-grained (<10 mm).

3.3 Minerals chemistry using LA ICP-MS

The apatite has high concentrations of Sr (5600-14600 ppm, ave. 11000 ppm), Y (234-967 ppm, ave. 442 ppm); Th (4.3-312 ppm, ave. 65.9 ppm); U (0.05-30.3 ppm, ave. 6.4 ppm) and low concentrations of Rb (0.03-0.20 ppm, ave. 0.08 ppm), and HFSE (Zr:0.47-24.6 ppm, ave. 4.52 ppm; Hf: 0.01-0.18 ppm, ave. 0.07 ppm; Nb:0.35-5.67 ppm, ave. 1.37 ppm; Ta:0.00-0.10 ppm, ave.0.02 ppm)

Two types of calcite were identified at the Miaoya REE prospect based on total REE concentrations: calcite from schist and syenite (low total REE concentration), and calcite from carbonatite (high total REE concentration). The schist/syenite calcite also has high Rb (0.15 - 29.8 ppm) and lower HFSE than the carbonatite calcite.

In terms of the REE patterns of these individual minerals, the chondrite-normalized REE patterns for apatite exhibit negative slopes and lack an Eu anomaly. Calcite from carbonatite has a right-dip trend patterns with (La)_N/(Lu)_N (0.24-322, ave. 57.1), while the calcite from schist and syenite has low concentration of all the trace elements, and has flat REE patterns. Columbite and ilmenite have an average REE up to 1000 ppm. The trace element concentrations in augite, biotite, plagioclase, and quartz are low, below 10 ppm, and they show a positive Eu anomaly.

3.4 Sr-Nd and C-O isotopes

Most samples have high Sr content, 3200 ppm to 5700 ppm in carbonatite, 2000 ppm to 2200 pp in mixed rocks and 4900 ppm in mixed carbonatite. The Sr in syenite (128 -11000 ppm) and schist (404 ppm) are relatively low. The initial ⁸⁷Sr/⁸⁶Sr (0.7038 to 0.7095) and ¹⁴³Nd/¹⁴⁴Nd (0.512269 to 0.512439) isotope ratios of different samples remain constant (Figure 1).

The carbonatite exhibits δ¹⁸O values of 11.1 ‰ to 13.8‰ and δ¹³C values of -5.4‰ to -3.1 ‰; these compositions fall outside of the field of the typical primary mantle-derived carbonatite on a δ¹⁸O_{V-SMOW} vs. δ¹³C_{V-PDB} diagram where the consistent δ¹³C_{V-PDB} value and highly variable δ¹⁸O_{V-SMOW}.

4 Discussion

4.1 REE enrichment at the Miaoya prospect

Three lines of evidence suggest that the Miaoya complex formed by unmixing of silicate magma: the syenites and carbonatites are spatially co-located, carbonatite and syenite yield similar Sr–Nd isotopic ratios, and trace element concentrations in syenite and carbonatite produce similar patterns on spider diagrams and REE plots (Hou et al.2015).

At the Miaoya prospect, measured Sr–Nd isotopic ratios for REE-mineralized carbonatites and syenites are similar to Sr–Nd ratios for fresh carbonatites and syenites. The Sr–Nd isotope ratios define isotopic arrays that deviate from the mantle array in a similar way to the EAFL (East African Carbonatite Line), which was derived directly from the mantle without the involvement of REE-

rich sedimentary material (Hou et al. 2015). Strontium and neodymium isotope ratios can be used to classify carbonatites as fertile or barren. Barren carbonatites follow the evolution trend of HIMU and EMI, while fertile carbonatites such as those at Bayan Obo, Weishan, and Mianning–Dechang deviate from this trend, as mentioned by Hou et al. (2015).

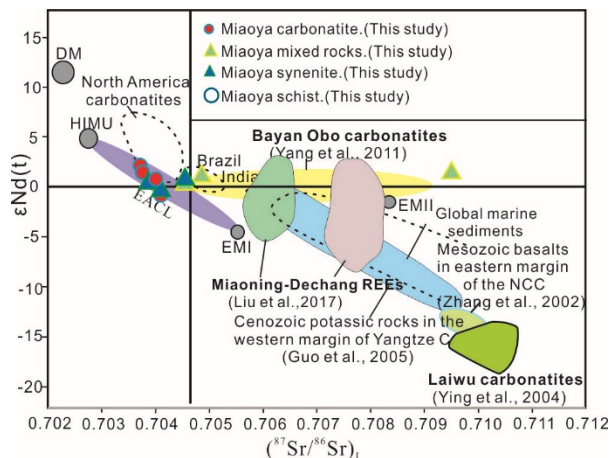


Figure 2. Whole rock Sr-Nd isotopic compositions of syenite and carbonates from the Miaoya REE prospect.

Carbonatites from the Miaoya prospect have high total REE concentrations (1300–4800 ppm) relative to the majority of the syenites (350–857 ppm REE), although one syenite sample contains 19,000 ppm REE. These concentrations, in combination with the genetic model inferred from the geological setting, suggest that carbonatites from Miaoya are typical fertile carbonatites, with potential for REE mineralization during magmatic–hydrothermal events. However, REE concentrations at Miaoya are lower than those at the Lizhuang, Maoniuping, and Dalucao deposits in the Mianning–Dechang REE belt (Hou et al. 2015).

Only calcite and apatite hosted by carbonatite contain elevated concentrations of REE, with total REE concentrations up to 35,000 and 14,000 ppm, respectively (Fig. 1). Columbite and ilmenite contain lower REE concentrations than apatite and cannot account for the REE mineralization. Monazite is one of the important REE minerals in carbonatite-related REE deposits (Chen et al. 2018) and is the most important primary REE mineral at the Miaoya prospect (Xu et al. 2010b; 2015; Ying et al. 2017). Both monazite and bastnäsite crystals are relatively small and rare.

Figure 2 shows the distinct isotopic arrays defined by barren and fertile carbonatite, dolomitic dikes with low REE concentrations have lower $^{87}\text{Sr}/^{86}\text{Sr}$ ratios than calcitic dikes at the Bayan Obo, suggesting that the Miaoya prospect involved lesser metasomatic refertilization and the addition of REEs and LILEs to the SCLM. DM, HIMU, EMI, and EMII are mantle end-members (i.e. depleted mantle (DM), High- μ mantle (HIMU), Enriched mantle 1 (EM1), and enriched mantle II (EMII); Hart et al., 1992).

4.2 Evolution of ore-forming fluids

Low-temperature isotope exchange between carbonates, meteoric water, and magmatic fluids produces positive shifts in $\delta^{18}\text{O}$ values in carbonates during the evolution of hydrothermal fluids. Such changes in C–O isotopic compositions are observed between bulk primary carbonatite and hydrothermal calcite at the Miaoya prospect ($\delta^{18}\text{O}_{\text{V-SMOW}} = 11.1\text{‰}$ to 13.8‰ and $\delta^{13}\text{C}_{\text{V-PDB}} = -4.9\text{‰}$ to -3.5‰). Carbon–oxygen isotopes, together with field observations of lithology, suggest that at least three possible fluid sources should be considered at the Miaoya prospect: meteoric water, magmatic water, and CO_2 derived from the decarbonation of carbonatite. In the absence of interaction with meteoric water, the syenite–carbonatite complex host rock and CO_2 produced by decarbonation would result in relatively high oxygen isotope ratios that are typical of hydrothermal fluids. At the Miaoya prospect, C–O isotope ratios suggest that meteoric water and CO_2 from decarbonation made minor contributions to the ore-forming fluids. Thus, magmatic water was the most likely primary contributor of fluid during mineralization.

4.3 Potential of carbonatite-syenite complexes for REE mineralization

Two REE-enrichment processes are necessary to form such deposits: production of fertile carbonatite and subsequent upgrade by magmatic–hydrothermal processes. Fertile carbonatites that host REE deposits commonly have high REE, Ba, and Sr contents, but fertility is not related to $\text{CaO}:\text{MgO}$ or $\text{FeO}:\text{MgO}$ ratios. Concentrations of REE, Ba, and Sr at Miaoya are lower than those at giant or large REE deposits elsewhere in the world, with data for Miaoya plotting in the barren field or near to the boundary between the barren and fertile fields in (REEs vs. $\text{CaO}:\text{MgO}$, $\text{FeO}:\text{MgO}$, Ba and $\text{Sr}:\text{Ba}$) diagrams (Fig. 2). The low REE contents suggest that the carbonatite–syenite complex at the Miaoya does not have the potential to host large or giant REE deposits.

During the early stages of mineralization, local tectonic activity generally will produce fractures or fissures in carbonatite–syenite complexes, facilitating fluid cycling and modifying the fluid chemistry by water–rock interaction. Circulation of ore fluids in tectonic fractures drives alteration within the carbonatite and leads to high concentrations of REE, F^- , Cl^- , CO_2 , $(\text{SO}_4)^{2-}$, and volatiles in the fluids. There is little evidence of tectonic activity within the Miaoya prospect, and petrography reveals a relatively intact inner structure in altered syenites and carbonatites. Microprobe and BSE imaging reveal that calcite grains show clear mineral boundaries and clear cleavages; these features are rare in the altered carbonatite complexes that host the Mianning–Dechang REE deposits, which would have hindered the cycling of hydrothermal fluids.

Sulfate and fluorite ions form stable complexes with the REE and could be important for REE transport and precipitation, respectively (Williams-Jones et al. 2012). REE-sulfate and -carbonate complexes are particularly

important at high-temperature and mildly acidic to near-neutral pH conditions (Williams-Jones et al. 2012; Migdisov and Williams-Jones 2014). Large and giant REE deposits generally contain large amounts of fluorine- and sulfate-bearing minerals, such as fluorite, fluorapatite, barite, and celestite, as the main gangue minerals. The abundance of these minerals implies high fluoride and sulfate contents in the ore-forming fluids (Kynicky et al. 2012). However, fluorite and barite are rare at the Miaoya prospect, suggesting that fluorine and sulfate contents were low in the ore-forming fluids, with a consequent reduction in transport and precipitation of REE. We conclude that a low concentration of suitable ligands for REE is another factor that inhibited REE mineralization at the Miaoya prospect.

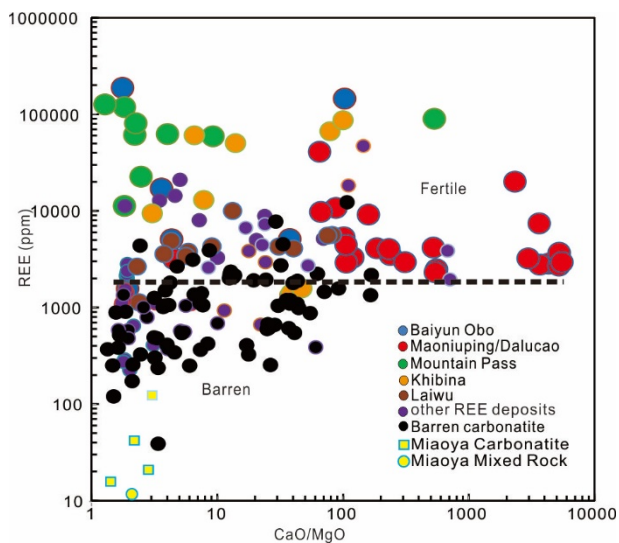


Figure 3. (A) REEs Vs. CaO/MgO diagrams of main global examples of carbonatites.

5 Conclusions

Two lines of the evidence suggest that REE at the Miaoya prospect were derived from the carbonatite–syenite complex itself: (1) the Sr–Nd isotope values of altered syenite and carbonatite are similar to those of fresh carbonatite and syenite; and (2) trace-element contents of apatite and calcite in mineralized samples are similar to those in unaltered samples, indicating that apatite and calcite in the carbonatites were the original source of REE for the deposit.

Three factors contributed to the low grade of ores at the Miaoya prospect: (1) REE concentrations in the carbonatite–syenite complex are lower relative to those in carbonatites at large and giant deposits; (2) there was little tectonic activity subsequent to intrusion, which restricted the extent of hydrothermal activity; and (3) low contents of fluorite, barite, calcite, and celestite in the prospective ores suggest that F^- , $(SO_4)^{2-}$, CO_2 , and other volatile components that are necessary to transport and facilitate the precipitation of REE were not present in sufficient concentrations at the Miaoya prospect.

Acknowledgements

Acknowledgments: This research was funded by [National Key R&D Program of China] grant number [2017YFC0601503] and [National Natural Foundation of Science of China] grant number [41672082], [41472301] and [41772044]. The authors sincerely thank Qisheng Hu and Qianyu Zhao from Eighth Geological Brigade of Hubei Province for their great assistance in field survey.

References

- Chen W, Lu J, Jiang SY, Ying YC, Liu YS (2018) Radiogenic Pb reservoir contributes to the rare earth element (REE) enrichment in South Qinling carbonatites *Chemical Geology*
- Hou Z, Liu Y, Tian S, Yang Z, Xie Y (2015) Formation of carbonatite-related giant rare-earth-element deposits by the recycling of marine sediments *Scientific Reports* 5:10231
- Kynicky J, Smith MP, Xu C (2012) Diversity of Rare Earth Deposits: The Key Example of China *Elements* 8:361-367
- Li XC, Zhou MF (2018) The Nature and Origin of Hydrothermal REE Mineralization in the Sin Quyen Deposit, Northwestern Vietnam *Economic Geology* 113:645-673
- Ma YX, Zhu HM, Gu TH (1981) Report for Detailed investigation of Miaoya Nb and REE deposit area in Zhushan County, Hubei Province (unpublished).
- Migdisov AA, Williams-Jones AE (2014) Hydrothermal transport and deposition of the rare earth elements by fluorine-bearing aqueous liquids *Mineralium Deposita* 49:987-997
- Williams-Jones AE, Migdisov AA, Samson IM (2012) Hydrothermal mobilisation of the Rare Earth Elements – a Tale of “Ceria” and “Yttria” *Elements*:355-360
- Xu C, Kynicky J, Chakhmouradian AR, Campbell IH, Allen CM (2010a) Trace-element modeling of the magmatic evolution of rare-earth-rich carbonatite from the Miaoya deposit, Central China *Lithos* 118:145-155
- Xu C, Wang L, Song W, Wu M (2010b) Carbonatites in China: A review for genesis and mineralization *Geoscience Frontiers* 1:105-114
- Xu C, Taylor RN, Li W, Kynicky J, Chakhmouradian AR, Song W (2012) Comparison of fluorite geochemistry from REE deposits in the Panxi region and Bayan Obo, China *Journal of Asian Earth Sciences* 57:76-89
- Xu C, Kynicky J, Chakhmouradian AR, Li X, Song W (2015) A case example of the importance of multi-analytical approach in deciphering carbonatite petrogenesis in South Qinling orogen: Miaoya rare-metal deposit, central China *Lithos* 227:107-121
- Ying Y, Chen W, Lu J, Jiang S-Y, Yang Y (2017) In situ U–Th–Pb ages of the Miaoya carbonatite complex in the South Qinling orogenic belt, central China *Lithos* 290-291:159-171

Graphite occurrences in Northern Norway (Vesterålen-Lofoten, Senja)

Janja Knežević, Iain H.C. Henderson, Håvard Gautneb, Jan Steinar Rønning, Frode Ofstad, Bjørn Eskil Larsen
Geological Survey of Norway

Abstract. Geological and geophysical investigations of graphite occurrences in Vesterålen (Nordland county) and Senja (Troms county), Northern Norway were carried out from 2015 to 2018. The main goal was to ground truth resistivity anomalies discovered by a helicopter-borne geophysical survey during the MINN project (Minerals in Northern Norway) from 2012-2014. All of the graphite occurrences are found in supracrustal granulite facies rocks of Archaean to Proterozoic age, comprising quartzites, migmatitic gneisses, iron formations, calcsilicates and graphite schist. The graphite localities have a range in total carbon (TC%) varying from 5% to 21%. The maximum content of TC is found at Vardfjellet, Senja with 40.3%. The graphite schists are all of the flake graphite type comprising rocks where the graphite flake size ranges from approximately 0.01 mm to 2 cm.

1 Introduction

In Northern Norway (Nordland and Troms counties) there are 76 occurrences of graphite; 47 in Nordland county and 29 in Troms county (12 deposits, 13 prospects, 51 occurrences). Historically, 3 mines have been in operation in Vesterålen area, (Jennestad, Golia, and Kråkberget). Four graphite mines are active in Europe, one of which is in Norway. The Skaland/Trælen mine has been in operation since 1917, producing about 10,000 tonnes per year from an ore with an average grade of 31% TC. This is the world's richest flake graphite mine in current operation.

Detailed geological and ground geophysical investigation of fourteen localities were investigated on Vesterålen and 6 localities on Senja (2015-2018) employing different geological and geophysical methods: geological mapping, structural analysis, sampling, chemical analyses, geological drilling, trenching and ground geophysical methods (CP, IP, SP, EM31 and 2D resistivity) (Fig.1-2). Samples were analysed for total carbon (TC) and total sulphur (TS) using a Leco SC-632 analyser. The detection limits are 0.06 % and 0.02 % for carbon and sulphur respectively (Table 1).

Table 1. Graphite occurrences with content of TC%

Locality	N Samples	Average TC%	Max TC%
Bukken	37	5.08	19.70
Grunnvåg	21	5.84	14.85
Vardfjellet	37	9.19	40.30
Hesten	21	5.77	12.81
Skardsvåg	31	0.98	5.41
Brenna	6	11.43	30.40
Haugneset	11	19.30	33.82
Kvernfordalen	5	6.06	13.70
Møkland	38	9	25.7
Morfjord	3	18.45	19.70
Raudhammaren	14	14.8	25.9
Romsetfjorden	12	14.5	31
Skogsøya	16	21	34.9
Smines	19	8	17.3
Sommarland	15	12.48	18.20
Vikeid	12	11.99	24.25
Sommarhus	7	24.07	37.70

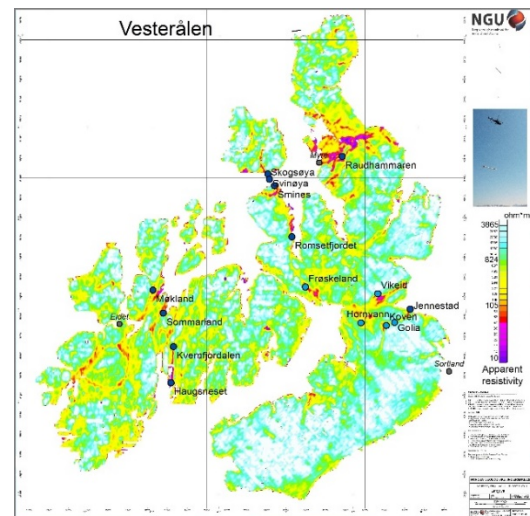


Figure 1. Vesterålen, Apparent resistivity (7000 Hz) with graphite occurrences (after Rodionov et al. 2013).

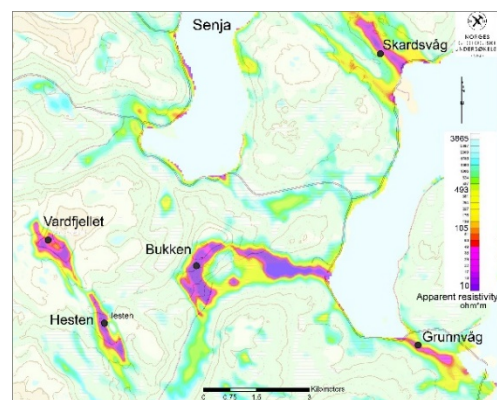


Figure 2. Apparent resistivity anomalies (6600 Hz) on Senja, with graphite occurrences

2 Geological setting

2.1 Vesterålen-Lofoten

The Lofoten-Vesterålen area in northern Norway is regarded as comprising part of the Baltic Shield. In broad terms, the area is composed of an Archaean to presumably mid-Proterozoic basement, intruded by a mangeritic suite composed of anorthosite-mangerite-charnockite-granite (AMCG) rocks (Davidsen & Skår, 2016) (Fig.3.).

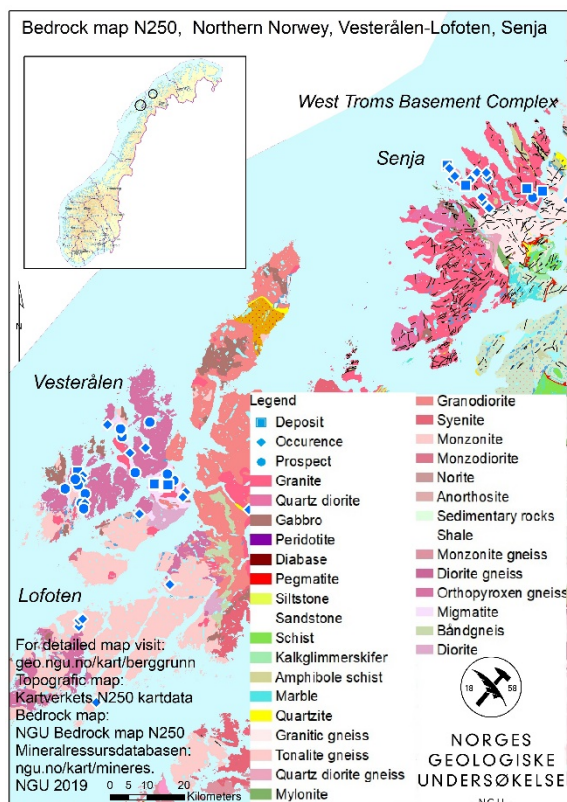


Figure 3. Bedrock map at scale 1:250 000, Vesterålen and Senja county Northern Norway, with graphite occurrences and investigated areas.

The rocks of the Lofoten-Vesterålen islands of Northern Norway are among the oldest yet reported from Scandinavia. The region has experienced at least five metamorphic and magmatic events during its history, but the later events had only local effects (Griffin, 1978). There have been two major periods in which new material was added to the crust; one at c. 2700 Ma, the other a protracted period from c. 2100 to 1700 Ma termed the Svecofennian Orogeny. Important metamorphic events occurred at 2700-2600 Ma, 1830 Ma and 1100-900 Ma. The first two events involved local anatexis, but large-scale re-melting of pre-existing crust to form granitic magma appears to have been limited to an episode at c.1400 Ma. The oldest rocks are migmatitic gneisses of generally intermediate composition, probably largely of supracrustal origin; these were intruded by a granodiorite/granite pluton at approximately 2600 Ma. Pb

isotope data indicate that the migmatites formed c. 2700 Ma ago, and the isotopic systems in some rocks have been disturbed by Proterozoic granulite-facies metamorphism.

A Proterozoic supracrustal series is composed predominantly of felsic meta-volcanic gneisses but includes marble, quartzite, graphite schist and iron formations (Griffin, 1978).

The supracrustal units containing the graphite schists are also often intruded by younger intrusions (AMCG). U-Pb dating indicates a three-stage magmatic history beginning at 1870–1860 Ma, with a dominant stage at 1800–1790 Ma, and the emplacement of pegmatites, local rehydration and retrogression between 1790 and 1770 Ma (Corfu, 2004). The basement and the early Proterozoic supracrustal sequence were subjected to regional metamorphism, which reached granulite facies over most of the area at about 1830 Ma (Griffin 1978). The Archaean to Palaeoproterozoic Gneiss Complex of Vesterålen, is dominated by orthopyroxene-bearing migmatitic gneisses. The gneiss complex includes horizons of quartzites, calc-silicates and amphibolites. The metamorphic event(s) reached peak conditions at $P=0.8\text{--}0.9$ GPa and $T=860\text{--}880$ °C (Engvik et al. 2016).

2.2 Senja

Senja is part of The West Troms Basement Complex (WTBC) which occupies the coastal islands of Troms county, North Norway (Fig. 1). The region is characterised by Archaean gneisses with varied protoliths, Archaean and Palaeoproterozoic greenstone belts and Svecofennian bimodal intrusions with ages of ca. 1.8 Ga. The WTBC is juxtaposed against the Caledonian nappe stack in the east by extensional and local thrust faults and represents a basement outlier in a similar tectonic position as Lofoten and Vesterålen. Geochronology from U–Pb of magmatic and migmatitic rocks collected in a transect perpendicular to the NW–SE strike of the complex records three main stages of Archaean magmatism and one superimposed, Neo-Archaean metamorphic high-grade event. The period from 2.75–2.70 Ga was particularly geologically active in the rest of the complex, with intrusion of diorite-granodiorite plutons on Kvaløya and Senja, followed by local migmatization and a subsequent pulse of diorite-granite magmatism from 2.70 to 2.67 Ga. The Archaean rocks were variably reworked, metamorphosed and intruded by felsic and mafic plutons during the Svecofennian (1.8–1.7 Ga) orogeny, and locally also formed the substrate to Palaeoproterozoic supracrustal rocks. Possible correlatives are found in the Lofoten and Vesterålen area (Myhre et al. 2013).

3 Petrology

3.1 Vesterålen-Lofoten

Graphite-bearing units comprise rocks with variable content of pyroxene (orthopyroxene, clinopyroxene) and plagioclase and are often abundant in biotite. The host

rock is also locally rich in iron sulfides and with mafic and mica veins enriched in pyrrhotite, pyrite, graphite, magnetite, biotite, amphibole, mica and clay minerals. Graphite-bearing rocks (granulite/pyroxene gneiss/felsic gneiss/biotite gneiss) are often intruded by charnockite and mangeritic intrusions (Rønningen et al. 2018).

Graphite schist is often complexly folded but can also occur with a brecciated texture (Fig. 4. a,b,c). Host rock identification can be problematic where graphite is abundant as the graphite schists are often strongly metamorphosed during granulite facies metamorphism. The average content of pyroxene (orthopyroxene, clinopyroxene) and plagioclase minerals can vary. Accessory minerals include magnetite, titanite, zircon, rutile, chlorite, apatite, and clay minerals.

Graphite rich zones can be from 30cm to up to 6m thick. In the wall rock adjacent to the graphite-rich zones graphite is often present in disseminated form at a lower grade (up to 20m thick) and can occur in mafic veins together with other minerals, such as biotite pyrrhotite pyrite, and mica. Graphite flake size can vary up to 2mm (Fig. 4d).

Millimetric to centimeter thick calcite veins and joints filled with calcite can also be found.

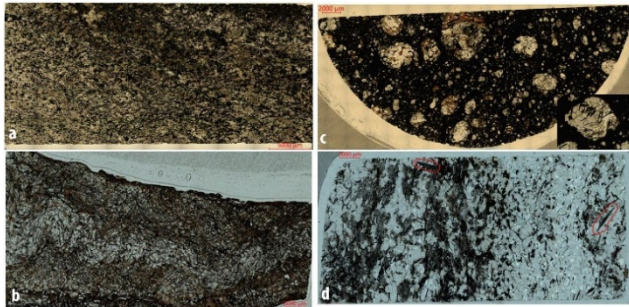


Figure 4 Thin sections in transmitted light, a) Iron-rich graphite schist (TC12,4%, TS 3,83%), b) Folded graphite schist, c) Iron and graphite rich breccia, pyrrhotite matrix, graphite flakes in silicate clasts, d) Graphite flakes up to 2mm.

3.2 Senja

Graphite occurs within graphite biotite gneiss which are abundant in feldspar, amphibole, sulfides, and mica minerals. Graphite occurs in lenses, veins and is also disseminated (up to 25m thick zones in drillcore).



Figure 5. Thin section hg39-16- biotite graphite gneiss

4 Structural geology

The WTBC on Senja consists of three main tectonic blocks juxtaposed along NW-SE crustal scale shear zones. The central block, termed *The Senja Shear Belt* (Zwaan, 1995) is a highly tectonised, predominantly granitoid block at granulite facies with complexly in-folded

metasedimentary units containing graphite. The graphite deposits on Senja were first mapped in detail by Haldal & Lund (1987). Henderson & Kenrick (2003) demonstrated that the graphite deposits on Senja are intimately associated with the development of NNW-SSE striking F_2 folds, and that the graphite is spatially associated with the F_2 fold hinges. However, the F_2 fold hinges are deformed by D_3 deformation on approximately E-W axes, creating complex interference geometries. Henderson & Kendrick (2003) also noted that graphite is most geographically extensive where F_3 structures intersect graphite-bearing F_2 structures. The extent of graphite outcrop is also strongly affected by the presence of both F_2 and F_3 shear zone structures which locally (F_2) or regionally (F_3) 'shear-out' the graphite outcrops, thereby limiting the extent of the graphite deposits, suggesting that a robust knowledge of the combination of the D_2 and D_3 structures allows for a better understanding of the geometry of the graphite deposits. Henderson & Kendrick (2003) carried out detailed 1:5000 structural mapping of 6 graphite deposits on Senja. In the present study, two of these deposits were re-mapped; Vardfjellet and Bukkemoen. Vardfjellet is the largest unexploited graphite deposit in Europe. Both deposits display a complex geometrical relationship.

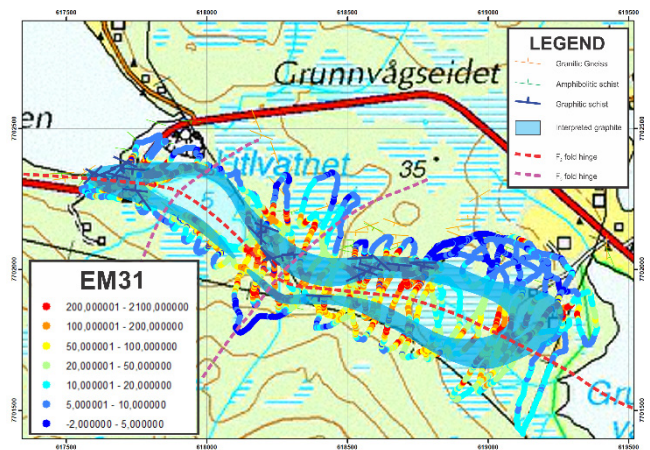


Figure 6. Map of the newly discovered Grunnvåg deposit with ground conductivity meter-EM31 (mS/m) measurements. The graphite is isoclinally folded around F_2 fold hinges.

The Bukkemoen deposit was thought to close towards the east (Henderson & Kendrick, 2003). However, this study shows that regionally the same tectonically attenuated lenses continue eastwards over a considerable distance. In the eastern extremity of the Precambrian Basement adjacent to late normal faulting, extensive graphite has been discovered in the Grunnvåg deposit (Figure 6). Here the graphite is complexly deformed in a similar way to the Vardfjellet and Bukkemoen deposits. Both detailed structural analysis, graphite sampling and ground geophysics have been undertaken and confirm the presence of an isoclinally folded (F_2), WNW-ESE striking graphite lense up to approximately 80m thick with thickening up to approximately 120m possible in the F_2 fold hinges. The graphite lense is weakly folded in very open F_3 folds on

NW-SE axes but the associated folding of the F₂ hinges is of limited extent compared to other deposits in the area.

The geophysical anomaly of the Bukkemoen deposit is approximately 2km in strike length, the outcropping graphite schist (up to 120 m wide) indicates a potential graphite resource. However, no detailed resource estimates are available at present. Grunnvåg represents the best exposed and longest graphite outcrop which is approximately 270m long, 90m wide with average graphite content of 5,84 TC%.

Bergh et al. (2010) proposed a regional tectonic model for the WTBC which is now demonstrably relevant for the whole of the Svecofennian orogeny in northern Fennoscandia (Henderson et al., 2015). Bergh et al. (2010) systematised the structural evolution of the West Troms Basement Complex (WTBC) west of the Caledonian nappe sequences and found that an initial phase of NE-directed contraction produced dip-slip fold and thrust belt geometries that were attenuated and segmented by subsequent orogenic scale sinistral lateral shearing. The combination of the F₂ and F₃ fold and shear structures leads to complex graphite deposit geometry.

Acknowledgements

Many thanks to Nordland and Troms counties who financed and supported these graphite investigations, we are also grateful to our coworkers from the Geological Survey of Norway (NGU) geophysics team; Harald Elvebakk, Jomar Gellein and Geir Viken. The NGU lab is thanked for sample preparation and analyses.

References

- Bergh, S.G., Kullerud, K., Armitage, P.E.B., Zwaan, K.B., Corfu, F., Ravna, E.J.K., Myhre, P.I. (2010) Neoproterozoic to Svecofennian tectono-magmatic evolution of the West Troms Basement Complex, North Norway. *Norwegian Journal of Geology*, 90:21-48.
- Corfu, F. 2004: U-Pb age, setting and tectonic significance of the anorthosite-mangerite-charnockite -Granite suite, Lofoten-Vesterålen, Norway. *Journal of Petrology*, 45:1799-1819.
- Corfu, F. 2007: Multistage metamorphic evolution and nature of the amphibolite-granulite facies transition in Lofoten-Vesterålen, Norway, revealed by U-Pb in accessory minerals. *Chemical Geology*, 241:108-128.
- Davidson, B. & Skår, Ø. 2004: Lofoten and Vesterålen: A Precambrian puzzle. (Abstract). The 26th Nordic Geological Winter Meeting, January 6th – 9th 2004, Uppsala, Sweden. Geologiske Förenings Föreläsningar. Vol 126, 20-21.
- Engvik, A.K., Davidson B., Coint, N., Lutro, O., Tveten, E. and Schiellerup, H. 2016: High-grade metamorphism of the Archean to Palaeoproterozoic gneiss complex in Vesterålen, North Norway. (Abstract) 32nd Geological Winter Meeting Helsinki, Bulletin of the Geological Society of Finland, special issue, 153-154.
- Engvik, A.K., Davidson B., Coint, N., Lutro, O., Tveten, E. and Schiellerup, H. 2016: High-grade metamorphism of the Archean to Palaeoproterozoic gneiss complex in Vesterålen, North Norway. (Abstract) 32nd Geological Winter Meeting Helsinki, Bulletin of the Geological Society of Finland, special issue, 153-154.
- Gautneb, H. & Tveten, E. 2000: The geology, exploration and characterization of graphite deposits in the Jennestad area, Vesterålen area northern Norway. *Norges geologiske undersøkelse Bulletin*. 436:67-74.
- Gautneb, H., Knezevic, J., Johannesen, N.E., Wanvik, J.E., Engvik, A., Davidson, B., Rønning, J.S. 2017: Geological and ore dressing investigations of graphite occurrences in Bø, Sortland, Hadsel and Øksnes municipalities, Vesterålen, Nordland County, Northern Norway 2015 – 2016. NGU Report 2017.015
- Griffin, W.L., Taylor, P.N., Hakkinen, J.W., Heier, K.S., Iden, I., Krogh, E.-J., Malm, O., Olsen, K.I., Ormåsén D.E. & Tveten, E. 1978: Archean and Proterozoic crustal evolution in Lofoten-Vesterålen N Norway. *Journal of the Geological Society of London* 135:629-647.
- Davidson, B. & Skår, Ø. 2004: Lofoten and Vesterålen: A Precambrian puzzle. (Abstract). The 26th Nordic Geological Winter Meeting, January 6th – 9th 2004, Uppsala, Sweden. Geologiske Förenings Föreläsningar. Vol 126, 20-21.
- Henderson, I.H.C., Kendrick, M. 2003: Structural controls on graphite mineralisation, Senja, Troms -2003, NGU report 2003.011
- Henderson, I.H.C., Viola, G. & Nazuti, A. 2015: A new tectonic model for the Palaeoproterozoic Kautokeino Greenstone Belt, northern Norway, based on high-resolution airborne magnetic data and field structural analysis and implications for mineral potential. *Norwegian Journal of Geology*, 95:339-364.
- Heldal, T. & Lund, E. (1987) Berggrunnsgeologisk kartlegging i Berg Kommune, Senja. Geologisk Kart (1:5000).
- Myhre, P.I., Corfu, F., Bergh, S.G. & Kullerud, K. 2013: U-Pb geochronology along an Archean geotranssect in the West-Troms Basement complex, North Norway. *Norwegian journal of Geology*, 93:1-24.
- Rodionov, A., Ofstad, F., Stampolidis, A. & Tassis G. 2013a: Helicopter-borne magnetic, electromagnetic and radiometric geophysical survey at Langøya in Vesterålen, Nordland. NGU report 2013.044.
- Rodionov, A., Ofstad, F. & Tassis, G. 2013b: Helicopter-borne magnetic, electromagnetic and radiometric geophysical survey in the western part of Austvågøya, Lofoten archipelago, Nordland. NGU Report 2013.045
- Rodionov, A., Ofstad, F., Stampolidis, A., Tassis, G. 2014: Helicopter-borne magnetic, electromagnetic and radiometric geophysical survey 2012:2013 and 2014, Troms County. NGU report 2014.039
- Rønning, J.S., Gautneb, H., Larsen B.E., Knežević J., Baranwal, V.C., Elvebakk, H., Gellein, J. Ofstad, F., & Brønner, M. 2018: Geophysical and geological investigations of graphite occurrences in Vesterålen and Lofoten, Northern Norway 2017, NGU report 2018.011
- Zwaan, K. (1995) Geology of the West Troms basement complex, Northern Norway, with emphasis on the Senja shear belt; a preliminary account. *NGU Bull.*, 42733-36.

Occurrences of energy critical elements; Lithium – Cobalt and Graphite in Europe, a preliminary overview.

Håvard Gautneb, Janja Knežević
Geological Survey of Norway, Norway

Eric Gloaguen, Jérémie Melleton, Blandine Gourcerol
BRGM

Tuomo Törmänen
Geological Survey of Finland, Finland

Abstract. In the EU, preliminary data show that there are 1167 registered occurrences, prospects or deposits of Li, Co and graphite, of these only 17 are active. This compilation is part of work package 5 of the FRAME project (Forecasting and Assessing Europe’s Strategic Raw Materials needs) a section within the framework of the GeoERA project. The data collected classify the occurrences according to their genetic type, their occurrence type and production status. The data have been collected from geological survey national databases and in this compilation we regard all Co deposits with a mean Co >100ppm as potential occurrences for Co. For the other commodities, Li bearing minerals or graphite must be positively identified or explored for to be included.

1 The data, collection and overview

The FRAME project is part of the H2020 GeoEra platform and consists of 11 partners from different geological survey in Europe. Li, Co and graphite are the most important materials in batteries. The project collected raw data extracted from each survey’s national database. In addition, a number of geological surveys that are not part of the project were requested to supply data. Basic geographical and geological information was collected including the genetic type of the different commodities. The occurrences were also divided into a) “Deposit” an occurrence where a value usually in the form of grade and tonnage exist. b) “prospect” an area with probability of deposits, but more detailed information is lacking c) “showing”, any occurrence of a type of mineralization usually with little additional information. The total number of localities for each commodity in each country is summarized in Fig.1 a, b and c.

2 Summary of the different commodities.

We show the distribution of Li, Co and graphite occurrences in the EU, classified according to their genetic types, in Fig 2, 3 and 4.

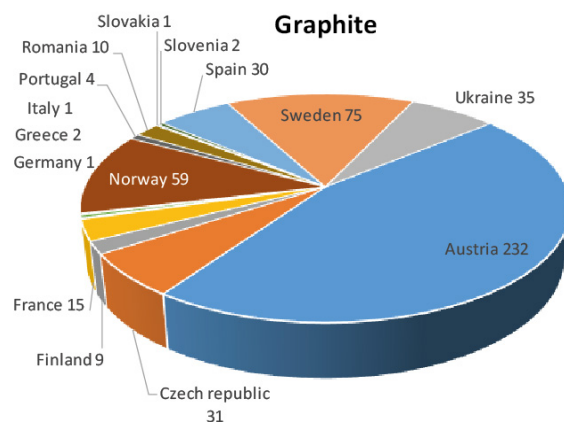
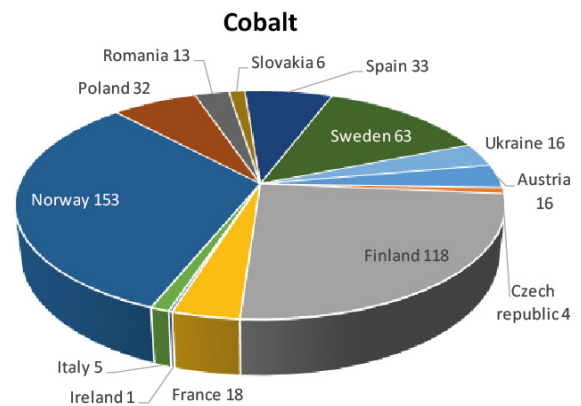
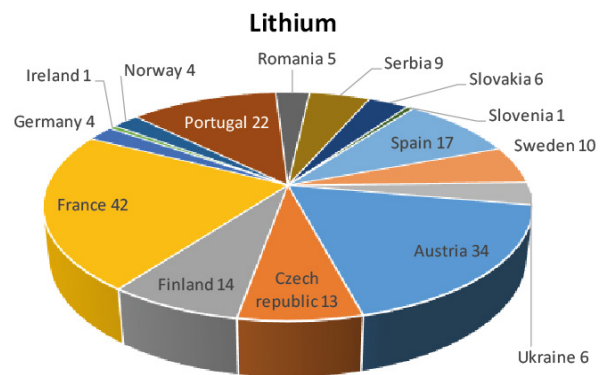


Figure 1 a b c Number of lithium, Cobalt and Graphite occurrences in Europe.

2.1 Lithium

High-grade Li deposits (Gourcerol et al., 2019; Gloaguen et al., 2018) are represented by numerous Li-rich LCT pegmatites, rare metal granites (Melleton et al., 2015) and atypical stratiform deposits such as Jadar. The distribution of lithium in Europe shows a strong clustering (fig. 2) highlighting the Li potential of the Variscan belt of south and central Europe. Representative examples (Gourcerol et al., 2019) are Wolfsberg pegmatites (236 366.46t Li₂O – grade 1.0%), Sepeda pegmatites (221 728.1t Li₂O – grade 1.0%) or Beauvoir rare-metal granite (375 000t Li₂O – grade 0.78%). Lithium is hosted by various minerals such as phosphates (amblygonite, montebasite, triphylite), inosilicate (spodumene) and phyllosilicates (lepidolite series, zinnwaldite, petalite). Co-products are generally Ta, Nb, Sn, Be. Jadar-type Li deposits are presently encountered in intramontane lacustrine evaporate basins in Serbia and Bosnia, where Li is hosted by Jadarite, a Li-bearing borosilicate. Its crystallisation is poorly constrained and may be related to the interaction of clastic sedimentary rocks with surrounding brine, possibly involving hydrothermal devitrification and hydration of andesitic-dacitic pyroclastic material or alteration of clay minerals. (Stanley et al., 2007; Stojadinovic et al., 2017). Jadarite occurs as 1-10 mm white ovoid grains in a mudstone matrix. The Li & B mineralisation of Jadar occurs as 1.5 to 35 m thick stratiform lenses of three identified gently dipping tabular zones covering a surface area of 3 km by 2.5 km. In 2017, the total mineral resources report 135.7 Mt of ore at a grade of 1.86 % Li₂O and 15.4 % B₂O₃ (Rio Tinto, 2017) that represents a giant deposit of 2.524 Mt of Li₂O.

Medium-grade Li deposits (Gourcerol et al., 2019) are represented by hydrothermal deposits such as greisens and Li-bearing quartz veins associated to some peraluminous rare metal granites. A typical example for greisen is Cinovec (Czech Republic, 5 652 990.2t Li₂O - grade 0.4 Li₂O) and for Li-bearing veins is Argemela mine (Portugal, 80 400t Li₂O – grade 0.4%). In greisens, lithium is mainly hosted by iron and fluorine-rich micas (zinnwaldite, lepidolite series) whereas in Li-bearing quartz veins, Li is hosted by phosphates (Montebasite, etc). Co-products are mainly Sn, Ta and Nb.

Various other types of rocks and/or geological formations may contain local high Li content with low tonnage or low to very low Li content with a high tonnage (Gloaguen et al., 2018): Li-rich (tosudite) hydrothermal alteration aureole around gold quartz veins; Cookeite/lithiophorite in black shales (Dauphiné: av. 441 ppm Li₂O, up to 1 847 ppm) or in bauxite deposits and Mn-(Fe) deposits. Li-rich clays (hectorite) are presently unknown in EU.

2.2 Cobalt

Cobalt is a common minor constituent in a number of different ore types but world mine production is dominated by three main types: 1) stratiform sediment-hosted deposits (60%), magmatic Ni-Cu(Co-PGE) deposits (23%), and lateritic Ni-Co deposits (15%), where cobalt is

recovered as a by-product (10-90 % recovery, Mudd et al., 2013). Other types of deposits containing Co include IOCG, VMS (Besshi-type), 5-element vein deposits, black-shale hosted Ni-Cu-Zn deposits, and Fe-Cu-skarn deposits (Slack et al., 2017). In most of these deposit types Co-grades are between 0.01-0.1%, highest grades occur in sediment-hosted deposits of the Central African Copperbelt (0.1-1.1% Co), lateritic Ni deposits (0.1-0.22% Co), some VMS deposit-types (Windy Craggy 0.66% Co, Outokumpu-type deposits 0.1-0.25% Co), and 5-element vein deposits and ultramafic-hosted hydrothermal deposits (up to %-level, e.g. Dobsina, Bou Azzer) (Hizman et al. 2017, Slack et al. 2017).

In Europe, most of the known Co-bearing deposits and showings are clustering in the Nordic countries (Finland, Sweden and Norway) while throughout southern-central Europe deposits are more scattered (Fig. 3). In the Nordic countries, the deposits mostly represent magmatic Ni-Cu and Fe-Ti-V deposits and VMS deposits, whereas elsewhere in Europe genetic types are more varied from sediment-hosted, to lateritic and 5-element vein types, among others. The only active mines producing cobalt are located in Finland. Kevitsa mine in northern Finland is a large low-grade Ni-Cu-PGE deposit, which produced 591 t of Co in 2018. Kylylahti mine is a small-sized Outokumpu-type Cu-Zn-Ni-Co deposit, which produced 278 t of Co in 2018 (New Boliden 2019). Terrafame is a large, low-grade black-shale hosted Zn-Ni-Cu-Co mine that produces Co as by product to Ni and Zn, but production figures for Co are not published (2013 286 t).

2.3 Graphite

Graphite is a common mineral in rocks throughout Europe. However it is rare to find economically interesting deposits. In this study we have divided graphite occurrences into flake and amorphous types which make up the bulk of the deposits. Vein deposits are known but are mostly geological curiosities in the EU (Luque et al 2014). The bulk of the graphite occurrences occur in Archean or Proterozoic rocks of Fennoscandia and Ukraine. In addition, a number of amorphous graphite occurrences are found in Phanerozoic rocks in Austria. There are also a large number of showings where the genetic type is unknown. Active mines are situated in Ukraine, Austria and Norway. The graphite bearing rocks are typically organic rich para-gneiss often associated with carbonates and iron formations. The graphite content varies from 2-3% up to over 40% (Gautneb & Tveten 2000). The Trælen deposit in Norway is the world's richest graphite deposit in current production with an average ore grade of 31%. Graphite deposits are good electrical conductors and relatively easy to locate using geophysics. In investigated (for instance in Norway) areas the graphite deposits are found to be polyphasally deformed and most commonly associated with high amphibolite or granulite facies metamorphism (Gautneb et al. 2017).

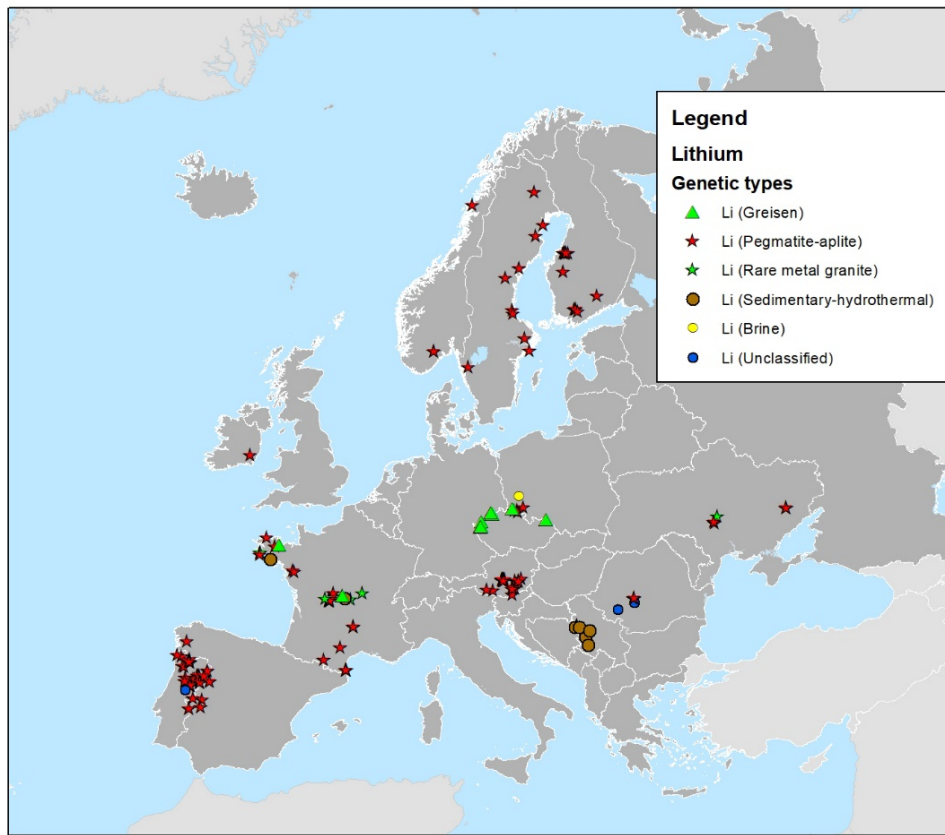


Figure 2. Genetic types of lithium.

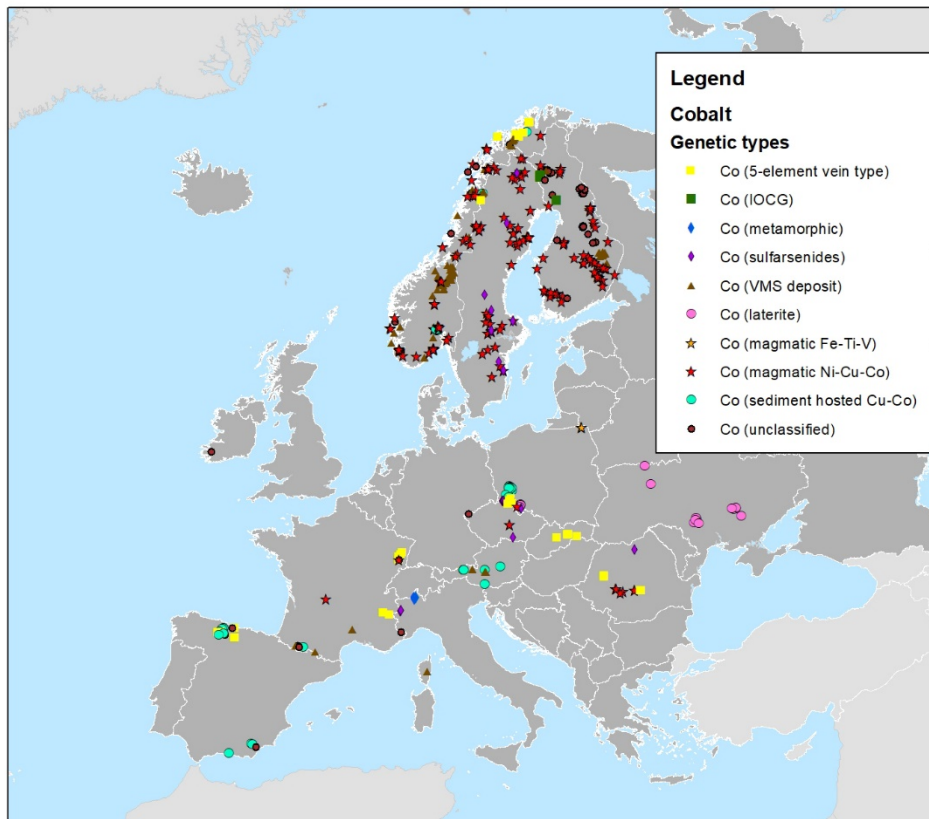


Figure 3. Genetic types of cobalt.

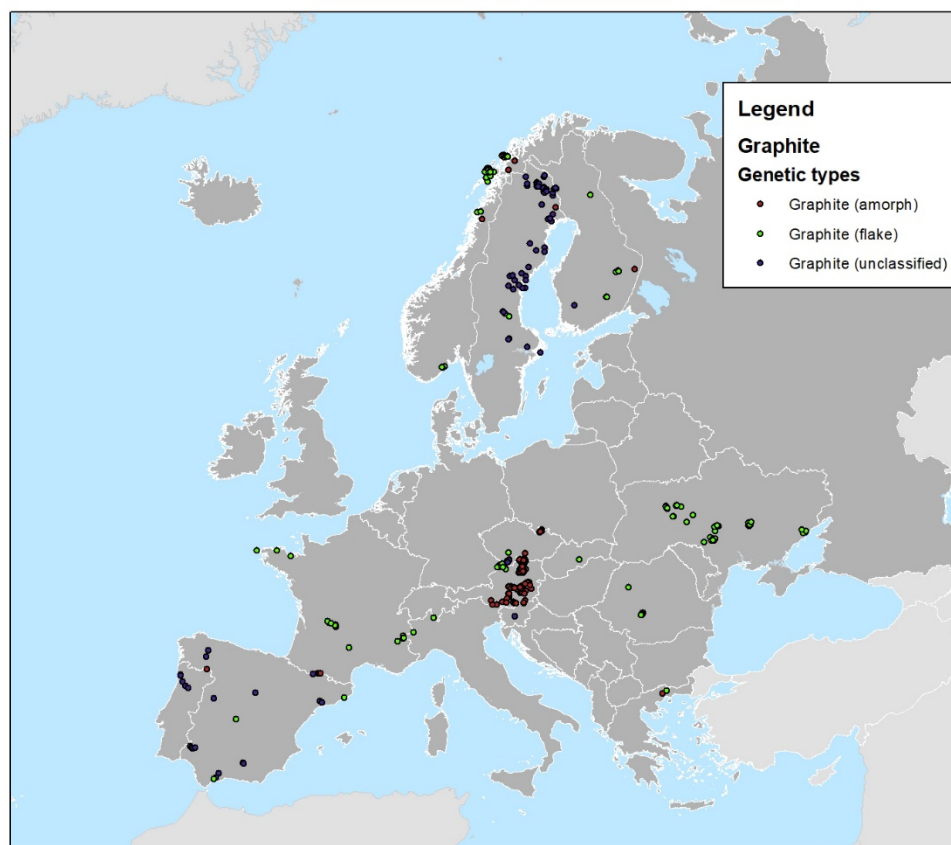


Figure 4. Genetic types of graphite

Acknowledgements

We thank the following persons and project partners for supplying data to this contribution; Anders Halberg (SGU), Daniel de Oliveira (LNEG), Boris Malyuk (GIU), Klemen Teran (GeoZs) Stanislav Soltes (SGIDS) Stanislav Mikulski (PGI), Roberto Martinez Orio (IGME Spain), Sebastian Pfeleiderer (GBA) Antje Wittenberg (BGR), Petr Rambousek (CGS), Mauro Lucarini (ISPRA), Eoin McGrath (GSI) Zoltan Horvath (MBFSZ), Kostas Laskarides (IGME Greece), George Tudor (IGR). This project has received funding from the European Union's Horizon 2020 research and innovation programme under grant agreement No 731166.

References

- Gautneb H. & Tveten E. 2000. The geology, exploration and characterisation of graphite deposits in the Jennestad area, north Norway, Norges geologiske undersøkelse Bull.436:67-74.
- Gautneb, H., Knežević, J., Johannesen N.E., Wanvik J.E., Engvik, A., Davidsen B., & Rønning J.E., 2017. Geological and ore dressing investigations of graphite occurrences in Bø, Sortland, Hadsel and Øksnes, municipalities, Vesterålen, Nordland County, Northern Norway, NGU report 2017.015.
- Gloaguen E., Melleton J., Lefebvre G., Tourlière B., Yart S., Gourcerol B. 2018. Ressources métropolitaines en lithium et analyse du potentiel par méthodes de prédictivité. Public report BRGM/RP-68321-FR, 126p. <http://infoterre.brgm.fr/rapports/RP-68321-FR.pdf>
- Gourcerol B., Gloaguen E., Melleton J., Tuduri J., Galiegue X. 2019. Re-assessing the European lithium resource potential – A review of hard-rock resources and metallogeny. *Ore Geology Reviews*, in press. doi: 10.1016/j.oregeorev.2019.04.015
- Hitzman, M.W., Bookstrom, A.A., Slack, J.F., Zientek, M.L., 2017. Cobalt—Styles of deposits and the search for primary deposits: U.S. Geological Survey Open-File Report 2017–1155:47.
- Luque F.J., Huizenga J.-M., Crespo-Feo E., Wada, H., Ortega L., Barrenechea J.F. 2014. Vein graphite deposits: geological setting, origin and economical significance. *Mineralium Deposita*, 49:261-277.
- Melleton J., Gloaguen E., Frei D. 2015. Rare-elements (Li-Be-Ta-Sn-Nb) magmatism in the European Variscan belt, a review. 13th SGA biennial meeting, 24-27 August 2015, Nancy, France. *Proceedings*, 2:807-810.
- Mudd G.M., Weng, Z., Jowitt, S.M., Turnbull, I.D., Graedel, T.E. 2013. Quantifying the recoverable resources of by-product metals: The case of cobalt. *Ore Geology Reviews*, 55:87-98.
- New Boliden 2019. Stable production, lower grades and metal prices. New Boliden Q4 and full year 2018 report. 37 p.
- Rio Tinto., 2017. Notice to ASX, Increase to Jadar Project Mineral Resources 2 March 2017, 22p. http://www.riotinto.com/documents/170302_Increase_to_Jadar_Project_Mineral_Resources.pdf
- Slack, J.F., Kimball, B.E., Shedd, K.B., 2017. Cobalt, chap. F of Schulz, K.J., DeYoung, J.H., Jr., Seal, R.R., II, and Bradley, D.C., eds., *Critical mineral resources of the United States—Economic and environmental geology and prospects for future supply*: U.S. Geological Survey Professional Paper 1802:F1–F40.
- Stanley C., Jones G.C., Rumsey M.S., Blake C., Roberts A.C., Stirling J.A.R., Carpenter G.J.C., Whitfield P.S., Grice J.D., and Lepage Y., 2007. Jadarite, LiNaSiB₃O₇(OH), a new mineral species from the Jadar Basin, Serbia; *European Journal of Mineralogy*, 19:575-580.
- Stojadinovic U., Matenco L., Andriessen P., Toljic M., Rundic L., and Ducea M., 2017. Structure and provenance of Late Cretaceous-Miocene sediments located near the NE Dinarides margin: Interferences from kinematics of orogenic building and subsequent extensional collapse. *Tectonophysics*, 710-711:184-204.

Typology of *hard-rock* Li-hosted deposits in Europe

Blandine Gourcerol, Eric Gloaguen, Johann Tuduri, Jérémie Melleton
Université d'Orléans, France

Abstract. Lithium became a strategic metal in the last decade due to its widespread use in electromobility and green technologies. Consequently, demand has increased significantly reviving European interest in lithium mining and leading many countries to assess their own mineral resources/reserves to secure their own supplies.

A compilation of European lithium *hard-rock* occurrences and a systematic assessment of metallogenic processes related to Li-mineralization have been produced. Accordingly, it appears that lithium is well represented through various deposit types related to several orogenies from Precambrian to Miocene ages. Thus, these deposits have been identified as mostly resulting from endogenous processes such as lithium-cesium-tantalum (LCT) pegmatites (e.g. Sepeda in Portugal; Aclare in Ireland; Lännta in Finland), rare-metal granites (RMG; Beauvoir in France; Argemela in Portugal) and greisens (e.g. Tregonning-Godolphin, Meldon in UK; Cinovec in Czech). Local exogenous processes may be related to significant Li-endowments such as jadarite precipitation in the Jadar Basin (Serbia) but are rarely related to economic grade and tonnage of lithium. Moreover, common parameters are identified in the Li endowment processes including: 1) a pre-existing Li-rich source; 2) a lithospheric thickening; and 3) an extensional regime.

1 Lithium: strategic and critical aspect

In the last decade, lithium has become a strategic metal due to its physical and chemical properties making it an excellent candidate for electromobility and green technologies such as Li-ion batteries and other energy storage devices (e.g. Manthiram et al. 2017). As a result, metal demand has increased significantly. In this context, identification and assessment of lithium mineral resources/reserves is a crucial step and lithium metallogeny has been identified as representing a major subject for discovery of new mineral resources.

A geographically- and geologically-based compilation of lithium occurrences with their corresponding features (deposit types, Li-bearing minerals and Li concentrations), has been produced. For the first time, this extended abstract gives a global overview of the identified Li deposit types and features, and their distribution throughout orogenies in Europe. Moreover, based on this compilation an effort was made to constrain Li endowments in terms of their metallogenesis, in order to present potential processes responsible for Li

endowment and introduce potential prospective areas.

2 An overview of the geological processes

Several deposit types show Li-bearing minerals. Herein, deposits have been divided into two distinct processes: 1) endogenous – related to magmatic process and high-temperature hydrothermal processes; and 2) exogenous process – related to sedimentary processes /hydrothermal fluids.

2.1 Endogenous processes related to lithium mineralization

Several Li-magmatic related events are identified through time (Fig. 1).

2.1.1 LCT pegmatites

LCT pegmatites, which may comprise spodumene, petalite, lepidolite and amblygonite-montebrazite minerals, are widely represented in Europe (Fig. 1) and show various ages from Paleoproterozoic to Miocene.

In the Svecofennian Orogen, LCT pegmatite ages range from 1.8 to 1.79 Ga suggesting a relatively late emplacement in the orogenic cycle, postdating the arc accretion and a regional metamorphism, and might be related to a crustal thickening and to the late amphibolite-facies metamorphic event (e.g. Eilu et al., 2012).

During the Sveconorwegian Orogen, emplacement of mixed niobium–yttrium–fluorine (NYF)-LCT pegmatites (910-906 Ma) appears coeval with gravitational collapse and post-collisional magmatism, as well as low pressure/high temperature metamorphism (e.g. Bingen et al., 2008).

The Ordovician Scottish and the ca. 412 Ma LCT pegmatites from Ireland (Barros, 2017), which are part

of the Caledonian orogenic belt, appear coeval with a crustal thickening and post-subduction magmatism. In the Variscan belt, various LCT pegmatites are widely distributed. Their respective ages suggest emplacement during the late Carboniferous reflecting extended fractionated magmatic events through the European core related to post-collisional stage of the orogenic cycle (Fig. 1; e.g. Melleton et al. 2012; Neace et al. 2016).

Finally, deposits within the Western Carpathians (Slovakia) as well as the Austroalpine pegmatites of the Eastern Alps, which form the extreme margins of the belt, indicate Permian ages coeval with a regional partial melting (e.g. Ilickovic et al. 2017).

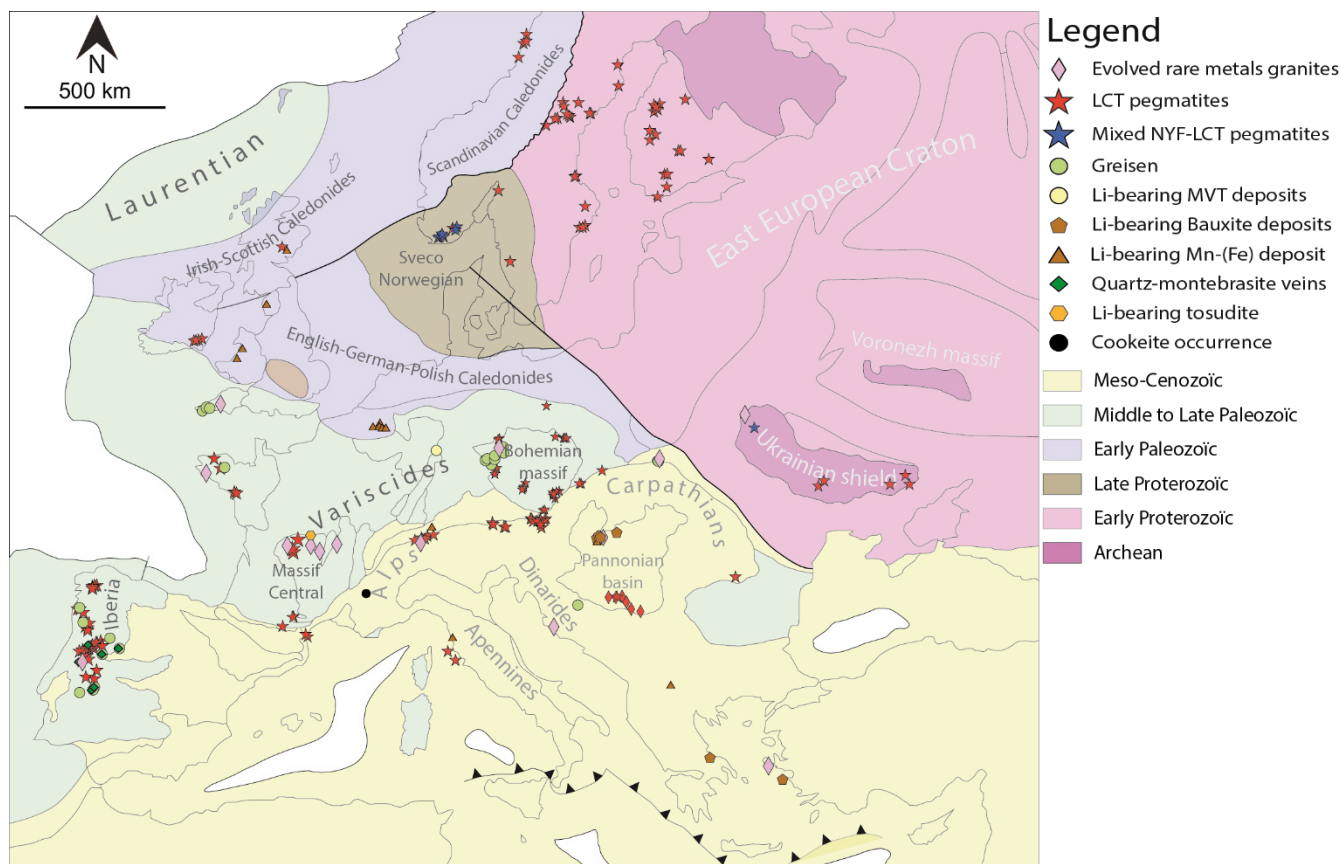


Figure 1. Simplified geotectonic map of Europe (modified after Charles et al., 2013) and distribution of various Li-bearing occurrences

2.1.2 Rare-metal granites (RMG)

RMG (Fig. 1), which comprises various types of Li-bearing minerals including Li-rich micas (e.g. lepidolite, zinnwaldite) are identified and are mainly Variscan in age (e.g. Beauvoir, Montebbras in France and Argemela in Portugal). They occur as very small, relatively subsurface granitic plugs, typically less than 1 km³ and two main types (e.g. Černý et al., 2005) are recognized. The first group is characterized by metaluminous to peraluminous, low to intermediate-phosphorus RMG with very high concentrations of Nb, Ta, Sn, which occur in both post-orogenic and anorogenic geodynamic settings. Li endowment is moderate (100 to a few 1000 ppm) and is mostly related to zinnwaldite mineralization (e.g. Cinovec and Podlesi granites in Czech Republic). The second group corresponds to peraluminous, high-phosphorus RMG with strong enrichments in Ta, Sn, Li and F, which occur in continental-collision settings. In this RMG type, Li concentrations are elevated varying from 0.5 % to 1.0 % Li₂O and Li is present in lepidolite, Li-rich muscovites and the amblygonite-montebbrasite series.

For both groups, their emplacements during the late Carboniferous are related to the post-collisional stage ending the Variscan orogeny (Fig. 1; e.g. Cuney et al. 2002; Melleton et al. 2012).

2.1.3 Greisens

Li-rich micas (Li-rich muscovite, lepidolite, zinnwaldite) and amblygonite-montebbrasite group minerals are also

well represented in Variscan greisen deposits (e.g. Cligga Head, Tregonning-Godolphin, Meldon in UK; DIha Dolina in Slovakia; Montebbras in France and Krasno-Konik, Krupka in Czech Republic).

This deposit type corresponds to high-T hydrothermal transformation of fractionated granitic intrusions (pegmatites, granites) within its upper part into a porous muscovite-quartz assemblage at the granite/host-rock contact and/or along multi-stage crosscutting Sn-W quartz veins (e.g. Černý et al., 2005). Greisen may form up to 100 m thick units with irregular to sheet-like bodies. Peraluminous RMG and metaluminous intrusions represent favorable granitic bodies for development of these deposit types.

2.1.4 Quartz-montebbrasite veins

Existence of Variscan quartz-montebbrasite hydrothermal veins associated with leucogranitic cupolas have been identified in the central part of the Central Iberian Zone in Spain (e.g. Valdeflores, Golpejas), Portugal (e.g. Argemela area) (Roda Robles et al. 2016) and France (Montebbras area). These veins are hosted by granitic bodies or metasedimentary rocks and are generally < 1m thick and fill out fracture sets. They show a high proportion of quartz and scarcity of minerals such as K-feldspars.

They appear to have been formed during the late stage of the Variscan orogeny and are spatially associated with peraluminous RMG.

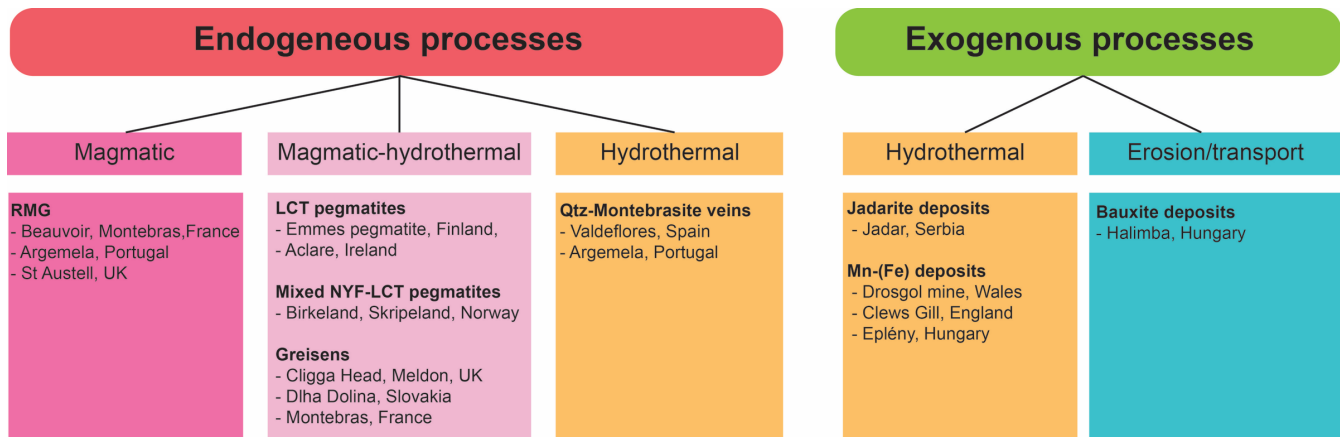


Figure 2. Various types of deposits related to Li-mineralization and selected examples.

2.2 Exogenous processes related to lithium mineralization

Li-occurrences in sedimentary formations are related to various exogenous processes such as hydrothermal and/or erosion/transport

2.2.1 Jadar deposit type

This deposit type is Neogene in age and related to jadarite mineralization. Occurrence of several other isolated intramontane lacustrine evaporate basins is suggested in Serbia (Fig. 1), as well as in Bosnia, such as the Lopare basins, where jadarite occurrence has been reported. Interestingly, the basement of these basins includes LCT pegmatite suggesting a local Li endowment in the basement (Stojadinovic et al. 2017). Formation of these basins occurred in the late stage of the Dinadric orogeny (Fig. 1), coeval with the extensional collapse and back arc extension due to the Carpathian slab retreat (Simić et al. 2017).

Precipitation of jadarite is poorly constrained and some authors suggested that interaction of clastic sedimentary rocks and surrounding brine, possibly involving hydrothermal devitrification and hydration of andesitic-dacitic pyroclastic material or alteration of clay minerals, may contribute to its precipitation (Stanley et al. 2007; Stojadinovic et al. 2017).

2.2.2 Mn-(Fe) deposits

The Li-bearing lithiophorite mineral, which precipitates from secondary fluid circulation, is widely present in Mn-(Fe) deposits. In Europe, two distinct periods show Mn-(Fe) deposit formation.

From Cambrian to Early Ordovician, deposits in Scotland, Wales (e.g. Drosgol Mine), Lake District of England (Clews Gill), Belgium (e.g. Otré) and Germany (Harz) (Fig. 1; Romer et al. 2011) represent a notable relic of the Cadomian orogeny (650 to 550 Ma). They are exclusively located in the Avalonian plate, constrained by the Rheic suture, and are formed from weathering of the Gondwana plate.

Mn deposits formed in Hungary (e.g. Eplény and Urkut deposits) are Jurassic in age (Fig. 1). These deposits are associated with marine sedimentary rocks composed

mainly of bioclastic limestones and black shales. Romer et al. (2011) suggested that the lithium component was derived from chemical weathering of continental crust and concentrated originally in siliciclastic or carbonate rocks. Moreover, distribution along regional faults appears as an important feature to focus fluid circulation (e.g. Candwr Fault in Wales, Cotterell et al. 2009).

2.2.3 Bauxite deposits

Li-bearing minerals (mainly lithiophorite and cookeite) occur in bauxite deposits. In Europe, these deposits are Jurassic to Cretaceous (Bardossy 1982) and are located northern shores of the Mediterranean Sea (Fig. 1).

These deposits are stratiform, related to non-uniform karst bedrock in which bauxite horizons are relatively large. The Halimba mining district is one of the largest area, thickness of the bauxite varies from 1 to 40 m. In these deposits, the Li-bearing mineral lithiophorite originated from secondary fluid circulation in the host rock (Bardossy 1982) forming Mn-rich crust layers in epi- and supergene crusts.

3 From sink to source

As suggested herein, several parameters may control Li mineralization in Europe.

Observable clustering of endogenous Li deposits such as LCT pegmatites, RMG and/or greisens may involve a crustal anomaly or a Li « pre-concentration » related to paleoenvironmental sedimentation conditions (e.g. type of basin, host rocks, climate) and/or post-deposition processes such as weathering, basinal fluid circulation in the crust, more generally preserved along paleo passive margins. Thus, this involves existence of a primary Li-source which can be of magmatic origin (e.g. erosional material from a continental magmatic arc and related Mn-(Fe) deposits and lithiophorite occurrences) or sedimentary origin. In that respect, a significant lithospheric thickening may reflect a favorable process to concentrate Li in a specific location.

Secondly, timing of fluid circulation appears an important feature for Li-endowment, which is either related to a regional or local extensional regime in an orogenic cycle. Thus, sedimentary/hydrothermal Li-deposits are mainly related to regional extension (e.g.

rifting or back arc extension) whereas, magmatic-related Li-deposits are associated with local decompression and/or transtension strike-slip deformation in late stages of the continent-continent orogenic cycle leading to formation of a volatile rich melt. Remarkably, sedimentary rocks enriched in Li during the extensional regime (e.g. Jadar Basin) may represent a favourable source for Li for a subsequent magmatic event. Unfortunately, data to confirm such a hypothesis are still lacking.

Finally, distribution of Li-occurrences is strongly influenced by the location and geometry of fracture sets. Thus, high permeability fractured zones seem to act as favourable channel for: 1) evolved magma and allowing emplacement of LCT pegmatite or RMG; or 2) hydrothermal fluid circulation throughout sedimentary successions (e.g. Jadar Basin, lithiophorite occurrences, the Aalenian black shales) leading to secondary Li-bearing mineral precipitation (e.g. lithiophorite, cookeite).

4 Perspectives for exploration

Lithium is not rare in Europe and is well distributed within several orogenic belts (Fig. 1). The Variscan orogeny (Fig. 1) shows the strongest Li-endowment through various Li-deposit types, whereas older orogenies mainly contain more localized LCT pegmatites (Fig. 1), potentially due to successive orogenic reworking. On the other hand, only very few studies report lithium occurrences related to the young Mediterranean orogens suggesting either a lack of exploration in this geographical area or a significant difference between the Variscan and the youngest orogenies.

Meanwhile, a heterogeneity of knowledge is observable regarding distinct countries and provinces. For instance, a great part of Europe appears underexplored/unstudied and may contain further lithium occurrences either as pegmatites or RMG and greisens. Moreover, description of Li-bearing minerals such as lithiophorite and Li-chlorite in sedimentary deposits such as bauxite, Mn-(Fe) and MVT deposits is/was not systematically reported as it was not of first interest in these deposit types, which may show a local significant Li-endowment such as in China (Wang et al. 2013).

Regarding jadarite occurrences, greenfield exploration in Balkan countries may identify potential deposits related to lacustrine evaporate basins. This area is relatively underexplored and several exploration and mining companies showed recent interest.

Acknowledgements

This study is supported by the LABEX VOLTAIRE (Geofluids and VOLatils, Earth, Atmosphere - Resources and Environment) in collaboration with the BRGM and the LEO of Orléans University.

References

Alviola R, et. al (2001) Svecofennian rare-element granitic pegmatites of the Ostrobothnia region, western Finland: their metamorphic environment and time of intrusion. In: Mäkitie H (ed) Svecofennian granitic pegmatites (1.86-1.79 Ga) and

quartz monzonite (1.87 Ga), and their metamorphic environment in the Seinäjoki region, western Finland, Geological Survey of Finland, 30, pp 9-29.

Bardossy G (1982) Karst bauxites, Bauxite deposits on carbonate rocks. In Elsevier Scientific publishing company (ed) *Developments in economic geology* 14, 442p.

Barros R (2017) Petrogenesis of the Leinster LCT (Li-Cs-Ta) pegmatite belt in southeast Ireland. PhD Thesis, University College Dublin, Ireland, 287 p.

Charles N, et al. (2013) Rare earth elements in Europe and Greenland: a geological potential? An overview. Mineral deposit research for a high-tech world, 12th SGA Biennial meeting 4:4 p.

Cotterell T (2009) Supergene manganese mineralization associated with the Camdwr fault in the Central Wales orefield. *Journal of the Russell Society* 12:15-25.

Cuney M., et al. (2002) The timing of W-Sn –rare metals mineral deposit formation in the Western Variscan chain in their orogenic setting: the case of the Limousin area (Massif Central, France). In Blundell DJ, Neubauer E, Von Quadt A (ed) *the timing of major ore deposits in an evolving orogeny*, Geological Society, London, Special Publications 204, pp 213-228.

Eilu P, et al. (2012) Metallogenic areas in Finland. *Geological Survey of Finland, Special Paper* 53:207-342.

Ilickovic T, Schuster R, Mali H, Petrakakis K, Schedl A (2017) Spodumene bearing pegmatites in the Austroalpine unit (Eastern Alps): distribution and new geochronological data. *Geophysical Research Abstracts*, EGU2017-7235, 19: Program with Abstract.

Manthiram A, Yu X, Wang S (2017) Lithium battery chemistries enabled by solid-state electrolytes. *Nat Rev Mater* 2:16103p.

Melleton J, Gloaguen E, Frei D, Novák M, Breiter K (2012) How are the emplacement of rare-element pegmatites, regional metamorphism and magmatism interrelated in the Moldanubian Domain of the Variscan Bohemian Massif Czech Republic. *Can Mineral* 50:1751-1773.

Neace ER, Nance RD, Murphy JB, Lancaster PJ, Shail RK (2016) Zircon La-ICPMS geochronology of the Cornubian Batholith, SW England. *Tectonophysics* 681:332-352.

Romer RL, Kirsch M, Kroner U (2011) Geochemical signature of Ordovician Mn-rich sedimentary rocks on the Avalonian shelf. *Can J Earth Sci*, 48:703-718.

Simić V, Andrić N, Životić D, Rundić L (2017) Evolution of Neogene Intramontane basins in Serbia. Pre-meeting Field trip B1 Abstract, 1p.

Stanley C, Jones GC, Rumsey MS, Blake C, Roberts AC, Stirling JAR, Carpenter GJC, Whitfield PS, Grice JD, Lepage Y (2007) Jadarite, LiNaSiB3O7(OH), a new mineral species from the Jadar Basin, Serbia. *Eur J Mineral* 19:575-580.

Stojadinovic U, Matenco L, Andriessen P, Toljic M, Rundić L, Ducea M (2017) Structure and provenance of Late Cretaceous-Miocene sediments located near the NE Dinarides margin: Interferences from kinematics of orogenic building and subsequent extensional collapse. *Tectonophysics* 710-711:184-204.

Wang DH, Li PG, Qu WJ, Yin LJ, Zhao Z, Lei ZY, Wen SF (2013) Discovery and preliminary study of the high tungsten and lithium contents in the Dazhuyuan bauxite deposit, Guizhou, China. *Science China. Earth Sci* 56:145-152.

Largest Spodumene lithium deposit of Western Europe

Catia G. Dias^{1,2}, Filipa L. Dias², Alexandre M. C. Lima^{1,2}

¹*Geosciences, Environment and Spatial Planning Department, Faculty of Sciences, University of Porto*

²*Institute of Earth Sciences – Porto Pole*

Abstract. Lithium (Li), as a strategic metal, is playing an important role in this century, mainly due to the growth prospect of Li-ion batteries for electric vehicles and for electricity storage (Low Carbon Technologies). Likewise, in this century, Portugal is considered an important and reliable Li source as a supplier for the European Union for its considerable quantity of lithium minerals and easily accessible location within Europe.

Li minerals are already being exploited at Barroso-Alvão Pegmatite Field (northern Portugal), which contains large amounts of spodumene, a Li-rich ore mineral.

Geochemical analysis has revealed that the Grandão pegmatite carries a spodumene mineralization (low tin and higher iron content) with absence of petalite.

Petrographic analysis highlighted different zones in the core section of the pegmatite: (i) shearing zones with microgranular spodumene, enriched in lithium content; (ii) non-affected zones with spodumene crystals larger than 2 mm.

Introduction

Lithium (Li) is a strategic metal with increasing importance due to the growth prospects of Li-ion batteries used in electric vehicles and for electricity storage (Low Carbon Technologies). The quantities of Li that Europe is expected to consume compromise its supply chain, meaning that sustained Li extraction and exploitation is fundamental in order to prevent Europe from a dependency on Li importation. Potential local suppliers in Europe are therefore of major importance.

Portugal is not far from becoming the major European source of Li, playing an important role in supporting the advancement of these Low Carbon Technologies (European Commission 2018)

Lithium minerals have been exploited in Portugal for a long time, but the majority of deposits were small local quarries simply for the ceramics and glass industry. However, the Barroso-Alvão aplite-pegmatite field (BAPF), in northern Portugal, contains large amounts of spodumene ($\text{LiAlSi}_2\text{O}_6$), a Li-rich ore mineral.

This work will present new geochemical data of the Grandão spodumene-bearing pegmatite, compared with previous data, proving that it is a spodumene-bearing vein similar to other bodies in the same field. Petrographic studies were also performed, to better understand its mineralogy and microstructures.

The knowledge of these veins can provide a better understanding of the BAPF, which can be very useful to enhance the importance of these resources and guarantee a full exploitation, minimizing unnecessary losses.

2 Geological Setting

The Barroso-Alvão aplite-pegmatite field (BAPF) is located in the Galicia Trás-os-Montes Zone (GTMZ), an essentially parautochthonous geotectonic zone using the classification proposed by Julivert et al (1974), but very close to the south boundary between the GTMZ and the Central Iberian Zone (CIZ) (Fig. 1). This region was affected by the Variscan orogeny, with three main deformation phases (D_1 , D_2 and D_3), leading to three superimposed schistositys (S_1 , S_2 and S_3) (Noronha et al. 1981). The first phase (D_1) is compressive and produces folds with NW-SE axis and vertical axial planes in the autochthonous terrains and differentiated vergence in parautochthonous terrains. The second phase (D_2) is tangential and induces sub-horizontal displacement with thrusts formation in the parautochthonous terrains and the obduction of ophiolite complexes in central Trás-os-Montes, and the third phase (D_3) covers all the terrains developing folds with subvertical axial planes (Ribeiro 1974; 2013).

Several types of granitic bodies outcrop near the pegmatite region, differing in composition and age: two-mica granites syn- D_3 (Cabeceiras de Basto granite; Barroso Granite) and post-tectonic biotite granites (Vila Pouca de Aguiar Massif) (Ferreira et al. 1987; Dias et al. 2010).

The BAPF contains several dozens of aplite-pegmatite dykes, whose size ranges from few to hundreds of meters, emplaced in low- to medium-grade Silurian metasedimentary rocks: quartziferous schists and micaceous schists with minor interbedded black schists (Ribeiro et al, 2000; Fig.1). The study area presents a prograde regional metamorphism of medium to low pressure and high temperature generated by the intrusion of the syntectonic Cabeceiras de Basto granite. The metamorphism isograds are parallel to this granite and to the lithostratigraphic units.

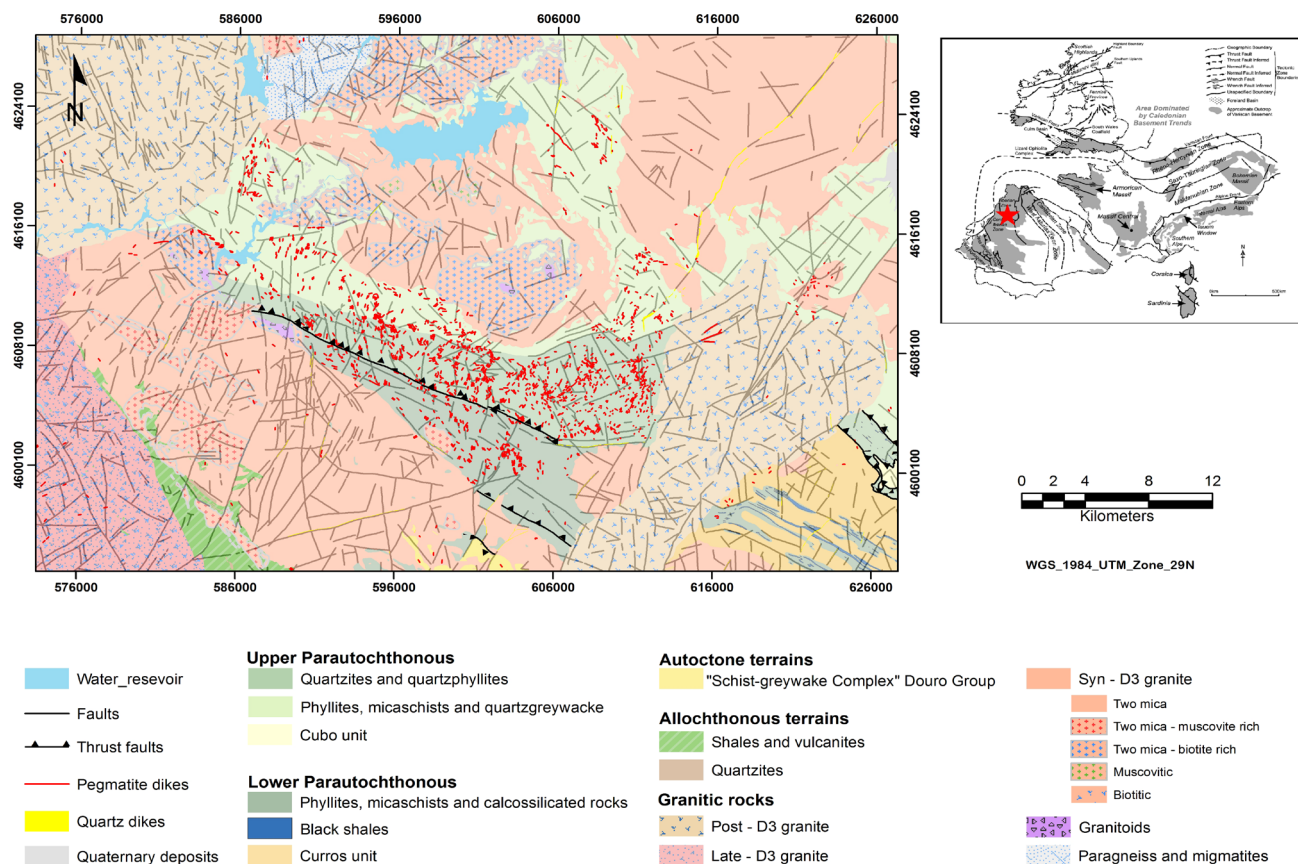


Figure 1. Geological setting of the Barroso-Alvão Aplite-pegmatite Field (Adapted from Silva 2014).

3 Pegmatites from the Barroso-Alvão pegmatite field (BAPF)

Five pegmatite types have been defined, by Martins (2009), according to their mineralogy, morphology, internal structure, relationship with hosting rock, and distribution: (i) intragranitic pegmatites; (ii) Li-barren pegmatites; (iii) Spodumene-bearing pegmatites; (iv) Petalite-bearing pegmatites; (v) Lepidolite-bearing pegmatites.

These pegmatites (excepting the intragranitic group) are hosted in low to medium grade metasedimentary rocks, exhibiting variable field relations among them. They belong to the rare element class and to the LCT family of Cerný and Ercit (2004).

Charoy et al. (1992) described these pegmatite bodies as concordant to highly discordant when compared to the host rocks; more or less deformed with variable dips, from vertical to flat-lying and with elongated or lenticular shape. Although the orientations vary, the veins are mainly controlled by S2 foliation, which has been locally deformed by S3 (crenulations with subvertical axial planes). The pegmatite emplacement suggests that the pegmatite-forming magma ascended along dilatation zones or preferential structural planes in the host rocks during and after the metamorphic peak (Charoy et al. 1992, 2001).

These bodies may be found with alternated textures from fine-grained (aplitic) to coarse-grained (pegmatitic)

and, therefore, are commonly called aplite-pegmatite veins. Generally, these bodies do not display an internal or even a regional zoning when considering their link to a parental granite (Charoy et al., 2001).

In the BAPF the major Li pegmatite mineralization corresponds to spodumene ($\text{LiAlSi}_2\text{O}_6$) and/or petalite ($\text{LiAlSi}_4\text{O}_{10}$), but there are also some outcrops with lepidolite ($\text{K}(\text{Li},\text{Al})_3(\text{Si},\text{Al})_4\text{O}_{10}(\text{F},\text{OH})_2$) in the northwest part of the BAPF (which will not be considered in this work).

Some of these aplite-pegmatites that carry tin (Sn) mineralization (cassiterite) are more aplitic in texture and are associated with petalite minerals, belonging to group iv, defined by Martins (2009). However, spodumene quartz intergrowths (SQI) can also be found within this type of Sn-bearing aplite-pegmatites and are thought to be formed by the breakdown of petalite (Cerný and Ferguson, 1972). This process could, for example, be explained by a drop of temperature during the normal process of the pegmatite cooling.

However, there is also another generation of Li aplite-pegmatite veins, presumably older, in this pegmatite field. These bodies have a different geochemical signature with less Sn and more iron (Fe), and usually have abundant spodumene crystals and no petalite. They are integrated in the group iii, according to Martins (2009). Moreover, these veins present a tendency to have more pegmatitic zones than the younger generation. Grandão, our case study, as Alijó and others falls in this last category (Fig. 2).

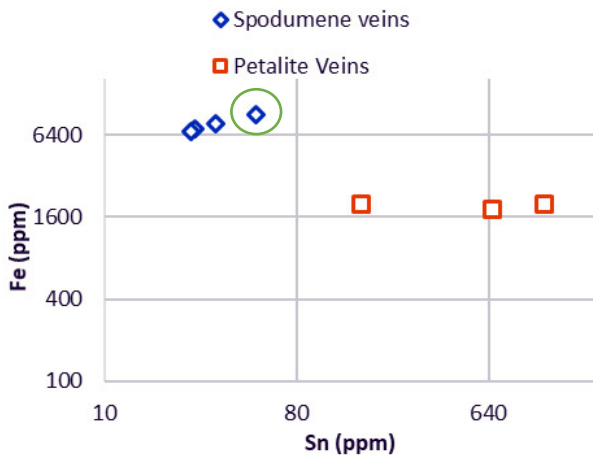


Figure 2. Iron (Fe) and tin (Sn) relation on a base-2 logarithmic scale. Elemental content from the whole-rock analysis of aplite-pegmatite veins at BAPF. Low Fe content and high Sn content indicates a petalite-bearing vein; high Fe content and low Sn content indicates a spodumene-bearing vein. Green circle represents Grandão pegmatite.

3.1 Spodumene pegmatites: Example of Grandão pegmatite

Grandão aplite-pegmatite is a large spodumene-bearing pegmatite, from Mina do Barroso, which is now a concession belonging to Savannah Lithium Lda, located in the BAPF. This concession has countless lithium-bearing pegmatite dykes that may contain petalite and/or spodumene. However, the Grandão aplite-pegmatite stands out because of its Li-mineralization (only spodumene which provides easier Li extraction when compared with petalite), its size and geometry.

This aplite-pegmatite is mainly sub-horizontal and covers an area of 600m north-south and 700m east-west and with a variable thickness from 10m-60m. The fact that it is so close to the surface, flat-lying and outcropping, makes this deposit an excellent opportunity for an open pit mining with low stripping ratio (fig. 3). The current mineral resource estimated for the Grandão Deposit is of 16.4Mt at 1.04% Li_2O for a total contained Li_2O of 171,400t.

3.1.1 Geochemistry and petrology of the Grandão pegmatite

The Grandão pegmatite geochemistry suggests a solely spodumene-bearing pegmatite with no petalite involved since it has an average of $\approx 0.91\%$ Fe and ≈ 51 ppm Sn (Savannah 2018).

An interesting fact about these pegmatites is that besides the spodumene crystals observed in the pegmatitic facies, the thin-sections from Grandão pegmatite drill cores have shown spodumene enrichments along preferential zones (fig. 4). These zones are sheared, which seems to have remobilized and concentrated lithium along them ($\text{Li}_2\text{O} \gg 3\%$). These shear zones contain very fine spodumene ($\sim 10 \mu\text{m}$) that occurs together with quartz. Although this particular texture could be described as Spodumene

Quartz Intergrowth (SQI) it does not seem to have any relation with former petalite crystals and therefore we can assume that it was formed at a later stage by Li remobilization from former bigger spodumene crystals.

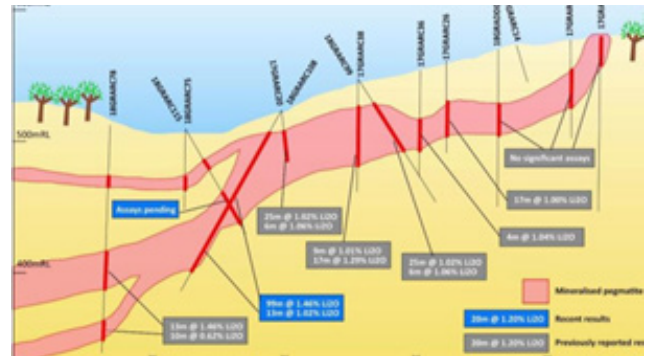


Figure 3. Grandão pegmatite cross section (Savannah 2018).

The major mineral phases observed in the thin sections were sodium-plagioclase (albite), quartz and spodumene and the accessory minerals include rare muscovite and potassium feldspar.

The mineral identification was confirmed by Backscattered Electron Detector (BSE) and Energy Dispersive X-Ray Spectrometry (EDS) analysis at the Materials Center of the University of Porto (CEMUP).

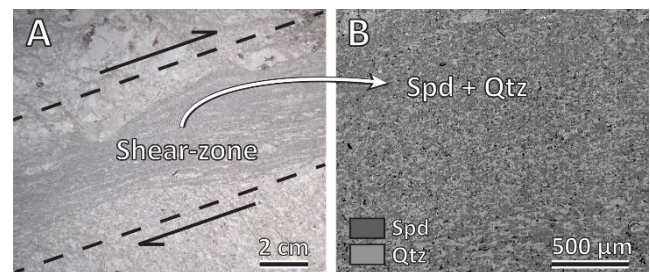


Figure 4. Thin-section made from chip cores of the Grandão pegmatite where a fine foliation marked by spodumene minerals (dark grey) can be observed as a result of strong deformation in a dextral shear zone (A) Stereo-binocular microscopy. (B) Backscattered electron image (BSE) focused on the fine foliation zone constituted by abundant spodumene (spd) together with quartz (qtz) in the proportion approximately 50%.

4 Final Remarks

The mineralogy of aplite-pegmatite veins from BAPF can be grouped in three different types, that carry Li mineralization: spodumene, petalite and lepidolite.

Grandão aplite-pegmatite geochemistry suggests a single lithium mineralization, being a spodumene-bearing pegmatite type, averaging Fe $\approx 0.91\%$ and Sn ≈ 51 ppm. Fe and Sn contents have the potential to provide a tool to define the potential of an unknown pegmatite, indicating if it is originally a spodumene-pegmatite or a spodumene-bearing vein where the spodumene formed by the breakdown of petalite. This small difference can be crucial to have an higher profit.

Moreover, petrographic studies led us to the conclusion that shear zones concentrate lithium

mineralization.

Therefore, these observations require further investigation to understand how, when and what type of pegmatite were affected by these ductile or brittle-ductile structures.

Acknowledgments

The authors of this paper appreciate the full collaboration and support of Savannah Lithium, Lda in this research. Work financially supported by FLAPSYS-Fiber Laser Plasma System for real time element analysis – POCl - 01 -0145 – FEDER – 031165.

References

- Černý, P, Ferguson R B (1972) The Tanco Pegmatite at Bernic Lake, Manitoba; IV, Petalite and Spodumene relations. *The Can Min* 11: 660-678.
- Černý P, Ercit T S (2005) The classification of granitic pegmatites revisited. *The Can Min* 43: 2005-2026.
- Charoy B, Lothe F, Dusaucy Y, Noronha F (1992) The crystal chemistry of spodumene in some granitic aplite-pegmatite from Northern Portugal. *The Can Min* 30: 639-651.
- Charoy B, Noronha F, Lima A (2001) Spodumene-Petalite-Eucryptite: mutual relationships and alteration style in pegmatite-aplite dikes from Northern Portugal. *The Can Min* 39: 729-746.
- Dias G, Noronha F, Almeida A, Simões P P, Martins H C B, Ferreira N (2010) Geochronology and petrogenesis of late-Variscan plutonism (NWPortugal): synthesis and inferences on crustal recycling and growth in the Central Iberian Zone. In: Coteló Neiva J M, Ribeiro A, Mendes Victor L, Noronha F, Magalhães Ramalho M (eds) *Ciências Geológicas: Ensino, Investigação e sua História*. Vol. I Geol Class 143-160 ISBN: 978-989-96669-0-0.
- European Commission 2018 Report on Raw Materials for Batteries Application SWD (2018) 245/2 final.
- Ferreira N, Iglesias M, Noronha F, Pereira E, Ribeiro A, Ribeiro M L (1987) Granitoides da Zona Centro Iberica e seu enquadramento geodinamica. In: F. Bea et al (eds) *Geologia de los Granitoides y Rocas Asociadas del Macizo*. Libro Homenaje a L.C. Garcia de Figuerola, Hesp Edit Rued 37-51.
- Julivert M, Fontbote J M, Ribeiro A, Conde L E (1974) Mapa tectónico de la Península Ibérica Y Baleares 1: 1 000 000. Memo exp Publicación IGME.
- Lima A, Vieira R, Martins T, Farinha J A, Noronha F, Charoy B (2003) Os filões applitopegmatíticos litiníferos da região Barroso-Alvão (Norte de Portugal). (Lithium-rich aplite pegmatite bodies from Barroso- Alvão region) Mem e Not, nº 2 (Nova Série) Public do DCT do MMG Univ de Coimbra, 169-190.
- London D (1984) Experimental phase equilibria in the system LiAlSiO₄-SiO₂-H₂O: a petrogenetic grid for lithium-rich pegmatites. *Am Min* 69: 995-1004.
- Martins T (2009) Multidisciplinary study of pegmatites and associated Li and Sn-Nb-Ta mineralisation from the Barroso-Alvão region. PhD Dissertation, University of Porto
- Noronha F, Ramos J M F, Rebelo J, Ribeiro A, Ribeiro M L (1981) Essai de corrélation des phases de déformation hercyniennes dans le NW de la Péninsule Iberique. *Leid Geol Meded* 52(1): 87-91.
- Ribeiro A (1974) Contribution à l'étude tectonique de Trás-os-Montes Oriental. (Contribution for the tectonic studies of Oriental Trás-os-Montes). Mem dos Serv Geol de Portugal, 24.
- Ribeiro, A. (2013) Evolução geodinâmica de Portugal: os ciclos ante-mesozóicos. (Geodynamic evolution of Portugal: pre-Mesozoic cycles) In: R. Dias, A. Araújo, P. Terrinha, J.C. Kullberg (Eds) *Geologia de Portugal Esc Edit* 1: 15-57.
- Ribeiro M A, Martins H C, Almeida A, Noronha F (2000) Carta geológica de Portugal, escala 1:50000, 6C (Cabeceiras de Basto). (Geological map of Portugal, scale 1:50000, 6C - Cabeceiras de Basto) Notícia Explicativa, Serv Geol de Port.
- Savannah Lithium Lda (2018) Continuity of Lithium Mineralisation Confirmed Through Further Drilling at the Grandao, Reservatorio and Pinheiro Deposits, at the Mina do Barroso Lithium Project. Report
- Silva D (2014) Spatial analysis applied to the Barroso-Alvão rare-elements pegmatite field (Northern Portugal). Master Thesis, University of Porto.

Tectono-magmatic constraints on tellurium-gold fertility, Fiji

Rose H. Clarke, Daniel J. Smith, David A. Holwell
University of Leicester, University Road, Leicester, UK

Jon Naden
British Geological Survey, Environmental Science Centre, UK

Stephen Mann
Lion One Metals, Waimalkia, Nadi, Republic of Fiji

Abstract. Low-sulphidation epithermal gold-telluride deposits form some of the world's largest and most important sources of both gold and tellurium. The association with a subset of these deposits with alkaline magmatism is well documented, but still poorly understood. Here we consider Fiji a type example of post-subduction extension related alkaline-hosted epithermal deposits, with the aim of constructing a process-based model for mineralisation. Preliminary findings from studies into the regional and local evolution, as well as mineralization styles and paragenesis are presented. This will aid further constraining of key processes in the model for their formation

1 Introduction

Tellurium is one of the rarest elements in the Earth's crust, along with the platinum-group elements (PGE) and Au (McDonough and Sun 1995), yet it is becoming increasingly significant in modern technology with uses in electronics, glass fibre, and perhaps most importantly, solar-PV panels.

Epithermal gold-telluride deposits, whilst rare, form some of the largest gold deposits in the world, with some gold tonnages exceeding 100t, e.g. Cripple Creek, Porgera, Vatukoula. Their exceptionally high grades and tonnages also extends to Te, making up some of the largest and most important deposits.

Specifically, they are found in low-sulphidation epithermal deposits associated with alkaline magmatism in post-subduction settings. This relationship has been studied for a century thanks to the presence of gold, however their endowment in critical and energy-critical elements including: Te, F, V, W, Bi, Sb and PGEs is becoming increasingly important (Pals and Spry 2003; Kelley and Spry 2016).

2 Current model for epithermal Au-Te deposits

Richards (2009) proposed a model for formation of these deposits, outlining the importance of the transition from subduction to post-subduction.

Subduction-associated basalts ascend, hit the base of the crust and stall in the MASH (melting, assimilation, storage and homogenization) zone. Here amphibole cumulates rich in chalcophile and siderophile elements,

are formed. Subduction may cease for a number of reasons; processes following cessation are determined by its cause. In the case of Fiji, post-subduction extension allows localized re-melting of asthenosphere and/or a shallow lithospheric root. Magmas encounter a boost of siderophile elements from the amphibole cumulates. Fluids formed in the upper crust may then form epithermal deposits, enriched in Te and Au.

3 Fiji case study

Although the model for post-subduction Au-Te mineralisation is theoretically robust, key causal and facilitating processes that define the model are poorly-constrained. Do the potassic, post-subduction magmas carry enhanced gold to the crust; if so is the enrichment owing to the tapping of a zone of fertility, or is it mantle derived?

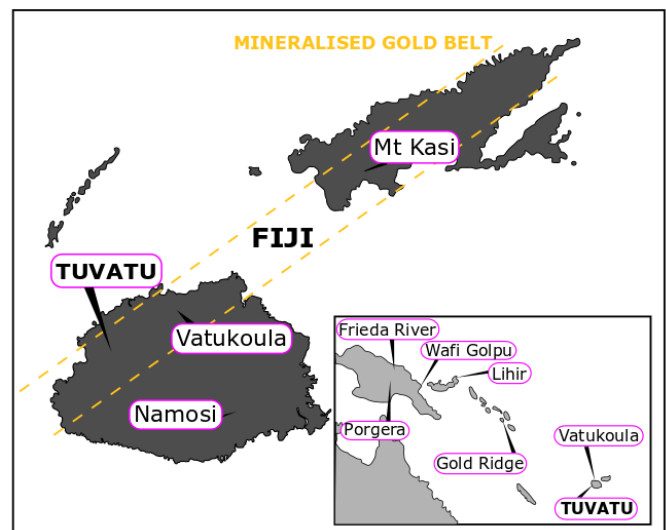


Figure 1. The mineralised gold belt, the Viti Levu Lineament shown on Viti Levu and Vanua Levu, with large mines annotated on. Inset: Western-Pacific islands with their respective large mines. All are epithermal Au-Te, or Cu / Cu-Au porphyries.

Fiji is the archetype for the post-subduction extensional deposits, and hence provides an exceptional case-study to support understanding. It is home to two major gold-telluride deposits (Vatukoula and Tuvatu; Figure 1) amongst other smaller mines and prospects along a >250 km mineralised belt, the Viti Levu

Lineament. Furthermore, due to its relatively young age and 'simple' oceanic-arc geology, lacking complications such as older interacting continental crust, or multiple phases of subduction, it is the perfect natural laboratory to study the model through petrology and mineralisation.

4 Tectonic setting

Fiji's setting is along the margin between the Pacific and Indo-Australian Plates, which consists of multiple microplates which have rapidly accreted to or become detached from the two major plates (Taylor *et al.* 2000). It is currently considered part of the Indo-Australian Plate. Current geographic location can be seen in Figure 2d.

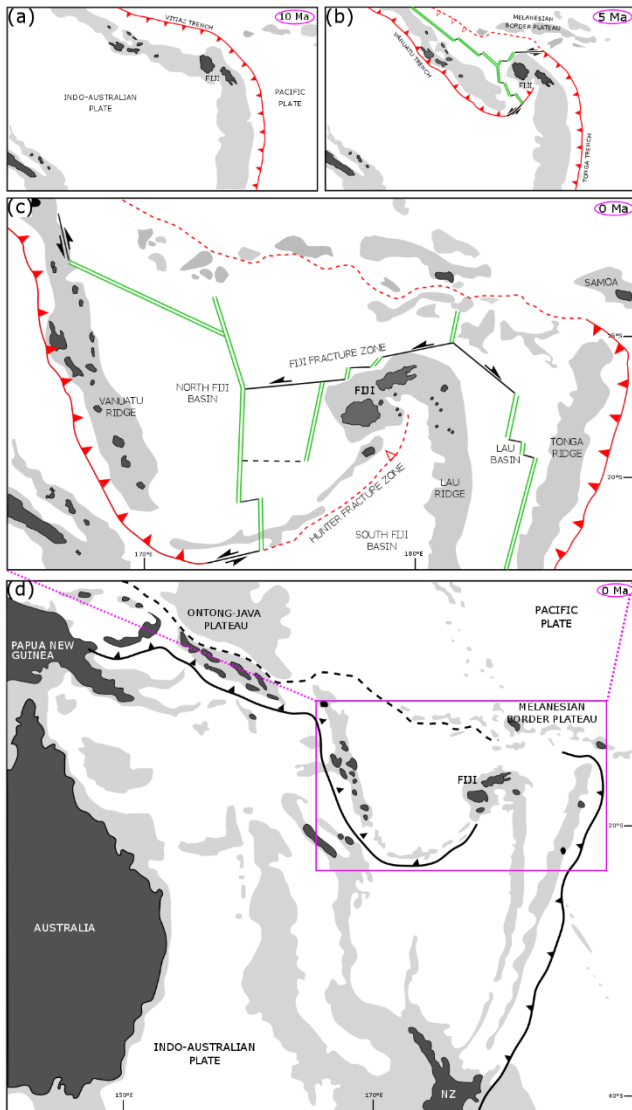


Figure 2. Tectonic configuration of Fiji showing the western-pacific islands and Ontong-Java Plateau; a more localized view of Fiji at present showing more complex plate boundaries; previous palinspastic reconstructions at 5 Ma and 10 Ma showing breakup of the previous Vitiav Arc.

The tectonic history can be split into 3 main stages which are comparable to those outlined in the model for ore formation (Figure 2): an arc phase, a transitional

phase and the remnant-arc phase.

Prior to the Late Miocene the Pacific Plate underwent subduction beneath the Indo-Australian Plate along the Vitiav Trench (Figure 2a). The oldest rocks in Fiji, the Yavuna Group, are of Late Eocene to Early Oligocene age (Hathway 1993); the lavas and intrusives record proto-arc activity (Wharton *et al.* 1995). Unconformably overlying this is the Wainimala Group (Hathway, 1993), 32-13 Ma, which is dominated by volcanic rocks representative of mature-arc activity.

Somewhere between 10–7.5 Ma active subduction beneath Fiji ceased with the oblique collision of both the Ontong-Java Plateau to the northwest and the Melanesian Border Plateau immediately north of Fiji itself (Hathway, 1993; Begg and Gray 2002). Subsequent events include: reversal of arc polarity and fragmentation (Gill and Whelan 1989); formation and propagation of a left-lateral transverse rift across the former Vitiav Arc, now between Vanuatu and Tonga (Gill and Whelan 1989); and rotation of Fiji, as can be seen from a–c in Figure 2 (Taylor *et al.* 2000),

Extension is now found north, east and west of Fiji (Figure 2c), primarily in the North Fiji Basin which may have initiated as early as 8 Ma, and the slightly younger Lau Basin (Stratford and Rodda 2000). Both ended direct subduction of the Pacific Plate beneath Fiji (Colley and Hindle, 1984).

Towards the very end of the Miocene 'post-subduction' shoshonitic lavas were erupted across Fiji (Gill and Whelan 1989), although their geochemical characteristics remained similar to subduction related rocks (Rogers and Setterfield, 1994). These rocks are associated with the mineralisation across Fiji. Their distribution suggests a strong NE-SW control due to faulting (Hathway 1993); the ascent of magma and subsequent eruptions have been attributed to movement through these deep-seated faults.

5 Magmatic setting

A significant amount of literature was produced on Fiji and Vatukoula in the 1980's in an attempt to characterize and understand the volcanic rocks, and their formation through subduction initiation, cessation and migration, as well as associated ore mineralogy. Whilst this produced some classic literature, little has been done since.

This study investigates the magmatic evolution of the extrusive and intrusive rocks, including both a regional scale study of Fiji, and a local scale study focusing on Tuvatu and the Navilawa caldera, incorporating comparisons to Vatukoula and the Tavua caldera. This will aid understanding of melt sources (and thus possibly ore-enriched sources) for post-subduction and shoshonitic magmas.

Preliminary results show distinct differences between subduction and post-subduction magmas. Post-subduction magmas have a stronger 'subduction

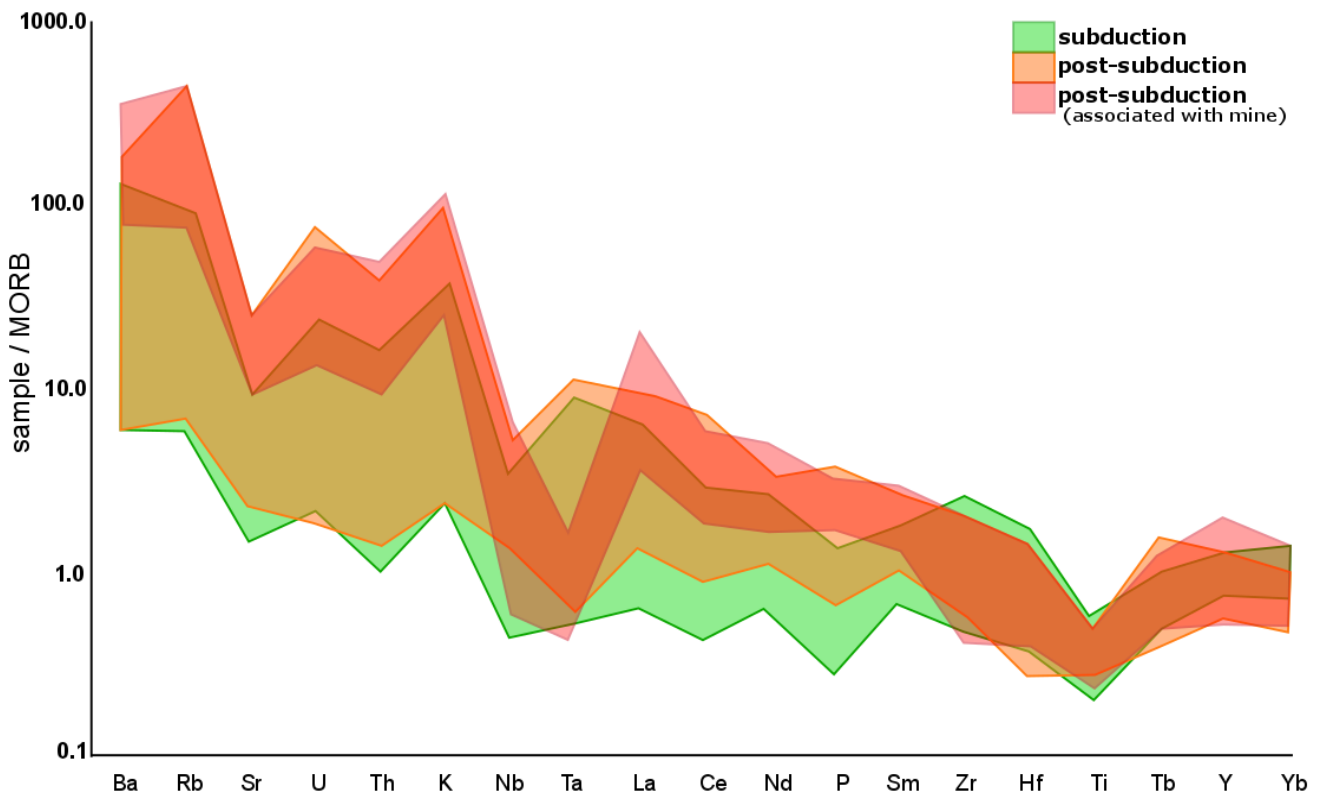


Figure 3. Multi-element diagram, showing the differences between magmatic rocks from during subduction in Fiji, post-subduction in Fiji, and post-subduction but with associated mines (Vatukoula and Tuvatu). Those associated with mineralisation especially show enrichments in LILE, particularly high K, a trough at Nb-Ta suggesting a metasomatised source. Overall however, there is still an arc-like signature.

signature' than those formed whilst active subduction was occurring. As well as being alkaline, they have an unusual potassic affinity, enrichments in LILE and low HFSE concentrations. These distinctions are even more pronounced in rocks at Tuvatu and Vatukoula, which are the post-subduction (associated with mine) data in Figure 3, which illustrates these differences.

This has previously been ascribed to enrichments from hydrous fluids from the subducting slab (Rogers and Setterfield 1994), though this was not considered with respect to mineralisation and potential implications for the economic geology of Fiji.

6 Mineralisation

The primary gold-telluride deposit being considered in the study is Tuvatu, although comparisons to the well-studied Vatukoula are also useful. A paragenesis for the Tuvatu deposit was constructed previously by Scherbarth and Spry (2006), and multiple iterations of a paragenesis of Vatukoula exist (e.g. Ahmad et al. 1987).

A link to nearby porphyry deposits has previously been postulated for both, but a closer look at spatial and temporal variation at the Tuvatu deposit suggest lodes within the Tuvatu mining license area have porphyry affinities themselves, with some samples hosting exclusively copper sulphides.

Multiple stages of mineralization within the epithermal deposit, identified through characterization using SEM and reflected light microscopy, include Pb-Zn-Cu sulphide mineralization, associated telluride mineralization, which in some places appears to overprint the sulphides, and later stage quartz veining which now hosts native gold and electrum.

Whilst it is known that the majority of gold at both deposits resides in auriferous pyrites, tellurides and occasionally occurs as native gold, mass balances have not been completed. Furthermore, zonation models and wall-rock interactions need (and are being) refined, so that the near-mine environment can be better understood. This will feed into constraining the aforementioned processes.

7 Summary

Fiji as a whole is a classic post-subduction, alkaline, gold-telluride district and hence provides an opportunity to study the key ore-forming processes so they may be constrained properly. Minor differences between Fiji and other deposits worldwide, such as Fiji's atypical potassic affinity and Tuvatu's abundance of exotic vanadium-bearing minerals also mean that comparisons between local, regional and global models can be interrogated.

Acknowledgements

This PhD project is funded by NERC CENTA DTP, with extra funding from the BGS University Funding Initiative (Project S392) and TeaSe. Thanks to Lion One Metals Ltd for allowing access to core from Tuvatu and geological insight, and Vatukoula Gold Mines PLC for allowing access and permission to publish and present this work. JN publishes with permission of the Executive Director, British Geological Survey, NERC

References

- Ahmad M (1987) Mineralogical and Geochemical Studies of the Emperor Gold Telluride Deposit, Fiji. 82.
- Begg G, Gray D R (2002) Arc dynamics and tectonic history of Fiji based on stress and kinematic analysis of dikes and faults of the Tavua Volcano, Viti Levu Island, Fiji. *Tectonics* 21:5-5-14.
- Colley H, Hindle W H (1984) Volcano-tectonic evolution of Fiji and adjoining marginal basins. Geological Society, London, Special Publications 16: 151.
- Gill J, Whelan P (1989) Early rifting of an oceanic island arc (Fiji) produced shoshonitic to tholeiitic basalts. *Journal of Geophysical Research: Solid Earth* 94:4561-4578.
- Hathway B (1993) The Nadi Basin: Neogene strike-slip faulting and sedimentation in a fragmented arc, western Viti Levu, Fiji. *Journal of the Geological Society* 150:563.
- Kelley K D, Spry P G (2016) Critical Elements in Alkaline Igneous Rock-Related Epithermal Gold Deposit. *Reviews in Economic Geology* 18:195-216.
- McDonough W F, Sun S -s (1995) The composition of the Earth, *Chemical Geology* 120:223-253.
- Pals D W, Spry P G (2003) Telluride mineralogy of the low-sulfidation epithermal Emperor gold deposit, Vatukoula, Fiji. *Mineralogy and Petrology* 79:285-307.
- Richards J P (2009) Postsubduction porphyry Cu-Au and epithermal Au deposits: Products of remelting of subduction-modified lithosphere. *Geology* 37:247-250.
- Rogers N W, Setterfield T N (1994) Potassium and incompatible-element enrichment in shoshonitic lavas from the Tavua volcano, Fiji. *Chemical Geology* 118:43-62.
- Scherbarth N L, Spry P G (2006) Mineralogical, Petrological, Stable Isotope, and Fluid Inclusion Characteristics of the Tuvatu Gold-Silver Telluride Deposit, Fiji: Comparisons with the Emperor Deposit. *Economic Geology* 101:135-158.
- Taylor G, Gascoyne K, and Colley H (2000) Rapid rotation of Fiji: Paleomagnetic evidence and tectonic implications. *Journal of Geophysical Research* 105:5771-5781
- Wharton M R, Hathway B, Colley H (1994) Volcanism associated with extension in an Oligocene--Miocene arc, southwestern Viti Levu, Fiji. Geological Society, London, Special Publications 81:95.

Pb-Sb/As sulfosalts from Săcărâmb Au-Ag-Te ore deposit (Romania)

George Dinca^{1,2}, Gheorghe C. Popescu¹, Daniel Birgaoanu^{3,4}, Oana-Claudia Ciobotea-Barbu^{5,6}

¹Dept. of Mineralogy, Faculty of Geology and Geophysics, University of Bucharest

²University of Bucharest, Research Center for Ecological Services (CESEC)

³Department of Geology, Faculty of Geography and Geology, "Alexandru Ioan Cuza" University

⁴Geological Institute of Romania

⁵University Politehnica of Bucharest, Faculty of Applied Chemistry and Materials Science, Depart. Of Inorganic Chemistry, Physical Chemistry and Electrochemistry

⁶Geological Institute of Romania

Abstract. Pb-Sb/As sulfosalts are commonly present in many hydrothermal gold deposits and can provide important physicochemical constraints on the metallogenesis. The abundant alabandite and gold-silver telluride veins in the Săcărâmb Au-Ag-Te deposit of the Metaliferi Mountains Neogene (Romania) contain an assemblage of sulfides, sulfosalts and tellurides. Pb-Sb/As-sulfosalts are characterized by replacement textures resulting from changes of fluid composition and mainly include bournonite-seligmannite, geocronite-jordanite, nagyagite, galena and tellurides. New Pb-Sb/As sulfosalts for Săcărâmb have been discovered: fullopite, falkmanite, robinsonite, liveingite and zinkenite. Furthermore, the presence of plagionite was chemically confirmed. These sulfosalts have direct contact with tellurides and the Sb-rich sulfosalts are found as inclusions in the alabandite, indicating that the Săcărâmb metallogenesis had antimony even in the sulfide stages. The sulfosalt assemblages also reveal that in the late stage of mineralization, the activity of arsenic and antimony was increased and influenced the telluride deposition conditions.

1 Introduction

Located in the south-eastern part of the Apuseni Mountains, Săcărâmb represents the most complex ore deposit from the South Apuseni Mountains (Metaliferi Mountains). This ore deposit is known for its Au-Ag-telluride assemblages and for the number of minerals identified (over 100 minerals; Udubasa et al. 2002). Despite having a long history of mineralogical research, Săcărâmb still has the potential for expanding its mineral catalogue.

This paper presents the discovery of new Pb-Sb/As sulfosalts from Săcărâmb ore deposit and brings a better understanding of the relationship between the sulfosalt and telluride assemblages.

2 Materials and Methods

To perform this study, over 50 polished sections of ore samples, collected from the Săcărâmb ore dumps were

analyzed by optical microscopy in reflected light. The optical microscope used was a Leitz Wetzlar reflected light microscope. For the determination of the chemical

composition, a scanning electron microscope (SEM) Zeiss Merlin with an attached EDS detector was used at the Geological Institute of Romania. The parameters of the SEM analysis were: acceleration voltage ranging between 15 and 20 kV, the electron beam intensity of 1–2 nA, background time of 20 s and using the Oxford Instruments X-MAX 50 EDS detector.

3 Results

All of the described sulfosalt associations were discovered in rhodochrosite-quartz veins that cut massive alabandite or are included in the alabandite.

The most common Pb-Sb/As sulfosalts identified at Săcărâmb are part of the bournonite-seligmannite series and geocronite-jordanite series. Both series are usually found together substituting galena crystals. Bournonite crystals can form large clusters (up to 1.5 cm), furthermore, the crystals show zonation, caused by Sb/As substitution. The chemical analyses of geocronite and jordanite from Săcărâmb indicate the existence of approximately perfect end members of the series (Table 1).

In bournonite and geocronite crystals, inclusions of tellurides and Te-sulfosalts have been identified: krennerite, sylvanite, nagyagite, goldfieldite and hessite.

Table 1 Representative chemical composition of bournonite (bnn), seligmanite (sel), geocronite (geo) and jordanite (jord) from Săcărâmb (wt%)

Element	bnn	sel	geo	jord
Cu	15.70	16.79	-	-
As	3.77	13.09	2.76	8.78
Sb	18.02	4.58	10.98	3.02
Pb	45.56	45.9	71.08	72.15
S	17.06	19.63	15.3	16.04
Total	100.00	100.00	100.00	100.00

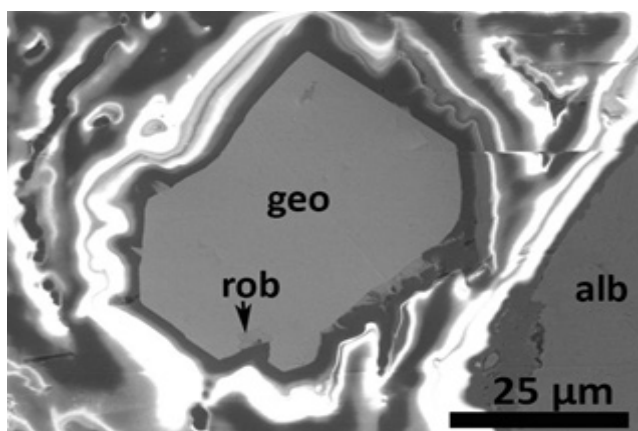


Figure 1. SEM-SE image of a geocronite (geo) and robinsonite (rob) in the rhodochrosite vein.

Zinkenite was found in association with galena and other Pb-Sb/As sulfosalts (boulangerite, geocronite) (Fig. 2). In one sample, zinkenite is developed on a krennerite crystal. Almost all of the analyzed zinkenite crystals from Săcărâmb contain arsenic in their chemical composition (Table 2). On the basis of 53 atoms, the empirical formula for zinkenite from Săcărâmb is $Pb_9Sb_{21.92}As_{3.62}S_{42}$.

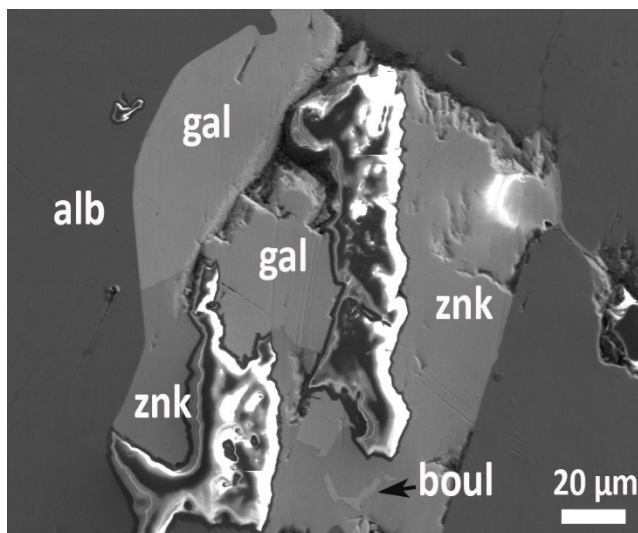


Figure 2. SEM-SE image of an association of galena (gal), zinkenite (znk) and boulangerite (boul) in alabandite (alb)

Benavidesite was identified frequently in the studied samples. It fills vugs together with rhodochrosite in the alabandite ore. In some samples, acicular benavidesite crystals have been found as an inclusion in alabandite (Fig. 3). Benavidesite from Săcărâmb has almost no iron in its composition, indicating that the iron present in alabandite did not participate in the sulfosalt formation stage (Table 2). Iron is found in marcasite and colomorph pyrite that fill corroded zones of alabandite. On the basis of 25 atoms, the empirical formula for benavidesite from Săcărâmb is $Pb_{4.1}Mn_{1.1}Sb_{5.68}S_{12.6}$.

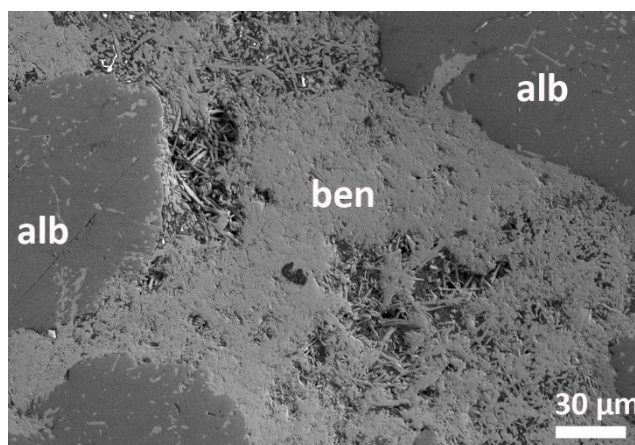


Figure 3. SEM-SE image of a mass of acicular benavidesite (ben) crystals in alabandite (alb)

Table 2 Representative EDS analyses of benavidesite (ben) and zinkenite (znk) from Săcărâmb (wt%)

Element	ben	ben	znk	znk
Mn	2.84	3.20	-	-
As	-	-	5.00	4.69
Sb	34.18	34.49	36.38	42.80
Pb	42.76	41.89	37.25	30.77
S	20.22	20.41	21.38	21.75
Total	100.0	100.0	100.0	100.0

Boulangerite and falkmanite were observed as inclusions in other lead sulfosalts (Fig. 2, 4). Boulangerite crystals from Săcărâmb have arsenic in their chemical composition similar to zinkenite (Table 3). The empirical composition of boulangerite and falkmanite from Săcărâmb are $Pb_{4.83}Sb_{3.57}As_{0.56}S_{9.12}$ and $Pb_{5.5}Sb_{3.93}S_{10.57}$.

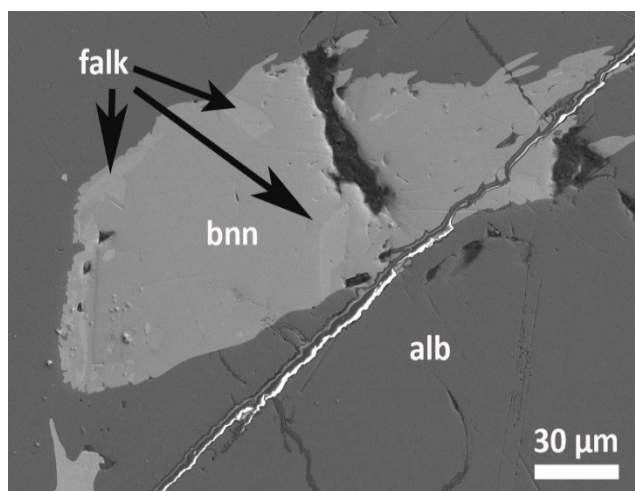


Figure 4. SEM-SE image of falkmanite (falk) crystals included in bournonite (bnn).

Robinsonite was identified in one sample as small crystals (under 5 μm) in association with geocronite and solitary in the carbonate veins (Fig. 1, 5). The calculated formula of robinsonite on the basis of 23 atoms is $Pb_{4.26}Sb_{5.86}S_{12.88}$ (Table 3).

Table 3 Representative EDS analyses of boulangerite (boul),

falkmanite (falk) and robinsonite (rob) from Săcărâmb (wt%)

Elem	boul	boul	falk	rob	rob
As	-	2.6	-		
Sb	26.8	27.3	24.3	35.1	36.4
Pb	55.0	53.1	58.3	44.1	43.3
S	18.2	17.1	17.4	20.8	20.2
Total	100	100	100	100	100

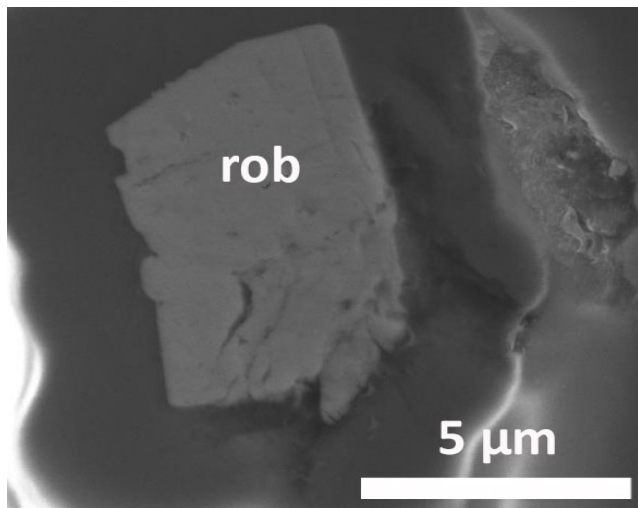


Figure 5. SEM-SE image of robinsonite (rob) in the rhodochrosite vein.

Liveingite, a rare sulfosalts was discovered at Săcărâmb, substituting galena crystals in the rhodochrosite veins. In reflected light the most striking feature observed is the abundant red internal reflections (Fig. 6). Liveingite from Săcărâmb has in its chemical composition antimony (Tab 4) similar to zinkenite where arsenic is present in the composition. This constant substitution between arsenic and antimony shows a frequent fluctuation of the ore forming fluid. The calculated formula of liveingite on the basis of 50 atoms is $Pb_{9.16}As_{12.59}Sb_{0.8}S_{27.45}$.

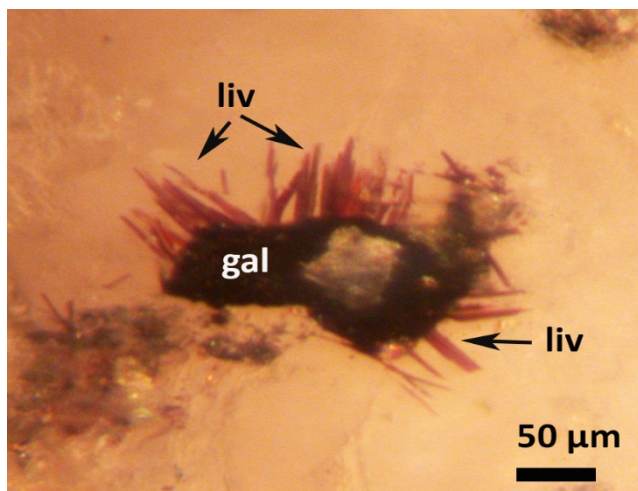


Figure 6. Cross-polarized photomicrograph in reflected light of liveingite (liv) crystals growing on galena (gal).

Plagionite was mentioned to be present at Săcărâmb

by Helke in 1934 but it was not confirmed. In this study, it was observed and confirmed to be present at the Săcărâmb ore deposit. Plagionite crystals were discovered together with tellurides and Te-sulfosalts. The most common association is with nagyagite, where it appears as inclusions within, or forming on the nagyagite crystals (Fig. 7). Arsenic has been detected in the analyses of plagionite from Săcărâmb, as in the other Pb-Sb sulfosalts (Table 4). The calculated empirical formula on the basis of 20 atoms of plagionite from Săcărâmb is $Pb_{5.25}Sb_{7.28}As_{0.91}S_{16.55}$.

Table 5 Representative EDS analyses of liveingite (liv) and plagionite (plg) from Săcărâmb (wt%)

Element	liv	liv	plg	plg
As	23.80	23.90	3.11	3.71
Sb	3.86	3.90	33.66	33.82
Pb	48.52	48.91	42.65	41.43
S	23.82	23.29	20.58	21.04
Total	100.00	100.00	100.00	100.00

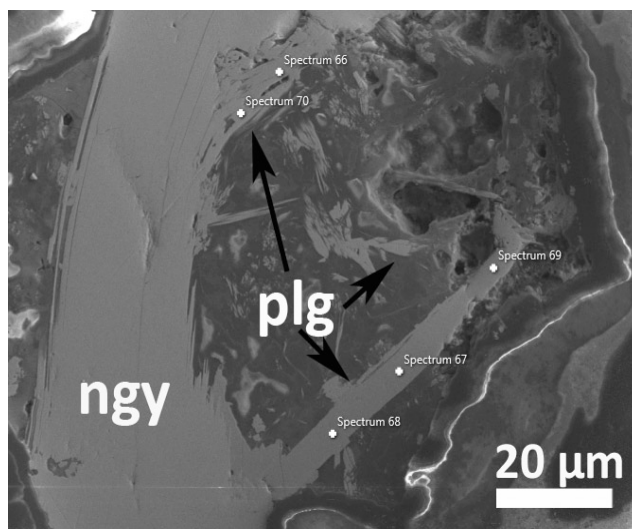


Figure 7. SEM-SE image of an association of nagyagite (ngy) and plagionite (plg).

Other rare Pb-Sb/As sulfosalts identified at Săcărâmb are fullopite and heteromorphite. Fullopite was found in only one sample, it is associated with famatinite and tennantite (Fig. 8). The empirical formula $Pb_{2.86}Sb_{8.07}As_{0.7}S_{14.36}$, was calculated on the basis of 26 atoms. Heteromorphite was observed in two samples from Săcărâmb. In the first sample, it is associated with nagyagite as inclusions in alabandite and in the second sample, it was found as an inclusion in bournonite. The empirical formula of heteromorphite on the basis of 24 atoms is $Pb_{7.05}Sb_{8.51}As_{0.59}S_{18.26}$. Both sulfosalts present arsenic in their composition.

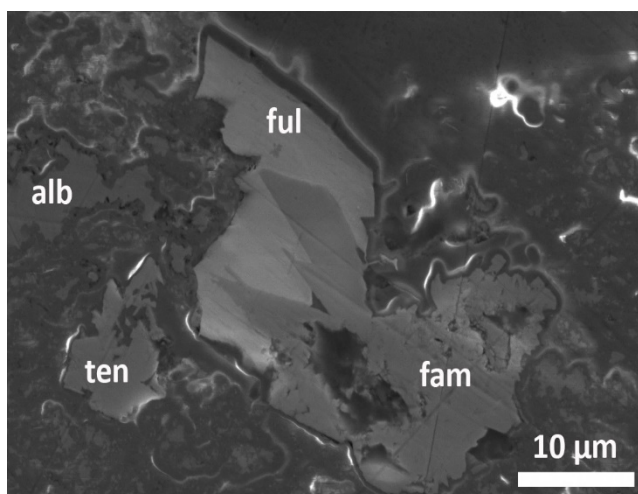


Figure 8. SEM-SE image of an association of fullopite (ngy), famatinite (fam), tennantite (ten) and alabandite (alb).

Table 5. Representative EDS analyses of fullopite (ful) and heteromorphite (het) from Săcărâmb (wt%)

Element	ful	ful	het	het
As	0.84	2.09	-	1.41
Sb	47.83	46.70	34.12	32.09
Pb	30.08	29.06	47.59	47.47
S	21.25	22.16	18.28	19.03
Total	100.00	100.01	100.00	100.00

4 Conclusion

Oscillatory zoning bands in bournonite crystals and As/Sb presence in the chemical composition of zinkenite, liveingite, fullopite, heteromorphite and plagionite indicate increased activity of Sb and As in ore fluids during the late stage of the mineralization.

Lead sulfosalts that are included in the massive alabandite, have little to no arsenic in their composition. Based on these observations we can assume that in the early stages antimony was dominant and in the late stage arsenic invaded the fluid. Pb-Sb/As sulfosalts from Săcărâmb ore deposit is most of the time found together with tellurides. Tellurides can be found as inclusions in the sulfosalts, and vice versa.

A new occurrence of Pb-Sb/As minerals has been identified, and chemically described at Săcărâmb: fullopite, zinkenite, heteromorphite, robinsonite and liveingite. Furthermore, plagionite was for the first time, chemically confirmed after its initial discovery at Săcărâmb by Helke in 1934.

Acknowledgements

We thank Eldorado Gold Corporation for the access on the Săcărâmb mine dumps. and the Microcosmos Laboratory, Geological Institute of Romania, for the SEM-EDS chemical analyses and SEM images. Data processing and the writing of the paper were done within the complex project INTER-ASPA, PN III, 34PCCDI/2018.

References

- Helke A. (1934) Die Goldtellurezlagerstätten von Săcărâmb (Nagyag) in Rumanien. N. J. Min. Geol. Pal., Beil. Band, 68, Abt. a, 19-85, Stuttgart.
- Udubaşa G., Đud'a R., Szakáll S., Kvasnytsya V., Koszowska E., Novák M., (2002) Minerals of the Carpathians. Granit, Prague

Pt- and Pd-bismuthotellurides: phase relations in the Pt-Bi-Te and Pd-Bi-Te systems

Polina V. Evstigneeva, Maximilian S. Nickolsky
IIGEM RAS, Russia

Natalia V. Geringer
Dubna State University, Russia

Anna Vymazalová
Czech Geological Survey, Czech Republic

Aleksey N. Nekrasov
IEM RAS, Russia

Dmitriy A. Chareev
IEM RAS, Russia
Ural Federal University, Russia
Kazan Federal University, Russia

Abstract. The phase relations in the Pt-Bi-Te and the Pd-Bi-Te systems have been studied in the temperature range of 350–550°C. In the case of the Pt-Bi-Te system, neither the mineral maslovite (PtBiTe), nor ternary phases were detected. In addition, maslovite was not obtained, even if Pd was involved in the system. Five solid solutions: ss-PtTe₂, ss-PtTe, ss-Pt₃Te₄, ss-Pt₂Te₃, ss-PtBi₂ forming all phase relations in the system have been found. The Pd-Bi-Te system has been studied in the PdBi – PdTe – Te – Bi region. Three solid solutions were found on the PdTe₂-PdBi₂ line: ss-PdTe₂, ss-PdBiTe and ss-PdBi₂. Besides, in the Pd-Bi-Te system, ss-PdTe – ss-PdBi equilibrium was detected; ss-PdTe has a wide range of homogeneity across all components.

1 Introduction

The tellurides of palladium, platinum and bismuth occur commonly in Cu-Ni-PGE mineral deposits associated with mafic and ultramafic igneous rocks but also can be found in less traditional environments e.g. porphyry copper deposits.

Platinum and palladium often accompany each other. In particular, there are close associations between Pt- and Pd-bismuthotellurides in nature (e.g. Viljoen et al. 2015). There are a number of natural phases that fall into the compositional fields of kotulskite (PdTe) – sobolevskite (PdBi), merenskyite (PdTe₂) – moncheite (PtTe₂), moncheite (PtTe₂) – maslovite (PtBiTe) series.

The kotulskite – sobolevskite series was reported by e.g. Evstigneeva et al. (1975), Cook et al. (2002) from Noril'sk; Kingston (1966) from Merensky Reef; Viljoen (2015) from Akanany project in northern Bushveld complex, among many other deposits.

Merenskyite – moncheite series are described by Zhu et al. (2010) in Xinjie layered intrusion in the Pan-Xi area of the Sichuan Province (SW China).

The moncheite – maslovite series was reported

Viljoen et al. (2015) in Akanany project in northern Bushveld complex.

The study of phase relations in the Pt-Bi-Te and Pd-Bi-Te systems is a crucial task. Information about phase relations in these systems will help to understand the conditions of their formation, as well as to predict stable mineral complexes in natural conditions.

The data on phase relations in the Pt-Bi-Te and Pd-Bi-Te systems are not complete (Vymazalová and Chareev 2018). The Pt-Bi-Te system has not been studied experimentally yet, only the phase relations in binary systems and a ternary mineral maslovite (PtBiTe, cubic, $a = 6.689 \text{ \AA}$; Kovalenker et al. 1979) are known.

The Pd-Bi-Te system is better studied compared to the Pt-Bi-Te system. The system has been studied by El-Boragy and Shubert (1970) in the Pd-rich corner at 480°C and by Hoffman and MacLean (1976) in the region Te-Bi₄Te₃-Bi₆₀Pd₄₀-PdTe at 480°C. In this system is the ternary mineral michenerite (PdBiTe, cubic, $a = 6.65 \text{ \AA}$).

In this study were present the phase relations in the Pt-Bi-Te and Pd-Bi-Te systems in the temperature range of 350–550°C at their own vapor pressure (nearly atmospheric pressure).

2 Materials and methods

The investigation of phase equilibria was carried out by analysis of quenched products obtained by the solid synthesis method. The synthesis was conducted from the pure elements in silica-glass evacuated ampoules ($\sim 10^{-4}$ bar). The mass of each sample was averaged ~ 400 mg. The ampoules with charges were heated in horizontal tube furnaces for 30–120 days, with one re-grinding during the experiment. The experimental run products were rapidly quenched in cold water.

Examination of run products was carried out using electron microscope with EDX system (TESCAN VEGA II XMU electron microscope) in polished sections and using powder X-Ray diffractometry (XRD, CuK α , Fe filter).

3 Results and discussion

3.1 The Pt-Bi-Te system

Based on the literature data on binary systems (Table 1) (Babanly et al. 2017; Okamoto 1991; 1994) and our experimental data three isothermal sections were assessed: at 350, 450 and 550°C. It was found that in the entire temperature range (and even at 200°C) there is no maslovite (PtBiTe) synthetic analogue or any ternary phases. Five solid solutions were observed: ss-PtTe₂ (with moncheite structure), ss-PtBi₂ (with insizwaite structure), ss-Pt₃Te₄ (analogue of the mitrofanovite), ss-PtTe and ss-Pt₂Te₃.

Table 1. Phases, their mineral analogues and temperature stability in the Pt-Te, Pt-Bi, Bi-Te and Pt-Bi-Te systems.

Phase	Mineral	Temperature stability, °C	Reference
<i>Pt-Te system</i>			
PtTe	–	<957	
PtTe ₂	Moncheite	<1147	Okamoto 1994
Pt ₂ Te ₃	–	<737	
Pt ₃ Te ₄	Mitrofanovite	<1017	
<i>Pt-Bi system</i>			
PtBi	–	<765	
α-PtBi ₂	–	<269	
β-PtBi ₂	Insizwaite	269–420	Okamoto 1991
γ-PtBi ₂	–	420–640	
δ-PtBi ₂	–	640–660	
Pt ₂ Bi ₃	–	570–685	
<i>Bi-Te system</i>			
Bi ₁₄ Te ₆ (Bi ₇ Te ₃)	Hedleyite	<312	
Bi ₂ Te	–	<375	
Bi ₄ Te ₃	–	<450	
BiTe	Tsumoite	<520	Babanly et al. 2017
Bi ₈ Te ₉	–		
Bi ₆ Te ₇	–	<540	
Bi ₄ Te ₅	Pilsenite	<562	
Bi ₂ Te ₃	Tellurobismuthite	<586	
<i>Pt-Bi-Te system</i>			
PtBiTe	Maslovite	–	Kovalenker et al. 1979

Three phase associations, that have been experimentally confirmed are: ss-PtTe₂ – Te(L)-Bi_xTe_{1-x}; ss-PtTe₂ – Bi_xTe_{1-x} – Bi(L); ss-PtTe₂ – Bi(L) – ss-PtBi₂; ss-PtTe₂ – ss-PtBi₂ – PtBi and ss-PtTe₂ – PtBi – Pt.

Three phase associations that have not been experimentally confirmed are ss-PtTe₂ – Pt – ss-Pt₂Te₃ and ss-PtTe – Pt – ss-Pt₃Te₄.

It is important that the determination of phase relations in the Pt-rich corner was complicated by the low kinetics associated with the metallic platinum presence and an

absence of the liquid phases. On the contrary, the Bi-rich corner is characterized by high kinetics. In a number of experiments Bi-Te phases released during cooling of the Te-rich bismuth melt (Fig. 1).

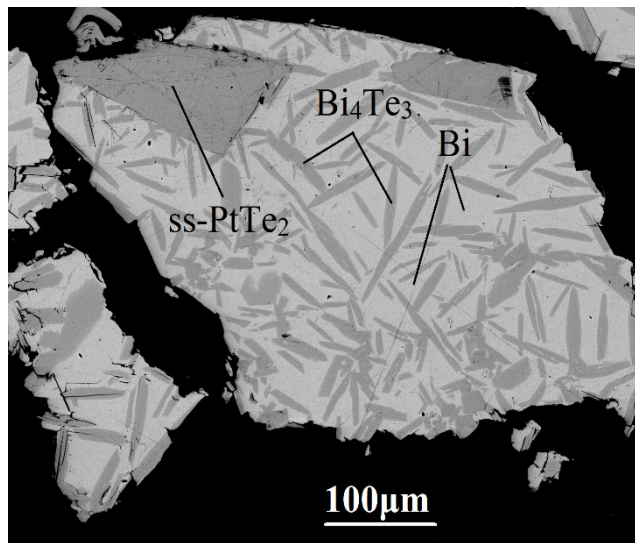


Figure 1. Back-scattered electron image of ss-PtTe₂ – Bi(L) phase association and Bi₄Te₃ released during bismuth melt cooling.

The phase relations in the system do not change significantly with a temperature decrease. Only the composition of the equilibrium phases change.

3.2 The Pd-Bi-Te system

In the case of the Pd-Bi-Te system, the PdBi – PdTe – Te – Bi part of phase diagram was studied. The binary phases were studied prior the ternary system (Table 2) based on Babanly et al. (2017), Okamoto (1992; 1994) and on our experiments series.

It was found that there are three solid solutions on the PdTe₂ – PdBi₂ line: ss-PdTe₂ (merenskyite structure), ss-PdBiTe (michenerite structure) and ss-PdBi₂. In addition, the ss-PdTe – ss-PdBi (kotulskite – sobolevskite) association was detected; ss-PdTe has a wide homogeneity range across all components.

As in the case of Pt-Bi-Te system the Bi-rich corner is characterized by high kinetics. However, in this case not just various bismuth tellurides are released during the cooling of the bismuth melt, but also other phases like ss-PdBiTe and ss-PdBi₂ (Fig. 2-3).

Table 2. Phases, their mineral analogues and temperature stability in the Pd-Te, Pd-Bi, Bi-Te and Pd-Bi-Te systems.

Phase	Mineral	Temperature stability, °C	Reference
<i>Pd-Te system</i>			
Pd ₁₃ Te ₃	—	<770	
Pd ₃ Te	—	727–785	
Pd ₂₀ Te ₇	Keithconnite	<750	
Pd ₈ Te ₃	—	563–905	
Pd ₇ Te ₃	—	<495	
Pd ₉ Te ₄	Telluropalladinite	<472	
Pd ₃ Te ₂	—	<507	
PdTe	Kotulskite	<746	
PdTe ₂	Merenskyite	<752	
<i>Pt-Bi system</i>			
α-BiPd ₃	—	<800	
β-BiPd ₃	—	800–935	
Bi ₁₂ Pd ₃₁	—	550–605	
Bi ₂ Pd ₅	—	<550	
γ (Bi ₃ Pd ₅)	—	400–683	Okamoto 1994
α-BiPd	—	<210	
β-BiPd	Sobolevskite	210–618	
α-Bi ₂ Pd	Froodite	<380	
β-Bi ₂ Pd	—	380(?)–485	
<i>Bi-Te system</i>			
See Table 1			
<i>Pd-Bi-Te system</i>			
PdBiTe	Michenerite	<480?	El-Boragy and Shubert 1970; Hoffman and MacLean 1976

Three phase associations, that have been experimentally confirmed are: ss-PdBiTe – Bi_xTe_{1-x} – Bi(L); ss-PdTe₂ – Te(L) – Bi_xTe_{1-x}; ss-PdTe – Bi(L) – ss-PdBi₂.

Two phase associations, that have been experimentally confirmed are: ss-PdBiTe – Bi_xTe_{1-x}, Bi(L) – Bi_xTe_{1-x}, ss-PdTe – Bi(L), ss-PdTe – PtBi₂ and ss-PtTe – PdBi.

3.3 The Pt-Pd-Bi-Te system

As noted above, in the Pt-Bi-Te system, a maslovite synthetic analogue was not obtained. This fact can probably be associated with a lower temperature of its formation (below 200°C) or with its stabilization by impurity components.

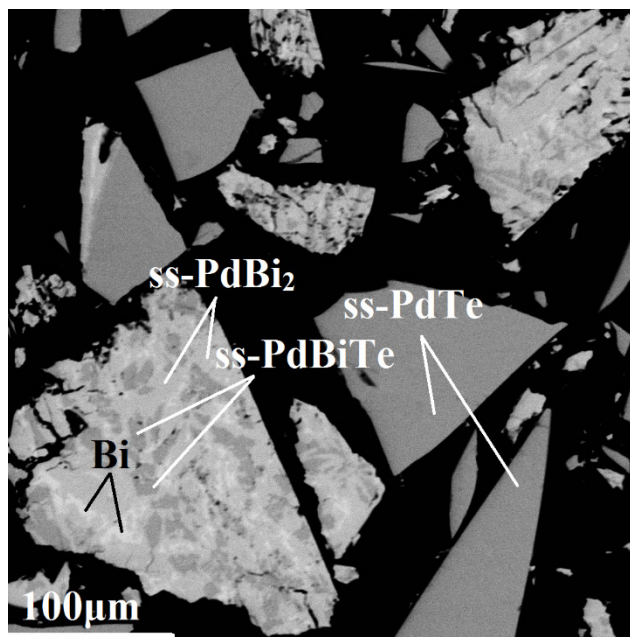


Figure 2. Back-scattered image of Bi(L) – ss-PdTe phase association and ss-PdBi₂ and ss-PdBiTe released during bismuth melt cooling.

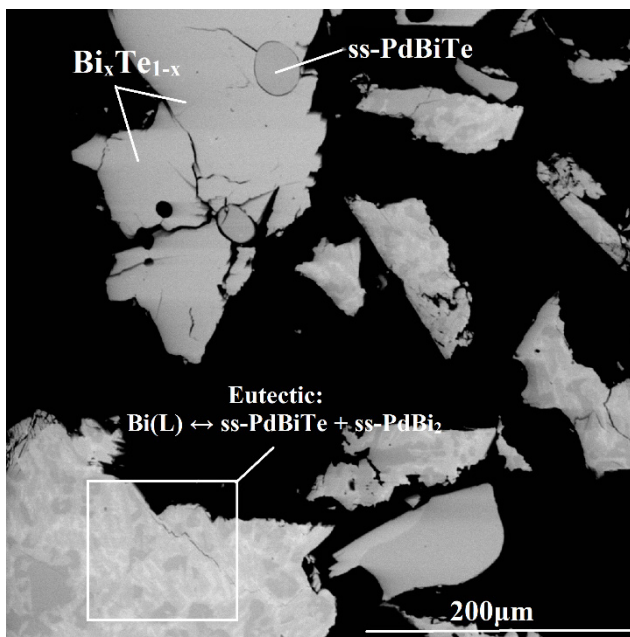


Figure 3. Back-scattered image of Bi(L) – ss-PdBiTe – Bi_xTe_{1-x} phase association and ss-PdBi₂ and ss-PdBiTe released during bismuth melt cooling.

Palladium-rich maslovite is common in nature. In connection with this fact, two experiments were carried out to obtain synthetic analogue of maslovite in the palladium bearing system, i.e. in the Pt-Pd-Bi-Te system.

Both samples were annealed for 30 days at 450°C with one re-grinding. The initial charges and the results of EPMA and XRD are presented in Table 3.

However, in both cases we did not obtain maslovite synthetic analogue (Table 3), which means an absence of the palladium effect on the stabilization of maslovite.

Table 3. Information about the initial charges and EPMA and XRD

results of the experiments in the Pt-Pd-Bi-Te system.

Run No	Starting material, at. %	EPMA results, at. %	XRD results
1	Pt 22.6	Pt _{5.7±1.6} Pd _{29.4±1.7} Bi _{62.9±1.1} Te _{2.0±0.3} Pt _{34.0±1.2} Pd _{0.7±1.0} Bi _{35.3±1.3} Te _{30.0±0.9} Pt _{9.6} Pd _{0.6} Bi _{82.6} Te _{7.3}	α-PdBi ₂ PtTe ₂ Bi
	Pd 9.0		
	Bi 45.1		
	Te 22.3		
2	Pt 17.6	Pt _{32.5±0.2} Pd _{2.3±0.2} Bi _{29.3±1.4} Te _{35.9±1.3} Pt _{3.0±1.5} Pd _{42.4±0.6} Bi _{38.2±1.3} Te _{16.4±0.7} Pt _{12.6±1.6} Pd _{20.0±2.5} Bi _{40.2±3.4} Te _{27.2±2.3} Pt _{2.7±1.6} Pd _{31.8±0.5} Bi _{61.8±1.7} Te _{3.7±0.5}	α-PdBi ₂ PtTe ₂ PdBiTe
	Pd 16.3		
	Bi 39.6		
	Te 26.6		

4 Conclusions

Based on experimental data, phase relations in the Pt-Bi-Te and Pd-Bi-Te systems were established in the temperature range of 350–550°C.

The synthetic analogue of maslovite (PtBiTe) is unstable in the studied temperature range. In addition, Palladium admixture does not affect stability of the maslovite. There are five solid solutions in the system: ss-PtTe₂, ss-PtBi₂, ss-Pt₃Te₄, ss-PtTe and ss-Pt₂Te₃. The solid solution PtTe₂ has the widest homogeneity range.

In the Pd-Bi-Te system there are three solid solutions on the PdTe₂ – PdBi₂ line: ss-PdTe₂, ss-PdBiTe and ss-PdBi₂. In addition, the ss-PdTe – ss-PdBi association was detected. The solid solution PdTe has a wide homogeneity range across all components.

We have proved a range of solid solutions in the systems Pd/Pt-Bi-Te, that have been often misinterpreted in natural samples and in some cases interpreted as a new unnamed phase. The associations observed are widely spread in Cu-Ni-PGE mineral deposits associated with mafic and ultramafic igneous rocks.

Acknowledgements

This study was supported by the Russian Science Foundation grant No. 17-17-01220 and by the Grant Agency of the Czech Republic grant No. 18-15390S. The work of DACH was supported by the program 211 of the Russian Federation Government, agreement No. 02.A03.21.0006 and by the Russian Government Program of Competitive Growth of Kazan Federal University.

References

- Babanly MB, Chulkov EV, Aliev ZS, Shevelkov AV, Amiraslanov IR Phase Diagram in Materials Science of Topological Insulators Based on Metal Chalcogenides (2017). *Rus J of Inorg Chem* 62(13):1703-1729.
- Cook NJ, Ciobanu CL, Merkle RkW, Bernhardt H-J (2002) Sobolevskite, taimyrite, and Pt₂CuFe (tulameenite?) in complex massive talnakhite ore, Talnakh Orefield, Russia. *Can Mineral* 40:329-340.
- El-Boragy M, Shubert K (1970) Über eine verzerrte dichteste Kugelpackung mit Leerstellen. *Z Metallkde* 61(8): 579-584.
- Evstigneeva TL, Kovalenker VA (1975) Sobolevskite, a new bismuthide of palladium, and the nomenclature of minerals of the system PdBi-PdTe-PdSb. *Int Geol Rev* 18:856-866.
- Hoffman E, MacLean WH (1976) Phase relations of Michenerite and

Merenskyite in the Pd-Bi-Te System. *Econ Geol* 71(7): 1461-1468.

Kingston GA (1966) The occurrence of platinoid bismuthotellurides in the Merensky Reef at Rustenburg platinum mine in the western Bushveld. *Miner Mag* 35:815-834.

Kovalenker VA, Begizov VD, Evstigneeva TL, Troneva NV, Ryabkin VA (1979) Maslovite PtBiTe, a new mineral from the Oktabrsky copper-nickel deposit. *Geol Rudn Mestorozh* 21(3):94-104 (in Russian).

Okamoto H (1991) The Bi-Pt (Bismuth-Platinum) System. *J of Phase Equil* 12(2):207-210.

Okamoto H (1992) The Pd-Te (Palladium-Tellurium) System. *J of Phase Equil* 13(1):73-78.

Okamoto H (1994) The Bi-Pd (Bismuth-Palladium) System. *J of Phase Equil* 15(2):191-194.

Okamoto H (1994) Comment on Pt-Te (Platinum-Tellurium). *J of Phase Equil* 15(4):456-457.

Viljoen F, Ramakoloi N, Rose D (2015) Mineral Chemistry of (Pt,Pd)-bismuthotelluride minerals in the Platreef at Zwartfontein, Akanani Project, Northern Bushveld Complex, South Africa. *The Can Min* 53:1109-1127.

Vymazalová A., Chareev DA (2018) Experimental aspects of Platinum-group minerals. In: Mondal SK and Griffin WL (eds) *Processes and Ore Deposits of Ultramafic-Mafic Magmas through Space and Time*. Elsevier, pp. 304-346.

Zhu W-G, Zhong H, Hu R-Zh, Liu B-G, He D-F, Song X-Y, Deng H-L (2010) Platinum-group minerals and tellurides from the PGE-bearing Xinjie layered intrusion in the Emeishan Large Igneous Province, SW China. *Miner Petrol* 98:167-180.

Separation of selenium and tellurium during low-temperature diagenesis

Magali Perez, John Parnell, Joseph Armstrong, Liam Bullock, Joerg Feldmann
University of Aberdeen, UK

Abstract. The mapping of selenium and tellurium in altered pyrite in an Ordovician shale shows that the two elements exhibit different mobility during alteration. Tellurium is enriched and Se is depleted in the in situ iron oxyhydroxide alteration product, relative to the unaltered sulphide. The data imply adsorption of additional Te from pore waters. More acidic conditions in adjacent environments would allow uptake of the Se into transported iron oxides. The different behaviour of Se and Te show how these two elements become separated during diagenesis, and results in a greater range of Se/Te ratios in continental deposits compared to marine shales.

1 Introduction

Selenium (Se) and tellurium (Te) are trace elements for which there is an increasing demand, because of their potential use in advanced technologies such as photovoltaic cells and thermoelectric devices. Both elements are currently obtained as by-products of the processing of copper. However, enhanced demand is driving a need for a better understanding of the geological cycling and distribution of these elements.

Some of the highest Se and Te contents in sedimentary rocks are in pyrite-bearing black shales (Parnell et al. 2016). Both elements occur at trace levels in pyrite, and in the case of early diagenetic pyrite precipitated from seawater sulphate, this represents their point of entry into the sedimentary system. Thereafter, they may be recycled during burial diagenesis, exposure to weathering, and eventually metamorphism. It is clear from sedimentary rocks that are relatively enriched in Se over Te, or vice versa (Bullock and Parnell 2017; Bullock et al. 2017), that there are circumstances where the two elements experience differential behaviour. A change of redox conditions, from a sedimentary environment in which Se and Te are resident in sulphide, to an oxidizing environment where they are likely to be adsorbed onto iron oxides (Harada and Takahashi 2009; Qin et al. 2017), is an opportunity for separation. Here we test this by detailed study of the distribution of Se and Te during the weathering of pyrite to iron oxide in black shale.

Pyrite in sedimentary rocks is readily oxidized (Rimstidt and Vaughan 2003). Since the evolution of an oxygenated atmosphere, the weathering of pyrite has played a critical role in the cycling of trace elements at the Earth's surface, by the liberation from pyrite into solution and transfer back into the oceans (Reinhard et al. 2009). However, some elements are liberated less readily than others, and may become adsorbed onto the iron oxyhydroxide weathering products, causing fractionation of element suites (Lu et al. 2005; Moncur et al. 2009).

Experimental studies of the weathering of pyrite similarly show that element differentiation occurs, whereby some are enriched within iron oxides while others are lost to solution (Parbhakar-Fox et al. 2013). Studies of the fate of trace elements during pyrite alteration have been undertaken using scanning electron microscopy (Moncur et al. 2009), electron microprobe analysis (Lu et al. 2005; Jeong and Lee 2003), micro-X-ray fluorescence (Carbone et al. 2012) and laser ablation-inductively coupled plasma-mass spectrometry (LA-ICP-MS; Parbhakar-Fox et al. 2013). LA-ICP-MS has the sensitivity to map fine-scale variations in Se and Te in sulphide minerals, including pyrite, (Gregory et al. 2015) and is the basis of this study.

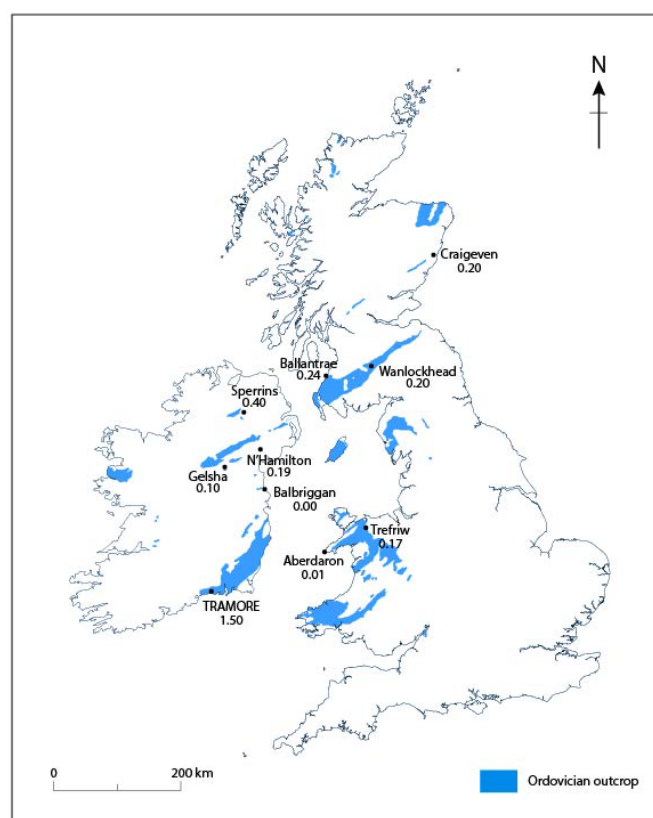


Figure 1. Location of Tramore in Ordovician outcrop, SE Ireland. Concentrations of Te in pyrite (ppm) recorded for 10 Ordovician shales, showing maximum at Tramore.

2 Methodology

Pyrite was studied in Ordovician black shale (Tramore Formation) from a coastal section at Tramore, Co. Waterford, Ireland (Fig. 1). The section of mixed shales

and limestones is described by Carlisle (1979). The site was selected because the pyrite exhibits alteration in an undisturbed section, and the rock is competent enough to allow polishing of the altered pyrite intact. The black shales at Tramore contain irregular crystals of pyrite, which are variably altered, from fresh sulphide to complete conversion to iron oxide.

LA-ICP-MS analyses were made of unaltered sulphide, pure oxide, and crystals showing partial alteration. The Te content of pyrite was measured using a New Wave laser ablation system UP213nm (New Wave Research, Fremont, CA) coupled to a inductive coupled plasma-mass spectrometer (ICP-MS) Agilent 7900 (Agilent Technologies, Tokyo). The laser beam had a round spot size of 100 μm moving in a straight line, 10 Hz repetition rate and 50 $\mu\text{m s}^{-1}$ ablation speed with 1 J cm^{-2} energy. Before ablation, a warm-up of 15 s was applied with 15 s delay between each ablation. Tellurium and selenium were measured (dwell time) using ^{78}Se (0.1 s), ^{82}Se (0.1 s), ^{125}Te (0.1 s), and ^{126}Te (0.1 s). Settings parameters were optimized daily by using NIST Glass 612, to obtain the maximum sensitivity and to ensure low oxide formation. In order to remove possible interferences, a reaction cell was used with hydrogen gas. The MASS-1 Synthetic Polymetal Sulfide standard (USGS, Reston, VA) was used to provide semi-quantification by calculating the ratio of concentration ($\mu\text{g g}^{-1}$)/counts per seconds, and multiplying this ratio by the sample counts.

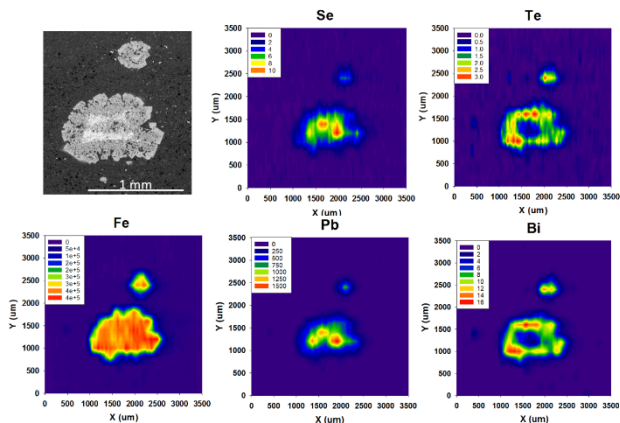


Figure 2. LA-ICP-MS maps for Fe, Se, Pb, Te and Bi in altered pyrite, Tramore. Note relative enrichments of Se in sulphide core, and Te in oxide halo.

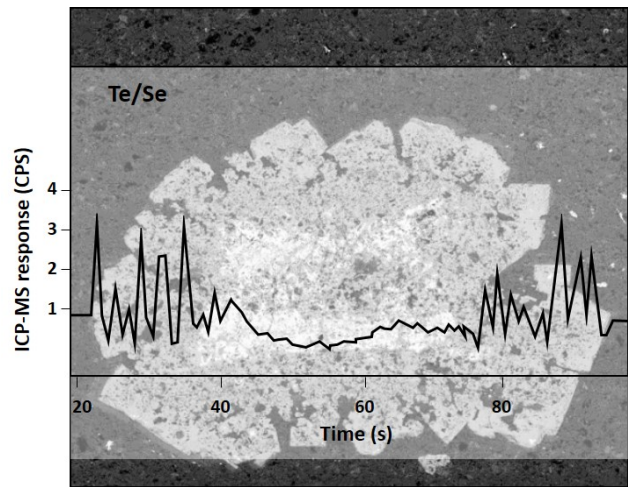


Figure 3. Te/Se ratios along a cross-sectional profile through altered pyrite, Tramore, showing increase in Te in iron oxide alteration halo, determined by LA-ICP-MS. [Profile superimposed on backscattered electron image].

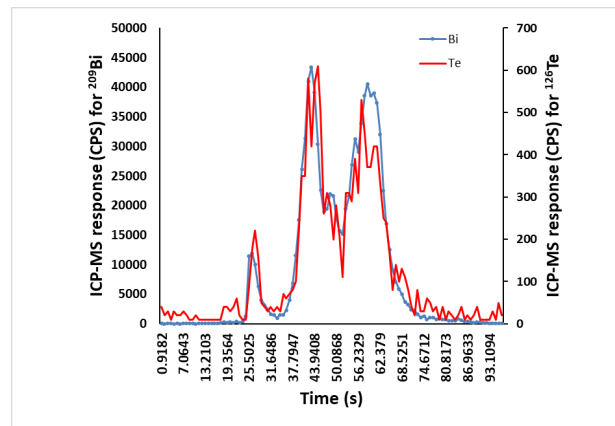


Figure 4. Profile of responses (CPS, counts per second) for ^{126}Te and ^{209}Bi across altered pyrite crystal, Tramore, showing close coincidence of Te and Bi ($R^2 = 0.93$). Two maxima for both elements occur at altered oxide margins, separated by lower responses from unaltered sulphide core.

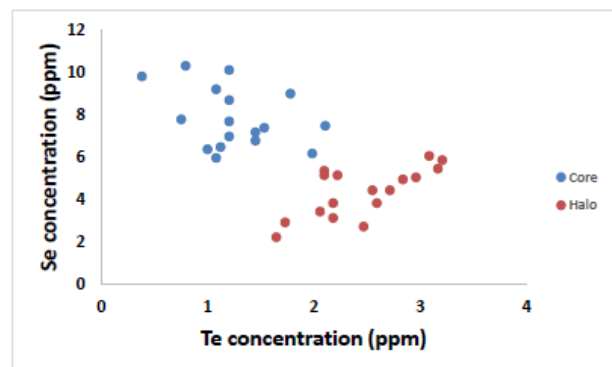


Figure 5. Cross-plot of Se and Te contents in unaltered sulphide and iron oxide alteration halo, Tramore pyrite, showing relative enrichment of Se in the sulphide and Te in the oxide, determined by LA-ICP-MS.

3 Results

Pyrite showing partial alteration consists of a core of unaltered sulphide, and a coating of iron oxide of variable thickness. The host shale has a calcareous matrix. LA-ICPMS maps of partially altered pyrite show a different concentration of trace elements in the oxide compared to the sulphide. The sulphide shows relative enrichment in Se and Pb, while the oxide shows relative enrichment in Te and Bi (Fig. 2). The pattern shown by the maps is further emphasized by cross-sectional profiles through the pyrite, which show decline in Se and increase in Te within the oxide relative to the sulphide (Fig. 3), and correspondence of Te with Bi (Fig. 4). Spot analyses from the laser maps quantify the Se and Te contents (Fig. 5), and yield mean compositions of 7.84 ppm Se and 1.26 ppm Te in the sulphide, and 4.36 ppm Se and 2.46 ppm Te in the oxide. These data equate to Se/Te ratios of 6.23 and 1.77 respectively. The shale has a mean concentration of 0.05 ppm Te (n=2).

4 Discussion

The data show that Se and Te behave differently during the weathering of pyrite, and consequently become differentially distributed. The pattern of Se and Te relative enrichment in sulphide and oxide respectively could be attributed, alternatively, as due to:

- (i) Depletion of Se from the oxide, with/without enrichment in the sulphide.
- (ii) Depletion of Te from the sulphide, with/without enrichment in the oxide.
- (iii) Enrichment of Te in the oxide from a source outside of the original sulphide.

The Se in the sulphide is evenly distributed, rather than concentrated at the margin, which makes enrichment of the sulphide from the surrounding oxide unlikely. Also, pyrite crystals showing no alteration rims have comparable Se contents. The reduced level of Se in the oxide suggests, therefore, that it was liberated into solution. Unaltered pyrite consistently contains less than 2 ppm Te. However, the mean content of 1.26 ppm Te in Tramore pyrite is high for pyrite in Ordovician shales elsewhere in Britain and Ireland (Fig. 1), suggesting that the unaltered Tramore pyrite has not been depleted in Te. This implies that the relatively high Te content in the oxide is due to addition of Te (over and above the total sum) from beyond the original sulphide crystal. Other studies have similarly shown that iron oxyhydroxide alteration products can adsorb higher concentrations of some trace elements than in the original sulphide and must do so from the pore waters rather than by inheritance from the replaced sulphide (Jeong and Lee 2003; Lu et al. 2005; Moncur et al. 2009). These data equate to about 3.5 times the Te/Se ratio in the iron oxyhydroxide compared to the sulphide, i.e. relative enrichment of Te in the in situ alteration products. The source of the additional Te is likely to be redistributed from within the shale, as whole rock analyses do not show any extra enrichment in Te, when compared to other Ordovician shales.

The distributions of Pb similar to that of Se, and of Bi

similar to that of Te (Figs. 2, 4), are typical of relationships found in pyrite elsewhere (Parnell et al. 2017). This probably reflects the common occurrence of Se and Te as lead selenide (clausthalite) and bismuth telluride minerals. If Se and Te occur in pyrite as micro-inclusions of minerals, they will most likely be as lead selenide and bismuth telluride.

The separation of Te and Se is a consequence of the relatively high solubility of Se (VI), while both Te (IV) and Te (VI) have a high affinity for Fe (III) hydroxides (Harada and Takahashi 2009; Qin et al. 2017). This differential behaviour may also explain the abundance of Te over Se in seafloor ferromanganese oxyhydroxide crusts (Harada and Takahashi 2009; Kashiwabara et al. 2014). Preferential precipitation of Te leaves pore waters relatively enriched in Se. However, Se does adsorb onto iron oxide, including iron oxides derived from the weathering of pyritic shale (Parnell et al. 2018). Indeed, iron oxides are deployed to extract Se out of groundwaters where there is a danger of environmental damage from toxic levels of dissolved Se (Rovira et al. 2008; Donovan and Ziemkiewicz 2013). The adsorption of Se onto iron oxyhydroxide increases at lower pH (Balistrieri and Chao 1990; Lee and Kim 2016). Selenium originally mobile in the fluid draining from shale could thereby become subsequently precipitated in more acidic, oxidizing groundwaters. Pyrite oxidation can occur in neutral and alkaline waters (Caldeira et al. 2003), and as the Tramore succession includes limestone beds, the pH within the shale may have been buffered, limiting Se adsorption. In contrast, Te adsorption is not so pH-dependent (Qin et al. 2017), allowing ready enrichment of Te in the iron oxyhydroxide alteration products.

The weathering of shale and coal, involving the breakdown of pyrite, yields iron oxide on a huge scale, as evident today in the need to filter out large quantities of it from old coal mines (Donovan and Ziemkiewicz 2013). This similarly occurred in the geological record when shale and coal were altered during periods of deep oxidation, such as in the Permian of Europe. Iron oxides generated by palaeo-weathering could have been recycled into the sedimentary record. Thus, any separation of Se and Te engendered by pyrite weathering would be conferred to younger sediments.

Previous studies of element distribution during pyrite alteration (Jeong and Lee 2003; Lu et al. 2005; Moncur et al. 2009; Carbone et al. 2012) were based on sulphide-bearing mine waste. Such artificial settings are characterized by high fluid content, high fluid drainage and throughput, high surface area, and access to oxygen-rich atmosphere. By contrast, the shale at Tramore is tightly compact (no visible porosity), with no fractures or veins within the volume of rock studied. This natural setting admits much less access to water and oxygen than in waste heaps, and the alteration of sulphides must occur at a slower rate. Given the limitation on fluid flow and oxidation, the separation of elements is especially notable. The timescale over which alteration occurs was likely to be many orders of magnitude greater in the shale than in a waste heap. This study clearly shows that element separation can occur on a geological timescale.

Recent research on the crustal cycling of Se and Te

(Bullock and Parnell 2017; Parnell et al. 2017; 2018) gives us a database to assess the evidence for their separation during diagenesis (Fig. 6). Data from black shales represent the Se/Te ratios incorporated into pyrite from sea water, while data from continental deposits (red sandstones/siltstones, and iron-rich precipitates) represent ratios evolved during diagenesis. The two sets of Se/Te data yield coefficients of variability (standard deviation/mean) of 1.7 for black shales and 4.9 for continental deposits, indicating greater decoupling of Se and Te in continental samples.

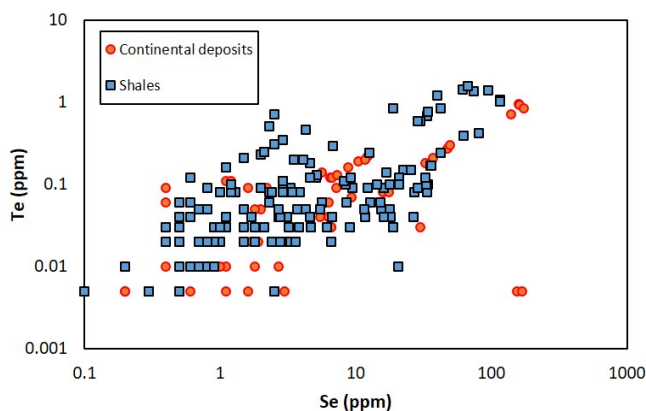


Figure 6. Cross-plot of Se and Te contents in black shales and continental deposits, based on database at University of Aberdeen. Data show greater coefficient of variability for continental deposits.

5 Conclusions

The LA-ICP-MS study of altered pyrite in the Tramore Shale shows that Se and Te become separated during alteration. In particular:

- (i) The Te/Se ratio is several times greater in the iron oxyhydroxide alteration product.
- (ii) The Te level in the oxyhydroxide is greater than in the sulphide, implying more uptake from pore waters.
- (iii) The Se level in the in the oxyhydroxide is less than in the sulphide, implying release into pore waters.

This evidence of separation of Se and Te during diagenesis is reflected in a greater diversity of Se/Te ratios in continental deposits rich in iron oxides, compared to black shales that record a signature of relatively homogenous sea water.

Acknowledgements

This work was supported by the NERC under Grant NE/M010953/1. J. Still gave skilled technical support.

References

Balistreri LS, Chao TT (1990) Adsorption of selenium by amorphous iron oxyhydroxide and manganese dioxide. *Geochim Cosmochim Acta* 54:739-751

Bullock LA, Parnell J (2017) Selenium and molybdenum enrichment in uranium roll-front deposits of Wyoming and Colorado, USA. *Jl Geochem Explor* 180:101-112

Bullock LA, Parnell J, Perez M, Feldmann J (2017) Tellurium enrichment in Jurassic coal, Brora, Scotland. *Minerals* 7:doi:10.3390/min7120231

Caldeira CL, Ciminelli VS., Dias A, Osseo-Asare K (2003) Pyrite oxidation in alkaline solutions: nature of the product layer. *Int J Min Process* 72:373-386

Carbone C, Marescotti P, Lucchetti G, Martinelli A, Basso R, Cauzid J (2012) Migration of selected elements of environmental concern from unaltered pyrite-rich mineralizations to Fe-rich alteration crusts. *Jl Geochem Explor* 114:109-117

Carlisl, H (1979) Ordovician stratigraphy of the Tramore area, County Waterford, with a revised Ordovician correlation for south-east Ireland. *Geol Soc Lond Spec Pub* 8:545-554

Donovan JJ, Ziemkiewicz PF (2013) Selenium adsorption onto iron oxide layers beneath coal-mine overburden spoil. *Jl Env Qual* 42:1402-1411

Gregory DD, Large RR, Halpin JA, Baturina EL, Lyons TW, Wu S, Danyushevsky L, Sack PJ, Chappaz A, Maslennikov VV, Bull SW (2015) Trace element content of sedimentary pyrite in black shales. *Econ Geol* 110:1389-1410

Harada T, Takahashi Y (2009) Origin of the difference in the distribution behaviour of tellurium and selenium in a soil-water system. *Geochim Cosmochim Acta* 72:1281-1294

Jeong GY, Lee BY (2003) Secondary mineralogy and microtextures of weathered sulphides and manganese carbonates in mine waste-rock dumps, with implications for heavy-metal fixation. *Amer Min* 88:1933-1942

Kashiwabara T, Oishi Y, Sakaguchi A, Sugiyama T, Usui A, Takahashi Y (2014) Chemical processes for the extreme enrichment of tellurium into marine ferromanganese oxides. *Geochim Cosmochim Acta* 131:150-163

Lee CG, Kim SB (2016) Removal of arsenic and selenium from aqueous solutions using magnetic iron oxide nanoparticle/multi-walled carbon nanotube adsorbents. *Desalin Water Treat* 57:28323-28339

Lu L, Wang R, Chen F, Xue J, Zhang P, Lu J (2005) Element mobility during pyrite weathering: implications for acid and heavy metal pollution at mining-impacted sites. *Environ Geol* 49:82-89

Moncur MC, Jambor JL, Ptacek CJ, Blowes DW (2009) Mine drainage from the weathering of sulphide minerals and magnetite. *Appl Geochem* 24:2362-2373

Parbhakar-Fox A, Lottermoser, B, Bradshaw D (2013) Evaluating waste rock mineralogy and microtexture during kinetic testing for improved acid rock drainage prediction. *Min Engin* 52:111-124

Parnell J, Brolly C, Spinks S, Bowden S (2016) Selenium enrichment in Carboniferous shales, Britain and Ireland: Problem or opportunity for shale gas extraction? *Appl Geochem* 66:82-87

Parnell J, Bullock L, Armstrong J, Perez M (2018) Liberation of Selenium from Alteration of the Bowland Shale Formation: Evidence from the Mam Tor Landslide. *Quart Jl Eng Geol Hydrogeol*, doi.org/10.1144/qjegh2018-026

Parnell J, Perez M, Armstrong J, Bullock L, Feldmann J, Boyce, AJ (2017) A black shale protolith for gold-tellurium mineralization in the Dalradian Supergroup (Neoproterozoic) of Britain and Ireland. *Appl Earth Sci* 126:161-175

Qin HB, Takeichi Y, Nitani H, Terada Y, Takahashi Y (2017) Tellurium distribution and speciation in contaminated soils from abandoned mine tailings: Comparison with selenium. *Env Sci Technol* 51:6027-6035

Reinhard CT, Raiswell R, Scott C, Anbar AD, Lyons TW (2009) A late Archean sulfidic sea stimulated by early oxidative weathering of the continents. *Science* 326:713-716

Rimstidt JD, Vaughan DJ (2003) Pyrite oxidation: A state-of-the-art assessment of the reaction mechanism. *Geochim Cosmochim Acta* 67:873-880

Iron-Oxide-Copper-Gold deposits as sources of tellurium, selenium, and other critical metals

David Holwell, Sally Worbey, Daryl Blanks, Kate Canham
University of Leicester, UK

Richard Lilly
University of Adelaide, Australia

Abstract. Tellurium and selenium are essential elements in third generation photovoltaic cells for solar power. Production is currently almost entirely as by-products from copper refining. Therefore, these elements are defined as 'critical' in terms of their projected increasing demand for future energy technologies, and their supply being determined by the economics of a separate commodity. Iron Oxide Copper Gold (IOCG) deposits are complex hydrothermal systems and whilst all deposits, by definition, contain economic Cu and Au, many deposits also have significant by-products, including U, REE, Co, Ag and As and a host of other potential by-products, including Te and Se. Thus, IOCGs represent vast potential resources for a number of critical elements. We show that resources of these elements can be effectively estimated using reliable ratios to the major, reported commodities. For example, Cu/Se and Au/Te ratios are consistent enough to be able to determine potential resources in the ores, but also an indication of recoverability by considering the respective ratios in the concentrates and tailings.

1 Introduction

Iron Oxide Copper Gold (IOCG) deposits are complex systems that exhibit a great deal of variation in their geochemistry, mineralogy and structural setting. Whilst all deposits, by definition, contain economic Cu and Au, many deposits also have significant by-products, including U, REE, Co, Ag and As. Indeed, some IOCG deposits, like Ernest Henry, Monakoff, E1 and others in the Cloncurry district, Queensland, contain elevated concentrations of a whole range of base, precious and semi metals. The latter include elements that are essential in new and environmental technologies, such as Te and Se (used in photovoltaic cells for solar power) and other elements such as Sb, Bi and Co. Although these elements are present, they are rarely included in routine analyses; are currently not recovered; and have no viable resource estimates available. Here we present a technique that provides an indication of the size and nature of potential resources of these by-product elements from IOCGs.

At present, all Te and Se production is as a by-product from porphyry Cu mining. Thus, IOCGs, which also contain large volumes of Cu sulfides, represent vast, undeveloped potential resources for these, and other, speciality elements. Here we use examples from the Cloncurry IOCG district (Ernest Henry and

Monakoff) and the Mumbwa region, Zambia (Kitumba) to illustrate the enrichment of a variety of speciality elements, and produce an estimate of the resources of Te and Se held within these deposits relative to its Cu and Au

2 IOCGs in the Cloncurry region, Australia

The Cloncurry district in Queensland, Australia, is one of the world's classic IOCG provinces. The world class Ernest Henry deposit (90 Mt @ 1.17% Cu and 1.6 g/t Au) is the largest known deposit in the region and has been mined by open pit, and now underground methods. At least one of the fluids responsible for the mineralization at Ernest Henry is thought to have been sourced from the nearby ~1505 Ma Malakoff granite (Kendrick et al. 2007); one of a number of granite bodies that make up the Williams-Naraku batholith that was emplaced towards the end of the ~1600–1500 Ma Isan orogen. Fifteen kilometers to the south of Ernest Henry lies the smaller, Monakoff deposit (52 Mt @ 0.77% Cu and 0.23 g/t Au), which was mined in 2013, and which also shows evidence of fluids derived from the Malakoff granite (Williams et al. 2015).

Both Ernest Henry and Monakoff are enriched in a host of elements in addition to the Cu and Au they are, or have been, mined for. These include Ag, REE, U, Ba, F, Sr, Te, Se, As, Bi, Co, Sb and Mo. Monakoff, in particular, has highly enriched concentrations of Te (up to 3.8 ppm), present as Te-bearing sulfosalts, and in solid solution in sulfides, including pyrite, and over 350 ppm in solid solution in galena (Williams et al. 2015).

3 IOCGs in the Mumbwa region, Zambia

The Mumbwa region of central Zambia is one of the most significant IOCG provinces in southern Africa. A number of deposits are associated with late stage syenite intrusions related to the ~540 Ma emplacement of the giant Hook Granite. One of the most significant of these is the Kitumba deposit, which is made up of a syenite and granite-hosted breccia with iron oxides, pyrite and chalcopyrite with carbonate and apatite. The highest grades are hosted within a zone of supergene enrichment, with stockworks of chalcocite, malachite, cuprite and native copper.

Concentrations of associated elements are less well defined that the Cloncurry deposits. Here we present initial results on the by-product potential of both the hypogene and supergene ores at Kitumba.

4 Estimating resources of potential by-product elements

By using a suite of samples with full bulk rock geochemistry, we are able to determine consistent Au/Te and Cu/Se ratios (but no reliable Cu/Te and Au/Se ratios) that can be used to back calculate the potential Te and Se resource at Monakoff from the measured Cu resource. Furthermore, we show that a similar approach can be undertaken at Ernest Henry, with the ratios comparable between the deposits, but not identical.

Further estimates of the 'recoverability' of these and other elements, at Ernest Henry were made possible by consideration of the same ratios of elements within samples of concentrates and tailings. Both Te and Se report to the concentrate, although they are not concentrated relative to the original ore in proportional amounts.

We therefore show that it is possible to make an estimate of the in situ resources of potential by-product elements like Te and Se, and their recoverability from concentrates and/or tailings from small, but representative datasets.

Acknowledgements

This work is funded by NERC SoS Minerals consortium grant NE/M010848/1 "TeaSe: tellurium and selenium cycling and supply" awarded to the University of Leicester. Ernest Henry Mines and Glencore are thanked for access to sampling from Ernest Henry and Monakoff. Consolidated Mines and Investment are thanked for access to Kitumba.

References

- Kendrick MA, Mark G, Phillips D (2007) Mid-crustal fluid mixing in a Proterozoic Fe oxide-Cu-Au deposit, Ernest Henry, Australia: Evidence from Ar, Kr, Xe, Cl, Br and I. *Earth and Planetary Science Letters* 256:328-343
- Williams, MR, Holwell, DA, Lilly, RM, Case, GND and McDonald, I. (2015) Mineralogical and Fluid Characteristics of the Monakoff and E1 Cu-Au Deposits, Cloncurry Region: Implications for Regional F-Ba-rich IOCG Mineralisation. *Ore Geology Reviews*, 64:103-127;

The critical elements (V, Co, Ga, Sc, REE) enrichment of Fe-Ti-V oxide deposits related to Mesoproterozoic AMCG complex in Poland

Mikulski Stanisław Z., Sadłowska Katarzyna
 Polish Geological Institute – National Research Institute

Abstract. Fe-Ti-V ores in the Krzemianka and Udryn deposits associated with Suwałki Anorthosite Massif (SAM) located in NE Poland were investigated for their critical element content. Complex geochemical and mineralogical investigation revealed significant concentrations, including V, Co, Ga, Sc, Hf and REE. Particularly a high concentration of vanadium (geometric mean = 861.6 ppm, for n = 39) cobalt (geom. mean = 111.8 ppm) and scandium (geom. mean = 21.6 ppm). Roughly estimated resources of critical elements in Fe-Ti-V ores are significant and reach about 1 million tons of vanadium, 150 thousand tons of cobalt, 56 thousand tons of gallium and 29 thousand tons of scandium. Moreover, other elements associated with sulphide ores were also documented (Zn, Ni, Cu and Cr), for which, estimated resources reach several hundred thousand tons, and their presence significantly increases the potential value of Fe-Ti-V ores, which are considered as subeconomic.

1 Introduction

Accumulations of critical elements in the magmatic Fe-Ti-V deposits from NE Poland were poorly covered by during exploration and their resource potential rarely evaluated. In the Krzemianka and Udryn deposits (Fig. 1), documented inferred resources (according to the Polish regulation of C₁ and C₂ category) of 1.34 billion tons of Fe-Ti-V ores, contain around 388,2 million tons of metallic iron, 98 million tons of TiO₂ and 4.1 million tons of V₂O₅. The average grade of ores are as follows: 27% Fe (range 20-50%), 7% TiO₂ and 0.3% V₂O₅ (Malon et al. 2018). Magnetite-ilmenite ores also contain Fe, Cu, Ni and Co sulphides from 1 to 3% of ore by volume and small amounts of REE in carbonatites (Ryka and Szczepanowski 1998). Inferred resources of Fe-Ti-V ore are considered as subeconomic despite a great amount of resources documented in the Fe-Ti-V oxide deposits from the Suwałki region. The current results from modern geochemical prospecting revealed that some of the critical and associated elements occur in quite high concentration (Mikulski et al. 2018).

2 Geological background of Fe-Ti-V deposits

The Krzemianka and Udryn Fe-Ti-V ore deposits are located in the Mesoproterozoic Suwałki anorthosite

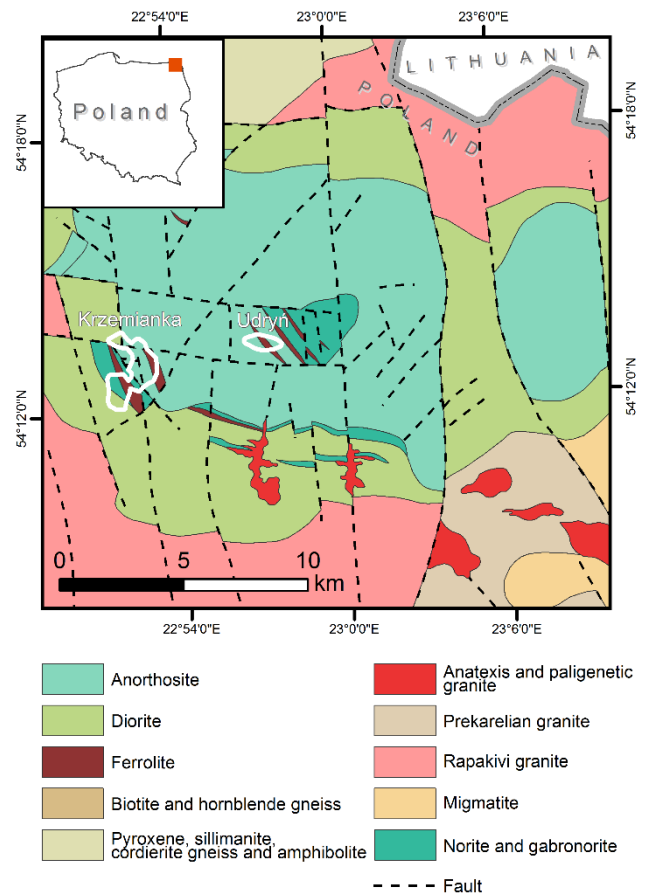


Figure 1 Geological map of the Suwałki Anorthosite massif (SAM) (Kubicki & Ryka 1982) with location of the Krzemianka and Udryn deposits in NE Poland

Massif (SAM) in NE Poland (Fig. 1; Ryka et al.). The SAM constitutes the eastern part of the Mazury Complex (Kubicki and Ryka 1982) and is covered by Mesozoic-Cenozoic sedimentary rocks of thickness from 500 m on the east to 1000 m on the north-west (Ryka 1998). Anorthosites and norites compose the core part of intrusion, which represents the AMCG association (Anorthosite-Mangerite-Charnockite-Granite) and are surrounded with diorites and gabronorites (Juskowiak 1998). Two N-S faults direction divide massif into three tectonic blocks. The western one, with the Krzemianka and Udryn Fe-Ti-V deposits, is uplifted.

The Krzemianka deposit has an arcuate shape (1.5 km wide and 4 km long) and is located in the western part of the Suwałki Massif close to its contact with metamorphic cover (Parecki 1998). The Udryn deposit is located in the

central part of the Suwałki intrusion, approximately 4 km east of the Krzemianka deposit. These deposits are in the form of lenses, schlieres, pseudo-seams and veins elongated medially and dipping generally at an angle of about 45° towards the SE (Kubicki and Siemiątkowski 1979). The ore bodies are variable in size with lengths up to 3 km and widths up to 0.6 km. Thicknesses vary from a few centimetres to 145 m. The majority of the Krzemianka deposit lies at a depth of 1100-1700 m. In the NE part of the anorthosite is the largest ore body. The deposit is made of titanium- and vanadium-bearing magnetite containing ilmenite and hematite-ilmenite occurring in various proportions from 1: 1 to 5: 1 and even 10: 1. The obtained Re-Os model age for pyrite, pyrrhotite and magnetite showed an age of 1536 ± 67 million years (Morgan et al. 2002; Wiszniewska et al. 2002). The Krzemianka and Udryn deposits belong genetically to the iron deposits of the Allard Lake type.

3 Analytical methods

In total 39 samples with economic ore mineralization representing a variety of Fe-Ti-V ore types were subject to a range of geochemical (ICP-QMS, ICP-OES, WD-XRF and GF AAS) and mineralogical (EPMA, CAMECA-SX100) techniques. 23 samples were collected from the Krzemianka deposit and 16 samples came from the Udryn deposit. Samples were collected mostly from the archive core material of boreholes drilled during the 1970s and 1980s. The analyses were performed at the Polish Geological Institute-National Research Institute using international and internal standards and included duplicate analyses (Mikulski et al. 2018).

4 Results and discussion

4.1 Geochemical investigation of a critical elements

Vanadium occurs in magnetite-ilmenite ores (e.g. Kubicki and Siemiątkowski 1979; Nieć 2003) and in the studied samples V concentrations range from 104 to 2208 ppm, and in approximately 38% of the population above 0.1% V. The population distribution is asymmetrical unimodal. The geometric mean for vanadium = 861.6 ppm ($n = 39$). Vanadium shows a good correlation with cobalt (correlation coefficient - $r = 0.70$, Fig. 2a) and very weak correlation with Fe_2O_3 ($r = 0.42$, Fig. 2b), and Ga (Fig. 2c) as well as with TiO_2 , Cd, Ni and Cr.

Cobalt is present in sulphides, mainly in pyrrhotite that accompany magnetite-ilmenite ores. The cobalt concentration ranges from 15 to 205 ppm. Samples with cobalt contents from 120 ppm to 180 ($n = 23$) are the most abundant. The average geometric content of cobalt is 111.8 ppm ($n = 39$). Cobalt shows a good correlation with vanadium, Fe_2O_3 and nickel ($r = 0.70$) and a weaker correlation with TiO_2 , chromium and gallium ($r = 0.6$).

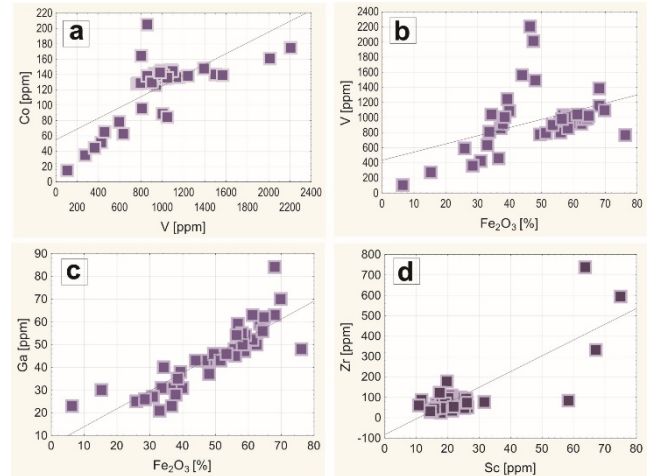


Figure 2 Bivariate diagrams of trace elements with trend lines in magnetite-ilmenite ores from the Krzemianka and Udryn deposits on the Suwałki Massif. (a)–V vs. Co; (b) Fe_2O_3 vs. V; (c) Ga vs. Fe_2O_3 ; (d) Sc vs. Zr

Gallium, determined using WD-XRF was also found in elevated concentrations in Fe-Ti-V ores, with contents ranging from 21 to 84 ppm. Most samples have gallium contents in the range from 30 to 60 ppm ($n = 26$). Geometric mean for gallium is 42 ppm ($n = 39$) and it shows a strong correlation with Fe_2O_3 ($r = 0.87$, Fig. 2c), nickel ($r = 0.82$), zinc ($r = 0.79$), TiO_2 ($r = 0.75$), and weaker one with cobalt and cadmium ($r = 0.57$).

Scandium is another important critical element occurring in elevated concentrations in the Fe-Ti-V deposits in Poland. Its contents in the ores range from about 17 to about 75 ppm. Geometric mean for occurrences of scandium is 21.6 ppm and it has a strong correlation with REE, P_2O_5 , thallium and zirconium ($r = 0.9-0.8$, Fig. 2d), MgO ($r = 0.74$), indium ($r = 0.73$) and MnO ($r = 0.72$), and a weaker correlation with the germanium ($r = 0.69$), tantalum ($r = 0.68$) and hafnium ($r = 0.57$).

In the Fe-Ti-V ores, there were also concentrations of hafnium, which range of 0.38 to 2.09 ppm, with the majority of data located from 0.4 to 1.2 ppm (about 74% of the population). The geometric mean for Hf is 0.87 ppm ($n = 39$). Hafnium shows a weak correlation with Ta, Th and Sc ($r =$ about 0.56), Ge and In ($r = 0.55$) and Nb and Zr ($r = 0.54$).

In the graph depicting REE concentrations normalized to chondrite there is a clear negative Eu anomaly (Fig. 3). In addition there is a significant (>400 x) enrichment in REE (especially in Ce, La and Nd) in 3 ore samples from the Udryn deposit. In total, the REE concentrations in the analysed samples are elevated (ΣREE approx. 0.1%). These associated with the enrichments in CaO and MgO and the presence of carbonatites related with Variscan-alkaline magmatism.

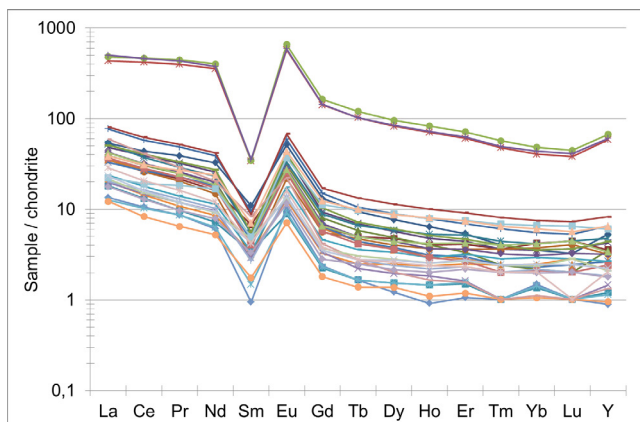


Figure 3 REE diagram normalized to chondrite (after McDonough, Sun1995) for the Fe-Ti-V ore samples from the Krzemianka and Udryn deposits in NE Poland

4.2 Ore mineralization in the light of the microscopic studies

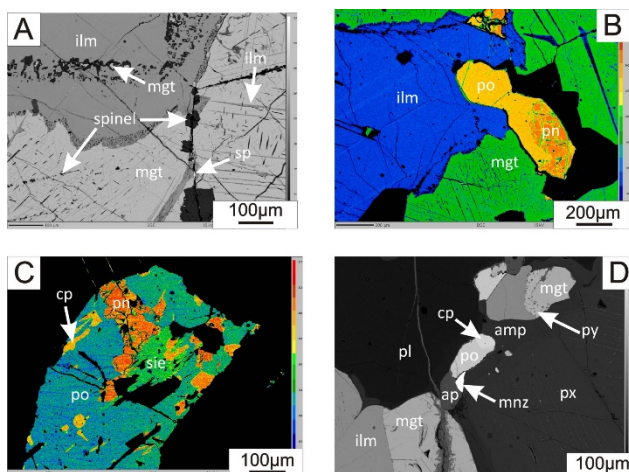


Figure 4 Typical Fe-Ti-V ores with sulphides from the SAM. BSE images; (a) Exsolution of ulvöspinel, ilmenite (ilm) and Al-Mg spinels (spinel) in magnetite (mg), sp – sphalerite; (b) Typical sulphide (pyrrhotite – po, pentlandite – pn) aggregates in magnetite-ilmenite ore; (c) Intergrowths of sulphides (po – pyrrhotite, cp – chalcopyrite, py – pyrite) and siegenite (sie); (d) Fe-Ti-V ore enriched with REE due to presence of monazite grain genetically related to F-apatite. pl – plagioclase, px – pyroxene, amp – amphibole, ap – apatite, mnz – monazite;

Microscopic studies of Fe-Ti-V ores confirm earlier research, which shows that main ore minerals are magnetite and ilmenite (e.g. Kubicki and Siemiątkowski 1979; Speczik et al. 1988; Kozłowska and Wiszniewska 1991; Wiszniewska 2002; Marcinkowski 2006).

Magnetite contains several generations of exsolution of ulvöspinel, ilmenite and Al-Mg spinels (Fig. 4a). Sulphides occur with Fe-Ti-V oxide ores and these comprise mainly pyrrhotite, chalcopyrite, pentlandite,

pyrite (Fig. 4B) with minor bravoite, violarite, siegenite (Fig. 4c), cubanite, galena, sphalerite, millerite and greenockite.

EPMA analyses reveal that Magnetite is the major V mineral here, V substitutes for Fe^{3+} in the magnetite crystal lattice. V content in magnetite is in the range 0.0X-0.59 wt. %, avg. 0.42 wt. % (Fig. 5a,b).

Ilmenite contains from 0.05 to 0.27 wt. % (avg. 0.14 wt. %) V (Fig. 6). Hemo-ilmenite enriched in V up to several wt. % occurs in barren rocks (Kubicki and Siemiątkowski 1979; Kozłowska and Wiszniewska 1991). Redistribution of V and Fe^{3+} ions substitution occurred under variable PT conditions during evolution of anorthosite massif (Speczik 1991).

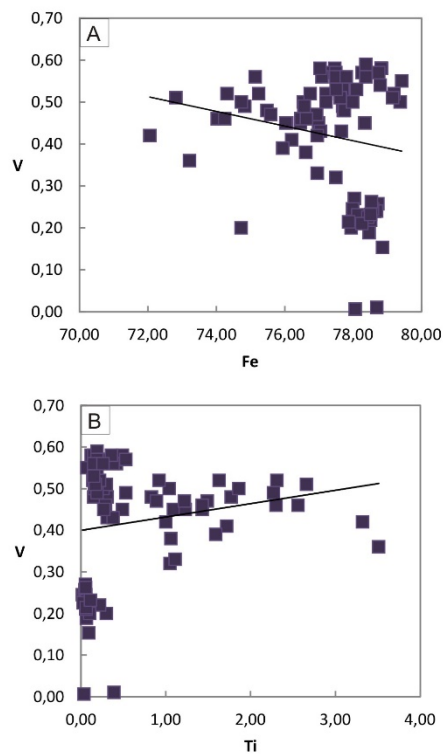


Figure 5 (a) Vanadium to iron ratio in magnetite; (b) Vanadium to titanium ratio in magnetite, showing Fe^{3+} ions substitution by V and positive correlation with Ti

The most abundant critical element in sulphide ore minerals is Co. Admixtures of Co in pentlandite which is the main phase bearing cobalt, may reach 15.3 wt.%. Siegenite contains up to 23.61 wt. % Co, but it occurs less frequently. Co admixtures in other sulphides such as pyrrhotite, chalcopyrite and pyrite are present and reach up to several wt. %. Other significant admixtures in Fe-Ti-V ores are Ni in pyrrhotite, chalcopyrite and

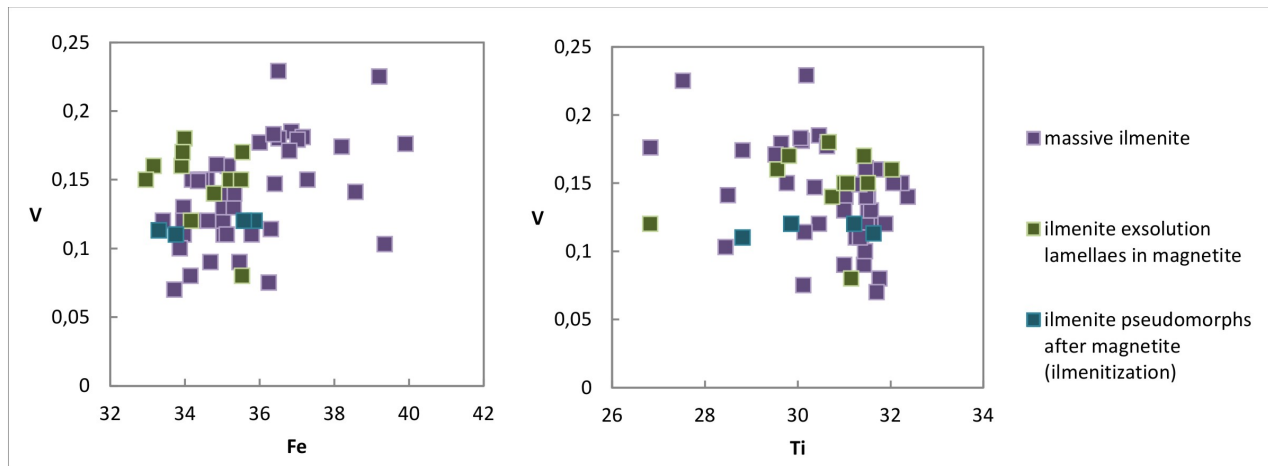


Figure 6 V/Fe and V/Ti ratio in ilmenite depending on crystal form

pyrite, moreover inclusions of native Bi in magnetite and pyrrhotite and inclusions of hessite and greenockite in chalcopyrite were identified. Samples less abundant in ore minerals (up to 40 %) are enriched in REE up to 0.1 wt. % due to presence of monazite genetically related to F-apatite (fig. 4D).

5 Conclusions

On the basis of geochemical (ICP-QMS, ICP-OES) and mineralogical (EPMA, CAMECA-SX100) investigation, elevated concentrations of critical elements such as V, Co, Ga, Sc, Hf and REE in magnetite-ilmenite ores from the Krzemianka and Udryn deposits in the Suwałki anorthosite massif in NE Poland have been found. The main minerals as carriers of critical elements identified and the estimated resources of these critical elements were also determined (Mikulski et al. 2018). Vanadium resources were estimated at ca. 1 million tons, cobalt on 150 thousand tons, gallium on 56 thousand tons and scandium on 29 thousand tons. Besides, associated elements such as Zn, Ni, Cu and Cr, have estimated resources up to several hundred thousand tons (Mikulski et al. 2018). The identification of critical and associated elements greatly increases the attractiveness of the considering deposits, which were documented in the 60-80. of the 20th century. They are considered so far subeconomic due to the low content of metals (Nieć 2003), depth of ore deposition and environmental protection aspects.

Acknowledgements

The project was financed by the National Fund for Environmental Protection and Water Management in accordance with Agreement No. 506/2015.

References

Juskowiak O (1998) Occurrence, structure and mineral diversity of rocks from the Suwałki Anorthosite Massif. *Prace Państw Inst Geol* 161:53–80
 Kozłowska A, Wiszniewska J (1991) Genetic aspects of ore minerals texture and structure in the Suwałki Massif *Arch. Mineral.* 44(2):69–88

Kubicki S, Siemiątkowski J (1979) Ore mineralization of the Kubicki S, Ryka W (1982) The geological atlas crystalline basement of the Polish part of the East European Craton. *Wyd. Geol Warszawa*, 24 pp
 Malon A, Tymiński M, Mikulski SZ, Oszczepalski S (2018) Metallic Raw Materials. In: Szuflicki M, Malon A, Tymiński M (eds) The balance of mineral resources deposits in Poland as of 31.12.2018, PIG-PIB, Warszawa, pp 49–63
 Marcinkowski B (2006) The regularity of occurrence of ore mineralization in selected complexes of the crystalline basement of north-eastern Poland. *Biul Państw Inst Geol* 421:53–90
 McDonough WF, Sun SS (1995) The composition of the Earth. *Chemical Geology* 120:223–253
 Mikulski SZ, Oszczepalski S, Sadłowska K, Chmielewski A, Małek R (2018) The occurrence of associated and critical elements in selected documented Zn-Pb, Cu-Ag, Fe-Ti-V, Mo-Cu-W, Sn, Au-As and Ni deposits in Poland. *Biul Państw Inst Geol* 472:21–52
 Morgan JW, Stein HJ, Hannah JL, Markey RJ, Wiszniewska J (2000) Re-Os study of Fe-Ti-V Oxide and Fe-Cu-Ni sulphide deposits, Suwałki Anorthosite Massif, Northeast Poland. *Mineral Deposita* 35:391–401
 Nieć M (2003) Geo-economic evaluation of vanadiferous titanomagnetite deposits in Suwałki massif in Poland. *Gospodarka Surowcami Mineralnymi* 19(2):5–27
 Parecki A (1998) Geological structure of Krzemianka and Udryn deposits. *Prace Państw Inst Geol* 161:123–136
 Ryka W (1998) Geological positions of the Suwałki Anorthosite Massif. *Prace Państw Inst Geol* 161:19–26
 Ryka W, Szczepanowski H (1998) Trace elements of the Suwałki Anorthosite Massif. *Prace Państw Inst Geol* 161:105–110
 Sadłowska K, Mikulski SZ (2019) Electron microprobe study of V, Co, Ni and Au admixtures in ore minerals from Fe-Ti-V deposits (NE Poland). *Przeegląd Geologiczny* 67(3):192-195
 Speczik S (1991) Distribution of vanadium in ore minerals of the Suwałki massif (NE Poland). *Archiwum Mineral* 44(2):19–36
 Speczik S, Wiszniewska J, Diedel R (1988) Minerals, exsolution features and geochemistry of Fe-Ti ores of the Suwałki district (northeast Poland). *Mineral Deposita* 23:200–210
 Wiszniewska J, Krzemińska E, Rosowiecka O, Petecki Z, Ruszkowski M, Salwa S (2018) New results of polymetallic, PGE and REE mineralizations research in the Suwałki Anorthosite massif (NE Poland). *Biul Państw Inst Geol* 472:271–284
 Wiszniewska J (2002) An age and genesis of Fe-Ti-V ores and associated rocks in the Suwałki Anorthosite Massif (NE Poland). *Biul Państw Inst Geol* 401:1–96

Indium and other critical elements enrichment in cassiterite-sulphide mineralization from the stratiform tin deposits in the West Sudetes (SW Poland)

MIKULSKI Stanisław Z., MAŁEK Rafał

Polish Geological Institute – National Research Institute

Abstract. A geochemical investigation (ICP-QMS, ICP-OES, WD-XRF and GFAAS) of 42 samples with cassiterite-sulphide mineralization taken from an abandoned tin mine and deposits in the Stara Kamienica Schist Belt in Poland was undertaken. This indicates elevated concentrations of critical elements (In, Bi, Ga, Co, Nb, Pt, Pd and Re) as well as some associated elements (Cu, Zn and Pb). In addition, EMPA studies (Cameca SX-100) enabled quantitative and qualitative identification of trace elements department in ore minerals (mostly sulphides). A number of rare ore minerals, which also contain interesting amounts of trace elements, have been identified. Some of these are the first recorded occurrence in tin deposits the Sudetes (e.g. In-bearing mineral - sakuraiite $[(Cu,Zn,Fe)_3(In,Sn)S_4]$). Identification of critical and associated elements may be considered as an added value to cassiterite ores.

1 Geological setting of Sn deposits

The stratiform tin deposits of the western Sudetes are located in the Lower Palaeozoic Stara Kamienica Schist Belt on the northern part of the Variscan Karkonosze Granite Massif, which is a part of the Karkonosze-Izera-Lausitz Block (Fig. 1; Michniewicz et al. 2006, and references therein). Cassiterite ores occur along a 15 km schist belt in two main zones, northern and southern, in which there are also several smaller mineralized zones. Ores associated with Co-Ni-As-Bi sulphide mineralization are hosted by quartz-mica schists, which are fine-grained rocks, light grey (often with a greenish shade), with clearly visible foliation and lamination (Szałamacha, Szałamacha 1974). The tin mineralized zones run latitudinally and strike from 37.5 to 57.5 degrees towards N. The thickness and grade of the main ore zones are highly variable. They occur in widths from 0.04 to 8.07 m and contain between 0.0001 % and 16.78% Sn (Michniewicz et al. 2006). These tin resources were classified as anticipated sub-economic and were estimated at 5.5 million tons of ore with an average content of about 0.5% Sn (Malon et al. 2018). Within the area the perspective resources of tin ore are estimated that it contains, approximately 20 million tons of ore with approximately 100,000 tons of metallic tin (Michniewicz et al. 2006). The genesis of tin (cassiterite-sulphide) mineralization is related to the activity of hydrothermal solutions, which are spatially, temporally and genetically linked to the intrusion of the Variscan Karkonosze Granitoid Massif (Wiszniewska 1984) or to

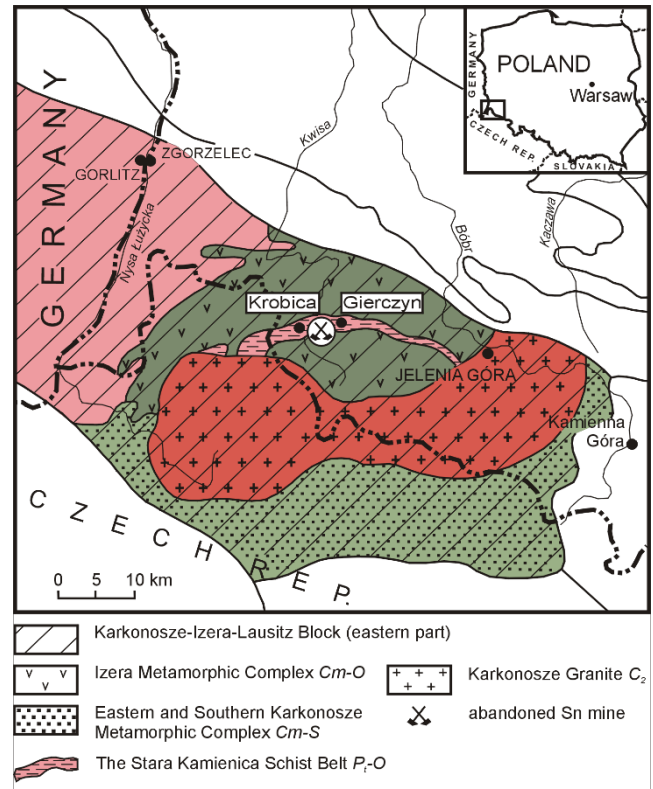


Figure 1 Location of the stratiform tin deposits in the Stara Kamienica Schist belt in the Sudetes (NE margin of the Bohemian Massif, SW Poland) on the geological background of the surrounding areas

the earlier development of magmatic-metamorphic processes (Michniewicz et al. 2006) as well as to the pre-, and Variscan multiple mineralization events (Cook and Dudek 1993, Mikulski et al. 2007).

2 Geochemical investigation of cassiterite-sulphide mineralization

42 samples with cassiterite-sulphide mineralization from the area of the Krobica and Gierczyn tin deposits were subject to geochemical investigation (ICP-QMS, ICP-OES, WD-XRF and GFAAS) (Mikulski et al. 2018). Tin concentrations range from 0.005 to 1.5%. The arithmetic mean of tin determined by WD-XRF is 806 ppm ($n = 42$). Tin shows a weak correlation with critical elements - bismuth and gallium (correlation coefficient - $r = 0.5$). and the investigated samples show an enrichment in In, La, Bi, Nb, Re, Co and W. In addition, the concentration of

other metals such as Zn (up to 0.7%), Pb (up to 0.7%) and Cu (up to 0.5%) are also of interest.

An important critical element occurring in elevated concentrations is indium, whose contents in some samples are up to 7.4 ppm. Arithmetic mean for indium concentration was 0.92 ppm and it shows strong correlation with copper ($r = 0.79$; Fig. 2a), and weak correlation with gold ($r = 0.50$), zinc ($r = 0.46$), uranium, bismuth, chromium and cobalt ($r =$ from 0.42-0.40). The main carriers of indium are sphalerite and chalcopyrite, which according to EMPA studies may have up to a several hundreds of ppm indium (in sphalerite up to 0.13 wt. %, and in chalcopyrite up to 0.16 wt. %). In addition, the indium mineral sakuraiite $(\text{Cu, Zn, Fe})_3(\text{In, Sn})\text{S}_4$ has been identified. This can contain indium up to approx. 19 wt. %.

Gallium concentrations are up to 84 ppm (Fig. 2b), with the majority of samples having gallium contents in the range of 20-25 ppm (about 35% of the whole sample population). The population distribution is unimodal symmetrical. Arithmetic mean for gallium is 20.2 ppm and it shows a weak correlation with Sn, W ($r =$ c.a. 0.5) and with REE, Zr, Rb and Th.

Cobalt is present in increased quantities in sulphides, mainly in cobaltite, pyrrhotite and pyrite, which accompany cassiterite ores. The cobalt concentration ranges from 6 to 168 ppm (Fig. 2c) and its arithmetic mean is 37.8 ppm. Cobalt shows a high correlation with As, Br and Sb ($r = 0.84-0.82$), and much weaker correlation with Au ($r = 0.53$) and Ag ($r = 0.48$).

Another critical element that occurs in samples is bismuth. WD-XRF and ICP-MS analyses show that bismuth contents are up to 1740 ppm and it Bismuth strongly correlates with U ($r = 0.74$), and much more weakly with Au ($r = 0.57$), Sn ($r = 0.54$), Cu, In and Ag ($r =$ about 0.4).

Niobium concentrations (WD-XRF) of compressed powder samples are up to 32 ppm (Fig. 2d). The arithmetic mean for Nb is 12.8 pp and it is correlated with m some elements, including from Ba, Ce, La, Rb, Sr, Th, V, Y, Zr, Hf, Ta, and W.

Platinum has interesting values up to 116 ppb (Fig. 2e). The arithmetic mean is about 56 ppb and it has a very weak correlation with Pd, U and Fe_2O_3 ($r =$ approx. 0.5).

Rhenium determinations using the ICP-MS methodology show that it is present in the range from 0.21 to 1.03 ppm with an arithmetic mean of 0.48 ppm. Rhenium shows a weak correlation with vanadium (Fig. 2f), zirconium, and yttrium distribution ($r = 0.54$).

In cassiterite-sulphide bearing samples, zinc contents range from 37 ppm to 0.56% and copper from 8 ppm to 0.33%. Arithmetic mean for zinc contents is 506 ppm. Zinc has a strong positive correlation with cadmium ($r = 0.87$), and weak correlation with indium ($r = 0.46$) and platinum ($r = 0.40$).

The arithmetic mean for copper concentration is 348 ppm. Copper has a strong correlation with indium and gold ($r = 0.78$; Fig. 2g), and much weak correlation with uranium, silver, cobalt, chromium and bismuth ($r =$ from 0.53-0.42).

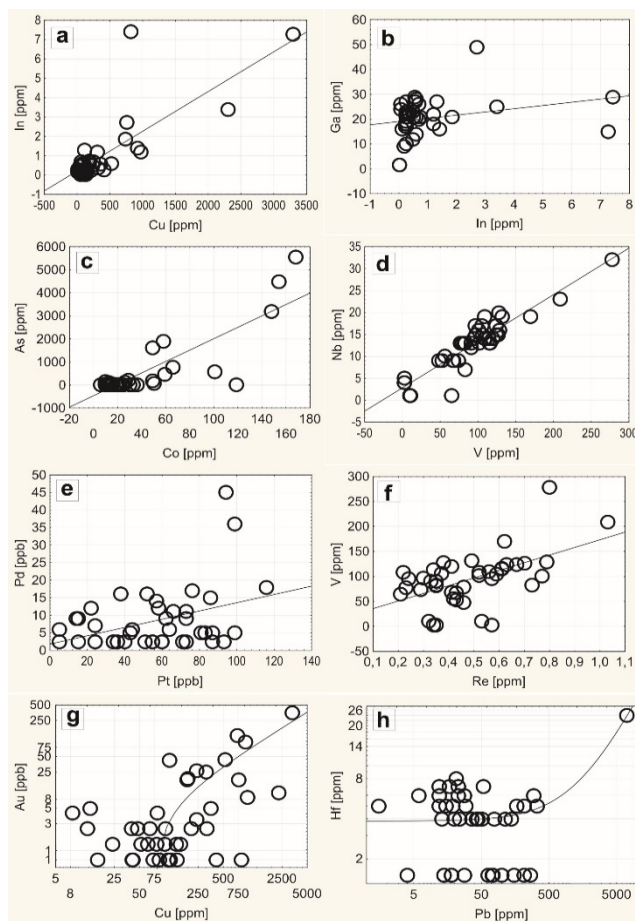


Figure 2. Bivariate and logarithmic diagrams of trace elements with trend lines in samples from Sn deposits in the Stara Kamienica Schist Belt (Sudetes, SW Poland)

(a) Cu vs. In; (b) In vs. Ga; (c) Co vs. As; (d) V vs. Nb; (e) Pt vs. Pd; (f) Re vs. V; (g) Cu vs. Au; (h) Pb vs. Hf

3 Ore mineralization

Ore mineralization in quartz-mica schists has a vein-impregnation character and it is represented mainly by cassiterite, pyrrhotite, chalcopyrite, sphalerite, arsenopyrite, ilmenite and rutile (Michniewicz et al. 2006; Wiszniewska, 1984). Also, a number of less frequently occurring ore minerals were identified and include pyrrargyrite $(\text{Ag}_3\text{SbS}_3)$, stannoidite $\text{Cu}_8(\text{Fe, Zn})_3\text{Sn}_2\text{S}_{12}$ (Piestrzyński and Mochnacka, 2003), and Ag-Sb-Bi minerals (Piestrzyński et al. 1990; 1992; Cook and Dudek 1993) as well as In-bearing mineral - sakuraiite (Małek and Mikulski 2019).

3.1 Cassiterite mineralization

In the studied samples, cassiterite is not visible macroscopically. It occurs as a small (max. 300 μm , usually up to 100 μm diameter) hypautomorphic or rarely automorphic grains forming grape-like clusters (Fig. 3a; or “spongy” ac. to Jaskólski and Mochnacka 1959;

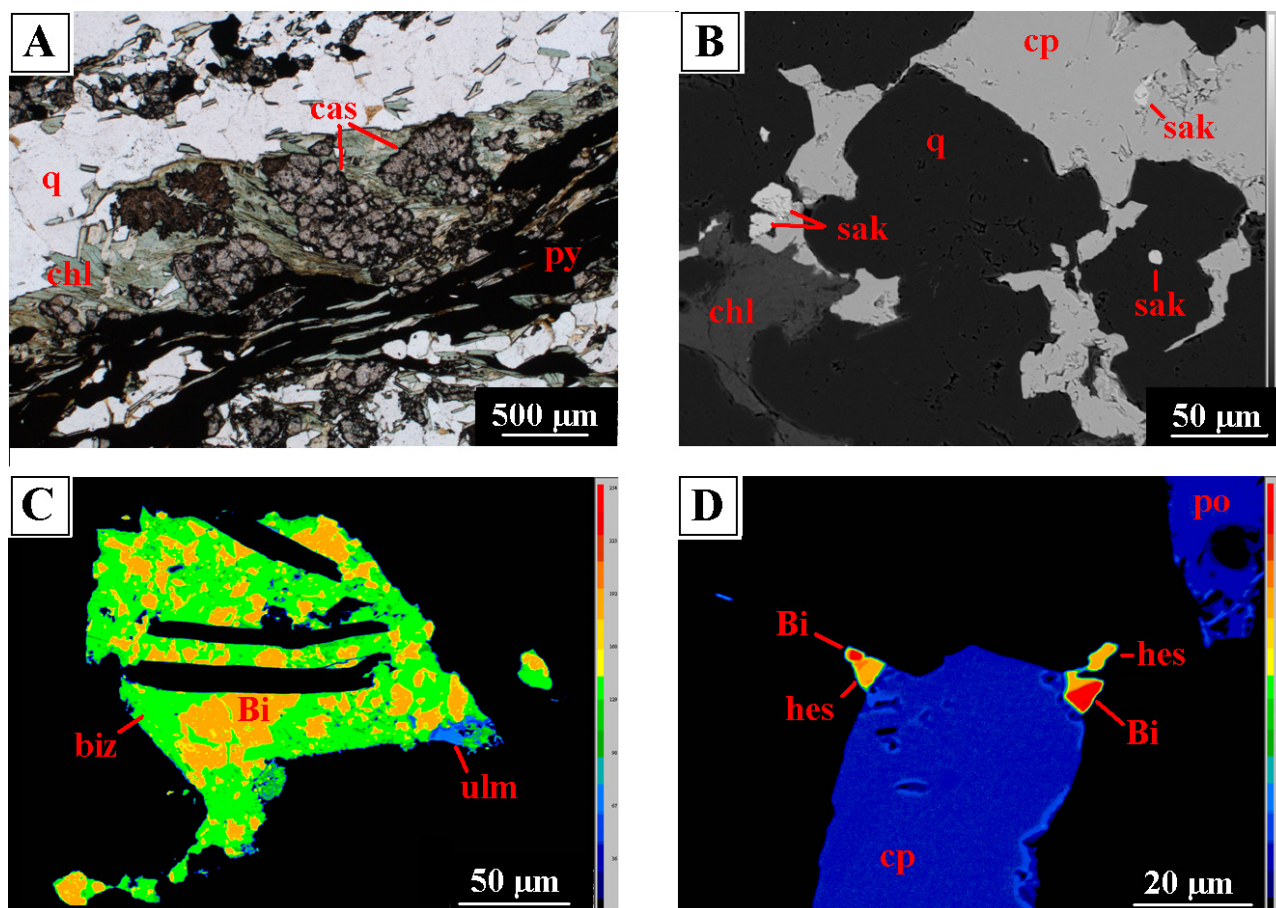


Figure 3 Cassiterite-sulfide mineralization from the Krobica tin deposit (a) cassiterite (cas) within chlorite laminae in association with sulphides, K11/3 borehole, depth 250,6 m, optical microscope, transmitted light, 1N; (b) chalcopyrite (cp) and sakuraiite (sak) in form of intergrowths and separate grains, C-X/46 borehole, depth 223,5 m, BSE; (c) overgrowths of native bismuth (Bi), bismuthinite (biz) and ullmannite [NiSbS] (ulm), C-X/46 borehole, depth 223,5 m, BSE; (d) characteristic sulfide aggregate with native bismuth (Bi) and hessite (hes), G-1/13 borehole, depth 154,25 m, BSE

Mochnacka 1985), that follow the main schistosity. Cassiterite mostly occurs in association with quartz, and chlorite and garnet, less often with sulphides, muscovite, chloritoid and biotite (Michniewicz et al. 2006). In addition, it is observed as intergrowths almost in every rock-forming mineral. Less often it forms aggregates with sulphides such as chalcopyrite, arsenopyrite or pyrrhotite. Occasionally cassiterite occurs as intergrowths in other ore minerals and sometimes contains wolframite inclusions.

3.2 Sulphide mineralization

Pyrrhotite and chalcopyrite are the main sulphides. Their xenomorphic crystals are forming big aggregates (up to 4 mm diameter) also with other sulphides (mostly pyrite, sphalerite and arsenopyrite). Pyrrhotite contains intergrowths of other minerals (mostly sulphides). Chalcopyrite definitely less often than pyrrhotite contain intergrowths, but most commonly occurs as an intergrowths itself (mainly in garnets). Sometimes it is replaced by covellite and bornite. Pyrite occurs less often than pyrrhotite or chalcopyrite and it co-creates sulphide aggregates with them, also makes growths with pyrrhotite. It shows a xenomorphic and occasionally

hypautomorphic form. Ilmenite is the most commonly occurring ore mineral in studied samples. It occurs both as a rock impregnation (grains up to 300-400 µm) and as a mineral aggregates with sulphides. It takes on a xenomorphic form (occasionally hypauto-morphic) - elongated crystals are oriented according to the direction of the shale foliation.

Arsenopyrite and sphalerite occur occasionally and they are forming aggregates with other sulphides (max. up to 100 µm diameter). Native bismuth and bismuthinite in the vast majority of observed cases occurs as intergrowths in sulphides (Fig. 3d). Sometimes they are also forming separate clusters overgrowing each other (up to 200 µm diameter). Magnetite and rutile like ilmenite occurs as a small rock impregnation but definitely less often. Qualitative and quantitative analyzes of ore minerals showed the content of interesting admixtures of the trace elements, such as cobalt, nickel, selenium, arsenic, zinc and silver. Chalcopyrite showed content of admixtures of Zn (max. 0.111 wt.%), sphalerite contained interesting admixtures of Ag (max. 0.289 wt.%) and Co (max. 0.137 wt.%), pyrite showed content of Ni (max. 0.661 wt.%). In turn, in arsenopyrite were found admixtures of Ni (max. 0.809 wt.%) and Co (max. 0.210 wt.%) and in bismuthinite: Te (max. 0.39 wt.%), Ni (max.

0.83 wt.%), Co (max. 0.63 wt.%) and also Au (max. 8.23 wt.%).

3.3 Rare ore minerals

They were identified in form of small intergrowths in sulphides or mutual mineral overgrowths with them (Figs. 3b-d). They occur definitely less often in the form of separate grains (the biggest grains – cobaltite and sakuraiite – up to 50 µm diameter; Fig. 3b). In general, these minerals occur sporadically and in small amounts. Among them, the most interesting metal contents in the chemical composition show: cobaltite (Co max. 34.7 wt.%, Ni max. 5.47 wt.%), costibite (Co max. 24.5 wt.%, Sb max. 57.03 wt.%, Ni max. 4.22 wt.%), gersdorffite (As max. 43.38 wt.%, Ni max. 26.63 wt.%, Co max. 11.22 wt.%), hedleyite (Te max. 32.92 wt.%, Ag max. 1.16 wt.%, Se max. 4.47 wt.%), hessite (Te max. 41.3 wt.%, Ag max. 61.3 wt.%), mimetite (Pb max. 70.56 wt.%, As max. 15.3 wt.%, Ni max. 0.14 wt.%, Co max. 0.29 wt.%, Hg max. 0.16 wt.%), safflorite (As max. 68.49 wt.%, Sb max. 0.27 wt.%, Ni max. 0.7 wt.%, Co max. 11.82 wt.%), sakuraiite (In max. 19.1 wt.%, Cd max. 0.65 wt.%, Ag max. 0.16 wt.%, Zn max. 36.86 wt.%), ullmannite (Sb max. 53.0 wt.%, Bi max. 23.38 wt.%, Se max. 0.33 wt.%, Cu max. 0.45 wt.%, Ni max. 26.46 wt.%) and wolframite (Ce max. 1.50 wt.%, W max. 60.39 wt.%).

4 Conclusions

- The modern geochemical investigation with application of ICP-QMS, ICP-OES WD-XRF and GFAAS methods to cassiterite-sulphide samples from the tin deposits in the Stara Kamienica schist belt in the Sudetes Mountains, revealed that they contain elevated concentrations of critical elements (In, Bi, Ga, Co, Nb, Pt, Pd and Re) as well as associated elements (Cu, Zn and Pb). Some of these critical elements show a strong positive correlation with tin or base metals distribution (e.g. In, Bi or Ga) what may increase an economic value of the considering Sn ores.
- Moreover, on the basis of detailed microscopic and microprobe (EMPA) studies, carriers of trace elements in sulphides associated with cassiterite ores were identified and, what is important, minerals so far unknown from the Krobica tin deposits were also found. As an example the main carrier of indium - sakuraiite [Cu, Zn, Fe)₃(In, Sn) S₄] and other tellurium (e.g. hessite – Ag₂Te) and bismuth minerals were recognized.

Acknowledgements

The project was financed by the National Fund for Environmental Protection and Water Management in accordance with Agreement No. 506/2015.

References

Cook N, Dudek K (1993) Petrography and geothermometry of rocks

- associated with Sn- and Co-Ni-As-Bi-Ag mineralizations at Przecznicza, Gierczyn-Krobica in the Izer Mountains, S.W. Poland. In: Seltmann R, Kämpf H, Möller P (eds) Metallogeny of collisional orogens focused on the Erzgebirge and comparable metallogenic settings. Czech Geological Survey, pp 247–254
- Jaskólski S, Mochnacka K (1958) Złoże cyny w Gierczyniu w Górach Izerskich na Dolnym śląsku i próba wyjaśnienia jego genezy. *Archiwum Mineralogiczne* 22:17–106
- Malon A, Tymiński M, Mikulski SZ, Oszczepalski S (2018) Metallic Raw Materials. In: Szuflicki M, Malon A, Tymiński M (eds) The balance of mineral resources deposits in Poland as of 31.12.2018, PIG-PIB, Warszawa, pp 49–63
- Małek R, Mikulski SZ (2019) Geochemical-mineralogical research of the rare and associated elements within cassiterite-sulphide mineralization in the Stara Kamienica schist belt in Western Sudetes - preliminary results. *Przegląd Geologiczny* 67(3): 179–182
- Michniewicz M, Bobiński W, Siemiątkowski J (2006) Mineralizacja cynowa w środkowej części pasma łupkowego Starej Kamienicy (Sudety Zachodnie). *Prace Państw Inst Geol* 185: 1–136
- Mikulski SZ, Kozłowski A, Speczik S (2007) Fluid inclusion study of gold-bearing quartz-sulphide veins and cassiterite from the Czarnow As deposit ore (SW Poland). In: Colin JA et al. (eds) Digging deeper. Proceedings of the Ninth Biennial SGA Meeting, Dublin 2007, pp 805–808
- Mikulski SZ., Oszczepalski S, Sadłowska K, Chmielewski A, Małek R (2018) The occurrence of associated and critical elements in the selected documented Zn-Pb, Cu-Ag, Fe-Ti-V, Mo-Cu-W, Sn, Au-As and Ni deposits in Poland, *Biuletyn Państwowego Instytutu Geologicznego* 472:21–52
- Piestrzyński A, Mochnacka K (2003) Discussion on the sulphide mineralization related to the tin-bearing zones of the Kamienica schists belt (Western Sudety Mts., S.W. Poland). In: Cieżkowski W, Wojewoda J, Żelaźniewicz A (eds) *Sudety Zachodnie: od wendy do czwartorzędz. WIND Wrocław*, pp 169–182 (in Polish with English summary)
- Piestrzyński A, Mochnacka K, Mayer W, Kucha H (1990) Scheelite and ferberite from the tin-bearing schists of the Kamienica Range (the Sudety Mts., S.W. Poland). *Mineralogia Polonica* 21:5–14
- Piestrzyński A, Mochnacka K, Mayer W, Kucha H (1992) Native gold (electrum), Fe-Co-Ni arsenides and sulpharsenides in the mica-schists from Przecznicza, the Kamienica Range, SW Poland. *Mineralogia Polonica* 23:27–43
- Szałamacha M, Szałamacha J (1974) Geologiczna i petrograficzna charakterystyka łupków mineralizowanych kasyterytem na przykładzie kamieniołomu w Krobicy. *Biuletyn Państwowego Instytutu Geologicznego* 279:59–89
- Wiszniewska J (1984) Geneza okruszczenia łupków izerskich Pasma Kamienickiego. *Archiwum Mineralogiczne* 40(1):115–188

A review of the resource potential of cobalt in Europe

Stefan Horn, Evi Petavratzi, Gus Gunn, Richard Shaw
British Geological Survey, UK

Frances Wall
Camborne School of Mines, University of Exeter, UK

Abstract. Cobalt is a technology metal used in rechargeable batteries, where the growing market for electric vehicles (EVs) is likely to significantly increase demand in the future. However, there are significant supply risks associated with this critical raw material. In Europe, only three mines in Finland currently produce cobalt, meaning that the EU is highly reliant on imports to meet current demand. However, a review of known cobalt deposits and occurrences has revealed that there are many other areas in Europe where cobalt could be produced as a by-product, including: (1) Sediment-hosted Cu deposits in Poland; (2) Ni-laterite deposits in south-eastern Europe; and (3) magmatic Ni-Cu-sulfide deposits in Scandinavia. Moreover, secondary resources with high cobalt contents, such as mine tailings and smelter slags, may also have potential to supply additional cobalt.

All this information will be used to produce a material flow analysis to gain a better understanding of the cobalt supply chain in Europe, which will cover future supply/demand scenarios that focus on electric vehicles.

1 Introduction

Transport is the second largest contributor of greenhouse gas emissions in the European Union (EEA 2018). Electric vehicles will play a major role in decarbonising the transport sector and their deployment has increased rapidly over the past few years. More than 3 million electric cars are currently in stock globally and an EV year-on-year sale increase of 56% was recorded in 2017 (IEA 2018). Consequently, there is increasing demand for raw materials used in EV batteries. For example, cobalt is widely used in Li-ion batteries (LIB) to provide the required high energy density. Depending on the chosen LIB chemistry, the cathode commonly requires several kilograms of cobalt. For example, the battery used in a Chevrolet Bolt contains 26 kg of cobalt (UBS 2017). Cobalt is classified as a critical metal (EC 2017), with 59% of world mine production coming from the Democratic Republic of Congo (DRC), some of which is linked to human rights abuses (Brown et al. 2019; Amnesty International 2016). Furthermore, the majority of cobalt ores and concentrates are exported to China, which now dominates global production of refined cobalt. Europe accounts for less than 2% of global mine production of cobalt and is thus highly dependent on imports (Brown et al. 2019). In view of the size of Europe's car manufacturing industry there is considerable interest in the development of indigenous resources for battery raw materials. The European Battery Alliance, launched in 2017 by the European Commission, aims to make the EU

a global leader in the complete value chain of EV battery production (EC 2018).

In order to help secure adequate and timely cobalt supply for the battery sector and support responsible sourcing, new research by the British Geological Survey (BGS) aims to analyse the cobalt supply chain in Europe and to quantify the future global demand for cobalt with a focus on the EV battery sector.

2 Primary cobalt deposits in Europe

Globally, most cobalt is produced from three deposit types: (1) stratiform sediment-hosted Cu-Co deposits; (2) magmatic Ni-Cu (-Co-PGE) sulfide deposits; and (3) Ni-Co laterite deposits. Furthermore, cobalt can also be

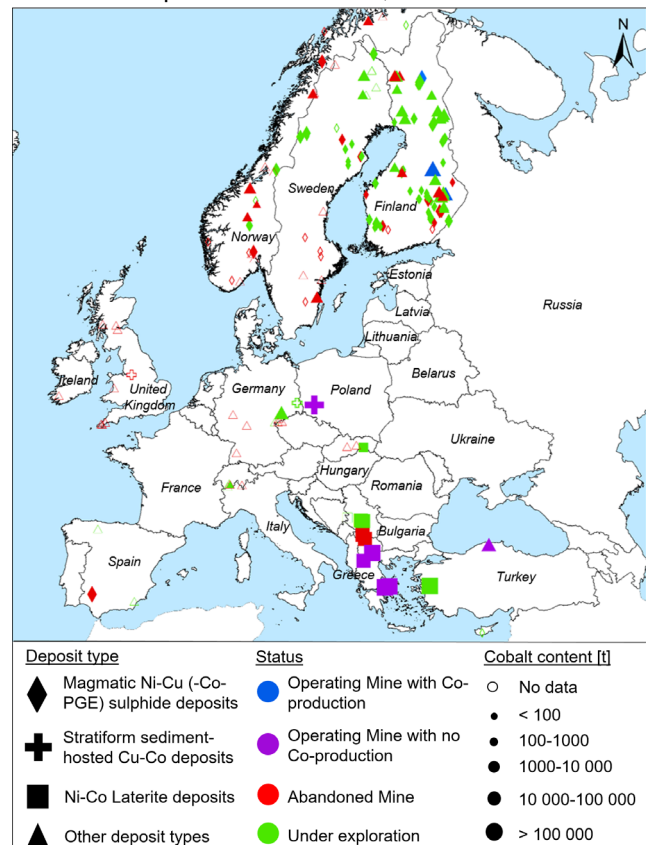


Figure 1. Preliminary map of potential cobalt resources in Europe classified by deposit type, status and cobalt content (Data from FODD 2011; Berger et al. 2011; Slack et al. 2017; Pazik et al. 2016 and company reports).

enriched in a variety of other deposit types, including: polymetallic Co-rich vein deposits; black shale-hosted

deposits; iron oxide-Cu-Au deposits; metasedimentary Co-Cu-Au deposits; volcanic-hosted massive sulphides (VHMS); Mississippi Valley type deposits; and Fe-Cu skarn and replacement deposits (Slack et al. 2017). In Europe, cobalt resources are associated with several of these deposit types, although production is limited to three mines in Finland, which together accounted for mine production of 2700 t cobalt in 2017 (Brown et al. 2019) (Fig. 1). At Sotkamo (also known as Talvivaara) a metamorphosed black-shale-hosted deposit contains an estimated 411 000 t cobalt metal (Slack et al 2017; FODD 2011). The ore is located in an organic and sulfur-rich black shale, which likely precipitated in an anoxic-euxinic environment. Subsequent metamorphism and deformation are considered to have contributed to further concentration of the metals in the deposit. (Luokola-Ruskeeniemi & Lahtinen 2013). Kevitsa is a magmatic sulfide deposit hosted in an ultramafic intrusion in the Lapland Greenstone Belt with an average Co grade of 0.01% (Santaguida et al. 2015; New Boliden 2017). The third mine, at Kylylahti, is located in the Outokumpu district, which is generally classified as a VHMS deposit (Slack et al. 2017). However, Peltonen et al. (2008) and references therein suggest a more complex polygenetic origin, including secondary Ni-enrichment, which is unusual for VHMS deposits, and late tectonic remobilisation. New Boliden (2017) reported an average grade of 0.12% Co in the Kylylahti deposit.

Figure 1 shows that Scandinavia is well endowed with deposits that have potential for cobalt extraction, especially magmatic sulfide ores. In Poland and Germany, stratiform sediment-hosted deposits comprise Europe's largest copper resources with reported average Co grades of between 50-80 ppm in the Polish deposits (Pazik et al. 2016). The so-called Kupferschiefer have been exploited for many centuries for chiefly Cu, Ag, Pb, Zn and even Co for a short time period, but the latter is not currently extracted (Borg et al. 2012). Co-rich Ni-Co-laterite deposits are abundant in Albania, Bosnia, Greece, Kosovo, Macedonia, Serbia and Turkey, with Co grades of up to 0.08% (Berger et al. 2011; Herrington et al. 2016). The laterites evolved on ophiolite complexes, which were obducted during the closure of the Tethyan Ocean during Late Jurassic to Early Cretaceous. Among various lateritic deposit subtypes which occur in the area oxide-dominated deposits are of special interest for cobalt recovery, due to late mobilisation and enrichment (Herrington et al. 2016). In these countries, ferronickel is produced by smelting these ores. Cobalt is typically enriched in the ferronickel and is, therefore, effectively lost for use in other applications (Berger et al. 2011; Crundwell et al. 2011).

3 Size and grade of primary deposits

Figure 2 illustrates the relation of Co grade and ore tonnage for Co-bearing deposits in Europe compared to major global cobalt producers. Globally magmatic sulfide deposits vary considerably in size, but most have a grade

between 0.01 – 0.1% Co. The Kevitsa mine, the Sakatti exploration project in Finland and the currently closed mine at Aguablanca in Spain each contain more than 10 000 t cobalt but are slightly smaller than Voisey's Bay in Canada (Slack et al. 2017; Anglo American 2018). Deposits in the Central African Copperbelt commonly have higher grades and contain more cobalt than the magmatic deposits. For example, the Kisanfu deposit has a grade of 1.08 % Co and 1.16 million tonnes of contained cobalt (Slack et al. 2017). In Europe there are significant resources of cobalt in the Kupferschiefer deposits in Poland, which are estimated to contain 122 360 t of cobalt metal (Szamalek et al. 2017). This highlights the significance of the resources in these deposits in Europe. Lateritic deposits which are currently major sources of cobalt production include Murrin Murrin in Australia and Moa in Cuba with a contained cobalt tonnage of 351 000t and 522 000t, respectively (Crundwell et al. 2011; Slack et al. 2017). The Mokra Gora laterite deposit in Serbia, and other deposits located in the Balkans, plot in the vicinity of these world class examples. The black shale deposit at Sotkamo is conspicuous on account of its low Co grade but very large size. These characteristics, together with the deportment of cobalt in the ore, make bioheap leaching the preferred method for metal recovery at the mine site (Brierley & Brierley 2001; Riekkola-Vanhanen 2013). In addition to the deposits highlighted above, potential cobalt resources are also known in other deposit types distributed widely in Europe.

Recent improvements in extraction and recovery technologies mean that secondary materials, such as copper slags and mine tailings, have the potential to be important sources of cobalt in Europe (Lutandula et al. 2013; Falagan et al. 2017). Therefore, it is important to understand the concentration and distribution of cobalt in these secondary materials, especially in wastes from processing ores known to be enriched in cobalt.

4 The cobalt supply chain

As a by-product of copper or nickel mining, information about flows and stocks of cobalt in the different stages of production is scarce. There are many uncertainties along the whole supply chain, including incomplete data, hidden flows (e.g. artisanal mining) and a lack of understanding of the processes, material transformations and material quantities involved (Fig. 3). A detailed analysis of the cobalt supply chain will enable the development of better models for future supply and demand requirements. This will help to develop improved standards and guidelines for responsible sourcing and cobalt traceability.

Acknowledgments

This project is funded by the NERC GW4+ Doctoral Training Partnership and hosted by the BGS in collaboration with Camborne School of Mines, University of Exeter.

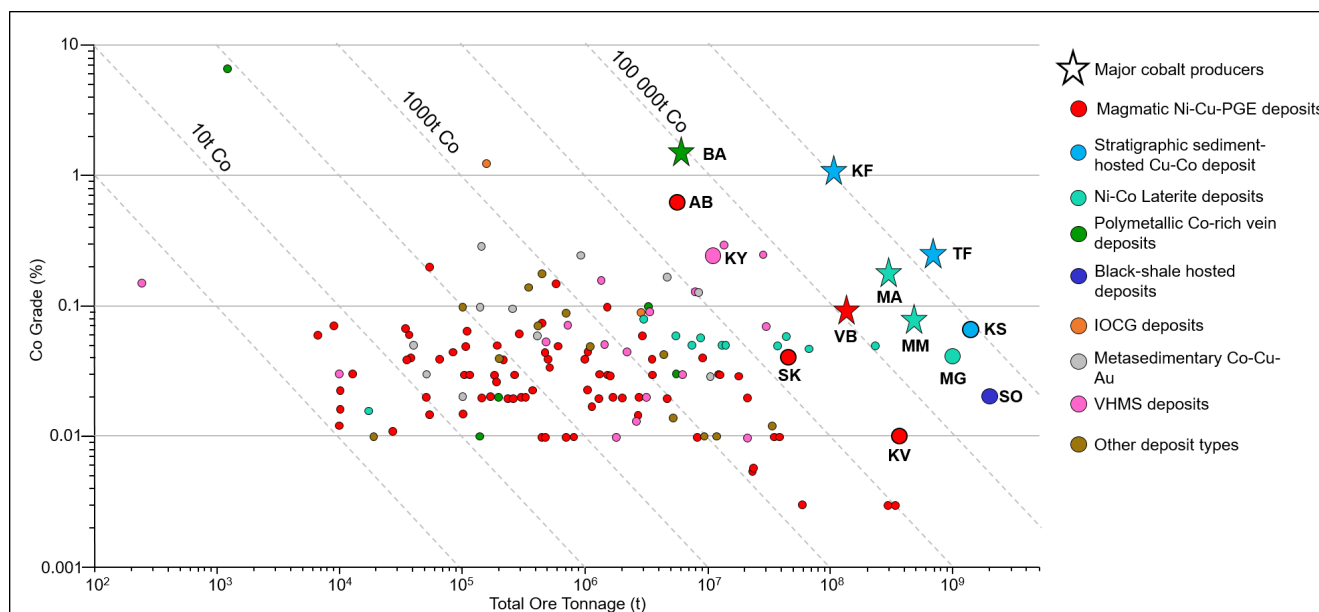


Figure 2. The relationship between ore tonnage and grade in Co-bearing deposits in Europe. Major cobalt producing mines are included for comparison (star-shape). Some large European deposits described in the text are highlighted as large dots and labelled. The total ore tonnage includes the mined ore, reserve and resources where known. Dashed lines represent isolines for contained Co. The quality of the grade and tonnage data are variable: Some data are taken from CRIRSCO-compliant resource estimates, while others are historic estimates or from codes not compliant with current reporting standards. AB = Aguablanca, Spain; BA = Bou Azzer, Morocco; KF = Kisanfu, DRC; KS = Kupferschiefer district, Poland; KV = Kevitsa, Finland; KY = Kylahti, Finland; MA = Moa, Cuba; MG = Mokra Gora, Serbia; MM = Murrin Murrin, Australia; SK = Sakatti, Finland; TF = Tenke Fungurume; SO = Sotkamo (Talvivaara), Finland; VB = Voisey's Bay, Canada (Data from FODD 2011; Berger et al. 2011; Slack et al. 2017; Pazik et al. 2016 and references therein as well as company reports).

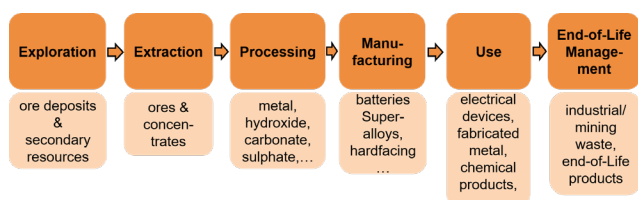


Figure 3. Simplified cobalt supply chain.

References

- Amnesty International (2016) "This is what we die for". Human rights abuses in the Democratic Republic of the Congo power the global trade in cobalt. London, U.K.
- Anglo American plc (2018) Ore reserves and Mineral resources report 2018.
- Berger VI, Singer DA, Bliss JD, Moring BC (2011) Ni-Co Laterite deposits of the world – Database and grade and tonnage models. Open-File Report. 2011-1058. U.S. Geological Survey.
- Brierley J, Brierley C (2001) Present and future commercial applications of biohydrometallurgy *Hydrometallurgy* 59:233-239.
- Borg G, Piestrzynski A, Bachmann G, Püttmann W, Walther S, Fiedler M (2012) An overview of the European Kupferschiefer deposits *Econ Geol Spec Publ* 16:455-486.
- Brown TJ, Idoine NE, Raycraft ER, Hobbs SF, Shaw RA, Everett P, Kresse C, Deady EA, Bide T (2019) World Mineral Production 2013-2017. British Geological Survey, Keyworth, Nottingham.
- Crundwell F, Moats M, Ramachandran V (2011) Extractive metallurgy of nickel, cobalt and platinum group metals. Elsevier, Amsterdam.
- EC - European Commission (2017) Study on the review of the list of Critical Raw Materials - Critical Raw Materials Factsheets. Luxembourg. doi:10.2873/398823.
- EC - European Commission (2018) Annex 2 - Strategic Action Plan on Batteries. COM(2018) 293, Brussels.
- EEA - European Environment Agency (2018) Greenhouse gas emissions from transport. Copenhagen.
- FODD - Fennoscandian Ore Deposit Database (2011) Geological Survey of Finland (GTK) Geological Survey of Norway (NGU), Geological Survey of Russia (VSEGEI), Geological Survey of Sweden (SGU), SC Mineral. <http://en.gtk.fi/information/services/databases/fodd/disclaimer.html>. Updated December 2017. Accessed 07 March 2019.
- Falagán C, Grail BM, Johnson DB (2017) New approaches for extracting and recovering metals from mine tailings. *Miner Eng* 106:71-78 doi:<https://doi.org/10.1016/j.mineng.2016.10.008>.
- Herrington R, Mondillo N, Boni M, Thorne R, Tavlan M (2016) Bauxite and Nickel-Cobalt Lateritic Deposits of the Tethyan Belt. In: Richards, J (ed) *Tectonics and Metallogeny of the Tethyan Orogenic Belt*. *Econ Geol Spec Publ* 19:349-387.
- IEA - International Energy Agency (2018) Global EV Outlook 2018 - Towards cross-modal electrification.
- Loukola-Ruskeeniemi K, Lahtinen H (2013) Multiphase evolution in the black-shale-hosted Ni-Cu-Zn-Co deposit at Talvivaara, Finland. *Econ Geol Rev* 52:85-99.
- Lutandula MS, Maloba B (2013) Recovery of cobalt and copper through reprocessing of tailings from flotation of oxidised ores. *J. Environ. Chem. Eng* 1(4):1085-1090 doi:10.1016/j.jece.2013.08.025.
- New Boliden (2017) Metals for Long-term Value Creation - 2017 Annual report. <https://www.boliden.com/investor-relations/reports-and-presentations/annual-reports>. Accessed 07/03/2019.
- Pazik PM Chmielewski T, Glass HJ, Kowalczyk PB (2016) World production and possible recovery of cobalt from the Kupferschiefer stratiform copper ore. *E3S Web of Conferences* 8. 01063. EDP Science.
- Peltonen P, Kontinen A, Huhma H, Kuronen U (2008) Outokumpu revisited: new mineral deposit model for the mantle peridotite-associated Cu-Co-Zn-Ni-Ag-Au sulphide deposits. *Ore Geol Rev* 33:559-617.
- Riekkola-Vanhanen M (2013) Talvivaara mining company—From a project to a mine. *Miner Eng* 48:2-9.
- Santaguida F, Luolavirta K, Lappalainen M, Yliinen J, Voipio T, Jones S (2015) The Kevitsa Ni-cu-PGE deposit in the Central

Lapland greenstone belt in Finland. In Maier WD, Lahtinen R, O'Brien H (eds.) Mineral Deposits of Finland. Elsevier, pp 195-210.

Slack FJ, Kimball BE, Shedd KB (2017) Cobalt. Chap. F of Schulz KJ, DeYoung JH Jr., Seal RR, Bradley DC (eds) Critical mineral resources of the United States – Economic and environmental geology and prospects for future supply. Professional paper 1802-F. U.S. Geological Survey.

Szamalek K, Szuflicki M, Malon A, Tymniski M (eds.) (2017) Mineral resources of Poland. Polish Geological Institute - National Research Institute, Warsaw. ISBN: 978-83-7863-718-9.

UBS (2017) UBS Evidence Lab Electric Car Teardown – Disruption ahead?, Q-series

Undiscovered Kuusamo-type cobalt-gold resources in Finland

Kalevi Rasilainen, Pasi Eilu

Geological Survey of Finland, Finland

Irmeli Huovinen, Jukka Konnunaho, Tero Niiranen, Juhani Ojala, Tuomo Törmänen

Geological Survey of Finland, Finland

Abstract. The potential metal resources in undiscovered Kuusamo-type cobalt-gold deposits in the Finnish bedrock were estimated down to one km depth using the three-part quantitative assessment method. A grade-tonnage model was constructed based on data from known deposits in the Kuusamo area in Finland. Eight permissive tracts were delineated, based on geological criteria. Most of the tracts are located in northern Finland. The number of undiscovered deposits was estimated for each tract by a group of experts at several levels of confidence. The mean estimate of the number of undiscovered Kuusamo-type cobalt-gold deposits in Finland is 58. The cobalt and gold resources in the undiscovered deposits was estimated using Monte Carlo simulation. The median estimate of undiscovered Kuusamo-type resources in Finland is 100,000 t of cobalt and 85 t of gold.

1 Introduction

Cobalt is known to occur as a minor or major commodity in several different types of mineral deposits in Finland, but the majority of the known cobalt endowment in the Finnish bedrock is in synorogenic intrusion-related Cu-Ni deposits, komatiite-related Ni-Cu-PGE deposits, Outokumpu-type Cu-Co-Zn deposits, Talvivaara-type Ni-Zn-Cu-Co deposits and Kuusamo-type Co-Au deposits. Undiscovered resources of cobalt in the three first mentioned deposit types in Finland have previously been estimated (Rasilainen et al. 2012, 2014). The undiscovered endowment of cobalt in Talvivaara-type deposits could not be assessed due to the lack of grade-tonnage information required for the construction of a deposit model (Rasilainen et al. 2010). Large mafic-ultramafic layered intrusions in northern Finland might contain significant cobalt resources, but the lack of cobalt grade information in layered intrusion-hosted Ni-Cu-PGE deposits has prevented the estimation of these resources.

We describe here the results of an assessment of cobalt and gold resources in Kuusamo-type Co-Au deposits in Finland. The assessment is part of an ongoing series of assessments started by the Geological Survey of Finland (GTK) in 2008 to estimate the undiscovered resources of several metals in the Finnish bedrock.

2 Kuusamo-type cobalt-gold deposits

The metal association Au-Co±Cu±U±LREE is

characteristic for numerous mineral deposits within the Kuusamo schist belt in eastern Finland (Fig. 1; Pankka 1992; Pankka and Vanhanen 1992; Vanhanen 2001). The reported ore tonnage and gold and cobalt grade values of the deposits show considerable variation (Table 1). Copper, uranium and rare earth elements (REE) are common minor components in the Kuusamo area deposits and occurrences (Vanhanen 2001; Dragon Mining 2013), but only in a few cases are there published resource estimates. The main economic interest in the Kuusamo deposits is in gold and cobalt, whereas copper and the REE have been regarded as potential by-products and uranium as a problematic waste (Dragon Mining 2013). None of the Kuusamo schist belt deposits has so far proven economic.

The Kuusamo deposits are hosted by a clastic sedimentary-dominated sequence deposited between 2.35 and 2.21 Ga, which also contains basaltic lavas and indications of evaporates (Vanhanen 2001). The sequence was intruded by basaltic dikes and sills prior to regional deformation. All deposits have a distinct structural control, and most of them are located at the intersection of a regional northeast-trending anticline with northwest-trending faults. The largest deposit, Juomasuo, is located in a doubly-plunging part of the northeast-trending anticline.

The rocks in the Kuusamo schist belt were affected by three regional and at least one localised alteration event (Pankka 1992; Pankka and Vanhanen 1992; Vanhanen 2001). The regional events were characterised by partial to total albitisation, sericitisation, spilitisation, scapolitisation and carbonatisation. The Au-Co±Cu±U±LREE mineralisation is related to the localised stage 4 alteration, which consists of weak to intense sulphidation with K±Fe, Mg alteration (Vanhanen 2001).

The main ore minerals in the Kuusamo-type deposits are pyrite, pyrrhotite, cobaltite, cobaltian pentlandite and chalcopyrite. Native gold occurs in free form within gangue and also associated with bismuth and tellurium minerals that are present as inclusions and in fractures in pyrite, pyrrhotite, cobaltite, and uraninite (Pankka 1992; Vanhanen 2001).

The metallic deposits in the Kuusamo schist belt have historically been classified into various types, including orogenic gold with atypical metal association, iron oxide-copper-gold (IOCG), Blackbird type, and syngenetic (e.g., Pankka 1992; Pankka and Vanhanen 1992; Vanhanen 2001; D.I. Groves personal communication 2006; Slack et al. 2010; Slack 2013). No exactly similar

deposits have yet been discovered elsewhere in Finland; therefore, they are classified as “Kuusamo-type”. However, there are similarities with some of the gold deposits in the Peräpohja belt, 200 km to the west of Kuusamo (Ranta et al. 2018).

Most of the available evidence suggest that the Kuusamo schist belt deposits are epigenetic. Early, premetamorphic, connate and possibly evaporite-derived brine circulation within the rifted basin caused alteration and rendered parts of the sequence competent. Such brines may survive into an orogeny and be able to transport metals also during orogenic processes (e.g., Yardley & Graham 2002). Premetamorphic alteration hardened the rocks and rendered them competent, and provided brines to transport the metals. Overall, the deposit characteristics are most consistent with the orogenic gold model with an atypical metal tenor. The main reasons for not including the Kuusamo deposits into *sensu lato* orogenic gold class include the multiple stages of alteration, the extensive mobility of most metals in the mineralising system, and the metal zoning within the deposits.

3 Data used and the assessment process

3.1 Data

Primary sources of information used in the assessment include geological maps in digital and paper format, databases of mineral deposits and occurrences, technical reports on deposits and occurrences, exploration and mining company websites, and published geological literature. The personal experience and knowledge of the assessment team members concerning many of the areas assessed was a valuable addition to the publicly available information.

Data for the deposit model was gathered from the GTK mineral deposit database and the Fennoscandian Ore Deposit Database (FODD 2018). Company web pages were accessed for updated grade and tonnage data.

3.2 Assessment process

The GTK assessments estimate the total amount of metals in undiscovered deposits down to a selected depth (usually one kilometre) using the three-part quantitative assessment method of the USGS (Singer 1993; Singer and Menzie 2010). The process consists of (1) evaluation and selection or construction of a descriptive model and a grade-tonnage model for each deposit type being assessed, (2) delineation of areas permitted by the geology for the deposit types (permissive tracts), and (3) estimation of the number of undiscovered deposits of each deposit type within the permissive tracts. The estimated numbers of deposits and the grade and tonnage distributions are used in Monte Carlo simulation to model the total undiscovered metal endowment.

The assessment process begun with the selection of the team of experts. The roles and responsibilities of the experts were agreed in the start-up workshop and the

characteristic features of Kuusamo-type deposits and their geological environments were discussed.

Preliminary permissive tracts were defined by the assessment team members who had personal working experience in the areas under study. The tracts were finalised after a review by other team members. For each permissive tract, a preliminary report was prepared. The report contained the delineation criteria for the tract, information on all existing mineral deposits and occurrences within the tract, information on the extent and intensity of exploration within the tract, and references to the sources of such information. The main criteria for delineating the Kuusamo-type tracts include: 1) a tectonic setting of an intracratonic rifted basin, 2) local indications of pre-existing evaporites, 3) extensive and intense sodic ± CO₂ (albite ± carbonate) and Na-Cl (scapolite) alteration predating the orogeny and mineralisation, 4) localised multi-stage, syn to late orogenic, structurally-controlled alteration proximal to Au-Co±Cu mineralisation.

The grade-tonnage model for Kuusamo-type Co-Au deposits was constructed using data from the above-mentioned databases.

The information gathered for the tracts was applied in two assessment workshops, where the experts estimated the numbers of undiscovered deposits possibly existing within each tract.

After the workshops, Monte Carlo simulations were run to estimate the probability distributions of the undiscovered cobalt and gold endowments in the permissive tracts. Detailed results of the assessment will be published in the report series of GTK.

4 Results and discussion

4.1 Grade and tonnage model

Kuusamo-type deposits are not with certainty known outside of Finland, and the number of deposits with a published resource estimate is small. Because of this, the grade-tonnage model is only based on 10 deposits, all within the Kuusamo area. Statistical tests indicate that the distributions of ore tonnage, gold grade and cobalt grade for the 10 deposits do not significantly differ from log normality (Table 1). There are weak correlations between logarithmic ore tonnage and metal grade values, but Bonferroni adjusted probabilities for the correlation coefficients indicate that the correlations are not significant.

Because of the small number of deposits used to construct the grade-tonnage model, and the uncertainties concerning the completeness of the reported resources, it is probable that the model gives a downward biased representation of the true resources of the Kuusamo-type cobalt-gold deposits.

Table 1. Summary statistics for the Kuusamo Co-Au deposits used for the grade-tonnage model.

	Tonnage (Mt)	Co (%)	Au (g/t)
Number of deposits	10	10	10

Minimum	0.050	0.014	0.040
Maximum	7.429	0.23	7.2
Arithmetic Mean	1.624	0.11	2.4
Standard Deviation	2.463	0.072	2.2
10 th percentile	0.090	0.022	0.20
50 th percentile	0.503	0.089	2.0
90 th percentile	6.054	0.22	5.6
Shapiro-Wilk p-value*	0.892	0.473	0.169

Mt: Million metric tons. Tonnages are rounded to full thousands and grades to two significant digits.

* Shapiro-Wilk normality test p-value was calculated for logarithmic tonnage and grade values.

4.2 Permissive tracts and number of deposits

In total, eight permissive tracts were delineated for Kuusamo-type Co-Au deposits (Table 2, Fig. 1). These tracts contain all the known Kuusamo-type deposits and occurrences in Finland. In total, the tracts cover an area of 21,082 km², which is approximately six per cent of the land area of Finland. The size of the permissive tracts varies from 780 km² to 5611 km² and the median area is 2254 km². Most of the tracts are located in Northern Finland.

The expected (mean) number of undiscovered deposits for a permissive tract, rounded to whole numbers, varies between two and 14, and the sum of the mean estimates across all tracts is 58 deposits (Table 2). Over 60 % of the undiscovered deposits are estimated to be located within three permissive tracts: Kuusamo (24 %), Peräpohja (21 %) and Pelkosenniemi (16 %).

Table 2. Permissive tracts for Kuusamo-type Co-Au deposits in Finland.

Tract name	Tract area (km ²)	Number of known deposits	Expected number of undiscovered deposits
Enontekiö	780	0	4.8
Kainuu	1075	0	6.7
Kittilä-Kolari	1279	0	4
Kuusamo	3684	10	14
Pelkosenniemi	5611	0	9.1
Peräpohja	4634	0	12
Pulju	790	0	2.3
Sodankylä	3228	0	5.5

4.3 Undiscovered endowment of cobalt and gold in Kuusamo-type deposits

The median estimate of the total in situ cobalt and gold content in undiscovered Kuusamo-type Co-Au deposits in Finland is at least 100,000 t of cobalt and 85 t of gold (Table 3). Approximately 50 % of this endowment is estimated to be located in undiscovered deposits in the Kuusamo and Peräpohja permissive tracts (Fig. 1). The assessment results indicate that at least 80 % of the remaining Kuusamo-type cobalt and gold endowment within the uppermost one kilometre of the Finnish bedrock is in poorly explored or entirely unknown

deposits.

Table 3. Identified and estimated undiscovered resources in Kuusamo-type Co-Au deposits in Finland.

	Identified resource	Median estimate	Mean estimate	Probability of mean or more
Co (t)	22,000	100,000	140,000	0.40
Au (t)	19	85	110	0.41
Ore (Mt)	16	83	100	0.42

Ore: Mineralised rock containing the metals. Identified resources as of 29th May 2017. All resources are rounded to two significant digits.

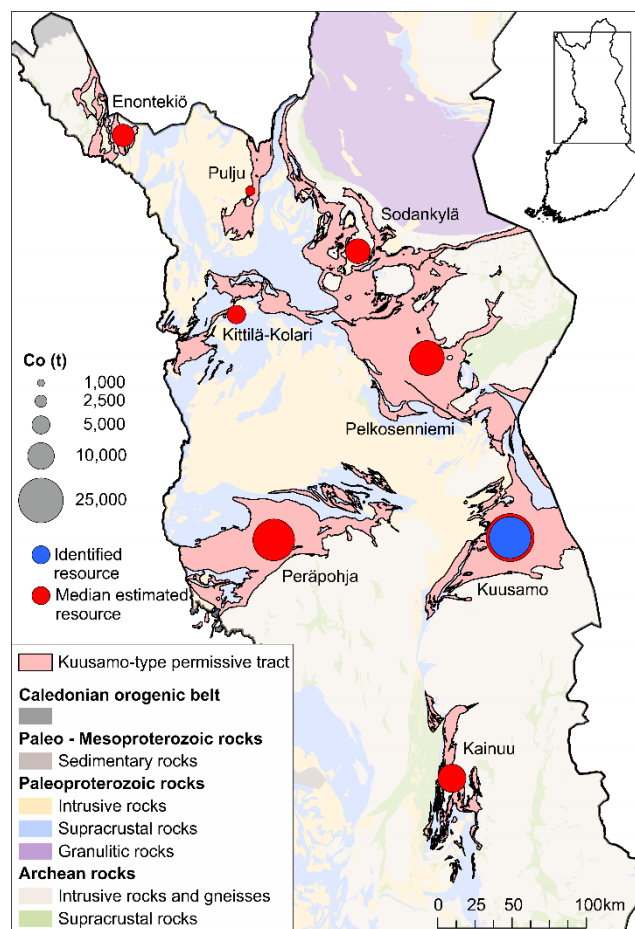


Figure 1. Permissive tracts for Kuusamo-type cobalt-gold deposits in Finland. Known and estimated undiscovered resources plotted on each tract do not indicate exact location of the resources.

Acknowledgements

We thank many of our colleagues at GTK for data, discussions and insights into details of the geology of cobalt-bearing deposits in Finland.

References

- Dragon Mining (2013) Annual Report 2012 http://www.dragonmining.com/static/files/31/2013-03-27_dra_annualreport_2012.pdf. Accessed 14 Feb 2018

- FODD (2018) Fennoscandian Ore Deposit Database. Geological Survey of Finland (GTK), Geological Survey of Norway (NGU), Geological Survey of Russia (VSEGEI), Geological Survey of Sweden (SGU), SC Mineral. <http://en.gtk.fi/informationsservices/databases/fodd/index.html>. Accessed 1 Nov 2018
- Pankka H (1992) Geology and mineralogy of Au-Co-U deposits in the Proterozoic Kuusamo volcanosedimentary belt, northeastern Finland. PhD Thesis, Michigan Technological University
- Pankka HS, Vanhanen EJ (1992) Early Proterozoic Au-Co-U mineralization in the Kuusamo district, northeastern Finland. *Precambrian Res* 58:387–400
- Ranta J-P, Molnar F, Hanski E, Cook N (2018) Epigenetic gold occurrence in a Paleoproterozoic meta-evaporitic sequence in the Rompas-Rajapalot Au system, Peräpohja belt, northern Finland. *Bull Geol Soc Finland* 52:733–746
- Rasilainen K, Eilu P, Äikäs O, Halkoaho T, Heino T, Iljina M, Juopperi H, Kontinen A, Kärkkäinen N, Makkonen H, Manninen T, Pietikäinen K, Räsänen J, Tiainen M, Tontti M, Törmänen T (2012) Quantitative mineral resource assessment of nickel, copper and cobalt in undiscovered Ni-Cu deposits in Finland. Geological Survey of Finland, Rep Invest 194
- Rasilainen K, Eilu P, Halkoaho T, Iljina M, Karinen T (2010) Quantitative mineral resource assessment of platinum, palladium, gold, nickel, and copper in undiscovered PGE deposits in mafic-ultramafic layered intrusions in Finland. Geological Survey of Finland, Rep Invest 180
- Rasilainen K, Eilu P, Halkoaho T, Karvinen A, Kontinen A, Kousa J, Lauri L, Luukas J, Niiranen T, Nikander J, Sipilä P, Sorjonen-Ward P, Tiainen M, Törmänen T, Västi K (2014) Quantitative assessment of undiscovered resources in volcanogenic massive sulphide deposits, porphyry copper deposits and Outokumpu-type deposits in Finland. Geological Survey of Finland, Rep Invest 208
- Singer DA (1993) Basic concepts in three-part quantitative assessments of undiscovered mineral resources. *Nonrenewable Res* 2:69–81
- Singer DA, Menzie WD (2010) Quantitative mineral resource assessments: An integrated approach. Oxford University Press, New York
- Slack JF, Causey JD, Eppinger RG, Gray JE, Johnson CA, Lund KI, Schulz KJ (2010) Co-Cu-Au deposits in metasedimentary rocks – A preliminary report. U.S. Geological Survey Open-File Report 2010–1212
- Slack JF (ed) (2013) Descriptive and geoenvironmental model for cobalt-copper-gold deposits in metasedimentary rocks (ver. 1.1, March 14, 2014). U.S. Geological Survey Scientific Investigations Report 2010–5070–G
- Vanhanen E (2001) Geology, mineralogy and geochemistry of the Fe-Co-Au-(U) deposits in the Paleoproterozoic Kuusamo Schist Belt, northeastern Finland. Geological Survey of Finland, Bull 399
- Yardley BWD, Graham JT (2002) The origins of salinity in metamorphic fluids. *Geofluids* 2: 49–256

Modelling ferromanganese crust distribution on seamounts for resource potential estimates

Sarah A. Howarth

University of Southampton, National Oceanography Centre Southampton, UK

Isobel A. Yeo, Bramley J. Murton

National Oceanography Centre Southampton, UK

Abstract. The expansion in renewable energy technologies is increasing demand for numerous elements, known as E-tech elements, such as cobalt (Co) and tellurium (Te). This is driving research into alternative sources of metal supply. Ferromanganese (FeMn) crusts present a potentially important future source of E-tech elements. Until now, most studies have used dispersed sample sets collected across ocean basins using spatially imprecise dredging techniques. Yet crust formation and composition depend upon a large range of local conditions, such as sediment supply, water depth and other oceanographic conditions. Here, we focus on the seamount-scale processes controlling FeMn crust formation and composition at Tropic Seamount, in the NE Atlantic. Outcrop mapping based on high-definition videos show that FeMn crust morphologies on the seamount can be related to a series of “type” environments. These have been combined with maps showing the presence or absence of FeMn crust within a distribution model to assess trends in crust growth. Building predictive models using empirical data allow for assumptions on the controls of crust formation to be tested at the scale of the individual seamount. Understanding the controls on both FeMn crust abundance and the distribution of economically important metals is key to developing mining strategies that maximise output and metal grade and minimise negative environmental impacts that may pose a potential barrier to future exploitation.

1 Introduction

Hydrogenetic ferromanganese (FeMn) crusts form from the precipitation of Fe-oxyhydroxides and Mn-oxides directly from seawater onto hard rock substrates, to form pavements and encrustations. Very slow formation rates, between 1–10 mm/Myr, combined with high specific surface areas of 325 m²g⁻¹ support the enrichment of many elements above continental crustal mean concentrations (Hein et al., 2000).

These high element concentrations mean that FeMn crusts are considered a potential resource of economically important metals, such as cobalt (Co) and platinum (Pt). Particular focus in recent years has been on the growing demand for these and other metals for use in green energy technologies, such as photo-voltaic cells and electric cars, and the security of their supply. The growth in this industry has led to shifts in demand patterns for raw materials and many of the elements vital to the production of these technologies are highly

concentrated in FeMn crusts (Hein et al. 2010; Hein et al. 2013). One such element is tellurium (Te), which is enriched in FeMn crusts by a factor of 10⁴ relative to continental crustal concentrations (Hein et al. 2003; Hein et al. 2010).

Ferromanganese crust formation is suggested to have four pre-requisites. Firstly, the precipitation of crusts requires a supply of the main constituent elements, Mn and Fe (Halbach et al., 1982). In the marine environment, the main sources of Mn are terrestrial inputs, seafloor hydrothermal fluids and diagenetic pore fluids from ocean basin and continental shelf sediments (Elderfield 1976; Bender et al. 1997). Iron fluxes to oceans are dominated by atmospheric dust inputs but also include rivers carrying continental runoff and groundwaters, hydrothermal fluids and diagenetic sediment pore fluids (e.g. Archer and Johnson 2000; Elrod et al. 2004). Secondly, crust formation requires oxidised waters to trigger the oxidation of aqueous Fe(OH)₃ and Mn²⁺ to form Fe-oxyhydroxide and Mn-oxide species (Koschinsky and Halbach 1995). Thirdly, crusts require a sediment-free hard substrate on which to form (Halbach et al. 1982). Hence areas with elevated current flow speeds, such as the turbulent flows generated around seafloor obstructions, promote crust precipitation. Finally, this substrate needs to be a stable surface to allow for the accretion of slow growing Mn-oxides and Fe-oxyhydroxides (Hein et al. 1988). Many of these pre-requisites are fulfilled by seamount and guyot environments, where FeMn crusts have been widely observed and studies have used models of global seamount coverage to estimate FeMn crust reserves (Manheim 1986; Yamazaki 1993; Hein et al. 2009; Hein et al. 2013).

Preferential formation on seamounts, in conjunction with leaching experiments, have supported the development of the widely applied colloid-chemistry model for the formation of hydrogenetic FeMn crusts that has been used to explain basin scale trends in FeMn crust composition (Halbach 1986; Koschinsky and Halbach 1995). Their formation has been linked to the concentration of reduced manganese, Mn²⁺, at the oxygen minimum zone (Johnson et al. 1996). Seafloor protrusions allow for upwelling and turbulent mixing of more oxygenated bottom waters, allowing Mn²⁺ to be oxidised and form oxide- and hydroxide- colloids. The mixed colloid species form due to the interaction of opposing surface charges between a central Mn- or Fe-core and other oxide and hydroxide elements (Koschinsky and Halbach 1995). Trace metals can then

be scavenged from the water column and adsorbed onto colloid surfaces of opposite charge (Fig. 1). Sequential leaching experiments show distinct elemental associations between Mn- and Fe-species (Koschinsky and Halbach 1995). Metal cations such as Co^{2+} and Ni^{2+} form colloid complexes with MnO_2 -colloids and anions such as MoO_4^{2-} are associated with Fe-oxyhydroxide colloid complexes.

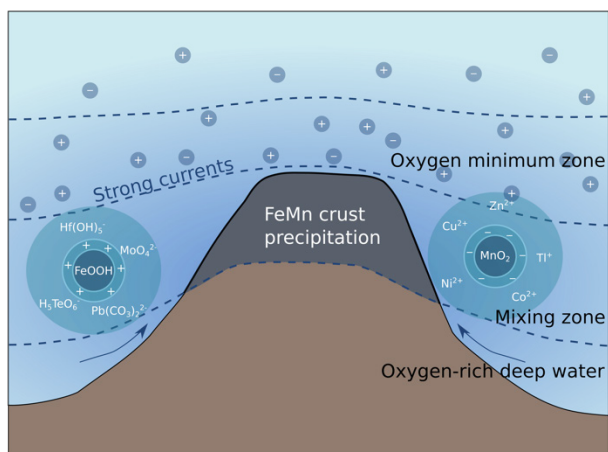


Figure 1 Schematic showing the proposed mechanism of formation for FeMn crusts on seamounts (adapted from Koschinsky and Halbach, 1995).

2 Geological setting

Tropic Seamount is an isolated submarine volcano in the NE Atlantic, ~470km off the West African coastline, at 23°N 21°W, south of the Canary Island Seamount Province (CISP) and Saharan Seamount chains. The structure is that of a flat-topped guyot that extends from 4000 m water depths up to 1000 m at its summit. Petrographic studies suggest the seamount is based upon alkaline ocean island basalts and petrogenetically has been grouped with the CISP, although this petrogenesis remains debated (e.g. Van Den Bogaard 2013; Patriat and Labails 2006). $^{40}\text{Ar}/^{39}\text{Ar}$ dating of feldspars indicates potential initial eruption ages from ~119–114 Ma, with late-stage eruptions until ~60 Ma (Van Den Bogaard 2013). A high-resolution age model for Tropic Seamount based on an FeMn core dates the earliest FeMn crust precipitation between 77–73 Ma (Josso et al. 2019).

3 Estimating FeMn crust resources

The resource potential of FeMn crusts has been widely discussed since the 1980s, following initial interest in the economic potential of FeMn nodules (e.g. Mero 1962; Halbach et al. 1982; Aplin and Cronan 1985; Manheim 1986). Estimates of global resources have developed through time with improvements in the understanding of the controls on FeMn crust formation and mapping techniques, alongside changes in technological mining constraints and metals of interest. A number of assumptions are commonly applied in resources estimate studies. Firstly, studies base FeMn site prospectivity on

economic element grade (for example for Co, Ni and Cu content) and estimated crust tonnages. Metal grades are generally estimated using regional-scale studies, as overall the global distribution in FeMn crust sampling is relatively sparse and the focus of the majority of studies is on samples from the Pacific Ocean (Hein and Koschinsky 2013). For example, the highest Co concentrations measured to date are for samples from the Prime Crust Zone of the Pacific Ocean (0.67 wt%, 362 crust samples) whereas Atlantic crusts have lower average Co concentrations (0.36 wt%, 43 crust samples) (Hein and Koschinsky 2013). These concentrations are also reported to vary with age and water depth (e.g. Hodkinson and Cronan 1990; Hein et al. 2000). These patterns have been applied to some mine site models in order to target the most promising crust horizons (Hein et al. 2009). Estimating crust tonnages remains a major challenge in FeMn resource assessment. Most models rely on the use of bathymetric maps to calculate the approximate number and surface area of seamounts and guyots to give a maximum surface area for crust coverage. This area is then refined using assumptions of optimum depths for crust formation and composition and technological constraints for mining, generally for water depths shallower than 2500 m (Hein et al. 2009; Muiños et al. 2013). However, few studies have had access to high-resolution maps of in-situ FeMn crust distribution.

The most significant unknowns in tonnage estimates are crust distribution and thickness variation. Crust distribution is proposed to depend on a number of environmental variables, such as water depth and sediment cover. Factors such as seamount age have been used to estimate crust formation and preservation potential (Hein et al. 1988). Modelling crust distribution based on the theoretical conditions of formation is limited by the low spatial resolution of samples collected by dredging, which has been the dominant method of FeMn crust sampling. Detailed investigation of crust thickness distribution on seamounts has as of yet only been described in two studies, with Usui et al. (2017) noting significant variation in crust thickness even down to the local, metre-scale and Yeo et al. (2018) discussing the optimal considerations for resource potential at Tropic Seamount.

Currently, the magnitude of deep-sea resources is highly uncertain. A key reason for this is the paucity of data on proven FeMn crust coverage and geochemical data with high spatial resolution. In particular, global estimates on FeMn crust resources have been hindered by an insufficient understanding of the controls on crust distribution and geochemistry at the regional- to local-scale of an individual prospective mine-site. The development of remotely operated underwater vehicle (ROV) and autonomous underwater vehicle (AUV) technologies have facilitated high resolution studies of in-situ FeMn crust distribution and well spatially constrained sampling campaigns (e.g. Usui et al. 2017; Teague et al. 2018; Yeo et al. 2018).

4 FeMn crust mapping for distribution modelling

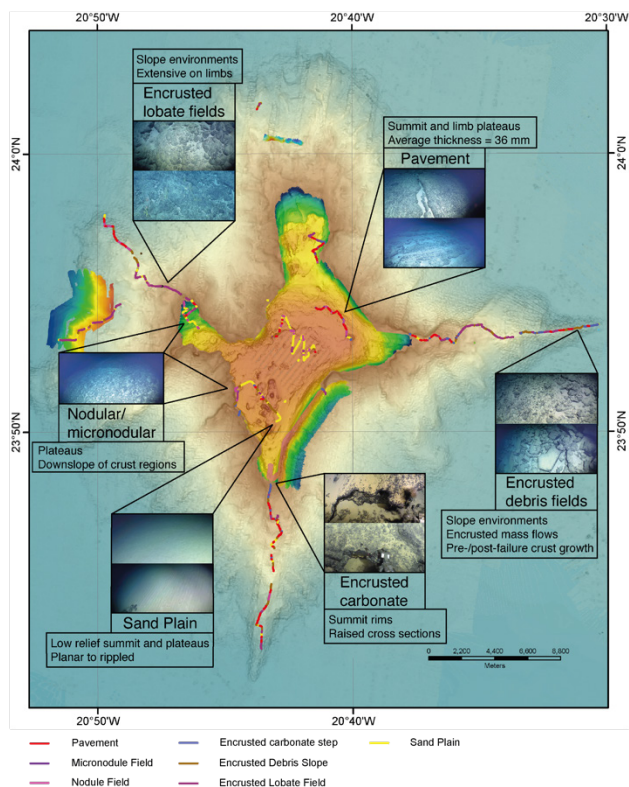


Figure 2 High-resolution lithological and environmental mapping from direct observation during remotely operated vehicle (ROV) dives. Systematic changes in crust are noted within distinct spatial environments on the seamount. Point data generated from these observations are used within the distribution model.

In this study, the FeMn crusts of Tropic Seamount display high heterogeneity at all scales. Crust growth is observed on all exposed surfaces as well as the lower substrate surfaces that are buried in sediment. Crust thickness varies from mm-thick FeMn coatings on rocks and coral debris, up to 20 cm thick crust on slabs and pavements. In general, the exposed upper surfaces display the thickest crust growth. Macro-textures vary over short distances from smooth to rough, with internal roughness commonly corresponding to high detrital grain content. Botryoidal textures exist on mm- to cm- scales, including in places where apparent individual nodules on the seabed are fused together to form irregular, sheet-like surfaces in outcrop. FeMn nodules take a range of forms, including micronodule and nodule fields. Internally the crusts alternate from layered to homogenous, with planar and botryoidal layering (Yeo et al 2018). Many crusts show a conglomeratic texture with internal clasts that display earlier FeMn crust growth included within younger crust matrices. Widespread observation of multiple crust growth events and growth hiatuses support a complex growth history (Josso et al. 2019).

Geological outcrop mapping was undertaken from ROV footage in order to investigate spatial trends in FeMn crust features. To facilitate mapping, different categories are delineated and these categories

compared to in-situ rock samples. The defining characteristics of these categories are the slope (flat/shallow/steep) and the overall outcrop texture. “Type” environments include sand plains (planar or rippled), crust slab fields, encrusted lobate fields, nodule fields, crust pavements, encrusted carbonate steps, encrusted debris slopes, and micronodule fields (Fig. 2). Flat summit regions are dominated by homogenous and rippled sand plains, crust pavements, and nodule fields. The crust pavement and nodule coverage vary widely, from full coverage with little underlying substrate visible to patches with <10% crust/nodule cover. Encrusted carbonate steps are focused around the edges of the summit. The transition to sloped environments leads to highly variable outcrops dominated by debris fields and cliffs. These include loose debris, such as coral debris with thin FeMn coatings, or encrusted debris in which underlying clastic rocks have been fused and covered in FeMn crust. Cliff environments display greater evidence of underlying substrate texture, including lava cooling joints, while intermittent shallow slopes show slumped slabs and lobate field interspersed with rippled sands. Where sampling was possible, example lithological samples from each environment were analysed.

In order to understand potential factors controlling the occurrence of FeMn crusts at the scale of an individual seamount a distribution model was built. Input data into this model include presence/absence data for FeMn crust outcrop, “Type” environment, FeMn crust thickness and substrate type. Given the four pre-requisites outlined in the current conceptual model of FeMn crust formation (a supply of Fe and Mn, oxidized waters, a hard, sediment-free substrate, and a stable long-lived surface), the interaction and spatial variation of two key features are considered within the FeMn crust distribution model. These are the bathymetric features of the seamount and the characteristics of the overlying water masses. Raster grids of features that capture bathymetric variance were generated, including slope, roughness and aspect. Key hydrographic inputs included dissolved oxygen from CTD casts and a current velocity model developed by HR Wallingford from in-situ current data. These grids are input as layers into an R-based generalized additive model (GAM) to build an FeMn crust distribution model that utilises the in-situ outcrop observations with environmental predictor variables that are thought to have direct or indirect effects on FeMn crust formation. A comparison between models with an empirical basis and theoretical focus is made in order to optimise FeMn distribution modelling. The model is then evaluated using a resampling method of Tropic Seamount to assess the accuracy of the model in predicting FeMn crust occurrence, by comparing model outputs with ground-truthed observations.

5 Outlook

Overall there is evidence for active crust growth at a range of depths and positions on Tropic Seamount. Established theories for crust growth suggest that active growth varies in relation to the position of the oxygen

minimum zone (e.g. Koschinsky and Halbach 1995). The observation of extensive crust development at all depths on the seamount and evidence for recent growth is contradictory to this view. High density, highly positionally-constrained sampling along depth profiles has allowed for further characterisation of the processes that were initially conceived based on dredge sampling, which is unlikely to fully capture spatially controlled geochemical trends at the of the mine-site scale. Mapping in-situ outcrop variation from ROV footage and assessments of resource viability using distribution modelling enables an integrated examination of the trends between crust abundance, texture and geochemistry and how the environmental conditions such as seamount morphology and water mass characteristics may influence these. Improved understanding is necessary of the sampling resolution required to fully encapsulate the variance of FeMn crust deposits and how sparse data points or localized datasets can be optimally interpreted and interpolated to predict deposit potential in unexplored regions.

Acknowledgements

SH was funded by the Natural Environment Research Council (NERC) SPITFIRE Doctoral Training Partnership (DTP) studentship (NE/L002531/1) and SH, IY and BM were supported the NERC MarineE-Tech project (NE/M011186/1 to BM and NE/M011151/1 awarded to P. Lusty at British Geological Survey). We thank the team of the 2016 expedition JC142 on the RRS James Cook for data acquisition and J. Spearman, J. Taylor and J. Crossouard from HR Wallingford for the current velocity modelling. T. Pearman of the University of Southampton is thanked for her advice on distribution modelling in R and to P. Lusty for reviews of the text.

References

- Archer DE, Johnson K. (2000) A model of the iron cycle in the ocean. *Global Biogeochemical Cycles* 14:269–279.
- Bender ML, Klinkhammer GP, Spencer DW (1997) Manganese in seawater and the marine manganese balance. *Deep-Sea Res* 24:799–812.
- Elderfield H (1976) Manganese fluxes to the oceans. *Mar Chem* 4: 103–132.
- Elrod VA, Berelson WM, Coale KH, Johnson KS (2004) The flux of iron from continental shelf sediments: a missing source for global budgets. *Geophys Res Lett* 31:L12307.
- Halbach P (1986) Processes controlling the heavy metal distribution in Pacific ferromanganese nodules and crusts. *Geol Rundsch* 75:235–247.
- Halbach P, Manheim FT, Otten P (1982) Co-rich ferromanganese deposits in the marginal seamount regions of the Central Pacific Basin - results of the Mid- Pac '81. *Erzmetall* 35:447–453.
- Hein JR, Koschinsky A (2013) Deep-Ocean Ferromanganese Crusts and Nodules. *Treatise on Geochemistry: Second Edition*, 273–291.
- Hein JR, Conrad TA, Staudigel H (2010) Seamount Mineral Deposits: A Source of Rare Metals for High-Technology Industries. *Oceanography* 23:184–189.
- Hein JR, Conrad TA, Dunham RE (2009) Seamount characteristics and mine-site model applied to exploration- and mining-lease-block selection for cobalt-rich ferromanganese crusts. *Marine Geores & Geotech* 27:160–176.
- Hein JR, Mizell K, Koschinsky A, Conrad TA (2013) Deep-ocean mineral deposits as a source of critical metals for high- and green-technology applications: Comparison with land-based resources. *Ore Geol Rev* 51:1–14.
- Hein JR, Koschinsky A, Halliday AN (2003) Global occurrence of tellurium-rich ferromanganese crusts and a model for the enrichment of tellurium. *Geochim Cosmochim Acta* 67:1117–1127.
- Hein JR, Koschinsky A, Bau M, Manheim FT, Kang JK, Roberts L (2000) Co-rich ferromanganese crusts in the Pacific. In: Cronan, DS (ed) *Handbook of Marine Mineral Deposits*, CRC Marine Science Series. CRC Press, Boca Raton, pp 239 - 279.
- Hein JR, Schwab WC, Davis AS (1988) Cobalt- and platinum-rich ferromanganese crusts and associated substrate rocks from the Marshall Islands. *Mar Geol* 78:255–283.
- Hodkinson RA, Cronan DS (1991) Regional and depth variability in the composition of cobalt-rich ferromanganese crusts from the SOPAC area and adjacent parts of the central equatorial Pacific. *Mar Geol* 98:437–447.
- Johnson KS, Coale KH, Berelson WM, Gordon RM (1996) On the formation of the manganese maximum in the oxygen minimum zone. *Geochim Cosmochim Acta* 60:1291–1299.
- Josso P, Parkinson I, Horstwood M, Lusty P, Chenery S, Murton B (2019). Improving confidence in ferromanganese crust age models: A composite geochemical approach. *Chem Geol*, 513: 108–119.
- Koschinsky A, Halbach P (1995) Sequential leaching of marine ferromanganese precipitates: Genetic implications. *Geochim Cosmochim Acta* 59:5113–5132.
- Manheim FT (1986) Marine Cobalt Resources. *Science* 232:600–608.
- Muñños SB, Hein JR, Frank M, Monteiro JH, Gaspar L, Conrad T, Pereira HG, Abrantes F (2013) Deep-sea Fe-Mn Crusts from the Northeast Atlantic Ocean: Composition and Resource Considerations. *Mar Geores & Geotech* 31:40–70.
- Patriat M, Labails C (2006) Linking the Canary and Cape-Verde hot-spots, Northwest Africa. *Mar Geophys Res* 27:201–215.
- Teague J, Allen MJ, Scott TB (2018) The potential of low-cost ROV for use in deep-sea mineral, ore prospecting and monitoring. *Ocean Eng* 147:333–339.
- Usui A, Nishi K, Sato H, Nakasato Y, Thornton B, Kashiwabara T, Urabe T (2017) Continuous growth of hydrogenetic ferromanganese crusts since 17Myr ago on Takuyo-Daigo Seamount, NW Pacific, at water depths of 800–5500m. *Ore Geol Rev* 87:71–87.
- Van Den Bogaard P (2013). The origin of the Canary Island Seamount Province—new ages of old seamounts. *Scientific Rep-UK*, 3:2107.
- Yamazaki T, Igarashi Y, Maeda K (1993) Buried cobalt rich manganese deposits on seamounts. *Resource Geol Special Issue* 17:76–82.
- Yeo IA, Dobson K, Josso P, Pearce RB, Howarth SA, Lusty PAJ, Murton BJ (2018). Assessment of the Mineral Resource Potential of Atlantic Ferromanganese Crusts Based on Their Growth History, Microstructure, and Texture. *Minerals*, 8:327.

Geochemistry of REE-rich karst bauxite ore deposits from the Sierra de Bahoruco, Dominican Republic

Thomas Aiglsperger, Bernhard Dold

Department of Civil Engineering and Natural Resources. Luleå University of Technology, Luleå, Sweden

Joaquín A. Proenza

Departament de Mineralogia, Petrologia i Geologia Aplicada, Universidad de Barcelona (UB), Spain

Cristina Villanova-de-Benavent

School of Environment and Technology (SET), University of Brighton, UK

Lisard Torró

Geological Engineering Program, Faculty of Sciences and Engineering, Pontifical Catholic University of Peru (PUCP)

Australia Ramírez, Jesús Rodríguez

Servicio Geológico Nacional, Dominican Republic

Abstract. In this work the geochemistry of REE-rich karst bauxite ore from several deposits of the Sierra de Bahoruco (Dominican Republic) has been investigated. The bauxite ores are geochemically heterogenous and show differences with respect to major, minor and trace elements. According to their major element geochemistry, the studied ores classify mostly as Fe-rich bauxites. The minor elements Cr and Ni are in general relatively high (up to 1250 and 2370 ppm, respectively), hence pointing towards a (ultra-)mafic source for the bauxite formation. The sum of REE contents range from ~400 to ~5400 ppm (average ~1200 ppm) at varying LREE/HREE between ~1 and ~25 (average ~8). In general, REE chondrite-normalized patterns for studied bauxites show negative Ce and Eu anomalies with rather flat segments for HREE. However, three samples from different bauxite ore deposits with the highest REE contents show significant enrichment trends for heavier REE, particularly for Pr, Nd, Sm, Gd as well as for Tb and Dy (one sample). Mineralogical studies reveal that formation of secondary REE-bearing minerals (i.e. phosphates, carbonates and oxides) occurred. Karst bauxite ores hosted in the Sierra de Bahoruco represent an excellent natural laboratory to study the geochemical behaviour of REE in weathering systems.

1 Introduction

Bauxite ores are the main source for Al in the world and two types can be distinguished: (1) lateritic bauxites, formed due to intense weathering of the source rock (e.g. granites, basalts, shales); and (2) karst bauxites, characterized by a strong association with carbonates hosting the bauxite ores. In addition to high Al contents, bauxite ores have recently also attracted economic geologists because of their capacity to accumulate rare earth elements (REE) (Torró et al. 2017 and references therein). Of special interest in this context are heavy rare earth elements (HREE, Eu to Lu) because of their greater economic value compared with light rare earth elements (LREE, La to Sm). However, the department

of different REE with respect to the evolution of bauxite profiles is still little studied. Hence, the aim of this work is to increase the whole-rock geochemistry database of bauxite ores by presenting geochemical data for major, minor and trace elements with special focus on REE enrichment trends from heterogenous karst bauxite ore deposits from the Dominican Republic.

2 Geological overview

2.1 Geology of the study area

The study area lies in the so-called Sierra de Bahoruco, which is located in the south-western part of the Dominican Republic, next to the border with Haiti (Fig. 1).



Figure 1. Map showing the Hispaniola island in the Caribbean; the study area, located in the province of Pedernales, is highlighted.

Its crystalline basement is formed by the basaltic Dumisseau Formation (Campanian to lower Eocene) which is overlain by a thick sequence of carbonates (Eocene to Quaternary), representing the major components of the Sierra de Bahoruco. The collision of the Greater Antilles belt with the Bahamas Platform caused a progressive uplift of the Sierra de Bahoruco which has been constrained from latest Middle Miocene to the present (Pérez-Valera 2010). Intense weathering

under tropical conditions resulted in the development of locally well-developed karst systems and bauxite formation (de León 1989; Pérez-Valera 2010; Pérez-Valera and Abad 2010). Numerous bauxite ore deposits of various sizes occur at different altitudes in the study area. For this study, only bauxite deposits that are located between 400 and 1600 m.a.s.l. were investigated (Fig. 2).

2.2 Bauxite mining in the study area

Mining activities in the province of Pedernales began in 1959 by the Alcoa exploration company which produced a total of ~23 million DMTU (dry metric ton unit) in 26 deposits until 1982 (Ramírez 2015). From 2006 until 2016 the only remaining, active mining operation in the study area was the Las Mercedes ore deposit. A detailed description on the geochemistry and mineralogy of the Las Mercedes ore deposit can be found in Torró et al. (2017).

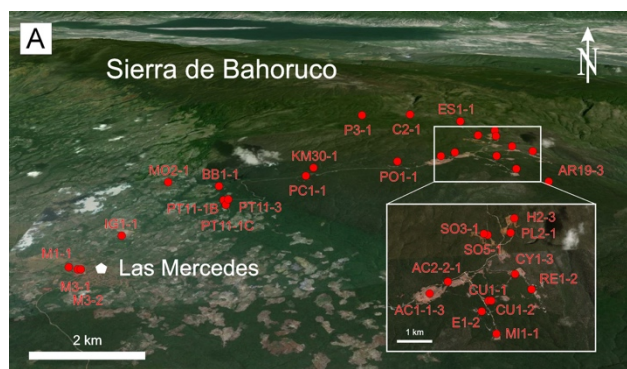


Figure 2. Google Earth aerophotograph showing the study area and the Sierra de Bahoruco together with sample points of this study.

3 Sample selection and methods

A total of 100 samples (1 kg each) of bauxite ore (incl. associated carbonates) from inactive mining sites was collected throughout the study area. 28 samples were selected (Fig. 2), homogenized and sent for geochemical analysis to Actlabs Laboratories (Ontario, Canada). Major, minor and trace elements of samples were determined using fusion inductively coupled plasma emission (FUS-ICP) and inductively coupled plasma emission mass spectrometry (ICP-MS).

4 Results

4.1 Major and minor element geochemistry and geochemical bauxite classification

The major elements Al_2O_3 , Fe_2O_3 and SiO_2 vary throughout the study area for different bauxite ore deposits: Al_2O_3 contents range from 43.5 to 50.5 wt.%, Fe_2O_3 contents from 16.5 to 22.5 wt.% and SiO_2 contents from 0.4 to 12.8 wt.%. According to the geochemical classification diagram for bauxitic ores by Bárdossy et al. (1982), samples studied in this work correspond mainly to iron-rich bauxites (Fig. 3). However, the majority of

samples plot close to, and a few samples also within the bauxite (*sensu stricto*) field. TiO_2 contents are rather constant for all analysed bauxite samples (avg. 2.4 wt.%).

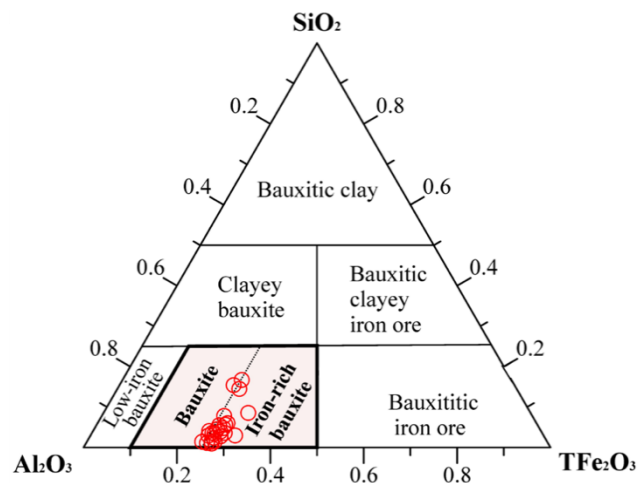


Figure 3. Whole rock SiO_2 - Fe_2O_3 - Al_2O_3 ternary plot of the studied bauxitic samples; bauxite classification fields are after Bárdossy et al. (1982) showing that most bauxites from the study area plot at the border between bauxite (*sensu stricto*) and iron-rich bauxite.

Minor elements such as Cr, Ni, V, Co and Zr show significant variations: Cr contents vary from 340 to 1250 ppm, Ni from 60 to 2370 ppm, V from 233 to 561 ppm, Co from 7 to 584 ppm and Zr from 81 to 618 ppm.

4.2 REE geochemistry

The bauxite ores reveal relatively high total REE (La-Lu) contents in the range from ~400 to ~5400 ppm (average ~1200 ppm) with varying LREE/HREE ratios from ~1 to ~25 (average ~8). On the other hand, the associated carbonates all have low total REE contents (~10 ppm on average) and reveal homogeneous LREE/HREE ratios around 5. In general, REE contents show a positive correlation with Al, Fe, Mn and P in studied bauxite ores. Similar as previously observed by Torró et al. (2017) in their survey on bauxite ores from the Las Mercedes ore deposit, the general REE chondrite-normalized patterns for bauxites from the study area reveal negative Ce and Eu anomalies with rather flat segments for HREE (Fig. 4).

However, three samples with the highest REE contents show also the lowest LREE/HREE ratios. As a consequence, their chondrite-normalized patterns are significantly different and are characterized by (i) a more pronounced negative Ce anomaly with strong relative enrichment trends for Pr-Sm and Gd; or (ii) relatively lower contents for La-Nd compared to heavier REE with positive Sm and Gd anomalies; or (iii) a slightly positive slope from Eu-Dy (Fig. 4).

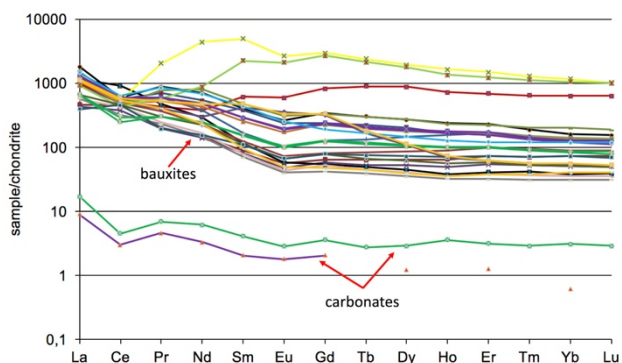


Figure 4. Chondrite-normalized REE patterns for studied bauxite ores from the Sierra de Bahoruco. Normalization values were taken from Anders and Grevesse (1989).

5 Discussion

The investigated bauxite ores in the study area are geochemically heterogeneous. For example, Al_2O_3 and SiO_2 contents significantly differ with respect to changing altitudes of the ore deposits. In general, higher Al_2O_3 with lower SiO_2 contents are observed at higher altitudes. This observation is probably linked to an *in-situ* bauxitization process at higher altitudes due to weathering of impure carbonates and subsequent transportation of bauxite ores to lower altitudes where they are deposited in depressions and voids within the karst system. The Las Mercedes ore deposit (Fig. 2) most likely represents an allochthonous bauxite ore deposit. However, the source of Al-bearing minerals within the impure carbonates that lead to bauxite formation under tropical weathering, is still an unresolved issue. The relatively high Cr and Ni contents of bauxite ores from the Sierra de Bahoruco point towards a (ultra-)mafic source that Torr o et al. (2017) identify as either the underlying basaltic Dumisseau Formation or Quaternary volcanic ashfall from major eruptions during carbonate sedimentation.

Karst Fe-rich bauxite ores from the Sierra de Bahoruco are characterized by relatively high REE contents and reach values up to 0.5 wt% total REE, suggesting potential as an unconventional source for REE. Variations in the chondrite-normalized REE patterns with local enrichment trends for specific REE (e.g. Nd, Sm and Gd) clearly show that geochemical conditions differ at the study area scale. Mineralogical results from heavy mineral separations reveal that presence of either primary phosphates (i.e. monazites) or secondary phosphates, carbonates and oxides can explain some of the observed differences with respect to the changing REE geochemistry between the bauxite ore deposits from the Sierra de Bahoruco.

Ongoing geochemical and mineralogical studies including REE-bearing clay minerals, the quantification of target minerals via automated mineralogy as well as sequential extraction experiments will help to better understand the REE geochemistry of the different bauxite ore deposits from the Sierra de Bahoruco and to get a more accurate idea on their economic potential as an alternative source for REE.

6 Concluding remarks

Karst bauxite ores hosted in the Sierra de Bahoruco represent an excellent natural laboratory to study the geochemical behaviour of REE in weathering systems.

The observed REE contents are economically significant, in case of favourable mineralogy for extraction, and when seen as cost-inexpensive by-products during the production of Al.

Results of this investigation contribute to a better understanding of REE cycling in the supergene environment.

Acknowledgements

This research has been funded by the project 2014-1B4-133 of the Ministerio de Educaci n, Ciencia y Tecnolog a of the Dominican Republic Government. The help and hospitality extended by the staff of DOVEMCO, SGN as well as by driver Mr. Wilson and assistants Mr. Jhonny and Mr. Lily during fieldwork are gratefully acknowledged.

References

- Anders E, Grevesse N (1989) Abundances of the elements: Meteoritic and solar. *Geochim Cosmochim Acta* 53:197-214
- B rdossy G (1982) Karst Bauxites: Bauxite Deposits on Carbonate Rocks; Developments in Economic Geology; Distribution for the U.S.A. and Canada, Elsevier Science Pub. Co: Amsterdam, The Netherlands; New York, NY, USA, 1982; ISBN 978-0-444-99727-2
- de Le n O (1989) Geolog a de la Sierra de Bahoruco (Rep blica Dominicana). Museo Nacional de Historia Natural, Santo Domingo
- P rez-Valera F (2010) Geologic Map Sheet 1:50.000 num. 5970-III and corresponding memoir. Proyecto 1B de Cartograf a Geom tica de la Rep blica Dominicana. Programa SYSMIN. Direcci n General de Miner a, Santo Domingo
- P rez-Valera F, Abad M (2010) Informe Estratigr fico y Sedimentol gico. Proyecto 1B de la Cartograf a Geom tica de la Rep blica Dominicana. Programa SYSMIN. Direcci n General de Miner a, Santo Domingo
- Ramirez RE (2015) El oro de Pedernales. *Geonoticias* 12-38:12-14
- Torr o L, Proenza JA, Aiglsperger T, Bover-Arnal T, Villanova-de-Benavent C, Rodr guez-Garc a D, Ram rez A, Rodr guez J, Mosquea LA, Salas R (2017) Geological, geochemical and mineralogical characteristics of REE-bearing Las Mercedes bauxite deposit, Dominican Republic. *Ore Geol Rev* 89:114–131

Sc redistribution during post-magmatic processes in the Cínovec/Zinnwald deposit

Sebastian Hreus^{1#}, Jakub Výravský^{1,2}, Jan Cempírek¹, Michaela Vašínová Galiová^{3,4}

¹Department of Geological Sciences, Faculty of Science, Masaryk University, Czech Republic

²TESCAN Brno s.r.o.

³Institute of Chemistry and Technology of Environmental Protection, Faculty of Chemistry, Brno University of Technology

⁴Central European Institute of Technology, Brno University of Technology, Czech Republic

Abstract. Post-magmatic processes on Li-Sn-W deposit Cínovec/Zinnwald were studied in order to assess Sc behaviour during alteration of Sc-enriched phases and other mineralogical changes. Focussing on the main rock types of the deposit, we describe several different alteration mechanisms that affect the most important carriers of scandium – zircon, columbite, wolframite, ixiolite, scheelite, zinnwaldite, and muscovite. The alterations include: 1) replacement of zinnwaldite (avg 63 ppm Sc) by muscovite (avg. 25 ppm Sc) 2) sheelitization of Sc-rich wolframite (0.58 wt% Sc₂O₃). The scheelite contains low Sc and is spatially associated with Sc-rich (up to 4.87 wt% Sc₂O₃) ixiolite. 3) Alteration of zircon possibly leading to Sc-enrichment 4) Replacement of wolframite I by Mn-dominant Sc-poor wolframite II. From above listed minerals, only wolframite and its Sc-bearing breakdown products are the most likely to have possible economic significance for Sc extraction.

1 Introduction

Cínovec-Zinnwald deposit is a world-class Li-Sn-W greisen deposit, located in the northern part of Krušné hory/Erzgebirge (Fig. 1), near the Czech-German border. It formed in a granite cupola of the post-collisional A-type Cínovec granite, which penetrates the Teplice rhyolite. The Cínovec granite cupola forms a N-S elongated elliptical body with surface dimensions 1.4 x 0.3 km. From geochemical point of view, the Cínovec granite is strongly fractionated, slightly peraluminous (Breiter and Škoda 2012), enriched in F, Li, Rb, Sn, W, Nb and Ta (Breiter et al. 2017a). Typical accessory minerals include fluorite, topaz, cassiterite, wolframite, columbite, Nb-rutile, zircon, monazite, xenotime and REE fluorocarbonates (Rub et al. 1998; Breiter and Škoda 2012; Johan and Johan 1994, 2005; Breiter et al. 2017b).

The Cínovec/Zinnwald deposit is located in the uppermost part of the granitic cupola, down to approximately 200 m below the current surface (Breiter et al. 2017a) and is composed of four distinct types of ore bodies (Nessler and Seifert 2015; Breiter et al. 2017a):

1) Flat, banded quartz-zinnwaldite veins, parallel to the granite-rhyolite contact. Associated minerals include topaz, K-feldspar, and wolframite > cassiterite;

2) Steep quartz-zinnwaldite veins striking from SW to NE, texturally similar to flat veins but locally enriched in base metals sulfides;

3) So called “massive greisens” that represent steep or flat zones of intensive metasomatic greisenization;

4) Flat-dipping bodies of “mineralized granites” with fine-grained cassiterite, known from the southern part of the deposit.

Exploitation of the deposit started in medieval times mainly for tin from cassiterite. In 19th century, production of tungsten as a main ore commenced. During a short episode in 1950's, Sc was extracted from wolframite (Petrů et al. 1956). In 1992, the mines were eventually closed. Nowadays, extensive exploration for Li, Sn, W and other elements is in progress on both sides of the border.

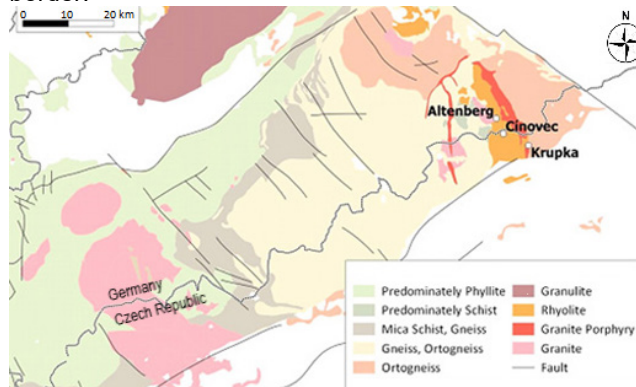


Figure 1. Geological Map of Krušné hory/Erzgebirge. European Metals, 2019, adjusted.

2 Methods

All the main Sc-bearing minerals from the main rock types of the Cínovec-Zinnwald deposit were studied in detail, which comprised granites, greisenized granites, greisens and hydrothermal veins. In total, 23 samples were examined and kindly provided by the company Geomet s.r.o.).

All essential minerals were investigated for main and minor elements content by CAMECA SX 100 electron microprobe at the Joint Laboratory of Electron Microscopy and Microanalysis of the Department of Geological Sciences, Masaryk University and Czech Geological Survey in Brno.

Micas were analyzed further for their trace element content using LA-ICP-MS (LSX-213 G2+ and Agilent 7900) at the Fun glass – Centre for Functional and Surface Functionalized Glass at Alexander Dubček University of Trenčín.

TIMA (Tescan Integrated Mineral Analyzer) was employed to characterize mineralogy of the thin sections, obtain modal composition of the rocks, grain size

distribution, associations of the relevant minerals and to improve understanding of their textural relationships.

3 Sc-bearing minerals at the deposit

According to Kempe and Wolf 2006, post-magmatic alterations of **zircon** on Cínovec/Zinnwald deposit affect its Sc content; altered zircons have generally higher Sc concentrations. However, plotting the Sc content against typical alteration indicators in zircons (analytical total, and Ca, Al, F, Fe) does not show any clear relationship between degree of alteration and Sc content (Fig.2). The situation is further complicated by near absence of unaltered zircons in our studied samples. Therefore, an unambiguous conclusion about influence of hydrothermal alteration on Sc content in zircons cannot be drawn at this point.

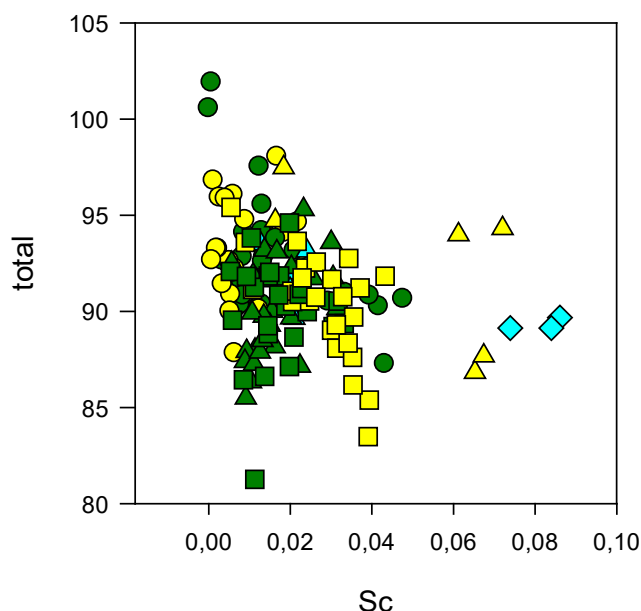


Figure 2. Total of measured elements and Sc content in zircon. Green symbols – granite, yellow – greisen, blue – hydrothermal veins.

3.1 Wolframite

Wolframite from greisen is characterized by two different alteration associations:

1) wolframite from “common” greisen forms two textural and chemical types with an unclear temporal relationship. Both form large crystals up to several mm in size. The first type occurs as solid, homogenous crystals which are relatively depleted in Nb and Sc (avg. 0.17 wt. % Sc_2O_3 ; 0.007 apfu), whereas the second type forms porous, oscillatory zoned crystals (Fig. 2), with preferential replacement of some zones and parts by Sc-ixiolite ($(\text{W},\text{Nb},\text{W},\text{Ta},\text{Mn},\text{Fe},\text{Sc})_4\text{O}_8$, scheelite and columbite. The second type of wolframite is enriched in Nb and Sc (avg. 0.55 wt. % Sc_2O_3 ; 0.025 apfu).

2) Late hydrothermal sulfidic mineralization locally breaks down thick-tabular wolframite I from greisens to aggregates and thin plates of wolframite II; the secondary

wolframite shows significantly higher Mn/(Mn+Fe) ratios and lower Sc content than wolframite I, and Sc was most likely released to fluid phase as there are no observed Sc-bearing alteration products. Sc content in the wolframite II is generally low (between 0 and 0.005 apfu, 0-0.11 wt. % Sc_2O_3 , compared to other samples.

Wolframite also occurs in hydrothermal veins it is characterized by very high Sc contents. Amounts of scandium range between 0.015-0.037 apfu (0.35-0.9 wt. % Sc_2O_3); similar to Sc-rich wolframites from greisens. These wolframites are partly replaced by Sc-poor scheelite and Sc-rich ixiolite. Sc enrichment of wolframite in hydrothermal veins as well as in greisens shows positive correlation with Nb (Fig. 3) indicating, that Sc enters the structure of wolframite via coupled substitution $\text{Fe}^{2+} + \text{W}^{6+} = \text{Sc}^{3+} + \text{Nb}^{5+}$.

3.2 Ixiolite

Ixiolite after wolframite from greisens as well as from hydrothermal veins generally has a significantly high Sc content (up to 4.87 wt % Sc_2O_3 (0.19 apfu), whereas, **scheelite and columbite** contain relatively low Sc amounts (0.033-0.034 apfu, 0.643-0.644 wt. % Sc_2O_3 for columbite after wolframite; 0-0.012 apfu, 0-0,323 wt. % Sc_2O_3 for scheelite). The lower content of Sc in scheelite may be explained by its incompatibility in the scheelite lattice, due to large difference in ionic radii of Sc and Ca, which contrasts with the similar ionic radius of Fe^{2+} and Sc in wolframite and ixiolite (see ionic radii in Shannon, 1976).

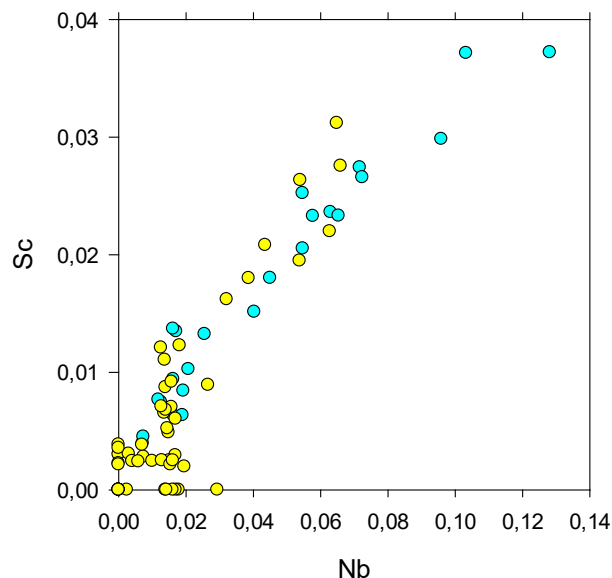


Figure 3. Plot of Nb vs. Sc contents in wolframite. Yellow symbols – greisen, blue – hydrothermal veins.

3.3 Zinnwaldite

Zinnwaldite (up to 87.6 ppm Sc, with average 63 ppm) is often altered to younger muscovite (fig. 4), with lower Sc content (up to 37.1 ppm, with average 25.3 ppm). Lower Sc contents in muscovite, compared to zinnwaldite, is in agreement with reported studies from Erzgebirge. However, the measured Sc-content in muscovite from

Cínovec is significantly higher than data from exocontact cassiterite–quartz veins in Ehrenfriedersdorf, Germany (2.2 vs. 18.9 ppm) and from hydrothermal muscovite from a wolframite-bearing quartz vein at Ulaan uul, Mongolia (13 ppm) (Kempe and Wolf, 2006). As it is one of the main rock-forming minerals, especially in greisens, zinnwaldite is an important Sc carrier.

Other important Sc-bearing minerals in the Cínovec-Zinnwald deposit include (from most common to rarest): columbite (up to 0.165 apfu; 3.04 wt. % Sc_2O_3), cassiterite (up to 0.007 apfu; 0.317 wt. % Sc_2O_3), Nb-rutile (up to 0.004 apfu; 0.16 wt. % Sc_2O_3) and xenotime (up to 0.014 apfu; 0.314 wt. % Sc_2O_3).

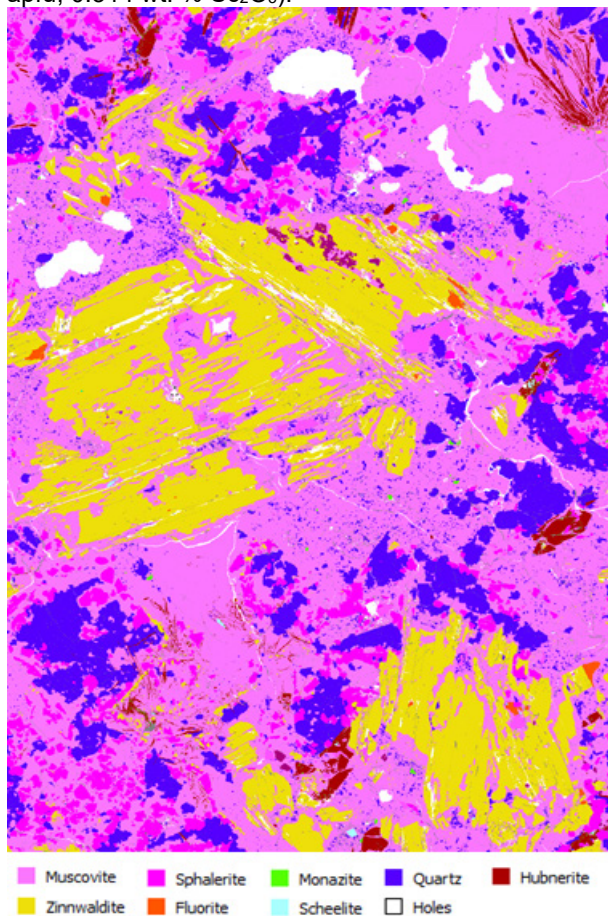


Figure 4. Muscovitization of zinnwaldite in hydrothermally altered greisen (sample P1/250) with TIMA mineral map. Original size of map 0.9x0.6 cm.

4 Conclusions

Several processes cause post-magmatic alteration of Sc-bearing minerals in Cínovec/Zinnwald Li-Sn-W deposit. Most of investigated zircons are significantly altered, but no clear connection between Sc content and degree of alteration was observed. Scheelitization of wolframite results in redistribution of Sc to secondary ixiolite due to Sc incompatibility in the scheelite structure. Zinnwaldite alteration results in lower Sc concentrations in secondary muscovite; the released Sc is stored in some of the ore minerals whose (re)-crystallization is related to muscovitization, most likely cassiterite.

In conclusion, Sc shows different behavior and degree of mobility during post-magmatic processes in distinct types of rocks and minerals. The most promising Sc-bearing minerals in the deposit are wolframite + ixiolite, cassiterite, and columbite. Due to the relatively high Sc concentrations in ore minerals, Sc in the Cínovec/Zinnwald deposit might potentially be a by-product of tungsten ore extraction.

Acknowledgements

This research was funded within the grant MUNI/A/1088/2017, and GA 19-05198S to JC. Authors are grateful to P. Reichl and V. Šešulka (Geomet s.r.o.) for possibility of access to the samples and for their help with data processing and sampling.

References

- Breiter K, Ďurišová J, Hrstka T, Korbelová Z, Hložková Vaňková M, Vašinová Galiová M, Kanický V, Rambousek P, Kněsl I, Dobeš P, Dosebaba M (2017a) Assessment of magmatic vs. metasomatic processes in rare-metal granites: a case study of the Cínovec/Zinnwald Sn–W–Li deposit, Central Europe. *Lithos* 292:198-217. doi: 10.1016/j.lithos.2017.08.015
- Breiter K, Korbelová Z, Chládek Š, Uher P, Knesl I, Rambousek P, Honig S, Šešulka V (2017b) Diversity of Ti–Sn–W–Nb–Ta oxide minerals in the classic granite-related magmatic–hydrothermal Cínovec/Zinnwald Sn–W–Li deposit (Czech Republic). *European Journal of Mineralogy* 29(4):727-738. doi: 10.1127/ejm/2017/0029-2650
- Breiter K., Škoda R (2012) Vertical zonality of fractionated granite plutons reflected in zircon chemistry: the Cínovec A-type versus the Beauvoir S-type suite. *Geologica Carpathica* 63(5): 383-398. doi: 10.2478/v10096-012-0030-6
- Johan V., Johan Z (1994) Accessory minerals of the Cínovec (Zinnwald) granite cupola, Czech Republic Part 1: Nb-, Ta- and Ti-bearing oxides. *Mineralogy and Petrology* 51(2-4): 323-343. doi: 10.1007/BF01159735
- Johan Z., Johan V (2005) Accessory minerals of the Cínovec (Zinnwald) granite cupola, Czech Republic: indicators of petrogenetic evolution. *Mineralogy and Petrology* 83(1-2): 113-150. doi: 10.1007/s00710-004-0058-0
- Kempe U, Wolf D (2006) Anomalously high Sc contents in ore minerals from Sn–W deposits: possible economic significance and genetic implications. *Ore geology reviews* 28(1): 103–122. doi: 10.1016/j.oregeorev.2005.04.004
- Nessler J, Seifert T, Gutzmer J (2015) New Sn-W potential at the Zinnwald/Cínovec deposit, Eastern Erzgebirge, Germany In: *13th SGA Biennial Meeting* Nancy – France 2015, Mineral resources in a sustainable world, pp 819-822
- Petrů F, Hájek B, Procházka V, Vít J (1956) *Chem. Listy* 50, 1696, in Czech
- Rub AK, Štemprok M, Rub MG (1998) Tantalum mineralization in the apical part of the Cínovec (Zinnwald) granite stock. *Mineralogy and Petrology*, 63(3-4): 199-222.
- Shannon RD (1976). Revised effective ionic radii and systematic studies of interatomic distances in halides and chalcogenides. *Acta crystallographica section A: crystal physics, diffraction, theoretical and general crystallography*, 32(5), 751-767. doi: 10.1107/s0567739476001551

Fenitisation associated with alkaline-silicate complexes. Implications for HFSE mobility in late-stage fluids, Gardar Rift, SW Greenland

Krzysztof Sokół, Adrian A. Finch
University of St Andrews, UK

Jonathan Cloutier
University of Tasmania

Madeleine C.S. Humphreys
127. Durham University, UK

Abstract. Alkali metasomatism associated with carbonatitic-alkaline magmatism (or fenitisation) is of interest for our understanding of chemical behaviour of economically important high-field-strength (HFSE) and rare-earth (REE) elements during late-stage magmatic-hydrothermal activity.

In this project, we explore the expression of alteration and the physico-chemical factors controlling fenitisation across the Proterozoic Gardar Province of Southern Greenland. We present our findings of bulk-rock (XRF/ICP-AES) and microbeam (BSE-SEM-EDAX/EPMA) analyses.

Our main case study, the Illerfissalik centre, comprises a series of nested syenitic intrusions. Fenites are exposed at its western margin, where a feldspar-poor Eriksfjord Formation quartz arenite protolith experienced intense metasomatism and deformation.

Detailed petrography demonstrates interstitial K-feldspar (commonly perthitic), mafic minerals including pyroxene or Na-amphibole, and titanite (often LREE-bearing) in the proximal high-grade fenite zone. The absence of feldspar in unaltered arenite (<5% mode further than 1.5 km distance from the contact zone) suggests that K-feldspar was introduced by early-stage fenitisation, along with the relatively Na-poor pyroxene. The presence of HFSE-rich phases i.e. Sr-chevkinite also attests to variable mobility of numerous alkali, alkali-earth metals and HFSE in fenitising fluids. Bulk-rock geochemical trends away from the contact are also presented. Further work including isotope systematics will constrain the geochemistry of fenitising fluids.

1 Introduction

The margins of alkaline magmatic complexes are often associated with forms of alteration characterised by the influx of alkalis and the loss of silica. The significance of fenitising fluids has long been debated with respect to HFSE-REE ore deposit genesis during late-stage activity and critical element prospectivity. Fenite is usually described around carbonatite (Elliott et al. 2018) and fenite around nepheline syenite is less well constrained.

This work focusses on the fenitised margins of alkaline-silicate centres within the Mid-Proterozoic

Gardar Province of SW Greenland (Figure 1). For the present contribution, we focus predominantly on the Illerfissalik and Ilimaussaq centres. We study the geological and mineralogical expression of fenitisation on a macro- and micro- scale in order to fingerprint the chemistry of the metasomatic fluid. To achieve our goals we analyse major and trace element chemistry of rocks in fenite aureoles.

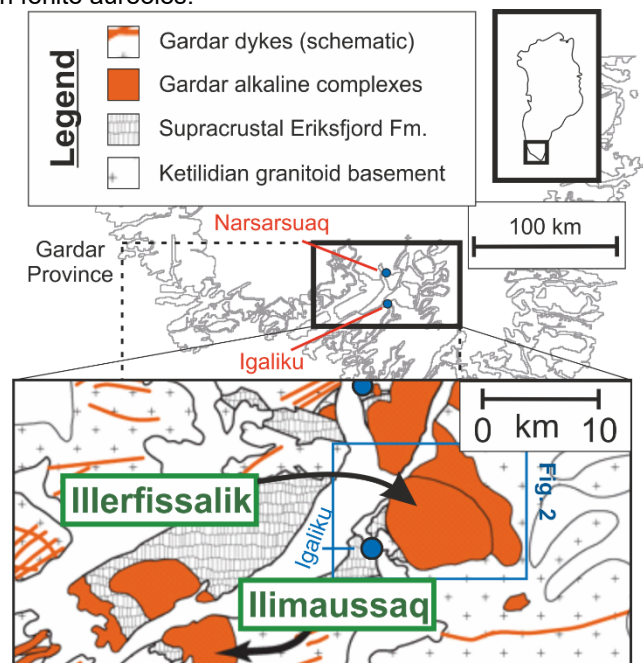


Figure 1. Location map & a broad overview of Gardar geology (modified after Garde et al. 2002; Ladenburger et al. 2016)

2 Illerfissalik centre, Gardar Province

The primary case study in our work is the Illerfissalik centre. It is part of a larger Igaliko Nepheline Syenite Complex, which comprises at least four distinct intrusive centres (Emeleus & Harry 1970) and consists of seven related subordinate syenitic bodies intruding during two major phases of activity (Figure 2). At its western margin, it abuts Ketilidian granitoid basement as well as supracrustal Eriksfjord Formation quartz arenite. The sediments show intense chemical alteration (Figure 3),

indicating where metasomatic fluid penetrated the country rocks pervasively through intergranular space and via pre-existing planar macroporosity (i.e. sedimentary cross-bedding and tectonic joint-fracture networks). Mylonitisation and evidence of rheomorphism can also be observed in a contact zone ~200m wide, in which the fenite grade is highest.

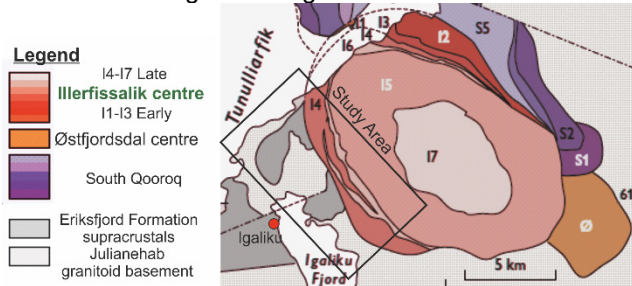


Figure 2. Simplified map of the Illerfissalik centre and the surrounding igneous bodies of 'Igaliko Nepheline Syenite Complex' (as in Emeleus & Harry 1970; map modified after Upton 2013)

We report the presence of metasomatic K-feldspar (up to 50% modal), pyroxene (augite, diopside, aegirine-augite) and Na-amphibole (richterite/arfvedsonite), and titanite (often LREE-bearing) - all restricted to interstitial domains in high-grade fenites. As low-grade fenites and unaltered sediments lack feldspar (<5% mode beyond ~1.5 km distance from the contact), we conclude that the K-feldspar was introduced to the country rocks by magmatic-hydrothermal fluids during an early-stage of fenite formation. Feldspar is often anhedral and intergrown with, or epitaxially overgrown by later Na-Ca-Ti phases and occasionally forms flame-perthite. EDAX analyses of the other main metasomatic phases introduced to Eriksfjord Fm. arenites reveal that prevalent $Di_{75-90}Hd_{1-20}Aeg_{3-11}$ pyroxene lacks Na (generally <2 wt%).



Figure 3. High-grade quartz fenite. Abundant richterite/ arfvedsonite with recrystallisation and sintering of original quartz.

Metasomatic Sr-chevkinite, columbite and zirconosilicates with HFSE as major components are also present in the contact mixed zone attesting to mobility of Na, K, Ca, Ti, Zr, Sr, Ba, Nb, Ta and LREE in multiphase fenitising fluids. Based on epitaxy of HFSE-rich precipitates upon earlier metasomatic phases introduced to Eriksfjord Fm., we infer at least two episodes of expulsion of such fluids into the envelope of Illerfissalik centre.

3 Other centres and future work

The Ilímaussaq Complex, also part of Gardar Province, provides a direct comparison due to the variety of hydrothermal veins (Figure 4), while the metasomatism of the granitoid envelope is reported to occur to at least ~120m distance (Ferguson 1964; Derrey 2012). Through this study we will gain further insight into chemical behaviour of HFSE in late-stage fluids associated with numerous alkaline igneous systems within Gardar such as Ilímaussaq, and magmatic-hydrothermal regimes in other crustal environments.



Figure 4. Late-stage vein networks resulting in autometasomatism of the marginal igneous units. Green alteration of the protolith is commonly associated with Na-rich fluid activity

Radiogenic (U-Pb, Sr-Nd) and stable (O-H-S) isotope systematics will be considered in this project in attempt to unravel geochronological relationships between magmatism and late-stage alteration episodes, and to constrain the geochemistry of fenitising fluids (i.e. temperature, fluid pH, redox state).

References

- Derrey I (2012) Element transport and mineral replacement reactions during alkali contact metamorphism: effects on the Julianehåb granite induced by the Ilímaussaq intrusion, SW-Greenland. Diplomathesis, Universität Tübingen
- Elliott HAI, Wall F, Chakhmouradian AR, Siegfried PR, Dahlgren S, Weatherley S, Finch AA, Marks MAW, Dowman E, Dedy E (2018) Fenites associated with carbonatite complexes: A review. *Ore Geol. Rev.* 93:36-59
- Emeleus CH, Harry WT (1970) The Igaliko Nepheline Syenite Complex, General Description. *Meddr. Grønland.* 186(3).
- Ferguson J (1964) Geology of the Ilímaussaq alkaline intrusion, South Greenland. *Bull. Grøn. Geol. Undersøgelse* 39:82
- Garde AA, Hamilton MA, Chadwick B, Grocott J, McCaffrey KJW (2002). The Ketilidian orogen of South Greenland: geochronology, tectonics, magmatism, and fore-arc accretion during Palaeoproterozoic oblique convergence. *Can. J. Earth. Sci.* 39:765-793
- Ladenburger S, Marks MAW, Upton BGJ, Hill P, Wenzel T, Markl G (2016) Compositional variation of apatite from rift-related alkaline igneous rocks of the Gardar Province, South Greenland. *Am. Min.* 101(3):612-626
- Upton BGJ (2013) Tectono-magmatic evolution of the younger Gardar southern rift, South Greenland. *Geol. Surv. Den. Green. Bull.* 29:124.

The Gakara Rare Earth Deposit, Burundi: geology, mineralogy, U-Th-Pb dating

Ntiharirizwa S^{1,2}, Boulvais P¹, Poujol M¹, Branquet Y^{1,3}, Midende G^{2,4}, Morelli C⁴, Ntungwanayo J⁴

¹Géosciences Rennes-UMR 6118, University Rennes, France

²Earth Sciences Department, University of Burundi, 2700, Bujumbura, Burundi

³Institut des Sciences de la Terre d'Orléans (ISTO) Université d'Orléans, France

⁴Rainbow Rare Earths, Boulevard du Japon, Bujumbura, Burundi

Abstract: One of the world's richest Rare Earth Elements (REE) deposits, Gakara, is in Burundi, near Lake Tanganyika, along the western branch of the East African Rift. It is enclosed in Mesoproterozoic rocks mainly composed of metasedimentary rocks and granitoids formed during the Kibaran orogeny. These rocks are intruded by a network of granite pegmatites and aplites clusters. Previous structures inherited from the Kibaran orogeny may have been reused during the REE mineralizing event. Hydrothermal fluids circulated along fractures and led to the formation of economic REE concentrations. Primary REE mineralization consists of bastnaesite (LREE-CO₃F), however, economically exploitable mineralization contains secondary monazite (LREE-PO₄) that formed by late hydrothermal processes. Evidence includes silicification of secondary mineralization which is associated with idiomorphic quartz crystals. Gakara REE mineralization share characteristics with other hydrothermal deposits from carbonatites such as Mountain Pass (California), Bayan Obo (China) and others. These observations are combined to better define the geodynamic and the magmatic context of the alkaline magmatism in the Gakara region, and to prospect for the presence of carbonatite in this region. The U-Th-Pb ages of bastnaesite and monazite (around 600 Ma), belong to the Pan-African cycle.

1 Introduction

During the recent years, the scientific community has made an important effort to better understand the metallogenic conditions for the emplacement of REE mineralization. Carbonatites and the associated hydrothermal activities are known to host the largest REE deposits (Goodenough et al. 2017; Jones et al. 1995; Verplanck et al. 2016). Carbonatites contain the greatest REE contents of any rock type and have the largest Light REE/Heavy REE ratio (Verplanck et al. 2016; Williams-Jones et al. 2012). The Gakara deposit in Burundi is described as a typical example of hydrothermal REE deposits likely linked to a carbonatitic magmatic-hydrothermal activity. Nevertheless, little is known or has been published (Lehmann et al. 1994; Van Wambeke et al. 1977) about this deposit, including the recent publication of our group (Ntiharirizwa et al. 2018). The Rainbow Mining Burundi (RMB) Company is exploiting REE mineralization in the Gakara region and many REE occurrences have been already identified (Figure 1B).

The Gakara deposit is the only deposit presently worked in Africa. With in-situ grades in the range of 47-67% Total Rare Earth Oxide (rainbowrareearths.com), Gakara is one of the world's richest rare earth deposits. The only geochronological data available so far for the Gakara area was obtained on bastnaesite (Nakai et al. 1988), using the ¹³⁸La-¹³⁸Ba isochron method, yielding a Pan-African age of 586.8 ± 3.7 Ma. In this paper, we use the U-Th-Pb in-situ LA-ICP-MS dating technique for bastnaesite and monazite. These new ages allow us to discuss the evolution of mineralization in the regional geodynamical context.

2 Regional geology

The geology of Burundi is dominated by the north-eastern trending Kibaran Fold Belt (Figure 1A) commonly named the Karagwe-Ankolean Belt (KAB) or Burundian Supergroup (Tack et al. 2010). The Burundian Supergroup consists of a highly deformed sequence of Mesoproterozoic granites, granitoids, metasedimentary and metavolcanic rocks (Tack et al. 2010; Deblond et al. 1999). The geology and tectonic framework of Burundi and adjacent countries have been strongly influenced by repeated episodes of rifting along existing structural discontinuities (Lehmann et al. 1994). This has resulted in numerous alkaline complexes and carbonatites (Lehmann et al. 1994) including the Upper Ruvubu Alkaline Plutonic Complex (URAPC) and the Matongo carbonatite in Burundi (Decrée et al. 2015) (Figure 1A). These alkaline rocks and carbonatites span a wide range in age from Late Proterozoic to Cenozoic (Lehmann et al. 1994). The late-Proterozoic events such as the URAPC, the Matongo carbonatite and the Gakara REE mineralization, have been related to Pan-African far-field tectono-thermal processes in the Western Rift area (Decrée et al. 2015; Midende et al. 2014; Tack et al. 1984). The Mozambique belt (Figure 1A) is the youngest of the Pan-African mobile belts (Kröner et al. 2014).

3 Local geology

The REE mineralization of Gakara is enclosed within Mesoproterozoic gneisses which are very heterogeneous in their lithologies and structures. The most widespread gneiss corresponds to an orthogneiss with K-feldspar phenocrysts, biotite, quartz, and less abundant muscovite. The deformation of these gneisses is significant. The foliation is affected by a system of ductile

shear bands at small scale and kilometeric scale. This partly explains the high variation of foliation orientations and dips at the regional scale. The gneisses are intruded by many pegmatitic bodies (Figure 3) composed of coarse-grained quartz, K-feldspar, Biotite and muscovite. When the outcrop is parallel to the main foliation, some pegmatites appear as classical dykes and sills crosscutting the foliation. However, most of them are intrafolial (i.e. within the foliation) and are strongly deformed (Ntiharirizwa et al. 2018). The granite pegmatites of Gakara have an age of 969 ± 17 Ma (Lehmann et al. 1994).

4 Mineralization

The REE mineralization is hosted within a network of bastnaesite/monazite-bearing veins and veinlets which range in thickness from a few centimeters to tens centimeters. The REE veins exhibit variable orientations and attitudes, although there appears to be a broad correlation with regional structures, which are predominantly in NE-SW and NW-SE directions (Figure 2). The emplacement of those veins is therefore structurally controlled (Van Wambeke et al. 1977), and their occurrence is independent of the various host lithologies formed between 1375 Ma to 986 Ma (Tack et al. 2010). The REE veins are younger [around 600 Ma, (Ntiharirizwa et al. 2018; Nakai et al. 1988)] and crosscut the main foliation of the host lithologies (Figure 2). There is evidence of post-REE mineralization deformation. Cenozoic rifting (Figure 1A) affected the whole area with a general uplift. Therefore, continuity of REE-veins is not ensured, and ore bodies correspond to discontinuous lensoid clasts within a cataclasite matrix with various amount of offset between them (Ntiharirizwa et al. 2018).

5 Petrography and mineralogy

Samples were collected during the RMB exploration campaigns (2011–2014), and during our field work (2017–2018). The mineralogical assemblage was made by Aderca and Van Wambeke (Van Wambeke et al. 1977, Aderca et al. 1971). Depending on the degree of alteration, different types of ore can be found: from massive pure bastnaesite ore to an almost pure monazite ore, and in-between, ores with various proportions of bastnaesite and monazite (Figure 3 A, B). Bastnaesite is invaded by monazite, mainly through the cleavages and by filling the fractures. In addition to bastnaesite and monazite, other less common REE minerals such as rhabdophane (Ce,La)PO₄.H₂O, cerianite (CeO₂) and fluorocerite (Ce,La)F₃ have been discovered in the Gakara ore (Van Wambeke et al. 1977). The most common gangue minerals are quartz, barite, biotite, galena, goethite and vermiculite. In comparison with other REE deposits associated with carbonatite, the Gakara deposit is characterized by the absence of simple carbonates especially calcite and dolomite.

As a summary, the mineralogical observations above

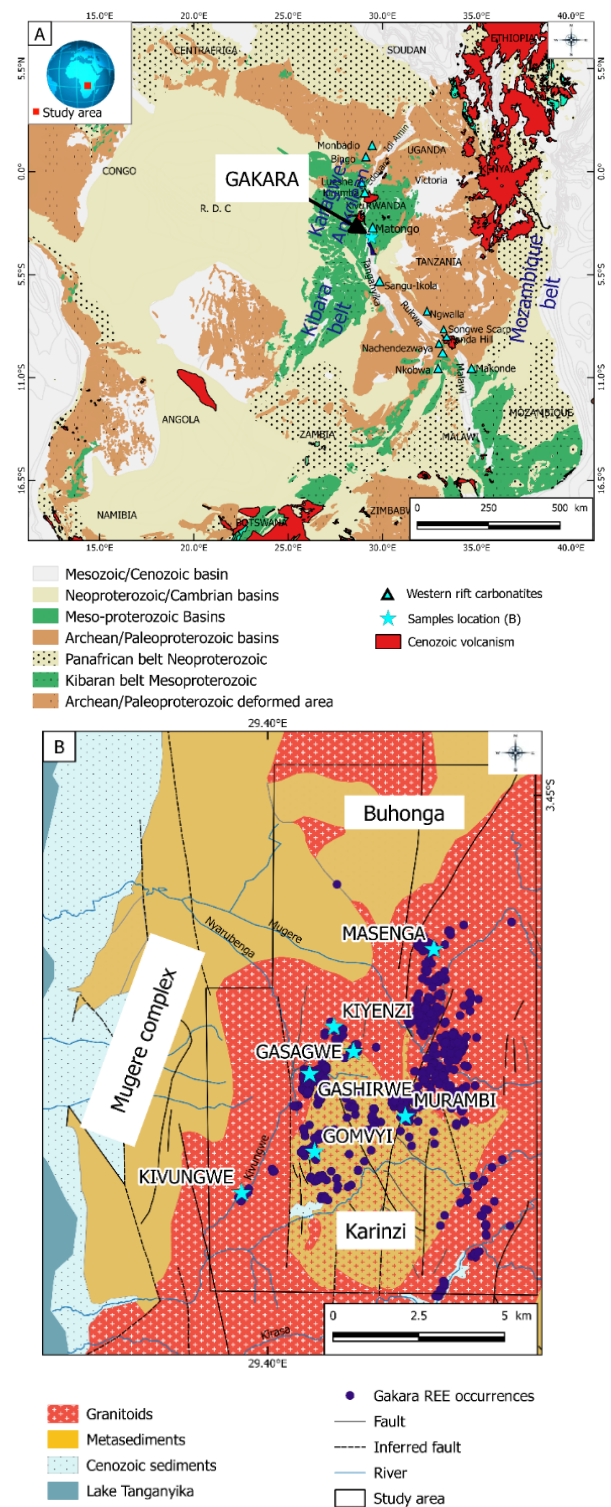


Figure 1. (A) Geological map of Central Africa showing Precambrian structures and locations of carbonatites complexes in the western branch of the East African Rift. The map is modified from Ntiharirizwa et al. 2018. (B) Geological map of the study area showing the occurrences of REE mineralization (RMB data) and their host rocks.

are presented in a paragenetic sequence (Figure 4). The REE mineralization consists of three successive stages (Ntiharirizwa et al. 2018). The first stage consists of the deposition of primary ore comprising bastnaesite, biotite,

galena, barite and quartz (1st generation). The second stage begins with the formation of monazite-Ce and quartz (2nd generation). The third stage corresponds to the formation of cerianite, a second type of La-rich monazite and rhabdophane; this last stage is indicative of a very oxidative, surficial, possibly lateritic environment.

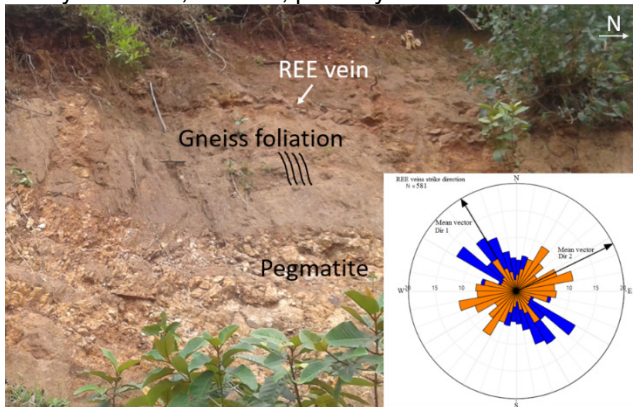


Figure 2. REE vein crosscuts the foliated gneiss at Masenga hill. The pegmatite vein is affected by the regional foliation. The rose diagram made by 581 structural measurements, highlights the variability of the REE vein's orientations.

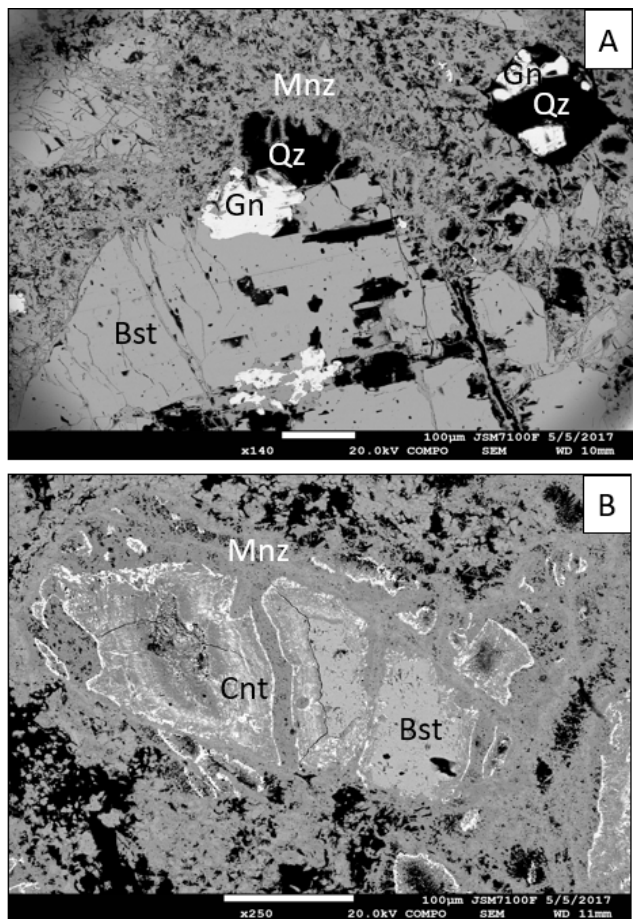


Figure 3. Microphotographs of samples from Gakara displaying the mineralogical assemblage: Bst=bastnaesite, Mnz=monazite, Qz=quartz, Gn=galena, Cnt=cerianite.

MINERAL	Time		
	ORE STAGE	ALTERATION STAGE	
		I	II
Bastnaesite	—		
Biotite	—		
Galena	—		
Barite	—		
Quartz	1	2	---
Goethite		—	---
Monazite		Ce	La
Rhabdophane			—
Cerianite			—

Figure 4. Synthetic paragenetic sequence for the Gakara REE mineralization (Nakai et al. 1988).

6 U-Th-Pb geochronology

U-Th-Pb geochronology of bastnaesite and monazite grains from the Gakara deposit was conducted by in-situ laser ablation inductively coupled plasma mass spectrometry (LA-ICP-MS) at Geosciences Rennes using an ESI NWR193UC Excimer laser coupled to a quadrupole Agilent 7700x ICP-MS.

6.1 Bastnaesite dating

Twenty-six (26) grains of bastnaesite have been dated

following a double-standardization protocol (Ntiharizwa et al. 2018). They have been first standardized with monazite. All the 26 analyses define a lower intercept date of 602.6 ± 9.5 Ma. When plotted in a $^{206}\text{Pb}/^{238}\text{U}$ versus $^{208}\text{Pb}/^{232}\text{Th}$ Concordia diagram, data are slightly discordant to discordant and define a lower intercept date of 597 ± 9 Ma (MSWD = 1.4). A second set of measurements has been done using a calcite standard. All the 26 analyses define a lower intercept date of 579 ± 27 Ma (MSWD = 0.27). If all the data acquired on bastnaesite (i.e., standardized with monazite and calcite) are plotted in a Concordia diagram (Figure 5A), they define a lower intercept date of 602.1 ± 7.2 Ma (MSWD = 1.5), a date interpreted as the age of the crystallization of bastnaesite.

6.2 Monazite dating

The monazite dating has been realized using the Moacir monazite standard (Ntiharizwa et al. 2018). Fourteen (14) monazite grains analyzed are characterized by rather homogeneous, although low, Pb, U and Th contents (1.8–3.5 ppm, 14–30 ppm and 17–48 ppm respectively) and very consistent Th/U ratios (1.0 to 2.1). The data have been reported in a $^{207}\text{Pb}/^{206}\text{Pb}$ versus $^{238}\text{U}/^{206}\text{Pb}$ Tera-Wasserburg diagram and in a $^{206}\text{Pb}/^{238}\text{U}$ versus $^{208}\text{Pb}/^{232}\text{Th}$ Concordia diagram. The data are concordant to discordant, demonstrating the presence of common Pb in some of the analyzed grains. The concordant data define a Concordia age of 588.7 ± 7.5 Ma (Figure 5B). Therefore, all the chronometers (U/Pb

and Th/Pb) return dates that are comparable within error at ca. 588 Ma, a date that we interpret as the age of the crystallization of these monazite grains.

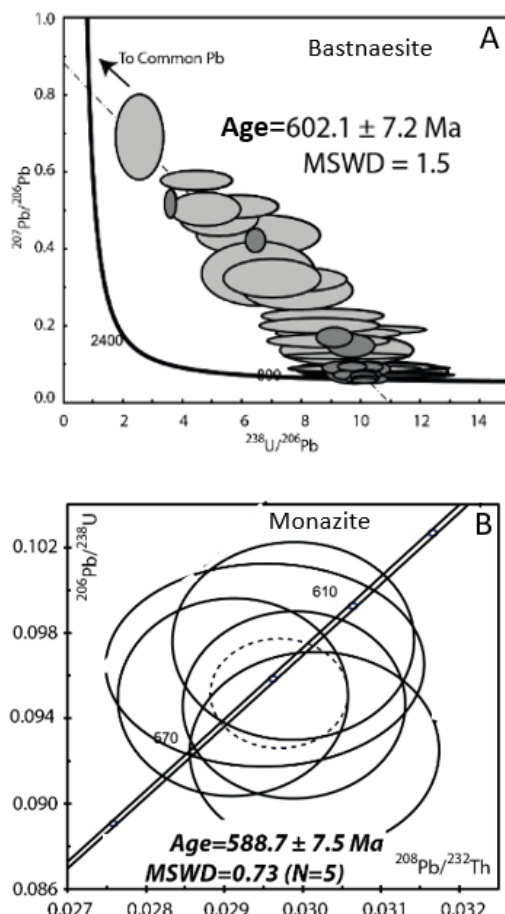


Figure 5. Tera–Wasserburg (A) and $^{206}\text{Pb}/^{238}\text{U}$ versus $^{208}\text{Pb}/^{232}\text{Th}$ Concordia (B) diagrams for Bastnaesite and monazite from Gakara.

7 Conclusion

The Gakara REE deposit, Burundi, formed by precipitation of bastnaesite and monazite veins from hydrothermal fluids. The hydrothermal origin is argued from the presence of fluid inclusions in bastnaesite and quartz crystals (Ntiharirizwa et al., in prep). Fluids were focused in pre-existing structural discontinuities. Although carbonatite is not yet found in the Gakara area, a carbonatitic body is suspected in depth (Lehmann et al. 1994; Van Wambeke et al. 1977; Ntiharirizwa et al. 2018). This suspicion is based on the strongly alkaline character of the ore system [4], and the REE differentiation similar to other carbonatite deposits (Verplanck et al. 2016; Tack et al. 1984). Geochronological data are compatible with the paragenesis sequence where monazite crystallization (near 588 Ma) followed the bastnaesite crystallization (near 600 Ma), likely in a continuum of hydrothermal activity. The varied types of ore bodies observed in the field must be reconciled into a unique mineralizing event (Ntiharirizwa et al. 2018), likely linked to the post-collisional tectonic context that prevailed at that time in the external zones of the Pan-African system.

Acknowledgements

We would like to thank the Rainbow Mining Burundi company for its assistance with the collection of data. Our special thanks are also extended to the staff of Geosciences Rennes for their administrative and technical support. We wish to thank also the Campus France Agency for the promotion of French higher education abroad.

References

- Goodenough, K.M.; Wall, F.; Merriman, D. The Rare Earth Elements: Demand, Global Resources, and Challenges for Resourcing Future Generations. *Nat Resour Res* 2017, 1–16.
- Jones, A.P.; Wall, F.; Williams, C.T. *Rare Earth Minerals: Chemistry, Origin and Ore Deposits*; Springer Science & Business Media, 1995; ISBN 978-0-412-61030-1.
- Verplanck, P.L.; Mariano, A.N.; Jr, A.M. Rare earth element ore geology of carbonatites. 2016, 2.
- Williams-Jones, A.E.; Migdisov, A.A.; Samson, I.M. Hydrothermal Mobilisation of the Rare Earth Elements – a Tale of “Ceria” and “Yttria.” *Elements* 2012, 8:355–360.
- Lehmann, B.; Nakai, S.; Höhndorf, A.; Brinckmann, J.; Dulski, P.; Hein, U.F.; Masuda, A. REE mineralization at Gakara, Burundi: Evidence for anomalous upper mantle in the western Rift Valley. *Geochimica et Cosmochimica Acta* 1994, 58:985–992.
- Van Wambeke, L. The Karonge rare earth deposits, Republic of Burundi: New mineralogical-geochemical data and origin of the mineralization. *Mineral. Deposita* 1977;12:373–380.
- Ntiharirizwa, S.; Boulvais, P.; Poujol, M.; Branquet, Y.; Morelli, C.; Ntungwanayo, J.; Midende, G. Geology and U-Th-Pb Dating of the Gakara REE Deposit, Burundi. *Minerals* 2018, 8:394.
- Nakai, S.; Masuda, A.; Lehmann, B. La-Ba dating of bastnaesite. *Chemical Geology* 1988:70:12.
- Tack, L.; Wingate, M.T.D.; De Waele, B.; Meert, J.; Belousova, E.; Griffin, B.; Tahon, A.; Fernandez-Alonso, M. The 1375Ma “Kibaran event” in Central Africa: Prominent emplacement of bimodal magmatism under extensional regime. *Precambrian Research* 2010:180:63–84.
- Deblond, A.; Tack, L. Main characteristics and review of mineral resources of the Kabanga-Musongati mafic-ultramafic alignment in Burundi. *Journal of African Earth Sciences* 1999, 29:313–328.
- Decrée, S.; Boulvais, P.; Cobert, C.; Baele, J.-M.; Midende, G.; Gardien, V.; Tack, L.; Nimpagaritse, G.; Demaiffe, D. Structurally-controlled hydrothermal alteration in the syntectonic Neoproterozoic Upper Ruvubu Alkaline Plutonic Complex (Burundi): Implications for REE and HFSE mobilities. *Precambrian Research* 2015:269:281–295.
- Midende, G.; Boulvais, P.; Tack, L.; Melcher, F.; Gerdes, A.; Dewaele, S.; Demaiffe, D.; Decrée, S. Petrography, geochemistry and U–Pb zircon age of the Matongo carbonatite Massif (Burundi): Implication for the Neoproterozoic geodynamic evolution of Central Africa. *Journal of African Earth Sciences* 2014:100:656–674.
- Tack, L.; De Paepe, P.; Deutsch, S.; Liégeois, J.P. The alkaline plutonic complex of the Upper Ruvubu (Burundi): geology, age, isotopic geochemistry and implications for the regional geology of the Western rift. In *African Geology*; Klerkx, J., Michot, J. (Eds), 1984:91–114.
- Kröner, A.; Stern, R.J. Pan-African Orogeny. *Encyclopedia of Geology* 2005, 1.
- Aderca, B.-M.; Tassel, R. van Le gisement de terres rares de la Karonge (République du Burundi); *Académie royale des sciences d’outre-mer*, 1971;

Magnetite formation in the serpentinization of ultramafic rocks from Bangong-Nujiang suture zone, Tibetan Plateau

Jing-Chao Li, Guo-Li Yuan*, Hua-Sheng Shao

School of Earth Sciences and Resources, China University of Geosciences, Beijing, China

Abstract. Serpentinized ultramafic rocks are widely distributed in the Bangong-Nujiang suture zone (BNSZ), and show close relationship with the regional mineralization. Here we investigate the serpentinized ultramafic rocks from Angwu in the central segment of the BNSZ, where the primary minerals include olivine, clinopyroxene, chromite, lizardite, magnetite, and chlorite. The alteration process of the ultramafic rocks, including serpentinization, can be divided into three stages: (I) formation of relatively Fe-rich serpentine (Mg#, 0.82), with no precipitation of magnetite; (II) formation of relatively Mg-rich serpentine (Mg#, 0.93), with precipitation of magnetite in serpentine veins; and (III) alteration of serpentine into chlorite. We computed the reactions associated with alteration process for the above stages. In addition, thermodynamic modeling in multicomponent mineral equilibrium phase diagrams indicate that during the serpentinization process, the desilication of pyroxene in caused the enhancement of SiO₂ activity and restricted the transformation from olivine to magnetite. The reaction temperature for the serpentinization of these rocks was relatively high, and within this temperature interval (100-300°C), lizardite was stable, and precipitation of magnetite was not favored.

1 Geology of the study area and sampling

In recent years, along with the discovery and exploitation of the Duolong large-scale mining area, the BNSZ has attained the status as one of the large polymetallic metallogenic belts on the Tibetan Plateau. Previous reports mainly focused on the nickel, pyrite (Luo et al., 2016) and chromite (Li et al., 2014), porphyry-type copper (gold) ore (Zhang et al., 2017) and skarn-type iron (copper) ore (Song et al., 2014). However, studies on magnetite deposits related to ultramafic rocks are relatively limited. Although large magnetite deposits have not been found in this zone as yet, several locations of magnetite mineralization related to ultramafic rocks were reported in the central section of the BNSZ, such as the Cebojiyi, Beila and at Daru Co (Figure 1b).

The serpentinized Angwu serpentinized ultramafic rocks (AUMRs) in the central section of the BNSZ occur approximately 50 km southeast of Duoma Town in Shuanghu County (Figure 1b), associated with magnetite mineralization. As shown in Figure 2a, the AUMRs represent a fragment at the contact of the fault with the Middle-Lower Jurassic Mugagangri Group (J1-2M). The Middle-Lower Jurassic Mugagangri Group consists of flysch and clastic rocks, which represent the abyssal to bathyal sediment of the Bangong-Nujiang Tethys Ocean (BNTO) (Cao et al., 2008). In the Angwu area, the Middle-

Lower Jurassic Mugagangri Group is dominated by greywacke and killas (metasediments).

The weathering front of AUMRs is characterized by emerald or dark green color, and the fresh surface is dark-green or black. The rock has a medium and coarse granular appearance and blocky structure, with locally strong serpentinization, with a soapy luster (Figure 2b). Six serpentinized AUMRs were sampled from the fresh outcrop and numbered as AW-GH1, AW-GH2, AW-GH3, AW-GH4, AW-GH5, and AW-GH6.

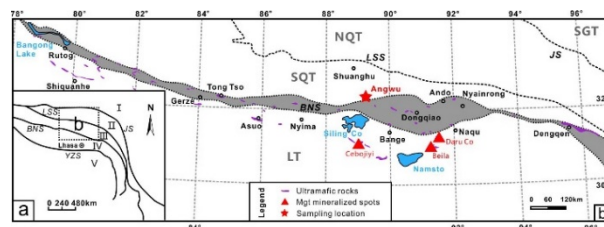


Figure 1. Tectonic sketch map of the Tibetan Plateau and sampling location of the Angwu ultramafic rocks.

I: Songpan-Ganzi Terrane, II: North Qiangtang Terrane, III: South Qiangtang Terrane, IV: Lhasa Terrane, V: Himalaya Terrane, JS: Jinshajiang suture zone, LSS: Longmuco-Shuanghu suture zone, BNS: Bangong-Nujiang suture zone, YZS: Yarlung Zangbo suture zone, SGT: Songpan-Ganzi Terrane, NQT: North Qiangtang Terrane, SQT: South Qiangtang Terrane, LT: Lhasa Terrane, Mgt: magnetite mineralization

2 Results

2.1 Petrography

Based on the mineral microstructures (Figure 2), the altered veins in the AUMRs can be divided into three types: (I) fine reticular serpentine veins with widths of approximately 0.05-0.1 mm that are developed in the cracks and grain margins of mainly olivine (Figure 2c); (II) coarse serpentine veins with widths of approximately 0.1-0.2 mm that cut through reticular veins, indicating later formation together with magnetite; and (III) chlorite veins with widths of approximately 0.05 mm developed in the serpentine veins within olivine and clinopyroxene (Figure 2d).

The results of X-ray diffraction (XRD) analyses for AUMRs indicate that the minerals mainly include forsterite, diopside, lizardite, magnetite, and clinocllore. Furthermore, XRD data identified subgroups, although some of these were not identified due to poor spectral peaks or due to abundance lower than the detection limit.

The backscattered electron (BSE) imaging and in situ component analysis for AUMRs were conducted with SEM-EDS. The results indicate mainly olivine,

clinopyroxene, serpentine, magnetite, and a mixture of serpentine and chlorite. In addition, chromite and ilmenite were also detected. The serpentine veins within altered olivine can be divided into two types: reticular serpentine veins with relatively low brightness correspond to the aforementioned type (I) veins, and the serpentine veins with the lowest brightness correspond to type (II) veins. Tiny magnetite crystals occur in the type (II) veins. Chlorite is mainly associated with the alteration of clinopyroxene corresponding to type (III) veins, although both serpentine and chlorite are developed on the grain margins of clinopyroxene.

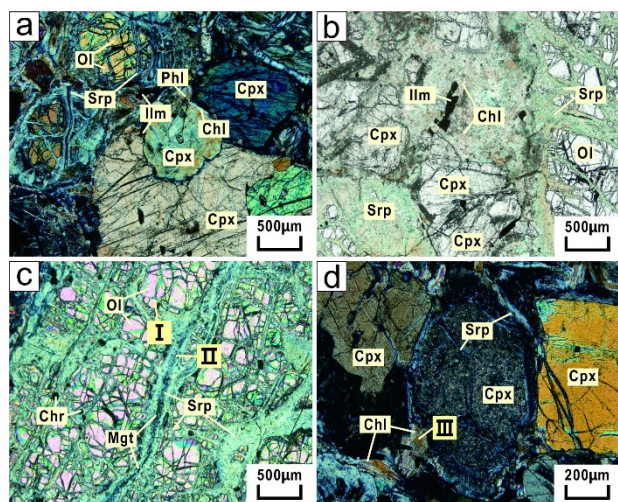


Figure 2. Photomicrographs of Angwu ultramafic rocks (sample: AW-GH1 and AW-GH6)

a: AW-GH1 (cross-polarized light), b: AW-GH6 (plane-polarized light), c: serpentinized olivine in AW-GH1 (cross-polarized light), d: serpentinized clinopyroxene in AW-GH1 (cross-polarized light), Ol: olivine, Cpx: clinopyroxene, Ilm: ilmenite, Srp: serpentine, Chl: chlorite, Phl: phlogopite, Mgt: magnetite, Chr: chromite, I: Type (I) serpentine veins, II: Type (II) serpentine veins.

2.2 Mineral chemistry

The olivine was normalized with 4 oxygen atoms, and all Fe was treated as Fe^{2+} while calculating mineral formulae. The olivine corresponds to that of low-Mg, Fe-rich type peridotite (Fo, 81-85), which is different from mantle peridotite, with a relative abundance of forsterite (Fo, >90) (Frost et al., 2013). The clinopyroxene was normalized with 4 cations. To balance the electrovalence of six oxygen ions in the molecular formula, Fe^{3+} is used to substitute for part of Fe^{2+} . Based on En-Wo-Fs classification diagram, the pyroxene in AUMRs is mainly clinopyroxene. Since there is strong alteration, the Mg# of clinopyroxene varies significantly (60-87). The results of the EPMA analysis of the spinel group minerals (mainly chromite and magnetite) and ilmenite are listed. The data were normalized with 3 cations, and ilmenite with 2 cations. To balance the electrovalence of cations, Fe^{3+} was used to substitute for some of the Fe^{2+} . The Cr# of chromite is 59-71, which is similar to that of spinel found in the Barru block of Sulawesi Island in Indonesia (Maulana et al., 2015). Magnetite is Fe-rich (in the unit molecule, $Fe^{3+} > Mg$). Ilmenite shows high Mg and low Mn ($MgO > 2wt.%, MnO < 0.5wt.%$) and occurs only in the

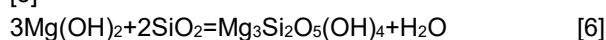
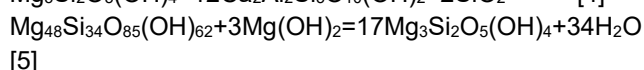
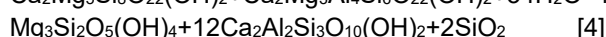
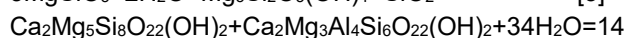
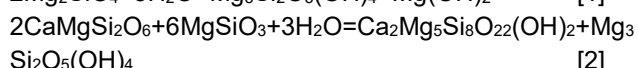
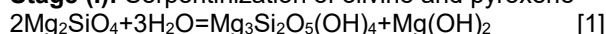
alteration zones of clinopyroxene.

3 Discussion

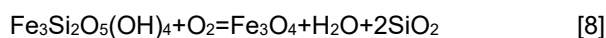
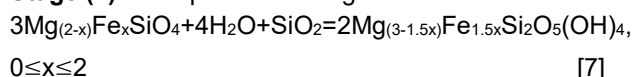
3.1 Factors influencing serpentinization

The serpentinization of AUMRs can be divided into three stages: (I) the alteration of olivine and clinopyroxene into serpentine; (II) the precipitation of magnetite from serpentine; and (III) the alteration of serpentine into chlorite. Mineral equilibrium modeling was based on phase diagrams (Holland and Powell, 2011) and mass balance. We computed the chemical reactions for the three stages of alteration of AUMRs. In this case, the ideal molecular formula was adopted for the major minerals. The results are as follows:

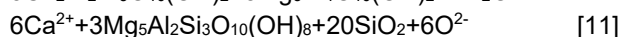
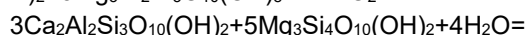
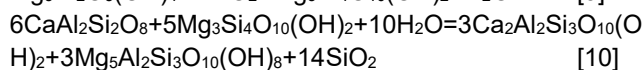
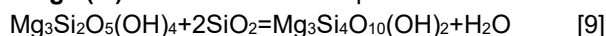
Stage (I): Serpentinization of olivine and pyroxene



Stage (II): Precipitation of magnetite



Stage (III): Chloritization of serpentine



3.2 Potential for magnetite mineralization

The Mg# of serpentine is positively related to the volume of magnetite precipitation. The range of Mg# of serpentine in the AUMRs is 77-95, suggesting the potential for small amount of magnetite precipitation (shaded area in Figure 3a). Experimental studies indicate that the release of Al and Si from pyroxene restrict the formation of iron oxide (Nozaka et al., 2017). Meanwhile, pyroxene would also cause the reduction of magnetite precipitation by gaining Fe from olivine during the serpentinization process. As discussed above, the desilication of pyroxene during serpentinization of the AUMRs enhanced the SiO_2 activity in the system (equations [3] and [4]), which reduced the amount of magnetite precipitation (Figure 3a). In addition, the mineral phase equilibrium (Figure 3b) indicates that higher temperatures are not favorable for the precipitation

of magnetite. Meanwhile, the lack of brucite indicates that the reaction temperature (200-300°C) in this case might be relatively high during serpentinization, which possibly hindered the large precipitation of magnetite. Thus, the possible reasons for the relatively low degree of magnetite mineralization in AUMRs are: (1) the significant increase of SiO₂ activity caused by desilication of pyroxene in the serpentinization process; and (2) the relatively high temperature in the system.

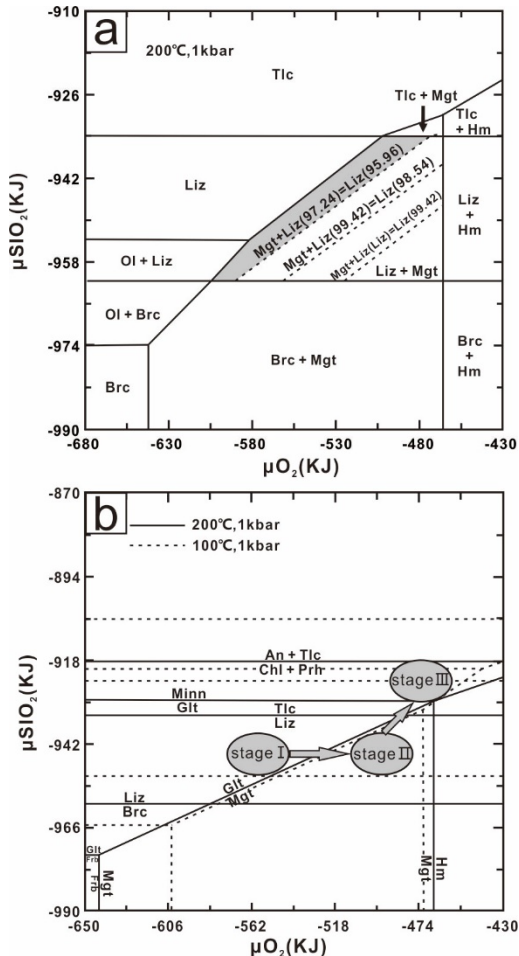


Figure 3. Phase diagrams of SiO₂ vs O₂ chemical potentials for serpentinization in Angwu Ultramafic Rocks. Ol: olivine, Hm: hematite, Brc: brucite, Mgt: magnetite, Liz: Lizardite, Tlc: talc, Frb: ferro-brucite, Glt: glaucophane, Minn: minnesotaite, An: anorthite, Chl: chlorite, Prh: prehnite

In summary, based on mineral phase equilibrium diagrams (Figure 3 and Figure 4), we predict two favorable conditions for magnetite precipitation during the serpentinization of ultramafic rocks: (1) lower SiO₂ activity under constant temperature and pressure, for example, less desilication of the primary minerals (e.g., pyroxene, amphibole); and (2) lower temperature within the temperature range (100-300°C) in the stability of lizardite.

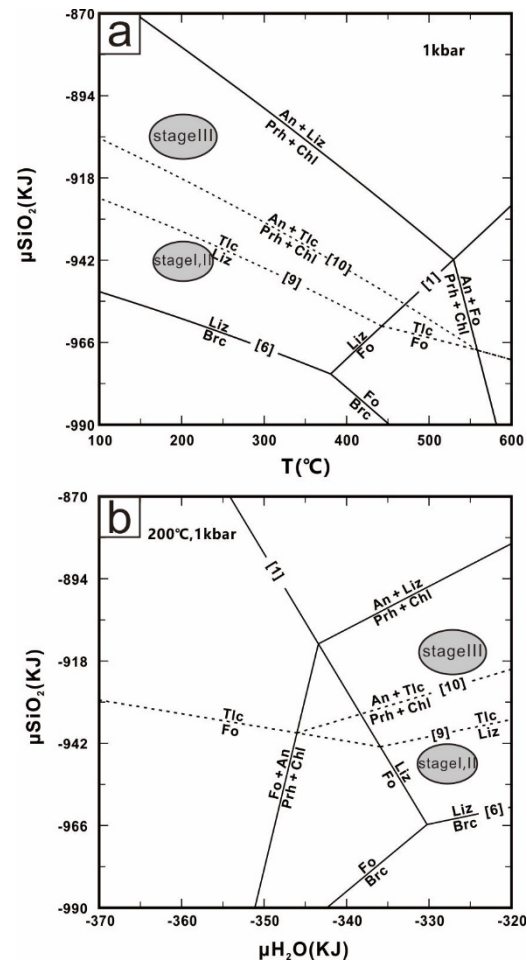


Figure 4. Phase diagrams for the serpentinization of olivine a: SiO₂ chemical potential vs temperature, b: SiO₂ vs H₂O chemical potentials, Fo: forsterite, Brc: brucite, Liz: Lizardite, Tlc: talc, An: anorthite, Chl: chlorite, Prh: prehnite

Acknowledgements

This research was partly funded by the National Key R & D Program of China (2018YFC0604106), and the Chinese Geological Survey Program (DD20160026), National Natural Science Foundation (41372249, 41872100), Fundamental Research Funds for the Central Universities (2652017239).

References

Luo, W., Li, Y.G., & Peng, J. (2016). Genesis of the nickel-sulfide-enriched ultrabasic rock in the Bangong Lake area, Tibet. *Journal of Mineralogy Petrology*, 36:29-36. (in Chinese with English abstract)

Li, X.K., Li, C., & Wang, M. (2014). The discovery of chromite in the Kangqiong area, middle-western segment of the Bangong Co-Nujiang River suture zone. *Geological Bulletin of China*, 33:1815-1819. (in Chinese with English abstract)

Zhang, Z., Fang, X., Tang, J.X., Wang, Q., Yang, C., Wang, Y.Y., Ding, S., & Yang, H.H. (2017). Chronology, geochemical characteristics of the Gaerqin porphyry copper deposit in the Duolong ore concentration area in Tibet and discussion about the identification of the lithoscaps and the possible epithermal deposit. *Acta Petrologica Sinica*, 33:476-494. (in Chinese with English abstract)

Song, Y., Tang, J.X., Qu, X.M., Wang, D.H., Xin, H.B., Yang, C., Lin,

- B., & Fan, S.F. (2014). Progress in the study of mineralization in the Bangongco-Nujiang metallogenic belt and some new recognition. *Advances in Earth Sciences*, 29:795-809. (in Chinese with English abstract)
- Cao, S.H., Xiao X.L., & Ouyang K.G. (2008). Renew-establishment of the Jurassic Mugangri Group and its geological significance on the Western side of the Bangong Co -Nujiang junction zone. *Acta Sedimentologica Sinica*, 26:559-564. (in Chinese with English Abstract)
- Holland, T.J.B., & Powell, R. (2011). An improved and extended internally consistent thermodynamic dataset for phases of petrological interest, involving a new equation of state for solids. *Journal of Metamorphic Geology*, 29:333-383.
- Nozaka, T., Wintsch, R.P., & Meyer, R. (2017). Serpentinization of olivine in troctolites and olivine gabbros from the Hess Deep Rift. *Lithos*, 282:201-214.

Can low-titanium lamproite magmas produce ore deposits? Evidence from Mesozoic Aldan Shield lamproites

Ivan F. Chayka, Andrey E. Izokh, Elena A. Vasyukova

V.S.Sobolev Institute of Geology and Mineralogy, SB RAS; Novosibirsk state university, Russia

Abstract. Lamproites and lamprophyres from Ryabinovoye gold deposit (Aldan Shield, Siberia) were studied. We demonstrate that these rocks, varying from Ol-Di-Phl-lamproites to syenite-porphyrries, form a continuous series of lamproite magma differentiation. At the stage of phlogopite and clinopyroxene crystallization, silicate-carbonate and then carbonate-salt immiscibilities occur. A suggestion is that during these processes LREE, Y, U, Sr and Ba distribute to a phosphate-fluoride fraction and probably accumulate in apatite-fluorite gangues. Based on our results and considering existing data on ore-bearing massifs within Central Aldan (Inagli, Ryabinoviy) and also of the Nam-Xe ore-bearing province (Vietnam), we concluded that Au, PGE and Th-U-Ba-REE deposits can be genetically connected with low-titanium lamproite magmas.

1 Introduction

The petrology and ore potential of lamproites, kimberlites and other high-potassic igneous rocks is a widely discussed topic. Lamproite magmatism is expressed in different tectonic settings from active-margin and collision to intraplate magmatic settings and, as well as kimberlite magmatism, provides information about deep mantle processes. On the other hand, lamproite rocks in numerous cases are spatially connected with trace-element deposits and some lamproites are diamond-bearing (Hoa et al. 2016; Vladykin 2008).

In the Central Aldan high-potassic province (Aldan shield, Russia) there are many synchronous mesozoic (125-134 Ma) (Shatov, et al. 2012; Mues-Schumacher et al. 1995) subvolcanic bodies of lamproites and lamproite-like rocks, spatially and temporally connected with Au-bearing (Ryabinoviy, Yukhtinskiy), PGE-bearing (Inagli) massifs and carbonatites (Murun massif). These occurrences were previously studied by a number of authors (Bilibin 1952; Vladykin 2008; Rokosova and Panina 2013; Mues-Schumacher et al. 1995). Although lamproites and lamprophyres are found all around Central Aldan and are united by some researchers into the Tobuk complex (Shatov et al. 2012), within the Ryabinovoye gold deposit (Ryabinoviy massif) a wide range of high-potassic dyke rocks outcrops on a very small area, being a unique case of differentiation of lamproite magma (from Ol-Di-Phl-lamproites to syenite-porphyry). Moreover, the rocks are well-preserved and are not weathered much. Hence, this complex can be considered as a “model example” for Aldan shield Mesozoic lamproites.

We studied in detail the mineralogical and chemical evolution of these lamproite-series rocks and compared some of their features with ones of Inagli dunites (Chayka and Izokh 2018) and with potassic rocks responsible for Ryabinovoye Au-porphyry deposit. Apatite-carbonate-fluorite assemblages, occurring as gangues and segregations within the lamprophyre dykes were studied in detail as well. In this paper we summarize all these results and briefly discuss ore potential of such lamproite magmas.

2 Geological setting

The Ryabinoviy massif is located in the central part of the Central Aldan high-potassic province in the Northern-Western part of Elkon horst. It is emplaced on the intersection of the Yakokutskiy and Yukhukhtinskiy faults, having an area (with apophysis) of about 50 km². Host rocks are granites and gneisses of the Aldan shield and Vend-Cambrian sedimentary layers (Maksimov et al. 2010). Lamproite-series rocks occur there within a small area of the Muskovitoviy location of the Ryabinovoye gold deposit. The complex includes a diatreme-like body, comprised of Ol-Di-Phl- and Di-Phl- lamproites and a sequence of dykes having composition from Ol-Di-lamproites to minettes and syenite-porphyry. It is noteworthy that the dykes cross-cut diatremes and each other in a homodrome sequence. Emplacement of these dykes is controlled by NE-striking faults.

3 Results

3.1 Mineralogical and chemical evolution of studied rocks

Petrographical study shows that rocks of these dykes form a continuous series from Ol-Di-Phl-lamproites via Di-Phl-lamproites and minettes to syenite-porphyrries. Ol-Di-Phl-lamproites consist of major olivine (in phenocrysts), diopside, phlogopite, K-feldspar (in groundmass); minor minerals are Cr-spinel (from Mg-chromite to Cr-magnetite), apatite, and pseudo-leucite. Di-Phl lamproites contain euhedral phenocrysts of diopside, zoned phlogopite, rare olivine replaced by carbonate and talc, and groundmass K-feldspar; minor minerals are magnetite and apatite. Minettes consist of euhedral zoned biotite and groundmass subhedral K-feldspar with minor magnetite, aegirine-augite, apatite and carbonate. Syenite-porphyrries are similar to

minettes, but contain less biotite, while K-feldspar is generally euhedral. Minettes and syenite-porphyrries also contain carbonate globules (see Chapter 3.2). The generalized sequence of crystallization is: (Cr-spinel+olivine+leucite) – (diopside+apatite) – (diopside+phlogopite (#Mg>70) +magnetite) – (aegirine-augite+biotite (#Mg<70)) – K-feldspar – carbonate.

The chemistry of major minerals was studied in detail and here we show only the essential chemical features of minerals:

1. Olivine cores have an extremely high #Mg up to 95 and high NiO content (up to 0,45 wt.%), rims' #Mg is about 75-88 (Chayka et al, 2018).
2. Cr-spinel composition varies from Mg-chromite (big euhedral grains, inclusions in olivine cores) to Cr-magnetite (groundmass grains);
3. Mica (annite-phlogopite series) phenocrysts are distinctly zoned: cores (#Mg=80-85) contain higher amounts of F (0,7-1,2 wt.%), than rims (#Mg=55-70, F – 0,5-0,9 wt.%), although other incompatible elements (Ba, Ti) are regularly higher in rims.
4. Apatite grains are inversely zoned in F content, as well as micas. Apatites from lamproites (less fractionated rocks) are about 5 to 15 times enriched in LREE, Y, U and Th in comparison with those from minettes and syenite-porphyrries (Fig.2a).

Major element composition was determined using XRF-analysis, alongside data published by Sharygin (1993). The geochemistry of major elements shows regular trends for MgO, SiO₂ and alkali content in the studied rocks. The studied series is subalkaline to alkaline, and high-potassic. A significant feature is dispersion of CaO content in minettes: CaO content varies in them from 4 to 12 wt.%, strongly deviating from the main CaO-MgO trend (Fig.1).

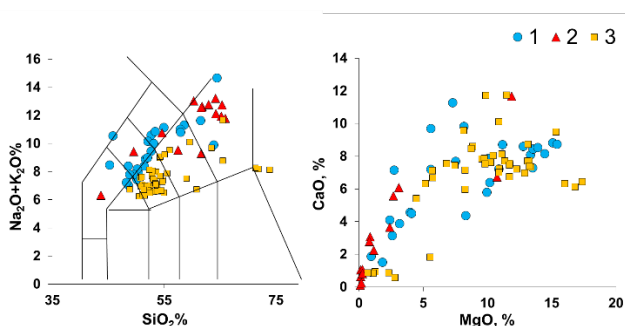


Figure 1. Binary diagrams for bulk compositions of the studied lamproite-series rocks (1), intrusive rocks of Aldanskiy complex (2), Northern Vietnam lamproite-series rocks (3)

3.2 Apatite-fluorite-carbonate mineralization

During field-works and further studies four different spatially-divided non-silicate associations were distinguished:

1. Silicate-carbonate and carbonate micro-globules in silicate matrix in minettes and syenite-porphyrries. They are round and oval-shaped, 0,05 to 2 mm in diameter and surrounded by laths of mica (Fig.3d). Their composition varies from dolomite+calcite+phlogopite to calcite+K-feldspar.

2. Big carbonate globules are found in some minette dykes. They are 1-3 cm in diameter and have a zoned structure (Fig.3a,c).
3. Calcite-apatite-fluorite gangue was found in dykes of syenite-porphry. It consists of major deep-purple fluorite, apatite and minor calcite, barite, celestine and various REE-minerals (bastnäsite, burbankite and others) (Fig.3d).
4. Carbonate in melt inclusions in olivine phenocrysts from Ol-Di-Phl-lamproites. According to Raman-spectroscopy, these inclusions contain up to 30 vol.% carbonate.

Based on chemical features of the minerals, structural relations and also considering results of previous researches (Rokosova 2013), we conclude that these associations can be united into a single phosphate-fluoride-carbonate mineralization, which was formed due to silicate-carbonate immiscibility and subsequent carbonate-salt separation (Chayka and Izokh 2017).

We also studied the distribution of trace elements in this mineralization and compared their concentrations with those in silicate portion. This problem was solved in two ways: by comparison of trace-element composition of studied minerals (calcite, dolomite, fluorite and apatite) with bulk trace-element composition of minettes (Fig.2b) and by comparison of trace-element composition of apatites from silicate rocks with gangue apatite (Fig.2a). The results show that apatite-fluorite gangue is enriched in LREE, U, Th, Sr and Ba, while carbonate globules are depleted in most of trace-elements.

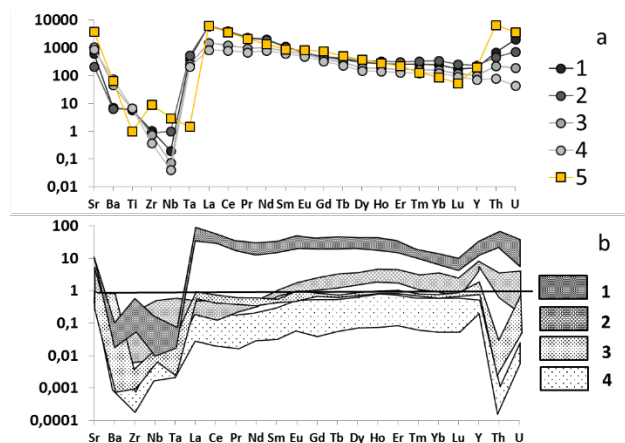


Figure 2. a) trace-element composition (by LA-ICP-MS and SIMS) diagram for apatite grains from Ol-Di-Phl-lamproites (1), Di-Phl-lamproites (2), minettes (3), syenite-porphyrries (4) and apatite-fluorite gangue (5); b) fields of trace-element composition, (normalized to bulk composition of minette) of apatite (1) and fluorite (2) from apatite-fluorite gangue, dolomite (3) and calcite (4) from big carbonate globules.

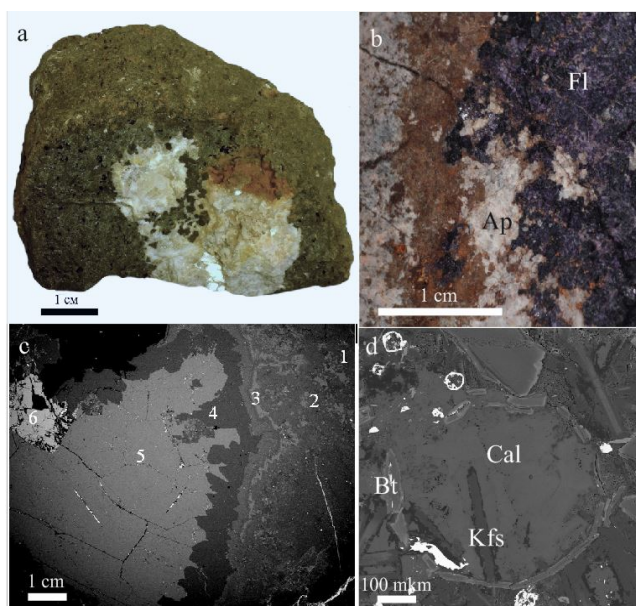


Figure 3. a) a big carbonate globule in minette sample; b) apatite-fluorite gangue in contact with syenite-porphry; c) BSE photo of big carbonate globule: silicate-carbonate zone (1), calcite-dolomite non-layered zone (2), calcite-dolomite layered zone (3), calcite core (4), fluorite segregation (5); d) electron microphotograph of silicate-carbonate micro-globule from minette

4 Discussion

4.1 Low-titanium lamproite melt as a parental melt for the Au-porphry Ryabinovoye deposit

Based on structural relations, the Aldanskiy potassic intrusive complex, which is responsible for Ryabinovoye Au-Cu-Mo- deposit, is considered to be an earlier phase than the studied dyke complex. But according to the previous researches (Shatov et al. 2012), there is no significant time-lapse between emplacement of these complexes. Moreover, there is a great similarity in their mineral compositions and major-element features. This background gives a reason to discuss a hypothesis that these complexes were produced from several magmatic pulses of similar parental melt. We considered bulk chemical composition and its evolution for rocks of both these complexes. Also we compared evolution of chemical compositions of micas and clinopyroxenes from rocks of these complexes. The comparison shows that rocks have the same composition ranges and correlations between main petrogenic oxides (Fig.1). Evolution of composition of clinopyroxenes and especially of micas are also very close (Chayka and Vasyukova, 2017). Trace-element compositions of lamproite-series rocks and Aldanskiy complex rocks are similar as well, although rocks of Aldanskiy complex show a wider range of compositions (which is quite typical for coarse-grained intrusive rocks due to fractionating). Thus we can conclude that the parental melt for Au-bearing Aldanskiy intrusive complex could have the composition of low-titanium lamproite melt. We have not appropriate data to state the full identity of parental melts, but it is very likely that they were identical at least in major-elements

composition and very similar in trace-element composition.

4.2 Low-titanium lamproite melt as a parental melt for PGE-bearing dunites of Inagli massif

The Inagli massif is a circular intrusion with dunite core and clinopyroxenite-shonkinite rim, situated at the Western part of the Central Aldan potassic province. It is well-known as a Cr-diopside deposit and a source for PGE placers. High degrees of secondary (hydrothermal and weathering) alternation makes it difficult to determine parameters of parental melt for this massif. Some researchers (Mues-Schumacher et al. 1995) suppose that the parental melt was very magnesian ($MgO \sim 25\%$) and add that it may be close to lamproites of Central Aldan. In order to test this hypothesis we studied in detail the chemical composition of Cr-spinel from both lamproites of Ryabinoviy massif and ultramafic rocks from the core of Inagli massif. The study was especially focused on composition of Cr-spinel hosted silicate inclusions (Chayka and Izokh 2018).

The results show similar compositions and evolution of Cr-spinel (considered Cr, Fe, Al, Mg, Ti). Accessory magnesian chromites from dunites (Inagli massif) and magnesian-chromite grains from Ol-Di-Phl-lamproites (Ryabinoviy massif) are most similar.

Study of silicate inclusions in Cr-spinel from lamproites from Ryabinoviy massif and dunites from Inagli massif show that their phase compositions are very close: they contain diopside and phlogopite as major minerals and minor apatite and sulphides such as pentlandite and chalcopyrite. The chemical features of phlogopite, diopside and apatite are close as well. We considered Na, Ti and Ba contents in phlogopite, Na and Al - in diopside, F and Sr content in apatite. These elements were chosen because they are relatively minor elements in Cr-spinel and are not significantly affected by silicate-spinel equilibrium. On the other hand their content in studied minerals is sensitive to their activity in melts.

The obtained results show that dunites from the core of PGE-bearing Inagli massif could represent metamorphosed cumulates of olivine and Cr-spinel, crystallized from low-titanium high-potassic, high-F parental melt, which is close to parental melt for lamproite series rocks of Ryabinoviy massif. This conclusion is also confirmed by previous researches (Mues-Schumacher et al. 1995; Okrugin 2004).

4.3 Low-titanium lamproites and REE deposits

In Northern Vietnam there are Cenozoic REE-U-F-Ba-deposits, located in the Nam Xe area and genetically related with lamproite and lamprophyre rocks of Fansipan uplift (Hoa et al. 2016). These rocks and the studied ones possess very similar major-element compositions and evolutionary trends (Fig.1). Both these series have unusual high forsterite (82-92) and NiO (0,1-0,5 wt.%) contents in phenocrystal olivines. We can suppose that chemical compositions of their sources and melting conditions were very close to each other.

As mentioned before, we studied apatite-fluorite-carbonate mineralization in dykes of the Ryabinoviy massif and supposed that it was a result of silicate-carbonate and carbonate-salt immiscibility (Chayka and Izokh 2017). At the stage of clinopyroxene and phlogopite crystallization in magmatic chamber, silicate-carbonate-salt immiscibility occurs. A hybrid carbonate-salt melt contains different amounts of P, F, Cl and SO₄, and then (probably with tectonically-caused decompression) it can separate into carbonatite and salt fractions (Rokosova and Panina 2013). Our study of trace-element distribution between parts of apatite-fluorite-carbonate mineralization shows that Th, U, LREE, Sr and Ba migrate into immiscible carbonate-salt part and then – into salt fraction, forming apatite-fluorite gangues with minor calcite, barite, celestine and REE-mineralization. This model suggests a genetic mechanism of trace-element deposits, related to high-potassic basic rocks and fluorite carbonatites, such as those at Fansipan uplift (Northern Vietnam).

5 Conclusions

Summing-up all the results, several conclusions can be made: firstly, the studied complex provides useful data on evolution of low-titanium lamproite magma and hence about Mesozoic lamproite magmatism all over Central Aldan. Concerning ore potential, obtained results indicate that evolution of low-titanium lamproite melts in certain conditions probably can lead to formation of Au, PGE and U-Ba-REE deposits. In addition, the similarity of Central Aldan and Fansipan lamproite-series rocks indicates the possible presence of Th-U-Ba-REE deposits, like Nam Xe, within the Central Aldan province.

Acknowledgements

We would like to thank Nikiforov A.V. (IGEM RAS, Moscow) for rock samples, Saprykin A.I. and Medvedev N.S. (NIIC SB RAS) for LA-ICP-MS analysis, Simakin S.G., (YB IPT RAS, Yaroslavl) for SIMS-analysis, Veksler I.V. (Potsdam University, Germany), for useful and interesting discussion. This study was supported by the Russian Scientific Foundation (project №19-17-00019).

References

- Bilibin YuA (1958) Selected works. Publishing of Academy of Sciences USSR, USSR (in Russian)
- Chayka IF, Izokh AE (2017) Phosphate-fluoride-carbonate mineralization in lamproite rocks of the Ryabinoviy pluton (Central Aldan): mineralogical and geochemical features and origin. *Mineralogiya* 3:39-51 (in Russian)
- Chayka IF, Izokh AE (2018) Dunites of the Inagli massif (Central Aldan), cumulates of lamproitic magma. *Russian Geology and Geophysics* 59: 1450-1460
- Chayka IF, Izokh AE, Sobolev AV, Batanova VG (2018) Low-titanium lamproites of the Ryabinoviy Massif (Aldan Shield): crystallization conditions and lithospheric source. *Doklady Earth Sciences* 481: 1008-1012
- Chayka IF, Vasyukova YeA (2017) Mineralogy, geochemistry and isotope chemistry of lamproite rocks of Tobuk complex and their relation to Au-ore Ryabinoviy massif (Central Aldan). *Metallogeniya Drevnikh I Sovremennykh Okeanov*. 1: 232-237

- (in Russian)
- Maksimov EP, Uytov VI, Nikitin VM (2010) The Central Aldan gold-uranium ore magmatogenic system, Aldan-Stanovoy shield, Russia. *Russian Journal of Pacific Geology* 4: 95-115
- Mues-Schumacher U, Keller J, Konova V, Suddaby P (1995) Petrology and age determinations of the ultramafic (lamproitic) rocks from the Yakokut complex, Aldan shield, Eastern Siberia. *Mineralogical Magazine* 59:409-428
- Okrugin AV (2004) Crystallization-immiscibility model of PGE-chromitite ores origin in mafic-ultramafic complexes. *Tikhookeanskaya Geologiya* 23: 63-75 (in Russian)
- Rokosova EYu, Panina LI (2013) Shonkinites and minettes of the Ryabinoviy massif (Central Aldan): composition and crystallization conditions. *Russian Geology and Geophysics* 54:613-626
- Sharygin VV (1993) Potassic picrites of Ryabinoviy massif. *Russian Geology and Geophysics* 4: 60-70
- Shatov VV, Molchanov AV et al (2012) Petrography, geochemistry and isotopic (U-Pb and Rb-Sr) dating of alkali magmatic rocks of Ryabinoviy massif (Southern Yakutia, Russia). *Regional Geology and Metallogeny* 51:62-78 (in Russian)
- Trong-Hoa Tran, Polyakov GV et al (2016) Intraplate Magmatism and Metallogeny of North Vietnam. Springer, Switzerland
- Vladykin NV (2009) Potassium alkaline lamproite-carbonatite complexes: petrology, genesis, and ore reserves. *Russian Geology and Geophysics* 50:1119–1128

Peraluminous pegmatoids with several thousands of ppm of LREE in the Central Grenville Province

François Turlin*, Aurélien Eglinger, Anne-Sylvie André-Mayer, Clara Deruy, Michel Cuney

GeoRessources lab., Université de Lorraine, CNRS, CREGU, Campus Aiguillettes, Faculté des Sciences et Technologies
**Now at Université du Québec à Montréal, Département des Sciences de la Terre et de l'Atmosphère, Montréal, Canada*

Olivier Vanderhaeghe, Marieke Van Lichtervelde

Géosciences Environnement Toulouse, Université de Toulouse, CNES, CNRS, IRD, UPS, 14 avenue Edouard Belin, 31400 Toulouse, France

Jean-Marc Montel

Centre National de la Recherche Scientifique, CRPG

Abdelali Moukhsil, Fabien Solgadi

Ministère de l'Énergie et des Ressources naturelles, Direction du Bureau de la connaissance géoscientifique du Québec

Abstract. Peraluminous pegmatoids (PGDs) from the central Grenville Province show LREE enrichments up to 7435 ppm hosted in monazite or allanite. These PGD are compared with their migmatitic metapelitic source to elaborate a petrogenetic model for these peculiar magmas.

The leucosome has low Σ REE content (39 ppm) consistent with its Pl+K-Fsp-dominated assemblage. The higher Σ REE contents (259 ppm) and negative Eu anomaly of the melanosome reflects the Bt+Grt-dominated assemblage and minor apatite+zircon+monazite. The strong fractionation of the LREE over HREE in the PGD points to HREE sequestration in the residual garnet. The decreasing Σ REE content and Eu negative anomaly from aplitic to pegmatitic facies are attributed to magmatic differentiation.

REE contents in the various rock types imply that the REE behaved as incompatible elements. Low degrees (<10%) of partial melting of the metapelites would be required to reach the Σ LREE content of the PGD but this is incompatible with melt migration, and with residual peritectic garnet. In turn, fractional crystallization is incompatible with flattening Eu anomaly nor with stable K/Rb ratios and Rb contents of K-feldspar during magmatic evolution. These data provide contradictory constraints on the contributions of partial melting and fractional crystallization in LREE enrichment of the PGD.

1 Introduction

For decades, experimental data and field observations demonstrated that peraluminous melts are not suitable hosts of LREE as shown by the solubility of monazite (Σ REE) that is below ca. 300 ppm (e.g. Montel 1986, 1993). However, Turlin et al. (2017) reported peraluminous pegmatoids (PGD) with up to 7435 ppm of REE hosted either in allanite or monazite. These PGDs were emplaced in the Allochthonous Belt of the central Grenville Province around ca. 1005-1000 Ma (Fig. 1, Turlin et al. 2017, 2019) and were derived by partial melting of Paleoproterozoic-Archean metapelites

belonging to the underlying Parautochthonous Belt (Fig. 1, Turlin et al. 2019).

This study aims to (i) compare the petrogeochemical characteristics of several facies of an example of a monazite-bearing LREE-rich PGD and of its metapelitic source (parautochthonous migmatites), and (ii) to discuss the magmatic processes that played a role in such important LREE accumulation in peraluminous melts.

2 Geological context

The Grenville Province is composed of two tectonometamorphic domains: the (i) Allochthonous Belt (terranes accreted to Laurentia during the Mesoproterozoic), and the (ii) Parautochthonous Belt (rocks of the Superior Province and its metasedimentary cover reworked during the Grenvillian Orogeny) (Fig. 1, e.g. Rivers 2008). The former recorded the Ottawa crustal thickening phase as early as ca. 1090 Ma with a HT-HP peak of metamorphism reaching granulite-facies at ca. 1070-1050 Ma (Rivers 2008; Lasalle et al. 2013; Turlin et al. 2018). It subsequently slowly cooled down to close to solidus conditions at ca. 1005-1000 Ma, and down to subsolidus condition of ca. 500°C at ca. 960 Ma (Turlin et al. 2018). The underlying Parautochthonous Belt (Fig. 1) was metamorphosed during the crustal thickening phase (ca. 1005-960 Ma) that reached partial melting conditions up to granulite-facies peak of metamorphism (Jannin et al. 2018; Jordan et al. 2006).

3 LREE-rich PGDs from the central Grenville

The LREE-rich PGDs from the Allochthonous Belt of the central Grenville Province show a strong peraluminous signature with ASI (Aluminum Saturation Index = $Al/(Ca - 1.67 \times P + Na + K)$; Frost et al. 2001; Shand 1943) between 1.18 and 1.36 (Turlin et al. 2017), which is uncommon for LREE-rich magmas. Among them, one PGD shows a Σ LREE content up to 6949 ppm hosted in monazite (Turlin et al. 2017). Its derivation by partial melting of parautochthonous metapelites has been

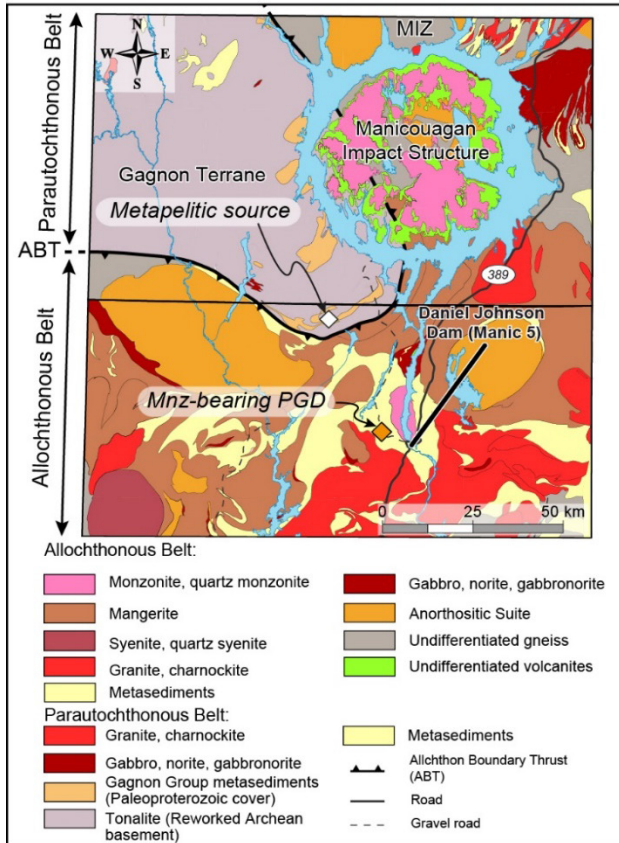


Figure 1. Geological map of the central Grenville Province (Quebec) with the localisation of the investigated LREE-rich pegmatitic granite dyke and of its metapelitic source (modified after Turlin et al. 2017). Abbreviations: MIZ = Manicouagan Imbricate Zone; Mnz = monazite.

shown by trace elements and U-Pb-Hf-O isotopes of zircon grains (Turlin et al. 2019).

4 Petrography

The parautochthonous metapelites correspond to migmatitic paragneisses dominated by the mesosome and the leucosome complemented with a thin melanosome (Fig. 2a). The leucosome is composed of a PI+K-Fsp+Qtz assemblage (Fig. 2b), the mesosome is composed of a Bt+Grt+PI+K-Fsp+Qtz assemblage (Fig. 2b), complemented with minor apatite and zircon, and the melanosome is composed of a Bt+Grt+PI assemblage and minor zircon, apatite and monazite, the latter generally enclosed into garnet (Fig. 2d). Garnet is peritectic as shown by the lack of zonation and their equilibrium with K-feldspar.

The PGD is composed of several facies that range from fine-grained (grain size <1 cm) to pegmatitic (grain size >5 cm). Both are dominated by a Qtz+K-Fsp+PI assemblage that is complemented with a high proportion of biotite, monazite and zircon in the fine-grained facies (Fig. 2e). In contrast, the pegmatitic facies only shows low proportion of biotite (Fig. 2f) and minor monazite and zircon. Monazite and zircon grains of the PGD do not show any inheritance from the protolith of the PGDs (Turlin et al. 2017, 2019).

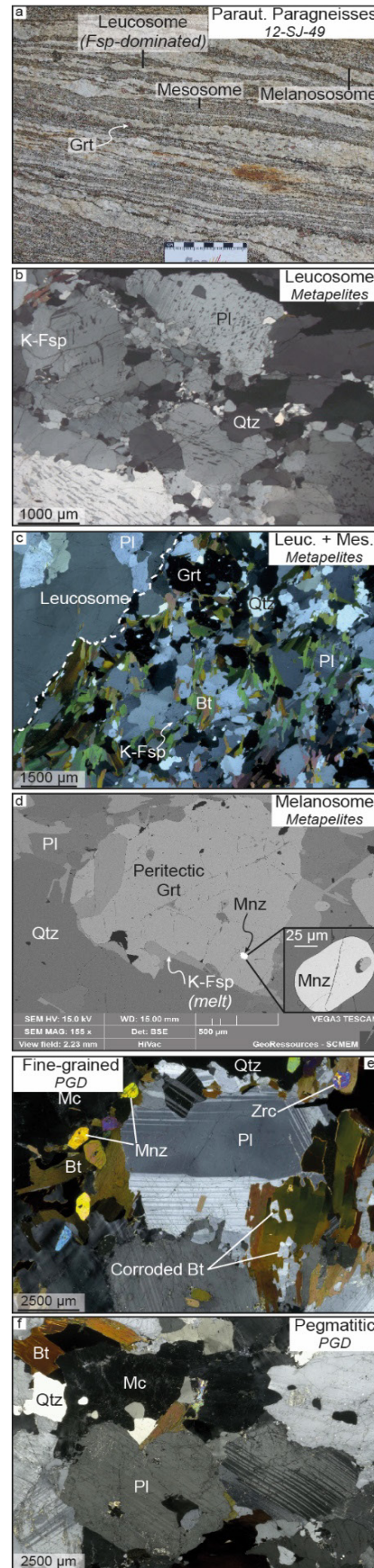


Figure 2. Petrography of the parautochthonous metapelites (a-d) and of the allochthonous-hosted pegmatitic granite dyke (e-f). a: migmatitic paragneisses dominated by mesosome and leucosome; b: leucosome are dominated by a PI+K-Fsp+Qtz assemblage; c: mesosome are complemented with biotite and peritectic garnet; d: melanosome with prograde monazite enclosed into peritectic garnet; e and f: fine-grained and pegmatitic facies of the pegmatitic granite dominated by a Qtz+K-Fsp+PI assemblage complemented with high or minor proportions of biotite, monazite and zircon, respectively. Abbreviations: Bt = biotite; Fsp = feldspar; Grt = garnet; Mnz = monazite; PI = plagioclase; Qtz = quartz; Zrc = zircon.

5 Genetic link between the metapelites and the PGD

Fractionation of pegmatites from their source can be traced using K-feldspar chemistry (K/Rb ratios and Rb contents, Černý et al. 1985; Hulsboch et al. 2014). Plotted in a K/Rb vs Rb diagram, data should follow a negative exponential distribution if one is fractionated from another (Hulsboch et al. 2014). In this study K and Rb contents of K-feldspar from the leucosome of the migmatites and of the various facies of the PGD were measured using EPMA and LA-ICP-MS, respectively.

The leucosome contains K-feldspar with Rb content of 18 ppm (S.D. of 6 ppm) and K/Rb ratios of 8229 (S.D. of 3868). The K-feldspars from the PGD show Rb contents between 28 and 60 (S.D. < 21) and K/Rb ratios between 2180 and 5798 (S.D. < 4283). The differences in these values is not correlated with magmatic evolution of the PGD from fine-grained to pegmatitic facies.

Plotted in a K/Rb vs Rb diagram, data obtained on K-feldspar from the leucosome of metapelites and from the PGD define a single trend following a negative exponential distribution (Fig. 3). Moreover, data from the PGD show (i) a slight fractionation from the leucosome and (ii) no distinction between the various facies (Fig. 3).

6 Whole rock geochemistry

The metapelites are characterized by a leucosome with a low Σ REE content of 39 ppm, and by a melanosome with a higher Σ REE content of 259 ppm. For the leucosome and the melanosome, the chondrite-normalized REE patterns indicate (i) similar fractionation of LREE over HREE (La_N/Yb_N of 3.4), (ii) no fractionation within the LREE (La_N/Sm_N of 1.1), and (iii) a slight fractionation within the HREE (Gd_N/Yb_N of 2.7) (Fig. 4). The leucosome and the melanosome have chondrite-normalized REE patterns with a strongly positive (Eu/Eu^* of 3.2) or negative (Eu/Eu^* of 0.5) Eu anomaly (Fig. 4), respectively. These features are consistent with the strong proportion of feldspar within the leucosome with no accessory minerals, and with the presence of apatite and monazite within the melanosome (Fig. 2d; Bea 1996). Similarly, the high Σ HREE content in the melanosome is consistent with the presence of garnet and zircon (Bea 1996; Hönig et al. 2014). The mesosome shows intermediate compositions between the leucosome and the melanosome consistent with the intermediate Bt+Grt+Pl+K-Fsp+Qtz assemblage (Fig. 2c) with minor apatite and zircon.

The PGD has a granitic composition (SiO_2 from 60.24 to 73.08 wt.%) and a strong peraluminous signature marked by ASI ranging between 1.12 and 1.36. From the fine-grained to the pegmatitic facies, the chondrite-normalized REE pattern is associated with decreasing (i) Σ REE content (from 7048 to 721 ppm), (ii) negative Eu anomaly (Eu/Eu^* from 0.1 to 0.6), (iii) fractionation of the LREE over the HREE (La_N/Yb_N from 1193 to 223), and (iv) within the HREE (Gd_N/Yb_N from 54 to 11) (Fig. 4). However, the LREE are not fractionated with this magmatic evolution (La_N/Sm_N of 6.8-7.2) (Fig. 4). These

REE patterns are consistent with the high proportion of monazite hosting the LREE (Bea 1996) in the fine-grained facies and that decreases towards the pegmatitic facies.

7 Discussion

The single trend defined in the K/Rb vs Rb diagram by the K-feldspar from the migmatitic metapelites and the various facies of the peraluminous PGD (Fig. 3) confirm their genetic link by partial melting discussed by Turlin et al. (2019). The peraluminous character of the PGD is not compatible with high proportions of monazite (Σ REE) which solubility in peraluminous melts is below ca. 300 ppm (Montel 1993).

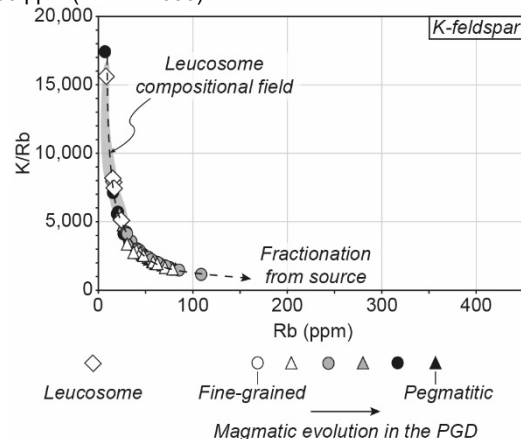


Figure 3. K/Rb vs Rb (ppm) diagram of K-feldspar. Note the little fractionated character of all investigated K-feldspar compared to the model of Hulsbosch et al. (2014) and that K-feldspar from the leucosome show a slightly lower fractionation compared to those from the dyke. No correlation between these fractionations and a specific facies of the latter can be outlined. Abbreviation: PGD = pegmatitic granite dyke.

If one considers the melanosome as the relict of the mesosome partial melting, the REE must be strongly compatible and strong REE enrichment is impossible. However, REE contents in the métapelites and in the PGD imply that the REE behaved as incompatible elements. The metapelites do not show strong Σ REE content (not higher than 259 ppm), therefore implying that the genesis of LREE-rich melts with contents up to thousands of ppm (Fig. 3) would result from a low degree (<10%) of partial melting. However, this is incompatible with (i) the lack of inherited monazite and zircon domains in the PGD that point to their total dissolution in the generated melts (Turlin et al. 2017, 2019), with (ii) the peritectic character of garnet that reflects the biotite destabilization and therefore higher degrees of partial melting, and with (iii) liquid migration in the crust (Vanderhaeghe 2009). In contrast, higher melting rates (>20-25%) would be consistent with the elements discussed above but are incompatible with the LREE enrichment of the PGD. Accordingly, these features point to the role of the fractional crystallization.

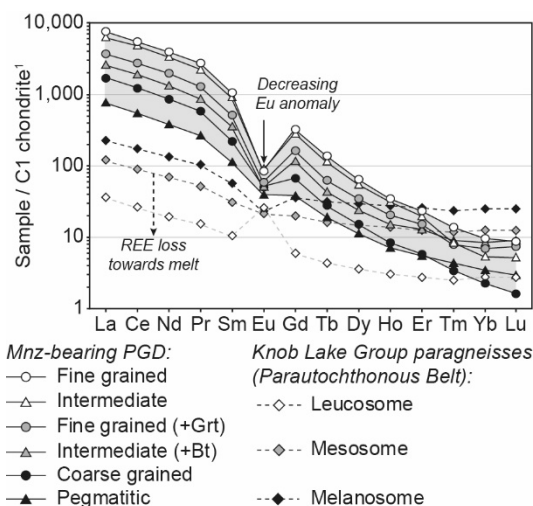


Figure 4. Chondrite-normalized REE patterns of the facies identified in the pegmatitic granite dyke and of the melanosome, mesosome and leucosome of its potential source. Abbreviations: ¹ = McDonough and Sun (1995); Bt = biotite; Grt = garnet.

The magmatic evolution from fine-grained to pegmatitic facies is associated with a decrease of the REE suggesting fractional crystallization (Fig. 3). However, the decreasing Eu negative anomaly and the stable K/Rb ratios and Rb contents from K-feldspar is in favor of a limited impact, if any, of fractional crystallization (Figs. 3-4).

Accordingly, this study challenges experimental data on LREE behavior within peraluminous melts, but the respective roles of partial melting and fractional crystallization in their genesis from partial melting of REE-unenriched metapelites is still challenging.

Acknowledgements

The authors thank the Ministère de l'Énergie et des Ressources naturelles (Québec, Canada) for technical and financial support for field work and analyses, to Andrei Lecomte (SEM) and Olivier Rouer (EMP) (GeoRessources, Nancy) for support in providing analytical data on SEM and EPMA, and to Chantal (GeoRessources, Nancy) for her help in LA-ICP-MS data acquisition. This work was funded by the Labex Ressources 21 (French National Research Agency – France), program “Investissements d’avenir” (ANR-10-LABX-21–LABEX RESSOURCES 21) and the Région Grand-Est. It benefited from the framework of the DIVEX “Rare earth element” research program.

References

- Bea F (1996) Residence of REE, Y, Th and U in granites and crustal protoliths; Implications for the chemistry of crustal melts. *J Petrology* 37:521–552
- Černý P, Meintzer RE, Anderson AJ (1985) Extreme fractionation in rare-element granitic pegmatites; selected examples of data and mechanisms. *Can Min* 23:381–421
- Frost BR, Barnes CG, Collins WJ et al. (2001) A geochemical classification for granitic rocks. *J. Petrology* 42:2033–2048
- Hönig S, Čopjaková R, Škoda R et al (2014) Garnet as a major

carrier of the Y and REE in the granitic rocks: An example from the layered anorogenic granite in the Brno Batholith, Czech Republic. *Am Min* 99:1922–1941

- Hulsbosch N, Hertogen J, Dewaele S et al (2014) Alkali metal and rare earth element evolution of rock-forming minerals from the Gatumba area pegmatites (Rwanda): Quantitative assessment of crystal-melt fractionation in the regional zonation of pegmatite groups. *Geochim Cosmochim Acta* 132:349–374
- Jannin S, Gervais F, Moukhsil A et al (2018a) Déformations tardigrenvilliennes dans la Ceinture parautochtone (Province de Grenville centrale): contraintes géochronologiques par couplage de méthodes U/Pb de haute résolution spatiale et de haute précision. *Can J Earth Sci* 55(4):406–435
- Jordan SL, Indares A, Dunning G (2006) Partial melting of metapelites in the Gagnon terrane below the high-pressure belt in the Manicouagan area (Grenville Province): pressure-temperature (P-T) and U-Pb age constraints and implications. *Can J Earth Sci* 38:1309–1329
- Lasalle S, Fisher CM, Indares A et al (2013) Contrasting types of Grenvillian granulite facies aluminous gneisses: Insights on protoliths and metamorphic events from zircon morphologies and ages. *Precambrian Research* 228:117–130
- McDonough WF, Sun SS (1995) The composition of the Earth. *Chem Geol, Chemical Evolution of the Mantle* 120:223–253
- Montel JM (1993) A model for monazite/melt equilibrium and application to the generation of granitic magmas. *Chem Geol* 110:127–146
- Montel JM (1986) Experimental determination of the solubility of Ce-monazite in SiO₂-Al₂O₃-K₂O-Na₂O melts at 800 °C, 2 kbar, under H₂O-saturated conditions. *Geology* 14:659–662
- Rivers T (2008) Assembly and preservation of lower, mid, and upper orogenic crust in the Grenville Province-Implications for the evolution of large hot long-duration orogens. *Precambrian Research* 167:237–259
- Shand SJ (1943) *The Eruptive Rocks*. New York: John Wiley
- Turlin F, Vanderhaeghe O, Gervais F et al (2019) Petrogenesis of LREE-rich pegmatitic granite dykes in the central Grenville Province by partial melting of Paleoproterozoic-Archean metasedimentary rocks: evidence from zircon U-Pb-Hf-O isotope and trace element analyses. *Precambrian Research* 327:327–360
- Turlin F, Deruy C, Eglinger A et al (2018) A 70 Ma record of suprasolidus conditions in the large, hot, long-duration Grenville Orogen. *Terra Nova* 30-3:233–243
- Turlin F, André-Mayer AS, Moukhsil A et al (2017) Unusual LREE-rich, peraluminous, monazite- or allanite-bearing pegmatitic granite in the central Grenville Province, Québec. *Ore Geology Reviews* 89:627–667
- Vanderhaeghe O (2009) Migmatites, granites and orogeny: Flow modes of partially-molten rocks and magmas associated with melt/solid segregation in orogenic belts. *Tectonophysics* 477:119–13

Geochemical variations in pegmatites of the Cape Cross-Uis tin belt and Sandamap-Kranzberg tin belt, Namibia

Filadelphia Mbingeneeko and Ansgar Wanke
University of Namibia, Geology Department, Namibia

Abstract. The Pan African Damara Orogenic Province of Namibia hosts world-renowned Sn- W metallogenic belts such as the Cape Cross-Uis tin belt and the Sandamap – Kranzberg tin belt (De Waal, 1985). For comparative purposes, this research aims to characterize the pegmatites based on geochemical variations at known deposits within the latter belts, namely; the Uis tin and the Sandamap Noord tin mineralization, respectively. The Uis tin mineralization is hosted in pegmatites, whilst the Sandamap Noord mineralization is hosted within pegmatitic quartz. Cassiterite is the main tin ore mineral (Petzel, 1986; Fuchsloch et al., 2018).

Three groups of pegmatites are distinguished within the Cape Cross-Uis belt, specifically at Uis tin mine, namely; the unzoned Nb-Ta-Sn type, the garnet-tourmaline, and the zoned lithium-bearing pegmatites. The classification of pegmatites within the Cape-Cross-Uis and the Sandamap - Kranzberg tin belts will serve as a guide to better explore for tin and associated mineralization within the Pan African Damara Orogenic Province. In future, this research will utilize new modern dating and geochemical analytical techniques to establish the genetic link between these polymetallic tin deposits.

1 Introduction

Critical high technology elements (Sn and associated W, Nb, Ta, Li, and Be among others) are essential to innovative and ecofriendly technologies, hence, they are of high importance to the global economy. These critical mineral commodities are associated with a high supply risk in the current global market. The Sandamap-Kranzberg tin belt and the Cape Cross-Uis tin belt of the Pan African Damara Orogenic Province in Namibia, host to the Sandamap Noord tin deposit and the world-renowned Uis tin deposits, respectively. The tin mineralization is hosted in pegmatites and pegmatitic quartz at, Uis Tin mine and Sandamap Noord deposit, respectively. Cassiterite is the main tin ore mineral at both deposits.

This research ultimately aims to contribute to the unresolved debate about the genetic link between Sn and associated mineralization within the pegmatites of the Pan African Damara Orogenic Province by classifying the pegmatites within the Province based on the classification scheme of Černý and Ercit (2005). For comparative purpose, the holistic understanding of the geochemical variation between pegmatites from the two tin deposits, namely; the Uis tin mine and the Sandamap Noord tin deposit will serve as a guide to better explore for tin and associated mineralization within the Pan African Damara Orogenic Province.

2 Geological setting

The Neoproterozoic Pan African orogenic belt surrounds and dissects the stable Kalahari and Congo Cratons in Namibia (Miller, 2008). This belt consist of the NE trending intracontinental Damara branch, the Gariiep branch in the southern part of Namibia and the NNW trending coastal Kaoko branch. The Damara branch and the Kaoko branch are subdivided into various tectonostratigraphic zones on the basis of metamorphic grade, igneous activity, stratigraphy and structure (Miller, 2008). Within the Kaoko branch, these zones are, namely; the Eastern Kaoko Zone (EKZ), the Central Kaoko Zone (CKZ), the Western Kaoko Zone (WKZ) and the Southern Kaoko Zone (SKZ) (Miller, 2008; Petzel, 1986).

The zones of the inland Damara branch, consists of; the Southern Zone, Central Zone and Northern Zone. The Cape Cross-Uis pegmatite belt (Uis Tin Mine) is situated in the Northern Zone (Richards, 1986; Fuchsloch, 2018). On the other hand, the Central Zone of the Damara branch is host to the Sandamap – Kranzberg tin belt, in which the Sandamap Noord Tin Deposit occurs, among others is situated (Keller, 1999).

Geological field investigations and whole rock geochemical analysis (Fuchsloch et al., 2018) indicated that the Sn mineralization within the Cape Cross- Uis pegmatite belt was emplaced during the relaxation of the Pan-African event. Moreover, Zhang (2017) conducted in situ U-Pb direct dating of cassiterite ore mineral to the Uis tin and the Goantagab tin deposits within the Damara Orogen. The resultant age indicated that the Pan-African tin mineralization event occurred during the period 501-524Ma and could be related to post-tectonic systems (Zhang, 2017). On the other hand, Steven (1993) conducted Rb-Sr whole-rock geochronological age dating for leucogranites (512"19 Ma) and pegmatites (473"23 Ma and 468"14 Ma) of Sandamap Noord.

3 Methodology

Pegmatite, country rock and granite samples were collected in October 2018 from the Sandamap Noord vicinity. A total of 19 pegmatite samples were selected for whole-rock geochemistry. Whole-rock geochemistry pegmatite samples were crushed using a carbon-steel jaw crusher and milled by using an agate disc mill at the Geological Survey of Namibia. Major and trace elements data were obtained using a WD-XRF at Aachen University. We are awaiting analytical results. These results will be compared against work done by Fuchsloch et al., 2018.

4 Results and Discussion

According to Fuchsloch et al., 2018, three generations of pegmatites are distinguished in the Northern Zone based on mineralogy, geochemistry and ore mineralogy. The generations of pegmatites are as follows; (1) un-zoned Nb-Ta-Sn type, the (2) garnet-tourmaline zoned pegmatites hosted in granites with higher REE, U, Th and Y contents, and (3) highly fractionated zoned lithium-bearing pegmatites with common Sn concentration of 10 000 ppm, Ta of 185 ppm and Nb of 206 ppm (Fuchsloch et al., 2018). On the other hand, the Central Zone of the Damara branch is host to the Sandamap – Kransberg tin belt, in which the Sandamap Noord Tin Deposit is situated (Keller, 1999). The Sandamap Noord deposit is linked with the white prominent blow of pegmatitic quartz hill. The hill consist of leucocratic pegmatites which intruded the schist of the Pan African System. Based on field investigation distinctive pegmatites were observed, such as; garnet pegmatites, tourmaline pegmatites, and a third type of pegmatite with no tourmaline nor garnet. There is very little published work on these pegmatites and almost nothing in the last 20 years, no modern age dating and very little if any mineral chemistry, except for tourmaline (Keller et al. 1999).

5 Conclusion

Fuchsloch et al., 2018, used the Classification Scheme by Černý and Ercit (2005), and identified different pegmatites within the Cape Cross-Uis pegmatite belt, including pegmatites from the Uis tin mine that they have high values of REE, U, Th, Y, with significant Li, Cs, Nb, and Ta values. On the otherhand, without whole-rock geochemistry data for the Sandamap Noord pegmatite data, only field investigation data is used to describe the pegmatites. In future, the first whole-rock geochemical study of the pegmatites will be used to classify the different pegmatites present at Sandamap Noord deposit.

References

- Fuchsloch WC, Nex PAM, Kinnaird JA (2018) Classification, mineralogical and geochemical variations in pegmatites of the Cape Cross-Uis tin pegmatite belt, Namibia. *Lithos* 296-299:79-95.
- Keller P, Robles ER, Pérez AP, Fontan F (1999) Chemistry, paragenesis and significance of tourmaline in pegmatites of the Southern Tin Belt, central Namibia. *Chemical Geology* 158:203-225.
- Miller R (2008) Namaqua Metamorphic Complex. In: Miller R (ed.) *The Geology of Namibia: Archaean to Mesoproterozoic*. Ministry of Mines and Energy, Geological Survey, Windhoek,
- Petzel VFW (1986) Vein and replacement type Sn and Sn-W mineralization in the Southern Kaoko Zone, Damara Province, South West Africa/Namibia. MSc thesis, Rhodes University.
- Richards, T.E., 1986. Geological characteristics of rare-metal pegmatites of the Uis type in the Damara Orogen, SWA/Namibia, 1845-1862. In: Anhausser, C.R. and Maske, S. (eds), *Mineral Deposit of Southern Africa*. Vol 1 & 2. Geol. Soc. S. Afr. Johannesburg.

Zhang R, Sun W, Lehmann B, Symons G, Seltmann R, Schmidt C, Li C (2017) Pan-African tin mineralization events in the Damara orogenic belt, Namibia, SW Africa: Constraints of cassiterite U-Pb dating and trace elements fingerprinting. SEG 2017 Conference.

New geochronological constraints on the Lagoa Real uranium province

Lucas Eustáquio Dias Amorim, Francisco Javier Rios, Lucilia Aparecida Ramos de Oliveira, Frederico Sousa Guimarães, Monica Elizetti Freitas, Ariela Costa Diniz
Centro de Desenvolvimento da Tecnologia Nuclear- CNEN-, Brazil

Mauro Cesar Gerales

Faculdade de Geologia, Universidade do Estado do Rio de Janeiro, Rio de Janeiro, Brazil

Evando Carele de Matos

Indústrias Nucleares do Brasil, Brazil

Abstract. The metalogenesis and petrogenesis of the Lagoa Real Uranium Province has been discussed since its discovery in the 1970's. Its magmatic association has been suggested to be the São Timóteo granite.

Here, we present new geochronological data that indicate different ages for the São Timóteo magmatic association, 2048 and 1742 Ma to charnockite, 1774 Ma to Lagoa do Barro granite, 1753Ma to Juazeirinho granite, 1739Ma to São Timóteo granite, and 1742 Ma to Albite-gneiss.

1 Introduction

The Lagoa Real Uranium Province (LRUP) is located in the Paramirim Aulacogen, São Francisco Craton in the northern Aracuaí Belt (Almeida 1977; Pedrosa-Soares et al. 2001). Currently, the LRUP comprises the largest uranium reserves of Brazil, and, extending over 35 km with 5 km in width

The LRUP has been studied since the 1970's. Its country rocks make up a Paleoproterozoic igneous association of granite – i.e., the São Timóteo granite –, orthogneiss and U-mineralized albitite and barren albitite (Costa et al. 1985) (Figure 1).

The granitic rocks are generically referred to as the São Timóteo granite. They are meta-igneous rocks that grade from undeformed granite to gneissic varieties (Cruz 2004). The contacts with the gneissic domains are either transitional or abrupt. The São Timóteo granite occurs as elongated bodies, from 4 to 10 km in length, and as dikes cutting the migmatitic basement (Costa et al. 1985; Maruejol 1989; Cruz 2004).

According to Maruejol (1989) and Amorim (2016), the São Timóteo granitic rocks form a batholithic body and display a compositional range from quartz-diorite to hornblende-granite, pyroxene-granite and charnockite, with clino- and orthopyroxene. Cruz (2004) distinguished

the LRUP granitic rocks between two distinct facies, São Timóteo and Jurema, due compositional and petrographical differences. The São Timóteo facies has porphyritic and cumulate fabrics, including phaneritic and pegmatoidal varieties. Its composition is predominantly syenogranitic in the porphyritic domains, whereas it is alkali-feldspar syenitic in the cumulate domains. The Jurema facies has porphyritic and phaneritic varieties. In the former, syenogranite predominates. In general, the Jurema facies looks similar to the São Timóteo facies, being distinguished from the latter by its biotite and amphibole contents, which make up 18% of the rock.

Several geochronological works were developed in the LRUP using different methods. Uranium/Pb zircon ages indicated crystallization at 1724 ± 5 Ma (Turpin et al. 1988). Cordani et al. (1992) provided Pb/Pb zircon ages that are indistinguishable within error (1710 ± 10 Ma). Pimentel et al. (1994) analyzed titanite crystals from U-mineralized albitite using U/Pb (ID-TIMS), for which ages of 960 Ma and 500 Ma were obtained and interpreted to represent metamorphic overprint.

Bettencourt et al. (2014) obtained an U/Pb (SHRIMP) zircon age of 1746 ± 7 Ma for the São Timóteo granite. Similar ages (1746 ± 5 Ma) were also reported in Lobato et al. (2015), who performed U/Pb analysis of zircon grains from the São Timóteo granite. These ages have been interpreted as the emplacement of the main-phase granitic magmatism of São Timóteo.

Recently, Amorim (2016) has identified five types of granitic rocks with respect to petrographical and geochemical characteristics: (i) charnockite, (ii) the Lagoa do Barro granite, (iii) the Juazeirinho granite, (iv) the São Timóteo granite and (v) albite-gneiss.. Here, we present zircon ages that have been obtained for all five types of granitic rocks that comprise the São Timóteo magmatic association of the LRUP.

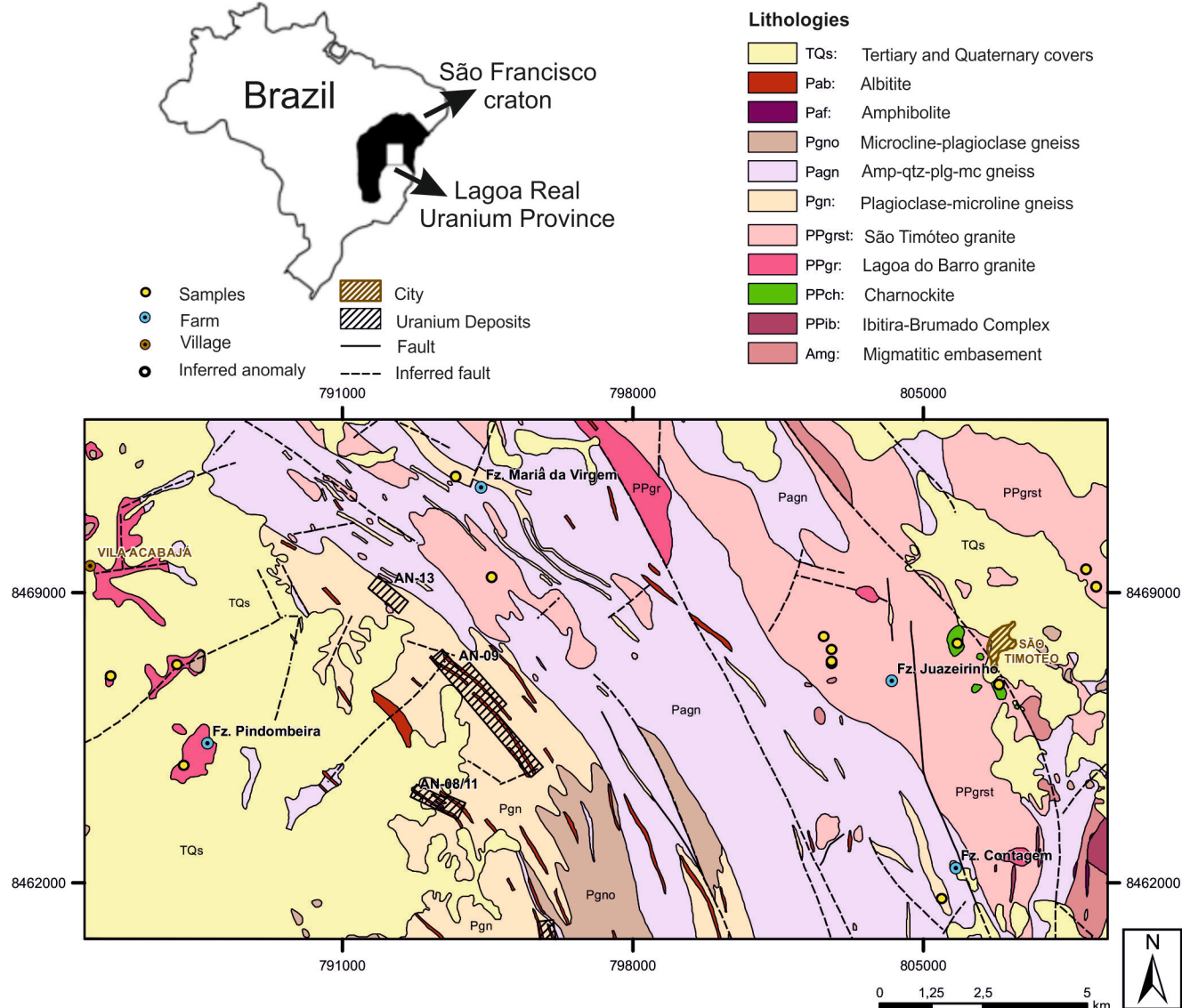


Figure 1. Geological Map of the Lagoa Real Uranium Province (Modified from Costa et al. 1985).

2 Methods

Zircon grains were recovered from samples of the five rock types of the São Timóteo association. Heavy-mineral concentration was performed at the the Geochronology and Geochemistry Laboratory (LOPAG), Universidade Federal de Ouro Preto (UFOP), Brazil. Zircon grains were mounted in resin and polished for backscattered-electron imaging, cathode luminescence and U/Pb-isotope work at the Multi-Laboratory of Chemical and Isotopic Analysis (MultiLab), of the Universidade Estadual do Rio de Janeiro (UERJ). The U/Pb isotope work was performed by means of laser ablation-inductively coupled plasma-mass spectroscopy (LA-ICP-MS), which combined a 192-nm Analyte G2 laser and a Finnigan NEPTUNE multicollector spectrometer.

3 Results

3.1 Charnockite

Charnockite crops out to the west and southwest of São Timóteo, and to the west of Lagoa Real (Figure 1). This rock has two zircon populations, with growth zones that are characteristic of igneous zircon. One population has contents of: (i) Pb = 28 - 136 ppm; Th = 38 - 199 ppm; and U = 57 - 325 ppm. Its $^{206}\text{Pb}/^{238}\text{U}$ - $^{207}\text{Pb}/^{235}\text{U}$ age is 2048 ± 6 Ma (MSWD = 0.5). The other population shows: Pb = 28 - 170 ppm; Th = 33 - 338 ppm; and U = 75 - 455 ppm. Its $^{206}\text{Pb}/^{238}\text{U}$ - $^{207}\text{Pb}/^{235}\text{U}$ age is 1742 ± 9 Ma (MSWD = 0.66) (Figures 2A, B).

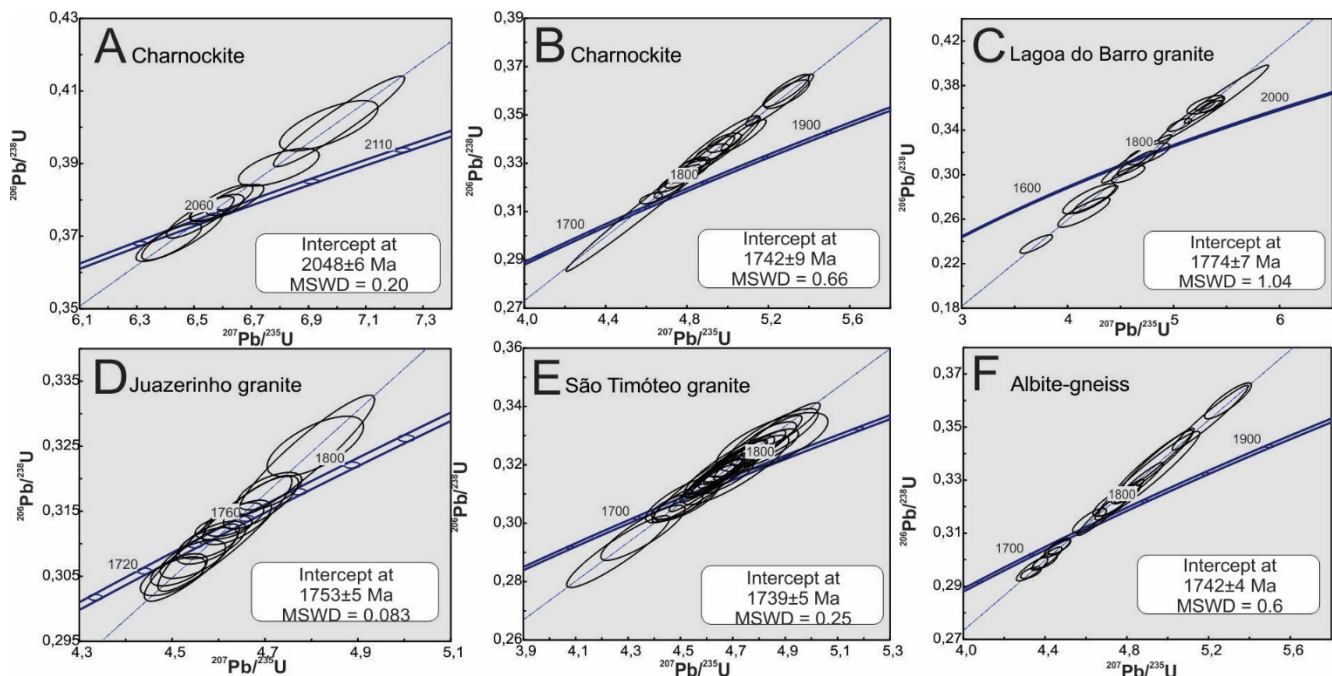


Figure 2. Discordia diagrams of charnockite and granitic rocks Lagoa do Barro, Juazeirinho and São Timóteo, and albite-gneiss.

3.2 Lagoa do Barro granite

Fine-grained granite, similar to those described by Costa et al. (1985), was sampled in the surroundings of Lagoa do Barro and Pindombreira farm, in the western section of the LRUP (Figure 1). Locally, it occurs as decimetric enclaves in augen gneiss. Zircon grains from the granite have Pb contents between 9 and 176 ppm, Th from 18 to 554 ppm, and U between 25 and 495 ppm. Their $^{206}\text{Pb}/^{238}\text{U}$ - $^{207}\text{Pb}/^{235}\text{U}$ age is 1774 ± 7 Ma (MSWD = 1.04) (Figure 2C).

3.3 Juazeirinho granite

The Juazeirinho granite is predominantly found near to the Juazeirinho farm and to the east of São Timóteo (Figure 1). Its zircon grains have Pb contents between 32 and 177 ppm, Th from 60 to 527 ppm, and U from 79 to 467 ppm. Their $^{206}\text{Pb}/^{238}\text{U}$ - $^{207}\text{Pb}/^{235}\text{U}$ age is 1753 ± 5 Ma (MSWD = 0.08) (Figure 2D).

3.4 São Timóteo granite

The least weathered outcrops of the São Timóteo granite were found in the southeast sector of the LRUP, near Monsenhor Bastos, and in the surroundings of the Juazeirinho farm, 4 km west of São Timóteo (Figure 1). In the latter, outcrops of three granite varieties – i.e., porphyritic, fine-grained and pegmatoid – occur in contact with the basement.

Classified as alkali-feldspar granite and quartz-feldspar granite, the São Timóteo granite has zircon grains containing Pb content between 15 and 51 ppm, Th from 28 to 254 ppm, and U from 40 to 312 ppm. Their age $^{206}\text{Pb}/^{238}\text{U}$ - $^{207}\text{Pb}/^{235}\text{U}$ age is 1739 ± 5 Ma (MSWD = 0.25) (Figure 2E).

3.5 Albite-gneiss

Albite-gneiss, erroneously classified as São Timóteo-associated leucodiorite in previous studies, was mainly found in the northeastern border (Maria da Virgem) and in the easternmost part (Morro da Contagem) of the LRUP (Figure 1). This lithology is composed of more than 60% albite without U mineralization, with variable proportions of mafic minerals. The rock has a gneissic coarse-grained fabric, and occurs in spatial association with orthogneiss rocks. The albite-gneiss shows albite with chessboard-type twinning, which is indicative of albitization of preexisting feldspar.

Zircon grains from the albite-gneiss has Pb contents between 10 and 209 ppm, Th from 17 to 513 ppm, and U from 30 to 530 ppm. Their $^{206}\text{Pb}/^{238}\text{U}$ - $^{207}\text{Pb}/^{235}\text{U}$ age is 1742 ± 4 Ma; (MSWD = 0.66) (Figure 2F).

4 Discussion

Our geochronological data indicate that the albite gneiss is temporally linked to the São Timóteo granite (1.74 Ga). Two explanations can thus be advanced. One is that the albite gneiss and the São Timóteo granite formed at the same time. The other is that the tectonic overprint and Na metasomatism, which are required for the petrogenesis of albite gneiss, post-dated the 1.74-Ga São Timóteo granite – i.e., the zircon age for the albite gneiss is inherited from a granitic protolith. On the other hand, the zircon age for the charnockite suggests that the rock formed at 2.05 Ga, having been assimilated by the ascent of the São Timóteo granite – i.e., charnockite-zircon population that crystallized at 1.74 Ga.

Our data further indicate two events of granitic magmatism: at 1774 Ma, which is a manifestation of the Algodão rift (Danderfer Filho et al. 2015), corresponding to the Lagoa do Barro granite; and at 1745 Ma, which can

be related to the Sapiranga rift (Danderfer Filho et al. 2015), being represented by the São Timóteo granite. An intermediate event seems to be the 1753-Ma Juazeirinho granite, which is at least 3 Ma older than the São Timóteo granite. A fourth event can potentially be recognized at 1724 Ma, an age determined by Turpin et al. (1988) and Cordani et al. (1992) for another granitic intrusion.

5 Conclusions

The granitic rocks of Lagoa Real comprise enclaves of charnockite that crystallized at 2.05 Ga. The enclave-forming assimilation took place at 1.74 Ga, which is the crystallization age of the São Timóteo granite. Three events of granitic magmatism have been distinguished: the 1774-Ma Lagoa do Barro granite; the 1753-Ma Juazeirinho granite; and the 1745-Ma São Timóteo granite. The U-barren albite-gneiss, which is similar to the U-mineralized albitite, has zircon grains that crystallized at 1741 Ma. The rock is either genetically related to the coeval São Timóteo granite or formed after it as a result of tectonic overprint and Na metasomatism.

Acknowledgements

We also thank the support of CDTN/CNEN, Project PPM 00493-15 (Fapemig), and Projects 424909/2016-2 and 308781/2014-7 (CNPq). Finally, we express gratitude for all that help with any advice in the review and elaboration of this work, in especial for A.R.Cabral.

References

- Almeida DE (1977) O Craton do São Francisco. *Rev Bras Geociências* 7:349–364
- Amorim LED (2016) Microquímica, geoquímica e geocronologia da associação magmática da Província Uranífera de Lagoa Real, BA: significado petrológico e evolutivo. Centro de Desenvolvimento da tecnologia Nuclear
- Bettencourt JS, Freitas ME De, Rios FJ, et al (2014) U-Pb SHRIMP zircon and Lu-Hf isotope systematics of Mesoproterozoic A-Type granites in Lagoa Real Uraniferous Province, State of Bahia, Brazil: a reconnaissance survey. In: 9. South American Symposium on Isotope Geology. São Paulo, p 117
- Cordani UG, Iyer SS, Taylor PN, et al (1992) PbPb, RbSr, and KAr systematics of the Lagoa Real uranium province (south-central Bahia, Brazil) and the Espinhaço cycle (ca. 1.5-1.0 Ga). *J South Am Earth Sci* 5:33–46. doi: 10.1016/0895-9811(92)90058-7
- Costa PHDO, Andrade ARF De, Lopes G., Souza SL d. (1985) Projeto Lagoa Real: mapeamento geológico, 1:25000, texto e mapas
- Cruz SCP (2004) A interação entre o Aulacógeno do Paramirim e o Orógeno Araçuaí-Oeste Congo. UFOP
- Danderfer Filho A, Lana CC, Nalini Júnior HA, Costa AFO (2015) Constraints on the Statherian evolution of the intraplate rifting in a Paleo-Mesoproterozoic paleocontinent: New stratigraphic and geochronology record from the eastern São Francisco craton. *Gondwana Res* 28:668–688. doi: 10.1016/j.gr.2014.06.012
- Lobato LM, Pimentel MM, Cruz SCP, et al (2015) U-Pb geochronology of the Lagoa Real uranium district, Brazil: Implications for the age of the uranium mineralization. *J South Am Earth Sci* 58:129–140. doi: 10.1016/j.jsames.2014.12.005
- Maruejol P (1989) Métasomatose alcaline et minéralisation uranifères: les albitites du gisement de Lagoa Real (Bahia, Brésil) et exemples complémentaires de Xihuashan (SE Chine), Zheltorechensk (Ukraine) e Chuling Khola (Népal central). Centre du Recherche sur la Geologie de l'uranium, Nancy

- Pimentel MM, Machado N, Lobato LM (1994) U-Pb geochronology of granitic and gneissic rocks of the Lagoa Real (BA) region and implications for the age of uranium mineralization. In: Congresso Brasileiro de Geologia. SBG, Balneário de Camburiú, pp 389–390
- Turpin L, Maruejol P, Cuney M (1988) U-Pb, Rb-Sr and Sm-Nd chronology of granitic basement, hydrothermal albitites and uranium mineralization (Lagoa Real, South-Bahia, Brazil). *Contrib to Mineral Petrol* 98:139–147. doi: 10.1007/BF00402107

Iberian Pyrite Belt massive sulphide deposit stockworks: styles and comparison

Emma Losantos, Guillem Gisbert, Fernando Tornos
Instituto de Geociencias (IGEO, CSIC-UCM), Madrid, Spain

Abstract. Despite of being a fundamental part of volcanic massive sulphide (VMS) systems, both for their importance in the comprehension of their genesis and their economic interest, stockworks have been often overlooked. The Iberian Pyrite Belt is an ideal place for their study as it entails a variety of VMS styles and their correspondent stockworks: shale hosted (Tharsis); igneous rocks hosted (Aguas Teñidas) and transitional (Río Tinto). The different styles share some common characteristics such as an irregular to stratabound morphology and a distinctive ore mineralogy, different to that of the overlying massive sulfides. The shale hosted stockworks show as well a unique chlorite-rich zone and an irregular enrichment in As-Co-Te-Bi-Au-bearing minerals more diverse than in the volcanic-hosted systems. Stockworks developed on volcanic rocks on the other hand, present in general an internal Cu enriched chloritic zone surrounded by a Zn enriched sericitic one with high contents in Ba and Na. Transitional ones show both types.

1 Introduction

The Iberian Pyrite Belt (IPB) hosts one of the largest concentrations of sulphides in the world. They are distributed in about 90 volcanogenic massive sulphide deposits (VMS) that entail over 1600 Mt of massive sulphides originally in place, and about 2500 Mt of stockwork ore (Tornos 2006 and references therein). Individual massive sulphide bodies can be up to 170 Mt (La Zarza), and in some cases smaller separate and nearby bodies could correspond to one larger original deposit dismembered by intense orogenic deformation (Río Tinto, Solomon et al., 1980; Tharsis, Tornos et al. 1998). However, in other cases small adjacent bodies seem to have been formed in independent sub-basins (Neves Corvo; Relvas 2000).

The stockwork is a fundamental, but often disregarded, part of volcanic massive sulphide systems. They are the fossil expression of the paleo-subsurface ascending path of the ore fluids that ultimately deposited the massive sulphides by mixing with cold and alkaline seawater (Nehlig et al. 1997 and references therein).

Traditionally, in the Iberian Pyrite Belt the massive sulphide deposits were classified as proximal when rooted on a stockwork and hosted by volcanic rocks, or distal and slumped away from their original position when not rooted and hosted by mudstones. Nowadays, advances in the structural knowledge have shown that most of the shale-hosted massive sulphides are also underlain by a stockwork and that the massive sulphides that are unrooted show a major fault in the footwall

(Tornos 2006).

2 Geological setting

The South Portuguese Zone, the tectonic domain hosting the IPB, has been interpreted as an exotic terrane accreted to the Iberian Autochthonous during the Variscan orogeny. The collision, with an oblique sinistral component, lead to the formation of pull apart basins where the IPB volcanic and sedimentary rocks would have been deposited (Tornos 2006).

Traditionally, the stratigraphy of the IPB has been divided into three distinctive groups (Schermerhorn 1971) which are, from footwall to hanging wall: 1) PQ group (Frasnian (?) to Late Famennian); 2) VS (Volcanic Sedimentary) Complex, Late Famennian to early Late Viséan; and, 3) Culm Group or Baixo Alentejo Flysch Group (Late Viséan to Middle-Upper Pennsylvanian) (Oliveira 1990; Oliveira et al. 2004).

The ore bodies are hosted by the VS Complex and show two distinct styles of mineralization (Tornos 2006).

Shale-hosted deposits occur mostly in the southern IPB. They have been interpreted as formed in sub-oxic to anoxic third order basins where upwelling, deep and sulphur-depleted fluids mixed with modified seawater, rich in biogenically reduced sulphur, lead to the precipitation of the massive sulphides dominantly on the seafloor. The stockwork-related hydrothermal alteration includes a single zone of chloritic alteration (Tornos et al. 1998).

VMS deposits hosted by felsic volcanic rock dominate in the northern IPB and where mudstones are minor. They have been interpreted as formed by the stratabound replacement of porous or reactive massive and volcanoclastic (vitriclast- or pumice-rich) volcanic rocks. Hydrothermal alteration in this deposits consists of an internal chlorite (ripidolite) – quartz – sulphides (-carbonates) zone surrounded by a peripheral stockwork zone with sericite-quartz-sulphides (-carbonates), with the white micas being characterized by high Ba-Na contents (Relvas et al. 1990; Costa 1996). In Rio Tinto area, which is geographically and lithologically transitional, both types of mineralization occur.

3 Description of the representative deposits

3.1 Aguas Teñidas

The Aguas Teñidas deposit is a classical deposit of the northern part of the IPB, with the massive sulphides being hosted by a rhyodacite showing a well-developed stockwork zone. It consists of a polymetallic (Cu-Zn-Pb)

massive sulphide body formed by host rock replacement in the permeable and reactive uppermost autobrecciated and partially devitrified in situ hyaloclastite of a subaqueous dome complex (Bobrowicz 1995; Conde 2016). This deposit grades to minor semi-massive and more abundant disseminated sulphides towards its footwall.

The VS Complex in the area includes 6 tectonostratigraphic units separated by tectonic contacts (shear zones), which are, from bottom to top: Footwall Felsic Unit, Volcano-sedimentary Unit, Hanging wall Felsic Unit, Sedimentary Unit, Upper Felsic Unit and Andesite Unit (Conde 2016).

The massive sulphide deposits, including Aguas Teñidas, are hosted in the Footwall Felsic Unit and Upper Felsic Unit. They are interpreted by Conde (2016) as a single felsic volcanic unit dismembered by tectonics. This unit was originally composed by dome and crypto-dome complexes of feldspar-quartz-phyric lava of rhyodacitic composition, with sills and dykes of similar composition, and coeval and cogenetic mass flow deposits rich in pumice and glass.

At the deposit scale, the Aguas Teñidas massive sulphide body has a mineral zonation similar to that in other VMS deposits, with a Cu-rich core at the base and Zn-Pb-rich ore towards the top and edges. However, a significant enrichment in Pb, Zn and Au by the footwall contact distinguishes this deposit from the classical VMS model (Bobrowicz 1995; McKee 2003). According to Hidalgo et al. (2000) the massive sulphide includes pyrite, sphalerite, chalcopyrite and galena in decreasing order of abundance. These phases represent over 95% of the sulphide mineralogy, with pyrite generally constituting between 50 and 80% of the ore. Tetrahedrite - tennantite, arsenopyrite, stannite, bournonite, native bismuth and trace amounts of fine-grained magnetite are also present. The metallic assemblage is accompanied by quartz, carbonates, white mica and chlorite.

Based on mineralogical composition, the ore has been divided into three broad types (Hidalgo et al. 2000):

1) Polymetallic banded Zn-Pb rich ore, which is found close to the hanging wall contact and the northern margin of the deposit. It is characterized by a fine grained compositional banding of sphalerite/galena, likely of tectonic origin, which bounds large lenses of massive and barren pyrite. Chalcopyrite commonly occurs in fractures.

2) Massive cupriferous ore, formed by structureless pyrite with fine-grained chalcopyrite occurring as replacements and fracture infills. Commonly occurs close to the footwall contact.

3) Copper-rich stockwork, formed by veinlets of pyrite and chalcopyrite within a groundmass of chlorite, quartz and white mica.

Alteration and stockwork

The stockwork area forms an asymmetric, concentric and funnel shaped east-west trending (in cross section) zone along the entire northern margin of the deposit and extends up to 70 m below the massive sulphide (Bobrowicz 1995; Hidalgo et al. 2000; McKee 2003).

Laterally it passes from quartz, to chlorite, white mica-chlorite, and white mica-quartz zones (Bobrowicz, 1995; Hidalgo et al., 2000; McKee et al., 2001; Tornos, 2006), with the ore being hosted by the two most internal ones.

Siliceous stockwork seems to be more abundant towards the western part of the deposit, whereas chloritic alteration predominates in the eastern part (McKee 2003). This is considered to indicate a non-uniform flow of hydrothermal fluids along the feeder system (McKee 2003). The described alteration pattern involves Fe + Mg enrichment and Ca + Na + Si ± K depletion within the inner chlorite zone, and Si + Na enrichment and Ca + Mg + Fe ± K depletion in the sericitic envelope (Bobrowicz 1995).

Rocks hosting the Aguas Teñidas Este deposit underwent three stages of alteration: 1) alteration by interaction with seawater during and soon after emplacement in submarine conditions, which transformed basalts into spilites and felsic rocks into keratophyres and quartz-keratophyres (McKee 2003); 2) intense hydrothermal alteration related to the mineralizing event; 3) metamorphic recrystallization in the prehnite-pumpellyite facies (Bobrowicz 1995; Sánchez-España et al. 2000; McKee 2003); and, 4) widespread oxidation related to thrust tectonics.

3.2 Tharsis

The Tharsis area, located in the southernmost IPB, is an exhalative shale-hosted deposit. The associated stockwork is currently overthrust above the massive sulphides (Strauss & Beck, 1990; Tornos 2006).

Alteration and stockwork

In this deposit, the hydrothermal alteration consists of a pervasive and monotonous chloritization and pyritization of the underlying shale, which is associated with the formation of mm- to cm-wide sulphide-rich veins. The stockwork is hosted by the lowermost shale belonging to the VS Complex and extends to unknown depths into the underlying PQ Group (Strauss and Beck 1990).

The ore system is tectonically dismembered but in general terms, it seems like the alteration and the amount and size of veins increase upwards, towards the massive sulphides, whilst laterally and downwards the stockwork seems to grade into unaltered shales (Tornos et al. 1998).

The metallic assemblage of the stockwork, more diverse than in the felsic-hosted systems, occurs within the veins and occasionally replaces the chloritized shales. It is formed by pyrite intergrown with abundant Co-As-Fe-S minerals and gold as minute inclusions (<10µm) (Strauss and Beck 1990; Tornos 2006). The sulphides show complex relationships of replacement, recrystallization and cementation and include, along with pyrite, variable amounts of chalcopyrite and also arsenopyrite, cobaltite, allocasite, pyrrotite, glaucodot, bismuthinite, Bi-tellurides and Bi-Pb-Cu-(Sb) sulfosalts (Tornos 2006). Gold occurs intergrown with these minerals as coarse grains (100-400 µm).

3.3 Rio Tinto

Rio Tinto consists of three mineralized zones (San Dionisio, San Antonio and Cerro Colorado units) now disconnected, but originally forming a single body of about 500 Mt of sulphides. The orebodies are autochthonous and underlain by three main stockwork zones (Nehlig et al. 1997).

Rio Tinto deposit shows characteristics from both northern and southern sectors, including exhalative deposits in the shale (Filón Sur) and replacive in the felsic volcanic rocks (Filón Norte zone) (Madeisky and Stanley 1993; Tornos 2008). The shale-hosted mineralization is located above a felsic dome and is likely infilling a small basin that could be related with a volcanic explosion. The volcanic-hosted mineralization occurs as large stratabound bodies within the felsic domes and likely replacing zones enriched in glass; this late mineralization is crosscut by the stockwork.

The structural frame in Rio Tinto is complex, with the major lithological contacts bounded by thrusts. As a whole, the sequence is similar to that deduced for the northern sector with a footwall basaltic unit involving submarine lava flows and volcanoclastic levels alternating with dark shales over the PQ group in concordant contact. Overlying these materials is the felsic unit with a very variable composition from place to place. In general, it consists on an acid complex with domes, sills and pumice mass flows covered by shales and capped by the Transition Series. This uppermost unit hosts the massive sulphides within shales on the Filón Sur orebodies and laterally grades into volcanoclastic sandstones containing fragments of the underlying volcanic rocks indicating that the sills predated the formation of the massive sulphides (Tornos 2006).

The massive sulphides appear in two distinctive types in Rio Tinto:

1) massive pyrite with only some local primary banding hosted by sedimentary breccia lenses interbedded with the shale within the Transition Series. This type of mineralization overlies the rocks with hydrothermal alteration and is equivalent to the shale-hosted deposits (Massive sulphides in Filón Sur, San Dionisio, Planes and San Antonio orebodies) (Williams et al. 1975; García Palomero 1980);

2) massive and semi-massive sulphide lenses hosted by coherent dacite of the Felsic Unit in the northern part of the district (Filón N; Salomón, Lago, Dehesa). Within this second type two stages of mineralization have been recognized: 1) an early one with sulphides precipitating in open spaces or as replacements in the margins of quartz-sericite/chlorite veins synchronous with the pervasive alteration of the host rocks and 2) a second stage of semi-massive to massive mineralization replacing the altered rocks (Tornos 2006).

Alteration and stockwork

The stockwork underlying the massive sulphide lenses has been followed down to 400 m depth with a downward

gradual diminution of the thickness and frequency of the veins (Williams et al. 1975). It hosts more than 2000 Mt of altered volcanic rocks with irregular copper grades.

In this stockwork two types of veins dominate (Nehlig et al. 1997): 1) small narrow micro-cracks and capillary flow channels (now mainly filled with quartz and mostly arranged sub-parallel to the base of the massive sulphide deposit); and 2) large and continuous veins filled with sulphides and quartz which can be strongly oblique to the base of the deposit. The quartz in this second type is mainly located along the margins, with the sulphides having a strong tendency to occupy vein centers. The pyrite-dominated veins have been found to postdate the quartz dominated veins, and the fact that most hydrothermal quartz-sulphide stockwork veins were sub-parallel to the base of the massive sulphide deposit is being explained as due to periodic over-pressures of at least 20 MPa. Such overpressure would have been produced by a sub- or super-critical phase separation within the root zones of the hydrothermal system that generates large volume increases of the hydrothermal fluids (Nehlig et al. 1997).

The hydrothermal alteration is irregular and controlled by the host lithology and the synsedimentary faults. On shale, breccia and basalt the alteration consists solely of a chlorite-rich zone. On dacitic rocks, it shows a zoned alteration with a pervasive sericitization that is crosscut by a later and more internal chlorite-rich alteration. Silica-chlorite-rich alteration zone is found adjacent to the faults (Tornos 2006). The sericitic zone is characterized by a sericitization of plagioclase fenocrystals and feldspar matrix crystals, and the presence of quartz, pyrite, and minor quantities of albite, chlorite, sphalerite, galena and carbonates (Toscano et al. 2002). This alteration entails an increase of K₂O and Ba contents and a minor one for Al₂O₃, TiO₂, S, Cu, Sr and F associated to a decrease of CaO, MgO, MnO. The chloritic zone, on the other hand, is characterized by a matrix of chlorite, quartz and abundance of sulphides, encompassing small granoblastic domains of quartz from the recrystallization of the igneous quartz fenocrystals, and minor quantities of sericite, epidote, rutile and chalcopyrite. The chloritic alteration increases the contents of TiO₂, Fe₂O₃, MgO, MnO and Al₂O₃ while depletes SiO₂, K₂O, CaO, Na₂O y Ba.

The distribution of the elements, and therefore the extension of the alteration zones, has been interpreted as dependent on the fluid/rock ratio and the temperature of the fluids. In the centre of the system the mineralogy would be more ferromagnesian and sulphur rich as a consequence of the higher fluid/rock ratio and temperature, whilst in the external halo the fluid/rock ratio and temperature fall would cause the elements which behave as mobile in the internal zone to be incorporated into the neoformed phyllosilicates (e.g. Ba rich sericites) (Toscano et al. 2002).

4 Discussion

Despite subsequent Variscan thrusting, most of the massive sulphide deposits in the IPB are emplaced

above a large stockwork made up of sulphide-bearing, anastomosing veinlets that represent the channel-ways through which the hydrothermal solutions ascended to the seafloor or the stratigraphic level where replacive deposits formed. Both massive sulphides and stockworks are shrouded by an intense hydrothermal alteration affecting the underlying rocks, the sulphides themselves, and the hosting felsic volcanic rocks and shales (Nehlig et al. 1997; Leistel et al. 1998).

There are varied stockwork morphologies, but both the shale hosted (e.g. Tharsis; Tornos et al. 1998) and the igneous hosted stockworks (e.g. Rio Tinto; Solomon et al. 1980), have been found to have an irregular to stratabound morphology. They display also characteristic ore mineralogy different to that of the overlying massive sulphides (Tornos 2006). The shale-hosted stockworks have a single hydrothermally altered chlorite-rich zone, and show an irregular enrichment in As-Co-Te-Bi-Au-bearing minerals that are usually found in the transition zone between the stockwork and the massive sulphides (Tornos 2006). In Tharsis, however, that mineral association can be traced downwards along the whole stockwork (Tornos et al. 1998).

Stockworks on volcanic rocks display an irregular division of the alteration zones, but in general present an internal zone rich in chlorite surrounded by a sericitic one with high contents in Ba and Na (Relvas et al. 1990; Costa 1996). However, there can also be stockworks developed on sericitized rocks with only minor chloritic alteration as in Rio Tinto (Tornos 2008). In general, there seems to be Zn enrichment in the sericitic stockwork, whilst the chloritic one is enriched in Cu (Rio Tinto, Solomon et al. 1980). In addition, an intense siliceous alteration is described in Aguas Teñidas Este (Bobrowicz 1995), and carbonate alteration is typical of many deposits such as the three being considered in this work: Rio Tinto (Williams et al. 1975), Aguas Teñidas Este (Bobrowicz 1995) and Tharsis (Tornos et al. 1998). This last alteration type can occur marginally to the mineralization, in the interface between massive sulphides and stockwork (e.g. Rio Tinto; Solomon et al. 1980), in independent veinlets of the stockwork or disperse in the system (e.g. Tharsis; Tornos et al., 1998).

Acknowledgements

This work is being funded by the European Commission Horizon 2020-776804 NEXT project (New Exploration Technologies).

References

Bobrowicz GL (1995) Mineralogy, geochemistry and alteration as exploration guides at Aguas Teñidas Este, Pyrite Belt, Spain Faculty of Science and Engineering, University of Birmingham.

Conde C (2016) Geology and hydrothermal evolution of massive sulphides of the Iberian Pyrite Belt, Spain Departamento de Geología, Universidad de Salamanca.

Costa I (1996) Efeitos mineralógicos e geoquímicos da alteração mineralizante em rochas vulcânicas félsicas de Rio Tinto (Faixa Piritosa Ibérica, Espanha). Dissertação de Mestrado. Univ. de Lisboa.

Hidalgo R, Guerrero V, Pons JM, Anderson IK (2000) The Aguas

Teñidas Este mine, Huelva Province, SW Spain.

Leistel J, Marcoux E, Thieblemont D, Quesada C, Sanchez A, Almodovar G, Pascual E, Saez RJMD (1998) The volcanic-hosted massive sulphide deposits of the Iberian Pyrite Belt. Review and preface to the Thematic Issue. 33:2-30.

McKee GS (2003) Genesis and deformation of the Aguas Teñidas Este massive sulphide deposit and implications for the formation, structural evolution and exploration of the Iberian Pyrite Belt. University of Birmingham.

Nehlig P, Cassard D, Marcoux EJMD (1997) Geometry and genesis of feeder zones of massive sulphide deposits: constraints from the Rio Tinto ore deposit (Spain). 33:137-149. doi: 10.1007/s001260050137.

Oliveira JT (1990) Stratigraphy and Synsedimentary Tectonism in: Dallmeyer RD, Garcia EM (eds) Pre-Mesozoic Geology of Iberia. Springer Berlin Heidelberg, Berlin, Heidelberg, pp 334-347.

Oliveira JT, Pereira Z, Carvalho P, Pacheco N, Korn DJMD (2004) Stratigraphy of the tectonically imbricated lithological succession of the Neves Corvo mine area, Iberian Pyrite Belt, Portugal. 39:422-436. doi: 10.1007/s00126-004-0415-2.

Relvas J, Massano CMR, Barriga FJAS (1990) Ore zone hydrothermal alteration around the Gaviao orebodies: implications for exploration in the Iberian Pyrite Belt. Proceedings VIII Semana de Geoquímica. Lisboa, pp 1-3.

Relvas J (2000) Geology and metallogeny at the Neves Corvo deposit, Portugal. University of Lisbon, Unpublished Doctoral Thesis, pp 319.

Sánchez España FJ (2000) Mineralogía y geoquímica de los yacimientos de sulfuros masivos en el área Nor-Oriental de la Faja Piritica Ibérica, San Telmo-San Miguel-Peña del Hierro, Norte de Huelva, España. Universidad del País Vasco, Unpublished Doctoral Thesis, pp 307.

Schermerhorn LJG (1971) An outline of the stratigraphy of the Iberian Pyrite Belt. Boletín Geológico y Minero 82:239-268.

Solomon M, Walshe JL, Garcia Palomero F (1980) Formation of massive sulfide deposits at Rio Tinto, Spain. Applied Earth Science 89:16-24.

Strauss GK, Beck JSJMD (1990) Gold mineralisations in the SW Iberian Pyrite Belt. 25:237-245. doi: 10.1007/bf00198992.

Tornos F, Clavijo EG, Spiro BJ (1997) The Filon Norte orebody (Tharsis, Iberian Pyrite Belt): a proximal low-temperature shale-hosted massive sulphide in a thin-skinned tectonic belt. 33:150-169. doi: 10.1007/s001260050138.

Tornos F (2006) Environment of formation and styles of volcanogenic massive sulfides: The Iberian Pyrite Belt. Ore Geology Reviews 28:259-307. doi: https://doi.org/10.1016/j.oregeorev.2004.12.005.

Tornos F (2008) La geología y metalogenia de la Faja Piritica Ibérica. Macla 10:13-23.

Topaz-rich breccias at the 1.9 Ga Kankberg Au-Te deposit, Skellefte District, Sweden.

Paulina Nordfeldt

Stockholm University, Laurentian University and Boliden Mines

Rodney L. Allen

Volcanic Resources AB

Iain K. Pitcairn

Department of Geological Sciences, Stockholm University

Harold L. Gibson

MERC, Harquail School of Earth Sciences, Laurentian University

Abstract. The Åkulla Au-Te deposit is a mineralogically distinct and newly recognized ore deposit style in the Skellefte District, Northern Sweden. The deposit is characterized by a quartz-rich alteration assemblage with abundant andalusite and topaz. Preliminary geochemical interpretation of this assemblage suggests that it formed under highly acidic conditions consistent with those of advanced argillic alteration. The rocks were subsequently metamorphosed to upper greenschist facies. Detailed textural analysis of core from centrally-located diamond drill hole AKULL869 allow the topaz-rich breccias to be subdivided into seven main breccia facies and suggests that topaz is a primary hydrothermal mineral, whereas andalusite grew during regional metamorphism. Consequently, this raises the important question as to the relationship between the conditions and setting of alteration and mineralisation at Åkulla Au-Te deposit and the more classic VMS mineralisation in the Skellefte district and elsewhere.

1 Introduction

The Paleoproterozoic (1.9 -1.8 Ga) Skellefte District is one of Sweden's premier mining districts hosting around 85 volcanogenic massive sulfide (VMS) deposits (Fig. 1), 5 of which are currently being mined, as well as orogenic gold and porphyry copper mineralisation (Allen et al. 1996; Weihed and Allen 2004). The VMS deposits are sulphide rich bodies that formed by hydrothermal activity at and below the seafloor. They are mined for base metals and precious metals (Zn, Pb, Cu, Ag and Au); some are significantly enriched in Au either as a by-product, or as the main commodity, such as the Boliden deposit and the Åkulla Au-Te deposits.

Here we describe the texture and mineralogy of felsic volcanic and volcanoclastic rocks at the Åkulla Au-Te deposit in the Skellefte District Sweden. Textural analysis of drill core has identified seven different breccia facies in the central mineralized zone. These breccias are in part preserved due to the resilience of the primary topaz-quartz hydrothermal alteration. The deposit allows new insight into the volcano-hydrothermal conditions of mineralization and alteration in the Skellefte District.

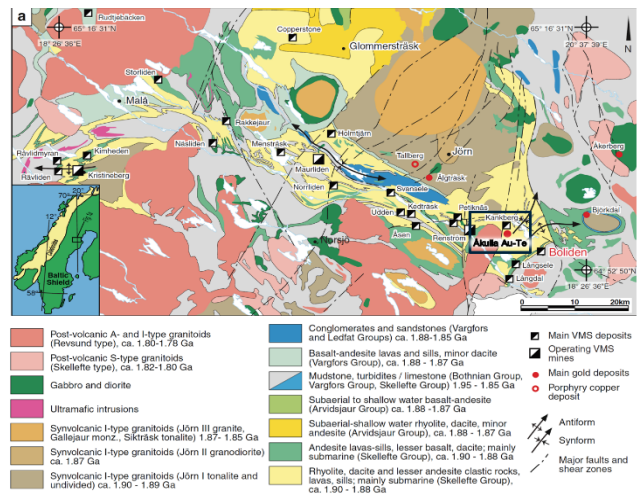


Figure 1. Simplified Skellefte District geological map, modified after Allen et al. 1996. Åkulla Au-Te deposit is located in the Kankberg area, visualized by the black box.

2 Geological setting

The Skellefte District is interpreted to be the remnant of a ca 1.9 Ga volcanic arc that was accreted to an Archean continental margin located to the north (Weihed et al. 2005). The Skellefte District comprises metavolcanic, metasedimentary and meta-intrusive rocks that were deformed and metamorphosed, locally to amphibolite facies, during the Svecofennian orogeny 1.90-1.80 Ga (Lundström et al. 1997; Mellqvist et al. 1999; Weihed et al. 2002; Kathol & Weihed 2005; Fig. 1). The district has undergone multiple deformation phases and the structural evolution strongly controls the distribution and shape of the VMS deposits in the district (Bauer et al. 2014). Regional metamorphism has modified the primary alteration association and caused remobilization of base- and precious metals within ore bodies (Mercier-Langevin et al. 2013; Bauer et al. 2014). Many of the Skellefte District VMS deposits show a strong spatial relationship to submarine, felsic cryptodomes (Allen et al. 1996). The deposits are related to a period of extensional volcanism and occur dominantly in the upper parts of the Skellefte Group volcanic and volcanoclastic rocks (Allen et al. 1996). Some of the VMS deposits are interpreted to have

formed on the sea floor, whereas others formed several tens to hundreds of meters below the sea floor (Allen et al. 1996; Doyle and Allen 2003).

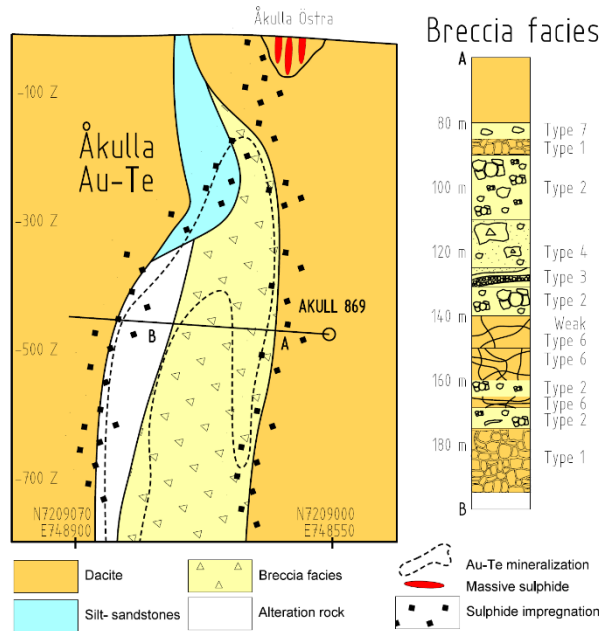


Figure 2. Cross-section of Kankberg Au-Te deposit looking south, showing simplified geology, position of Au-Te mineralization, and sulphide occurrences. For simplicity, alteration is excluded. Åkulla Östra open pit is projected in to the cross-section. Coordinates are in SWEREF99. Detailed graphic log of the breccia facies in AKULL869 is shown to the right. See Table 1 for Textural description



Figure 3. a. Least-altered coherent dacite surrounding the deposit DDC AKULL809, 140m depth. b. strongly altered in situ brecciated dacite displaying perlitic fractures from the central dacitic body DDC AKULL869, 177m depth.

The Åkulla deposit is a mineralogically distinct and newly recognized ore deposit style in the Skellefte District that is characterized by the abundance of topaz-quartz alteration, Au-Te enrichments and a paucity of sulfide within the main ore assemblage, and is therefore distinct from the known base metal and precious metal deposits in the district (Allen et al. 1996; Weihed and Allen 2004). The deposit, located in the Kankberg area (Figs. 1), contains 2.7 million tons of proven mineral reserve grading 3.8 g/t Au and 182 g/t Te (Boliden Annual report 2018). The Kankberg area has three previously mined massive sulphide ore bodies within 1km² (Kankberg deposit, Åkulla Västra and Åkulla Östra), all having the

traditional Skellefte District VMS composition. The Åkulla Au-Te deposits sits spatially under one small surface deposit, Åkulla Östra (Fig. 2). Preliminary geochemical investigation indicates that topaz-quartz altered rocks are depleted in Na⁺, Ca⁺², Mg⁺², Fe⁺² and enriched in SiO₂, which indicates extensive leaching typical of highly acidic conditions associated with advanced argillic alteration (Sillitoe et al. 1996; Barrett et al. 2005; Mercier-Langevin et al. 2013). The andalusite is interpreted to have formed during later regional metamorphism but the topaz and quartz appear to be primary hydrothermal minerals.

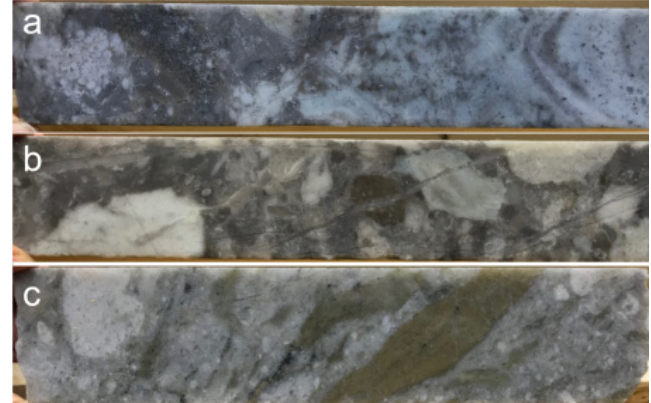


Figure 4. AKULL869 a. Type 2a breccia facies; poorly sorted, clast to matrix supported polymict breccia with clasts of in situ brecciated dacite (162m depth). b. Type 2b breccia facies; poorly sorted, clast to matrix supported polymict breccia without in situ brecciated dacite clasts or mafic clasts (163m depth). c. Type 2c facies; poorly sorted, clast to matrix supported polymict breccia containing up to 15% sericite-altered mafic clasts (173m depth)

3 Rock types

Strata in the Åkulla Au-Te deposit area are steeply dipping, and the deposit is surrounded by weakly to moderately altered (chlorite and or silica) coherent dacitic intrusions (Figs. 1, 2 and 3a). Lithochemical data indicates two different dacitic intrusions, one dominating the north and the other the south. Silt- and sand-sized volcanoclastic deposits containing small massive sulphide lenses and stringers occur above the Åkulla deposit. The deposit is defined by a central, 200m wide, minimum 400m deep and 300m elongated, strongly quartz, topaz, andalusite and white mica altered core shown as the breccia facies unit in Fig. 2. Coherent and breccia facies are recognized in the altered core area. The contacts are interdigitating and either the coherent dacites intrude in to the breccias or the breccias overprint and/or intrude across the dacite.

The breccias include six main facies and an undifferentiated group (Table 1 and Fig. 2). The units are often 5cm to 7m thick and are randomly intercalated through 100m of the drill hole AKULL869 (subhorizontal hole at the -500m mine level, Fig. 2). Alteration is dominated by quartz (amorphous flooding and several generations of veining), topaz (amorphous flooding, irregular thin veining and rare anhedral mineral spots found in very mica altered and foliated rocks), white mica (defining tectonic fabric) and andalusite (within matrix and fabric, euhedral to subhedral porphyroblasts and late coarse quartz, andalusite and fluorite veinlets). The

alteration affects coherent units, as well as clasts and the matrix of the breccia units resulting in, for example, topaz fragments within a topaz-altered matrix. Beautiful topaz and quartz zoning are common in coherent, locally even perlitic and porphyritic (quartz and relict feldspar phenocrysts) dacite and dacitic fragments (Fig. 4a). The dominant fragments in these units are 1) coherent, porphyritic, sometimes topaz altered and/or zoned dacite, 2) aphyric silicic fragments variably topaz altered and more deformed, and 3) mica altered leucoxene-bearing mafic clasts. Ore mineralization occurs as fracture fills of Au-telluride minerals <0.5% and locally visible gold. Sulphides are generally lacking in the central body but disseminations and fracture fillings of pyrite (1-10 %), are common in the periphery of the central body and towards the surface (Fig. 2).

Table 1. Description of the seven different breccia facies in drill hole AKULL869 at the Åkulla Au-Te deposit.

1	Monomict in-situ brecciated dacite; 0.5m to 4m thick intervals with perlitic texture and cusped to serrated clast boundaries (Fig. 3b).
2	Polymict poorly sorted breccia; 0.4m to 7m thick, clast- to matrix-supported with granular matrix. Many clasts with serrated, hackly, angular margins (Fig. 4). This breccia type is subdivided into a) with patches/intervals of in situ brecciated dacite; b) without in situ brecciated dacite and without mica altered mafic clasts; c) with up to 15% yellow to brown mica altered deformed mafic clasts.
3	Polymict moderately to well sorted, clast-supported breccia, 0.1m to 3m thick with moderately abraded to sub-rounded clasts (Fig. 5). This breccia type is subdivided by grain size into a) pebble breccia; b) breccia with sand-size matrix and <5% pebbles; normal-graded in places; and c) breccia with very fine sand to silt-size matrix and <2% pebbles.
4	Breccia with breccia/volcaniclastic clasts, 0.3m to 4m thick with a sandy well-sorted matrix that is commonly in situ brecciated (Fig. 6); a) with sandy unbreciated clasts up to 20cm; b) with larger clasts of polychromatic breccia.
5	Moderately to poorly sorted, polymict breccia, 0.5-6 m wide with pale brown to bluish, silty to fine sand matrix of amorphous topaz and quartz, resulting in a "slurry" like texture. Irregular sharp contacts and wall rock fragments with jigsaw-fit texture imply sprawling of clasts and wall rock. Clast shapes moderately abraded to some sub-rounded (Fig. 7a)
6	Qtz-cemented in-situ breccia, 1m to 6m wide, defined by abundant sub-planar veinlets with hydrothermal cement (Fig. 7b).
7	Undifferentiated breccia; 1m to 10m; Breccia that we cannot easily allocate to the types above; including mica-altered apparent breccia that contains some apparent 0.5 – 5 cm clasts (Fig. 7c).

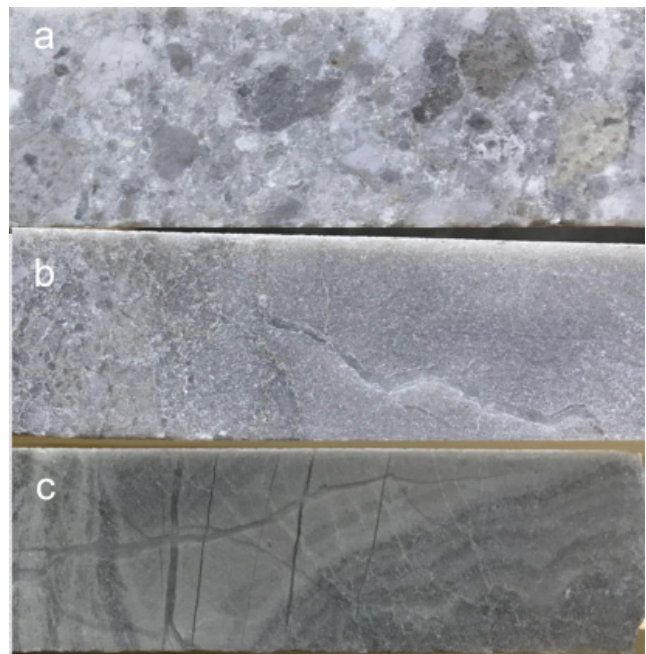


Figure 5. AKULL869 a. Type 3a facies; moderately to well sorted, clast supported, polymict, sand to siltstone matrix breccia (124m depth). b. Type 3b facies, moderately to well sorted, mainly sand size polymict breccia, coarser fragments to the left (123m depth). c. Type 3c facies, moderately to well sorted, very fine sand to siltstone matrix breccia, at 130m depth.

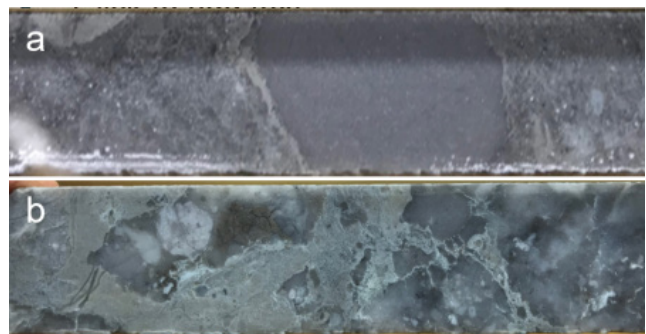


Figure 6. AKULL869. a. Type 4a facies, well sorted sand-sized matrix breccia, in situ brecciated matrix with volcanic sandstone intact clasts (120m depth). b. Type 4b facies, well sorted sand-sized matrix, with in situ brecciated larger clast of polymict pebble breccia, visible to the top left. Polymict pebble breccia fragment to the right display jig saw fit, in situ brecciation (116m depth).

4 Discussion

In this abstract, we present results of detailed textural logging of AKULL869 that is a key in interpretation of the breccias in the Åkulla Au-Te deposit. Interpretations are preliminary. However, the matrix supported, poorly sorted breccias (breccia facies 2) indicate transport and rapid deposition through mass movement of a clastic aggregate. The clast-supported breccia with moderate to good sorting (facies 3 and 4) imply traction transport and deposition. Facies 5 slurry-textured breccia occurs as vein-like units, cross cutting all other breccia facies, and include fragments of the wall rocks (Fig.6a); they are interpreted to be intrusive breccia dykes. The in situ breccia of facies 6 most likely formed by hydraulic fracturing and/or collapse, whereas perlitic textures and

cusped clast boundaries in facies 1, suggest a component of hyaloclastic fragmentation.

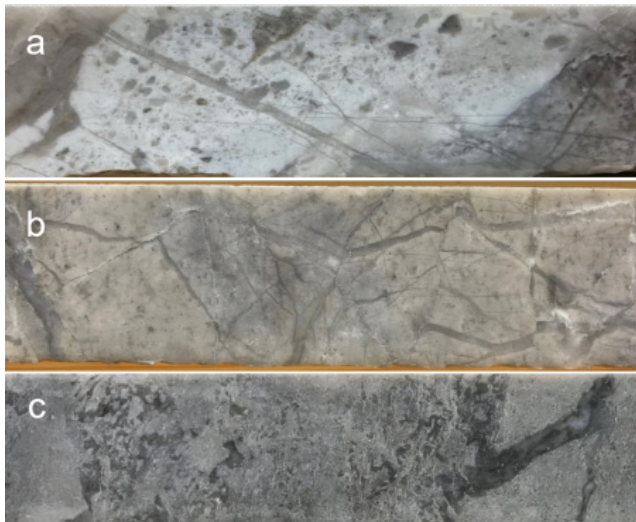


Figure 7. AKULL869 **a.** Type 5 facies, poorly sorted polymict breccia, silty to fine sand-sized matrix that is amorphous topaz and quartz with irregular and sharp contacts. Clasts are subrounded and to the left there is a fragment almost detached from the surrounding unit giving it a slurry vein texture, (184m depth). **b.** Type 6 facies, in situ breccia with subplanar thin cemented quartz veins (56m depth). **c.** Undifferentiated breccia with sericite alteration, (250m depth).

The breccia facies described above could potentially have formed through volcanic, sedimentary and hydrothermal processes at the sea floor, or alternatively through magmatic-hydrothermal processes in cavities within the subsurface. For example, topaz-quartz altered clasts occur in bedded, stratiform sedimentary-like deposits that are not topaz altered in their matrix. These rocks could have formed either as sedimentary units on the sea floor carrying erupted hydrothermal clasts, or as hydrothermal deposits formed in cavities in the subsurface containing clasts transported from deeper in the alteration system. Whether the deposit formed at the sea floor or mainly or entirely in the subsurface has important implications for ore genesis and for exploration for further similar deposits.

We interpret the topaz-quartz mineral assemblage as being a primary assemblage that formed during hydrothermal alteration based on the following evidence: a) Topaz- and quartz-rich assemblages are the alteration assemblages that best preserve primary “volcanic” rock textures. The rigid properties and low permeability of topaz-quartz altered rocks did not allow ductile deformation nor infiltration of disseminated sulphide mineralization, both of which surround the quartz-topaz core zone. b) Topaz occurs as both clasts in the breccias and in the matrix. c) Topaz alteration is overprinted by, and consequently we infer partly altered to coarse quartz, muscovite, andalusite and fluorite. d) Topaz-quartz alteration is amorphous, non-porphyroblastic and less metamorphically coarsened than the other alteration assemblages. The physical and chemical setting for advanced argillic alteration generating topaz as a primary mineral is yet to be constrained but clearly requires F-bearing hydrothermal fluids. This raises the important

question as to the relationship between the conditions and setting of alteration and mineralisation at the Åkulla Au-Te deposit and the more classic VMS mineralisation in the Skellefte district and elsewhere.

Acknowledgements

This research is a PhD project is funded by Boliden Mines organized via a cosupervision agreement between Laurentian and Stockholm Universities.

References

- Allen RL, Weihed P, Svenson SÅ, (1996) Setting of Zn-Cu-Au-Ag massive sulphide deposits in the evolution and facies architecture of a 1.9 Ga marine volcanic arc, Skellefte district, Sweden. *Econ Geol* 91: 1022–1053.
- Bauer TE, Skyttä P, Hermansson T, Allen RL, Weihed P (2014) Correlation between distribution and shape of VMS deposits and regional deformation patterns, Skellefte district, northern Sweden. *Miner Deposita* 49(5):1-19.
- Barrett TJ, MacLean WH, Årebäck H. (2005). The Palaeoproterozoic Kristineberg VMS deposit, Skellefte district, northern Sweden. Part II: chemostratigraphy and alteration. *Miner Deposita* 4:368.
- Boliden (2018) Boliden Annual and Sustainability Report 2018. <https://www.boliden.com/investor-relations/reports-and-presentations/annual-reports>.
- Doyle MG, Allen RL (2003) Subsea-floor replacement in Volcanic-hosted Massive Sulphide Deposits. *Ore Geol Rev* 23:183-222.
- Kathol B, Weihed P (2005) Description of regional geological and geophysical maps of the Skellefte district and surrounding areas. *Geol Surv of Sweden Ba* 57.
- Lundström I, Albino B (1997) The Björkdal area. *Geol Surv of Finland Guide* 41:72–75.
- Mellqvist C, Öhlander B, Skiöld T, Wikström A (1999) The Archaean-Proterozoic Palaeoboundary in the Luleå area, northern Sweden: Field and isotope geochemical evidence for a sharp terrane boundary. *Precambrian Research* 96:225–243.
- Mercier-Langevin P, McNicoll V, Allen RL, Blight JHS, Dubé B (2013) The Boliden gold-rich volcanogenic massive sulfide deposit, Skellefte district, Sweden: new U–Pb age constraints and implications at deposit and district scale. *Miner Deposita* 48:485-504.
- Sillitoe RH, Hannington MD, Thompson JFH (1996) High sulfidation deposits in the volcanogenic massive sulfide environment. *Econ Geol* 91:204–212.
- Weihed P, Allen RL, (2004) Overview of Porphyry-Style Cu-Au and Mesothermal Gold Deposits in the Skellefte District. In: Allen RL, Martinsson O, Weihed P, (ed) *Svecofennian Ore-Forming Environments Field Trip Volcanic-associated Zn-Cu-Au-Ag and magnetite-apatite, sediment-hosted Pb-Zn, and intrusion-associated Cu-Au deposits in northern Sweden*. Society of Economic Geologists Guidebook Series. Littleton, Colorado: Society of Economic Geologists 33:51-56.
- Weihed P, Arndt N, Billström K, Duchesne JC, Eilu P, Martinsson O, Paounen H, Lahtinen R (2005) 8: Precambrian geodynamics and ore formation: The Fennoscandian Shield. *Ore Geology Reviews* 27:273–322.
- Weihed P, Bergman J, Bergström U (1992) Metallogeny and tectonic evolution of the Early Proterozoic Skellefte district, northern Sweden. *Precambrian Research* 58:143-167.
- Weihed P, Billstrom K, Persson PO, Weihed JB (2002). Relationship between 1.90-1.85 Ga accretionary processes and 1.82-1.80 Ga oblique subduction at the Karelian craton margin, Fennoscandian Shield. *GFF UPPSALA* 3:163.

Indium and Gallium in Cu-Pb (Ag) sulphide deposits of the Otavi Mountain Land, Namibia; a LA-ICP-MS study

Ester Shalimba, Ansgar Wanke

University of Namibia, Geology Department, Namibia

Sven Sindern

RWTH Aachen University, Institute of Applied Mineralogy and Economic Geology, Aachen, Germany

Abstract. Chalcopyrite and bornite are two common sulphide minerals of copper ores. Their crystal structures can accommodate significant amounts of trace elements. The herein presented study focuses on the concentration of gallium and indium associated with chalcopyrite and bornite of the Cu-Pb (Ag) deposit of Otavi Mountainland, Namibia. The research aims to correlate base metal element concentrations with Ga and In concentrations in the sulphide minerals. Trace elements in bornite and chalcopyrite were determined by LA-ICP-MS. Both, bornite and chalcopyrite show large concentration variation for minor and trace elements (e.g. $191,87 \text{ ppm} \geq \text{Ag} \leq 257,48 \text{ ppm}$ and $2,78 \text{ ppm} \geq \text{Ag} \leq 3,57 \text{ ppm}$ respectively). Gallium concentration are $>1 \text{ ppm}$ in bornite, while chalcopyrite has significantly higher concentration of Ga ($<14 \text{ ppm}$). Indium concentrations are below the detection limit in bornite and they are relatively low in chalcopyrite grains ($<0,1 \text{ ppm}$). Element correlation plots show that high Ga concentrations correlate with low Ag and correlation between Ag and Pb is weak. Additionally, chalcopyrite grains with significant amount of Ga always contain traces of In. Further studies will investigate the influence of base metals concentration on the distribution of the above.

1 Introduction

Critical raw materials are essential for economic growth, especially in terms of technological evolution. Economic importance and supply risks are the two parameters frequently used to determine how critical the raw materials are (Graedel et al. 2011). Gallium (Ga) and Indium (In) are critical for a variety of high technology applications; such as in semiconductors, wide angle camera lenses as well as pharmaceutical industries (Paradis 2015). These elements are mainly recovered as byproducts of base metals from Zn and Cu deposits.

The trivalent Ga is considered as a trace element with a crustal abundance of 17 ppm, which is commonly associated with aluminum ores, zinc ores, iron ores and coal (Redlinger et al. 2015; Frenzel et al. 2016).

Indium is typically associated with minerals such as zinc, copper and iron-tin sulphides. It dominantly occurs as indium-bearing mineral in (Pb)-Zn ores as well as concentrates is sphalerite (Cook et al. 2011). Indium is a highly volatile chalcophile, with a crustal abundance estimated to be at about 0.05-0.072 ppm (Taylor and McLennan 1985)

The research presents a combined mineralogical and

geochemical study of sulphide mineralization from a Cu-Pb (Ag) deposit hosted in carbonate rocks of Otavi Mountainland, Namibia. This study aims to correlate the relations between base metal elements and Ga and In concentration in the sulphide mineralization.

2 Geological setting

The OML province is situated at the transition between the Northern Zone and Northern Platform of the Neoproterozoic Damara Orogen. The Damara orogenic belt is best described in Martin and Porada (1977), Miller (1983, 2008) and Pirajno and Joubert (1993) as a late Proterozoic suture zone between the Kalahari and Congo Craton. The Otavi Mountainland province consists of various base metal sulphide deposits, which are hosted within the sedimentary units of the Damara sequence (Kamona and Günzel 2007). Pirajno and Joubert (1993) argued that there must have been at least two separate events that led to the metal concentration in Tsumeb, Kombat and Berg Aukas deposits. They concluded that Berg Aukas was formed by the first event, which was associated with compaction and dewatering of sediments of a northern rift; whereas, Kombat and Tsumeb deposits were a result of a much later episode that was associated with devolatilization reactions during regional prograde metamorphism of the sediments in this Northern rift.

3 Methodology

Samples collected during a field campaign were prepared into epoxy mount polished section at the Geological Survey of Namibia, for petrographic study and LA-ICP-MS analyses.

A petrographic study was conducted using a Leica DM 4500p microscope, in RWTH, Aachen University, Germany.

Laser ablation-inductively plasma-mass spectrometry (LA-ICP-MS) was used to measure trace element concentrations in bornite and chalcopyrite. Spot analysis was done on pre-selected site base on petrographic study conducted on the samples. The LA-ICP-MS system comprises a NewWave UP193Fx (ArF-Excimer-Laser) operated with a 150 μm laser beam diameter and 6Hz repetition rate connected to a quadrupole ICP-MS system (PerkinElmer Elan DRCe). Total analysis time was 100s, approximately 40s on background and 60s on signal. MASS-1 reference material was used as an external calibration standard, and sulfide stoichiometric

concentrations of bornite (25.56% S) and chalcopyrite (34.94% S) were used as internal standards. Analytical reproducibility is better than 10% for all trace elements.

4 Results and Discussion

4.1 Petrography

The primary ores are massive, disseminated and to a certain extent brecciated. There are three distinct ore assemblages observed in the samples; (1) bornite-chalcopyrite-covellite, (2) bornite-galena-chalcocite and (3) bornite-chalcopyrite (Fig. 1).

The primary sulphide mineralization formed bornite, galena and chalcopyrite, while covellite, chalcocite are the secondary minerals. The common gangue minerals are dolomite and calcite. The primary ore textures are subhedral-anhedral grains, dissemination, intergrowth and replacement texture.

Bornite is characterized by anhedral coarse grained texture, and it is replaced by chalcopyrite and chalcocite in most samples (Fig. 1a, b). Most of the bornite grains are light orange in color, while some exhibit a light grey color. Galena is fine grained, and mainly appearing as inclusions in the bornite (Fig.1 c). Chalcopyrite displays a replacement texture, and it is massively distributed within the dolomite. Covellite is mainly observed in the brecciated zone, and it appears as veinlets and intergrowths in bornite that is replaced by chalcopyrite (Fig. 1a).

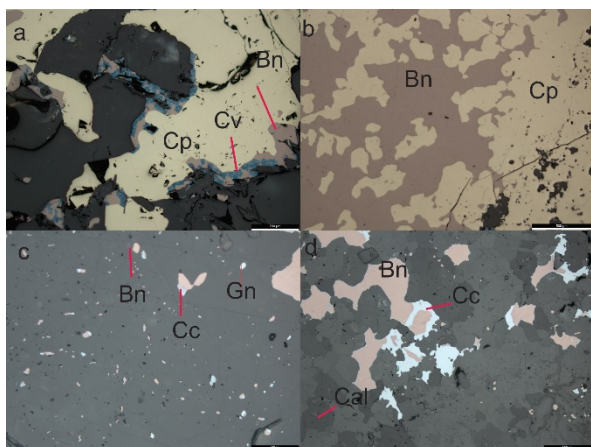


Figure 1. Microphotography in reflected light showing ore mineralogy and textures observed. **a)** Bornite replaced by chalcopyrite with intergrowth of covellite. **b)** Bornite replaced by chalcopyrite. **c)** dissemination of bornite, chalcocite and galena. **d)** Intergrowth of bornite and chalcocite. Abbreviations: Bn-bornite, Cp= chalcopyrite, Cc=chalcocite, Cv=covellite, Cal=calcite.

4.2 LA-ICP-MS Data

Trace analyses by LA-ICP-MS for bornite and chalcopyrite element concentration's mean, median, max and min are listed in Table 1 and 2 respectively. The data obtained consists of 342 spot analyses in bornite and 184 spot analyses in chalcopyrite. Representative time-resolved LA-ICP-MS depth profiles are shown in figure 3.

Bornite has significantly high concentrations of Ag in

all the samples analyzed. All bornite contains Ag with a mean concentration ranging between 100 and 290 ppm.

Pb values are typically >1 ppm, except for several bornites in KH0517 and KH0515 with values as high as ±1200 ppm, indicating a possible galena inclusion in the bornite.

All samples contain measurable Ga concentration in bornite which is relatively low. There are no absolute values for In in bornite. If detectable, Cd, Sb and W are all in low concentration in all the samples.

Gallium has a significantly higher concentration in chalcopyrite compared to bornite in all the samples studied. KH0517 has a high concentration of Ga (<16.61 ppm, mean=13.22 ppm) and moderate concentration of Ag and Pb (<14.57 ppm, mean =3.57 ppm; <11.11 ppm, mean= 6.10 ppm respectively). V concentration is low (up to 5 ppm, mean= 1.94), while In is low with a single spot.

Table 1. LA-ICP-MS Mean concentration analyses for minor and trace elements in Bornite (ppm)

	V	Ga	Ag	Cd	Sb	W	Pb
KH0517							
Mean	4.6	1.5	257	2.4	0.3	0.9	93
Median	3.8	1.1	259	2.5	0.3	0.8	5.9
MIN	2.2	0.7	207	1.9	0.2	0.4	1.4
MAX	12.	7.6	281	2.7	0.4	2.3	1270
KH0516							
Mean	13.3	1.5	242	-	-	-	1.1
Median	5.3	1.3	244	-	-	-	1.1
MIN	2.3	0.9	213	-	-	-	0.7
MAX	75	2.9	292	-	-	-	1.8

	V	Ga	Ag	Cd	Sb	W	Pb
KH0515							
Mean	-	1.3	191	-	-	-	74
Median	-	1.3	195	-	-	-	12.6
MIN	-	0.8	100	-	-	-	2.6
MAX	3.59	3.1	239	1.9	-	-	656

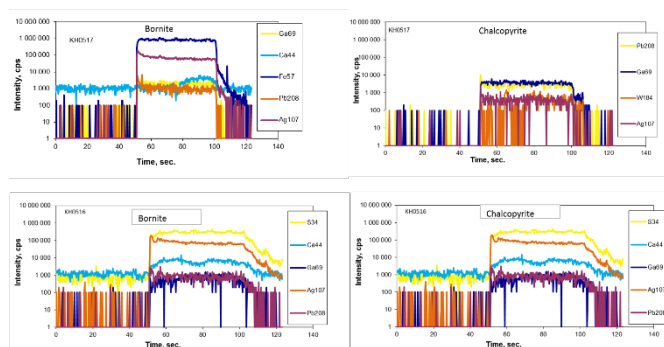


Figure 2. Representative time-resolved LA-ICP-MS depth profiles for analyzed bornite and chalcopyrite. Irregular signals of ⁴⁴Ca indicate local occurrence of carbonate inclusions.

Table 2. LA-ICP-MS Mean concentration analyses for minor and trace elements in Chalcopyrite (ppm). Owing to restrictions of the MASS1 standard, In is given as information value.

	V	Ga	Ge	Ag	In	W	Pb
KH0517							
Mean	1.9	13.2	-	3.6	-	0.9	6.1
Median	1.3	12.9	-	2.1	-	0.9	4.9
MIN	0.8	11.6	-	0.9	-	0.5	3.3
MAX	5.	16.6	2.9	14.6	0.9	1.4	11
KH0516							
Mean	30.5	12.5	-	2.8	0.4	-	1.6
Median	30.6	13.2	-	2.3	0.4	-	1.6
MIN	23.4	10.5	-	1.2	0.3	-	0.8
MAX	37.4	13.9	-	5.1	0.4	-	2.3
KH0515							
Mean	-	14.1	3.7	3.1	0.2	-	8.5
Median	-	14.3	3.7	1.5	0.2	-	3.6
MIN	-	10.8	3.6	0.5	0.1	-	0.6
MAX	-	16.6	3.9	19.2	0.2	5.3	43.3

5 Conclusion

Pb does not correlate with Ga in both, bornite and chalcopyrite (Fig.3&4). Chalcopyrite accommodates higher concentrations of Ga compared to bornite. Furthermore, the higher Ga concentrations in chalcopyrite correlate with In concentrations above the detection limit. Ag is more accommodated in bornite than in chalcopyrite, indicating that substitution for Ag may explain the limited accommodation of Ga in bornite. However, neither within bornite, nor within chalcopyrite a conclusive correlation of Ga with Ag was observed. In order to fully study the association of the selected high-tech metals with base metals, significantly more data need to be collected.

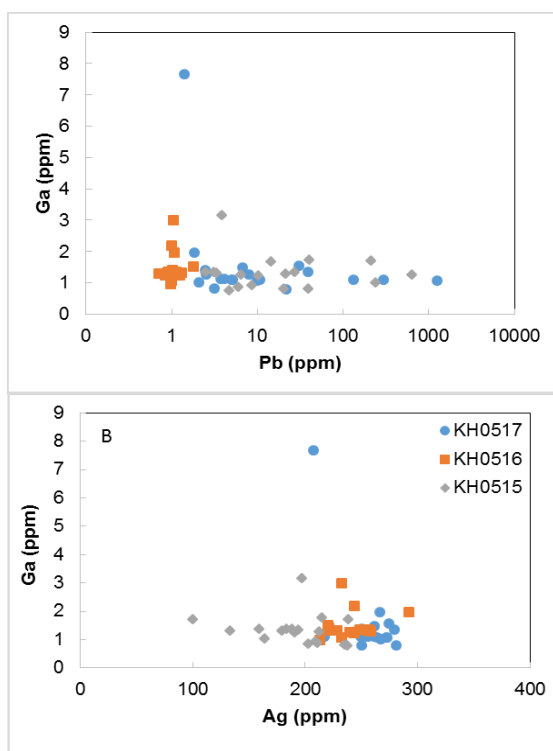


Figure 3. Comparison of Ag-Ga and Pb-Ga by LA-ICP-MS analysis for bornite

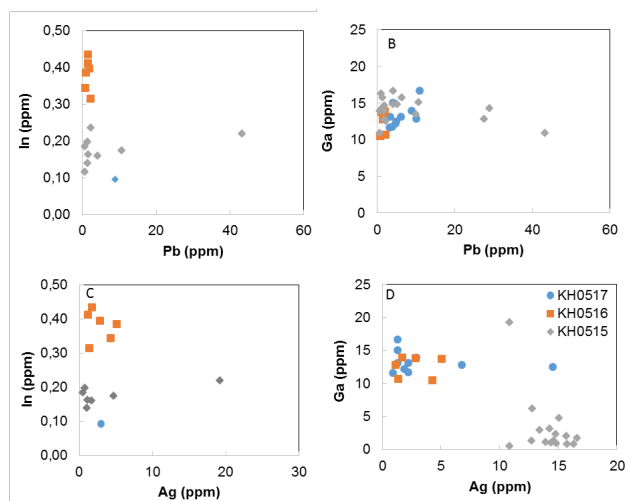


Figure 4. Comparison of Pb-In, Ag-In, Ag-Ga and Pb-Ga by LA-ICP-MS analysis for chalcopyrite.

Acknowledgements

The project is funded by BMBF through the LoCoSu project. LA-ICP-MS analyses were carried out at the Institute of Applied Mineralogy and Economic Geology at RWTH Aachen University. We would like to acknowledge The University of Namibia, Geology Department for the logistical field support.

References

- Cook NJ (2011) The mineralogy and mineral chemistry of indium in sulphide deposits and implications for mineral processing. *Hydrometallurgy* 108:226-228.
- Graedel TE, et al. (2012) Methodology of Metal Criticality Determination. *Environ. Sci. Technol.* 46:1063-1070.
- Frenzel M, Ketris MP, Seifert T, Gutzmer J (2016) On the current and future availability of gallium. *Resources Policy* 47(3):38-50.
- Kamona F, Günzel A (2007) Stratigraphy and base metal mineralization in the Otavi Mountain Land, Northern Namibia- a review and regional interpretation. *Gondwana Res.* 11:396-413.
- Martin H, Porada H (1977) The intracratonic branch of the Damara orogen in South West Africa I. Discussion of geodynamic models. *Precambrian Res.* 5:311-338.
- Miller RM (1983a) The Pan-African Damara Orogen of South West Africa/ Namibia. In Miller RM (Ed.) Evolution of the Damara Orogen of South West Africa/Namibia. Special Publication, Geological Society of South Africa 11:431-515.
- Miller RM (2008) Neoproterozoic and early Palaeozoic rocks of the Damara Orogen. In: Miller, R.M. (Ed.), *The Geology of Namibia*, 2. Geological Survey of Namibia, Windhoek, 13-1-13-410.
- Paradis S (2015) Indium, germanium and gallium in volcanic- and sediment-hosted base-metal sulphide deposits. In Simandl, GJ and Neetz M (Eds.) Symposium on Strategic and Critical Materials Proceedings, November 13-14, 2015, Victoria, British Columbia. British Columbia Ministry of Energy and Mines, British Columbia Geological Survey Paper 2015-3:23-29.
- Pirajno F, Joubert BD (1993) An overview of the carbonate-hosted mineral deposits in the Otavi Mountainland, Namibia; implications for the ore genesis. *J. Afr. Earth. Sc.* 16: 265-272.
- Redlinger M, Eggert R, Woodhouse M (2015) Evaluating the availability of gallium, indium, and tellurium from recycled photovoltaic modules. *Solar Energy Materials & Solar Cells* 138(7):58-71.
- Taylor SR, McLennan SM (1985) *The Continental Crust: Its Composition and Evolution*. Blackwell Scientific Publishing, Oxford.

Chemical characteristic of gersdorffite solid solutions in Stan Terg area, Kosovo

Marcin Wojślaw¹, Jaroslav Pršek¹, Sławomir Mederski¹, Burim Asllani², Jakub Kanigowski¹

¹AGH University of Science and Technology, Kraków, Poland

²E&E Experts LLC, Prishtina

Abstract. A listwaenite-hosted Ni-As-Sb-S assemblage occurs in the Stan Terg Zn-Pb(Ag) district within the Vardar Zone structure and is closely related to a Neogene calc-alkaline and volcanic-intrusive complex. In this paper, results of gersdorffite chemical analyses performed using electron microprobe analysis from Vllahi, Melenica and Mazhiq is presented. Small irregular inclusions of gersdorffite from Vllahi are enclosed in galena and shows enrichment in Co (up to 3 wt.%) in comparison to Co-free Melenica and Mazhiq samples. In Melenica the initial Ni association is replaced by gersdorffite and later by Sb-bearing gersdorffite. Mazhiq samples are dominated by oscillatory zoned crystals of gersdorffite and Sb-rich gersdorffite rimming arsenopyrite cores or irregular masses filling free spaces between euhedral crystals of arsenopyrite. Zoning is related to variable As (up to 42 wt.%), Sb (up to 15 wt.%) and Fe (up to 9 wt.%) indicating fluctuations of arsenic and antimony fugacity in hydrothermal fluids. Melenica and Mazhiq gersdorffite performs strong replacement trend of a mixture of Co and Ni by Fe. In addition, extensive substitution of As by Sb led to deposition of intermediate member of gersdorffite-ullmannite series, maximum content of Sb reaches 0.47 apfu.

1 Introduction

Gersdorffite is common Ni-bearing sulphoarsenide occurring at hydrothermal veins at moderate temperatures and magmatic sulfide system with general formula NiAsS. It belongs to the pyrite structure group. Three crystal structure variants of gersdorffite have been described: an ordered structure (P2₁2, ullmannite subgroup) (Bayliss & Stephenson 1967), disordered structure (Pa3, pyrite supergroup) (Bayliss 1982), and distorted disordered structure P1 (Bayliss & Stephenson 1968).

Gersdorffite incorporates Ni, Co and Fe in varying proportions (Klemm 1965) thus forming solid solutions in the ternary gersdorffite-cobaltite-arsenopyrite series. Ni and Co end-member of the series exhibit complete miscibility above 550°C, meanwhile transition of Ni by Fe is limited (Yund 1962). Moreover, the As and S content may vary from the molar 1:1 ratio thus forming solid solutions towards krutovite (NiAs₂) and vaesite (NiS₂) (Yund 1962). In addition to that, ullmannite (NiSbS) displays extensive substitution of As for Sb results in a variety phases between gersdorffite and ullmannite (Bayliss 1969).

The aim of this paper is chemical comparison of gersdorffite solid solutions from Ni-As-Sb-S assemblage

in Vllahi, Mazhiq and Melenica within the Stan Terg area.

2 Analytical samples and methodology

2.1 Investigated material

Samples of Ni-As-Sb-S mineralization were collected from debris and outcrops from three localization in Stan Terg region: Mazhiq, Vllahi and Melenica.

Material obtained in Vllahi is mostly porous and deformed breccia and volcanic tuff. Material indicates strong silicification (layered chalcedony). Free spaces are filled up with quartz, calcite and barite. Samples are slightly weathered, which is indicated by the presence of brownish iron oxide. Ore minerals, galena and sphalerite are usually massive or fill up free spaces

Melenica's samples are mostly brecciated listwaenites exhibiting strong quartz and calcite alteration. Nickel sulphides occur as irregular aggregates, several mm in size within listwaenites clasts cemented with carbonates and silica. Thin veinlets of galena and sphalerite occur in the strongly silicified zones.

Mazhiq's specimens are deformed listwaenites with massive gersdorffite impregnations accompanied by pyrite and needles of sulphosalts.

2.2 Analytical methods

Preliminary investigation of gersdorffite from Stan Terg area was conducted in reflected-light microscopy in Economic Geology Department AGH in Cracow. Chemical analyses were carried out by electron microprobe (EPMA) using EOL Super Probe JXA-8230 at the Critical Elements Laboratory AGH-KGHM in Kraków, Poland. Operating conditions were an accelerating voltage of 20 kV, a beam current 20 nA, peak time of 20 sec, and a background time of 10 sec with following standards natural: (pyrite, stibnite, chalcopyrite, arsenopyrite) or synthetic (native nickel, native cobalt, Bi₂Se₃) and spectral lines: S(Kα), Sb(Lα), Co(Kα), Ni(Kα), Cu(Kα), Fe(Kα), Bi(Mα), As(Lα).

3 Geological background of Stan Terg area

Stan Terg deposit is placed in northern Kosovo within the Vardar Zone, which is an elongated trending NNW-SSE regional suture between the Serbo-Macedonian Massif to the east and the Dinarides to the west. The Vardar Zone is marked by late Proterozoic metamorphic successions, and the Dinarides, which consists of Mesozoic rocks affected by Alpine deformation. The regional junction comprises Paleozoic crystalline schist and phyllite,

Triassic clastics, phyllites, volcanoclastic rocks and Upper Triassic carbonates, Jurassic serpentinitized ultramafic rocks, gabbros, diabases and sediments of the ophiolite association. The Cretaceous sequence consists of a complex series of clastics, serpentinite, mafic volcanics and volcanoclastic rocks, and carbonates. The Tertiary (Oligocene-Miocene) andesite, trachyte and latite sub-volcanic intrusives, volcanics and pyroclastic rocks occur at several centers within central part of Vardar Zone, covering large areas (Hyseni et al. 2010).

Ni-As-Sb-S occurrences in Stan Terg district are genetically connected to the Neogene calc-alkaline and volcanic-intrusive complex. Metals in these assemblage were probably sourced from the serpentinite basement and surroundings and were mobilized during magma ascent through the ophiolite complex (Carter 2008). Nickel mineralization is hosted mainly in listwaenite rocks, developed within contact between hanging wall serpentinites and footwall volcanic- intrusive rocks. During pre-mineralization processes, intensive silicification of serpentinites led to the formation of listwaenites (Miletic 1995). On contrary, listwaenites have also been considered to be formed after complete silicification and carbonatization during hydrothermal processes (Borojevic-Sostaric et al. 2013).

4 Mineralogy of gersdorffite

4.1 Mazhiq

Gersdorffite recognized in Mazhiq constitutes the major ore mineral, and occurs as follows: a) irregular masses rimming/replacing euhedral crystals of arsenopyrite or pyrite or chalcopyrite (Fig. 1a) b) intergrowth of euhedral to subhedral square or hexagonal zoned crystals (Fig.

1b). It is characterized by having moderately high reflectance with white to creamy or greyish tint. Tetrahedrite often replaces or fill up cracks or crystallizes along bands within zoned gersdorffite crystals. Under EPMA, crystals of gersdorffite are zoned with clearly visible dark grey and white bands following the forms of the crystal. Difference in colors in BSE images is caused by variability in Fe content as well as As-Sb content.

EPMA of the gersdorffite from Mazhiq yielded Sb-bearing and As-bearing gersdorffite. The chemical composition of gersdorffite is $(\text{Ni}_{0.93}\text{Fe}_{0.07})_{\Sigma 1}(\text{As}_{0.93}\text{Sb}_{0.07})_{\Sigma 1}\text{S}_{0.92}$ (Tab. 1). For an intermediate As-Sb member EPMA yielded a composition $(\text{Ni}_{0.98}\text{Fe}_{0.01})_{\Sigma 0.99}(\text{As}_{0.80}\text{Sb}_{0.18})_{\Sigma 0.98}\text{S}_{0.94}$.

Gersdorffite from Mazhiq exhibits enrichment in Sb up to 15 wt.% and As content differs from 32 wt.% to ~37 in Sb-bearing gersdorffite and 37wt. % to 47 wt.% in gersdorffite. Moreover, it displays zoning in terms of Fe, varying from 0.25 wt.% to 1.14 wt.% and 0.36 wt.% to 8,91 wt.% in gersdorffite and Sb-bearing gersdorffite, respectively. Ni-bearing sulphoarsenide shows depletion in Co and Cu.

Arsenopyrite is found as crystallization core or small (up to 50 μm) subhedral to euhedral inclusion within gersdorffite crystals. The chemical composition of arsenopyrite corresponds to average formula $(\text{Fe}_{0.95}\text{Ni}_{0.02}\text{Co}_{0.02})_{\Sigma 0.99}(\text{As}_{0.93}\text{Sb}_{0.01})_{\Sigma 0.94}\text{S}_{1.03}$ (Tab. 1). Arsenopyrite is slightly enriched in Ni (up to 0.84 wt.% as well as Bi up to 0.51 wt.% and Co up to 0.84 wt.%).

Based on textural relations, the following crystallization sequence was suggested: 1) arsenopyrite, pyrite, 2) gersdorffite 3) Sb-bearing gersdorffite. However, rhythmical zoning can sometimes be noted indicating occasional interruption and changing chemistry of the ore-bearing solutions.

Table 1. Representative average EMPA and atomic proportions of gersdorffite and arsenopyrite from Vllahi, Melenica and Mazhiq (in wt.%); n – number of analyses.

Locality	Mineral (n)	S	Sb	Fe	Co	Ni	Cu	Bi	As	Total
Vllahi	Gersdorffite (4)	18.44	1.65	0.54	1.85	31.59	0.04	b.d	43.55	97.67
Melenica	Gersdorffite (18)	19.09	3.52	0.99	1.56	31.83	0.06	b.d	40.99	98.07
	Sb-bearing gersdorffite (4)	17.50	21.71	0.18	0.94	31.27	0.04	b.d	26.72	98.37
Mazhiq	Gersdorffite (39)	17.69	4.94	2.25	0.15	32.47	0.08	0.13	41.80	99.51
	Sb-bearing gersdorffite (19)	17.64	12.65	0.48	0.05	33.57	0.05	0.33	34.80	99.57
	Arsenopyrite (15)	20.30	0.74	32.61	0.84	0.84	0.21	0.51	42.90	98.65
Atomic proportions										
Vllahi	Gersdorffite	0.99	0.02	0.02	0.05	0.93	-	-	1.00	3.02
Melenica	Gersdorffite	1.01	0.05	0.03	0.05	0.92	-	-	0.93	2.99
	Sb-bearing gersdorffite	0.99	0.32	0.01	0.03	0.96	-	-	0.64	2.95
Mazhiq	Gersdorffite	0.92	0.07	0.07	-	0.93	-	-	0.93	2.92
	Sb-bearing gersdorffite	0.94	0.18	0.01	-	0.98	-	-	0.80	2.91
	Arsenopyrite	1.03	0.01	0.95	0.02	0.02	0.00	0.00	0.93	2.98

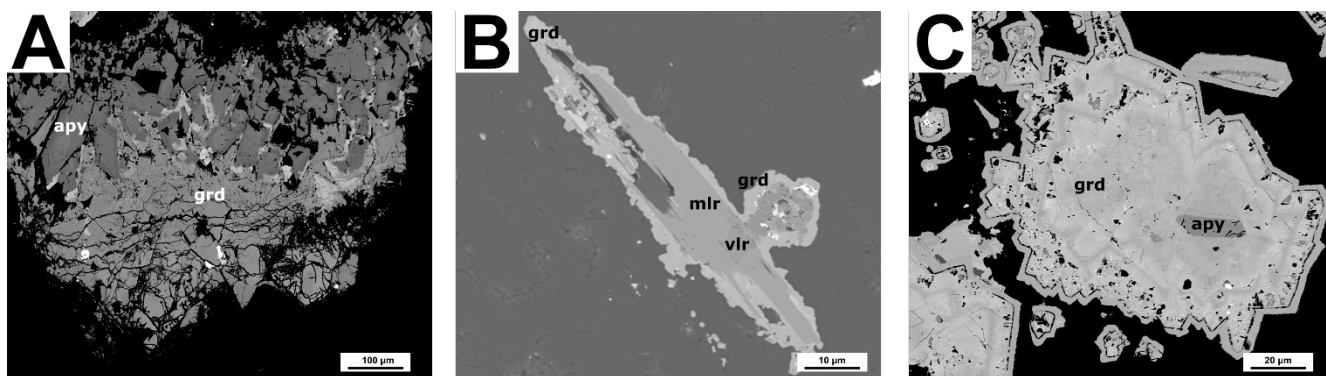


Figure 1. Back-scattered electron image showing **a.** irregular masses of gersdorffite (grd) filling free spaces between euhedral crystals of arsenopyrite (ars), Mazhiq; **b** gersdorffite rimming millerite (mlr) and violarite (vlr), Melenica; **c.** oscillatory zoned crystals of gersdorffite with arsenopyrite crystallization core, Mazhiq.

4.2 Melenica

Ni-rich sulphoarsenide appears in association with Ni, Fe, Zn and Co sulphides, replacing violarite, millerite or siegenite (Fig. 1b). Occurrence of single crystals is very rare. Ni or Ni-Co sulphides form cores of the Ni bearing mineral aggregates and they are replaced by Sb-gersdorffite or gersdorffite.

On the basis of chemical analysis Sb-bearing gersdorffite was distinguished, with an average formula of $(\text{Ni}_{0.96}\text{Co}_{0.03}\text{Fe}_{0.01})_{\Sigma 1}(\text{As}_{0.64}\text{Sb}_{0.32})_{\Sigma 0.96}\text{S}_{0.99}$. Meanwhile the composition of gersdorffite is $(\text{Ni}_{0.92}\text{Co}_{0.05}\text{Fe}_{0.02})_{\Sigma 1}(\text{As}_{0.93}\text{Sb}_{0.05})_{\Sigma 0.98}\text{S}_{1.01}$ (Tab. 1). Both, Sb-bearing and As-bearing gersdorffite are characterized by strong depletion in Co, Fe and Cu. Ni content is relatively constant in both varieties, approximate 32 wt.%. Arsenic content reaches up to 29.26 wt.%, which affects the low content of sulphur ~20 wt.%.

4.3 Vllahi

Gersdorffite occurs as small irregular inclusion enclosed in galena, up to 100 μm in size. Besides macroscopic observations reveal horseshoe-shaped zoning, micro analyses does not exhibit any chemical variability. It is associated with violarite, rammersbergite, millerite and pyrite.

EPMA analyses of gersdorffite yielded an average chemical composition $(\text{Ni}_{0.93}\text{Co}_{0.05}\text{Fe}_{0.02})_{\Sigma 1}(\text{As}_{0.99}\text{Sb}_{0.02})_{\Sigma 1.01}\text{S}_{0.99}$ (Tab. 1), which is nearly stoichiometric. Gersdorffite from Vllahi shows limited fluctuations of Co, Fe and Sb, varying from 0.69 wt.% to 3.06 wt.%, 0.27 wt.% to 1.48 wt.% and 0.84 wt.% to 3.39 wt.%, respectively.

5 Discussion

As a result of reflected-light microscopy and EPMA analyses, Ni-As-Sb-S listwaenite-hosted associations were recognised in Stan Terg area within Vardar Zone. Minerals of the gersdorffite solid solution occur in broad association of other Ni-minerals (Bal et al. unpublished). Gersdorffite from Mazhiq and Melenica shows strong negative correlation between Sb and As (Fig. 2a), which

Pearson correlation coefficient is equal 0.97 and 0.9, respectively. This is indicative for mutual substitution between Sb and As. Sb-bearing gersdorffite occurs replacing gersdorffite in zonal crystals. Zonation of crystals is a result of variability of new hydrothermal solutions which are usually enriched in antimony and depleted in arsenic. Meanwhile, Vllahi gersdorffite displays strong negative correlation ($R=0.79$) of As and Sb. Extensive replacement of As by Sb is manifested by gersdorffite-ullmannite solid solution.

In addition to that, gersdorffite from Mazhiq and Melenica performs almost perfect linear correlation of Ni+Co with Fe (Coefficient of correlation is 0.99 for Mazhiq and Melenica) (Fig. 2b), which is a result of substitution of Ni by small amount of Co and both elements by Fe. The opposite trend was documented in arsenopyrite where Fe is substituted by Ni+Co. The above factor may indicate metal-rich environment (Hem et al. 2004). Vllahi does not follow this trend, however as a strong negative correlation is found between Ni and Fe ($R=0.97$). The analyses of gersdorffite from Melenica, Mazhiq and Vllahi were plotted on a ternary diagram of the Ni-Co-Fe system (Fig. 2c). Mazhiq and Melenica confirm substitution of Ni by Fe. Moreover, huge miscibility gaps between and disagreement of arsenopyrite and gersdorffite based on (Klemm 1965) indicate low temperature of crystallization between 300-400°C. On a ternary system of Ni-Co-Fe Vllahi gersdorffite Ni seems to be replaced by Co, which is in disagreement with binary plot Ni+Co with Fe. Nevertheless, analyses of Vllahi gersdorffite should be taken with lack of confidence with regard to small amount of measurements points and tiny size of inclusions. Ni-As-Sb-S mineralization of the Pb-Zn deposit within Vardar Zone have been already noticed in the Kizhnica (Mederski 2019, unpublished) and Rogozna ore field (Radosavljevic et al. 2015). Kizhnica gersdorffite tends to be similar to Stan Terg gersdorffite – constituent Fe-poor region in Ni-Co-Fe system, common substitution of Fe by Ni and deficiency in Co. In Kizhnica area, ullmannite within gersdorffite crystals has been found. Rogozna ore field is characterised by complete gersdorffite-ullmannite series. Although, mentioned above, the assemblage exhibits opposite

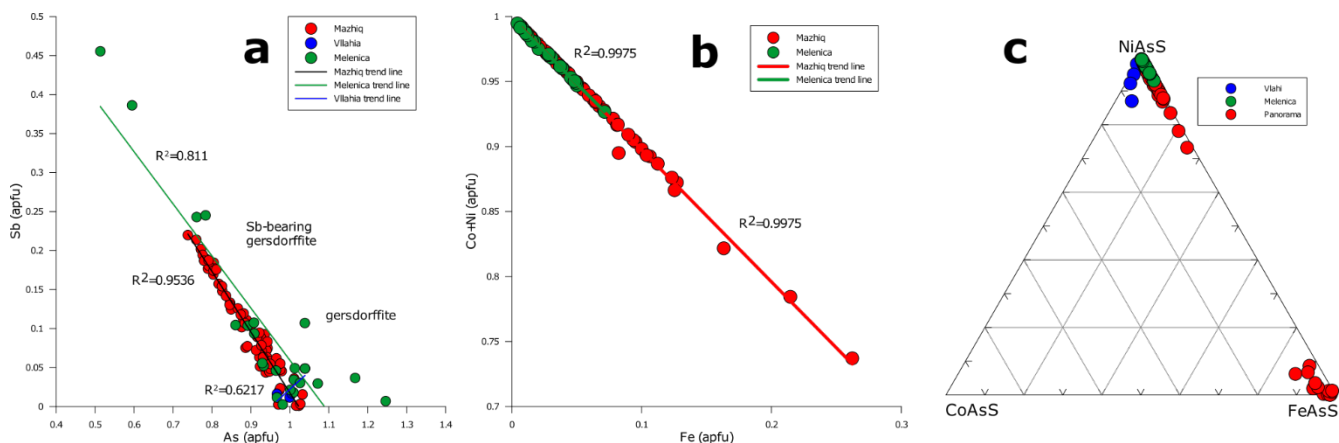


Figure 2. Composition of gersdorffite and Sb-bearing gersdorffite from Stan Terg area on **a.** a binary diagram Sb vs As; **b.** a binary diagram Co+Ni vs Fe; **c.** ternary diagram of NiAsS-CoAsS-FeAsS system.

trends to the Mazhiq and Melenica - As-bearing ullmannite crystallized first and was followed by Sb-bearing gersdorffite.

Textural relations of Melenica gersdorffite, rimming violarite, bravoite or siegenite and transformation of sulphides to sulphoarsenides exhibit slight drop in sulphur fugacity and slight increase in arsenic fugacity. Associations of Melenica gersdorffite is familiar with “km3” district within Lavrion district in Greece where deposition of Ni sulphides was followed by formation of gersdorffite (Voudouris et al. 2018). However, the originate of Lavrion district is assumed to be from intrusion of a Miocene granodiorite body and related to felsic and mafic dikes and sills. This can be excluded in our region of investigation. In addition, occurrence of native bismuth and Bi-rich sulphosalts were observed.

Leaching and remobilization of Co, Ni, Fe and As from mafic and ultramafic is favoured for Bou Azzer deposit (Ahmed et al. 2009). However, at Bou Azzer, where no Bi-minerals were reported, acidic magmatic fluids under moderately reducing conditions at high fluid ratio leached Co, Ni, Fe and As from serpentinites. In comparison to Bou Azzer, Stan Terg district is depleted with precious metals and Co, which may refer to relatively high bulk content of these elements in serpentinites.

Oscillatory zoned gersdorffite was reported from San Juan de Plan deposit in Spain (Fanlo et al. 2004) and the high grade Ni-Co-Fe-As hydrothermal ore veins from Dobšiná in Slovakia (Kiefer et al. 2017). The oscillatory variations in As, Sb, Ni and Co content of individual zones observed within Mazhiq gersdorffite suggest physical or chemical fluctuations within the bulk system and disequilibrium in the ore fluids.

Acknowledgements

Research was founded by AGH-UST Rector Grant assigned to Studenckie Koło Naukowe Geologów. Authors are grateful to Mr. Adam Włodek from Critical Elements Laboratory AGH-KGHM in Kraków for conducting EMPA analyses.

References

- Ahmed AH, Arai S, Ikenne M (2009) Mineralogy and paragenesis of the Co-Ni arsenide ores of Bou Azzer, Anti-Atlas, Morocco. *Econ. Geol.* 104:249–266.
- Bayliss P (1967) The crystal structure of gersdorffite. *Mineral. Mag.* 36:38–42.
- Bayliss P (1982) A further crystal structure refinement of Gersdorffite. *Am. Mineral.* 67:1058–1064.
- Bayliss P, Stephenson NC (1968) The crystal structure of gersdorffite (III), distorted and disordered pyrite structure. *Mineral. Mag.* 36:940–947.
- Borojević-Šoštaric S, Palinkaš LA, Neubauer F, Hurai V, Cvetković V, Roller-Lutz Z, Mandić M, Genser J (2013) Silver-base metal epithermal vein and listwanite hosted deposit Crnac, Rogozna Mts., Kosovo, part II: A link between magmatic rocks and epithermal mineralization. *Ore Geol. Rev.* 50:98–117.
- Fanlo I, Subial, Gervilla F, Panaiagua A, Garcia B (2004) The composition of Co–Ni–Fe sulfarsenides, diarsenides and triarsenides from the San Juan de Plan deposit. *Central Pyrenees, Spain. Can. Mineral.* 42:1221–1240.
- Hyseni M, Durmishaj B, Fetahaj B, Shala F, Berisha A, Large D (2010) Trepça Ore Belt and Stan Terg mine – Geological overview and interpretation, Kosovo (SE Europe). *Geologija* 51:87–92
- Kiefer S, Majzlan J, Chovan M, Števko M, (2017) Mineral composition and phase relations of the complex sulfarsenides and arsenides from Dobšiná (Western Carpathians, Slovakia). *Ore Geol. Rev.* 89:894–908.
- Klemm DD, (1965) Synthesen und analysen in den dreiecksdiagrammen FeAsS–CoAsS–NiAsS und FeS₂–CoS₂–NiS₂. *Neues Jahrb. Mineral. Abh.* 103:205–255.
- Miletić G, (1995) The structure of the lead and zinc deposit “Crnac”. In: Janković, S. (Ed.), *Geology and Metallogeny of the Kopaonik*
- Radosavljević SA, Stojanović JN, Vuković NS, Radosavljević-Mihajlović AS, Kašić VD, (2015) Low-temperature Ni-As-Sb-S mineralization of the Pb(Ag)-Zn deposits within the Rogozna ore field, Serbo-Macedonian Metallogenic Province: Ore mineralogy, crystal chemistry and paragenetic relationships. *Ore Geol. Rev.* 65:213–227.
- Voudouris P, Melfos V, Spry PG, Bonsall T, Tarkian M, Solomos C (2008) Carbonate replacement Pb-Zn-Ag±Au mineralization in the Kamariza area, Greece: mineralogy and thermochemical conditions of formation. *Miner. Petrol.* 94:85–106.
- Yund RA, (1962) The system Ni-As-S; phase relations and mineralogical significance. *Am. J. Sci.* 260:761–782.

Thalcusite - a new mineral from the Kupferschiefer, Sieroszowice deposit, Poland

Jadwiga Pieczonka¹, Adam Piestrzyński¹, Roman Jedlecki²

¹AGH-UST, Faculty of Geology, Geophysics and Environmental Protection, Krakow, Poland

²KGHM-Polska Miedź S.A., Poland

Abstract. Here we report the first discovery of thallium copper sulfide in Poland. Thalcusite - $Tl_2Cu_3FeS_4$ was found in the Kupferschiefer horizon in the Sieroszowice Mine. This horizon contains an economic concentration of copper. Thalcusite occurs in association with native-Ag, stromeyerite, galena, sphalerite, chalcocite and covellite. The presence of thallium minerals suggests a low temperature stage in the famous Cu-Ag Kupferschiefer type deposits in Poland. The calculated chemical composition is as follows: $Tl_{2.023}Cu_{3.025}Fe_{0.909}S_{3.989}$

1 Introduction

There are only few places with occurrences of thallium minerals in the World. Two of the most important occurrences are known in Europe. The first place is located in Macedonia. The Allchar deposit has been known since the Roman Empire but now it is an abandoned mine. An Sb-As-Tl mineral association was documented by Jankovic (1989). A second locality is in Lengenbach quarry Binntal valley, Switzerland. This deposit is characterized by Pb-Zn-As-Ba-Tl mineralization (Hofmann and Kniel 1996). Two deposits are also known from China. Nanhua deposit in Yunnan Province (Zhang et al. 1996), and Lanmuchang deposit in Guizhou province (Zhang et al. 1997). Au-As-Tl mineralization is also common in Carlin-type deposits (Percival and Radtke 1993).

The Lubin-Sieroszowice Cu-Ag deposit is relatively well recognized. For more than 50 years there has been intensive underground mining. Each year 0.7 sq. km of deposit is mined out. This gives the opportunity to have continuous access to a new section of this giant deposit. Additional data comes from both drilling and regular channel sampling. All mentioned deposits are recognized as a low temperature hydrothermal deposits located within the clastic carbonate organic-rich sediments.

2 Geological setting

In the Lubin area (Sieroszowice Mine) thalcusite was found in samples from the drill core which was recovered from the one of the underground exploration drillings. Position of the sample is difficult to assess. The sample was taken 114 m away from the mining corridor. The sample represents typical carbonate ore containing economic copper grade. This dolomite is characterized with presence of anhydrite-gypsum micro nests with secondary dolomite – calcite sparite occurring on the border with the host rock. In this deposit more than 140 minerals have been identified. Thalcusite was found in

the profile characterized with presence of a secondary oxidation system (SOS) (Piestrzyński and Pieczonka 1997; Pieczonka and Piestrzyński 2008).

3 Analytical methods

All samples were examined with optical microscope and EDS EM using a Quanta-Fei electron microscope. Quantitative WDS analyses were carried out in the Critical Elements Laboratory of the Faculty of Geology, Geophysics and Environmental Protection, AGH-UST Cracow using a JEOL SQ8200 microprobe (EMP). The EMP was operated in the wavelength-dispersive mode at an accelerating voltage of 20 kV, and a probe current of 40 nA, with a focused beam diameter of 1 μ m. The following standards and measurement lines have been used: SK α , FeK α (Pyrite), AgL α (100 %), CuK α (CuFeS₂), TlM α (Lorandite), SbL α (Sb₂S₃), AuM α (100%), HgM α (HgSe), AsL α (As₂S₃), SeL α (PbSe) Counting times on peak/background (in sec.) were as follows 10/5. Original Jeol ZAF procedures were used for a final correction of all measured elements.

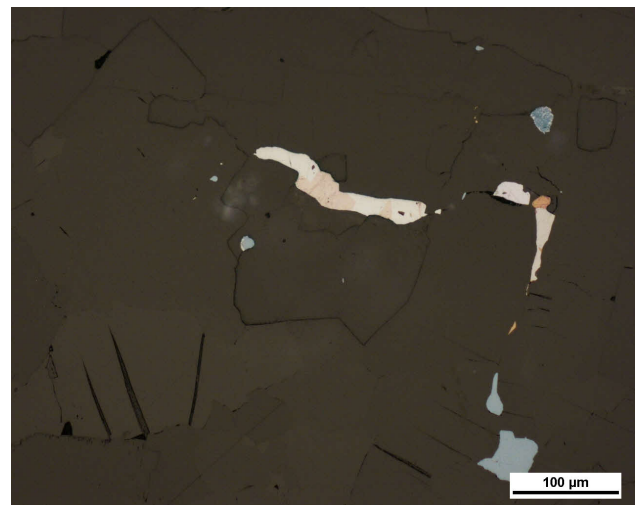


Fig. 1. Intergrowth of thalcusite with chalcocite in the carbonate nest. In the vicinity bornite, and covellite are present. Reflected light

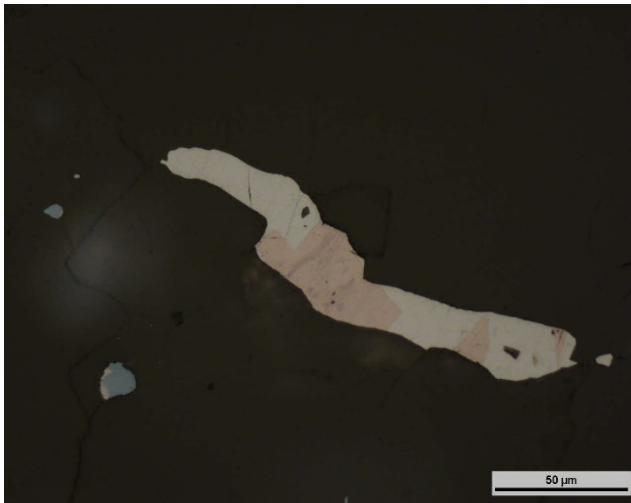


Fig. 2. Intergrowth of thalcosite with Chalcocite. Reflected light, magnification from fig. 1

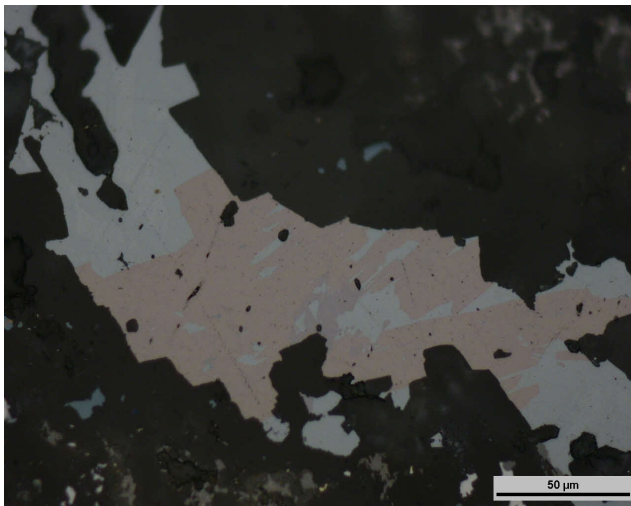


Fig. 3. Intergrowth of thalcosite with chalcocite. Reflected light.

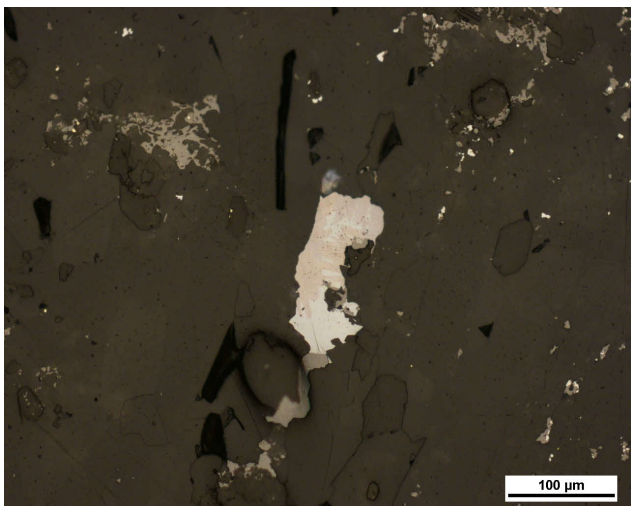


Fig. 4. Intergrowth of galena with thalcosite, black is organic matter Reflected light.

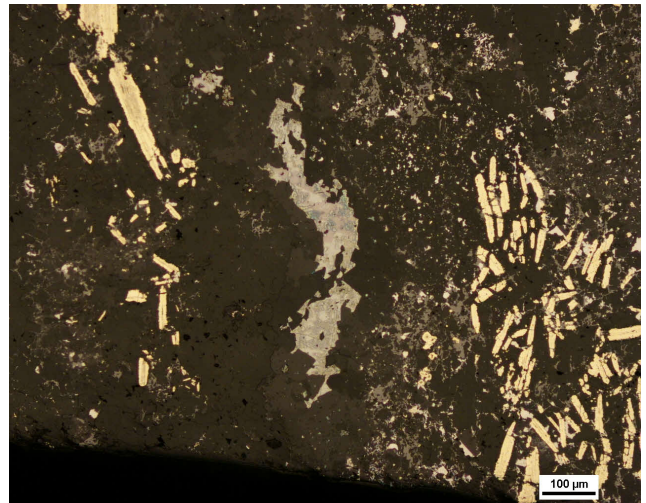


Fig. 5. Position of thalcosite - chalcocite agregate in the ore containing pyrite – sphalerite and covellite. Reflected light

4 Mineralogy and geochemistry

Thalcosite was initially recognized as luzonite (Cu_3AsS_4). It is characterized with a very similar white-pink-lilac color, visible bi-reflectance and anisotropy. Thalcosite often forms intergrowths with copper sulfides like chalcocite (Fig. 1, 2, 3), digenite and covellite. In the nearest vicinity, galena, sphalerite, pyrite (Fig. 5) and stromeyerite have also been noted. Framboidal pyrite as well as bornite are very common in the dolomite matrix. Locally pyrite forms elongated aggregates (Fig. 5) which are probably result of the replacement of organogenic remnants. The host rock is dolomite with minor secondary calcite which rimmed gypsum-anhydrite nests. Secondary nests are composed of elongated gypsum and anhydrite crystals often replaced by younger copper sulfides and idiomorphic calcite sparite (Fig. 3). In the both dolomite matrix and sulphate nests organic matter forming irregular concentrations and free space filling are observed (Fig. 4).

All analyzed thalcosite grains reveal almost stoichiometric composition (Table 1). The average content of major elements is as follow: TI – 53.12 wt%, Cu- 26.692 wt%, Fe- 6.751 wt% and S- 16.426 wt% (Table 1). Small amounts of Ag, Sb, Au and As were also documented (Table 1). From all the measured admixtures in thalcosite, gold content seems to be possible. The average content of Au is on the level of 0.087 wt% and maximum concentration reach 0.139 wt% (Tab. 1) In point 9 - 0.056 wt% of Se was additionally measured (Table 1). Standard deviation (s.d) and coefficient of variability (C.o.V) of all measured elements are as follow: for S- 0.120 and 0.73%, Cu- 0.225 and 0.91%, TI- 0.504 and 0.95% and Fe- 0.13 and 1.93% respectively. The statistic parameters of minor elements are much higher (Table 1) and in the case of As, coefficient of variability overprint 100%. Very low statistical parameters of major constituents confirm also high quality of WDS analyses. Based on WDS measurement the atomic proportions have been calculated (Table 2). The average atomic composition of thalcosite is as follows:

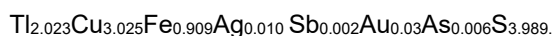


Table 1. WDS composition of thalcosite in wt%

no	SKα	AgLα	CuKα	FeKα	TiMα
1	16,394	0,104	24,562	6,796	52,594
2	16,598	0,168	24,817	6,655	53,980
3	16,280	0,233	24,891	6,575	52,704
4	16,415	0,129	24,616	6,588	53,588
5	16,493	0,042	24,611	6,754	52,830
6	16,542	0,165	24,214	6,914	53,005
8	16,481	0,069	24,914	6,930	52,477
9	16,498	0,184	24,980	6,874	53,083
10	16,353	0,148	24,595	6,771	53,226
17	16,210	0,179	24,716	6,648	53,713
Avg.	16,426	0,142	24,692	6,751	53,120
s.d	0,120	0,057	0,225	0,131	0,504
C.o.					
V	0.73%	40.36%	0.91%	1.93%	0.95%

Hg- sought but not detected

Table 1 continued

no	SbLα	AuMα	AsLα	Total	Comment
1	0,055	0,035	0,065	100,605	AP467 Fot9_p3
2	0,043	0,068	0,140	102,469	AP467 Fot7_p1
3	0,021	0,133	0,105	100,942	AP467 Fot7_p2
4	0,023	0,049	0	101,408	AP467 Fot9_p1
5	0,007	0,059	0,046	100,842	AP467 Fot9_p2
6	0,040	0,056	0,049	100,985	AP467 Fot9_p3
8	0,021	0,096	0	100,988	AP467 Fot10_p2
9	0,040	0,107	0,180	102,002	AP467 Fot10_p3
10	0,012	0,124	0	101,229	AP467 Fot10_p4
17	0	0,139	0	101,605	Ja21-G-fot5_p4
av.	0,026	0,087	0,059	101,308	
s.d	0,018	0,038	0,065	0,576	
C.o.V	67.5%	43.7%	110%	0.57%	

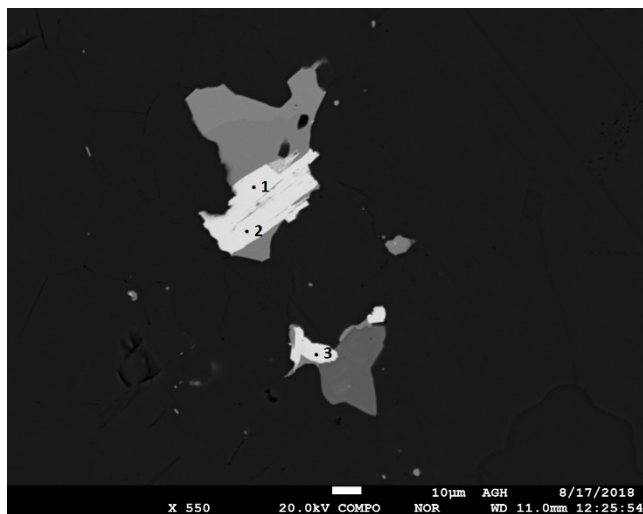


Fig. 6. BSE image of thalcosite (white) and copper sulphides, 1, 2, 3 analytical points, sample A467 Fot9

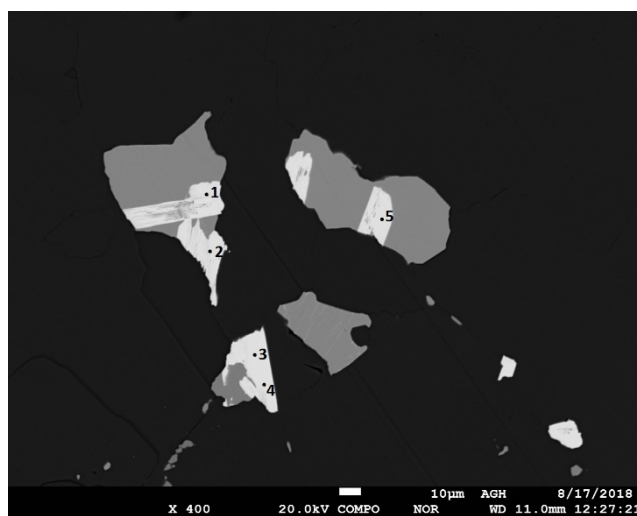


Fig. 7. BSE image of thalcosite (white) and copper sulphides, 1, 2, 3, 4, 5 analytical points, sample AP 467 Fot. 10

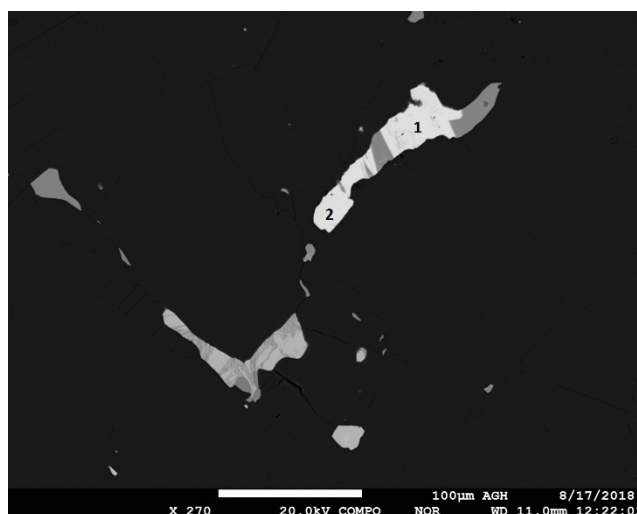


Fig. 8. BSE image of thalcosite (white) and copper sulphides, 1, 2 analytical points, sample AP 467 Fot. 7, compare fig. 1

Table 2. Atomic proportions based on WDS quantitative measurements (Table 1) and apf calculation for 10 atoms

No.	SKα	AgLα	CuKα	FeKα	TiMα	SbLα
1	3.9969	0.0075	3.0211	0.9512	2.0115	0.0035
2	3.9958	0.0120	3.0140	0.9196	2.0386	0.0027
3	3.9687	0.0168	3.0612	0.9200	2.0155	0.0013
4	3.9964	0.0093	3.0234	0.9207	2.0466	0.0014
5	4.0112	0.0030	3.0196	0.9429	2.0155	0.0004
6	4.0216	0.0119	2.9698	0.9649	2.0215	0.0025
8	3.9904	0.0049	3.0431	0.9631	1.9931	0.0013
9	3.9701	0.0131	3.0325	0.9495	2.0038	0.0025
10	3.9822	0.0106	3.0215	0.9465	2.0331	0.0007
17	3.9538	0.0129	3.0414	0.9308	2.0553	0.00
Av.	3.989	0.010	3.025	0.909	2.023	0.002
s.d.	0.020	0.004	0.024	0.093	0.020	0.001
C.o.V	0.51%	40.50%	0.79%	10.19%	0.97%	69.23%

Table 2 continued

No.	AuMα	AsLα	Total	Comment
1	0.0014	0.0068	100.505	AP-467 Fot9 p3
2	0.0026	0.0144	102.469	AP-467 Fot7 p1
3	0.0052	0.0110	100,942	AP467 Fot7 p2
4	0.0019	0.00	101,408	AP467 Fot9 p1
5	0.0023	0.0047	100,842	AP467 Fot9 p2
6	0.0022	0.0051	100,985	AP467 Fot9 p3
8	0.0037	0.00	100,988	AP467 Fot10 p2
9	0.0042	0.0185	102.002	AP467 Fot10 p3
10	0.0049	0.00	101,229	AP467 Fot10 p4
17	0.0055	0.00	101,605	Ja21-G-fot5 p4
Av.	0.003	0.006	101.298	
s.d..	0.001	0.007	0.590	
C.o.V	44.16%	110.04%	0.58%	

5 Discussion

The discovery of thalcosite which usually occurs in hydrothermal environments may be an important factor in discussions of the genesis of Kupferschiefer type deposit, which belong to the low temperature family (Borg et al. 2012). Most of the ore minerals were precipitated in temperatures below 100°C degree. This mineral has been also documented in VMS type deposits (Kovalenker et al. 1976) and alkaline complexes Karup-Moeller (2001), but in these cases, the temperature of precipitation might be higher.

For more than 200 years discussion on deposit genesis has continued in international publications. Till now more than 600 publications were already published. The copper deposit was described in over 600 papers and books, e.g. Harańczyk (1972); Kucha and Pawlikowski (1986); Vaughan et al. (1989); Wodzicki and Piestrzyński (1994); Piestrzyński (2007); Borg et al. (2012) and many others. The mineralogy of this deposit was described in details by Piestrzyński (2007); Pieczonka and Piestrzyński (2000, 2008); Pieczonka et al. (2007). In general, copper sulphide mineralization transgresses all sediments close to the Lower-Upper Permian border. The Kupferschiefer organic shale contains the highest metals concentrations, however i.e. the Permian Weissliegende sandstone that overlies Rotliegende sandstone, host the biggest Cu-Ag reserves. In samples from the deposit thallium wasn't recorded in the bulk chemical analyses. In the Lubin-Sieroszowice deposit thalcosite have been detected within the dolomite type of ore, containing numerous of carbonate - sulphate micro-nests. The pink-lilac color and the reflectivity of thalcosite are very similar to the one of mineral from the bornite family. Therefore, during the standard microscopic observations it is very easy to miss this mineral. This work described the place and new localization of thalcosite in the World.

Acknowledgements

The authors are grateful to MSc eng. Gabriela Kozub-Budzyn for WDS measurements and the AGH-UST for

the financial support, grant 11.11.140.161.

References

- Borg G, Piestrzyński A, Bachman GH, Puttmann W, Walther Sabine, Fidler M (2012) An overview of the European Kupferschiefer deposits. SEG Special Publication 16:455-486
- Harańczyk C (1972) Ore mineralization in the lower Zechstein euxenic sediments in the Fore-Sudetic monocline. *Archiwum Mineralogiczne* XXX:1-172. (in Polish)
- Hofmann BA, Knill MD (1996) Geochemistry and genesis of the Lengnabach Pb-Zn-As-Tl-Ba-mineralization, Binn Valley, Switzerland. *Miner Deposita* 31:319-339
- Jankovic S, (1989) Sb-As-Tl mineral association in the Mediterranean region. *Inter Geol Rev* 31: 262-273
- Karup-Moeller S, Makovicky E (2001) Thalcosite from Nakkaalaaq, the Ilimaussaq alkaline complex, South Greenland, South Greenland, *Geology of Greenland Survey Bulletin* 190:127-130
- Kovalenker VA, Laputina IP, Evstigneeva TL, Izoitko VM (1976) Thalcosite, $Cu_3-xTl_2Fe_{1+x}S_4$, a new thallium sulfide from copper-nickel ores of the Talnakh deposits. *Zap Vses Mineral Obshch* 105: 202–206 (in Russian)
- Kucha H, Pawlikowski M (1986) Two-brines model of the genesis of strata-bound Zechstein deposits (Kupferschiefer type), Poland. *Miner Deposita* 21: 70-80
- Zhang Z, Zhang X, Zhang B, Chen Y, Gong G (1996) Topomorphic characteristics of realgar in the Nanhua As-Tl deposit. *Acta Miner Sin* 16:315-320
- Zhang B, Zhang Z, Zhang X, Chen G (1997) A research into environmental Geochemistry of Lanmunchang thallium deposit in Xingren of Guizhou Province. *Guizhou Geology* 14:71-77
- Percival TJ, Radtke AS (1999) Thallium in disseminated replacement gold deposits of the Carlin-type; a preliminary report. *Neues Jahrbuch fuer Mineralogie Abhandlungen* 166:65-75
- Pieczonka J (2000) Oxidation zones in the copper deposit in Fore-Sudetic monocline. *Prace Specjalne PTMin* 16:9-54. (in Polish)
- Pieczonka J, Piestrzyński A (2000) Genetical model of Au concentration in the area of Copper deposit in the Fore-Sudetic monocline. *Prace Specjalne PTMin* 16:55-82. (in Polish)
- Pieczonka J, Piestrzyński A (2008) Mineralogy and geochemistry of ore minerals from secondary oxidized zones. In: Pieczonka et al. 2008: The red-bed-type precious metal deposit in the Sieroszowice-Polkowice copper mining district, SW Poland. *Annales Societatis Geologorum Poloniae* 78/ 3:195-241
- Piestrzyński A (2007) Historical development of opinions on genesis of copper ore deposit in Fore-Sudetic monocline – discussion. *Biuletyn Państwowego Inst Geol* 423:69-76. (in Polish)
- .Piestrzyński A, Pieczonka J (1997) Noble metals from the Kupferschiefer-type deposits, Lubin-Sieroszowice, SW Poland. In: *Mineral Deposits: Research and Exploration*, Heikki Papunen ed. Turku: 563-566
- Vaughan DJ, Sweeney M, Diedle GFR, Harańczyk C (1989) The Kupferschiefer: an overview with an appraisal of the different types of mineralization. *Econ Geol* 84:1003-1927
- Wodzicki A, Piestrzyński A (1994) An ore genetic model for the Lubin-Sieroszowice mining district, Poland. *Miner Deposita* 29:30-43

Nickel in shungite deposits

Connor Brolly, John Parnell
University of Aberdeen, Scotland, UK

Abstract. Hydrothermal fluids are a major medium for metal redistribution and deposition in the Earth's crust. The spatial relationship of metallic ores and hydrocarbons suggests that fluid hydrocarbons play a role in the transportation of metals and can be found in sufficient quantities to be economically exploitable. Examples of these include Carlin-type and Mississippi Valley-type (MVT) deposits. Paleoproterozoic carbonaceous metasediments are host to several metal-rich deposits across Scandinavia and Russia. Ni occurs in the low-grade black-shale hosted Talvivaara deposit, Finland, which has been intermittently mined since 2008.

This study aims to investigate mineralization found in shungite, a carbonaceous metasediment from Karelia, Russia as an analogue to mineralization found at the Talvivaara deposit. Two samples of shungite were analysed using SEM. The first sample which was dull and bedded-type shungite, showed no evidence of metal enrichment. The second sample from a vein-type shungite, a product of hydrocarbon migration, showed an enrichment of Ni, which demonstrates that Ni was transported by hydrocarbons. Given the similarity and proximity of shungite deposits and the Talvivaara host rocks, we infer that hydrocarbons played a role in metal transport in Ni mineralization.

1 Ore deposits associated with hydrocarbons

Aqueous solutions are the normal medium of metal transport, other than magmatic fluids, capable of concentrating metals into ore deposits (Migdisov et al. 2017). The role of hydrocarbons for metal concentration is usually as a reductant, reducing metals out of solution, as opposed to an organo-metallic fluid which transports metals (Banks 2014). There is however an increasing body of evidence which suggests that hydrocarbons play a role in metal transport, when spatially associated with metallic ores (Watkinson 2007; Williams-Jones and Migdisov 2007). Carlin-type deposits in Nevada are the second largest type of Au deposits in the world associated with hydrocarbons. Au and other metals were remobilized and transported as organic-metallic fluids during hydrocarbon migration (Emsbo and Koenig 2007). Mississippi Valley-type (MVT) deposits which are epigenetic, carbonate-hosted sulphide bodies are a major source of lead and zinc resources (Anderson and Macqueen 1982; Paradis et al. 2007). Oil inclusions associated with MVT deposits contain high concentrations of metals compared with natural crude oils. This is thought to be a result of oil and metal-rich brines interacting, which mobilizes metals (Banks 2014).

2 Ni in Paleoproterozoic carbonaceous metasediments

The Talvivaara Ni-Cu-Zn-Co deposit, Finland is the largest black-shale hosted deposit in the world. It has been mined intermittently since 2008 and has an estimated resource of 1550 Mt of ore with 2.22% Ni, 0.13% Cu, 0.02% Co and 0.49% Zn (Talvivaara Mining Company 2011). The sediments are rich in organic carbon (7.6 %) which is graphitic. Talvivaara is located near the Archean-Proterozoic boundary in the mining district of Outokumpu (Loukola-Ruskeeniemi and Lahtinen 2012). It was discovered in 1977 and was originally considered uneconomic but became economic through developments in extraction techniques. At full production an estimated 50,000 tonnes of nickel was extracted (Kontinen 2012). The deposit is located in the Karelia schist belt and occurs as two ore bodies (Kuusilampi and Kolmisoppi) over 2 km. The Ni enrichment in the black schists at Talvivaara is a result of increased Ni concentration in Paleoproterozoic seawater (Konhauser et al. 2009), and the spatial association of ultramafic intrusions (Loukola-Ruskeeniemi et al. 1991).

Shungite rocks from the Zazhogino deposit, found near lake Olega, Karelia, Russia, are of the same age, and found in close proximity to the Talvivaara deposit (Fig. 1). This deposit contains an estimated 25×10^{10} tonnes of organic carbon and represents one of the richest accumulations of organic material from the Paleoproterozoic. Ni in shungite has a median abundance of 390 ppm (Melezhik et al. 1999), significantly higher than the global median of 70 ppm in black shales (Ketrin and Yudovich 2009). The analysis of shungite for metal enrichment could give a useful insight to the role of migrating hydrocarbons for ore transport at Talvivaara, and other Paleoproterozoic black schists.



Figure 1. Geographic locations of the Talvivaara and Zazhogino deposits.

3 Samples

3.1 Shungite

The highly carbonaceous rocks of the Shunga district, found northwest of Lake Onega, Karelia in Russia called shungite (Inostrantsev 1879), has been mined for its technical properties - including the use as an antifriction agent, electromagnetic shielding and ecological remediation through adsorption (Solovov et al. 1990; Efremov et al. 2013). Bedded and vein shungite represent the source rock and migration product of a

petroleum system (Melezhik et al. 1999; Melezhik et al. 2004).

Two samples were analysed by scanning electron microscopy (SEM) in this study; a dull, bedded-type shungite, and a bright vein-type shungite, the latter of which is a product of hydrocarbon migration.

Figure 2A-C are images of bedded-type shungite which is rich in authigenic orthoclase feldspars. The bedded texture is evident in figure 2A, and shows dark shungite bands, interbedded with quartz and orthoclase feldspar. Orthoclase feldspars display overgrowths of the same mineralogy shown in figure 2C. Similar mineralogy and textures are observed by Parnell et al. (1994).

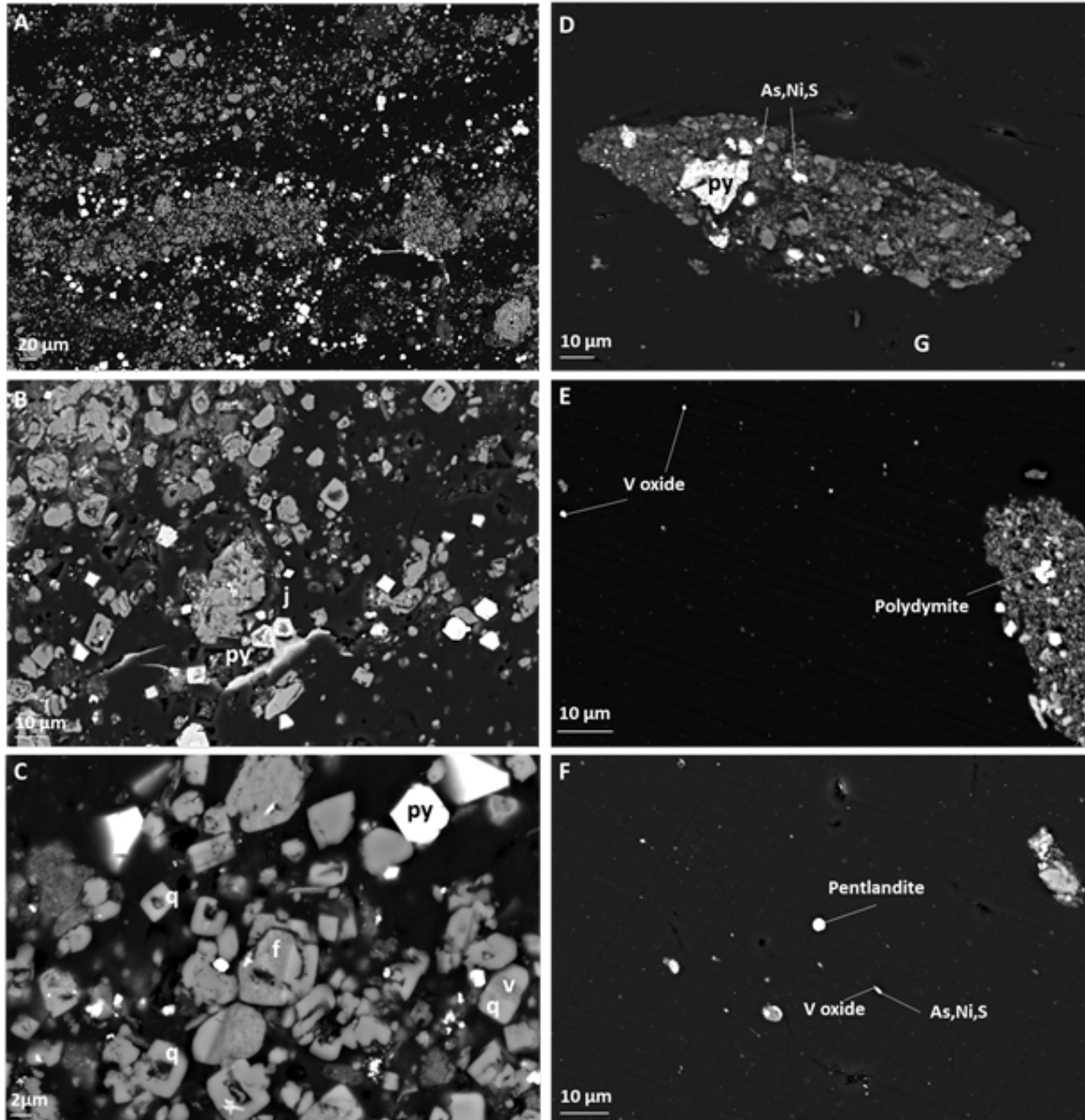


Figure 2. SEM images of shungite. (A-C) – bedded-type shungite with orthoclase feldspars (f), quartz (q), pyrite (py) and vanadium mica (v). (D-F) - bright, vein-type shungite with mineral inclusions and Ni phases, graphite (G).

Pyrite is abundant and occasionally occurs with trace levels of arsenic. Pyrite as recrystallized framboids occur in all types of shungite (Melezhik et al. 2004). Vanadium mica can also be seen in the mineral rich bands. The bedded-type shungite shows no Ni mineralization.

Figure 2D-F are images of vein-type shungite which is typically characterized by mineral inclusions in a carbonaceous matrix which was also observed by Strakhov (2007). Mineral inclusions show preferential orientation, indicating fluid migration. Nickel is more abundant in the mineral inclusions and can be seen in gersdoffite and polydymite (a weathering product of pentlandite) and occurs as isolated pentlandite spheroids in the matrix. Vanadium oxide is abundant in the matrix and is observed as isolated grains and adhered to an As, Ni and S phase interpreted to be gersdoffite. The Ni mineralogy in vein-type shungite described here are similar to that found in the black schists at Talvivaara which are rich in pentlandite (Riekkola-Vanhanen 2010).

4 Origin of and mobilization of Ni in shungite

Ni naturally occurs in hydrocarbons at concentrations of several hundred ppm, compared with other trace metals (<20 ppm) (Banks 2014). In addition, Paleoproterozoic seawater had elevated levels of Ni (Konhauser et al.

2009; Loukola-Ruskeeniemi and Lahtinen, 2012), which could account for the widespread distribution of Ni in the Talvivaara metasediments. The black schists are spatially associated with ophiolitic rocks in Jormua, Finland (Loukola-Ruskeeniemi et al. 1991), which would have been a major source of Ni and other metals, enriching the surrounding metasedimentary host rock (Loukola-Ruskeeniemi et al. 1991). Black shale does not tend to be Ni-rich, with a global median Ni content of 70 ppm (Ketris and Yudovich 2009), therefore Ni in high concentrations must be sourced from elsewhere. Melekestseva et al. (2013) showed that a high Ni/Co ratio is consistent with an ultramafic source.

The rocks at the Zazhogino deposit are analogous to the rocks of the Talvivaara, given that they are the same age, and are carbonaceous rocks spatially associated with ultramafic rocks. The two deposits are located around 200 km apart. Hydrocarbons could have played a role as an ore fluid, scavenging and transporting metals throughout the Karelia Schist belt during the Paleoproterozoic.

The process of Ni mobilization in shungite is summarized in a schematic sketch (Fig. 3). Hydrocarbons liberated from carbon-rich shungite rocks, migrated and scavenged Ni from ultramafic rocks and mineralized as bright vein-type shungite within joints and bedding planes (Melezhik et al. 1999) rich in Ni.

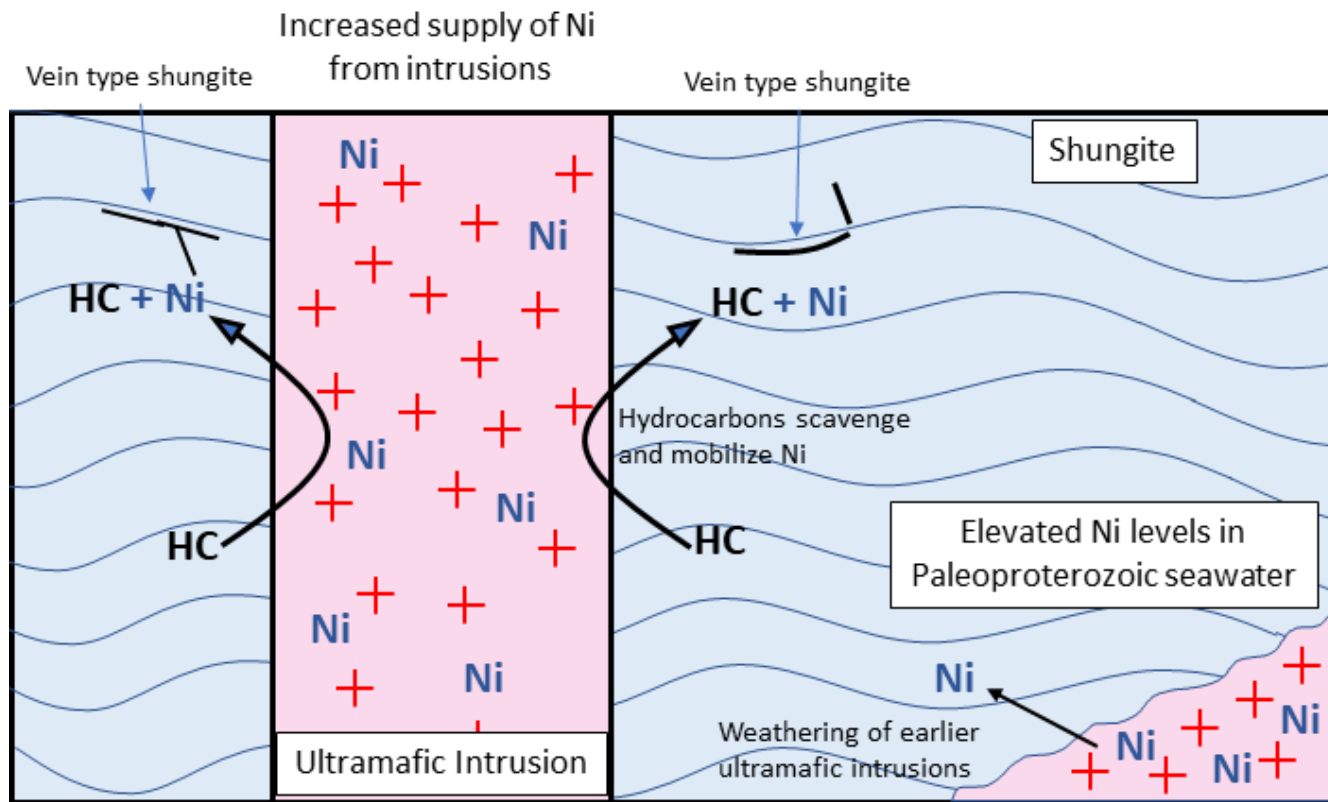


Figure 3. Schematic sketch of Ni mobilization in shungite. Liquid hydrocarbons from bedded-type shungite scavenge Ni from cross-cutting ultramafic intrusion and are mineralized as vein-type shungite in joints and bedding planes. Ni could also be supplied to the depositional environment from weathering of earlier ultramafic intrusions. HC – hydrocarbons, Ni-nickel.

Acknowledgements

This work was supported by NERC grant RG12966-10.

References

- Anderson GM, Macqueen RW (1982) Ore deposit models - 6. Mississippi Valley-type lead-zinc deposits: *Geosci Can* 9:108-117
- Banks DA (2014) Transport of metals by hydrocarbons in MVT deposits. *Acta Geol Sin* 88:145-146
- Efremov S, Nechipurenko S, Kazankapova M, Washington W, Tassibekov K, Nauryzbaev M (2013) Physico-chemical characteristics of shungite rock of Kazakhstan. *Eurasian Chem Tech Jour* 15:241-249
- Emsbo P, Koenig AE (2007). Transport of Au in petroleum: evidence from the northern Carlin trend, Nevada. In: Andrew CJ, Borg G (eds) *Digging Deeper, Proceedings of the Ninth Biennial SGA Meeting*. Irish Assoc for Econ Geol pp 695–698
- Inostrantsev AA (1879) New extreme example in the series of amorphous carbon. *Gornoi Jour* 2:314-342 (in Russ)
- Ketris MP, Yudovich YaE (2009) Estimations of Clarkes for carbonaceous biolithes: World averages for trace element contents in black shales and coals. *Int Jour of Coal Geol* 78:135-148
- Konhauser KO, Pecoits E, Lalonde SV, Papineau D, Nisbet EG, Barley ME, Arndt NT, Zahnle K, Kamber BS (2009) Oceanic nickel depletion and a methanogen famine before the Great Oxidation Event. *Nature* 458:750–754
- Kontinen A (2012) F029 Talvivaara Ni-Zn-Cu. In: Eilu P (ed) *Mineral Deposits and Metallogeny of Fennoscandia*, *Geol Surv of Finl*, pp 276-280
- Loukola-Ruskeeniemi K (1991) Geochemical evidence for the hydrothermal origin of sulphur, base metals and gold in Proterozoic metamorphosed black shales, Kainuu and Outokumpu areas, Finland. *Miner Deposita* 26:152–164
- Loukola-Ruskeeniemi K, Lahtinen H (2012) Multiphase evolution in the black-shale-hosted Ni–Cu–Zn–Co deposit at Talvivaara, Finland. *Ore Geol Rev* 52:85-99
- Melezhik VA, Fallick AE, Filippov MM, Larsen O (1999) Karelian shungite—an indication of 2.0-Ga-old metamorphosed oil-shale and generation of petroleum: geology, lithology and geochemistry. *Earth-Sci Rev* 47:1-40
- Melezhik VA, Filippov MM, Romashkin AE (2004) A giant Paleoproterozoic deposit of shungite in NW Russia: genesis and practical applications. *Ore Geol Rev* 24:135-154
- Melekestseva IYu, Zaykov VV, Nimis P, Tret'yakov GA, Tessalina, SG (2013) Cu–(Ni–Co–Au)-bearing massive sulfide deposits associated with mafic–ultramafic rocks of the Main Urals Fault, South Urals: Geological structures, ore textural and mineralogical features, comparison with modern analogs. *Ore Geol Rev* 52:18–36
- Migdisov AA, Guo X, Xu H, Williams-Jones AE, Sun CJ, Vasyukova O, Sugiyama I, Fuchs S, Pearce K, Roback R (2017) Hydrocarbons as ore fluids. *Geochem Persp Lett* 5:47-52
- Paradis S, Hannigan MD, Dewing K (2007) Mississippi Valley-Type lead-zinc deposits. In: Goodfellow WD (ed) *Mineral deposits of Canada: A synthesis of major deposit types, district metallogeny, the evolution of geological provinces, and exploration methods*. *Geol Assoc of Can, Mineral Deposits Division, Spec Pub* 5:185-203
- Parnell J, Carey PF, Bottrell SH (1994) The occurrence of authigenic minerals in solid bitumens. *Jour of Sediment Res* 64:95-10
- Riekkola-Vanhanen M (2010) Talvivaara Sotkamo mine — bioleaching of a polymetallic nickel ore in subarctic climate. *Nova Biotechnol* 10-1:7–14
- Solovov VK, Tupolyev AG, Zaidenberg AZ, Zveryev AA, Kalinin YuK (1990) Electromagnetic spectral analysis of conducting composites. In Fridlyander IN, Kostikov VI (eds) *MICC-90 Moscow Int Composites Conf*. Elsevier, pp 343-347.
- Strakhov VM (2008) Structure and physiochemical properties of Karelian shungite. *Solid Fuel Chem* 42:4-9
- Talvivaara Mining Company (2011). Stock Exchange Release van Zuilen MA, Fliegel D, Wirth R, Lepland A, Qu Y, Schreiber A, Romashkin AE, Philippot P (2012) Mineral-templated growth of natural graphite films. *Geochim et Cosmochim Acta* 83:252-262
- Watkinson P (2007) Deposition from crude oils in heat exchangers. *Heat Transf Eng* 28:177–184
- Williams-Jones AE, Migdisov AA (2007) The solubility of gold in crude oil: implications for ore genesis. In: Andrew CJ, Borg G (eds) *Digging Deeper, Proceedings of the Ninth Biennial SGA Meeting*. Irish Assoc for Econ Geol pp 765-768

Coastal garnet and magnetite sands in the Erongo and Kunene regions of Namibia

Stephanie Lohmeier, Bernd Lottermoser, Alexander Hennig

RWTH Aachen University, Institute of Mineral Resources Engineering, Germany

Daniela Gallhofer

University of Graz, Institute of Earth Sciences, Austria

Abstract. Coastal placers are present in the Erongo and Kunene regions of Namibia at current and past shorelines. The thickness of these mineral sands varies distinctly, being mostly at the dm-scale. The placer horizons consist of alternating mm to cm thick strata enriched in heavy minerals (pink-red-black) and quartz-rich layers (yellow-white). All coastal placer occurrences show similar bulk mineralogical compositions, consisting of rock-forming minerals (quartz, feldspar, micas, carbonates) and heavy minerals (Al_2SiO_5 -phases, apatite, epidote, Fe(Ti)-oxides, garnet (almandine, ferrous pyrope), monazite, pyrite, pyroxene, rutile, schorl, staurolite, titanite, zircon, zoisite). All sample locations have heavy mineral associations that are garnet-dominated except for the southernmost sampling point near Swakopmund. Placer occurrences with REE and Ti resource potentials are the Fe oxide-dominated sands close to Swakopmund, with ratios of valuable minerals to gangue minerals of max. 1:30 for zircon plus monazite and 1:5 for Ti minerals. The bulk sediment load is from the Orange river in the source. Contributions of the Kuiseb and Swakopmund rivers are minor, contributions of other ephemeral hinterland rivers are negligible.

1 Introduction

Abundant information is available concerning the diamondiferous Plio-Pleistocene placer deposits of southern Africa (Corbett and Burrell, 2001; Jacob et al., 2006; Spaggiari et al., 2006), but little is known about heavy mineral-bearing sands along the narrow Namibian coastal plain. Coastal Namibia is a hyperarid region (Lancaster, 2002) where chemical weathering is negligible and sediment composition is largely controlled by physical processes (Garzanti et al., 2014a, b). Strong winds transport sand all year long from south to north (Lancaster, 1985). Temporally floods feed hinterland rivers only for few weeks a year depositing their sediment load into flat interdune playas (Jacobson et al., 1995). Three large dune fields occur along the coast, however, the Erongo coast is characterized by a large, ~350 km wide dune-free gap.

Since late Pliocene (van der Wateren and Dunai, 2001) sediments of coastal Namibia have been largely supplied by the Orange river and its tributary the Vaal river (Vermeesch et al., 2010; Garzanti et al., 2014a; Gehring et al., 2014). The detrital material is transported northward over distances of hundreds of kilometers from the Orange delta up to southern Angola by ultra-long

littoral and aeolian transport (Garzanti et al., 2014a; Garzanti et al., 2015). However, ephemeral hinterland rivers in the Erongo and Kunene regions draining Damara metasediments and granitoids of the Hinterland Branch (Kuiseb, Swakop, Omaruru, Ugab), as well as the Kaoko belt (Huab), and Etendeka flood basalts (Koigab), contribute likewise to the recent beach and dune sands (Lancaster, 1982; Garzanti et al., 2014a; Garzanti et al., 2015). An additional sand source is the partially lithified Tertiary Tsondab sandstone (Garzanti et al., 2012; Garzanti et al., 2015).

Hydrodynamic-sorting processes and winnowing lead to the formation of placer deposits on the foreshore and on beaches in Namibia where ultradense minerals are enriched up to 200 times (Garzanti et al., 2015). They are easily distinguishable as small layers and deep pink to dark red and black patches in which garnet or magnetite are concentrated (Garzanti et al., 2014b; Garzanti et al., 2015) set into feldspatho-quartzose to litho-feldspatho-quartzose (volcaniclastic) beach and dune sands (Garzanti et al., 2014a; Garzanti et al., 2015).

2 Geological setting

The coast of the Erongo region is a rocky plain with outcrops of metamorphic and minor igneous rocks, forming largely small hills and inselbergs. This landscape is characteristic for the total ~350 km long dune-free area between Walvis Bay and the Skeleton coast. Northwards, it passes over into the Skeleton coast erg where local diamond-bearing (pocket) beaches are known (Moore and Moore, 2004). However, higher diamond-potential is by placers in the Sperrgebiet bordering the dune-free area in the south (Corbett and Burrell, 2001; Jacob et al., 2006; Spaggiari et al., 2006). To the east the narrow coastal plain is bounded by the Great Escarpment, which is a prominent topographic rise towards the mountainous hinterland.

Placers are located either directly along the current shoreline or close-by retracing Quaternary paleo-shorelines. They are separated from the hinterland by a prominent 3-5 m high cliff impeding sand movement away from the beach. The thickness of the placers varies distinctly, but is mostly in the dm-scale. Layers of conspicuous deep pink to dark red or black color alternate with brighter, coarser-grained quartzose layers. The coast-parallel surficial placer bodies have narrow to lenticular shape. The individual dimensions are controlled by the underlying irregular basement as well as by

hydrodynamic sorting processes.

3 Coastal sands of Namibia

3.1 Mineralogical composition

The bulk mineralogical composition of placer sands along the Namibian coast is quite uniform, but the proportions of the respective minerals are distinctly variable. Generally, coastal placer sands comprise a varying portion of rock-forming minerals (quartz, plagioclase, K-feldspar, biotite, muscovite, clay minerals, dolomite, siderite, chlorite), and a small portion of unclassified minerals, beside heavy minerals. Lithoclasts are negligible. The relative abundance of heavy minerals versus light rock-forming minerals varies between ~3 and 75 vol% and is largest in the placers north of the Omaruru river. The most enriched mineral sands with heavy mineral proportions of ~94 vol% are located close to Swakopmund. In the placers close to the Ugab and Huab rivers the heavy mineral fraction amounts between ~74 and 84 vol%. Quartz (≤ 55 vol%) prevails distinctly over altered plagioclase (≤ 10 vol%). K-feldspar is mostly < 1 vol%.

Mineralogically, the heavy mineral fractions can be subdivided into three groups coinciding with their spatial distribution. The first group comprises placers in the southern area in the surroundings of Swakopmund, the second those north of the Omaruru river. All remaining sands belong to the third group and are located in the northern area. All heavy mineral suites are garnet-dominated (≤ 73 vol% of the total sand mass), except for those placers close to Swakopmund where Fe-oxides (≤ 62 vol%) prevail, which provoke the characteristic pink to red color. Pyroxene (up to ~27 vol%) and staurolite (up to ~14 vol%) are abundant in all northern placers. Altered ilmenite (≤ 17 vol%) pertains to the main components at all locations, in particular in the southern placers. Zoisite occurs in significant quantity (up to ~6 vol. %) in the central area. Apatite is likewise minor with proportions of ~4 to 6 vol% in the central domain. The highest zircon proportions are in the southern placers with up to ~3 vol%. The Ti phases titanite and rutile belong likewise to the trace minerals with < 2 vol% in all domains and absolute bulk proportions of 0.2 to 1.0 vol% titanite and 0.3 to 0.8 vol% rutile, respectively. The highest monazite proportions are close to Swakopmund with 0.6 vol%. Bulk monazite proportions are between 0.0 and 0.6 vol%. All remaining minerals share in general less than 1 vol% of the mineral suite.

3.2 Minerals of economic interest

The ratio of total valuable minerals to total gangue minerals is of economic interest. Considering zircon and monazite combined as possible carriers of REE (rare earth elements), the ratio is between 1:30 and 1:1300 with the most promising placers located close to Swakopmund (ratios 1:30 and 1:40) and in the central area (NAM-SM44). Titanium-bearing minerals (ilmenite, rutile, titanite) are likewise of interest for industry. The ratios are between 1:5 and 1:70 displaying the

Swakopmund placers likewise as most promising. Notwithstanding these positive Ti ratios the largest portion is represented by altered ilmenite with unknown loss of Ti. Moreover, microscopy revealed that ilmenite occurs intergrown with Fe-oxides. All three textures of ilmenite-magnetite intergrowths expressed as trellis type, composite type and sandwich type are present. Individual, non-altered ilmenite crystals are quite rare. Likewise magnetite shows incipient to advanced martitization to hematite. Both, magnetite and ilmenite show indications of leaching and/or decomposition into secondary phases although the products are mostly sorted out of sands. The reason is seen by the deposition in a formerly active, high-energy environment where less stable minerals are destroyed and washed out. Garnet can be of economic interest, as an abrasive substance, but, grains are probably too small for industrial use.

4 Discussion – linkage of sand composition and source regions

The southernmost placers are located north of the mouths of the Kuiseb and the Swakop rivers. Whereas the Kuiseb drains amphibolite-facies quartzites and mica-schists, the Swakop drains granites and metasediments. The Kuiseb carries quartzose to feldspatho-quartzose-metamorphiclastic sands with abundant biotite and a moderately-rich amphibole-epidote-garnet suite with minor apatite and tourmaline (Garzanti et al., 2014a). Zircon, rutile, titanite, staurolite, kyanite and monazite are rare (Garzanti et al., 2012). Feldspatho-quartzose sands with biotite and a moderately-rich amphibole-garnet-staurolite suite with some clinopyroxene, tourmaline, apatite, titanite and minor kyanite and sillimanite are characteristic for the Swakop sediment load. The composition of these larger hinterland rivers is hardly reflected in the placer assemblages close to Swakopmund, which contain only very minor proportions (< 1 vol%) of epidote, apatite, staurolite, titanite and Al_2SiO_5 phases. The only significant mineral is garnet (< 25 vol%), but the feldspatho-litho-quartzose to lithofeldspatho-quartzose Orange river sand with a clinopyroxene dominated heavy mineral suite and subordinate opaque Fe-Ti-Cr-oxides, epidote, amphibole and garnet (Garzanti et al., 2012; Garzanti et al., 2014a) is a more likely source for the bulk of the heavy minerals. However, a certain portion of garnet might be from the Damara formations. In addition, also the Coastal Namib sand sea with feldspatho-quartzose sands rich in clinopyroxene and minor garnet, amphibole and epidote (Garzanti et al., 2014a) might contribute a certain garnet portion. Monazite and zircon can be supplied, in parts, by the Kuiseb.

The situation is different north of the mouth of the Omaruru river delivering feldspatho-quartzose sands with a moderately-poor tourmaline-garnet-amphibole-epidote-titanite mineral suite and minor sillimanite (Garzanti et al., 2014a). Whereas the southern placers are largely composed of hardly only heavy minerals, the three following to the north have a large proportion of rock-forming minerals. In particularly quartz (≤ 55 vol%) and

plagioclase (≤ 10 vol%) share larger proportions. Pyroxenes represent ~ 5 -6 vol%, biotite ~ 2 vol% of bulk sand. The heavy mineral suite is dominated by garnet and minor staurolite, zoisite and apatite, heavy minerals not carried by the Omaruro river, but staurolite, apatite, biotite and minor titanite are within the sediment of the Swakop river. As zoisite shows a similar distribution as staurolite a river-derived origin is likely. Pyroxenes and low epidote contents as well as Fe-oxide and ilmenite are traced back to the Orange river load. Zircon and monazite show similar distribution curves as Fe-Ti-oxides implying the Orange river as likely source. Traces of tourmaline, epidote and titanite might be related to the Omaruro sediment load.

The impact of the Orange river is still apparent in all placers further north, reflected by the occurrence of larger proportions of Fe-Ti-oxides and minor pyroxene. Subordinated apatite, staurolite and zoisite might be traced back to the Swakop river.

Ugab sediment is quartzo-feldspathic with clinopyroxene, hornblende, garnet and epidote, as well as zircon and tourmaline (Garzanti et al., 2014a). However, a significant distribution of Ugab sediment is not distinguishable in none of the northern placer sands. Differences in pyroxene, epidote and schorl occurrence are subtle. Distinguishable are only subtle higher average contents of dolomite and Al_2SiO_5 -phases.

Although three different heavy mineral sand assemblages can be distinguished, their sediment load can largely be traced back to the Orange river. In the southern area, a distribution of Swakop and/or Kuiseb sediment load is hardly reflected in the placers. The central and northern placers show a certain Swakop and/or Kuiseb-derived sediment load. The contributions of the ephemeral Omaruru and the Ugab rivers are insignificant. Uncertain is the provenance of garnet in all placers due to its presence in all rivers, however, Garzanti et al. (2014a) showed that only one-third of beach sand in the 350 km dune-free gap between the Namib and the Skeleton coast erg is Orange river-derived. The remaining two-third are supplied by the Swakop river. Concerning garnet, a mixed provenance is likely with significant distribution of both, the Swakop river and the Orange river. In particular the local supply of amphibolite-facies metasedimentary rocks of the Damara Inland Branch to beach sands north of Walvis Bay, as shown by Garzanti et al. (2014a) argues for this. However, large shares of the Omaruru and the Ugab can be excluded. The latter is also indicated by distinctly minor long-term supply of only $\sim 1 \times 10^9$ t/a of all rivers draining the Damara Orogen in the Erongo region in comparison to $\sim 11 \pm 2 \times 10^6$ t/a supply of only the Orange river (Garzanti et al., 2014a).

5 Conclusions

The mineral suites of all placers argue for the Orange river as dominant sediment source, however, a certain contribution of the Swakop and Kuiseb rivers is traceable. The contributions of other ephemeral hinterland rivers are

insignificant. Although the geological conditions are not ideal, the relatively high total heavy mineral content and the favorable ratio of ore to gangue minerals concerning Ti minerals render at least the southern placer deposits an economically considerable resource. Minor zircon and monazite contents, good access to the locations and simple mineability upgrade the deposits.

References

- Corbett I, Burrell B (2001) The earliest Pleistocene(?) Orange river fan-delta: an example of successful exploration delivery aided by applied Quaternary research in diamond placer sedimentology and paleontology. *Quat Int* 82:63-73.
- Garzanti E, Andò S, Vezzoli G, Lustrino M, Boni M, Vermeesch P (2012) Petrology of the Namib sand sea: long-distance transport and compositional variability in the wind-placed Orange delta. *Earth Sci Rev* 112:173-189.
- Garzanti E, Vermeesch P, Andò S, Lustrino M, Padoan M, Vezzoli G (2014a) Ultra-long distance littoral transport of Orange sand and provenance of the Skeleton Coast Erg (Namibia). *Mar Geol* 357:25-36.
- Garzanti E, Vermeesch P, Padoan M, Resentini A, Vezzoli G, Andò S (2014b) Provenance of passive-margin sand (Southern Africa). *J Geol* 122:17-42.
- Garzanti E, Reentino A, Andò S, Vezzoli G, Pereira A, Vermeesch P (2015) Physical controls on sand composition and relative durability of detrital minerals during ultra-long distance littoral and aeolian transport (Namibia and southern Angola). *Sedi* 62:971-996.
- Gehring AU, Riahi N, Kind J, Almqvist BSG (2014) The formation of the Namib Sand Sea from the spatial pattern of magnetic rock fragments. *Earth Planet Sci Lett* 395:168-172.
- Jacob J, Ward, JD, Bluck BJ, Scholz RA, Frimmel, HE (2006) Some observations on diamondiferous bedrock gully trapsites on late Cainozoic, marine-cut platforms of the Sperrgebiet, Namibia. *Ore Geol Rev* 28:493-506.
- Jacobson PJ, Jacobson KM, Seely MK (1995) Ephemeral rivers and their catchments: sustaining people and development in western Namibia. Desert Research Foundation of Namibia, Windhoek.
- Lancaster N (2002) How dry was dry? – Late Pleistocene palaeoclimates in the Namib desert. *Quat Sci Rev* 21:769-782.
- Lancaster N (1982) Dunes on the Skelton Coast, Namibia (South East Africa): geomorphology and grain size relationships. *Earth Surf Proc Land* 7:575-587.
- Lancaster N (1985) Winds and sand movements in the Namib sand sea. *Earth Surf Proc Land* 10:607-619.
- Moore JM, Moore AE (2004) The roles of primary kimberlitic and secondary Dwyka glacial sources in the development of alluvial and marine diamond deposits in Southern Africa. *J Afr Earth Sci* 38:115-134.
- Spaggiari RI, Bluck BJ, Ward JD (2006) Characteristics of diamondiferous Plio-Pleistocene littoral deposits within the paleo-Orange river mouth, Namibia. *Ore Geol Rev* 28:475-492.
- Vermeesch P, Fenton CR, Kober F, Wiggs GFS, Bristow CS, Xu S (2010) Sand residence times of one million years in the Namib sand sea from cosmogenic nuclides. *Nat Geosci* 3:862-865.
- van der Wateren FM, Dunai TJ (2001) Late Neogene passive margin denudation history – cosmogenic isotope measurements from the central Namib desert. *Glob Planetary Change* 30:271-307.

Detection of subsidence related to mining activity by using interferometric radar data: the Seruci-Nuraxi Figus coal mine case study (Sardinia, Italy)

Ammirati Lorenzo, Calcaterra Domenico, Di Martire Diego, Mondillo Nicola

Department of Earth, Environment and Resources Sciences, University of Naples "Federico II", Italy

Abstract. In this study subsidence related to mining activity in the Nuraxi Figus coal district was detected by means of the Advanced Differential Interferometric Synthetic Aperture Radar (A-DInSAR) technique, applied to COSMO-SkyMed (CSK) data. The interferometric results, covering 2011 and 2014, have been obtained in the framework of the so-called "Third Not-ordinary Plan of the Environmental Remote Sensing Project". The remote sensing revealed a maximum subsidence of about 23 cm related to coal extraction, carried out in correspondence of two production panels, 400 m wide and 1300 m long, at a depth of about 500 m below the ground level.

Time-lapsed vertical deformation profiles have been carried out to analyze the dynamic ground-deformation development. The study allowed demonstration that subsidence was still active for a year after the mine panel production.

1 Introduction

Sometimes, underground mining produces subsidence, which can be coincident with mining activities or delayed in response to the time-dependent deformation of the rocks. Soil deformation due to underground mining has been reported from almost all parts of the world (e.g. Pickering and Lewis 1994, Zhou et al. 2015, Przyłucka M. et al. 2015) and can be dangerous when affecting surface infrastructures (Ge et al. 2006, Vervoort 2016), also causing major damages to buildings and houses (Asadi et al. 2005). Therefore, it is essential to not underestimate the potential effects of mining subsidence. Indeed, monitoring surficial deformations in active or closing mining areas is a key point to minimize negative environmental and social impacts. The management of subsidence has increased in importance over the last years and several monitoring methods have been used, comprising Advanced Differential Interferometric Synthetic Aperture Radar (A-DInSAR) techniques (Herrera et al. 2010; Tomás et al. 2014; Yerro et al. 2014; Fan et al. 2015; Przyłucka et al. 2015).

In this work, we have studied surficial deformations which occurred between 2011 and 2014, in association with deep underground mining in the Seruci-Nuraxi Figus coal district (Carbonia – Iglesias, Sardinian region, Italy) (Tessitore et al. 2018). To pursue this aim, we used COSMO-SkyMed data (2011-2014), processed by a PS-like technique (Costantini et al. 2008).

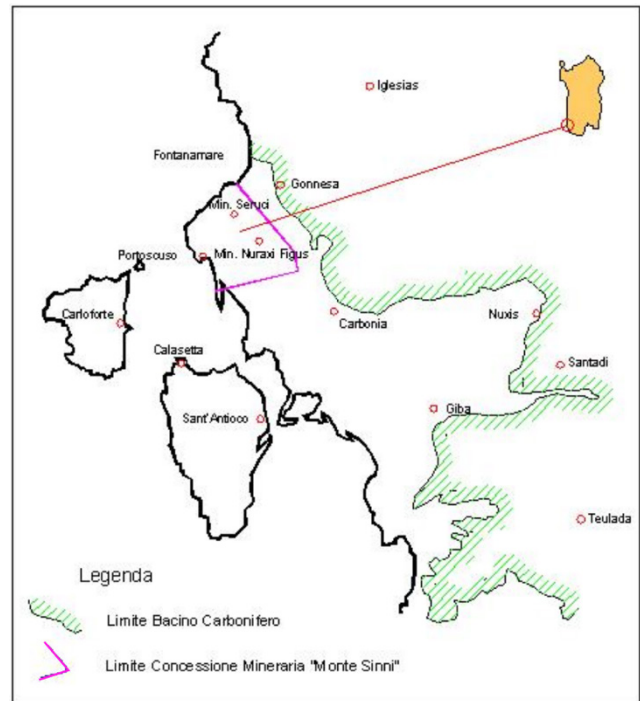


Figure 1. The study area. Green line is the Sulcis carboniferous basin limit, the pink line represents the Carbosulcis mining district (<http://www.carbosulcis.eu>).

2 The study area

The Seruci-Nuraxi Figus coal mine is located in Sardinia (Italy), within the Sulcis coalfield, an area extending for about 60 hectares between the Carbonia, Gonnessa and Portoscuso towns (Fig.1). In recent years, the mining licenses have been owned by Carbosulcis S.p.A., which mined the coal seams in several sectors of the Seruci-Nuraxi Figus concession (also named "Monte Sinni" concession) until 2012, to supply coal fuel to the nearby thermal electric power station owned by ENEL S.p.A. The production panels were mined underground, by an infrastructure comprising 30 km of tunnels, at a depth of ca. 400 m below the sea level, up to about ca. 500 m below the ground surface. On the 1st of October 2014, the European Commission approved, for the Seruci-Nuraxi Figus coal mine, a closure plan, which intended to stop coal mining before the end of 2018 and to complete environmental remediation before the end of 2027 (<http://www.carbosulcis.eu/>). Thus, the present activities carried out in the Seruci-Nuraxi Figus mine are mainly focused on the maintenance and safety measures.

2.1 Geological setting

The study area is in a paleostructure of the continental south-western Sardinia margin, where an Eocene sedimentary basin, called “Sulcis carboniferous basin”, is situated (Fig. 2). The sedimentary rocks occurring in this area from the Paleozoic to the Quaternary. The basement is featured by Paleozoic and Mesozoic rocks, which crop out on the eastern and northern borders of the Sulcis basin (Pasci et al. 2012). The sedimentary succession filling the basin, uncomfortably covering the basement, can be subdivided from the bottom to the top, in four Formations: Calcari a Macroforaminiferi Fm. (limestones); Miliolitico Fm., consisting of sandstones, marls and limestones (20-70 m thick); Lignitifero Fm., an association, 70 to 150 m thick, of clays, marly limestones, bituminous limestones, marls and conglomerates, interbedded with coal seams, and the Cixerri Fm., consisting of sandstones, conglomerates and marls (average thickness = 300 m) (Pasci et al. 2012). The Lignitifero Fm. coal seams have a thickness comprised between 1 and 10 m and consist of pure coal layers commonly 10 cm thick, rarely reaching 30-50 cm of thickness, interbedded with clays. In the Seruci-Nuraxi Figus area, the mined horizon is located at 350-450 m below the surface. Sedimentary rocks are covered by 100-300 m of volcano-pyroclastic rocks and ignimbrites (Fadda et al. 1994; Pasci et al. 2012).

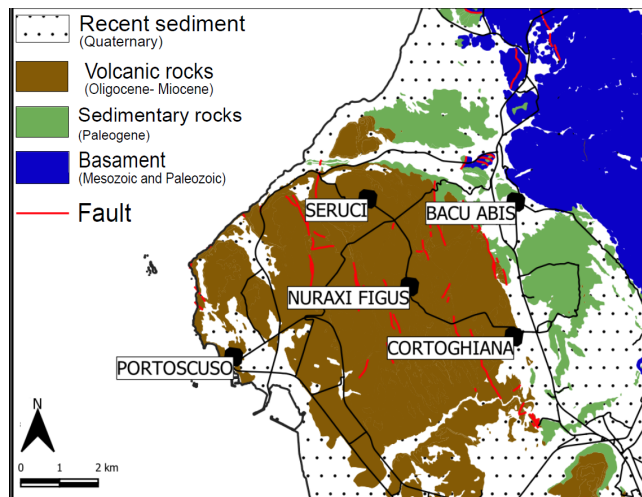


Figure 2. Geological map.

3 Satellite data

COSMO-SkyMed dataset (91 images) obtained in the framework of the Third Not-ordinary Plan of Environmental Remote Sensing project (Piano Straordinario di Telerilevamento Ambientale, PST-A-3 in Italian) promoted by the Italian Ministry for the Environment, Land and Sea (Costantini et al. 2017; Di Martire et al. 2017), have been used in this work. The PSP-SAR algorithm (Costantini et al. 2008) has been applied to high-resolution CSK images acquired in ascending and descending orbits, respectively covering the periods May 2011-January 2014 and May 2011-

March 2014. Specifically, cumulated displacements, projected along the satellite Line of Sight (LoS), (for each observation period) are of -6 ± 16 mm (ascending) and of -13 ± 32 mm (descending) on average for the whole study area. By means of the composition of LoS velocity data (ascending and descending), have been obtained the vertical deformation maps and profiles.

4 Results and discussion

From the processing of the COSMO-SkyMed data, scattered subsidence was detected in correspondence of the Seruci-Nuraxi Figus mine panels (Fig. 3) which are 400 m wide, 1300 m long and 3 m high.

The deformation maps obtained from interferometric processing, acquired in both geometries, allowed exact determination of the vertical displacements.

The subsidence started in the year 2011, and developed until 2014, with maximum cumulated vertical displacements of ca. 23 cm. It is important to note that the maximum deformation was detected in correspondence with post-mining operations, considering that the Carbusulcis mining activity records indicate that most of the extraction was carried out in the period 2011-2013, with a peak of coal production in 2012 (Fig. 4). On the other hand, between 2013 and 2014, the extraction activities had to stop for long periods due to technical reasons, which prevented any further excavation of the panels and only allowed to carry out limited maintenance works to the main and tail tunnels.

5 Conclusions

According to existing regulations, mine monitoring is mandatory also after their closure.

Several monitoring techniques can be used to manage subsidence and other kinds of post-mining issues, improving technical, economical, and environmental aspects related to sustainable development of mining areas. From our study, A-DInSAR has turned out to be very sensitive for identifying subsidence at a centimetric scale, then may be very useful during the preliminary phases of post-mining environmental remediation plans, but also for ground monitoring in active mining areas.

The DInSAR study on the Nuraxi Figus mining area, allowed detection of subsidence phenomena that started during mining activity and developed until post-mining operations. The good correlation between position and timing of subsidence and mining activity, strongly suggests that the coal extraction in this area has produced the observed surface deformation phenomena.

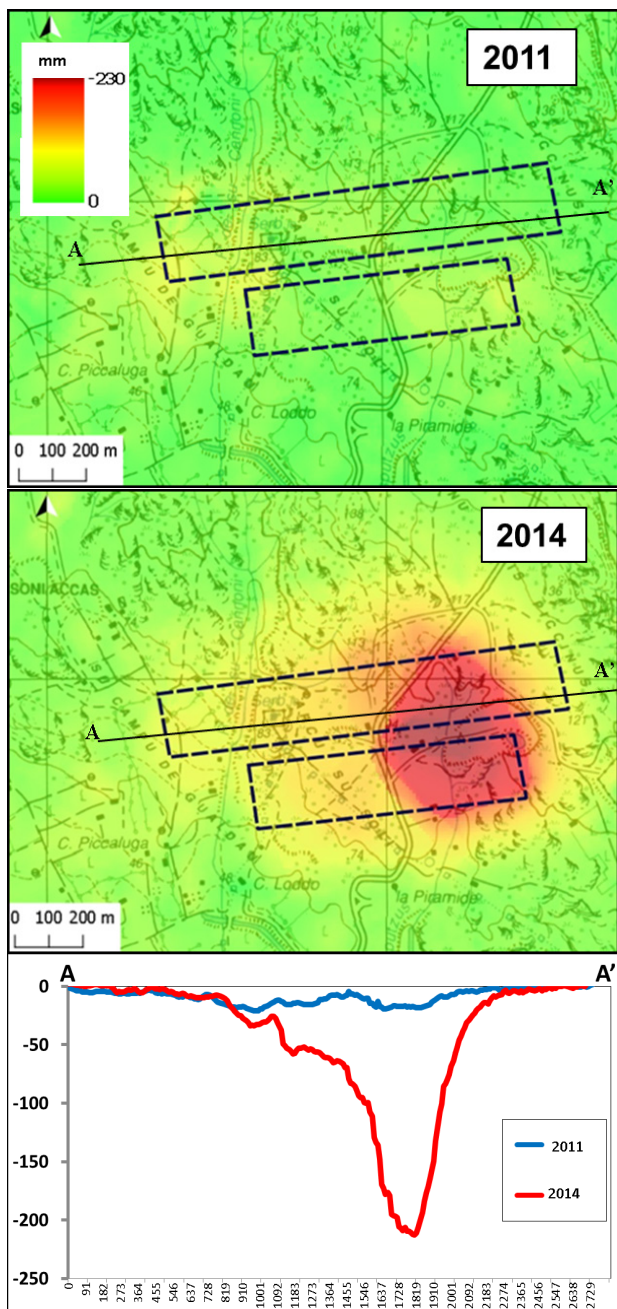


Figure 3. InSAR vertical deformation maps (top) and vertical deformation A-A' profiles (below) cumulated in the periods 2011-2014; black dashed lines in the figure represent the mining panels.

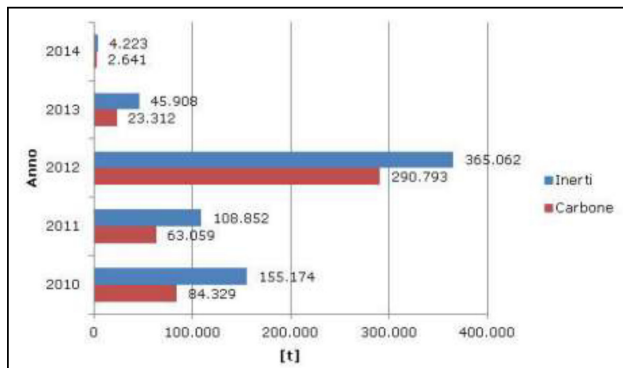


Figure 4. Carbosulcis mining activity records. Red and blue

represent the tons materials productions (www.carbosulcis.eu).

The study also confirms that ground surface deformations can occur also a few years after completion of mining work. However, for better investigating and understanding the cause-effect mechanism between extraction and ground deformation, external data must be acquired, especially in the areas where predominantly horizontal and vertical components have been observed.

Future prospective will be to apply A-DInSAR monitoring in other study cases. Two subsidence phenomena, which are causing damage to buildings and houses, will be examined. The first study case is the well-known Kiruna mine (Sweden) (Henry et al. 2004), whereas the second is represented by Zaruma (Ecuador), that is an area heavily affected by illegal mining.

Acknowledgements

COSMO-SkyMed data have been used thanks to a cooperation protocol between Italian Ministry for the Environment, Land and Sea (MATTM) and Federico II University of Napoli. The authors are grateful to Carbosulcis S.p.A. for allowing publication of mine data.

References

- Asadi, A.; Shahriar, K.; Goshtasbi, K.; Najm, K. Development of a new mathematical modelling for prediction of surface subsidence due to inclined coal seams mining. *J. South Afr. Inst. Min. Metall.* 2005:105, 15–20
- Carbosulcis S.p.A. website: <http://www.carbosulcis.eu/> (last consultation 05/10/2017)
- Costantini M, Falco S, Malvarosa F, Minati F (2008) A new method for identification and analysis of persistent scatterers in series of SAR images in: *IGARSS 2008-2008 IEEE International Geoscience and Remote Sensing Symposium* 2:449
- Costantini M, Ferretti A, Minati F, Falco S, Trillo F, Colombo D, Novali F, Malvarosa F, Mammone C, Vecchiolli F, Rucci A, Fumagalli A, Allievi J, Ciminelli MG, Costabile S (2017) Analysis of surface deformations over the whole Italian territory by interferometric processing of ERS, Envisat and COSMO-SkyMed radar data. *Remote Sensing of Environment*, in press <https://doi.org/10.1016/j.rse.2017.07.017>
- Di Martire D, Paci M, Confuorto P, Costabile S, Guastaferrero F, Verta A, Calcaterra D (2017) A nation-wide system for landslide mapping and risk management in Italy: The second Not-ordinary Plan of Environmental Remote Sensing. *International Journal of Applied Earth Observation and Geoinformation* 63:143–157. doi: 10.1016/j.jag.2017.07.018
- Fadda A, Ottelli L, Perna G (1994) *The Sulcis Carboniferous Basin - Geology, Hydrogeology, Mines.* Carbosulcis s.p.a., Cagliari, Italy (in Italian)
- Fan H, Gao X, Yang J, Deng K, Yu Y (2015) Monitoring Mining Subsidence Using A Combination of Phase-Stacking and Offset-Tracking Methods. *Remote Sensing* 7:9166–9183. doi: 10.3390/rs70709166
- Ge, L.; Chang, H.-C.; Rizos, C. Monitoring Land Surface Subsidence using Radar Interferometry: The Challenges. In *Proceedings of the Shaping the Change XXIII FIG Congress, Munich, Germany, 8–13 October 2006.*
- Henry, Emmanuel & Mayer, Christoph & Rott, Helmut. (2004). Mapping mining-induced subsidence from space in a hard rock mine: example of SAR interferometry application at Kiruna mine. *CIM Bulletin*. 97:1-5.
- Herrera G, Tomás R, Vicente F, Lopez-Sanchez JM, Mallorquí JJ, Mulas J (2010) Mapping ground movements in open pit mining areas using differential SAR in-terferometry. *International*

- Journal of Rock Mechanics and Mining Sciences 47:1114-1125.
doi: 10.1016/j.ijmms.2010.07.006
- Pasci S, Carmignani L, Pisanu G, Sale V (2012) Notes to 1:50.000 Geological Map of Italy, Sheet 564, Carbonia. Servizio Geologico d'Italia - ISPRA and Regione Autonoma della Sardegna (in Italian)
- Pickering KT, Owen LA (1994) An introduction to global environmental issues. Routledge, London, New York
- Przyłucka M, Herrera G, Graniczny M, Colombo D, Béjar-Pizarro M (2015) Combination of Conventional and Advanced DInSAR to Monitor Very Fast Mining Subsidence with TerraSAR-X Data: Bytom City (Poland). Remote Sensing 7:5300–5328. doi: 10.3390/rs70505300
- Tessitore S., Di Martire D., Mondillo N., Ammirati L., Boni M., Calcaterra D. (2018). Detection of Subsidence by Radar Interferometric Data in the Seruci-Nuraxi Figus Coal Mine Area (Sardinia, Italy). IAEG/AEG Annual Meeting Proceedings. Volume 3 pages 51-5.
- Tomás R, Romero R, Mulas J, Marturià JJ, Mallorquí JJ, Lopez-Sanchez JM, Herrera G, Gutiérrez F, González PJ, Fernández J, Duque S, Concha-Dimas A, Cocksley G, Castañeda C, Carrasco D, Blanco P (2014) Radar interferometry techniques for the study of ground subsidence phenomena: a review of practical issues through cases in Spain. Environ Earth Sci 71:163–181. doi: 10.1007/s12665-013-2422-z
- Vervoort A (2016) Surface movement above an underground coal longwall mine after closure. Nat. Hazards Earth Syst. Sci. 16:2107–2121. doi: 10.5194/nhess-16-2107-2016
- Yerro A, Corominas J, Monells D, Mallorquí JJ (2014) Analysis of the evolution of ground movements in a low densely urban area by means of DInSAR technique. Engineering Geology 170:52–65. doi: 10.1016/j.enggeo.2013.12.002
- Zhou, Dawei & Wu, Kan & Cheng, Gong-Lin & Li, Liang. (2014). Mechanism of mining subsidence in coal mining area with thick alluvium soil in China. Arabian Journal of Geosciences. 8. 10.1007/s12517-014-1382-2.

Developing adaptive expertise in exploration decision-making

Marianne J. Davies

Dynamics Development

Rhys S. Davies

Centre for Exploration Targeting, School of Earth and Environment, The University of Western Australia

Dynamics Development

Abstract. The declining discovery rate of world-class ore deposits represents a significant obstacle to the future of global metal supply. To counter this trend, there is a requirement for mineral exploration to be conducted in increasingly challenging and uncertain search spaces. Faced with such an increase in task complexity, an important limitation from an exploration perspective is the human behavioural aspect of information interpretation and decision-making.

By adapting and developing upon existing research from a broad range of disciplines, this paper introduces the Dynamics learning curve, part of the Dynamics model of decision-making and learning. Its application for developing adaptive expertise within the mineral exploration industry is discussed. The model takes into account behavioural and motivational aspects of the individual, as well as the wider context and complexity in which the individual and the decision-making behaviour are embedded. This model can be used as a diagnostic tool for situational analysis and to inform learning interventions. The model can also be used for designing working and training environments to promote learning and adaptive decision-making, to improve success rates in the mineral exploration industry.

1 Introduction

Despite increased exploration expenditure, the global discovery rate of world-class ore deposits has been in decline for over a decade (Schodde, 2017). Without access to these materials, society is unlikely to realise long-term goals towards achieving sustainability, such as the transition to renewable energy sources and evolution of the automotive industry to predominantly battery-driven vehicles (Sykes et al. 2016).

Mineral exploration has traditionally followed an empirical approach, searching for evidence of mineralisation upon the surface of the planet, then targeting drilling to define the extent of an ore body beneath the surface. As outcropping deposits in well-defined areas are depleted, there is a need for exploration to extend to less well-explored search spaces (Hronsky and Welborn, 2018). These include regions where surficial evidence for deposits are absent, requiring a predictive, conceptual approach to targeting, guided by an understanding of underlying mineralising processes (McCuaig and Hronsky, 2014). As the mineral exploration industry experiences a transition from

empirical to conceptual targeting, human expertise and creativity are key to realising long-term, recurring success (Davies and Davies, 2018).

This paper proposes a complete model of learning and decision making, to guide our industry in adapting training and working environments, as well as management styles, that enable employees to achieve their maximum potential and develop expertise in exploration targeting.

2 Adaptive expertise

2.1 Human decision-making

Exploration datasets are, by definition, incomplete, allowing for multiple interpretations. In an exploration context, competing hypotheses can only be fully tested through further exploration activities. A number of studies have delved into the process of subjective assessments and interpretation of geoscientific data. Polson and Curtis (2010) and Bond et al. (2012) discuss the role of heuristics in geological interpretations based on uncertain data. They highlight the potential for experts to reach contradictory conclusions when analysing the same data, bringing the adequacy of expert opinion into question. However, Bond et al. (2012) recognised that Master's or Ph.D. qualifications significantly improved expert performance in interpreting a seismic dataset, highlighting the importance of developing genuine expertise, through relevant training and experience.

Research into human decision-making has resulted in two broad camps. Naturalistic decision-making focuses on the intuitive judgments of highly skilled professionals. The recognition-primed decision-making model (Klein, 1998; 2008) defines the conditions in which intuitive judgement may become skilful. On the other hand, research into heuristic biases has focused on understanding common flaws in human cognitive performance that have a negative impact on decision making (Kahneman 2011).

In their seminal paper, Kahneman and Klein (2009) agreed that whether or not intuitive decisions are highly accurate and skilful, or hugely flawed, depends on the experience, knowledge and skill level of the decision-maker, specific to the context in which the decision is being made.

2.2 Developing expertise

Shwartz et al. (2005) proposed a model to define transferable and adaptive expertise, outlining the balance between innovation and efficiency (Fig. 1). The level of task complexity needs to lie within an 'optimal adaptability corridor;' where the individual is just outside their current knowledge and ability, but not overwhelmed by the task or situation. Should the learner be overwhelmed by the complexity of the task, then learning opportunities will be limited, and they will remain a frustrated novice. However, a learner who is insufficiently challenged by a task will only develop limited, routine expertise for that specific task. The risk faced by experts is that their skills are too narrow, and are therefore not transferable into different contexts or environments, as outlined by Kahneman and Klein (2009).

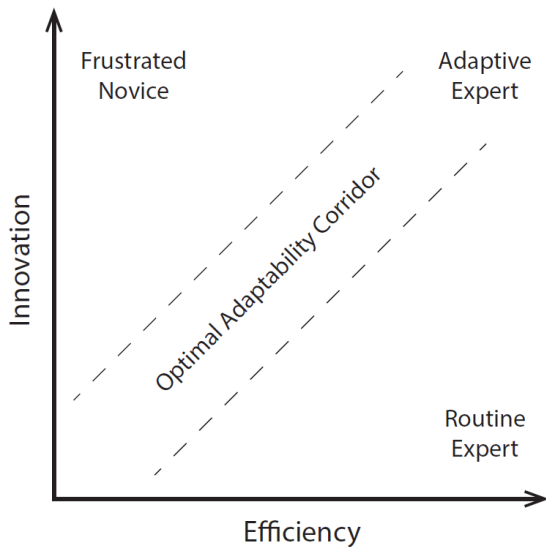


Figure 1. Adaptive expertise represents a balance between innovation and efficiency, after Shwartz et al. (2005)).

3 Discussion

To better understand the process of decision-making and skill development, Davies and Davies (2018) proposed the Dynamics model of decision-making and learning (Fig 2). This model combines Newell's Constraints model (1985) and Wulf & Lewthwaite's OPTIMAL model of learning (2016), and includes a feedback loop, to define an autopoietic (i.e. self-organising and self-regulating) system.

The constraints model is embedded within an ecological dynamics (ED) theoretical perspective (Newell 1985). ED incorporates dynamical systems theory to understand how complex non-linear systems, such as people, companies, and marketplaces, behave (Zohar 1997). For learning to be effective, it must take place in an authentic environment, representative of those environments into which the skill will later be transferred (Headrick et al. 2015). Learning occurs through attunement to relevant information. This information must be present and consistent, such that the learner is able to recognise regularities between the environment and their decisions (Kahneman and Klein 2009).

The information influencing decision-making behaviour comprises affordances and constraints. These are broadly categorised as individual, environment and task (Newell, 1985). Although the defined task is well recognised as a decision-making constraint, the individual and environment are often overlooked or misunderstood in the decision-making process. Differences in individual perception, motivation and meaning will shape the influence of constraints and account for the diversity of decisions, when identical constraints are presented to separate explorers (Davids et al. 2015).

Key elements recognised in the model are that learning is a non-linear process and that motivation, effort and focus of attention are the initial start points, defining the quality of individual input into learning and decision-making tasks (Ryan and Deci 2002; Wu and Magill 2011).

In addition to this, we present the 'Dynamics learning curve' (Fig 3). This model builds on biological system curves, the Catastrophe Curve (Fazey and Hardy, 1988) and the Challenge Point Framework (Gudagnoli and Lee 2004). Here, the complex relationship between the demands of a task and the expected performance output are represented by a performance curve. Individual, task and environmental demands are combined to represent the overall challenge to the individual (Kahneman 2011; Gudagnoli and Lee 2004). Where the demands of the task are limited, the performer will remain under-challenged and lack the opportunity to develop adaptive expertise. Should task difficulty increase, the learner's performance will trend upwards to a point where they are optimally challenged.

An important feature of this is the 'ugly zone' a term coined by rugby coach Dave Alred (2015). In the model, this zone describes the point where there is instability in performance and risk of a bifurcation point. This zone is where new and innovative ideas and understanding become possible, but typically involves the learner feeling unnatural, regressive and awkward. An integral risk of learning in the 'ugly zone' is the potential for a collapse in performance, arising from the learner being overwhelmed or over-challenged. For this reason, it's important to recognise that developing adaptive expertise presents a significant risk of failure. In fact, this will probably be the *status quo* for the majority of the learning period. It is advised that exploration-specific training courses are developed, so that learners can test novel ideas and risk failure without the serious financial consequences faced in industry.

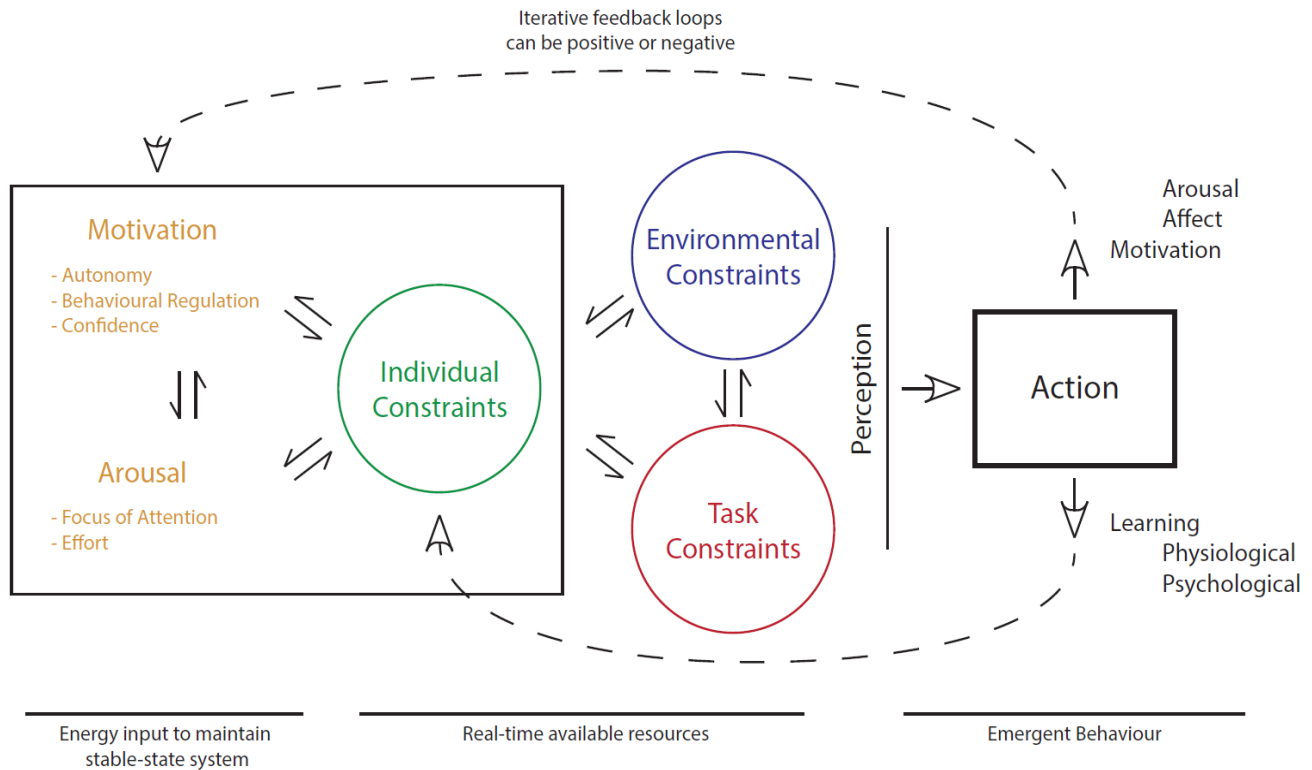


Figure 2. The Dynamics model of decision-making and learning, after Davies and Davies (2018). Developed from Newell's Constraints model (1986) and Wulf & Lewthwaite's OPTIMAL model (2016).

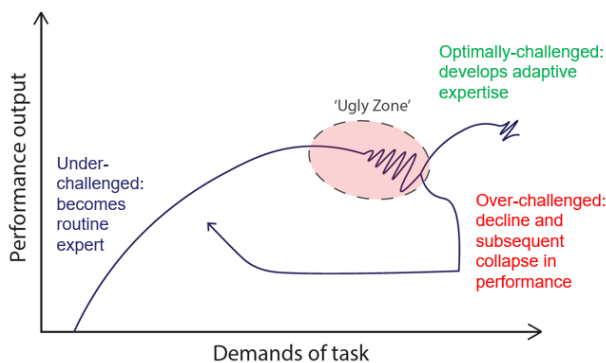


Figure 3. The Dynamics learning curve shows how adaptive expertise is developed through learning in the 'ugly zone,' after Davies and Davies (2018).

4 Conclusions

The mineral exploration industry is experiencing a major transition as surface deposits are depleted. Predictive targeting for buried or 'blind' deposits requires explorers to conduct conceptual exploration based on an understanding of underlying mineralising processes. As such, there is a need for explorers to develop adaptive and transferable expertise in exploration decision-making, so that the exploration industry might avoid a metal supply crisis.

It is likely that exploration targeting currently

represents a low-validity task (Kahneman, 2011), since the practice climate in industry presents limited opportunity for attunement to relevant information or feedback (Hogarth 2001; Kahneman and Klein 2009).

As such, it is advised that training courses are developed, and working environments are adapted, such that exploration geologists are presented the opportunity to develop adaptive expertise. Although an element of risk remains in all exploration decisions, due to limitations inherent within exploration datasets, the objective of such training courses is to improve the base-rate quality of exploration decisions, across the minerals industry.

The Dynamics learning curve provides a clear understanding of what the optimal adaptability corridor represents, and how to recognise whether a learner is being sufficiently challenged and supported such that they may develop adaptive expertise. Together, the Dynamics models incorporate disparate research topics, to guide the exploration industry in designing training programmes, working environments and management styles that enable employees to develop adaptive expertise.

Acknowledgements

This research was supported by an Australian Government Research Training Program (RTP) Scholarship and Society of Economic Geologists (SEG) Graduate Student Fellowship Grant.

References

Alred, D., (2015). *The Pressure Principle; Handle Stress, Harness Energy, and Perform When it Counts.* Penguin Life,

- London:272p
- Bond CE, Lunn RJ, Shipton ZK, Lunn AD (2012) What makes an expert effective at interpreting seismic images? *Geology* 40:75–78.
- Curtis A (2012) The science of subjectivity. *Geology* 40:95–96.
- Davids K, Araújo D, Ludovic S, Orth D (2015) Expert Performance in Sport: An ecological dynamics perspective. In: Baker J, Farrow D, Ed. *Handbook of Sport Expertise*, Routledge, pp 130-145
- Davies MJ, Davies RS (2018) Beyond below-ground geological complexity: Developing adaptive expertise in exploration decision-making. In: Australasian Institute of Mining and Metallurgy, *Proceedings of Complex Orebodies Conference*, 19-21 November, Brisbane, Australia, pp 95-98
- Fazey J, Hardy L (1988). The inverted-U hypothesis: a catastrophe for sport psychology? *British Association of Sports Sciences Monograph 1*. The National Coaching Foundation, Leeds
- Guadagnoli MA, Lee TD (2004) Challenge Point: A Framework for Conceptualizing the Effects of Various Practice Conditions in Motor Learning. *Journal of Motor Behaviour*, 36(2):212-224
- Headrick J, Renshaw I, Davids K, Pinder RA, Araujo D (2015) The dynamics of expertise acquisition in sport: the role of affective learning design. *Psychology of Sport and Exercise* 16(1):83-90.
- Hogarth RM (2001) *Educating intuition*. University of Chicago Press, Chicago:352p
- Hronsky JMA, Welborne J (2018) Western Mining Services, Senior Exploration Management (SEM) course. Perth, July 2018.
- Kahneman D, Klein G (2009) Conditions for Intuitive Expertise: A Failure to Disagree. *American Psychologist* 64:515–526
- Kahneman D (2011) *Thinking, fast and slow*. Penguin Books Ltd, London:504p
- Klein G (1998) *Sources of power: How people make decisions*. MIT Press, Cambridge, MA:352p
- Klein G (2008) Naturalistic Decision Making. *Human Factors* 50:456-460
- McCuaig TC, Hronsky JMA (2014) The mineral system concept: the key to exploration targeting. *SEG 2014: Building Exploration Capability for the 21st Century*, pp 153–175.
- Newell KM (1985) Coordination control and skill. In: Wilberg RV, Franks IM, Ed. *Differing perspectives in motor learning, memory, and control*, Elsevier Science, Amsterdam, pp. 295-317
- Ryan RM, Deci EL (2002) An overview of self-determination theory. In: Deci EL, Ryan RM, Ed. *Handbook of self-determination research*, University of Rochester Press, Rochester, NY, pp. 3-33.
- Schodde RC (2017) Long-term forecast of Australia's mineral production and revenue. *The outlook for gold: 2017-2057*. Special study commissioned by the Australian government and industry by MinEx Consulting, October 2017:89p
- Schwartz DL, Bransford JD, Sears D (2005) Efficiency and innovation in transfer. In Mestre J, Ed. *Transfer of learning: Research and perspectives*, Information Age Publishing, Greenwich, CT, pp 1-51
- Sykes JP, Wright JP, Trench A (2016) Discovery, supply and demand: From Metals of Antiquity to critical metals. *Applied Earth Science* 125:3-20
- Wu WF, Magill RA (2011) Allowing learners to choose: Self-controlled practice schedules for learning multiple movement patterns. *Research Quarterly for Exercise and Sport* 82(3):449-457.
- Wulf G, Lewthwaite R (2016) Optimizing Performance through Intrinsic Motivation and Attention for Learning: The OPTIMAL theory of motor learning. *Sychonomic Bulletin & Review* 23:1382-1414
- Zohar D (1997) *ReWiring the Corporate Brain: Using the New Science to Rethink How We Structure and Lead Organizations*, Berrett-Koehler Publishers, San Francisco:172p.



15th Biennial SGA Meeting
Glasgow, Scotland
August 27 -30 2019

Life with Ore Deposits on Earth